IGARSS'96

1996 International Geoscience and Remote Sensing Symposium

IEEE

University of Nebraska Lincoln

NASA

NOAA

OFFICE OF NAVAL RESEARCH 50th Anniversary 1946-1996

U.R.S.I.

Remote Sensing for a Sustainable Future

Volume II

Burnham Yates Conference Center
Lincoln, Nebraska USA
27-31 May 1996

IEEE Catalog Number 96CH35875
Library of Congress Number: 95-80706



IGARSS'96

1996 International Geoscience and Remote Sensing Symposium

Remote Sensing for a Sustainable Future

Volume II

DTIC QUALITY INSPECTED 2

19970520 020

IEEE Catalog Number 96CH35875
Library of Congress Number: 95-80706

Editor: Tammy I. Stein
Editorial Assistant: Jennetta Brunk
Production: IEEE Publications

Copyright and Reprint Permission: Abstracting is permitted with credit to the source. Libraries are permitted to photocopy beyond the limit of U.S. copyright law for private use of patrons those articles in this volume that carry a code at the bottom of the first page, provided the per-copy fee indicated in the code is paid through Copyright Clearance Center, 222 Rosewood Drive, Danvers, MA 01923. For other copying, reprint or reproduction permission, write to the IEEE Copyrights Manager, IEEE Service Center, 445 Hoes Lane, P.O. Box 1331, Piscataway NJ 08855-1331. All rights reserved. Copyright @1996 by the Institute of Electrical and Electronics Engineers, Inc.

IEEE Catalog Number 96CH35875
ISBN 0-7803-3068-4 (softbound edition)
ISBN 0-7803-3069-2 (casebound edition)
ISBN 0-7803-3070-6 (microfiche edition)
Library of Congress Number 95-80706

Additional copies of the IGARSS'96 Digest are available from the following source:

Institute of Electrical and Electronics Engineers, Inc.
Single Copy Sales
445 Hoes Lane
PO Box 1331
Picataway NJ 08855-1331

IGARSS'96 SPONSORS

IEEE

IEEE Geoscience and Remote Sensing Society

University of Nebraska Lincoln

University of Nebraska, Lincoln

NASA

National Aeronautics and Space Administration (NASA)

NATIONAL OCEANIC AND ATMOSPHERIC ADMINISTRATION
NOAA
25 YEARS of SCIENCE & SERVICE
U.S. DEPARTMENT OF COMMERCE

National Oceanic & Atmospheric Administration (NOAA)

ONR . . . Investing in the Future
OFFICE OF
50
Anniversary
NAVAL RESEARCH
1946 - 1996

Office of Naval Research (ONR)

IGARSS'96 TECHNICAL SPONSOR



U.S. National Committee
Union Radioscientifique Internationale

IGARSS'96 COOPERATIVE SPONSORS

Canon/Modern Methods Inc.

Center for Advanced Land Management Information Technologies, UNL

Center for Communication and Information Science, UNL

Center for Electro-Optics, UNL

Center for Laser Analytical Studies of Trace Gas Dynamics, UNL

Centurion International, Inc.

College of Engineering and Technology, UNL

Department of Electrical Engineering, UNL

ERDAS, Inc.

High Plains Climate Center, UNL

Li-Cor, Inc.

U.S. Geological Survey EROS Data Center

IGARSS'96 ORGANIZING COMMITTEE

Ram Narayanan
General Chairman

Robert McIntosh
Technical Program Co-Chairman

Calvin Swift
Technical Program Co-Chairman

Barbara Emil
Finance Chairman

James Merchant
Publications Chairman

Steve Reichenbach
CD ROM Chairman

Jim Lacy
WWW Chairman

Tammy Stein
Director of Conferences and Information Services, GRSS

LOCAL HOST COMMITTEE

Dennis Alexander
Mark Anderson
Ezekiel Bahar
Blaine Blad
John Boye
Mark Cockson
Natale Ianno
Robert Maher
Robert Palmer
Donald Rundquist
Karen St. Germain
Khalid Sayood
Tracy Soukup
Elizabeth Walter-Shea
Jon Welles

IGARSS'96 TECHNICAL PROGRAM COMMITTEE

Dennis Alexander, University of Nebraska-Lincoln
Werner Alpers, University of Hamburg
Mark Anderson, University of Nebraska-Lincoln
Ghassem Asrar, NASA Headquarters
Kultegin Aydin, Penn State University
Ezekiel Bahar, University of Nebraska-Lincoln
Ronald Birk, Sverdup Technology Inc.
Andrew Blanchard, University of Missouri-Columbia
Dan Cress, Sandia National Laboratories
John Curlander, Vexcel Corporation
John Curtis, US Army WES
Don Deering, NASA Goddar Space Flight Center
Craig Dobson, University of Michigan
Fernando Echavarria, University of Nebraska-Lincoln
Edwin Engman, NASA Goddard Space Flight Center
Stephen Frasier, University of Massachusetts
Prasad Gogineni, University of Kansas
Richard Gomez, US Army TEC
Bill Grant, NASA Langley
Martti Hallikainen, Helsinki University of Technology
Jim Irons, NASA Goddard Space Flight Center
Akira Ishimaru, University of Washington
Thomas Jackson, USDA Hydrology Lab
James Kalshoven, NASA Goddard Space Flight Center
Timothy Kane, Pennsylvania State University
Roger Kassebaum, Millard North High School-Omaha
Wolfgang Keydel, Institut fur Hochfrequenztechnik
Nahid Khazenie, NASA Goddard Space Flight Center
Roger Lang, George Washington University
Ellsworth LeDrew, University of Waterloo
Fuk Li, Jet Propulsion Laboratory
Charles Luther, Office of Naval Research
Harlan McKim, US Army CRREL
David McLaughlin, Northeastern University
James Mead, University of Massachusetts
Nasir Memon, Northern Illinois University
James Merchant, University of Nebraska-Lincoln
David Meyer, EROS Data Center
Wooil Moon, University of Manitoba
Richard Moore, University of Kansas
Ram Narayanan, University of Lincoln-Nebraska
Eni Njoku, Jet Propulsion Laboratory
Robert Palmer, University of Nebraska-Lincoln
William Plant, University of Washington
Jeff Plaut, Jet Propulsion Laboratory
Paul Racette, NASA Goddard Space Flight Center
John Reagan, University of Arizona
Steven Reichenbach, University of Nebraska-Lincoln
Jack Rinker, US Army TEC
Christopher Ruf, Pennsylvania State University
Donald Rundquist, University of Nebraska-Lincoln
Khalid Sayood, University of Nebraska-Lincoln
Thomas Schmugge, USDA/ARS Hydrology Laboratory
Khalid Siddiqui, SUNY College at Fredonia
Alois Sieber, Joint Research Centre-Ispra
Karen St. Germain, University of Nebraska-Lincoln
Mikio Takagi, University of Tokyo
Jim Tilton, NASA Goddard Space Flight Center
Dennis Trizna, Naval Research Labs
Leung Tsang, University of Washington
Fawwaz Ulaby, University of Michigan
Bruce Wallace, Army Research Laboratory
Elizabeth Walter-Shea, University of Nebraska-Lincoln
JoBea Way, Jet Propulsion Laboratory
Edward Westwater, NOAA/ERL/WPL
Simon Yueh, Jet Propulsion Laboratory



IGARSS'96

1996 International Geoscience and Remote Sensing Symposium

Table of Contents

INTERACTIVE AREA 1 -- Atmosphere

1. Dual-Frequency Three-Dimensional Images of Clouds 1
Firda, J.M., S.M. Sekelsky and R.E. McIntosh

2. Preliminary Backscatter Lidar Measurements of Atmospheric Boundary Layer and Cirrus Clouds in Buenos Aires 34.6 S / 58.5 W 4
Lavorato, M.B., G.J. Fochesatto , E.J. Quel and P.H. Flamant

3. Improvement of a Standard Doppler Dealiasin Technique for Weather Radars Operating in Heavy Clutter Environment 7
Giuli, D., L. Facheris, F. Frattura and L. Baldini

4. Time-Frequency Analysis of Backscattered Lidar Signal to Study Atmosphere Dynamics 10
Molinaro, F., H. Bencherif, M. Bessafi and J. Leveau

5. Estimating RCS of the Sea Surface Perturbed by Rain for Rainfall Rate Retrieval 13
Capolino, F., D. Giuli , L. Facheris and F. Sottili

6. Assessment of Multiple Scattering Effects on Aerosol Retrievals from AVHRR NA
Ignatov, A., L. Stowe and R. Singh

7. Dielectric Constants for Melting Hydrometeors as Derived from a Numerical Method 16
Meneghini, R., and L. Liao

8. Analysis and Modeling of Atmospheric Transport of Water Vapor and Other Trace Constituents NA
Johnson, D.R.

9. Second Order Microwave Radiative Transfer Equation Solution with SSM/I Data NA
Souffez, S.H., and J.R. Givri

10. Adaptive Optical Aerosol Model of the Earth's Atmosphere NA
Smokty, O., and N. Kobjakova

11. Monitoring of Clouds Moisture for Problems of Increase Precipitation Artificially NA
Ruzhentsev, N.V., Yu.A. Kuzmenko and V.P. Bakhanov

12. Optical Remote Sounding of Aerosol Formations on the Base of Numerical Simulation of the Scattering Radiation 19
Belyaev, B.I., L.V. Katkovsky, V.P. Kabashnikov and V.P. Nekrasov

13. Investigation of the Anisotropy of the Atmospheric Turbulence Spectrum in the Low Frequency Range 22
Lukin, V.

14. Benguela Upwelling System: Satellite and Shipborne Data Analysis NA
Kazmin, A.S.

INTERACTIVE AREA 1 -- SAR Processing and Applications

15. A Simulation-Based Validation of Some Improvements in Automatic Stereo-Radargrammetry 25
Nocera, L., S. Dupont and M. Berthod

16. Detection and Localization of Lost Objects by SAR Technique 28
Dionisio, C.

NA -- Not available at time of printing.

INTERACTIVE AREA 1 *continued* -- SAR Processing and Applications

17. REX -- An Automated Road Extraction Algorithm for SAR Imagery NA
Bergen, Z.D., D. Kaiser and R.E. Carande

18. Automated Matching Experiments With Different Kinds of SAR Imagery 31
Gelautz, M., G. Jakob, G. Paar, S. Hensley and F. Leberl

19. Detecting Man-Made Features in SAR Imagery 34
Carlotto, M.J.

20. Texture Analysis by Universal Multifractal Features in a Polarimetric SAR Image 37
Martinez, P., D. Schertzer and K. Pham

21. Reading CEOS-SAR Tapes: A New General Reader and a Proposed New Standard 40
Pierce, L.

22. RADARSAT Processing at ASF 43
Leung, K., M. Chen, J. Shimada and A. Chu

23. Radar Speckle: Noise or Information? 48
Xia, Z.G., and Y. Sheng

24. SAR and One-Bit Coding: New Ideas 51
Franceschetti, G., M. Tesauro and S. Wall

25. Preserving Exponentials in Synthetic Aperture Radar Data 54
Pepin, M.P., and J.J. Sacchini

26. Improved Multiple Look Technique 57
Yeo, T.S., W.L. Lay, Y.H. Lu, W.E. Ng, I. Lim and C.B. Zhang

27. Partially Correlated K-Distribution for Multi-Look Polarimetric SAR Imagery 60
Yu, Y., A. Torre and S. Huan

28. Speckle Reduction and Enhancement of SAR Images in the Wavelet Domain 63
Sveinsson, J.R., and J.A. Benediktsson

29. Adaptive Filtering Algorithms for SAR Speckle Reduction 67
Lu, Y.H., S.Y. Tan, T.S. Yeo, W.E. Ng, I. Lim and C.B. Zhang,

INTERACTIVE AREA 2 -- Marine/Ocean

1. Multispectral and Multisatellite Data for Investigation of Black Sea Upper Layer Processes NA
Stanichny, S.V., and D.M. Solov'ev

2. A Software Package for the Quality Assessment of the Low Bit Rate Mediterranean Scatterometer and Altimeter Products:ERS-1.WSC.DWP and ERS-1.ALT.MPR NA
Bartoloni, A., C. Celani, C. D'Amelio, G. Milillo and R. Viggian

3. Estimation of Adjacent Effects Over the Coastal Zone by Polarization Measurements NA
Kusaka, T., S. Sado and Y. Kawata

4. An Eolian and Marine Phenomena Characterization in Dune Sectors by Image Processing 70
Delignon, Y., L. Moreau and P. Clabau

5. Retrieval of Arctic Surface Conditions and Cloud Properties from AVHRR Data: A Time Series for the Beaufort Sea 73
Meier, W., J. Maslanik, J. Key and C. Fowler

6. Sensitivity Study of the Aerosol Size Parameter Derived from AVHRR's Channels 1 and 2 Over Oceans NA
Ignatov, A.

7. Evaluation of Remote Sensing Algorithms for the Retrieval of Optically-Active Components in Turbid Natural Waters 76
Kutser, T., A. Blanco and H. Arst

8. Comparison of Sea Traffics in Tokyo and Osaka Bays With JERS-1/OPS Data 79
Takasaki, K., T. Sugimura and S. Tanaka

9. NASA Scatterometer Near-Real-Time, Value Added Products for Meso/Synoptic-Scale Marine Forecasting 82
Spencer, M.W.

10. Wavelet Analysis of AVHRR Images for Feature Tracking 85
Liu, A.K., W.Y. Tseng and S.Y.S. Chang

11. Flourescence as a Potential Indicator of Coral Health 88
Holden, H., D. Peddle and E. LeDrew

12. Satellite Synthetic Aperture Radar, CODAR, and In Situ Measurements of Oceanic Features in Monterey Bay NA
Fernandez, D.M.

13. Variability of Rossby Wave Propagation in the North Atlantic from TOPEX/POSEIDON Altimetry 91
Cipollini, P., D. Cromwell and G.D. Quartly

14. Chlorophyll Retrieval from CZCS: Influence of Atmospheric Aerosols 94
Moldenhauer, O., M.L. Steyn-Ross and D.A. Steyn-Ross

15. A Global Sea Level Variability Study From Almost a Decade of Altimetry 97
Naeije, M.C., and R. Scharroo

16. Variability and Frontogenesis in the Large-Scale Oceanic Frontal Zones Derived from the Global Satellite Measurements NA
Kazmin, A.S.

17. Vertical Distribution of PAR and Diffuse Attenuation Coefficient Modeling and In Situ Measurements 100
Volynsky, V.A., A.I. Sud'bin and J. Marra

18. Determination of Optical Properties of Ocean Upper Layers by Reflectance Spectra Measurements NA
Parishikov, S.V., M.E. Lee and O.V. Martynov

19. Oil Spills Detection in the Sea Using ALMAZ-1 SAR NA
Ivanov, A.Yu., V.V. Zaitsev, O.V. Ivlev and V.Yu. Raizer

20. Detection of Convective Instability in Atmospheric Boundary Layer Over the Ocean by Airborne Ku- Band Real Aperture Radar 103
Mityagina, M.I., Y.A. Kravtsov, V.G. Pungin, K.D. Sabinin and V.V. Yakovlev

21. Analyzing the Discharge Regime of a Large Tropical River Through Remote Sensing, Ground-Based Climatic Data, and Modeling 106
Schloss, A.L., C.L. Vorosmarty, C.J. Willmott and B.J. Choudhury

INTERACTIVE AREA 3 -- Sea Ice

1. Using Temporal Information in an Automated Classification of Summer, Marginal Ice Zone Imagery 109
Haverkamp, D., and C. Tsatsoulis

2. Texture Representation of SAR Sea Ice Imagery Using Multi-Displacement Co-Occurrence Matrices 112
Soh, L.K., and C. Tsatsoulis

3. Phase Correction for Coherent Noise Reduction in Short-Range Radar Measurements 115
Beaven, S.G., S.P. Gogineni and P. Kanagaratnam

4. In-Situ Measurement of the Complex Dielectric Constant of Sea Ice From 1 to 10 GHz 118
Nassar, E., R. Lee, K. Jezek and J. Young

5. Nearshore Ice Surface Roughness Surveys on Lake Superior 121
Pilant, D.

6. Error Characteristics of the SIRF Resolution Enhancement Algorithm 124
Early, D.S., and D.G. Long

7. The Quantification of Sea Ice Melt Features from Low Level Aerial Photographs 127
Derksen, C.P., J.M. Piwowar and E.F. LeDrew

8. Electromagnetic Waves Scattering From Sea Ice with Inhomogeneous Dielectric Permittivity Profile NA
Timchenko, A.I., and A.O. Perov

9. Investigation of the Fast Troposphere Parameters Variations by Using Method of the Radioacoustic Sounding NA
Rapoport, V.O., N.I. Belova, V.V. Chugurin, Y.G. Fedoseev, Y.A. Sazonov and V.A. Zinichev

10. Applications of the Remote Sensing for Experimental Study of the Boundary Layer's Dynamics in the Coastal Zone of the Black Sea NA
Kontar, E.A., A.I. Ginzburg and M.M. Domanov

11. Modelling Inter-Annual Snow Variability in Eastern Canada NA
Lewis, J.E., and L. Lee

12. Mapping Snow Properties for Spatially Distributed Snow Hydrological Modeling in Mountainous Areas Using Passive Microwave Remote Sensing Data 130
Wilson, L.L., L. Tsang and J.N. Hwang

13. Snow Classification from SSM/I Data over Varied Terrain Using an Artificial Neural Network Classifier 133
Sun, C., C.M.U. Neale, J.J. McDonnell and H.D. Cheng

14. Snow Mapping with SIR-C Mulpolarization SAR in Tienshan Mountain 136
Li, Z., and J. Shi

15. Recent Progress in Development of the Moderate Resolution Imaging Spectroradiometer Snow Cover Algorithm and Project 139
Riggs, G., D.K. Hall and V.V. Salomonson

16. Relation Between Radiative and Microphysical Properties of Snow: New Efficient Approach NA
Zege, E.P., and A.A. Kokhanovsky

17. Variations in Radar Backscatter Across the Great Ice Sheets 142
Noltimier, K.F., and K.C. Jezek

18. Geophysical Data Management System 145
Baggeroer, P.A., K.C. Jezek and D.G. Hart

19. Ice Sheet Margin Detection Using ERS-1 Synthetic Aperture Radar 148
Sohn, H.G., and K.C. Jezek

INTERACTIVE AREA 3 -- Soil

20. Microwave Effective Permittivity Model of Frozen Soil and Applications to Passive Remote Sensing NA
Tikhonov, V.V.

21. Flood Monitoring in Norway Using ERS-1 SAR Images 151
Weydahl, D.J.

22. Relating Microwave Satellite Radiometer Observations to Land Surface Parameters: A Physical Approach 154
Karam, M.A., and A. Stogryn

23. Analysis of ERS-1 SAR Data to Study Soil Moisture Content in Rocky Soils 157
Sano, E.E., A.R. Huete, D. Troufleau, M.S. Moran and A. Vidal

24. Determining Water Stress in Potato Fields Using Infrared Thermometry NA
Peterson, J.R., J.M. Giarrusso and M.C. MacDonald

25. An Automated Overland Flow Model Based Upon Remote Sensing and GIS 160
Leu, C.H.

26. Analysis for Soil Moisture and Land Cover Studies ERS-1 and JERS-1 SAR Data 163
Rao, Y.S., P.V.N. Rao, L. Venkataratnam and K.S. Rao

27. Spatio-Temporal Dynamics of Soil Moisture in Tallgrass Prairie Using ERS-1 SAR Image Time Series: First Year Results 166
Henebry, G.M., and A.K. Knapp

28. Mapping Methane Emission from Arctic Tundra Using Satellite Data, a Digital Elevation Model, and Discriminant Functions Based on Field Data 169
Shippert, M.M.

INTERACTIVE AREA 4 -- Crustal Movements/Vegetation

1. Neogene-Quaternary Kinematics of the Northern Mediterranean Microplates NA
Yutsis, V.V., and V.N. Vadkovsky

2. Water Content Influence on Scattering Properties of Vegetation Cover 172
Roenko, A.N., Yu.F. Vasilyev, B.D. Zamaraev and V.L. Kostina

3. Experimental Study of Fire Risk by Means of Passive Microwave and Infrared Remote Sensing Methods 175
Liberman, B., A. Grankov, A. Milshin, S. Golovachev and V. Vishniakov

4. Investigation and Cataloguezation of Backscattering Characteristics of Different Earth Covers in Millimeter Wave Band 178
Vasilyev, Yu.F., B.D. Zamaraev, V.L. Kostina and A.N. Roenko

5. Classification Using Multi-Source Data Using and Predictive Ability Measure 180
Chong, C.C., and J.C. Jia

6. Center Pivot Irrigation System Analysis Using Airborne Remotely Sensed Imagery: A Commercial Remote Sensing Case Study 183
MacDonald, M.C.

7. The Sensitivity of a Land Surface Parameterization Scheme to the Choice of Remotely-Sensed Landcover Data Sets 186
Oleson, K.W., K.L. Driese, J.A. Maslanik, W.J. Emery and W.A. Reiners

8. Using the Wavelet Method for a Multispectral Remote Sensing Study of Plant Community Spatial Processes in Broad Range of Spatial Scales 189
Mikheev, P.V., S.S. Kheeroug, G.Y. Yakin and J. S. Todhunter

9. A Multi-Parameter Land Data Set for Regional Modeling 192
Thames, P., J. Maslanik, K. Oleson and W. Emery

10. Coincident Diurnal and Spatial Variations in Dielectric Constant Properties as Measured Along a Vertical Gradient in Stems of Norway Spruce NA
McDonald, K., R. Zimmermann and E.D. Schulze

11. Spatio-Temporal Land Cover Dynamics in the Pantanal Assessed Using Lacunarity Analysis on an ERS-1 SAR Image Time Series 195
Henebry, G.M., and H.J.H. Kux

12. Accuracy Analysis and Validation of Global 1 Km Land Cover Data Sets 198
Scepan, J., J.E. Estes and W.J. Starmer

13. Potential of SIR-C Data to Study Vegetation Over Gujarat Test Site, India 201
Rao, K.S., Y.S. Rao, L. Venkataratnam and P.V.N. Rao

14. Intercomparison of Several BRDF Models for the Compositing of Spaceborne POLDER Data over Land Surfaces 204
Hautecoeur, O. and M. Leroy

15. Monitoring Arid and Semi-Arid Regions with ERS-1 Wind Scatterometer Data NA
Frison, P.L. and E. Mougin

16. Estimation of Seasonal Dynamics of Pasture and Crop Productivity in Kazakhstan Using NOAA/AVHRR Data 209
Gitelson, A., F. Kogan, E. Zakarin and L. Lebed

17. The Reflectance of Pleurozium Schreberi as a Function of Water Status and Its Implications on Understory Reflectance Variations for BOREAS Sites 212
Fernandes, R., H.P. White, D.R. Peddle, J.R. Miller and L.E. Band

18. Mapping Species Rich Boreal Wetlands Using Compact Airborne Spectrographic Imager (CASI) NA
Jelinski, D.E., J.R. Miller, R. Steinauer, S. Narumalani and J. Freemantle

19. Seasonal NDVI Trajectories to Response to Disturbance: Toward a Spectral-Temporal Mixing Model for Tallgrass Prairie 215
Goodin, D.G., and G.M. Henebry

20. Analysis of the Canadian Boreal Forest Using Enhanced Resolution ERS-1 Scatterometer Imagery 218
Wilson, C.J., III, and D.G. Long

21. Comparison of Interferomertic SAR and Radar Profiling in Forest Mapping NA
Axelsson, S.R.J.

22. Land Cover Change Dynamics of a Himalayan Watershed Utilizing Indian Remote Sensing Satellite (IRS) Data 221
Krishna, A.P.

23. Classification of Cover Types in the Lower Delta of the Parana River Using a Multitemporal Approach NA
Karszenbaum, H., P. Kandus, L.A. Frulla and D.A. Gagliardini

24. Remote Sensing of Crop Responses to Ozone and Carbon Dioxide Treatments 224
Leblanc, E., C.S.T. Daughtry and C.L. Mulchi

25. Radar Profiling for Forest Inventory NA
Axelsson, S.R.J., M. Eriksson and S. Hallidin

26. Examination of Multi-Temporal ERS-1 Radar over the Rainwater Basin 227
Keithley, C., and M. Roberts

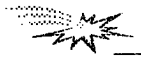
27. Application of Remote Sensing Measurements for Research an dService of Agriculture in Bulgaria NA
Kazandjiev, V.

28. A Comparison of NDVI and Spectral Mixture Analysis for Estimating Biophysical Properties in Boreal Forest Terrain 230
Peddle, D.R., F.G. Hall and E.F. LeDrew

29. Global Landcover Classification Training and Validation Issues and Requirements 233
Muchoney, D., J. Borak and A. Strahler

30. An Automatic Road Extraction Method Using a Map-Guided Approach Combined with Neural Networks for Cartographic Database Validation Purposes 236
Fiset, R., F. Cavayas, M.C. Mouchot, B. Solaiman and R. Desjardins

31. Plant Condition Remote Monitoring Technique 239
Fotedar, L.K., and K. Krishen



INTERACTIVE AREA 4 -- Geophysical Modelling

32. Feature Selection Using Decision Trees -- An Application for the MODIS Land Cover Algorithm 243
Borak, J.S., and A.H. Strahler

33. Regional Land Cover Characterization Using Multiple Sources of Intermediate-Scale Data 246
Vogelmann, J.E., S. Howard and T. Sohl

34. Multisensor Studies Using Landsat TM, SPOT and ERS-1 in Monitoring of Vegetation Damage in Nikel (Russia) and Varanger (Norway) NA
Lauknes, I. and H. Tommervik

35. Calibration and Classification of SIR-C SAR Data in Moderate Slope Areas 248
Holecz, F., T.R. Michel and M. Keller

36. A New Quick-Look Optical SAR Processor with Digital Input/Output 251
Litovechenko, K., P. Lemaire and C. Barbier

37. The Modeling of Forested Areas for Real and Synthetic Aperture Imaging Radar Simulation 254
Stuopis, P.A., J.M. Henson, R.E. Davis and K. Hall

38. Use of Geometrical SAR Simulation for Visibility Prediction: Application to Mission Planning and Urban Study 257
Gouinaud, C., and I. Pons

39. Modelling of Microwave Backscatter Using a Tree-Growth Model for Boreal Forests Within the NOPEX Test Site 260
Woodhouse, I.H., and D.H. Hoekman

INTERACTIVE AREA 4 *continued* -- Geophysical Modelling

40. Modeling Wetland Vegetation Using Polarimetric SAR 263
Slatton, K.C., M.M Crawford, J.C. Gibeaut and R.O. Gutierrez

41. Rain Pattern Detection by Means of Packet Wavelets 266
Marazzi, A., P. Gamba and R. Ranzi

INTERACTIVE AREA 5 -- Missions and Programs

1. The Development of the Seawinds Scatterometer Electronics Subsystem (SES) 269
Boller, B.D., R.D. Crowley, M.C. Smith and R.S. Roeder

2. Phase B and Breadboard Results for the TOPEX POSEIDON FOLLOW-ON Mission 273
Rey, L., N. Suinot, P. Oudart and G. Carayon

3. Science Data Collection with Polarimetric SAR 276
Dall, J., K. Woelders and S.N. Madsen

4. Spaceborne Rain Radar Mission and Instrument Analysis 279
Vincent, N., J. Chenebault, N. Suinot and P.L. Mancini

5. SIR-C/X-SAR Campaign on Ruegan Island, Germany - First Results 282
Prietzsch, C., and A. Bachem

6. The Indian Remote Sensing (IRS) Mission NA
Yang, J.

INTERACTIVE AREA 5 -- Electromagnetic Problems

7. Phase Fluctuations for Waves of Different Spatial Frequencies and Their Use in Determination of Inhomogeneous Dielectric Permittivity Profile NA
Timchenko, A.I.

8. Volume Scattering Function of Light for a Mixture of Polydisperse Small Particles with Various Optical Properties 285
Haltrin, V.I., A.D.Weidemann and W.E. McBride III

9. Simulation of RAR Reflectivity Maps of the Sea Surface for Remote Sensing Applications 290
Corsini, G., G. Manara and A. Monorchio

10. A Simplified Hybrid Model for Radiation Under Discontinuous Canopies 293
Li, X., W. Ni, C. Woodcock and A. Strahler

11. Estimation of Some Characteristics of Ocean Waters Using Optical Data (Case I) 296
Volynsky, V.A., J. Marra and C. Knudson

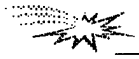
12. The Synthesis of Optimal Structure of Radar Using Polarization Adaptation 299
Loutin, E.A., A.I. Kozlov and A.I. Logvin

13. A Method and Algorithm of Computing Apparent Optical Properties of Coastal Sea Waters 305
Haltrin, V.I., and A.D. Weidemann

14. Scene Understanding from SAR Images 310
Datcu, M.

15. Microwave Specific Attenuation by Lossy Raindrops of Spheroidal Shapes: An Exact Formulation NA
Li, L.W., T.S. Yeo, P.S. Kooi and M.S. Leong

16. Theoretical Research on New Concepts for the Remote Sensing of Hydrometeors 315
Martin-Neira, M., J. Bara, A. Capms, F. Torres, I. Corbella and O. Gasparini



INTERACTIVE AREA 6 -- Educational Initiatives

1. Helping Students and Teachers Make Sense of Remote Sensing Via the Internet NA
Croft, S.K., and R.J. Myers

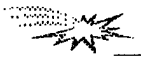
2 "Winds of Change" A Multi-Media Tool to Aid Teachers in Teaching Global Climate 321
Yanow, G., A. Sohus and B. Payne

3 From Surfer to Scientist: Designing a Canadian Remote Sensing Service for the Internet Audience 324
Langham, C.W., A.M. Botman and T.T. Alfoldi

4 Earth System Science Education Using Remote Imagery and Environmental Data Access NA
Fortner, R.W.

5 Using Weather Satellite Images in the Classroom of the Future NA
Keck, C.L.

6 The Use of Technology Driven Investigations in Geoscience and Remote Sensing Education: Findings from an Evaluation of the JASON Project NA
Coan, S.M., and C.J. Moon



INTERACTIVE AREA 7 -- SAR Interferometry

1. Linear Structures in SAR Coherence Data 330
Hellwich, O., and C. Streck

2. Detection and Velocity Estimation of Moving Objects in a Sequence of Single-Look SAR Images 333
Kirscht, M.

3. A Discrete Minimization Approach to Phase Unwrapping NA
Bartoloni, A., C. D'Amelio, A., Mariani, G. Milillo and M. Mochi

4. Comparison of Multigrid and Wavelet Techniques for InSAR Phase Unwrapping NA
Datcu, M.

5. Comparative Analysis of Phase Unwrapping Methods Using Self-Affine (Fractal) Models 336
Valero, J.L., and I. Cumming

6. A Workstation for Spaceborne Interferometric SAR Data 339
van der Kooij, M.W.A., B. Armour, J. Ehrismann, H. Schwichow and S. Sato

7. A Comparison of Phase to Height Conversion Methods for SAR Interferometry 342
Small, D., P. Pasquali and S. Fuglistaler

INTERACTIVE AREA 7 *continued* -- SAR Interferometry

8. Along-Track SAR Interferometry for Motion Compensation NA
Pasquali, P., B. Fritsch and D. Nuesch

9. SAR Interferometry: A Multigrid Markovian Approach for Phase Unwrapping with a Discontinuity Model 345
Labrousse, D., S. Dupont and M. Berthod

10. Echoes Covariance Modelling for SAR Along-Track Interferometry 347
Lombardo, P.

11. On the Survey of Volcanic Sites: The SIR-C/X-SAR Interferometry 350
Coltelli, M., G. Fornaro, G. Franceschetti, R. Lanari, M. Migliaccio, J.R. Moreira, K.P. Papathanassiou, G. Puglisi, D. Riccio and M. Schwabisch

12. DEM Generation by Repeat-Pass SAR Interferometry NA
Herland, E.A.

INTERACTIVE AREA 8 -- Techniques and Instrumentation

1. Atmospheric Induced Errors on Interferometric DEM Generation 353
Kenyi, L.W., and H. Raggam

2. Wavelet Projection Pursuit for Feature Extraction and Cloud Detection in AVIRIS 356
Bachmann, C.M., E.E. Clothiaux and D.Q. Luong

3. Atmospherical Correction of Satellite and Aircraft Spectral Image Without Calibration NA
Zege, E.P., I.L. Katsev and A.S. Prikhach

4. Absolute in Flight Calibration of Airborne Multichannel MM-Wave Imaging Radiometer 360
Cherny, I.V., A.A. Pankin and S.Y. Pantzov

5. Analysis of Map Speckle Suppression Algorithm 363
Zaitsev, V.V., and V.V. Zaitsev

6. Space "MSU-E" and "MSU-SK" Scanner Images Using for Evaluation of Antropogenic Pollution of Snow Cover NA
Mironov, V.L., S.A. Komarov, A.V. Yevtyushkin, I.N. Dubina, V.N. Yushakov and T.V. Baikalova

7. Laboratory and In-Flight Spectrometer Calibration Technique in Visible and Near Infrared Spectral Ranges 366
Belyaev, B.I., L.V. Katkovsky and V.P. Nekrasov

8. An Attempt to Differentiate Specific Absorption Characteristics by Solving Inverse Problem NA
Volynsky, V.A.

9. Secondary Processing Algorithm for Two-Frequency Aircraft Radiomapping System NA
Ruzhentsev, N.V., Yu.A. Kuzmenko and V.P. Churilov

10. Duct Detection over the Sea by TRANSIT Measurements 369
Gaikovich, K.P., A.N. Bogaturov, A.S. Gurvich, S.S. Kashkarov, S.N. Krivonozhkin, B.M. Shevtcov, V.K. Ivanov and V.D. Freylikher

11. The Abilities of Radioacoustical Sounding Method for Atmosphere Processes Diagnostic NA
Rapoport, V.O. and V.V. Tamoikin

12. An Investigation of the Textural Characteristic for Geological Purposes 372
Pasaribu, D.P.

13. Estimating Microwave Observation Depth in Bare Soil Through Multi-Frequency Scatterometry NA
Troch, P.A., F. Vandersteene and Z. Su

14. Validation of ERS-1/SAR Data to Map the Rio Amazonas Floodplain According to the Cartographic Accuracy Standards 374
Kux, H.J.H., and V. Barbosa da Silva

15. Detail-Preserving Segmentation of Polarimetric SAR Imagery 377
Andreadis, A., G. Benelli and A. Garzelli

16. Detection and Analysis of Ship Waves in ERS-1 SAR Imagery 380
Peng, C.Y., A.K. Liu and S.Y.S. Cheng

17. ROME: The Rosetta Microwave Experiment for the Investigation of the Cometary Nucleus 383
Fedele, G., G. Picardi and R. Seu

18. On the Use of Whitening Filter and Optimal Intensity Summation to Produce Multi-Look SAR Images 387
Bruniquel, J., A. Lopes, J.G. Planes, F. Cazaban and M. Deschaux-Beaume

19. Channel Design of the ADEOS-II/GLI (Global Imager) 390
Nakajima, T.Y., T. Nakajima and M. Nakajima

20. Atmospheric Effects on CO2 Differential Absorption Lidar Performance 393
Petrin, R.R., D.H. Nelson, J.R. Quagliano, M.J. Schmitt, C.R. Quick, R.K. Sander, J.J. Tiee and M. Whitehead

21. Improved Feature Classification by Means of a Polarimetric IR Imaging Sensor 396
Sadjadi, F., and C. Chun

22. A Comparison of Scintillation Crosswind Methods 399
Poggio, L., M. Furger and W.K. Graber

23. A Multi-Frequency, Dual-Polarization, Microwave Link for Rainfall Estimation 402
Rincon, R.F., S.W. Bidwell, A.R. Jameson and O.W. Thiele

24. Radiometric Normalization of Landsat/TM Images in Multitemporal Classification Procedures NA
Frulla, L., J. Milovich and H. Karszenbaum

25. Cost-Effective Parallel Processing for Remote Sensing Applications 405
Kim, H.J., and H.S. Kim

26. Design of a Geographic Information System Using OPS5 408
Menon, A.K., P. Jayaprakash and P.V. Usha

27. Multiresolution De-Speckle Based on Laplacian Pyramids 411
Alparone, L., B. Aiazzi, S. Baronti and C. Susini

28. Classification and Feature Extraction with Enhanced Statistics 414
Benediktsson, J.A., K. Arnason, A. Hjartarson and D. Landgrebe

29. Modeling and Simulation of Real Aperture Radar Images NA
Menegasssi Menchik, M.T., and D. Fernandez

30. A Rain Profiling Algorithm for the TRMM Precipitation Radar NA
Iguchi, T., T. Kozu, R. Meneghini and K. Okamoto

31. Application of Radar Target Decomposition Technique for Flood Detection: Results from SIR-C Data NA
Hess, L.L., Y. Wang and J.M. Melack

32. Solar Irradiance Determination by Using ATSR-2 Data 417
Xue, Y., D.T. LLewellyn-Jones and S.P. Lawrence

33. Automatic Interaction Detector (Aid) Application on Image Classification NA
Ho, L.L. and J.A. Quintanilha

34. Comparison of Linear Least Squares Unmixing Methods and Gaussian Maximum Likelihood Classification 420
Fernandes, R., J. Miller and L.E. Band

35. Development and Test of a Raster Scanning Laser Altimeter for High Resolution Airborne Measurements of Topography 423
Rabine, D.L., J.L. Bufton and C.R. Vaugh

36. Optical Correction of Scene Fractions for Estimating Regional Scale Ocean Coral Abundance in Fiji 427
Peddle, D.R., E.P. LeDrew and H.M. Holden

37. Development of SAR Interferometry at I.I.T. Bombay, India 430
Sukhatme, J.S., V. Walavalkar, Y.S. Rao, G. Venkataraman, M.V. Khire and K.S. Rao

38. Improved Procedures for the Retrieval of Stratospheric Trace Gases from Spectra of a Ground-Based Millimeter Wave Radiometer 433
Kuntz, M.

39. A New 278 GHz Ground-Based Radiometer for Vertical Profile Sounding of C10 and 03 in the Upper Atmosphere 436
Hochschild, G., and R. Krupa

40. Polarimetric SAR Image Classification Based on Target Decomposition Theorem and Complex Wishart Distribution 439
Du, L.J., and J.S. Lee

41. Hydrometeors Investigation by Means of 3 Millimeter Coherent Radar 442
Kosov, A.S., V.D. Gromov, S.N. Maleev, S.S. Kiselev, D.P. Skulachev and I.A. Strukov

42. Vegetation Obscuration Effects on Mid-Infrared Laser Reflectance of Soil 445
Guenther, B.D., and R.M. Narayanan

43. Applying Principal Components Analysis to Image Time Series: Effects on Scene Segmentation and Spatial Structure 448
Henebry, G.M., and D.R. Rieck

44. D.A.T.E. -- Dip Algorithm Testing and Evaluating Workbench 451
Kerzner, M.G.

45. High Resolution VHF SAR Processing Using Synthetic Range Profiling 454
Lord, R.T., and M.R. Inggs

46. A Region-based Approach to the Estimation of Local Statistics in Adaptive Speckle Filters 457
Fjortoft, R., F. Lebon, F. Sery, A. Lopes, P. Marthon and E. Cubero-Castan

47. A Precision Processor for Radarsat NA
Hughes, W., I. Arnon, K.A. Gault, D. MacGregor, L. Mikulin, L. Lightstone and J. Princz

48. Reversible Inter-Frame Compression of Multispectral Images Based on a Previous-Closest-Neighbor Prediction 460
Aiazzi, B., P.S. Alba, L. Alparone, S. Baronti and P. Guarnieri

49. Color Correction of HSI Transformed Images Using Color Space Transformation NA
Hosomura, T., and K. Katou

50. Lossless Compression of Multispectoral Images Using Permutations 463
Arnavut, Z., and S. Narumalani

51. Algoritms to Compute the Top-of-the-Atmosphere ALBEDO for Clear-Sky Conditions from Multi-Angle Data NA
Borel, C.C., and S. A.W. Gerstl

52. Parametric Representation of Atmospheric Disturbances NA
Mukherjee, D.P., P. Pal and J. Das

53. Radar Altimeter Return Noise Signals Identification 466
Maotang, L., J. Jingshan, W. Jingli and Y. Zhiqiang

54. Range and Angle Error Correction Measure for the Low Elevation Angle in Remote Sensing Data Analysis 469
Choi, J.

55. Potential and Use of Radar Images for Characterization and Detection of Urban Areas 474
Gouinaud, C., F. Tupin and H. Maitre

56. Phase Preservation in SAR Processing: The Interferometric Offset Test 477
Rosich Tell, B., and H. Laur

57. The Automation of Radar Operation and Calibration of NASA/JPL Airborne Multi-Frequency Polarimetric and Interferometric Synthetic Aperture Radar System NA
Lou, Y., and Y. Kim

58. Robust Restoration of Microwave Brightness Contrasts from the DMSP SSM/I Data 481
Petrenko, B.Z.

59. Advanced Airplane Version of the HUT 93 GHz Imaging Radiometer 484
Kemppinen, M., T. Auer, I. Mononen and M. Hallikainen

60. Ingara Dual Pass Cross Track Interferometry NA
Stacy, N.J.S., and G.G. Nash

61. A Low Range-Sidelobe Pulse Compression Technique for Spaceborne Rain Radar 487
Sato, K., H. Hanado and H. Kumagai

62. Pulse Compression With - 65 dB Sidelobe Level for a Spaceborne Meteorological Radar 490
Vincent, N., J. Richard, N. Suinot, M. Yarwood and C. Mavrocordatos

63. A SAR Antenna Calibration Method 493
Stevens, D., P. Bird and G. Keyte

64. Inflight Vertical Antenna Patterns for SIR-C from Amazon Rain-Forest Observation 496
Fang, Y., and R.K. Moore

65. A Contribution to Imaging Radiometer Sampling and Integration Period Determination 499
Kemppinen, M.

66. Radarclinometry for ERS-1 Data Mapping 503
Paquerault, S., H. Maitre and J.M. Nicolas

67. Millimeter-Wave Backscatter Measurements in Support of Surface Navigation Applications 506
Snuttjer, B.R.J., and R.M. Narayanan

68. A Novel Design of Return Signal Simulator for Radar Altimeters 509
Wu, J., and L. Lin

69. Polarimetric Calibration of Bistatic Radars Using Active Calibrators NA
Hevizi, L.G., and D.J. McLauglin

70. Calibration of Airborne Multiparameter Precipitation Radar with an Active Radar Calibrator 512
Hanado, H., H. Kumagai, T. Iguchi, T. Kozu, K. Nakamura and H. Horie

71. On the Accurate Calibration of the Sea Winds Radar Antenna: A Cylindrical Near-Field Measurement Approach 515
Hussein, Z.A., and Y. Rahmat-Samii

72. Detection of Pollutants in Liquids by Laser Induced Breakdown Spectroscopy Technique 520
Arca, G., A. Ciucci, V. Palleschi, S. Rastelli and E. Tognoni

73. Review of Vicarious Calibration of the Visible and Near-Infrared Channels of the Advanced Very High Resolution Radiometer NA
Rao, C.R.N., and J. Chen

74. Contextual Dynamic Neural Networks Learning in Multispectral Images Classifications 523
Solaiman, B., M.C. Mouchot and A. Hillion

TPAM -- Land Cover Mapping: Models and Applications

1. The Use of AVHRR Data for Creation of a New Global Land Cover Product for IGBP/DIS — NA
Belward, A., and T.R. Loveland

2. From Leaf to Scene: A Scaling Problems in Remote Sensing of Vegetation — 526
Goel, N.S., and W. Qin

3. Global Land Cover Classes Compatible with Radiative Transer Theory — NA
Nemani, R., S. Running and R. Myneni

4. ART Neural Networks for Remote Sensing: Vegetation Classification from Landsat TM and Terrain Data — 529
Carpenter, G.A., M.N. Gjaja, S. Gopal and C.E. Woodcock

5. New Approaches to Classification in Remote Sensing Using Hybrid Decision Trees to Map Land Cover — 532
Brodley, C.E., M.A. Friedl and A.H. Strahler

6. Proportional Estimation of Land Cover Characteristics From Satellite Data — 535
DeFries, R., M. Hansen and J. Townshend

7. Fuzzy ARTMAP Classification of Global Land Cover From AVHRR Data Set — 538
Gopal, S., C.E. Woodcock and A.H. Strahler

8. Exploring the Interannual Variability of Vegetation Activity Using Multitemporal AVHRR NDVI Imagery — 541
Mora, F., and J.W. Merchant

9. Correction of Land-Cover Area Estimates from Low Spatial Resolution Remotely Sensed Data — 544
Moody, A.

10. Landsat Pathfinder Data Sets for Landscape Change Analysis — 547
Dwyer, J.L., K.L. Sayler and G.J. Zlystra

TPAA -- Radar Remote Sensing and Precipitation

1. Factors Affecting NEXRAD-Based Point Rainfall Rate Estimation in the Seattle Area — 551
Seliga, T.A., and C. Chen

2. Analysis of Dual-Wavelength Dual-Polarization Returns from Frozen Hydrometeors — 554
Meneghini, R., T. Iguchi and L. Liao

3. Polarimetric Method for Ice Water Content Determination — 557
Ryzhkov, A.V., and D.S. Zrnic

4. Simulation of Dual-Polarization Bistatic Scattering from Rain and Hail — 560
Aydin, K., and S.H. Park

5. Computational Study of Millimeter Wave Scattering form Bullet Rosette Type Ice Crystals — 563
Aydin, K., and T.M. Walsh

6. Multiparameter Radar Snowfall Estimation Using Neural Network Techniques — 566
Xiao, R., and V. Chandrasekar

TPAA *continued* -- Radar Remote Sensing and Precipitation

7. Probing Electric Fields Near Sprites and Jets Using Multiparameter Radar and Chaff 569
Seliga, T.A., J.D. Sahr and R. H. Holzworth

8. Weather Radars with Pulse Compression Using Complementary Codes: Simulation and Evaluation 574
Mudukutore, A., V. Chandrasekar and R.J. Keeler

TPCP -- Remote Sensing: Boreal Ecosystems

1. Mapping of Boreal Forest Biomass Using SAR 577
Ranson, K.J., G. Sun, B. Montgomery and R.H. Lang

2. Carbon Dynamics in Northern Forests Using SIR-C/X-SAR Imagery 580
Bergen, K.M., M.C. Dobson and L.E. Pierce

3. Winter and Spring Thaw as Observed with Imaging Radar at BOREAS NA
Way, J.B., R. Zimmermann, K. McDonald and E. Rignot

4. Land Applications of ERS-1 Wind Scatterometer in Boreal Forest Zone 583
Pullianinen, J., N. Walker, T. Manninen, M. Hallikainen and J. Grandell

5. Monitoring Boreal Ecosystems in Siberia with the ERS-1 Windscatterometer NA
Schmullius, C., V. Wismann and K. Boehnke

6. Changes in Water Flux, Xylem Sap Composition, and Dielectric Constant Along a Vertical Gradient in Stems of Norway Spruce NA
Zimmermann, R., K. McDonald and E.D. Schulze

7. Spatial and Temporal Variability of Surface Cover at BOREAS Using Reflectances from a Helicopter Platform 586
Loechel, S.E., C.L. Walthall, E. Brown de Coulston, J.M. Chen and B.L. Markham

8. Use of Compact Airborne Spectrographic Imager (CASI) Data and Separability Measures for Classifying Complex Wetland Vegetation NA
Shepherd, P.R., D.E. Jelinski and J.R. Miller

9. Modeling Solar Radiation Transmission in Boreal Conifer Forests 591
Ni, W., X. Li, C.E. Woodcock, R.J. Roujean, R. Davis and A. Strahler

10. The Impacts of Environmental Conditions on Microwave Radiometry of Vegetation: A Physical Approach 594
Karam, M.A.

TPED -- Remote Sensing Applications of Sea Surface Modelling

1. Optimization of a Composite Surface Model for the Radar Backscattering Cross Section of the Ocean Surface as Measured by Wind Scatterometers 597
Romeiser, R.

2. A Physically-Based Two-Scale Electomagnetic Model for Backscatter From Ocean-Like Surfaces 600
Elfouhaily, T., and B. Chapron

3. An Application of the Two-Scale Model from the Point of View of the Small Slope Approximation to Radar Observations from the Ocean 603
Skirta, E.A., and A.N. Keane

4. A Comparison of Wind Wave Spectra Used in Ocean Remote Sensing Modeling 606
Elfouhaily, T., and B. Chapron

5. Evolution of Surface Waves of Finite Amlitude in Field of Inhomogeneous Current 609
Bakhanov, V.V., O.N. Kemarskaya, V.P. Pozdnyakova, J.A. Okomel'kova and I.A. Shereshevsky

6. Study of the Second Order Approximation of the Velocity Bunching in SAR Imaging Process Using the Bispectrum 612
Le Caillec, J.M., R. Garello and B. Chapron

7. Bistatic Sea Clutter: Simulations and Measurements 615
Khenchaf, A., F. Daout, Y. Hurtaud and J. Saillard

8. Verification of Microwave Scattering Mechanisms Using Optical Polarimetric Imagery 618
Barter, J.D., and P.H.Y. Lee

9. Fetch and Wind Speed Dependence of SAR Azimuth Cutoff and Higher Order Statistics in a Mistral Wind Case 621
Kerbaol, V., B. Chapron, T. Elfouhaily and R. Garello

10. Combined Radar and Cross-Polarizational Radiometer System for Detection and Identification of Some Anomalous Formations Originated on Sea Surface Due to Changes of Long and Short Waves Characteristics 625
Arakelian, A.K., and A.K. Hambaryan

TPES -- Youth Enhancing Space: KidSat

1. KidSat: Youth Enhancing Space 628
Choi, M.Y, G. Nagatani, J.B. Way and E.J. Stork

2. The Education Element of the KidSat/Youth Enhancing Space Project 631
McGuire, J., B. Fisher, R. Kassebaum, D. Barstow, K. Rackley, P. Bixler, M.A. Jones and J. Hunt

3. The Space Element of the Youth Enhancing Space Project NA
Lane, J., A. Leach, S. Davis, A. Ramirez and J. Baker

4. Mission Operations in the Classroom NA
Rackley, K., P. Bixler and H. Haugen

5. Youth Enhancing Space: Data System Element NA
Kirchner, C., M. Minino, R. Kassebaum, J. Lawson and P. Andres

6. Exploration Results from Charleston NA
Cowen, R., K. Rackley and the Fifth Grade Students of Buist Academy

7. Exploration Results from San Diego NA
Austin, A., S. Akpa, R. Anderson, P. Bixler and R. Ebel

8. Exploration Results from Pasadena NA
Brammer, C., M.A. Jones and the Fifth Grade Students of Washington Accelerated

TPF -- Remote Sensing for the Arctic Climate System

1. Future Opportunities and Issues in Radar Remote Sensing of Earth's High Latitudes 634
Carsey, F., and C. Wales

2. Satellite Remote Sensing of Atmosphere and Ice over the Arctic Ocean: A Perspective NA
Rothrock, D.A.

3. Expected Errors in Satellite-derived Estimates of the High Latitude Surface Radiation Budget 636
Key, J.R., R.S. Stone and A.J. Schweiger

4. Multitemporal Analysis of Fast Sea Ice Albedo Using AVHRR Data 639
De Abreu, R.A., and E.F. LeDrew

5. Assessing Variability and Trends in Arctic Sea Ice Distribution Using the Satellite Data 642
Belchansky, G.I., I.N. Mordvintsev and D.C. Douglas

6. Image Time Series Analysis of Arctic Sea Ice 645
Piwowar, J.M., G.R.I. Wessel, and E.F. LeDrew

7. An Analysis of Odden Event Intra- and Inter-Annual Variability 648
Fischer, K.W., C.A. Russel, R.A. Shuchman and E.G. Josberger

8. Remote Sensing Data Availability from the Earth Observation System (EOS) via the Distributed Active Archive Center (DAAC) at NSIDC 651
Weaver, R.L., and V.J. Troisi

9. CIDAS Climatological Ice Data Archiving System NA
Chagnon, R.

10. The Radarsat Geophysical Processor System NA
Rothrock, D., H. Stern, and R. Kwok

TPP -- SAR Interferometry: Processing Algorithms and Systems

1. Algorithms for Calculation of Digital Surface Models from the Unwrapped Intereferometric Phase 656
Goblirsch, W., and P. Pasquali

2. Elevation Correction and Building Extraction from Interferometric SAR Imagery 659
Burkhart, G.R., Z. Bergen, R. Carande, W. Hensley, D. Bickel and J.R. Fellerhoff

3. Unbiased Estimation of the Coherence from Multi-Look SAR Data 662
Touzi, R., A. Lopes, J. Bruniquel and P. Vachon

4. Automated Rapid Mapping with Interferometric Synthetic Aperture Radar Data 665
Ngai, F.M., and R.E. Carande

5. Ultra-Wideband and Low-Frequency SAR Interferometry 668
Ulander, L.M.H., and P.O. Frolind

6. Medium Resolution Efficient Phase Preserving Focusing for Interferometery 671
Gatelli, F., A. Monti Guarnieri, C. Prati and F. Rocca

7. EMISAR Single Pass Topographic SAR Interferometer Modes 674
Madsen, S.N., N. Skou, K. Woelders and J. Granholm

8. Parametric Estimation of Time Varying Baselines in Airborne Interferometric SAR 677
Mohr, J.J., and S.N. Madsen

9. On the Baseline Decorrelation 680
Franceschetti, G., A. Iodice, M. Migliaccio and D. Riccio

TPT -- Daytime Operation of Lidar Systems

1. Micro Pulse Lidar Daytime Performance: Simulations and Observations 683
Reagan, J.A., A.E. Galbraith and J.D. Spinhirne

2. Daytime Raman Lidar Measurements of Atmospheric Water Vapor NA
Whiteman, D., S.H. Melfi, G. Schwemmer, R. Ferrare and K. Evans

3. Lidar Studies of the Atmosphere NA
Carswell, A.I.

4. Daytime Temperature Measurements with a Sodium-Vapor Dispersive Faraday Filter in Lidar Receiver NA
Chen, H., M.A. White, D.A. Krueger and C.Y. Che

5. Rayleigh Lidar Observations During Arctic Summer Conditions 686
Thayer, J.P., N.B. Nielsen, R.B. Kerr and J. Noto

6. Daytime Tropospheric Water Vapor Profile Measurements by Raman Lidar 691
Bisson, S.E., and J.E.M. Goldsmith

7. A Differential Absorption Lidar System for Day and Night Measurements of Tropospheric Ozone NA
Langford, A.O., amd M.H. Proffitt

8. Spatial Properties of the Atmospheric Boundary Layer as Observed by Lidar NA
Cooper, D.I., and W. Eichinger

9. High Spectral Resolution, Low-Coherence Technique for Daytime Doppler Wind Measurements with Lidar 694
Fischer, K.W.

10. Field Calibration and Sensitivity Analysis of Coherent Infrared Differential Absorption Lidars 697
Richter, P.I., I. Peczeli, S. Borocz, L. Gazdag, J. Leonelli and T. Dolash

TPV -- Image Segmentation

1. Task-Specific Segmentation of Remote Sensing Images 700
Xuan, J., and T. Adah

2. Hybrid Image Segmentation for Earth Remote Sensing Data Analysis 703
Tilton, J.C.

3. Unsupervised Statistical Segmentation of Multispectral SAR Image Using Generalized Mixture Estimation 706
Marzouki, A., Y. Delignon and W. Pieczynski

4. Segmentation of SAR Images by Means of Gabor Filters Working at Different Spatial Resolution 709
Baraldi, A., and F. Parmiggiani

5. Markov Random Field Based Image Segmentation with Adaptive Neighborhoods to the Detection of Fine Structures in SAR Data 714
Smits, P.C., S. Dellepiane and S.B. Serpico

TPV *continued* -- Image Segmentation

6. Unsupervised Multiresolution Segmentation of Textured Image and Its Interpretation Using Fully Polarimetric SAR Data — NA
Liu, G., S. Huang and A. Torre

7. SAR Image Segementation by Mathematical Morphology and Texture Analysis — 717
Ogor, B., V. Haese-Coat and J. Ronsin

TPZ -- Microwave Remote Sensing of Vegetation

1. Analysis of Polarimetric Radar Backscatter of Moss-Bedded Conifers in Boreal Forest — NA
Saatchi, S.S., and M. Moghaddam

2. Scattering from Cultural Grass Canopies: A Phase Coherent Model — 720
Stiles, J.M., and K. Sarabandi

3. Scattering from Cultural Grass Canopies: Measured and Modeled Data — 723
Stiles, J.M., K. Sarabandi and F.T. Ulaby

4. Forest Backscatter Modeling: Simulation Versus Discrete Random Media Approach — 726
Lang, R.H., and R. Landry

5. Wave Scattering and Scene Image of Trees Generated by Lindenmayer Systems — 728
Zhang, G., and L. Tsang

6. Extraction of Biomass from SAR Data: A Realistic Approach — NA
Amar, F., M.S. Dawson, A.K. Fung and M.T. Manry

7. Estimation of Moisture Content of Forest Canopy and Floor From SAR Data, Part I: Volume Scattering Case — 730
Moghaddam, M., and S. Saatchi

8. Estimation of Moisture Content of Forest Canopy from SAR Data — NA
Moghaddam, M., and S. Saatchi

9. Investigating Correlations Between Radar Data and Characteristics of Mangrove Forests — 733
Proisy, C., E. Mougin and F. Fromard

10. Monitoring Vegetation Features with Multi-Temporal SAR Data — 736
Amodeo, G., P. de Matthaeis, P. Ferrazzoli, S. Paloscia, P. Pampaloni, G. Schiavon, S. Sigismondi and D. Solimini

TEAM -- Microwave Sensor Calibration

1. RADARSAT Calibration Studies NA
Lukowski, T.I., R.K. Hawkins, C. Cloutier, L.D. Teany, J. Iisaka and T. Sakurai-Amano

2. Near-Field Effect of Extended Targets on Absolute Calibration of Microwave Sensors 739
Wu, J., and J. Jiang

3. Calibration of an Airborne W-Band Polarimeter Using Drizzle and a Trihedral Corner Reflector 743
Galloway, J., A. Pazmany and R. McIntosh

4. Calibration of Bistatic Polarimetric Scatterometers 746
Daout, F., A. Khenchaf and J. Saillard

5. Accurate Antenna Reflector Loss Measurements for Radiometer Calibration Budget 749
Skou, N.

TEF -- Volume Scattering I

1. Electromagnetic Scattering Based on Pair Distribution Functions Retrieved from Planar Snow Sections 754
Zurk, L.M., L. Tsang, J. Shi and R.E. Davis

2. Modeling of Electromagnetic Wave Scattering from Time-Varying Snowcover 757
Ding, K.H., Y.E. Yang, S.E. Shih, J.A. Kong and R.E. Davis

3. Pulsed Beam Scattering from a Layer of Discrete Random Medium: With Applications to Spaceborne Weather Radars 760
Kilic, O., and R.H. Lang

4. TM Wave Scattering by Multiple Two-Dimensional Scatterers Buried Under One-Dimensional Multi-Layered Media 763
Cui, T.J., and W. Wiesbeck

5. TE Wave Scattering by Multiple Two-Dimensional Scatterers Buried Under One-Dimensional Multi-Layered Media 766
Cui, T.J., and W. Wiesbeck

TEH -- Subsurface Sensing and Material Properties I

1. High Resolution Imaging Techniques in Step-Frequency Subsurface Radars NA
Martinez-Madrid, J.J., J.R. Casar Corredera and G. de Miguel-Vela

2. Numerical Simulation of Scattering from Objects Embedded in a Medium with Randomly Rough Boundary 772
Tjuatja, S., Z.J. Li, A.K. Fung and C. Terre

3. A High-Resolution Imaging of Small Objects for Subsurface Radar Data Processing 775
Sato, T., T. Wakayama, K. Takemura and I. Kimura

4. Ground-Penetrating Radar Antenna Modeling 778
Haung, Z., K. Demarest and R. Plumb

5. 3-D SAR Imaging of Targets Obscured by Dielectric Media NA
Fortuny, J., and A.J. Sieber

TEM -- Land Cover: Innovation Classification Methods I

1. A Hierarchial Fuzzy Clustering Algorithm Using Pyramid Linking Data and Land-Cover Classification Experiments 781
Naka, M., T. Miyazaki and Y. Iwata

2. Fractal Concept to the Classification of Crop and Forest Type in IRS Data 784
Jeyarani, K., and K. Jayaram Hebbar

3. A Comparison of Three Neural Network Classifiers for Remote Sensing Classification 787
Gopal, S., and M. Fischer

4. A Decision Tree Classifier Design for High-Dimensional Data with Limited Training Samples 790
Tadjudin, S., and D.A. Landgrebe

5. Classification Accuracy Improvement and Delineation of Mixed Pixels Using Hierarchical Image Classification 793
Ediriwickrema, D.J., and S. Khorram

TEP -- SAR Interferometry

1. High Resolution 3-D SAR via Multi-Baseline Interferometry 796
Homer, J., D. Longstaff and G. Callaghan

2. Interferometric Analysis of Multifrequency and Multipolarisation SAR Data 799
Papathanassiou, K.P., and J.R. Moreira

3. Fusing L, C, and X Band Interferometric Phase Images by Means of Kalman Filtering Techniques NA
Loffeld, O., R. Kraemer, A. Hein, L. Dutra, G. Fornaro, R. Lanari, M. Migliaccio, J.R. Moreira, K.P. Papathanassiou, D. Riccio and M. Schwabisch

4. Quality Assessment of InSAR-Derived DEMs Generated with ERS Tandem Data 802
Schwabisch, M., M. Matschke,W. Knopfle and A. Roth

5. Atmospheric Heterogeneity: Effects on Multi-Pass Space Borne SAR Interferometry NA
Rossi, M., H. Vadon and A. Arnaud

TES -- Ocean Winds and Waves I

1. Surface Winds in a Midlatitutde Storm Seen by Satellites and Numerical Models 805
Katsaros, K.B., S. Dickinson, A. Bentamy, Y. Quilfen, S.S. Atakturk and R.A. Brown

2. The Comparison Between Active and Passive Microwave Data for Geophysical Ocean Surface Parameters Retrieval NA
Givri, J.R., S.S. Souffez and K. Bourbigot

3. Microwave Backscatter from the Sea Surface at Grazing Incidence 808
Buckley, J.R., and R.S. Johnson

4. Doppler-Radar-Radiometer Method of Near Sea Surface Wind Speed, Long Waves Roughness Degree, Water and Air Temperatatures Determination 811
Arakelian, A.K., and A.K. Hambaryan

5. An Offset between Scatterometer Directional Anisotropy and Wind Direction across the Equatorial Pacific Ocean 814
Rufenach, C.L.

TET -- Educational Initiatives

1. The Role of Remote Sensing in Training Activity of Tuscany Region 817
Cuomo, S., D. Giuli and G. Federici

2. Development of a Remote Sensing Core Curriculum Submitted for the Sessions on Educational Initiatives in Geoscience and Remote Sensing 820
Estes, J.E., and T. Foresman

3. NASA/JPL's Imaging Radar Outreach Program 823
Freeman, A., E. O'Leary, B. Chapman and J. Trimble

4. What Kind of Images Do I Need? What Is the Delay to Obtain Them? NA
Houzelle, S., P. Bellemain, J. Amalric and P. Herry

5. Geoscience Field Trainings in Russian Universities NA
Yutsis, V.V., and V.T. Trofimov

WAAM -- Land Cover: Tropical Forests and Vegetation

1. Discrimination of Africa's Vegetation Using Reconstructed ERS-1 Imagery 827
Hardin, P.J., D.G. Long and Q.P. Remund

2. The JERS-1 Amazon Multi-Season Mapping Study (JAMMS) 830
Freeman, A., B. Chapman and M. Alves

3. Forest Classification by Means of Pattern Recognition Method Applied to Scatterometer Data 833
Dechambre, M., and M. Bourdeau

4. Use of Polarisation Synthesis for Deforestation Studies Based on SIR-C/XSAR Data Analysis 836
Soyris, J.C., T. Le Toan, N. Floury, L. Thomasson, C.C.Hsu and J.A. Kong

5. Can the ERS-1 Scatterometer Be Used to Forecast the Inundation Extent in the Pantanal Wetland? 839
Wismann, V.R., and K. Boehnke

6. Forest Mapping and Monitoring in French Guiana: From Deforestation Mapping to a GIS for a Future National Park NA
Vedel, S., and D. Girou

7. Use of ERS-1 SAR Data for Forest Monitoring in South Sumatra 842
Le Toan, T., F. Ribbes, T. Hahn, N. Floury and U.R. Wasrin

8. Tropical Forest Monitoring Using Data from the ERS-1 Wind Scatterometer 845
Woodhouse, I.H., and D.H. Hoekman

9. Mapping and Monitoring the Mangrove: First Regional Map of Mangrove Using Remote Sensing and Geographic Information Systems NA
Girou, D., S. Vedel and O. Laroussinie

10. A Comparison of Reconstructed Ku-Band Scatterometry, C-Band Scatteromentry, and SSM/I Imagery for Tropical Vegetation Classification 848
Hardin, P.J., D.G. Long, Q.P. Remund and D.R. Dawn

WAAA -- Sensors and Remote Methods for Detecting Environmental Contaminants

1. Advances in Fiber Optic Based Laser-Induced Flourescence Sensors for In Situ Measurement of Petroleum Hydrocarbons in Soils — NA
Lieberman, S.H., and D.S. Knowles

2. Determination of Contaminants in the Enviroment Using Instrumentation Based on Laser-Induced Breakdown Spectroscopy — NA
Cremers, D.A., and M.J. Ferris

3. Trace Detection of Environmental Contaminants by Laser Photogragmentation / Fragment Detection Spectrometry — 851
Sausa, R.C.

4. Detection of Environmental Contaminants by Time Resolved Laser Induced Breakdown Spectroscopy Technique — 854
Arca, G., A. Ciucci, V. Palleschi, S. Rastelli and E. Tognoni

5. Influences on Detectability of Heavy Metals in Soils by Laser-Induced Breakdown Spectroscopy — 857
Alexander, D.R., D.E. Poulain, M.S. Khlif and E.R. Cespedes

6. Development and Testing of Electrochemical Sensors for Rapid Detection of Explosive Contaminants in Soils — NA
Cespedes, E.R.

7. Commercialization of the Laser Spark Continuous Metal Emissions Montor — NA
French, N.B.

8. Measurements of the Radar Backscattering Over Different Oceanic Surface Films During the SIR-C/X-SAR Campaigns — 860
Gade, M., W. Alpers , M. Bao and H. Huehnerfuss

9. Airborne CASI Imaging Spectrometer Used in Monitoring of Vegetation Damage in the Pasvik Area — NA
Tommervik, H., I. Lauknes and B. Johansen

10. Preliminary Evaluation of a Millimeter-Wave System for Air Pollution Monitoring — 863
Nadimi, S.A., and J.W. Bredow

WACP -- Microwave Synthetic Aperture Interferometric Radiometry

1. Two-Dimensional Aperture Synthesis Radiometers in a Low Earth Orbit Mission and Instrument Analysis — 866
Kraft, U.R.

2. Integration of MIRAS Breadboard and Future Activities — 869
Martin-Neira, M. , J.M Goutoule, A. Knight, J. Claude, J. Bara, A. Camps, F. Torres, I. Corbella, A. Lannes, E. Anterrieu, V. Laursen and N. Skou

3. Design and Implementation of the MIRAS Digital Correlator — 872
Batz, O., U. Kraft,W. Lindemer and H. Reichel

4. Characteristics of the Baseline Off-Nadir Angle of Supersynthesis Radiometer — 875
Komiyama, K., and Y. Kato

5. Icestar: Next Major Advance in Sea Ice Remote Sensing — NA
Cavalieri, D.J., L.L. Thompson, D.M. Le Vine and J.A. Weinman

6. Calibration of Synthetic Aperture Radiometers in Space: Antenna Effects 878
Le Vine, D.M., and D.E. Weissman

7. RADSAR Synthetic Aperture Radiometer Test Results NA
Edelsohn, C.R.

8. Development of a 37GHz Synthetic Apeture Microwave Radiometer NA
Goodberlet, M.A., C.S. Ruf and C.T. Swift

9. Application of Sparse Phased Arrays to Millimeter-Wave Radiometry 881
Loveberg, J., S. Clark, D. Wilkner and B. Wallace

10. Radiometer System with Cross-Polarization and Correlation of the Channels of Observation 885
Arakelian, K.A., and A.K. Arakelian

WAED -- Remote Sensing of Littoral Submesoscale Processes I

1. Spatial Variations of Microwave Backscatter Magnitude and Angular Distribution: Response of the Short Waves to Wind and Surface Changes 888
Weissman, D.E., W.J. Plant, W.C. Keller and V. Hesany

2. Seagulls and SAR: Atmospheric Convection Effects in SAR Images over the Ocean 891
Vesecky, J.F., F.L. Ludwig, J.M. Daida, N. Chinchilla and G. Kimbreau

3. Evidence of a Land Breeze in an ERS-1 SAR Image of the New Jersey Coastline 893
Sikora, T.D., D.R. Thompson, G.S. Young and N.S. Winstead

4. Atmospheric Signatuares in SAR Imagery 896
Beal, R.C., D.R. Thompson, G.S. Young, H.N. Shire and T.D. Sikora

5. SAR Response to Spatially and Temporally Varying Wind Fields 899
Lyzenga, D.R.

6. Synthetic Aperture Radar Imagery of the Coastal Ocean Near Cape Hatteras, NC NA
Marmorino, G.O., D.R. Lyzenga, J.A.C. Kaiser and C.L. Trump

7. An End-To-End Simulation of Radar Signatures from the HI-RES 1 Rip Feature 902
Chubb, S.R., A.L. Cooper, R.W. Jansen and C.Y Shen

8. Low Grazing Angle Dual Polarized Doppler Radar Measurements of Oceanic Fronts 905
Allan, N., D.B. Trizna and D.J. McLaughlin

9. Effects of Wave Breaking on SAR Signatures Observed Near the Edge of the Gulf Stream 908
Lyzenga, D.R.

10. Issues Surrounding Surfactant Effects Upon Radar Imagery of Convergent Ocean Surface Flows with Application to the Hi-Res I Rip Feature 911
Cooper, A.L., S.R. Chubb and J.A.C. Kaiser

WAES -- Educational Initiatives I

1. Satellite Remote Sensing of the Environment: New Opportunities for the Educator NA
Winokur, R.S.

2. An Overview of Remote Sensing Education Projects Sponsored by the NASA Space Grant Program 914
Wersinger, J.M., and E. Ward

3. Mission to Planet Earth On-Line Earth Systems Science Course 917
Blurton, C., and S. McGee

4. Remote Sensing Data for Educational Purposes: The Policy of the European Space Agency and Its Achievements with the Meteosat Data NA
Le Ber, J.

5. Earth Observation Satellite Date and its Application to Environmental Education 920
Goto, A.

6. Applications of Satellite Imagery, Visualizations and Remote Sensing in Environmental/Science: An Earth Systems Science Approach 922
Moore, J.D.

7. Do We Really Understand What We See? Cognitive Issues in Remote-Sensing From the Perspective of a Scientist and an Educator 925
Barstow, D., and E. Frost

8. National Weather Service Portable Multimedia Presentations to Teachers and Students NA
Gird, R., and J. Von Ahn

9. Interdisciplinary Earth System Science and Earth Observations From the International Space Station: Partners in Education 929
Willis, K.J., D.L. Amsbury, C.D. McLaughlin and T. Miewald

10. Applied Environmental Problem-Solving Using Remote Sensing Technology: A Summer Practicum for Undergraduate Faculty NA
Panah, A.A.

WAF -- Sea Ice Remote Sensing (Models, Techniques and Applications) I

1. Global Sea Ice Monitoring from Microwave Satellites 932
Johannessen, O.M., M.W. Miles and E. Bjorgo

2. Sea Ice Identification Using Dual-Polarized Ku-Band Scatterometer Data 935
Yueh, S.H., R. Kowk, S.H. Lou and W.Y. Tsai

3. Temporal Mixture Analysis of SMMR Sea Ice Concentrations 938
Piwowar, J.M., D.R. Peddle and E.F. LeDrew

4. Polarimetric Backscattering at 23 cm Wavelength from Antarctic Lead Ice and Estimation of Ice Thickness 941
Winebrenner, D.P.

5. Characterization of Ice in the Chukchi Sea at the Start of the Growing Season Using Satellite SAR 944
Onstott, R.G.

6. Bistatic Microwave Investigations of Sea Ice-Like Media 947
May, G.C., J.W. Bredow, J. Juying, S.A. Nadimi and A.K. Fung

7. Validation of a Sea Ice Model Using Forward Simulation of ERS-1 SAR Data: A Case Study in the Beaufort Sea 950
Heinrichs, J., J. Maslanik and K. Steffen

8. The Influence of Cloud Cover on the Microwave Scattering Coefficient (σ°) of First-Year and Multiyear Sea Ice 953
Barber, D.G., and A. Thomas

9. Comparison of Aircraft and DMSP SSM/I Passive Microwave Measurements over the Bering Sea in April 1995 956
Cavalieri, D.J., D.K. Hall and J.R. Wang

10. Multi-Channel Algorithm Approach to Determining Melt for Arctic Sea Ice Using Passive Microwave Data 959
Anderson, M.R.

WAP -- SAR Interferometry and Geoscience Applications

1. Differential SAR Interferometry for Detection of Small Terrain Movements NA
Cavallo, A., D. Tarchi and A.J. Sieber

2. Satellite Radar Measurements of Land Subsidence 963
van Halsema, D., and M.W.A. van der Kooij

3. Flood Monitoring Using ERS-1 SAR Interferometry Coherence Maps 966
Geudtner, D., R. Winter and P.W. Vachon

4. Determination of Vegetation Height from SAR Interferometry: A Theoretical Study 969
Sarabandi, K.

5. Application of Interferometry to Studies of Glacier Dynamics 972
Mohr, J.J., and S.N. Madsen

6. Relating Forest Paramters to Interferometric Data 975
Floury, N., T. Le Toan and J.C. Souyris

7. Estimating Vegetation and Surface Topographic Parameters from Multibaseline Radar Interferometry 978
Treuhaft, R., M. Moghaddam, J. van Zyl and K. Sarabandi

8. On the Detection of Spatially Varying Current Fields at the Ocean Surface by Along-Track Interferometric Synthetic Aperture Radar 981
Romeiser, R., and D.R. Thompson

9. Study of Integration Time Effects on Coherent Radar Imagery of the Sea Surface 984
Moller, D., S. Frasier and R.E. McIntosh

10. Recent Earth Crust Movement of the Black Sea and Adjacent Areas: Application of Remote Sensing Data NA
Yutsis, V.V., V.G. Talitsky and A.F. Vasilevsky

WAT -- Lidar/Spectrometry

1. Daytime Performance Simulation of PN-Code Modulated Micro-Joule Lidar 987
Schoening, V.L., J.A. Reagan and P.A. Delaney

2. Application of Wideband Signals to Airborne Laser Bathymetry 990
Pillai, S.R., and A. Antoniou

3. Low Light-Level IR Detectors for Use in Lidar Systems 993
Mayer, T.S., and T.J. Kane

4. Scanning for a Satellite Radar Wind Sounder (RAWS) 996
Moore, R.K., B. Beh and S. Song

5. Feasibility Study of a Compact Low Cost Correlation LIDAR Using a Pseudo Noise Modulated Diode Laser and an APD in the Current Mode 999
Bundschuh, B.O., D. Schneider and M. Grindel

6. Remote Sensing Spectrometry of a Temperate Deciduous Forest -- A Modeling Approach 1002
Demarez, V., J.P. Gastellu-Etchegorry, F. Zagolski, E. Mougin, G. Marty, E. Dufrene and V. Le Dantec

7. A Revised Measurement Methodology for Spectral Optical Properties of Conifer Needles 1005
Middleton, E.E., S.S. Chan, M.A. Mesarch and E.A. Walter-Shea

8. Airborne Imaging Spectrometry in National Forest Inventory 1010
Makisara, K., and E. Tomppo

9. An Approach for Obtaining Best Estimates of Spectral Optical Depths and Calibration Intercepts from Solar Radiometer Data Corrupted by Temporal Variations 1014
Erxleben, W.H., and J.A. Reagan

10. Estimation of Abundances in Two-Component Mineral Mixtures Using Mid-Infrared Laser Reflectance Ratios 1017
Narayanan, R.M., K.K. Warner and R.F. Diffendal, Jr.

WAV -- Data Compression in Remote Sensing

1. Near Lossless Transform Coding of Multispectral Images 1020
Tescher, A.G., J.T. Reagan and J. A. Saghri

2. Progressive Model-Based VQ for Image Data Archival and Distribution 1023
Manohar, M., and J.C. Tilton

3. Effect of Compression on Physical Parameters Derived from Polar Ice Radiances 1026
St. Germain, K.M., and K. Sayood

4. Lossless Seismic Data Compression Using Adaptive Linear Prediction 1029
Mandyam, G., N. Magotra and W. McCoy

5. Performance of An Enhanced DCT Compression System for Space Applications 1032
Yeh, P.S., W.H. Miller and S. Hou

6. End-to-End System Consideration of the Galileo Image Compression System 1035
Cheung, K., K. Tong and M. Belongie

7. A Bounded Distortion Compression Scheme for Hyper-Spectral Image Data 1039
Memon, N.D.

8. Lossless Image Compression Based on a Generalized Recursive Interpolative DPCM 1042
Aiazzi, B., P.S. Alba, L. Alparone and S. Baronti

9. Image Sequence Compression Using Adaptive Wavelet Packet 1045
Sarita, S., and P. Nagabhushan

10. Using ATM Networks for Processing Global Earth Data 1048
Kess, B.L., P.R. Romig III, S.E. Reichenbach and A. Samal

WAZ -- Soil Moisture I

1. Applications of Passive Microwave Observations of Surface Soil Moisture 1051
Schmugge, T.

2. Spatial and Temporal Trends in Land Surface Moisture and Temperature Observable Using Data from the Nimbus-7 Microwave Radiometer 1054
Njoku, E.G., and B.W. Rague

3. Application of Microwave Remotely Sensed Surface Soil Moisture for Estimation of Sub-Surface Soil Hydraulic Properties 1058
Engman, E.T., N.M. Mattikalli, L.R. Ahuja and T.J. Jackson

4. Investigation of the Accuracy of Soil Moisture Inversion Using Microwave Data and Its Impact on Watershed Hydrological Modeling 1061
O'Neill, P.E., A.Y. Hsu, T.J. Jackson, E.F. Wood and M. Zion

5. Surface Soil Moisture Estimation with Radarsat: Early Results NA
Brisco, B., R.J. Brown and T.J. Pultz

6. SIR-C/X-SAR as a Bridge to Soil Moisture Estimation Using Current and Future Operational Satellite Radars 1064
Jackson, T.J., T.L. Li, E.F. Wood, A. Hsu, P.E. O'Neill and E.T. Engman

7. Backscattering over Bare Soils: Measurements and Simulations Using SIRC/XSAR and ERASME 1994 Data over Orgeval 1067
Zribi, M., Taconet, O., S. Le Hegarat-Mascle, D. Vidal-Madjar, C. Emblanch, C. Loumagne and M. Normand

8. Polarimetric Backscattering Measurements of Herbaceous Vegetation: A Sensitivity Study for Soil Moisture Retrieval 1070
Chiu, T.C., K. Sarabandi and F.T. Ulaby

9. Comparison of Spatial Statistics of SAR-Derived and In-SITU Soil Moisture Estimates 1073
Hirsave, P.P., R.M. Narayanan, B.T. Tracy , B.L. Gwilliam R.L. Bolus, T. Pangburn and H.A. McKim

10. Soil Moisture and Temperature Determination by Recursive Assimilation of Multifrequency Observations Using Simplified Models of Soil Heat and Moisture Flow and Emission 1076
Galantowicz, J.F., and D. Entekhabi

WPAM -- Land Cover: Radar for Forest Mapping

1. Radar Backscatter Components from Ponderosa Pine Forests 1077
Wang, Y., and F.W. Davis

2. The Applications of Space Born SAR on Forestry NA
Zeng, Q., J. Jiao, Z. Li and X. Che

3. The Suitability of Multifrequency, Multipolarimetric and Multitemporal Radar Data for Forest Monitoring 1080
Haas, A., and B. Forster

4. Sensitivity of Modeled C-Band from Loblolly Pine Forest Backscatter to Soil Surface Roughness and Moisture 1083
Wang, Y., J.L. Day and F.W. Davis

5. Multifrequency and Polarimetric Analysis of Forests with SIR-C/X-SAR Data 1086
Seifert, F.M., H. Kietzmann and M. Zink

6. Optimization of a Scanning Radar Altimeter for Forest Inventory: A Simulation Method 1089
Hyyppa, J., and M. Hallikainen

7. Temporal Stability of Northern Forest Biophysical Retrievals Using SIR-C/X-SAR 1092
Dobson, M.C., L.E. Pierce, K.M. Bergen and F.T. Ulaby

8. Regional Stability of an ERS/JERS-1 Classifier 1093
Kellndorfer, J.M., M.C. Dobson and F.T. Ulaby

9. Radar Modeling of Forest Spatial Structure 1096
Sun, G., and K.J. Ranson

10. Comparative Analysis of Forests Types Classification Methods Using SIR-C Multifrequency, Multipolarization and Repeated Orbits Interferometry Data NA
Zaitsev, V.V., and A.I. Zakharov

WPAA -- Weather Information Systems

1. Knowledge Based System for Weather Information Processing and Forecasting 1099
Siddiqui, K.J.

2. A Database Program to Archive and Analyze Current Weather Data 1102
Parkin, S.H. and J.P. Refling

3. Neural Network-Based Cloud Detection/Classification Using Textural and Spectral Features 1105
Azimi-Sadjadi, M.R., M.A. Shaikh, B. Tian , K.E. Eis and D. Reinke

4. An FFT-Based Algorithm for Computation of Gabor Transform with its Application to Cloud Detection/ Classification 1108
Tian, B., M.R. Azimi-Sadjadi, M.A. Shaikh and K.E. Eis

5. A Prototype Sea Ice Mapping System Using a Geographical Information System and Expert Knowledge 1111
Williams, R.N., and J. Hartnett

6. Campaign of Validation of Aerosol Optical Depth from Satellites in the Canary Islands Zone NA
Exposito, F.J., J.P. Diaz, M. Arbelo, J.C. Guerra and F. Herrera

7. A Split-Window Equation with Variable Coefficients to Obtain SST in Midlatitudes NA
Arbelo, M., V. Caselles, F.J. Exposito and F. Herrera

8. Pluviometry and Vegetation Monitoring in the Canary Island Zone Using the NOAA Advanced Very High Resolution Radiometer NA
Hernandez, P.A., M. Arbelo, F.J. Exposito and F. Herrera

9. Combined Use of Radar and Satellite Information for Precipitation Estimation in Hungary 1114
Csiszar, I., and J. Kerenyi

10. DSP Architecture for Dual Waveband Meteorological Data Processing NA
Malinovski, V.

WPCP -- Polarimetric Radiometry

1. The AEOLIS Program: Prospects for Future Low-Cost, Space-Borne Vector Wind Sensors 1117
Van Woert, M.L.

2. Polarimetric Scanning Radiometer for Airborne Microwave Imaging Studies 1120
Piepmeier, J.R., and A.J. Gasiewski

3. Ocean Surface Wind Direction Retrievals Using Microwave Polarimetric Radiometer Data 1123
Gaiserl, P.W., P. Chang and L. Li

4. Polarimetric Observation of Ocean Internal Waves by Microwave Radiometers During the Coastal Ocean Probing Experiment 1126
Irisov, V.G., and Yu.G. Trokhimovski

5. Broadband Phenomena in Oceanic Passive Wind Direction Signatures: The Sensitivity to Wave Asymmetry, Foam, and Atmospheric Profile 1129
Kunkee, D.B., and A.J. Gasiewski

6. A Numerical Study of Ocean Thermal Emission NA
Johnson, J.T., R.T. Shin, J.A. Kong, L. Tsang and K. Pak

7. A Comparison of Sea Emission Between Experimental Data and Model Predictions NA
Chen, K.S., S.J. Lai, A.K. Fung and S.Y. Yueh

8. Modelling of Wind Direction Signals in Polarimetric Sea Surface Brightness Temperatures 1132
Yueh, S.H., W.J. Wilson and F.K. Li

9. The Atmosphere Influence on Sea-Surface Polarized Microwave Emission 1135
Pospelov, M.N.

10. Oceanic Wind Vector Determination Using a Dual-Frequency Microwave Airborne Radiometer - Theory and Experiment 1138
Jacobson, M.D., W.J. Emery and E.R. Westwater

WPED -- SAR Applications for Oceanography

1. A PC-Based Remote Sensing System for Detection and Classification of Oceanic Fronts 1141
Askari, F., E. Malaret, D. Lyzenga, M. Collins, T. Donato, A. Skoelv, T. Jenserud and C. Brownsword

2. A Lightweight Spectrasat Concept for Global Ocean Wave Monitoring 1143
Beal, R.C., D.Y. Kusneirkeiwicz, J.L. MacArthur, F.M. Monaldo and S.F. Oden

WPED *continued* -- SAR Applications for Oceanography

3. Using the CCRS Along Track InSAR to Measure and Interpret Ocean Surface Currents 1146
Campbell, J.W.M., A.L. Gray, J.H. Clark, J. Gower and K.E. Mattar

4. Comparison of Wave Parameters Measured from the SIR-C On-Board Processor with WAM Predictions in the Southern Ocean 1149
Monaldo, F.M.

5. Estimation of Thermocline Depths From SAR Imagery and a Two Layer Density Model 1152
Porter, D.L., and D.R. Thompson

6. Validation of SAR Ocean Wave Measurements: ERS-1 and CV-580 Cross Spectra and CV-580 Along-Track InSAR 1155
Vachon, P.W., C. Bjerkelund, J. Buckley, J. Campbell, F.W. Dobson, A.L. Gray, H. Johnsen and R. Lalbeharry

7. Coast Watch - 95: ERS - 1/2 SAR Applications of Mesoscale Upper Ocean and Atmospheric Boundary Layer Process off the Coast of Norway 1158
Johannessen, O.M., J.A. Johannessen, A.D. Jenkins, K. Davidson, D.R. Lyzenga, R Shuchman, P. Samuel, H.A. Espedal, J. Knulst, E. Dano and M. Reistad

8. Evaluation of RADARSAT Synthetic Aperture Radar Data for Ocean Wave Measurements and Ship Detection NA
Olsen, R.B., P. Bugden, P. Hoyt, M.Henschel and M.R. Lewis

9. The Imaging of Submarine Sandwaves with Multi-Band SAR NA
Vogelzang, J.

10. Ocean Surface Slope Measurement Using Polarimetric SAR 1162
Lee, J.S. and D.L. Schuler

WPES -- Educational Initiatives II

1. Studying the Earth's Environment From Space - A Curriculum Workshop 1165
Alfultis, M.A.

2. NASA-NOAA Summer School for Earth Science - Processes of Global Change and Global Change Workshop for Teachers NA
Syvertson, M., S. Ride, D. McCleese and W. Mohling

3. Mission: Arkansas - Curriculum Enhancement and Dissemination of K-12 Science Mathematics Using Space Based Data and Geographic Information Systems NA
Hehr, L.H.

4. Constructing Earth System Science Learning Through Multidisciplinary Studies of Global Change 1166
Fortner, R.W., and V.J. Mayer

5. A CD-ROM Study Package on Current Forest Issues for Use in Secondary School Science Classes 1169
Hassol, S., and C.J. Tucker

6. Using Distributed Multimedia Systems to Enable Earth Systems Education in the Earth System Science Community NA
Keeler, M.,and F. Mahootian

7. Our Role in the Earth System: One K-12 School District's Science Education Initiative 1172
Lindgren, P.D.

8. Earth System Science Education: A Continuing Collaboration 1175
Johnson, D.R., M. Ruzek and M. Kalb

9. OMSI-NSF Young Scholars Research Participation Program, Oregon Museum of Science and Industry 1178
Gottfried, J.

10. Alaska SAR Facility Education Outreach 1181
Sandberg, D., and F. Carsey

WPF -- Research Progress Under the ONR Sea Ice Electromagnetics ARI

1. Observations of Sea Ice Physical Properties During the Sea Ice Electromagnetics Initiative 1184
Gow, A.J., and D.K. Perovich

2. Physical and Electrical Characteristics of Snow on Sea Ice: Implications for Forward Scattering Model Development 1187
Barber, D.G., S.D. Drobot and J. Iacozza

3. Sea Ice Polarimetric Backscatter Signatures at C Band 1190
Nghiem, S.V., R. Kwok, S.H. Yueh, J.A. Kong, A.J. Gow, D.K. Perovich, S. Martin and R. Drucker

4. Polarimetric Properties of Simulated Sea Ice with Special Focus on Property Retrieval and Important Scattering Processes 1193
Onstott, R.G.

5. Ultra-Wideband Radar Measurements of over Bare and Snow-Covered Saline Ice 1196
Gogineni, S.P., P. Kanagaratnam and K. Jezek

6. Microwave and Thermal Infrared Emission from Young Sea Ice and Pancake Ice 1199
Grenfell, T.C.

7. Modeling of Ice Thickness Effect and Its Application to Data Interpretation 1202
Fung, A.K, and R.G. Onstott

8. Electromagnetic Inversion of the Physical Properties of Sea Ice NA
Golden, K.M.

9. Inversion of Wideband Microwave Reflectivity to Estimate the Thickness of Arctic Lead-like Sea Ice 1205
Winebrenner, D.P., and J. Sylvester

10. Thickness Retrieval Using Time Series Electromagnetic Measurements of Laboratory Grown Saline Ice 1208
Shih, S.E., K.H. Ding, S.V. Nghiem, C.C. Hsu, J.A. Kong and A.K. Jordan

WPP -- SAR Processor Systems and Algorithms

1. ASF SAR Processing System Performance Overview NA
Jin, M., K. Leung, M. Chen and A. Chu

2. Vexcel Corporations' SAR Processing Ground Station: An Overview 1211
Compton, M., and R.E. Carande

3. Azimuth and Range Scaling for SAR and ScanSAR Processing 1214
Moreira, A., R. Scheiber and J. Mittermayer

WPP *continued* -- SAR Processor Systems and Algorithms

4. High Precision Processing of SIR-C ScanSAR Data 1217
Mittermayer, J., A. Moreira, G. Davidson, R. Bamler and Y.L. Desnos

5. A Comparison of the Range-Doppler and Chirp Scaling Algorithms with Reference to RADARSAT 1221
Hughes, W., K.A. Gault and J. Princz

6. Comparison of Medium Resolution Algorithms for Spacecraft On-Board SAR Image Generation 1224
Vidal, A., and J. Rosello

7. Registration SAR Images Using the Chrip Scaling Algorithm 1227
Fernandes, D., G. Waller and J. R. Moreira

8. Autofocus of Wide Azimuth Angle SAR Images by Contrast Optimisation 1230
Berizzi, F., G. Corsini, M. Diani and M. Veltroni

9. High Frequency Phase Errors in SAR Imagery and Implications for Autofocus 1233
Marechal, N.

10. Phase Errors Compensation in SAR Imaging 1241
Isernia, T., V. Pascazio, R. Pierri and G. Schirinzi

WPT -- Clouds, Aerosols and Boundary Layer

1. Cirrus Cloud Detection by Micro Pulse Lidar: Algorithm Development and Testing 1244
Galbraith, A.E., J.A. Reagan and J.D. Spinhirne

2. Cloud Masking with Satellite Infrared Images over Polar Oceans 1247
Schlueter, N., and T. Markus

3. Cloud Corrections for Satellite Images NA
Peltoniemi, J.I.

4. The Estimation of Aerosol Models by the Reflectance Analysis of the Airborne POLDER Data 1250
Yamazaki, A., K. Ueda, Y. Kawata and T. Kusaka

5. Particle Size Distributions and Extinction Determined by a Unique Bistatic Lidar Technique 1253
Stevens, T.D., and C.R. Philbrick

6. Remote Sensing of the Marine Atmospheric Boundary Layer and Oean Surface Winds: Observations from the LITE Correlative Flights 1257
Palm, S.P., G. Schwemmer, D. Vandemark, D. Hines and S.H. Melfi

7. Remote Measurement of Coastal Marine Atmospheric Boundary Layer (MABL) Features 1260
Jordan, M.S., C.H. Wash and K.L. Davidson

8. Estimation of the Ocean/Atmosphere Boundary Layer Height of Water Vapor from Space 1263
Ruf, C.S., and S.E. Beus

9. Rain Measurement with SIR-C/X-SAR 1266
Moore, R.K., A. Mogili, Y. Fang, B. Beh and A. Ahamad

10. Investigations of Atmospheric Boundary Layer by Using 5-Millimeter Radiometer NA
Kadygrov, E.N., and A.V. Troitsky

WPV -- Calibration and Correction Algorithms for Radiometric and Reflectance Measures

1. Artifact Correction and Absolute Radiometric Calibration Techniques Employed in the Landsat 7 Image Assessment System 1270
Boncyk, W.C., B.L. Markham, J.L. Barker and D.L. Helder

2. Landsat-7 Enhanced Thematic Mapper Plus In-Flight Radiometric Calibration 1273
Markham, B.L., J.L. Barkerm,W.C. Boncyk, E. Kaita and D.L. Helder

3. Short Term Calibration of Landsat TM: Recent Findings and Suggested Techniques 1276
Helder, D., W. Boncyk, J.L. Barker and B.L. Markham

4. Comparison of Scene-Dependent Radiometric Validation Methodologies for EOS-AM1 MODIS Level-1 Products NA
Barker, J.L., and S.G. Ungar

5. In-Flight Radiometric Calibration Plans for the Earth Observing System -- Multi-Angle Imaging Spectroradiometer 1279
Bruegge, C., R.Woodhouse, and D. Diner

6. Cross-Calibration of Two Small Footprint Sensors 1283
Gustafson-Bold, C.L., and K.J. Thome

7. Evaluation of The Aerosol Scattering Phase Function from PGAMS Observation of Sky Path Radiance 1286
Schiller, S., and J. Luvall

8. RADARSAT CALIBRATION: The Operational System and Initial Results 1290
Srivastava, S.K., T.I. Lukowski, R.K. Hawkins, C. Cloutier, L.D. Teany, N.W. Shepherd, R.B. Gray, A.P. Luscombe and R. Banik

9. Calibration Methods and Results for the Advanced Solid-State Array Spectroradiometer (ASAS) NA
Dabney, P.W., M.R. Tierney, J.R. Irons,W.M. Kovalick, M.C. Bur and C.A. Russell

10. Calibration of the AVHRR Thermal Infrared Channels: Determining the Temperature of the Internal Calibration Target 1293
Steyn-Ross, D.A., M.L. Steyn-Ross and S. Clift

WPZ -- Soil Moisture II

1. The Influence of Soil Moisture on Temporal CVV- and LHH- Signatures from Vegetated Fields - Summary of the DLR E-SAR Cleopatra Campaign NA
Schmullius, C., and J. Nithack

2. A Modified IEM Model for Scattering from Soil Surfaces with Application to Soil Moisture Sensing 1297
Fung, A.K., M.S. Dawson, K.S. Chen, A.Y. Hsu, E.T. Engman, P.O. O'Neill and J. Wang

3. Soil Moisture Retreival Using the Danish L- & C-Band Polarimetric SAR 1300
Ji, J., P. van der Keur, A. Thomsen and H. Skriver

4. Remote Sensing of Soil Moisture Using EMAC ESAR Data 1303
Su, Z., P.A. Troch and F.P. De Troch

5. Use of Polariztion Synthesis From Polarimetric SAR Data for Roughness Estimation over Bare Fields 1306
Mattia, F., J.C. Souyris, T. Le Toan, G. De Carolis, N. Floury, F. Posa and G. Pasquariello

6. Microwave Remote Sensing of Land Surfaces Soil Moisture at Global Hydrology and Climate Center 1309
Wu, S.T.S.

WPZ *continued* -- Soil Moisture II

7. Soil Hydraulic Characterization Derived from Landsat TM-5 Data 1312
Bresci, E., and I. Becchi

8. An Optical Reflectance Technique for Soil Moisture Measurement - Part I: Theory, Description and Application 1315
Belisle, W.R., A. Sharma and T.L. Coleman

9. Accuracy of Soil Moisture Determination by Means of Passive Microwave Remote Sensing Method: Modeling and Experiments 1320
Liberman, B., and A. Milshin

10. Microwave Dielectric Behavior of Wet Soils in Region of Transition Moisture 1323
Belyaeva, T.A., and Yu.M. Sosnovsky

WEAM -- Infrared and Optical Remote Sensing of the Ocean Surface

1. Ocean Skin Temperature Modulation by Swell Waves NA
G.A. Wick, Hesany and A.T. Jessup

2. Monitoring of the Sea Surface Thermal Patterns in a Marginal Sea Affected by an Ocean NA
Nakamura, S.

3. Sensitivity Analysis of a Coupled Optical Remote Sensing and Three Dimensional Hydrodynamic Model NA
Bostater, C., and T. McNally

4. Ocean Ripple Statistics Measured with a Scanning-Laser Glint Sensor 1328
Shaw, J.A., and J.H. Churnside

5. The Remote Technique of Sea Surface Waves by Optical Sensors 1331
Titov, V.I., and E.M. Zuykova

WEF -- Volume Scattering II

1. Radio Wave Propagation Along Mixed Paths Through Four-Layered Model of Rain Forest: A Closed Form Solution NA
Li, L.W., T.S. Yeo, P.S. Kooi and M.S. Leong

2. A Coherent Scattering Model for Forest Canopies Based on Monte Carlo Simulation of Fractal Generated Trees 1334
Lin, Y.C., and K. Sarabandi

3. A Numerically Derived Electromagnetic Scattering Model for Grass Grain Heads 1337
Siqueira, P., and K. Sarabandi

4. Electromagnetic Scattering by Multiple Three-Dimensional Scatteres Buried Under One-Dimensional Multi-Layered Media 1340
Cui, T.J., and W. Wiesbeck

5. Electromagnetic Wave Transmission in Randomly Distributed Inhomogeneous Spherical Particles NA
Osharin, A.M.

WEH -- Subsurface Sensing and Material Properties II

1. Wave Reflection From a Target Immersed into Disordered Medium — NA
Kanzieper, E., and V. Freilikher

2. The Modified Rayleigh-Gans Approach and Scattering Waves — 1343
Yildirim, O.

3. An Inverse Algorithm for Integral Equation Formaultion of Dielectric Loaded Cavities — 1346
Sabet, K.F., K. Sarabandi, J.G. Yook and L.P.B. Katehi

4. Method for Retrieval of Media Structural Parameters from Frequency Dependence of Transmission Coefficient — NA
Boyarskii, D.A.

5. Application of SIR-C L/C/X-Band Radar Data for Mineral Exploration Experiment in Hwanggangni Mining District, Korea — NA
Jiang, W.W., C.S. So, Y. Yamaguchi, W.M. Moon and S.K. Choi

WEM -- Remote Sensing Missions and Programs

1. Early Images from the RADARSAT Synthetic Aperture Radar — 1352
Luscombe, A.P., R. Gray, N. Shepherd, S. Srivastava, D. Meier and W. Jeffries

2. The Development of the ENVISAT-1 Advanced Synthetic Aperture Radar — 1355
Mancini, P., J.L. Suchall, Y.L. Desnos, R. Torres, J. Guijarro and G. Graf

3. Processing and Validation of the ERS-1 Radar Altimeter Data at the Italian PAF — NA
Celani, C., A. Bartoloni, G. Milillo and F. Nirchio

4. An Alaska SAR Overview in the RADARSAT Era — 1358
Cuddy, D., and K. Leung

5. Cassini Radar Investigation of Titan — NA
Wall, S., C. Elachi and L. Roth

WEP -- Active and Passive Remote Sensing of Precipitation

1. Validation and Ground Truth for TRMM Precipitation Radar Using the MU Radar — 1361
Sato, T., T. Teraoka and I. Kimura

2. Preliminary Results of Ground-Based Rain Measurements with a Dual-Frequency Multiparameter Radar-Radiometer — 1364
Horie, H., R. Meneghini and T. Iguchi

3. Active and Passive Microwave for Rainfall Monitoring — 1367
Nativi, S., L. Baldini, D. Giuli and P. Mazetti

4. Study of Potential of a Profile-Based Algorithm for Precipitation Retreival from MIMR — NA
Panegrossi, G., S. Dietrich, F.S. Marzano and A. Mugnai

5. Investigation of Multifrequency Multipolarisation Radar Signatures of Rain Cells, Derived From SIR-C/X-SAR Data — 1370
Melsheimer, C., W. Alpers and M. Bao

WESF -- Land Cover: Innovative Classification Methods II

1. Mathematical Morphology, Urban Change, Image-Oriented Geographic Information Systems 1373
Maupin, P., and B. Solaiman

2. Fuzzy Classification Techniques for Urban Area Recognition 1376
Console, E., and M.C. Mouchot

3. Robust Mixed Pixel Classification Using the Hypothesis Testing Hough Transform 1379
Bosdogianni, P., M. Petrou and J. Kittler

4. Improving Automated Land Cover Mapping by Identifying and Eliminating Mislabeled Observations from Training Data 1382
Brodley, C.E., and M.A. Friedl

5. An Automatic Technique for Detecting Land-Cover Transitions NA
Serpico, S.B., L. Bruzzone, F. Roli and M.A. Gomarasca

WES -- Ocean Waves and Winds II

1. A Not Pointwise Approach to the Wind Field Retrieval from Scatterometer Data NA
Bartoloni, A., C. D'Amelio and G. Milillo

2. X-Band Coherent Measurements of Ocean Backscatter from an Airship NA
Hesany, V., W.J. Plant, W.C. Keller and K. Hayes

3. Observations of the Ocean Surface Using an Aircraft Radar Altimeter, Scatteromenter and ROWS 1385
Vandemark, D., D. Hines, B. Chapron, J. Carswell and W. Donnelly

4. Dependence of Altimeter Returns on Wind Stress and Wave Age 1389
Elfouhaily, T., B. Chapron, V. Kerbaol, J. Gourrion, J. Tournadre, K. Katsaros and D. Vandemark

5. Correcting SeaWinds Scatterometer Measurements for Atmospheric Attenuation 1392
Moore, R.K., N. Kambhammettu and S. Song

WET -- Remote Sensing of Surface Waters

1. Spectrometry of Turbidity in Surface Water 1395
Han, L.

2. Validation of an Optical Remote Sensing Model Using Reflectance Signatures Collected From an Airborne Sensor NA
Bostater, C., W. Ma, T. McNally, M. Keller and M. Gimond

3. Quantitative Remote Estimation of Algal Density, Pigment Concentrations and Non-organic Suspended Matter in Aquatic Environments, Principles and Techniques NA
Gitelson, A.A., Y.Z. Yacobi and S. Plotnizky

4. SeaWiFS and MERIS: A Comparison of Their Performance for the Estimation of Optically Active Components in Ocean Water 1398
Cipollini, P., and G. Corsini

5. A Numerical Study of the Composite Surface Model for Ocean Scattering 1401
Johnson, J.T., R.T. Shin, J.A. Kong, L. Tsang and K. Pak

6. Algorithm Requirements for Operational Use of Airborne Remote Sensing in Inland Water Management NA
Dekker, A.G., H.J. Hoogenboom and M. Rijkeboer

THAAM -- Retrieval of Ecosystem Parameters from BRDF Data and Models

1. Kilometer-Scale Global Albedo from MODIS 1405
Wanner, W., A.H. Strahler, B. Zhang and P. Lewis

2. The Influence of Directional Sampling on Bidirectional Reflectance and Albedo Retrieval Using Kernel-Driven Models 1408
Wanner, W., P. Lewis and J.L. Rougean

3. Semiempirical Modelling of Bidirectional Utilizing the MODIS BRDF/Albedo Algorithm Models 1411
White, H.P., J.R. Miller, R. Soffer and W. Wanner

4. Analytic Forms of Bidirectional Reflectance Functions for Earth Radiation Budget Studies 1414
Manalo-Smith, N., and G.L. Smith

5. The Use of Bidirectional Reflectance to Estimate Broadband Hemispherical Albedo Over Tasmania 1417
Russell, M., and M. Nunez

6. A Technique for Combining Geometrical and Spectral BRDF Information for Retrieval of Plant Canopy Characteristics Uing AVHRR Optical Data NA
Braswell, B.H., J.L. Privette and D.S. Schimel

7. Estimating Hemispherical Reflectance and Selected Biophysical Parameters for Boreal Forest Canopies Using Spectral Bidirectional Reflectance Data Acquired by ASAS NA
Russell, C.A., J.R. Irons and P.W. Dabney

8. An Integrated Approach to Estimating LAI Using Multitemporal and Multidirectional Remote Sensing Measurements 1420
Qi, J., and M.S. Moran

9. Comparison of Vegetation Index Compositing Scenarios: BRDF Versus Maximum VI Approaches 1423
van Leeuwen, W.J.D., A.R. Huete, S. Jia and C.L. Walthall

10. Retrieval of Canopy Structural Parameters from Multi-Angle Observations Using an Artificial Neural Network 1426
Abuelgasim, A.A., S. Gopal and A.H. Strahler

THAAA -- Microwave/Millimeter-Wave Atmospheric Absorption and Scattering Models

1. Observations and Modelling of Radiometric Signatures of Storms in the Frequency Range of 90-220 GHz 1429
Wang, J.R., C. Kummerow, P. Racette, W. Olson and J. Zhan

2. Atmoshperic Water-Vapor Microwave Absorption - A Review of Models and Measurements NA
Rosenkranz, P.W.

3. Model Based Retrievals of Water Vapor Profiles from Microwave Radiances NA
Wilheit, T.T., C.B. Blankenship and S.L. Moore

4. Observed and Theoretical Millimeter Wave Emission in the Tropics 1432
Snider, J.B., and D.A. Hazen

5. Atmospheric Microwave Absorption Parameter Estimation Near 22 GHz 1435
Cruz Pol, S.L., C.S. Ruf and SJ. Keihm

6. Atmospheric Water Vapor and the Total GPS Signal Delay NA
Gutman, S.I., D.E. Wolfe and R.B. Chadwick

THAAA *continued* -- Microwave/Millimeter-Wave Atmospheric Absorption and Scattering Models

7. Recent Advances in Satellite Sounding at the U.K. Meteorological Office 1438
Barwell, B.R.

8. Wind Speed and Total Integrated Water Vapor Measurements Over the Ocean Using the Special Sensor Microwave/Imager (SSM/I) NA
Manning, W.

9. Influence of Scattering in the Absorbing Line Structure in Two-Phase Media 1441
German, M.L., V.P. Nekrasov and E.F. Nogotov

10. Atmospheric Effects Due to Different Particle Shapes on Propagation 1444
Yildirim, O.

THACP -- Microwave Remote Sensing of Ocean Surface Winds I

1. JPL Wind Radiometer Measurements NA
Wilson, W.J., and S.H. Yueh

2. Surface and Airborne Radiometric Observations During the Coastal Ocean Probing Experiment: An Overview 1450
Westwater, E.R., V.G. Irisov, L.S. Fedor and Yu.G. Trokhimovski

3. Surface Wind Measurements by Radiometer- Polarimeters in Frame of Russia Airspace Programs 1454
Kravtsov, Yu.A., A.V. Kuzmin, M.N. Pospelov and A.I. Smirnov

4. Observation of the Ocean Brightness Temperature Anisotrophy During the Coastal Ocean Probing Experiment 1457
Irisov, V.G., and Yu.G. Trokhimovski

5. High Altitude Aircraft Mapping of Near Surface Ocean Winds 1460
Hood, R.E., and R.W. Spencer

6. Performance Analysis for the Sea Winds Scatterometer 1463
Long, D.G., and M.W. Spencer

7. Remote Sensing of the Near Surface-Ocean Wind Vector Under Low-Wind Conditions Using Scatterometry 1466
Carswell, J., W. Donnelly and R. McIntosh

8. Ku-Band Ocean Backscatter Functions for Surface Wind Retrieval 1469
Nghiem, S.V., F.K. Li and G. Neumann

9. Scatterometer Measurements of Ocean Surface Stress Magnitude and Direction from Aircraft During SWADE and from ERS-1 1472
Weissman, D.E.

10. Statistics of Radar Backscatter from Wind Waves 1475
Long, D.G., R. Reed and D.V. Arnold

THAED -- Remote Sensing of Littoral Submesoscale Processes II

1. An Analysis of Drainage Flow Exit Jets Over the Chesapeake Bay as Seen in an ERS-1 SAR Image NA
Winstead, N.S., G.S. Young, D.R. Thompson and H.N. Shirer

2. Study of Katabatic Wind Fields by Using ERS-1 Synthetic Aperture Radar Imagery of the Ocean Surface 1478
Alpers, W., U. Pahl, G. Gross and D. Etling

3. A Coupled Wind — Internal Wave System 1481
Smirnov, A.V.

4. A Large-Scale Evaluation of Features for Automatic Detection of Oil Spills in ERS SAR Images 1484
Schistad Solberg, A.H., and R. Solberg

5. Ocean Features Evaluation from RADARSAT SAR Imagery NA
Staples, G.C.

6. Meteorological Explanation of a Sea Surface Roughness Streak Imaged by ERS-1 SAR Near Block Island, New York NA
Winstead, N.S., H.N. Shirer, T.D. Sikora and R.C. Beal

7. Internal Waves in the Strait of Messina Observed by the ERS1/2 Synthetic Aperture Radar 1487
Brandt, P., A. Rubino and W. Alpers

8. Studies of Rainfall Footprints on the Sea Conducted by Spaceborne SAR "Almaz" and Shipborne Microwave Radiometers 1490
Bulatov, M.G., M.D. Raev and E.I. Skvortsov

9. The Microwave Radar Signal Doppler Spectrum and the Problem of Ocean Surface Slicks Detection 1493
Kanevsky, M.B., and V.Y. Karaev

10. The Remote Sensing of the Ocean Surface in the Frontal Zone 1495
Lavrenov, I.

THAES -- Educational Initiatives III

1. The Weather Visualizer: A Java Tool for Interactive Learning 1498
Hall, S.E., M.K. Ramamurthy, R.B. Wilhelmson, J. Plutchak, D. Wojtowicz and M. Sridhar

2. Lessons Learned From Using GIS/RS as an Integrative Tool for Interdisciplinary Learing and Teaching in a Senior-Level Capstone Course on Global Change at Westminster College of Salt Lake City 1501
Ford, R.E., and J. Hipple

3. Classroom Applications of Marine and Environmental Remote Sensing Data 1504
Alfultis, M.A., and M.R. Hicks

4. A Model for Environmental Earth Science Module Design 1506
Meyers, R.J., J.A. Botti and K.D. Gonzalez

5. Remote Sensing and Inner City Youth: A Pilot Collaboration of the Aspen Global Change Institute's Ground Truth Studies and the 4-H After School Programs 1509
Katzenberger, J.

6. The Arctic Observatory: An Educational Tool for Intercomparison Studies and Time-Series Analysis Using Five Arctic Parameters on CD-Rom NA
Keeler, M., and F. Mahootian

7. Texas Space Grant Consortium: Educational Opportunites in Earth Science and Remote Sensing 1512
Neuenschwander, A.

THAF -- Sea Ice Remote Sensing (Models, Techniques and Applications) II

1. The SIMMS'93 SAR Polarimetry Experiment: Combined Surface and Airborne Radar Measurements for Winter Sea Ice — 1515
Livingstone, C.E., D.G. Barber, F. Spring and W. Liu

2. Ice Roughness Classification and ERS SAR Imagery of Arctic Sea Ice: Evaluation of Feature-Extraction Algorithms by Genetic Programming — 1520
Daida, J.M., R.G. Onstott, T.F. Bersano-Begey, S.J. Ross and J.F. Vesecky

3. A Microwave Technique for Mapping Ice Temperature in the Arctic Seasonal Ice Zone — 1523
St. Germain, K.M., and D.J. Cavalieri

4. A Neural Network Sea Ice Edge Classifier for the NASA Scatterometer — 1526
Alhumaidi, S.M., W.L. Jones, J.D. Park, S. Ferguson and M.H. Thursby

5. Fusion of Satellite SAR and SSM/I Data for Thin Sea Ice Concentration — NA
Beaven, S.G.

6. Comparison of Open Water and Thin Ice Areas Derived from Satellite Passive Microwave Data with Aircraft Measurements and Satellite Infrared Data in the Bering Sea — 1529
Markus, T., and D.J. Cavalieri

7. Lake Superior Ice Concentration Using SSM/I — NA
Pilant, D.

8. Measuring Sea Ice Floe Size During Summer with ERS SAR Imagery — NA
Holt, B., and S. Martin

9. Separating Ice-Water Composites and Computing Floe Size Distributions — 1532
Soh, L.K., D. Haverkamp and C. Tsatsoulis

THAH -- Emerging Technologies and Techniques

1. Laser Diode Based New Generation Lidars — 1535
Reagan, J.A., H. Liu and J.F. McCalmont

2. Antartic Miniature Lidar — 1538
Rall, J.A.R., and J.B. Abshire

3. Fulfilling the Promise of Imaging Spectrometry: Underappreciated Aspects of Sensor Performance Which Affect Data Utility — NA
Chrien, T.G., M.L. Eastwood, R.O. Green, C.M. Sarture and G.H. Bearman

4. Use of FT-IR and UV Spectrometers for Monitoring Multiple Pollutants in the Lower Troposphere — 1541
Gibbs, D.P., and B. Krenek

5. Multimeter Wave Imaging Technology — 1544
Huguenin, G.R.

6. Synthetic Aperture Radiometers for Microwave Remote Sensing from Space — 1547
Le Vine, D.M., and C.T. Swift

7. Capabilities and Recent Results From the ER-2 Doppler Radar (EDOP) — 1550
Bidwell, S.W., G.M. Heymsfield and I.J. Caylor

8. Millimeter-wave Radars for Remotely Sensing Clouds and Precipitation 1553
Mead, J.B., A.L. Pazmany, S.M. Sekelsky, R. Bambha and R.E. McIntosh

9. Airborne SAR Interferometry: Potential and Future Applications NA
Moreira, J.

10. Satellite SAR Interferometry: Present Status and Future Technologies NA
Guarnieri, A. M., C. Prati and F. Rocca



THAP -- SAR Speckle and Classification

1. Polarimetric Image Classification Using Optimal Decomposition of Radar Polarization Signatures 1556
Dong, Y., B. Forster and C. Ticehurst

2. A Comprehensive Evaluation of Filters for Radar Speckle Suppression 1559
Sheng, Y., and Z.G. Xia

3. SIR-C Polarimetric Image Segmentation by Neural Network 1562
Sergi, R., G. Satalino, B. Solaiman and G. Pasquariello

4. Determining the Number of Classes for Segmentation in SAR Sea Ice Imagery 1565
Soh, L.K., and C. Tsatsoulis

5. A Multi-Temporal Classifier for SIR-C/X-SAR Imagery 1568
Bergen, K.M., L.E. Pierce, M.c. Dobson and F.T. Ulaby

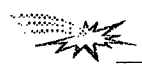
6. Study on Target Detection Using Multi-Look Polarimetric SAR Data NA
Xiong, H., G. Liu and S. Huang

7. Optimal Multi-look Polarimetric Speckle Reduction and Its Effects on Terrain Classification 1571
Liu, G., S. Huang, A. Torre and F. Rubertone

8. Polarimetric Signature Preservation in SAR Speckle Filtering 1574
Lee, J.S., G. De Grandi, M.R. Grunes and E. Nezry

9. Reduction of Multiplicative Noise in SAR Imaging by Wiener Filtering 1577
Pascazio, V., and G. Schirinzi

10. Statistical Characterization of the Phase Process in Interferometric SAR Images 1580
Di Bisceglie, M., and C. Galdi



THAV -- Image Processing: Restoration Problems

1. Aerosol Properties From Blurring Effect in Remotely Sensed Images 1584
Leone, A., B. Bulgarelli, M. Garello and G. Perona

2. Deriving the Anisotropic Atmospheric Point Spread Function of ASAS Off-Nadir Images and Removal of the Adjacency Effect by Inverse Filtering 1587
Hu, B., X. Li and A.H. Strahler

3. Quantitative Evaluation of Edge Preserving Noise-Smoothing Filter 1590
Pasaribu, D.P.

THAV *continued* -- Image Processing: Restoration Problems

4. A Constructive Deconvolution Procedure of Bandpass Signals by Homomorphic Analysis 1592
Marenco, A.L., and V.K. Madisetti

5. Cubic Covolution for One-Pass Restoration and Resampling 1597
Reichenbach, S.F., and K. Haake

THAV -- Image Processing: Registration and Resampling

6. Quantitative Aspects of the Radiometric Normalization of Multi-Temporal Satellite Scenes in the Creation of Large Area Image Mosaics NA
Guindon, B.

7. Landsat Thematic Mapper Band-to-Band Registration 1600
Barker, J.L., and J.C. Seiferth

8. Digital Resampling for Image Processing and Fusion of SSM/I Data 1603
Pellegrini, P.F., E. Piazza and A. Nervi

9. Spatial Resolution Enhancement of SSM/I Data: Vegetation Studies of the Amazon Basin 1606
Long, D.G., D.R. Daum and P.J. Hardin

10. Automated Image Registration for Change Detection from Landsat Thematic Mapper Imagery 1609
Dai, X., S. Khorram and H. Cheshire

THAZ -- The World's Airborne SAR Facilities I: Conventional Frequencies & Respective Applications

1. NASA/JPL Airborne Three-Frequency Polarimetric/Interferometric SAR System 1612
Kim, Y., Y. Lou, J. van Zyl, L. Maldonado, T. Miller, T. Sato and W. Skotnicki

2. Hughes Integrated Synthetic Aperture Radar 1615
Bayma, R.W.

3. Ingara: An Integrated Airborne Imaging Radar System 1618
Stacey, N.J.S., M.P. Burgess, M.R. Muller and R. Smith

4. The Canadian Airborne R&D SAR Facility: The CCRS C/X SAR 1621
Livingstone, C.E., A.L. Gray, P.W. Vachon, M. Lalonde, R.K. Hawkins, T.I. Lukowski, K. Mattar and J.W. Campbell

5. The DLR Airborne SAR Project E-SAR 1624
Horn, R.

6. EMISAR: C- and L-Band Polarimetric and Interferometric SAR 1629
Lintz Christensen, E., J. Dall, N. Skou, K. Woelders, J. Granhohm and S.N. Madsen

7. First Results and Status of the PHARUS Phased Array Airborne SAR 1633
Greidanus, H., P. Hoogeboom, P. Koomen, P. Snoeij and H. Pouwels

8. Development of NASDA Airborne Synthetic Aperture Radar (NASAR-1) 1636
Shimada, M., H. Oaku and M. Yamanashi

9. The NEC Interferometric SAR System "NEC-SAR" 1639
Nagata, H., H. Shinohara, M. Murata, M. Miyawaki, H. Nagata, H. Shinme, M. Sugawara, H. Totuka, Y. Ohura and H. Nohmi

THPAM -- BRDF Model Development, Validation and Inversion II

1. Angular Signatures, and a Space-Borne Measurement Concept 1642
Gerstl, S.A.W.

2. Estimation of Leaf Size from Hotspot Observation 1645
Qin, W., N.S. Goel and B. Wang

3. Multiple Scattering Approximations and Coherent Backscattering Theory for Soil Bidirectional Reflectance 1648
Liang, S.

4. A Four-Level Bidirectional Reflectance Model Based on Canopy Architecture and its Inverstion 1651
Chen, J.M., and S.G. Leblanc

5. Validation of a BRDF Model for Boreal Forest 1654
North, P.R., S.E. Plummer and D.W. Deering and M. Leroy

6. Assessing Canopy Biomass and Vigor by Model-Inversion of Bidirectional Reflectances: Problems and Prospects 1657
Brakke, T.W., J. Otterman, J.R. Irons and F.G. Hall

7. Retrieval of Forest Biophysical Parameters from Remote Sensing Images with the DART Model 1660
Pinel, V., J.P. Gastellu-Etchegorry and V. Demarez

8. Extracting Sub-Pixel Vegetation Endmember Bidirectional Reflectance for Canopy Model Inversion Using NOAA AVHRR Satellite 1663
Asner, G.P., J.L. Privette, C.A. Wessman and C.A. Bateson

9. Estimation of Bidirectional Reflectance Distribution Function from Land Surfaces Using Airborne POLDER Data 1666
Takemata, K., T. Yonekura, M. Asae and Y. Kawata

10. Validation of Kernel-Driven Semiempirical BRDF Models for Application to MODIS MISR Data 1669
Hu, B., W. Wanner, X., Li and A.H. Strahler

THPAA -- Passive Remote Sensing of the Environment

1. A Scanning 60 GHz Radiometer to Measure Air-Sea Temperature Difference: Recent Results During Cope 1672
Trokhimovski, Yu.G., E.R. Westwater, V.G. Irisov and V.Ye. Leuskiy

2. Measurements of Integrated Water Vapor and Cloud Liquid from Microwave Radiometers at the DOE ARM Cloud and Radiation Testbed in the U.S. Southern Great Plains 1675
Liljegren, J.C., and B.M. Lesht

3. Performance Evaluation of a Spinning Flat Reflector for Millimeter-Wave Radiometry 1678
Jacobson, M.D., and W.M. Nunnelee

4. Observations of Water Vapor and Cloud Liquid from an Airborne Dual-Frequency Radiometer During VORTEX'95 1681
Fedor, L.S., E.R. Westwater and M.J. Falls

5. Applications of Kalman Filtering to Derive Water Vapor Profiles from Raman Lidar and Microwave Radiometers 1685
Han, Y., E.R. Westwater and R.A. Ferrare

THPAA *continued* -- Passive Remote Sensing of the Environment

6. Application of Neural Nets to Rain Rate Retrieval from Simulated Multichannel Passive Microwave Imagery 1688
Gasiewski, A.J., G.A. Showman and G.M. Skofronick

7. Prediction of Water Vapor Scale Height from Integrated Water Vapor Measurements 1692
Boback, J.P., and C.S. Ruf

8. Feasibility of a New Ground-Based Microwave Measurement Method for the Atmospheric Water Vapor 1695
Hashimoto, S., N. Yamashita and T. Mikami

9. Determination of Humidity Profiles from Measurements of Up Going Radiation at Wavelengths 0.3 and 1.35 cm 1698
Markina, N.N., and A.P. Naumov

10. Recovering of Atmospheric Water Vapor and Liquid Water Contents by Multifrequency Radiometer: Experiments and Modeling 1701
Perfiliev, Y.P.

THPCP -- Microwave Remote Sensing of Ocean Surface Winds II

1. A Simple Model for Deriving Ocean Surface Wind Direction from the DMSP Special Sensor Microwave Imager (SSM/I) 1704
Boucher, D.J., B.H. Thomas, D.N. Ricci and A.M. Kishi

2. Ocean Surface Wind Speed and Direction Retrievals from the SSM/I 1707
Li, L., and P. Chang

3. Assessing the Ocean Surface Vector Wind Signal in SSM/I Data Using Neural Networks 1710
Bates, J.J., and K.C. McColl

4. The Effects of Tropospheric Water Vapor and Cloud Liquid Water on Ocean Surface Wind Vector Retrievals Using Polarimetric Radiometers NA
Gaiserl, P.W., and P. Chang

5. Surface Winds from the SSM/I Using Neural Networks 1712
Krasnopolsky, V.M., L.C. Breaker and W.H. Gemmill

6. Development of a Statistical Method for Eliminating Improbable Wind Aliases in Scatterometer Wind Retrieval 1715
Oliphant, T.E., and D.G. Long

7. Advanced Techniques for Improving Wind Direction Ambiguity Removal in Scatterometry 1718
Huddleston, J.N., R.D. West, S.H. Yueh and W.Y. Tsai

8. Geophysical Modeling Error in Wind Scatterometry 1721
Johnson, P.E., D.G. Long and T.E. Oliphant

9. Cramer-Rao Bound for Wind Estimation from Scatterometer Measurements 1724
Oliphant, T.E., and D.G. Long

10. Atmospheric Effects on the Wind Retrieval Performance of Satellite Radiometers 1727
West, R.D., and S.H. Yueh

THPED -- Remote Sensing of the Space/Time Characteristics of Water Surfaces

1. Laboratory Studies on Frequency-Wavenumber Spectrum of Short Wind Waves — NA
Hara, T., E.J. Bock and M. Donelan

2. Nonlinearities and Reverse Travelling Energy Observed in Wavenumber-Frequency Spectra of X-Band Ocean Backscatter — 1730
Frasier, S., and R. McIntosh

3. In Situ Measurements of Small Scale Wind-Waves and Their Moduation by Ocean Currents and Atmospheric Forcing — NA
Bock, E.J., T. Hara and J.B. Edson

4. Observed Space-Time Structure of Radar Backscatter from the Ocean Surface — 1733
Hesany, V., W.J. Plant, W.C. Keller and K. Hayes

5. Surface Wave Dispersion Observed With Airborne Spotlight Imaging Systems — NA
Dugan, J.

6. Optical, Radar and In Situ Measurements of Internal Wave Dispersion — 1736
Gotwols, B.L., E. Aarholt, R.D. Chapman and R.E. Sterner II

7. The Coastal Ocean Probing Experiment: Further Studies of Air-Sea Interactions with Remote and In-Situ Sensors — 1739
Kropfli, R.A. and S.F. Clifford

8. The Estimation of Ocean Current From ω-k Analysis of Radar Data — 1742
Lamont-Smith, T.

9. High Resolution Polarimetric Radar Scattering Measurements of Low Grazing Angle Sea Clutter — 1745
Twarog, E.M., D.J. McLaughlin and N. Allan

10. Simultaneous CODAR and OSCR Measurements of Ocean Surface Currents in Monterey Bay — 1749
Fernandez, D.M., and J.D. Paduan

THPES -- Land Cover: Multitemporal Analysis and Change Detection

1. A Comparative Analysis of ERS-1/SAR and Landsat/TM Multitemporarl Scenes for Land Use Studies in Sao Paulo State, Brazil — NA
Damiao, D.P., and H.J.H. Kux

2. A Multitemporal Land-Cover Change Analysis Tool Using Change Vector and Principal Components Analysis — 1753
Parra, G.A., M.C. Mouchot and C. Roux

3. Assessing Inter-Annual Variability for the Central Grassland Region of the US Using the 1990 Seasonal Land Cover Classification — NA
Stretch, L., B. Reed and D. Ojima

4. Land-Cover Dynamics in Eastern Amazonia, 10 Years of Change as Viewed by Landsat TM — NA
Roberts, D.A., G. Batista, J. Pereira and B. Nelson

5. Monitoring Land Cover of the Desert Fringes of the Eastern Nile Delta, Egypt — 1756
El-Khattib, H.M., N.M. El-Mowilhi and F. Hawela

6. Temporally Invariant Classifiers and the Classification of Floristics — NA
Fitzgerald, R.W.

THPES *continued* -- Land Cover: Multitemporal Analysis and Change Detection

7. Retrieval of Forest Parameters from Multitemporal Spaceborne SAR Data 1759
Kurvonen, L., J. Pulliainen, M. Hallikainen and P. Mikkela

8. Monitoring of the Change of Vegetative Conditions Using Multitemporal SAR Data 1763
Suga, Y., S. Takeuchi and H. Tsu

9. C- and L-Band Multi-Temporal Polarimetric Signatures of Crops 1766
Skriver, H., F. Nielsen and A. Thomsen

10. Characterization of Oklahoma Reservoir Wetlands for Preliminary Change Detection Mapping Using IRS-1B Satellite Imagery 1769
Mahlke, J.

THPF -- Microwave Remote Sensing of the Antarctic

1. RADARSAT Antarctica Mapping System: System Overview 1772
Norikane, L., B. Wilson and K. Jezek

2. RADARSAT: The Antarctic Mapping Project 1775
Jezek, K.C., J. Curlander, L. Norikane, F. Carsey, J.P. Crawford, C. Wales and J. Muller

3. The McMurdo Ground Station (MGS): Ready for SAR Acquisition 1777
Wales, C.

4. Calibration of Data from the Antarctic Mapping Mission 1780
Williams, J.

5. A Robust Threshold Retracking Algorithm for Extracting Ice-Sheet Surface Elevations from Satellite Radar Altimeters 1783
Davis, C.H.

6. Individual Weather Correction for Antarctic Sea-Ice Concentration from SSM/I 1788
Thomas, C.H., and G.C. Heygster

7. The Effect of the Grounded Tabular Icebergs in Front of Berkner Island on the Weddell Sea Ice Drift as Seen from Satellite Passive Microwave Sensors 1791
Markus, T.

8. Mueller Matrix Associated with Diffuse Scattering from Two-Dimensional Random Rough Surfaces -- Full Wave Analysis 1794
Lee, B.S., and E. Bahar

THPH -- Optical Remote Sensing Instrumentation and Techniques

1. Development and Present Configuration of the NASA GSFC/WFF Helicopter-Based Remote Sensing System 1797
Walthall, C.L., D.L. Williams, B.L. Markham, J.E. Kalshoven and R.F. Nelson

2. System Requirments for Active Optical Search and Rescue 1800
Field, C.T., and P.S. Millar

3. Shortwave Infrared Spectral Reflectance of Plant Litter and Soils 1803
Nagler, P.L., C.S.T. Daughtry and S.N. Goward

4. Using Laser Echo Recovery and a Scannable Field-of-View Telescope to Determine Vegetation Structure and Sub-Canopy Topography Over Wide Swaths 1806
Blari, J.B., D.J. Harding and D.B. Coyle

5. An Active Optical Remote Sensing System for Vegetation Index Determination 1809
Kalshoven, J.E., and D.P. Rosten

6. Effects of Excitation Wavelength on the Chlorophyll Flourescence Ratio F685/F730 nm 1812
Corp, L.A., J.E. McMurtrey, E.W. Chappelle, M.S. Kim and C.S.T. Daughtry

7. An Improved Aircraft Underflight Instrument for the Derivation of Band Gains in Satellite Sensors 1816
Abel, P., and B. Subramanya

8. Radiometric Corrections of Visible/Infrared Satellite Data Over Terrestrial Environments: Angular, Atmospheric and Topographic Effects 1823
Moreno, J.F.

9. Comparison of Lidar Water Vapor Measurements Using Raman Scatter at 266 nm and 532 nm 1826
Harris, R., F. Balsiger and C.R. Philbrick

10. Computer Modeling of Adaptive Optics and Sites for Telescopes Design 1830
Lukin, V.P.



THPP -- SAR Applications and Signal Processing

1. Mapping Geologic Structure on Barrier Islands Using Polarimetric SAR NA
Slatton, K.C., M.M. Crawford, J.C. Gibeaut and R.O. Gutierrez

2. Integration of SIR-C/X-SAR and Landsat TM Data for Geologic Mapping and Resource Exploration 1833
Wever, T., and M. Frei

3. Retrieval of Man-Made Structures in Siberia with INSAR Techniques Using ERS SAR Data 1836
Streck, C., and O. Hellwich

4. Angular Dependence of SAR Backscatter Around Mt. Taranaki, New Zealand 1839
Pairman, D., and S. Belliss and S. McNeill

5. Edge Detection in Speckled SAR Images Using the Continuous Wavelet Transform 1842
Chabert, M., J.Y. Tourneret and G. Mesnager

6. Heterogeneity in SAR Images NA
Mueller, H.J

7. Intersystem Normalization of Multifrequency Radar Imagery for Discrimination of Unvegetated Lava Surfaces NA
Kaupp, V.H., J.F. Hug, W.P. Waite, H.C. MacDonald and C.M. Ting

8. Removing RF Interferences from P-Band Ariplane SAR Data 1845
Cazzaniga, G., and A. Monti Guarnieri

THPV -- Methods of Data Analysis

1. Hybrid Consensus Theoretic Classification 1848
Benediktsson, J.A., J.R. Sveinsson and P.H. Swain

2. A Framework for Multi-Date Multi-Sensor Image Interpretation 1851
Murni, A., A.K. Jain and J. Rais

3. Optimal Projection Selection for Projection Pursuit in High Dimensional Feature Reduction NA
Velipasaoglu, E.O., and O.K. Ersoy

4. Automated Training Sample Labeling Using Laboratory Spectra 1855
Hsieh, P., and D.A. Landgrebe

5. Modified Divisive Clustering Useful for Quantitative Analysis of Remotely Sensed Data 1858
Prakash, H.N.S., S.R. Kumar, P. Nagabhushan and K.C. Gowda

6. Surface Information Retrieval From Optical/Microwave Data: Potentials and Limits of Synergistic Approaches 1861
Moreno, J.F., and S.S. Saatchi

7. Sensor Data Simulations Using Monte-Carlo and Neural Network Methods 1864
Kiang, R.K.

8. Model-Based Technique for Super Resolution and Enhanced Target Characterization Using a Step-Frequency Radar: A Simulation Study 1867
Chakrabarti, S., P. Kanagaratnam and P. Gogineni

9. Contextual Simulation of Landscape Based on Remotely Sensed Data 1870
Jung, M.,THPF: Microwave Remote Sensing of the Antarctic and M.M. Crawford

10. Intelligent Fusion and Analysis of AIRSAR Data for SEIDAM 1873
Bhogal, A.S., D.G. Goodenough, D. Charlebois, H. Barclay, S. Matwin and O. Niemann

THPZ -- The World's Airborne SAR Facilities II: Extraordinary Frequencies and Special Applications

1. Multi-Channel SAR with Phased Array: The Experimental Airborne System AER-II NA
Ender, J.H.C.

2. The German DO-SAR Sytem Abstract NA
Fritsch, B.

3. The Experimental Airborne VHF SAR Sensor CARABAS: A Status Report 1877
Gustavsson, A., L.M.H. Ulander, L.E. Anderson, P.O. Frolind, H. Hellsten, T. Jonsson, B. Larsson and G. Stenstrom

4. A H igh Resolution, Four-Band SAR Testbed with Real-Time Image Formation 1881
Walker, B., G. Sander, M. Thompson, B. Burns, R. Fellerhoff and D. Dubbert

5. The Lincoln Laboratory Millimeter-Wave Synthetic Aperture Radar NA
Murphy, T.J., and J.C. Henry

6. ONERA Airborne SAR Facilities NA
Boutry, J.M.

7. The Army Research Laboratory Ultra Wideband BoomSAR
Ressler, M.A. 1886

8. Status of the SASAR System 1889
Inggs, M.

9. Overview of the P-3 UWB SAR System NA
Sheen, D.R., and T.B. Lewis

10. YSAR: A Compact, Low-Cost Synthetic Aperture Radar 1892
Thompson, D.G., D.V. Arnold, D.G. Long, G.F. Miner and T. Karlinsey



FAAM -- Land Cover Characterization Using BRDF Models and Data

1. Nadir and Bidirectional Surface Measurements of Arctic Tundra: Site Differentiation and Vegetation Phenology Early in the Growing Season 1897
Vierling, L.A., D.W. Deering and T.F. Eck

2. Analysis of Airborne POLDER Data on Boreal Forest Covers 1901
Bicheron, P., M. Leroy and O. Hautecoeur

3. Variability of BRDF with Land Cover Type for the West Central HAPEX-Sahel Super Site 1904
Brown de Colstoun, E.C., C.L. Walthall, A.T. Cialella, E.R. Vermotel, R.N. Halthore and J.R. Irons

4. Use of BRDF Models to Normalize Angular Reflectances to NADIR for Temporal Compositing Schemes NA
Jia, S., A.R. Huete and W.J.D. van Leeuwen

5. Detection and Correction of the Bidirectional Effects in AVHRR Measurements Over Northern Regions NA
Li, Z., J. Cihlar, X. Zheng and L. Moreau

6. Conifer Shoot Bidirectional Scattering: Methodology and Preliminary Results 1908
Walter-Shea, E.A., M.A. Mesarch and L. Chen

7. Assymmetry in the Diurnal Variation of Surface Albedo 1911
Mayor, S., W.L. Smith, Jr., L. Nguyen, T.A. Alberta, P. Minnis, C.H. Whitlock and G.L. Schuster



FAAA -- Active Remote Sensing of the Lower Atmosphere

1. Retrieval of Boundary-Layer Turbulence Using Spaced-Antenna Wind Profilers 1914
Holloway, C.L., R.J. Doviak, S.A. Cohn and R.J. Lataitis

2. A Buoy-Mounted Wind Profiler for Remote Measurement of Ocean Winds 1917
Mead, J.B., P.M. Langlois and R.E. McIntosh

3. Frequency Domain Interferometry in the Planetary Boundary Layer: First Results 1920
Corner, B.R., R.D. Palmer and R.M. Narayanan

4. A Digital Beamforming Radar Profiler for Imaging Turbulence in the Atmospheric Boundary Layer 1923
Mead, J.B., G. Hopcraft, B. Pollard, R.E. McIntosh

5. Preliminary Results From the Arecibo 430 MHz Spatial Interferometry System 1926
Howell, P.B., R.D. Palmer, R.M. Narayanan, M.F. Larsen and J.Y.N. Cho

6. Measurements of Vertical Velocities and Divergence in the Atmosphere Using the MU Radar in Japan 1929
Ren, Y., R.D. Palmer, S. Fukao, M. Yamamoto and T. Nakamura

FAAA *continued* -- Active Remote Sensing of the Lower Atmosphere

7. Structure of the Atmosphere in an Urban Planetary Boundary Layer from Lidar and Radiosonde Observations NA
Eichinger, W., and D. Cooper

8. Volume Imaging Lidar Observations of the Convective Boundary Layer NA
Eloranta, E., and A. Piironen

9. Low-level Jet Detection in Snow with a Noncoherent Weather Radar NA
Melnikov, V.M., and A.V. Ryzhkov

FACP -- Subsubsurface Electromagnetic Sensing at Deeper Depths

1. Radar Sounding of Glaciers in Greenland 1932
Allen, C., B.P. Wolhletz and S. Gogineni

2. Sensing of Gradient Electromagnetic Fields from Subsurface Conducting Targets 1935
Cress, D.H., and L.C. Bartel

3. Modeling the Electromagnetic Detection of Buried Cylindrical Conductors 1938
Moses, R.W., R.E. Kelly and J.M. Mack

4. Marine Sediment Mapping with Airborne Electromagnetics NA
Mozley, E.C., and J. Reynaud

5. Electromagnetic Modeling of Subsurface 3D Structures 1941
Newman, G.A., and D.L. Alumbaugh

6. Demonstration of the Lasi High-Resolution Electromagnetic Sounding System at the Nevada Test Site NA
Sternberg, B.K., and M.M. Poulton

7. Statistical Law of Surface Impedance Distribution 1945
Bashkuev, Yu.B., V.B. Haptanov and L.H. Angarkhaeva

8. The Prediction Map of Geoelectric Sections of Australia, New Zealand and New Guinea 1947
Bashkuev, Yu.B., V.R. Advokatov and L.H. Angarkhaeva

9. The Influence of Ground Stratification Upon a Field of Magnetic Loop 1950
Dmitriev, W.V.

FAED -- Remote Sensing of Littoral Submesoscale Processes III

1. Frontal Signatures in Radar Imagery NA
Vogelzang, J., K.G. Ruddick and J.B. Moens

2. Detection and Location of Internal Waves in Ocean SAR Images by Means of Wavelet Decomposition Analysis 1953
Rodenas, J.A., and R. Carello

3. Imaging the Multiscale Structure of Atmospheric Turbulence Using Satellite-Based Synthetic Aperture Radar (SAR) NA
Mourad, P.D.

4. Spectral Analysis of Non-Stationary Ocean SAR Images Using the Wigner-Ville Transform 1956
Grassin, S., R. Garello and M. Prevosto

5. Results of Airborne Backscatter Measurements During the Surface Wave Dynamics Experiment 1959
Nghiem, S.V., F.K. Li G. Neumann and S.H. Lou

6. Quantitative Analysis of Radar Signatures of Underwater Bottom Topography According to a Bragg-Based Composite Surface Model 1962
Romeiser, R.

7. Near Nadir Microwave Specular Returns From the Sea Surface -- Measurements of Winds From Breeze to Hurricane 1965
Wu, J.

8. Spectral Variations of Sea Surface Emission at MM-Wave Frequencies Under Influence of Synoptical Oceanic Eddies 1968
Cherny, I.V., and V.P. Nakonechny

9. Examination of Sea Surface by Airborne Microwave Radar and Radiometers in Joint US/Russia Internal Waves Remote Sensing Experiment NA
Kuzmin, A.V., M.I. Mityagina and V.V. Yakovlev

10. Surface Wave Observation in the Gulf Stream Area Using ALMAZ-1 SAR 1971
Grodsky, S.A., V.N. Kudryavtsev, A.Y. Ivanov, V.A. Zaitsev and D.M. Solov'ev

FAES -- Land Cover: Agricultural

1. Land Cover Mapping in the Eastern Slopes of the Andes Using ERS-1 and Landsat Data NA
Echavarria, F.R., and C. Keithley

2. A Multisensoral Approach for Landuse Classifications and Grassland Monitoring Based on the Possibility Theory 1974
Stolz, R., and W. Mauser

3. Spectral Angle Mapper Classification and Vegetation Indices Analysis for Winter Cover Monitoring Using JERS-1 OPS Data 1977
Kim, C., and S. Cho

4. Comparison of Classification Techniques for Agricultural Crops Using Temporal Multiparameter Airborne DLR E-SAR Images NA
Schmullius, C., S. Erasmi and P. Hurlemann

5. SIR-C Polarimetric Backscatter Features of Agricultural Land Cover Types Early and Late During the Growing Season 1980
Davidson, M.W.J., R. Steingießer, W. Kuhbauch, F. Vescoui and F. Tano

6. Use of ERS-1 SAR Data for Field Rice Mapping and Rice Crop Parameters Retrieval 1983
Ribbes, F., and T. Le Toan

7. Textural Processing of Multi-Polarization SAR for Agricultural Crop Classification 1986
Treitz, P.M., O.R. Filho, P.J. Howarth and E.D. Soulis

8. Early Diagnostic of Disease Erisiphe Graminis with Using Remote Sensing Measurements NA
Kazandjiev, V.

9. Study on Auto-Extraction of Winter Wheat Planting Area from TM Image Based on Pattern Recognition Technology 1989
Yang, X., N. Wang and P. Qin

10. Spring Wheat Yield Prediction for Western Canada Using Weekly NOAA AVHRR Composites 1992
Hochheim, K.P., D.G. Barber and P.R. Bullock

FAF -- Microwave Remote Sensing of Snow

1. Snow and Ice Observations During the European Multi-Sensor Airborne Campaign in 1995 — 1995
Noll, J., M. Wooding and E. Attema

2. Overview of EMAC-95 Snow and Ice Airborne Campaign in Finland — 1998
Hallikainen, M., P. Ahola, K. Rautiainen, J. Pihlflyckt, T. Tirri, M. Makynen, J. Lahtinen, H. Servomaa, P. Makkonen, J. Grandell, M. Kemppinen, M. Nikulainen, H. Taskinen, S. Tauriainen and M. Roschier

3. First Results From EMAC '95 Snow Experiment in Norway — NA
Guneriussen, T., R. Solberg, K. Sand, J. Noll and D. Weydal

4. Estimation of Snow Water Equivalence Using SIR-C/X-SAR — 2002
Shi, J., and J. Dozier

5. Estimation of Snow Water Equivalent Using Passive Microwave Radiation Data — 2005
Tait, A.

6. Microwave Remote Sensing of Snow: Modeling and Measurements — NA
Hallikainen, M., J. Grandell, T. Pyhalahti and V. Jaaskelainen

7. Scattering and Emission from Dry Snow in the Range 35-120 GHz — 2008
Tjuatja, S., A.K. Fung and J.C. Comiso

8. Multi-Frequency FMCW Radar Profile of Snow Cover — NA
Koh, G., and N.E. Yankielun

9. Observations of Snow Crystal Shape in Cold Snowpacks Using Scanning Electron Microscopy — 2011
Foster, J.L., D.K. Hall, A.T.C. Chang, A. Rango, W. Wergin and E. Erbie

10. Dramatic Decrease in Radar Cross Section over Greenland Observed by the ERS-1 Scatterometer Between 1991 and 1995 — 2014
Wismann, V.R., and K. Boehnke

FAH -- UWB and Ground Penetration Radar

1. An Ultrawideband Imaging Radar for Sea Surface Studies — 2017
Sletten, M.A., and D.B. Trizna

2. Development of a Low Cost SFCW Ground Penetrating Radar — 2020
Langman, A., S.P. Dimaio B.E. Burns and M.R. Inggs

3. A Range Algorithm for Ground Penetrating Radar — 2023
Caffey, T.W.H.

4. Results of a Remote Sensing Experiment Using a Low Frequency Ultra-Wideband SAR to Investigate the Phenomenology of Landmines — 2027
Sturgess, K., L. Happ, J. Kurtz and M. Collins

5. Processing the Ground Penetrating Radar Data Using Its Correlation Property — NA
Jen, L., J. Li and M.X. Wang

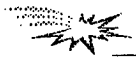
6. Signal Processing Aspects of Polarimetric Random Noise Radar Data for Shallow Subsurface Imaging — 2030
Xu, Y., P.D. Hoffmeyer, R.M. Narayanan and J.O. Curtis

7. An Interferomic Techniques for Synthetic Aperture Ground-Penetrating Radar 2033
Leuschen, C., N. Goodman, C. Allen and R. Plumb

8. Subsurface Imaging Using Ground-Penetrating Radar Measurements 2036
Goodman, N., C. Leuschen, R. Plumb and C. Allen

9. Multi-Layer Detection Tracking for Monostatic Ground Penetrating Radar 2038
Rampa, V., and U. Spagnolini

10. Analysis of Response of the Electromagnetic Induction for Detecting of Buried Objects 2041
Zhu, K.



FAP -- SAR Interferometry Processing Algorithms

1. Region Growing Algorithm for InSAR Phase Unwrapping 2044
Xu, W., and I. Cumming

2. A Comparison of Phase Unwrapping Techniques NA
Collins, J.D., G. Sessenrath and N. Marechal

3. A Theoretical Analysis on the Robust Phase Unwrapping Algorithms for SAR Interferometry 2047
Fornaro, G., G. Franceschetti, R. Lanari and E. Sansosti

4. SAR Interferometry: A Multigrid Markdown Approach to Phase Unwrapping with a Discontinuity Model NA
Labrousse, D., and M. Berthod

5. A Multiresolution Approach to Improve Phase Unwrapping 2050
Davidson, G.W., and R. Bamler

6. Maximum Entropy Solution for Interferometric SAR Phase Unwrapping 2054
Datcu, M.

7. Consistent 2-D Phase Unwrapping Guided by a Quality Map 2057
Flynn, T.J.

8. Absolute Phase Determination in SAR Interferometry 2060
Chiaradia, M.T., L. Guerriero, G. Pasquariello, A. Refice and N. Veneziani

9. Determination of Absolute Interferometric Phase Using the Beam-Amplitude Ratio Technique 2063
Bickel, D.L., and W.H. Hensley



FAV -- Method of Data Analysis

1. Multisource Data Integration Using Neural Networks: Optimal Selection of Net Variables for Lithologic Classification 2068
Yang, G., M.J. Collins and P. Gong

2. Multisensor Data Analysis Based on Neural Networks NA
Blonda, P., G. Pasquariello, V. la Forgia, A. Bennardo, G. Stalino, R. Sergi and R. Loizzo

3. A Completely Fuzzy Classification Chain for Multispectral Remote Sensing Images 2071
Gamba, P., A. Marazzi, A. Mecocci and P. Savazzi

4. A Raster-Based Fuzzy Expert System for Forestry Evolution 2074
Saint-Joan, D., and J. Desachy

FAV *continued* -- Method of Data Analysis

5. Evolving Feature-Extraction Algorithms: Adapting Genetic Programming for Image Analysis in Geoscience and Remote Sensing 2077
Daida, J.M., T.F. Bersano-Begey, S.J. Ross and J.F. Vesecky

6. Radar Imaging of Three-Dimensional Targets in the Laboratory 2080
Bertrand, J., and P. Bertrand

7. Use of Confocal Techniques in the Generation of Three Dimensional Images Using Conventional SAR NA
Byrd, M., A.J. Blanchard and B. Krenek

8. Reconstrucion of Complex Dielectric Profiles via Quadratic Models 2083
Pierri, R., T. Isernia, V. Pascazio and A. Tamlourrino

9. Topographic Measurements Using Polarimetric SAR Data 2086
Schuler, D.L., J.S. Lee and G. De Grandi

10. A New Method for Extracting Topographic Information From a Single Multispectral Image 2089
Carlotto, M.J.

FAZ -- Surface Temperatures: Observations and Applications

1. Thermal Emission from Rough Terrain: Anisotropy and Its Possible Consequences on Satellite Image Interpretation 2092
Jamsa, S.

2. Validation of Land-Surface Temperature Retrieval from Space 2095
Wan, Z., W. Snyder and Yulin Zhang

3. Model Simulations of the Effect of the Atmosphere on the Remote Sensing of Earth Surface Parameters with the Advanced Very High Resolution Radiometer NA
Rao, C.R.N., and N. Zhang

4. Land Surface Temperature Retrieval From AVHRR: Influene of Surface Emissivity and Atmospheric Water Vapor 2098
Steyn-Ross, M.L., and D.A. Steyn-Ross

5. TIR Observations in FIFE From Field, Aircraft and Satellite Platforms 2101
Schmugge, T.J., and G.M. Schmidt

6. A Simple Method for Estimating Surface Energy Fluxes and Air Temperatures From Satellite Observations 2104
Anderson, M.C., J.M. Norman, G.R. Diak and W.P. Kustas

7. Unmixing of Satellite Thermal Images: Simulation and Application to TM/Landsat Data 2107
Zhukov, B., D. Oertel, F. Lehmann and P. Strobl

8. SSM/I-Based Surface Temperature Retrieval Method for Boreal Forest Zone 2110
Pullianinen, J., J. Grandell and M. Hallikainen

9. Analyzing Thermal Properties of Forests Using Multitemporal Space Borne Thermal Data NA
Lohi, A., and Y. Awaya

10. Visualisation of Urban Surface Temperatures Derived from Satellite Images 2113
Nichol, J.

FPAM -- Rough Surface Scattering Effects on Remote Sensing of Terrain

1. A Further Study of the IEM Surface Scattering Model 2116
Fung, A.K., and C.Y. Hsieh

2. On the Use of the Quasi Specular Model for Surface Parameter Estimation 2119
Marchand, R., and G.S. Brown

3. Electromagnetic Scattering from Slightly Rough Surfaces with Inhomogeneous Dielectric Profile 2122
Sarabandi, K., and T. Chiu

4. Electromagnetic Wave Scattering From Real-Life Rough Surface Profiles and Profiles Based on Averaged Spectrum 2125
Pak, K., L. Tsang, R. Weeks, J.C. Shi and H. Rott

5. Analytical, Experimental, and Numerical Studies of Angular Memory Signatures of Waves Scattered from One-Dimensional Rough Surfaces 2128
Kuga, Y., C.T.C. Le and A. Ishimaru

6. The SIR-C/X-SAR Experiment: The Sensitivity of Microwave Backscattering to Surface Roughness of Bare Soils 2131
Coppo, P., G. Macelloni, P. Pampaloni, S. Paloscia and S. Sigismondi

7. Using SIR-C SAR and Cloude's Decomposition for the Determination of Soil Moisture in Vegetated Areas 2134
Chadwick, D.J., and J.R. Wang

8. Interferometric Technique of Determining the Average Height Profile of Rough Surfaces 2137
Ishimaru, A., C.T.C. Le, Y. Kuga, J.H. Yea, K. Pak and T.K. Chan

9. Detection of a Target in a Inhomogeneous Medium Using Angular Correlation Function 2140
Chan, T.K., Y. Kuga and A. Ishimaru

10. Numerical Study of Detection of a Buried Object Under a Single Random Rough Surface with Angular Correlation Function 2143
Tsang, L., G. Zhang and K. Pak

FPAA: Earth Radiation Budget

1. Remote Sensing of Land Surface Temperature: The Directional Viewing Effect 2146
Smith, J.A., N. Chauhan and J. Ballard

2. A Simulation of Topographic Solar Radiative Forcing over a Mountainous Region Using Geostationary Satellite Data 2149
Loechel, S., R.O. Dubayah, J. Barnett, C. Gautier and M. Landsfeld

3. Modeling Area-Averaged Fluxes over Partially Vegetated Land Surfaces Using Aircraft and In-Situ Thermal Data 2152
Friedl, M.A.

4. A One-Dimensional Hydrology/Radiobrightness Model for Freezing/Thawing Bare Soils 2155
Liou, Y.A., and A.W. England

5. On the New Long-Wave Radiation Determination from Satellite Data 2158
Xue, Y., S.P. Lawrence and D.T. Llewellyn-Jones

FPAA *continued* -- Satellite Measurements

6. Landsat 7 System Design Overview 2160
Andary, J., P. Spidaliere, S. Jurczyk and T. Arvidson

7. Landsat 7 and Beyond 2161
Irons, J.R., D.L. Williams and B.L. Markham

8. Reducing the Effects of Space-Varying Wavelength-Dependent Scattering in Multispectral Imagery 2164
Carlotto, M.J.

9. RADARSAT for Landuse Monitoring: Early Results NA
Brown, R.J., T.J. Pultz, B.G. Brisco, Y. Crevier and L. Tighe

FPCP -- Surface Scattering

1. An Exact Technique for Calculating Low Grazing Angle Backscatter from Rough Surfaces NA
Kasilingam, D.

2. Fractal Analysis of Bidimensional Profiles and Application to Electromagnetic Scattering of Soils 2167
Rouvier, S., P. Borderies, I. Chenerie, J.C. Souyris, T. Le Toan and N. Floury

3. Like and Cross Polarized Cross Sections for Two Dimensional Random Rough Surfaces: Bistatic Single and Double Scatter 2170
El-Shenawee, M., and E. Bahar

4. A Knowledge-Based Inversion of Physical BRDF Model and Three Examples 2173
Li, X., and A. Strahler

5. Scattering Cross Sections of Composite Rough Surfaces New Unified Full Wave Solutions 2177
Bahar, E., and Y. Zhang

6. Scatter Cross Sections for Two-Dimensional Random Rough Surfaces-Full Wave Analysis 2180
Bahar, E., and B.S. Lee

7. The Measured Polarized Bidirectional Reflectance Distribution Function of a Spectralon Calibration Target 2183
Betty, C.L., A.K. Fung and J. Irons

8. Energy Conservation in Soil Surface Scattering in the Optical Region 2186
Li, Z., A.K. Fung, S. Tjuatja, C. Betty and J. Irons

9. Optical Versus Radar Roughness in Agricultural Tillage 2189
Colpitts, B.G.

10. The Soil Surface Reflectivity in the Partial Coherent Microwaves at the Frequencies 300 and 900 MHz 2192
Bobrov, P.P., and I.M. Schetkin

FPED -- Laboratory Studies of Ocean Surface Scattering

1. Laboratory Investigations of the Hydrodynamics and Radar Backscattering Properties of Breaking Waves 2195
Meadows, G., E.B. Dano, D.R. Lyzenga, H. VanSumeren, R. Onstott and D.E. Lund

2. Doppler Characteristics and Angular Dependence of Radar Backscatter From Laboratory Breaking Waves 2198
Dano, E.B., D.R. Lyzenga and G. Meadows

3. Dependence of Polarimetric Doppler Spectra on Breaking-Wave Energy 2201
Lee, P.H.Y., J.D. Barter, K.L. Beach, B.M. Lake, H. Rungaldier, J.C. Shelton, H.R. Thompson, Jr., and R. Yee

4. Laboratory Study of the Fine Structure of Breaking Waves for Scatterometry Applications 2204
Rozenberg, A., W.K. Melville and M. Ritter

5. Small Grazing Angle Radar Scattering from a Breaking Water Wave: Demonstration of Brewster Angle Damping 2207
West, J.C., J.M. Sturm and M.A. Sletten

6. Dominant Wave Effects in Wavetank Measurement of Microwave Doppler Spectra 2210
Plant, W.J., V. Hesany, W.C. Keller and M.A. Donelan

7. Comparison of Experimental and Theoretical Ocean Wavenumber Spectra for Gravity-Capillary and Capillary Waves NA
Keller, M.R., and B.L. Gotwols

8. Depolarization in Microwave Scatterometry 2213
Lee, P.H.Y., J.D. Barter, K.L. Beach, B.M. Lake, H. Rungaldier, J.C. Shelton, H.R. Thompson, Jr., and R. Yee

9. Influences of Wind Bursting on Radar Return 2216
Savtchenko, A., S. Tang and J. Wu

10. Measuring Small-Scale Water Surface Waves: Nonlinear Interpolation and Integration Techniques for Slope-Image Data 2219
Daida, J.M., R.R. Bertram, D.R. Lyzenga, C. Wolf, D.T. Walker, S.A. Stanhope, G.A. Meadows, J.F. Vesecky and D.E. Lund

FPES -- Spatial Decision Support Systems: Cost/Benefit Analysis

1. Remote Sensing: Economic Viability Environmental Monitoring 2222
Macauley, M.K., and T.J. Brennan

2. Ecosystem Management: A Decision Support GIS Approach 2225
Ji, W.

3. Dawn of a New Era: The Image Information Age 2228
Jordan, III, L.E.

4. Non Point Source Pollution 2231
Subra, W., and J. Waters

5. A Genetic Approach to Ecosystem Modeling: Do the Benefits Warrant the Costs? NA
Morain, S., and A. Budge

6. Cost-Effective Environmental Consulting Using Geographic Information Systems and Remote Sensing 2234
Gibas-Tracy, D.R.

FPES *continued* -- Spatial Decision Support Systems: Cost/Benefit Analysis

7. Land Surface Remote Sensing and Geographical Information Systems for Water Quality Modeling 2237
Mattikalli, N.M., and E.T. Engman

8. Satellite Remote Sensing and Geographic Information System for Monitoring Morphodynamics of the Active Yellow River Delta, China 2240
Yang, X., M.C.J. Damen, R. van Zuidam, A. van Gelder, J.H. van den Berg and G. Chen

9. Remote Sensing and Core Data Needed to Support Planning and Policy Decision Making 2242
Foresman, T.W., J.E. Estes, J.J. Garegnani and D.L. Porter

FPF -- Snow, Glaciers and Permafrost

1. Analysis of Snow Cover in Alaska Using Aircraft Microwave Data (April 1995) 2246
Hall, D.K., J.L. Foster, A.T.C. Chang, D.J. Cavalier, J.R. Wang and C.S. Benson

2. Estimation of Snow Surface Albedo Using Landsat Thematic Mapper 2249
Shi, J., T.H. Painter and J. Dozier

3. Estimating Alpine Snow Cover with Unsupervised Spectral Unmixing 2252
Rosenthal, W.

4. Airborne and Spaceborne SAR Interferometry: Application to the Athabasca Glacier and Area 2255
Vachon, P.W., D. Geudtner, L. Gray, K. Mattar, M. Brugman, I. Cumming, and J.L. Valero

5. Effects of System Errors on Combined MM/IR Neural Network Inversion of Surface Snow Properties 2258
Jackson, S.R., and R.M. Narayanan

6. Machine-Based Snow Line Determination and the Identification of Ice Sheet Features in Visible and SAR Imagery 2261
Lin, I.I., and W.G. Rees

7. Thawing of Soils in Siberia Observed by the ERS-1 Scatterometer Between 1992 and 1995 2264
Boehnke, K., and V.R. Wismann

8. Passive Microwave Freeze/Thaw Classification for Wet Tundra Regions 2267
Kim, E.J., and A.W. England

9. Freeze / Thaw Classification for Prairie Soils Using SSM/I Radiobrightnesses 2270
Judge, J., J.F. Galantowicz, A.W. England and P. Dahl

FPH -- Advanced Sensors

1. Integrating Global Positioning Systems with Satellite Remote Sensing: Avoiding Major Pitfalls 2273
Leavitt, B.C., and S.L. Payton

2. Remote Sensing with Hyperspectral Imagery Using DASI -- An Imaging Interferometer 2276
Hammer, P.D., D.L. Peterson, W.H. Smith, S.E. Dunagan, L.F. Johnson, A.W. Strawa, J. Zott and G. Langford

3. Multi-Mission Radar Altimeter: Concept and Performance 2279
Jensen, J.R., and R.K. Raney

4. Backscatter Characteristics of Buried Targets Measured Using an Ultrawideband Polarimetric Random Noise Radar 2282
Hoffmeyer, P.D., Y. Xu, R.M. Narayanan and J.O. Curtis

5. Airborne 14-Channel Microwave Radiometer HUTRAD 2285
Hallikainen, M., M. Kemppinen, K. Rautiainen and J. Pihlflyckt

6. Experimental Investigation of Diffraction Gratings for Millimeter/Submillimeter-Wave Instruments 2288
Nadimi, S.A., J.W. Bredow and G.C. May

7. Ground Segment for ERS-2 GOME Sensor at the German D-PAF 2291
Balzer, W.

8. Dual Polarized L-Band Microstrip Patch Array for the AIRSAR/TOPSAR System 2294
Rostan, F., W. Wiesbeck and J.J. van Zyl

9. Self-adapting Sensor for Atmospheric Electricity Measuring 2297
Yanovsky, F.J.

10. Spectrometry From Airborne Platforms: Examples and Analysis of the Italian Research Council (CNR) MIVIS Campaigns Over Different Test Sites NA
Bianchi, R., R.M. Cavalli and S. Pignatti

FPP -- Land Cover: Inventory and Monitoring

1. Integration of Multispectral Land Ecological Data for Characterizing Montane Meadow Communities in the Greater Yellowstone Ecosystem 2300
Jakubauskas, M.E., D. Debinski and K. Kindscher

2. Case-Based Reasoning and Software Agents for Intelligent Forest Information Management 2303
Charlebois, D., D.G. Goodenough, A.S. Bhogal and S. Matwin

3. The Suitability of Future High-Resolution Satellite Imagery for Forest Inventory 2307
Solberg, R., A.H. Schistad Solberg, H. Koren and K. Aas

4. Applications of Multi-Frequency, Multi-Polarization and Multi-Incident Angle SAR Systems in Urban Land Use and Land Cover Mapping 2310
Xia, Z.G.

5. Variations in Land Cover Areas Estimated from Remotely Sensed Data 2315
Yang, W., and J.W. Merchant

6. Recent Experiences in Mapping Land Cover From AVHRR Data: People's Republic of China Test Sites 2318
Qiu, Z., L. Yang and T.R. Loveland

7. Validating Global Landcover Classification Pattern Using Spatial Resoluton -- Independent Landscape Metrics 2321
Frohn, R.C., and J.E. Estes

8. Using Geoinformation System and Space Imagery to Monitor Environmetal Changes in the Aral Sea Ecological Disaster Area 2324
Glushko, E.V., A.V. Ptichnokov and V.S. Tikunov

9. Limitations for Multispectral Classification of Temperate Forests -- Scaling Problems of Groundtruth and Satellite Data 2326
Kellenberger, T.W., and K.I. Itten

FPV -- SAR Geocoding and Orthorectification

1. Practical SAR Orthorectification 2329
Pierce, L., J. Kellndorfer, F. Ulaby and L. Norikane

2. Optimization of the Tie-Pointing Procedure for the Terrain Correction of SAR Data 2332
Roth, A., W. Knoepfle and M. Matschke

3. Applicability of Automatic Tie-Pointing for Geocoding and Mosaicking of Overlapping SAR Images NA
Raggam, H., A. Bauer and W. Hummelbrunner

4. Geocoding and Classification of ERS/JERS-1 Composites 2335
Kellndorfer, J.M., M.C. Dobson and F.T. Ulaby

5. Experiences In Multi-Sensoral SAR Geocoding 2338
Roth, A., D. Kosmann, M. Matschke, B. Mueshen and H. John

6. Design, Performance and Technology Aspects in Relation to a Next Generation High Resolution Spaceborne SAR Instrument 2341
Bottger, H., C.Heer and J.J. Wilson

7. Development of a High-Resolution Ground-Based Synthetic Aperture Radar 2344
Morrison, K., and J.C. Bennett

8. Integrated Design of Synthetic Aperture Radars for Unmanned Aircraft 2347
Vesecky, J.F., and J.M. Cornwall

9. ER-2 IFSAR Digital Terrain Matrix Collection System 2349
Malliot, H.A.

FPZ -- Vegetation Properties

1. Novel Algorithms for Remote Sensing of Chlorophyll Content in Higher Plant Leaves 2355
Gitelson, A.A., M.N. Merzlyak and Y. Grits

2. Chlorophyll Flourescence Measurements of Several Plant Species Compared with MNDVI-Images in Air Pollution Affected Sites in Varanger, Northern Norway NA
Tommervik, H.

3. An Approach for Mapping Light-Use Efficiency on Regional Scales Using Satellite Observations 2358
Norman, J.M., M.C. Anderson and G.R. Diak

4. Detecting Spatial and Temporal Patterns of Aboveground Production in a Tallgrass Prairie Using Remotely Sensed Data 2361
Su, H., J.M. Briggs, A.K. Knapp, J.M. Blair and J.R. Krummell

5. Assimilation of Shortwave Remote Sensing Observations Within an Agrometeorological Model -- Crop Production Estimation 2366
Moulin, S., A. Fischer and G. Dedieu

6. Mapping Field Crop Evapotranspiration Using Airborne Multispectral Imagery 2369
Ahmed, R.H., and C.M.U. Neale

7. Effects of Shadows on Vegetation Indices 2372
Huemmrich, K.F.

8. Multisensor Estimation of Vegetation Characteristics 2375
Zhang, J., R.M. Narayanan, B.T. Tracy, B.L. Gwilliam, R.L. Bolus, T. Pangburn and H.L. McKim

9. Subpixel Spatio Temporal Pattern Analysis of Remote Sensing Observations for Predicting Grassland Ecological and Biophysical Parameters 2377
Csillag, F., A. Davidson , S. Mitchell, B. Wylie, D. Wedin, H. Peat and M. Kertesz

10. Retrieval of Crop Biomass in 1989 by Using ANN MODEL of 1988 2380
Jin, Y.Q.



IGARSS'96

1996 International Geoscience and Remote Sensing Symposium

Technical Papers

Discrimination of Africa's Vegetation Using Reconstructed ERS-1 Imagery

Perry J. Hardin[1], David G. Long[2], and Quinn P. Remund[3]
Microwave Earth Remote Sensing Group
690 SWKT, Brigham Young University, Provo, Utah 84602
Phone: 801-378-6062 Email: perry_hardin@byu.edu

I. INTRODUCTION

Currently there is an extended international effort to inventory and monitor equatorial vegetation. Because of persistent cloud cover typical of equatorial regions, active microwave imagery such as ERS-1 SAR is preferred over high-resolution visible and near infrared spaceborne sensors for this task. However, no active microwave instrument designed to provide continental coverage at resolutions similar to the popular AVHRR has ever flown -- neither are any planned for the future.

Satellite scatterometers are calibrated active microwave radar instruments originally designed to measure the radar backscatter of the ocean's surface under all-weather conditions. The first spaceborne scatterometer flew as part of the Skylab missions. The European Space Agency (ESA) successfully launched its ERS-1 satellite into a quasi-polar mission-adjustable orbit in the summer of 1991. The instrument payload included the Active Microwave Instrument (AMI) which is capable of operating in a wind scatterometer mode (5.3 Ghz) for the production of wind vector products.

The primary mission of the ERS-1 scatterometer is the determination of ocean surface wind direction and velocity. This is not surprising, because most land imaging applications require spatial resolutions finer than its 50 km footprint appropriate for large ocean expanses. However, an image reconstruction technique developed [1] has improved the AMI scatterometer resolution to 14 km, making it a candidate for coarse monitoring of cloudy global areas such as the Arctic, Antarctic, and continental equatorial forests.

The goal of the research reported in this paper is to evaluate reconstructed ERS-1 scatterometry for discriminating between vegetation classes of continental Africa.

II. METHODOLOGY

One of the first examinations of ERS-1 scatterometry over land was reported by Mogin *et al.* [2]. As described in that paper among many others, the ERS-1 scatterometer is a C-band instrument consisting of three antennae, one pointing 45° forward, another pointing 45° aft, and one pointing normal to the flight path. The 4.8 kW instrument with VV polarization, orbiting at approximately 785 km, has a swath width of 500 km, incident angle ranges between 18° and 59°, and produces imagery with a spatial resolution of 50 km.

Reconstruction of scatterometry to higher resolutions by using multiple satellite passes is described at length elsewhere [1]. Originally developed for Seasat-A scatterometer data (SASS), reconstruction of ERS-1 data does not produce equally high resolution. Summarizing, the SASS cell on the earth has an irregular hexagon shape with well defined geographic coordinates for each vertex. The generous overlapping of these hexagonal cells of different sizes at a variety of incidence angles allows for high sampling rates in the reconstruction. The result is reconstructed imagery with a cell resolution between 5 and 10 km.

In contrast, the tapered circular footprint of the ERS-1 scatterometer cell, with its cos^2 rolloff function provides insufficient definitive locational information for the same high-rate of sampling (with confidence), resulting in a lower resolution image (20 km). The reduced number of measurements produced by the single-sided operation further contributes to the problem.

The ERS-1 data used in the reconstruction for this research was acquired between April, 1992 and May, 1995 and covered 3 seasons. Twelve monthly average backscatter images were reconstructed, corresponding to each of the twelve calendar months. One of the reconstructed scatterometer images used is shown in Figure 1.

Reconstructing the entire African continent created an analysis problem. Since Africa spans both the northern and southern hemispheres, a vegetation class (e.g. tropical woodland) common to both hemispheres would have different backscatter averages dependent on the northern or southern hemisphere season. To rectify this problem, the twelve monthly images were split along the equator, and reconstituted so that corresponding months (*seasonally speaking*) were analyzed together.

[1] Department of Geography
[2] Department of Electrical and Computer Engineering
[3] Department of Electrical and Computer Engineering

0-7803-3068-4/96$5.00©1996 IEEE

The map database used for this study is produced by the World Data Center-A (WDC-A) for Solid Earth Geophysics in cooperation with the Data Management and Information Systems Working Group of the International Geosphere-Biosphere Program (IGBP). The purpose of the database is to provide a series of digital maps for global change analysis and climatic modeling. The database is used extensively by the United Nations Environmental Program (UNEP) and other international organizations. The database contains several vegetation-related grid-cell maps of continental Africa. Regrettably, none of the digital maps has the same high resolution as the reconstructed ERS-1 imagery, and all are highly tentative. The experiments described in this paper refer to the Matthews Vegetation map. Despite its low 1° cell resolution, it was chosen in preference to the others because of its broad categories of vegetation based on characteristic physiognomic classes. The original map consists of 21 vegetation classes, ranging from tropical evergreen forest to desert. Due to the inaccuracies typical in any map of such coarse resolution, vegetation classes with fewer than 600 cells on the continent were discarded, leaving 13 classes for the discrimination experiments.

The goal of this preliminary analysis was to determine whether sufficient information exists in the reconstructed ERS-1 imagery to distinguish between the Matthews vegetation classes. Three procedures were used:

- Calculation of simple descriptive statistics for each vegetation class for spring, summer, fall, and winter.
- Graphical analysis of backscatter change through the season for each vegetation class.
- Rudimentary discriminant analysis.

To conduct these analyses, the 12 monthly ERS-1 images were registered with the digital vegetation map, and the backscatter values for each underlying vegetation cell were extracted and recorded.

In the discriminant analysis, the vegetation classes were the dependent variables, and pixels from the twelve seasonal images formed the independent variables. In the tests described below, only one-third of the pixels for each of the 13 vegetation formations were used for training. The remaining two-thirds were reserved for testing the discrimination.

The fundamental approach used in the exploratory discriminant analysis was to continually regroup the original 13 vegetation categories into a much smaller set until the classification accuracy produced by discriminant functions reached an acceptable level. An effort was made to maintain logically consistent groupings. For example, while we felt free to combine equatorial forest categories with some woodland categories, we did not combine forest categories with unrelated categories such as desert. The quality of the supervised classification was assessed by a simple percentage of agreement between the map and predicted vegetation class.

III. RESULTS AND DISCUSSION

Backscatter values for the 13 vegetation classes, calculated for summer and winter seasons, are presented in Table 1. In general, regardless of the season, backscatter is the highest among the tropical forest classes and decreases progressively through the woodland and grassland categories. Desert produces the lowest backscatter.

Figure 2 is a graph of vegetation backscatter changes for the 12 composite months. To improve legibility, only nine of the 13 classes are shown. The graph shows how the backscatter for the equatorial forest classes changes little throughout the year. This is to be expected, since the equatorial forest vegetation is largely evergreen, and does not drop its leaves in response to seasonal changes in temperature or moisture. In fact, most of the evergreen classes show the same general behavior -- consistent backscatter throughout the year. Few of these classes are strongly affected by the shift of the Intertropical Convergence zone (ITC).

The desert class has consistently low backscatter throughout the year -- there is little vegetation to provide seasonally changing surface or volume backscatter.

In contrast to the classes which exhibit little change, the savanna woodlands and grasslands show a profound increase in backscatter during certain months as the grassy vegetation becomes greener, or as the trees leaf-out. As the ITC drifts away from these regions, and these savanna vegetation classes come under the influence of subtropical high pressure, the climate becomes more droughty, the vegetation rapidly browns, and the trees lose their leaves. The backscatter decreases during these months.

Initial attempts to discriminate between all 13 classes were disappointing. Furthermore, a final grouping of four classes produces an overall accuracy of only 63.5%, far less than the accuracy produced when a similar experiment was conducted over South America [3]. Class accuracy figures for this four group solution are presented in Table 2.

As the table shows, the evergreen forest and woodland classes are the most accurately classified, whereas the shrubland and mixed grass-shrubland are correctly classified less than 1/2 the time.

IV. CONCLUSION

Given the vegetation class seasonality depicted in the ERS-1 imagery, the mediocre classification accuracy is unexpected. Further investigation has indicated that the digital map being used for "ground-truth" is extremely generalized -- the satellite imagery depicts more detail in the vegetation than the map. We think that vegetation

mixtures along the vegetative region borders combined with the generalization in the map contributed to the lack of discrimination accuracy. In previous work with higher quality map sources and more selective sampling, classification accuracy exceeded 80%, although the same problems were cited [3].

Given the dramatic seasonal changes in the savanna classes, and the lack of seasonal changes in the tropical forest classes, there is strong evidence that reconstructed ERS-1 imagery can be used for regional vegetation mapping and monitoring. However, other evidence suggests that a single reconstructed image used alone would be insufficient -- a temporal sequence would likely be required. Inclusion of AVHRR or another reconstructed image type would also prove valuable. Mid-latitude and boreal forest research using reconstructed C-band scatterometry may also prove fruitful, especially when combined with high resolution SAR imagery.

V. REFERENCES

[1] D.G. Long, P.J. Hardin, and P.T. Whiting, "Resolution enhancement of spaceborne scatterometer data," IEEE. Trans. Geo. Remote Sensing, vol. 31, no.3, pp. 700-715, 1993.

[2] E. Mougin, A. Lopes, P.L. Frison, and C. Proisy, "Preliminary analysis of ERS-1 wind scatterometer data over land surfaces.," Int. J. Remote Sensing, vol. 16, no.2, pp. 391-398, 1995.

[3] P.J. Hardin and D.G. Long, "Discriminating between tropical vegetation formations using reconstructed high-resolution Seasat-A scatterometer data," Photo. Eng. Remote Sensing, vol. 60, no. 12, pp. 1453-1462, 1994.

Vegetation Formation	Summer	Winter
Tropical evergreen rainforest	-8.02	-8.28
Trop. broad-leaved seasonal evergreen forest	-8.44	-8.93
Evergreen broad-leaved sclerophyllous woodland	-10.22	-10.23
Grassland with < 10% woody trees	-9.47	-11.13
Tropical drought-deciduous woodland	-9.86	-11.15
Grassland with 10-40% woody trees	-10.35	-11.35
Meadow, short grassland, no woody cover	-10.77	-11.80
Tall grassland, no woody cover	-10.35	-12.10
Xeromorphic shrubland	-11.95	-12.19
Evergreen broad-leaved shrubland	-12.43	-12.37
Medium grassland, no woody cover	-11.64	-12.60
Grassland with shrub cover	-12.76	-13.41
Desert	-15.67	-15.97

Table 1. Seasonal backscatter averages

Vegetation class	Percentage of map pixels accurately classified
Evergreen forest and woodland	82.2%
Deciduous woodland and grassland	64.5%
Shrubland and mixed grass-shrubland	44.6%
Desert	72.2%

Table 2. Results from the discrimination analysis.

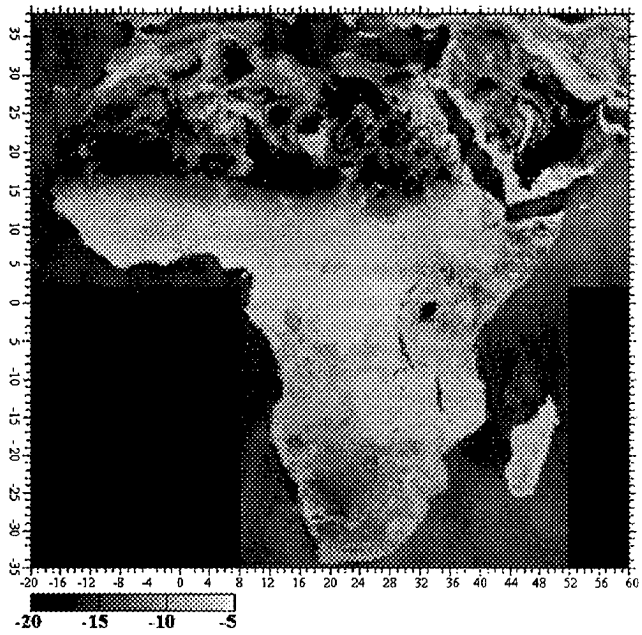


Figure 1. Reconstructed ERS-1 summer image.

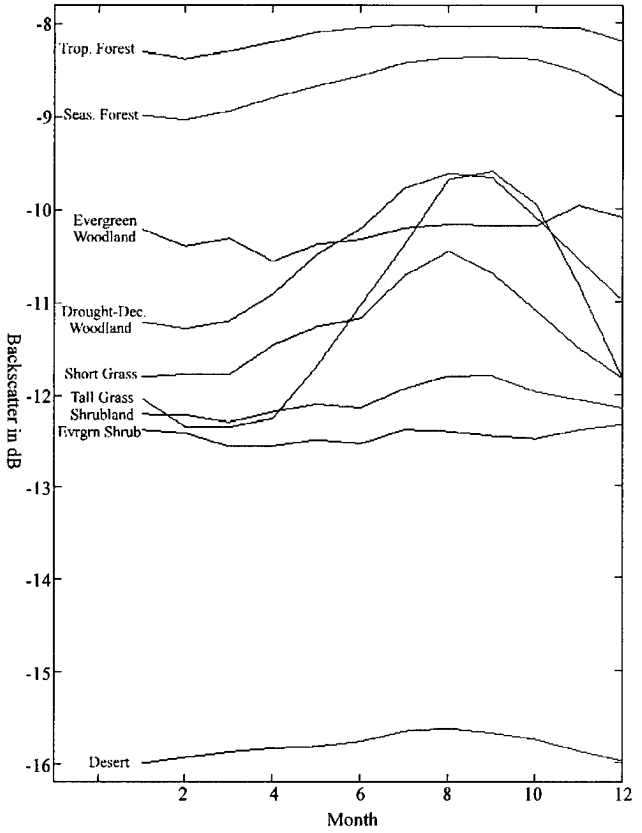


Figure 2. Seasonal change in backscatter for selected vegetation classes

Monitoring of the Sea Surface Thermal Patterns in a Marginal Sea Affected by an Ocean

Shigehisa Nakamura
Shirahama Oceanographic Observatory
DPRI, Kyoto University at Katada
Shirahama 649-22 Japan

Abstract-This work concerns monitoring of thermal patterns on the sea surface in a marginal sea.Some timely variations of the thermal patterncan be well detected by using the NOAA's APT(Automatic Picture Transform) imageries.Special reference is an eddy tracking in the Japan Sea as a marginal sea. The evolution of the eddy suggests us a dynamical process in the sea where effects of the ocean can be seen.Geographic and bathymetric effects must be contributive for the process.

INTRODUCTION

In order to realize monitored satellite thermal variations on the sea surface, this work is undertaken.For the purpose, the NOAA'sAPT imageries are directly received at the author's station. For convenience,the western part of the Japan Sea as a marginal sea is taken for the author's interest area.In this area,evolution of an eddy had been observed at an ocean flow variations.This result should be realized as a dynamic process.

By this time,the author has used the NOAA's APT imageries in the Northwestern Pacific for realizing the western boundary flow"Kurosio" just south of the Japanese Islands (1).Several works were monitoring of thermal variations of Kurosio flow in relation to storm flood spread(2-5).These work areas were a part of the Pacific as an ocean. In this work,the Japan Sea is the author's interest and the effects in the Pacific is seen also in the Japan Sea.

INFRARED APT DATA

For promoting this work,the data of the directly received infrared imageries were used, through a simple parabora antenna and a simple receiver and tranformer. A desk-top type of personal computer was utilized for processing the received data and displaying. When the imagely of AVHRR is used the size of the piksel is about 1 km square.Nevertheless,in this work the size of the piksel is adjusted as about 4 km square in order to fit the adjusted for our display after transforming the received signals.Even though, the imageries show us how are the variations of the thermal pattern on the sea surface.The APT data obtained after receiving as the real-time data can be utilized for the various purposed fields.

MARGINAL SEA

In the author's understanding, many of the contributions have been presented for the problems on the sea surface thermal variations in the ocean.In this work, an application for the existing marginal sea is considered. For convenience,the Japan Sea just neibor the Pacific is the case for this work.By this time, only a limitted scientist has payed his attention for detecting the sea surface variations which can be found by looking at thermal imageries of the NOAA's APT data. Special interest in tnis work is to describe a life of an eddy in the Japan Sea as a marginal sea.

0-7803-3068-4/96$5.00©1996 IEEE

THERMAL PATTERN

The area of the interested in this work is shown in Fig.1 where the bathymetry is not so simple. Even though, it should be in mind that a northern peak in the Korean Plateau is the location of the author's interest in this work.

A filament was found on 1st April 1993 as seen in the first block in Fig.2.The author had watched the filament on the sea surface to see an evolution of the filament that can be identified by the isotherms specifying the eddy and filament as seen in blocks in Fig.2.

Looking at the thermal patterns around the eddy and filament, the author has to consider that a cold core of the eddy is trapped by the northern peak of the Korean Plateau.

The filament in Fig.2 is specific because the filament is warm and creeping along the eastern coast of the Korean Peninsula. The water consisting the filament should be an inflow of the Kurosio flow through the East China Sea and the Tsushima Strait.

Considering about the variations of the sea surface thermal pattern in the Japan Sea,the peak seems to control cold core eddy there and to form a circular warm filament around the eddy.The filament must be driven by the shear forcing of the eddy.

This eddy must be found even by the Korean scientists though no contribution is seen even now.

In the other oceanic zone, for example,in the areas of the Gulf Stream and the Kuroshio flow,warm core ring has been well discussed though no detailed remark is here noticed.

With this work,it is clarified that the satellite thermal pattern in a marginal sea is useful at detecting effects of the ocean.

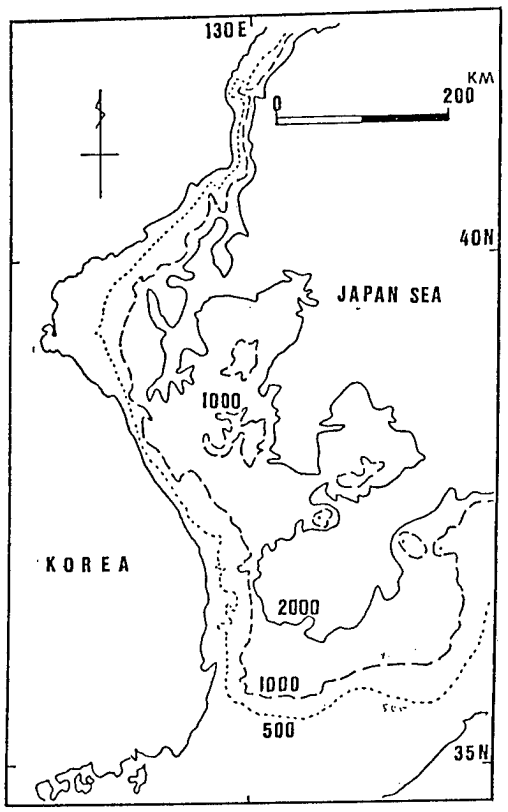


Fig.1 Bathymetry of the western Japan Sea.
The contours for 5oo,1000 and 2000 m deep.

REFERENCES

1)Nakamura,S."Satellite monitoring of storm runoff",Proc.5thConf.on Urban Storm Drainage,1990,pp.639-645.

2)Nakamura,S."Satellite thermal variations of Kuroshio," Proc. PORSEC92,vol.2,pp.835-840.

3)Nakamura,S."Satellite monitoring of storm flood spread as a land-ocean interaction,"IEEE Proc.of IGARSS93,Tokyo,pp.203-205.

4)Nakamura,S."Infrared monitoring of the Kuroshio in storms," in PORSEC93(eds.by I.S.F.Jones, Sugimori,Y. and R.W.Stewart), pp.465-472.

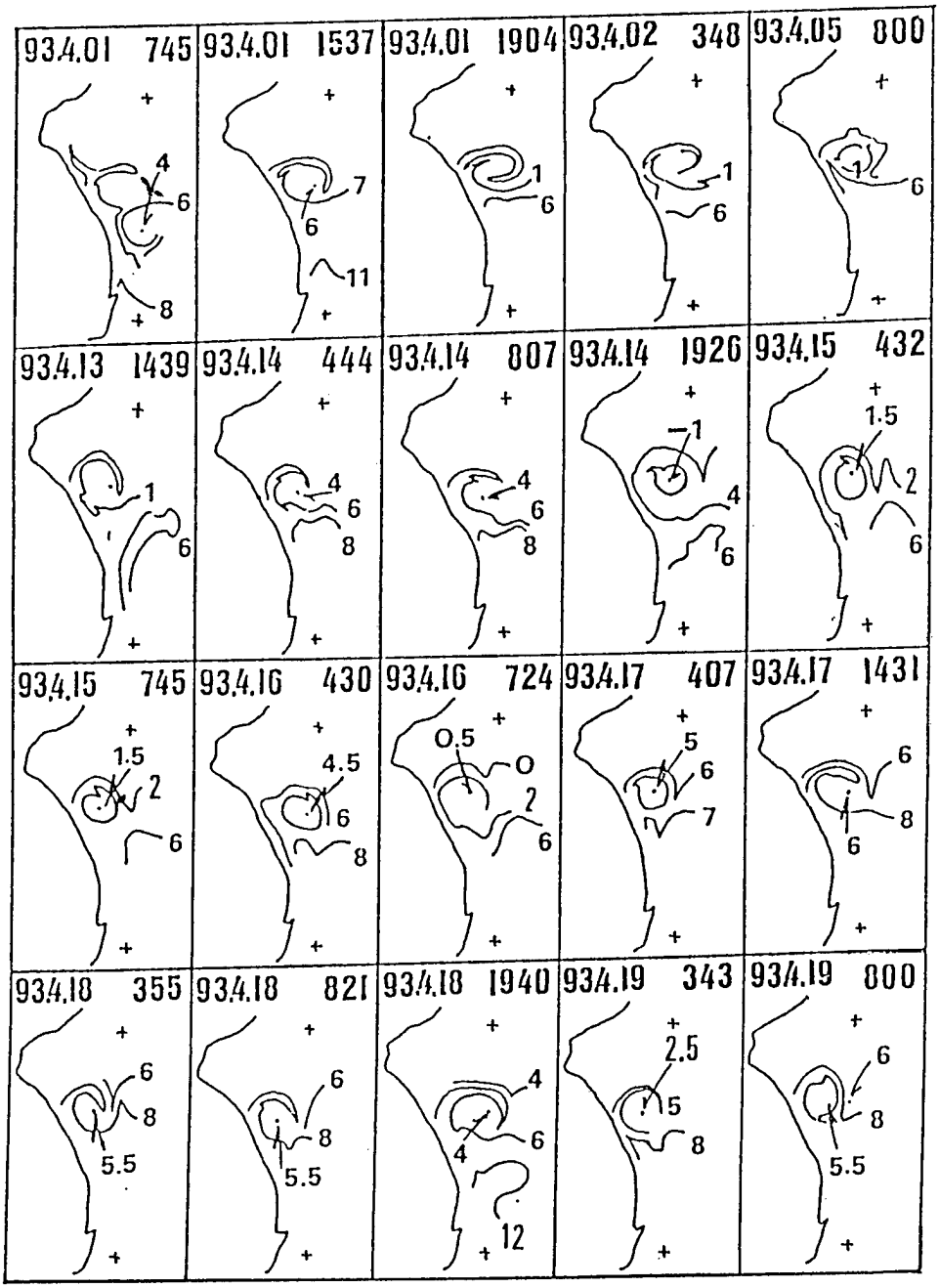


Fig.2 Sea surface thermal variations in the Japan Sea as a marginal sea where effects of the Pacific Ocean are seen.

1)The area is located in the western part of the Japan Sea as seen in Fig.1.

2)The two cross marks for the locations of 35°N and 40°N on the meridian of 135°E in each block.

3)The date and time is notated as 93.4.01 and 745 for 1993 April 1st and for 07h45m JST for example.

4)The numerals in the blocks for the apparent sea surface isotherms(°C).

Forest Classification by means of Pattern Recognition Method Applied to Scatterometer Data

M. Dechambre* and M. Bourdeau**

* CETP/CNRS 10 - 12 Av. de l'Europe 78140 FRANCE
phone : 33-1-39 25 48 51, fax : 33-1-39 25 48 72 email : dechambr@cetp.ipsl.fr
**Ecole Polytechnique, C.P. 6070-Centre Ville, Montréal, Québec, H3C-3A7
phone : 1-514-340 49 41, fax : 1-514-340 44 63, email : bourdm@ere.umontreal.ca

ABSTRACT

This paper presents vegetation classification results using C-band helicopterborne scatterometer data acquired over different forested areas during two experimental campaigns in France(1991) and in French Guiana (in the framework of the ESA SAREX campaign in 1992). The scatterometer involved in the two campains was ERASME, a small, low power, high resolution (1m), ranging radar. It operated as a sounder of the trees, in a nadir looking mode. A new pattern recognition method, which we call morphodecomposition, has been used to process the data and is presented also here. The results of this statistical method of analysis applied to four classes of forests are promising.

INTRODUCTION

Helicopterborne radar measurements have been carried out, firstly, during summer and winter of 1991 over a temperate forest in France [1], and secondly, during April 1992, over the French Guiana Rain Forest and Mangrove[2] (in the frame work of the SAREX-92 campaign organized by ESA and supported by ESA, CNES, and the French National Program for Spatial Remote Sensing).
The French radar involved was ERASME [3], a bi-frequency FM/CW high resolution (1m) ranging radar, used in a specific configuration, i.e., a nadir looking mode and a low flight altitude giving an antenna footprint, at 3 dB, of about 20m by 5m along the radar track. The X-band data (9.65 GHz) were only studied. One of the principal aim of that experiment was to test, in natural conditions,the capacity of microwaves to penetrate into the canopy, leading to a vertical description of it. A statistical processing of the data has been conducted, using a new method of pattern recognition, called morphodecomposition which provides a classification of the different types of forest from the radar data. A description of the data is given before a brief presentation of the morphodecomposition method. The results are presented in a last paragraph.

DESCRIPTION OF THE DATA

The return signal has not been processed in terms of a classical radar cross section, the raw data were directly used. These data are in the form of "spectra" (fig.1), which represent the power return in terms of the vertical range distance. Because of the good penetration of microwaves into the canopy, the shapes of those spectra are strongly related to the vertical structure of the sounded forest. This consideration is the starting point of our work : an attempt of classification of different types of forest by means of a pattern recognition method applied to raw nadir looking radar data.
We have plotted on fig.1 four typical spectra, corresponding to the four forests that we have observed with our radar :

- a deciduous French forest during summer (#1)
- the same forest during winter.(#2)
- the coastal swamp covered with mangrove.(#3)
- the tropical rain forest in French Guiana(#4))

In the sites #1 and #2, about 12 species of trees are present, with (#1) or without (#2) leaves. The site #4 is characterized by a great biodiversity (about 100 species/ha), and the shapes of the radar spectra are quite variable. On the contrary, the site #3 is covered with mangrove composed with only one species of tree.
In order to compare the four classes of forests in terms of the vertical structure of the vegetation, we made two transformations on the data -on the length of the spectra and the surface of its- which did not affect, obviously, the shapes of the spectra.
The lengths of the spectra. The first echo of the spectra corresponds to the top of the trees, the second one, which is, nevertheless, not always present (#4), corresponds to the ground echo. Then the length of a spectrum represents the height of the trees. This parameter is not a characteristic of a type of forest and has not to be taken into account in our analysis. We eliminated this parameter by shrinking or stretching the length of the spectra to a same value, arbitrarily taken equal to 100.
The surfaces of the spectra. The surfaces delimited by the curves are related to the flight altitude of the radar which is not constant from one data to another one. The volume of vegetation included into the antenna beam depends on this altitude. We have normalized the surfaces of all the spectra in order to compare them in a same manner.
We built four test files for the analysis corresponding to the four types of forests. Each file contains 15 spectra, chosen to be uncorrelated and to have representative shapes, that is to say, true to the majority of the spectra in a class.

0-7803-3068-4/96$5.00©1996 IEEE

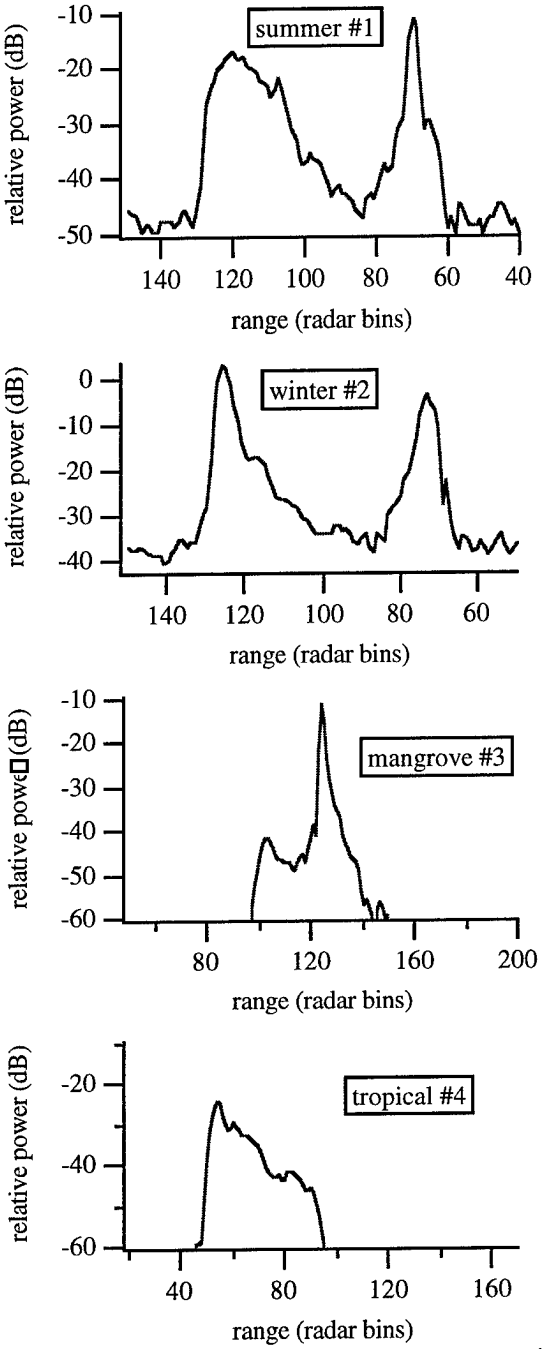


Fig.1 : Four examples of an ERASME spectrum acquired in the same radar configurations over the four types of forests investigated

MORPHODECOMPOSITION OF SAMPLES

The main ideas of our methodology, that we call *morphodecomposition*, were devised to identify manners of speech in linguistics [4]. An adaptation of this methodology to identify the time series has given promising results [5]. Morphodecomposition of a sampled signal is a two-step technique, an *analysis* of the given signal into simpler elements, and a *synthesis* of these elements into a signature comprising a number of features. Signals do not come alone, but usually are taken from a large collection or samples. The result of morphodecomposition then, forms a data matrix that can be analysed in view of the purposes of the applications, whether it is identification, determination of the number of classes of patterns, verification (as in signatures)...

Analysis. From a sequence of observations, $(t_i; y_i)_{i=1}^{L}$, equally spaced or not, we first obtain the sequence of first differences $\Delta y_i \equiv y_{i+1} - y_i, i = 1,\ldots, L-1$. The two-state case can be based, for example, on the sign of these differences. Let us say that the state a_i is *1* or *2* according to the sign of Δy_i. Actually, within certain limits, any cutpoint can be used for that purpose :

$$a_i = \begin{cases} 1 \text{ if } \Delta y_i \le c \\ 2 \text{ otherwise} \end{cases}$$

To generalize to the n-state case, one has to define $n-1$ cutpoints giving rise to n intervals on the real line, and a_i is the number of the interval containing Δy_i. Defined from the first differences of the samples, we have replace the L samples by $N=L-1$ states. The determination of the cutpoints and the production of the chains of states constitute the first step, the analysis of the methodology. The cutpoints can be determined according to one of the two following choices : either one uses equally spacing, or one uses equals masses, to determine them. The two alternatives were tested, and we decided the masses choice. They are calculated from the set of all first differences calculated from the data set under consideration. When ordered the cutpoints are their regular quantiles. For the two-state case, c can be the median. Similarly for the n-state case, the first cutpoint can be the $(1/n)$th quantile, and so forth. Now a sample signal is represented by a sequence of states or primitives $a_1, a_2, \ldots a_N$. This step is now followed by a synthesis providing a signature of each sampled sequencing properties of the units. A signature takes the form of a vector of features.

Synthesis : selection properties. Let us assume that we have n states and denote by $P_1 = \{p_{11},\ldots, p_{1n}\}$ their empirical probabilities observed on a given spectrum, by $P_2 = \{p_{21},\ldots p_{2n^2}\}$ the empirical distribution of the n^2 pairs of states, etc. The first order entropy associated to a given spectrum is given by

$$H_{n,1}(P_1) = -\sum_{i=1}^{n} p_{1i} \log_2(p_{1i}),$$

which is the average of the set $\{\log_2(p_{1i})\}_{i=1}^{n}$. It is to be noted that any perturbation of the a_i will give the same first

entropy. The second entropy of P_1 will begin to take into account some sequencing properties of the states :
$H_{n,2}(P_1) = H_{n,1}(second\ states\ /\ first\ states)$.
An easy calculation shows that
$H_{n,2}(P_2) = H_{n^2,1}(P_2) - H_{n,1}(P_1)$.
One can similarly define $H_{n,3}(P_1), H_{n,4}(P_1)$ and so on.

Synthesis : sequencing properties. Although the higher order entropies provide some sequencing characteristics for a signal, they describe mainly selection properties. In order to describe more precisely the former ones, we simply use the empirical transition matrix of the states, and calculate its eigenvalues and eigenvectors. We will keep only the *n-1* eigenvalues other than *1* (the transition matrix is a Markov matrix), and the *n-1* angles of the eigenvectors to the eigenvalue *1*. Those *2(n-1)* parameters provide a summary of the transition matrix structure.

RESULTS

In the application described here, we consider the states form $n = 2$ to $n = 5$, and order entropies up to the order 4. The signature resulting in the synthesis step comprises then 36 features. Sets of data are fed into statistical procedures, discriminant analyses, clustering procedures, factor analyses, etc.
We present now two sets of results, the first one corresponding to data with normalized lengths only, and the second one corresponding to data with both normalized lengths and surfaces. The statistical procedure adopted here is the discriminant analysis, but the other classical procedures cited have been tested and give almost same results. The results are presented in terms of diagonals of the confusing matrix, giving the percentage of success for each classification. We applied our method to the 4 classes of forets, i.e. #1,#2,#3,#4, and to 2 classes to times, i.e. #1, #2 (deciduous forest with and without leaves) and #3 ,#4 (mono-species forest and large biodiversity forest).

Data with normalized lengths

from type	#1	#2	#3	#4
#1	**85%**	8%	5%	2%
#2	5%	**93%**	2%	0%
#3	3%	7%	**81%**	9%
#4	5%	9%	14%	**72%**

from type	#1	#2
#1	**91%**	9%
#2	7%	**93%**

from type	#1	#2
#1	**91%**	9%
#2	18%	**82%**

Data with normalized lengths and surfaces

from type	#1	#2	#3	#4
#1	**89%**	6%	4%	1%
#2	6%	**91%**	3%	0%
#3	3%	6%	**83%**	8%
#4	3%	6%	13%	**79%**

from type	#1	#2
#1	**91%**	9%
#2	5%	**95%**

from type	#3	#4
#3	**95%**	5%
#4	13%	**87%**

These results are quite promising,we have done a comparison between the morphodecomposition efficiency and other classical methods one and we have presented it in a forthcoming paper[6]. We found that this new method seems to be more efficient than others. The badest results are obtain for the tropical site, which is not surprising. We observed great variations of the shapes of the spectra along a flight track. This variability is certainly caused by the apparent confusion of the canopy. In addition, the ground peak is not always present, du to a high absorption of the wave by the vegetation, which leads to a confusion in the classification. The results of the second set of data seems to be slightly better than those of the first set, but not for all the groups. The difference between the two sets of data is not very relevant.
As a conclusion, we may say that a pattern recognition method applied to nadir looking radar data can provide a classification of different types of forest. The next step of our investigations could be the same work applied on only one type of forest, in order to distinguish different vertical structures of a forest linked to natural disposition, desease, etc...In that case, other difficulties would appeared du to an unsupervised classification.

REFERENCES

[1] M. Dechambre, R. Bernard, E..Krasteva, "Nadir looking helicopter-borne radar observations over a forest of a temperate region", proceedings of the microwave signature conference, 1992, (Innsbruck, Autriche,01-03 Juillet).
[2] M. Dechambre," Radar measurements over the French Guiana mangrove", proceedings of the IGARSS'94, CALTECH, Pasadena, august 8-12, 1994, California, USA
[3] R. Bernard, D.Madjar-Vidal, F. Baudin, and G.Laurent, "Data processing and calibration for an airborne scatterometer," IEEE trans. on geoscience and remote sensing. Vol. GE-24, no.5, September 1986.
[4] M. Bourdeau, L. Dagenais, L. Santerre,"A quantitative framework for phonology",J. of Applied Linguistics, vol.87-88, pp121-150, 1990.
[5] M. Bourdeau & B. Burtschy, "Syntactic identification of ARMA processes", Ame. Stat. Ass. Proc. of the Business and Economic statistics section, pp169-171, 1994.
[6] M. Bourdeau & M. Dechambre, "Morphodecomposition compared to other techniques in the search for typical forms in radar spectra obtained from observation of forests", unpublished.

Use of Polarisation Synthesis for Deforestation Studies based on SIR-C/XSAR Data Analysis

Jean-Claude SOUYRIS - Thuy LE TOAN - Nicolas FLOURY - Laurent THOMASSON
CESBIO, 18 Av. Edouard Belin, BPI 2801, 31055 Toulouse Cedex, France
Ph : +33.61.55.85.84 E-mail : souyris@cesbio.cnes.fr

Chih-Chien HSU - Jin Au KONG
Department of Electrical Engineering and Computer Science,
Massachusetts Institute of Technology, Cambridge, MA 02139, USA
Ph : +1.617.253.8209 E-mail : chih@ewt.mit.edu

Abstract - This paper addresses the use of polarisation synthesis techniques for deforestation studies, through the analysis of polarimetric data acquired by the Spaceborne Imaging Radar-C/XSAR (polarimetric L- and C- bands, X band VV), in April and October 1994. For any basis of orthogonal polarisations, a collection of polarimetric discriminators is calculated. The following conclusions are derived : *1)* The degree of coherence at C band between HH and VV signals provides the best results for forest/non forest segmentation. *2)* L band HV is the more appropriate radar configuration for biomass estimation. *3)* The use of circular polarised intensity signals enhances the roughness effect over bare soils surfaces.

INTRODUCTION

In previous studies [1]-[2], SIR-C/XSAR data acquired over the Landes forest test site in South-Western France have been analysed at various incidences (26°, 51°) for forest/non-forest segmentation and regenerating forest mapping applications. Data analysis has been made conjointly with the development of a theoretical modeling using radiative transfer theory, coupled with a branching model taking into account coherent scattering effects due to the clustered vegetation structures [3]. L band HV configuration was found to offer the highest sensitivity to biomass content in the range [0 tons/ha, 100 tons/ha]. Besides, C band degree of coherence between HH and VV signals at low incidence angle (26.4°) led to the best results regarding forest/non forest segmention.

Using polarisation synthesis techniques, the objective of this work is to demonstrate the consistency of the above-mentioned configurations, but also to investigate the polarisation dependence of backscattering from forested and non forested areas. It consists in deriving the target response for any set of transmitting and receiving polarisation, from the knowledge of the polarimetric response derived in a linear polarisation basis $(\hat{h}, \hat{v})$. For every configuration, the degree of coherence between copolarised signals and the corresponding intensity signatures are calculated.

0-7803-3068-4/96$5.00©1996 IEEE

POLARIMETRIC FEATURES

Intensity information : The knowledge of the full polarimetric information, included either in the 3*3 covariance matrix $\left[\overline{\overline{C}}\right]$ or in the 4*4 Muller matrix $\left[\overline{\overline{M}}\right]$, permits the application of polarisation synthesis techniques in order to maximize/minimize the contrast between various types of targets. The simulated incident Stokes vector is given by : ${}^t\tilde{S}^i = (1, \cos 2\psi_i \cdot \cos 2\tau_i, \sin 2\psi_i \cdot \cos 2\tau_i, \sin 2\tau_i)$, where ψ_i and τ_i are respectively the orientation with respect to $\hat{h}$ direction, and the ellipticity of the polarisation ellipse (τ_i = 0° is a linear polarised wave, whereas $\tau_i = \pm 45°$ is a circular polarised wave) [4]. The free space backscattered energy is given by $\tilde{S}^{fs} = \left[\overline{\overline{M}}\right].\tilde{S}^i$ where $\tilde{S}^{fs}$ is the free space backscattered Stokes vector. Considering a receiving polarisation $\tilde{S}^{rec}$, the synthetised intensity response is linked to the measured power at the terminal of the receiving antenna, propotional to : $P^{rec} = {}^t\tilde{S}^{rec} \cdot \left[\overline{\overline{M}}\right] \cdot \tilde{S}^i$

The choice of optimal polarisations accordingly to a given objective has been extensively discussed in the past. A great deal of work has been done either to determine the optimal polarisations of incoherently reflected waves [5], [6], or to determine the optimal transmitting and receiving polarisations for maximizing the polarimetric contrast between two targets [7]. Regarding the contrast maximisation issue, the basic principle is a two-step process : *1)* The incident polarisation $\tilde{S}^i$ is chosen in such a way that the ratio P^{fs1}/P^{fs2} is maximum, where P^{fs1} and P^{fs2} are respectively the free space backscattered power density coming from *Target 1* and *Target 2*. This step is subject to alternative methods, which are either to derive an optimisation based on total intensities, or to consider the ratio between the adjustable intensity parts only, namely the polarised parts of the backscattered waves. Regarding the issue of optimal polarisations for incoherently reflected

waves, a numerical comparison between the two approaches [5]-[6] showed that the resulting mathematical and numerical problems turn out to be quite similar. *2)* Once $\tilde{S}^i$ is determined, the receiving polarisation $\tilde{S}^{rec}$ is adjusted so that $p^{rec\,2}$ is minimum. The interest of this approach is a total decoupling between the choice of the transmitting wave polarisation and the one of the receiving wave.

Coherence information : In addition to intensity-based information (which are shown to be critically dependent on site and measurement conditions, including calibration uncertainties), polarisation synthesis can be further applied to coherence information. The generalized *pp-qq* degree of coherence [8] is defined as :

$$\rho_{pp-qq} = \frac{\langle S_{pp} \cdot S_{qq}^{*} \rangle}{\sqrt{\langle |S_{pp}|^2 \rangle \cdot \langle |S_{qq}|^2 \rangle}}$$

where $(\hat{p}, \hat{q})$ is a basis of orthogonal elliptical polarisations. The notion of *contrast optimisation* between *Target 1* and *Target 2* has been assessed using the degree of coherence. The selected criterion is a maximisation of the difference between $|\rho_1|$ and $|\rho_2|$ estimated over the two extended targets under consideration. The search for other types of criteria remains nevertheless a topic for further studies.

APPLICATIONS

The contrast optimisation procedure has been applied to SIR-C data acquired over the Landes forest test site in South-Western France. This artificial forest is almost totally formed of maritime pine (pinus pinaster), and constitutes nearly one million hectares on a flat topography. The study area (Nezer test site) located within the Landes forest includes a collection of maritime pine stands ranging between *5* and *150 tons/ha.*

Over the Nezer test site, 4 different targets have been considered to assess the polarisation synthesis aspect. *Target 1* is a 46 years old forest (characterized by a biomass rate of 150 tons/ha). *Target 2* is a low vegetated area (clear-cut), *Target 3* is a smooth soil surface (r.m.s. height is 1.2 cm) and *Target 4* is a rough soil surface (r.m.s. height is 2.5 cm).

Forest / non forest segmentation

At C band and low incidence angle (24°), polarisation synthesis applied to the degree of coherence confirmed that $\rho\ hh - vv$ provided the best results for forest/non forest segmentation (the result of optimisation using *Target 1* and *Target 2* led actually to a basis of polarisations with ellipticity of 1°). L and C band coherence maps have been subsequently constructed, showing an enhanced contrast between classes, compared with the corresponding color composite images generated from intensity information [2]. Based on these maps, the unsupervised extraction of forest stands lower than 33 tons/ha has been achieved with an accuracy higher than 85%, whereas the discrimination between forest and clear-cut areas indicated an accuracy of 87%.

Biomass mapping

Once the segmentation forest/non-forest is achieved using C band $\rho\ hh - vv$, the objective is to investigate the most appropriate set of transmitting and receiving polarisations to enhance intensity contrast (considering the adjustable intensity part only) between *Target 1* and *Target 2*, and consequently stretching out the dynamic between forest stands of different ages, in order to set up a biomass estimation process of the forested areas. Using 24° L band data, the result of this optimisation is given by :

$$\psi^{i} = 0.5°,\ \tau^{i} = -0.5°,\ \psi^{rec} = 90°,\ \tau^{rec} = -1°$$

The optimal transmitting polarisation is a linear polarisation in the $\hat{h}$ direction, whereas the receiving polarisation is linear in the $\hat{v}$ direction. The result of the optimisation consequently confirms LHV as the more appropriate configuration for biomass estimation. Taking *Target 3* or *Target 4* instead of *Target 2* in the contrast optimisation process led to a similar result. **Fig. 1** shows a biomass map in the range [0, 100 tons/ha] derived from this configuration. The image was first segmented into two classes (forest / non forest) using C band $\rho\ hh - vv$. The original SIR-C image is 12 looks, which has been further processed with a Kuan filter applied with a 9*9 moving window.

Roughness mapping

In order to derive a roughness mapping over non forested areas, as a preliminary step to a moisture inversion process, contrast optimisation has been subsequently applied to *Target 3* and *Target 4*, which have the same moisture content. In this case, the optimisation result led to :

$$\psi^{i} = 43°,\ \tau^{i} = -37°,\ \psi^{rec} = 40°,\ \tau^{rec} = -30°$$

$\tilde{S}^i$ and $\tilde{S}^{rec}$ are fully elliptical polarisations, close to the circular configuration. It should be noted that circular polarisations provides similar results. **Fig. 2a-b** display respectively the 24°, L band filtered image over a bare soils area for this synthesis, and the corresponding filtered LHV image. The different roughness states over the bare soil surfaces clearly show up in **Fig. 2-a**, whereas the intensity level is almost constant in the LHV configuration (**Fig. 2-b**). A similar result has been presented in [4], considering lava flows of different roughness. In a parallel study [8], the degree of coherence expressed in a circular polarisation basis has been chosen as a roughness estimator.

CONCLUSION

The overall objective being to assess the capability of spaceborne polarimetric data for biomass inversion and deforestation monitoring, SIR-C/XSAR data acquired over the Landes test site showed the consistency of polarisation synthesis for biomass or roughness effects enhancement.

The preliminary results show also an obvious complementarity between intensity and coherence images, as well as the interest of polarisation synthesis. The study is currently applied to tropical forest areas in Brazil (Manaus Cabaliana, Sena Madureira), where extensive deforestation activities are in progress.

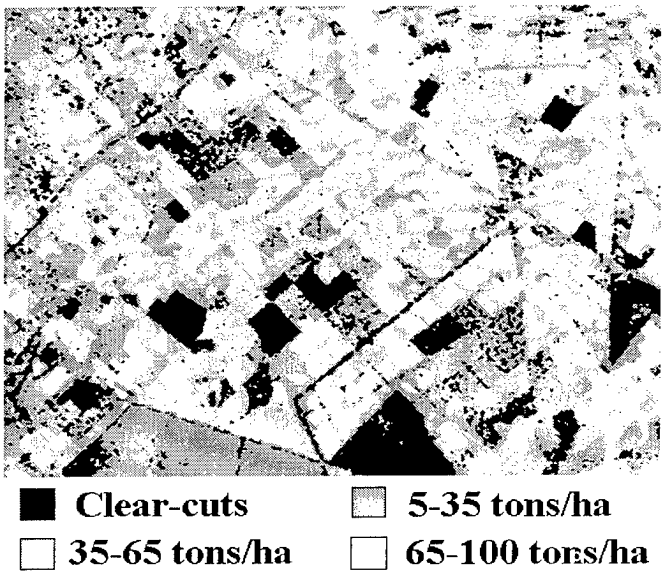


Fig. 1 : Biomass map of the Nezer test site

REFERENCES

[1] : J.C. Souyris, T. Le Toan, C.C. Hsu, J.A. Kong, « Inversion of Landes Forest Biomass using SIR-C/XSAR Data : Experiment and Theory, » in Proceedings IGARSS'95, Volume II, pp. 1201-1203, Firenze, Italy.

[2] : J.C. Souyris, T. Le Toan, N. Floury, C.C. Hsu, J.A. Kong, « Inversion of forest biomass using SIR-C/XSAR data, », submitted to IEEE Transations on Geoscience and Remote Sensing, March 1996.

[3] : Hsu, C.C., H.C. Han, R.T. Shin, J.A. Kong, A. Beaudoin and T. Le Toan, "Radiative transfer theory for polarimetric remote sensing of pine forest", International Journal of Remote Sensing, Vol. 15, no. 14, pp. 2943-2954, September 1994.

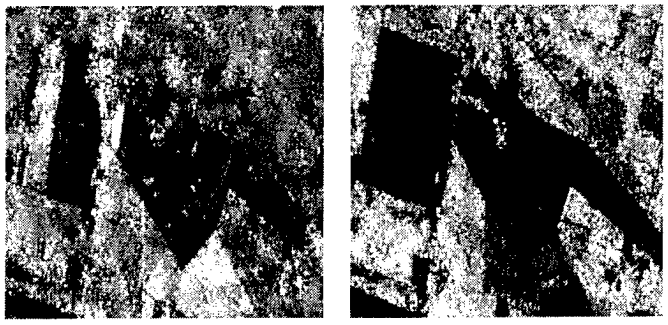
[4] : Zebker, H.A., J.J. Van Zyl, D.N. Held, « Imaging radar polarimetry from wave synthesis », Journal of Geophysical Research, vol. 92, no. B1, pp. 683-701, January 1987.

[5] : Van Zyl, J.J., C.H. Papas, C. Elachi, « On the optimal polarisations of incoherently reflected waves », IEEE Transations on Antennas and Propagation, vol. AP-35, No. 7, July 1987.

[6] : Kostinski, A.B., B.D. James, W.M. Boerner, « Optimal Reception of Partially Polarized Waves », J. Opt. Soc. Am. A, Vol. 5, No. 1, January 1988.

[7] : Kostinski, A. B., W.M. Boerner, « On the polarimetric contrast optimisation », IEEE Transations on Antennas and Propagation, Vol. AP-35, No. 8, August 1987.

[8] : De Carolis, G., F. Mattia, G. Pasquariello, F. Posa, P. Smacchia, N. Floury, T. Le Toan, J.C. Souyris, « Soil moisture estimation from multipolarisation and multifrequency SAR data », Proceedings IEEE Workshop « Retrieval of bio- and geophysical parameters from SAR data for land applications », Toulouse, 10-13 October 1995.



(a) **(b)**

Fig. 2 : L band, 24° image over bare soils of varying roughness. **(a)** $\psi^i = 43°, \tau^i = -37°, \psi^{rec} = 40°, \tau^{rec} = -30°$ **(b)** $\psi^i = 0.5°, \tau^i = -0.5°, \psi^{rec} = 90°, \tau^{rec} = -1°$ (HV)

ACKNOWLEDGMENTS

This work was supported by the Direction des Recherches et Etudes Techniques (DRET) under contract n° 94-091, the Centre National d'Etudes Spatiales (CNES) and NASA contract n° 958461. The authors thank Jerôme Bruniquel for image filtering work.

Can the ERS-1 Scatterometer be used to Forecast the Inundation Extent in the Pantanal Wetland ?

Volkmar R. Wismann and Kai Boehnke

Institute for Applied Remote Sensing, Bahnhofstrasse 54, 22880 Wedel, Germany,
T : +49 (0)4103 13922; F : +49 (0)4103 7469; E : 100412.1731@compuserve.com

ABSTRACT

Radar backscatter measurements obtained by the ERS-1 scatterometer over the Pantanal region between November 1991 and August 1995 are investigated. During this period the inundation extent varied considerably, a relatively wet year, 1992, was followed by dry years, 1993 and 1994, while in 1995 a maximum in inundation was encountered. This interannual variation is well reflected in the NRCS measurements. Furthermore, for the northern part of the Pantanal a very high correlation was found between the increase in radar cross section and the inundation extent if a time shift of 1-2 months is applied to the scatterometer data. Thus the radar measurements may allow to predict the inundation extent since the signal in NRCS is 1-2 months ahead of the flooding.

INTRODUCTION

In July, 1991, the European Space Agency (ESA) launched the First European Remote Sensing Satellite ERS-1 carrying a C-band (5.3 GHz) wind scatterometer for global wind measurements over the ocean. This sensor operates at vertical polarization (VV), its three antennae are looking 45 degrees forwards, sideways, and 45 degrees backwards with respect to the satellite flight direction, the incidence angle ranges from 18 to 57 degrees, the illuminated swath is 500 km wide, and the along-track and cross-track spatial resolution is 50 km. The normalized radar cross section (NRCS) measurements are independent of cloud coverage and illumination by the sun and provide a global coverage within 3 to 4 days.

The Pantanal in South America is one of the world's largest tropical wetlands. It is located in the upper Paraguay River basin, occupying an area of 137,000 km², located mainly in Brazil, only in the West, small parts are in Bolivia and Paraguay. Presently, the main river system is still unregulated. The climate of the Pantanal is tropical with a marked wet season between November and March. The annual rainfall across this region is generally 1000-1700 mm/a. The maximum inundation occurs in February in the northern regions and due to the delayed drainage of the river system as late as June in the southern part. The total area inundated can vary from 11,000 to 110,000 km². It has been demonstrated by [1] that passive microwave remote sensing can be used to monitor the inundation in the Pantanal area. The difference between vertically and horizontally polarized brightness temperatures at 37 GHz is used as an indicator for the presence of surface water. In our investigation we are using active microwave measurements of the normalized radar cross section (NRCS) at 5.3 GHz. We found not only a correlation between the inundation extent and the NRCS, but also a phase shift between both time series of 1-2 months where the radar signal leads the inundation extent.

RADAR BACKSCATTER DATA

In this investigation the NRCS measurements obtained between November, 1991, and August, 1995, are analysed. Until March, 1995, the full data set distributed on CD-ROM by CERSAT, the French Processing and Archiving Facility (F-PAF) was available and for the period April to August, 1995, Fast Delivery Copy (FDC) products were used.

For the analysis, monthly averaged NRCS values for two incidence angle ranges (18°-30° and 40°-57°) were computed on a grid with a resolution of 0.5° in latitude and 1° in longitude which corresponds roughly to the instrument resolution of 50 by 50 km. Fig. 1 depicts a sequence of NRCS maps of the Pantanal area constructed from the monthly averaged radar cross section measurements. These maps show distinct spatial variations of the NRCS as well as its seasonal and interannual variability. It is worth noting an area (marked by the arrow in Fig.1) of relatively low radar cross section which starts to development in summer 1993 and was detectable throughout the entire year,1994. While in 1995 the NRCS of this spot *returned* to it nominal value. The evolution of this spot correlates very well with the water level of the river Paraguay and the extent of the inundation.

CORRELATION WITH INUNDATION

Daily water level data for numerous stations along the Paraguay River were provided by the Departamento Nacional de Águas e Energia Elétrica (DNAEE), Brazil, for the period January 1991 to May / June 1995 [2]. These waterlevel data were used to extend the time series of inundation extent given by [1]. Fig. 2 depicts the time series of the total inundated area in the Pantanal between November 1991 and May 1995. This curve shows not only the seasonal variation of the

This research was funded by the European Space Agency within the Earth Observation Preparatory Programme (EOPP) under ESTEC contract 11103/94/NL/CN.

0-7803-3068-4/96$5.00©1996 IEEE

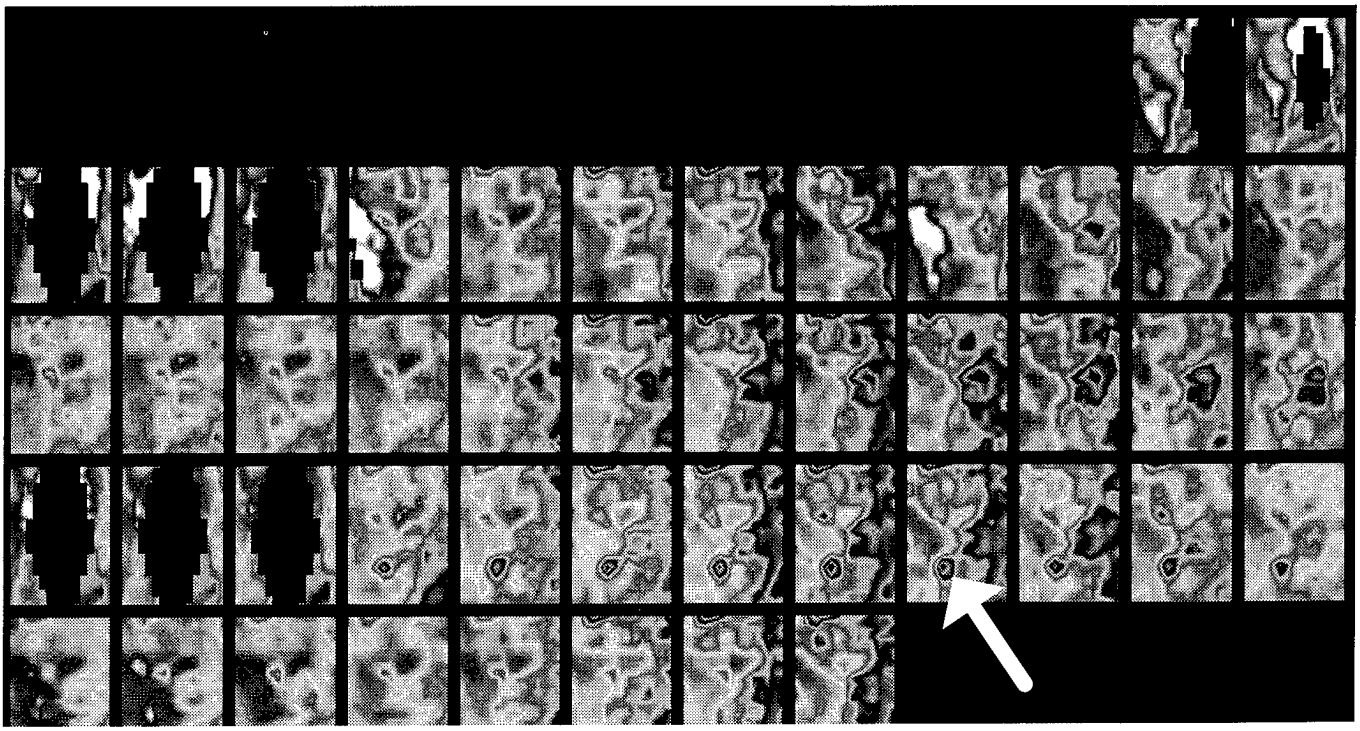


Fig. 1: A sequence of NRCS maps of the Pantanal area (corner coordinates are 16-22 °S; 54-60°W) for the years 1991 (top row) to 1995 (bottom row). Monthly averages from January (left) to December (right) show a distinct seasonal and spatial variation of the NRCS. Note the dark spot located at 20°S;58°W, south of the city of Corumba (marked by the arrow) which develops at the end of 1993, is clearly visible in 1994, and vanishes in 1995.

inundation extent but also a significant interannual variability with relatively low values between the end of 1993 and the end of 1994 and relatively large flooding after the rainy season in 1995. On top of this time series plot a Hovmoeller diagram depicts monthly averaged NRCS along a longitudinal transect at 57°W from 16°S to 22° S through the Pantanal area. Beside the spatial variation of the NRCS along the transect (see also Fig. 1) the seasonal and interannual variation of the NRCS can be delineated which seems to be correlated to the inundation extent shown in the same figure.

Fig. 3 depicts the correlation between the monthly averaged NRCS for the incidence angle range between 40°and 57° and the inundation extent. The NRCS data originate from the northern part of the Pantanal 17°S and 56.5°W close to Cuiabá, Brazil. Although the dynamic range in radar cross section is not very large there is a clear increase in NRCS with increasing flooding extent. Included in the plot is a linear regression line which represents the data points quite well. From monthly weather reports the 4 data points well above the regression line could be identified as months with exceptionally high precipitation events. The best correlation between the NRCS and the inundation extent was found when the inundation time series was shifted by 2 months with respect to the NRCS time series, which has been applied in this figure. Fig. 4 shows the correlation coefficient of the

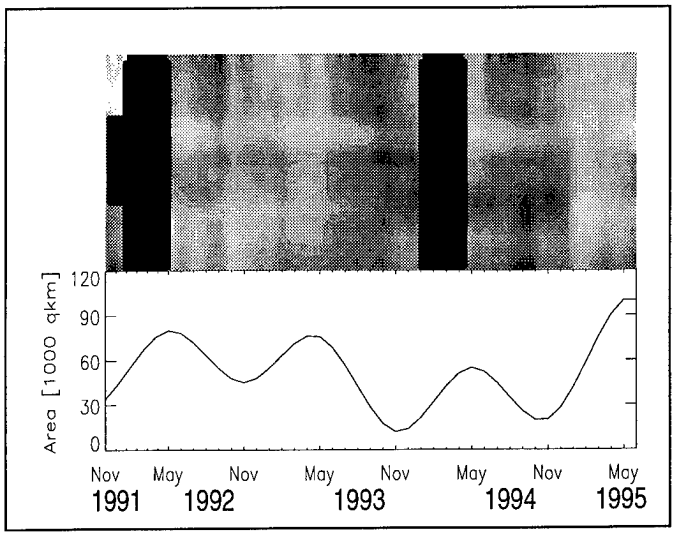


Fig. 2: Time series of the extent of the inundated area of the Pantanal (bottom) and a Hovmoeller diagram (top) of monthly averaged NRCS along a longitudinal section from 16°S to 22°S at 57°W. The black bars are due to data gaps during the two ice orbits in 1992 and 1994, respectively. Brighter tones correspond to higher radar cross section.

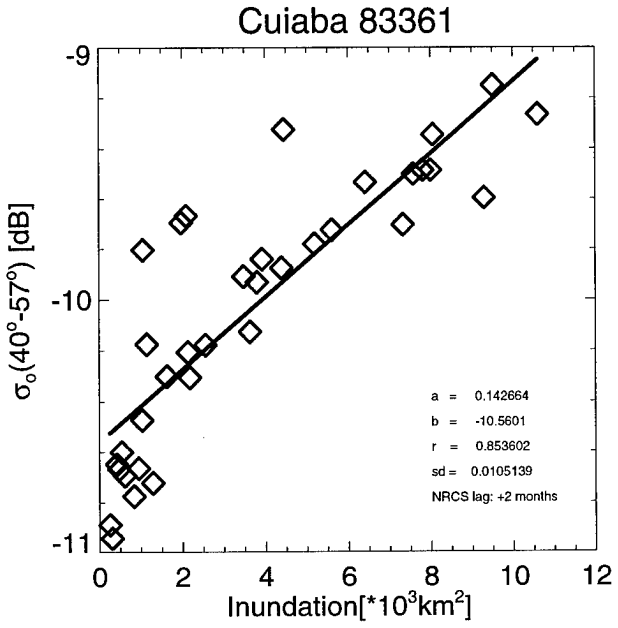


Fig. 3: Correlation between inundation extent and NRCS at 40°-57° incidence angle for an area in the northern part of the Pantanal south of Cuiabá, Brazil.

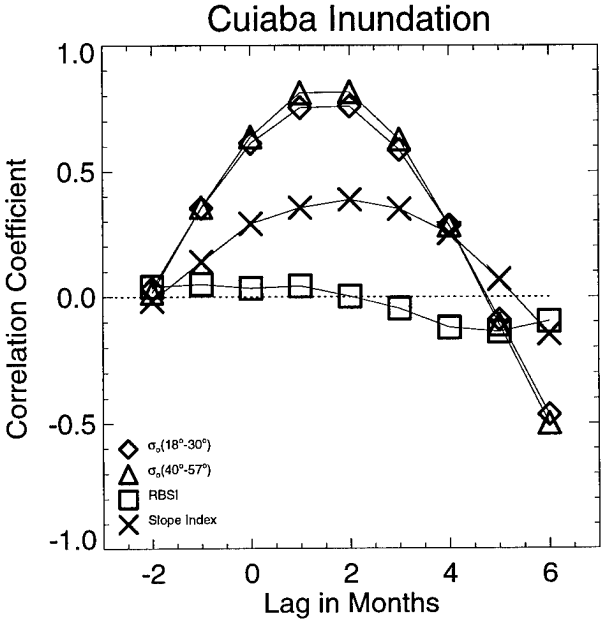


Fig. 4 : Correlation coefficient as a function of the time lag between the inundation and radar parameter time series. Data for the for the same location as in Fig. 3. Different symbols are used for different incidence angles and radar parameters

linear regression between the inundation extent and NRCS at 2 incidence angle ranges as a function of time lag between both time series (also shown are the curves for the RBSI and slope index, these parameters have been introduced by [3] in order to describe the radar backscatter from vegetation, but they are of no interest here). The best correlation can be found for a phase of 1-2 months between the NRCS and the flooding extent.

DISCUSSION

A high correlation between the NRCS and the inundation extent in the Pantanal area was found. The same correlation analysis was applied to the NRCS and precipitation data. Here, the precipitation curve was 1 month ahead the NRCS curve. Furthermore, we could not delineate any dependence on incidence angle of the scatterometer measurements. In summary this indicates that in this case the scatterometer is more sensitive to the vegetation than to the surface characteristics. The radar cross reacts to the onset of vegetation growth in the rainy season which happens timely between the actual precipitation and the flooding. Since the latter two are closely related the NRCS measurements may provide information on both parameters. The Pantanal is not a very inhomogeneous area in terms of NRCS as depicted in Fig.1 and in vegetation cover. This has to be taken into consideration when developing a retrieval algorithm for flooding extent in this area. But, the prospective of predicting the inundation extent by means of scatterometer measurements taken at least 1 month in advance will have a great impact on various ecological and economic aspects related to the rivers Paraná and Paraguay.

ACKNOWLEDGMENT

We are grateful to Senhor Vinicius and Senhor Avila of Departamento Nacional de Águas e Energia Elétrica (DNAEE), Brazil, for providing the water level data for numerous stations along the Paraguay River.

REFERENCES

[1] Hamilton, S. K., S.J. Sippel, and J.M. Melack, Inundation patterns in the Pantanal wetland of South America determined from passive microwave remote sensing, submitted to Water Resources Research, 1995.

[2] Avila, C., Departamento Nacional de Águas e Energia Elétrica (DNAEE), Brasilia, Brazil, pers. Communication, 1996.

[3] Wismann, V., A. Cavanie, D. Hoekman, I. Woodhouse, K. Boehnke and C. Schmullius, Land surface observations using the ERS-1 scatterometer, Report for the European Space Agency, ESTEC Contract 11103/94/NL/CN, 57 pages, Feb., 1996.

Use of ERS-1 SAR Data for Forest Monitoring in South Sumatra

Thuy Le Toan, Florence Ribbes, Thomas Hahn, Nicolas Floury
CESBIO - CNES/CNRS/Université Paul Sabatier, Toulouse, France
bpi 2801, 18 Avenue Edouard Belin, 31055 Toulouse Cedex
Tel : (33) 61 55 66 71 Fax : (33) 61 55 85 00
E-mail : letoan@cesbio.cnes.fr

Upik Rosalina Wasrin
Forest Ecology and Mapping - SEAMO BIOTROP
Jl Raya Tajur Km 6, PO Box 116, Bogor, Indonesia
Ph :(19) 62 251 323 848 Fax : (19) 62 251 326 851

ABSTRACT

In the frame of the joint ESA-CEC TREES project, the capacity of ERS-1 SAR data for mapping tropical forest, has been evaluated.

In this paper, we investigate new methods of discriminating forests from deforested areas using ERS-1 data over South Sumatra. The method developed is based on the temporal variation of the radar backscatter assessed by the ratio between two images, which permit to reduce the effect of terrain topography. The results show that using multitemporal data, with optimal acquisition periods, good forest/non forest discrimination could be achieved with the ratio based classifier.

The investigation of 5 multitemporal ERS-1 images permitted to build a forest/non forest map of the South of Sumatra (60 000 km²).

1- INTRODUCTION

Tropical rain forest covers 80 to 90 % of the terrestrial standing biomass. Three countries possess more then half of the total tropical dense forest : Brazil (33 %), Indonesia (10%) and Zaire (10 %) [1]. In Indonesia, Sumatra constitutes the most important forest resource. The South of Sumatra is characterised by the rapid depletion of the rain forest, mainly due to logging and permanent or semi-permanent settling of transmigrated population. The deforestation rate has been estimated to be of 1.6 % per year from 1978 to 1985. Thus there is an important need for surveying tropical forests in Sumatra.

This study has been initiated in the frame of the TREES ERS-1 project in order to develop methods for the discrimination of forest from deforested areas from SAR data in regions where cloud cover is almost permanent. The method developed is be applied to ERS-1 data in order to make a forest/non forest map of an extensive region of South Sumatra covered by multitemporal frames.

0-7803-3068-4/96$5.00©1996 IEEE

2 - STUDY SITE AND DATA ACQUISITION

The study site is situated in the South of Sumatra where the deforested land is either allocated to transmigration or to industrial plantation of palm tree and rubber. The remaining forests are located mainly on hilly or mountainous terrain, with various degradation stages due to access roads and logging.

Maps of land use have been realised by BIOTROP on 2 study areas covering 2 of the SAR frames using Landsat TM data and ground check. Three main vegetation units have been recorded :

1 - Non swampy vegetation including : a) primary forest, b) secondary, logged-over and depleted forest, c) secondary growth and d) grassland.

2 - Swampy vegetation including : a) primary forest, b) secondary forest, c) secondary growth, d) grassland and e) mosaic of secondary vegetation.

3 - Cultivated areas including : a) paddy, b) crops and c) plantations.

4 - Other land use including : a) habitat + reforestation, b) urban area, c) barren land, d) coast, e) fish ponds, f) area of transmigration.

The available ERS-1 data have been acquired on 8 SAR frames from the 22/09/93 to the 11/09/1994 with an average of 3 to 4 multitemporal acquisitions (fig. 1).

3 - ERS-1 DATA ANALYSIS

The radar backscattering coefficient (σ°) has been extracted from ERS-1 SAR data for different land cover types identified on the 2 SAR frames, at different acquisition dates.

Fig. 2 shows an example of σ° values extracted from images corresponding to the wet season (15/11/93) and to the dry season (09/06/94). The analysis can be synthesised as follows :

- Forest areas have shown a good temporal stability in σ°. Lowland forest have in addition a good spatial stability values. Small temporal changes in the responses (> 1 dB) can

be attributed to heavy rainfall or dry conditions. Between the forest classes, only small differences (< 1 dB) have been measured. The same trend in temporal variation has been observed with forests in mountainous areas. However, the backscatter values are spatially variable due to the relief effect (as much as 10 dB, from -12 dB to -2 dB).

Non-forest classes have a wide range of backscatter responses and can present a large temporal changes :

- In general agricultural crops have significant temporal changes due to the combined effect of vegetation growth, soil moisture and soil roughness.
- Tree plantations can have a variable backscatter. Mature plantation were found stable in time with σ° that can be confused with the forest. However some plantations such as coconut or palm tree have higher backscatter than the forest. Young plantations, less dense in terms of biomass, tree density and tree height were characterised by a temporal change of σ°.
- Clear cut areas can have a large range of backscatter responses according to the clear cutting practices, which result in a diversity of surface conditions (soil roughness, presence of tree trunks, vegetation regrowth).
- Other non temporally stable land covers include swamps, savannah and water bodies, whereas urban areas appear particular with high backscatter values and no temporal variation.

3 - METHODOLOGY

Based on the above observations, in lowland areas, the forest classes can be characterised by their backscatter values (e.g. : 7.5 dB ± 1 dB) together with their temporal change (e.g. : ≤ 0.5 dB). In areas with relief, only the temporal change can be used as classifier, unless a precise DEM is available.

The method developed here is based on the temporal variation classifier. The threshold for forest areas corresponds to a temporal change of less than 1 dB. The optimum data acquisition dates should maximise the temporal change of non forest classes. A minimum pair is one acquisition at the wt season and one at the dry season. The method consists of :

1 - Speckle reduction filtering using a multitemporal filter that reduces the speckle effect significantly while providing relatively less damage in the spatial resolution and preserving fine structure [2]. This filter was combined with a simple mean filter.

2 - *Temporal image ratioing* : a normalised ratio (called Temporal Change Index) of the mean backscatter values acquired at different dates has been developed to quantify the temporal change between 2 acquisitions. Moreover, the ratio, when applied to perfectly overlaid images, permit to get rid of the relief effect. As the ratio is very sensitive to the speckle noise, the images have to be strongly filtered. The Effective Number of Looks (ENL) must be 128 for detecting changes ≥ 1 dB with an accuracy of 80 % [3]. The filtering process described above permitted to reach the appropriate ENL.

3 - *Forest/Non forest Segmentation*: the forest / non forest image is generated using a threshold on the Change Index image. On frames with no relief it was possible to improve the result using the backscatter value of forests in order to discriminate forests from other temporal stable land cover such as urban areas or tree plantations.

Fig. 3 to 6 show respectively 2 ERS-1 acquisitions on one SAR frame, the corresponding Change Index image and the resulting forest/Non forest segmentation.

5 - FOREST / NON FOREST MAP OF SOUTH SUMATRA

The forest/non forest map of South Sumatra was obtained by making a mosaic of the resulting forest/non forest maps over the different ERS-1 frames.

Fig. 7 shows the result of the mosaicking of forest/non forest maps of a large part of South Sumatra (200x300 km). The resulting pixel size after the different averaging processes is about 150 m.

6 - CONCLUSION

The forest/non forest mapping method appears very promising in spite of the complexity of the land-cover distribution and the effect of the relief.

Current work consists in evaluating quantitatively the results which are provided at an intermediate resolution (150 m) compared to high resolution optical data (SPOT, Landsat) and low resolution data such as NOAA/AVHRR. At a specific site, the remaining uncertainties are due to the confusion with other temporally stable cover classes. In mountainous areas those classes include also the shadow and the bright parts of the images due to the SAR viewing effect. The small size of the cover classes will also be a limiting factor which increases the uncertainties in the backscatter values and their temporal ratio.

Nevertheless, the forest/non forest mapping results appear very promising. A strategy for deforestation monitoring will consist in updating regularly the results with new ERS1/2 data in regions of active deforestation.

ACKNOWLEDGMENTS

The work has been conducted partly in the frame of ESA-JRC TREES-ERS1 94 project. ERS-1 data have been provided by ESA.

REFERENCES

[1] J.P. Lanly, 1982. « Tropical forest resources ». FAO, Rome, 113 p.
[2] J. Bruniquel and A. Lopes, 1994. « Analysis and enhancement of multi-temporal SAR data », SPIE/EUROPTO Symp., Rome, vol. 2315, pp. 342-353.
[3] E.J.M. Rignot and J.J. Van Zyl, 1993. " Change detection techniques for ERS-1 SAR data ". IEEE Transactions on Geoscience and Remote sensing, Vol. 31, N° 4, pp. 896-906.

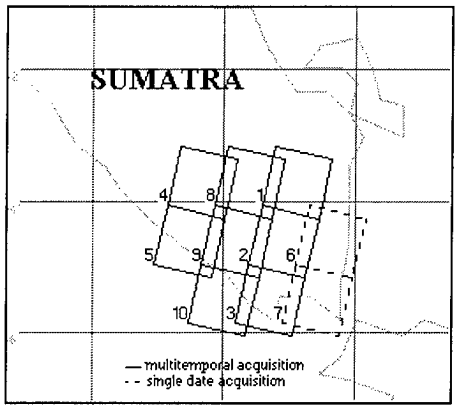


Fig. 1 : ERS-1 SAR data available over South Sumatra

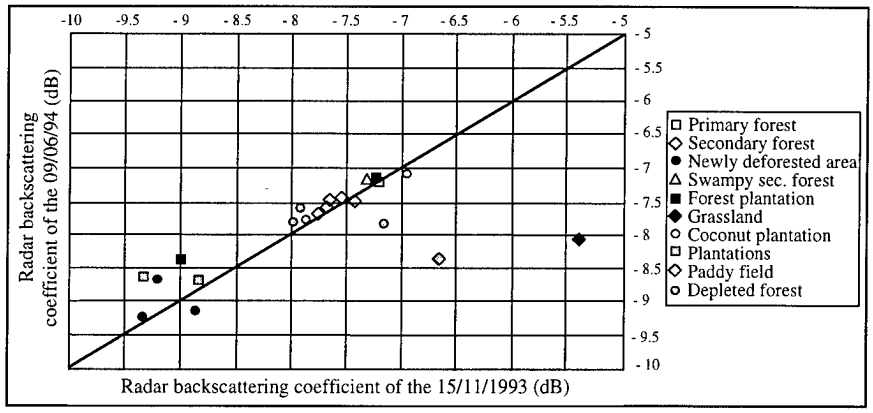


Fig. 2 : σ° of different land covers at one test area in South Sumatra



Fig. 3 : ERS-1 image (01/12/93)



Fig. 4 : ERS-1 image (05/08/94)



Fig. 5 : Change Index image



Fig. 6 : □ Forest / ■ Non forest map

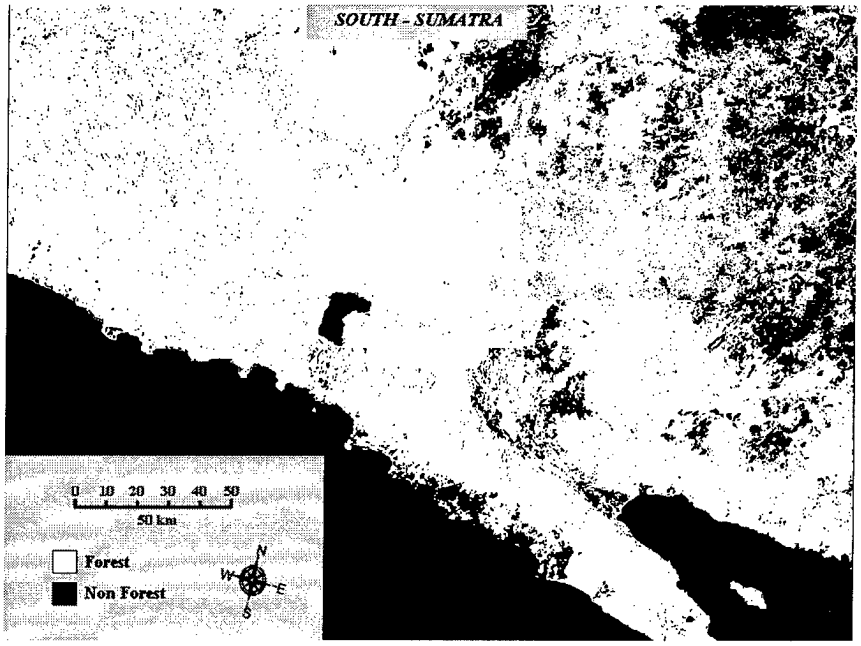


Fig. 7 : Mosaicked Forest / Non forest map of South Sumatra

Tropical Forest Monitoring Using Data From The ERS-1 Wind Scatterometer

Iain H. Woodhouse and Dirk H. Hoekman

Wageningen Agricultural University
Department of Water Resources, Nieuwe Kanaal 11
6709 PA Wageningen, The Netherlands
tel: +31-317-484288 fax: +31-317-484885 email: woodhouse@rcl.wau.nl

ABSTRACT

In this study, ERS-1 Wind Scatterometer data is used to map regions of tropical rainforest in the Amazon Basin, Africa and Borneo. Within these regions the seasonal and spatial variations of the backscatter characteristics are investigated. Through the use of additional spaceborne SAR data some possible explanations are presented for the characteristics observed. The results demonstrate the potential of scatterometer data for meso-scale monitoring of tropical forest.

INTRODUCTION

The ERS-1 Wind Scatterometer (WSC) instrument was designed to measure the near-surface wind field over the ocean by inferring the wind from measurements of the surface radar backscatter. Backscatter measurements, however, are also made over land and several studies have highlighted the ability of space-borne low resolution scatterometers to distinguish between general land cover classes by considering their backscatter characteristics as functions of incidence angle and time [1].

The WSC can provide frequent global coverage with a repeat cycle of <4 days, and unlike optical and IR instruments is not affected by persistent cloud cover. While the nominal resolution of the data is coarse (50-km) it is well suited for meso-scale land cover monitoring for use in global climate models.

BACKGROUND

"Tropical rain forest" is a term often loosely used to describe the relatively homogenous areas of dense forest found astride the equator in Latin America, Africa, South East Asia and Australia. For the purposes of forest monitoring, however, such a general class of forest type is grossly oversimplified. The UNESCO regional scale land cover maps of South America, for example, divides forest into six sub-categories [2]. Such sub-categories were used by Long and Hardin (1994) [3] to perform a supervised classification of the Amazon Basin which distinguished four sub-classes of tropical forest using enhanced resolution Seasat (Ku-band) Scatterometer data. These sub-classes contained a mixture of a number of forest types (as defined by the UNESCO data) with the classes of higher backscatter having progressively more formations of "extremely moist forest", and "wet submontane forest".

Analysis of the monthly averaged ERS-1 C-Band scatterometer data, however, indicates that the distinction between regional-scale forest classes is not so clear. Over the range -5.5 to -7.5 dB (in $\gamma=\sigma^0/\cos\theta_i$) the distribution is approximately Gaussian with a mean at around -6.5 dB. Such results are supported by other studies which have tried to use C-band VV polarisation backscatter to distinguish forest types in tropical areas. The histograms in Fig. 1 come from a study of ERS-1 PRI SAR data of Guyana and Colombia [4] and illustrates that although it may be relatively easy to distinguish between forest and non-forest, there is little opportunity to discriminate forest types.

TROPICAL FOREST MAPPING

In global terms tropical forests exhibit the following backscatter characteristics:

1.A very stable backscattering signal throughout the year, with an annual variation of less than 1 dB;

2. Very high backscatter (γ > -7dB) at angles of incidence

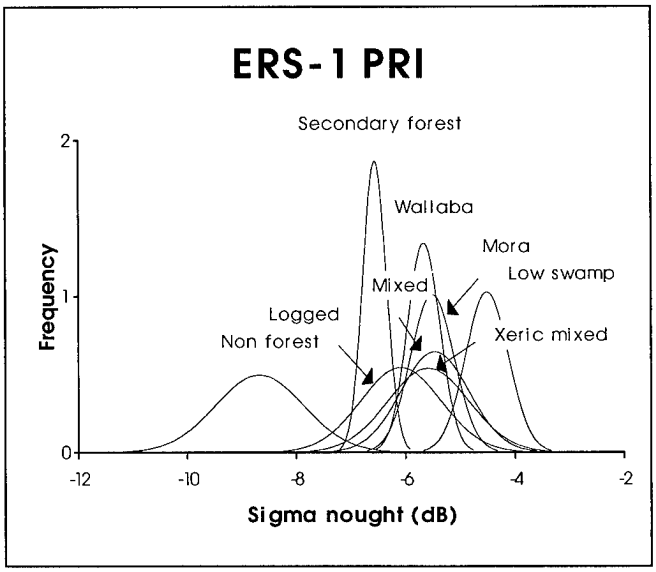


Figure 1. Backscatter histograms for studied cover types in Guyana and Colombia. Data derived from ERS-1 SAR.PRI images on April 29 1992 and May 26 1992 (from [4]).

0-7803-3068-4/96$5.00©1996 IEEE

above 45°; and

3. Backscatter as a function of incidence angle characteristic of volume scattering (defined here as (average γ in 15-30° range) -(average γ in 45-60° range) < 0.4 dB).

Using these characteristics as classification criteria maps of regions composed mainly of dense tropical rainforest have been made for the Amazon Basin, Africa and Borneo and are shown in Fig. 2 (a) to (c). Areas classed as forest have been density sliced as a function of their γ at large incidence angles with the density slices in steps of 0.25 dB in mean gamma from -7.0 to -5.75.

While there are no discrete regions to be identified in these data, the maps do show a spatial variation in the backscatter over large areas. Analysis of the asymmetry of the measurements in these regions indicates that the variation is not related to the variation in topography (directly) but may be due to variations in levels of annual precipitation and therefore regional plant vigour or surface conditions (either directly in the form of increased soil moisture and/or flooding, or indirectly as a consequence of changes in understory vegetation). Such conclusions are supported by analysis of ERS-1 SAR PRI images over the Mabura Hill area in Guyana in [4]. This study has identified a seasonal difference in the mean backscatter of forested regions of as much as 1dB between wet and dry seasons, with the wettest season giving the highest backscatter. Small seasonal variations (<0.75dB) are also observed in the scatterometer data. The small magnitude of these fluctuations has meant that such variations have often been overlooked or ignored in the past. Figure 6 illustrates the seasonal behaviour of the backscatter in the Mabura Hill area of Guyana. Both the ERS-1 SAR and the WSC data show a minimum around October during the dry season. The magnitude of the seasonal variation is a consequence of the different incidence angles: at the high incidence angles of the plotted WSC data the backscatter is less dependent on the surface conditions than the steeper incidence angles of the ERS-1 SAR. This result supports the suggestion that the surface characteristics are the prime factor determining the seasonal behaviour.

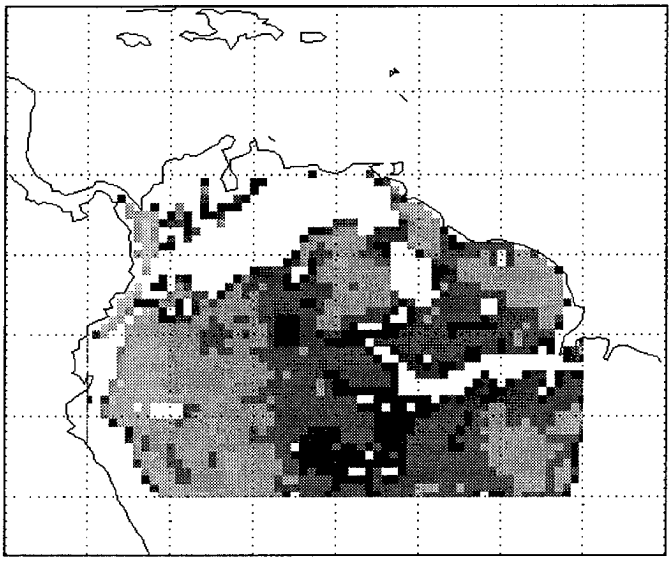


Figure 2 (a) See next page for description.

CONCLUSIONS

Space-borne low resolution scatterometer data clearly has potential as a means of monitoring tropical forests. However it is likely that such data will be most efficiently used in conjunction with complimentary satellite data. Further analysis of the scatterometer data over tropical forest regions with the use of backscatter models to predict expected microwave responses should help to identify the main biophysical parameters influencing the scatterometer observations.

REFERENCES

[1] V. Wismann, K. Boehnke, and C. Schmullius, "Radar signatures of land surfaces measured by the ERS-1 scatterometer". Space at the Service of our Environment, Proceedings of Second ERS-1 Symposium held in Hamburg, Germany, 11-14 October 1993, ESA SP-361 (European Space Agency), pp. 405-410.

[2] UNESCO, Vegetation map of South America, 1:5,000,000. Institut de le Carte Internationale du Tapis Vegetal, Toulouse, France, 1980.

[3] D.G. Long, and P.J. Hardin, "Vegetation studies of the Amazon Basin using enhanced resolution Seasat Scatterometer data". IEEE Transactions on Geoscience and Remote Sensing, Vol. 32, No. 2, pp. 449-460, 1994.

[4] J.J., van der Sanden, "Analysis of ERS-1 SAR data for Mabura Hill, Guyana". Proceedings of the TREES ERS-1 Study 94 Final Workshop, held in Ispra (JRC), 23-24 February 1995 (European Space Agency)., in press.

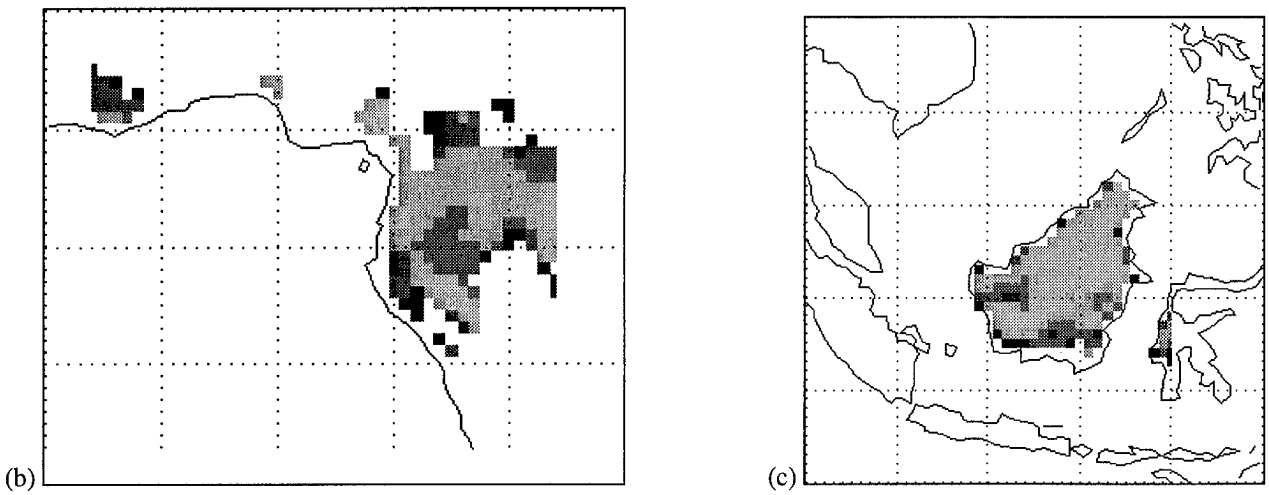


Figure 2. Density sliced images of tropical forest regions in (a) Amazon, (b) Africa, and (c) Borneo. The density slices are in steps of 0.25 dB with the darkest regions representing γ in the range -7.0 to -6.75 dB.

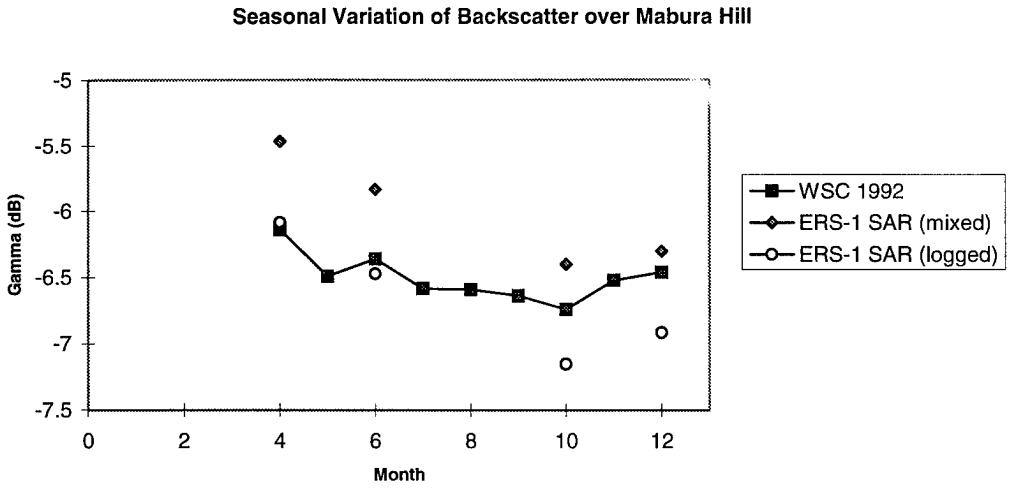


Figure 3. Seasonal behaviour of backscatter in the Mabura Hill area of Guyana. Solid line represents the WSC measurements made over a 9 month period in 1992. The individual points are measurements made from ERS-1 SAR data for different land cover types (mixed forest and logged forest) in April, June, December 1992 and October 1993 (from [4]). The minimum occurs during the dry season.

A Comparison of Reconstructed Ku-band Scatterometry, C-band Scatterometry, and SSM/I Imagery for Tropical Vegetation Classification

Perry J. Hardin[1], David G. Long[2], Quinn P. Remund[2], and Douglas R. Daum[2]
Microwave Earth Remote Sensing Group
690 SWKT, Brigham Young University, Provo, Utah 84602
Phone: 801-378-6062 Email: perry_hardin@byu.edu, david_long@byu.edu

I. LOW-RESOLUTION MONITORING OF EARTH

In support of efforts to detect and measure global climate and landcover change, remotely sensed imagery is frequently employed. Because these monitoring efforts are truly *global*, low-resolution sensors are frequently preferred over high resolution Landsat and SPOT sensors. For example, Advanced Very High Resolution Radiometer (AVHRR) imagery and its derivative vegetation indices are utilized for inexpensive low-resolution monitoring of equatorial forests where high-resolution imaging with Landsat-type satellites would be inappropriate.

The AVHRR instruments that flew on polar orbiters NOAA-7, NOAA-9 and NOAA-11 were five-channel radiometers capable of continuously scanning the earth with 1 km ground resolution. While these 1 km data are available for limited portions of Earth, AVHRR global area coverage (GAC) data are resampled on-board the satellite to 4 km resolution and stored for later transmission. The popular global vegetation index products derived from GAC data are further resampled to resolutions between 13 km and 26 km. The two AVHRR channels typically used for vegetation inventory include:

1. 0.58 to 0.68μm
2. 0.725 to 1.10μm

In contrast to AVHRR, *microwave* radiometers are electromagnetic receivers which measure radiation in the frequency band of 1-300 Ghz. Microwave radiometers have proven invaluable for collecting global geophysical information. The Special Sensor Microwave / Imager (SSM/I), part of the Defense Meteorological Satellite Program, has been used to measure cloud water content, precipitation, snow cover, and surface temperature. Currently two SSM/I instruments are operational. SSM/I is a seven channel, four frequency radiometer. The frequencies include:

1. 19.35 Ghz, Vertical and horizontal polarizations
2. 22.235 Ghz, Vertical polarization only
3. 37.0 Ghz, Vertical and horizontal polarizations
4. 85.5 Ghz, Vertical and horizontal polarizations

The 3dB footprint for the SSM/I ranges from 13 to 69 km -- it is dependent on frequency and direction (along-track vs. cross-track).

Whereas microwave radiometers are passive, satellite scatterometers are active microwave instruments originally designed to measure the radar backscatter of the ocean's surface under all-weather conditions. The first spaceborne scatterometer flew as part of the Skylab missions. Between June and October of 1978, the Seasat-A Scatterometer (SASS) was able to obtain nearly continuous global, dual polarization Ku-band coverage at a spatial unit cell resolution of 50 km for nearly 100 days. The European Space Agency (ESA) successfully launched its ERS-1 satellite into a quasi-polar mission-adjustable orbit in the summer of 1991. The instrument payload included the Active Microwave Instrument (AMI) which is capable of operating in a vertically polarized wind scatterometer mode (5.3 Ghz) for the production of 50 km resolution cell wind vector products. Other scatterometer launches are planned.

With the exception of AVHRR, the primary mission of all the instruments described has been the remote sensing of the earth's atmosphere and ocean. This is not surprising, because most land imaging applications require spatial resolutions finer than the footprints appropriate for large ocean expanses or atmospheric sounding. However, a new multivariate image reconstruction technique [1] has improved the resolution of imagery produced by SASS, the ERS-1 scatterometer, and SSM/I to resolutions between 5 and 20 km, making them candidates for medium-scale monitoring of cloudy global areas such as the Arctic, Antarctic, and continental equatorial forests. Furthermore, successful efforts have been made to remove atmospheric distortion in the SSM/I data [2].

One goal of the research reported in this paper is to combine these reconstructed image data sets with AVHRR vegetation index images for discriminating between vegetation formations in central South America. This also provides an opportunity to compare the utility of the various image types for equatorial vegetation discrimination in general.

[1] Department of Geography
[2] Department of Electrical and Computer Engineering

0-7803-3068-4/96$5.00©1996 IEEE

II. METHODOLOGY

Reconstruction of SASS imagery is discussed elsewhere [1]. The reconstructed image used for this project (Figure 1), was composited from data collected over central South America from July 1 to October 10, 1978. Only vertically polarized data acquired with incidence angles between 23° and 55° degrees with noise below a certain predetermined level were used. Additionally, orbits for which the spacecraft attitude determination were in error were excluded.

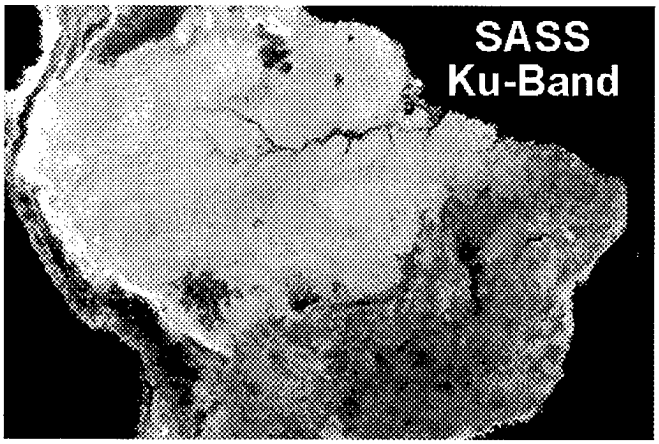


Figure 1. Reconstructed SASS image.

In order to maximize the fairness of any comparison with SASS (which had a limited life), an NDVI composite was constructed for the same seasonal period, albeit in 1982 (Figure 2). This was the earliest AVHRR imagery available. The process of creating the NDVI composite has already been described [3].

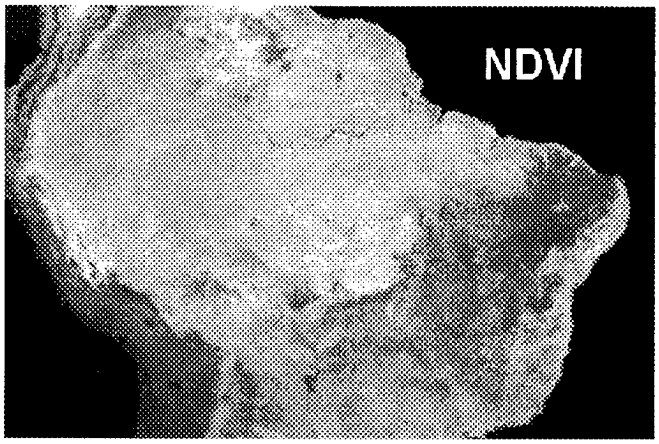


Figure 2. The AVHRR-derived NDVI image

The SSM/I data used in this project was acquired during September of 1992. Since SSM/I has seven channels, seven images were reconstructed. A discussion of the SSM/I reconstruction process is reported in these proceedings [4] and will not be repeated here. The images used in this research are also available in that reference.

Discriminating between equatorial vegetation using reconstructed ERS-1 imagery is also reported in these proceedings [5] for the interested researcher to review. Although ERS-1 data for that research was acquired between April, 1992 and May, 1995, only the data from July 1 through September 30, 1992 were composited for this project -- roughly the seasonal time-frame associated with the SASS imagery.

Since all the images were reconstructed to differing resolutions between 5 and 20 km, the images were all resampled to the lowest common resolution (20 km), cast to a common projection using nearest neighbor resampling, and registered.

A simple experiment was devised to test the utility of the reconstructed imagery and AVHRR for discrimination between broad vegetation classes within the study area of central South America. Using the 1:5,000,000-scale *Vegetation Map of South America* [6], large homogeneous rectangular regions for 15 different vegetation formations were delimited. A total of 21 rectangular regions were delineated, totaling over 566,000 km^2. Once these regions were defined, the pixels from the SSM/I, SASS, ERS-1 and NDVI images were extracted for each and saved for further analysis. In the discrimination to be described next, only one-third of the pixels for each of the 15 formations were used for training. The remaining two-thirds were reserved for testing the discrimination.

To establish a baseline estimate of discrimination ability, there was an initial analysis to classify the 15 vegetation formations using linear discriminant functions generated from the training set classes. After the baseline classification was established, the original 15 categories were regrouped into a set of 10 categories to improve the accuracy. This was done primarily by combining the forest formations.

To limit the complexity of the iterative discrimination, we selected only one SMM/I band to include with the SASS, ERS-1 and NDVI images. From initial tests, we found the 85H channel to be slightly superior to the others for discriminating between the vegetation classes. It was used in the discrimination analysis.

Since the goal of this research is to combine these data sets and compare them for discrimination of vegetation, all possible combinations of ERS-1, SASS, NDVI and SSM/I 85H were tried in the experiments in order to find the optimum combination for classification. Coefficients for Fisher's linear discriminant function were generated using the training data. The functions were then applied to each pixel in the test data set. Accuracy was assessed by counting the number of pixels in each vegetation class which were correctly classified by the discriminant

functions. The results were also summarized in confusion matrices.

III. RESULTS

The average image values for the 15 original classes are shown in Table 1. Variance values, some substantial, are not shown in order to conserve space. In general, there is agreement in trend between the values. The equatorial forests have the highest backscatter, while the shrublands and grasslands have the lowest.

As shown in Table 2, the best single image for classifying the 15 vegetation classes is ERS-1. However, the performance of all the single images is abysmal, with accuracy ranging from 22% to 30%. When two images are used together, the highest classification accuracy is obtained when 85H is combined with either ERS-1 or NDVI (51% - 52%). As might then be expected, when ERS-1 is combined with both NDVI and 85H, the accuracy increases further (63%). Using all four images produces an accuracy of 67%. For the sake of comparison, we also report that the classification accuracy using the seven SSM/I channels alone is 61%. When all ten images are utilized together, the classification accuracy exceeds 74%.

Grouping the forest classes substantially improves the classification accuracy, as does grouping two *campos cerrados* classes. The trend in the discrimination analyses for the ten collapsed groups follows the pattern established for the previous experiment. Using SASS, ERS-1, NDVI, and 85H together produces an accuracy of 90%. When the experiment is repeated with all seven SSM/I bands, the classification accuracy increases significantly to 93%.

IV. CONCLUSION

Given the results of the discrimination experiments, the following conclusions can be made.

1. Reconstructed radiometer imagery appears to have greater potential for discriminating between equatorial vegetation than either reconstructed C-band or Ku-band imagery.
2. Reconstructed C-band imagery is only slightly better than reconstructed Ku-band imagery for vegetation discrimination when combined with other reconstructed image types.
3. Use of all possible reconstructed images achieves the highest possible classification accuracy.
4. The different forest classes are difficult to distinguish between, although easily distinguishable from non-forest classes.

Perhaps the most intriguing aspect of the discrimination analysis is the superior value of reconstructed SSM/I imagery for distinguishing between equatorial vegetation. Clearly more research is warranted in SSM/I reconstruction.

Vegetation Formation	SASS A	ERS-1 A	NDVI	85H K
Very moist forest	-7.7	-8.1	0.29	286.1
Moist seasonal forest	-7.5	-8.0	0.29	287.2
Ombrophilous submontane forest	-7.5	-7.9	0.29	284.4
Extremely moist forest	-7.2	-7.7	0.28	286.1
Tropical seasonal lowland forest	-7.8	-8.2	0.28	287.1
Degraded forest formation	-7.6	-8.0	0.26	282.6
Degraded deciduous woodland	-8.6	-9.0	0.25	288.8
Campos sujos / limpos	-10.14	-10.4	0.19	288.7
Campos cerrados south	-10.9	-11.1	0.18	280.6
Chaco	-9.5	-9.7	0.16	283.8
Campos cerrados north	-10.0	-10.3	0.15	286.4
Degraded lowland woodlands	-10.7	-10.8	0.15	**
Degraded *campos cerrados*	-11.18	-11.3	0.14	280.0
Degraded *caatinga* formation	-9.8	-10.0	0.09	286.3
Caatinga	-9.3	-9.6	0.08	286.1

Table 1. Mean values for the 15 vegetation classes.
*** Unavailable at publication time.*

Images used	Accuracy %
NDVI	21.6
SASS	23.8
85H	24.2
ERS-1	29.8
SASS, ERS-1	40.0
ERS-1, NDVI	48.6
SASS, 85H	48.9
SASS, NDVI	49.1
ERS1, 85H	51.1
NDVI, 85H	51.5
SASS, ERS-1, NDVI	53.8
SASS, ERS-1, 85H	58.7
SASS, NDVI, 85H	58.8
ERS-1 NDVI, 85H	62.8
SASS, ERS1, NDVI, 85H	66.7
Seven SSM/I channels alone	60.9
SASS, ERS1, NDVI, seven SSM/I channels	74.4

Table 2. Results from the 15 group discrimination analysis.

V. REFERENCES

[1] D.G. Long, P.J. Hardin, and P.T. Whiting, "Resolution enhancement of spaceborne scatterometer data," IEEE. Trans. Geo. Remote Sensing, vol. 31, no.3, pp. 700-715, 1993.

[2] D. Daum, "Application of enhanced resolution imaging to SSM/I data," M.S. Thesis, Department of Computer and Electrical Engineering, Brigham Young University, 1994.

[3] P.J. Hardin and D.G. Long, "Integrating reconstructed scatterometer and Advanced Very High Resolution Radiometer data for tropical forest inventory," Optical Engineering, vol. 34, no. 11, pp. 3146-3153.

[4] D.G. Long, D.L. Daum, and P.J. Hardin, "Spatial resolution enhancement of SSM/I data: vegetation studies of the Amazon Basin," Proceedings, IGARSS '96, Lincoln Nebraska, May, 1996.

[5] P.J. Hardin, D.G. Long, and Q.P. Remund, "Discrimination of Africa's vegetation using reconstructed ERS-1 imagery," Proceedings, IGARSS '96, Lincoln Nebraska, May, 1996.

[6] UNESCO. "Vegetation map of South America," Paris: UN Educational, Scientific, and Cultural Organization, 1981.

Trace Detection of Environmental Contaminants by Laser Photofragmentation/Fragment Detection Spectrometry*

Rosario C. Sausa
U.S. Army Research Laboratory, AMSRL-WT-PC
Aberdeen Proving Ground, MD 21005-5066
Phone: (410) 278-7070 Fax: (410) 278-7333 Email: Sausa@ARL.MIL

Abstract: Trace concentrations of NO_2, other nitrocompounds, R-NO_2, and brominated species are detected by one color, laser-induced photofragmentation/ fragment detection spectrometry. Laser radiation near 226 nm is used to both photolyze the nitrocompound and to facilitate the detection of the characteristic NO fragment by 1+1 resonance-enhanced multiphoton ionization (REMPI) via its $A^2\Sigma^+$-$X^2\Pi$ (0,0) transitions. Similarly, laser radiation at 260.63 nm is used to fragment the target brominated compound and excite the characteristic Br atom photofragment via its two-photon $4p^4 5p\ ^4D^o_{3/2} \leftarrow 4p^5\ ^2P^o_{3/2}$ transition. Detection of Br is accomplished by 2+1 REMPI, and by laser-induced fluorescence and stimulated emission via the $4p^4 5p\ ^4D^o_{3/2} \rightarrow 4p^4 5s\ ^4P_{5/2,3/2}$ transitions at 844 and 751.5 nm. The analytical merits of the technique are evaluated and discussed, and the limits of detection for various compounds reported.

INTRODUCTION

Concerns related to public health and the environment have generated great interest in the development of fast, sensitive, and cost effective devices for monitoring trace contaminants in the atmosphere, water, and soil. Laser photofragmentation/fragment detection (PF/FD) techniques offer real-time monitoring capabilities with high sensitivity and selectivity, and can be used for either point or remote sensing [1]. The PF/FD approach is particularly useful for large molecules which are weak fluorophors or predissociate with the absorption of laser radiation. One-color PF/FD is based on the use of a single laser operating at a fixed frequency to photofragment the target compound into characteristic atomic or diatomic fragments, and to facilitate their detection by laser-induced fluorescence (LIF), resonance-enhanced multiphoton ionization (REMPI) or possibly by stimulated emission (SE). The detection of these species by such methods is feasible since they possess favorable combination of strong optical transitions, and sharp, well resolved spectral features. Reported in this paper are studies of PF/FD techniques for measuring trace levels of various nitrocompounds and brominated compounds.

EXPERIMENTAL

The experimental apparatus has been described in detail elsewhere [2,3]. Briefly, the experimental set up consists of a tunable laser with frequency doubling crystal, a simple flow cell (350 cm^3) equipped with an ion and photodetector, and a data acquisition and analysis system. REMPI detection is accomplished with miniature electrodes (1.5 cm^2), while LIF and SE detection is accomplished by a photomultiplier/filter combination (10 nm fwhm). The data acquisition system consists of a 125 MHz digital oscilloscope, boxcar integrator, and PC-AT computer.

RESULTS/DISCUSSION

The relevant reactions pertinent to NO_2 detection by PF/FD at 226 nm may be written as follows:

$$NO_2 + h\nu_1 \rightarrow NO(X^2\Pi) + O(^1D) \quad (1)$$
$$NO(X^2\Pi) + 2h\nu_2 \rightarrow NO^+(X^1\Sigma^+) + e^- \quad (2)$$

where (1) represents the laser photofragmentation step yielding NO, and (2) represents the 1+1 REMPI of the NO fragment via its $A^2\Sigma^+$ intermediate state. An enhancement in the NO ion signal is observed since the $A^2\Sigma^+$ state is resonant with the energy of the 226-nm photon. The processes represented by (1) and (2) are very fast, occurring in the duration of the laser pulse, approximately 10^{-6} s for our experiment. Also, $h\nu_1 = h\nu_2$ since the same laser frequency is used for both photofragmentation and subsequent fragment ionization.

Fig. 1 shows the ionization spectra of trace levels of NO and NO_2 in air at different pressures. The spectra were recorded at 10 Hz with a scan rate of 0.005 nm/s, 3 pulse averaging, and an electrode voltage of 150 V. A comparison of the ionization spectra reveals that the

* *This research was supported by the ARL Director's Research Initiative Program and the Strategic Environmental Research and Development Program (SERDP) on Cleanup, projects Army-713-94 and Army-729-94.*

0-7803-3068-4/96$5.00©1996 IEEE

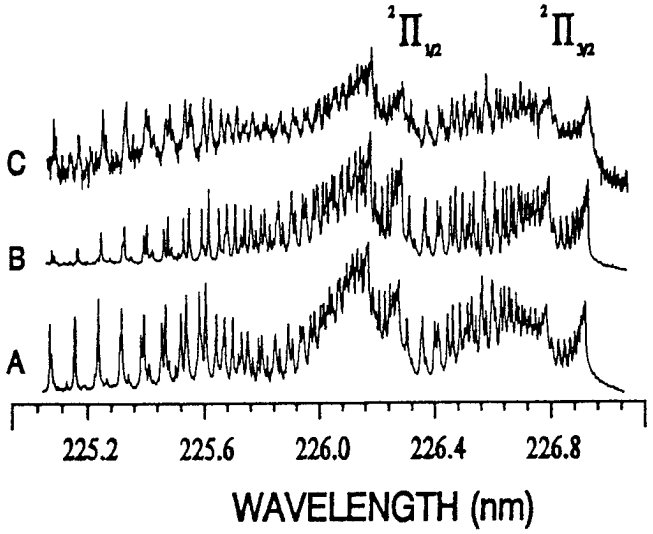


Fig. 1. Ionization spectra of 6 ppm of NO at 100 Torr (A), and NO generated from 6 ppm of NO_2 at 100 Torr (B) and 760 Torr (C).

features are similar, corresponding to the NO $A^2\Sigma$ - $X^2\Pi$ (0,0) band. The bandheads displayed in the spectra arise from the $^2\Pi_{1/2}$ and $^2\Pi_{3/2}$ spin-orbit components of the NO ground electronic state. As shown in Fig. 2C, the majority of the rotational features are resolved at 760 Torr to the baseline, confirming their identification. The ionization spectra collectively demonstrate both the spectral selectivity and feasibility of the method for ambient measurements. NO and NO_2 are easily discriminated from other interfering species based on excitation wavelength, but cannot be differentiated from each other since only the total ion signal is measured. Recent results from our group reveal that the 226-nm photolysis NO_2 yields NO with significant rovibrational excitations. Thus, NO_2 can be differentiated from ambient NO by monitoring the internal energy distributions of both fragment and ambient NO.

The limits of detection (LODs) of NO_2 and other nitrocompounds are presented in Table I. In the present study, the LOD is defined as the concentration of the analyte equal to three times the standard deviation of the background noise evaluated from 16 independent measurements either in the absence of sample or by tuning the laser to 227.4 nm, an off-resonance transition. The signals were integrated for 10 s at 10 Hz with 100 pulse averaging. As shown in Table I, the LODs for NO and NO_2 are 1 and 22 ppb, respectively, while those of the other nitrocompounds range in the sub to low ppm. The high sensitivities achieved is a reflection of the high efficiency of both the photofragmentation and ionization processes employed. The extension of this technique using visible laser radiation for NO_x detection and near

Table I. LODs (ppm) of various nitrocompounds using PF/FD at 226 nm. Laser energy ~10 μJ.

Species:	NO	NO_2	CH_3NO_2	$C_6H_5NO_2$	TNT
LODs:	0.001	0.022	0.220	~1	~1

ultraviolet radiation for nitrocompound detection is presently being investigated.

In the case of brominated compounds, the laser is tuned to the strong two-photon $4p^45p^4D^o_{3/2} \leftarrow 4p^52P^o_{3/2}$ transition of Br at 260.634 nm, and is used to both photofragment the target molecule and facilitate the detection of characteristic Br fragment by 2+1 REMPI, LIF, and SE (see Fig. 2). The SE signal is distinct from the LIF signal in that it is coherent, bidirectional, and propagated coaxially with the laser beam. Also, it is approximately two orders of magnitude larger than the LIF signal as a result of photophysical amplification.

A comparison study of REMPI, LIF, and SE detection techniques has been performed for CF_3Br and $CHClBr_2$, and estimates of their LODs are presented in Table II. The PF/REMPI technique exhibits excellent sensitivity with LODs in the ppb range. Arepalli et al. have also used this technique and estimated an LOD of 0.4 ppb for Br atoms generated from HBr and other brominated compounds [4]. It should be noted, however, that the compounds were sampled in pure form and at much lower pressures (10^{-3} Torr) than were used in the present studies, and extrapolation of their results to

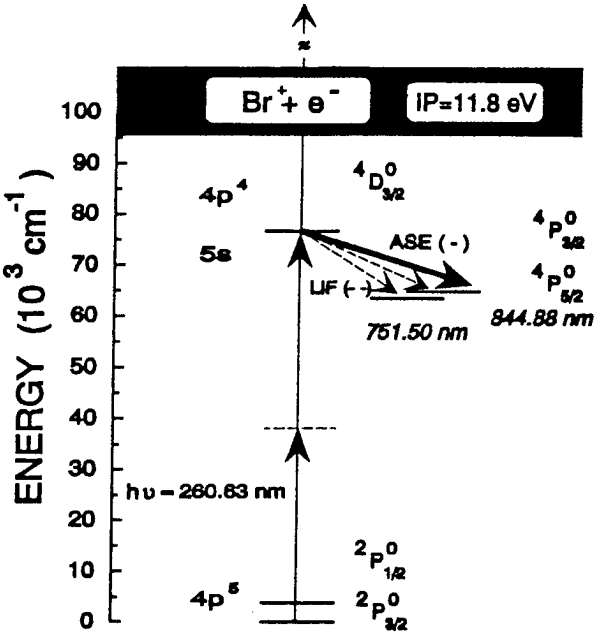


Fig. 2. A partial potential energy diagram of Br.

Table II. LOD estimates (ppm) of $CHClBr_2$ and $CHBr_3$ at 260.635 nm. Laser energy ~ 100 μJ.

	PF/REMPI	PF/LIF[a]	PF/SE[b]
$CHClBr_2$	0.022	0.25	10
$CHBr_3$	0.025	0.35	20

[a] Detection at 5 cm from sample
[b] Detection at 2 m from sample

dilute samples in a buffer gas matrix is difficult. Nonetheless, in both studies the absolute number of Br atoms detected at the LOD are very similar, on the order of 10^4-10^6.

Although high sensitivities are achieved with the PF/REMPI approach, it is susceptible to high background noise and interference due to nonresonant multiphoton ionization. It was observed experimentally that the magnitude of the background near 260 nm represented as much as 50% of the total ionization signal when the laser is resonant with the Br transition. This indicates that alternative ionization processes originating from parent molecule and/or other daughter fragments are operative. Thus, the technique appears to be limited to relatively low laser pulse energies.

Table II reveals that the sensitivities obtained by PF/LIF are an order of magnitude lower that those obtained by PF/REMPI. This difference in sensitivity results primarily from the high background and laser scatter inherent in these PF/LIF measurements, and is not necessarily characteristic of the technique. The analytical capability of this approach can be improved, however, by better system design, i.e. the addition of light baffles, signal collection optics, and/or spectrometer.

Table II also reveals that ppm levels of $CHClBr_2$ and $CHBr_3$ can be detected by PF/SE. It should be noted that the LODs were determined by measuring the signal with the detector at 2 m from the sample. The analytical potential of the technique is also high and it's capabilities can be improved. The background noise of the SE approach is low, unlike REMPI and LIF, and can be made even lower with appropriate shielding of the detector. Furthermore, since the signal is coherent and the background emission is incoherent, increasing the laser intensity to saturation conditions will greatly enhance the sensitivity without compromising the signal-to-noise ratio. The SE signal is also coaxial with the laser beam, and thus can easily be separated with filters or prisms. Moreover, since it is bidirectional, it only requires "one window access" to the sample environment. This has important implications for accessing remote or hostile environments and also for coupling to fiber optic probes. The extension of the PF/FD techniques to other halogenated compounds such as chlorofluorocarbons is also being investigated.

CONCLUSION

The analytical utility of laser photofragmentation with subsequent fragment REMPI, LIF, and SE detection has been demonstrated for trace ambient concentrations of various brominated and nitrocompounds. The characteristic spectral features of the NO and Br fragments are sufficiently resolved at 1 atm, indicating that the PF/FD technique is highly selective based on wavelength excitation. The LODs for the various compounds range from low ppb to low ppm with an instrument response time of 10 s and relatively low laser pulse energy (tens of microjoules). An increase in sensitivity is projected with an improved system design and utilizing higher pulse energies. Faster response times are also possible by operating the laser at a higher repetition rates, i.e 100 Hz, without compromising the number of pulses averaged. The attributes of the PF/FD approach and the simplicity of the instrumentation make it a viable alternative to conventional methods for continuous monitoring of trace contaminants.

ACKNOWLEDGMENTS

The author thanks Drs. R. Pastel, J. Simeonsson, G. Lemire, and E. Cespedes for many valuable discussions.

REFERENCES

[1] J.B. Simeonsson and R.C. Sausa, "A Critical Review of Laser PF/FD Spectrometry for Gas-Phase Chemical Analysis", *Appl. Spect. Rev.*, in press.

[2] J.B. Simeonsson, G.W. Lemire and R.C. Sausa, "Laser-Induced Photofragmentation/Fragment Photoionization Spectrometry: A Method for Detecting Ambient Oxides of Nitrogen", *Anal. Chem.* Vol. 66, pp. 2272-2278, 1994.

[3] J. Simeonsson and R. Sausa, "Trace Detection of Ambient Brominated Compounds by Laser PF/FD Detection Spectrometry", *Spectrochimica Acta*, Vol. 49B, pp. 1545-1555, 1994.

[4] S. Arepalli, N. Presser, D. Robie and R.J. Gordon, "The Detection of Br Atoms by REMPI", *Chem. Phys. Lett.* Vol. 117, pp. 64-66, 1985.

Detection of Environmental Contaminants by Time Resolved Laser Induced Breakdown Spectroscopy Technique

G.Arca, A.Ciucci*, V.Palleschi, S.Rastelli and E.Tognoni

IFAM - Istituto di Fisica Atomica e Molecolare del C.N.R.
Via del Giardino, 7 - 56127 PISA
Tel. +39 (50) 888109 - Fax: +39 (50) 888135
e-mail: vince@risc.ifam.pi.cnr.it
WWW: http://www.ifam.pi.cnr.it

* ENEA - Ente per le Nuove tecnologie, l'Energia e l'Ambiente
Centro Ricerche Ambiente Marino
Pozzuolo di Lerici CP 316 - 19100 (SP) I
Tel. +39 (187) 536291

ABSTRACT

The Laser Induced Breakdown Spectroscopy (LIBS) technique has become, in these last years, a reliable tool for very fast multi-elemental pollutants' analysis in atmosphere, solid matrix and liquids [1].

Its principle of operation lies in the avalanche ionization effect (optical breakdown) produced by an intense laser beam focused on the sample to be investigated. Under the effect of the intense EM field of the laser, the material is separated in its atomic constituents, with a very high degree of ionization and electron temperatures reaching several tens of eV. With the recombination of atoms and electrons, an extremely intense emission of light (laser spark) takes place. The latter is collected and analysed for discerning the characteristic emission lines of the different elements in the sample.

Among the many advantages of LIBS technique with respect to standard methods, either chemical or laser-based, it may be appropriate to quote the possibility of getting quantitative information on the whole sample composition in a single run, through the simultaneous detection of the emission line patterns of different elements present in the material under analysis.

This peculiar feature of the LIBS system allows for very fast sample analysis and thus, when necessary, for continuous monitoring of its composition. The applications of the LIBS technique to industrial exhausts monitoring take a great advantage of this characteristics, along with the possibility of LIBS operation in hostile environment.

In fact, being the LIBS method essentially non-invasive, remote controllable and fully automated, it is possible to arrange a setup in which the most delicate parts of the apparatus are kept protected in a safe environment far apart from the dangerous and/or potentially damaging site to be monitored. Remote operation is also useful in polluted soil and water analysis.

APPLICATIONS

The LIBS system is composed by the following elements (Tab.1)

• Laser source	Q-switched Nd:YAG
Pulse width	8ns
Energy/pulse	400mJ
Repetition rate	10Hz
• Spectrograph	
type	Czerny-Turner
focal length	1 m
grating	1200g/mm
• O.M.A.	
Spectral range	2000-9000Å
resolution	0.8Å
• PC 386	

0-7803-3068-4/96$5.00©1996 IEEE

Its main elements are a Q-Switched Nd:YAG laser operating at the fundamental wavelength (1064 nm), a monochromator, an optical multichannel analyser and the acquisition system.

In last years, the IFAM LIBS prototype has been used for pollutants diagnostics in gas, solid and liquid samples, both in laboratory and "on the field".

Mercury detection in air (laboratory measurement)

Due to its intrinsic danger even at very small concentrations, mercury is one of the most interesting pollutant that can be successfully monitored with our technique. It should be noted that usual chemical techniques for detection of mercury in air, although very precise, require a quit lengthy procedure involving pumping of a great quantity of the air for increasing the quantity of metal to be detected, reduction of mercury on gold, flushing in inert gas and optical analysis of the extracted residual by fluorescence methods. On the other hand, laser based techniques as DiAL can give precise results in real time, but it is not possible to use them for short-range analysis.

With the aim of testing the sensitivity of our LIBS system we simulated a mercury contamination in atmosphere by filling the experimental vessel with an air sample at NTP with known mercury concentration. We can estimate the maximum sensitivity of our LIBS system as the smallest mercury concentration for which a spectral line signal is still detectable against the background. With our experimental set-up we were able to detect, without particular difficulties, mercury concentration as low as 5 parts per billion (ppb), a figure quite interesting since it corresponds to a concentration well below the health danger threshold for this pollutant.

Diagnostics of smokes from power plant (*in situ* measurement)

The field measurements have been carried out on the 150 MW oil-fired Livorno power plant. Figure 1 shows the arrangement of the instrument on the plant. Smoke temperature was about 150°C; solid particulate volume fraction was about 10^{-8}.

The laser beam was focused into the flue duct by means of a small lens; the U.V-visible light emitted by the plasma was collected by the same lens and focused, through a second lens, onto the fiber optic, which transmitted the light to the entrance slit of the spectrometer (slit width 5 μm).

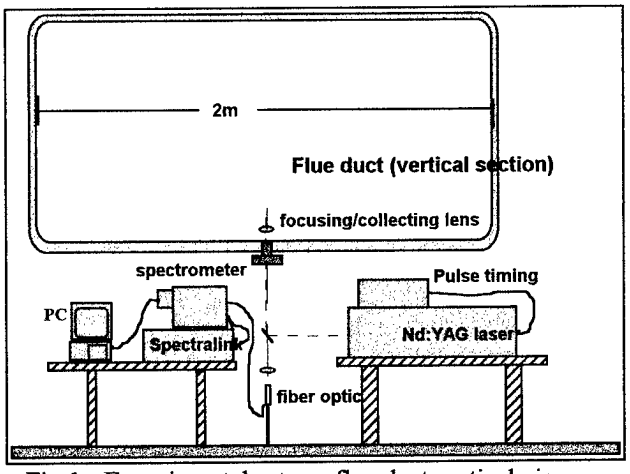


Fig.1 - Experimental set-up; flue duct vertical view.

No optical windows were needed since the plant is operating at low pressure; a short focal length lens (250mm)was used, directly inserted inside the duct in order to obtain an intense plasma signal.

Different spectral regions were scanned; the rotation of the grating was computer controlled. The acquisition of optical multichannel analyser was delayed with respect to the breakdown process in order to obtain a better selectivity; decay of background continuous emission occurs in fact faster than line emission. In order to optimize the S/N ratio, in the present field tests the delay time was fixed at 2.2μs.

Figures 2 and 3 show some experimental spectra resulting from the averaging of 250 pulses.

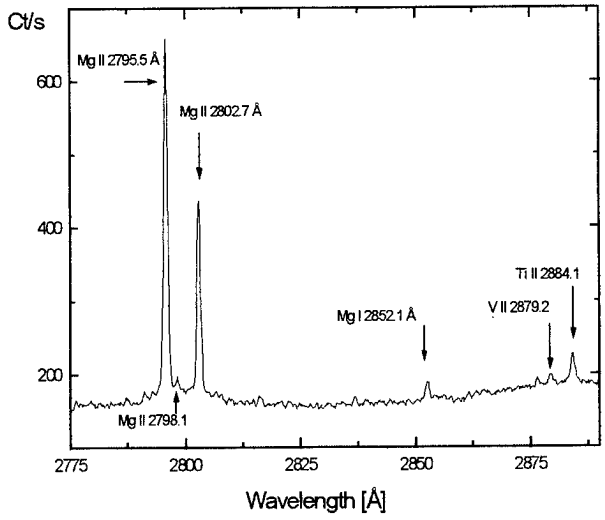


Fig.2 - LIBS spectrum from power plant smokes.

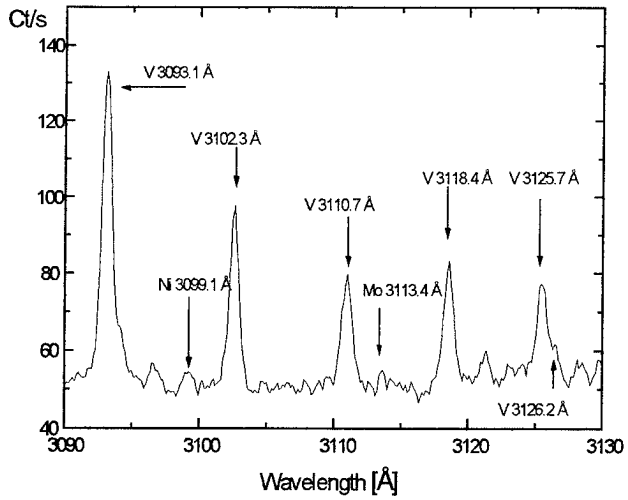


Fig.3 - LIBS spectrum from power plant smokes.

Acquisition and spectral scanning was performed with a commercial software. The analysis software has been purposely developed by CNR/IFAM (DataLIBS), which automatically marks the peaks of emission lines, compares the corresponding wavelengths with a database of atomic and molecular lines and finally supplies the operators with a list of the trace pollutants identified. During the software development, particular care has been taken to the proper handling of multiple assignations.

Before starting the measurements inside the duct, a number of acquisitions outside the duct were performed in order to evaluate the background signal and to be sure that the spectral lines detected were in fact emitted by metals present in the smokes.

The analysis of the spectra shows that many metallic elements are clearly identifiable in the power plant smokes: among them it's worth to mention Ni, V, Ti, Mg, Fe. The laboratory analysis of a sample of the heavy oil confirmed the presence of the same elements.

Diagnostic of pollutants in soil (laboratory measurement)

The LIBS technique has been also applied to investigate the presence of heavy metals in certified soil samples, where pollutant species were contained in the concentration range of a few ppm. Due to a large number of atomic constituents in soil samples, the problem of a correct identification of spectral lines arises with the need to discriminate, within the spectral resolution of the system, among the various emitting species.

A certified soil sample (GXR-2) from US Geological Survey [12] has been used to tests the performances of the LIBS set-up. The investigated soil sample has been pressed to form solid pellets prior to LIBS analysis. A list of constituents identified is given in table 2, along with the reported concentrations in the sample (recommended values, following the review of Gladney et al. [1]).

Table 2. GXR-2 sample

Element	Recommended values	Experimental S/N
Al	18.6 ± 0.4 %	> 10
Ca	8200 ± 400 ppm	> 10
Co	9 ± 2 ppm	7
Cr	37 ± 10 ppm	3
Cu	not given	4
Fe	1.9 ± 0.23 %	> 10
Hg	3.2 ± 0.2 ppm	2
Mg	0.88 ± 0.05 %	> 10
Mn	960 ± 100 ppm	> 10
Mo	1.5 ± 0.5 ppm	4
Ni	18 ± 3 ppm	8
Pb	615 ± 15 ppm	2
Sb	48 ± 5 ppm	6
Si	23.0 ± 2.2 %	> 10
Sr	280 ± 60 ppm	4
Ti	2800 ± 300 ppm	> 10
W	1.8 ± 0.2 ppm	4
Zn	500 ± 60 ppm	8

CONCLUSION

The applicability of the LIBS technique for laboratory and *in situ*, on-line detection of pollutants in gas, solid and liquid samples has been demonstrated.

The technique has shown an high selectivity and sensitivity. Continuous and simultaneous monitoring of several atomic species is possible due to its fast time response.

REFERENCES

[1] see G.Arca, A.Ciucci, V.Palleschi, S.Rastelli and E.Tognoni, "Detection of Pollutants in Liquids by Laser Induced Breakdown Spectroscopy Technique", (same proceedings) and references therein.

[2]] E.S. Gladney, D.R. Perrin, J.W. Owens and D. Knab, Anal.Chem. 51, 1557 (1979).

Influences on Detectability of Heavy Metals in Soils by Laser-Induced Breakdown Spectroscopy

D.R. Alexander, D.E. Poulain, M.S. Khlif, and E.R. Cespedes*

Department of Electrical Engineering and Center for Electro-Optics
University of Nebraska, Lincoln, NE 68588-0511, USA
T: 402.472.3091 F: 402.472.5083 EMail: dalexander@unl.edu

*U. S. Army Corps of Engineers, Waterways Experiment Station
Environmental Engineering Division
3909 Halls Ferry Road, Vicksburg, MS 39180-6199, USA
T: 601.634.2855 F: 601.634.2732

Abstract— Laser-induced breakdown spectroscopy (LIBS) is a rapid remote measurement method for determination of levels of metals in the environment. A major factor in the acceptance of this technique involves the detection limits under both laboratory and field operations. Research on limits of detection of heavy metals in different types of soils under various conditions using LIBS has been carried out. Pulses from a Nd:YAG laser operating at 150 mJ at $\lambda = 1.06$ μm are focused on sample surfaces to produce laser sparks (plasmas). Atomic emissions from the plasmas are recorded using an optical multichannel analyzer after delays of a few microseconds when interference from broadband emissions is reduced.

Research has been performed on the detection limits of As, Cd, Cr, Hg, Pb, and Zn in soil matrices. Results are reported on the detectability of Cr in sand samples.

The LIBS method described is well-suited to monitoring of subsurface soils using this technique installed in a cone penetrometer. Conditions that would be encountered by a cone penetrometer-based LIBS system are simulated by compressing soil samples and then allowing them to relax for specific intervals before LIBS analysis. Results are presented of the dependence of LIBS measurements on the relaxation time after soil sample compression. This data is important to understand how to implement field-deployable LIBS systems.

I. Introduction

Recently interest in sensors to accurately assess and monitor the extent of environmental contamination around waste disposal sites and research facilities has grown markedly. There is an ever-increasing need to quickly and accurately perform concentration measurements of chemical species *in situ*. Previously these measurements could only be performed in the laboratory. However, the volume of measurements to be performed today and in the future have a prohibitive cost of time and finances to acquire soil or water samples and return them to a laboratory for analysis. Thus, new methods are needed to perform remote measurements quickly and efficiently, while maintaining comparable analysis capabilities.

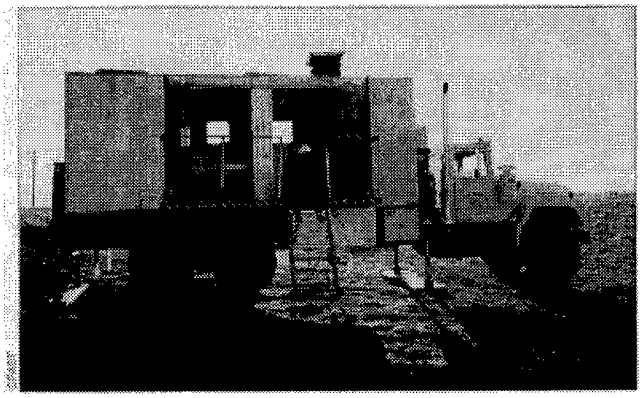


Fig. 1.Cone penetrometer vehicle during a field test at Hill Air Force Base near Salt Lake City, Utah. (From *Spectroscopy*, 10(7) (1995):34.)

LIBS is one method with the potential to satisfy these requirements. In this method the laser source serves to vaporize, atomize, and excite the sample material in the course of one laser pulse. This method, termed laser-induced breakdown spectroscopy (LIBS), has been used in analyses of gases [1], liquids [2, 3], solids [4], solid aerosols [5–7], liquid aerosols [8–10], and soils [11–13]. Because of the relative simplicity of LIBS, it is well-suited for use in the field. One existing field-deployable site characterization system to which LIBS could be adapted is the Site Characterization and Cone Penetrometer System (SCAPS) developed by the Army Corps of Engineers' Waterways Experiment Station (WES), shown in Fig. 1. SCAPS sensors, housed in a cone penetrometer, are driven into the soil by a hydraulic ram to depths of up to 200 feet. Measurements are performed *in situ* during the descent and/or ascent of the penetrometer. This makes it possible to determine contaminant plume boundaries on-

The partial support of this work by the U.S. Army Corps of Engineers, Waterways Experiment Station under Contract #DACA39-95-K-0053 is gratefully acknowledged.

0-7803-3068-4/96$5.00©1996 IEEE

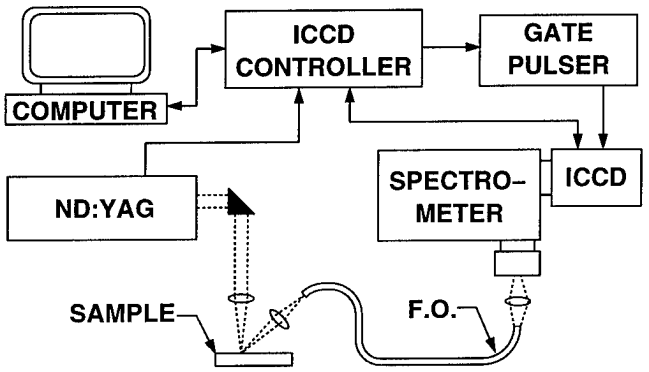


Fig. 2.Schematic of a typical LIBS system utilizing a Nd:YAG laser and an optical multichannel analyzer.

site.

As part of an on-going effort to develop LIBS for use with SCAPS, the current work describes the effect of soil compression and subsequent relaxation on LIBS measurements of chromium in sand. Results are also presented on the detection limits of Cr in sand are presented.

II. Experimental Technique for LIBS

A schematic of the experimental arrangement used in performing the experimental research is shown in Fig. 2. A pulsed Nd:YAG laser (Big Sky Laser, Model 100R), operating at the principal wavelength ($\lambda = 1.06$ μm) and 10 ns pulse width, serves as the excitation source. The laser radiation is focused by a plano-convex BK7 lens (diameter (ϕ) = 15 mm, focal length (f) = 100 mm) on the soil sample. An optical multi-channel analyzer (OMA), consisting of a spectrometer (Instruments SA, Model HR-320, f = 320 mm) equipped with an intensified CCD camera (ICCD)(Princeton Instruments, Model ICCD-1024MG-E), is used to analyze the spectra of the plasma emissions. Emission from the laser-produced plasma is focused by a fused silica lens into an optical fiber (3M, TECS FT-1.0-UMT) for transmission to the OMA. Transmitted light from the fiber is coupled into the OMA with a bi-convex fused silica lens (ϕ = 25 mm, f = 50 mm). An aperture between the lens and OMA slit matches the F/# of the lens to the spectrometer. The entrance slit of the spectrometer is typically opened 25 μm. The region of the plasma imaged by the spectrometer is approximately 1 mm in diameter. The spectrometer is equipped with a 1200 lines/mm holographically ruled diffraction grating. The OMA was able to acquire individual spectra from the LIB plasma at the rate of approximately two per second. To increase the signal-to-noise ratio for the atomic emission lines, and thus reduce the limits of detection, the ICCD is gated. A Q-switch sync signal from the Nd:YAG triggers a gate pulse generator (Princeton Instruments, Model PG-200). The gate pulse generator triggers the OMA and provides for delay of the gate pulse after the laser pulse and variation of the gate pulse width (integration time).

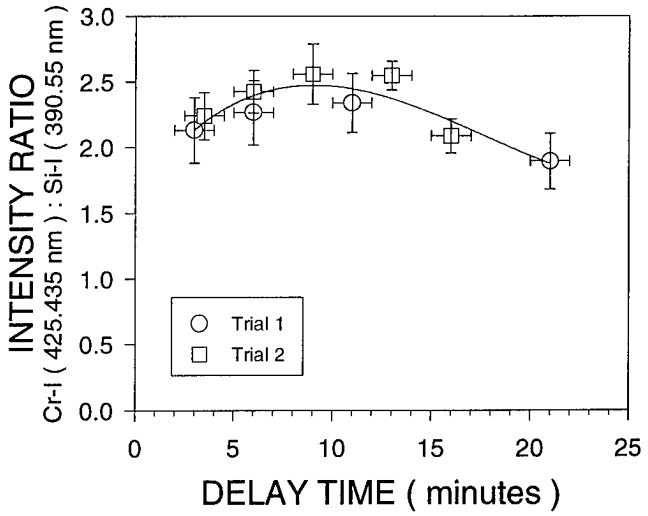


Fig. 3.Effect of "relaxation time" after soil compression (20 tons for 1 minute) on LIBS measurements of 50 ppm chromium in sand.

For the detection limit analysis washed and dried sand (Mallinckrodt Chemical, Inc., No. 7062 KPTN) was necessary because "naturally" occurring sand samples were found to contain up to 4 ppm chromium.

III. Results and Discussion

A. Soil Compression Effects

A cone penetrometer inherently requires large forces to be applied to the soil in the immediate vicinity of the tip. To understand the effect of soil compression on LIBS measurements, soil samples contaminated with chromium were compressed then allowed to relax for various periods before LIBS analysis. Sand samples ($\sim$ 75 g) were doped with 50 ppm Cr (w/w). Samples were then compressed in aluminum sample holders under a load of 20 tons for one minute. Different samples were allowed to relax from 2 to 20 minutes before being analyzed using LIBS. Data for less than two minutes was not possible due to sample preparation location and the time required to perform the first LIBS measurements. Results of two trials are shown in Fig. 3. The emission intensity ratio of Cr-I (425.435 nm) to Si-I (390.55 nm) increases during the first 6 to 10 minutes before decreasing to a level approximately equal to the initial measurement.

We believe that two competing processes are responsible for the observed time-dependence of the measurements. One effect is related to the soil moisture content which is known to decrease the intensity ratio as the moisture content increases. As the soil moisture increases a greater portion of the laser pulse is required to excite water adsorbed on the sand granules. As the soil is compressed, moisture is expelled from the soil matrix. Dur-

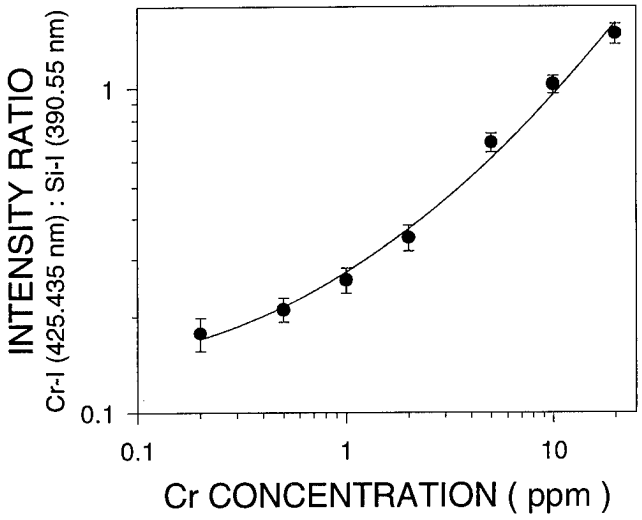


Fig. 4.Calibration curve for LIBS measurements of chromium concentration in sand for 200 ppb to 20 ppm.

ing the relaxation period humidity from the ambient air is readsorbed by the sand. A second contributing effect is due to energy being stored in the sand particles by the compression process. Since the energy introduced by the compression process is stored mainly in the silicon (silicon dioxide) there will be a trend for the silicon line intensity to increase over the chromium line intensity. In addition, any stored energy makes it easier to produce slightly higher plasma temperature. The stored energy effect is not permanent and relaxes in time ($\sim$ 20 minutes).

B. Calibration

Shown in Fig. 4 is a calibration curve for LIBS measurement of chromium in sand for the concentration range from 200 ppb to 20 ppm (w/w). The detection limit was computed according to the relation $C_L = (2\sigma)/S$, where C_L is the detection limit, σ is the standard deviation of the emission intensity ratio, and S is the slope of the calibration curve near it's lower limit. Based on the application of this relation to the data in Fig. 4, the detection limit for chromium in sand was determined to be 360 ppb.

IV. Conclusions

Tests have been performed to demonstrate the variation of LIBS measurements as a function of soil compression and relaxation time. Results indicate that in the application of LIBS to a cone penetrometer system, consistency must be maintained in the analysis method to achieve repeatable results. A calibration curve has been developed for chromium in sand for concentrations between 200 ppb and 20 ppm. The lower detection limit for chromium in sand was estimated to be 360 ppb.

References

[1] D.A. Cremers and L.J. Radziemski, "Detection of chlorine and fluorine in air by laser-induced breakdown spectrometry." *Anal. Chem.*, 55, (1983):1252-1256.

[2] D.A. Cremers, L.J. Radziemski and T.R. Loree, "Spectrochemical analysis of liquids using the laser spark." *Appl. Spectrosc.*, 38, (1984):721-729.

[3] J.R. Wachter and D.A. Cremers, "Determination of uranium in solution using laser-induced breakdown spectroscopy." *Appl. Spectrosc.*, 41, (1987):1042-1048.

[4] K.J. Grant, G.L. Paul and J.A. O'neill, "Quantitative elemental analysis of iron ore by laser-induced breakdown spectroscopy." *Appl. Spectrosc.*, 45, (1991):701-705.

[5] L.J. Radziemski, T.R. Loree, D.A. Cremers and N.M. Hoffman, "Time-resolved laser-induced breakdown spectrometry of aerosols." *Anal. Chem.*, 55, (1983):1246-1252.

[6] D.K. Ottesen, L.L. Baxter, L.J. Radziemski and J.F. Burrows, "Laser spark emission spectroscopy for in situ, real-time monitoring of pulverized coal particle composition." *Energy & Fuels*, 5, (1991):304-312.

[7] W.L. Flower, *et al.*, "A laser-based technique to continuously monitor metal aerosol emissions." *Fuel Proc. Tech.*, 39, (1994):277-284.

[8] H.A. Archontaki and S.R. Crouch, "Evaluation of an isolated droplet sample introduction system for laser-induced breakdown spectroscopy." *Appl. Spectrosc.*, 42, (1988):741-746.

[9] K.W. Holtzclaw, J. Moore and C.L. Senior, "Real-time optical measurement of alkali species in air for jet engine corrosion testing." *31st Aerospace Sciences Meeting & Exhibit*, Reno, Nevada (1993).

[10] D.E. Poulain, and D.R. Alexander, "Laser-induced breakdown spectroscopy of liquid aerosols: droplet salt concentration measurements." *Appl. Spectrosc.*, 49, (1995):569-579.

[11] R. Wisbrun, I. Schechter, R. Niessner, H. Schröder and K.L. Kompa, "Detector for trace elemental analysis of solid environmental samples by laser plasma spectroscopy." *Anal. Chem.*, 66, (1994):2964-2975.

[12] D.R. Alexander, D.E. Poulain, R.D. Kubik, and M.U. Ahmad, "Automated element identification in laser-induced breakdown spectroscopy studies of contaminated soils." Final Report on U.S. Army Corps of Engineers, Waterways Experiment Station, Contract DACA39-93-K-0052, (1993).

[13] D.A. Cremers, J.E. Barefield II, and A.C. Koskelo, "Remote elemental analysis by laser-induced breakdown spectroscopy using a fiber-optic cable." *Appl. Spectrosc.*, 49, (1995):857-860.

Measurements of the Radar Backscattering over Different Oceanic Surface Films During the SIR-C/X-SAR Campaigns

Martin Gade, Werner Alpers, Mingquan Bao,
Institute of Oceanography, University of Hamburg, D–22529 Hamburg, Germany,
phone: +49 (40) 4123 5450, fax: +49 (40) 4123 5713, e-mail: gade@ifm.uni-hamburg.de

Heinrich Hühnerfuss,
Institute of Organic Chemistry, University of Hamburg, D–22529 Hamburg, Germany

Abstract – Results of the analyses of SIR-C/X-SAR images from the test site North Sea as well as from other sea areas showing radar signatures of natural surface films and of oil spills are presented. Damping ratios (i.e., the ratios of the normalized radar cross section from a slick-free and a slick-covered water surface) and polarization signatures have been calculated and compared. A strong wind dependence of the damping ratio for the same substance is shown and explained by means of the source terms for the spectral energy in the ocean wave spectrum. It is therefore concluded that surface films of different visco-elastic properties can only be discriminated at low to moderate wind speeds. Furthermore, polarization signatures from film-covered as well as from film-free water surfaces have been calculated and compared. Differences between them are found only at low wind speeds and small incidence angles which is in accordance to Bragg scattering theory.

INTRODUCTION

The damping of ocean waves by different surface films has been subject of several investigations (see, e.g., [1] and literature cited therein). Since the backscattered radar power depends on the spectral power density of the Bragg waves (i.e., waves with a wavelength $\lambda_B = \lambda_0 / 2\sin\vartheta$, where λ_0 denotes the radar wavelength and ϑ the incidence angle), ocean surface films appear as dark patches on radar images. However, ocean surface films are not only of man-made origin, like mineral oil spills from ships. Also natural surface slicks produced by plankton, algae, or fish appear on the sea surface, especially in coastal regions. To allow effective oil spill surveillance using active radar techniques, the discrimination between the different kinds of surface films is therefore necessary. During the two SIR-C/X-SAR campaigns in 1994, controlled surface film experiments were carried out in the test site North Sea, west off the German island of Sylt, where biogenic surface slicks as well as small spills consisting of mineral oil were deployed on the sea surface. The goal of these experiments was to investigate whether the spaceborne L, C, and X band multi-polarization SARs are capable of discriminating between the films of different chemical properties. In this paper, an overview is given of the results obtained from the SAR images of this test site as well as from other sea areas showing radar signatures of natural surface films and of oil spills.

MEASURED DAMPING RATIOS

In Fig. 1 a composite of two SAR images of the test site North Sea taken during the first mission on April 18, 1994, at 05:26 UTC is shown. The images were taken at L band (left) and X band (right), both at VV polarization. The dark patch is due to a biogenic slick consisting of oleyl alcohol (herein abbreviated as OLA) which had been deployed on the sea surface directly before the image was taken. During this experiment, the wind speed was moderate (5 m/s). It can be seen that the slick contrast is higher at X band, i.e., X band Bragg waves are more damped by OLA than L band Bragg waves. From these SAR images damping ratios (i.e., the ratios of the normalized radar cross section from a slick-free and a slick-covered water surface) have been calculated by averaging the same number of pixels from a slick-free and a slick-covered area and by calculating the ratio of the obtained values. Since, in general, surface films are not homogeneous, only pixels from one scan were used for calculating the damping ratios of each radar band (instead of averaging over the whole slick-covered area). The obtained results from various scans are shown in Fig. 2.

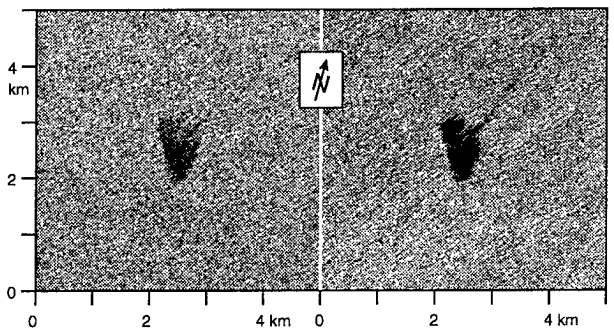


Fig. 1: composite of two SIR-C/X-SAR images of the test site North Sea showing the same biogenic slick (OLA, see text), left: L band, VV polarization, right: X band, VV polarization (SRL-1, datatake 143.30, April 18, 1994, 05:26 UTC, dimensions 5 km by 5 km).

This work has been supported by the German Space Agency (DARA) under contract 01QS9016 / 50QS90165.

0-7803-3068-4/96$5.00©1996 IEEE

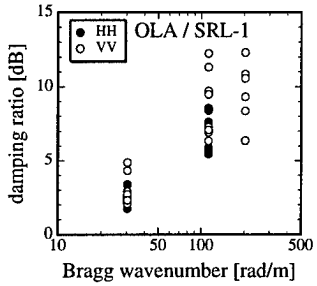


Fig. 2: damping ratios for OLA at moderate wind speed obtained from the SIR-C/X-SAR images of the first surface film experiment in the testsite North Sea (see Fig. 1).

On October 06, 1994, a second surface film experiment was performed, again, in the test site North Sea. The SAR image shown in Fig. 3 was taken at 08:12 UTC at X band, VV polarization (SRL-2, datatake 96.20, image dimensions are 12 km by 5.5 km). The dark patches originate from the set of different surface films which had been deployed on the sea surface. Directly before the image was taken a front passed the test site, so that the wind speed increased to more than 10 m/s.

Results obtained for the biogenic slicks consisting of oleyl alcohol (OLA, patch B), oleic acid methyl ester (OLME, patch C), and triolein (TOLG, patch D) as well as for the oil spill consisting of heavy fuel (IFO 180, patch A) are depicted in Fig. 4. It can be seen, that OLA (which was deployed during both missions) shows a different damping behavior at high wind speed. In particular, the damping ratios obtained from C and X band SAR images have decreased and are comparable with the L band damping ratios (whereas the damping ratios increased monotonously with Bragg wavenumber under moderate wind conditions, see Fig. 2). For all substances shown in Fig. 4 the damping ratios under high wind conditions are comparable (only TOLG shows slightly higher damping characteristics).

In order to compare the results of the dedicated experiments, several other SIR-C/X-SAR images showing natural surface films as well as oils spills have been analyzed. Typical examples are presented in Fig. 5 and Fig. 6. The natural

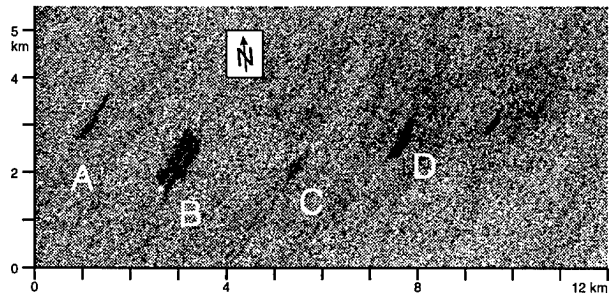


Fig. 3: X-SAR image showing a set of surface films (see text) in the test site North Sea taken on October, 06, 1994, at 08:12 UTC, X band, VV polarization (SRL-2, datatake 96.20)

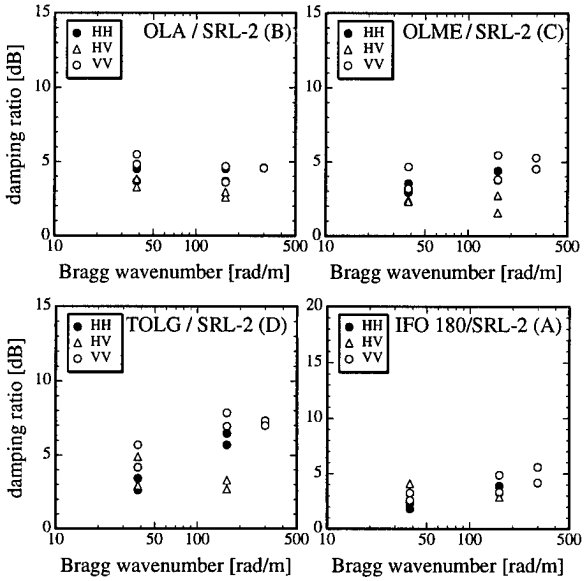


Fig. 4: damping ratios for differ ent surface films at high wind speed obtained from the SIR-C/X-SAR images of the second surface film experiment in the testsite North Sea (see Fig. 3).

surface films (Fig. 5, image dimensions are 7 km by 7 km) were imaged under low wind conditions (up to approx. 4 m/s) and show high damping ratios, especially at L and X band. In comparison with OLA at moderate wind speed it can be seen that the L band values are most different, which might be due to the large slick-covered sea area (cf. [1]).

In the sea areas where oil spills have been imaged the wind conditions were moderate (approx. 5 m/s). In comparison with the natural surface films, the damping ratios obtained from the oil spills are lower, especially at low Bragg wavenumbers (L band). Again, an increasing damping characteristic has been found, which seems to be typical for (thick) oil layers.

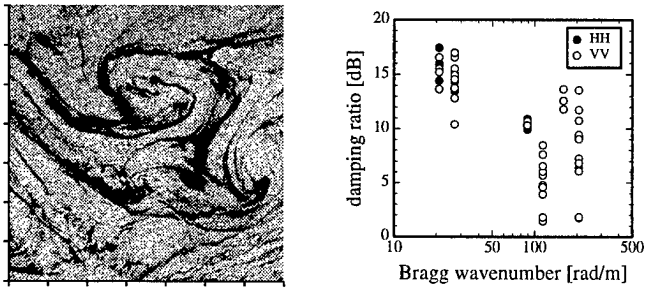


Fig. 5: left: X-SAR image taken on April 12, 1994, at 07:28 UTC and showing enlarged natural surface films due to an algae bloom in the North Sea west of North Denmark (SRL-1, datatake 47.10, X band, VV polarization, dimensions 7 km by 7 km); right: sample of damping ratios obtained from SAR images of natural slicks.

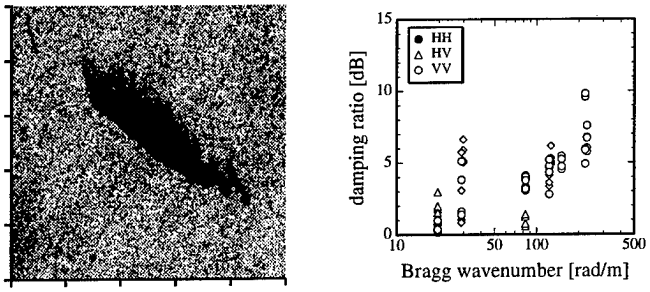


Fig. 6: left: X-SAR image taken on April 17, 1994, at 18:47 UTC from the Strait of Malacca (North of Sumatra). Dark patches of this shape are very likely due to oil spills (SRL-1, datatake 136.00, X band, VV polarization, 5 km by 5 km); right: sample of damping ratios of different oil spills obtained from SIR-C/X-SAR images.

In all damping curves presented here, no significant dependence on the polarization has been found.

POLARIZATION SIGNATURES

In order to profit from the multi-polarization capabilities of the SIR-C system polarization signatures have been calculated for film-covered and film-free water surfaces. At low to moderate wind speeds the polarization signature of an sea surface area which was very likely covered by mineral oil is quite different from that of the surrounding sea. The pedestal of the polarization signature is significantly higher at the oil-covered area (see Fig. 7) which is due to a lower signal-to-noise ratio (i.e., a higher portion of speckle noise). The different shape of the two polarization signatures shown in Fig. 7 can be explained with a different ratio of Bragg and specular scattering at low incidence angles (here 24°). However, at high wind speed the polarization signatures are similar for the different artificial surface films and are comparable to those measured over the surrounding (slick-free) ocean surface (not shown here).

DISCUSSION

For the interpretation of the obtained results a constant spectral action density is assumed,

$$0 = S_{in} - S_{dv} + S_{nl} - S_{db} , \qquad (1)$$

where S_{in} , S_{dv} , S_{nl} , and S_{db} are the source terms for energy input by the wind, viscous dissipation, nonlinear wave interaction, and dissipation by wave breaking, respectively. Inserting into (1) the expressions for the first two source terms (which can be found, e.g., in [3]) one obtains for the ratio of the (normalized) radar cross sections:

$$\frac{\sigma_0}{\sigma_s} = \frac{\Psi_0}{\Psi_s} = \frac{\beta_s - 2\Delta_s c_g}{\beta_0 - 2\Delta_0 c_g} \cdot \frac{S^0_{nl} - S^0_{db}}{S^s_{nl} - S^s_{dl}} \qquad (2)$$

Here Ψ is the spectral power density, β is the wind-induced spectral growth rate, Δ is the coefficient for spatial viscous damping, and c_g is the group velocity of the water surface waves. The subscripts/superscripts 0 and s denote a slick-free and slick-covered water surface, respectively. For monomolecular surface films the ratio of the viscous damping coefficients, Δ_s/Δ_0 , shows a resonance-like behavior which is typical for *Marangoni damping* (for details see [1]). From (2) it can be inferred, firstly, that the characteristic damping behavior of the surface films can have a strong influence on the damping ratio only at low to moderate wind speeds (where the wind-induced spectral growth rates are relatively small). Differences due to the characteristic damping behavior should therefore be observed only at low to moderate winds. At high wind speeds, the ratio of the spectral growth rates (i.e., the ratio of the friction velocities, see [3]) should become dominant and the film-induced differences of the damping ratios should vanish. Secondly, the reduction of wave breaking in the presence of surface films should be more important at high wind speeds, whereas at low wind speeds nonlinear wave interaction cannot be neglected. The presented results are in good agreement with these theoretical considerations (in [2] these hypotheses are also compared with data obtained by an airborne scatterometer).

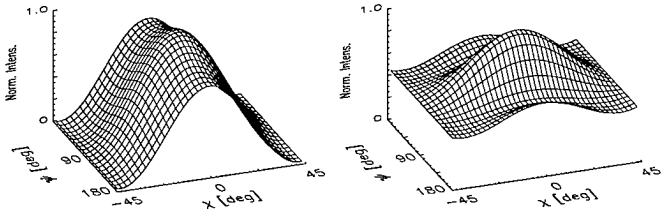


Fig. 7: C band polarization signatures of a film-free (left) and a film-covered (right) water surface obtained from SAR images taken from an oil spill on the West Pacific Ocean off the Mexican coast (SRL-1, datatake 65.10, April 13, 1994, 09:51 UTC)

ACKNOWLEDGMENTS

The authors are grateful to M. Kessler and G. Tanck for their engaged help in processing the SAR data.

REFERENCES

[1] W. Alpers and H. Hühnerfuss, "The damping of ocean waves by surface films: a new look at an old problem," J. Geophys. Res., vol. 94, pp. 6251–6265, 1989.

[2] M. Gade, "Untersuchungen zur Abbildung verschiedenartiger Oberflächenfilme auf der Meeresoberfläche mit Hilfe unterschiedlicher Radarsensoren," PhD thesis, Univ. of Hamburg, Hamburg, Germany, unpublished.

[3] O.M. Phillips, "Spectral and statistical properties of the equilibrium range in wind-generated gravity waves," J. Fluid Mech., vol. 156, pp. 505–531, 1985.

PRELIMINARY EVALUATION OF A MILLIMETER-WAVE SYSTEM FOR AIR POLLUTION MONITORING

Nadimi S. A., Bredow J. W.
University of Texas at Arlington-Wave Scattering Research Center
Department of Electrical Engineering, Box 19016, Arlington, Texas 76019
PH:817-273-3522/Fax:817-273-3443/Email:nadimi@uta.edu

Abstract – The progress of a spectrometer for environmental monitoring being developed at the University of Texas at Arlington will be discussed. This spectrometer is an active/ passive millimeter-wave (MMW) spectrometer that will operate over the 75-110 GHz (W-band) atmospheric window. Final laboratory testing of the system is projected to be the reflection and the transmission study of random dense media, and/or frequency-selective gratings.

INTRODUCTION

The priliminary design concept of the millimteter-wave system was discusse by Bredow *et al.* [1]. In this paper, we discuss the current status of the system development. To improve on accuracy and identification/quantification of pollutants, the task of design, and development of an active/ passive millimeter-wave (MM-wave) spectrometer was started in the fall of 1993. The 75-110 GHz (W-band) atmospheric window is relatively quiet and rotational resonances for many pollutants occur in this region. Therefore, this region could considerably enhance the environmental studies when used in association with UV and IR: (I) W-band can supply additional spectral information that can be useful in identifying and quantifying pollutants and in quantifying the presence of interferers, e.g., H_{20}; (2) W-band can penetrate through fog, haze and regions of particulates much more readily than IR and UV; and (3) radar techniques at W-band can supply information about particulate pollutants including size and concentration.

Substantial progress has been made in the design, development and testing of the MM-wave spectrometer. Testing of the system in the laboratory to determine power levels, frequency stability and overall performance of the system has been accomplished. Enclosure of most of the sections of the system is completed and the development of some of the software libraries needed to control the system via a multifunction analog, digital I/O board for PC has been realized. The construction of the anechoic chamber for the indoor study of the pollutants is essentially complete.

ASSESSMENT OF THE SYSTEM

The block diagrams of the system are shown in Figs. 1-3, and two pictures of the system are provided in Figs. 4&5. The W-band instrument will operate in 4 primary modes: (1) as a spectrometer measuring absorption over the 75-110 GHz region; (2) as a radiometer measuring blackbody-type emissions over the entire 75-110 GHz region; (3) as a pulse radar with peak power of 200 mW, over a 500 MHz bandwidth centered at about 93.1 GHz; and (4) as a step frequency radar (when used in combination with a HP 8510 network analyzer) over selected 9 GHz bandwidth segments of the 75-110 GHz band. The first 3 modes will be used primarily in the field to study air pollution (including particulate). The last mode is primarily for related studies in a new millimeter wave anechoic chamber that has been set up at UTA.

Testing on various sections of the system were performed. The if processor of the W-band spectrometer/radar (fig. 2) was tested in the laboratory. The filters in the two filter banks, the YIG-multiplier, mixer, and the two Low Noise Amplifiers (LNA) were tested for comparison to the design specifications. The if signal from the receiver antenna is filtered through the quasi-optical section into two bands of 75-93 GHz and 93-110 GHz. Each of these bands is then processed as four subbands covering 75-84, 84-93, 93-102 and 102-110 GHz of the received signal. Each subband is down converted to an if frequency range of 4.5-13.5 GHz which is then processed in the if processor by using a bank of filters, a YIG multiplier, and a bank of detectors.

The YIG multiplier was tested at frequencies of 4 to 12 GHz. At 4.0 GHz the output power was measured to be 5.5 dBm. The power levels of the multiplier decreased with increasing frequency. At 12 GHz the output power was measured to be below -3.0 dBm; however, the levels are controlled by a combined amplifiers/attenuator network before supplying the mixer's LO port To insure no drifting effect by the multiplier, tests were repeated several times and no drifting was noticed in any of the tests.

Acknowledgment: This study was supported by the National Science Foundation under grant number ECS-9214363.nology, Aug. 8-12, 1994, pp. 693-695.

REFRENCES

[1] Bredow, J., Fung, A.K., Gibbs, D.P. and Tjuatja, S., "A 75-110 GHz millimeter-wave spectrometer for pollution studies," Proc. IGARSS'94, California Institute of Technology, Aug. 8-12, 1994, pp. 693-695.

0-7803-3068-4/96$5.00©1996 IEEE

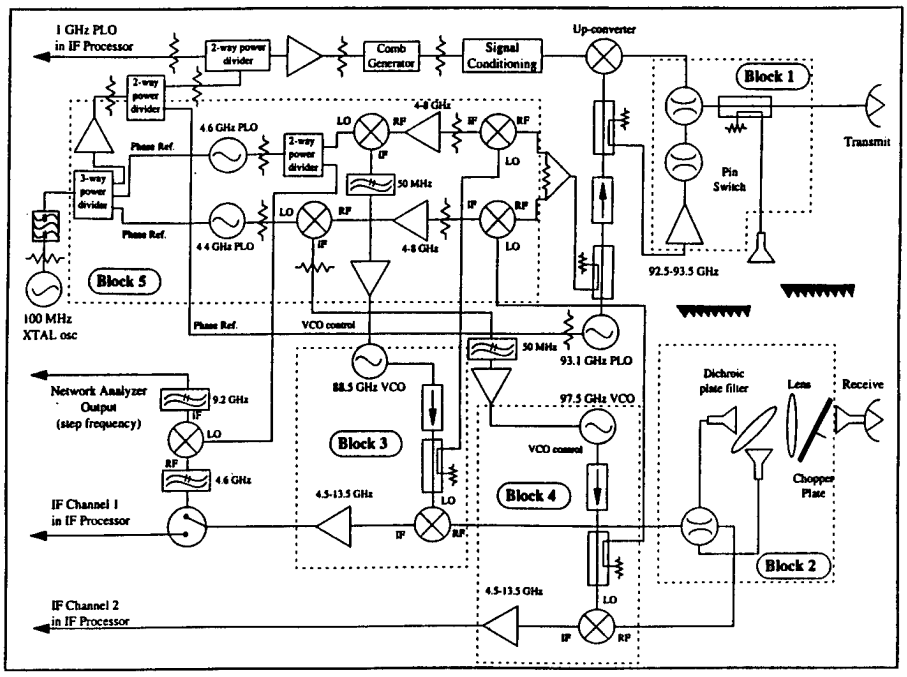


Fig.1 W-band Spectrometer/Radar RF Circuitry

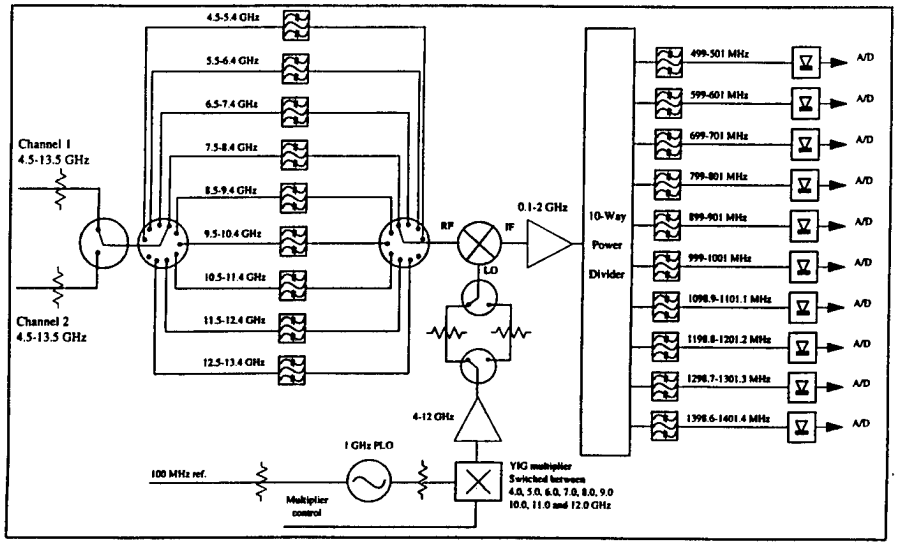


Fig.2 W-band Spectrometer/Radar IF Circuitry

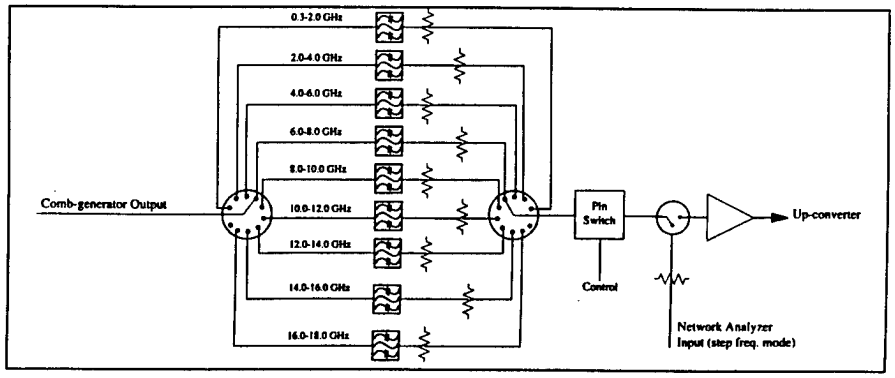


Fig. 3 W-band Spectrometer Signal Conditioning

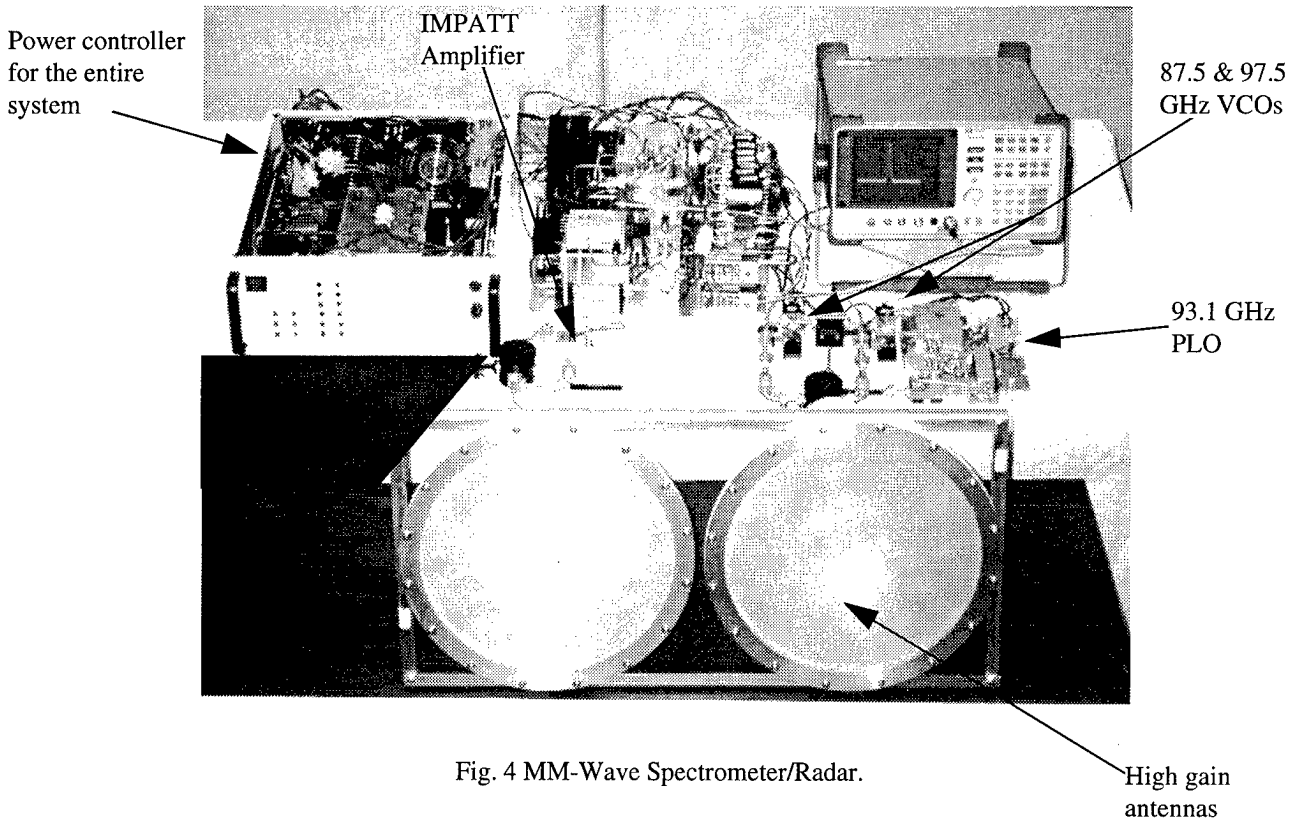


Fig. 4 MM-Wave Spectrometer/Radar.

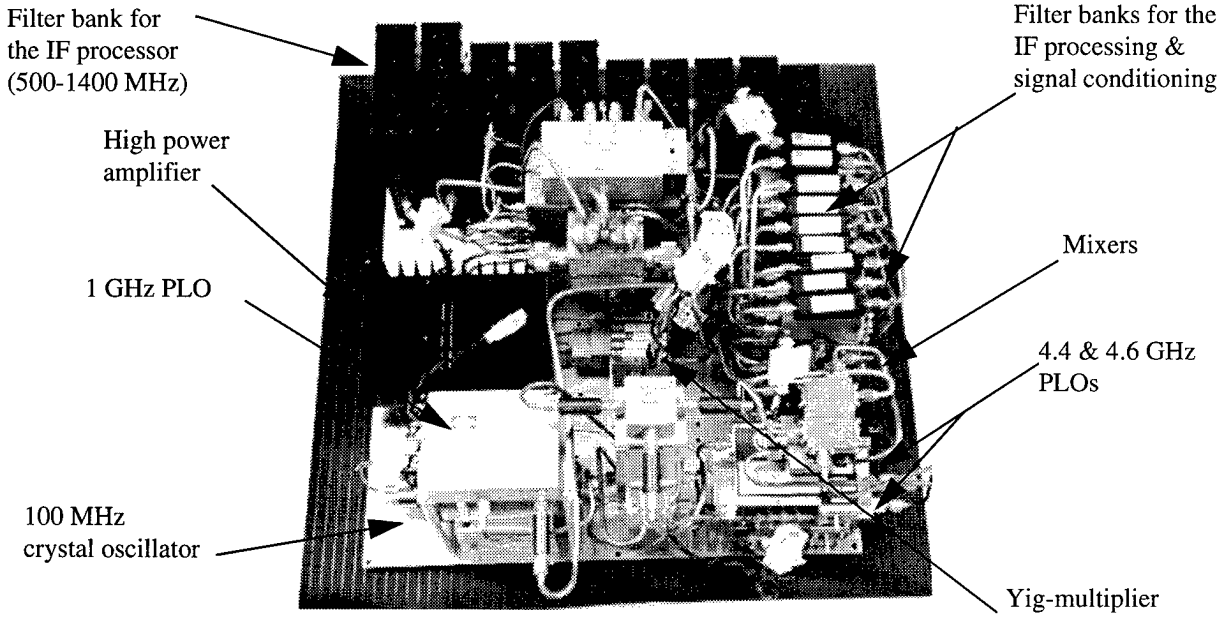


Fig. 5 Showing some of the components of the, PLOs, IF processor, and part of the signal conditioning.

TWO-DIMENSIONAL APERTURE SYNTHESIS RADIOMETERS IN A LOW EARTH ORBIT MISSION AND INSTRUMENT ANALYSIS

Ulrich R. Kraft

Dornier Satellite Systems GmbH, Dept. RST 21

P.O Box 801169, D-81663 Munich, Germany

Phone : (+89) 607 20591, Fax : (+89) 607 23384

ABSTRACT Mission and configuration of spaceborne two-dimensional synthetic aperture radiometers are considered in order to assess the possibilities and limits of this sensor type for global soil moisture monitoring. Results are presented which include the selection of orbit, scan type and basic sensor parameters as well as predictions for performance and mass/power requirements of different sensor options.

INTRODUCTION

Microwave radiometers operating at comparably low frequencies can play an important role in the monitoring of our environment since they permit measurements of ecological key parameters like soil moisture under all weather conditions and at any desired time.

Whereas the low microwave frequency range offers the advantage of a high penetration ability through clouds and into the top layer of the earth surface, its specific disadvantage is the poor spatial resolution which is achievable with moderately sized antennas. For global monitoring from space, antenna dimensions of up to 10 m or even more can be required which implies serious problems for any practical implementation of such a sensor.

A possible solution to the problem is the concept of passive aperture synthesis which has been implemented and successfully demonstrated with the airborne ESTAR sensor [1]. Investigations of corresponding spaceborne sensors based on one-dimensional aperture synthesis have been reported earlier by the author [2].

In Europe, the possibility to implement two-dimensional aperture synthesis for future spaceborne soil-moisture sensing is being investigated by the European Space Agency (ESA). The mission analysis for such an instrument (MIRAS) together with parts of the instrument analysis have been carried out by the author within this frame.

The following contribution gives an overview of key results based on an extension of the work performed for MIRAS. Results are presented which include the selection of orbit, scan type and basic sensor parameters as well as predictions for performance and mass/power requirements of different sensor options.

0-7803-3068-4/96$5.00©1996 IEEE

MISSION ANALYSIS

The basis for the mission analysis is formed by the scientific requirements given in Fig. 1 which have been established during the MIRAS study and subsequently agreed with a variety of specialists [3]. These requirements ask for a ground resolution of 10-20 km with 60 km as the acceptable limit matched to the 6.8 GHz channel of MIMR. The preferred geometry is a conical scan with 50° incidence (45-55°permitted) and dual-polarization which would avoid the need for auxillary temperature information through the use of the polarization ratio. The second option is a nadir line scan (similar to ESTAR) with incidences of 0-35° and one polarization which leads to a simplified sensor but implies the need for auxillary data.

For these options, the selection of the preferred orbit is based on the requirements for global coverage until ±85° lattitude with revisit times of 1-3 days. In order to achive constant conditions a polar near-sun-synchronous dawn-dusk orbit is preferred whereby 'standard' (700-800 km) as well as 'dedicated low' (400-500 km) orbits have been considered. The results of a first-cut assessment on instrument impacts are shown in Fig. 2. Whereas 1 day revisit is generally not possible, 2.3 days may be feasible with the concical scan approach at 700-800 km but imply the need for a large FOV which leads to increased problems with RFI, decorrelation and sample spacing selection. The same holds for a conical scanner in a 400-500 km orbit with about 3 days revisit time. Here, these aspects plus increased lifetime problems due to increased atmospheric drag have to be traded against a resolution improvement of about 34-40%. Taking into account these considerations, a 'standard' orbit of 799.8 km which has a minimum swath of about 880 km and matches both scan approaches has been selected.

A comparison of the basic geometries is shown in Fig. 3. Whereas an increased swath of about 890 km provides the desired global coverage until ±85° for all options, it is clearly shown that a conical scan geometry using only 50°-incidence pixels would imply a very poor use of available data since only a few of all possible pixels are utilized. For this reason, the investigated sensor options are limited to the 45-55° conical and the nadir line scan approach for which the corresponding instrument requirements are given

in Fig. 4. For both cases, decorellation is not a problem for up to 25 MHz bandwidth and up to 20 m aperture size due to the limited FOVs which is fully in line with the results of earlier system studies on 1-dim. synthesis [2].

INSTRUMENT CONFIGURATION

For the implementation of the selected sensor options, 3 antenna configurations as shown in Fig. 5 have been considered which provide the same, fully sampled circular area in the uv-plane for a given armlength L. Whereas T- and U-shape generate a regular, rectangular uv-grid which can be handled by conventional fourier processing, the Y-shape provides a hexagonal grid which permits a larger sample spacing Δ but requires a more complex processing with some remaining open questions. Taking into account mechanical stability, spaceraft accommodation and deployment, the U-shape is not very attractive because of the 90°-bends and the horizontal arm which would imply a larger 'free' volume on the satellite. Consequently, only T- and Y-shape have been considered further, whereby only samples within the the circular region (w/o redundancies) are used in order to ensure symmetry and minimum power demand.

The selection of the processing window affects accuracy, resolution and sensitivity of the sensor as discussed already in [2] for 1-dim. synthesis. Since most sidelobes of the antenna pattern are pointed towards the earth surface (200-300 K) an accuracy of about 3 K requires beam-efficiencies of about 99% which implies the unavoidable need for a highly tapered window. The selected Blackman-window ensures such a high beam-efficiency and improves the sensitivty but degrades the resolution slightly.

The sample spacing Δ is selected as a compromise to minimise both the impact of possible image lobes (aliasing) on the sensor accuracy as well as the number of antennas, receivers and correlators. This optimum occurs, if the worst case image lobes point towards the cold sky background or off-axis angles where they are suppressed by the antenna elements. For a T-shape (Y-shape) antenna, this selection corresponds to spacings of 0.720 (0.831) and 0.780 (0.900) for the nadir and the conical scan geometry, respectively.

In order to estimate the sensor sensitivity ΔT, a simplified model for the center pixel [2] using a homogenous scene of 300 K and identical receivers of 100 K has been assumed. Here, the array thinning for a circular uv-area and Blackman weighting as well as the effect of the one-bit digital correlators which have been selected in order to minimise power consumption and sensor complexity are taken into account.

The mass estimate is based on a structural mass of 7.8 kg/m for the three arms as well as 0.5 kg, 9 g and 60 kg for each receiver chain, each complex correlator and a fixed contribution, respectively. Similarly, the power estimates are based on 1.5 W per reciver chain, 90% efficiency of the power unit and 20 W fixed contributions. For the complex correlators figures of 50 mW (realistic) as well as 15 mW (most optimistic) have been used.

INSTRUMENT RESULTS

Based on the previously described selections estimates for performances and budgets of both the nadir-view and the conical scan sensor matching the given mass and power limits are shown in Fig. 6 and Fig. 7, respectively

For the nadir geometry the mass and power allocations permit an antenna size of 9-10 m per arm which leads to a good resolution of 20-35 km. Here, the Y-shape offers an improvement of about 13-14% with the disadvantages described before. The desired sensitivity of 1 K is possible but requires multilook processing of 4 looks (8-14 looks available). An accurcay of 3 K is possible through Blackman-window processing. Mass and power figures are about 270 kg and 400/600W (optimistic/realistic).

For the conical scan geometry an antenna size of 10-11 m is possible which permits only a moderate resolution of 35-60 km again with slight advantages for the Y-shape. A sensitivity of 1 K requires also multilook processing (4-5) but is more critical here since only 4-7 looks are available. Mass and power figures are about 270-280 kg and again 400/600W (optimistic/realistic).

The results show that only the nadir geometry permits spatial resolutions down to 20 km and should be reconsidered, therefore, from a scientific point-of-view. (resolution vs. aux. data requirements). Furthermore, a more detailed investigation of the pros and cons of T- and Y-shape is recommended, since the possible resolution improvements of the Y may not balance out the processing problems.

REFERENCES

[1] D. M. LeVine, A. J. Griffis, C. T. Swift, T. J. Jackson, "ESTAR : A Synthetic Aperture Microwave Radiometer for Remote Sensing Applications", Proc. IEEE, Vol. 82, No. 12, (1994), pp. 1787-1801

[2] U. R. Kraft, "Spaceborne Synthetic Aperture Interferometric Radiometers for Global Monitoring of the Earth", Proc. IGARSS 91, (1991), pp. 971-974

[3] D. Guyenne (ed.), Proceedings of the Consultative Meeting on Soil-Moisture and Ocean Salinity Measurement Requirements and Radiometer Techniques, ESA-Publ. ESA-WPP-87, (1995)

Parameter	Optimum Figure	Acceptable Figure
Spatial Coverage	global	global up to ±85° NS
Spatial Resolution	10-20 km	up to 50-60 km
Temporal Coverage	full year	n.a.
Temporal Resolution	1 day	up to about 3 days
Local Time of Measurement	dawn-dusk	arbitrary
Nominal Incidence Angle	50°	0°
Range of Incidence Angles	45°-55°	0°-35°
Polarisation	H+V	H or V
Sensor Frequency	1.4 GHz	n.a.
Sensor Bandwidth	≤ 25 MHz	n.a.
Radiometric Sensitivity	0.5 K	up to about 1.0 K
Radiometric Accuracy	1.0 K	up to about 3.0 K

Fig. 1 Scientific requirements for soil-moisture sensing

Heading	Parameter	Allocation		
	Revisit Time	1.0 d	2.3 d	3.2 d
DEDICATED LOW ORBIT	Mean Orbit Altitude	466.1 km	429.0 km	466.1 km
	Orbit Inclination	97.3°	97.1°	97.3°
	Required Swath	2617 km	1136 km	818 km
NADIR SENSOR		not feasible for global coverage at 0-35° incidence		
OFF-NADIR SENSOR	Off-Nadir Angle COC	not feasible for	not feasible for	15.5°
	IFOV-CR	global coverage	global coverage	± 40.6° (!)
	Incidence Angles	at	at	45-55°
	Res. (10 m) 45°	45-55°	45-55°	25.8 x 16.4 km
	Res. (10 m) 55°	incidence	incidence	41.4 x 19.6 km
STANDARD ORBIT	Mean Orbit Altitude	799.8 km	740.5 km	799.8 km
	Orbit Inclination	98.6°	98.4°	98.6°
	Required Swath	2800 km	1215 km	880 km
NADIR SENSOR	Off-Nadir Angle COC	not feasible for	not feasible for	0.0°
	IFOV-CR	global coverage	global coverage	± 28.6°
	Incidence Angles	at	at	0-32.6°
	Res. (10 m) COC	0-35°	0-35°	20.6 x 20.6 km
	Res. (10 m) EOC	incidence	incidence	32.2 x 23.9 km
OFF-NADIR SENSOR	Off-Nadir Angle COC	not feasible for	18.6°	31.3°
	IFOV-CR	global coverage	±44.2° (!)	±24.5°
	Incidence Angles	at	45-55°	45-55°
	Res. (10 m) 45°	45-55°	38.8 x 25.7 km	39.4 x 27.6 km
	Res. (10 m) 55°	incidence	60.2 x 30.3 km	58.8 x 32.5 km

Fig. 2 System impacts of orbit options

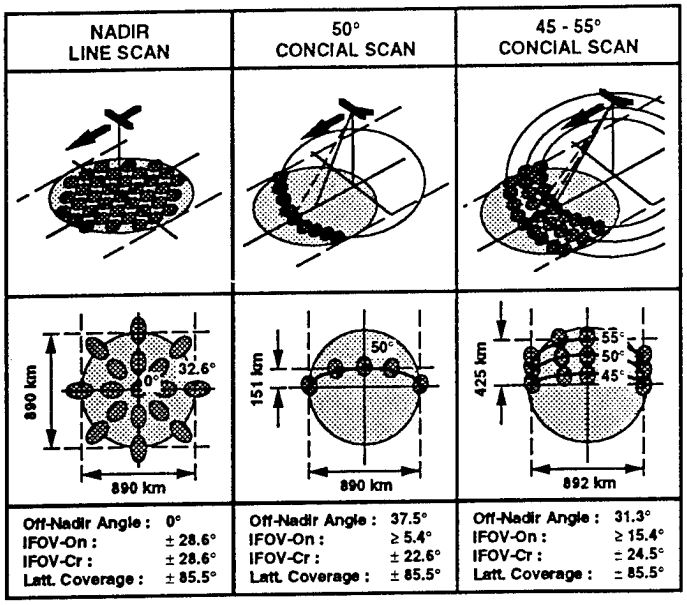


Fig. 3 Overview of scan options

Sensor Type	NADIR LINE SCAN	45 - 55° CONICAL SCAN
Orbit Type	sun-synchronous	sun-synchronous
Mean Orbit Altitude	799.8 km	799.8 km
Orbit Inclination	98.6°	98.6°
Nodal Crossing Time	10:00 h AM	10:00 h AM
Off-Nadir Angle	0°	31.3°
IFOV-CR	±28.6°	±24.5°
IFOV-ON	±28.6°	≥15.4°
Swath	890 km	890 km
Sensor Frequency	1.4 GHz	1.4 GHz
Sensor Bandwidth	≤ 25 MHz	≤ 25 MHz
Sensor Polarisation	H or V	H + V
Spatial Resolution	20-60 km	20-60 km
Temporal Resolution	1/3.2 d	1/3.2 d
Radiometric Sensitivity	≤1.0 K	≤1.0 K
Radiometric Accuracy	≤3.0 K	≤3.0 K
Total Sensor Mass	≤200-300 kg	≤200-300 kg
Total Sensor Power Consumption	≤300-600 W	≤300-600 W

Fig. 4 Deduced instrument requirements

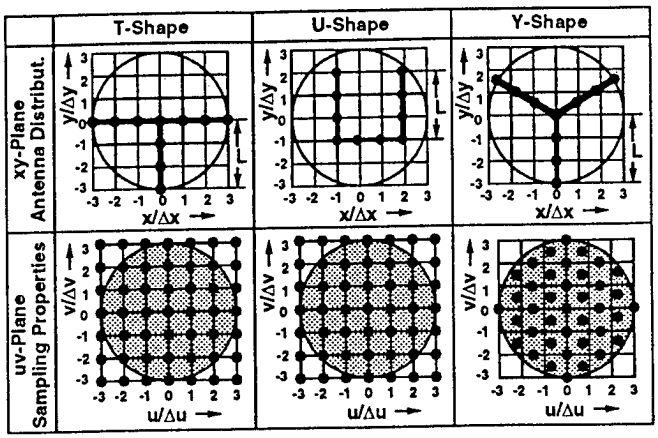


Fig. 5 Overview of antenna configuration options

Parameter	Requirement	T-Shape Approach	Y-Shape Approach
Length of One Antenna Arm	n.a.	8.95 m	10.33 m
Number of Antenna Elements	n.a.	175	175
Number of Receiver Chains	n.a.	175	175
Number of Complex Correlators	n.a.	5375	5133
Sensor Frequency	1.4 GHz	1.4 GHz	1.4 GHz
Sensor Bandwidth	≤ 25 MHz	20 MHz	20 MHz
Sensor Polarisation	H or V	H or V	H or V
Off-Nadir Angle	0°	0°	0°
IFOV ON x CR	n.a.	±28.6° x ±28.6°	±28.6° x ±28.6°
Used Footprint ON x CR	n.a.	890 x 890 km	890 x 890 km
Sample Spacing ON x CR	n.a.	0.720 x 0.720	0.831 x 0.831
Spatial Coverage	global, ≥ ±85°	global, ±85.5°	global, ±85.5°
Revisit Time	up to about 3 days	3.2 days	3.2 days
Incidence Angle Variation	0° - 35°	0° - 32.6 °	0° - 32.6 °
Spatial Resolution	20-60 km		
0° Incidence (COC) B-Window		23.0 x 23.0 km	19.9 x 19.9 km
32.6° Incidence (EOC) B-Window		36.1 x 26.7 km	31.3 x 23.1 km
Radiometric Sensitivity (ΔT)	≤1.0 K		
ΔT-Snapshot B-Window		1.86 K	2.00 K
ΔT-Processed B-Window		0.93 K	1.00 K
Multilook Requirement		4	4
Multilook Availability		8 ... 11	9...14
Radiometric Accuracy	≤3.0 K	poss. w. Blackman	poss. w. Blackman
Total Mass	≤200-300 kg	about 270 kg	about 270 kg
Total Power Consumpt. (realist.)	≤300-600 W	about 600 W	about 600 W
(optimist.)		down to 400 W	down to 400 W

Fig. 6 Performances and budgets (NADIR LINE SCAN)

Parameter	Requirement	T-Shape Approach	Y-Shape Approach
Length of One Antenna Arm	n.a.	9.69 m	11.19 m
Number of Antenna Elements	n.a.	175	175
Number of Receiver Chains	n.a.	175	175
Number of Complex Correlators	n.a.	5375	5133
Sensor Frequency	1.4 GHz	1.4 GHz	1.4 GHz
Sensor Bandwidth	≤ 25 MHz	20 MHz	20 MHz
Sensor Polarisation	H + V	H/V switched	H/V switched
Off-Nadir Angle	0°	31.3°	31.3°
IFOV ON x CR	n.a.	15.4° x ±24.5°	15.4° x ±24.5°
Used Footprint ON x CR	n.a.	250 x 890 km	250 x 890 km
Sample Spacing ON x CR	n.a.	0.780 x 0.780	0.900 x 0.900
Spatial Coverage	global, ≥ ±85°	global, ±85.5°	global, ±85.5°
Revisit Time	up to about 3 days	3.2 days	3.2 days
Incidence Angle Variation	45-55°	45-55°	45-55°
Spatial Resolution	20-60 km		
45° Incidence B-Window		40.7 x 28.5 km	35.2 x 24.7 km
50° Incidence B-Window		48.9 x 30.8 km	42.3 x 26.6 km
55° Incidence B-Window		60.7 x 33.5 km	52.6 x 29.0 km
Radiometric Sensitivity (ΔT)	≤1.0 K		
ΔT-Snapshot B-Window		1.97 K	2.12 K
ΔT-Processed B-Window		0.99 K	0.95 K
Multilook Requirement		4	5
Multilook Availability		4 ... 6	4... 7
Radiometric Accuracy	≤3.0 K	poss. w. Blackman	poss. w. Blackman
Total Mass	≤200-300 kg	about 270 kg	about 280 kg
Total Power Consumpt. (realist.)	≤300-600 W	about 600 W	about 600 W
(optimist.)		down to 400 W	down to 400 W

Fig. 7 Performances and budgets (45-55° CON. SCAN)

Integration of MIRAS Breadboard and Future Activities

M.Martín-Neira[1], J.M.Goutoule[2], A.Knight[3], J.Claude[2],
J.Bara[4], A.Camps[4], F.Torres[4], I.Corbella[4],
A.Lannes[5], E.Anterrieu[5], B.Laursen[6], N.Skou[6]

(1) European Space Agency, ESTEC, Postbus 299, 2200 AG Noordwijk, The Netherlands
(2) Matra Marconi Space France, 31 rue des Cosmonautes, Z.I. du Palays, 31077 Toulouse, France
(3) Matra Marconi Space UK, Anchorage Road, Portsmouth, Hampshire PO3 5PU England
(4) Polytechnic University of Catalonia, ETSE Telecommunications, 08071 Barcelona, Spain
(5) CERFACS/LAT, 14 Avenue Edouard Belin, F-31400 Toulouse, France
(6) Danish Center for Remote Sensing, TUD, B-348, DK-2800 Lyngby, Denmark

ABSTRACT

The European Space Agency (ESA) is conducting a feasibility study on MIRAS, a Microwave Imaging Radiometer using two dimensional Aperture Synthesis, for the mapping of soil moisture and ocean salinity from space. An aircraft breadboard of this instrument is currently being integrated and will be flown in Spring 1996. This paper concentrates on the results achieved following the integration of the prototype. The breadboard consists of an 11 element Y-shaped bi-dimensional L-band interferometer which can be switched to measure the two polarizations.

In addition the future activities related to MIRAS are presented. A technology demonstrator of MIRAS is proposed as a first major step towards a future spaceborne sensor.

AIRBORNE DEMONSTRATOR

The second part of the MIRAS program is devoted to the demonstration of the concept capabilities through a breadboard to be flown on a C 130. Miras breadboard is identical to the central part of Miras spaceborne instrument, i.e. it works at L band and has a Y shape antenna with 0.65 m long arms and 11 Elementary Radiating Elements. The 11th one enables the phase restoration capability to suppress phase errors due to mechanical deformation of the antenna and residual receiver errors.

The main elements of MIRAS breadboard are: a Y-shaped 11 element array, the L-band receivers with switched polarization, an optical harness which distributes the clock reference to the receivers and a correlator unit which digitizes in 1 bit the receivers outputs and correlates them during an integration time of 0.285 seconds. Two kinds of calibration signals are provided to the receivers within the breadboard: a common noise reference supposed to produce a known output correlation and 11 independent 50 ohms loads supposed to produce a zero output.

MIRAS Antennas

The 11 cup dipole antennas of MIRAS demonstrator have been manufactured and tested with their environment. Their diagram patterns are very similar with directivities lying between 9 and 9.2 dB (18.5 cm aperture), including the effects of the thermal box side walls simulated during the measurements. The half power beamwidth is between 65° and 70° depending on the cut plane and the polarisation. The normalized phase discrepancy between antennas is less than 5° within the IFOV. The cross polarisation level is −20 dB but −30 dB inside the IFOV. The coupling between antennas is less than −25 dB.

L-band Receivers

The low noise amplification, radio interferences filtering, and I and Q demodulation are achieved by 11 receivers units installed around the structure, phase locked onto a common clock distributed by optical fibers. They exhibit 100 dB gain and 1.3 dB noise figure at 1.41 GHz.

Correlator Unit

MIRAS demonstrator requires 55 complex (or 110 real) correlators. They are implemented in a single 10 dm^3 unit based on FPGA circuits for the digital sections. The

0-7803-3068-4/96$5.00©1996 IEEE

two critical performances of the correlators are the noise and the accuracy. MIRAS correlator perfectly fits to the 1 bit correlator theory, no additional noise being observed. As far as the correlation accuracy is concerned the almost only contributor is the offset of the A/D 1 bit converter. Using independent noise sources as input signals, the correlators give outputs as low as 10^{-4}, some of them reaching 3×10^{-3} which has a negligible impact on MIRAS breadboard performances.

SYSTEM PERFORMANCE AND ERROR ANALYSIS

The system basic performance of the spaceborne version of MIRAS has been further studied in terms of spatial resolution and radiometric sensitivity. Spatial resolution has been computed including all the available (u,v) samples given by the Y-array. The synthesized half-power beamwidth ranges from 0.77° to 1.10° at boresight, depending on the weighting function. It broadens up to 0.82° or 1.14° respectively due to fringe-washing effects at the swath edge. The radiometric sensitivity has been studied taken into account predetection filters shape, the use of DSB receivers and the effect of the digital correlator being used. Snap–shot radiometric sensitivity for 0.3 seconds integration time is between 13 and 5 K, depending on the weighting function. This sensitivity is improved by a factor of 6 when the complete dwell time corresponding to the pixel is used as integration time. The radiometric resolution reaches a saturation threshold for large signal to noise ratios due to discretization errors.

The sources of error have been classified according to their origin and the feasibility of their calibration into the following three main groups:
1) antenna errors: amplitude and phase ripple in the pattern, coupling, mispointing, in–plane and out–of–plane position errors, polarization cross–talk;
2) receiver errors: in–phase channel errors (phase and delay time offsets), I/Q quadrature errors and amplitude errors;
3) baseline errors: phase and amplitude errors (differences of frequency response between receivers chains), offset errors due to unwanted correlated signals (i.e. LO leakage), as well as 1 bit quantizer threshold offsets.

Receiver errors appear as separate amplitude factors or phase summand errors in the measured visibility samples and can be calibrated by a distributed network of noise sources. On the contrary, baseline amplitude and phase errors appear as mixed terms with parameters coming from the particular pair of receivers and must be calibrated by noise injection from a single noise source.

The analysis of system errors shows that the most important contributors to the radiometric resolution are the antenna pattern amplitude and phase ripple (must be known to 0.25% and 0.5°), antenna mutual coupling (mutual impedances to within 5%) and the baseline phase and amplitude errors which requires very well matched filters. These errors must be known to the mentioned levels in order to be able to correct them during the inversion process.

ON–BOARD MIRAS CALIBRATION PROCEDURE

An original hardware calibration scheme is proposed for MIRAS spaceborne sensor whose potential can be tested with the aircraft breadboard [2, 4]. The method avoids the problems of a centralized noise distribution network, namely, the mass of the cables and their electrical matching. This is possible by using several noise sources distributed along the array which inject calibration noise into groups of 8 receivers with an overlapping of 4 receivers between groups. Only the half of the noise sources which is connected to non overlapping groups of receivers is switched at a time, so that the noise sources are switched sequentially.

This scheme provides a set of calibration measurements that allows to solve for the receiver phase and quadrature error terms. It also allows to compute the equivalent noise temperature of the receivers and the amplitude of the calibration noise signals themselves (except the reference one which is assumed to be known), which determine the gain factors of the normalized visibility samples. The main hardware calibration steps are:
1) correlators offset calibration by injection of uncorrelated noise (matched loads);
2) inversion of the 1–bit/2–level digital correlator response to find the normalized visibility samples ;
3) estimation of the in–phase and quadrature receiver errors by alternated correlated noise injection;
4) removal of the noise contribution of the noise distribution network and addition of the noise induced by the antenna network;
5) application of the normalization gain factors to the normalized visibility samples (antenna temperature measured by the total power radiometer and receiver noise temperatures);
6) calibration of in–phase and quadrature receiver errors using (3) through (5);
7) calibration of antenna coupling using ground antenna measurements.

INVERSION ALGORITHM

An inversion algorithm is proposed based on the hexagonal FFT presented in [5] which is able to operate directly with the measured (u,v) samples over the hexagonal grid given by the Y–shaped array, avoiding any interpolation process, signal to noise ratio degradation and induced artifacts. Hexagonal processing can be performed efficiently with standard rectangular FFT's provided that the

(η, ξ) direction cosines grid is chosen over the reciprocal grid of the (u,v) one: memory savings are 13.4% and the computational load is reduced by a 25%. The number of brightness temperature pixels in the basic hexagonal cell is the same as the total number of correlations, redundant or not. The number of visibility samples which must be set initially to zero is equal to the number of redundant correlations.

The image reconstruction procedure can be decomposed into three main steps. In order to get rid of phase errors due to antenna deformations and residual errors from the on–board hardware calibration, an operation of redundant spacing calibration is performed first. The cost for this spectral reduction of phase closure data is a translation indetermination in the real space [3]. The very process of image reconstruction comes next based on the linear relationship between the visibilities and the brightness temperature distribution. The final step consists in raising the translation indetermination for which several strategies can be adopted.

The initial guess of the reconstruction algorithm is obtained by direct Hexagonal Fourier inversion of the calibrated visibilities and compensation by the average antenna radiation pattern [2, 5]. The inversion process is accelerated by processing zero mean differential visibilities, which are obtained by subtracting the visibility contributions of the sky and that of an hypothetical constant brightness temperature Earth as measured by the total power radiometer. This technique has been tested in a preliminary MIRAS spaceborne software simulator [1] and has shown to converge in a few iterations.

LABORATORY TESTS ON MIRAS CONCEPT

A bi–dimensional synthetic aperture radiometer has been used to simulate the Y-shaped antenna structure used in MIRAS. This demonstration model consists of a calibrated 2-channel Ku-band (16 GHz) correlation radiometer with two horn antennas and an antenna mounting structure enabling the horns to be mounted in relevant positions within a certain aperture. A total aperture synthesis is obtained by sequentially placing the two antenna elements in all required pairs of positions and measure the corresponding samples of the visibility function. Pointing the instrument at a stationary target and accepting a longer total time for a measurement, the synthetic aperture principle can be demonstrated in this way.

The number of samples with different positions taken one by one add up to a thousand and the total measurement takes several hours. The spacing between the antennas in the Y–shaped structure is 0.8λ which is comparable to the 0.89λ in MIRAS. The demonstration model has been used to simulate a two dimensional aperture with 16 elements on each arm which is more representative of the spaceborne design. The tests are performed on targets like the horizon with simple structures like a power plant and a 50 meter chimney [6]. The two channel demonstration has been used to evaluate calibration topics as well. However, the two channel set-up is less useful for the demonstration of overall instrument calibration because errors tend to add up in the image reconstruction as the same channels are used for all measurements.

FUTURE ACTIVITIES ON MIRAS

In the near future (Spring 1996) the aircraft MIRAS breadboard will be flown on board an Hercules C–130 of the Danish Air Force over a site in the north of Denmark. It is expected that these measurements together with the integration ground tests which are currently being performed will demonstrate the feasibility of the L–band two–dimensional aperture synthesis MIRAS radiometer.

Further hardware developments on a LIght weight Cost EFfective L–band antenna/receiver assembly (LICEF) and on an advanced DIgital COrrelator for aperture Synthesis applications (DICOS) are being undertaken by ESA at present. These developments aim at building a spaceborne MIRAS demonstrator to test key functions of the system in orbital flight conditions.

References

[1] Matra Marconi Space, "MIRAS: Microwave Imaging Radiometer with Aperture Synthesis", Final Report, ESTEC Contract No. 9777/92/NL/PB

[2] J.Bara, A.Camps, I.Corbella, F.Torres, "Bi–dimensional Discrete Formulation for Aperture Synthesis Radiometers", CNN 2 of WO-10 to ESTEC Contract No. 9777/92/NL/PB

[3] A.Lannes, E.Anterrieu, "Image Reconstruction methods for Remote Sensing by Aperture Synthesis", IGARSS'94, Pasadena, 2892–2903,1994

[4] F.Torres, A.Camps, J.Bara, I.Corbella, R.Ferrero, "On-board Phase and Module Calibration of Large Aperture Synthesis Radiometers: Application to MIRAS", in press for TGARS, Dec.1995

[5] A.Camps, J.Bara, I.Corbella, F.Torres, "Inversion Algorithms over Hexagonal Sampling Grids in Interferometric Aperture Synthesis Radiometry", PIERS'95, Seattle US, 1995

[6] B.Laursen,N.Skou, "A Spaceborne Synthetic Aperture Radiometer Simulated by the TUD Demonstration Model", IGARSS'94, pp 1314-1316

Design and Implementation of the MIRAS Digital Correlator

Ottfried Bätz, Ulrich Kraft, Willi Lindemer, Hans Reichel
Dornier Satelliten Systeme GmbH, Dept. RST 15, P.O.Box 80 11 69, D-81663 Munich, Germany
Phone: (+89) 607 26188, Fax: (+89) 607 35180

Abstract — The MIRAS imaging radiometer presented in other papers so far, includes a digital one-bit correlator array. The configuration of a future MIRAS flight model features more than 100 antenna elements. This requires a correlator array with more than 10 thousand correlators.

The feasibility of MIRAS will be demonstrated by a breadboard with 11 complex channels and 110 correlators. The sampling frequency is 50 MHz and the integration time is 285 msec. The described demonstrator is using high speed comparators for analog-to-digital conversion and field-programmable gate arrays (FPGAs) for digital processing.

The tests using a specific testbed have turned out the difficulty of stimulating the correlators for the purpose of precise calibration.

The described correlator has been developed for the European Space Agency.

I. INTRODUCTION

Techniques of radiometry using frontends with aperture synthesis has been widely reported and discussed in [1], [2], [3], [4] and others. Suitable and affordable implementation techniques, in particular for the correlators, are extensively traded. Performance efficiency of the technique and power consumption of the technologies are the major competing criteria. Now, when radiometers of this kind have been taken into consideration for deployment on space platforms, mass and volume have become additional critical benchmarks.

The major design drivers of a correlator are the analog section (EMI robustness), the sampler (only for digital implementations), the multiplier and the integrator. The noise bandwidth is usually bound to the baseband limit frequency of analog amplifiers and/or to the realizable sampling and processing frequency in digital correlators. The references are unanimously confirming that the digital technology appears most promising for an implementation of huge correlator arrays.

With a Nyquist sampling frequency f_s related to the noise bandwidth, the performance of a complex correlator in terms of the standard deviation of the visibility value is defined by the relation

$$\Delta T/T = 1/[\eta\,(0.5 f_s\,\tau)^{1/2}]\,. \qquad (1)$$

where τ is the integration time of the correlator, η is the efficiency.

The choice of a suitable technology is mainly determined by the maximum possible product (η fs1/2).

It is evident that a sampler followed by a one-bit ADC (analog-to-digital converter) and a correlator offers the highest sampling and processing speed but features only moderate efficiency (η=0.64). Higher efficiency can be obtained by more levels, e.g. η=0.8 for a 3-level (2-bit) correlator or a 1-bit by multi-bit correlator [1], but the processing rate is significantly worse than for the simple 1-bit correlator. A technological step off the 1-bit correlator reduces the processing speed by at least a factor of 2. Hence the ($\eta\, f_s^{1/2}$)-product of the 1-bit correlator is very close to that of a multi-bit correlator. The ultimate choice in favor of a 1-bit correlator will finally be taken upon power consumption, technological complexity and low sensitivity to absolute level variations.

These issues have been the base for the design of MIRAS (Microwave Imaging Radiometer with Aperture Synthesis).described in [4]. A breadboard has been implemented and constructed for a demonstration on a C 130 aircraft.

II. ARCHITECTURE OF THE CORRELATOR

The MIRAS breadboard includes a CPMU (Correlator and Power Measurement Unit) tailored to an antenna and RF configuration with 11 complex channels (each consisting of an in-phase and a quadrature-phase branch). The correlator unit is composed of 110 individual correlators thus offering full redundancy for the purpose of comprehensive experimental studies. As the 1-bit correlator eliminates the absolute noise level, a Power Measurement subunit has been added.

The functional elements of the CPMU are drawn in Fig. 1. The unit is fed by 21 noise channels band-limited to 25 MHz. All channels are synchronously sampled at 50 MHz. Thereafter, the digital signals are distributed to the 110 correlators. Each correlator performs an integration over 285 msec. A 24-bit accumulator is split into a fast and a slow counter in order to save electrical power. The 16 most significant output bits are multiplexed along with the output of the Power Measurement Unit (PMU) and dumped through an IEEE-488 interface to a PC (personal computer).

The PC performs a linearisation with a sine-conversion and, then, a correction of the CPMU output data by applying data from a calibration map.

III. DESIGN AND IMPLEMENTATION

The critical elements of the CPMU hardware are the comparator and the fast counter. Moreover, the distribution network between the samplers (latches) and the correlators proper will become a challenge when in future large scale systems thousands of correlators are to be fed.

The comparator is the high speed device MAX 902. Its output port is linked to a D-flip-flop sampler. All samplers

0-7803-3068-4/96$5.00©1996 IEEE

are synchronously clocked. The sampling rate of 50 MHz is limited by the capability of the following fast counter. All signal lines from CPMU input up to the samplers and all clock lines from the common generator to the samplers are carefully aligned to a maximal differential delay of 30 ps in order to keep undesired de-correlation effects $\Delta\rho$ below 10^{-4}. After sampling, the timing constraints are relaxed to some nano-seconds (about one quarter of the clock period).

Correlators of a future operational MIRAS instrument are needed in a great volume and, therefore, they should be implemented in ASIC´s (application specific integrated circuits). The correlators of the CPMU breadboard, however, have been implemented in FPGA´s (field programmable gate arrays), for financial reasons. An ACTEL 1225 device has been used for operation up to 50 MHz. Each device accommodates both a sub-matrix of 5x5 correlators and its associated data distributor. Each correlator is composed of an EXOR element (multiplier) and a 5-bit counter.

Another FPGA type, ACTEL 1280, accommodates 14 post accumulators with 19 stages, each, clocked at 6.25 MHz in order to save electrical power.

The circuitry for timing and control of the CPMU as well as the integrator of the Power Measurement Unit are brought into one ACTEL 1280. So the entire CPMU with 110 correlators and all control functions is using 15 FPGA´s.

The CPMU is housed in a 19-inch drawer with 4 height units. The power consumption is below 12 Watts.

The accumulator of a correlator is a straight up-counter; this to realize is easier than an up/down-counter mentioned in the literature. The content n of the accumulator is $n_{max} = f_s \tau$ at full correlation, and $n_{max}/2$ at zero correlation. The normalized non-linear visibility value V_n is obtained by $V_n = 2n/n_{max} - 1$. The linearized visibility value V_l is derived by $V_l = \sin(V_n \pi/2)$.

Finally, the corrected visibility value V_c is obtained by three calibration values, one characteristic triplet per correlator. The approximation $V_c = a + b\ V_l + c\ V_l^2$ calibrates the individual offset, tilt and first-order bend of a correlator response. The corrections allow for electro-magnetic interference and imperfections of the hardware implementation in particular of the analog section. 110 triplets of parameters *a, b, c* are stored in a PC. Eventual recording of triplets vs. temperature allows thermal calibration of the correlators.

IV. TEST CONFIGURATION

The measurement of the correlation response of the unit requires two sources of bandlimited white noise whose cross-correlation can be preset. The selected test set-up is sketched in Fig. 2. One noise source is directly linked to one correlator input port, while the other port is fed by a mix of two uncorrelated noise signals. The power ratio of the mix is denoted as *NPR* (noise power ratio). The preset correlation ρ of the correlator input signals is determined by

$$\rho = (1 + NPR)^{-1/2} . \qquad (2)$$

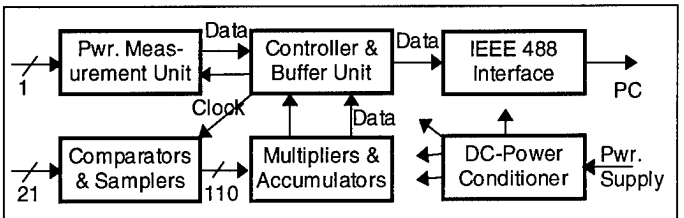


Fig.1: Architecture of the MIRAS Correlator and Power Measurement Unit

The accuracy of ρ depends on the measurement of the *NPR*. The test bed is arranged such that the same power meter is used for both noise ingredients at the second port. The accuracy of ρ is highest at $NPR = 1$, i.e. at $\rho = 0.707$.

All other settings of the *NPR* suffer from the residual error of the power ratio measurement. With the available power meter, HP 436A & 8481A, the error is bound to about 0.2 dB within the same measurement range, and to 0.4 dB over two ranges.

A relative precise prediction of ρ is supposed at $\rho=0$ where the two noise sources are separately feeding the two correlator input ports. Careful shielding is required in order to avoid adverse effects through finite cross-coupling and environmental spurious signals like from computer networks.

The case at $\rho=1$, where one source is feeding the two correlator inputs ports, constitutes a configuration easy to implement and reliable in prediction. However, it is not an operational mode that may occur in MIRAS.

Statistical properties of the correlator have been obtained by evaluating 50 consecutive measurements, one every 285 msec.

V. TEST RESULTS

Fig. 3 shows the linearized response of correlator No.1. Fig. 4 shows the deviation from a linear response. The response is essentially due to the imperfect setting and measurement of the input correlation ρ. This becomes evident by the small deviation at ρ=(0, 0.707 and 1) where the knowledge of the power ratio is most precise.

The standard deviation (Fig. 5) complies with the expected values.

A survey of all 110 correlators at ρ=0.707 exhibits some groups of correlators which, prior to calibration, significantly deviate from the expected value (see Fig. 6). This is due to deficiencies in the layout of the analog part of the CPMU. Signal coupling and interference from clock lines into the signals are resulting in a de-correlation effect. After calibration, the CPMU was performing adequately.

VI. CONCLUSION

The demonstrator of the CPMU has met the relevant performance objectives. The use of FPGA´s have paved the way for future large scale correlator systems in space.

VII. REFERENCES

[1] J.B.Hagen, D.T.Farley, "Digital-correlation techniques in radio science", Radio Science, Vol. 8, pp. 775-784, Aug./ Sept. 1973.

[2] D.M. LeVine, M.Koa, A.B.Tanner, C.T.Swift, A.Griffis, "Initial Results in the development of a Synthetic Aperture Microwave Antenna", IEEE-Trans. on GRS, Vol. 28, No. 4, pp. 614-619.

[3] U.R.Kraft, "Spaceborne Synthetic Aperture Interferometric Radiometers for Global Monitoring of the Earth, Proc. of IGARSS 91, Espoo/Finland, 1991, pp. 971-974.

[4] J.M.Goutoule, "MIRAS Spaceborne Instrument and its Airborne Demonstrator", Proc. of the Consultative Meeting on Soil Moisture and Ocean Salinity, Noordwijk / The Netherlands, 20-21April 1995, pp. 65-69.

[5] M.Martin-Neira, "Calibration of MIRAS Spaceborne Radiometer", Proc. of the Consultative Meeting on Soil Moisture and Ocean Salinity, Noordwijk/The Netherlands, 20-21 April 1995, pp. 79-80.

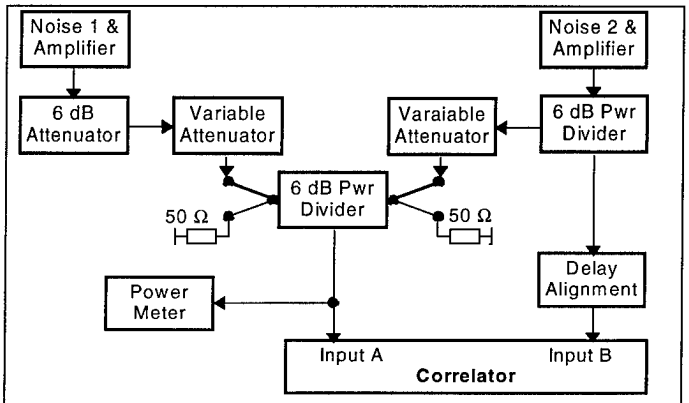


Fig.2: Generation of the Test Signals

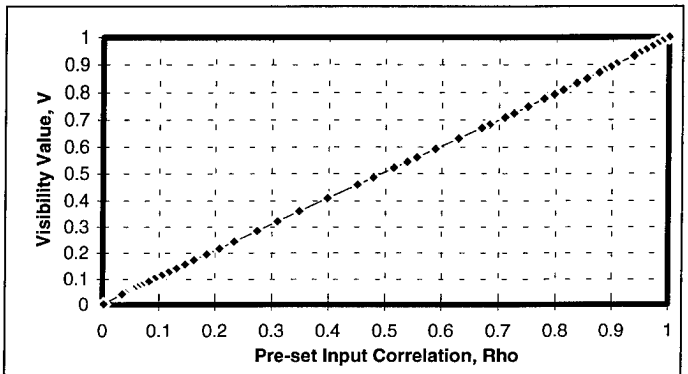


Fig.3: Linearized and Calibrated Correlator Response

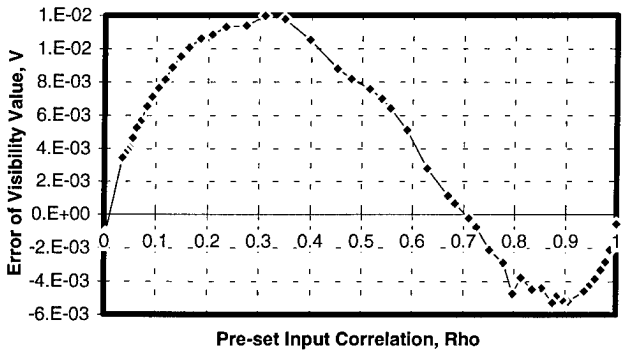


Fig.4: Deviation from Optimum Correlator Response incl. effects from imperfections of test equipment

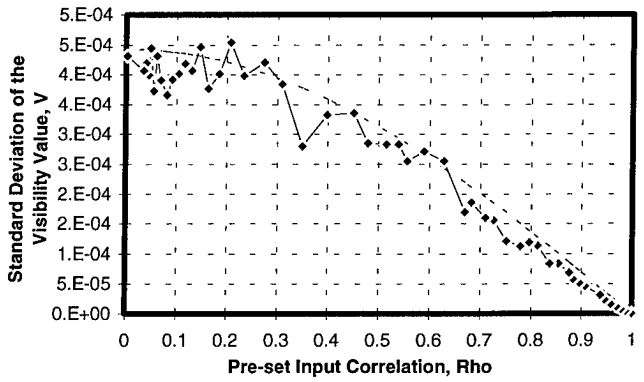


Fig.5: Standard Deviation of Linearized Visibility Value

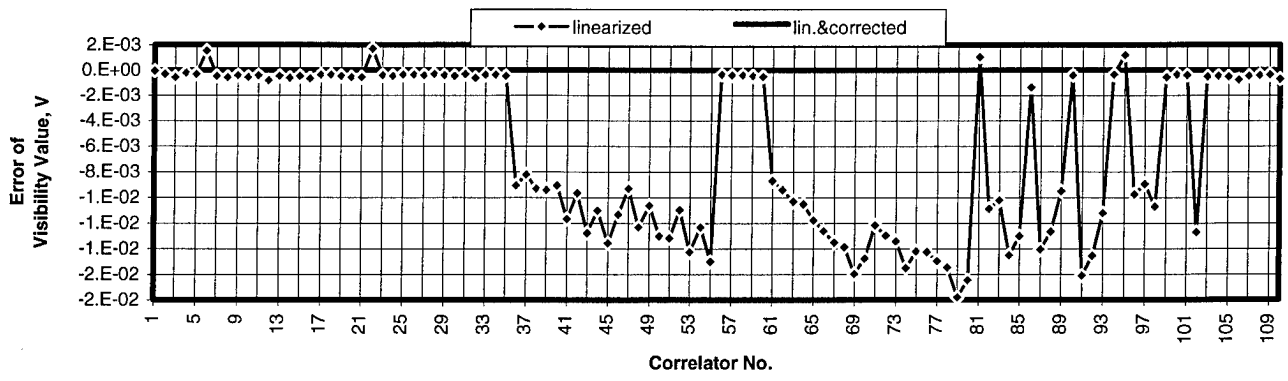


Fig. 6: Survey of the Visibility Values of 110 Correlator at ρ=0.707

Characteristics of the Baseline Off-Nadir angle of Supersynthesis Radiometer

Koji Komiyama and Yoshihiko Kato

Electrotechnical Laboratory, AIST, MITI

1-1-4, Umezono, Tsukuba, Ibaraki, Japan 305

Tel.+81-298-58-5637, Fax. +81-298-58-5640, komiyama@qm.etl.go.jp

ABSTRACT-- The spatial resolution made by matched filtering along a track of a supersynthesis radiometer is evaluated with different baseline off-nadir angle of the interferometer used for the synthesis. A nearly vertical baseline is convenient for the synthesis, but a combination of multiple interferometers is possible to make a finer spatial resolution.

INTRODUCTION

A supersynthesis radiometer(SSR)[1]-[3] is a kind of synthetic aperture interferometric radiometer. The principle is a synthesis on the basis of the phase change of the correlation signal between signals received by two antennas aligned along vehicle track. The phase history of the correlation signal is caused by the varying incidence angle of a ground microwave emission to the baseline of the interferometer composed of two receiving antennas. Since the beam-widths of these antennas must be broad to receive ground microwave with a wide incidence angle change to the interferometer baseline, small antennas are required along the track. Therefore, they are easily attached to a vehicle, for example, to a small satellite.

Imaging procedures of the SSR is expressed and the characteristics of the off-nadir angle of the interferometer baseline particularly concerning the spatial resolution is discussed.

BASICS OF SUPERSYNTHESIS

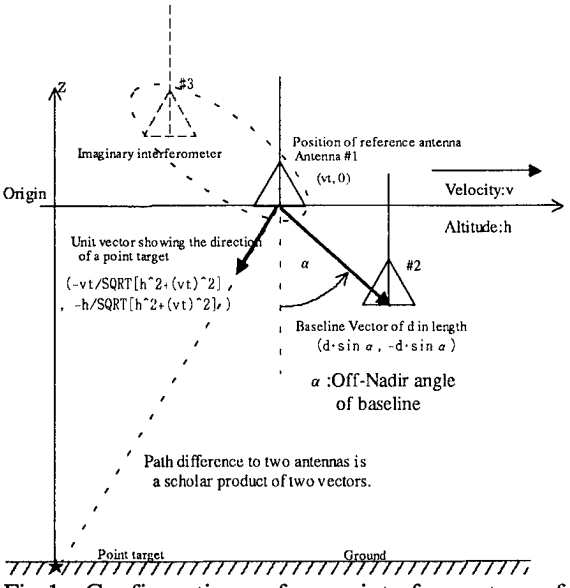


Fig.1 Configuration of an interferometer of supersynthesis radiometer

0-7803-3068-4/96$5.00©1996 IEEE

A configuration of an interferometer used for a supersynthesis radiometer is shown in Fig. 1. The synthesis is effective only along the track, and the performance is discussed in the vertical plane of Fig.1. A point target is adopted for simplicity to illustrate the performance of the radiometer and the process of image retrieval. Two vectors denoting the direction of the target and the interferometer baseline from the reference antenna #1 are mathematically described in Fig.1. The phase of the correlation output, that is, a visibility function is expressed from a scholar product of these two vectors:

$$\phi(t) = \frac{2d\pi(hCos\alpha - vtCos\alpha)}{\lambda\sqrt{h^2 + v^2t^2}} \qquad (1)$$

The frequency of the visibility function is a time differential of the $\phi(t)$ and some calculated examples of the frequency history are shown in Fig.2 with a model of the altitude h, velocity v and the baseline length d of 700Km, 7Km/s and 50 wavelength, respectively.

Since the frequency curve near the position just over the target, that is, the origin presents a linear and monotonous variation, a matched filtering is possible for the retrieval of the target image. It is an analogy to the imaging process of a synthetic aperture radar.

When the ground is far enough from the interferometer, the incident signal is assumed to have a planer wavefront. Therefore, if the antenna #2 is redefined as a phase reference, the complex conjugate of the measured visibility function is the same as that of the imaginary interferometer illustrated in Fig.1. The frequency curve of the complex conjugate function is shown in Fig.2 corresponding to the original one with the off-nadir angle of 30 degree. This is a special feature that an interferometric synthesis can utilize almost twice the measured visibility function data, and the composite interferometric synthesis improves a spatial resolution only when the resultant frequency range after the duplication is continuous. That corresponds to the condition

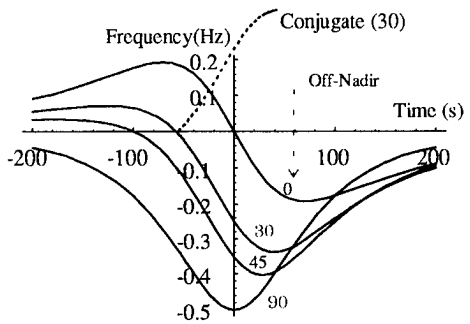


Fig. 2 Frequency histories of visibility functions

that zero frequency must be included in the frequency history of the visibility function used. Since the position of the zero frequency is far from the origin in the case of large off-nadir angle of the baseline, the composite interferometric procedure is not efficient due to the excessively long integration range.

The procedure of the retrieval is illustrated in Fig.3 on the basis of an ordinary matched filtering with the off-nadir angle 30 degree. Only the real part of a complex visibility function is shown with the frequency (b) and its gradient (c) histories of a point target. A reference function (e) which is a complex conjugate to the above visibility function is used for the matched filtering. For the image retrieval around the target, the integration of the product of the visibility and reference functions is executed. By scanning the position:dx, a point target response (h) is obtained.

Since the frequency history is not exactly linear, a specific taper window (f) is applied in addition to a triangular taper (g) which is also modulated to be triangular in frequency domain.

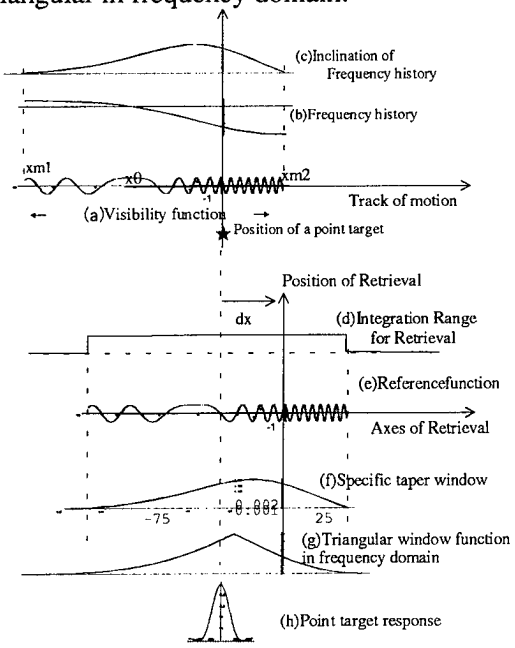


Fig.3 Procedure of Ordinary matched filtering

A retrieval procedure of the composite interferometric synthesis is shown in Fig.4. When the conjugate visibility function is additionally used, their frequencies are partly overlapped around zero frequency. Therefore, the data (a) and (b) used without redundancy are shorter than that for the ordinary matched filtering. The composite frequency range becomes nearly twice the original. The integration are separately executed using each reference functions (g) and (i). The triangular taper window must have its maximum at zero frequency, that is, the center of the whole data used as shown by (h) and (j). The resolution by the composite interferometric synthesis is better by about 40% than that by an ordinary matched filtering.

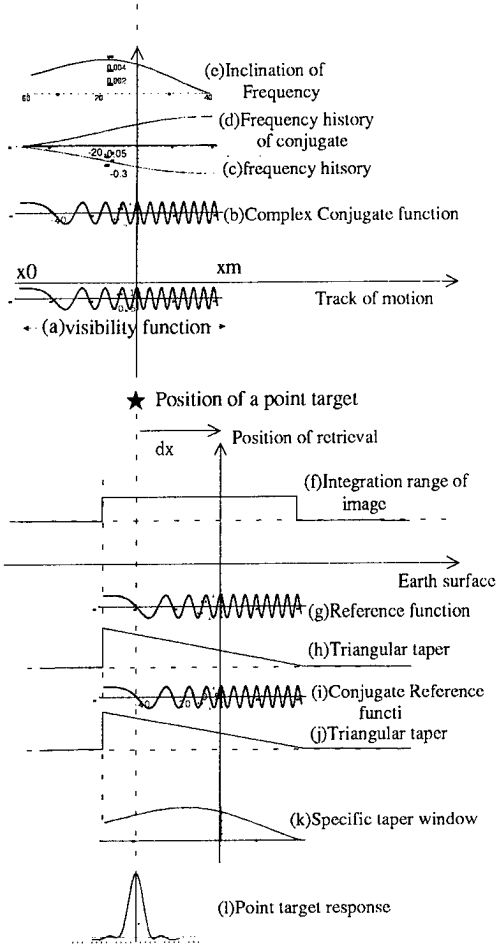


Fig. 4 Procedure of Composite Interferometric Synthesis

CHARACTERISTICS OF OFF-NADIR ANGLE OF INTERFEROMETER BASELINE

A large bandwidth of the visibility function makes a fine resolution by matched filtering. Therefore, it is not efficient to use the data with small frequency gradient. Fig. 5 shows the relation between the spatial resolution and the length of the visibility function used for the ordinary matched filtering with different off-nadir angle. The length of the visibility function is exactly denoted by the minimum(breaking-off) gradient limit of the frequency of the visibility function used for the image retrieval. It

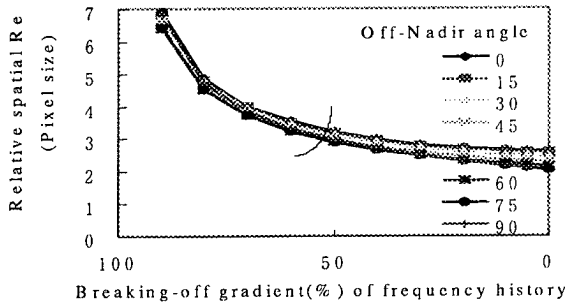


Fig.5 Spatial resolution in relation to off-nadir angle by ordinary matched filtering

shows the data with small frequency gradient under 50% of the maximum gradient do not contribute to the improvement of the resolution. This is true to all the off-nadir angles.

The resolution by the composite interferometric synthesis is improved as shown in Fig.6, when it is applicable. The procedure is not applicable due to lack of zero frequency part in the visibility function, if the small frequency gradient part of the visibility function is not used. The best improvement is obtained at 30 degree in off-nadir angle with the breaking-off gradient of 50%.

From the view point of spatial resolution the best design parameters are 30 degree in off-nadir angle and 50% in breaking-off gradient of the frequency of visibility function.

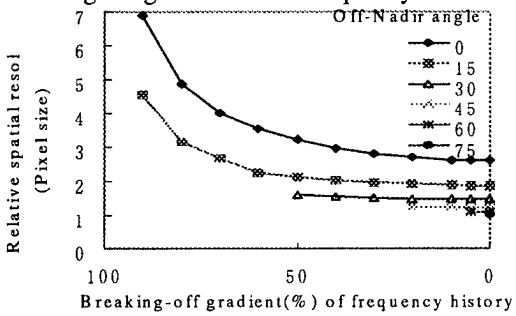


Fig.6 Spatial resolution by composite interferometric synthesis in relation to the breaking-off gradient of the frequency of visibility function

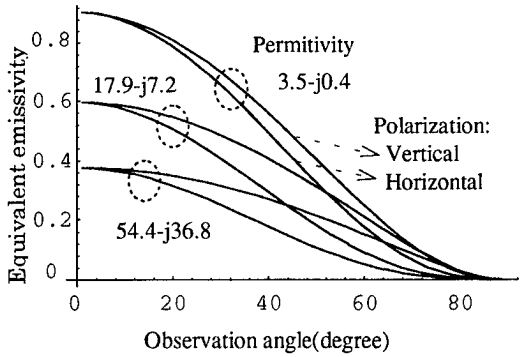


Fig.7 Effective emissivity after propagation attenuation through slant path

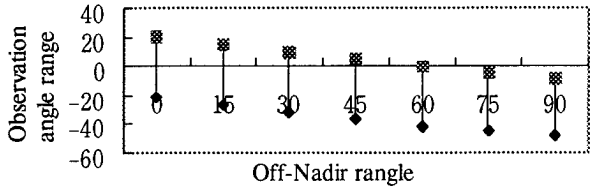


Fig.8 Observation angle range through which a visibility function is measured to 50% breaking-off gradient for different off-nadir angle of interferometer baseline(15 degree step)

The angular characteristic of ground emission is not considered above. But the angular characteristic is important not only for getting a physical information of the target but for the retrieval itself of a ground image by supersynthesis, since the integration data for image retrieval are too long for a large off-nadir angle.

The angular change of the power of the microwave ground emission incident to the interferometer is shown in Fig.7. It includes the effect of the propagation attenuation which is proportional to the square of the varying distance from the ground to the interferometer. The emission signal seriously decreases over 30 degree of the observation angle.

The range of the observation angle necessary for the image retrieval is shown in Fig. 8 with the breaking-off gradient of 50% in the visibility function. The angular range of 0 degree off-nadir is symmetrical around the nadir, but the horizontal baseline (90 degree in off-nadir) has an angular range which is displaced far from the nadir to 49 degree where the signal strength decreases to lower than a half of that of the nadir case. Since the maximum observation angle of 30 degree off-nadir is about 32 degree and the signal decrease is small, the best specification is 30 degree off-nadir and the breaking-off gradient of 50% for single interferometer design.

MULTIPLE INTERFEROMETER DESIGN

By using an interferometer with a large off-nadir angle, the visibility function with high frequency can be obtained though the necessary data around zero frequency is not included. Fig.9 shows a method of a composite multiple interferometer combining two interferometers of small and large off-nadir angles. They are used to get two consecutive parts of visibility function as shown by bold lines. By using an additional interferometer of short baseline and small off-nadir angle, even a horizontally aligned interferometer can gather a combined wideband visibility function useful for the dual interferometer synthesis through a reasonable narrow angular range near the nadir.

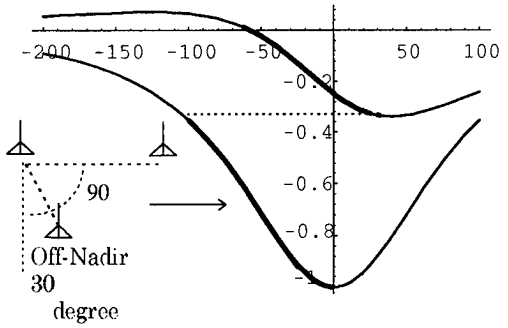


Fig.9 Combination of a composite interferometer for super synthesis

CONCLUSIONS

The best design of the SSR with single interferometer is 30 degree in off-nadir angle of the baseline and 50% in breaking-off gradient of the visibility function. Multiple interferometer is possible to get a fine spatial resolution along the track of flight.

REFERENCES

[1]K. Komiyama, "Supersynthesis radiometer for passive remote sensing," IGARSS'92 1992.

[2]K. Komiyama, Y. Kato, and T. Iwasaki, "Indoor experiment of two-dimensional supersynthesis radiometer," IGARSS'94 1994.

[3]K.Komiyama, Y.Kato,"Two-dimensional Supersynthesis Radiometer for Field Experiment ," IGARSS'95 1995.

Calibration of Synthetic Aperture Radiometers In Space: Antenna Effects

D.M. Le Vine
Code 975, Goddard Space Flight Center, Greenbelt, Maryland, 20771
Phone: 301-286-8059 FAX: 301-296-1761 email: dmlevine@meneg.gsfc.nasa.gov

D.E. Weissman
Department of Engineering, 133 Hofstra University
Hempstead, New York 11550-1090
Phone: 516-463-5546 FAX: 516-463-4939 email: eggdew@vaxc.hofstra.edu

Abstract: The measurement of mutual coupling is being investigated as a technique to aid in the calibration of synthetic aperture microwave radiometers. The technique is based on recent research suggesting that the antenna patterns that are needed for calibration can be reconstructed from a measurement of the mutual coupling between elements in the thinned array. A synthetic aperture radiometer is particularly suited to the measurement of mutual coupling because the basic hardware (a correlation interferometer) measures the product for each antenna pair in the array. This paper describes research to evaluate the role of mutual coupling on the antenna patterns and describes a technique to adapt the mutual coupling measurement for calibration of radiometers deployed for remote sensing from space.

INTRODUCTION

Recent research has demonstrated that synthetic aperture radiometers can be calibrated at levels needed to measure surface soil moisture [1,2]. As a matter of convenience, the calibration procedure can be divided into two steps: image reconstruction and scaling.

Image reconstruction involves converting the instrument output (voltage from each antenna pair) into a map of the scene (voltage as a function of position). Scaling is the process of assigning a brightness temperature to each voltage in this image. Assuming an adequate image reconstruction algorithm, the later can be done conventionally (i.e. by observing a "hot" and a "cold" scene and assuming linear receivers). On the other hand, the image reconstruction procedure is unique to synthetic aperture radiometers. In principle, it is a Fourier transform on a discretely sampled transform space (i.e. one sample for each baseline). Among the issues affecting the image is the distribution of these samples in the transform space; however, more serious problems arise because the basis vectors needed to execute this transform (impulse response of the instrument) are not ideal in real instruments. The antennas in the array are a major factor contributing to the departure of the basis functions from ideal.

One problem arises because the individual antennas in the array are not ideal (i.e. not isotropic). This adds a taper to what would otherwise be nearly sinusoidal basis functions. In addition, coupling between antennas can cause distortions in what otherwise would be a symmetrical pattern. Because the elements in the array need not be symmetrically positioned, coupling can result in basis vectors which are different for each baseline (antenna pair). In fact, this is the case with the aircraft instrument, ESTAR, as illustrated in Figures 1 and 2. Figure 1 shows the pattern (magnitude) of the antennas on the edges (left and right) of the array. The antenna on the right has been reversed to illustrate the symmetry in the fine structure of the pattern, which we believe to be due to mutual coupling. Figure 2 shows the basis functions associated with this pair of antennas. The solid line is the output from the "inphase" channel and the dashed line is the "quadrature" output. These curves are the output as a point source is moved across the field-of-view [1]. Ideally, these two curves would be sinusoidal, oscillating at a frequency determined by the baseline ($7\lambda/2$).

The image reconstruction procedure adopted with the aircraft radiometer ESTAR to account for the departure of the basis functions from ideal, was to implement a numerical inversion using the measured basis functions [3,1]. This works well for ESTAR; however, in applications such as a remote sensing from space, where changes might occur in the radiometer antenna upon deployment, one would like to have an in situ check on the basis functions. An in situ measurement of mutual coupling might provide the required check.

ROLE OF MUTUAL COUPLING

An important question to be resolved about antenna

0-7803-3068-4/96$5.00©1996 IEEE

patterns such as shown in Figure 1 is the reason for their departure from the patterns of the isolated antennas. We sought to test the hypothesis that this was due largely to mutual coupling by making measurements on a version (vertically polarized copy) of the antenna employed by ESTAR. As a first step, measurements of mutual coupling were made in the laboratory using a network analyzer and then these values were used in a simple model to calculate patterns. In this exercise it was assumed that all antennas initially had an identical isolated pattern equal to the theoretical pattern for a dipole over a ground plane. Figure 3 shows the result of this calculation for antenna #5 (right edge of the array) together with the measured pattern (solid line).

As a second step in establishing that mutual coupling was a major factor in determining the structure of the measured patterns, established theory for dipoles above a ground plane was used to compute the mutual coupling. Given dimensions for the dipoles comprising this antenna, the elements of the impedance matrix (a five port network since there are 5 antennas) were computed using formulas in Elliot [4] and the impedance matrix was transformed to a scattering matrix using standard procedures [5]. Figure 4 shows a comparison of the mutual coupling (magnitude of S_{12}) computed in this manner with the measured values.

CALIBRATION

If the antenna structure is completely stable, one could measure the antenna patterns (or basis functions) in the laboratory and then use them in the image reconstruction process as has been done successfully with ESTAR. However, in a cases such as an instrument in space, one would like some assurances that the patterns measured on the ground are, in fact, the ones after deployment.

Assuming that the antennas themselves don't change, the results above and recent research on antenna arrays suggests that the patterns can be computed from the mutual coupling [6]. Synthesis radiometers are particularly suited for the measurement of mutual coupling. For example, the aircraft instrument, ESTAR, employs a switch just behind the antenna where an internal reference source is periodically coupled into the system to correct for phase and amplitude drift. By modifying this switch so that an active element can be coupled to the antenna, one can obtain a measure of mutual coupling. For example suppose signal is coupled both into the antenna and the receiver normally connected to that antenna. Since the radiometer measures the product from each receiver pair, each baseline which normally would be formed with this (active) antenna now has an output which is proportional the mutual coupling between the two antennas.

Work is underway at GSFC to test this concept in the laboratory. A circuit to test this procedure using a laboratory research radiometer built at Goddard [7] is currently underway. As of the writing of this manuscript the circuit has been assembled and testing will begin soon.

REFERENCES

[1] Le Vine et al, "ESTAR: A Synthetic Aperture Microwave Radiometer for Remote Sensing Applications", Proc. IEEE, Vol 82 (#12), pp 1787-1801, December, 1994.

[2] Jackson et al, "Large Area Mapping of Soil Moisture Using the ESTAR Passive Microwave Radiometer in Washita'92", Remote Sens. Envir., Vol 53, pp 27-37, 1995.

[3] Tanner, A.B., "Aperture Synthesis for Passive Microwave Remote Sensing: ESTAR", Ph-D dissertation, Dept of EE, U of Mass., Feb, 1990.

[4] Elliot, R.S., Antenna Theory and Design, Chap 7, Prentice-Hall, New Jersey, 1981

[5] Pozar, D.M., Microwave Engineering, Chap 5, Addison-Wesley, 1993.

[6] Kelly and Stutzman, "Array Antenna Pattern Modeling Methods that Include Mutual Coupling Effects", IEEE Trans. AP, Vol 41 (#12), pp 1625-1632, 1993.

[7] Le Vine, D.M., J.A. Gatlin and J.G. Maruschak, "Development of a Two Dimensional Synthetic Aperture Radiometer", Proc. IGARSS-93 (Kogakuin Univ., Tokyo, Japan) pp 1441-1443, 1993

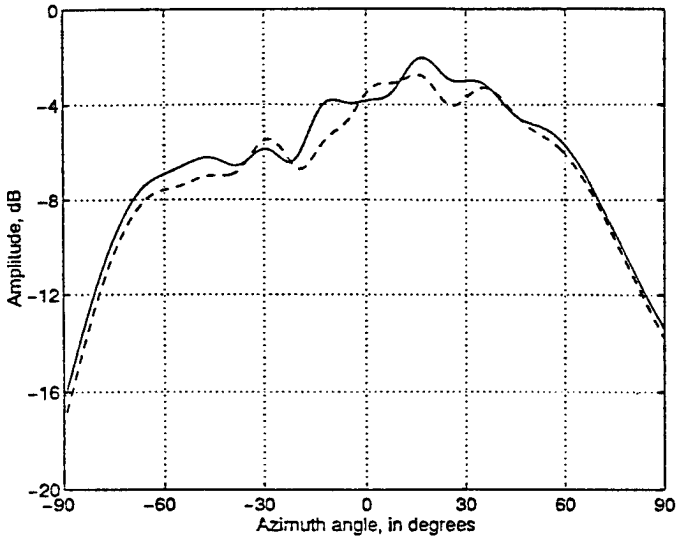


Figure 1: Measured antenna patterns for antennas #1 (solid line) and #5 (dashed line). These antennas are on the left and right edges of the array, respectively and the amplitude is presented in db. The pattern for antenna # 5 has been reversed to emphasize the symmetry.

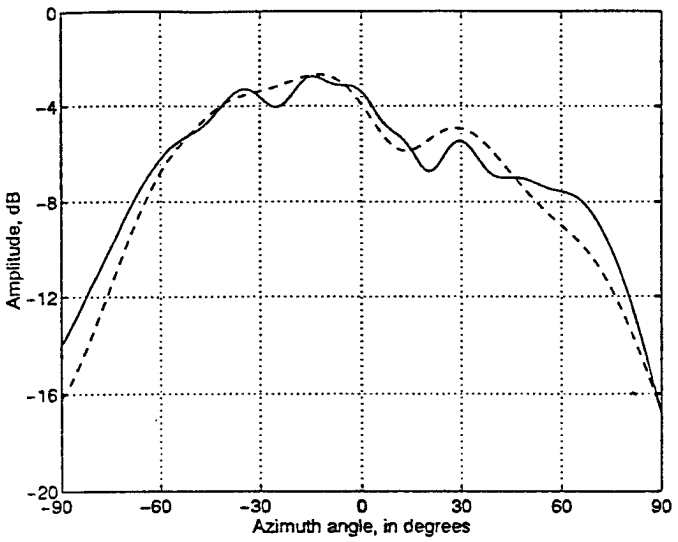


Figure 3: Comparison of measured (solid) and computed (dashed) patterns for antenna #5. The mutual coupling between nearest neighbors was -15 and -22 db.

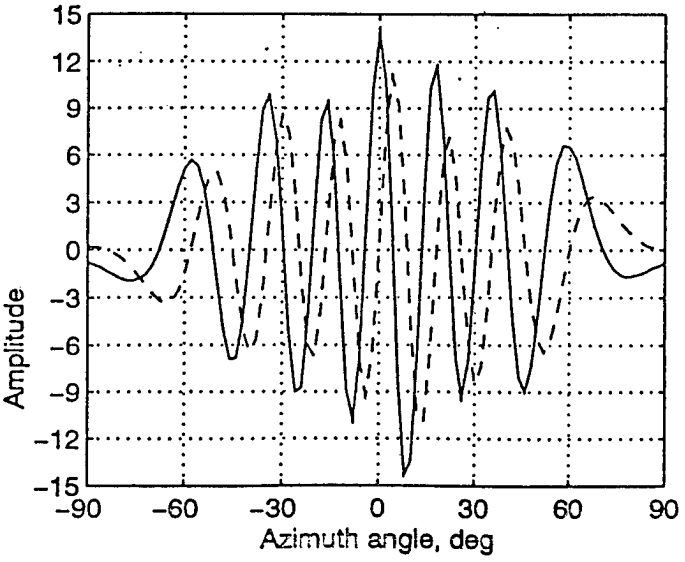


Figure 2: Basis functions for the antenna pair with $7\lambda/2$ spacing. The solid line is the inphase channel and the dashed line is the quadrature channel.

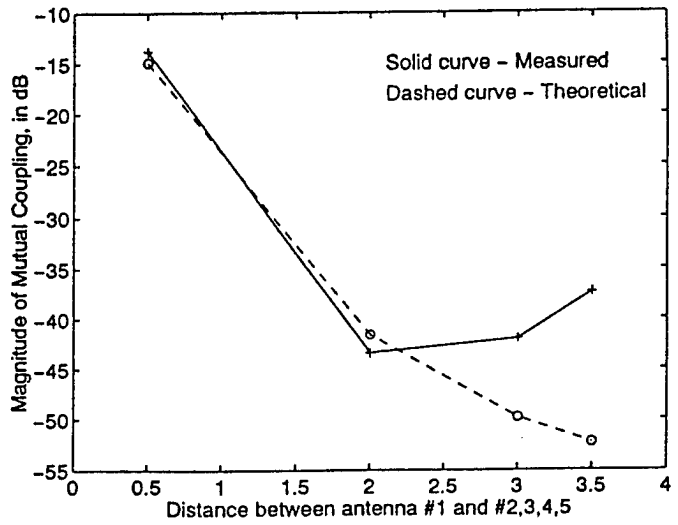


Figure 4: Comparison of measured (solid) and computed (dashed) mutual coupling. The data were obtained from measurements on the ESTAR antennas and the computations were based on theory for dipoles.

Application of Sparse Phased Arrays to Millimeter-Wave Radiometry

John Lovberg and Stuart Clark
ThermoTrex Corporation,
9550 Distribution Ave., San Diego, CA 92121
Phone (619) 578-5885, FAX (619) 578-1419

David Wikner and Bruce Wallace
Army Research Laboratory
2800 Powder Mill Road, Adelphi, Md 20783
Phone (301) 394-3170, FAX (301) 394-5132

ABSTRACT

Although radiometry has been used in imaging applications for many years, it is only recently that radiometric imaging at millimeter-wave frequencies has become practical and relatively common. Unfortunately while millimeter-wave radiometers offer much better cloud, fog and solid object penetration than either visible or infrared systems, the obtainable spatial resolution is often too poor to produce a useful imagery. In this paper we present an array-based concept that has already demonstrated good image performance and is scalable to very large sparse apertures (for high spatial resolution) while still preserving a high frame rate. Approaches and techniques to help mitigate the effects of array sparseness are discussed in some detail.

INTRODUCTION

Radiometers operating at millimeter wavelengths are afforded much better penetration through atmospheric obscurants such as clouds and fog than their infrared (IR) counterparts, due to their longer operational wavelength. This long wavelength also reduces the directionality of millimeter-wave (MMW) radiometers relative to IR radiometers, a drawback in applications such as thermal imaging, for which typically-useful spatial resolution (<0.1 mrad) is achievable only through diffraction-limited performance from detector apertures of the order of thousands of wavelengths across. At MMW frequencies, filled apertures of this size, such as focal plane detectors and arrays using reflective dish collectors or refractive lenses, are unwieldy and difficult to fabricate at such extreme sizes. Phased array radiometers can be built in flat pupil-plane architectures for real-time imaging applications [1], but at this size, filled arrays are impractical, and even extremely sparse arrays require several tens to hundreds of detector elements, along with hundreds or thousands of electronic correlators and associated computational electronics .

A new approach which makes increasingly populated phased arrays feasible involves the use of optical array processing. Phased array direction finders conceived in the late 70s [2] used the optical interference pattern from the multiple-slit aperture of a multi-channel Bragg cell to locate the azimuthal direction of an active signal incident on a linear array of omnidirectional spiral antennas. Extension to two-dimensional passive imaging arrays has been recently accomplished [3], using frequency-scanned antennas in place of spirals to distinguish elevation through spectral analysis. These passive imaging arrays, and their application to wide-instantaneous-field radiometric imaging, are the subject of this paper.

TECHNICAL APPROACH

A frequency-scanned antenna is typically constructed of an extended feedline with an array of periodically-spaced radiation elements along its length. The antenna beam direction θ relative to antenna broadside is given by:

$$\sin\theta = \frac{\lambda}{\lambda_g} - \frac{n\lambda}{s}$$

where λ is the free-space wavelength of the detected radiation, λ_g is its wavelength in the feedline, s is the distance between radiation elements along the feedline, and n is the mode number for which the antenna is made operational. A broadband, low-noise receiver connected to the antenna receives thermal noise from blackbody radiation incident on the antenna, but in any scan direction the antenna is capable of detecting only that wavelength for which eq. 1 is satisfied. Spectral decomposition of the broadband receiver signal thus provides a one-dimensional spatial intensity map for MMW thermal emissions from a scene within the antenna field of view. A phased array of such antennas can be configured, such that by monitoring the relative phase of incident wavefronts in each spectral bin, a two-dimensional intensity map can be obtained for real-time imaging.

The use of an optical processor to perform the required spectral analysis is straightforward. An acoustic transducer on an acousto-optic modulator (Bragg cell) is fed with the heterodyne-downconverted and amplified signal from the radiometer receiver. Acoustic waves propagating in the Bragg cell crystal form a diffraction grating, whereupon a laser shone onto the crystal is diffracted in real time into the same one-dimensional angular intensity distribution as the MMW distribution incident on the fre-

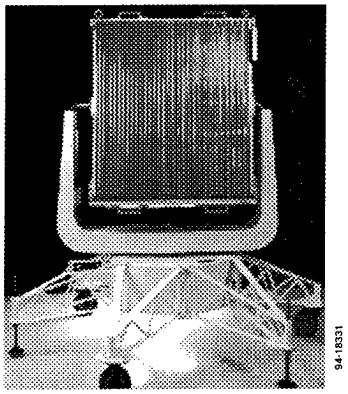
0-7803-3068-4/96$5.00©1996 IEEE

quency-scanned antenna. The diffracted laser light is then Fourier transformed by a lens to produce a 1-dimensional image of the MMW scene. A phased array of such modulators is comprised simply of a multiplicity of acoustic transducers arrayed on a single Bragg cell crystal. For any arbitrarily populated and spaced array of antennas in the radiometer receiver, a Bragg cell with a self-similar array of acoustic transducers will act as a multi-slit phased diffraction grating to cohere light wavefronts with the same (now two-dimensional) directionality as that received in MMW by the antenna array. After the MMW radiation pattern has been converted to a laser light pattern, a low-cost monochromatic CCD camera can function as the focal-plane power detector for tens of thousands of MMW image pixels.

This real-time staring imager is characterized by a wide instantaneous field of view, spatial resolution which can (by using large highly sparse arrays) be made to approach that of typical wide-field, pixel-limited IR cameras, and operation in adverse weather well beyond where IR imagers are blinded. For military applications there are further significant advantages to MMW radiometric imagers. Chief among these is the fact that they are totally passive, and as such do not violate radio silence for covert mission applications. Countermeasures for sparse array radiometers comprise a new and different class from IR and active radar countermeasures; in fact, many countermeasures for IR and radar actually enhance passive MMW signatures and vice-versa.

EXPERIMENTAL RESULTS

Since 1992, the Army Research Laboratory has funded research with MMW sparse phased array radiometers of the type described here. During that time, the technology has progressed from proof-of-concept through laboratory breadboard to demonstration of a 32-channel, 94 GHz phased-array imager which has been tested in the field. Figure 1 shows the imager in its most recent configuration, with a 3-foot square aperture and a depth (including discrete MMW receiver behind the antenna) of only 10 inches. The optical processor is located remotely in a 19-inch rack with power supplies and a computer for image processing. The demonstration imager currently generates 40-horizontal by 30-vertical-beamwidth images at a rate of about 1 per second. The MMW beamwidths are 4-times oversampled to produce images of 160 by 120 pixels. The imager's spatial resolution is 0.2 degrees, over a 6° V x 8° H instantaneous FOV; a wider field is obtainable by stitching instantaneous frames, as demonstrated in figure 2. At the 1/30 second integration time of the CCD camera in the optical processor, the system thermal sensitivity is approximately 15 Kelvins, but near-term retrofit with MMW low-noise amplifiers and a higher performance video camera should improve this by at least a factor of three. Further improvement in effective thermal resolution is possible through the application of image post-processing to mitigate losses resulting from array sparseness (up to about a factor of 3 in the current imager).



SLOTTED METAL WAVEGUIDE ARRAY ANTENNA

Fig 1: Passive Millimeter-wave Camera (PMC) at 94 GHz has a 3-foot square by 2 inch deep antenna and generates over 1000 pixels instantaneously from only 32 antenna/receiver channels.

SPARSE ARRAY LOSS COMPENSATION

The application of sparse arrays allows for high spatial resolution without the complication and expense of thousands of individual MMW correlators. The price paid for this advantage is a loss in antenna array performance relative to filled arrays, in the form of higher sidelobes and in the introduction of grating lobes into the antenna pattern. In addition phase aberrations a can arise from incorrectly positioned antennas and/or path-length variations in the individual signal or reference oscillator channels. These features lead to an overall reduction in signal-to-noise ratio (image contrast) and to the introduction of image artifacts (ghosts) into image data. In theory, such image degradations can be undone through post-processing either in the image plane (using for example CLEAN [4], or other numerical deconvolution) or in the pupil plane [5], using adaptive signal processing techniques to remove phase errors or null

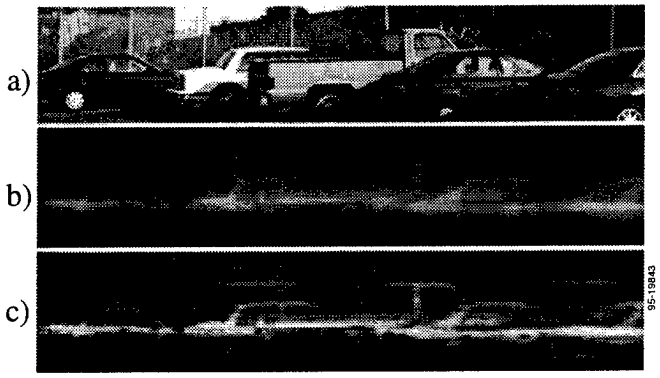


Fig 2. Sparse-array MMW imaging data. (a) Visible light scene, (b) MMW data with 0.7-second integration time, stitching 4 overlapped scenes to create a 564 x 120 pixel image, (c) MMW data with sparse array loss compensation.

sidelobes. Since pupil plane techniques typically require access to the phase of the object's correlation function, the image plane must be adequately sampled so that the Van-Cittert-Zernike theorem (VCZT) can be invoked to determine an object's correlation function from its image plane intensity.

Outside of the presence of noise and ignoring the finite size of the individual antennas, the spatial Fourier transform of an image collected by a sparse array must yield a series of delta functions at spatial frequencies corresponding to all individual antenna pairs (for N antennas, this amounts to N(N-1)/2 correlations minus any repeated correlations arising from redundant antenna spacings), assuming that the Nyquist sampling criterion is met. The Nyquist criterion, in this case, requires that the CCD array be capable of at least twice oversampling the difference between successive spatial frequencies. An estimate of the required number of CCD pixels can be obtained by dividing the array size by the difference between the 2 closest pairs of antennas and multiplying by 2 to satisfy Nyquist. For the imager shown in figure 1, the array is 80 cm wide with a 0.4 mm difference between the 2 closest pairs of antennas, resulting in about 4000 CCD pixels being required per line. With the correlation amplitudes and phases recovered from the CCD data, one can null sidelobes (up to N of them with an N element array), [by inverse tapering the correlation function] sharpen the imager's modulation transfer function for "improved spatial resolution" and use advanced techniques such as Redundant Spacings Calibration (RSC) [6] to adaptively remove phase aberrations in the array. In its simplest form, RSC works by forcing pairs of antennas with the same spacing (i.e. baseline) between them to produce the same value for their correlation using the fact that in the far field, the correlation function depends only upon relative and not absolute position of the antennas. In the extreme, this technique can make actual phase-matching of the receiver channels unnecessary. To first order, the addition of noise in the signal data simply propagates noise to the Fourier-reconstructed image.

Some more simple techniques for sparse-array loss compensation are somewhat effective even when the Nyquist criterion is not met by the CCD camera. One example is shown in figure 3. Here the CCD array does not sufficiently sample Fourier space to allow preservation of individual correlation functions. However, it is easily shown that the "DC" or zero spatial frequency (i.e. the correlation of an antenna with itself) is strongly overweighted in a very sparse array, since the "zero spacing" of each antenna with itself occurs N times for an N element array, while in an optimum sparse array design, all other spacings are forced to occur only a few times at most. Reweighting the corresponding DC term in the Fourier plane appropriately and then transforming back to the image plane, produces an image with significantly less smearing and contrast degradation. Since only the DC term has to be changed, this can actually be done very quickly in the image plane without having to perform any Fourier transforms by determining the average intensity on each line in the image and subtracting an appropriate fraction of this value from each and every point in the line in question. That this simple approach produces such a dramatic improvement is not surprising since it is the absence of baselines near the zero frequency that causes the smearing, and it is precisely these baselines that we have opted to replace with longer ones in order to obtain higher resolution with a fixed number of array elements. Note the power line extending across the field of view in figure 3(a). It is barely, if at all, evident in the raw image data (Fig 3(b)). With DC correction, it stands out sharply, despite being physically far smaller (< 0.1 times) than one diffraction-limited beamwidth wide

OTHER PROCESSING TECHNIQUES

To overcome the limited bandwidth capability of an acousto-optic cell and thereby substantially improve imager frame rate, we are currently developing a new optical processor that uses modulated light in fibers coupled to a high finesse Fabry-Perot interferometer to perform the frequency processing and provide 12 GHz of instantaneous bandwidth for a 30 Hz frame rate. In the future reweighting of spatial frequencies to compensate sparse array losses can in principle be accomplished in real time using filter masks in the Fourier plane of the optical processor. Improvements in the speed and size of digital electronics will likely make frequency multiplexers and large

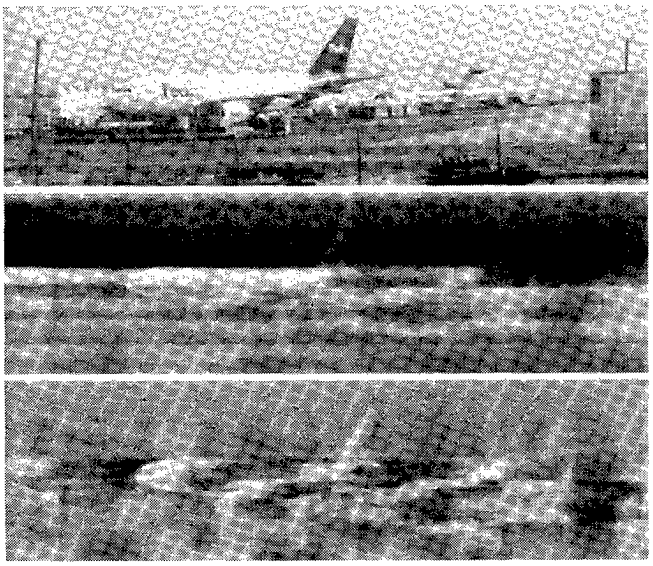


Fig 3: DC attenuation of MMW images. (a) Visible light scene. (b) MMW raw data. (c) DC component of each horizontal line reduced by 97%. Note the power line, not evident in the raw data above.

banks of two-bit correlators feasible for microwave and perhaps someday even millimeter-wave, direct digital processing. Phase and frequency multiplexing might also be accomplished through various implementations of MMW constant-k, Rotman, and Archer lenses in conjunction with MMW low-noise amplifiers.

CONCLUSIONS

The high speed attainable with optical processors has made sparse array pupil-plane imaging radiometers practical at MMW. Advances in sparse array loss compensation have the potential to substantially reduce the losses associated with sparse arrays and provide high-contrast, high-resolution imagery with unique long-wavelength atmospheric penetration capability.

[1] Le Vine, D. M. et al, "ESTAR: A Synthetic Aperture Microwave Radiometer for Remote Sensing Applications", Proc. IEEE Vol 82, pp 1787-1801, 1994

[2] Lindley, J.P. "Angle of Arrival Sensors Using Acousto-Optical Processing," Applied Technology Division of ITEK Corporation, N00173-76-C-0333-(A002), 1977.

[3] Lovberg, J. A., Chou, R., Martin, C., "Real-Time Millimeter-Wave Imaging Radiometer for Avionic Synthetic Vision", pp 234-244, SPIE Vol. 2220, 1994

[4] Thompson, A. R., Moran, J. M., Swenson, G. W. , "Interferometry and Synthesis in Radio astronomy", Wiley-Interscience, New York 1986

[5] Clark, S. E. , "Phase Error Compensation in Optical Phased Arrays", pp. 154-165, SPIE Vol. 2120, 1994.

[6] Greenaway, A. H. "Optical Aperture Synthesis", Meas. Sci. Technol. Vol. 2 pp 1-12, 1991

RADIOMETER SYSTEM WITH CROSS-POLARIZATION AND CORRELATION OF THE CHANNELS OF OBSERVATION

Karen A.ARAKELIAN and * Artashes K ARAKELIAN

Yerevan State Medical University
Faculty of General Medicine, 4-th Year, 407 Group
2 Koryouni St., Yerevan, 375009, Armenia

* Institute of Radiophysics and Electronics
of Armenian National Academy of Sciences
Ashtarak-2, 378410, Armenia
Tel: (+7-8852) 287 850, E-mail:irphe@arminco.com

ABSTRACT

Microwave, bi - polarization radiometer method of detection and identification of observed surfaces anomalous formations and estimation of principal characteristics some of them are developed. Detection and classification are carried out by taking into account correlative features of vertically and horizontally polarized components of observed surfaces proper radiothermal radiation signals.

Microwave, bi-polarization radiometer detector-identifier, as well as radiometer system for wind and temperature fields characteristics determination are suggested.

INTRODUCTION

One of the main methods of remote sensing in radio frequency range is microwave radiometer method, based on measurement of proper radiothermal radiation of environment objects. Space microwave radiometry is successfully used, for instance, to identify the parts of the Earth surface, to determine parameters of snow fields, such as: boundaries, thickness and melting time. These methods are particularly useful to carry out the global oceanographic researches since they deal with relatively homogeneous objects, whose topography and chemical composition are relatively constant on large areas. The main parameters determined by microwave radiometry are sea water temperature and salinity, near sea surface wind speed and direction, degree of sea surface roughness, etc. Microwave radiometry is successfully used to control the ecological state of environment, to detect, classify and estimate the main parameters of various surface pollutions. Usually, these problems are solved by registration of proper radiothermal radiation vertically and horizontally polarized components. But these components may be correlated in time and in space. Therefore, for effective detection and classification it is necessary to take into account correlative relationships between cross polarized components of environment objects proper radiothermal radiation.

In this paper cross polarized, microwave pasive method for under spread surfaces anomalous formations detection and identification, as well as cross polarization and correlative radiometer detector-identifier and system for near sea surface wind speed and water temperature determination are described.

RADIOMETER DETECTION METHOD

Microwave radiometry is successfully used to detect environmental anomalies such as cloudiness, ice and snow covers, plants, spills of oil or other surface active substances, internal waves, streams, temperature distributions, foam formations and other phenomena of artificial and natural origin. At the incidence angle $\vartheta > 0^{\circ}$ the characteristic features of some formations is not only the changes of

0-7803-3068-4/96$5.00©1996 IEEE

proper radiothermal radiation cross polarized components variances [1], but also a cross-correlation of these components and its fluctuations. The value and the change of this correlation existing for various inhomogeneities, enable us to improve the characteristics of detection and identification by simultaneous use of the results of bi -polarization and cross-correlation observations.

Assuming, that vertically ξ and horizontally η polarized radiometer receivers input signals cross-correlation coefficient is ρ_k ($k=0$ corresponds to the background and $k = 1$ - to anomalous formation situation), and using the optimally criterion of Neyman-Pearson, we will obtain following equation for decision rule of detection:

$$S = S_\xi + S_\eta + S_{\xi\eta} > S_o \quad (1)$$

where

$$S_\xi = \alpha \sum_1^N \xi_i^2 \; ; \; S_\eta = \beta \sum_1^N \eta_i^2 \; ; \; S_{\xi\bar{\eta}} = \gamma \sum_1^N \xi_i \eta_i$$

$$\alpha = \frac{(\sigma_{1\xi}^2 - \sigma_{o\xi}^2)(\rho_1^2 \sigma_{1\xi}^2 - \rho_o^2 \sigma_{o\xi}^2)}{2(1-\rho_o^2)(1-\rho_1^2)\sigma_{1\xi}^2 \sigma_{o\xi}^2} \; ;$$

$$\beta = \frac{(\sigma_{1\eta}^2 - \sigma_{o\eta}^2)(\rho_1^2 \sigma_{1\eta}^2 - \rho_o^2 \sigma_{o\eta}^2)}{2(1-\rho_o^2)(1-\rho_1^2)\sigma_{1\eta}^2 \sigma_{o\eta}^2} \; ;$$

$$\gamma = \frac{\left[\rho_1 (1-\rho_o^2)\sigma_{o\xi}^2 \sigma_{o\eta}^2 - \rho_o (1-\rho_1^2)\sigma_{1\xi}^2 \sigma_{1\eta}^2\right]}{(1-\rho_o^2)(1-\rho_1^2)\sigma_{1\xi}\sigma_{o\xi}\sigma_{1\eta}\sigma_{o\eta}} \; ;$$

$\sigma_{k\xi}^2$ and $\sigma_{k\eta}^2$ are the variances of vertical and horizontal polarization channels input signals, S_o - threshold, providing the necessary false alarm level.

Detection characteristics of above mentioned method are considerably higher than of the method described in [1].However, in spite of the advantages of this detection method it has such a drawback as a low classification probability. This drawback can be elininated by simultaneous consideration of output signals of separate channels, formed as a result of preliminary filtration of anomalies in each channel. Indeed, according to the Neyman-Pearson criterion, and using the independence of components ξ and η the decision rule (1) can be represented as three independent decision rules:

$$S_\xi > S_1 \; ; \; S_\eta > S_2 \; ; \; S_{\xi\eta} > S_3 \quad (2)$$

Fig.1 shows a block-diagram of detector-identifier, based on decision rules (2). For this system the false alarm probability is defined by expression:

$$P_o(S_{1,2}) = P_{o\xi}(S_1)\, P_{o\eta}(S_2)\, P_{o\xi\eta}(S_3) \quad (3)$$

For detection probability the following estimation is true:

$$P_1(S_{1,2}) > \max\{P_{1\xi}(S_1); P_{1\eta}(S_2); P_{1\xi\eta}(S_3)\} \quad (4)$$

Taking into account, that only a correlation of anomalous formations radiothermal images internal

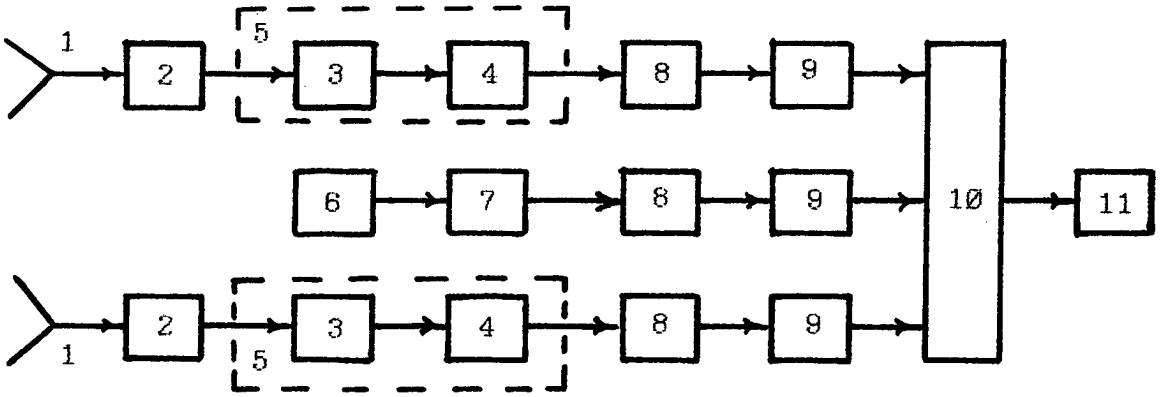


Fig. 1 A Block Diagram of Detector-Identifier
1.- Antenna, 2.- Polarizer, 3.- Microwave Module, 4.- Low Frequency Module, 5.- Radiometer Receiver, 6.- Multiplier, 7.- Integrator, 8.- Module of Normalization, 9. Thresholder, 10.- Identifier, 11.- Register

structures represents principal interest in practice, we can change decision rules (2) by detection to:

$$S_\xi > S_1 \; ; \; S_\eta > S_2 ; \; S^1_{\xi\eta} > S_4 \quad (5)$$

where $$S^1_{\xi\eta} = \gamma^1 \sum_1^M \left(S^1_\xi S^1_\eta - \sum_1^N \xi_i^2 \sum_1^N \eta_i^2 \right)$$

$$S^1_\xi = \sum_1^Q \xi_i^2 ; \quad S^1_\xi = \sum_1^Q \eta_i^2$$

In a time scale $Q < M << N$, $\gamma \approx \gamma^1$ and may have both positive and negative values.

In Fig.2 a block-diagram of detector-identifier, based on decision rules (5) are presented. For false alarm and detection probabilities may be used expressions (4) and (5) by replacement of $P_{k\xi\eta}(S_4)$ instead of $P_{k\xi\eta}(S_3)$.

WIND SPEED DETERMINATION

As shown in [1], bi-polarizing radiometer system may be used for sea surface wind speed and water temperature determination. But, since, in practice, by radiometers we can measure the antenna noise temperature only, then for unambiguous determination of water temperature t and wind speed v it is necessary to have a priori information on a brightness temperature of Atmosphere on the antenna level T_{AAO} and the Atmosphere optical width τ_{AO} This information must complete the others described in [1]. In Fig.3 a block diagram of bi-polarization radiometer system for near sea surface wind speed and water temperature determination are represented.

CONCLUSION

Thus, we have developed bi-polarization microwave radiometer methods and systems of environment anomalous formations remote detection and identification, as well as near sea surface wind speed and water temperature determination.

REFERENCE

1.A.K.Arakelian and K.A.Arakelian "Efficiency of Bi-Polarization Radiometer Sensing Method in Environment Investigations" The Digest of ICEMI'95, Shangai, China, 1995.

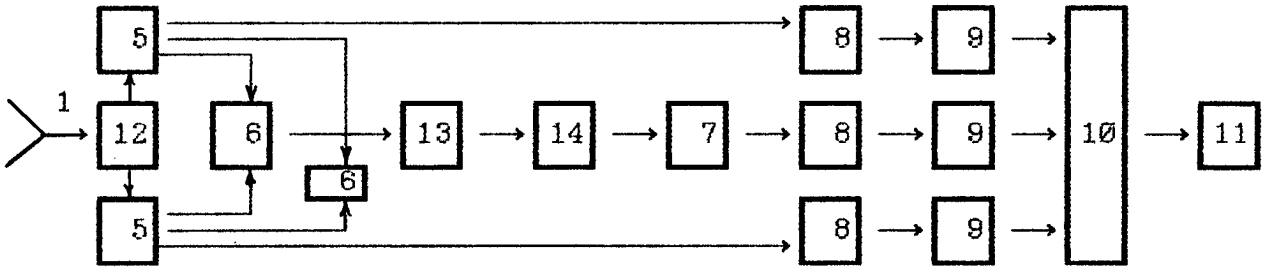


Fig.2

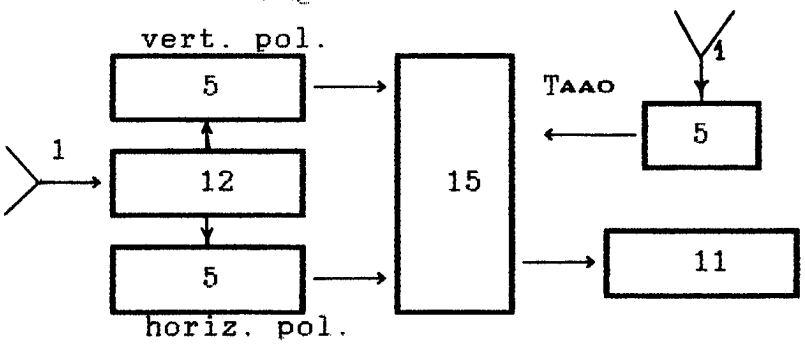


Fig.3

12.- Polarization Splitter, 13.- Delay Module , 14.- Subtracter, 15.- Solver, (for all oters see Fig.1)

Spatial Variations of Microwave Backscatter Magnitude and Angular Distribution: Response of the Short Waves to Wind and Surface Changes

David E. Weissman
Hofstra University
Hempstead, New York 11550
Tel:(516) 463-5546, FAX:(516)269-5920, (E-Mail): eggdew@vaxc.hofstra.edu

William J. Plant, William C. Keller and Vahid Hesany
Applied Physics Laboratory
University of Washington
Seattle, WA 98105-6698

Abstract: Comparisons among submesoscale sea surface Ku-band backscatter, wind speed, air and sea temperatures, friction velocity and laser altimeter wave height spectra were made to observe the dynamic responses in time and space of the centimeter waves within kilometer sized areas. Measurements were made in October 1993 off the Oregon coast from an airship carrying a dual polarized Ku-band radar with a suspended package of meteorological and physical instruments, and a laser altimeter.

INTRODUCTION

The present effort focusses on measurements made off of the Oregon coast in October 1993. The airship provided a unique platform because of its slow velocity and low altitude. Its instrument complement consisted of a dual polarized 14 GHz CW radar, with video and infrared imagers attached to the gondola plus an airborne suspended package (ASP) tethered to the gondola to lie about 10 meters off the sea surface. This ASP contained the meteorological and oceanographic instrumentation.

One mode of the 14 GHz CW radar provides a full 360° azimuthal scan every 60 seconds (simultaneous H & V-pol) at incidence angles of 20°,30° and 40° degrees. This omnidirectional data record senses the angular variation of the 1 to 3 cm capillary wave spectrum for each sweep. The measurements provided by the airborne suspended platform that are of interest here are: coincident wind (3 components) and wave height, air and sea temperature and heat fluxes. A laser altimeter measures altitude and wave height spectra. A separate mode of the radar, which operates with coherent detection and Doppler measurements, will be used to measure the surface currents to see if current gradients exist and to assess their possible effects on the azimuthal radar response.

DATA ACQUISITION

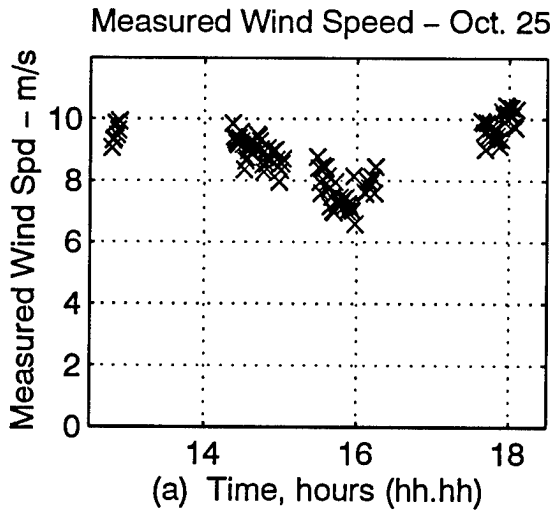
All the radar data were acquired by instruments located on the gondola of the airship, whose normal operating altitude was in the range of 70 to 85 meters above the surface. The meteorological and sea surface measurements were performed by instruments mounted on a sled suspended from the blimp gondola with a tether. This sled was typically positioned about 10 meters above the surface. The net ground speed of this entire blimp system is in the range from 5 to 15 m/s.

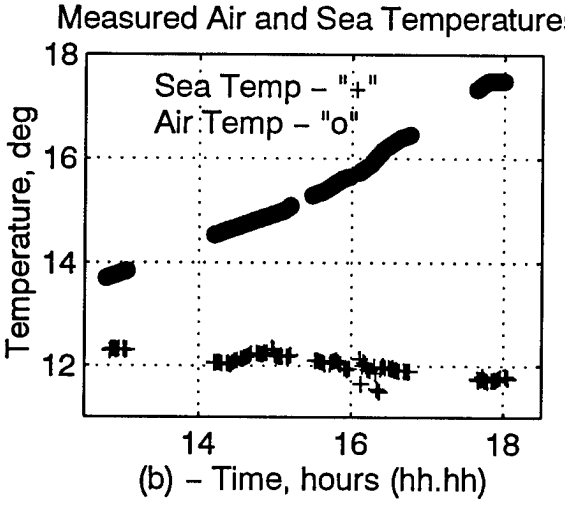
The rotating K_u-band antenna is held at a fixed incidence angle and scanned azimuthally to span a full circle in 30 seconds. Subsequent data analysis groups the data into 36 bins of 10 degrees each. Two of these scans are averaged to form one minute data points. In most cases, this means that the distance covered by the blimp during this interval is less than 1 km. Linear regression analysis is used to compute the 3 Fourier series coefficients; A0, A1 and A2 for each one-minute data set. These are usually part of the scatterometer model function. The results presented here focus attention on how the A0 term responds to changes in incidence angle, temporal fluctuations of horizontal wind speed, friction velocity and the air & sea temperatures under the blimp. Surface stress is measured with the dissipation technique.

MEASURED RESULTS

The data collection runs on October 25 spanned 5 hours. Throughout this period the wind speed stayed mostly within the 7 to 10 m/s range. (see Fig. 1(a)). The sea temperarure encountered within a rectangular region of 12 Km (E-W) by 20 Km (N-S) was fairly constant at 12° C (within +/- 0.3°). The air temperature encountered at 13:00 (PDT) was 13.7°, then it monotonically increased along the flight path

0-7803-3068-4/96$5.00©1996 IEEE





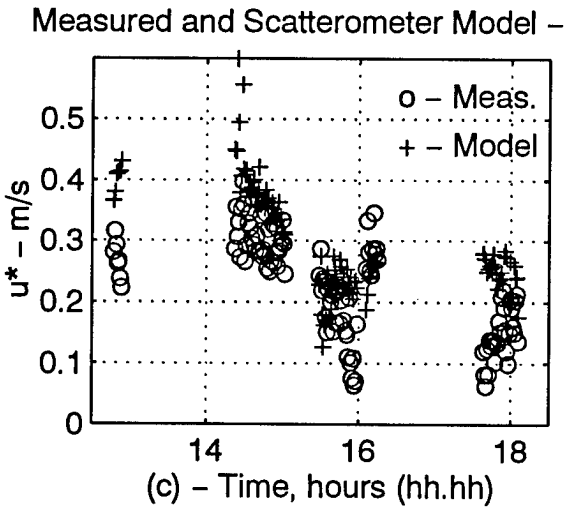


Figure 1: (a) Wind speed, (b) Air and sea Temperature, (c) Friction velocities

over a 5 hour duration to 17.5° C (see Fig. 1(b)). This resulted in a strongly stable air-sea statification of 5.5° C. This change in stratification is known to affect the drag coefficient and friction velocity. R.A. Brown's analysis of stratification effects [1] indicate that a change of air-sea temperature difference from +1.7° to +5.5° can reduce the drag coefficient by a factor of 2, thereby reducing the friction velocity with a multiplying factor 0.7, at a constant wind speed of 8 m/s. This expectation is realized in the u_* measurement (Fig. 1(c)). At the time of 18:00, we see that while the wind has stayed close to 10 m/s, the measured u* value is reduced appreciably from its earlier value, by about a factor 2 from its initial value.

This effect is also seen in the average radar cross section measurements. While the incidence angle of both V-pol and H-pol were varied from 20° to 50° during this time, each A0 can be related to the friction velocity using the FASINEX model function for u_* [2]. These model results agree fairly well with the measured u_* (Fig. 1(c)).

On October 29, a 30 minute run at a constant incidence angle of 40° is shown in Figure 2(a) amd (b). A steady wind of approximately 5.5 m/s during the first 22 minutes was followed by a sharp drop in speed to 2 m/s. The average RCS in Fig. 2(b) shows a corresponding large drop in both the V-pol and H-pol by about 15 dB. However the laser spectra (each data run is 10 minutes long) are plotted in Figure 3, and they do not display any appreciable change in spectrum shape or level. Of the 4 runs shown in Fig. 3, the first 2 cover the time before the wind change, and the latter 2 cover the 20 minutes after the change. Because the blimp and laser are moving at a speed of 10 m/s, the encounter spectrum (with 8 Hz sampling limited to a 4 Hz maximum) only responds to wavelengths of about 2 meters and longer. The conclusion here is that smaller scale centimeter wave roughness responds rapidly to the wind variations, but longer gravity waves do not.

ACKNOWLEDGMENT

This research program was supported by the Office of Naval Research, Ocean Sciences Division, Remote Sensing Program. The authors wish to acknowledge the other principal participants in this experiment. From APL/UW: Dr. Andrew Jessup, Ken Hayes and Chris Zappa. The Naval Research Laboratory participants: Karl Hoppel, Al Uliana, Joe Montgomery and Phuc Nyugen.

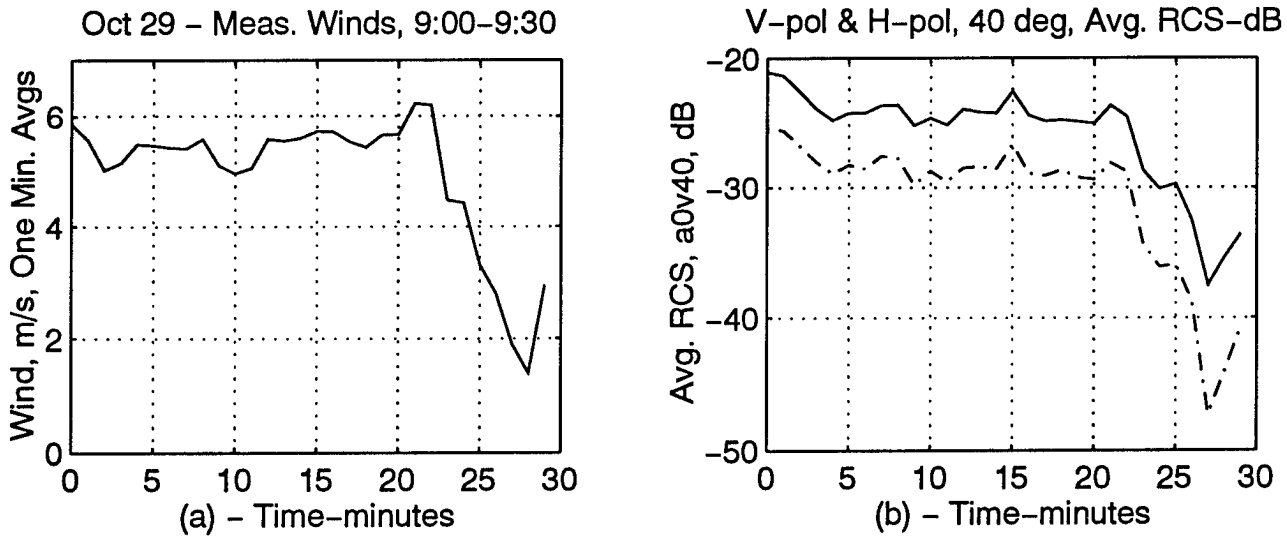


Figure (2) - Simultaneous monitoring of wind speed and 40° incidence average RCS (V-pol: solid curve, H-pol: dashed curve) across rapid wind change on October 29

consecutive 10 minute runs, coincident with observations in Figure 2.

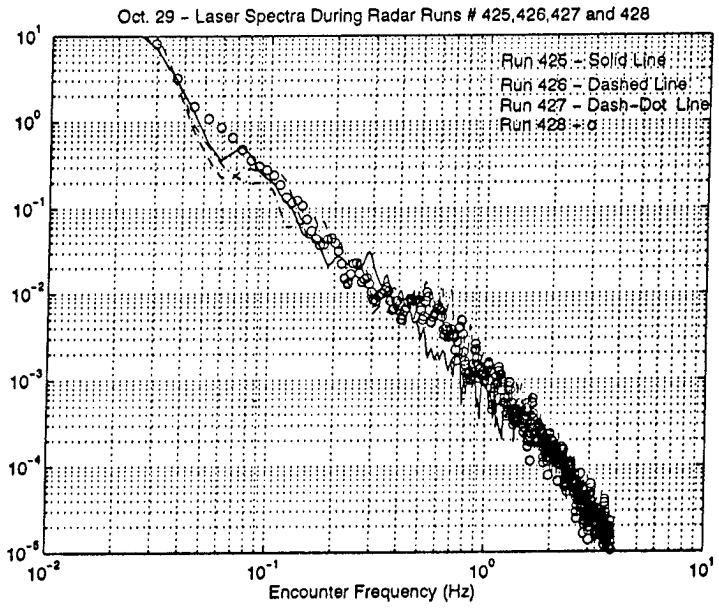


Figure 3: Laser altimeter wave height spectra for 4

REFERENCES

[1] R.A. Brown, Surface Fluxes and Remote Sensing, Chapt 2. *Surface Waves and Fluxes, Vol. I*, G.L. Geernaert and W.J. Plant, Eds., Kluwer Academic Publishers, 1990

[2] D.E. Weissman, K.L. Davidson, R.A. Brown, C.A. Friehe and F. Li, "The relationship between the microwave radar cross section and both wind speed and stress: model function studies using FASINEX experiment data", J. Geophys. Res., Vol. 99, No. C5,. pp 10,087-10,108, May 15, 1994

Seagulls and SAR: Atmospheric Convection Effects in SAR Images over the Ocean

J. F. Vesecky, F. L. Ludwig*, J. M. Daida, N. Chinchilla and G. Kimbreau

Atmospheric, Oceanic and Space Science Dept.
The University of Michigan, Ann Arbor MI 48109-2143
Tel: 313-764-5151, FAX: 313-764-5137, jfv@umich.edu

***SRI International, Menlo Park CA 94025**
Tel: 415-859-2915, fludwig@unix.sri.com

Interpretation of features in synthetic aperture radar (SAR) ocean images has most often dealt with oceanic phenomena. Here we focus on atmospheric boundary layer processes that express themselves in SAR images via spatial variations in the surface wind field that drives small scale ocean ripple waves (< 1 m wavelength) and hence SAR image intensity. Since the 1930's, observations (from seagull soaring to satellite images) have revealed geometric patterns in the air flow related to convection in an unstable atmospheric boundary layer. Woodcock (1948) noted that patterned sea gull soaring and cloud layers occurred where the boundary layer was thermally unstable, whereas uniform cloud layers corresponded to a stable boundary layer. When wind shear was low, polygonal cloud patterns prevailed; but when wind shear was high, the clouds were formed into horizontal columns, referred to as cloud streets. We along with others (Alpers & Brummer, 1994; Sikora, et al., 1995 and P. Moreau, 1995) argue that the geometrical 'puff' patterns in SAR images are the surface counterpart to the cloud patterns and result from convective air flows in an unstable marine atmospheric boundary layer. Further, it is thought that these patterns contain information on the convective processes and bulk wind flow going on and that this information can be extracted by pattern analysis on the SAR images.

ANALYSIS

We have searched the Space Radar Laboratory CD Rom data base from the flights in April and October, 1994. A number of cases were found and are under investigation. In this paper we analyze SAR observations of atmospheric convection over the Gulf of Mexico in the Yucatan Strait between Cuba and Mexico. L-band VV SAR images from the October, 1994 flight of the Space Radar Laboratory show a 50 km by 500 km region containing tropical rain cell features as well as regions of varied cellular patterns. Fig. 1 shows a portion of this image swath. The vertical dimension of the image is 53.2 km and the tick marks along the bottom are at 1 second intervals of flight time. We analyze these cellular patterns using 2-D Fourier analysis with the results shown as contour plots displaced to the right from the region under investigation. Note the white outlined squares at left indicating the region analyzed by the Fourier power spectrum contour plots.

RESULTS

The array of power spectrum contours shows the spatial variation of the cellular patterns. We note typical cell sizes of 1-3 km. The cell shapes are approximately circular and are organized of into larger scale patterns (horizontal columns or streets). The cellular patterns vary from dense, overlapping-cell structures at upper, left to less dense structures with separated cells at center left and below. As one moves lower in the figure, it is clear that cells become aligned in rows tens of km long, separated by about 3 km.

The 2-D power spectra show the anisotropic nature of the cells as they are organized into rows. The lowest contour plot shows a good example of the spatial nature of the cells and their larger organizational structure. Note the longer spatial wavelength variation along the direction of the rows and the shorter spatial wavelength across the rows. We suspect that the longer wavelength along the rows is due to wind shear above about 10 to 15 kts.

CONCLUSIONS

We conclude that spatial analysis of SAR images can reveal useful information regarding convective processes in the marine boundary layer. What is probably most useful aside from the wind direction is the large scale view of convective processes given by the large area observed in SAR images. Thus, one may be able to map the spatial evolution of convective processes in the marine boundary layer and with multiple SAR images the temporal evolution as well.

REFERENCES

Alpers, W. R. & B. Brummer, J. Geophy. Res., vol. 99, num. 12,613-12,621 (1994).

Moreau, P., SAR observations of marine boundary layer processes, Seminar, University of Michigan, 1995.

Sikora, T.D., G.S. Young, R.C. Beal and J.B. Edson, **Monthly Weather Rev. 123**, 3623-3632 (1995).

Woodcock, A. H. & J. Wyman, Ann. N Y Acad. Sci., vol. XLVIII, 749-777, 1948.

0-7803-3068-4/96$5.00©1996 IEEE

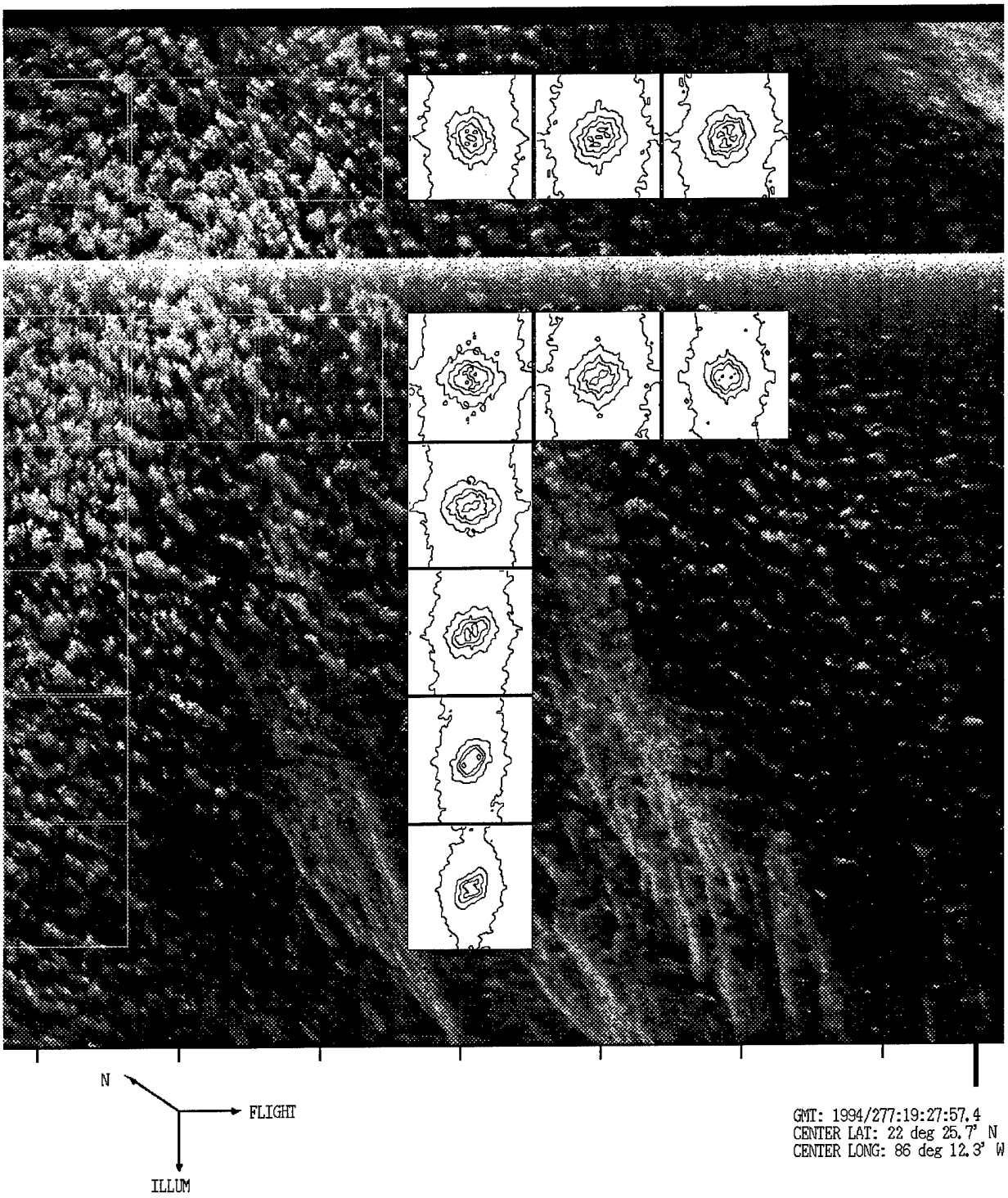


Fig. 1. L-band SAR image collected by the Space Radar Laboratory, October 4, 1994 at ≈ 1330 local time in the Yucatan Strait. Two-dimensional Fourier power spectra are shown displace to the right from the location of their input image data. The bright horizontal band is an artifact. Data kindly provided by Jet Propulsion Laboratory.

Evidence of a Land Breeze in an ERS-1 SAR Image of the New Jersey Coastline

T. D. Sikora[1,2], D. R. Thompson[2], G. S. Young[1], and N. S. Winstead[1]
[1]The Pennsylvania State University, 503 Walker Bldg., University Park, PA 16802

[2]The Johns Hopkins University, Applied Physics Laboratory, Johns Hopkins Rd., Laurel, MD 20723-6099
Tel: (301) 953-6000 Fax: (301) 953-5548 email:sikora@nansen.jhuapl.edu

1. INTRODUCTION

The modulation patterns observed in microwave synthetic aperture radar (SAR) images of the ocean surface depend strongly on the spatial variation of those components of the surface wave height spectrum whose scales are comparable to the wavelength of the SAR. Because the magnitude of these spectral components depends on the local wind vector, meso- and sub-mesoscale flow variations in the marine atmospheric boundary layer will produce characteristic signatures in SAR imagery via their momentum exchange with the ocean surface. We therefore expect SAR to be a powerful sensor for studying the vast array of phenomena that are found in the marine atmospheric boundary layer. Initial confirmation of these expectations have, in fact, already been realized [e.g., 1-5].

For example, in [4,5], we analyzed backscatter variations present in an ERS-1 SAR image in order to reveal the existence and depth of an atmospheric mixed layer. In the present paper, we show how the intensity variations in a SAR image can be employed to reveal the sea surface manifestation of a land breeze.

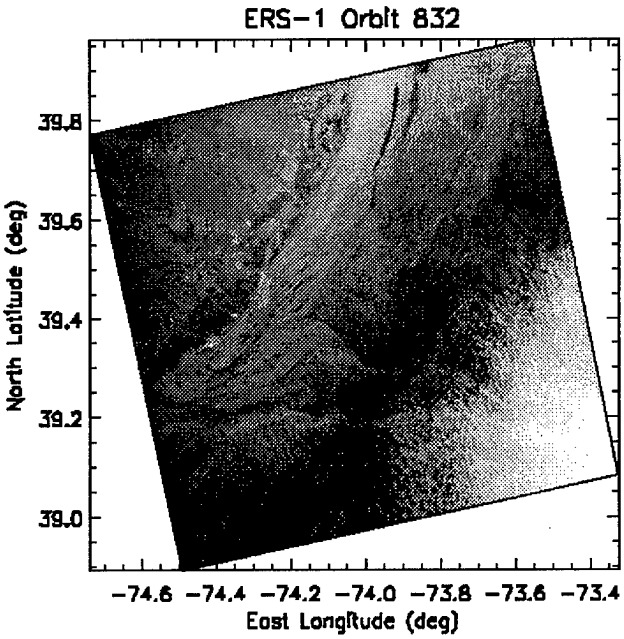


Fig. 1: ERS-1 SAR Image of the New Jersey Coastline

2. SAR IMAGE

In Fig. 1, we present an ERS-1 SAR image acquired over the southern New Jersey Coastline on 13 September 1991 at 0311 GMT. The ERS-1 SAR operates at 5.4 GHz vertical polarization and has a 23° incidence angle. Within the image in Fig. 1, there exists two dominant SAR backscatter regimes over the ocean surface that we suggest are atmospherically induced. The first is an extensive mottled regime which occurs well off the coast in the southeast corner of the image. In [4], we concluded that mottling is, in fact, the SAR signature of marine atmospheric mixed cellular convection. In [5], we demonstrate how the existence of mottling can be used to estimate mixed layer depth via spectral analysis of radar backscatter.

The second regime in Fig. 1 is an area of enhanced backscatter directly adjacent to the coast. This area of enhanced backscatter uniformly decreases in intensity with distance from the coast. There is a narrow region of relatively weak backscatter between the first and second regime. Given the date, time, and location of the image, as well as the existence of mottling, we hypothesize that the second backscatter regime is the footprint of a land breeze. Our hypothesis will be supported using routine meteorological data and boundary layer theory.

3. THEORY

A land breeze is the near-surface component of a typically nocturnal coastal thermal circulation. Fig. 2 shows an idealized land breeze circulation. During the night, all else being equal, the land and the air adjacent to the land radiatively cools more so than their maritime counterparts. A lower boundary layer temperature contrast develops in response to this differential cooling. This temperature contrast induces a lower boundary layer wind flow, a density current, from the cool, dense, air over the land towards the relatively warm, less dense, air over the water. As night time progresses and the temperature contrast increases, the land breeze increases in horizontal scale and strength. In the absence of appreciable synoptic-scale background flow, land breeze wind speeds are typically on order of a few meters / second and the wind direction veers with time as the land breeze increases in strength. This veering of the wind is due

0-7803-3068-4/96$5.00©1996 IEEE

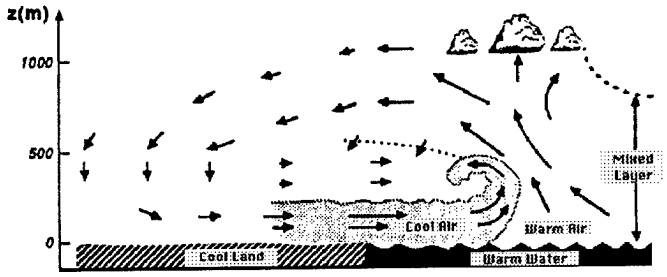


Fig. 2: Schematic of a Land Breeze Circulation (modified from [6])

to the coriolis force. At some distance over the water, the influence of the thermal contrast between the land and the water can no longer maintain a land breeze and the wind speed diminishes. The surface layer air then converges at what is referred to as the land breeze front. Air then rises, flows back inland, and descends to complete the circulation. Typical depths of a mature land breeze circulation are hundreds of meters to a few kilometers. The day time counterpart to the land breeze is known as the sea breeze and is typically stronger than the land breeze. For a more in depth review of the physics of coastal thermal circulations see [7].

The phenomenon of the land and sea breeze has been extensively studied via a vast array of atmospheric models [e.g., 8,9]. Observational studies of the sea breeze have also been conducted helping to provide thorough understanding of the phenomena [e.g., 10,11]. In contrast, detailed observational studies of the land breeze are lacking. This gap is due in part to the cost and man power requirements needed to readily and frequently sample the marine atmospheric boundary layer using *in situ* instrumentation. Remote sensing studies are therefore an ideal means of filling this observational gap.

4. DISCUSSION

Several qualitative arguments can be made for the existence of a land breeze footprint in Fig. 1. First, the image was taken during the night, the preferred time for the existence of a land breeze. Second, the area of enhanced backscatter along the New Jersey Coastline seen in Fig. 1 conforms well with the theoretical model of a land breeze given in Section 1; the intensity of backscatter implies a light and steadily decreasing wind immediately offshore. Third, the area of little or no backscatter seen to the southeast of the hypothesized land breeze may indicate the existence of land breeze frontal convergence. Finally, the mottling seen in the southeastern portion of Fig. 1 indicates the presence of a deep mixed layer, a relatively warm sea surface, and quiescent synoptic-scale weather conditions [4]; all else being equal then, the meteorological and sea surface background conditions are ideal for the existence of a land breeze (warm water and calm synoptic-scale winds). In order to confirm the presence of a land breeze at the time of the ERS-1 SAR overpass, routine meteorological temperature and wind data must be employed.

4.1 Meteorology

Review of National Meteorological Center synoptic analyses (not shown) corroborate the qualitative assessment in Section 3 that no large scale synoptic disturbances existed in the region during the ERS-1 SAR overpass. At image time, the imaged area, as well as the entire northeastern United States was under the influence of a large fair weather high pressure system which was centered near 50.00 N, -75.00 E. The backscatter variations seen in Fig. 1 are therefore not of synoptic origin.

Fig. 3 shows four stream line analyses covering the imaged area of Fig. 1. They were generated from synoptic and surface airways data for 0000 GMT, 0300 GMT, 0600 GMT, and 0900 GMT, 13 September 1991. Arrows indicate the direction of the wind and the distance between stream lines is proportional to wind speed. It should be noted that these analyses were generated by interpolating between a rather sparse number of data points. Interpolated wind directions and speeds at any one point may therefore be in error. For example, the wind speed at the Atlantic City New Jersey Airport (the only ground station within the imaged area) (ACY) was less than 1 m / s for all four analysis times (ACY can be found on Fig. 1 at 39.45 N, -74.57 E and near the left center of the maps in Fig. 3). However, these analyses are appropriate for judging the larger scale characteristics of the flow field.

Within Fig. 3, it can be seen that as time progressed from 0000 GMT to 0900 GMT, winds along the New Jersey Coast veered from a predominately easterly flow early at night to a westerly flow at 0900 GMT. As discussed in Section 3, this nocturnal veering of the wind is characteristic of the life

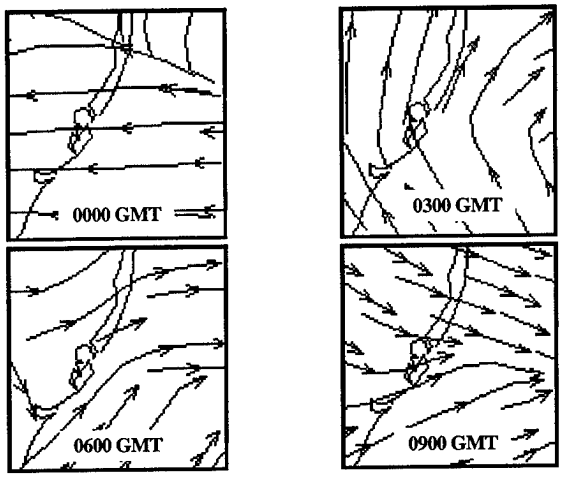


Fig. 3: Stream line analyses from 13 September 1991

cycle of a land breeze.

Unfortunately, these stream line analyses do not conclusively support the existence of a land breeze at the time of the ERS-1 SAR overpass. The 0300 GMT analysis only indicates offshore flow in the northern half of the plot. A possible explanation for this discrepancy is that the 0300 GMT analysis is revealing the onset of the land breeze. Note that the 0300 GMT analysis uses data recorded at approximately 0245 GMT. Note also that the ERS-1 SAR overpass occurred at 0311 GMT. It is plausible that the land breeze was developing from north to south between these two data acquisition times. To add credence to our argument, note that the backscatter signature from the hypothesized land breeze in Fig. 1 is stronger in the northern half of the image indicating stronger wind flow there. In fact, wind direction data from a buoy located near the mouth of the Hudson River, north of the imaged area, almost identically matches the veering pattern seen in the streamline analyses.

The cause of this hypothesized land breeze event can be found by simply analyzing temperature data from ACY and that of the adjacent coastal waters for the night of 13 September 1991. Table 1 shows the nocturnal temperature change at ACY.

Table 1: Temperature Data from ACY for 13 Sept. 1991

0000 GMT	0300 GMT	0600 GMT	0900 GMT
57° F	51° F	51° F	50° F

While the temperature at ACY dropped through the evening, ship and buoy reports indicate maritime air temperatures near the imaged ranged from the mid 60's to low 70's ° F. Given the above qualitative and quantitative assessments, we believe but can not conclude, this nocturnal temperature difference between the land and the sea is what induced the backscatter variations seen along the New Jersey Coast in Fig. 1 and that the backscatter variations are the SAR footprint of a land breeze.

5. CONCLUSIONS

Basic boundary layer theory combined with ERS-1 SAR image, and surface meteorological data, analysis suggest the existence of a land breeze footprint off the New Jersey Coast in Fig. 1. The image time combined with the horizontal extent and intensity of the backscatter regime in question qualitatively conforms with the boundary layer thought model of a land breeze. This qualitative evidence is partially supported by routine meteorological wind and temperature data. However, it is obvious that more ground truth is needed to conclude without a doubt that our hypothesis is correct. To further this type of research, we are currently planning several large and small scale experiments who's purposes are to meteorologically ground truth SAR imagery. This type remote sensing research can be of interest to the defense, merchant, and recreational coastal marine community.

6. ACKNOWLEDGMENTS

The authors wish to thank the European Space Agency for supplying the ERS-1 SAR image used in this study. This ongoing research is supported by the Office of Naval Research under Grant N00014-93-1-0252.

7. REFERENCES

[1] R. C. Beal, V. Kudryavtsev, D. R. Thompson, S. Grodsky, D. G. Tilley, V. Dulov, and H. C. Graber, "Interpretation of ERS-1 SAR imagery of the Gulf Stream using near-surface measurements," unpublished.

[2] T. W. Gerling, "Structure of the surface wind field from the Seasat SAR," J. Geophys. Res., vol. 91, pp. 2308- 2320, 1986.

[3] J. F. Vesecky and R. H. Stewart, "The observation of ocean surface phenomena using imagery for the SEASAT synthetic aperture radar: An assessment," J. Geophys. Res., vol. 87, pp. 3397-3430, 1982.

[4] T. D. Sikora, G. S. Young, R. C. Beal, and J. B. Edson, "Use of ERS 1 synthetic aperture radar imagery of the sea surface in detecting the presence and structure of the convective marine atmospheric boundary layer," Mon. Wea. Rev., vol. 123, pp. 3623-3632, 1995.

[5] T. D. Sikora and G. S. Young, "Investigating the marine atmospheric boundary layer using synthetic aperture radar spectra," Eighth Conference on Air-Sea Interaction, AMS, pp. 45-49, 28 January-2 February 1996.

[6] R. B. Stull, An Introduction to Boundary Layer Meteorology, Dordrecht: Kluwer Academic Publishers, 1988.

[7] G. S. Young and J. W. Winchester, "Association of non-marine sulfate aerosol with sea breeze circulation in Tampa Bay," J. Appl. Meteor., vol. 19, pp. 419-425, 1980.

[8] M. A. Estoque, "A theoretical investigation of the sea breeze," Quart. J. Roy. Meteor. Soc., vol. 87, pp. 136-146, 1961.

[9] J. Neumann and Y. Mahrer, "A theoretical study of the land and sea breeze," J. Atmos. Sci., vol. 28, pp. 532-542, 1971.

[10] M. A. Fosberg and M. J. Schroeder, "Marine air penetration in Central California," J. Appl. Meteor., vol. 5, pp. 573-589, 1966.

[11] J. E. Simpson, D. A. Mansfield, and J. R. Milford, "Inland penetration of sea-breeze fronts," Quart. J. R. Met. Soc., vol. 103, pp. 47-76, 1977.

ATMOSPHERIC SIGNATURES IN SAR OCEAN IMAGERY

R. C. Beal[1], D. R. Thompson[1], G. S. Young[2], H. N. Shirer[2], and T. D. Sikora[1,2]
[1] The Johns Hopkins University Applied Physics Laboratory, Laurel, MD 20723
[2] The Pennsylvania State University Dept of Meteorology, University Park, PA 16802
Tel: 301-953-5009 / Fax: 301-953-5548 / email: r.beal@jhuapl.edu

ABSTRACT

This paper reviews some of the important steps necessary to interpret multiscale atmospheric phenomena in SAR imagery, using examples from ERS-1. In some cases, it may be practical, with a combination of SAR imagery and conventional meteorological analysis, to effectively specify the MABL, including its depth and stability, surface wind speed and direction, and sea-surface stress or friction velocity, all on spatial scales down to a km or less. Such an application of SAR would represent a significant advance over conventional scatterometry, with typical spatial resolution of >20 km. This resolution is insufficient to resolve the turbulence structures in the MABL, and therefore also insufficient to deduce the surface wind corrected for atmospheric stability.

1. INTRODUCTION

Synthetic aperture radar (SAR) imagery, now routinely collected from space, reveals a vast array of phenomena related to the behavior of both the ocean mixed layer and the marine atmospheric boundary layer (MABL). The spatial variation of the SAR backscatter is a direct measure of the roughness of the ocean surface on scales comparable to the SAR transmission wavelength, typically a few cm. These roughness variations, in turn, are the result of a broad range of oceanic and atmospheric processes and their interactions. To the extent that the spectral energy density of the cm-scale waves is a direct measure of the surface stress, SAR imagery can be used to examine surface stress variations resulting from atmospheric phenomena. Previous work with atmospheric signatures in SAR imagery can be found in [1-6].

Processes that affect the spectral density of the cm-scale surface waves (and hence the value of the radar backscatter σ_0), but are not directly related to the ambient wind field, can contaminate the wind estimates. Such processes include the damping of cm-scale waves by surfactant films and the modulation of the local wave field via interactions with local currents.

2. HIGH RESOLUTION SAR SCATTEROMETRY

From 17 April to 25 May 1992, a large coordinated ERS-1 SAR data set was collected over the NW Atlantic [7]. The original goal was to construct an 800 km square mosaic covering the western Gulf Stream and the coastal regions from Cape Hatteras to Cape Cod, and, through comparisons with NOAA Advanced Very High Resolution Radiometer (AVHRR) imagery, to deduce whether SAR could reveal anything new about the large-scale current dynamics.

Any one of several physical processes can lead to a modulation of the SAR intensity in the vicinity of a current gradient: wave-current interactions can cause a local excess or deficiency of scatterers and/or local wave breaking; surfactants can collect at the interface of two converging water masses and be carried along by the mean current parallel to the interface; sharp stability gradients can occur at the boundaries of water masses of varying temperatures, causing a step-like change in backscatter intensity. Although these processes are useful for revealing a current boundary, they can also contaminate the wind signature. Moreover, these are the same contaminating influences that can introduce errors into wind estimates from conventional scatterometry, although they are ordinarily masked by the large footprint of the scatterometer. Fortunately, they are often recognizable in the higher resolution SAR imagery.

Figure 1 shows the set of 12 ascending ERS-1 SAR passes, constructed from 87 100 km square frames, that were collected over a 38 day interval during April/May 1992, in a region from Cape Hatteras in the SW to Cape Cod in the NE. Adjacent pass overlap was ~30% ; the passes are separated here for clarity. Each frame was smoothed to 100 m pixels, and each pass (4 to 8 frames) was corrected for both cross-track antenna pattern and backscatter fall-off with incidence angle. The latter correction was estimated by dividing each pass by the mean cross-track trend for all 12 passes, since no geophysical basis exists for such a cross-track trend over the 38-day collection interval. Relative radiometric calibration from pass-to-pass was preserved by linearly scaling all passes identically. The resulting pixel intensity is linearly proportional to radar backscatter σ_0 at a specific incidence angle (or cross-track position). With this correction method, and in the absence of contaminants, a spatially homogeneous, unidirectional, neutrally-stable wind U_{10N} should produce a uniform backscatter (pixel value) over the ocean for all passes.

The SAR imagery in Fig 1 is rich with spatial variations on many scales, and from many sources. For a unidirectional wind at neutral stability, σ_0 is nearly linearly proportional to wind magnitude (see Fig 2, calculated from [8]). Associating the most probable SAR intensity (pixel value of 87 from ocean histogram of Fig 1) with the most probable U_{10N} for April/May in the NE Atlantic (5.5 m/s from climatological data), leads to an absolute relationship between pixel value and U_{10N}, σ_0, and friction velocity u_*. These relationships are summarized in the four columns on the right side of Fig 1.

In general, of course, the wind is not unidirectional, and the

0-7803-3068-4/96$5.00©1996 IEEE

MABL is not neutral. For example, Fig 2 shows that the same σ_0 can result from any wind speed from 5 to 10 m/s, depending upon wind direction and MABL stability. Note that σ_0 = 0.4 (–4 dB) can result, e.g., from 1) a neutral upwind of 5 m/s; 2) a neutral cross wind of 8.5 m/s; 3) a stable upwind of 6 m/s with +4°C air-sea temperature difference. At lower winds, the stability effects are even more pronounced. For $U_{10} < 3$ m/s, stability increasing beyond neutral can actually quench the backscatter. Note, however, that changes on the unstable side of neutral have little effect on σ_0.

In general, to extract useful wind estimates from the SAR, an estimate of both wind direction and MABL stability must be available. But if an unstable MABL can be assumed *a priori*, then the major errors will come from the unknown wind direction. Fortunately, in many cases, the SAR imagery itself provides clues from which wind direction and/or stability can be inferred. Several examples of ERS-1 SAR imagery, in which such clues are more or less evident, are shown in Fig 3. Panel A shows 2-D roll vortices [1,2], panel B shows island shadowing, and panel C is an example of atmospheric gravity waves [3]. Panel D evidently shows an enhanced mesoscale convergence region [9], and panel F shows sharp stability changes induced by the warm Gulf Stream [6]. Panels E and G, perhaps suggestive of gravity waves, are presently unexplained.

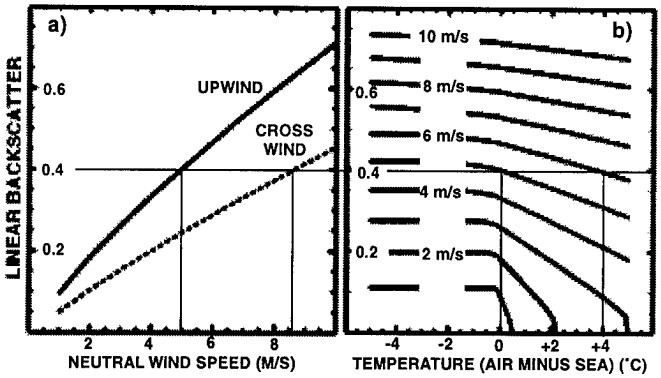


Figure 2. Dependence of backscatter σ_0 on a) wind speed U_{10N} for two directions, and b) air-sea temperature difference for various upwind wind speeds, calculated from [9]. A σ_0 of 0.4 can result from infinite combinations of wind speed and direction, and stability (see text).

3. SUMMARY

SAR imagery is rich with surface signatures related to the atmospheric boundary layer. Although many of these signatures have been observed since Seasat, only recently have some of the spaceborne SAR platforms been sufficently radiometrically stable that quantitative estimates of the radar backscatter are possible. However, armed with a robust absolute calibration strategy, a good understanding of the spatial scales and

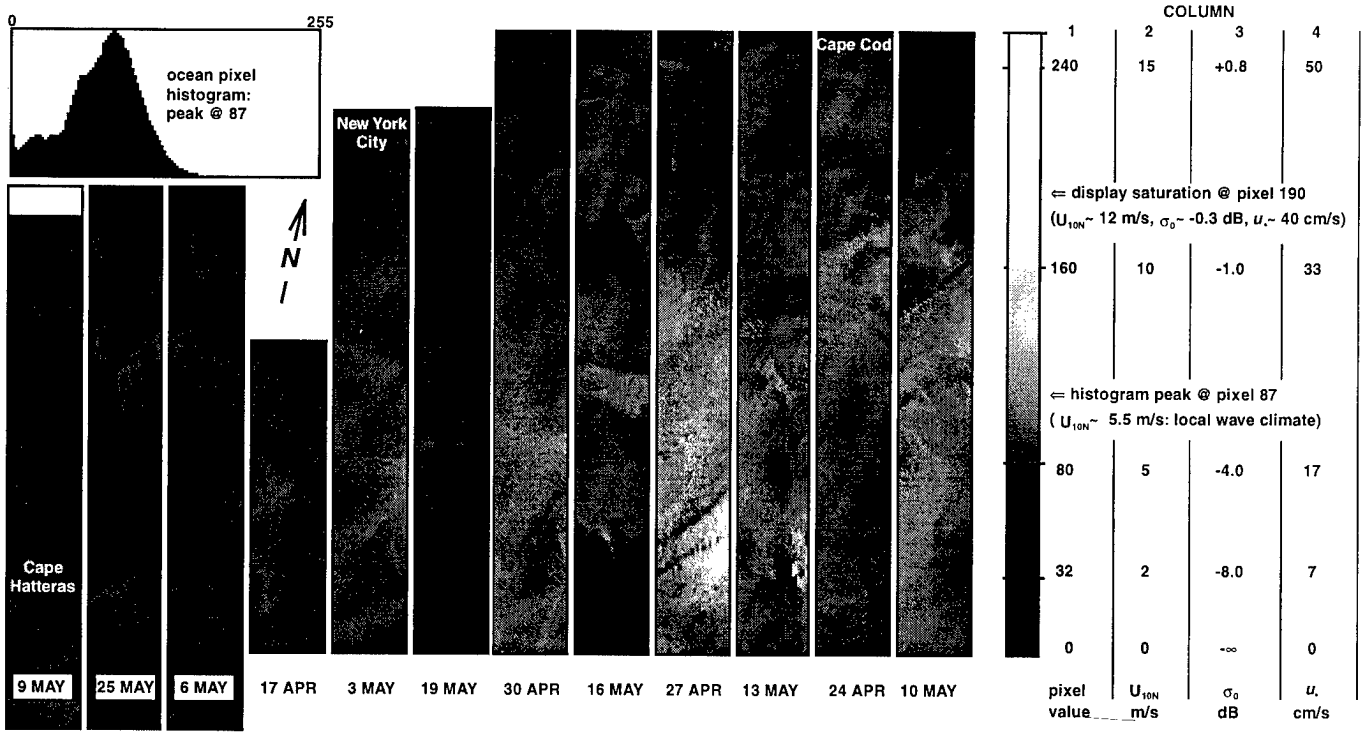


Figure 1. Set of 12 ERS-1 SAR passes collected in April/May 1992. Calibration method (see text) preserves relative backscatter for all passes. Ocean histogram peak value of 87 (column 1) is associated with mean April/May wind speed (column 2) of 5.5 m/s. Wismann algorithm (Fig 2) permits σ_0 estimates (column 3) and, for a uniform neutral MABL, u_* estimates (column 4). The many caveats are discussed in the text.

patterns associated with various atmospheric processes, and a sensitivity to the intrinsic information in the SAR imagery itself, a complete specification of the MABL appears to be feasible, at least over a limited range of conditions.

Even when clues of the MABL are completely lacking in the SAR imagery, a careful surface analysis combined with larger scale wind fields from a spaceborne scatterometer should produce a good first guess wind direction at the few tens-of-km scale, which could then be iterated down to a few km with a refined SAR image analysis.

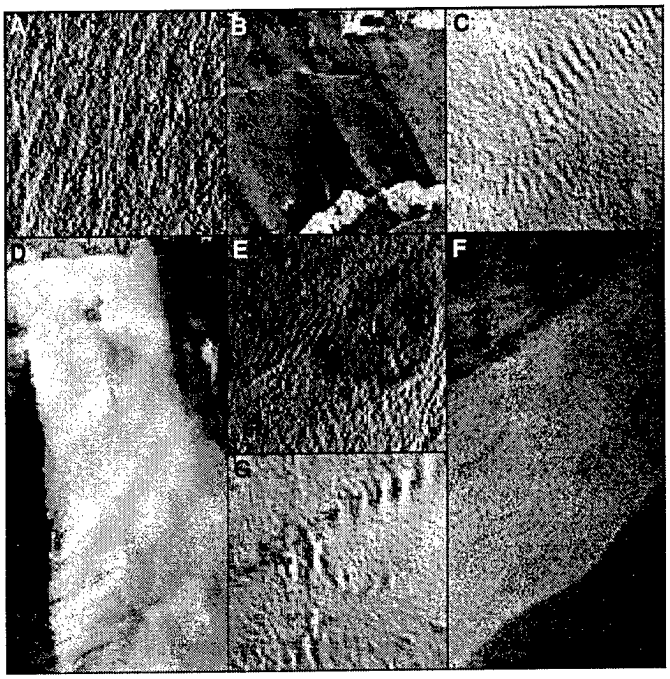


Figure 3. Some interesting examples of atmospheric expressions contained in Fig 1. Panels A and B are 20 km wide. All others are 80 km wide. Panels A, C, E, and G have been enhanced via spatial differentiation. A: 2D roll vortices; B: land shadowing; C: gravity waves [3]; D: mesoscale convergence region [9]; E: unexplained; F: warm Gulf Stream [6]; G: unexplained.

4. REFERENCES

[1] Gerling, T. W., 1986: Structure of the surface wind field from the Seasat SAR. *J. Geophys. Res.*, **91**, 2308-2320.

[2] Alpers, W. R. and B. Brümmer, 1994: Atmospheric boundary layer rolls observed by the synthetic aperture radar aboard the ERS-1 satellite. *J. Geophys. Res.*, **99**, 12613-12621.

[3] Thomson, R. E., P. W. Vachon, and G. A. Borstad, 1992: Airborne synthetic aperture radar imagery of atmospheric gravity waves. *J. Geophys. Res.*, **97**, 14249-14257.

[4] Vachon, P. W., O. M. and J. A. Johannessen, 1994: An ERS-1 synthetic aperture radar image of atmospheric lee waves. *J. Geophys. Res.*, **99 C11** 22,843-22490.

[5] Sikora, T. D., G. S. Young, R. C. Beal, and J. B. Edson, 1995: On the use of spaceborne synthetic aperture radar imagery of the sea surface in detecting the presence and structure of the convective marine atmospheric boundary layer. *Mon. Wea. Rev.* **23**, 3623-3632.

[6] Beal, R. C., V. Kudryavtsev, D. R. Thompson, S. Grodsky, D. G. Tilley, V. Dulov and H. C. Graber, 1996: Interpretation of ERS-1 SAR imagery of the Gulf Stream using near surface measurements. *J. Geophys. Res.* (in review).

[7] Beal, R.C., V. Kudryavtsev, D. R. Thompson, S. Grodsky, D. Tilley, and V. Dulov, 1993: Large and small scale signatures of the ERS-1 SAR over the Gulf Stream, *Proc. 2nd ERS-1 Symposium*, Hamburg, Germany, 547-552.

[8] Wismann, V., 1992: A C-band scatterometer model derived from the data obtained during the ERS-1 calibration/validation campaign. *Proc. First ERS-1 Symposium*, Cannes, 55-59.

[9] Winstead, N.S., H. N. Shirer, T. D. Sikora, and R. C. Beal, 1996: Meteorological Explanation of a Sea Surface Roughness Streak Imaged by ERS-1 SAR Near Block Island, New York, *Proc. IGARSS '96,* Lincoln, Nebraska.

ACKNOWLEDGEMENT

This work was supported by the U. S. Office of Naval Research, Remote Sensing and Space Division.

SAR Response to Spatially and Temporally Varying Wind Fields

D.R. Lyzenga
Department of Naval Architecture and Marine Engineering
University of Michigan
Ann Arbor, MI 48109-2145
Tel 313-764-3216, Fax 313-936-8820
lyzenga@umich.edu

Abstract -- This paper discusses some considerations involved in modeling the transient effects associated with unsteady or non-uniform wind fields over the ocean. The spectral energy balance equation is solved for some simple cases in which the wind varies in time or space, using various formulations for the wind input and dissipation terms. An overshoot effect is shown to occur when the energy dissipation rate is assumed to be proportional to the velocity variance due to longer waves in the spectrum. Examples are presented and some implications for SAR image interpretation are discussed.

INTRODUCTION

Manifestations of sub-mesoscale atmospheric phenomena such as wind fronts and convection cells are frequently observable in SAR images collected over the oceans. These image features are apparently caused by spatial variations in the surface wind fields. However, the relationship between the radar cross section and the local wind speed in these cases is not necessarily the same as for the case of uniform and steady winds, because the wave field may not have reached its final equilibrium state even at the short wavelengths that most strongly influence the radar backscatter.

The relationship between the surface wind and wave fields is described by the spectral energy balance equation, which is discussed in the following section. The remainder of the paper presents the results of some numerical experiments using this equation along with various formulations for the wave growth and dissipation terms. Since there is considerable uncertainty about these term, the results of these experiments are not to be considered as definitive, but are intended to illustrate possible behaviors and to stimulate further research into the underlying interaction mechanisms.

THE SPECTRAL ENERGY BALANCE EQUATION

The spectral energy balance equation can be written, in the absence of surface currents, as

$$\frac{\partial E}{\partial t} + c_g \cdot \nabla E = F_E(E) \qquad (1)$$

where E is the energy spectral density, c_g is the group velocity, and $F_E(E)$ is the net source function for wave energy, which can be written as

$$F_E(E) = \alpha + \beta E - D + T_{nl} \qquad (2)$$

where α is a linear growth parameter (Phillips mechanism), β is an exponential (Miles) growth parameter , D is the energy dissipation rate, and T_{nl} represents the rate of energy transfer due to nonlinear wave-wave interactions.

The linear growth mechanism is necessary to initiate wave growth, since it is the only term that is non-zero when E=0. However, this term is frequently assumed to be negligible in comparison with the second growth term soon after wave growth is initiated.

A number of formulations for the exponential growth rate have been published. The results shown in this paper were obtained using the form proposed by Donelan and Pierson [1] which can be written as

$$\beta = 0.194\frac{\rho_a}{\rho_w}\left[\frac{\bar{U}(\lambda/2)}{c}\cos(\Phi - \Phi_w) - 1\right]^2 \omega \qquad (3)$$

where $\bar{U}(\lambda/2)$ is the mean wind speed at a height equal to half the wavelength of the surface waves under consideration. This mean wind speed is obtained by assuming a logarithmic wind profile under neutral stability conditions.

Various forms for the energy dissipation rate have also been used, including those proposed by Hughes[2], Komen *et al.* [3], and Phillips [4]. The dissipation rate used by Komen *et al.* is proportional to the energy spectral density, with a constant of proportionality that depends on certain integral properties of the spectrum, while the forms used by Hughes and Phillips are proportional to the second and third power of the (local) spectal density, respectively.

The nonlinear energy transfer term as originally formulated by Hasselmann requires extensive computing time for its evaluation, and various approximations have been used to improve computational efficiency. It is considered to be an important mechanism, particularly near the peak of the spectrum, and it has also been cited as an explanation for the "overshoot" effect, which is discussed below. However, because of its complexity and unceratinties regarding the proper formulation of this term, it has been neglected in the following numerical experiments.

Research supported by ONR Contract # N00014-93-1-0105.

0-7803-3068-4/96$5.00©1996 IEEE

SOLUTIONS OF THE ENERGY BALANCE EQUATION

The simplest form of the energy balance equation which reproduces the basic observations of an exponential growth followed by a transition to an equilibrium state can be written as

$$\frac{\partial B}{\partial t} + c_{gx}\frac{\partial B}{\partial x} = \beta B - \gamma B^2 \qquad (4)$$

where B is the "degree of saturation," defined as k^4 times the height spectrum, and c_{gx} is the x-component of the group velocity. If a spatially uniform wind field is applied at t=0 and is assumed to be constant thereafter, the second term on the left side of this equation vanishes, and the resulting equation has the analytical solution

$$B(t-t_o) = \frac{\beta e^{\beta t}}{\gamma(1+e^{\beta t})} \qquad (5)$$

for arbitrary t_o. This solution is shown in Fig. 1 using values of β calculated from (3) for a wind speed of 5 m/s, at wavenumbers of 10, 20, and 40 rad/m, and assuming $\gamma = 100\beta$. Although it yields reasonable values of the equilibrium spectrum, this assumption is not entirely satisfactory because it makes the dissipation rate dependent on the wind speed, rather than on only the wave state.

Similar values can be obtained for the equilibrium spectrum by making γ proportional to the velocity variance. There is some experimental as well as theoretical justification for such an assumption [5], but physical arguments would suggest that the dissipation rate for any given wavenumber should depend only on the orbital velocities associated with longer waves in the spectrum. These arguments motivate a re-definition of the dissipation parameter as

$$\gamma = \gamma_o \left(\frac{\sigma_v^2(k)}{c^2}\right)\omega \qquad (6)$$

where $$\sigma_v^2(k) = \int_0^k \int_0^{2\pi} c^2(k')\, B(k', \phi')\, d(\ln k')\, d\phi' \qquad (7)$$

and γ_o is a dimensionless constant. Using this definition, a numerical solution of (4) was accomplished by stepping from lower to higher wavenumbers, assuming $\gamma = 0$ at the lowest wavenumber and recomputing $\sigma_v^2(k)$ and γ at each successive wavenumber. The time integration was done using the second order finite difference equation

$$B(t+\Delta t) = B(t) + B'(t)\Delta t + \frac{1}{2}B''(t)(\Delta t)^2 \qquad (8)$$

where

$$B'(t) = \beta B - \gamma B^2 \quad \text{and} \quad B''(t) = (\beta - 2\gamma B)\, B'(t)\,. \qquad (9)$$

This procedure was found to accurately reproduce the analytic solution (5) when a constant value of γ was used, with a time step $\Delta t = 0.2/\beta$. The results obtained by using (6) with $\gamma_o = 10$ are shown in Fig. 2 for the same wind speed and wavenumbers as shown in Fig. 1.

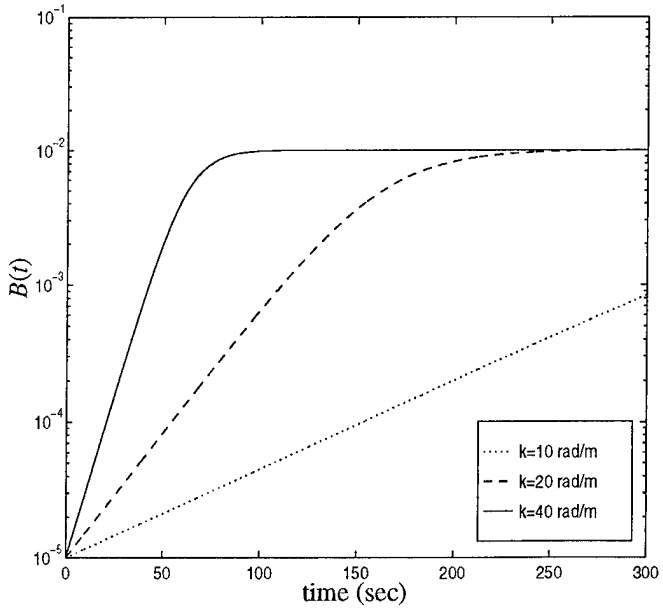


Fig. 1. Analytical solution of the energy balance equation (4) at three wavenumbers, using Donelan and Pierson's growth rate (3) and a constant dissipation rate parameter

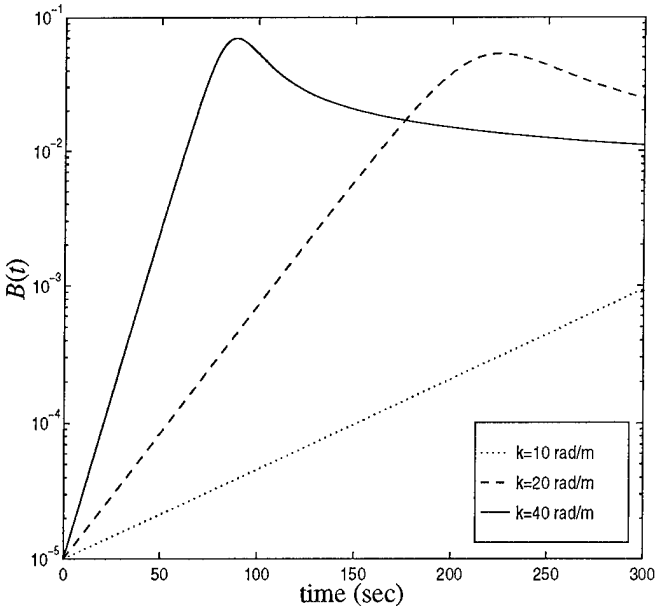


Fig. 2. Numerical solution of the energy balance equation (4) using a variable dissipation rate coefficient γ as given by (6) and (7), for the same conditions as in Fig. 1.

A second case of interest is that of a wind front moving at a velocity U_f in the x direction, with a wind speed U_w behind the front. In a coordinate system moving with the front, the spectral energy balance equation can be written as

$$(U_f - c_{gx}) \frac{\partial B}{\partial x'} = \begin{cases} \beta B - \gamma B^2 & x' > 0 \\ -\gamma B^2 & x' < 0 \end{cases} . \qquad (10)$$

For constant γ and $U_f > c_{gx}$, the solution of this equation can be obtained from (5) by substituting $t = x'/(U_f - c_{gx})$. As $U_f - c_{gx} \to 0$, the time axis shrinks and the solution approaches a step function at $x' = 0$. Waves with negative values of $U_f - c_{gx}$ are in equilibrium for $x' > 0$, and are radiated ahead of the front where they decay as

$$B(x') = \frac{U_f - c_{gx}}{\gamma\,(x' + x_o)} \quad \text{for} \quad x' < 0 \qquad (11)$$

Using (6) for the dissipation rate, the numerical solution described previously can be used by making the substitution $t = x'/(U_f - c_{gx})$ for waves with $U_f > c_{gx}$, and assuming that longer waves, if they exist, have reached an equilibrium state in the region $x' > 0$. Results obtained using this procedure with U_w=5 m/s and U_f=2 m/s are shown in Fig. 3.

DISCUSSION

The numerical experiments described in this paper show that an overshoot effect is predicted for a growing wave field using a simple wave growth model in which the dissipation is assumed to be proportional to the velocity variance associated with longer waves in the spectrum. L-band SAR images collected during the High Resolution Field Experiment (Fig. 4) captured an advancing wind front with characteristics similar to those used in the above calculations. A pronounced brightening can be observed at the leading edge of the front, which may be interpreted as a manifestation of this overshoot effect. Calculations at the Bragg wavenumber of 40 rad/m show at least a qualitative agreement with these observations.

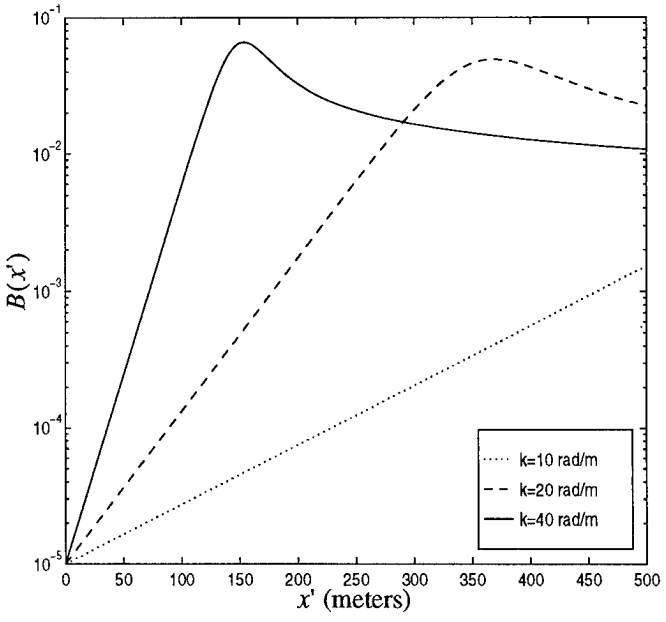


Fig. 3. Spectral density vs. position for three wavenumbers

REFERENCES

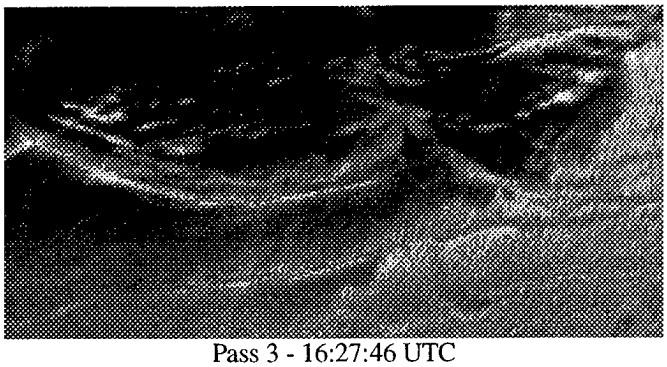
[1] M.Donelan and W.Pierson, "Radar scattering and equilibrium ranges in wind-generated waves with application to scatterometry," J. Geophys. Res, vol. 92, pp. 4971-5029, 1987.

[2] B.Hughes, "The effect of internal waves on surface wind waves, 2.Theoretical analysis," J. Geophys. Res., vol. 83, pp. 455-465, 1978.

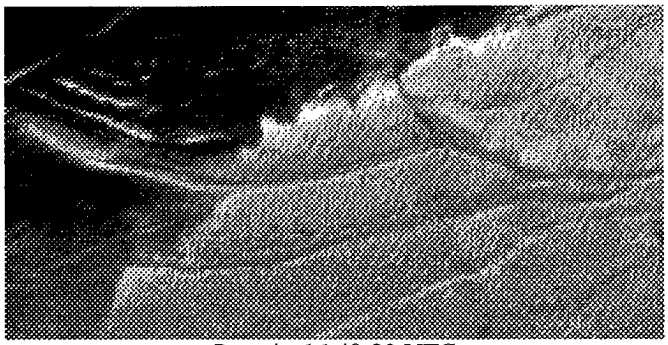
[3] G.Komen, S.Hasselmann and K.Hasselmann, "On the existence of a fully developed wind-sea spectrum," J. Phys. Oceanogr., vol. 14, pp. 1271-1285, 1984.

[4] O.Phillips, "Spectral and statistical properties of the equilibrium range in wind-generated gravity waves," J. Fluid Mech., vol. 156, pp. 505-531, 1985.

[5] O.Phillips and M.Banner, "Wave breaking in the presence of wind drift and swell," J. Fluid Mech., vol. 66, pp. 625-640, 1974.



Pass 3 - 16:27:46 UTC



Pass 4 - 16:49:23 UTC

Fig. 4. ERIM / NAWC L-band SAR images showing wind front near the edge of the Gulf Stream on 9/16/91

An End-to-End Simulation of Radar Signatures From The HI-RES 1 Rip Feature

S. R. Chubb, A. L. Cooper, R. W. Jansen, C. Y. Shen
Remote Sensing Division
Naval Research Laboratory
Washington, D. C. 20375-5351, U. S. A.
T: 202.767.5270, F: 202.767.3303, EMAIL: chubb@ccf.nrl.navy.mil

Abstract -- We examine the origin of the strong radar signatures from the rip-like feature observed during the First High Resolution Remote Sensing (HIRES-1) experiment, based on an "end-to-end" strategy in which radar signatures are modelled from a full-spectrum wave approach, using surface and subsurface currents, derived from the underlying hydrodynamics. We find that it is necessary to include wave-breaking (WB) effects to obtain satisfactory agreement with experiment for the magnitude of the observed radar signature. We accomplish this using an earlier WB model and by introducing an improved WB model. The new model combines the statistically-based, composite model of radar backscatter with a deterministic, feature model that relates the predominant backscatter from breaking waves to a particular geometrical model of a spilling breaker. This is accomplished by using localized WB criteria, based on critical crest acceleration Λ_c information, to determine the probability of breaking, and by extending the feature model so that its assumed geometry may be determined statistically. This allows us to eliminate all of the unknown parameters of the feature model using calculations of wave-height spectra.

INTRODUCTION

In this paper we investigate the underlying dynamics associated with a strong, rip-like sub-mesoscale feature that was observed in radar imagery[1] at the boundary between Gulf Stream and Shelf water near Cape Hatteras during the first NRL High Resolution Remote Sensing Experiment (HIRES-1). In situ current measurements[2] have shown that this rip-like signature occurs along the boundary of a sharp current convergence front. These measurements also indicate that the frontal dynamics involves the subduction of denser Gulf Stream water under lighter shelf water. In the resulting radar signature, the radar cross-section (RCS) increases by ~10-13 dB along a line-shaped feature, extending several kilometers, predominantly in the east-west direction, normal to the associated front[1].

Jansen et al[3] performed calculations, using a 1-dimensional model of the surface current structure. Consistent with the entire set of in situ current measurements[2], Mied et al[4] developed a considerably richer model for the surface currents and dynamics of current flow at the Gulf Stream/shelf water boundary when the Gulf Stream advances onto the shelf. The present work provides an overview of a detailed study[5], where we have extended the earlier calculations[3] by incorporating the more extensive surface current structure of the Mied et al model. We have combined these calculations of subsurface and surface current flow with modelling of the wave field, using a spectral model of wave-current interaction, and the electromagnetic composite scattering (CS) model for relating wave field to radar return, to simulate the underlying imaging and dynamics, thereby incorporating surface, sub-surface and electromagnetic effects. When the RCS is derived from this approach, using the CS model, the radar signature is underpredicted by a factor of ~4. Consistent with earlier measurements[2] and calculations[3], we have hypothesized that WB effects, not included in the CS model, are responsible for this deficiency. To investigate this point, we have performed new calculations based on the earlier Sparse Breaker Model[3,5] (SBM) of WB backscatter effects and by introducing an improved WB model[5]. The improved model makes use of Localized Wave-Breaking Criteria (LWBC) for relating the probability $P(x,y)$ of WB to occur at a point (x,y) to the probability that a wave obtains a critical wave crest acceleration Λ_c[5]. WB effects are included by replacing the deterministic "feature modelling" approach due to Wetzel[6], with a modified "statistically determined" model in which information provided by $P(x,y)$ and the wave spectrum are used to determine values for the unknown parameters of the feature model.

SUMMARY OF END-TO-END PROCEDURE

A key result of the Mied et al[4] study is that irrespective of the initial boundary configuration, the density-current boundary at the Gulf Stream/shelf water interface evolves into a propagating surface front, and the boundary is always unstable. Because of the insensitivity with respect to the initial boundary configuration, we have been able to model[5] the underlying current structure (in good agreement with measurement[2,4,5]), from a single choice of initial conditions. Here, we have initialized the

0-7803-3068-4/96$5.00©1996 IEEE

subsurface current calculations using density ρ, and (Along-Front) velocity U profiles corresponding to a vertical interface representing the density boundary and a broad jet representing the adjoining Gulf Stream flow. Geographically, the density interface simulates the northern inshore edge of the Gulf stream water on the shelf. Initial velocity U is directed eastward in the positive x direction. The other directions are positive y north and positive z up.

The density across the interface decreases in the northward, positive y direction, with a density change $\Delta\rho$=0.9 kg/m^3 across a width of ~1 km. The value for $\Delta\rho$ is consistent with the observations[2,4], and the width scale is assumed. The density interface is centered at the mid point of the model domain, which has linear dimension L=10 km. The width of the current is set at 4 km so that the current is contained well within the model domain. A surface velocity of U_o= 1 m/s is used, and this velocity is assumed to decrease linearly with depth to a zero value from the surface z=0 to the bottom z= -30 m.

In the model, the sea surface is rigid, stress free and insulated; the shelf bottom is flat, no slip and also insulated. To simplify the calculations, in the horizontal direction, periodic boundary conditions are imposed on the velocity and on the deviation $\rho'(=\rho-\bar{\rho})$ between ρ and the mean stratification $\bar{\rho}$ of the density (defined by $\bar{\rho}=\rho_o-\Delta\rho(y/L)$.

As in the model by Mied et al[4], the motion is uniform in the direction parallel to the density-current boundary (in the east-west direction that points along the rip), so that $\rho\equiv\rho(y,z)$, $U\equiv U(y,z)$, and the remaining (Across-Front) current component $V\equiv V(y,z)$. Using these assumptions and the requirement of incompressibility and the additional assumption of the Boussinesq approximation, two-dimensional calculations of the subsurface current structure (based on the Navier Stokes equation) are carried out. Details of the calculational procedure are outlined elsewhere[4,5].

From these calculations, at the surface, the surface currents V and U are constructed. Because the currents do not depend on x, and the sea surface is rigid, at the surface $U\equiv U(y)$, $V\equiv V(y)$, and there are two non-vanishing current gradient components, $\partial V/\partial y$ (the Cross-Front divergence) and $\partial U/\partial y$ (the Along-Front shear). Using these quantities, the wave action density $N(\boldsymbol{k},\boldsymbol{r},t)$ is determined for each wave-vector $\boldsymbol{k}$, and location $\boldsymbol{r}$ on the surface of the ocean. The procedure for deriving N is similar to one used by Jansen et al[3]. The one important difference occurs because in our model, non-vanishing Along-Front currents and current gradient components are present. As a consequence, in the present case, to solve for N, we use

$$\frac{\partial\omega}{\partial k_y}\frac{\partial N(\boldsymbol{k},\boldsymbol{r})}{\partial y}-\left(\frac{\partial U}{\partial y}k_x+\frac{\partial V}{\partial y}k_y\right)\frac{\partial N(\boldsymbol{k},\boldsymbol{r})}{\partial y}=S(\boldsymbol{k},\boldsymbol{r}), \quad (1)$$

in place of the simpler equation that they have solved[3]. Here,

$$\omega(k)=\omega_o(k)+k_xU+k_yV, \quad (2)$$

$k\equiv|k|\equiv(k_x^2+k_y^2)^{1/2}$, $\omega_o\equiv(gk+T/\rho_w k^3)^{1/2}$ (with $T\equiv$surface tension of water, $\rho_w\equiv$density of water) is the intrinsic angular frequency of the wave, and S (in Eq. 1) is the same source function that was used previously[3].

RCS values were determined from the wave-height spectrum $F\equiv k/(\omega_o\rho_w)N$, using the CS model[3,5]. A potentially important point is that during the present work, it was found that for X-band, when the CS model is applied either for our currents or for the Jansen et al[3] currents, the small slope approximation[5] that was used in Jansen et al[3] overpredicts the radar signature by~2 dB.

WAVE-BREAKING EFFECTS

As discussed in the Introduction, two procedures, the SBM and LWBC, were used to investigate the potential effects of WB. The SBM refers to the procedure initially formulated by Jansen et al[3]. The LWBC is based on a generalization of this approach. In the LWBC, it is assumed that the probability $P(x,y)$ for wave-breaking to occur at a specific point can be obtained and $P(x,y)$ can then be used to infer values of σ_{tot} based upon the further assumption that electromagnetic backscattering processes from regions involving breaking and non-breaking events are not coupled to each other. Based on this strategy, we write the total specific cross-section σ^{sp}_{tot}(≡specific cross-section≡ RCS per unit illuminated area), using

$$\sigma^{sp}_{tot}=(1-P(x,y))\sigma^{sp}_{CS}+P(x,y)\sigma^{sp}_{WB}, \quad (3)$$

where σ^{sp}_{CS} is the CS specific cross-section.

The two new quantities, $P(x,y)$, σ^{sp}_{WB}, required in Eq. 3, are derived by assuming that the contribution to the RCS from $P(x,y)\sigma^{sp}_{WB}$ can be represented using a predominant (average) geometrical shape (based on an average effective geometry), and by approximating $P(x,y)$ using a procedure outlined by Snyder and Kennedy[7], in which it is assumed that when the local crest acceleration Λ_c exceeds a critical value, breaking occurs with 100% certainty. Using this assumption, these authors showed that when $P(x,y)$ can be equated with the fractional white-cap coverage and the variance of the crest acceleration Δa_c is known, $P(x,y)$ can also be related to the associated (normally-distributed) probability that Λ_c is exceeded. Our procedure is to evaluate $P(x,y)$ using this method for each value of Λ_c, based on a new idea: estimate Δa_c(x,y) from the vertical acceleration spectra that apply to our calculated

spectra F; i.e., $\Delta a_c(x,y) \equiv [\int \omega_o^4(k) F(\boldsymbol{k},\boldsymbol{r}) d^2\boldsymbol{k}]^{1/2}$ at each point of the ocean surface. To compare with earlier SBM results, the integration used in these calculations excludes values of $k > 4\pi$ m^{-1}. Also, then, consistent with Lyzenga's observation[8], $gk >> T/\rho_w k^3$, and $\omega_o^2 \sim gk$, so that $\Delta a_c(x,y) \equiv g\Delta m(x,y)$, where $\Delta m(x,y)$ is the local slope variance.

The remaining quantity σ_{WB}^{sp} is derived from an adaptation of Wetzel's[6] feature model of spilling breakers. Here, instead of assuming particular values for the crest length $\mathcal{L}$ and height $\mathcal{H}$, as Wetzel did, average effective values $\mathcal{L}_{ave}$ and $\mathcal{H}_{ave}$ are derived using information about $P(x,y)$, the spectrally-averaged value of F, and an average representation of Wetzel's expression for the total cross-section σ_{WB}. In particular, by equating the average value σ_{WB}^{ave} that results when σ_{WB} is averaged (as a function of $\mathcal{L}$) over radar footprint size Q with $P(x,y)\sigma_{WB}^{sp}$ Q, it is possible to derive an expression for σ_{WB}^{sp} that depends only on $\mathcal{H}_{ave}$ and not on $\mathcal{L}_{ave}$, provided within each footprint, $P(x,y)$ can be equated with the fractional coverage of breakers found within the footprint. Details of the calculation are presented elsewhere[4]. The result is $\sigma_{WB}^{sp}(x,y) \approx k_o \mathcal{H}_{ave}(x,y)/2$, where $k_o \equiv 2\pi/\lambda$, and $\lambda \equiv$radar wavelength.

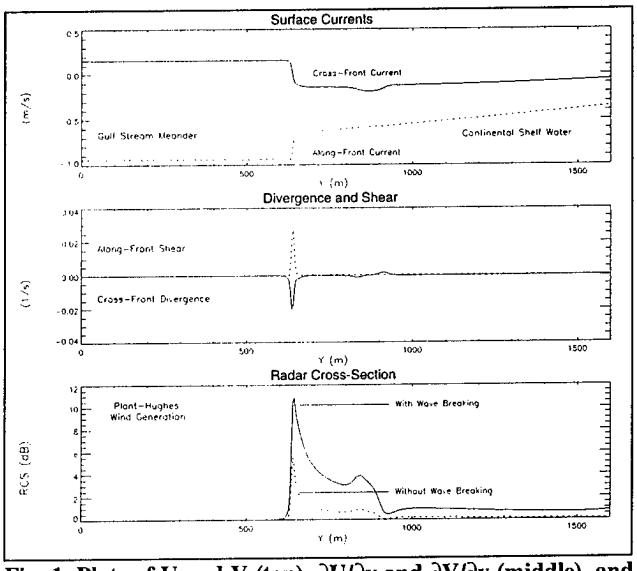


Fig. 1. Plots of U and V (top), $\partial U/\partial y$ and $\partial V/\partial y$ (middle), and RCS with and without WB versus position (Y), as discussed in text.

RESULTS

Fig. 1 shows plots of the V (solid line) and U (dashed line) surface currents (top panel), surface current gradients (middle panel) $\partial V/\partial y \equiv$Cross-Front divergence (solid line) and $\partial U/\partial y \equiv$ Along-Front shear (dashed line), and (in the bottom panel) the RCS from the CS (dashed line) and the RCS that results when WB effects are included using the LWBC procedure described above.

The variation in V ~0.4 m/s (top panel), maximum value of $\partial V/\partial y \sim .019$ s^{-1} (directly over the rip), and width of the regions where $\partial V/\partial y$ and $\partial U/\partial y$ are appreciable all are in good agreement with in situ measurements[2]. RCS values vary with $\partial V/\partial y$ qualitatively in agreement with the relaxation model. When $\partial U/\partial y$ is omitted (in calculations that are not shown), however, the peak value from the enhancement in σ_{CS} is reduced by 1.5-2 dB, indicating that indirect tilt-modulation effects not included in the relaxation model play a role. As shown in Fig. 1, WB effects enhance the peak value of the RCS from 5.8 dB to 10.9 dB, in quantitative agreement with the data (which shows the RCS varying between ~9 and ~13 dB) and with bounds derived from SBM calculations[3,5]. The WB effect that is shown, which occurs when $\Lambda_c = 0.4g$ ($g \equiv 9.8$ m/s^2), corresponds to the maximum enhancement that is found[5]. Pronounced (>~ 9 dB) radar signatures are obtained for a range of critical accelerations, $0.3\ g < \Lambda_c < 0.5\ g$, indicating that the values of Λ_c from the simulation that are consistent with the radar measurements over the rip are also consistent with results for Λ_c that have been obtained in wave-tank and field experiments[5].

REFERENCES

[1]F. Askari, EOS **73**, #43/supplement, 247 (1992). R. P. Mied et al., "High Resolution Remote Sensing." 1992 NRL Review, pp. 181-183, (1992).

[2]G.O. Marmorino and C.L. Trump, C.L., J. Geophys. Res.,99, C4, 7627 (1994).

[3]Jansen, R. W., et al., Proc IGARSS'94, v. 1, 460 (1994).

[4]R.P. Mied et al, "Frontogenesis with Ageostrophic Vertical Shears and Horizontal Density Gradients: Gulf Stream Meanders onto the Continental Shelf," J. Geophys. Res., to appear (1996).

[5]R. W. Jansen, C. Y. Shen, S. R. Chubb, A. L. Cooper, and T. E. Evans, "Subsurface, Surface, and Radar Modelling of a Gulf-Stream Current Convergence," submitted to J. Geophys. Res. (1995).

[6]L. B. Wetzel, in *Wave Dynamics and Radio Probing of the Ocean Surface*, (O. M. Phillips and K. Hasselmann, eds., Plenum Press, NY, 1986), pp. 273-284.

[7]D. R. Kennedy and R. L. Snyder, J. Geophys. Res. 13, 1482 (1983).

[8]D. R. Lyzenga, private communication (1994).

Low Grazing Angle Dual Polarized Doppler Radar Measurements of Oceanic Fronts

Nicholas Allan
Sachs-Freeman and Associates
NRL T-A9, 1401 McCormick Dr
Landover, MD 20785, USA
tel: 1-202-767-7082
nallan@seascat.nrl.navy.mil

Dennis B. Trizna
Naval Research Laboratory
Code 7255, 4555 Overlook Ave
Washington, DC 20375, USA
tel: 1-202-404-7891
triznad@onrhq.onr.navy.mil

David J. McLaughlin
Northeastern University
ECE Department
Boston, MA 02115, USA
tel: 1-617-373-2032
dmcl@cdsp.neu.edu

ABSTRACT

This paper presents low grazing angle dual polarized Doppler radar measurements of oceanic fronts made from a ship-borne platform during the 2nd ONR/NRL High Resolution Remote Sensing experiment (HIRES-II). These are compared with in-situ Acoustic Doppler Current Profiler (ADCP) measurements and occurrence of whitecap events recorded using a closed circuit TV camera. The results show that dual polarized radar operating in this angular regime can provide useful information about the current variability, occurrence of wave breaking and the effects of fronts on the propagation of ocean waves. This information is important for understanding and modeling the physical mechanisms governing the radar imaging of oceanic fronts.

INTRODUCTION

Wave-current interaction along oceanic fronts cause an increase in surface roughness to occur, allowing them to be detected by imaging radars. Modeling electromagnetic scattering from such features usually involves predicting the modulation of the ocean surface wave spectral density from knowledge of the behavior of the currents across the front. These predictions are then combined with the composite surface scattering model to estimate radar cross section variations. It has been found that agreement with observations is seen only when a contribution due to wave breaking is included in the scattering model [1]. Therefore, the current variability, frequency of wave breaking events and the effect of the varying flow on the propagation of ocean waves are important for understanding and modeling the physical mechanisms governing the radar imaging of oceanic fronts.

Recently, it has been demonstrated that scattering from the sea surface for vertical polarization at low grazing angles can be reasonably well explained using the Bragg scattering model, whereas, that for horizontal polarization is sensitive to wave breaking events [2]. Using the Bragg model the Doppler peak spectral shift can be related to motions of the ocean surface, such as currents and orbital velocity of the waves [3]. Therefore, dual polarized Doppler radar measurements offer the potential to provide information about the processes involved in the radar imaging of oceanic fronts.

This paper presents dual polarized Doppler radar measurements of oceanic fronts made during the 2nd ONR/NRL High Resolution Remote Sensing experiment (HIRES-II). This experiment took place off the coast of Cape Haterras, North Carolina, where distinct radar signatures frequently occur as Gulf Stream water interacts with coastal waters. Average radial scatterer velocity and consecutive Short-Time Fourier Transforms (STFT's) are computed and compared with concurrent ADCP measurements and whitecap events detected with a closed circuit television camera. The results are used to investigate the utility of dual polarized Doppler radar operating in the low grazing angle regime for remotely sensing the current variability, occurrence of wave breaking and the effects of fronts on the propagation of ocean waves.

MEASUREMENT CONCEPT

The dual polarized Doppler radar was deployed on the port side of the USNS Bartlett as shown in fig.1 [4]. Coherent radar scattering measurements were made over a range swath of 1 km using a range resolution of 3.75 m. A total of 64 range cells spaced 15 m apart were placed across the 1 km swath. A range resolution smaller than the range cell spacing was used so that a large range extent could be covered while maintaining high range resolution. Data were collected as the ship transected individual fronts and stored on Exabyte 8 mm magnetic tapes for off-line processing. A Global Positioning System (GPS) receiver interfaced to a PC computer recorded the position of the ship. The TV camera mounted on the bow of the ship collected video imagery of the sea surface from which whitecaps were detected. The ADCP measurements were made using NRL's TOwed ADCP (TOAD). The ADCP is mounted on a 3 m long tubular body and was towed in the undisturbed water on the starboard side of the ship. Currents observed at the shallowest bin at a depth of 1.7 m were compared with the Doppler radar radial scatterer velocity measurements.

0-7803-3068-4/96$5.00©1996 IEEE

SURFACE VELOCITY MEASUREMENTS

At low grazing angles shadowing of the smaller waves by larger ones can occur. For the dual polarized Doppler radar in the configuration used in the HIRES-II experiment the grazing angles ranged from 0.5 degrees at the farthest range to 1.8 degrees at the nearest range. The change in the grazing angle across the swath causes the shadowing to become more severe with increasing range. Therefore, as range increases only the larger waves with higher orbital velocities are visible to the radar, causing the Doppler peak spectral shift to move to a higher velocity. This effect is a problem as it could mask the current variation.

Since the radar has enough range resolution to resolve individual wave crests, the largest radar cross section crests can be isolated from those with a smaller cross section. These peaks should have on average the same orbital velocity independent of range. Therefore, by averaging the radial scatterer velocities associated with the largest radar cross section peaks only will lessen the effect of the shadowing. To accomplish this task, consecutive 0.5 s averages of the backscatter power and radial scatterer velocity time series were computed for each individual range cell over a two minute time interval. Backscatter power was averaged incoherently and the radial scatterer velocity was computed using the cross Wigner-Ville instantaneous frequency estimator [4], [5]. For each range cell, the average radial scatterer velocity was formed by computing the average of the velocities associated with the 21 highest backscatter power averages in the two minute interval.

Fig.2 shows average radial scatterer velocity versus range (top) and TOAD measured current vectors (bottom) for a front separating green-colored water to the north from light-blue-colored water to the south. The front was oriented approximately southwest to northeast and the radar viewed it from the north side with a line of sight direction of 192 ^{o}T. Waves were propagating towards the radar in a direction approximately along the radar line of sight. Positive velocities are towards the radar. The

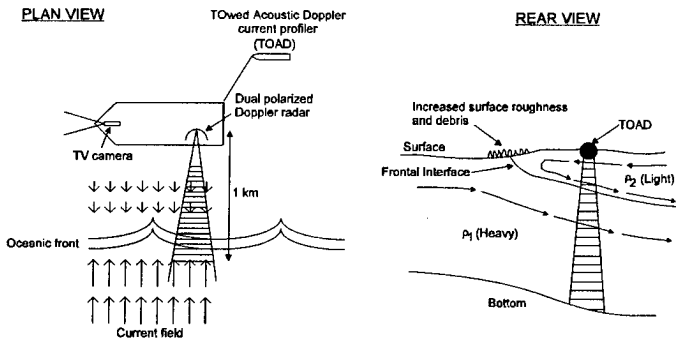


Figure 1. Measurement concept.

radial scatterer velocity on the north and south sides of the front were found by averaging the velocities over the range intervals 250 m to 400 m and 850 m to 1000 m, respectively. These velocities were 100 cm/s on the north side and 142 cm/s on the south side. The radial scatterer velocity on the south side of the front is larger than that on the north side of the front by 42 cm/s, indicating that the water masses were converging there. The largest velocity is seen at the front with a speed of 178 cm/s.

The TOAD measured velocity projected in the radar line of sight direction is shown below the current vectors in fig.2 and is 75 cm/s for the south side of the front and 37 cm/s for the north side. The difference between the projected velocities across the front is 38 cm/s which is in good agreement with the difference in the radial scatterer velocity measurement across the front. This results shows that except at the immediate vicinity of the front, vertically polarized Doppler radars have the potential to measure current variations across it.

Radial scatterer velocity versus range for a similar case is shown in fig.3. For this particular scenario the front was again oriented approximately southwest to northeast and the radar viewed it from the north side with a line of sight direction of 151 ^{o}T. Waves were propagating in a direction nearly perpendicular to the line of sight. TOAD current vector observations indicate that the water masses were converging at the boundary. However, the radial scatterer velocity on the north side of the front is larger than that on the south side, indicating a diverging flow in contradiction with the TOAD observations. A study of the TV video recording showed that the waves were propagating in a more northerly direction on the north

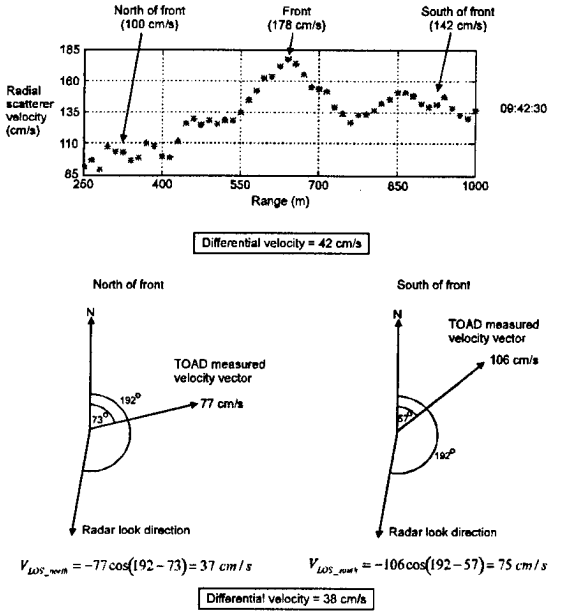


Figure 2. Radial scatterer velocity and TOAD measured currents showing convergence at a front.

side of the front due to the interaction of the waves with the changing current, giving rise to the apparent divergence observed by the radar. Since the radial scatterer velocity is a function of the cosine of the angle between the line of sight direction and the wave propagation direction, the radial scatterer velocity is very sensitive to changes in the direction of wave propagation for this particular case. This result shows that vertically polarized Doppler radars also have the potential to study the effects of fronts on wave propagation.

WAVE BREAKING OBSERVATIONS

Whitecap events were detected from the video recordings off-line. The time that whitecaps of length greater than 0.25 m reached their maximum were recorded. These times were then used to form a time series of the number of detected whitecap events per minute. Fig.4 (top) shows this quantity for video recordings made as the ship traversed a front separating rough green-colored water from calm blue-colored water. The number of detected whitecap events falls from 16 on the rough water side to 7 on the calm water side. Fig.4 (bottom) shows consecutive STFT's of both horizontally and vertically polarized scattering from a single range cell for the same front crossing. The individual broadband events result from scattering from individual wave crests as they pass through the radar resolution cell. A significant change in the Doppler spectral characteristics occurs as the cell crosses the front. For vertical polarization the magnitude and bandwidth are smaller on the calm water side of the front. For horizontally polarized scattering, however, the magnitude drops dramatically as the front is traversed and is scarcely detectable for scattering on the calm side of the front. These changes occur coincidentally with the decrease in the number of detected whitecap events per minute, indicating that Doppler characteristics may be potentially useful for determining the spatial variability of whitecap occurrences across an oceanic front.

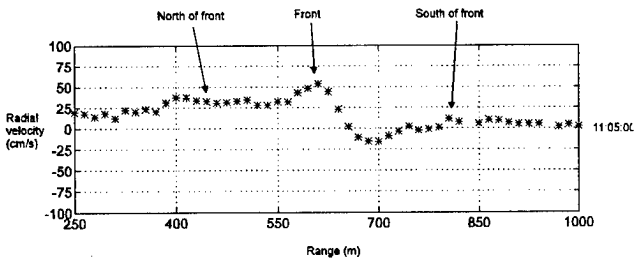


Figure 3. Radial scatterer velocity showing divergence at a front.

SUMMARY

Dual polarized Doppler radar measurements of oceanic fronts were made off the coast of Cape Hatteras, North Carolina. Radial scatterer velocity and STFT's were computed and compared with current measurements made with an ADCP and whitecap events observed with a closed circuit TV video camera. The results show that dual polarized Doppler radar measurements provide useful information about the current variability and the occurrence of wave breaking across oceanic fronts and the effects of fronts on wave propagation.

REFERENCES

[1] G.O. Marmorino, R.W. Jansen, G.R. Valenzuela, C.L. Trump, J.S. Lee, and J.A.C. Kaiser, "Gulf Stream convergence imaged by synthetic aperture radar," J. Geophys. Res., vol. 99, no. C9, pp. 18,315-18,328, 1994.

[2] P.H.Y. Lee, J.D. Barter, K.L. Beach, C.L. Hindman, B.M. Lake, H. Rungaldier, J.C. Shelton, A.B. Williams, R. Yee, H.C. Yuen, "X band microwave backscattering from ocean waves," J. Geophys. Res., vol. 100, no. C2, pp. 2,591-2,611, 1995.

[3] D.B. Trizna, "A model for Doppler peak spectral shift for low grazing angle sea scatter," IEEE J. Oceanic Eng., vol. 10, no. 4, pp. 368-374, 1985.

[4] N. Allan, "Dual polarized Doppler radar measurements of oceanic fronts," unpublished.

[5] B. Boashash, "Estimating and interpreting the instantaneous frequency of a signal-part 2: Algorithms and applications," Proc. IEEE, vol. 80, no. 4, pp. 540-568, 1992

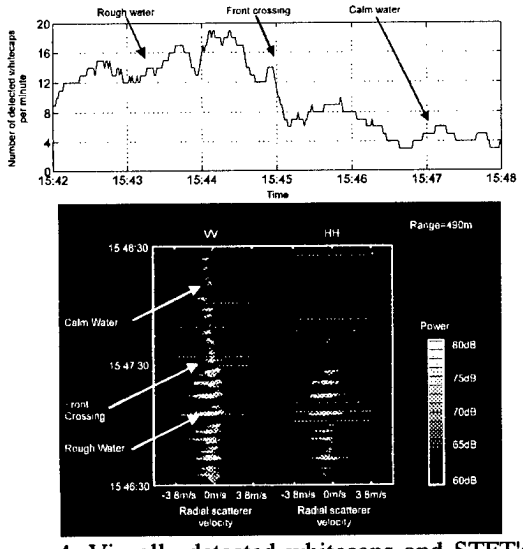


Figure 4. Visually detected whitecaps and STFT's of backscattered signals

Effects of Wave Breaking on SAR Signatures Observed near the Edge of the Gulf Stream

D.R. Lyzenga
Department of Naval Architecture and Marine Engineering
University of Michigan
Ann Arbor, MI 48109-2145
Tel 313-764-3216, Fax 313-936-8820
lyzenga@umich.edu

Abstract -- This paper examines the role of wave breaking in the formation of the bright linear features that appear in SAR images collected near the edge of the Gulf Stream. Results from a recent set of laboratory experiments are used to develop a relationship between the rate of energy dissipation and the generation of small-scale roughness by breaking waves. This source function is found to exceed the direct generation of waves by the wind at high wavenumbers when there are large current gradients. The changes in the small-scale roughness and radar backscatter due to this mechanism are estimated and the results are compared with SAR observations from the High-Resolution Field Experiment.

INTRODUCTION

SAR images collected near the edge of the Gulf Stream contain bright linear features that appear to coincide with regions of strongly converging surface currents associated with ocean fronts, internal waves, and flow over bottom topographic features. Wave-current interaction models based on the wave action equation have been used with some success to predict the changes in the surface roughness and radar backscatter for such features [1,2]. However, the changes in the wave spectra predicted by these models decrease rapidly with increasing wavenumber, due to the wavelength dependence of the relaxation rate. When coupled with a Bragg scattering model, these results imply much smaller changes in the radar backscatter at higher radar frequencies such as X-band (3 cm wavelength) than at L-band (25 cm wavelength). This behavior is observed for some types of SAR image features, but not for the bright linear features considered in this investigation.

One possible explanation for this discrepancy is the effect of wave breaking. An increased radar backscatter has been observed from breaking surface waves by many investigators, and several mechanisms have been proposed to explain these observations. The proposed mechanisms include specular scattering from large surface slopes, edge diffraction effects from the sharp crests of waves just before breaking, and Bragg scattering from the small-scale surface roughness generated during the breaking process. In this paper, the latter mechanism is evaluated by extrapolating laboratory measurements of breaking waves to the ocean, using the rate of energy disspation in the breaking wave as the scaling parameter.

SMALL-SCALE ROUGHNESS GENERATED BY BREAKING WAVES

Some empirical information regarding the generation of small-scale surface roughness by wave breaking can be drawn from recent laboratory experiments by Walker *et al.*[3]. These experiments indicate that small-scale surface disturbances are created in a localized region on the forward face of the breaking wave, and are swept backward over the crest into the following trough. Due to the interaction of these short waves with the diverging surface currents on the rear face of the breaking crest, their wavelengths are increased and their associated height variance is reduced by about an order of magnitude by the time they reach the zero crossing following the breaking wave crest. However, a significant amount of short wave energy also escapes from this region and subsequently decays more slowly due to the effects of viscosity and turbulence.

Surface roughness measurements were made during these experiments using an optical technique, and two-dimensional wavenumber spectra were estimated at various locations along the breaking wave surface. The rate of energy dissipation in the breaking wave was controlled by changing the angle of attack of the hydrofoil that was used to generate the breaking wave, and the energy dissipation per unit crest length was inferred from measurements of the wave kinetic energy at the zero crossings on either side of the breaking crest. The spectra measured near the breaking crest have a significantly different shape depending on the energy dissipation, but outside of the breaking region the spectra all have a similar shape, with an amplitude that is proportional to the energy dissipation rate. This observation suggests that the rate of production of short wave energy may be described by means of a source function which has the form

$$S_b \equiv C(K)\ E(k,\phi) = f(k,\phi)\ D_\lambda \qquad (1)$$

where $C(K)$ is the phase speed of the breaking wave, $E(k,\phi)$ is the short wave spectral energy density and D_λ is the energy disspation rate per unit crest length. The function $f(k,\phi)$ was estimated by computing the energy spectrum from each of the measured height spectra and scaling the results by $C(K)/D_\lambda$. The resulting data points were then fit to a function of the form

0-7803-3068-4/96$5.00©1996 IEEE

$$f(k,\phi) = a\,k_o\left\{1-\left(\frac{k_o}{k}\right)^2\right\}k^{-3} \quad \text{for} \quad k>k_o \qquad (2)$$

where $a \approx 0.0026$ and $k_o \approx 15.4$ rad/m. This function appears to fit the experimental data quite well, as shown in Figure 1. However, the breaking waves in this experiment all had a wavelength of about 80 cm, so it is necessary to make some assumptions to generalize these results to other wavelengths. Noting that the cutoff wavenumber k_o is about twice the wavenumber of the breaking wave for this case, we will assume that this is true in general. It may also be noted that the integral of $f(k,\phi)$ over all wavenumbers is independent of k_o and is equal to about 0.011, which would imply that a little over one percent of the energy dissipated during breaking is converted into shorter wave energy in the "far field" of the breaking wave.

For a random sea containing a wide range of breaking wave lengths, the total rate of production of short wave energy due to wave breaking is predicted on the basis of this model to be

$$S_b(k,\phi) = \int\!\!\int f(k,\phi)\; D(K,\Phi)\; K\; dK\; d\Phi \qquad (3)$$

where $D(K,\Phi)$ is the rate of energy dissipation per unit wavenumber. If the wave field is in a state of equilibrium, with the energy input from the wind being balanced by dissipation, the total rate of energy dissipation is given by

$$D_{tot} = \int\!\!\int \beta(K,\Phi)\; E_o(K,\Phi)\; K\; dK\; d\Phi \qquad (4)$$

where $\beta(K,\Phi)$ is the growth rate or wind input parameter and E_o is the equilibrium energy spectrum. Ignoring the energy transfer due to nonlinear wave-wave interactions, there is also an approximate "local" energy balance, so that

$$D(K,\Phi) \approx \beta(K,\Phi)\; E_o(K,\Phi)\;. \qquad (5)$$

This equation was evaluated using the growth rate proposed by Donelan and Pierson [4], *i.e.*

$$\beta = 0.194\frac{\rho_a}{\rho_w}\left[\frac{\overline{U}(\lambda/2)}{c}\cos(\Phi-\Phi_w)-1\right]^2\omega \;-\; 4\nu k^2 \qquad (6)$$

along with an equilibrium energy spectrum of the form

$$E_o(k,\Phi) = \rho_w\, g\, S_{PM}(k)\left\{1-\left(\frac{k}{k_c}\right)^2\right\}^{-1} A(\Phi-\Phi_w) \qquad (7)$$

where $S_{PM}(k)$ is the Pierson-Moskowitz wave height spectrum converted into wavenumber coordinates, $k_c = 60$ rad/m is a high wavenumber cutoff inferred from measurements by Jaehne and Riemer [5], and

$$A(\Phi-\Phi_w) = \frac{4}{3\pi}\cos^4[(\Phi-\Phi_w)/2] \qquad (8)$$

is the normalized angular distribution of the energy spectrum. The dissipation rate from (5) was substituted into (3), which was numerically integrated to obtain the short wave energy production rates for several wind speeds. The results for a wind speed of 5 m/s are shown in Fig.2 along with the rate of energy production due to direct wind growth.

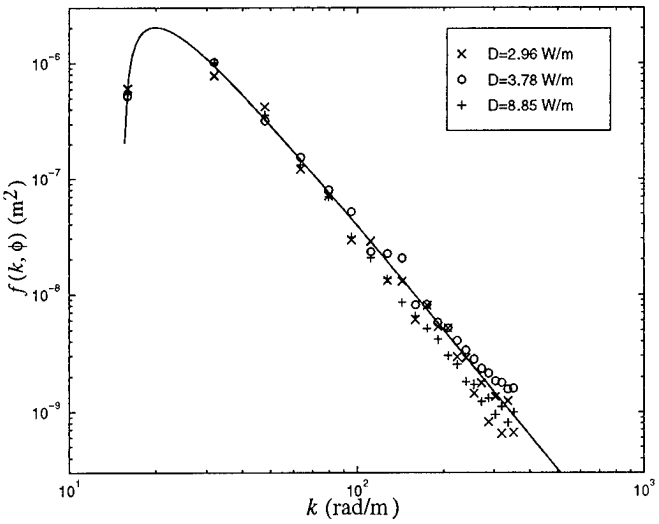


Fig. 1. Breaking wave source distribution function derived from laboratory measurements by Walker *et al.* [3].

WAVE-CURRENT INTERACTION MODELING

The interaction of a continuous spectrum of ocean waves with a surface current which varies only in the x-direction can be described by the equation

$$\frac{\partial N}{\partial t} + (c_{gx}+u)\frac{\partial N}{\partial x} - \left[k_x\frac{du}{dx} + k_y\frac{dv}{dx}\right]\frac{\partial N}{\partial k_x} = F_N(N) \qquad (9)$$

where N is the action spectral density, c_{gx} is the x-component of the group velocity, u and v are the x and y components of the surface current, k_x and k_y are the x and y components of the wavenumber, and $F_N(N)$ is the net source function for wave action [6, 7]. This equation can be rewritten in terms of the energy spectrum $E = \omega N$, where ω is the wave intrinsic frequency, as

$$\frac{\partial E}{\partial t} + (c_{gx}+u)\frac{\partial E}{\partial x} - \left[k_x\frac{du}{dx} + k_y\frac{dv}{dx}\right]\left(\frac{\partial E}{\partial k_x} - \frac{c_{gx}}{\omega}E\right) = F_E(E) \qquad (10)$$

where
$$F_E(E) = \beta E - D + T_{nl}^{\cdot}\;. \qquad (11)$$

In the absence of any currents, the energy input from the wind is balanced by dissipation as discussed in the previous section. When currents are present, additional energy is put into the wave field by the currents and the rate of energy dissipation also increases. In order to estimate the change in the energy dissipation rate due to a given current gradient we will assume that dissipation imposes a hard upper limit to the energy spetrum, so that the spectral density remains close to its equilibrium value E_o. In this case the first two terms on the left hand side of (10) may be neglected. If the energy transfer term is assumed to depend only on the spectral shape, the first and last terms on the right-hand side of (11) are also nearly constant, implying an increase in the energy dissipation rate of

$$\Delta D = \left[k_x\frac{du}{dx} + k_y\frac{dv}{dx}\right]\left(\frac{\partial E_o}{\partial k_x} - \frac{c_{gx}}{\omega}E_o\right). \qquad (12)$$

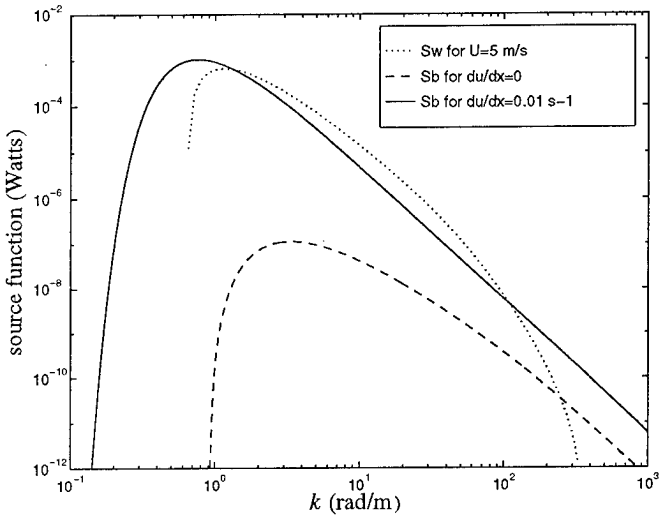


Fig. 2. Comparison of source functions due to direct wind generation (dotted line), breaking waves with no current gradients (dashed line), and breaking waves in the presence of a strong current gradient (solid line).

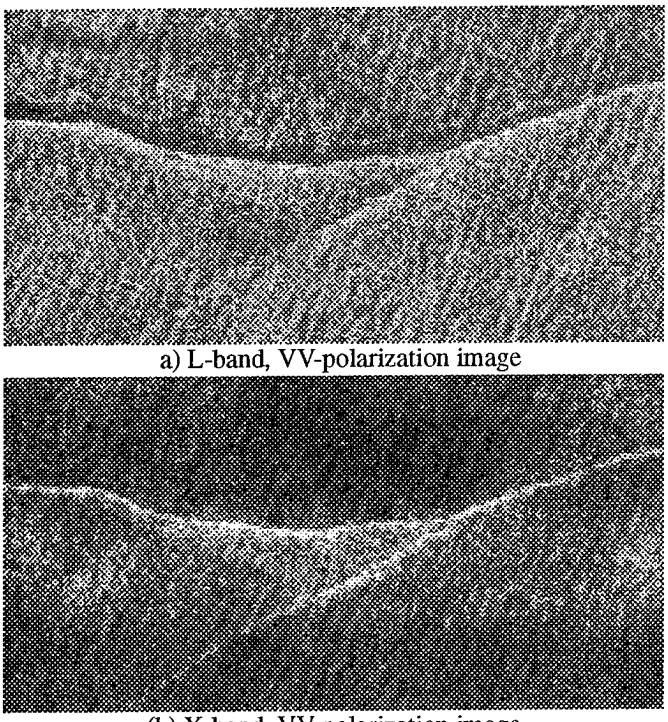
Adding this change to the dissipation rate in (3) produces changes in the source function as shown in Fig. 2 for a strain rate of 0.01 sec^{-1}, which is representative of the features discussed below [8].

DISCUSSION

Segments of simultaneously collected L-band and X-band, VV-polarized SAR images from the High-Resolution Field Experiment are shown in Fig. 3. For an incidence angle of 50° the Bragg wavenumber is 40 rad/m at L-band and 300 rad/m at X-band. The results shown in Fig. 2 indicate that waves at the L-band Bragg wavenumber are primarily wind-generated, but that wave breaking is the dominant source of X-band Bragg waves. Thus, variations in the amount of wave breaking due to wave-current interactions are expected to have little effect at L-band but a large effect at X-band for this case. Although additional modeling is required to evaluate the changes in the wave spectral density, it seems reasonable to assume that the spectral density and thus the radar backscatter is roughly proportional to the source strength in this spectral region. The observed modulations, which are on the order of 8-10 dB for the X-band image and 3-4 dB at L-band, are consistent with the results shown in Fig. 2 if this assumption is correct.

ACKNOWLEDGMENTS

This work was supported by the Office of Naval Research under Contract No. N00014-93-1-0105. The laboratory measurements upon which this work is based were made under the ONR University Research Initiative project at the University of Michigan. SAR images were processed at the Environmental Research Institute of Michigan.



a) L-band, VV-polarization image

(b) X-band, VV-polarization image

Fig. 3. ERIM/NAWC SAR images collected near the edge of the Gulf Stream on September 16, 1991 (pass 15).

REFERENCES

[1] B.A.Hughes and R.F.Gasparovic, "Introduction," J. Geophys. Res., vol. 93, p. 12217, 1988.

[2] D.Lyzenga,"Interaction of short surface and electromagnetic waves with ocean fronts," J. Geophys. Res., vol. 96, pp. 10765-10772, 1991.

[3] D.Walker, D.Lyzenga, E.Ericson, and D.Lund, "Radar backscatter and surface roughness measurements for stationary breaking waves," Proc. Roy. Soc. Lond. A, in press.

[4] M.Donelan and W.Pierson, "Radar scattering and equilibrium ranges in wind-generated waves with application to scatterometry," J. Geophys. Res, vol. 92, pp. 4971-5029, 1987.

[5] B.Jaehne and K.Riemer, "Two-dimensional wave number spectra of small-scale water surface waves," J. Geophys. Res., vol. 95, pp. 11531-11546, 1990.

[6] B.Hughes, "The effect of internal waves on surface wind waves, 2.Theoretical analysis," J. Geophys. Res., vol. 83, pp. 455-465, 1978.

[7] O.Phillips, "On the response of short ocean wave components at a fixed wavenumber to ocean current variations," J. Phys. Oceanogr. vol. 14, pp. 1425-1433, 1984.

[8] G. Marmorino, personal communication, 1996.

Issues Surrounding Surfactant Effects Upon Radar Imagery of Convergent Ocean Surface Flows with Application to the Hi-Res I Rip Feature

A. L. Cooper, S. R. Chubb, and J. A. C. Kaiser
Remote Sensing Division
Naval Research Laboratory
Washington, D. C. 20375-5351, U. S. A.
T: 202.767.2292, F: 202.767.3303, EMAIL: cooper5@nrlfs1.nrl.navy.mil

Abstract -- X-band radar signatures of a current rip convergence, resulting from denser Gulf stream fluid interacting with fresh coastal shelf water near Cape Hatteras, were observed during the First High Resolution (Hi-Res I) experiment[1]. These signatures, which appeared as intense (~10 dB) enhancements in radar cross section (RCS) in the form of meandering linear segments, were accompanied by secondary parallel meandering segments of reduced (~5-10 dB) RCS on the shelf water side. The effects of wave-current interaction scale with the surface velocity (u) while the effects of surfactants scale as the ratio of surface current to phase velocity (u/c). Unlike internal waves which 'graze' upon the ambient surface film material, current rips 'herd' the ambient surface film material to a convergence point where u/c=1. The latter features can induce singular behavior for a monomolecular surface film. A number of fundamental issues need to be resolved including: continuity of the surface film in regions of wave breaking[2]; buckling of the monomolecular film; and subduction of the surfactant at the frontal boundary. These issues are highlighted through application to the Hi-Res I rip feature using a simplified one-dimensional model of the feature as well as the surface manifestation of currents derived from the associated depth-dependent structure.

Introduction

It is well known that the presence of an elastic surface film can have a profound effect upon an ocean surface wave field. The short gravity-capillary and capillary waves are most strongly modulated by the elastic film. A surface flow-field convergence tends to concentrate or compress these materials whereas a flow-field divergence tends to dilute or reduce their local concentration. The surface currents may also modulate the ocean wave spectrum directly through wave-current interactions. In order to characterize the effects of surface active materials upon the surface wave field and to distinguish them from the more direct effects due to wave-current interactions, it is necessary to solve the wave action equation including surfactant-induced wave damping in combination with an evolution equation and equation of state of the surfactant material.

During recent experiments, associated with the Naval Research Laboratory (NRL) Accelerated Research Initiative (ARI), High Resolution Remote Sensing sponsored by the Office of Naval Research, X-band real aperture radar (RAR) images of a current rip feature off the coast of North Carolina in the vicinity of Cape Hatteras were obtained by Askari [1]. Additionally, "simultaneous" ground truth was gathered from the two ships involved in the experiment. These measurements have defined the feature to be that of a strong current rip convergence front. In those experiments, the resulting radar images of this feature displayed a corrugated bright image with an amplitude of approximately 300 m and a wavelength of the order of 1.5 km. Running essentially parallel to the bright signature was a dark band displaced slightly to the shelf-side. The existence of this dark band suggests wave damping due to accumulated surfactant as a possible mechanism. In this paper, we model the ocean wave spectral modulations and the radar signatures produced by current rip convergent features of that type in the presence of surfactants. We simulate the current rip feature surface velocity field similar to that observed in the recent High Resolution Remote Sensing ARI experiments. It is the objective of this study to examine the simultaneous effects of wave-current interaction and surfactant damping for current rip type features of this type in order to assess the relative contributions of each of these phenomena in the modulation of the spectral density and the generation of the radar imagery and to highlight some of the important scientific issues associated with these types of features.

Modeling of Surfactant Effects

For the one-dimensional, steady, situation considered here, the wave-action equation is written as

$$(c_{gx}+u-c)\left(\frac{\partial N}{\partial x}\right)-\left(k_x\frac{\partial u}{\partial x}+k_y\frac{\partial v}{\partial x}\right)\frac{\partial N}{\partial k_x}=-\beta\frac{N}{N_o}(N-N_o)-\gamma N+\Pi$$

where c_{gx} represents the x-component of the group velocity of the waves of wave number **k**, u represents the x-component of the local surface velocity, c represents the phase velocity of the entire rip feature (x-direction), y is the

0-7803-3068-4/96$5.00©1996 IEEE

wave damping rate to be defined below, N denotes the wave action spectral density, and π is the resonant regrowth term due to Phillips. The first term on the right hand side is the Plant-Hughes relaxation term (Eq. 21), discussed above, where N_o the equilibrium spectrum and ß the relaxation rate.

The damping rate, $\gamma(k,E)$, is taken as that of the linearized form due to Dorrestein [9] and Levich [13] is a function of wave number, k, and the film elasticity, E, and is given as

$$\gamma(k,E)=4\theta\omega_0\left[\frac{2\theta-\sqrt{2\theta}\chi+\chi^2/\sqrt{8\theta}}{2\theta-\sqrt{8\theta}\chi+2\chi^2}\right]$$

where:

$$\chi=(Ek^3)/(\rho\omega^2)\ ,\quad \theta=(\nu k^2)/\omega.$$

and ω represents the intrinsic frequency of the wave which is approximately defined by

$$\omega=\sqrt{gk\ +\ \sigma k^3/\rho}$$

with σ denoting the surface tension, ν the kinematic viscosity, g the acceleration of gravity, and p the mass density of the fluid. Note that in the limit of zero elasticity $\gamma=\gamma_{vis}=4\nu k^2$ (viscous damping).

The spreading pressure of the film material is defined as the change in surface tension due to the presence of the film . That is, $p = \sigma_0 - \sigma$ where the subscript 0 denotes the clean (film-free) surface properties. The elasticity is readily computed from a pressure area relationship for the film material and is given as

$$E\ \equiv\ -A(\partial p/\partial A)\ .$$

For an insoluble surfactant, neglecting any vertical transport at the interface, we have

$$\partial\Gamma/\partial t\ +\ \nabla_s\cdot(\Gamma\boldsymbol{u}_s)\ =\ 0$$

where Γ represents the surface surfactant concentration, $\mathbf{u}_s$ represents the surface velocity, and ∇_s the surface gradient operator. If we assume that the behavior is quasi-steady, as a consequence of a Galilean transformation in which the coordinate system is propagated at the phase velocity, **c**, of the feature, we obtain, relative to the translating coordinate system,

$$\partial(\Gamma(u-c))/\partial x=0.$$

Here, we have specialized to a one-dimensional feature flow-field with variation in the x-direction only (u is the velocity component in that direction) with c representing the x-component of the phase velocity of the feature.

The solution of Eq. (1) is simply given as

$$\Gamma/\Gamma_1=A_1/A=(1-(u_1/c))\ /\ (1-(u/c))$$

where Γ_1 represents the uniform ambient surfactant concentration and A_1 represents the ambient film area corresponding to the approaching fluid where $u=u_1$. We note that this predicts singular behavior for the film concentration, Γ, and film area, A, approaching zero when $u/c\rightarrow 1.0$. This is a consequence of the neglect of diffusion or vertical advection of surfactant. In practice, the huge resultant surface concentration would initiate significant diffusion along the surface film and into the bulk material and/or the surfactant film monolayer would be destroyed by buckling.

In order to circumvent the singular behavior predicted by the surfactant evolution equation solution and to model monolayer film buckling, a pressure-area relation due to Barger [3] is used in which the pressure is finite as the area tends to zero.

$$pA\ =\ 51.6\ +\ 102.7p\ -3.9p^2$$

This relation was determined from the behavior of a large number of surfactant samples from various parts of the world evaluated at film pressures from 0 to 10 d/c. The extrapolation to the limiting pressure represents the 'buckling' pressure for the film and defines a zero film elasticity at the singular point. This extrapolation does not represent an accurate description of the film behavior, but it effectively simulates film buckling by limiting the maximum film pressure while establishing a relatively realistic response throughout most of the pressure range. Most importantly, the singular behavior, which is non-physical, is conveniently bypassed.

Results

For simplicity, emphasizing the strong convergence of the basic feature, a simulated velocity has been generated in one-dimension. To approximate the basic north-south flow corresponding to the Hi-Res I rip feature, representing a convergent flow field with a 20 c/s relative convergence velocity occurring across a transition region of approximately 20 m is modeled as

$$U(x)\ =\ -\ 0.1\ \tanh(x/10)$$

Early estimates of the phase velocity of the current rip were that c=0.1 m/s so that the convergence point where u=c would occur on the extremely small velocity gradient portion of the feature. The estimated wind speed was 3 m/s from the south west. With these quantities input into the wave action equation, combined with an assumed uniform ambient surfactant pressure, the surface film distribution can be computed, the modulated spectral density may be

evaluated and the RAR signature can be generated through a composite Bragg scattering model. The resulting rcs is summarized in Fig. 1. For ambient p_0 = 0.5 d/c (upper left plot), the predicted radar return displays a region of reduced backscatter followed by one of increased backscatter with the total signature variation coinciding with the location of the steep values of the velocity gradient, du/dx < 0.0 and | du/dx | >>1. This simulated signature is quite different than that observed in the experiment, in that the relative order of the bright and dark signatures appear to be reversed and the separation between them is grossly underpredicted. In order to retard the occurrence of the dark band in the simulated radar image and thereby shift it relative to the bright variation, a number of additional simulations were made with reduced initial film pressures. These simulations for various levels of initial ambient film pressure are also depicted in Fig. 1. A systematic trend shifting the dark signature to the right (northward in the experiment) is apparent as the ambient film pressure is reduced. The results corresponding to an ambient film pressure of 0.0001 dyne/cm. agree most closely with the experiment. Clearly this represents an extremely low value of the ambient pressure. In fact, this value is lower than the measurement threshold for surface films. One might question the predictions of these extremely small values of film pressure relative to the unique predictions for zero pressure. However, it should be recalled that the convergence considered here is so strong that it predicts singular behavior for the relative concentration ratio driving the film area toward zero. This is due to the fact that we have neglected diffusion, considered an insoluble film and have not allowed for submergence or downwelling of the surface film material due to the convergence. Within these constraints, any finite initial film pressure, regardless of how small, would attain singular concentrations through the assumed rip type convergent flow. For real flows, surfactant diffusion,film buckling and other non-equilibrium effects would retard and hence reduce this compression to finite levels. Additionally, if significant wave-breaking results from the wave-current interaction, any existing compressed surface films would be destroyed with subsequent regeneration and compression retarding the establishment of the compressed surfactant band. The extremely low values of film pressure required in the simulations may be due to the fact that we cannot completely characterize wave breaking and the attendant film destruction. Included within the figure is the case corresponding to zero film pressure or a "clean" surface for comparison. This cross-section variation therefore illustrates the effect of wave-current interactions only; that is, no film damping.

The sensitivity of the relative location of the dark signature due to surfactant damping to the level of ambient film pressure is in large part due to the extremely small value of the velocity gradient at the convergence point for the modeled feature velocity field. Subsequent estimates from experiment for the velocity field and the results of the end-to-end models of Mied et al.[6] and Chubb et al. [2] indicate that the convergence point is located more centrally on the rip convergence where the velocity gradient is close to its maximum value. The migration of the dark signature with ambient film pressure would be almost entirely eliminated. The parallel dark features are possibly due to an upwelling of surfactant associated with a subsurface rotor predicted by Mied et al.[6].

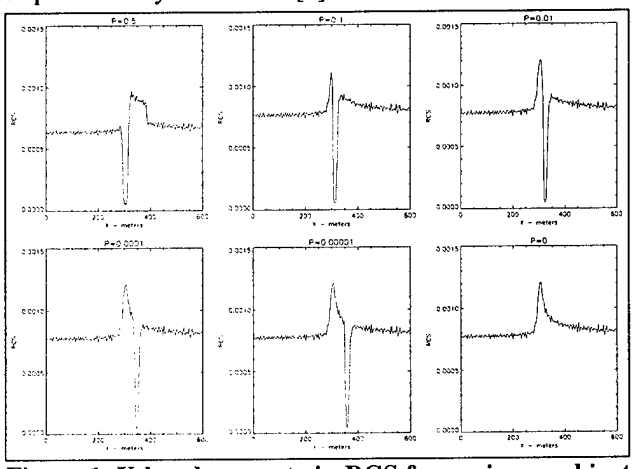


Figure 1. X-band current rip RCS for various ambient film pressures.

REFERENCES

[1] F. Askari, EOS **73**, #43/supplement, 247 (1992). R. P. Mied et al., "High Resolution Remote Sensing." 1992 NRL Review, pp. 181-183, (1992).

[2] S.R. Chubb, A.L. Cooper, R.W. Jansen and C.Y. Shen, "An End-to-End Simulation of Radar Signatures from the Hi-Res I Rip Feature", IGARSS '96, these proceedings, 1996.

[3] W.R. Barger and M.A. Klusty, "Common Features of Natural Surface Films from the Coastal Waters of Maine, Virginia, and Bermuda. I. Pressure and Modulus Data", unpublished Naval Research Laboratory Report, 1993.

[4] R. Dorrestein, "General Theory of the Effect of Surface Films on Water Ripples. I", Proc. Acad. Sci. Amst., pp. 260-272, 1951.

[5] V.G. Levich, "Physiochemical Hydrodynamics", Chapter XI, Prentice Hall, 1962.

[6] R.P. Mied et al, "Frontogenesis with Ageostrophic Vertical Shears and Horizontal Density Gradients: Gulf Stream Meanders onto the Continental Shelf," J. Geophys. Res., to appear (1996).

An Overview of Remote Sensing Education Projects Sponsored by the NASA Space Grant Program

J-M Wersinger
National Aeronautics and Space Administration / George C. Marshall Space Flight Center
Mail Code DS01
Marshall Space Flight Center, AL 35812
Voice: 205-544-9699/Fax: 205-544-5893/Email: j.m.wersinger@msfc.nasa.gov

and

Elizabeth Ward
National Aeronautics and Space Administration
Mail Stop 221
Langley Research Center, Hampton, VA 23681-0001
Voice: 804-864-3299/Fax: 804-864-9083/Email: e.b.ward@larc.nasa.gov

Abstract -- Congress established the NASA National Space Grant College and Fellowship Program (Space Grant) with legislation enacted in 1988. Congress conceived the program to ensure continued US strength in space-related research and education and to capitalize on the multiple opportunities afforded by the space environment. Space Grant consists of a national network of 52 university-based consortia in the 50 states, the District of Columbia, and Puerto Rico. These consortia partner over 550 affiliate institutions. Members include colleges, universities, business and industrial partners, state and local government agencies, and other nonprofit organizations. Space Grant consortia actively engage in remote sensing education on a variety of fronts that span informal education to faculty internships. With its presence in every state, Space Grant provides an effective interface for the formation of partnerships among NASA program offices, university and precollege educators, researchers, business and industry, and state and local governments. Specifically, Space Grant is presently building partnerships with NASA's Mission to Planet Earth (MTPE) and with the Cooperative Extension Service (CES). The partnership with MTPE will bring space imagery to class rooms from kindergarten through college. As a facilitator with a multidimensional interface, Space Grant may help to alleviate the duplication of effort that often plagues educational projects. The partnership with CES will bring information and expertise about RS data and products to local communities in the areas of agriculture, land use, wetlands, forestry, water management, and others.

THE NATIONAL SPACE GRANT COLLEGE AND FELLOWSHIP PROGRAM

With legislation enacted during the late 1980s, Congress created the Space Grant Program to insure a continued and adequate workforce in space endeavors, to promote space and science literacy and to provide public service by bringing the benefits of space to US citizens. During the first five years of its operation, Space Grant developed thousands of successful education, research and public service programs. Cumulatively, the consortia have awarded over 6500 fellowships and scholarships to US citizens. With a matching funds component, consortia members have leveraged non federal funds to approximately double the Space Grant budget. A significant number of education programs involve satellite imagery and RS data. Space Grant is now poised to expand its RS efforts on two fronts: in education in a partnership with MTPE and in outreach in partnership with CES. After a description of RS education programs now in place at Space Grant institutions, we shall present the efforts underway in developing these partnerships.

REMOTE SENSING EDUCATION PROGRAMS AT SPACE GRANT INSTITUTIONS

Over half of the 52 Space Grant consortia report the use of remote sensing in Earth Systems Science education. The range of activity spans informal science museum programs through university faculty training. Space Grant consortia employ diverse education vehicles such as precollege teacher training seminars, elementary through secondary school classrooms, university level courses, and faculty training at Earth Observing System Data Centers. Space Grant developed courses and materials focus on the interdisciplinary use of remotely sensed data and instrumentation. Space Grant contributes thousands of dollars annually to provide student and faculty training in remote sensing. In addition to traditional education venues, Space Grant consortia have also used remote sensing to aid state and local economic development.

0-7803-3068-4/96$5.00©1996 IEEE

Individual state consortia boast many outstanding programs and materials in remote sensing; a few examples follow. The University of Alaska Science Museum, with support from the Alaska Space Grant Consortium, has developed a set of user-friendly materials designed to teach Alaskan precollege students how to interpret satellite images of the environment. Similarly, the GAIA Crossroads project, co-sponsored by Apple Computer, the Maine Space Grant Consortium and others, teaches precollege students in 86 Maine schools how to interpret images of their local communities. As a GAIA participant, Wiscasset Primary School purchased what is believed to be the first school-owned real-time satellite receiving station that can access data from the NOAA polar orbiting satellites and the GOES stationary satellites. The receiving satellite has increased educational opportunities in the classroom and has led to non-school related requests for information by state and local officials. In Kennebunk, image-savvy students assisted town fire marshals in discovering fire ponds for use with local fire-fighting needs.

The Hawaii Space Grant consortium provided expert consultation to determine GIS applications for the state, to assess the need for remotely sensed data in American Flag territories in the South Pacific, to interpret lava flow information from island volcanoes, and to develop a low-cost remote sensing device for a local business. The consortium has used these and other experiences to implement undergraduate level courses in remote sensing using satellite data gathered from the islands. The Nevada Space Grant consortium has funded faculty research that studies the application of remotely sensed data to traffic problems on the nation's highways. Wyoming's Space Grant consortium has funded a full-time faculty member to develop courses in remote sensing. The consortium created and distributed a Wyoming CD ROM to all secondary science and mathematics school teachers in the state. The CD contains images of Wyoming for use in image processing tasks. Wyoming has joined with several other state Space Grant consortia and the EOS data center (SD) to form the Upper Midwest Consortium. This new consortium plans to take full advantage of the Earth Systems Science Education initiative by offering courses, teacher and faculty training, and technology transfer products to meet the agricultural needs of local communities.

As a student project partially funded by the National Space Grant program, Arizona State University is building and will launch AUSat 1, a satellite designed to collect meaningful data on the Earth's aurora. Mississippi Space Grant, in cooperation with Stennis Space Center, has developed a community college project that places remotely sensed images and other data on the World Wide Web for use in Earth Systems science courses.

Maryland Space Grant has co-developed the *Educators' Manual for Satellite Image Interpretation,* a teacher's guide for using remotely sensed imagery in the classroom. The California Space Grant consortium, introduced the KIDSAT project--designed to place relevant space imagery into the hands of precollege teachers and students for practical local application. Space Grant institutions have conceived and implemented myriad other projects or activities that employ the use of remotely sensed Earth systems data. The National Space Grant program, through its network of state consortia, will continue to fund these and other yet to be developed projects with the vision of making remote sensing a user-friendly, economically important, educational tool for the 21st century.

BRINGING THE BENEFITS OF REMOTE SENSING TO CITIZENS THROUGH PARTNERSHIPS

NASA organizes its activities around strategic enterprises. A premier NASA strategic enterprise is MTPE, a scientific research program designed to study global climate change. This study is made by collecting large amounts of data from remote sensing satellites which are used for scientific modeling of the global climate. In parallel, at its Stennis Space Center, NASA is also involved in collaborations with space industries to develop satellites and sensors for commercial remote sensing. Space Grant has defined as one of its objectives to provide the benefits of NASA's MTPE and commercial RS data and products to the public. This is to be done through partnerships. To explore possible partnerships with MTPE and Cooperative Extension Service, Space Grant has organized two conferences in 1995.

The "NASA Space Grant Conference on Extending Remotely Sensed Data to Local Communities in the Southeastern US" took place in Huntsville, AL on June 12-13, 1995. This first conference brought together about 60 participants from CES, Space Grant, MTPE, universities and corporations. This was a Get-Acquainted meeting whose goal was for participants of such varied backgrounds to learn about each others interests and concerns. The discussion made it clear that MTPE data and products would find their best use in education rather than with CES since they will have less resolution, will be more global and will be available on a less timely basis than commercial RS data. On the other hand, commercial RS data and products will be more suitable for applications like agriculture, forestry, land use, etc. and could be extended to local communities through the CES network. A second meeting took place in Biloxi, Mississippi Nov. 30-Dec. 1, 1995 entitled "The NASA Space Grant Extension Workshop on Remote Sensing". Its goal was to identify pilot projects in education and extension facilitated by Space Grant. The workshop brought together over 120 participants from all

parts of the country. Topics discussed were college and precollege education, precision agriculture, land use, weather and agriculture, wetlands and forestry, plant stress detection, and water management. The CES specialists and county agents present (about 30% of the participants) expressed great interest in using RS and GIS products with the public they serve. A number of commercial RS and GIS providers present encouraged CES personnel to be trained in RS and GIS to provide expertise to the public they serve. Several pilot projects were identified. The outlines for partnerships and projects with MTPE and CES as recommended at the last conference follow.

Space Grant educational initiatives and partnership with MTPE

In precollege education, Space Grant universities may organize teacher training workshops in their States using education materials produced by MTPE. They may also monitor the effectiveness of these materials. Space Grant as a whole could act as a clearinghouse for such materials and help reduce duplication of efforts. This could be a very effective way for Space Grant to support national education initiatives.

In college education, Space Grant may help establish a curriculum for an undergraduate RS/GIS program and use its banner to accredit this program and thus help universities to establish such a curriculum. Another recommendation is for Space Grant to establish fellowships for professionals to work with some of the data providers like MTPE to create instructional materials. That would benefit both MTPE people in learning what educational products are needed and the faculty fellow who would learn what is available in the MTPE archives and what it takes to produce the products.

Space Grant partnership with CES

The Cooperative Extension Service is an association between the US Department of Agriculture, Land Grant universities and county governments whose purpose is to improve people's lives. It has a national network with offices in over 3,000 counties in the US. Historically, CES focused on agriculture and rural community problems. Recently, its emphasis has shifted to modern day issues. Its programs now emphasize help to communities in economic transition, people's health, food safety and quality, the plight of young children, sustainable agriculture, waste management, water quality and help to youth at risk. Land Grant Universities organize and monitor the work done by CES county agents in their State. Thus, CES has a nationwide network devoted to helping people in local communities at the county level.

Land Grant Universities have specialists in agriculture, home economics, environmental issues, land use, weather, etc. These specialists are often researchers and teachers in various departments on the Land Grant campuses. They train and support CES county agents who directly help citizens in their communities and play a role in city councils, civic clubs and county government. Space Grant sees the CES network as a conduit with access to local communities for its outreach and public service effort. CES sees Space Grant as a partner that gives it access to space technology, training and information.

Many Space Grant universities are also Land Grant institutions and can work in partnerships with CES in their State. Initially, these partnerships' will be to inform local communities on the potential uses of RS/GIS products. Later, as use of RS/GIS products will become commonplace, the partnerships will provide expert advice on new products and on how to solve specific problems encountered in the use of products. In both steps Space Grant consortia will facilitate the training of CES personnel in RS/GIS for specific uses (agriculture, disaster relief, land use, environmental issues, etc.). Training CES specialists has a considerable leveraging effect since the specialists in every State will train and support the county agents in that State. A goal would be to have a RS/GIS specialist in CES in each State, perhaps partially funded by NASA.

At the Biloxi Workshop, it was recommended that Space Grant initiate a campaign of information on the potential of RS/GIS through media, through CES at the local community level, at farmers' fairs and at county agents' national meetings. This campaign could influence the rate of adoption of RS/GIS products by farmers, foresters, city developers, etc., and facilitate the onset of a booming remote sensing industry.

CONCLUSION

Since 1991 more than half of the nation's Space Grant consortia have produced and implemented the use of remotely sensed products for curriculum and instruction at both the precollege and university levels. Faculty are being trained to understand and transform raw data for classroom use. Space Grant students and faculty engage in satellite design and construction. Expanding on these achievements, the Space Grant Program is now initiating a partnership in education with NASA's Mission to Planet Earth. Space Grant has also started an aggressive outreach effort in association with Cooperative Extension Service personnel to provide local communities with the benefits of RS/GIS products.

MISSION TO PLANET EARTH
ON-LINE EARTH SYSTEMS SCIENCE COURSE

Craig Blurton, Ph.D.
NASA Classroom Of The Future
316 Washington Avenue
Wheeling, WV 26003
Telephone: 304/243-2388
FAX: 304/243-2497
Email: craigb@cotf.edu

Steven McGee, Ph.D.
NASA Classroom Of The Future
316 Washington Avenue
Wheeling, WV 26003
Telephone: 304/243-2388
FAX: 304/243-2497
Email: mcgee@cotf.edu

ABSTRACT

The National Aeronautics and Space Administration (NASA) has a leadership role in Earth Systems Science research for the United States with the Mission to Planet Earth (MTPE) program, which, making use of satellite technology, remote sensing, and image processing, is altering our understanding of our planet.

Although significant effort is going into the MTPE program, and although the implications of this research will have widespread impact on environmental, scientific, social, political, economic, and health policies worldwide, few teachers and far fewer students are aware of these efforts, or have the skills and knowledge necessary to understand them. Typically, students and teachers do not have experience with analyzing problems on an ecosystem or biosphere scale. But MTPE's scientific studies hold great potential to enhance, enrich, and extend the K-12 science and mathematics curricula. Many curriculum materials have been developed for this purpose by MTPE, Project Globe, and others.

In order to provide middle school educators from across the United States with the skills, knowledge, and materials necessary to teach their students about Earth Systems Science and NASA's MTPE research efforts, the NASA Classroom of the Future will design, develop, field test, and disseminate an on-line course making use of World Wide Web and Virtual Reality Mark-up Language (VRML) technologies.

The development of the on-line inservice course will be a collaborative effort involving classroom teachers, education personnel and scientists from NASA's Mission to Planet Earth (MTPE), the Classroom of the Future (COTF), and Space Grant Consortia members.

INTRODUCTION

The Earth as a system and the impact of human beings on that system have become the focus of extensive national and international research efforts. For example, the International Council of Scientific Unions' (ICSU) International Geosphere-Biosphere Programme (IGBP), the United States Global Change Research Program, and the National Research Council have focused on global change as a major part of their research agenda.

The National Aeronautics and Space Administration (NASA) has taken a leadership role in this research for the United States with the Mission to Planet Earth (MTPE) program, which makes use of satellite technology, remote imaging, and image processing, and is altering our understanding of the Earth as a system.

Although significant effort is going into the MTPE program, and although the implications of this research will have widespread impact on environmental, scientific, social, political, economic, and health policies worldwide, few teachers and far fewer students are aware of these efforts, or have the skills and knowledge necessary to understand them. Typically, students and teachers do not have experience analyzing problems on an ecosystem or biosphere scale. MTPE's scientific studies hold great potential to enhance, enrich, and extend the K-12 science and mathematics curricula.

The NASA Classroom of the Future at Wheeling Jesuit College, in cooperation with NASA Headquarters Education and MTPE program personnel, is planning and field testing a World Wide Web-based teacher training program to provide middle school teachers from across the United States with the skills, knowledge, and materials necessary to understand and teach their students about Earth Systems Science and NASA's MTPE research efforts.

This effort includes course development, development of a WWW-based VRML interface, field testing of these materials, and dissemination to NASA-funded Space Grant Consortium for regional implementation. If successful, it is anticipated that the COTF will, in subsequent years, develop similar on-line courses for elementary and high school teachers.

The use of VRML and the World Wide Web, will place this project at the forefront of on-line teacher training initiatives.

Dr. Robert Tinker and Dr. Sarah Haavind, in a recent paper [1], describe the results of a study of the current state of the art in on-line course development. In the paper, they identify "common elements" of such courses:

> The majority of netcourses studied utilized conferencing software or bulletin boards for the instructional part of the course. Some required up to four face-to-face meetings with the whole class so participants can "know" who their on-line colleagues are, other courses are marketed nationally, even internationally, and face-to-face meetings are not

0-7803-3068-4/96$5.00©1996 IEEE

possible, with the exception of occasional subgroups who sign up together and build in local meetings. Some courses are augmented by a media package of materials up-front that include such resources as videotapes, software, or information on disk, as well as the traditional photocopied set of readings. The courses we reviewed varied widely in the level of structure, but all synchronized student activity by having topics that changed weekly. (p. 16)

After exploring the strengths and weakness of current efforts in this area, they noted that current implementations were technically limited for a variety of reasons and concluded, "The World Wide Web will become the technology of choice for netcourses because of its universality and openness" (p. 30).

We will use WWW technology for the Earth Systems Science course under development, but to go a step further than that under current consideration by developers. We propose to use Virtual Reality Mark-up Language (VRML) to build an interactive learning environment for use by class members and instructors. (For more information about VRML, see the Chronicle of Higher Education, February 23, 1996, p. A21 or visit the San Diego Supercomputer Center's WWW site at http://www.sdsc.edu/vrml/.) Such an environment will allow participants to explore virtual settings and interact with embedded tools and resources.

Curriculum Development

This project will develop the on-line materials for teacher training but will not develop K-12 *classroom* curriculum materials. Instead, the project will identify and incorporate existing K-12 classroom Earth System Science curriculum materials. NASA personnel have developed MTPE materials that can be used in teacher training and by teachers in their classrooms. Many other federally-funded programs are developing Earth Systems Science materials for use in K-12 classrooms. For example, Project GLOBE has developed a nationwide program to prepare teachers to teach Earth Systems Science and a special opportunity exists to collaborate with the NASA HPCC-funded "Exploring the Environment" (ETE) project at the COTF. ETE is developing a WWW site that contains Earth System Science investigations which can be incorporated into the MTPE curriculum (http://www.cotf.edu/ETE/).

Planning Team

This spring, the COTF is bringing together a course development team consisting of representatives from NASA Headquarters (MTPE and Education Division), COTF, Space Grant Consortia, a VRML software developer Earth System scientists, and middle school science teachers. The group will meet at the COTF for three days to develop the outline for the course, supporting materials and the virtual environment. Once this meeting is completed, development will continue with the participants collaborating using the Internet as the medium for communications. The materials will be ready for field testing in the winter of 1996-97.

COURSE DESCRIPTION

The content of the class will be Earth Systems Science, appropriate for middle school teachers and students, as well as an introduction to curriculum materials developed by NASA and other federal agencies for use in middle school science classes. The class will be delivered on-line, making use of WWW technology, including VRML to enable multimedia and virtual environments to be part of the educational experience. The project will do preliminary work developing interactive environments that enable participants to "enter" a virtual environment and interact with other participants as well as embedded tools and resources.

Each participant in the class will receive a class "kit" that will contain materials such as print media, software, manipulatives, videotape, and curriculum materials from MTPE, GLOBE, and other federally-funded Earth System Science projects.

The class will be taught by an Earth System scientist and middle school science teacher, both of whom will help in its development. The class will be held on-line, with group problem solving, discussion, and peer support central to the activities. Original videotape in support of the curriculum will be developed as well.

The on-line course materials will be field tested by 40 middle school science teachers across the country during the winter '96-'97. Participants in the field test will receive the course, course kit of materials, and two continuing education credits for participation. In addition, these individuals will attend a two-day workshop at the COTF during the fall of 1996 to receive instruction related to data collection and materials use during the field test.

COTF will make the class available to Space Grant Consortia colleges and universities to install on local Internet servers. By doing so, it will be possible for participating Space Grant Consortia members to offer it to teachers in their geographic region.

This approach--regional dissemination and delivery--may seem counterintuitive due to the Internet's ability to deliver the course anywhere. However, such an approach will help address two critical issues--scalability (How does one mentor 50,000 teachers on-line?) and degree bearing credit (each participating institution will award credit to its participants). It is also anticipated that because of this approach, participating institutions will also be able to modify the course to meet local needs, integrating it into existing efforts.

RESEARCH AND EVALUATION

Both formative and summative evaluation will be an integral part of the project, with a formal research agenda developed as part of the program that will further the COTF's research mission. Dr. Steven McGee, COTF Educational Research, will be part of the development team from the inception of the project.

As mentioned earlier, the on-line course will be piloted in the fall of 1996 with 40 teachers across the country being recruited to participate in the field test and being awarded 2 CEUs for their efforts.

Each participants' interactions with the course materials on the Web site and with the instructors and each other will be monitored and analyzed. Participants in the field test will be required to participate in an on-going dialog about the effectiveness of both the on-line course materials and discussions as well as the classroom science activities and materials implemented as part of the course requisites.

COTF DEVELOPMENT TEAM

Craig Blurton, Ph.D.

Dr. Blurton, Associate Director of the NASA Classroom of the Future, will serve as principal investigator for this project. Dr. Blurton's duties will include coordinating the work of the various participants, arranging and facilitating meetings, managing the field test of the on-line course, and as science education advisor to the development team.

Stuart Ullman, Ph.D.

Dr. Ullman will serve as co-principal investigator and computer scientist on the project, responsible for the development of the Virtual Reality Mark-up Language (VRML) environment which will be created for use on the COTF web site. Dr. Ullman's current position at Carderock Division, Naval Surface Warfare Center in Maryland is as computer scientist and operations research analyst for the Methodology and Computation Branch, Operations Research Department..

Dr. Steven McGee

Dr. Steven McGee, COTF Educational Research, will serve as program evaluator and researcher. Dr. McGee will be responsible for developing the project's research design. Dr. McGee's work will capture lessons learned both during the development process and the field test

Mr. Bruce Rosen

Mr. Bruce Rosen, Computer Support Analyst at the COTF, will serve as "Webmaster" for the duration of the project, assisting in the development of the VRML interface, installing and testing software, and maintaining the system during the field test. Mr. Rosen has a Bachelors of Science in Computer Science with a minor in mathematics and currently is developing the COTF web site and manages the COTF Internet server.

Other Team Members

As of this writing, other members of the development team can only be identified by role. Specific individuals will be selected to fill these positions in consultation with NASA Headquarters personnel from Education, MTPE, and Space Grant.

Earth System Scientists– These individuals will provide the content expertise to the group. One of these individuals will serve as the on-line course instructor during the field test of the course materials.

Middle School Earth Science Teachers– These individuals, selected because of leadership in the field of Earth Science as well as exemplary teaching skills and an understanding of the National Science Education Standards, will assist with the development of the on-line instructional content and serve as on-line mentors during the field test of the course materials.

NASA Headquarters Personnel – At least one NASA Headquarters staff from MTPE, Education, and Space Grant will be invited to participate in the development process. Staff participation will ensure that the project developed meets NASA's education goals and is well connected to NASA human and material resources.

Space Grant Consortium Representatives – One or two representatives from colleges and universities that are members of NASA Space Grant Consortium will participate in the development process. Their inclusion will ensure that the project staff are informed about existing Space Grant resources and activities related to teacher training in Earth System Science and that the materials developed will be such that they can be integrated into Space Grant Consortium activities once development and field testing are completed.

CONCLUSION

Making use of high performance computing and communications technologies, the COTF, in collaboration with NASA personnel, is designing, producing, and delivering a high quality on-line Earth System Science course to educators across the United States making use of cutting edge technologies in support of NASA's Mission to Planet Earth.

[1] R. Tinker and S. Haavind, "Netcourses and netseminars: current practice and new designs," in press.

Earth Observation Satellite data and its Application to Environmental Education

Akiko Goto
National Space Development Agency of Japan
1-29-6 Hamamatsu-cho, Minato-ku, Tokyo, 105, JAPAN
Phone: 81-3-5401-8694, Fax:81-3-5401-8702
E-mail:AGOTO@rd.tksc.nasda.go.jp

INTRODUCTION

Generally speaking, "Think globally, act locally" is one of the most important element in environmental education. More and more middle schools in Japan start activities to learn environmental changes in their resident area, like measuring polluting matters in their near river, but it is difficult for teachers to find materials to organize environmental program to relate local changes with global environmental issues such as green house effects.

Earth observation satellites proved us vast area information about what's going on earth surface. Earth observation satellite data might contribute to environmental education in the aspect of "Think globally."

In this view, National Space Development Agency of Japan(NASDA) begins the program that offers satellite date and its application to environmental education in schools.

PROGRAM SCOPE

The primary goals of the NASDA's environmental education program are

(1) to encourage understanding of global environmental changes;
(2) to familiarize results of earth observation activities;
(3) to explore potential earth observation satellite data users in schools;and
(4) to contribute to other domestic/international environmental education program.

The approach that we designed for this program includes the following elements;

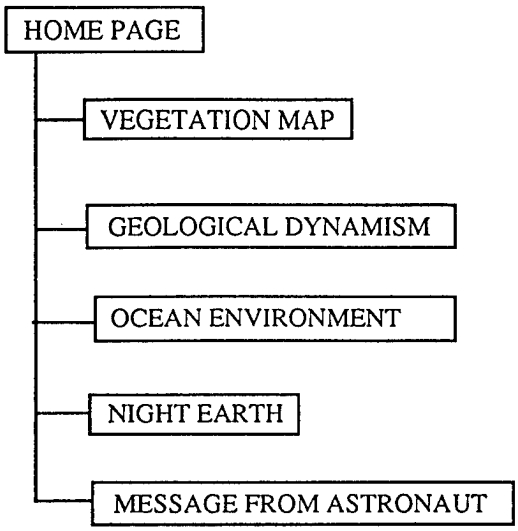
(1) a focus on junior and senior high school students and teachers;
(2) development of instructional material for environmental education;
(3) use of computer technology;and
(4) cooperation with other educational organization

NASDA's long-term program involves;

(1)conducting requirement survey;
(2)designing and developing educational courseware (text, CD-ROM, sample data-set and curriculum);
(3)conducting pilot seminar and test courseware;and
(4)evaluating the program, to make improvements and asses its responsiveness to education requirement.

0-7803-3068-4/96$5.00©1996 IEEE

Fig. 1, Structure of multimedia CD-ROM



CD-ROM

According to our survey conducted in 1994, more than 90% junior and senior high schools in Japan have personal computers. Interactive multimedia can contain various kinds of datasourses such as satellite images, motion video and socio-economic statistics, and teachers and students can manipulate these data to meet their own needs. NASDA developed multimedia CO-ROM as a prototype educational tools to initiate teachers to organize their original class by using earth observation satellite data as one of materials.

This CD-ROM titled "The changes of earth environment" consists of 5 components .(shown in Fig. 1,)

(1)vegetation map - World vegetation map, Deforestation of Amazon, urbanization of Tokyo.
(2)geological dynamism - Volcanic activities such as Mt. Pinatubo and Mt.Unzen, Earthquake
(3)ocean environment - seasonal changes of sea surface temperature, water pollution,
(4)night earth - night earth looking from space, energy consumption,
(5)message from astronaut - video message of Japanese astronaut.

Each part includes text, sound, graphs, pictures, statistics well as Earth observation satellite data. User can operate this

CD-ROM only by mouse clicks, so it is easy to treat even for beginner of computer.

PILOT SEMINAR

We tested our newly developed educational courseware on a one day pilot seminar held by Ministry of education and Tokyo gauge university. About 100 junior or senior high school teachers engaged in environmental education participated form all over the country. The seminar consists of lecture about Earth Observation Satellite date, computer training, and an internet demonstration. We distributed text and CD-ROM to all participants.

Most of teachers had strong interest about using satellite images for environmental education. They gave highest evaluation to CD-ROM. We expected that internet was effective communication tool, but investigation on participants shoed that many teachers are not familiar with computer networks.

THE FUTURE

NASDA will continue to develop the courseware, to have a seminar, and to improve the environmental education program. In the future, we try to use various communication options and international cooperation.

Applications of Satellite Imagery, Visualizations and Remote Sensing in Environmental/Science

An Earth Systems Science Approach

John D. Moore
Burlington County Institute of Technology
Medford, New Jersey 08055
jdmoore@njlink.pppl.gov

INTRODUCTION

Imagery generated from international remote sensing satellites provide real time data for monitoring global natural resources and other atmospheric and environmental phenomena. These images present *interdisciplinary* opportunities for students and teachers to examine and study Planet Earth on a local to global scale, and opens a new chapter in the field of ***environmental interpretation***.

RATIONALE

In 1983 an advisory council of NASA established an Earth Systems Sciences Committee to review the science of Earth as an integrated system of interacting components. The stated goal of Earth Systems Science is to "obtain a scientific understanding of the entire Earth System on a global scale by describing how its component parts and their interactions have evolved, how they function, and how they may be expected to continue to evolve on all time scales." In 1990 the U.S. Congress adopted the Global Change Research Act. The U.S. Global Change Research Program was established "aimed at understanding and responding to global change, including the cumulative effects of human activities and natural processes on the environment ..."

The education component of this program has identified the following objectives:

- Involve public and institutional decision makers in program planning and examination of policies and options
- Expand public awareness of global change, including awareness of the prominent issues, their scientific complexity, and research needed for predicting consequences and evaluating national and international policy options for responding
- Train future scientists, engineers, and educators by promoting understanding among educators and decision makers of the multidisciplinary nature of global change

Early "Mission to Planet Earth" documents did not include the K-12 curriculum as a potential user. Recently. the document "Public Use of Earth and Space Science Data over the Internet" (NASA 94) which was a solicitation to "stimulate broad public use, via the Internet, of very large remote sensing databases maintained by NASA, and other agencies. The potential applications of remote sensing databases, and areas of interest include: atmospheric, oceanic, and land monitoring; publishing; agriculture; forestry; transportation; aquaculture; mineral exploration; land-use planning; libraries; cartography; **education** (***especially K-12***); entertainment; environmental hazards monitoring; and space science data applications" (CAN-OA-94-1, NASA, 94). More recently, NASA issued a research announcement for "opportunities to participate in NASA Mission to Planet Earth and Earth Observing System Science and Education Programs (NRA-95-MTPE-03). The objective of the announcement in Science Education is for investigators to become actively involved with local schools and/or undergraduate colleges; as well as appropriate public educational institutions. The purpose is to provide educational opportunities and/or materials that promote general scientific literacy, especially with respect to the understanding of the Earth as an integrated, dynamic system. These programs are representative of the future impact of dialog between teachers, students, schools, and scientists in science education.

A SHIFT IN THE PARADIGM

Three distinct educational disciplines have been evolving somewhat independently over the past three decades. Science Education, Technology Education, and Environmental Education have the opportunity to unite their common educational goals and objectives and embark in a new direction leading education towards the classroom of the 21st Century, a classroom where students practice real science, using real data, in real time, and the opportunity to interact with international scientists representing an array of agencies and organizations. Development of critical thinking skills, collaborative project based, cooperative and hands-on learning utilizing the power of technology, when applied to real world applications, can lead to improvement in math, geography, as well as other academic disciplines. Environmental Education has long been established as *interdisciplinary*. With the rapidly increasing availability and access to the Internet by the K-12 educational

0-7803-3068-4/96$5.00©1996 IEEE

community, coupled with the incredible explosion of data, information, imagery, and visualizations, students and teachers have a unique opportunity to reform much of what is taught, and certainly how it is taught. Many organizations have already developed on-line curricula in support of use of the data/images. Educational applications has a brief history, less than a decade. In K-12 education, those working to incorporate these resources collaborated to bring about a rapid evolution, namely, determining how to capture satellite imagery and real time data in the classroom, interpretation of images, how to generate funds and support for new programs, how to share this resource with other educators, to writing curriculum that supports the use of the technology and its products.

National science standards have been published. An Earth Systems Science approach to science education models current science research. Part of the educational agenda is to address the need for future generations to move into the scientific research community. As students develop proficiency in the identification, acquisition and applications of available real time data, student initiated research can begin. In the process, students have exposure to real issues, and real applications, factors that have been identified in science education research as improving student interest and performance. Ground truth verification of satellite data is an essential component of data reliability, and therefore, students from around the planet may have the opportunity to contribute to the process.

SATELLITE IMAGERY AND DIRECT READOUT DATA

Students can *today* utilize NOAA weather satellite data and experience the following practical applications of science concepts and principles which include but are not limited to:

- Develop a knowledge and understanding of environmental satellites, their operation, and application of data
- Application of satellite images as they apply to: weather forecasting, identification of land masses, location of geographical areas via coordinates, tracking weather phenomena, and developing forecasting skills from a visual data base
- Develop a knowledge and understanding of global conditions and how environmental factors such as weather are globally interconnected
- Develop and conduct individual research projects using data and/or the technology to expand student experiences in the areas of Meteorology and/or the use of technology
- Acts as a demonstration project to encourage and develop interest by women and other minorities in the study of environmental sciences.

GEOGRAPHIC INFORMATION SYSTEMS (GIS)

GIS applications have advanced considerably in the past two years. Once viewed as a domain of researchers and highly experienced professionals in the field, today it is available to the K-12 community. *Arc View 2.0* is a complete GIS system. Educational applications identified in the science curriculum include:

- Expand analyses of environmental relationships by displaying the micro and macro systems as they occur
- Expand local environmental analyses by seeking similar patterns in other places
- Study the impact on visible patterns altering the electromagnetic radiation received in satellite imagery
- Overlay satellite imagery with ground mapping to examine the impact of environmental characteristics on people and vice versa.

Through incorporating local, state, and regional data bases into classroom studies, students have the ability to utilize real data associated with real life studies including "natural resource management, environmental assessment, business and marketing operations, urban planning, utilities planning and operations, forestry and a variety of other geosciences," in the classroom.

AMS DATASTREME PROJECT

During the 1993-94 school year, a pilot study of the American Meteorological Society's Project Atmosphere, designed to "investigate the educational potential of *real-time scientific data* for use across the curriculum K-12 was implemented. The objectives were as follows:

- The determination of the technical and economic feasibility of delivering a real-time meteorological data stream to schools across the country at no additional recurring costs to schools
- The investigation of the educational potential of using real-time scientific data in school learning environment through the development, implementation, and evaluation of prototypical instructional strategies and materials
- The preliminary identification and teaching of understandings and skills employed in the processing, analysis, evaluation, application, and interpretation of a continuous data stream to seek answers, trends and predications.

National Science Foundation funding has been received for implementation of The DataStreme Project that will develop and deliver a distance-learning course for teachers based on the current meteorological data stream.

THE GLOBE PROGRAM

The *GLOBE* Program (**G**lobal **L**earning and **O**bservations to **B**enefit the **E**nvironment), first introduced by Vice President Al Gore on April 22, 1994 (Earth Day), links students worldwide in an effort to monitor changes in the world's environment. GLOBE is an international science and education program that creates a partnership between students, teachers, and the scientific research community that actively involves the students in data collection and observation. Participating scientists will use these data in their research programs to improve our understanding of the global environment. The objectives of GLOBE are to:

- Enhance the environmental awareness of individuals throughout the world
- Enable students to make environmental observations that will contribute to improving our understanding of planet Earth
- Give students the opportunity to work with respected scientists, collaborating through a worldwide network
- Involve students, teachers, and scientists in sharing information about the global environment
- Enrich and supplement existing curricula in science and mathematics
- Support higher student achievement in science, mathematics, and technology.

GLOBE surface based observations of many environmental parameters will prove helpful in satellite remote sensing studies. Measurements from space can be calibrated with respect to "*ground truth.*"

LEARNING THROUGH COLLABORATIVE VISUALIZATION (CoVIS)

The CoVis Project (Northwestern University) is attempting to transform science learning to better resemble the authentic practice of science. "The CoVis project will explore issues of scaling, diversity, and sustainability as they relate to the use of networking technologies to enable students to work in collaboration with remote students, teachers, and scientists." Participating students and teachers will study atmospheric and environmental sciences through inquiry-based activities. The CoVis Project "provides students with a range of collaboration tools which include:

- desktop video conferencing
- shared software environments for remote/ real time collaboration
- access resources of the internet
- a multimedia scientist's notebook
- scientific visualization software.

SUMMARY

In order to understand global change and the demands on human activity, the science community is documenting global environmental systems so we can better comprehend how the Earth works as a system. The science education community can likewise respond by encouraging students to begin use the data and technology in the classroom that will prepare them to transition into the rapidly emerging professions of the 21st Century. An ***Earth Systems*** approach applies environmental systems principles to the traditional Earth Science, Biology, Chemistry, and Physics core proficiencies, and more importantly provides the structure, or focus of instruction. The Earth Systems Science Approach is science for the 99%. The Earth Systems Science approach to environmental /science education will model and teach skill proficiencies that represent science and research. Equally as important, the Earth Systems approach will develop interest and prepare students for careers in the science, technology, and environmental fields, while fostering an environmentally literate and conscious society leading towards better local and global decision makers.

REFERENCES

[1] American Meteorological Society. 1993. "Project ATMOSPHERE: Teachers Manual."

[2] Baker, D. J. 1990. "Planet Earth: The View from Space," Harvard University Press.

[3] Barstow, D. 1994. Geographic Information Systems: New Tools for Student Exploration. "Hands On!" TERC, Vol. 17, No. 1: 10-13.

[4] Bednarz, S. 1994. GIS in Schools? Why? How? "ArcSchool Reader," Winter 1994, p. 3.

[5] NWU, "Learning through Collaborative Visualization."

[6] NASA, "EOS: A Mission to Planet Earth," EOS Program Office.

[7] NJ State Mapping Advisory Committee, "New Jersey GIS Resource Guide," 1995

[8] Report of the Earth Systems Sciences Committee, 1988, "Earth System Science: A Closer View."

[9] Report by the Committee on Environment and Natural Resources Research of the National Science and Technology Council. 1995, "Our Changing Planet: The FY 1995 U.S. Global Change Research Program."

[10] The GLOBE Program. 1994. The White House, Washington D.C.

Do We Really Understand What We See?

Cognitive issues in remote-sensing from the perspective of a scientist and an educator

Daniel Barstow
Principal Investigator, "Visualizing Earth"
TERC, 2067 Mass Ave., Cambridge, MA 02140
tele: 617-547-0430/fax: 617-349-3535/email: Dan_Barstow@terc.edu

Dr. Eric Frost
Co-Principal Investigator, "Visualizing Earth"
Director, Computer Imaging, Visualization and Animation Center
Department of Geological Science, San Diego State University, San Diego, CA 92182
tele: (619) 594-5003/fax: 619-594-4372/email: frost@imagine.sdsu.edu

As remote-sensing specialists, we all use images and visualizations as the life-blood of our work. We receive data in the form of images, we use software to manipulate images, we cross-reference among images, and we use images to communicate our findings. And yet, how well do we understand the cognitive and perceptual issues which make our images more or less effective? These cognitive issues become all the more important when we try to use images to convey essential concepts to the general public, and when we promote the use of images in education.

Such cognitive and perceptual issues are the focus of "Visualizing Earth," an educational research project funded by the National Science Foundation, Applications of Advanced Technology program. "Visualizing Earth" combines the expertise of educators, remote-sensing scientists and cognitive psychologists, to explore cognitive issues which are central to more effective use of remote-sensed images and visualization software tools in education. In this paper, two of the Principal Investigators, a scientist and an educator, share their initial findings in relation to their efforts to use images in education and public information.

I. THE EDUCATOR'S PERSPECTIVE

Daniel Barstow is a senior curriculum developer at TERC, a non-profit educational research and development company. He is Principal Investigator for a group of projects designed to promote more effective use of remote-sensed images and visualization software in education, including Visualizing Earth, GLOBE education element, Mars Exploration Education Program, and Mapping Our City. He is also on the Core Curriculum Development Team for KidSat.

When atmospheric scientists look at this satellite image of Earth, they see patterns of clouds which are indicators of broad weather systems on Earth. They see the Intertropical Convergence Zone, with its band of equatorial cumulonimbus clouds. They see mid-latitude storm systems, as cold polar air masses interface with warm tropical air masses. They see climatic variations, such as the clear skies over parts of Mexico and the broad areas of stratus clouds over South American rain forests.

When elementary school students look at the same image, they wonder whether the white areas are snow or clouds. They try to see their home and school. They wonder why the oceans are gray instead of blue. They see a group of clouds that look like a dragon. And they think about being an astronaut so they could see Earth from space. Clearly, students and scientists see images differently, based on substantive differences in their background and cognitive development.

As we develop education and public outreach programs, it is crucial for us to understand these differences. What is obvious to scientists, as they look at images, is based, in fact, on years of experience and research. In the case of meteorologists, it is based on learning about the signatures of certain weather patterns, on experience comparing visible satellite images with ground-based Doppler radar, on having seen numerous sequences of hourly GOES images to know how storms move and change over time. With this background, a glance at a single image evokes a rich set of associations and background, enabling the scientist to find deep meaning in the image. Most students have neither the experience nor (in the case of elementary school students) the cognitive maturity to find such meaning in the same images.

0-7803-3068-4/96$5.00©1996 IEEE

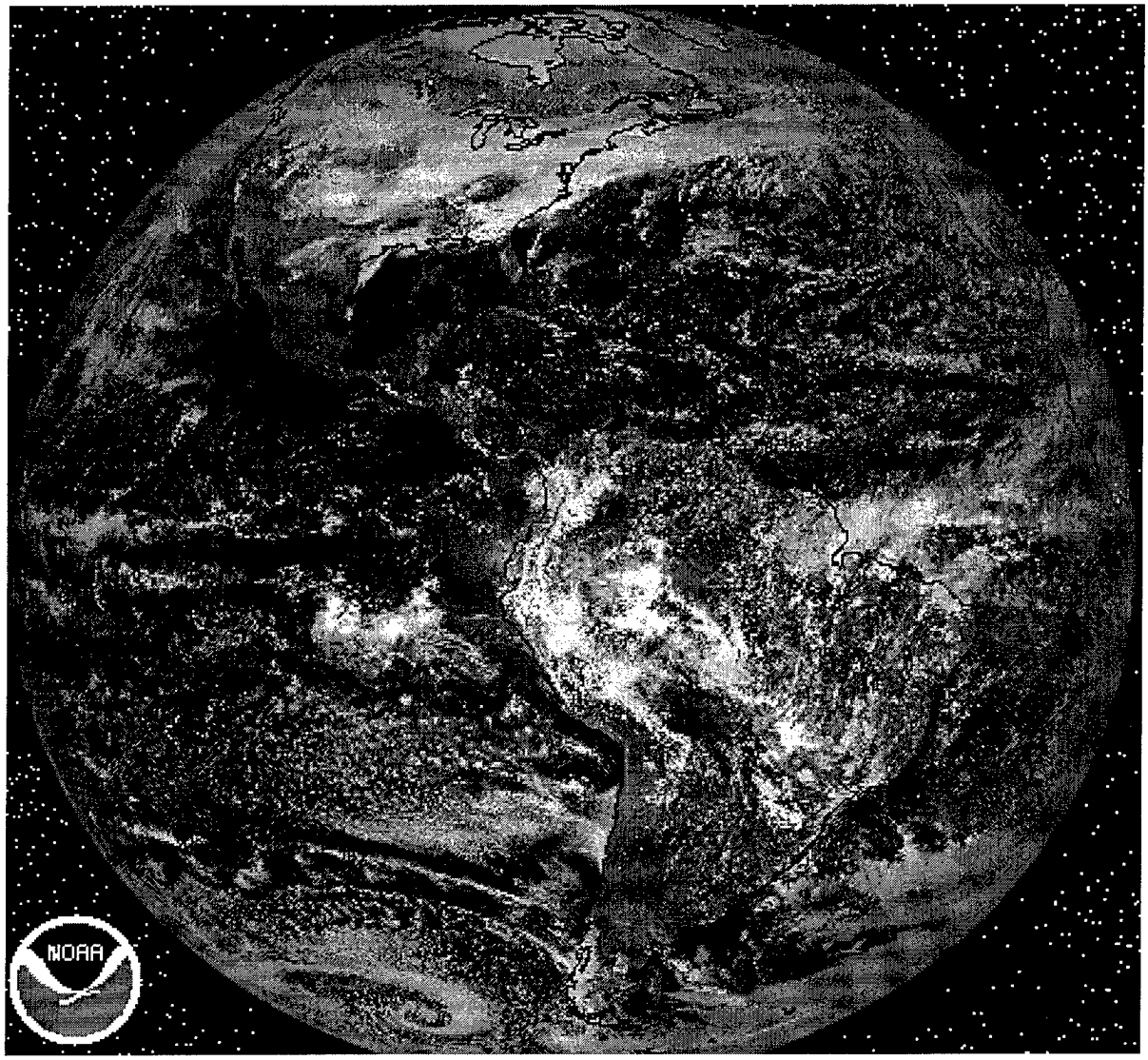


Fig. 1, Full-disk visible light image of Earth from the GOES-8 (Geostationary Orbital Environmental Satellite) weather satellite

We are still in early stages of our "Visualizing Earth" cognitive research. However, it is clear that effective educational use of remote-sensed images must go beyond simply making the images available on the World Wide Web. Access is only one part of the equation. We (as scientists and educators) also must provide:

1. educational materials which help students develop the skills and knowledge base to use these images
2. opportunities for students to pursue their own image-based investigations, enabling them to do the same kind of inquiry and exploration that scientists do

GLOBE is one example of a project that is striving to implement these goals. Conceived and initiated by Vice President Al Gore, the program engages students and scientists, working together, in environmental research. Using carefully designed protocols, students in thousands of schools around the world do local environmental observations, such as daily weather, which they submit to a central data base. The scientists use these data for their own research, and the students use the data for investigations-based learning. In addition, through GLOBE's web-page, the students have direct access to GOES and other remote-sensed images.

GLOBE had to go through a paradigm shift in its design. The original concept was that the scientists would use the data in their research, then create a "visualization" such as a map with the relevant data, which would clearly communicate the findings to the students. However, this one-way approach did not engage the students directly in the data. The new model is that the students will have direct access to the same data as the scientists, and do their own investigations. They may not be exploring the same issues as the scientists, but their ability to make meaning of the science content is greatly enhanced by their own direct involvement.

A second example is KidSat, in which students have direct and exclusive use of a camera in space, initially flown on the Space Shuttle, and eventually on the Space Station. This NASA-funded project is a collaboration of NASA JPL, Johns Hopkins University Institute for the Academic Advancement of Youth, and UCSD California Space Institute. The key educational concept is that students are much more engaged with their use of remote-sensing resources (such as the KidSat digital camera) if they are an integral part of the process, including the selection of target sites. With KidSat, students learn about orbital paths, camera resolution, telecommunications and image analysis, in the process of conducting their own investigations of volcanoes, urban growth, cloud patterns and other topics of personal interest.

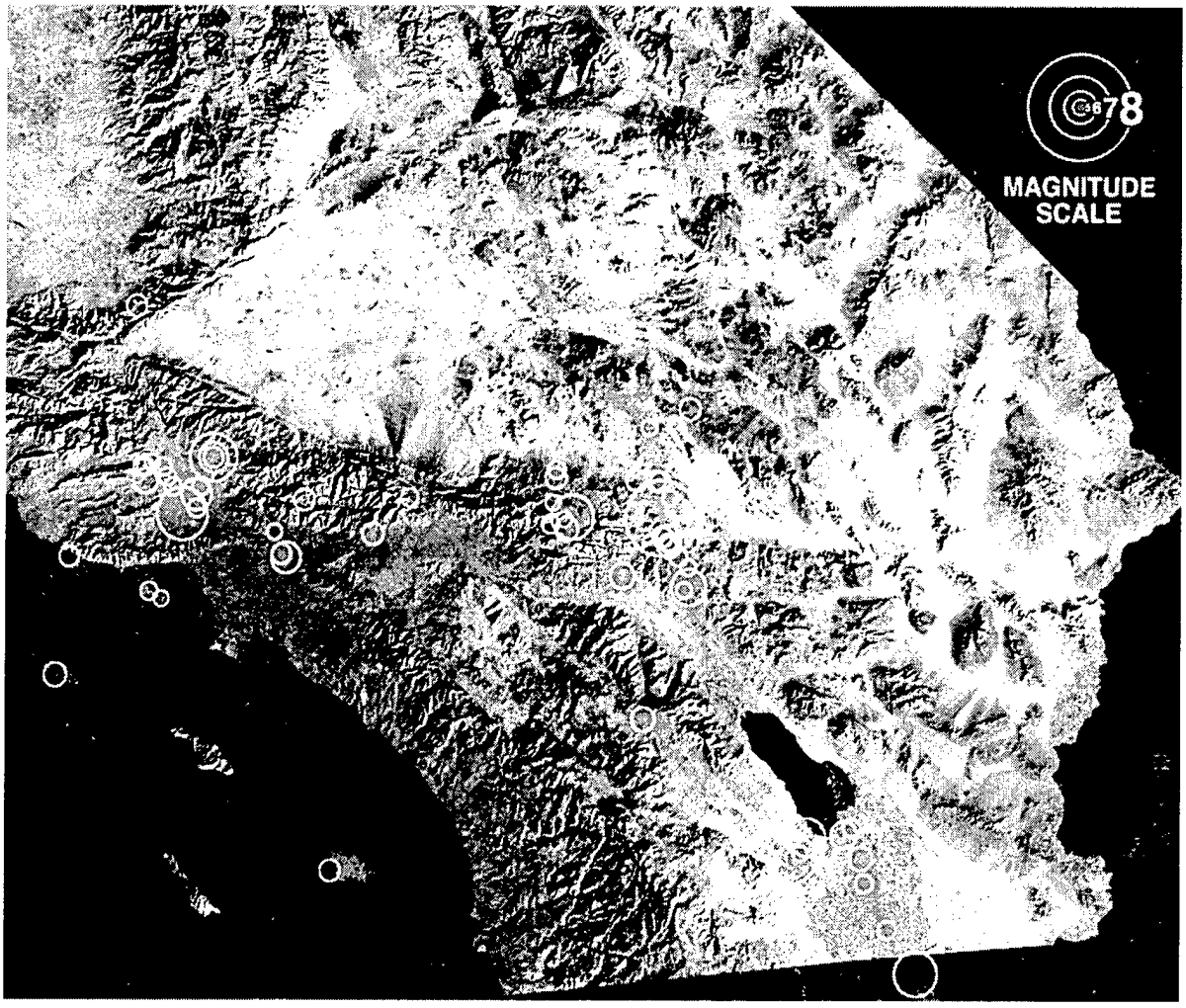


Fig. 2, Landsat composite of Southern California with epicenters, from "Putting Down Roots in Earthquake Country", published by Southern California Earthquake Center

II. THE SCIENTIST'S PERSPECTIVE

Dr. Eric Frost is Associate Professor of Geological Sciences, and Director of the Computer Imaging, Visualization and Animation Center at San Diego State University. He has specialized in structural geology, remote-sensing and plate tectonics. In California, he has been actively involved in public information and safety programs relating to earthquakes. He is a co-Principal Investigator on the "Visualizing Earth" project.

Visualization of earth systems, such as plate tectonics, has significant implications for both scientists and the general public. For example, understanding how and why faults form, anticipating the effects of earth motion during seismic events, and evaluating the overall seismic risk for homes or businesses involve decisions that we all make. If scientists and non-scientists alike cannot visualize the complex, 3-D relationships of geologic structures, then much of the effort of earth scientists will languish in earth science journals without affecting society, especially through education in K–16 classrooms.

By studying different parameters for how people are able to effectively visualize complex spatial relationships, we are endeavoring to provide a framework of tools that will assist others in creating more effective learning and teaching tools. Some of the principal factors that we have found that increase most peoples' spatial cognition include:

1. Perspective views, such as space shuttle photography provide orientation and relationships.

2. Stereoscopic views, done with colors, offset photos or polarized light make visualizations "real."

3. Motion, especially to enhance change detection or show geometries and kinematics with fly-throughs.

4. Colors, where the colors (IHS) have a genetic link to attributes of the visualization.

5. Virtual reality, (QTVR), creates illusion of manipulation and explorability.

6. Non-visible spectra, views of specialized relations like IR and plants, radar and ice, sound and reflections.

7. Video and slow motion video, show motion and cause-and-effect, including using flicker for change.

8. Morphing of before and after or of one feature into another to show change.

9. GIS of one data set on another to show correlation of both position and weighted value.

10. Model building and destruction, ESP in conjunction with other techniques such as video.

11. Temperature changes, to duplicate changes in spatial position within the earth (brittle to ductile).

12. Spatial queuing of inhomogeneous cross sections.

To mimic temporal changes (space to time) combinations of these different tools and the interactive ability to alter them and allow different parameters to assist in the earth visualizations produces strikingly higher degrees of effective spatial cognition in both scientists and non-scientists.

"Visualizing Earth" is funded by the National Science Foundation, Grant # RED-9554504. All opinions, findings, conclusions, and recommendations expressed herein are those of the authors and do not necessarily reflect the views of the National Science Foundation.

Interdisciplinary Earth System Science and Earth Observations from the International Space Station: Partners in Education

Willis, Kimberly J.
Lockheed Martin Engineering and Science Services
Mail Code C102, P.O. Box 58561, Houston, TX 77258-8561
(713) 333-7125 FAX (713) 7791 e-mail "willis@ersaf.jsc.nasa.gov"

Amsbury, David L., and McLaughlin, C. Diane
NASA Lyndon B. Johnson Space Center
Mail Code SN5, Johnson Space Center, Houston, TX 77058
(713)483-5160 (713) 483-4089 FAX (713) 483-2911 e-mail "amsbury@snmail.jsc.nasa.gov", "mclaughlin@snmail.jsc.nasa.gov"

Miewald, Thomas
University of Nebraska at Lincoln
(402) 472-2865 e-mail "tmiewald@unlinfo2.unl.edu"

ABSTRACT

The monitoring of the global environment will be aided by a nadir-viewing, optical quality window located in the United States Laboratory of the International Space Station (ISS). Through this window Earth observations data of significant scientific and educational value will be acquired and made available to scientists, educators, and the general public. The analysis of data from the ISS will require the integration of many Earth science disciplines. It is this integration of science in a global context that will make the data a value added educational resource for students from kindergarten to graduate school. Educational technologies such as database of descriptive information on over 200,000 Earth-viewing images, laser videodiscs containing 180,000 digital images, World Wide Web Home Pages containing Earth observations information and digital images, and 35 mm discipline slide sets exist now and will be improved for the ISS.

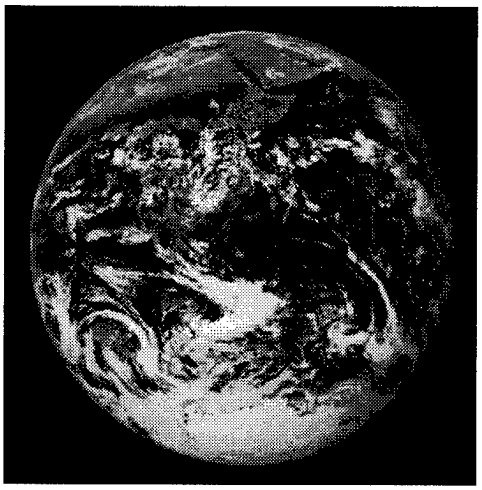


Figure 1. Full Earth view taken by Apollo 17 astronauts.

INTRODUCTION

Images of the Earth from space offer a unique global perspective whereby the interactions between white clouds, blue oceans, and green and brown continents are visible on a broad scale. These images are used to document change over time and are especially illustrative of multiple processes effecting environmental change in many areas of the world. An Earth observing program will begin on the ISS in early 1999 with the addition of an optical quality, nadir viewing window located in the United States Laboratory. The global perspective of environmentally monitored sites allows students and scientists to see the effects of the relationship between the atmosphere, oceans, biosphere, and solid Earth. Educational technologies such as databases and digital images of the Earth, that matured during the Space Shuttle Program will be expanded and refined with the ISS.

INTERDISCIPLINARY EARTH SYSTEM SCIENCE AND EARTH-VIEWING IMAGERY

Astronaut photographs of the Earth are a versatile classroom resource that can readily be integrated into existing curricula from Kindergarten to Graduate School. The body of photography provides an integrated, global view of dynamic Earth processes in geographic context. Students and teachers can identify and measure changing shorelines, observe regional structures in mountain belts, effects of volcanic eruptions, forest conversion, changing sediment loads in rivers, smoke palls, and ocean currents. Documentation of Earth observations in the form of photographs and electronic images also allows scientists and students to share in the orbital experience of the astronauts.

Astronaut photography of the Earth has unique features that can complement data from other sensors such as satellites. From Mercury to the Space Shuttle astronauts have acquired over 200,000 images of the Earth in a time span of over 30 years. This unique data set showing environmental change

0-7803-3068-4/96$5.00©1996 IEEE

over time will be expanded with the completion and operation of the International Space Station (ISS). Environmental monitoring programs presently being applied in the Space Shuttle program will be enhanced because of the longer increment flights of 90 days on the ISS, as opposed to a maximum of 16 days on Shuttle. Piloted platforms can image target sites from differing altitudes as well as from different look angles. The human observer is the most important component of the piloted platform because a trained observer in space can accurately describe and document Earth features and phenomena, assimilate and interpret what has been observed; rapidly select observational sites, sensor systems, and parameters; and modify planned activities as needed.

OPTICAL-QUALITY, NADIR VIEWING WINDOW IN THE UNITED STATES LABORATORY MODULE ON THE INTERNATIONAL SPACE STATION

The current configuration of the ISS contains an optical-quality, nadir viewing window in the United States Laboratory, Earth-viewing cupola windows in node 2, and two windows in the United States Habitation module. The optical-quality window is made of fused silica with a clear viewing aperture of 50.8 cm diameter. Infrared and ultraviolet images can be acquired with the removal of the inner scratch pane assembly. The United States Laboratory is currently scheduled for attachment to the Space Station in November 1998.

Situated above the nadir-viewing window will be a rack facility that will allow for attachment points for various sensors. The rack will facilitate multiple sensors where viewing angles can be varied as much as 45 degrees. Sensors currently planned to be manifested for the ISS are Nikon, Hasselblad, Linhof, and IMAX film cameras, an Electronic Still Camera (ESC, digital), and a Video Camcorder.

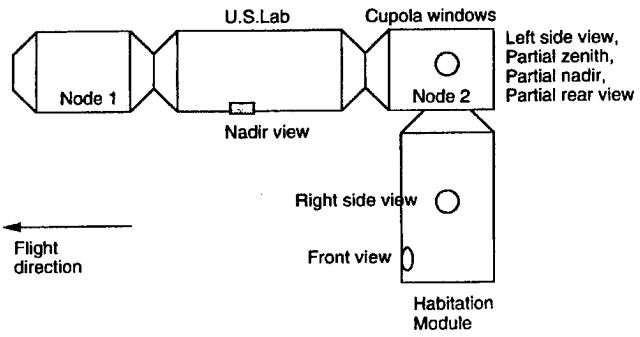


Figure 2. International Space Station window locations in the United States Laboratory.

EARTH OBSERVATIONS EDUCATIONAL TECHNOLOGIES: FROM SPACE SHUTTLE TO THE ISS

Digitized images with textual information are now available on several home pages on the World Wide Web and can be accessed by students, educators, scientists, and the general public by using the following URL's:

Space Shuttle Earth Observations Project Database of Photographic Information and Images
http://eol/sseop.html

Earth Science Branch Home Page
http://ersaf.jsc.nasa.gov/sn5.html

JSC Imagery Services Digital Image Collection
http://images.jsc.nasa.gov/

The Space Shuttle Earth Observations Projects (SSEOP) textual database with geographic information about each Earth-viewing photograph taken by astronauts can be accessed through the JSC Home Page, the Earth Science Home Page, or can be accessed directly by telnet.

telnet sseop.jsc.nasa.gov
Username: **PHOTOS**

For more information about the SSEOP textual database see Nelson, R. M., K. J. Willis, W. J. Daley, and F. R. Brumbaugh [1] and Pitts et al. [2].

Astronaut photographs of the Earth are also available on videodisc. Two 12-inch laser videodiscs contain over 150,000 images of the Earth. Disc 1 contains the first 44 Shuttle missions and can be ordered from the Johnson Space Center. Disc 2 includes Shuttle missions from 1992 to 1993 as well as some press release images. Disc 2 is available from NASA Central Operation of Resources for Education (CORE). For more information about the laser videodiscs see McKay and Willis [3].

Astronaut photographs of the Earth have been made into slide sets. Cities of the United States, the Geography of the United States, which is divided into 5 regions: Pacific Coast States; Southwest States and Rocky Mountains; Great Plains States and Mississippi River Valley; Appalachians, Ohio River Valley, Great Lakes; and East Coast States are 35 mm slide sets that can ordered from CORE. Each slide set consists of approximately 20 slides and comes with a brief description of each slide.

Educational technologies will continue to evolve with the ISS. Continued growth of the worldwide communications networks will increase global access and involvement from the educational community with each flight increment of the ISS.

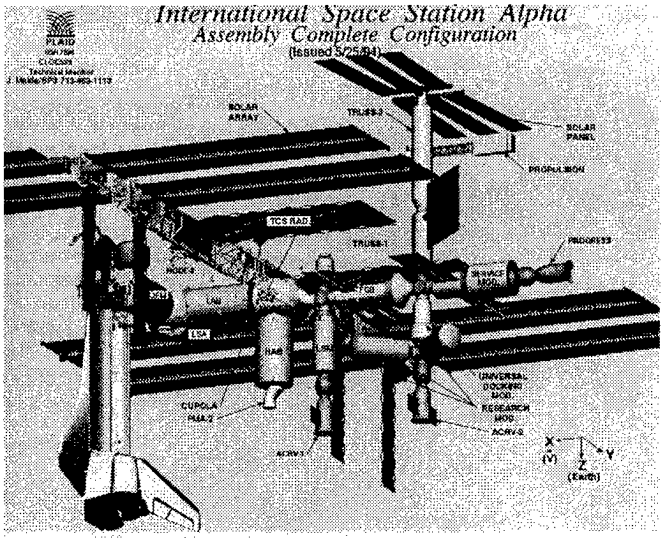


Figure 3. The International Space Station as it will appear when the assembly is complete.

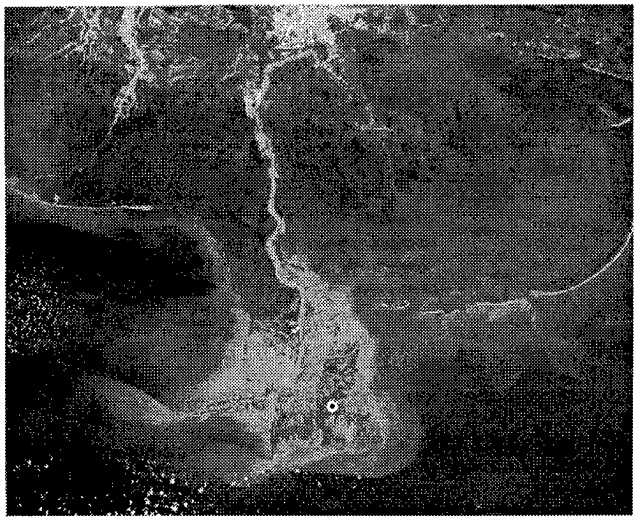


Figure 4. The Mississippi River Delta photographed by the STS-51C crew in January 1985 (STS51C-143-027).

CONCLUSION

Earth observations from human tended spacecraft have increased in scope and complexity, enhanced science contributions, and increased public awareness and understanding of the sensitivity of the global environment. This understanding of the global environment will be further developed with the addition of an optical quality, nadir viewing window from the ISS. A partnership between the science and education communities has been cultivated with the Shuttle program, but will be further developed and expanded with the ISS. Educational technologies that result from this partnership will benefit both communities nationally and internationally.

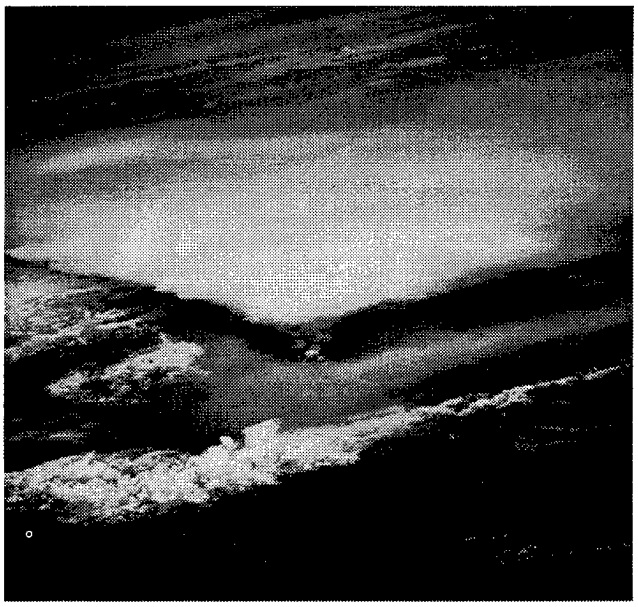


Figure 5. Rabaul volcanic eruption plume on Papua, New Guinea. This photograph was taken by the STS-64 crew in September 1994 (STS064-116-064).

REFERENCES

[1] R. Nelson, K. Willis, W. Daley, F. Brumbaugh, and J. Bremer, "Cataloging and indexing - the development of the space shuttle mission data base and catalogs from earth observations hand-held photography," in International Geoscience and remote Sensing Symposium Digest, 1992, pp. 155-157.

[2] D. Pitts, et al., "Space shuttle digital data base," in International Geoscience and Remote Sensing Symposium Digest, 1994.

[3] M. McKay and K. Willis, "Space shuttle photography-a classroom resource," in International Geoscience and Remote Sensing Symposium Digest, 1994, pp. 520-522.

Global Sea Ice Monitoring from Microwave Satellites

Ola M. Johannessen[1], Martin W. Miles[2] and Einar Bjørgo
Nansen Environmental and Remote Sensing Center
Edvard Griegsvei 3a, N-5037 Solheimsviken/Bergen, Norway
tele: +47 55 29 72 88 fax: +47 55 20 00 50
e-mail: ola.johannessen@nrsc.no
[1]and Geophysical Institute, University of Bergen, Norway
[2]and Department of Geography, University of Bergen, Norway

Abstract — The global sea ice covers can be regularly and frequently monitored using satellite passive microwave sensors. Recent studies using passive microwave have detected significant decreases in Arctic ice extent and ice area, with no significant changes in the Antarctic. Here we analyze microwave data through mid-1995, to identify changes in ice extent, ice area, and, for the first time, overall ice concentration. We find continued decreases in the Arctic ice extent and ice area, and establish a decrease in the ice concentration. We also include a seasonal analysis of the Arctic trends, which establishes the greatest decreases to be in summer and spring. The relatively large summer decreases imply a reduction in the multi-year ice area, suggesting reduced ice thickness, though observational data are lacking.

INTRODUCTION

Global warming related to increases in so-called greenhouse gases can be studied using models and observations. Greenhouse warming scenarios using atmospheric general circulation models (GCMs) tend to predict enhanced warming in the polar regions, especially the Arctic [1], including a marked retreat of the sea ice cover [2]. Some GCM results even show the complete or near-complete removal of the summer sea ice cover in the Arctic Ocean [3]. Systematic observations of the global sea ice covers may be useful for the early detection of global climate change [4,5].

Satellite passive microwave sensors provide the most consistent means to monitor and estimate global sea ice variability. Algorithms developed for multi-frequency microwave data can retrieve sea ice concentration for a given pixel, from which ice extent (the area within the ice edge, defined conventionally as the 15% ice concentration isopleth), ice area (the area of ice-covered ocean), water area (the difference between ice extent and ice area) and overall ice concentration (the average ice concentration within the ice edge; i.e., the ratio ice area/ice extent) can be derived. Earlier studies using microwave data have emphasized the Nimbus-7 Scanning Multichannel Microwave Radiometer (SMMR) data set 1978-1987. An analysis of SMMR data using the NASA Team algorithm revealed a 0.032 x 10^6 km^2 yr^{-1} (2.4% per decade) decrease in Arctic sea ice extent, with no significant trend in water area, and no significant trends at all in the Antarctic [6]. The subsequent sensor, the Special Sensor Microwave Imager (SSM/I) on Defense Meteorological Satellite Program (DMSP) satellites, has provided comparable data since 1987, including a 6-week period of overlap with SMMR. Analysis of the SSM/I data 1987-94 revealed greater negative trends in Arctic ice extent and ice area, again with no significant changes in water area or any of the Antarctic ice parameters [7].

The SMMR-SSM/I overlap period allows for sensor intercalibration, such that the satellite-derived sea ice record can be extended beyond the operational period of a single sensor system. The creation and analysis of continuous SMMR-SSM/I time series of ice extent, ice area, and water area 1978-94 has been recently discussed [8]. The trends estimated in that analysis were between those found in the separate SMMR and SSM/I time series [7], suggesting that the intercalibration was successful. Again, significant decreases were found in Arctic ice extent and ice area, with no trend in the water area.

The lack of significant trends in Arctic water area [6-8] is usually taken to imply that there have been no changes in the compactness of the sea ice cover. However, we consider the water area parameter (extent minus area) to be a relatively poor indicator, compared to overall ice concentration (area/extent), a parameter that has not been systematically investigated previously. Another important remaining scientific issue is the seasonal character of the negative trends found in Arctic ice extent and ice area [6-8].

The research presented here serves to extend and expand on [8]. The objectives here are to: 1) create time series of ice extent, ice area, and overall ice concentration from 1978-95 SMMR and SSM/I T_Bs, 2) estimate trends in the parameters in the Arctic and Antarctic and 3) investigate the seasonal components of any significant overall trends.

METHODS

Creating the sea ice time series

The SMMR data are polarized T_Bs measured at 7, 11, 18, 21, and 37 GHz, acquired at 2-day intervals, and the SSM/I data are 1-day polarized T_Bs at 19, 22, 37, and 85 GHz. These data are provided on CD-ROM from the National Snow and Ice Data Center (NSIDC), Boulder, Colorado. The sensor system considerations in constructing geophysical time series from SMMR-SSM/I data are described in [9], in which it is recommended that such time series should be constructed at the geophysical parameter level, rather than the measured radiance level (T_B). In the present research, ice concentration in each individual pixel is the geophysical parameter of interest. Individual-pixel ice concentrations were computed using the NORSEX algorithm [10], which uses vertically-polarized T_Bs at 18 and 37 GHz (SMMR) and 19 and 37 GHz (SSM/I). The details of the SMMR-SSM/I intercalibration that we performed are provided in [8]. Time series of ice extent, ice area, and overall ice concentration were then derived from individual-pixel ice concentrations.

Analyzing the sea ice time series

Monthly mean were computed to reduce the high-frequency variability. The overall mean and seasonal cycle were then removed, resulting in anomalies (departures), from

0-7803-3068-4/96$5.00©1996 IEEE

which trends were estimated using generalized least-squares linear regression. Associated with each trend is a particular significance value; here, results were considered to be statistically significant at the 0.05 significance (95% confidence) level. In the cases where trends were found to be "statistically significant", the possible effects of temporal autocorrelation were tested for and accounted for re-running the regressions after randomly subsampling the time series to remove the autocorrelation.

An analysis was then performed to identify the seasonal contribution to each of the overall trends that was found to be statistically significant. Month-by-month time series were created for each of these ice parameters, then analyzed using regression, with the same criteria for statistical significance.

RESULTS

Overall trends

The statistically significant trends and departures 1978-95 are shown in Fig. 1, and the statistical parameters are summarized in Table 1. We find significant decreases ($p < 0.05$) in ice extent, ice area, and overall ice concentration in the Arctic. In the Antarctic, there are no statistically significant trends.

In the Arctic, the estimated trends in ice extent and ice area are - 0.033 x 10^6 km^2 yr^{-1} and - 0.036 x 10^6 km^2 yr^{-1}, respectively. These represent rates of decrease of 4.5% and 5.6%, respectively over the observation period. The decrease in overall ice concentration was 1.8% from 1978-95. This means that ice cover became less compact the period, the first time that such a trend has been established.

In the Antarctic, very slight (< 0.01 x 10^6 km^2 yr^{-1}) decreases were found in the ice extent and ice area, but the trends are not statistically significant. This hemispheric asymmetry is consistent with most global climate model results, for example [10].

Seasonal trends

The overall negative trends in the Arctic ice cover should not be expected to be monotonic geographically or temporally. Here we investigate the latter aspect, using a monthly breakdown of the overall time series. The seasonal contribution to the overall trend in Arctic sea ice area is shown in Fig. 2. The greatest reductions have occurred in summer (July, August and September). For example, the decreases in August ice area were 0.054 x 10^6 km^2 yr^{-1}, compared to the overall mean trend of - 0.036 x 10^6 km^2 yr^{-1}. Statistically significant decreases were found in the Arctic in each season, except in the freeze-up period (October, November, and December).

An earlier study [11] found significant decreases in the Arctic only in summer. Our results indicate not only a deepening of summer reductions, but that decreases are happening in the spring as well. A preliminary investigation into the "temporal dependencies" in the time series reveals that the late summer (August and September) anomalies are correlated with the anomalies the following late spring (May and June). Accordingly, the recent reductions in the Arctic minimum ice cover, occurring in September, may reinforce reductions in the ice cover in the following late spring, although this remains speculative.

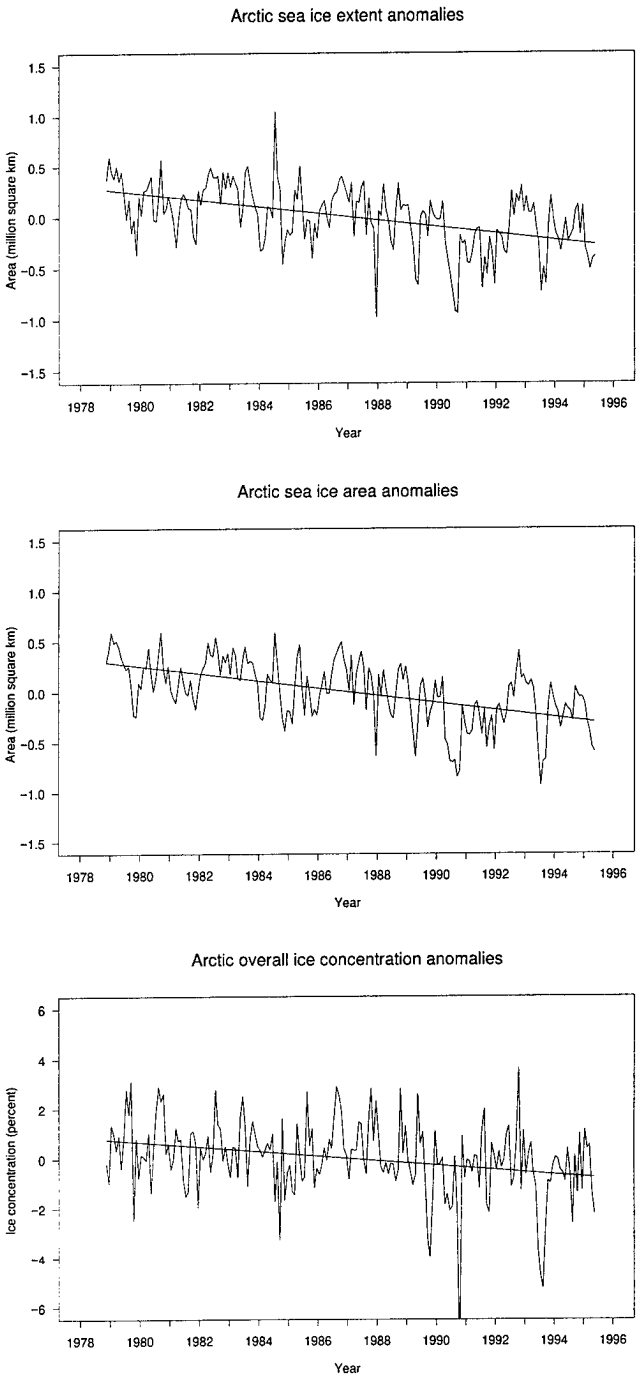


Fig. 1. Anomalies in monthly averages of Arctic ice extent, ice area, and overall ice concentration, November 1978 - May 1995, derived from SMMR and SSM/I passive microwave satellite data. The parameters are derived from individual-pixel ice concentrations derived using the NORSEX algorithm [10]. Units are 10^6 km^2. Lines represent the slope estimated by least-squares linear regression, and are considered statistically significant at the 95% confidence level.

Table 1. Summary of trend analysis of Arctic and Antarctic ice extent, ice area, and overall ice concentration (area/extent). In the Arctic, we use area/extent < 84° N, because of the data gap poleward. The observation period, T_{obs}, is the length of the time series, i.e., 16.5 years. The slope is in 10^6 km^2/yr for ice extent and ice area, and %/year for ice concentration.

Parameter	Slope	$\Delta_{\%}$ during T_{obs}	Δ_A during T_{obs} (x 10^6km^2)	Conf. level
ARCTIC				
Ice extent	- 0.033	- 4.5	- 0.54	99
Ice area	- 0.036	- 5.6	- 0.60	99
Ice concentration	- 0.094	- 1.8	N/A	99
ANTARCTIC				
Ice extent	- 0.008	- 1.2	- 0.14	79
Ice area	- 0.004	- 0.7	- 0.07	48
Ice concentration	0.018	0.4	N/A	42

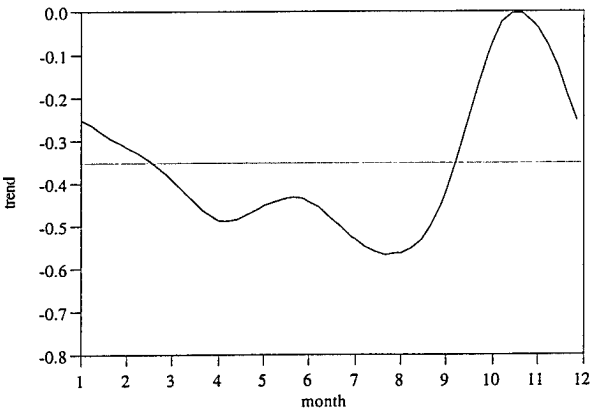


Fig. 2. Seasonal distribution of trends in Arctic sea ice area 1978-1995, derived from microwave satellite data. Units are 10^6 km^2 decade^{-1}. The curve represents the trend as a function of season. The horizontal line represents the overall trend of - 0.36 x 10^6 km^2 decade^{-1}.

CONCLUSIONS

The most noteworthy results of our research are: 1) a 1978-95 time series of microwave-derived ice extent, ice area, and overall ice concentration, 2) the estimation of significant decreases in each parameter in the Arctic, and 3) the determination of substantially greater decreases in the summer and spring ice cover in the Arctic.

The time series can serve as a baseline for monitoring the global sea ice covers. New SSM./I data can be incorporated and analyzed as they become available. The inclusion of SSM./I data through the end of 1995 is of great interest, as U.S. National Ice Center maps reveal the 1995 Arctic minimum ice extent to be near the 1990 record low.

While it is tempting to infer that this is a global warming signal, some caveats need to be considered. The negative trends in Arctic ice parameters, while statistically significant, are small compared to the overall mean and seasonal variability. Also, the record remains short, such that even one or two anomalous years can greatly affect the estimated slopes.

Further, the interannual variability of the ice cover and associated atmospheric forcing mechanisms is high, such that the tendencies in recent years are not necessarily indicative of the near-future situation. Recent analysis of SSM/I data and meteorological data has revealed that most of ice reductions in the 1990s have been in the Siberian sector, in response to synoptic-scale atmospheric forcings, unpublished [12]. It is not known whether these broad meteorological tendencies are related to global warming, and it is of course not known whether they will continue.

The relatively large summer decreases imply a reduction in the multi-year ice area, suggesting reduced ice thickness, though observational data are lacking. In addition to its relevance to global warming, the substantially greater decreases in Arctic spring and summer have implications for operations in the Arctic, especially in the marginal seas.

REFERENCES

[1] R.J. Stouffer, S. Manabe, and K. Bryan, "Interhemispheric Asymmetry in Climate Response to a Gradual Increase in Atmospheric CO_2," *Nature* vol. 342, pp. 660-682, 1989.

[2] C.A. Senior, and J.F.B. Mitchell, "Carbon Dioxide and Climate: the Impact of Cloud Parameterization," *J. Clim.* vol. 6, pp. 393-418, 1993.

[3] S. Manabe, M.J. Spelman, and R.J. Stouffer, "Transient Responses of a Coupled Ocean-Atmosphere Model to Gradual Changes of Atmospheric CO_2," *J. Clim.* vol. 5, pp. 105-126, 1992.

[4] J.E. Walsh, "The Arctic as a Bellwether," *Nature* vol. 352, pp. 19-20, 1991.

[5] J.E. Walsh, "Long-Term Observations for Monitoring of the Cryosphere," *Clim. Change* vol. 31, pp. 369-394, 1995.

[6] P. Gloersen, and W.J. Campbell, "Recent Variations in Arctic and Antarctic Sea-Ice Covers," *Nature* vol. 352, pp. 33-36, 1991.

[7] O.M. Johannessen, M. Miles, and E. Bjørgo, "The Arctic's Shrinking Sea Ice," *Nature* vol. 376, pp. 126-127, 1995.

[8] O.M. Johannessen, M.W. Miles, and E. Bjørgo, Time series analysis of SMMR and SSM/I data for climate change detection. *Proc. IGARSS95*, 1995.

[9] I.H.H. Zabel, and K.C. Jezek, "Consistency in Long-Term Observations of Oceans and Ice from Space," *J. Geophys. Res.* vol. 99, pp. 10109-10120, 1994.

[10] E. Svendsen, et al., "Norwegian Remote Sensing Experiment: Evaluation of the Nimbus 7 Scanning Multichannel Microwave Radiometer for Sea Ice Research," *J. Geophys. Res.* vol. 88, pp. 2781-2791, 1983.

[11] W.L. Chapman, and J.E. Walsh, "Recent Variations of Sea Ice and Air Temperature in High Latitudes," *Bull. Am. Met. Soc.* vol. 74, pp. 33-47, 1993.

[12] J.A. Maslanik, M.C. Serreze, and R.G. Barry, "Arctic Sea Ice Reductions Linked to Anomalies in Atmospheric Circulation," unpublished.

Sea Ice Identification Using Dual-Polarized Ku-Band Scatterometer Data

Simon H. Yueh, Ronald Kwok, Shu-Hsiang Lou, and Wu-Yang Tsai

Jet Propulsion Laboratory, MS 300-235
California Institute of Technology
4800 Oak Grove Drive, Pasadena, CA 91109, USA
Tel: 818-354-3012, Fax: 818-393-5285
E-mail: simon@malibu.jpl.nasa.gov

Abstract – This paper describes a classification algorithm using dual-polarized scatterometer measurements to identify the edge of the sea ice cover. The distinct polarization scattering signatures of sea ice and open water are discussed and illustrated with the dual-polarized radar measurements from the Seasat-A scatterometer (SASS). The analysis of SASS data suggests that the ratio of vertical and horizontal polarization backscatter, denoted as the copol ratio, is a useful discriminator of sea ice and open ocean. A simple classification algorithm using the thresholds of the copol ratio and backscatter levels is proposed. The feasibility of this algorithm is demonstrated using the SASS data from the single-sided, dual-polarization mode. The results indicate that the dual-polarized measurements from the NASA scatterometer (NSCAT) can be used to produce routine maps of sea ice extents.

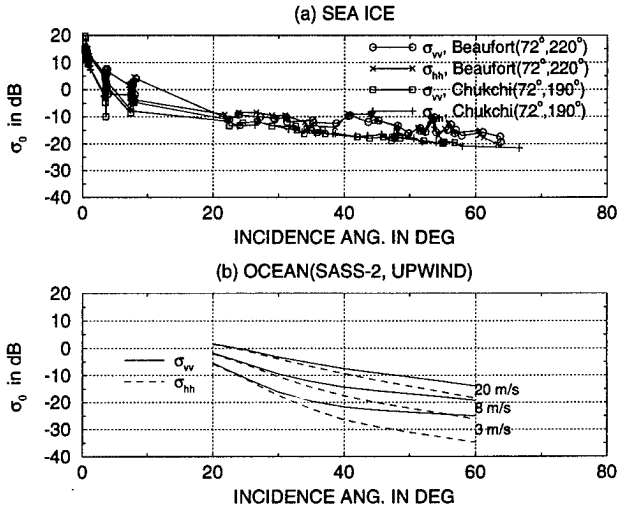


Figure 1. Examples of dual-polarized backscatter data from Seasat scatterometer versus incidence angle. (a) two selected sea ice areas in the Arctic ocean and (b) averaged upwind observations of ocean backscatter [5]

INTRODUCTION

In this paper, we describe the potential of using dual-polarized scatterometer returns from the polar oceans to identify the edge of the ice cover. This ice edge could be used to compute the ice extent which is defined as the area enclosed by the outer boundary of the ice pack. The trends in the maxima and minima of the annual ice extents of the Arctic and Antarctic sea ice covers have been suggested as useful indicators of climatic change. Recent investigations have been based on the ice extent derived from data collected by the Scanning Multichannel Microwave Radiometer (SMMR) instrument and its successor, Special Sensor Microwave Imager (SSM/I). We suggest here that a dual-polarized scatterometer could be used to discriminate sea ice from open water and that a routine ice edge product derived from active microwave data could provide an interesting complement to the SSM/I estimates.

SEA ICE/WATER CLASSIFICATION ALGORITHM

A. Scattering Signatures of Sea Ice and Open Water

Sea ice consists of freshwater ice, brine, and air bubbles. The salinity, size, shape, and number densities of brine inclusions and air bubbles in the ice layer are strongly influenced by the temperature during ice growth and desalination. The surface is composed of meltponds, hummocks, ice ridges and snow cover with roughness at a range of scales [4]. Scattering from a complex medium like sea ice involves both volume and surface scattering mechanisms. Air bubbles, brine pockets, and snow grains are sources of volume scattering. Because these volume scatterers are randomly oriented or almost spherical, the levels of vertical and horizontal polarization returns, σ_{vv} and σ_{hh}, are thus similar. In other words, the copol ratio σ_{vv}/σ_{hh} is near unity for volume scattering. Surface scattering is contributed by the rough surfaces of ice ridges, sea ice and snow cover at all length scales. In general, the surface roughness of sea ice, except thin ice, is comparable with or much larger than the wavelength ($\sim$ 2 cm) of SASS. This means that the geometric optics scattering from surface facets facing the scatterometer may become significant even at large incidence angles. Consequently, the levels of Ku-band σ_{vv} and σ_{hh} will be similar for most sea ice surfaces. From the described characteristics of volume and surface scattering, we anticipate that the copol ratio is close to unity for sea ice at Ku-band, regardless of

This work was performed under a contract with the National Aeronautics and Space Administration at the Jet Propulsion Laboratory, California Institute of Technology.

0-7803-3068-4/96$5.00©1996 IEEE

which scattering mechanism dominates. Figure 1(a) illustrates the SASS data for two areas, one in the Beaufort sea and the other in the Chukchi sea centered at $(72°, 220°)$ and $(72°, 190°)$, respectively. The size of each area is 1° in latitude by 1° in longitude. As shown, the copol ratio is less than 2 dB from 0° to 60° incidence angles, consistent with the physical scattering mechanism described above. The higher backscatter in the Beaufort Sea is probably due to scattering from the more deformed sea ice cover in this region.

The scattering mechanisms of open ocean are quite different from those of sea ice. Sea surfaces roughened by wind forcing are comprised of gravity waves, capillary waves, breaking waves, and foam. The dependence of σ_{vv} and σ_{hh} on the incidence angle and wind speed is illustrated in Figure 1(b) using the SASS-2 model function for upwind observations [5]. The characteristics illustrated here are similar for observations made at other wind directions. The sea surface backscatter is dominated by the Bragg scattering from capillary waves at large incidence angles. The Bragg scattering mechanism provides a unity copol ratio at small incidence angles. However, the copol ratio for Bragg scattering increases with increasing incidence angles and may reach as high as 10 dB at 60° incidence at low winds. Figure 1(b) also indicates that the copol ratio of sea surface backscatter depends on wind speed. This might be due to the increasing coverage of breaking waves and foam with increasing wind speed. It has been suggested that breaking waves significantly increase the level of σ_{hh} at high incidence angles beyond what is predicted from the Bragg scattering mechanism. An increase in σ_{hh} leads to a reduction of the copol ratio of ocean backscatter. In general, the copol ratio of ocean backscatter increases with increasing incidence angles, unlike that of sea ice.

Comparative analysis of Figures 1(a) and (b) indicates that the backscatter levels from sea ice overlap with the range of backscatter from open water, which depends on wind speeds. This clearly makes it difficult to distinguish sea ice and open water using only backscatter levels. However, the SASS data suggest that the copol ratio for ocean backscatter is larger than that of sea ice backscatter at large incidence angles. To verify whether the above observation is true over a larger area, the copol ratios of the SASS data from the entire polar regions are examined. The ratio of consecutive σ_{vv} and σ_{hh} measurements made by the same antenna beam is calculated for incidence angles between 43° and 58° and grouped into 0.5° by 0.5° bins. The results show that the copol ratio is close to 0 dB for the areas expected to be covered by sea ice and is as large as 5 dB over the open ocean. This supports our conclusion drawn from Figure 1.

B. Sea Ice/Water Classification Algorithm

The preceding discussion suggests that the copol ratio is a good discriminator of sea ice and open water. Analysis of SASS-2 geophysical model function [5] for several wind speeds shows that the copol ratio for open water is greater than 2 dB at above 43° incidence angles for winds up to 20 m/s. Hence, if a value of 2 dB is selected for γ_t, the threshold algorithm should work rather well for a large range of wind speeds with the backscatter observations at incidence angles greater than 43°.

Besides the threshold for copol ratio, the thresholds of backscatter levels are also required to reduce erroneous classification at high and low winds. The copol ratio data for the south polar region show that there will be substantial misclassifications of open water into ice if the copol ratio is used as the only discriminator. The classification can be improved by bracketing the range of backscatter levels. The upper backscatter threshold (σ_1) is selected to be small enough so that extraordinarily strong wind conditions resulting in high backscatter and small copol ratios will not be confused as sea ice, but is large enough to include as many ice types as possible so that strong backscatter from some winter Antarctic sea ice will not be excluded. The lower threshold (σ_2) is needed to exclude the noisy backscatter data from open ocean at low winds. We found that the values of 0 dB and -25 dB for σ_1 and σ_2, respectively, work well for the summer Arctic and winter Antarctic sea ice with our current data set. Hence, we propose the following algorithm for sea ice and open water discrimination using the data from above 43° incidence:

A pixel is classified as sea ice if

- $\sigma_{vv}/\sigma_{hh} \leq \gamma_t$, and
- $\sigma_1 > \sigma_{vv}$ and $\sigma_{hh} > \sigma_2$.

Otherwise, this pixel is classified as open water.

APPLICATIONS TO SEASAT DATA

Here, the copol ratio algorithm for sea ice and open water classification is demonstrated with the data from the Seasat scatterometer [3]. SASS used four dual-polarized fan-beam antennas to produce an X-shaped illumination pattern on the earth surface. There were eight science operational modes for beam/polarization scanning. Modes 3 and 4 are single-sided, dual-polarization modes illuminating the left and right sides of the satellite velocity vector, respectively. In early July 1978, SASS operated continuously in mode 4 from revs 142 to 223 with the antenna/polarization scanning sequence (1V,1H,2V,2H). These 82 revs ($\sim$ 6 days) of dual-polarized backscatter data are used to test the sea ice/open water classification algorithm described in the previous section.

The data in the range of incidence angles from 43° to 58° were averaged and grouped into 0.5° latitude and 0.5° longitude bins. The copol ratio was calculated from each pair of consecutive σ_{vv} and σ_{hh} measurements from the same antenna beam and averaged over all the SASS observations for each bin. The averaged σ_{vv}, σ_{hh}, and copol ratio are used to determine whether a bin is sea ice or water. Note that there are bins with no SASS observations from 43° to 58° incidence angles. For this case, no classification is performed.

The classification results are shown in Figures 2 and 3. σ_0 of classified sea ice pixels is indicated with a range of gray levels. As expected in summer, the ice edge is located to the north of the Chukchi sea in the Arctic ocean.

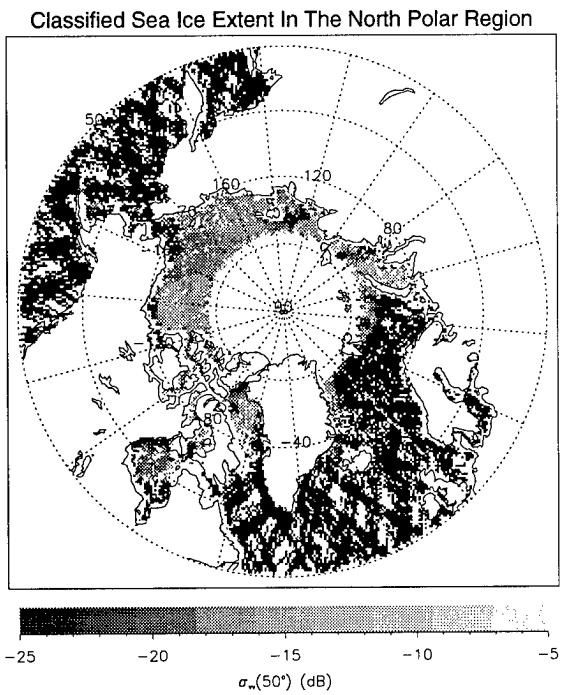


Figure 2. Sea ice backscatter σ_{vv} interpolated at 50° for the north polar regions. Black represents ocean, and white represents land or no data.

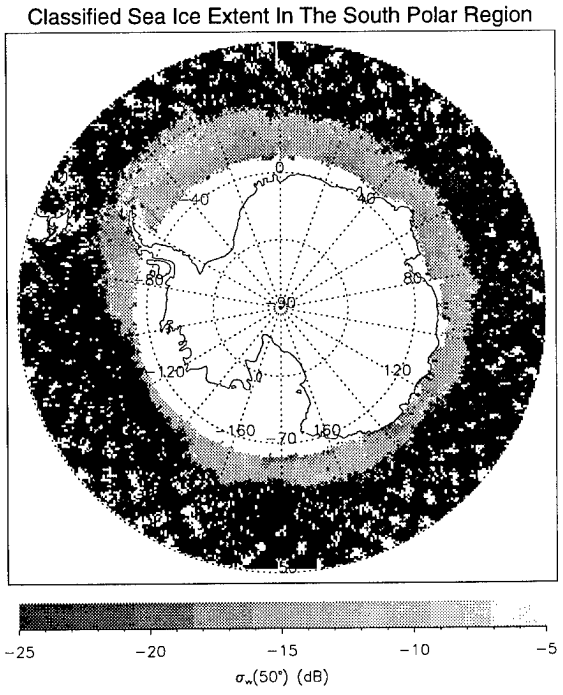


Figure 3. Sea ice backscatter σ_{vv} interpolated at 50° for the south polar regions. Black represents ocean, and white represents land or no data.

A large portion of Baffin Bay was still covered by sea ice, and a large portion of coastal water in the Hudson Bay was open. There was also sea ice off the east Greenland coast. These features agree with the climatological coverage of sea ice in the north polar region [6]. There are only a few obvious misclassifications: A few bins in the north Pacific were classified as sea ice and a few within the ice edge in the Arctic ocean to the north of Chukchi sea classified as open water. For the south polar region, Fig. 3 indicates that the ice edge nearly reached the maximum extent and extended into the mid-latitudes of the south Atlantic, consistent with the climatological ice edge [6]. The clearly identifiable misclassifications are also very limited with very few black pixels well within the ice edge. Although no ground truth information is available to determine the absolute accuracy, the small number of apparent classification errors indicated by the sea ice pixels in the mid-latitude oceans and open water pixels within the ice edges suggests reasonable results from this copol ratio algorithm.

SUMMARY

A classification algorithm using the dual-polarized radar backscatter is presented for the identification of sea ice cover. This algorithm is demonstrated with the SASS data from the single sided, dual-polarized modes. A small number of obvious classification errors suggests that this algorithm performs reasonably well for the summer Arctic and winter Antarctic sea ice. Work is being carried out to further reduce these classification errors with the sea ice identification algorithm developed for ERS-1 [1]. If this algorithm proves to be useful and accurate for other seasons, the sea ice extent can be produced routinely from the NSCAT data [2] and is expected to complement the current products used for monitoring the extent of sea ice cover.

REFERENCES

[1] Gohin, F., and A. Cavanie, "A first try at identification of sea ice using the three beam scatterometer of ERS-1," *Int. J. Remote Sensing*, Vol. 15, No. 6, 1221-1228, 1994.

[2] Naderi, F. M., M. H. Freilich, and D. G. Long, "Spaceborne Radar Measurement of Wind Velocity Over the Ocean — An Overview of the NSCAT Scatterometer System," *Proc. of The IEEE*, Vol. 79, No. 6, 850–866, 1991.

[3] Boggs, Dale H., Seasat Geophysical Data Record Users Handbook, JPL-D129 (internal document), Jet Propulsion Laboratory, Pasadena, August 1982.

[4] Tucker, W. B., D. K. Perovich, A. J. Gow, and W. F. Weeks, "Physical properties of sea ice relevant to remote sensing," Microwave Remote Sensing of Sea Ice, Frank D. Carsey ed., American Geophysical Union, Washington, DC, 1992.

[5] Wentz, F. J., S. Peteherych, and L. A. Thomas, "A model function for ocean radar cross sections at 14.6 GHz," *J. Geophy. Res.*, Vol. 89, No. C3, 3689-3704, 1984.

[6] Gloersen, P., D. J. Cavalieri, J. Comiso, C. L. Parkinson, and H. J. Zwally, Arctic and Antarctic Sea Ice, 1978-1987: Satellite Passive-Microwave Observations and Analysis, *Electromagnetics*, NASA Spec. Publ., SP-511, 289 pp, 1992.

Temporal Mixture Analysis of SMMR Sea Ice Concentrations

Joseph M. Piwowar, Derek R. Peddle, and Ellsworth F. LeDrew
Waterloo Laboratory for Earth Observations
Department of Geography
University of Waterloo
Waterloo, ON, Canada N2L 3G1
e-mail: piwowar@wateol.uwaterloo.ca

Abstract -- In this paper we introduce the idea of Temporal Mixture Analysis (TMA) for analyzing long sequences of hypertemporal remote sensing imagery. The basis of this approach is spectral mixture analysis, which we adapt from the spectral domain to the time domain and apply it to a 9-year record of sea ice concentrations in the Northern Hemisphere. We find that endmember fraction images provide a unique summary of spatial arrangements and temporal characteristics of the mapped phenomenon during a specific period.

INTRODUCTION

The basic premise behind remote sensing is that the identity of targets within a sensor's field-of-view can be retrieved based on their unique spectral and/or spatial properties. The detectability of a surface target is limited by its size, relative to the spatial resolution of the sensing instrument, and the uniqueness of its spectral attributes in the recorded spectral bands. As a result, a large proportion of remotely sensed data are spectrally mixed because the scales of spatial variation of natural phenomena are often smaller than the spatial resolutions of sensors [2]. Thus a fundamental, yet often overlooked, concept is that each single radiance value recorded by a sensor actually contains contributions from several individual surface components [1].

Spectral mixture analysis (SMA) is a procedure which attempts to extract the fractional radiance components from the pixels in an image. It has been shown to be quite effective at addressing a wide range of remote sensing issues from a variety of sensors. In particular, SMA has been used extensively for the analysis of hyperspectral data from imaging spectrometers where conventional image analysis techniques have been shown to be inadequate [2].

The basic premise in temporal monitoring using remote sensing data is that changes in surface features must result in changes in sensed radiance values and that the changes in radiance due to surface changes must be large with respect to radiance changes caused by other factors [3]. Thus in addition to having sufficient magnitude, the detectability of changed features is also dependent on the timing and frequency of observation. Unlike traditional change detection methods (such as image ratioing or differencing), *hypertemporal* image sequences record temporal signatures with sufficient temporal sampling to allow direct identification of changed features and quantitative analysis of subtle temporal changes on a pixel-by-pixel basis.

In this research, the SMA paradigm is extended to evaluate temporal spectra instead of electromagnetic radiance spectra. Specifically, *temporal* mixture analysis (TMA) is examined within the context of identifying the significant temporal patterns of sea ice concentrations in the Arctic.

0-7803-3068-4/96$5.00©1996 IEEE

SCANNING MULTICHANNEL MICROWAVE RADIOMETER DATA

The Scanning Multichannel Microwave Radiometer (SMMR) was a 10-channel instrument which operated on the Nimbus-7 spacecraft between November 1978 and August 1987. It measured emitted Earth radiation at five dual-polarized frequencies between 6.63 and 37 GHz in the microwave portion of the electromagnetic spectrum. The SMMR data used in this study are derived from those published on the *Nimbus-7 SMMR Radiances and Sea Ice Concentrations* CD-ROM (Volume 7) produced by the NASA Oceans and Ice Branch at the Goddard Space Flight Center.

We are interested in assessing the variability of Arctic sea ice concentrations over time within the context of a changing climate. It was anticipated that TMA could define a regional classification of the Arctic sea ice zone based on average monthly sea ice concentrations. To facilitate this investigation, all of the ice concentration files within each month were averaged to create 108 monthly images. A 12 month annual summary of mean sea ice concentration was then created by averaging the monthly concentration images for each month over the 9 year data record. This 12-slice image was used in the following modelling experiments.

TEMPORAL MIXTURE ANALYSIS

The primary objective of spectral mixture analysis is the isolation of the main spectral contributions in each pixel. First, endmembers are defined which characterize the most extreme, or "pure" spectra present in the data. They are then entered into a (generally linear) mixing model which defines the spectral mixing of the scene components from which a set of fraction images (one per endmember) is produced [2].

In a spectral mixture analysis, spectral endmembers are defined as radiometrically "pure" features (e.g., vegetation, soil, etc.). In this study, the SMA technique is extended to analyze temporal spectra of SMMR sea ice concentrations to determine if endmember fractions could be created from temporally "pure" ice concentration features (e.g. always ice-covered, always ice-free, seasonally ice-covered). Three sea ice endmembers, each describing a different seasonal pattern of ice growth and decay, were defined by sampling temporal spectra from the SMMR data. A fourth endmember was defined manually as 100% concentration for each month of

the year to represent non-seasonal sea ice. The SMMR data were unmixed into four corresponding endmember fraction images (Fig.1).

The first seasonal endmember highlights some of the most dramatic seasonality in the Arctic sea ice zone. The spectral curve exhibits near total ice concentration from November through May. There is a steady opening up of the ice cover in June and July until August when it is ice-free. Ice rapidly forms again in the fall so that by November, complete coverage is again realized. Spatially, the fraction image shows regions exhibiting these characteristics as most of the peripheral seas ringing the non-seasonal sea ice of the central Arctic Ocean.

The second seasonal sea ice fraction image was derived from those image pixels which had 100% concentration in March (the general time of maximum winter sea ice) and were ice-free in September (the usual ice minimum). Regions with these temporal characteristics have almost total ice coverage from December to June, experience a rapid clearing in June and July, remain ice free for August and September, and quickly freeze-up to high ice concentrations during October and November. The fraction image identifies these characteristics to be primarily located in Hudson and Baffin Bays, and in the Chukchi, Kara and Barents Seas. Each of these regions are locations of relatively limited ice movement throughout the year (although this is not unique to these regions), possibly due to the restrictive presence of landmasses which partially segregate these areas from the main Arctic drift streams, and to shallow bathymetry. This limited ice motion could promote the quick ice formation and ice stagnation observed in the endmember spectrum.

The third seasonal sea ice endmember characterizes much of the ice in the more southerly extents of the seasonal sea ice zone: in the Sea of Okhotsk, and in parts of the Bering and Labrador Seas. The annual cycle of ice cover in these areas is split approximately equally between periods of total ice coverage and times of ice absence. After reaching a peak concentration of about 80-90% in February or March, the ice coverage decreases steadily so that by June the region is ice-free. It remains devoid of ice for five months until November, when the coverage begins to increase again.

The highest non-seasonal ice fractions are found in the central Arctic Ocean, above the Canadian Archipelago. This is the location of the oldest and slowest drifting ice in the Arctic. The non-seasonal ice fractions in the bulk of the Arctic Basin are all over 70%. Towards the periphery, the non-seasonal fractions drop off rapidly, but are complemented by corresponding increases in seasonal ice fractions.

SUMMARY

Temporally mixed images provide a unique summary of the spatial arrangement of the temporal characteristics of the mapped phenomenon during a specific period. A key distinction which differentiates temporally mixed imagery from similar images derived through other means (e.g., principal components analysis or image classification) is that the data presented are derived from the temporal characteristics of the analyzed phenomenon and not the type of feature present. For example, a region which is highlighted by a non-seasonal ice endmember is not necessarily dominated by multiyear ice. It is, however, dominated by ice whose month-to-month variation is closely aligned with the temporal spectrum defined for this endmember.

An interesting phenomenon about the temporal character of Arctic sea ice was revealed in this analysis: the need for endmembers which had maximum or minimum concentrations between 20% and 80% was not identified during the TMA procedure. This suggests that regions tend to remain generally ice-free or ice-covered during the year and there are forces at work which cause sea ice to resist a change of state (freezing or thawing) well beyond the point at which the atmospheric conditions dictate. Once a certain threshold has been passed, however, the state change occurs rapidly and totally as the system regains equilibrium.

In this study, a simple model consisting of only four distinct temporal processes - three describing seasonal variations; one identifying a non-seasonal component - was required to describe the temporal characteristics of Arctic sea ice concentrations on an annual cycle. These new methods have the potential to improve how climate models treat the polar ice covers, as many existing models treat the Arctic sea ice cover as a solid slab of ice one metre thick. More realistic climate models will help in the development of a better understanding of the Earth's climate system and the significant role played by the polar ice covers.

ACKNOWLEDGMENTS

Financial Support from the Natural Science and Engineering Research Council and the Institute for Space and Terrestrial Science is acknowledged.

REFERENCES

[1] Derek R. Peddle, Ellsworth F. LeDrew and Heather M. Holden, "Spectral Mixture Analysis of Coral Reef Abundance from Satellite Imagery and In Situ Ocean Spectra, Savusavu Bay, Fiji", *Proceedings, Third Thematic Conference on Remote Sensing for Marine and Coastal Environments*, Vol. II, pp. 563-575, Seattle WA., September 1995.

[2] John B. Adams, Milton O. Smith and Alan R. Gillespie, "Imaging Spectroscopy: Interpretation Based on Spectral Mixture Analysis", in *Remote Geochemical Analysis: Elemental and Mineralogical Composition.* C.M. Pieters and P. Englert, Eds. Cambridge: LPI and Cambridge University Press, pp. 145-166, 1993.

[3] Ashbindu Singh, "Digital Change Detection Techniques Using Remotely-Sensed Data", *Int. J. Remote Sensing*, Vol. 10, No. 6, pp. 989-1003, 1989.

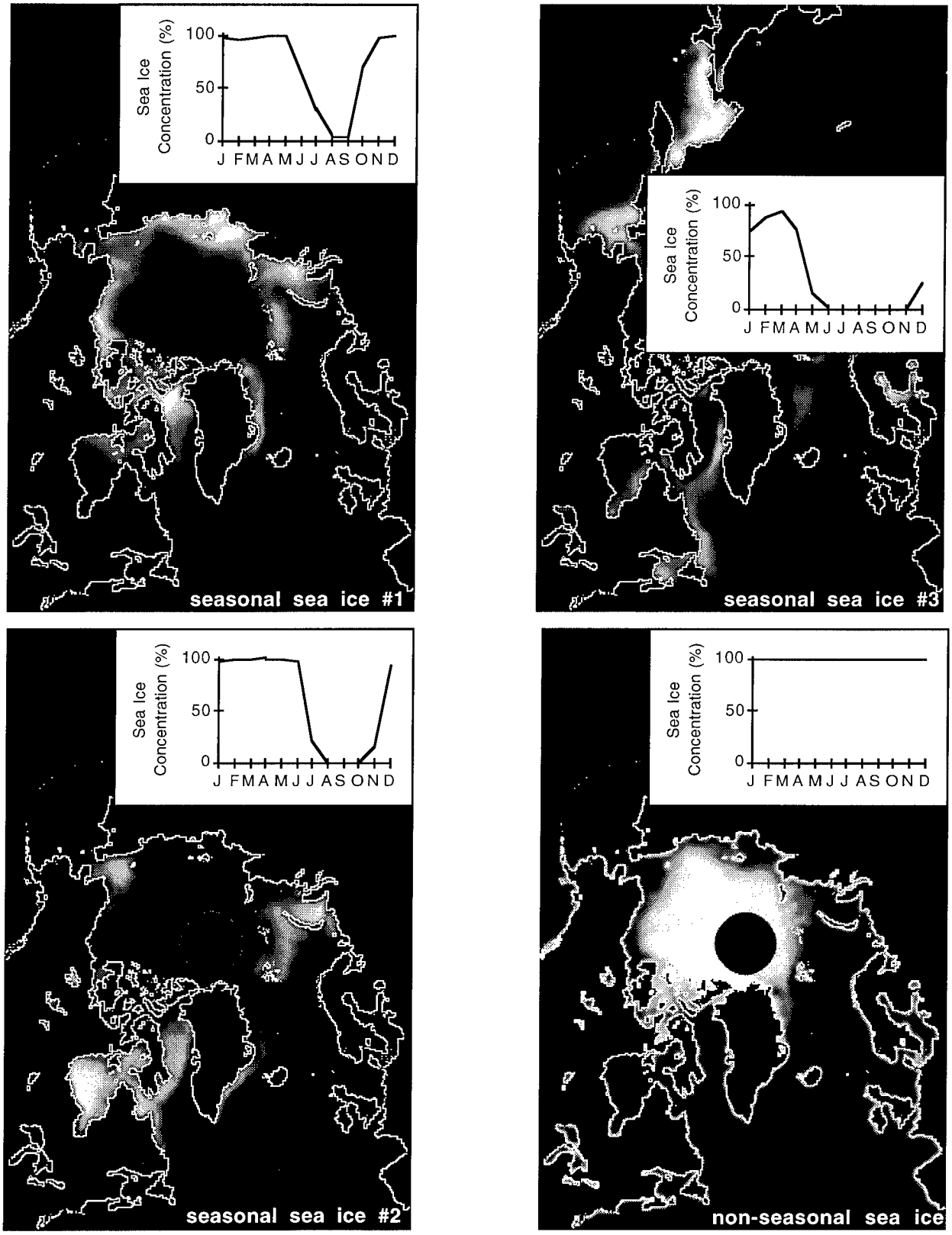


Fig. 1: Spectral Endmembers and Corresponding Fraction Images

Polarimetric Backscattering at 23 cm Wavelength from Antarctic Lead Ice and Estimation of Ice Thickness

D. P. Winebrenner

Applied Physics Laboratory - University of Washington, 1013 NE 40th St., Seattle, WA 98195, (206)543-1393, (206)543-1393 fax, dpw@apl.washington.edu

ABSTRACT

Copolar ratios and phases in backscattering from Beaufort Sea ice at 23 cm wavelength (L-band) vary with apparent ice thickness [1]. Specifically, copolar ratios for multiyear and apparently thick first-year ice agree with those expected for Bragg scattering from an effectively infinitely thick slab with small surface roughness (relative to the radiation wavelength). Copolar phases for multiyear ice cluster tightly around one value, which was taken as a reference value (early data were not phase-calibrated). Copolar phases for apparently thick first-year ice cluster around the same reference value, but are slightly more variable. Both ratios and phases for lead ice, however, display large departures from thick ice values. A scattering model proposed to explain those variations predicts approximately equal likelihoods for copolar phases greater than and less than the reference value. The Beaufort Sea data, however, show negative copolar phase values (i.e., values below the reference value) in all but one case. While this may be because all leads imaged in the data set were of similar ages, the paucity of positive copolar phases was a significant gap in observational support for the theory. I present here new data from the Shuttle Imaging Radar - C (SIRC) mission during October 1994 showing leads in the northern Weddell Sea. As in the Beaufort, essentially no surface observations are available, but conventional SAR imagery suggests the presence of lead ice of at least two distinct ages in close proximity in the Weddell scene. Ice regions in the two categories show spatially coherent, but quite different, polarimetric signatures at L-band, including copolar phases larger than neighboring thicker ice in one case and smaller in the other. The copolar phase also varies between regions. I present a quantitative analysis of the observations and a comparison with theory. I conclude with an assessment of the possibility of estimating lead ice thickness directly from snapshot and time-sequential L-band polarimetric synthetic aperture radar (SAR) imagery.

1. INTRODUCTION

Thin Arctic sea ice exerts an influence on the ocean and atmosphere far out of proportion to its area on the Earth's surface, because of its dominant influence on the heat balance of the Arctic during winter [2]. ("Thin" sea ice typically refers to ice less than about 70 cm in thickness.) The location and distribution of such sea ice is also important in determining the cost and difficulty of various surface and subsurface operations in the Arctic basin and many coastal waters. Thus the remote estimation of sea ice thickness has long been a goal.

Existing microwave remote sensing methods for estimating sea ice thickness rely on the observation of processes at the upper surface of the ice (either the air/ice or snow/ice interface), which are hoped to serve as reliable proxies for ice thickness via one physical link or another. Increasing understanding of such links, however, shows them to be tenuous. For example, the development of frost flowers and rough slush on new ice surfaces, which is visible in backscatter at 5.3 GHz, fails to occur under some conditions of ice growth; thus there is no one-to-one relation between backscattered intensity, or even a given history of backscattered intensity, and new ice thickness. A method of sea ice estimation based on a direct signature response to ice thickness itself is therefore highly desirable.

Jet Propulsion Laboratory airborne SAR observations of apparently thin sea ice in Arctic leads seem to show a strong variation with ice thickness, and this may be understandable in terms of the effect of interference between up- and down-going waves in the ice on scattering at the air/ice interface (the up-going waves being the result of reflection at the ice/water interface)[1]. Such a theory predicts, however, that copolar phases both greater and less than those observed for (effectively infinitely) thick ice should be observed. The observational evidence for copolar phases greater than those from thick ice was not strong in the Beaufort Sea data. Here I present observations of copolar ratios and phases in 24-cm wavelength backscattering from apparently new ice in the Weddell Sea, which were obtained by the SIR-C SAR during October 1994. The imagery shows well-defined regions of ice of apparently differing thicknesses, with reasonably stable but differing polarimetric signatures in differing regions. In particular, spatially coherent regions displaying copolar phases greater than those for neighboring thicker ice are found adjacent to equally spatially coherent regions displaying phases less than those for thicker ice. The absolute phase calibration of the imagery may not yet be sufficiently precise to support a precise comparison of theory and data [3], but such a comparison is the goal of forthcoming work.

2. OBSERVATIONS

Figure 1 shows a conventional, total power SAR image of sea ice in the Weddell Sea during October 1994, acquired using the SIR-C SAR. The location of the image center

0-7803-3068-4/96$5.00©1996 IEEE

is approximately 58°14′S, 21°35′E, and the incidence angle at the center of the image is approximately 32°. The image shows rough first year ice pack, presumably of morphology and thickness similar to that observed previously in the Weddell [4], riven by a lead containing new ice of two or more apparent thicknesses, perhaps resulting from separate opening episodes.



Figure 1. Conventional, total-power SAR image of sea ice in the Weddell Sea acquired by the Shuttle Imaging Radar - C during October 1994.

Figures 2 and 3 show corresponding images of copolar phase and ratio, respectively. These images are derived by using a square, 6x6 pixel moving spatial average of covariance matrices in the original data and computing polarimetric signatures from the averaged covariance matrices (for standard, precise definitions, see [1]). The correspondences between gray scale and signature values, according to initial calibration supplied by JPL, are shown beneath the images.

Both images show regions of reasonably stable but differing signatures corresponding rather precisely to regions of differing apparent age in Figure 1. In particular, it seems clear that most probable copolar phase values for pack ice fall *between* corresponding values observed in separate, spatially well-defined areas of new ice.

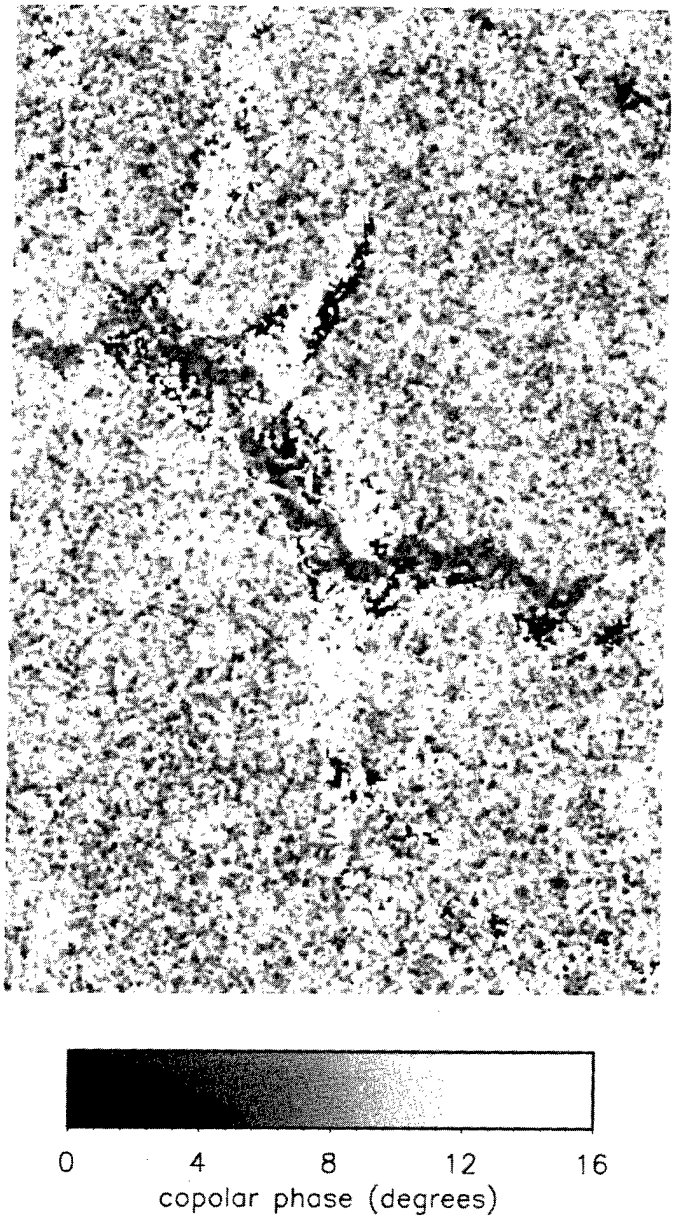


Figure 2. Copolar phase image corresponding to the conventional image in figure 1, based on a 6x6 pixel moving average of covariance matrices.

3. DISCUSSION

The set of observations above is not an exception – several other instances in the SIR-C data of lead systems running through pack ice show similar signature variations. I believe the relative (i.e., within scene) calibration of signatures is likely to be highly reliable, and therefore that the observation of thin ice signatures with copolar phases bracketing those of pack ice significantly strengthens the proposed explanation for signature variations in terms of interference-modulated rough surface scattering [1]. Understanding the mechanism of signature variation opens the door to inverting signature time series to estimate ice thickness history, and the mechanism proposed in [1] is amenable to such inversion.

However, the absolute calibration of copolar ratio and phase remain, as of this writing, sufficiently uncertain [3] to make a quantitative comparison with theory difficult. The multiyear ice sea ice that provided a calibration target of sorts in earlier work [1] is not present in these observations, but orbits on which sea ice data were acquire typically also saw the acquisition of open ocean data just off the ice edge. Because the polarimetric backscattering from wind-roughened sea water is relatively well understood, observations of this surface type should be useful in tightening the radar calibration and acheiving a precise comparison of theory with data. This is subject of a study now underway, to be reported in the near future.

4. ACKNOWLEDGMENTS

This work was sponsored by the Office of Naval Research, grant N00014-96-1-0266. I would like to thank Ben Holt and Ellen O'Leary of the Jet Propulsion Laboratory for expeditiously providing SIR-C SAR data.

5. REFERENCES

[1] Winebrenner, D.P., L.D. Farmer and I.R. Joughin, "On the Response of Polarimetric SAR Signatures at 24-cm Wavelength to Sea Ice Thickness in Arctic Leads", *Radio Science*, 30(2), pp. 373-402, 1995.

[2] Maykut, G.A., "The surface heat and mass flux", pp. 395-464 in *The Geophysics of Sea Ice*, N. Untersteiner, ed., NATO ASI Series B, Physics vol. 146, Plenum Press, New York, 1986.

[3] Freeman, A., M. Alves, B. Chapman, J. Cruz, Y. Kim, S. Shaffer, J. Sun, E. Turner, and K. Sarabandi, "SIR-C Data Quality and Calibration", *IEEE Transactions on Geoscience and Remote Sensing*, 33(4), pp. 848-857, 1995.

[4] Tucker, W.B. III, D.K. Perovich, A.J. Gow, W.F. Weeks, and M.R. Drinkwater, "Physical Properties of Sea Ice Relevant to Remote Sensing", chapter 2 in *Microwave Remote Sensing of Sea Ice*, F.D. Carsey, ed., Geophysical Monograph 68, American Geophysical Union, 1992.

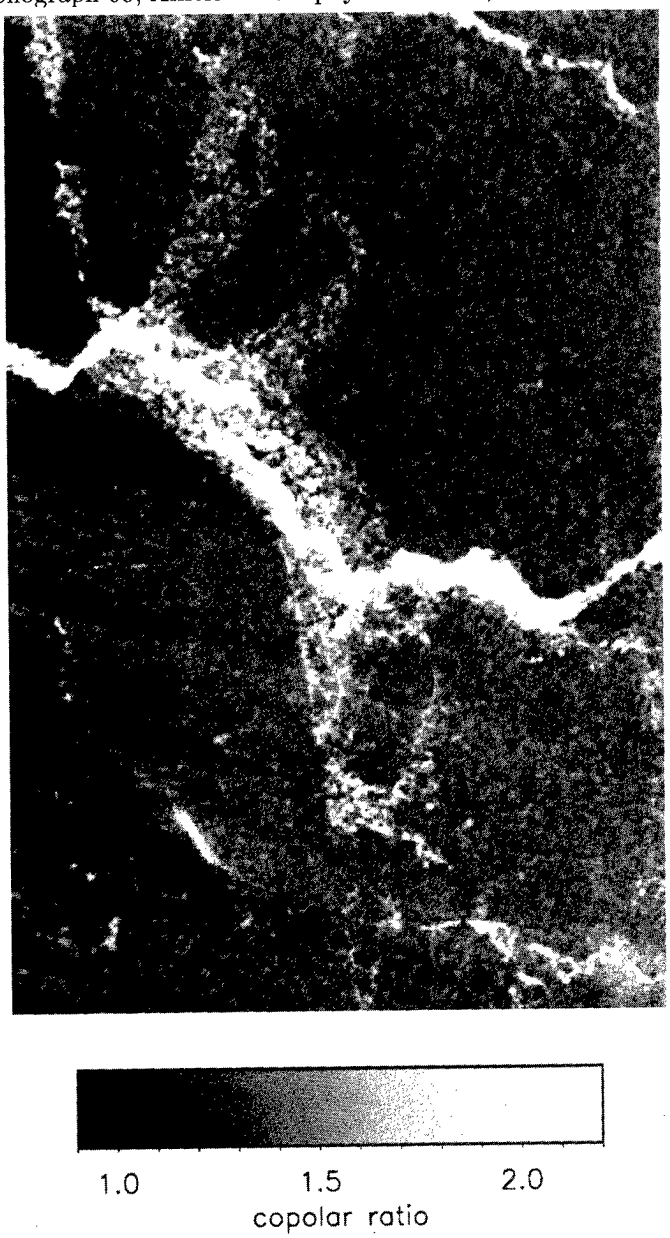


Figure 3. Copolar ratio image corresponding to the conventional image in figure 1, based on a 6x6 pixel moving average of covariance matrices.

Characterization of Ice in the Chukchi Sea at the Start of the Growing Sea Using Satellite SAR

Robert G. Onstott
Center for Earth Sciences / Environmental Research Institute of Michigan
P.O. Box 134001, Ann Arbor, MI 48113-4001
Phone: (313) 994-1200 FAX:(313) 994-5824 Email: Onstott@ERIM.org

Abstract - The distribution of ice forms and thickness is believed to be important to the study and monitoring of changes in our global environment. Distribution information is known to vary with region. Satellite and in-situ observations were conducted in the Chukchi Sea with the intent to learn more about sea ice physical and microwave properties during the period of transition from summer to winter. Comparisons are made with observations from a well studied region, the Beaufort Sea. A regional knowledge of sea ice properties and microwave behavior is important to the application of SAR remote sensing methods to retrieve geophysical properties.

INTRODUCTION

Previous microwave and physical property investigations have often concentrated on the Beaufort Sea and the marginal ice zone in the Fram Strait. Regions such as the Chukchi Sea are less well studied. The character of ice conditions presented in synthetic aperture imagery (SAR) is found to be different from that of the Beaufort Sea, a region immediately to the East. This provides an illustration that processes unique to a region influence the microwave behavior of its floating ice.

We participated in an U.S. Geological Survey cruise during the fall freeze-up period (e.g. August and September 1992) during which the United States Coast Guard (USCG) Ice Breaker *Polar Star* operated in the Chukchi and Western Beaufort Sea in a region between 75 and 76 N, and 154 and 165 W. Based on *in-situ* observations made during this cruise an opportunity to compare ERS-1 SAR signatures with ice transitioning from summer-to-fall conditions and the production of new ice in an area associated with the Chukchi Sea and which contains seasonal ice was made possible. This also provided the opportunity to examine ice which was also studied during an intensive spring 1992 Beaufort Sea investigation [1,2], and had transited northwest..

OBSERVATIONS CONDUCTED IN SITU

During this cruise *in situ* observations were made to characterize sea ice physical and electrical properties. In addition, a microwave scatterometer which operates at the ERS-1 SAR frequency and a color video recording system were positioned on the bridge of the ship to view perpendicular to the ship's track. When at station, detailed angular response information was obtained to support studies of the backscatter mechanisms at play. When in transit, observations were made at the ERS-1 SAR observation angle of 25 degrees for a statistical study of backscatter intensity and ice form.

DISCUSSION

ERS-1 SAR imagery were obtained for the period of 24 August to 12 October to characterize the transition from summer melt to fall-freeze up. About thirty 100 km x 100 km images were used in characterizing this period and region. Measures of multiyear ice and total image backscatter were made and are provided in Fig. 1. Backscatter intensities range from a low of about -13 to a high of about -7.5 dB. There are three characteristics to the observed time response: (a) a rapid level shift in intensity which occurred near the end of August and associated with the drop in ambient temperature (see Fig. 2) to below the freezing point of fresh water, (b) a level shift in total image intensity occurring mid September, and (c) a third level shift in total image intensity at the end of September. The modulation in backscatter intensity at late summer may be explained based on whether a floe has a wet or frozen surface, or if a floe is covered with large areas of open water filled meltpools, or whether the meltpools are largely drained

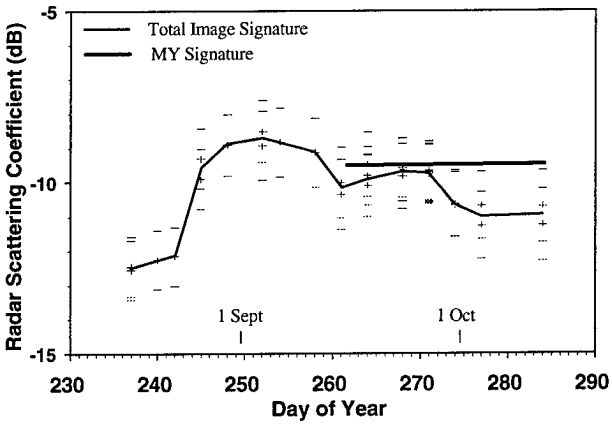


Fig. 1. ERS-1 SAR radar scattering coefficients for multiyear ice and total image backscatter is shown.

0-7803-3068-4/96$5.00©1996 IEEE

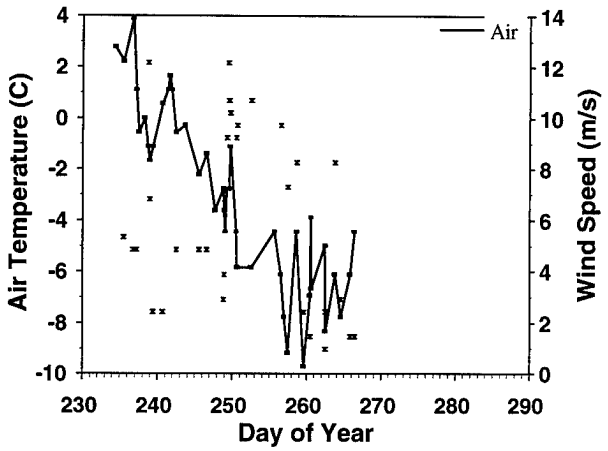


Fig. 2. Periodic air temperature and wind speed were taken at a height of about 19 meters.

and frozen [3]. Once freeze-up occurs, multiyear signatures are found to stabilize at about -9.5 dB. Based on SAR image analysis, the level shifts in total image backscatter which occur after mid September are associated with the divergence in the ice fields after storms and the filling in of the divergence areas with newly produced ice. As the fraction of the ice field in first year ice increases the total image backscatter decreases. This suggests that storms may be the primary mechanism forcing divergence and that changes in ice fraction may occur in concert with storm frequency.

The character of ice fields in both the Chukchi and Beaufort as observed at the end of summer is illustrated in the 25 August SAR image shown in Fig. 3. Over a region of 100 km square, there is great homogeneity. Modification of this character began 6-14 September in association with a storm which produced wind speeds of 11m/s. Individual floe structures resulted and regions of newly formed ice become a small percentage of the ice field. By mid October, it is observed that the old ice has conglomerated further into masses with distinct boundaries which is frozen into a matrix of recently formed ice. This is a major change in character and is illustrated in Fig. 4. A key difference between the Beaufort and Chukchi Sea is that divergence is less constrained in the Chukchi Sea and that the size of the conglomerations which result are smaller than those observed in the Beaufort Sea.

During fall, new ice is produced. *In situ* observations were made of the evolution of newly formed ice and of the variety of new ice forms present in the region. New ice production occurs in concert with the divergence of the ice fields which exposes open water to a cold atmosphere. The production of new ice in a region such as the northern extent of the Chukchi Sea is very much a dynamic process. How much new ice is produced, how long it survives, and its

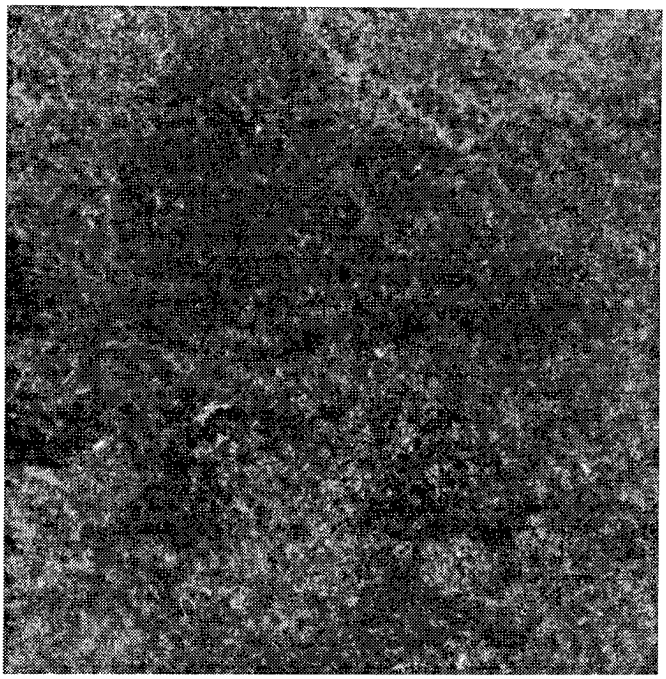


Fig. 3. European Space Agency SAR (©) image of ice locate at the northern extent of the Chukchi Sea area on 24 August 1992 (73.8 N, -156 W).

microwave properties have one thing in common, they are temporally dynamic. As an example, the variation in the signature of newly produced ice is shown for thicknesses from 3 to 20 cm for various formation states in Fig. 5. Open water driven by an 11 m/s wind is provided as a reference. Signature are shown for formation conditions which include nilas, frost flower covered ice, and grey ice. This investigation also contributed to the correlation of backscatter response and formation state. The backscatter response of ice is often dominated by it's surface roughness and formation conditions as seen in the time series response shown in Fig. 6 for a region of recently formed ice.

CONCLUSIONS

Utilizing *in situ* physical and electromagnetic property information we have improved our understanding of the amplitude and textural information provided in ERS-1 SAR products of sea ice in the Chukchi Sea. ERS-1 SAR data are used to document the transition from summer-melt to fall freeze-up conditions. Sea ice conditions and microwave properties observed about the ship during the cruise provide guidance of the important mechanisms at play. Comparisons of ERS-1 SAR products of the Beaufort Sea and the northern Chukchi Sea shows that differences in SAR image character is attributable to floe size. This difference is found to be associated with how these two ice fields respond to meteorological forcing.



Fig. 4. European Space Agency SAR image (©) of ice located at the northern extent of the Chukchi Sea on 11 October 1992 (75.2 N, -159 W).

The results from this investigation support a quantitative assessment of the ability of satellite SAR to map Chukchi and Western Beaufort Sea ice types, and potentially thickness, for the fall freeze-up condition.

REFERENCES

[1] Onstott, R.G. and R.A. Shuchman, "Arctic Sea Ice Microwave Signature and Geophysical Processes Study," Cannes, France, 4-6 November 1992 .

[2] Shuchman, R.A. and R.G. Onstott, "ERS-1 SAR Snow and Sea Ice Signatures During LEADEX," ERIM Technical Report 231500-12-T, ERIM, Ann Arbor, Michigan, August 1992.

[3] Onstott, R.G., "SAR and Scatterometer Signatures of Sea Ice," Chapter 5, Microwave Remote Sensing of Sea Ice (ed. by Frank Carsey), American Geophysical Union, Washington, D.C., 1993.

ACKNOWLEDGMENTS

This study was funded by the National Science Foundation, Office of Polar Programs under Grant No. OPP-9224190. We thank the U.S. Geological Survey for the opportunity to participate in this cruise, the USCG *Polar Star* for their accommodations. We would especially like to thank M.O. Jefferies and K. Schwartz for operating the ship-board scatterometer during this cruise and providing the *in situ* information.

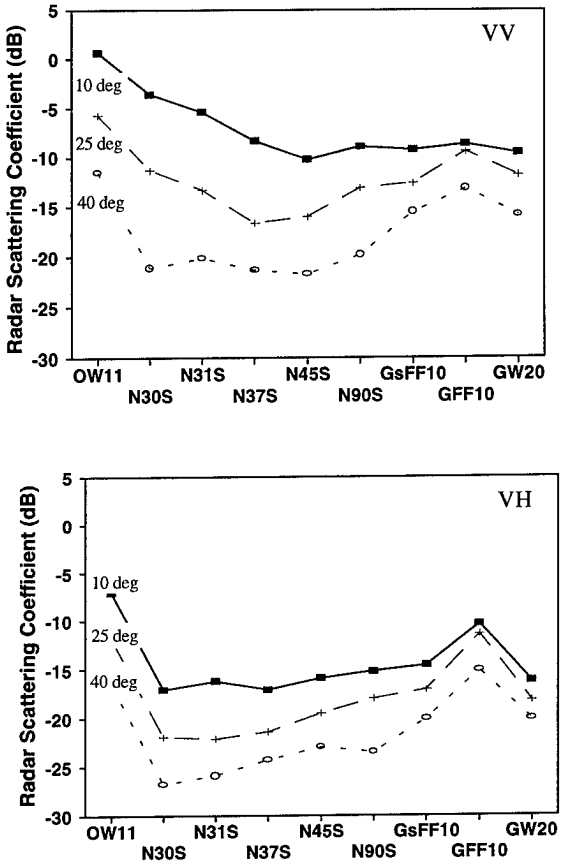


Fig. 5. The signature of newly produced ice is shown at VV and VH polarizations for various formation conditions. Legend: N- nilas, S-smooth, 30-30 mm, s-sparse coverage, FF-frost flowers, G-grey, 10-10 cm, GW-grey white.

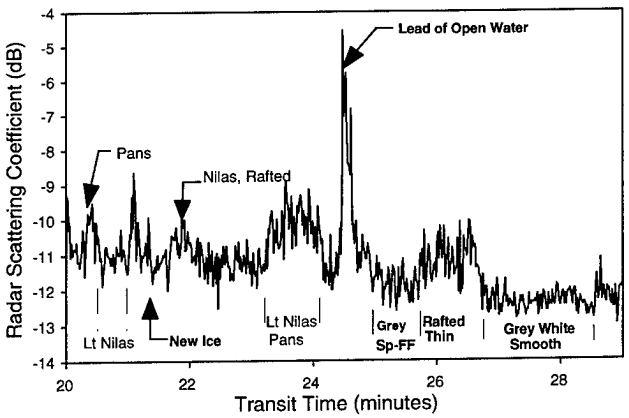


Fig. 6. The backscatter response of ice is often dominated by it's surface roughness and formation conditions as seen in this time series response for a region of recently formed ice.

Bistatic Microwave Investigations of Sea Ice-Like Media

May G.C., Bredow J.W., Juying J., Nadimi S.A., Fung A.K.
University of Texas at Arlington-Wave Scattering Research Center
Department of Electrical Engineering, Box 19016, Arlington, Texas 76019
PH:817-272-5660 FAX:817-272-3443 Email:gcm3629@omega.uta.edu

Abstract -- For purposes of verifying inverse and forward scattering models for sea ice, and to develop a better understanding of scattering and emission behaviors from sea ice, a target is built whose dielectric properties are similar to those of sea ice. This paper briefly describes the investigation of materials leading to the construction of a 12 layer epoxy target, dielectric measurements regarding how well this target followed the desired dielectric profile, and microwave measurements of the target made using several bistatic angles.

INTRODUCTION

In the past, numerous measurements were made in order to determine and quantify important scattering and emission mechanisms of sea ice. During the initial phase of these activities, field campaigns determined and quantified fundamental differences in scattering and emission behaviors between different types of ice. It was later found that the structural and electrical complexity and spatial variability of natural sea ice precluded more detailed studies of scattering and emission behaviors in the field.[1]

This led to research conducted in facilities such as the US Army Cold Regions Research and Engineering Laboratory (CRREL). Though these have led to a better understanding of a number of scattering and emission behaviors from sea ice, the structural and electrical characteristics of laboratory ice are sufficiently complex that some important questions have not been answered.[2]-[3]

These unanswered questions include the structural and electrical parameters of sea ice which can be retrieved from a set of remote sensing data. In addition, what frequencies, polarizations, and angular geometries are needed to obtain the best retrieval of these parameters. The specific mechanisms which cause dense medium scattering to deviate from the well-known sparse medium scattering behavior also need to be determined. There is also the question of whether brine and air pockets in sea ice can be adequately modeled by a monodispersion or polydispersion of spheres, or whether the use of ellipsoids is necessary.

Some of these questions may better be answered by performing microwave measurements of man-made targets that are fabricated so as to incorporate only those parameters that are thought to have the greatest influence on scattering/emission from sea ice. To this end, the Wave Scattering Research Center (WSRC) at the University of Texas at Arlington (UTA) has undertaken the construction of sea ice-like media using epoxy mixed with filler so as to create the desired dielectric profile corresponding to various types of sea ice.

Using this approach is expected to lead to improved quantitative interpretations as to how well the models perform, as opposed to parameter retrieval for actual ice which, due to its complex structure, almost always permits considerable leeway in interpretation, often making it unclear as to how well the models actually worked.

EXPERIMENTAL APPROACH

In order to find a suitable material which could be used for construction of the target, a study was made of commercially available materials which could be easily molded into the appropriate shape. The second phase consisted of identifying a number of filler materials which could be added to these other base materials in order to vary both the magnitude and loss of the dielectric constants.

A wide variety of base materials were allowed to harden in small containers, followed by the measurement of their dielectric constants using a Hewlett Packard HP85070A Dielectric Probe Kit. In addition to the values of the dielectric constants, other factors were noted as well, such as the amount of time required for the material to cure or harden into the desired shape, and whether the material cracked or developed other undesired imperfections upon reaching its final state. Among these, materials such as caulking and mending-type substances were rejected due to their tendency, when used in large volumes, to take several days to cure and then to crack or otherwise deform upon hardening.

The most favorable materials investigated were epoxies, which are available in large quantities at reasonable cost. In addition, these epoxies, created by mixing a resin with a hardener material, have permittivities only slightly lower than sea ice, with relatively low loss. The final choice of epoxy was a Shell product, the liquid resin EPON 828, with its corresponding Epicure 3140 hardener, which are available for an effective cost of less than $60 per mixed gallon. The base mixture consists of 2 parts of resin to 1 part of hardener, and has a dielectric constant which varies from 3.09-j0.09 at 3 GHz, to 2.93-j0.19 at 18GHz.

0-7803-3068-4/96$5.00©1996 IEEE

The second phase of the materials research involved the investigation of various materials available in powdered form, which have dielectric constants with magnitudes and losses which are greater than the base epoxy. Thus by adding these materials to the epoxy in varying quantities, a desired dielectric property can be achieved. The dielectric properties of materials such as mica and aluminum oxides were measured, and then the material was mixed with the epoxy at various concentrations. These samples were then measured as well, and plots of the dielectric constant versus the amount of the material added were obtained.

The most suitable filler material was activated carbon available in a 325-Mesh powder form. When added to the Shell epoxy, the dielectric constant is raised to the values given in Table 1, by varying the concentrations as shown.

Table 1. Dielectric Constant of 828 Epoxy as a Function of Frequency and Concentration of Carbon Filler.

2:1:X	3GHz	9GHz	18GHz
X=0.25 parts carb.	4.10-j0.14	3.95-j0.36	3.85-j0.32
X=0.50 parts carb.	5.06-j0.15	4.80-j0.46	4.68-j0.40
X=1.00 parts carb.	12.9-j0.50	12.2-j1.30	12.2-j1.00

With the choice of filler narrowed to carbon, and the base material chosen as 828 epoxy, experiments were then conducted to develop more information on the variance of the dielectric constant for various concentrations of carbon. In addition, several small prototype layers were poured to achieve the desired dielectric constant profiles, to develop confidence both in the results and in the mixing procedures.

TARGET DESCRIPTION

A sea ice profile was designed for a frequency of 4GHz, consisting of 12 layers of 1cm thickness. Fig. 1 shows the real part of the dielectric constant, and Fig. 2 shows the imaginary component. The expected profile for the real part is the same as the desired profile. The imaginary portion is driven by the corresponding real values for a given concentration, and thus the expected imaginary values are not the same as the desired profile.

The designed profile was achieved by pouring one layer at a time into a circular form, making sure each layer spread out to a uniform depth. For the first few layers, a 24 hour curing time was used, but it was quickly determined that two layers could be poured in a 24 hour time frame, one in the morning and one at night.

The materials for each layer were combined by parts by weighing the container into which each portion was added, until the weight equal to that calculated had been reached. Mixing was achieved using a large paint-mixing bit in conjunction with a variable speed electric drill. Initial layers were somewhat thinner than designed as no material losses had been accounted for in the pouring process. The epoxy

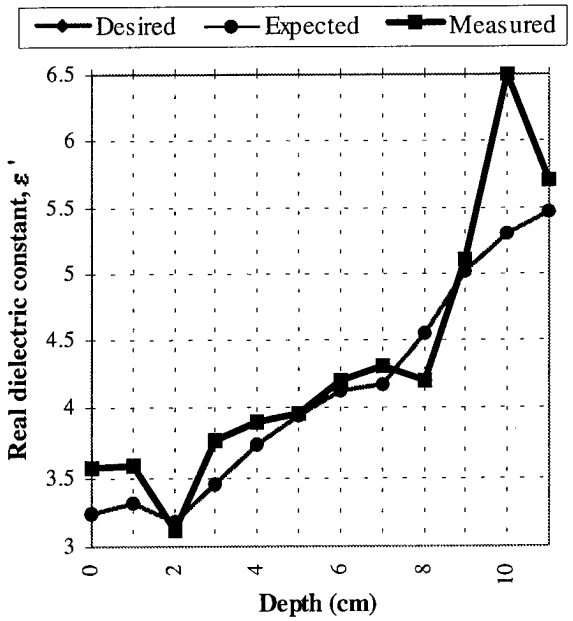


Fig. 1. Real dielectric constant versus depth for designed, expected, and measured profiles.

resin and hardener have the consistency of a very thick molasses, and the resulting combination with the carbon results in a very viscous material which pours and spreads very slowly. Some material losses are inevitable. By increasing the mixture amount to account for this waste, the desired thickness can be achieved.

The resulting target, shown in Fig. 3, is 4 feet in diameter, 4.7 inches thick, and weighs about 250 lbs. The

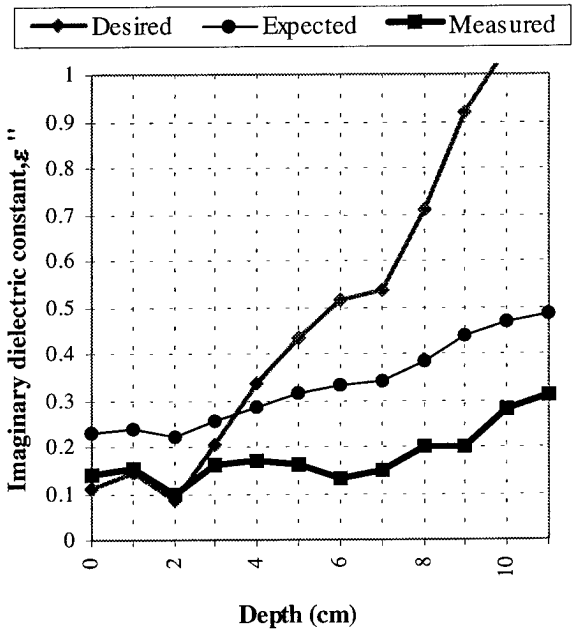


Fig. 2. Imaginary dielectric constant versus depth for designed, expected, and measured profiles.

extraction of the target from the form proved easier than anticipated, as the form had been initially sprayed with silicone. In a few areas on the bottom corners the epoxy mixture had seeped under the aluminum foil used on the bottom of the form, making it somewhat difficult to remove the foil, but this was accomplished with minimal target deformation.

MEASUREMENT RESULTS

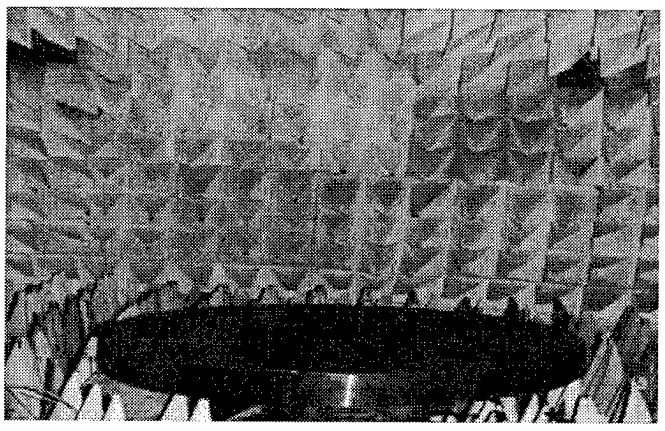
RCS measurements were made in the Wave Scattering Research Center's anechoic chamber. Pictured in Fig. 3 is the epoxy target positioned on the pedestal, located in the center of a quarter sphere shown in the background. Broadband conical antennas are located at various positions around the quarter sphere to give a wide range of bistatic angles. The transmit antenna, not shown, is located to the upper right of the picture, at an angle of 45°. Measurements were made with a Hewlett Packard HP8510A vector network analyzer.

For the measurements made, the displaced antenna calibration approach was used.[4] This entails calibrating the receive antenna at a bistatic position which will result in a good calibration for all 4 polarizations: VV, VH, HV, and HH. The antenna, which is attached to a 20ft. phase stable cable, is then moved to various locations where the target and background measurements are made. All target measurements were made rotating the target into 10 equal azimuthal positions, each 36° apart. These are then averaged to obtain the radar cross section plots of Fig. 4.

Measurements were made using several bistatic angles, but due to the absence of discrete scatterers and to the layered nature of the target, appreciable scattering is noticeable only near and around the specular region. Fig. 4 shows several results over 13-17GHz near the specular direction. Results show substantial agreement with predictions of a simple layer model.

DISCUSSION

This initial synthetic target was developed to demonstrate



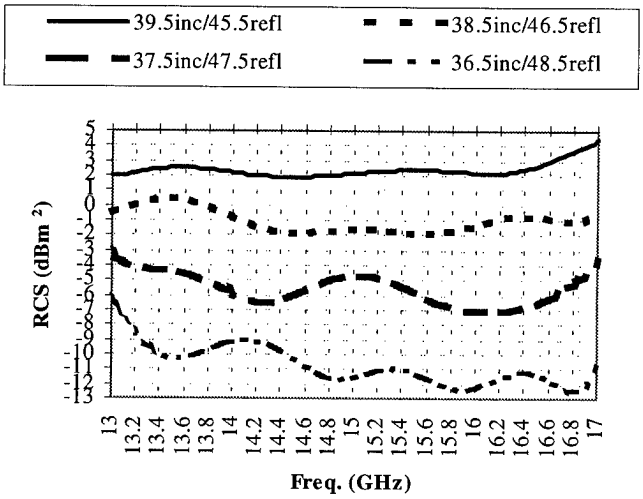


Fig. 4. RCS values for various angles near specular.

the feasibility of simulating a sea ice-like profile using commonly available materials. This target will be used as a standard against which the results of other scatterer containing targets can be compared.

These future activities will include the addition of scatterers into the target. The goal will be the simulation of air pockets and brine pockets which are found in sea ice, by the addition of various types of material such as foam spheres or metal-coated spheres.

ACKNOWLEDGMENT

This study was supported by ONR grant N00014-95-1-0441.

REFERENCES

[1] J.W. Bredow, "A Laboratory Investigation Into Microwave Backscattering from Sea Ice", Doctoral Dissertation, University of Kansas, 1989

[2] J.W. Bredow, R.L. Porco, A.K. Fung, S. Tjuatja, K.C. Jezek, S. Gogineni, A.J. Gow,"Determination of Volume and Surface Scattering from Saline Ice Using Ice Sheets with Precisely Controlled Roughness Parameters", *IEEE Transactions on Geoscience and Remote Sensing,* vol. 33, No. 5, pp. 1214-1221, September, 1995

[3] C.E. Nance, "Scattering and Image Analysis of Conducting Rough Surfaces", Doctoral Dissertation, University of Texas at Arlington, May 1992.

[4] B.D. Jersak," Bistatic, Fully Polarimetric Radar Cross-Section Calibration Techniques and Measurement Error Analysis ",Doctoral Dissertation, University of Texas at Arlington, Dec. 1993.

Validation of a Sea Ice Model Using Forward Simulation of ERS-1 SAR Data: A Case Study in the Beaufort Sea

John Heinrichs, James Maslanik, and Konrad Steffen
Cooperative Institute for Research in Environmental Sciences
Campus Box 216 University of Colorado at Boulder Boulder, CO 80309
Phone: (303) 492-6881, email: jheinric@albedo.colorado.edu

Abstract--A sea ice dynamics/thermodynamics model is validated using a one-year time series of data from the C-band Synthetic Aperture Radar (SAR) instrument aboard Earth Resources Satellite 1 (ERS-1). Common validation problems using geophysical parameter estimates produced by operational algorithms are avoided by coupling a simple backscatter model to the physical model to generate a time series of estimated SAR backscatter values, which can be directly compared to the observed time series. Comparison of actual and estimated SAR backscatter shows good agreement during the winter and spring seasons. Differences during the summer and early autumn period are attributed to surficial changes, namely wet snow, meltponds, and young ice covered by frost flowers, that are not included in the ice physics model but affect the C-band backscatter. After adding these effects to the backscatter model, very good agreement is observed throughout the year between the sea ice/backscatter model and the ERS-1 time series, with RMS differences about 10% of the full range of backscatter values. The paper demonstrates the utility of the forward simulation approach for model validation and discusses potential future improvements and applications.

1. INTRODUCTION

Numerical models have been increasingly used in studies of sea ice. As the General Circulation Models (GCMs) used for global climate simulations become more detailed, sea ice models have become important components. These models must be validated (i.e., have their predictions compared with reality) before they can be used. A typical approach to validation is to compare model-generated estimates of such variables as ice concentration and extent with those obtained from satellite-borne sensors, particularly microwave sensors. A major difficulty is that errors in the model predictions, combined with errors in the geophysical parameter estimates from the remote sensing data, render a direct comparison of predictions and observations problematic. The research described in this paper has had, as its primary goal, the development of an alternative strategy for validating sea ice models with SAR data. SAR instruments offer high spatial resolution and have a demonstrated ability to respond to the changes in sea ice as it grows and melts [1]. Our strategy is to couple a simple backscatter model to a physical sea ice model and compare estimates of the radar backscatter the sensor would receive to the actual observed backscatter. With this approach, the ambiguities inherent in statistical geophysical parameter estimation algorithms can be avoided and a more accurate validation of the model performed. This technique has been successfully used in other contexts, most notably in retrieving atmospheric temperature and water vapor profiles from satellite-borne sounders [2] and detecting areas of snowmelt on the Greenland ice sheet [3].

0-7803-3068-4/96$5.00©1996 IEEE

2. APPROACH

An area in the Beaufort Sea at at 78° N, 153° W (Fig. 1) that had high variability in ice concentration estimates from visible and passive microwave sensors and thickness estimates from submarine sonar data was selected as the study location. A series of 32 low-resolution (100 m) ERS-1 C-band SAR images covering the study area from October 1991 to November 1992 was obtained from the Alaska SAR Facility (ASF) and calibrated using the operational ASF algorithm [4].

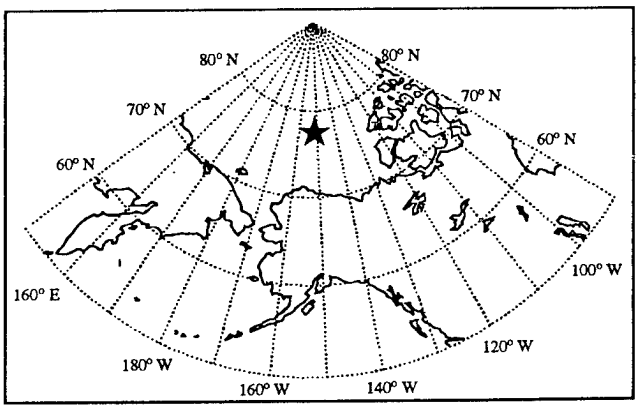


Figure 1 Location of the study area in the Beaufort Sea

Simulations of the Arctic ice cover were performed using a two-layer thermodynamic ice model based on the original formulations of Hibler and Walsh [5] with revised parametrizations of downwelling radiation. Separate thermodynamic and dynamic calculations were done for first year ice, second-year ice, and multiyear ice. Model runs were carried out at 160 km spatial resolution with a 24-hour time step over the entire 13-month study period. Daily geostrophic winds estimated from National Meteorological Center (NMC) air pressures were used to drive the model. Other forcings included climatological air temperatures and humidity and oceanic heat flux and geostrophic ocean currents.

After the model run was completed, model output for the study location was extracted. In general, this time series of surface cover (shown in Fig. 2) is consistent with observed long-term averages from passive microwave instruments [6] and shows temporal changes (i.e., the increase of open water (OW) and decrease of multiyear (MY) ice during the summer, the disappearance of first-year (FY) ice in the summer, and large amounts of FY ice forming in the autumn) that would be expected in typical pack ice.

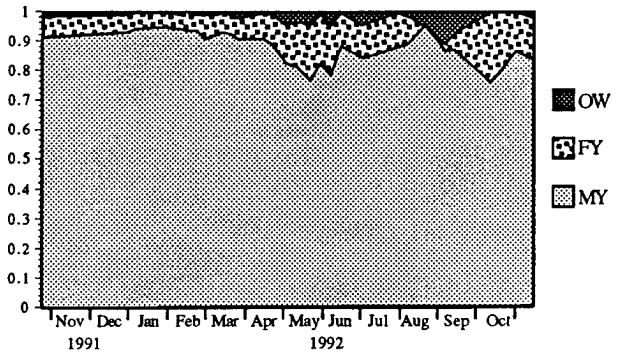


Figure 2. Time series of coverage for open water, first-year ice, and multiyear ice from the sea ice model.

In order to validate the output of the ice physics model against ERS-1 SAR data, we developed a simple model of the mean C-band backscatter of the grid point containing the study domain. If only OW, FY ice, and MY ice are considered, the average backscatter of the entire scene (σ^0) is given by

$$\sigma^0 = \sigma^0_{OW}A_{OW} + \sigma^0_{FY}A_{FY} + \sigma^0_{MY}A_{MY} \quad (1)$$

where σ^0_{OW}, σ^0_{FY}, and σ^0_{MY} are the backscatter contributions for open water, first year, and multiyear ice respectively; and A_{OW}, A_{FY}, and A_{MY} are the corresponding areal fractions covered by each surface type (obtained from the ice model).

The backscatter of MY ice varies on short time scales [7], and to eliminate this variation as a source of error we obtained values for σ^0_{MY} by sampling the backscatter of several MY floes in each SAR image in which distinct floes were visible. For FY backscatter, such a sampling procedure is impractical, and a constant value of -16.0 dB for σ^0_{FY} was chosen based on the results of a recent study comparing Landsat and ERS-1 SAR data [8]. Finally, the backscatter of open ocean areas is known to vary with wind speed due to the formation of capillary waves on the ocean surface. To determine σ^0_{OW}, we used a formula developed empirically by Wismann [9] relating open ocean backscatter to the wind speed.

3. RESULTS

Fig. 3 shows both the estimated and actual SAR backscatter values through the study period. Agreement between the two is clearly seasonally dependent. During the late autumn, winter, and early spring (November through May), agreement between the estimated and actual SAR time series is quite good. The combined model substantially overestimates the backscatter during the summer and underestimates it during the winter. We attribute these differences to physical changes in the sea ice that affect the observed SAR signal, but are not incorporated into the model. The first is the melting of the snow cover at the start of summer, which has been noted to cause a large drop in backscatter values [1]. The second is the formation of meltponds which, being liquid, would tend to have wind speed-dependent backscatter values closer to open water than sea ice. Supporting this hypothesis, concurrent variations in backscatter and wind speed were observed in the actual SAR time series. The third surface change is the formation, under particular atmospheric conditions (namely a large air/surface temperature contrast and atmospheric supersaturation), of crystalline "frost flowers" on young ice [10]. Well-developed frost flower populations have been shown to increase the backscatter of young ice by as much as 12-15 dB [1]. In images taken during the freezeup period, high-backscatter areas appear between MY floes, supporting this explanation.

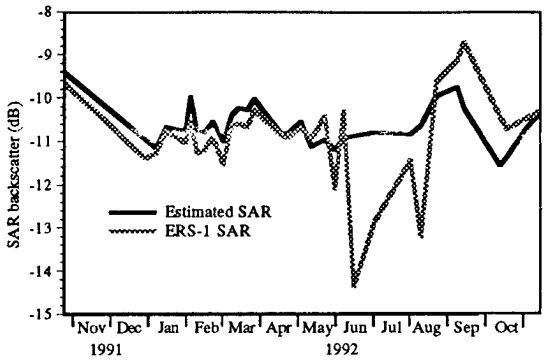


Figure 3. Comparison between actual ERS-1 SAR backscatter time series and estimates from the ice model.

By incorporating these three major surficial changes into the backscatter model, their effects on the observed SAR time series can be evaluated and a more accurate validation test of the ice model performed. By considering them as new surface types, (1) above can be rewritten as

$$\sigma^0 = \sigma^0_{OW}A_{OW} + \sigma^0_{FY}A_{FY} + \sigma^0_{MY}A_{MY} + \sigma^0_{WS}A_{WS} + \sigma^0_{MP}A_{MP} + \sigma^0_{FF}A_{FF} \quad (2)$$

where A_{WS}, A_{MP}, and A_{FF} are the fractions of the scene that are covered by wet snow, meltponds, and frost flowers on young ice respectively and σ^0_{WS}, σ^0_{MP}, and σ^0_{FF} are the corresponding backscatter values.

Based on snow depth statistics gathered in the southern Beaufort Sea we estimated a value of 0.42 for the fraction of MY ice covered by snow with a depth large enough to affect the SAR signal. A_{WS} is set to this value at the start of the summer and decreases linearly with time to zero on the date the meltponds reach their maximum size. σ^0_{WS} is very low (the water acting as a near-perfect absorber) and we used a constant value of -22.0 dB. Water from melting snow collects in areas of low ice topography until mid-summer after which it drains into the ocean. A_{MP} is set to 0 at the beginning of summer, after which it increases linearly to a maximum value (0.29, from measurements made by the authors as part of the 1993 Seasonal Sea Ice Monitoring Site (SIMMS) field program) and then decreases linearly to 0 at the end of the summer. Since meltponds are liquid water pools open to the surface, their backscatter is dominated by wind-driven capillary waves just as for open ocean, and σ^0_{MP} was set equal to σ^0_{OW}. To capture the effects of frost flowers, we moved all the new FY ice to the FF category whenever the surface temperature is below -10°C. On the basis of a statistical analysis of sampled points, a value of -6.0 dB was

used for σ^0_{FF}. After inclusion of all three new surface types in the backscatter model, the time series of surface cover shown in Fig. 4 was obtained.

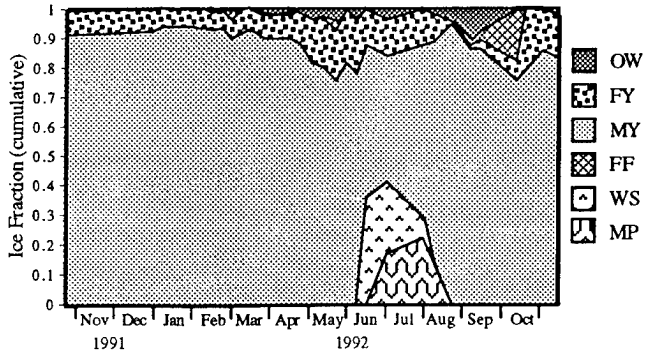


Figure 4. Time series of coverage by six different surface types used for the final ice/backscatter model. Types included are open water, first-year ice, multiyear ice, frost-flower-covered young ice, wet snow, and meltponds.

Fig. 5 shows the mean backscatter estimated by the modified physical/backscatter model compared with the actual ERS-1 SAR time series. The improved fit during the melt and freezeup periods is obvious, although a few individual days with large differences can be seen. In most cases, these are days on which the NMC geostrophic wind speeds are high but no corresponding high-backscatter open water areas are observed in the SAR imagery. From this, we conclude that either the derived NMC winds are in error or the time difference between the NMC analysis and the satellite observation was sufficient for the wind speed to vary.

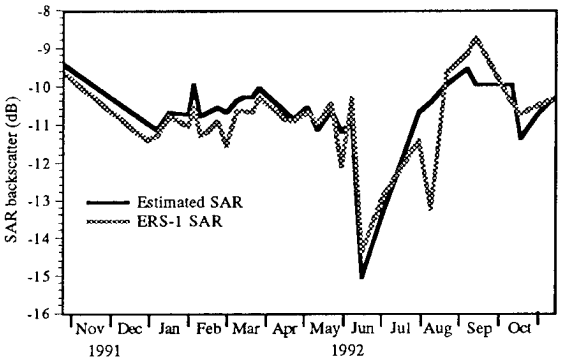


Figure 5. Comparison between actual ERS-1 SAR backscatter time series and estimates from the modified ice/backscatter model.

The RMS difference between the estimated and actual SAR time series is 0.69 dB, approximately 10% of the full range of observed backscatter values. We interpret this as an upper limit on the error of the surface cover fractions of the ice model. The average difference between the actual and estimated SAR backscatter values is 0.18 dB, indicating that there is no significant overall bias in the comparison. Sensitivity studies showed that the inclusion of wet snow had the greatest beneficial effect, followed by meltponds.

4. CONCLUSIONS

The most important conclusion of our research is that the use of even a simple backscatter model coupled to a model of ice physics is a valuable validation tool. We were able, using this approach, to show that the performance of one particular ice model during winter and spring is quite good. Discrepancies between the observed and estimated backscatter in other seasons were examined and identified as being due primarily to surficial changes that are not included in the ice model but affect the SAR signal. By incorporating these effects in the backscatter model, we were able to confirm that the good performance of the ice model continues through the melt and freeze-up portions of the annual cycle. Finally, we obtained a time series of surface cover in the Beaufort Sea that can be demonstrated as accurate within about 10% by comparison with observed SAR data. We would like to acknowledge the ASF Distributed Active Archive Center (DAAC) for supplying the digital ERS-1 SAR data used in this study and the National Aeronautics and Space Administration (NASA), which supported our research under NASA Grant NAGW-2598.

5. REFERENCES

[1] Onstott, R. , 1992, SAR and scatterometer signatures of sea ice, in Microwave Remote Sensing of Sea Ice, edited by F. Carsey, *Geophysi. Monogr. Ser. vol. 68*, AGU, Washington, D.C., 1992.

[2] Le Marshall, J., An Intercomparison of Temperature and Moisture Fields Derived from TIROS Operational Vertical Sounder Data by Different Retrieval Techniques. Part I: Basic Statistics, *J. Appl. Met.*, 27, 1282-96, 1988.

[3] Mote, T., and M. Anderson, Variations in snowpack melt on the Greenland ice sheet based on passive microwave measurements, *J. Glac.*, 41(137), 51-63, 1995.

[4] Kwok, R., and G. Cunningham, *Geophysical processor system data user's handbook*, Rep. D-9526, 91 pp., Jet Propulsion Lab., Pasadena, Calif., 1993.

[5] Hibler, W. , and J. Walsh, On modeling seasonal and interannual fluctuations of Arctic sea ice, *J. Phys. Oceanogr.*, 12, 1514-23, 1987.

[6] Gloersen, P., W. Campbell, D. Cavalieri, J. Comiso, C. Parkinson, and H. Zwally, *Arctic and Antarctic Sea Ice, 1978-1987: Satellite Passive-Microwave Observations and Analysis*, National Aeronautics and Space Administration, NASA SP-511, Washington D.C., 1992.

[7] Kwok, R., and G. Cunningham, Backscatter characteristics of the winter ice cover in the Beaufort Sea, *J.Geophys.Res.*, 99(4), 7787-804, 1994.

[8] Steffen, K., and J. Heinrichs, Feasibility of sea ice typing with synthetic aperture radar: Merging of Landsat Thematic Mapper and ERS-1 SAR satellite imagery, *J.Geophys.Res.*, 99(C11), 22413-424, 1994.

[9] Wismann, V., A C-band wind scatterometer model derived from the data obtained during the ERS-1 calibration/validation campaign, *Proc. First ERS-1 Symp.*, Cannes, 4-6 Nov. 1992, ESA SP-359, 55-9.

[10] Martin, S., R. Drucker, and F. Meredith, A laboratory study of frost flower growth on the surface of young sea ice, *J. Geophys. Res.*,100(C4), 7027-36, 1995.

The Influence of Cloud Cover on the Microwave Scattering Coefficient (σ°) of First-Year and Multiyear Sea Ice

David G. Barber and Andrew Thomas

Centre for Earth Observation Science, Department of Geography,
University of Manitoba, Winnipeg, Manitoba, Canada, R3T 2N1.
Ph. (204) 474-6981. Fx. (204) 275-8281, dbarber@cc.umanitoba.ca

ABSTRACT -- Over sea ice, the shift from predominantly clear conditions in winter to persistent stratus cloud cover in late spring and early summer coincides with a dramatic increase in the net radiation balance at the sea ice surface. Transformation of the boundary layer climate and the geophysical properties of the snow covered sea ice result from this cloud-induced rise in surface energy balance. In this paper we examine the extent to which changes in surface radiation, sea ice physical and electrical properties, and microwave scattering are a function of clear versus cloudy conditions over first-year and multi-year sea ice types.

INTRODUCTION

The impacts of cloud on the surface radiation balance of sea ice have been well documented. The arrival of increasing cloudiness in the Arctic in the later stages of winter has marked effects on the radiation regime over sea ice. Over high albedo surfaces, cloud cover results in an increase in the net radiation balance at the surface. This has lead many studies to conclude that cloudiness is a critical factor in determining the survival rate of snow and ice cover in high latitudes. Net radiation at the surface is the primary vehicle for facilitating physical (and thereby dielectrical) changes in the ocean-sea ice-atmosphere interface.

Active microwave remote sensing of sea ice is a mature science in the areas of tactical marine navigation and ice kinematics and is an active research field in the areas of climatology and global change research. A commonly held axiom is that synthetic aperture radar (SAR) at 5.3 GHz is not affected by cloud cover. By stating that a relationship exists between the influence of clouds on surface energy balance and the ability of microwave remote sensing to detect these changes, it is implied that a shift from clear to overcast conditions is accompanied by changes in sea ice physical and/or electrical properties which have the potential to affect microwave scattering.

In this work we consider a specific subset of the seasonal co-evolution of physical, electrical, energy balance, and microwave scattering characteristics by specifically examining the influence of clouds within the later portion of the winter season (i.e., air temperatures less than -10°C). We investigate two sites (first-year and multi-year) under completely clear and 100 percent overcast (stratus cloud) conditions. A relationship is sought between physical property changes induced by cloud cover, associated dielectric changes in the snow cover and corresponding variations in the microwave scattering coefficient (σ°). This knowledge will assist in determining the physical mechanisms responsible for any observed change in microwave scattering and will provide a preliminary step required to exploit space borne microwave remote sensing data in the measurement of sea ice energy balance characteristics under clear and cloudy conditions. In specific, we address the following questions:

1) Is there a detectable change in the average scattering coefficient (σ°) of the snow and/or sea ice within the case study contrasts?
2). Is there a detectable change in the physical and/or electrical properties of the snow covered sea ice within the case study contrasts?

METHODS

Data used in this investigation were collected during the Seasonal Sea Ice Monitoring and Modeling Site (SIMMS'93) experiment [1]. Detailed physical, electrical, and energy balance variables were measured at a multi-year (MY1) and first-year (FY1) sea ice sites (Fig. 1) over the period 22 April to 20 June, 1993. Detailed methods are available elsewhere [2].

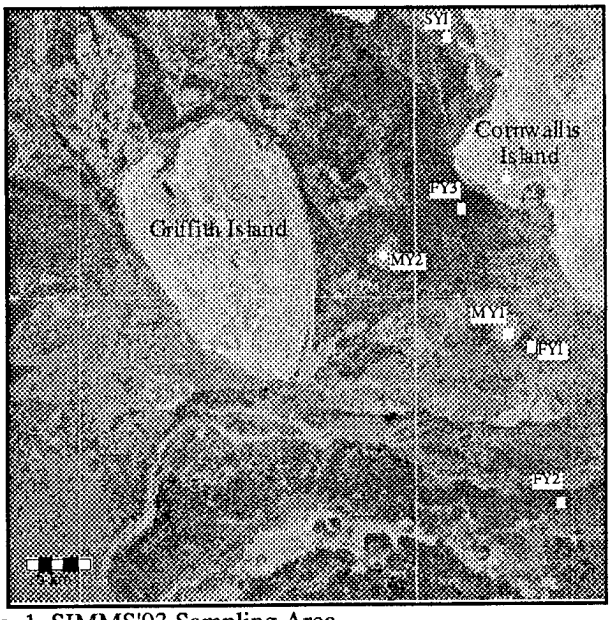


Fig. 1 SIMMS'93 Sampling Area.

0-7803-3068-4/96$5.00©1996 IEEE

RESULTS AND DISCUSSION

In our first objective we investigate whether there is a detectable change in the average scattering coefficient ($\sigma°$) of the snow covered sea ice between the clear and cloudy case study contrasts. The analysis of variance (Table 1) indicates that there is a significant effect of both 'Site' and 'Date' in the difference of means amongst the clear and cloudy sites. There also appears to be a significant interaction between 'Site' and 'Date' ($P<0.0001$; Table 1). Pairwise comparison of the box plots of $\sigma°$ (Fig 2) indicate that a statistically significant difference occurred for cloudy versus clear over the first-year sea ice (FY1 $P=0.006$) and no statistical difference was observed for the multi-year sea ice contrast (MY1 $P=0.999$). Of the other two FY sites only FY2 showed a statistically detectable difference ($P=0.0001$). The FY3 site was slightly rougher (surface roughness on the order of 2 cm) and it showed no detectable difference between clear and cloudy conditions ($P=0.737$). The other multi-year sites (MY2 and second year ice (SYI)) showed no detectable effect of the cloud cover on $\sigma°$.

Table 1. Analysis of Variance results for the effect of 'Date' and 'Site' on the average scattering coefficient ($\sigma°$)

	DF	Sum of Squares	Mean Square	F-Value	P-Value
Site	5	8559.761	1711.952	2037.528	<.0001
Date	1	21.604	21.604	25.712	<.0001
Site * Date	5	47.594	9.519	11.329	<.0001
Residual	288	241.981	.840		

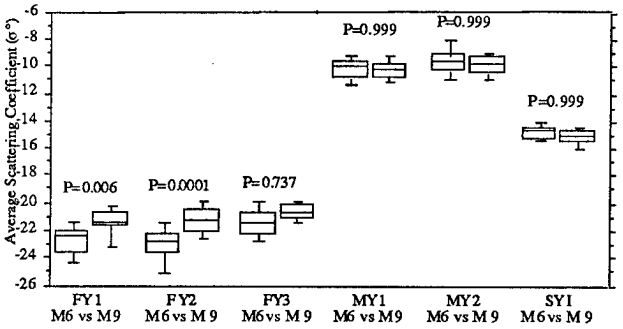


Fig. 2. Effect of Cloud on the ERS-1 Average Scattering Coefficient ($\sigma°$) of first-year ice and multi-year sea ice. P-values are denoted above each pair of box plots illustrating the statistical significance of the clear versus cloudy $\sigma°$ contrasts.

These results indicate that cloud cover appears to affect the scattering coefficient from smooth first-year sea ice but not for slightly rough first-year or multi-year sea ice (Fig. 2). This suggests that the cloud effect is manifested in a level of scattering lower than the volume contribution from the surface layer in the multi-year forms or from the higher surface scattering created from the rougher first-year ice surface geometry. Throughout the entire ERS-1 sub scene the change in $\sigma°$ between clear and cloudy conditions is much larger in the lower magnitude range of $\sigma°$ (Fig 3). The bivariate histogram shows that there is agreement in scattering between the cloudy and clear conditions over most of the range in $\sigma°$ from about -20 to -6 dB. The most significant departure is illustrated by an increase in scattering in the May 9 (cloudy) case relative to the May 6 (clear) case (Fig. 3). These results show that an increase in scattering occurs between the noise floor and about -20 dB under a cloudy relative to a clear atmosphere.

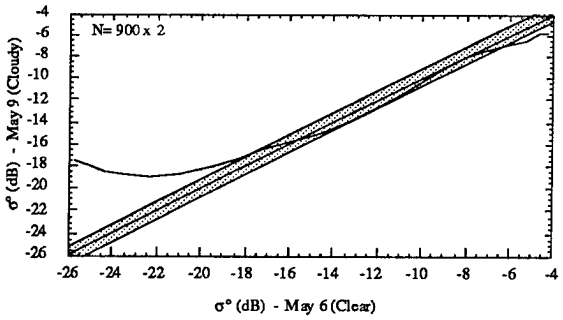


Fig. 3. Clear and cloudy ERS-1 subscene bivariate histogram showing the relative change in $\sigma°$ as a function of the magnitude in $\sigma°$ (dark curve). The agreement line is denoted as the diagonal line bounded by a 1.5 dB error envelope (shaded box).

In our second objective we tested to determine whether a detectable change in the physical and/or electrical properties of the snow covered sea ice occurred between the case study contrasts. Results of the Kolmogorov-Smirnoff test (Fig. 4) for the FY1 site indicated that for all of the vertical profile contrasts only snow temperature illustrated a statistically significant difference between clear and cloudy conditions ($P=0.01$; Fig. 4). All the other variables were determined to be statistically indistinguishable. It is interesting to note however that the volume of brine increased in the basal layer of the snow volume (because of the temperature increase) and that the permittivity and loss increased at the 8 cm level. The change in the dielectric constant at the 8 cm level occurred at the surface of the original snow layer (i.e., above this point new snow was deposited during the SIMMS experiment and is distinguishable because of a decreasing density towards the surface [Fig. 4D). The presence of a small amount of brine at this level in combination with the relatively high density created the dielectric change. A slight increase in loss at the 2cm (basal snow layer) and the ice surface (Fig. 4) reflects the increase in the temperature profile in both the snow and ice volumes. Although a decrease was observed for grain size in the basal layer.(Fig. 4C) we consider the average change observed to be within the error limits of the method.

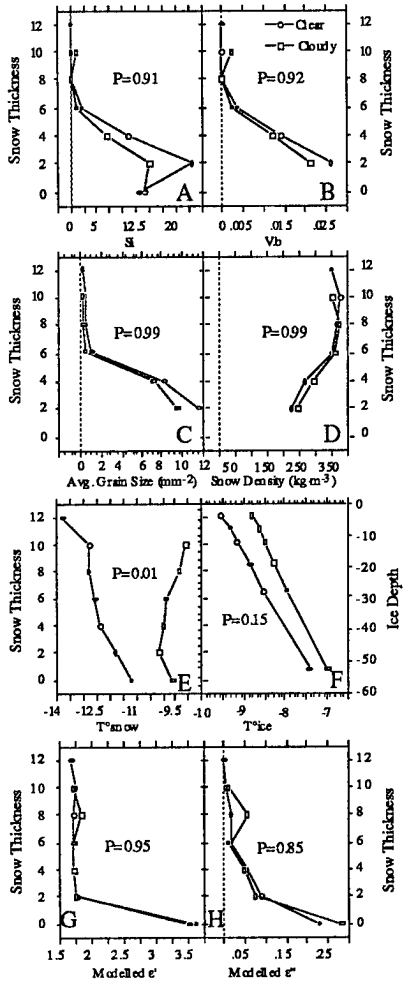


Fig. 4. Profile plots of first-year (FY1) snow and ice surface salinity (A), brine volume (B), average grain area (C), snow density (D), temperature of the snow volume (E) and ice volume (F), modelled dielectric permittivity (G) and loss (H). All variables were measured through the snow and sea ice volumes during the cloudy and clear cases. P-Values (P) are denoted for a Kolmogorov-Smirnov test of the difference in the profile distributions between the clear and cloudy case contrasts.

At the MY1 site there was also a statistically distinguishable change in the profile of the snow temperature (P=0.05, Fig. 5C) but not for the ice volume temperature (Fig. 5D). Although there was a slight increase in both permittivity and loss (particularly within the upper layers of the snow volume), the magnitudes were considerably smaller than in the FY1 case. No significant differences were observed for either snow grain size (Fig. 5A) or density (Fig. 5B). Both permittivity and loss were statistically indistinguishable between the cloudy and clear cases (Figs. 5E and F). Note that the similarity in grain size and density between the FY and MY cases and the lower magnitudes in permittivity and loss for the MY versus the FY cases (c.f., Fig 4 and 5).

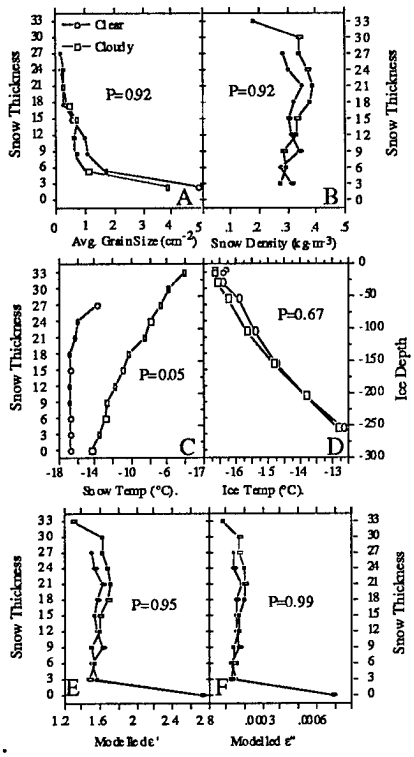


Fig. 5 (right). Profile plots of multi-year (MY1) average snow grain area (A), snow density (B), temperature of the snow volume (C) and ice volume (D), modelled dielectric permittivity (E) and loss (F). All variables were measured through the snow and sea ice volumes during the cloudy and clear cases. P-Values (P) are denoted for a Kolmogorov-Smirnov test of the difference in the profile distributions between the clear and cloudy case.

LITERATURE CITED

[1] E.F. LeDrew and D.G. Barber, "The SIMMS program: A study of change and variability within the marine cryosphere," *Arctic*, vol. 47, no.3, pp 256-264, 1994.

[2] D.G. Barber and A. Thomas. The Influence of Cloud Cover on the Radiation Budget, Physical Properties and Microwave Scattering Coefficient ($\sigma°$) of First-Year and Multiyear Sea Ice. IEEE Transactions on Geoscience and Remote Sensing. In Review.

ACKNOWLEDGMENTS

Data used in this paper have been obtained from the collective efforts of the SIMMS'93 participants - thanks to each. This work was supported by an NSERC and Office of Naval Research Grant (N00014-94-1-03-86) to D. Barber Thanks to the Polar Continental Shelf Project for the SIMMS logistical support and to E. LeDrew for discussions throughout this project.

Comparison of Aircraft and DMSP SSM/I Passive Microwave Measurements Over the Bering Sea in April 1995

D. J. Cavalieri, D. K. Hall, and J. R. Wang
Laboratory for Hydrospheric Processes
NASA Goddard Space Flight Center Greenbelt, Maryland 20771 U.S.A.
Tel: (301) 286-2444 Fax: (301) 286-0240 Email: don@cavalieri.gsfc.nasa.gov

Abstract – During April 1995 a NASA ER-2 high-altitude aircraft carrying a Millimeter-Wave Imaging Radiometer (MIR) made two flights over the Bering Sea as part of a mission to study sea ice and snow for improving retrievals of these parameters from passive microwave radiometers. MIR measures radiances at 89 GHz, 150 GHz, three frequencies near 183 GHz, and at 220 GHz. Sea ice features are observable at all frequencies except at 183 GHz, because of strong atmospheric water vapor absorption. The radiometric brightness over ice-free ocean increases with frequency as expected, but the situation is more complex over sea ice.

INTRODUCTION

A NASA ER-2 high-altitude aircraft made a series of flights over Alaska and the Bering Sea in April 1995 in support of sea ice and snow algorithm development for the NASA MTPE EOS AMSR and MODIS instrument science teams. The two primary sensors aboard the ER-2 were a six-channel, total power Millimeter-Wave Imaging Radiometer (MIR) and a Moderate Resolution Imaging Spectroradiometer Airborne Simulator. This paper reports on the results obtained with the MIR over the Bering Sea ice cover on April 8.

Sea ice retrievals from satellite passive microwave radiometers are sensitive to atmospheric water vapor variability. This is particularly the case in the vicinity of the ice edge and in marginal sea ice zones where ice concentrations are low. Some studies have examined the effect of water vapor variability on sea ice retrievals at lower frequencies (18 and 37 GHz) [1], but little work has been done at higher frequencies (85 GHz and higher). The MIR range of frequencies (89 GHz to 220 GHz) have been used previously for determining water vapor profiles over the ocean surface [2] and may, in combination with the lower frequency channels on the Defense Meteorological Satellite Program (DMSP) Special Sensor Microwave/Imager (SSM/I), also be useful in assessing and improving current methods of eliminating the effects of water vapor variability on sea ice retrievals [3]. This paper examines the spectral variation of MIR radiances over the Bering Sea ice cover and compares this variation to the known properties of the ice cover as determined from the DMSP SSM/I.

0-7803-3068-4/96$5.00©1996 IEEE

DATA

The DMSP SSM/I radiances are used with the NASA Team sea ice algorithms [4,5] to provide a description of the Bering Sea ice cover. On April 8 the ice cover extended to 55.6° N, 194° E in the southeastern portion of the Bering Sea and to 60° N, 180° E in the western portion. The sea ice concentration was generally high (85-100%), except in the marginal ice zone and in coastal polynyas. The largest coastal polynya was located south of St. Lawrence Island (SLI) where the minimum observed concentration at the mapped resolution of 25 km was 45%. From the NASA thin ice algorithm [5] only two areas along the aircraft flight path show the presence of new and young ice; one is a coastal polynya in the eastern most end of Norton Sound and the other is the SLI polynya.

The ER-2 MIR is a cross-track scanner that has a 3-dB beam width of 3.5° and an angular swath of 100°. At a nominal aircraft altitude of 18.5 km, the ground resolution at nadir is about 1 km. It measures a mixture of horizontal and vertical polarizations at 89 GHz, 150 GHz, 183±1 GHz, 183±3 GHz, 183±7 GHz, and at 220 GHz. The polarization mix varies with incidence angle, but this effect is small over sea ice. There is generally good agreement between the MIR 89 GHz observations and the averaged 85.5 GHz horizontally and vertically polarized DMSP SSM/I data. The ER-2 aircraft flight tracks over the Bering Sea were planned to optimize coverage of as many SSM/I footprints as possible while still imaging a range of sea ice types and ice-free ocean.

RESULTS

The April 8 MIR radiance maps for 89 GHz, 150 GHz, and 220 GHz are shown in Fig. 1, 2, and 3 respectively. These figures show sea ice areas which exhibit contrasting spectral variations along the flight path. The first is an area of consolidated sea ice off of Nome, Alaska. MIR brightness temperatures range from 190 K to 210 K at 89 GHz, from 175 K to 200 K at 150 GHz, and from 200 K to 210 GHz at 220 GHz. The lower radiances observed at 150 GHz are not consistent with the expected increase in brightness with frequency resulting from atmospheric water vapor emission. Examination of the 85 GHz SSM/I data at horizontal and vertical polarization also shows this area of relatively low brightness. This is not observed,



Figure 1: MIR 89 GHz image of the Bering Sea ice cover for April 8, 1995.

however, at lower frequencies or in the polarization, (V-H)/(V+H), at 85 GHz. This decrease in brightness at 150 GHz relative to the other two MIR frequencies is also observed in the region just north of SLI.

In contrast to this spectral variation is the increase in brightness temperature with frequency observed in the polynya south of SLI (see Fig. 1, 2, and 3). Near the SLI coastline, the MIR brightness temperatures increase from about 200 K at 89 GHz, to 220 K at 150 GHz, and to 240 K at 220 GHz. The spatial pattern of radiances observed in the figures suggests the presence of clouds (or water vapor) emanating from over the polynya and spreading southward. This is not inconsistent with a characteristic feature of polynyas. An increase in brightness with MIR frequency is also observed farther south in the marginal ice zone, a transition region of lower ice concentration, and over ice-free ocean.

CONCLUSIONS

The contrasting spectral variations observed in MIR data at 89, 150, and 220 GHz over the Bering Sea ice cover on April 8 suggest that both atmospheric emission and surface influences are affecting the received radiances. In a region off of Nome, Alaska and just north of SLI, the lower brightness at 150 GHz relative to the other two frequencies suggests the occurrence of surface scattering. This scattering may result from a particularly heavy snow cover on the sea ice. This effect has been observed north of SLI in previous aircraft missions [6]. Over ice-free ocean or areas of low ice concentration, as for example, in the vicinity of coastal polynyas, the increase of brightness temperature with frequency is consistent with a spectral response one would expect from an atmosphere with appreciable water vapor. Further work is needed to determine quantitatively the contributions from surface scattering and atmospheric water vapor variability.

ACKNOWLEDGMENTS

The aircraft flights and data analysis were supported by the NASA MTPE EOS Project Office. We thank the High Altitude Missions Branch at NASA Ames Research Center for the successful ER-2 aircraft mission.

REFERENCES

[1] Wang, J. R. and L. A. Chang, Retrieval of water vapor profiles from microwave radio-metric measurements near 90 Hz and 183 GHz, Journal of Applied Meteorology, 29, 1005-1013, 1990.

[2] Cavalieri, D. J., K. St. Germain and C. Swift, Reduction of Weather Effects in the Calculation of Sea Ice Concentration with the DMSP SSM/I, J. Glaciology, 41, 455-464, 1995.

[3] Maslanik, J. A., Effects of weather on the retrieval of sea ice concentration and ice type from passive microwave data, Int. J. Remote Sensing, 13, 37-54, 1992.

[4] Cavalieri, D. J., J. Crawford, M. R. Drinkwater, D. Eppler, L. D. Farmer, R. R. Jentz and C. C. Wackerman, Aircraft active and passive microwave validation of sea ice concentration from the DMSP SSM/I, J. Geophys. Res., 96, 21,989-22,008, 1991.

[5] Cavalieri, D. J., A microwave technique for mapping thin sea ice, J. Geophys. Res., 99, 12,561-12,572, 1994.

[6] Cavalieri, D. J., P. Gloersen and T. T. Wilheit, Aircraft and satellite passive microwave observations of the Bering Sea ice cover during MIZEX-West, IEEE Transactions on Geoscience and Remote Sensing, GE-24, 368-377, 1986.

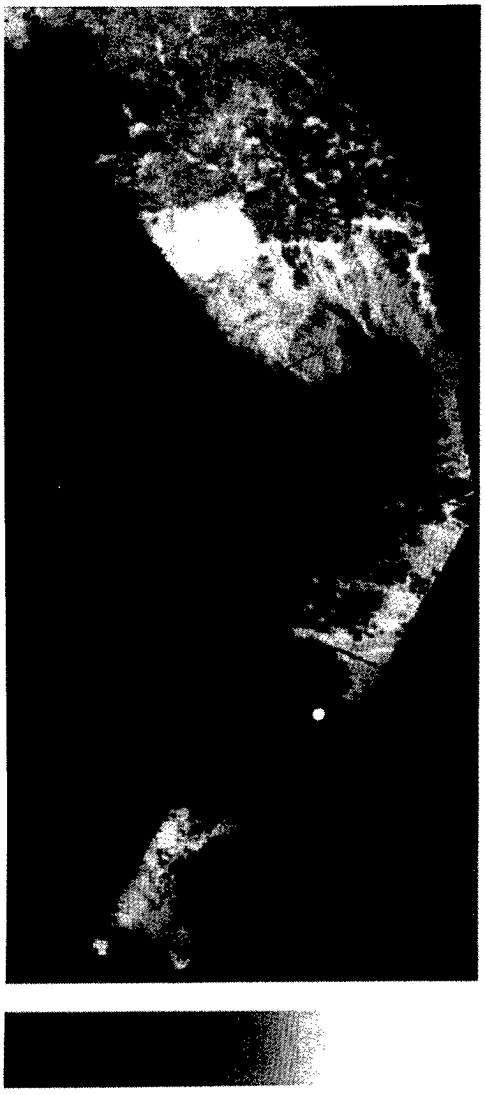


Figure 2: MIR 150 GHz image of the Bering Sea ice cover for April 8, 1995.



Figure 3: MIR 220 GHz image of the Bering Sea ice cover for April 8, 1995.

Multi-channel algorithm approach to determining melt for Arctic Sea Ice using passive microwave data.

Mark R. Anderson
324 Avery Hall
Department of Geography
University of Nebraska-Lincoln
Lincoln, NE 68588-0135
(402) 472-6656
(402) 472-1185 fax
mra@unlinfo.unl.edu

INTRODUCTION

Scientific interest in the potential effects of climate change on the polar regions have increased since computer simulations have shown that high latitudes are likely to experience enhanced warming. The response of sea ice regions to a projected warming has been of particular interest. To decide how snowmelt on the sea ice responds to climate variations, surface snowmelt must be examined. This project produces a new approach to determine melt onset for the Arctic sea ice region using passive microwave data from SSM/I platforms. Previous work has shown strong variations in the onset of melt on sea ice from passive microwave remote sensing [1,2,3]. More recent research using similar passive microwave techniques on the Greenland ice sheet have determined annual melt variations in surface snowcover [4,5]. Results from these studies have been used to produce a new algorithm that detects snowmelt on sea ice. This is accomplished because of the large increase in emissivity that occurs when liquid water is present in the snowpack. Additionally, the penetration depths of the SSM/I channels differ, aiding in the development of a new multi-channel algorithm.

An investigation was launched to verify the new algorithm in its detection of initial snowmelt for the Arctic sea ice basin. Using the whole basin allowed the melt algorithm to be applied in any ice type situation, since early development showed that ice type was an important factor in detecting melt.

0-7803-3068-4/96$5.00©1996 IEEE

ALGORITHM DEVELOPMENT

The melt algorithm uses the difference between the 19 Ghz and 37 Ghz horizontally polarized channel (HR algorithm). The horizontal channels have a strong dependence on snow grain crystal size that is rapidly altered during melt conditions. This rapid change is observed in the brightness temperatures. During melt conditions, the brightness temperatures first increase than a rapid decrease occurs because of the change in snow grain size. During these melt periods, it was observed that the HR algorithm showed a reversal in the trend of the differences. A threshold was determined by examining regions in the Arctic basin when this reversal occurred. Through analysis of several regions in the Arctic basin, both first-year and multiyear ice types, a melt threshold was assigned when the difference was less than 2K or when the 37 Ghz horizontal channel became warmer than the 19 Ghz horizontal channel.

Other known algorithms were examined but were found unexceptable, since they were ice type dependent. For example, two algorithms that detect melt onset on the Greenland ice sheet were investigated. The first, the 37 Ghz horizontal threshold technique [4] could not be used since brightness temperatures varied too much because of the thickness of the snow and ice surfaces. On the Greenland ice sheet, the snowcover is thick enough to not allow penetration of the underlying surface to interfere with the snow signal. The other method, the

cross polarization gradient ratio (XPGR) [5] used to show melt on the Greenland ice sheet was also not acceptable. The XPGR removes the dependence of the physical temperatures, however, the algorithm reacted differently depending on the ice type conditions. These were determined to be important deficiencies, therefore these algorithms were not pursued. The two techniques were used to help develop the HR algorithm. For example, melt onset was detected by the XPGR algorithm but apriori information was needed to determine ice type.

MELT ONSET

To show the capabilities of the melt algorithm, two examples will be discussed although many more locations have been investigated (Table 1). These locations were chosen because they represent both first-year and multiyear ice conditions. The analysis was completed for three years, 1989-1991, though only 1989 will be discussed here. The first location, is a first-year ice region located in the Laptev Sea. The melt algorithm determined that the initial melt occurred between Julian days 123 thru 134 for the three years (Table 1). Time series of the brightness temperatures, ice concentrations and the various algorithms including the HR melt algorithm were also analyzed (Fig. 1). During all three years, the ice concentrations go to zero confirming that the locations are first-year ice locations. The multiyear ice fraction also indicates that during melt, the calculation of multiyear ice gives a false representation of ice type. The HR melt algorithm, however, shows melt initiation occurring before the change in multiyear ice, allowing the melt algorithm to also be used a precursor. The analysis also shows that melt occurs in events and not continuous through the melt season. This is confirmed by all locations.

The time series for the multiyear ice location, found in the central Arctic Ocean (seventh site Table 1), shows similar results (Fig. 2). The ice concentrations remain high throughout the year, though the multiyear ice fraction still displays a rapid increase during melt. The initial melt occurrences showed a greater range than the first-year regions. The HR algorithm indicated that melt occurred between Julian day 138 and 174, a 36-day variation among the three years analyzed. Melt occurrences were also more sporadic than the first-year locations.

Dates of initial melt for the entire basin were produced for the entire Arctic basin for the three years to show the spatial distribution. An example plot of the initial dates is given in Fig 3. Several generalizations can be made for this analysis. The first shows the robust nature of the algorithm. In each year, the initial dates are spatially consistent and show the poleward progression of melt taking place as one would expect. There are small variations within different regions that are probably caused by atmospheric

Table 1. Locations studied and melt onset dates

Lat.	Long.	Location	Melt Onset Date		
			1989	1990	1991
72 N	135 E	Laptev Sea (FYI)	134	123	129
71 N	165 E	East Siberian Sea (FYI)	99	92*	91*
69 N	176 W	Chukchi Sea (FYI)	141	101	142
70 N	167 W	Chukchi Sea (FYI)	96	115	111
80 N	120 E	Laptev Sea (MYI)	169	149	147
72 N	62 E	Barents Sea (FYI)	104	103	98
83 N	180 E	Arctic Ocean (MYI)	174	138	158
83 N	177 W	Arctic Ocean (MYI)	174	138	185
83 N	136 W	Arctic Ocean (MYI)	173	157	186
70 N	60 W	Baffin Bay (FYI)	108	115	122
60.5N	88 W	Hudson Bay (FYI)	104	93	97*
59 N	85 W	Hudson Bay (FYI)	117	92*	111
57 N	82.5W	Hudson Bay (FYI)	134	93*	111
			* First date of analysis		

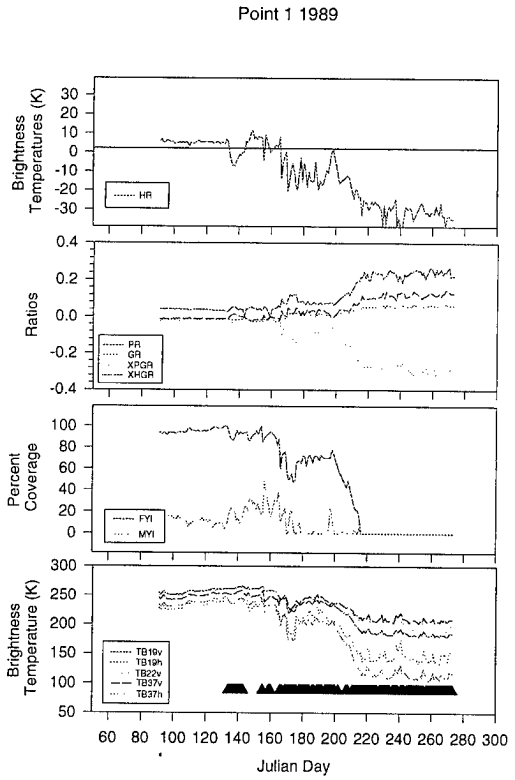


Figure 1. Time series analysis for a first-year ice location in the Laptev Sea (72 N,135 E) for 1989. Triangle shapes represent melt occasions detected by the HR melt algorithm.

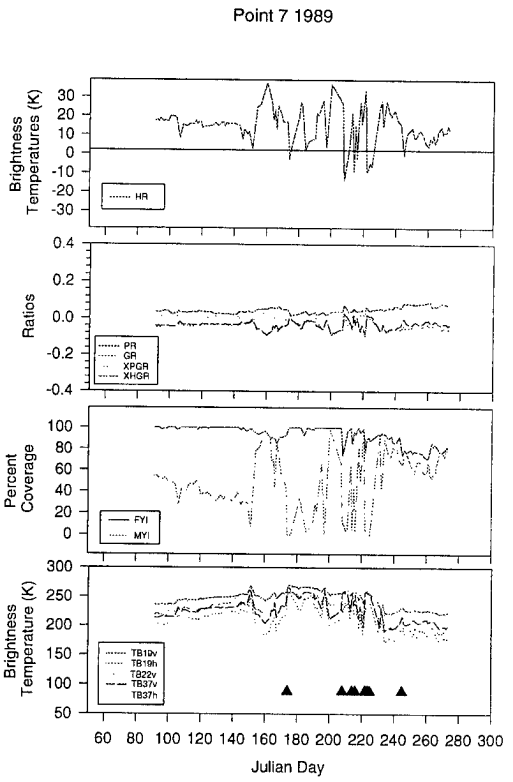


Figure 3. Time series analysis for a multiyear ice location in the central Arctic Ocean (83 N, 180 W) for 1989. Triangle shapes represent melt occasions detected by the HR melt algorithm.

conditions, but this would be expected. The other major generalization that can be concluded, is that the actual differences between years for most locations are quite small. Again, this would enhance the current thinking that melt occurrence in the Arctic basin is mainly regulated by the radiational changes that take place in the Arctic throughout the spring period. However, the variations in initial date for each location are going to be driven by local atmospheric variations controlling the solar radiation received.

The spatial analysis also demonstrates that many locations in the ocean region that do not have an ice cover but the algorithm still analyzed a melt date needed to be filtered and removed from the data set. It was thought originally that these point were removed through the filters applied to the data set before the algorithm was applied. However, the spatial analysis gives a different picture. New filters will have to be developed and applied to insure an accurate melt data set.

SUMMARY/CONCLUSIONS

A study was launched to develop a new melt algorithm that would detect the onset of melt from the entire Arctic sea ice basin with no dependence on ice type. The HR melt algorithm developed produces initial dates when sea ice snowpack begins to show melt in the passive microwave remotely sensed data. The melt algorithm was then applied to three years of data to show the robust nature of the algorithm for different ice type locations. The results show that the entire data set now needs to be analyzed to produce a melt climatology.

Since a melt algorithm has been established and a melt climatology will be produced, In

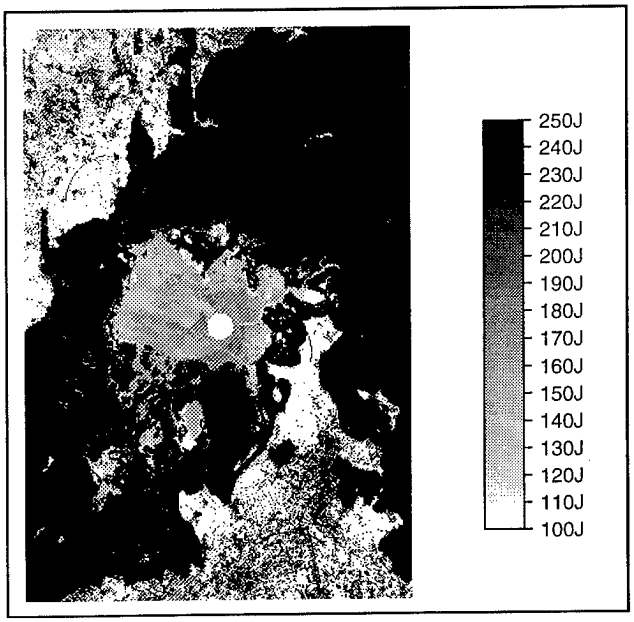


Figure 3. Initial melt onset dates as detected by the HR melt algorithm for 1989.

addition, other locations can be analyzed, since the algorithm produces dates of melt onset that can be compared to other locations within the Arctic Basin. This will allow a more complete understanding of the relationships between the atmospheric effects and the ice conditions, especially considering modeled climate variations.

REFERENCES

[1] Anderson, M.R., R.G. Crane and R.G. Barry, "Characteristics of Arctic Ocean ice determined from SMMR data for 1979: Case studies in the seasonal sea ice zone," Advances in Space Research, 257-261, 1985.

[2] Anderson, M.R., "The onset of spring melt in first-year ice regions of the Arctic as determined from SMMR data for 1979 and 1980," J. of Geophyl Res, 92(C12), 13,153-13,163, 1987.

[3] Anderson, M.R., "Snow melt on sea ice surfaces as determined from passive microwave satellite data," Large Scale Effects of Seasonal Snow Cover, edited by B.E. Goodison, R.G. Barry and J. Dozier, IAHS Publication No. 166, 329-352, 1987.

[4] Mote, T.L. and M.R. Anderson, "Variations in snowpack melt on the Greenland ice sheet based on passive microwave measurements," J. of Glaciol., 41(137), 51-60, 1995.

[5] Abdalati, W. and K. Steffen, "Passive microwave-derived snow melt regions on the Greenland ice sheet," Geophy. Res. Let., 22(7), 787-790, 1995.

ACKNOWLEDGMENTS

This work was supported at the University of Nebraska by NASA grant NAGW-1266 and by NASA contract NAS-5-32392 to the University of Colorado. The SSM/I gridded brightness temperatures obtained on CD-ROM were from the National Snow and Ice Data Center, Boulder, CO.

Satellite Radar Measurements of Land Subsidence

D. van Halsema and M.W.A. van der Kooij[1]
TNO Physics and Electronics Laboratory
P.O. Box 96864, 2509 JG The Hague, the Netherlands
Tel: +31(70)3740433 (direct) or ~374 0000; fax: +31(70)328 0961
email: vanHalsema@fel.tno.nl

Abstract -- The potential of satelliteborne interferometric measurements for the mapping of slow land subsidence has been investigated. Two test sites, covered by the ERS-1 satellite, were selected in the Netherlands: the provinces of Groningen and Zeeland. In situ measurements on the weather and the actual subsidence were gathered. It will be shown that under favorable conditions measurement accuracy's for land subsidence in the range of mm's are feasible. Atmospheric effects together with temporal decorrelation are the major limitations to the accuracy of the technique for this type of long term measurement.

INTRODUCTION

The winning of natural gas in the northerly provinces of the provinces of the Netherlands causes bottom subsidence in a bowl-shaped area with a diameter of approximately 40 km. The final largest subsidence is currently estimated at 36 centimeter. The change in a year is generally less than one cm. Measurement of this change is very important since even a small subsidence does have major consequences for the infrastructure in the area. A budget of 300,000 till 700,000 Dutch guilders is spent every year for conventional levelling campaigns. Disadvantages of this technique are the price, the limited accuracy (1 cm) and the fact that only few point measurements become available. Repeat orbit SAR interferometry might provide a relatively cheap tool to monitor the subsidence with high accuracy and resolution.

For the assessment of the applicability of SAR interferometry for measurement of small deformations the error sources need to be addressed. We made a distinguishment between local ~ and systemic error sources. The effect of the first type of errors can be expressed by their effect on the coherence of the interferogram which is a quantitative measure of the phase consistence and therewith of the quality of the interferogram (e.g. Zebker and Villasenor, 1992). Three major sources of decorrelation can be distinguished: decorrelation due to thermal noise, baseline decorrelation and temporal decorrelation.

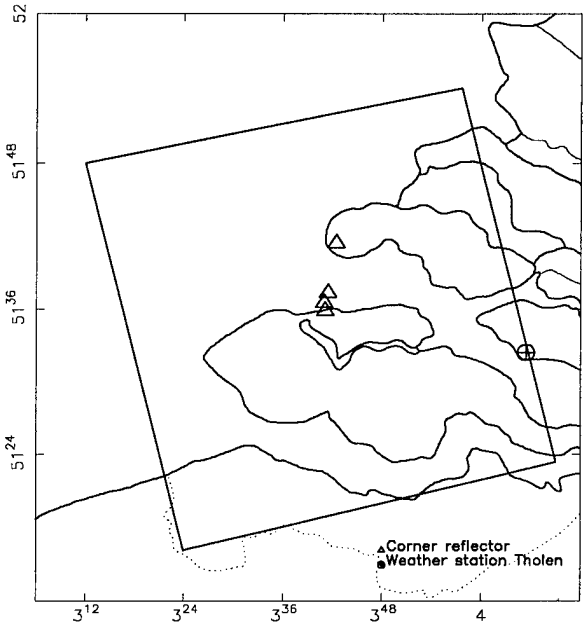


Figure 1: The Zeeland test area with the frame of the ERS-1 quarter scene as well as the positions of the corner reflectors and the weather station

In order to circumvent loss of accuracy because of low coherence we studied subsidence on objects with high backscatter (good SNR) and from interferograms with very small (< 100 m) baselines (little baseline decorrelation). For slow processes like subsidence due to natural gas winning, temporal decorrelation is unavoidable. However the amount of temporal decorrelation strongly depends on the nature of the scattering object. Solid scatterers like houses and rocks, but also artificial (corner) reflectors hardly do decorrelate and can therefore be used for the purpose of long term monitoring.

The second important error source in interferometric measurements of ground deformation is the presence of systematic phase effects. Three effects can be identified:

1. Effects caused by topography.
   This effect depends on the baseline, a large baseline gives a high 100-200 m and the land is very flat, like in

[1] Now at Atlantis, 1827 Woodward Dr, K2C OP9 Ottawa, Canada

0-7803-3068-4/96$5.00©1996 IEEE

the Netherlands, these effects are very small. It can be corrected for by using accurate (radar) DEM's.

2. Atmospheric/ionospheric effects.
   Hartl et. al. (1993) have found evidence of systematic effects and argue that these effects are caused by local variations in the atmospheric conditions that are different for the two passes. Only little quantitative information on this effect is available at the moment to the knowledge of the authors.
3. Effects individual agricultural fields
   This effect has been observed and reported a few times and it might be caused by irrigation or human activities (Hartl et. al, 1993).

EXPERIMENT

Figure 1 shows the Zeeland area including the frame of the 50 x 50 km ERS-1 quarter scene coverage. The location of the corner reflectors and the location of the weather station is indicated.

In the project the magnitude of decorrelation and systematic effects have been investigated for data collected in Zeeland and Groningen. This was done in order to study the potential and limitations of multi-pass interferometry in general and the mapping of deformation in particular.

A total of 50 SAR images have been acquired and used in the interferometric processing. Approximately 30 interferograms of the Zeeland and Groningen areas have been produced.

RESULTS AND ANALYSIS

For the Groningen area interferograms over time spans of more than one year are necessary in order to measure the small (< 1 cm) subsidence. Temporal decorrelation causes a 100% loss of information over agricultural and water areas. However, the man-made objects such as factories and buildings remain coherent and contain enough information for the measurement to be useful. First results indicate that coherence is maintained in urbanized areas and areas with little vegetation, even for a time interval of 2-3 years. This will probably enable interferometric measurement of slow processes like land subsidence.

Figure 2 gives an example of an interferogram of Zeeland taken during the second ice phase of the satellite. The time between both data acquisitions is 3 days. Phase values this figure range from 0 (black) to 2 pi (white). A 2 pi cycle of phase corresponds to a path length difference of 2.75 cm. Since the area is very flat within 20 meters, and no subsidence occurs here, other effects must be the cause of the observed phase variations.

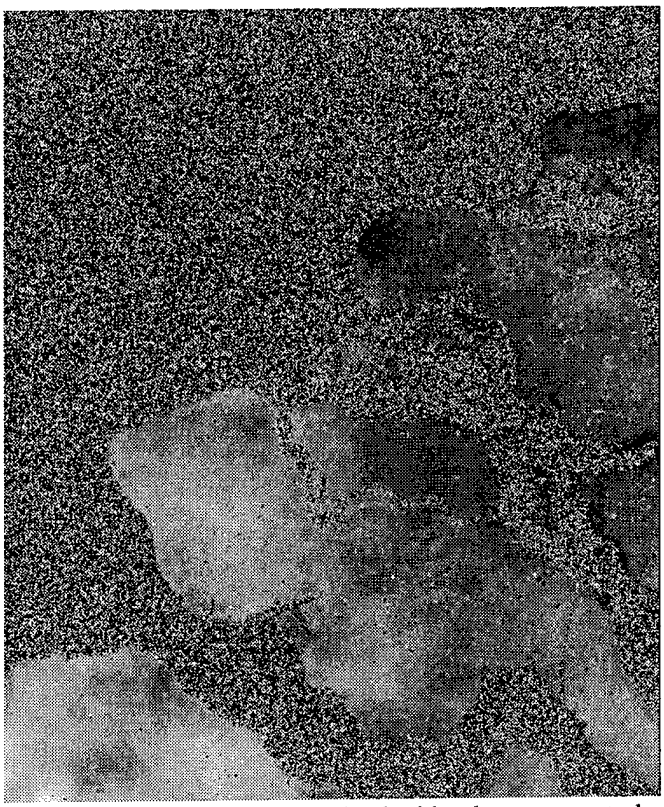


Figure 2: Interferogram of Zeeland with what appears to be atmospheric effects.

Many of the studied interferograms contain, similar to figure 2, spatial variations in phase. Typical dimensions of the patterns are 1-5 km. These patterns are most probably caused by atmospheric variations in water vapor content, which have changed during the time interval.

It appears that there is a relationship between the atmospheric conditions during the the two passes and the magnitude of the phase effect. In the interferograms with at least one pass under rainy and heavily clouded conditions the phase effect is approximately 2 radians maximum. When the situation is more favorable for both passes (e.g. sunny, cold), the effects are between 0.5 and 1 radians at the most, which corresponds to a height change error between 2 and 4 mm.

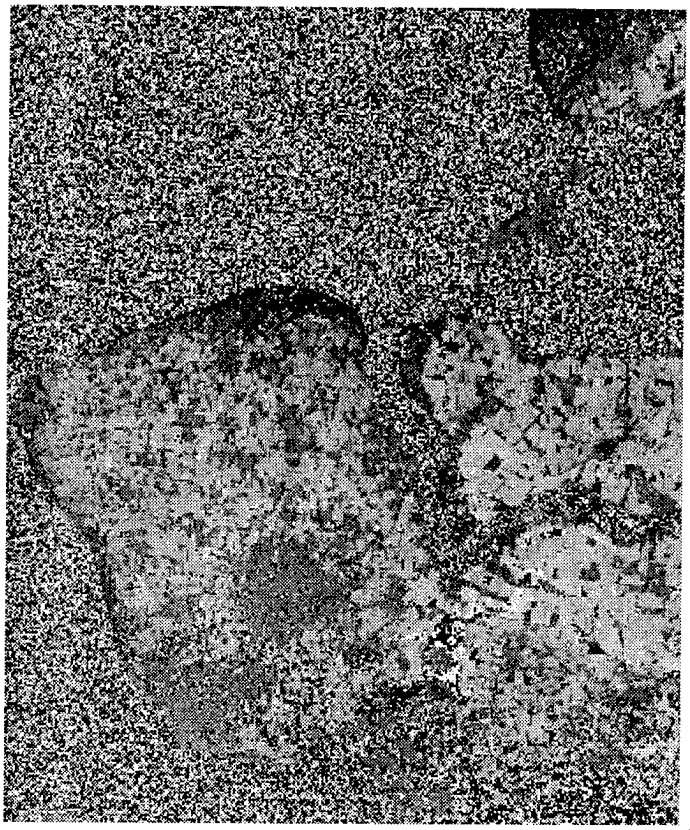


Figure 3. Interferogram of Zeeland. The first image of the interferogram was taken during freezing conditions, the second under thawing conditions.

Some of the interferograms (6 out of 19) contain systematic phase effects that are clearly correlated to the land use or the soil type. The best example is shown in figure 3, which shows an interferogram made from data acquisitions at 23/2 and 26/2 1994.

It is a blowup on the Island of Noord Beveland similar to figure 2. Clearly visible are local phase variations that are related to land use. It appears that there is also a relation between soil type and differential phase.

It seems very likely that the observed systematic phase effects in figure 3 are due to frost/thaw events during the time interval between the ERS-1 passes. In similar interferograms during this period, the largest phase effects can be found for combinations of an ERS-1 pass with sub-zero temperatures and an ERS-1 pass with temperatures above zero degrees Celsius. In other words: the effects are large if a change from freezing to thaw conditions occurred in the time interval between the passes. In figure 3 the phase of most of the agricultural fields is higher than that of the urbanized areas and sandy soils. The first areas are more sensitive to ice heave of the ground caused by frost because of the larger water content of clay ground. Different clay concentrations in the agricultural fields or different surface structures might give rise to the observed differences between agricultural fields. The magnitude of the effect ranges from several mm's up to 1 cm.

CONCLUSIONS

A quantitative investigation into the accuracy of interferometric SAR measurements has been performed. Systematic effects of 2-10 mm have been discovered due to atmospheric moisture variations. These effects appear to be dependent on the weather conditions. Systematic phase were also found when a frost or thaw event occurred between the passes of the ERS-1. This is probably a real effect of shrinking and swelling of the soil with typical magnitudes of 5 mm. Coherence images of the Groningen subsidence area with time intervals of 2-3 years suggest that the technique might be usable to investigate slow processes like land subsidence caused by gas exploitation with typical magnitudes of 5 mm/year. Future research will be directed towards operational applications and the optimum conditions for multi-pass interferometric measurements.

Acknowledgments. The authors thank ESA for the ERS-1 data made available and for the weather data of Zeeland. The research was supported by the Netherlands Remote Sensing Board.

REFERENCES

Hartl, Ph, Thiel, K, Wu, X and Xia, Y (1993) Practical application of SAR Interferometry; experiences made by the Institute of Navigation. Proceedings of the 2nd ERS-1 symposium, p 717, Hamburg, 1993.

Villasenor, J and Zebker H.A. (1992) Temporal Decorrelation in Repeat-Pass Radar Interferometry. IEEE transactions on Geoscience and Remote Sensing, 1992

FLOOD MONITORING USING ERS-1 SAR INTERFEROMETRY COHERENCE MAPS

D. Geudtner [1*], R. Winter [2], P. W. Vachon [1]

[1] Canada Centre for Remote Sensing ; 588 Booth St., Ottawa, Canada, K1A 0Y7
Phone: 1-613-998-9060, Fax: 1-613-993-5022, email: geudtner@ccrs.emr.ca

[2] EC Joint Research Centre, 21020 Ispra, Italy
Phone: 39-332-78-9765, Fax: 39-332-78-9536, email: rudolf.winter@jrc.it

Abstract -- The potential of satellite repeat-pass SAR interferometry (InSAR) for flood monitoring is discussed. Using ESR-1 SAR images covering the 1993/94 flood event in the river Rhine, Germany, it is shown that, by evaluating the scene coherence, a reliable mapping of flood extent is feasible, even in cases of rough water surfaces where the analysis of conventional SAR intensity and multi-temporal images may fail.

INTRODUCTION

The generation of flood assessment maps as well as the development and validation of hydrological models which are essential for flood prevention activities require an accurate knowledge of the flood extent. Previous studies of flood monitoring have been mainly based on aerial photography as well as on images from optical and radar spaceborne sensors [1]. Most common are change detection techniques using multi-sensor or multi-temporal color composite images for comparison of the flood situation with the normal water stage. However, due to the all-weather acquisition capability of radar sensors, SAR images are often the only available image data during the flood event.

The interpretation of SAR data, including derived multi-temporal SAR images, is usually based only on the evaluation of the expectation value of the intensity image, which is related to the radar backscatter coefficient σ^0. Due to the imaging geometry, i.e. the projection onto the ground, this relationship exhibits a $1/\sin\theta_i$ dependence, where θ_i stands for the local incidence angle [2]. Therefore, particularly in cases of sloped terrain, small temporal changes in geophysical surface parameters may not be detectable as a difference in image intensities. Additionally, the typical speckle phenomenon in SAR intensity images limits the radiometric resolution. In particular, if SAR images from different imaging geometries are used, then, because of their various speckle contributions, a discrimination of σ^0 differences may be difficult.

Generally, inundated areas can be reliably delineated if the land was completely covered by a smooth water surface having low σ^0 values. However, this approach is not applicable under even light wind conditions during the SAR data acquisition which may have roughened the water surface causing an increase in the backscatter intensity, which is comparable to the surrounding land.

In InSAR, the phase derived from a pair of single look complex images, acquired from slightly different imaging geometries, is related to the terrain height and may contain information about possible surface displacements provided that the phase of the surface reflectivity has remained stable between the two passes. Small variations of the geometric and/or dielectric properties of the scatterer within the resolution cell may decrease the degree of coherence, a measure of phase correlation, between the two data sets. This relationship has been used to map temporal surface changes for classification of land signatures [3].

In this paper, the suitability of InSAR coherence measurements for flood monitoring is demonstrated. We start in Section 2 with a short review of the required precessing steps for the estimation of the scene coherence. In Section 3 the results of our coherence analysis are discussed and Section 4 concludes the paper.

2. SCENE COHERENCE ESTIMATION

The degree of coherence between two complex SAR images z_1 and z_2 is defined as:

$$\gamma = \frac{\left|E\{z_1 \cdot z_2^*\}\right|}{\sqrt{E\{|z_1|^2\}\, E\{|z_2|^2\}}} = \gamma_{scene} \times \gamma_{S/N} \times \gamma_H \qquad (1)$$

where $E\{.\}$ is the expectation value

It has been shown in [4] that the coherence γ, measured from the SAR data, contains information about temporal changes of geophysical surface parameters, referred to as the scene coherence γ_{scene}, and other contributions which are affected by thermal noise $\gamma_{S/N}$, and spectral misalignment γ_H due to baseline and antenna pointing decorrelation effects. Therefore, an accurate estimation of γ_{scene} for a reliable interpretation and comparision of coherence maps acquired at different times and with different imaging geometries is required. The interferometric processing steps which are described in detail in [5] and [6] include a phase preserving image co-registration, an oversampling of the images by a factor of two, a bandpass filtering both in range and azimuth, and the removal of systematic geometry phase trends related to an ellip-

* D.G. thanks the DAAD/Germany for supporting this work.

0-7803-3068-4/96$5.00©1996 IEEE

soidal earth model. According to (1) the expectation value has been calculated over a 30 x 6 window size (azimuth and range) to reduce an overestimation of γ over areas with low coherence. After a compensation of the noise floor decorrelation, γ_{scene} values may related to surface changes, where bright areas represent high coherence, while dark areas denote low coherence, as seen in Figs. 4 and 5.

3. DATA AND RESULTS

In December 1993, a period of heavy rainfall in Germany caused a rise of river levels, combined with an increase in soil saturation, and led to flooding. The selected test site covers about 20 by 20 km of the nearly flat area arround the city of Dormagen that was furthermore affected by a high tide in the river Rhine during Dec. 22-28, 1993. The acquisition dates of the ERS-1 data, the orbit numbers, and the interferometric baselines B_N for corresponding image pair combinations considered here, are summerized in Table. 1. Suitable interferometric pre-flood images were not available due to the change of the ERS-1 repeat cycle from the Multidisciplinary Phase (35 days) to the Second Ice orbit (3 days) during Dec. 20-24, 1993. Unfortunately, on Dec. 28, 1993 no SAR data for this test site were collected.

The SAR intensity image for Dec. 25, 1993, Fig.1, shows the situation at the flood peak. The inundated areas along the Rhine are easily distinguishable from the land and also from the normal river course because of their low intensity values, indicating a smooth water surface. The intensity image for Dec. 31, 1993, Fig. 2, was acquired during a falling low water period, and in Fig. 3, for Jan. 3, 1994, the river is shown in an almost non-flood stage.

In the following, we focus particularly on the meander and the oxbow-lake regions, marked in these images with (1) and (2), respectively. In Fig.1, it is clearly discernable that parts of these grassland covered regions were inundated. However, comparing all three images, it is not recognizeable to what extent the other areas within those regions, characterized by their relativly high intensity values, were actually affected by the flood. The rough water surface during the second SAR data acquisition, Fig.2, creating a speckle-like pattern, makes an evaluation of the intensity values more difficult. The additional use of a multi-temporal SAR image based on the combination of the three single intensity data sets facilitates the visual comparison of the flood peak situation with the normal river course, but does not allow a detailed mapping of the flood extent.

In the coherence image, Fig. 4, derived from the complex image pair of Dec. 25 - 31, 93, the regions, marked with (1) and (2), appear completely decorrelated. Considering the relativly high coherence (close to unity) for the surrounding land, the significant loss of coherence for both the meander and oxbow-lake regions can be attributed to flooding of these areas at the acquisition time on Dec. 25, 93, and causing, therefore, a change in the phase of the surface reflectivity.

Table. 1 Analysed ERS-1 SAR images of the flooded area

Image pair acquisition dates	orbit number	B_N [m]
Dec. 25, 93 & Dec. 31, 93	12778/12864	275
Dec. 25, 93 & Jan. 3, 94	12778/12907	335
Dec. 31, 93 & Jan. 3, 94	12864/12907	60

The low correlation of those areas, located in (1) and (2), with higher intensity values, as seen in Fig.1, indicates that these areas were also flooded at the time, but the grassland vegetation was not entirely covered by water. A similar coherence map has been generated from the second image pair in Table. 1, which confirms this interpretation. On the other hand, the coherence map derived from the image pair of Dec. 31, 93 and Jan. 3, 94, shows relativly high coherence values for both areas, attributed to the falling low water level on Dec. 31, 1993. In other words, most of those areas were no longer inundated at the time of data acquisition. However, the high intensity values in these areas, Figs. 2 and 3, indicate highly saturated soils on both acquisition dates. This assumes that, except for the explanation given above, no other decorrelation effect, such as volume scattering due to a change in the penetration depth or vegetation, has caused the decrease in coherence in Fig. 4. Besides the flooded areas, a forest region (3) also appears as decorrelated in the coherence maps, Figs. 4 and 5, because of the typical volume scattering effect.

An improved classification of the test site in terms of separation of flooded areas from deep water bodies and surrounding land, respectively, and a distinction of different land cover categories, has been achieved by merging SAR intensity and coherence images using the well-known principal component transformation. From the available six information layers, three intensity and three coherence images, the principal components 1, 2 and 4 were extracted and combined to a RGB image which will be presented at the symposium.

4. SUMMARY AND CONCLUSIONS

Using a sequence of ERS-1 SAR images covering the 1993/94 flood event in the river Rhine, we have demonstrated the potential of InSAR coherence analysis for flood monitoring. Due to the sensitivity of the interferometric phase to temporal changes of the surface reflectivity between passes, coherence maps can provide additional information about the flood extent which otherwise may be difficult to derive from conventional SAR intensity and multi-temporal images. However, this approach requires the availability of suitable interferometric data sets and the application of advanced processing steps to accurately estimate the scene coherence.

REFERENCES

[1] ESA, ESRIN, "Proc. First ERS Thematic Workshop Group Meeting on Flood Monitoring", 26-27 June, 1995

[2] R. Bamler, B. Schättler, "SAR Data Acquisition and Image Formation," in SAR Geocoding: Data and Systems, G. Schreier, Karlsruhe, Wichmann, 1993, 53-102
[3] U. Wegmüller, C. L.Werner, "SAR Interferometric Signatures of Forest," IEEE Trans. Geosci. Rem. Sens., vol. 33, no. 5, pp. 1153-1161
[4] R. Bamler, D. Just, "Phase Statistics and Decorrelation in SAR Interferograms," Proc. IGARSS '93, Tokyo, pp. 980-984
[5] D. Geudtner, "Generation of Coherence Maps Using SAR Interferometry: A Promising Tool for Surface Change Monitoring", Proc. The Space Congress, 1995, Bremen, Germany
[6] P.W. Vachon, D. Geudtner, A.L. Gray, and R. Touzi," ERS-1 Synthetic Aperture Radar Repeat-Pass Interferometry Studies: Implications for RADARSAT", Can. J. Rem. Sens. 21 (4), 1995, pp. 441-454

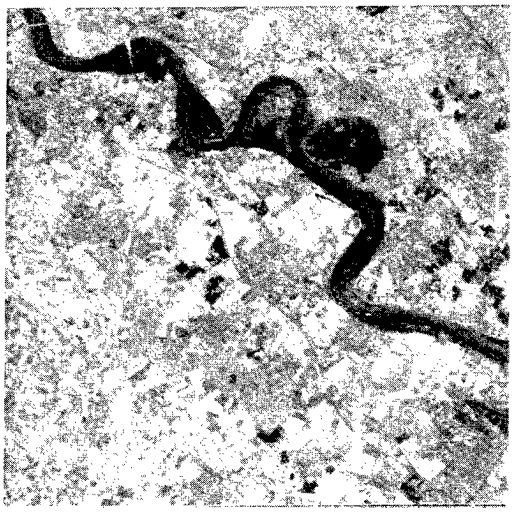


Fig.1 ERS-1 SAR intensity image during the flood, acquired on Dec. 25, 1993

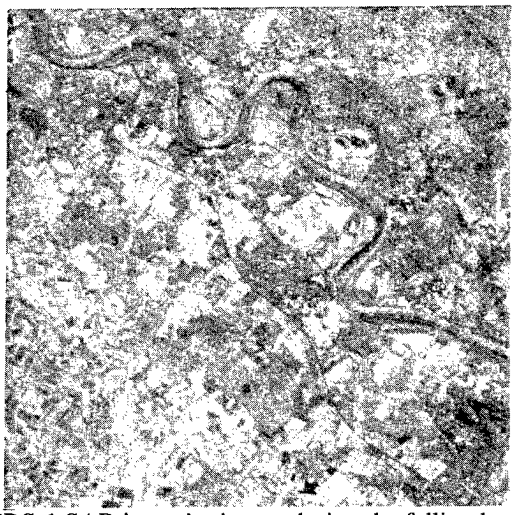


Fig.2 ERS-1 SAR intensity image during the falling low water period, acquired on Dec. 31, 1993

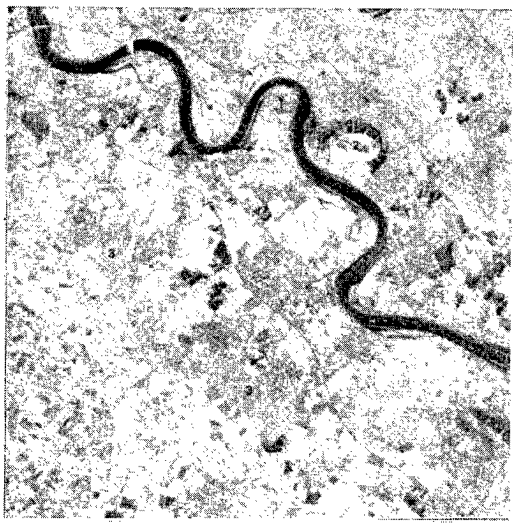


Fig.3 ERS-1 SAR intensity image after the flood, acquired on Jan. 3, 1994



Fig.4 ERS-1 SAR coherence map, derived from the image pair of Dec. 25 and 31, 1993



Fig.5 ERS-1 SAR coherence map, derived from the image pair of Dec. 31, 1993 and Jan. 3, 1994

Determination Of Vegetation Height From SAR Interferometry: A Theoretical Study

Kamal Sarabandi

The University of Michigan, Radiation Lab
Ann Arbor, MI 48109-2122 USA
FAX: +1-313-747-2106 email: saraband@eecs.umich.edu

ABSTRACT

In this paper the theoretical aspects of estimating vegetation parameters from SAR interferometry is presented. In conventional applications of interferometric SAR (INSAR), the phase of the interferogram is used to retrieve the location of the scattering phase center of the target. Although the location of scattering phase center for point targets can be determined very accurately, for a distributed target such as a forest canopy this is not the case. For distributed targets the phase of the interferogram is a random variable which in general is a function of the system and target attributes. To relate the statistics of the interferogram phase to the target attributes, first an equivalence relationship between the two-antenna interferometer system and an equivalent Δk radar system is established. This equivalence relationship is needed to related the frequency correlation function of distributed targets, which can conveniently be obtained experimentally, analytically, or numerically, to the phase statistics of the interferogram. It is shown that the frequency correlation function of distributed targets which in turn is a function of scattering mechanisms and system parameters determines the accuracy with which canopy height can be estimated. It is also shown that for a uniform closed canopy the extinction and the physical height of the canopy top can be estimated very accurately. Some analytical and numerical simulations are demonstrated.

1. INTRODUCTION

The interferometric technique relies on a coherent imaging process to find the range or distance to the scattering phase center of the scatterers in the radar image[1]. It is shown that the phase of the interferogram is proportional to the wavelength, slant range, look angle, distance between the antennas (baseline distance), orientation of the antennas with respect to each other, and the height of the scattering phase center above a reference line [2]. For non-vegetated terrain, the scattering phase centers are located at or slightly below the surface depending upon the wavelength of the SAR and the dielectric properties of the surface media. Whereas for vegetated terrain, these phase centers lie at or above the surface depending upon the wavelength of the SAR and the vegetation attributes.

The significant vegetation attributes are: (1) the type of vegetation, (2) the quantity or biomass of the vegetation and (3) the dielectric properties of the vegetation. As pertains to SAR interferometry, the type of vegetation refers to the structural attributes of vegetation elements and includes the shapes and sizes of foliage and woody stems relative to wavelength and their three-dimensional organizational structure. The biomass refers to attributes such as the height of the vegetation, the thickness and density of the crown layer that contains foliage and stems, and the number of plants per unit area. The dielectric properties of the vegetation elements determine scattering and propagation through the media; these may vary with time due to seasonal changes in plant physiology and the phase of water (liquid or frozen) or due to the presence of water films resulting from intercepted precipitation or dew.

The main objective of this paper is to establish a thorough understanding of the relationship between the INSAR parameters and the vegetation attributes. the accuracy with which the vegetation scattering phase center can be measured. To accomplish these goals an equivalence between INSAR and Δk-radar techniques is established which facilitates numerical simulations and controlled experiments using scatterometers. Monte Carlo simulation of a forest canopy which preserves the absolute phase of the radar backscatter allows for quantifying the role of vegetation attributes in determining the location of the scattering phase centers as measured by SAR interferometry.

2. ΔK-RADAR EQUIVALENT OF AN INSAR

In this section an equivalence relationship between an interferometric SAR and a Δk-radar is obtained. As will be shown later the statistics of the phase of the interferogram or equivalently the location of the scattering phase center and its statistics is a very strong function of the location and number density of the forest constituent particles and their dielectric and scattering properties. Understanding the relationship between the tree height and the corresponding location of the scattering phase centers requires numerical simulations (Monte Carlo

0-7803-3068-4/96$5.00©1996 IEEE

simulation of a fractal generated forest stand) or controlled experiments using scatterometers are needed. The scattering phase center of a target can also be obtained using a Δk-radar assuming that the incidence angle is known.To demonstrate the equivalence between an ISAR and a Δk-radar consider a two-antenna interferometer. In this scheme one of the antennas is used as the transmitter and receiver and the other one is used only as the receiver, the phase of the interferogram (ϕ) is related to the difference in path lengths from the antennas to the scattering phase center (δ) by

$$\delta = \frac{\lambda_0}{2\pi}\phi \tag{1}$$

where $\lambda_0 = c/f_0$ is the wavelength. Now let us consider a radar capable of measuring the backscatter at two slightly different frequencies $f_1 = f_0$ and $f_2 = f_0 + \Delta f$. Denoting the phase difference between the two backscatter measurements by ϕ, it can be shown that

$$\phi = 2\Delta k r = 4\pi\Delta f\, r/c \tag{2}$$

where r is the radar distance to the target scattering phase center. Comparing (1) with (2) the desired relationship between the Δk-radar and INSAR can be obtained. Basically by requiring the backscatter phase differences once obtained from a small change in the aspect angle and the other one obtained from a small change in the frequency of operation we have

$$\Delta f = f_0 \frac{B}{2r}\sin(\theta - \alpha) \tag{3}$$

Noting that $r = H/\cos(\theta)$, it can easily be shown that Δf is almost independent of incidence angle over the angular range $30° - 60°$. For example, an C-band (5.3 Ghz) interferometer with a horizontal baseline distance 2.4 m at an altitude 6 Km is equivalent to a C-band Δk-radar with $\Delta f = 530$KHz.

What remains to be shown is the algorithm by which the target height can be extracted from a Δk-radar. By measuring the radar response of the target at the same viewing angle but at a slightly different frequency and calculating the change in the phase of the scattered field ($\phi = \Phi_2^s - \Phi_1^s$) due to the change in the wavenumber ($\Delta k = k_2 - k_1$) it can be shown that

$$h = \frac{1}{2\cos(\theta)}\ \frac{\phi}{\Delta k} \tag{4}$$

3. SENSITIVITY ANALYSIS

In estimating the height of the scattering phase center of a distributed target using (4), random fluctuations of the calculated or measured phase as a function of frequency due to fading must be considered. Since the location of the scatterers in the illuminated volume is random, the process describing the scattered field is a Wiener process and for large number of scatterers the process is Gaussian. It is shown that the pdf for the difference between phases of E_2^s and E_1^s ($\phi = \Phi_2 - \Phi_1$) is related to the elements of the covariance matrix and is and can be expressed in terms of only two parameters (α and ζ). When the scattered fields are completely correlated $\alpha = 1$ and the pdf of ϕ is a delta function. In this case the calculation of the height from (4) has no error in principle. For $\phi = \zeta$ the pdf assumes its maximum and this point corresponds to the average height of a uniform distributed target over a flat ground plane. In this analysis the objective is to establish a relationship between the height resolution and the frequency shift for a given error probability criterion. Let us define the normalized correlation function of the process by

$$R(\Delta f) = \frac{|< E_1 E_2^* >|}{< |E_1|^2 >} \tag{5}$$

which is also known as the frequency correlation function [4]. It can be shown that $\alpha = R(\Delta f)$. To quantify the accuracy of the height estimation for a given distributed target, let us assume that the normalized frequency correlation function of the target is known. The objective is to estimate ζ from which the mean height can be obtained. Suppose $\delta\phi = \phi - \zeta$ represents the error in the phase measurement which corresponds to an error in height measurement given by

$$\delta h = \frac{\delta\phi}{2.4\Delta f\cos\theta} \tag{6}$$

where δh is in meters, $\delta\phi$ is in degrees, and Δf is in MHz. The uncertainty in the estimation of height can be quantified according to a prescribed error probability criterion. For example, $\delta\phi$ can be chosen such that the probability of measuring the phase within the $\delta\phi$ neighborhood of the coherent phase difference to be 90%, that is

$$P(\phi \in [\zeta - \delta\phi, \zeta + \delta\phi]) = 0.9\ .$$

Hence, using this criterion the estimate of the height is

$$\tilde{h} = \bar{h} \pm \delta h$$

with a probability of 0.9.

The uncertainty in the height measurement defined by this criterion is a complex function of Δf noting that $\delta\phi$ is a function of α which is related to Δf through the correlation function. Referring to (6), it seems that the height uncertainty decreases when Δf is increased; however, it should also be noted that $\delta\phi$ increases when Δf is increased. This behavior suggests that there may exist a frequency shift Δf for which δh is minimized. This particular frequency shift will be referred to as the critical frequency shift. In order to investigate the possibility of finding the critical frequency shift, the relationship between the height uncertainty and the frequency shift must be obtained. The relationship between $\delta\phi$ and α can be directly obtained from the cumulative distribution function (cdf) of $\Delta\phi = \phi - \zeta$. Note that for most practical cases $\alpha > 0.95$ (baseline distance or equivalently the frequency shift is rather small). The relationship between $\delta\phi$ and α is shown in Fig. 1 for the 80% and 90% probability criteria.

Assuming a Gaussian form for the normalized frequency correlation function the uncertainty in height estimation can be related to the frequency shift. Suppose the normalized frequency decorrelation function is approximated by

$$R(\Delta f) \approx 1 - (\Delta f / F_d)^2$$

where F_d is a free parameter equal to the frequency decorrelation bandwidth of an equivalent Gaussian correlation function. Figure 2 shows the product of the height uncertainty and the equivalent decorrelation bandwidth versus frequency shift normalized to the decorrelation bandwidth for both the 80% and 90% criteria. Thus the uncertainty in height measurement for a distributed target with known equivalent decorrelation bandwidth is independent of frequency shift or equivalently the baseline distance.

4. FREQUENCY CORRELATION FUNCTION

As was shown in the previous section the frequency correlation function of a distributed target is the most important parameter in estimating the height of the scatterer accurately. In a recent study [4] it was shown that the frequency correlation function, in general, depends on two sets of parameters: (1) radar parameters such as incidence angle, frequency, polarization, and footprint size, and (2) target parameters such as penetration depth and albedo. It is also shown that when the scattering is localized, that is, the field correlation distance in the random media is small, the frequency correlation function can be expressed in terms of product of two expressions: (1) a system dependent term only a function of radar parameters, and (2) a target dependent term only a function of the target attributes. For a homogeneous layer of random scatterers such as leaves and small branch over a smooth ground plane the FCF was calculated as a function of the layer thickness and number density of the constituent particles [4]. The equivalent decorrelation bandwidth F_d is computed and plotted in Fig. 3. It is shown that as the layer thickness and extinction increases, F_d and as a result of which the accuracy in height estimation increases.

5. REFERENCES

[1] Li, F.K., and R.M. Goldstein, "Study of multibaseline spaceborne interferometric synthetic aperture radars," *IEEE Trans. Geosci. Remote Sensing*, vol. 28, pp. 88-97, 1990.

[2] Zebker, H.A., S.N. Madsen, J. Martin, K.B. Wheeler, T. Miller, Y. Lou, G. Alberti, S. Vetrella, and A. Cucci, "The TOPSAR interferometric radar topographic mapping instrument," *IEEE Trans. Geosci. Remote Sensing*, vol. 30, no. 5, pp. 933-940, 1992.

[3] Sarabandi, K., "Derivation of phase statistics of distributed targets from the Mueller matrix," *Radio Sci.*, vol. 27, no. 5, pp 553-560, 1992.

[4] Sarabandi, K., and A. Nashashibi, "Analysis and applications of backscattered frequency correlation function,"*IEEE Trans. Geosci. Remote Sensing*, submitted for publication.

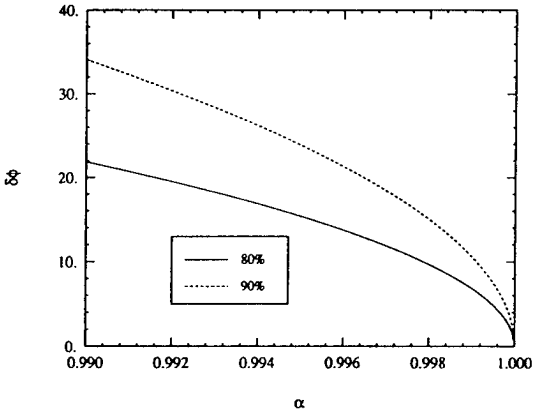


Figure 1: The phase uncertainty for 80% and 90% percent error probability criteria as a function of α.

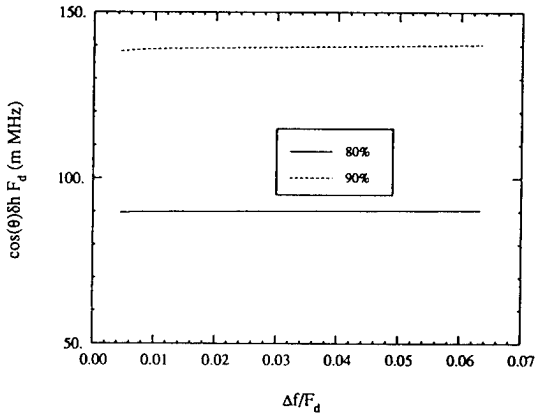


Figure 2: Product of the height uncertainty and decorrelation bandwidth versus frequency shift normalized to F_d.

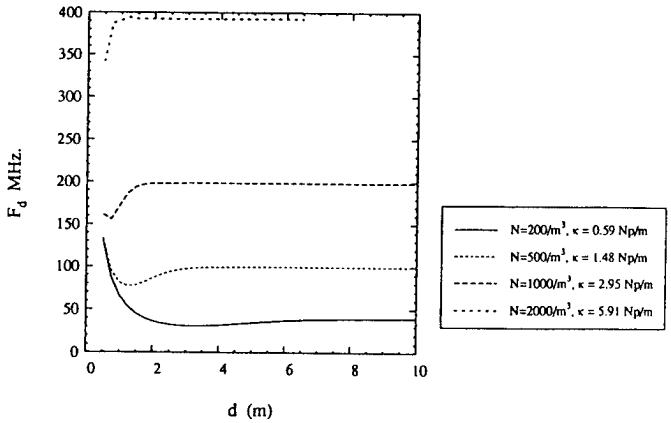


Figure 3: F_d as a function of depth for a homogeneous layer of a random medium at 5.3 GHz and $\theta = 30°$.

Application of Interferometry to Studies of Glacier Dynamics

Johan Jacob Mohr, Søren Nørvang Madsen

Danish Center for Remote Sensing, Dept. of Electromagnetic Systems
Technical University of Denmark, B-348, DK-2800 Lyngby, Denmark
Phone: +45 4525 3800, Fax: +45 4593 1634, Email: jm@emi.dtu.dk

ABSTRACT

Multi baseline repeat track interferometry (RTI) can potentially be used to measure both velocities and the micro topography of glaciers. The Danish Center for Remote Sensing† (DCRS) in corporation with the Danish Polar Center (DPC) has established a test cite for studies of glacier dynamics on the Storstrømmen glacier in North East Greenland. DCRS has acquired RTI data over the glacier in 1994 and 1995 and ERS-1/2 tandem mode data are also available. This paper presents recent results from this study. The advantages of satellite and airborne RTI respectively is described. The paper concludes with an analysis of different configurations of the spatial and temporal baselines.

INTRODUCTION

The ice sheets of Greenland and Antarctica are important components in the global climate system. Glaciers might act as indicators of changes in the ice sheet, thus monitoring methods are of significant interest. A joint project between the Danish Center for Remote Sensing (DCRS) and the Danish Polar Center (DPC) addresses the utility of airborne as well as satellite repeat track interferometry (RTI) for studies of glacier dynamics particularly as it relates to mass balance estimation.

Repeat track interferometry can provide measurements of surface displacements at sub-centimeter levels and/or relative topography with decimeters accuracy. However, the successful combination of two or more aircraft images to interferograms requires control of the trajectory to within a few meters. In the repeat pass mode the aircraft carrying EMISAR†† is controlled by the radar control computer via the Instrument Landing System (ILS) which again receives its navigational information from a P-code GPS receiver, thus allowing routine acquisitions of RTI data.

For the interpretation of the interferograms the required accuracy is even more stringent, since all errors in the knowledge of the spatial baseline directly translate into the same errors in the displacement measurements. This is essential, due to the small temporal baselines achievable in airborne interferometry. When a spatial baseline is present the topography as well contributes to the interferogram phase, but with the application of multi-baseline techniques this component can, in principle, be removed.

EXPERIMENTS ON STORSTRØMMEN

The two DCRS studies investigating the utility of repeat track interferometry for studies of glacier dynamics uses airborne EMISAR data and data from the ERS-1/2 satellites respectively. For both studies Storstrømmen is selected as the primary test area.

The airborne EMISAR experiments are conducted in a 10 km (N-S) by 30 km (E-W) area in the lower part of Storstrømmen. In 1994 DPC deployed four corner reflectors on solid rock in the test area and surveyed their positions by GPS. In 1995 the four reflectors were checked and their position resurveyed.

The reflectors serve as reference points for the RTI data. In august 1994 the area was covered by C-band RTI data acquisitions on a one day mission. In august 1995 L-band data were acquired on two consecutive days, thus giving a one day temporal baseline - an order of magnitude greater than for the 1994 data.

Airborne interferograms from 1994 as well as 1995 shows very low phase noise and are easily unwrapped.

The spatial baselines, extracted from the combination of GPS and the radar Inertial Navigation Unit (INU), have been refined with a parametric error model tuned with co-registration errors from numerous small image patches, [1]. The uncertainties on the baseline estimates, though reduced from several meters to the centimeter level, are still not sufficiently accurate to be used for an extraction of the glacial velocity know to be on the order of meters per year. The major unknown, is probably a very low frequency INU drift which is presently being studied.

The satellite project concerns data from the European Space Agency (ESA) ERS-1 (launched June, 1991) and ERS-2 (launched April , 1995) sensors. The satellites are presently operated in a tandem mode such that, seen from the earth, ERS-2 repeats the ERS-1 trajectory with a one day delay. The satellites are in a 35 day repeat cycle, thus allowing the

† The Danish Center for Remote Sensing (DCRS) is established and funded by the Danish National Research Foundation.

†† Development of the EMISAR was sponsored by the Thomas B. Thriges Foundation, the Danish Technical Research Counsil (STVF), the Royal Danish Air Force (RDAF), the Technical University of Denmark and the Joint Research Centre (JRC).

0-7803-3068-4/96$5.00©1996 IEEE

generation of one interferogram with a one day temporal baseline every 35 day for any area.

After correcting the ERS data for missing lines and digitization window changes we generated single look complex images, estimated baselines, and formed interferograms. On Fig. 1 a raw interferogram covering a 100 km by 200 km area around Storstrømmen is shown. On the left the interferogram phase is shown, on the right the amplitude. The phase is color coded and is repeated for each 2π, in this case corresponding to either a change in the terrain height of 800 m or a line of sight motion of 2.8 cm/day. Two interferograms with a 35 day separation have presently been generated. However, one of the interferograms is rather difficult to phase unwrap, likely due to temporal decorrelation thus resulting in a low correlation interferogram.

Manually counting the fringes on the mountains shows that a minor tilt of 1-2 fringes is still present. It is also noted that the topography in this area can account for at most 2 fringes. Thus the fringe pattern on the upper part of the glacier (with an eastward flow) must be due to a horizontal surface velocity of approximately 300 m/y in the central part decreasing to approximately zero at the sides. The almost vanishing fringe pattern on the lower part (with a southward flow) can not easily be interpreted as only the line of sight component of the motion can be determined, thus providing virtually no sensitivity to velocity measurement in this flow direction.

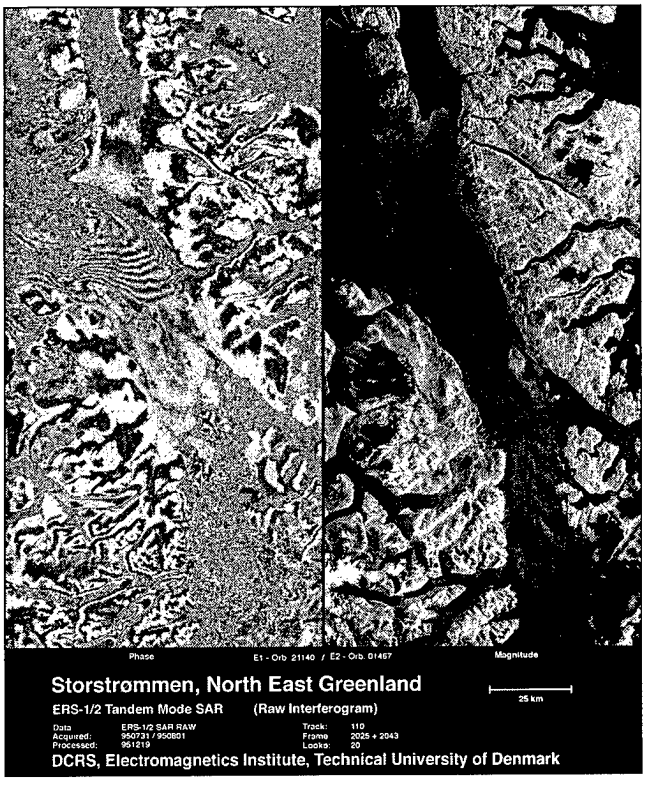


Fig 1. Raw interferogram from ERS-1/2 tandem data.

AIRBORNE VS. SATELLITE INTERFEROMETRY

From a users point of view the most significant advantages and disadvantages of airborne vs. satellite interferometry are:

- **Coverage and resolution.** Satellite images have large coverage and coarse resolution. Data amounts as well as acquisition time limits the coverage of an airborne sensor. One airborne data file of the 10 km times 30 km test fields has approximately the same size (1 Gbyte) as a full 100 km times 200 km ERS image.
- **Spatial availability.** Areas coverage for a satellite is inflexible since the satellite tracks are predetermined, as opposed to airborne interferometry. On the other hand, satellites does obtain global coverage in just a few days.
- **Temporal availability.** The satellite data generally have a fixed temporal baseline. The spatial baseline for an airborne system can in principle be chosen freely, but of course cost issues are of major importance
- **Velocity modeling**. Again since the satellite tracks are predetermined only one velocity component can be measured (two, if ascending and descending orbits are combined). In the ERS case the angle between the tracks is small (20°-30°) and ascending tracks are unfortunately not acquired at the moment. With airborne interferometry images can be acquired from different angles, in principle enabling the measurement of the 2-D (or even the 3-D) velocity pattern.
- **Viewing geometry.** Satellites usually uses steep incidence angles inhibiting mapping of rough terrain.

From an engineering point of view airborne data are usually easy to unwrap as opposed to satellite data. On the other hand baseline estimation is much more difficult for airborne systems.

SENSITIVITY ANALYSIS

The application of RTI to studies of glacier dynamics, has the inherent problem that topography as well as glacial movement contributes to the interferogram phase. The phase of a pixel, φ_{ij}, in an interferogram formed from two images denoted i and j, see Fig. 2, are (to first order)

$$\varphi_{ij} = -\frac{4\pi}{\lambda}\left(B_{\parallel,ij} + B_{\perp,ij}\Delta\theta - \Delta\rho_{ij}\right) + \varepsilon_{ij}. \qquad (1)$$

In (1) λ denotes the wavelength, $B_{\parallel,ij}$ and $B_{\perp,ij}$ the parallel and perpendicular baselines (assuming a flat earth), $\Delta\theta$ the angular deviation from the reference surface, $\Delta\rho_{ij}$ the line of sight (LOS) motion of the scene in the pixel and ε_{ij} the phase noise, [2]. Note that motion compensation to a common reference line or the removal of the flat earth phase are two alternative means to remove the parallel baseline component before the interferogram is interpreted. It is obvious that topography and displacement can not be determined unambiguously from (1). The ambiguity can be solved in one of the following ways:

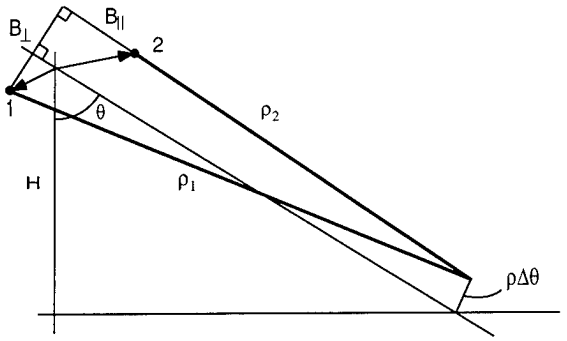


Fig. 2. Geometry for interferometric pair.

I. The topography term, $\Delta\theta$, can be supplied from another source, – a digital elevation model (DEM), [3].

II. Multiple interferograms can be utilized. If the flow field is stationary the displacements $\Delta\rho_{ij}$ can be collapsed into one unknown velocity v, since the temporal baseline are usually well known, [4].

III. The spatial baseline can be chosen to (or by change be) zero, such that the sensitivity to topography is zero, [5].

Though III is simplest, it is usually difficult to acquire such data and one must rely on either I or II. The following will focus on II as DEM's of Arctic regions are not widely available.

With a multi baseline technique (option II) the height and velocity of each pixel in the interferogram is 'optimally' found by solving a set of linear equations similar to (1) in a least square sense. To analyze the sensitivity of the solution, the equations corresponding to two interferograms, denoted 12 and 23, are investigated. To simplify the analysis the perpendicular spatial baselines and the temporal baselines are written as

$$B_{\perp,12} = B\sin\alpha, \quad B_{\perp,23} = B\cos\alpha, \quad \alpha\in[-\pi/2;+\pi/2]$$
$$T_{12} = tT, \quad T_{23} = (1-t)T, \quad t\in[0;1]$$

If $\delta_{\|}$ denotes the standard deviation of the parallel baseline estimates (assumed common for all (i,j)) and $\delta_{\perp}$ the perpendicular baseline, it can be shown that the uncertainties on the topography, $\Delta\tilde{\theta}$, and velocity, $\tilde{v}$, estimates are

$$\delta^2_{\Delta\tilde{\theta}} = \frac{1}{B^2}\frac{t^2+(1-t)^2}{\left((1-t)\sin\alpha - t\cos\alpha\right)^2}\left(\delta^2_{\|}+\Delta\theta\,\delta^2_{\perp}\right) \qquad (2)$$

$$\delta^2_{\tilde{v}} = \frac{1}{T^2}\frac{1}{\left((1-t)\sin\alpha - t\cos\alpha\right)^2}\left(\delta^2_{\|}+\Delta\theta\,\delta^2_{\perp}\right) \qquad (3)$$

It turns out that the uncertainty due to phase noise with a variance denoted σ^2_{ε} can be calculated from (2)-(3) as well, by substituting $(\lambda/4\pi)^2\,\sigma^2_{\varepsilon}$ for $(\delta^2_{\|}+\Delta\theta\delta^2_{\perp})$.

The most significant conclusion is that the topography uncertainty is independent of the total time span, T, and is minimized by choosing a configuration with large spatial baselines, B. Reversely the velocity uncertainties is independent of the magnitude of B and minimized by choosing a large T. This is of course only valid to a certain extend, since other issues such as temporal decorrelation, geometrical decorrelation and phase unwrapping must be taken into account.

If the temporal baselines can be chosen freely the global minimas are reached when (t,α) are chosen such that one interferogram has a zero temporal baseline and a large spatial baseline and the other conversely has a large spatial and a zero temporal baseline.

When the temporal baselines can not be chosen freely, the optimal spatial baseline ratio is easily found from (2) or (3). An interesting special case is the ERS-1/2 tandem mode data where $t = 0.5$. In that case the optimal spatial baselines for a velocity estimation has same magnitude but opposite sign. Note that as long as the baselines have opposite sign the standard deviation is at most a factor of $\sqrt{2}$ larger than the optimal.

CONCLUSION

Raw data from the ERS-1/2 satellites have been processed and the spatial baselines are estimated to within 10 cm. Precision orbit data with a similar accuracy, now available from ESA, might be used in the future. Manual fringe counting on the upper part of Storstrømmen shows horizontal surface velocities of approximately 300 m/y in the central part decreasing to approximately zero at the sides, in good agreement with in-situ measurements. The interferograms, though, need to be augmented with airborne data, since the flow of the lower part of the glacier is almost perpendicular to the ERS line of sight. Airborne data unwraps well. The uncertainty on the spatial baselines has been reduced from several meters to the centimeter level, but since the residual errors are not linear but rather caused by a small drift in the INU, this is not sufficiently accurate. Work on the estimation of such a non-linear baseline uncertainty is in progress.

REFERENCES

[1] Johan J. Mohr and Søren N. Madsen, "Parametric Estimation of Time Varying Baselines in Airborne Interferometric SAR," these proceedings.

[2] Søren N. Madsen and Howard Zebker, "Imaging Radar Interferometry," chapter 17 in Manual of Remote Sensing, Vol III, 1996, in press.

[3] D. Massonnet et al., "The displacement field of the Landers earthquake mapped by radar interferometry," Nature, Vol. 364, July 8. 1993, pp. 138-142.

[4] R. Kwok and M.A. Fahnestock, "Ice Sheet Motion and Topography from Radar Interferometry," IEEE trans. Geosci. Remote Sensing, Vol. 34, No. 1, Jan. 1996, pp. 189-200.

[5] R.M. Goldstein, H. Engelhardt, B. Kamb and R.M. Frolich, "Satellite Radar Interferometry for Monitoring Ice Sheet Motion: Application to an Arctic Ice Stream," Science, Vol. 262, pp. 1282-1285.

Relating forest parameters to interferometric data

N. FLOURY, T. LE TOAN and J.C. SOUYRIS
CENTRE d'ETUDES SPATIALES DE LA BIOSPHERE
CNES - CNRS - Université Paul Sabatier
bpi 2801, 18 avenue Edouard Belin
31055 Toulouse Cedex
France
Tel: (33) 61 55 85 84 Fax: (33) 61 55 85 00
E-mail: Nicolas.Floury@cesbio.cnes.fr

Abstract -- This paper presents the use of ERS-1 repeat-pass interferometric data for forest environment study. The overall objective is to assess the potentialities of interferometric information - degree of coherence and phase difference - to retrieve forest parameters.

Coherence is shown to be a good discriminator between forest stands and bare soil surfaces. The resulting map using coherence for different interferometric couples is in good agreement with ground data. Phase difference statistics are shown to be helpful in discriminating forest stands of different heights.

INTRODUCTION

Several studies have shown the potentialities of repeat-pass interferometry for the extraction of DEMs over temporally stable terrains or for the detection of small terrain movements. The interest in interferometry as a tool to study forests is more recent [1]-[2]. The objective of this paper is to analyse interferometric data over a well known test site, the Landes Forest in France, for a better understanding of the relations between interferometric information and forest parameters.

TEST-SITE AND DATASET

The site under test is the Landes forest, located in South-Western France. It represents the largest plantation forest in France, constituting nearly one million hectares on flat topography. This artificial forest is almost totally formed of maritime pine (pinus pinaster) and is managed in a consistent fashion, which ensures the canopy to be homogeneous.

The ground data consist in a biomass map which provides information about location and age of more than 50 stands of maritime pine, covering about 20 ha each. The age of these stands ranges between 2 and 50 years old, while the corresponding biomass is between 5 and 150 tons / ha. Clear cuts and agricultural fields are also present in the area. Other parameters such as tree densities and dendrometric information are also available.

Interferometric data consists of 3 interferometric couples based on ERS-1 SLC images acquired in 1991 and processed by the CNES.

The characteristics of the interferometric data are summarized in Table1.

The complex degree of coherence of the two co-registered complex image values s1 and s2, is given by:

$$\rho\, e^{j\phi} = \frac{\left\langle s_1 . s_2^* \right\rangle}{\sqrt{\left\langle s_1 s_1^* \right\rangle . \left\langle s_2 s_2^* \right\rangle}}$$

where ρ is the degree of coherence and ϕ the phase difference between the two signals.

Interferometric Set	Date of acquisition	Time interval (days)	Baseline given by ESA (m)
A	15 oct 91 / 20 nov 91	35	10
B	20 nov 91 / 02 dec 91	12	142
C	15 oct 91 / 02 dec 91	47	130

Table 1: Characteristics of available interferometric data

COHERENCE

Fig. 1 presents the variations of the coherence versus stand age for the 3 interferometric sets.

High temporal coherence is obtained for clear cuts and open fields whereas it decreases with stand age. Regarding the ERS-1 configuration over the Landes Forest, previous experiment and modeling studies [3] have shown that backscattered signal for low age stands comes principally from the soil contribution, (Fig. 2) which is time-coherent. As vegetation grows, the proportion of volume backscattered signal increases. However, the volume scatterers such as needles or branches are more sensitive to variations due to growth or wind. For different acquisitions, these scatterers have a high probability to move. This leads to a decrease of the overall correlation in the case of a forested area.

The overall coherence of sets A and C is shown to be lower than coherence of set B. This could be the result of two effects: (a) the degree of coherence could decrease as a function of time interval between acquisitions as shown in [4] or (b) the strong precipitation which occured on October

0-7803-3068-4/96$5.00©1996 IEEE

15th (34 mm) caused a drop of coherence for the interferometric sets which include this acquisition. Lower coherence of A and C compared to B observed over clear cuts can be explained by changes in the remaining vegetation cover (growth of herbaceous, cleaning of a stand after a cut) or by strong modifications of the roughness state.

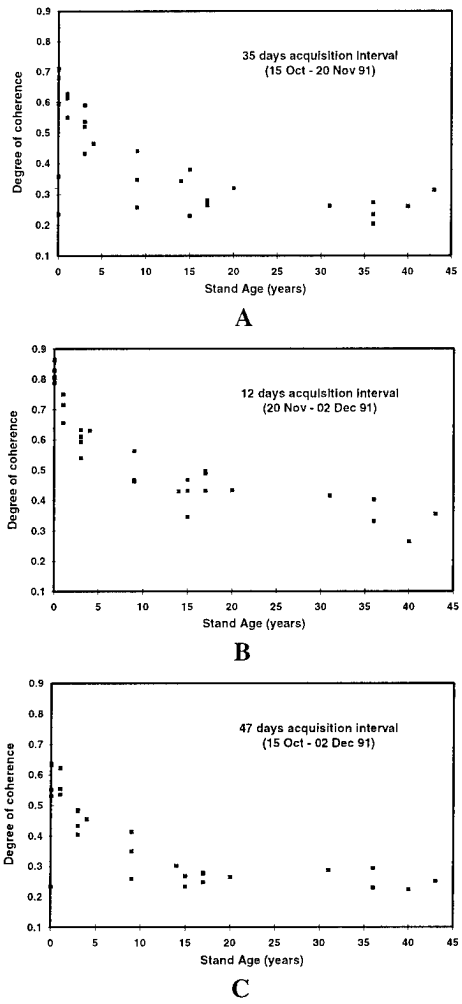


Fig. 1: Variations of the degree of coherence with stand age

The degree of coherence between two separate acquisitions can be a good discriminator between forests and bare soil surfaces (or surfaces with low vegetation cover). The example in Fig. 3b shows a map of forest / non-forest obtained from a thresholding of the degree of coherence of A and B interferometric sets (3a for set A). The resulting map is in good agreement with the forest map established from ground data. White areas are ground surfaces which did not change between the two extreme acquisition dates (15 oct / 2 dec). Black areas are forest stands characterized by a low correlation. Areas in grey are fields or stands which correlation state has changed. This could have been caused by plough, harvest (on agricultural fields), growth of herbaceous or cleaning of stands.

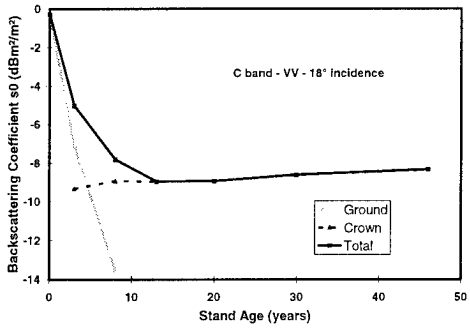


Fig. 2: Decomposition of scattering mechanisms derived from theory described in [7]

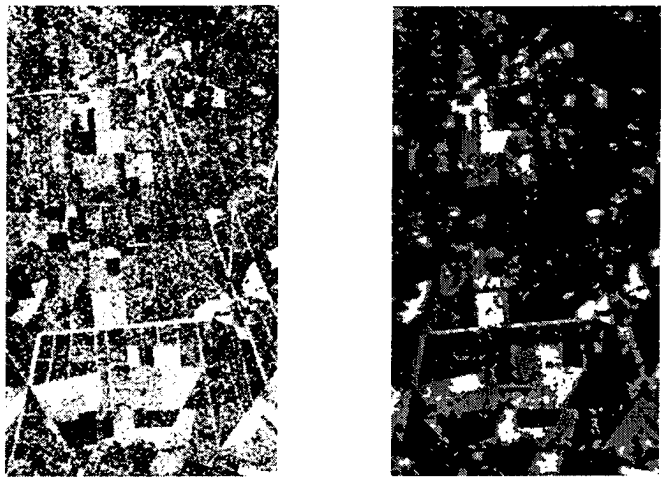


Fig. 3: Map of (a) coherence of set B and (b) forest / non-forest areas based on the degree of coherence. Nezer test-site.

PHASE DIFFERENCE

The interferometric phase shift is related to the height of the scatterers. In the forest case, this distance depends on the trees height and on the penetration depth. Since the phase difference rms decreases with an increase of the degree of coherence, the measurements were extracted from the interferometric set B, which presents the highest overall coherence. The larger baseline of B is also well suited to reducing the rms-height error [5].

The digital elevation model of the area of study is not available. However, the general topography of the test-site is flat (as a rule, the slope is less than 0.5%). We chose to restrict the study to a small area around a clear cut which was considered as ground level.

Probability density functions (pdf) of the phase difference for stands of different ages surrounding the selected clear-cut are calculated. Fig. 4 presents pdfs of the

clear-cut and of stands of 17 and 40 years old. The pdfs show an overall good agreement with the theoretical pdfs given by [6].

The offset between the mean phase difference for a forested area and the mean phase difference for the clear cut (ground reference) is related to the scatterers height. The spreading of the pdf is linked to the degree of coherence. We can observe that the variation of the mean value of the phase difference is a monotonous function of the stand age.

The mean value of the phase difference is extracted from each stand and the corresponding height difference is computed. This leads to the effective heights given in Table 2.

Discrepancies exist between computed and actual heights. The measured height is not the height of the top of the trees, but the height of scatterers distributed over a thickness equal to the penetration depth and is smaller than the actual height. Further work will consist in using the modified radiative transfer model developped in [7] to estimate the effective penetration depth for each stand. Moreover, despite the low slope, forest stands are large enough to induce a shift of a few meters in the ground level. This shift could be corrected by using a DEM

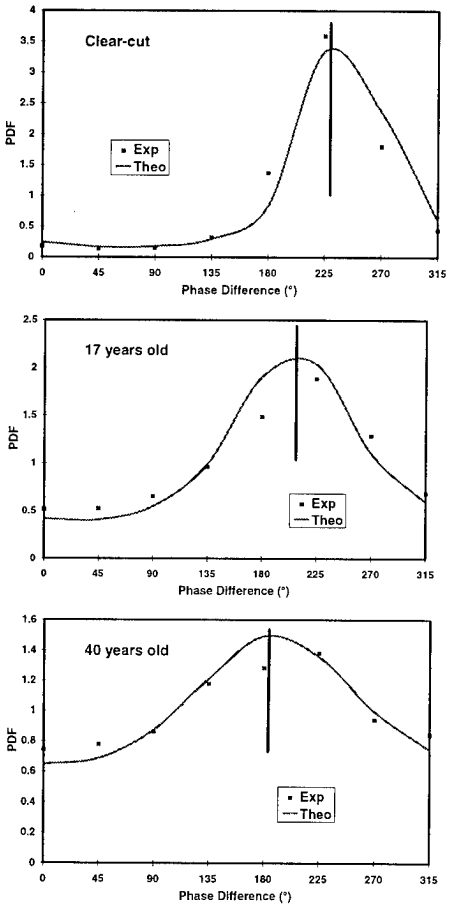


Fig. 3: Pdfs of the phase difference of interferometric set B. Experiment vs Theory

Stand Age	Measured Effective Height	Actual Height
0	*0 m*	*0 m*
9	6.0 m	5.35 m
17	6.9 m	10 m
36	10.1 m	16 m
39	10.2 m	17.2 m

Table 2: Computed vs measured tree heights

The rms errors on estimated height are very important. The errors could be reduced (a) by using interferometric pairs with a larger baseline to reduce rms height dependence on rms phase difference, and (b) by enhancing the overal degree of coherence using interferometric pairs with a smaller time interval.

CONCLUSION

This study has underlined the relations between the interferometric degree of coherence and the forest age (or biomass). Coherence has been shown to be efficient to discriminate forest areas from clear-cuts. Qualitative use of phase difference may be undertaken to classify forest stands of different heights (related to biomass).

Optimal interferometric pairs with a smaller time interval and a larger baseline should (a) enhance the use of the degree of coherence to discriminate young forest stands and (b) permit a more quantitative use of the phase difference to extract forest height.

ACKNOWLEDGMENTS

The work is carried out under CNES/CESBIO Contract n°833/2/95/CNES/171. The interferometric data have been provided by CNES/QTIS.

BIBLIOGRAPHY

[1] J.O. Hagberg, L.M.H. Ulander and J. Askne: « Repeat-Pass SAR Interferometry over Forested Terrain », IEEE TGRS, Vol. 33, No. 2, March 1995, pp 331-340.

[2] U. Wegmüller and C.L. Werner: « SAR Interferometric Signatures of Forest », IEEE TGRS, Vol. 33, No. 5, September 1995, pp 1153-1161.

[3] J.C. Souyris, T. Le Toan, C.C. Hsu and J.A. Kong: « Inversion of Landes Forest Biomass using SIR-C/XSAR Data: Experiment and Theory », IGARSS'95, July 95, Vol. 2, pp 1201-1203.

[4] H.A. Zebker and J. Villasenor: « Decorrelation in Interferometric Radar Echoes », IEEE TGRS, Vol. 30, No. 5, September 1992, pp 950-959.

[5] F.K. Li and R.M. Goldstein: « Studies of Multibaseline Spaceborne Interferometric Synthetic Aperture Radars », IEEE TGRS, Vol. 28, No. 1, January 1990, pp 88-97.

[6] J.S. Lee, K.W. Hoppel, A. Mango, A.R. Miller: « Intensity and Phase Statistics of Multilook Polarimetric and Interferometric SAR Imagery », IEEE TGRS, Vol. 32, No. 5, September 1994, pp 1017-1028.

[7] C.C.Hsu, H.C.Han, R.T.Shin, J.A.Kong, A. Beaudoin and T. Le Toan: « Radiative transfer theory for polarimetric remote sensing of pine forest at P band », IJRS, Vol. 15, No. 14, September 1994, pp 2943-2954.

Estimating Vegetation and Surface Topographic Parameters From Multibaseline Radar Interferometry

Robert Treuhaft[1], Mahta Moghaddam[1], Jakob van Zyl[1], and Kamal Sarabandi[2]

[1]Jet Propulsion Laboratory, MS 300-235
California Institute of Technology
4800 Oak Grove Drive
Pasadena, California 91109
Telephone: 818-354-6216 email: bob_treuhaft@radar-email.jpl.nasa.gov
[2]University of Michigan, Ann Arbor, MI 48109
Telephone: 313-936-1575 email: saraband@eecs.umich.edu

ABSTRACT

Interferometric synthetic aperture radar (INSAR) data are sensitive to characteristics of the vertical distribution of vegetation and the underlying surface topography, both of which are of critical importance in successional ecological modeling and hydrology. However, even with the simplest scattering model, the number of parameters describing the vegetation and surface topography needed to characterize the INSAR response exceeds the number of independent INSAR observations. Introducing INSAR measurements across two baselines extends the observation set and potentially enables the estimation of all the parameters in a homogeneous-layer scattering model described below. The baseline lengths and INSAR accuracies needed for multibaseline INSAR parameter estimation are discussed below. A demonstration of multibaseline INSAR with TOPSAR data over the BOREAS Southern Test Site yields estimates of the vegetation layer depths and extinction properties.

1. INTRODUCTION

INSAR data can potentially be used to infer the vertical structure of vegetation and the underlying surface topography. In order to estimate vegetation and surface topographic parameters from INSAR, a physical model relating the INSAR data to the properties of the vegetation and surface topography must be used. A simple homogeneous-layer model outlined below suggests that a minimum of three physical parameters are needed to describe the INSAR response to a vegetation layer [1] (see Fig. 1): 1) the depth of the vegetation layer h_v, 2) the extinction coefficient (power loss per unit length) σ_x, and 3) the altitude of the underlying ground surface z_0. However, for single-baseline, single-frequency, single-polarization, and single-incidence-angle INSAR, there are only two effective observations: 1) the amplitude and 2) phase of the INSAR complex cross-correlation (introduction of the backscattered power observation requires another parameter [1], and will be ignored here). Thus the estimation of the above three parameters is underdetermined. Introducing a second INSAR baseline extends the observation set and facilitates the estimation of vegetation and surface parameters. In the next section, the modeling of the INSAR return with a homogeneous vegetation layer is described with expressions relating the above parameters to the INSAR observations. Section 3 explores the baseline combinations and noise characteristics required to uniquely estimate all parameters, and shows the results of parameter estimation from the BOREAS data. Section 4 contains a summary and recommendations for future data acquisition and analysis improvements.

The research described in this paper was carried out in part by the Jet Propulsion Laboratory, California Institute of Technology, under contract with the National Aeronautics and Space Administration.

2. HOMOGENEOUS-LAYER MODELING OF THE INSAR RETURNS

This section will summarize a model of the vegetation layer as a homogeneous scattering medium, which is completely described in [1]. Fig. 1 schematically shows a horizontal baseline and ground surface for simplicity. The principal INSAR observations are contained in the normalized complex cross-correlation, C_N, which is defined as

$$|C_N| \equiv \frac{|<E(\vec{R}_1)E^*(\vec{R}_2)>|}{\sqrt{<E^2(\vec{R}_1)><E^2(\vec{R}_2)>}} \quad (1)$$

0-7803-3068-4/96$5.00©1996 IEEE

where $E(\vec{R}_1)$ and $E(\vec{R}_2)$ are the signals at each end of the baseline. The received fields contributing to $E(\vec{R}_1)$ and $E(\vec{R}_2)$ can be thought of as a sum of fields originating from vegetation constituents such as that located at $\vec{R}_j$ in Fig. 1. It is shown in [1] that, after correction for signal-to-noise characteristics, which are discussed, for example, in [1], [2], and [3], and after neglecting small refractivity effects, also discussed in [1], the magnitude and phase of C_N can be written as

$$\begin{aligned} 1)\ |C_N| &= \left[\frac{A_R}{A_R|_{\alpha_r=0}}\right]\left[\frac{A_v(\sigma_x,h_v)}{A_v(\sigma_x,h_v)|_{\alpha_z=0}}\right] \\ 2)\ \phi_{obs} &\equiv \arg(C_N) = \phi_v(\sigma_x,h_v)+\phi_0(z_0) \end{aligned} \quad (2)$$

where the term in the first set of brackets is the correlation amplitude due to the finite extent of the range cell, and the term in the second set of brackets is due to the finite vertical extent of the vegetation. The A_R and A_v functions are defined in [1], and are only shown here to demonstrate that $|C_N|$ depends on the vertical depth of the vegetation h_v and the extinction coefficient σ_x, which is defined as

$$\sigma_x \equiv \frac{4\pi\rho_0 Im < f_f >}{k_0} \quad (3)$$

where ρ_0 is the average number density of vegetation scatterers, $Im < f_f >$ is the average imaginary part of the forward scattering amplitude of the vegetation scatterers, and k_0 is the wave number at the center of the radar pass band. The terms α_r and α_z are the partial derivatives of the interferometric phase with respect to the distance and altitude of a reference point taken to be at the ground surface; they depend on the experimental configuration, and in particular on baseline. The observed phase ϕ_{obs} in the second line of (2) is a sum of a vegetation-induced phase, ϕ_v and the phase ϕ_0 due to scattering at a reference point chosen to be at the bottom of the layer. While the three parameters, h_v, σ_x, and z_0 cannot be determined from one complex C_N measurement, they can be estimated by adding data from another baseline, for which the functional form of (2) is changed, via A_R and A_v, without introducing any new parameters.

3. USING MULTIBASELINE INSAR FOR VEGETATION PARAMETER ESTIMATION

The standard TOPSAR baseline is 2.5 m [4], which is realized by transmitting from one end of the baseline and receiving at both ends of the baseline. An effective 5-m baseline was generated by transmitting at both ends of the baseline and receiving at both ends. Although multibaseline INSAR potentially provides enough observations (4 total observations for 2 baselines) to estimate all three parameters mentioned above, this paper will concentrate only on the vegetation depth and extinction coefficient for brevity. The vegetation depth and extinction coefficient will be determined by using the first line of (2) twice, once for each baseline, and solving for the two parameters. The vegetation phase ϕ_v also has information on these two parameters, but it is not expected to be as sensitive to the h_v and σ_x parameters as $|C_N|$. Once those 2 parameters are estimated, z_0 can be estimated from the induced ϕ_v and ϕ_{obs} using the second line of (2). In the absence of noise, the parameters would be uniquely determined. Noise on the cross-correlation magnitudes, for example, induces an uncertainty in the values of h_v and σ_x. For typical TOPSAR baselines of 2.5 m and 5 m, h_v and σ_x are frequently not well-determined. Fig. 2 shows the set of h_v and σ_x values which are allowed for an old jack pine stand in the BOREAS Southern Test Site, measured at a wavelength of 5.6 cm, at about 28° incidence, for which the noise on the normalized cross-correlations was taken to be 0.001. This seemingly low noise value was achieved by averaging over a few thousand pixels, which yields areas of the order of 1 km^2. For longer baselines, the averaging would not have to be over such a large area. As can be seen from Fig. 2, the 2.5-m or 5-m baselines alone will not constrain the parameters, because the h_v parameter on the abscissa has a wide range of allowed values, which actually extends to infinity. But the intersection of the allowed values for each baseline (in white in Fig. 2), which is the multibaseline solution, constrains the solutions to the overlap region in Fig. 2. The multibaseline h_v solution is 24-34 m, while σ_x is constrained to the range 0.22-0.29 db/m. Fig. 3 shows a similar plot for a stand of young jack pine, at an incidence angle of about 29°. Because the young jack pine stand is shorter, the correlation signature between baselines is less distinct, and these two TOPSAR baselines were insufficient to determine the two parameters, as their intersection, which is equivalent to the 5-m baseline solutions, contains values of h_v out to infinity. Approximate ground truth vegetation depths are 15 and 4 m for old and young jack pine, repectively. The multibaseline solutions are therefore consistently high. Potential reasons for overestimating h_v will be discussed in the next section.

4. INTERPRETATION AND FUTURE DATA ACQUISITION/ANALYSIS IMPROVEMENTS

From Fig. 2 and Fig. 3, it can be seen that the simultaneous use of 2 INSAR baselines has the potential for estimating the vegetation depth and extinction coefficient parameters. Although not shown here, the ground surface altitude z_0 can also be estimated from the multibaseline data. Fig. 3 demonstrates that even for the large averaging areas (approximately 1 km on a side) used in this study, the 2.5-m and 5-m baseline pair are not useful for estimating the complete parameter set. It has been shown by

simulation that a 5-m and 10-m baseline would be better suited to parameter estimation with typical noise values of about 0.005 on areas with linear dimensions of the order of 100 m. The bias toward high values of vegetation depth in the current study can arise from a number of instrumental and modeling factors detailed in [1]. Chief among them are correlation loss, due to an effectively larger range resolution cell, which is larger than the nominal loss calculable from the standard radar step-chirp. A larger range bite would tend to lower the correlation amplitude which would cause estimates of vegetation depth to be too high, and extinction coefficients and surface altitudes to be too low. One inadequacy in the modeling may be the failure to account for ground and ground-trunk returns, which should be negligible at the 5.6-cm wavelength, but would induce a lower cross-correlation amplitude. Future model improvements will include the ground and ground-trunk returns, at the expense of introducing more parameters describing the surface reflection properties. A data acquisition/analysis strategy involving multifrequency and multibaseline INSAR may be capable of estimating all the parameters in the extended set.

5. REFERENCES

[1] R. N. Treuhaft, S. N. Madsen, M. Moghaddam, and J. J. van Zyl, "Interferometric Remote Sensing of Vegetation and Surface Topography," Submitted to Radio Science, 1995.

[2] F. K. Li and , R. M. Goldstein,"Studies of Multibaseline Spaceborne Interferometric Synthetic Aperture Radars," IEEE Trans. Geosci. Remote Sensing, 28, 88-97, 1990.

[3] E. Rodriguez, and J. M. Martin, "Theory and Design of Interferometric Synthetic Aperture Radars," IEE Proceedings-F 139, 147-159, 1992.

[4] H. A. Zebker et al., "The TOPSAR Interferometric Radar Topographic Mapping Instrument," IEEE Transactions on Geoscience and Remote Sensing, 30, 1992.

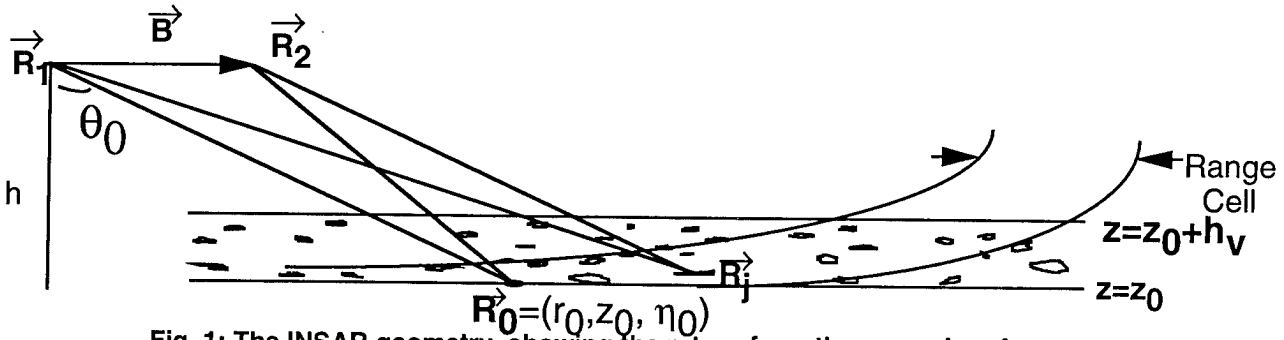


Fig. 1: The INSAR geometry, showing the return from the ground surface altitude at R_0 and from the vegetation scatterer at R_j.

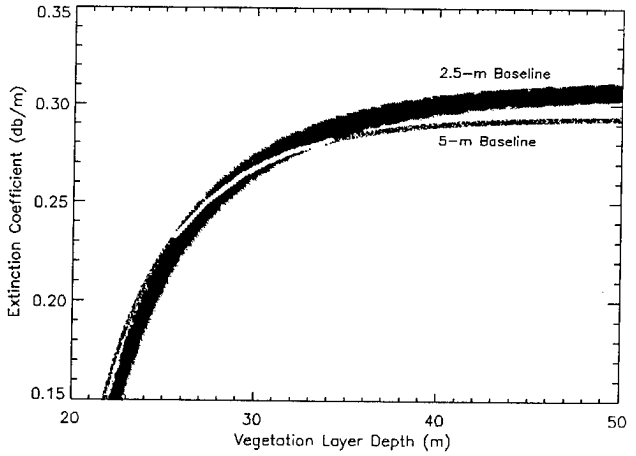


Fig. 2: Old jack pine (~15 m tall) allowable extinction-coefficient and vegetation-depth solutions for 2.5 m (dark), 5 m (light) baselines, and their intersection (white).

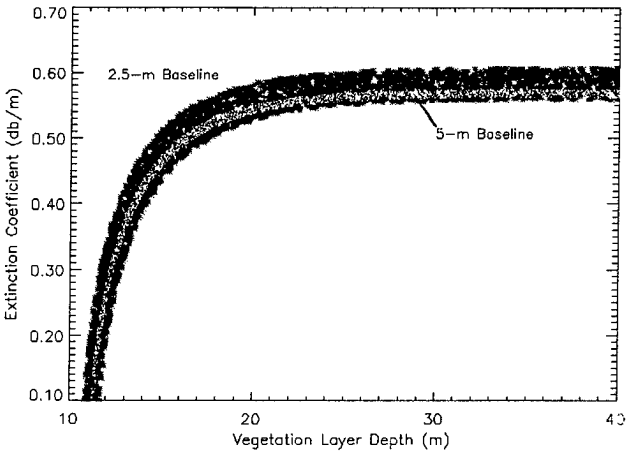


Fig. 3: Young jack pine (~4 m tall) allowable extinction-coefficient and vegetation-depth solutions for 2.5 m (dark) and 5 m (light) baselines.

On the Detection of Spatially Varying Current Fields at the Ocean Surface by Along-Track Interferometric Synthetic Aperture Radar

Roland Romeiser[1] and Donald R. Thompson[2]

[1]University of Hamburg, Institute of Oceanography, Troplowitzstr. 7, 22529 Hamburg, Germany
Phone: +49 40 4123 5430 Fax: +49 40 4123 5713 E-Mail: romeiser@ifm.uni-hamburg.de

[2]Johns Hopkins University, Applied Physics Laboratory, Johns Hopkins Road, Laurel, MD 20723, USA
Phone: +1 301 953 6000 X 4559 Fax: +1 301 953 5548 E-Mail: thompson@nansen.jhuapl.edu

Abstract -- The phase information in along-track interferometric synthetic aperture radar (along-track INSAR, ATI) images is a measure of the Doppler offset of the backscattered signal and thus of the line-of-sight velocity of the scatterers. It is hoped that this information can be exploited for oceanic surface current measurements from aircraft or spacecraft. However, the Doppler offset of the radar backscatter from the ocean arises not exclusively from the mean surface current, but it includes contributions associated with surface wave motions. We have developed a very efficient model for the computation of these contributions and of the complete Doppler spectra. In this work, we present the theoretical concept of the model and discuss the actual possibilities and limitations of oceanic current measurements by ATI.

INTRODUCTION

A radar signal which is backscattered by a moving target experiences a Doppler shift in frequency proportional to the target's line-of-sight velocity. The Doppler spectrum of the radar return from the ocean surface represents a distribution of the line-of-sight velocity of the scatterers, weighted by their contribution to the backscattered power. The bandwidth of the Doppler spectrum depends on the amplitudes of the ocean waves within the illuminated area. The first moment of the Doppler spectrum, the Doppler offset, can be converted into a weighted mean line-of-sight velocity of the scatterers.

Along-track interferometric synthetic aperture radar (along-track INSAR, ATI) systems can directly detect the Doppler offset associated with each pixel of a SAR image [1]. This technique is promising for remote measurements of spatial surface current variations and of the orbital motions of long waves. Conventional radars can measure only the normalized radar backscattering cross section (NRCS) variations which result from such features.

However, the Doppler offset is not simply proportional to the component of the mean surface current parallel to the radar look direction. It includes also contributions associated with the phase velocity of the short waves that give rise to resonant Bragg scattering and, via higher-order effects, with the orbital motions of all ocean waves that are long compared to the Bragg waves. Comparisons of simultaneously acquired radar and in-situ data have shown that measured "Doppler velocity fields" can deviate strongly from the actual surface current fields [2]. Also a clear dependence of the Doppler offset on the polarization of the radar, which is known from Doppler scatterometry, indicates that wave motion effects may not be neglected when converting Doppler offsets into currents. ATI data must be corrected for these effects.

Measured Doppler spectra can be relatively well explained by fundamental radar backscattering models based explicitely on Maxwell's equations (e.g., [3]). However, such models are quite complex, and computations are time-consuming. For a better understanding of the ATI imaging mechanism and for extensive numerical analyses, it would be desirable to have a simplified model which reduces the calculation of Doppler offsets to an evaluation of a few key expressions. As far as NRCS calculations are concerned, this has been achieved with the development of composite surface models based on the simple equations of Bragg scattering theory (e.g., [4]).

In fact, we have developed a new model which combines the advantages of a composite surface model with the capability of Doppler calculations. In this paper we present the theory of the proposed model, compare model predictions with results of a more fundamental model, and discuss the resulting theoretical possibilities and limitations of oceanic current measurements by ATI.

THEORY OF THE MODEL

In general, the Doppler shift f_D of the radar signal backscattered by a moving target is given by

$$f_D = -k_e v_p / \pi \,, \tag{1}$$

where k_e is the magnitude of the electromagnetic wave vector and v_p is the line-of-sight component of the target velocity. Since the backscattering of microwaves at the ocean surface is, for moderate incidence angles, dominated by Bragg scattering, some Doppler shift will always result from the phase speed of the short Bragg waves at the ocean surface that give rise to resonant interaction with the electromagnetic waves. If no surface currents and longer waves were present, the Dop-

This work has been supported by the Deutsche Forschungsgemeinschaft, Grant No. Al 88/2, and by the Office of Naval Research, Grant No. N00014-95-1-0046.

0-7803-3068-4/96$5.00©1996 IEEE

pler spectrum would consist of two lines associated with the Bragg waves traveling towards and away from the radar. The intensity of the two lines would be proportional to the wave-height spectral densities of the two Bragg wave components.

However, the orbital motions of longer waves within the footprint of the radar and the corresponding velocity distribution must lead to a broadening of the two lines. The variation of the Doppler shift with the line-of-sight velocity along a sinusoidal wave can be related to the surface slope by a complex linear modulation transfer function D. If the amplitude of the wave is ζ_0 and its wavenumber is k, one obtains for the probability density function (pdf) of the Doppler frequencies associated with the sinusoidal wave

$$p_x(f) = \frac{1}{\pi} \frac{1}{\sqrt{f_0^2 - f^2}} \text{ where } |f| \le f_0 \equiv |D| k \zeta_0 . \quad (2)$$

The shape of this distribution is similar to a capital letter M. Together with the Doppler shift, however, also the NRCS varies along the sinusoidal wave. Looking at the Doppler spectrum, this results in a weighting of the different values of $p_x(f)$ with the corresponding contributions to the backscattered power. Accounting for variations of the NRCS up to second order in the surface slope, an "elementary" Doppler spectrum associated only with the motions of a given sinusoidal wave will be proportional to

$$p_\sigma = \frac{1}{(1+b_1)\pi} \left(1 + b_1 + \frac{af}{f_0} + b_2 \left(1 - 2 \left(\frac{f}{f_0} \right)^2 \right) \right) \frac{1}{\sqrt{f_0^2 - f^2}} \quad (3)$$

where the coefficient a accounts for the effect of NRCS variations of first order in the surface slope, and b_1, b_2 account for the effect of constant and oscillating second-order contributions to the NRCS, respectively. The distribution p_σ is similar to p_t, but it may be asymmetric and have a slightly different bandwidth and mean value. The coefficients a, b_1, b_2 can be derived from the equations of Bragg scattering theory. In general, they depend on the two-dimensional wavenumbers of the modulating sinusoidal wave, and they may be different for the distributions associated with the two Bragg wave components. In addition to pure geometric effects, we include also the effect of hydrodynamic modulation of the Bragg wave intensity by longer waves. The resulting model is then completely consistent with a previous version that was employed for NRCS simulations [4].

On a real ocean surface, a full two-dimensional spectrum of surface waves is present. Assuming that all waves are propagating independently of each other, their mean effect on the Doppler shift and the NRCS will be equal to the sum, or integral, of their single effects. In principle, the shape of the longer-wave related Doppler spectrum associated with each of the two Bragg wave components is then given as the convolution of an infinite number of infinitely narrow distributions of the form (3), representing an integral of all wave effects over the full two-dimensional waveheight spectrum. According to the central limit theorem, the resulting distribution will be Gaussian. We obtain for its variance

$$\langle f^2 \rangle - \langle f \rangle^2 = \iint \left(\frac{1}{2} - \frac{a^2(\underline{k}) + b_2(\underline{k})}{4 + 4 b_1(\underline{k})} \right) |D(\underline{k})|^2 k^2 \Psi(\underline{k}) d^2k \quad (4)$$

and for its mean value

$$\langle f \rangle = \iint \frac{a(\underline{k}) |D(\underline{k})|}{1 + b_1(\underline{k})} k^2 \Psi(\underline{k}) d^2k , \quad (5)$$

where Ψ is the waveheight spectrum.

Finally, the actual Doppler spectrum $S(f)$ is obtained by centering the two Gaussian distributions at the positions corresponding to the respective lines associated with the Bragg wave phase speed and multiplying them by the corresponding zeroth-order NRCS and by a factor $(1+\iint b_1(\underline{k}) d^2k)$ which accounts for the second-order contributions to the NRCS. The integral of $S(f)$ will then yield the NRCS, and the first moment of $S(f)$ yields the Doppler offset in the absence of a mean surface current. The current-related Doppler offset will lead to a further frequency shift of the spectrum. In order to retrieve currents from ATI data, the data must be corrected for the wave-related contributions.

MODEL RESULTS

Fig.1 shows examples of some Doppler spectra obtained from the proposed model and from a time-dependent model based on fundamental equations as described in [3]. For these model simulations, the radar frequency was assumed to be 1.0 GHz (L band) at vertical (VV) polarization, the incidence angle is 30°, and the azimuthal radar look direction is 75° with respect to the downwind direction. Doppler spectra are shown for wind speeds of 3, 6, and 12 m/s at a height of 10 m; there is no mean surface current.

Both models predict Doppler spectra of similar shapes and with comparable bandwidths and Doppler offsets. In particular, both models show two separate peaks for the two Bragg wave components in the 3 m/s case, which are broadened with increasing wind speed until a quasi-Gaussian spectrum is obtained at 12 m/s winds. The proposed model, which reduces computing times by a factor of more than 10, appears to reproduce basic properties of the Doppler spectra quite well. Remaining differences between the two models can be mainly attributed to the fact that different parameterizations of the waveheight spectrum have been used. Another difference is the inclusion of hydrodynamic modulation effects in the proposed model, which are neglected in the other model.

Fig.2 shows examples of simulated "Doppler velocity" signatures of a simple current feature similar to typical currents over underwater sandwaves in tidal waters. A surface current change from 0.9 m/s to 1.1 m/s within 50 m causes a hydrodynamic modulation of the ocean wave spectrum. Due to this effect, the contribution of the surface waves to the Doppler ve-

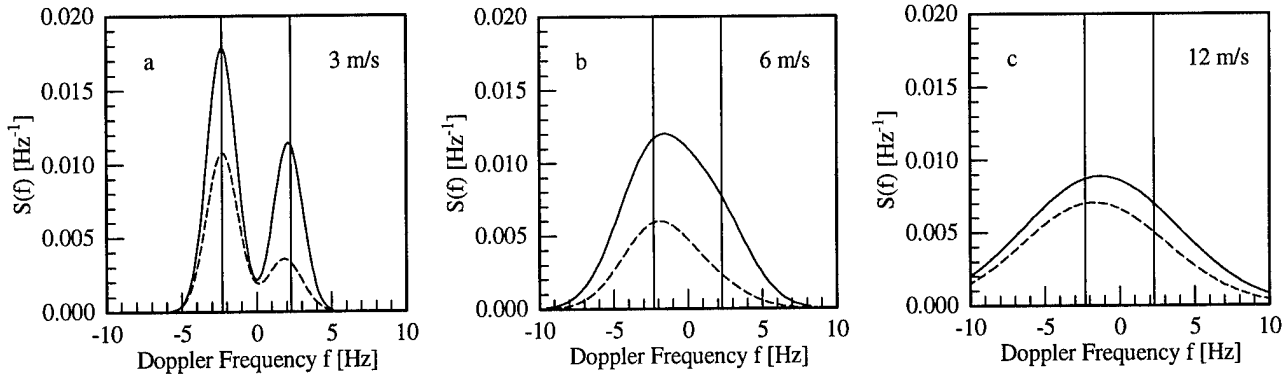


Figure 1: Simulated Doppler spectra for L band (1.0 GHz), vertical (VV) polarization, an incidence angle of 30°, and an azimuthal radar look direction of 75° with respect to the wind direction. Wind speeds are a) 3 m/s, b) 6 m/s, c) 12 m/s. Solid lines: results of the proposed model; dashed lines: results of a more fundamental model (see text for details).

locities will not differ by a constant offset but by a spatially varying offset from the true surface current.

For the computation of the spatially varying wave spectra we have used a numerical model based on the equations of weak hydrodynamic interaction, as described in [5]. A special feature of this model is a correction of the wind speed for the local current, i.e., only relative wind speeds enter into the equilibrium waveheight spectrum. In order to demonstrate the dependence of the Doppler velocity variations on the wind direction, simulations were carried out for wind directions ranging from 0° to 180° with respect to the current direction, while the radar look direction was always aligned with the current direction.

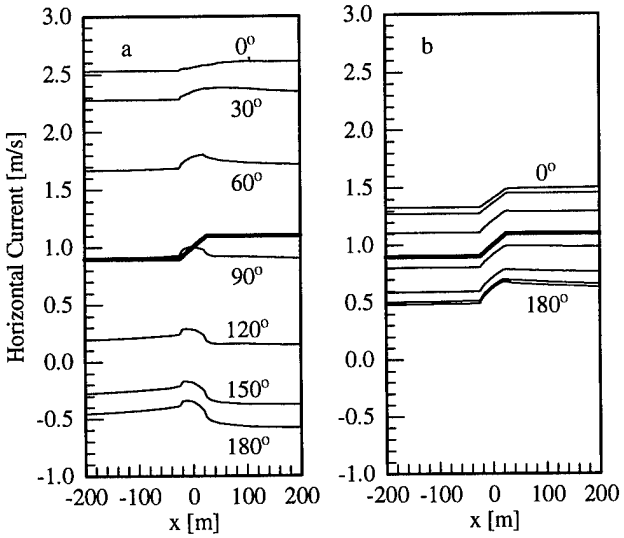


Figure 2: Simulated Doppler velocity signatures of a simple surface current feature (bold line) for a downstream looking radar and wind directions between down- (0°) and upstream (180°); a) L band (1.0 GHz), HH, incidence angle = 30°, wind speed = 10 m/s; b) X band (10.0 GHz), VV, 60°, 5 m/s.

Fig.2a shows model results for a relatively low radar frequency, horizontal polarization, a relatively steep incidence angle, and a relatively high wind speed. Here the Doppler signatures look quite different than the original current field. The situation is much less complicated in the case shown in Fig.2b, i.e., for a high radar frequency, VV polarization, a high incidence angle, and a low wind speed.

According to these first results, a retrieval of oceanic surface currents from ATI data appears to be feasible if the right parameters, in particular high radar frequencies and incidence angles, are chosen. We will soon present results of a more detailed study.

REFERENCES

[1] R.M. Goldstein, T.P. Barnett, and H.A. Zebker, "Remote sensing of ocean currents," Science, vol. 246, December 1989, pp. 1,282-1,285.

[2] D.R. Thompson and J.R. Jensen, "Synthetic aperture radar interferometry applied to ship-generated waves in the 1989 Loch Linnhe experiment," J. Geophys. Res., vol. 98, 1993, pp. 10,259-10,269.

[3] D.R. Thompson, "Calculation of microwave Doppler spectra from the ocean surface with a time-dependent composite model," in Radar Scattering from Modulated Wind Waves, edited by G.J. Komen and W.A. Oost, Kluwer Academic Publishers, 1989, pp. 27-40.

[4] R. Romeiser, "Optimization of a composite surface model for the radar backscattering cross section of the ocean surface as measured by wind scatterometers," Proc. IGARSS '96, Lincoln, NE, 1996.

[5] R. Romeiser, "Quantitative analysis of radar signatures of underwater bottom topography according to a Bragg-based composite surface model," Proc. IGARSS '96, Lincoln, NE, 1996.

Study of Integration Time Effects on Coherent Radar Imagery of the Sea Surface

Delwyn Moller, Stephen Frasier, Robert E. McIntosh
Microwave Remote Sensing Laboratory
University of Massachusetts, Amherst, MA 01003
T: 413.545.0779 / F: 413.545.3690 / moller@alex.ecs.umass.edu

Abstract— **Remote sensing of the ocean surface using Interferometric SAR techniques is of significant interest due to the potential for synoptic measurement of ocean wave and surface current patterns. INSARs use the phase difference between colocated SAR images separated by a small time lag to infer surface radial velocities, and hence wave orbital velocities and currents. The quality of such measurements is affected both by the integration time used in forming SAR images and by the much smaller time lag separating the images.**

In March 1994, the FOPAIR imaging radar obtained near-instantaneous imagery of ocean surface backscatter and Doppler velocity at 64 frames per second. In this paper we investigate explicitly sea surface motion effects on INSAR imagery by subsampling the radar's data stream. Through sub-sampling, longer coherent integration times are synthesized yielding INSAR-like images which may be compared to coincident high-speed radar images. Through this analysis, the effects of integration time on image quality and current measurements are revealed.

I Introduction

In recent years the innovation of Interferometric Synthetic Aperture Radar (INSAR) has provided the potential for imaging of near-surface ocean currents [1]. INSAR operates in a similar manner to SAR except two antennas spatially separated in the along-track direction receive the backscattered signal yielding separate complex SAR images. Through the motion of the platform, it is possible to coregister the two images. When co-registered the SAR images are separated by a time lag equal to the antenna separation divided by the platform velocity, and the covariance of the two images is the interferometric product. The magnitude is akin to a conventional SAR image while the phase contains Doppler velocity information. Typically the time lag between images is much smaller (O(msec)) than the integration time used for either image (O(1 second)).

In a manner similar to INSAR, the FOcused Phased Array Imaging Radar (FOPAIR) [2] utilizes a pulse-pair technique applied to successive images to infer the scene velocity. FOPAIR is an X-band system consisting of a single transmit horn and a sequentially sampled, 64-element receive array. By scanning the receive array very rapidly, one obtains an instantaneous snapshot of the ocean surface complex backscatter, and the covariance of successive temporal images yields Doppler velocity information. Usually, the time lag between the images is larger than the integration time for each image. If, however, the array is sampled more slowly, the effects of gross surface motions and decorrelation during the integration time can be observed.

In this investigation INSAR imaging is emulated by subsampling the FOPAIR data stream thereby extending the integration time. For example, an aperture may be synthesized by combining the response of element 1 from scan 1, element 2 from scan 2, element 3 from scan 3, and so on. This method will yield a total integration-time which is 64 times the original frame rate. If a smaller integration time is desired then subgroups of elements can be used from each scan to synthesize the aperture. Using this technique, half-second integration-time images are compared with instantaneous images in the next section.

II Data Application

Fig. 1 shows imagery obtained on March 25, 1994 from the end of the USACE research pier at Duck, NC. This data was acquired at a frame rate of 64 Hz with a pulse-pair interval of 2.5 msec. The upper panel exhibits instantaneous imagery of a surface slick. The slick region corresponds to a lower power return. Note also the difference in Doppler velocity measured across the slick. These images represent a ten-second average (post-beamforming), thereby illustrating the mean intensity and velocity characteristics. Averaging spatially or temporally is necessary to average out orbital velocities and other wave effects.

The lower panel of Fig. 1 shows the same data, but subsampled to give a half-second integration time. Again, a ten-second average is shown. It is immediately apparent that the half-second integration time images are degraded in comparison to the instantaneous imagery. Both the Doppler velocity and magnitude images of the half-second integration-time images are blurred. This is especially evident when looking at the transition between the slick and non-slick regions. Very noticeable is a negative bias in the half-second integration-time velocity measurement along the border of the slick. There is also a slight azimuthal shift, or squint, in the half-second integration-time images due to radial motion of scatterers during the aperture synthesis. The mean radial velocity over the image would imply an azimuthal shift of seventeen degrees. This mean shift has been removed, although some residual shifts remain in the image.

In the next section a simple model will be introduced to

This work was supported by the Office of Naval Research (Remote Sensing) under grant N00014-93-1-0261

0-7803-3068-4/96$5.00©1996 IEEE

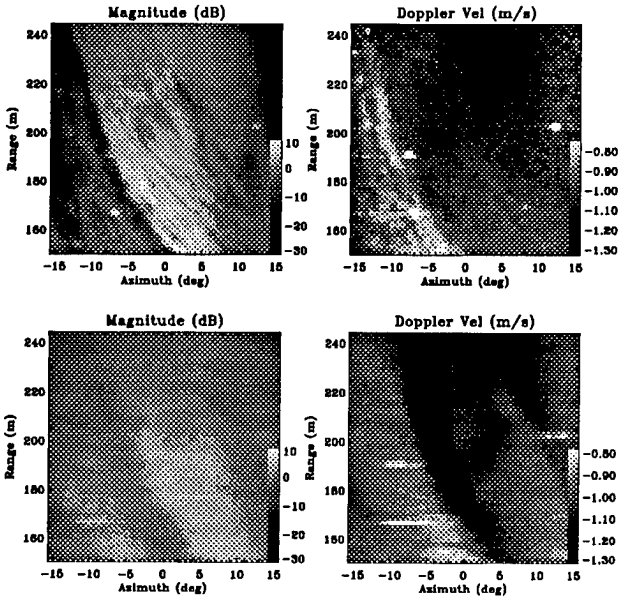


Fig. 1. Radar images of the ocean surface obtained on March 25, 1994. Top: Near-instantaneous imagery. The left image is the magnitude of the covariance while the right image shows mean Doppler velocity over 10s averaging time. Bottom: Half-second integration-time imagery. The left image is the magnitude of the covariance while the right image shows mean Doppler velocity over 10s averaging time.

help explain the effects observed in Fig. 1. Subsequently, in the light of this model, we shall compare the integration time effects in more detail by considering a single range gate of the slick data and compare these scans to results from a preliminary simulation.

III Discussion

In order to predict the integration time effects on image quality and velocity measurement, we will present a simple model for interferometric ocean imaging.

Considering a single range gate, the beamformed result for a single scan is:

$$I(t,u) = \sum_{n=0}^{N-1} \left[\int_{-1}^{1} r(u', t + n\delta t) e^{-jnu'} du' e^{(jnu)} \right] \quad (1)$$

where the integral term represents the response of the nth element to the field-of-view, $u = kdsin\theta$, k is the radar wavenumber, d is the interelement spacing, and θ is the angle from broadside. Furthermore, δt is the time between element illumination, and $r(u,t)$ is the complex ocean return including range and antenna pattern. If the pulse-pair interval is Δt then the interferometric response is given by the covariance:

$$C(u,t) = < I(u,t) I^*(u', t + \Delta t) > \quad (2)$$

where the angle brackets denote expectation. We characterize ocean surface backscatter as a product of slowly varying amplitude and frequency modulation terms due to the motion of the surface and a rapidly varying (fading) term such that the autocovariance of the surface can be represented by:

$$\begin{aligned} < r(u,t) r^*(u',t') > \; = \; & \sqrt{\sigma(u,t)\sigma(u',t')}. \\ & e^{jk(v(u,t)t - v(u',t')t')}. \\ & e^{-(t-t')^2/\tau^2} \delta(u-u') \end{aligned} \quad (3)$$

where $\sigma(u,t)$ is the backscattered power return (AM modulation), $v(u,t)$ is the scene radial velocity (FM modulation), the exponential $e^{-(t-t')^2/\tau^2}$ is a temporal decorrelation term and $\delta(u-u')$ is a spatial Dirac delta function. The spatial and temporal fading terms account for the rapid decorrelation of the scattering scene. In particular, the $\delta(u-u')$ term in (3) assumes complete spatial decorrelation as in [3].

Applying (3), to (2) yields:

$$\begin{aligned} C(u,t) \; = \; & \sum_{n=0}^{N-1} \sum_{m=0}^{N-1} e^{-(t_n - t_n)^2/\tau^2} e^{-ju(n-m)}. \\ & \int_{-1}^{1} \sqrt{\sigma(u,t_m)\sigma(u,t_n)}. \\ & e^{jk(v(u,t_n)t_n - v(u,t_m)t_m)} e^{ju(n-m)} du \end{aligned} \quad (4)$$

where:

$$t_n = t + m\delta t$$

$$t_m = t + n\delta t + \Delta t$$

Examining (4), reveals that if the scene decorrelates significantly during the integration time, then contributions from temporally disparate elements will be small reducing the effective interferometric aperture size as expected. The presence of the time-varying Doppler velocity in the integral biases the phase of the element responses and it is this mechanism which causes the imagery to squint. These predictions may be verified by looking at the Fig. 1 images in more detail. Clearly the fine detail in the original images is lost.

Fig. 2 shows magnitude and phase scans for a single range gate of the images of Fig. 1. In both the intensity and phase scans, the half-second integration-time scan exhibits a smoothed response which is attributed to decorrelation effects. From scene coherence estimates of the near-instantaneous imagery, a decorrelation time of approximately 11 msec was calculated for this data. Referring back to (4), an integration-time of a half-second will result in severe decorrelation between all but the nearest few neighboring elements.

To further verify (4), a simulation was developed to approximate the slick data. A simple scene was defined with

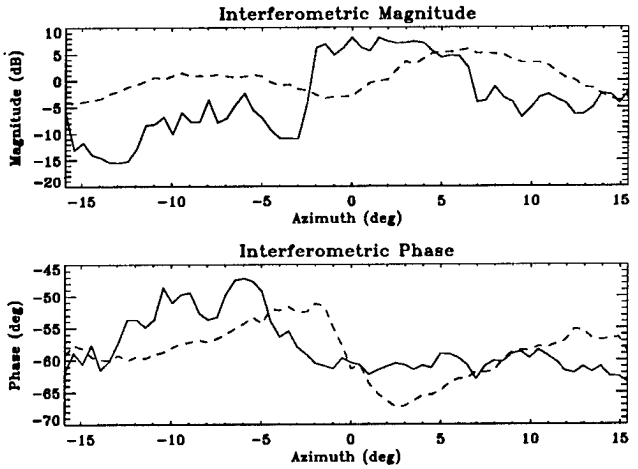


Fig. 2. Azimuthal profiles of interferometric magnitude and phase for instantaneous imagery (solid line) and half-second integrated imagery (dashed line).

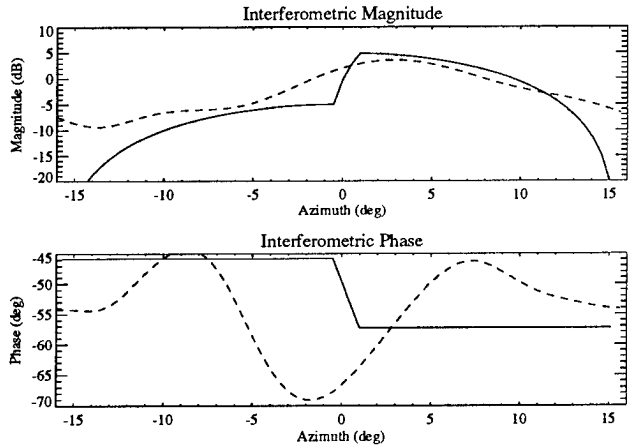


Fig. 3. Simulated azimuthal profiles of interferometric magnitude and phase for instantaneous imagery (solid line) and half-second integrated imagery (dashed line).

two distinct levels of magnitude and phase-speed across the field-of-view. A Gaussian decorrelation function with a decorrelation time of 11 msec was used. The instantaneous case may be approximated by setting $\delta t = 0$ in (4). For this ideal the simulation is able to recreate the scene exactly.

The results of these simulations are shown in Fig. 3. The magnitude response rolloff in the instantaneous case is a result of the window function applied to the scene. The windowing effects have not been removed to more clearly represent the ability of the imaging process in reconstructing the power-weighted field-of-view. For the same reason, the antenna pattern window has not been removed in Fig. 1 or Fig. 2 and the full field-of-view of the array has been displayed.

In Fig. 3, both the magnitude and phase of the half- second integration time simulation are smoothed functions. For this simple scene azimuthal shifts were compensated. In the magnitude response the half-second integration-time scan matches the peak of the instantanteous scan reasonably well. For the phase response, the half-second integration-time scan differs substantially. The response both overshoots and undershoots the instantaneous phase scan.

The simulation results in Fig. 3 appear to be consistent to first-order when compared with the data scans of Fig. 2. It is important when comparing these figures to remember that the half-second integration-time scans in Fig. 2 is squinted by approximately 5 degrees. The half-second integration-time phase scans exhibit a peak, trough, peak characteristic in both the data and simulated scans. For each, the first peak matches the higher phase reasonably well but the trough undershoots the lower phase by about 10 degrees. The next peak overshoots in both cases. In a similar manner, the magnitude responses for the simulated and data cases can be compared. Qualitatively, the high power region is matched reasonably well, with the lower power areas being overestimated in both cases.

IV Future Plans

The results of the simulation are preliminary but encouraging. When examining these results for the case where a distinctive spatial feature is present, it is evident that some error would occur in velocity estimates inferred from long-integration time interferometric imagery. Further analysis needs to proceed for more general conditions to help classify what the ocean-current imaging limitations are. We hope to pursue more systematic investigations during our future radar deployments.

References

1. Goldstein, R.M., T.P. Barnett, H.A. Zebker, "Remote Sensing of Ocean Currents", *Science*, Vol.246, pp. 1282-1285, Dec 1989.
2. McIntosh, R.E., S.J. Frasier, J.B. Mead, "FOPAIR: A Focused Array Imaging Radar for Ocean Remote Sensing", *IEEE Trans. on Geoscience and Remote Sensing*, 33(1), pp. 115-124, Jan 1995.
3. Hasselmann, K. et al.,"Theory of Synthetic Aperture Radar Ocean Imaging: A MARSEN View.",*Journal of Geophysical Research*, Vol.90, pp. 4659-4686, May 1985.

Daytime Performance Simulation of PN-Code Modulated Micro-Joule Lidar

V.L. Schoening, J.A. Reagan, P.A. Delaney
University of Arizona
ECE Department, Bldg. 104
Tucson, AZ 85721
(502) 621-2434, (520) 621-8076 (fax), schoen@ece.arizona.edu

ABSTRACT

Laser radar (LIDAR) has proven to be beneficial for retrieving atmospheric information. While most lidars to date have been mono-pulse systems that record the responses to individually transmitted pulses of light at significant energy levels (a few tenths to a few joules), more research is now focusing on low-power, eye-safe systems. One method for obtaining range information from lidars transmitting with low peak power lasers is to implement pulse code modulation wherein the lidar transmits a CW pseudo-noise code modulated signal (e.g., [1], [2], [3]). This paper presents a simulation of the pn-code modulated lidar scheme. By choosing an appropriate maximal-length code and bit length, atmospheric ranges of interest can be sensed by statistical correlation analysis of the temporal return signal. A key issue concerning the viability of this approach is the signal to noise ratio (SNR). The averaging time needed to achieve an acceptable SNR in daylight conditions, when noise is high, is compared to that of a conventional monopulse lidar system. Input parameters and considerations such as detector limitations and model noise levels are discussed.

INTRODUCTION

The monopulse lidar operates by transmitting one laser pulse into the atmosphere and recording the return photons as they arrive in time. Accumulating returns from several pulses yields the profile of the atmosphere. The pn-code modulated lidar method transmits a series of pulses and the received photoelectrons at any instant are due to scattering contributions from several range bins. Hence, the atmospheric scattering response cannot be range resolved by the simple time-range relation that applies for conventional monopulse lidar. To extract the atmospheric profile, the accumulated histogram of return photoelectrons is correlated with the original transmitted pulse sequence.

The recorded photoelectron counts for the monopulse and pn-code modulated approaches are both governed by the same photon/photoelectron statistics, namely, the Poisson distribution. The probability function of the Poisson distribution is

0-7803-3068-4/96$5.00©1996 IEEE

$$P(x,\mu) = \exp(-\mu)(\mu^x/(x!)). \quad (1)$$

The average count of x is an estimate of the mean, μ, of the Poisson distribution. For this distribution the mean equals the variance and the standard deviation is the square root of the variance. The variability in the received photoelectron counts as characterized by the Poisson distribution must be properly accounted for in any complete simulation of expected lidar performance.

BACKGROUND THEORY FOR PN-CODE MODULATED LIDAR

The transmitted pulse code is a maximum length pseudo random binary sequence. This array of length m can be generated with an n-stage shift register, where the maximal achievable period is

$$m = 2^n - 1 \quad (2)$$

An XOR gate performs modulo-2 addition at the feedback taps. A generated sequence will have an almost equal number of zeros and ones (one more one than zero). This property allows the laser to operate at approximately 50 percent duty cycle. This sequence is also useful when computing the autocorrelation function, which determines the degree of agreement between a code and a time delayed version of itself. The normalized magnitude of this function will be one for zero relative delay between the two codes and will be close to zero for all other time delays.

The range resolution for the lidar system is

$$\Delta R = t_b(c/2) \quad (3)$$

where t_b is the pulse bit period, c is the speed of light, and the factor of two accounts for the round trip distance traveled. The maximum unambiguous code range measurable with a sequence of length m is given by

$$R_{max} = m(c/2)t_b \quad (4)$$

The code length must have a larger R_{max} than the expected maximum range.

The expected mean count of received photoelectrons in bin j scattered from a single range R_k can be expressed as

$$N_{j,k} = [\,Eo \cdot \gamma \cdot \Delta R \cdot \beta(\lambda_L, R_k) \cdot T^2(R_k)]/R_k^2 \qquad (5)$$

where

$$\gamma = (\eta A_o\, \tau_{sys})/(hc/\lambda) \qquad (6)$$

and

$$T^2(R_k) = \exp[-2 \int \kappa(\lambda_L, R_k)]dR \qquad (7)$$

Eo is the energy per transmitted '1' bit in the code, η is the detector quantum efficiency, the quantity hc/λ is the laser photon energy (h is planck's constant, c is the speed of light and λ_L is the operational wavelength), A_o is the effective area of the receiver telescope, τ_{sys} is the lidar receiver optical transmission efficiency, β is the atmospheric backscatter coefficent ($km^{-1} \cdot sr^{-1}$) for a specific wavelength and range, ΔR is the range bin size, and $\kappa(\lambda_L, R)$ is the total attenuation coefficient (km^{-1}). Summing over k, where k is modulo-m, will include the effects of contributions from all the pulses in the transmitted code.

For every '1' bit in the transmitted sequence, a pulse of light energy is sent into the atmosphere and generates a Poisson distributed response of returned photons due to atmospheric scattering versus range. Each of these bits will generate a response delayed from the time the first photoelectron is received from the first pulse in the sequence by an amount T_N, where

$$T_N = \text{bit number} \cdot t_b \qquad (8)$$

The responses are measured by a photon detector at the receiver. The detector is assumed to have the capability to count all arriving photons and not saturate. Every '0' bit in the sequence will not generate a response.

For each iteration of the code, a histogram Nj is constructed by accumulating return photons for each '1' bit transmitted. Background noise is addressed independently of the signal. A Poisson distribution due to noise is added to each bin of the histogram. Histograms generated for all iterations are then summed together. To extract the atmospheric extinction profile, the final histogram is cross-correlated with a shifted version of the original code.

Two sources of noise are present in this system. One is "photon noise" or shot noise inherent in the signal itself, and the other is also shot noise due to background. Both are generated using the Poisson distribution model. The signal-to-noise ratio (SNR) for this PN code lidar for range j is [2]

$$SNR(R_j) = \langle S(j) \rangle / \sqrt{\sum_{j=0}^{m-1} S(j) + \langle B \rangle T} \qquad (9)$$

where S(j) is the number of signal counts for bin j, <B> is the average number of background counts, and

$$T = m \cdot t_b \cdot L \qquad (10)$$

where L is the number of iterations.

For the monopulse lidar, the SNR is given by

$$SNR(j) = (S(j) \cdot \sqrt{K}) / \sqrt{S(j) + B} \qquad (11)$$

where K is the number of pulses. The SNR for each system is a suitable performance parameter for direct analysis and comparison between the two types of lidars.

DISCUSSION OF SIMULATION PARAMETERS

Code lengths of 255 and 1023 are used in the simulations. Nominal aerosol profiles of various ranges of the atmosphere are used to compute the backscatter coefficients in the lidar equation. Since the atmosphere has more variability at short distances, these ranges are beneficial for verifying the retrieved extinction profile. However, practical lidars typically do not achieve full overlap of the transmitted beam path by the receiver field of view before a few hundred meters to even a few kilometers. Characteristic parameter values for a monopulse lidar system that has been simulated and tested in the field [4] are shown in Table 1. These nominal values will be used in the pn-code lidar simulations for direct comparison with a monopulse lidar. To compare the performance of a pn-code lidar with that of the monopulse lidar, the range of atmosphere to be studied will begin at approximately 4km because prior to this level, complete overlap has not occurred for this system.

Table 1 Characteristics of a Typical MPL System	
Wavelength	523 μm
Laser Energy	4 μJ
Range Resolution	150 m
Effective Receiver Aperture	0.016 m^2
Receiver Field of View	110 E-6 radians
Detector Quantum Efficiency	0.5
Sky Spectral Radiance	0.05 $w/m^2/sr/nm$
Receiver Spectral Bandpass	2 nm
Receiver Optical Transmission	0.08

WORK TO BE REPORTED

One issue under investigation is finding the advantage, if any, to using a long maximum length code over a shorter one. A longer code will allow one to study more ranges of the atmosphere, but if the altitude of interest is relatively close, then the longer code may introduce more noise than would occur by using a shorter code. Code lengths implemented in the simulation are 255 bits and 1023 bits for comparison.

A few questions arise when considering the scenario of using a long code to study a small range of atmosphere. A 1023 code with a system PRF of 1MHz will allow one to study a range of approximately 0-153km. If the range of interest is 10km, to use the entire code is not very efficient. The possibility of only using a portion of the code is under investigation. A point relevant to this issue is that the expected atmospheric return from distant ranges will become fairly negligible relative to the near range returns, both due to the inherent inverse range squared drop off and the normal decrease in atmospheric scattering with height. Hence, if one can assume the signal counts are negligible beyond some range, say 20 km, when attempting to recover near range information, say within 8 km, the simulations can be implemented more efficiently. If this case is true, one must still be cautious when modeling background noise. The mean value of background noise is the same for all bins, regardless of range. Current simulations explore methods for increasing efficiency while accounting for the full effect of noise.

Other work focuses on computing the SNR of the pn-code lidar signal in daylight conditions. To make a comparison with the monopulse case, one must know how several parameters relate between the two systems. For example, the energy per pulse of a monopulse lidar appears analogous to the average energy transmitted over a code length in the pn-code lidar system in the comparison of the performance of a pulse of the former with that of a full code sequence of the latter. One choice of performance evaluation is to measure the time required for each lidar to achieve the same SNR. Results of these various investigations will be discussed in the symposium presentation of this paper.

REFERENCES

[1] J. A. R. Rall, "Differential Absorption Lidar Measurements of Atmospheric Water Vapor Using a Pseudonoise Code Modulated AlGaAs Laser," NASA Technical Memorandum 104610, 145 pp., July, 1994.

[2] J. B. Abshire and J.A.R. Rall, "AlGaAs Aerosol Lidar - Theory & Measurements," *OSA 6th Topical Meeting on Optical Remote Sensing of the Atmosphere*, Salt Lake, UT, Paper # ThE29, March, 1993.

[3] N. Takeuchi, H. Baba, K. Sakurai, and T. Ueno, "Diode-laser random-modulation cw lidar," Appl. Opt., **25**, pp. 63-67, 1986.

[4] J. A. Reagan, A. E. Galbraith, and J.D. Spinhirne, "Micro Pulse Lidar Daytime Performance" Simulations and Observations," *Proc. IGARSS '96*, May, 1996.

APPLICATION OF WIDEBAND SIGNALS TO AIRBORNE LASER BATHYMETRY*

S. Radhakrishnan Pillai and Andreas Antoniou
Department of Electrical and Computer Engineering
University of Victoria
Victoria, B.C., V8W 3P6
Fax: (604) 721 6052
e-mail: radha@ece.uvic.ca, andreas@ece.uvic.ca

Abstract

A new technique for the estimation of time delay for ocean depth measurement has been introduced. The technique involves the transmission of a chirp-like signal and the processing of the reflection by an appropriate matched filter. The proposed scheme improves the resolution between the blue-green surface and bottom returns thereby enhancing the accuracy of the time-delay estimation. It is shown here that a chirp-like signal in conjunction with an appropriate matched filter can improve the resolution between the surface and bottom reflection of a bathymetric signal.

I. Introduction

Bathymetry refers to sea depth measurement and ocean bed characterization using scattered returns from the upper and bottom surfaces of the ocean. The conventional acoustic echo sounding hydrographic methods provide hydrographic data only along a single path directly beneath the track of a surveying ship. Sonar systems based on acoustic echo sounding methods require surface vessels to carry them and thus the speed of acquisition of bathymetric data is limited by the speed of the vessel. Moreover, the hydrographic survey ships cannot operate safely in shallow waters [1]-[3].

To increase the accuracy and the rate of coverage of a given area in shallow coastal waters, light-detection and ranging (lidar) airborne laser systems have been introduced. In the lidar system of interest, the LARSEN 500 [4], a series of short pulses of blue-green laser light as well as infrared pulses are projected simultaneously from the aircraft into the ocean. The blue-green laser light is reflected back from the surface and bottom of the ocean whereas the infrared (IR) pulse is scattered by the water surface. The ocean depth can be measured from the time-delay between the surface and bottom reflections. The infrared (IR) pulse serves as a surface marker and is used for calibration and correction purposes. The blue-green surface and bottom returns are used to estimate sea depth. The LARSEN 500 offers high efficiency and flexibility but it is prone to a number of depth measurement errors which are usually minimized by careful system design and by choosing operational parameters. Since the backscattered bottom return is much weaker than the surface return, the most critical performance factor in the depth measurement accuracy is the resolution between the surface and bottom reflections. The major factors that influence depth measurement are sea turbidity, sea-surface roughness, shape and texture of sea bottom, and the angle of the laser beam with respect to the sea surface [3, 4].

Several signal processing techniques for enhancing the precision of depth estimation have been proposed in recent years. In this paper, a new technique is developed to detect and enhance weak reflections from the bottom of the sea, thus improving the accuracy of the sea depth measurement.

II. Resolution Enhancement

Let us assume that the target region is irradiated by a transmitter that sends a time-dependent signal $s(t)$. The leading edge of the transmitted signal $s(t)$ reaches the first target (ocean surface) and after reflection travels backward (or is echoed back) towards the transmitter/receiver T_1 seconds later. The remaining portion of the signal travels towards the second target (ocean bottom) and is also reflected back. The receiver records the echoes from all the reflectors from the target scene which can be represented as

$$r(t) = \sum_{i=1}^{m} a_i s(t - T_i) + n(t), \quad 0 < t < T \qquad (1)$$

where T_i represents the two-way round trip delay to the ith target and $n(t)$ represents the noise present. In bathymetry, the signal-to-noise ratio (SNR) is extremely poor and the problem is to estimate the unknown delays $T_1, T_2, \ldots, T_m$ from the received waveform $r(t)$, $0 < t < T$.

Naturally, the input signal shape is important in this case, and we propose to make use of a chirp signal and its modified version for the input signal. In conjunction with an appropriate matched filter, such signals have a remarkable energy localization property. Note that in a chirp signal,

*THIS RESEARCH IS SUPPORTED BY THE NATURAL SCIENCES AND ENGINEERING RESEARCH COUNCIL OF CANADA AND MICRONET, NCE PROGRAM.

0-7803-3068-4/96$5.00©1996 IEEE

the phase angle change is quadratic and thus [5, 6]

$$s_1(t) = A\cos(\omega_0 t + bt^2), \quad 0 < t < T. \tag{2}$$

If we take the derivative of the phase, we get the instantaneous frequency to be $\omega_0 + 2bt$. Thus in a chirp signal, the instantaneous frequency varies with time, but it has excellent localization properties after matched filtering.

When the transmitted signal $s(t)$ is a rectangular pulse of duration τ_0, then its Fourier transform is a sinc function with its first zero crossing at

$$\omega_0 = \frac{2\pi}{\tau_0} \tag{3}$$

and hence the bandwidth of $s(t)$ determines the range resolution. Clearly, when $s(t)$ is a rectangular pulse, one cannot achieve long duration in both time and frequency domains since ω_0 (the bandwidth) is inversely proportional to the pulse duration τ_0 in the time domain. This problem is solved by using a chirp pulse whereby the transmitted signal is a frequency modulated pulse. Thus an increase in τ_0 results in a better output signal-to-noise ratio for chirp signals [6, 7].

Interestingly, it is possible to formulate (2) using variations of the above idea. For example, bringing in an additional t^3 term into (2) further improves the energy localization property of chirp signals. In severe noise conditions these 'super-chirp' pulses can be detected using a corresponding matched filter. For example,

$$s_2(t) = A\cos(\omega_0 t + bt^2 + ct^3), \quad 0 < t < T, \tag{4}$$

where b and c are appropriate constants, and the quadratic variation of the instantaneous phase term helps to strongly reject all other signal (and noise) at the matched filtering stage.

With $r(t)$ representing the received signal, the matched filter output $R(t)$ is given by

$$R(t) = r(t) * s_2(T - t) \tag{5}$$

The output $R(t)$ peaks at the unknown delays T_1, T_2, ..., T_m and due to the energy compactification property in the 'super-chirp' signal $s_2(t)$, these peaks are quite dominant. Thus an increase in the pulse duration τ_0 in chirp signalling can simultaneously increase the overall transmitted power (i.e., an increase in the output SNR), and the bandwidth of the transmitted pulse thereby effectively improving the depth resolution.

As an illustrative example, consider a received signal corrupted by heavy noise as shown in Fig. 1. The SNR is 3 dB. The waveform in Fig. 1(a) is the received signal with three delayed returns corresponding to T1=1000, T2=1500 and T3=1700. Observe that they are barely noticeable in the received signal because of the dominant noise.

The next waveform in Fig. 1(b) is the FFT of the first time signal. Notice that the delayed returns cannot be detected from this waveform either. The third waveform in Fig. 1(c) shows the matched filter output using the above 'super-chirp' signal as the transmitted signal. Notice that all three time delays are accurately recovered here using the above matched filter.

By utilizing a frequency modulated pulse we can achieve frequency-spread characteristics of a short pulse within the envelope of a long duration signal. Thus using a quadratic frequency-modulated pulse with the frequency span set by the resolution required and with the duration set by the energy required for depth range performance can enhance the resolution between the blue-green laser signal thereby increasing the depth measurement accuracy.

III. Conclusions

A new technique for time-delay estimation from signals corrupted with noise or clutter is introduced. It is well known that for a given level of noise, a matched filter produces the largest possible peak output in response to each echo signal. In this way it maximizes the probability of detecting valid signals with a threshold detector. Results obtained so far show that the technique works very well for return signals corrupted with heavy noise or noise-like clutter that can originate at the bottom of the ocean.

REFERENCES

[1] K. Muirhead and A. P. Cracknell, "Airborne lidar bathymetry," *Int. J. Remote Sensing*, vol. 7, no. 5, pp. 597-614, 1986.

[2] R. M. Measures, *Laser Remote Sensing: Fundamentals and Applications*, New York: John Wiley & Sons, 1984.

[3] F. E. Hoge, R. N. Swift, and E. B. Frederick, "Water depth measurement using an airborne pulsed neon system," *Appl. Opt.*, vol. 19, no. 6, pp. 871-883, Mar. 1980.

[4] R. W. J. Dirks and D. Spitzer, "Laser remote sensing of aquatic environment: First and second order scattering model," *Appl. Opt.*, vol. 30, pp. 443-452, Feb. 1991.

[5] D. R. Wehner, *High Resolution Radar*, Artech House, Boston, 1987.

[6] M. Soumekh, *Fourier Array Imaging*, Englewood Cliffs: NJ, Prentice Hall, 1994.

[7] J. R. Klauder, A. C. Price, S. Darlington, and W. J. Albersheim, "The theory and design of chirp radars," *The Bell System Technical J.*, vol. 39, no. 4, pp. 745-808, July 1960.

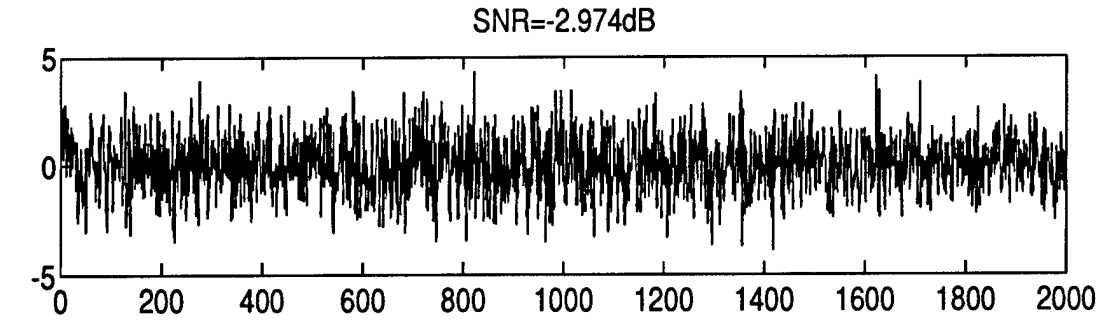


Fig. 1(a) Three signal returns in noise

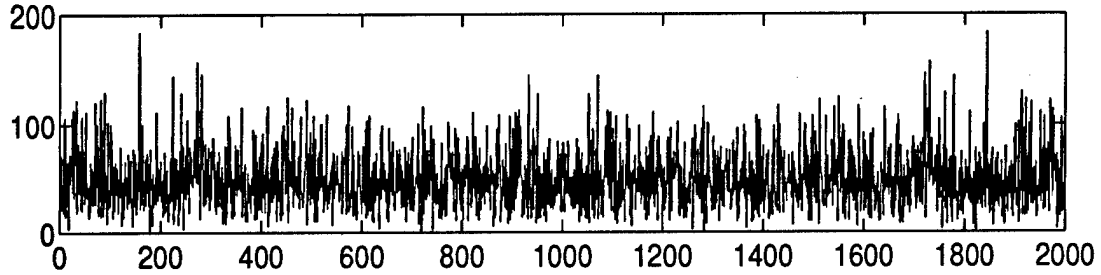


Fig. 1(b) FFT of Return Signals

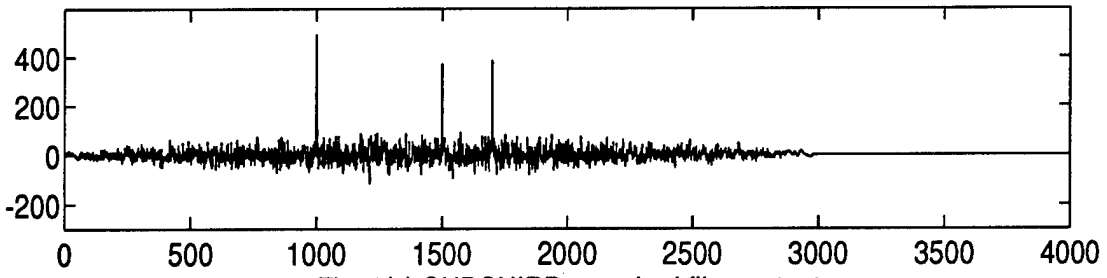


Fig. 1(c) SUPCHIRP: matched filter output

Figure 1. Resolution enhancement using a chirp-like signal.

Low Light-Level IR Detectors for Use in Lidar Systems

Theresa S. Mayer and Timothy J. Kane
Department of Electrical Engineering, The Pennsylvania State University
121 Electrical Engineering East, University Park PA, 16802
(814) 863-8458 tsm@toolbox.psu.edu
(814) 863-8727 kane@ecl.psu.edu

Abstract – Field operation of lidar would be facilitated greatly by the availability of portable, eye-safe systems that are based on solid-state lasers and detectors operating at wavelengths in the near infrared. The operating principles and design requirements of Indium Gallium Arsenide-based avalanche photodetectors capable of single photon detection in the 0.8 μm to 1.6 μm wavelength range are discussed in this paper.

INTRODUCTION

Lidar has proven to be a powerful technique for measuring the distribution and evolution of atmospheric aerosols and clouds. In particular, elastic-backscatter lidar systems are capable of probing a wide range of constituents from large aerosols down to background atmospheric density. When coupled with radar and photometry, these systems can be used to study a variety of atmospheric phenomena including the formation processes of clouds, the dispersion characteristics of aircraft contrails, and optical extinction through high Cirrus [1]. Unfortunately, the field operation of lidar systems has been hindered by their large size, high cost, and complexity as well as their relatively poor reliability and stability. Moreover, these systems generally require the use of high-power laser sources that are not eye-safe. Recent advances in solid-state laser and detector technology, however, offer for the first time the opportunity to build portable, eye-safe lidar systems that are capable of reliable field operation with minimal supervision.

A compact lidar system based on such solid-state components was demonstrated recently by Spinhirne at the Goddard Space Flight Center [2]. The system used a diode pumped Nd:YLF laser (532 nm), a Silicon (Si) Geiger-mode avalanche photodetector (GAPD), and a single-card multichannel scalar data acquisition system. In order to provide eye-safe operation at this wavelength, the laser was operated using microjoule-level pulse energies and pulse repetition rates of several thousand hertz. Excellent performance was achieved for detecting and profiling cloud and aerosol scattering throughout the troposphere and into the stratosphere. For more extensive measurements of the stratosphere, however, the operating wavelength must be extended from the visible to the near infrared (IR) where the eye-safe power densities are higher. In particular, three wavelengths of interest for lidar applications are 1.064 μm, 1.54 μm, and 2.1 μm due to the availability of solid-state laser sources. Unfortunately, these wavelengths are beyond the detection limits of the commercially available GAPD's. Therefore, further advances in portable, eye-safe lidar systems require the development of high-performance solid-state GAPD's capable of single photon detection at wavelengths beyond 1.0 μm.

In this paper, we will first present an overview of the operation of solid-state avalanche photodetectors (APD's). This will be followed by a discussion of an APD design that is suitable for Geiger mode operation in the range of wavelengths between 0.8 μm and 1.6 μm. Finally, the applications to lidar remote sensing that would benefit from the availability of this detector technology will be presented.

AVALANCHE PHOTODETECTOR BACKGROUND

The principles of operation of solid-state APD's are similar to those of photomultiplier tubes (PMT's). For example, both devices rely on the generation and multiplication of charged carriers in response to an incoming photon. In the case of a PMT [3], when a photon strikes the photocathode an electron is emitted and is accelerated in an electric field towards the first electrode. The collision of the electron with the first electrode will result in the emission of multiple secondary electrons. In multistage PMT's, this multiplication of carriers is repeated at successive electrode stages. In a similar manner, an electron-hole pair is created in an APD when the photon incident on the device has an energy greater than the semiconductor bandgap energy [4]. In contrast to the PMT, however, the electron-hole pair generated by the incident photon is separated and accelerated in an electric field caused by a reverse-biased p–n junction. If the electric field is of sufficient strength, each carrier will generally acquire enough energy while traversing the so-called depletion region of the p–n junction to experience an ionizing collision with the crystal lattice. These ionizing collisions will result in the generation of two additional electron-hole pairs. These new carriers along with the original carriers can also experience ionizing collisions. In this way, there is a multiplication (avalanching) of carriers that results in an internal gain which is reflected in a detectable terminal current.

Solid-state APD's offer several advantages over PMT's. These advantages include smaller size, improved durability,

0-7803-3068-4/96$5.00©1996 IEEE

lower cost, and lower operating voltages. Presently, Si-based APD's that are suitable for single-photon detection are available commercially from a several vendors. At typical operating temperatures, however, these APD's can not be used for detection of light with wavelengths that exceed 1.0 μm because of the relatively large bandgap of Si (E_g = 1.2 eV at T = 77 K where $\lambda(\mu m) = 1.24/E_g(eV)$). Therefore, in order to extend the detection wavelength, an APD must be designed and fabricated using a semiconductor that possesses a narrower bandgap. The bandgaps of several common semiconductors are given in Table 1 [4]. Based on the bandgap energy, the two materials that are best suited for detection beyond 1.0 μm are Germanium (Ge) and Indium Gallium Arsenide (InGaAs). In addition to appropriate wavelength detection, however, an APD that is used for single photon counting applications must possess low dark current (leakage that is present with no incident photons) and excellent noise performance. In both cases, the performance of InGaAs which is a direct-bandgap semiconductor surpasses that of the indirect-bandgap Ge [5]. Moreover, the long-wavelength (> 1.4 μm) response of InGaAs is superior to that of Ge. Therefore, solid-state APD's based on InGaAs are a better choice for lidar applications requiring detection at wavelengths greater than 1.0 μm and will be the focus of the remainder of the paper.

Table 1. Bandgaps of Common Semiconductors (T = 300K). The dependence of the bandgap on temperature varies as $E_g = E_g(0) - AT^2$, where A is a constant that is independent of temperature.

Semiconductor	E_g (eV)
Si	1.12
GaAs	1.42
Ge	0.67
InP	1.35
InGaAs	0.74
InAlAs	1.49

AVALANCHE PHOTODETECTOR DESIGN AND OPERATION

In addition to the excellent electrical and optical performance that can be achieved with devices based on InGaAs, there are several additional properties of the material system that can be exploited to enhance the design of detectors capable of single photon counting over the range of wavelengths extending from 0.8 μm to 1.6 μm. One of the most important features is the ability to form lattice matched heterojunctions using the wider bandgap material, InAlAs. With this added flexibility, APD's can be designed such that the longer wavelength radiation will be absorbed in the narrow bandgap material while the carrier avalanche will be contained in the wider bandgap material [6]. A simplified schematic of this device is shown in Fig. 1. This fundamental design procedure can be used to maximize the detector quantum efficiency and responsivity while minimizing the noise due to the higher dark currents typically associated with narrow bandgap materials. InGaAs APD's based on these principles are currently being designed and fabricated in the Electronic Materials and Processing Research Laboratory at Penn State University [7].

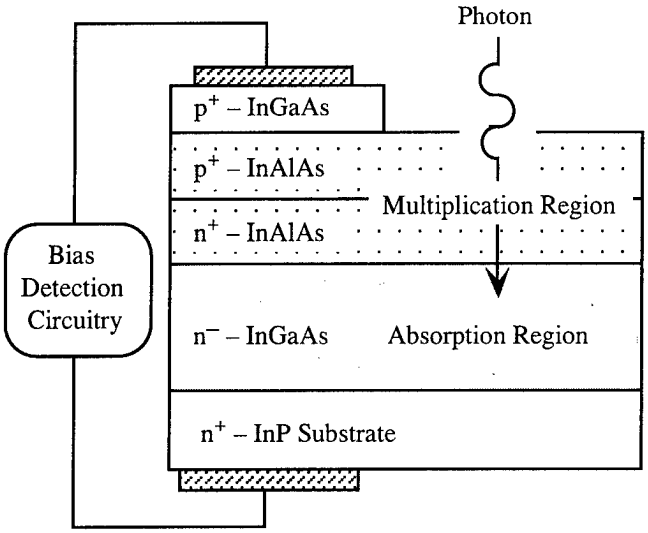


Fig. 1. Simplified diagram of InGaAs-based APD.

In applications where low light-level analog detection is desired, APD's are typically operated at a bias slightly below the breakdown voltage of the p–n junction (the breakdown voltage is the voltage required to create an electric field across the junction that is large enough to sustain ionizing collisions – between 20 V and 50 V for most APD's). In this mode of operation, however, the gain of the APD generally ranges only from 10 to 100. Devices with such low gains cannot be used satisfactorily in applications that require single photon detection because of the difficulty of detecting such small photon induced currents. In order to achieve the higher gains that are required for single photon detection, the APD must be operated slightly beyond the breakdown voltage of the p–n junction. This requires that the APD be cooled to a temperature for which the dark current is zero independent of the bias [8]. Under this condition, a photon generated electron-

hole pair will initiate an avalanche process that results in large device gains (terminal current). Once the detector is triggered by a photon, however, the current will not return to zero until the bias across the device is lowered below the junction breakdown voltage. Therefore, to count subsequent photons, the bias must be lowered to quench the avalanche process and reset the device.

APPLICATIONS

Avalanche photodetectors capable of single photon detection at 1.0 μm coupled with commercially available diode-pumped Nd:YAG's or Nd:YLF's operating at their fundamentals (1.064 mm and 1.046 mm, respectively) will allow the implementation of portable, eye-safe lidar systems capable of high-resolution measurements of atmospheric aerosols. There are several advantages of operating an aerosol lidar in the IR as opposed to the visible region. These advantages include the ease with which aerosols and Rayleigh scatterers can be delineated, an increase in eye-safe power levels by an order of magnitude, and an improvement in the stability of the laser output. Therefore, lidar systems based on 1.0 μm operation are expected to outperform considerably their visible counterparts. The meteorological research that would result from such portable, eye-safe mini lidar systems includes cirrus cloud studies, contrail dispersion investigations, and upper atmospheric probing for polar stratospheric clouds.

A diode-pumped Nd:YAG mini-lidar system is currently being developed in the Communications and Space Science Laboratory at Penn State University. Initially, this lidar system will operate in the visible wavelength range using standard PMT detection. In the future, it will be used to test the solid-state GAPD's that are currently being investigated.

CONCLUSIONS

Field operation of lidar would be facilitated greatly by the availability of portable, eye safe systems. These systems would be based on solid-state lasers and detectors, which offer smaller size, lower cost, and enhanced reliability and stability. Development of such advanced systems, however, requires high-performance solid-state GAPD's capable of single photon detection at wavelengths beyond 1.0 μm. In this paper, the operation of InGaAs-based APD's suitable for single-photon detection in the 0.8 μm to 1.6 μm wavelength range was considered. Such APD's are currently being designed and fabricated at Penn State University and, when completed, will be incorporated in a diode-pumped Nd:YAG mini-lidar system also being developed at Penn State University.

REFERENCES

[1] J. A. Reagan *et al.*, "Lidar sensing of aerosols and clouds in the troposphere and stratosphere," *Proceedings of the IEEE*, vol. 77, pp. 433-448, 1989.

[2] J. D. Spinhirne, "Micro Pulse Lidar," *IEEE Transactions on Geoscience and Remote Sensing*, vol. 31, pp. 48-55, January 1993.

[3] R. W. Engstrom, *Photomultiplier Handbook, Theory, Design, and Application*, RCA Corporation, 1980.

[4] S. M. Sze, *Physics of Semiconductor Devices*, J. Wiley and Sons, 1984.

[5] G. H. Olsen, "InGaAs fills the near-IR detector-array vacuum," *Laser Focus World*, pp. A21-A30, March 1991.

[6] P. Bhattacharya, *Semiconductor Optoelectronic Devices*, Prentice Hall, Inc., 1994.

[7] W.-Y. Hwang, R. Kochhar, M. Micovic, T. S. Mayer, D. L. Miller, and S. M. Lord, "Molecular Beam Epitaxy of $In_{0.74}Ga_{0.26}As$ on InP for Near Infrared Detectors," submitted to *J. Vac. Sci. and Tech. B.*, 1995.

[8] A. Lacaita, P.A. Francese, F. Zappa and S. Cova, "Single-photon detection beyond 1 μm: performance of commercially available germanium photodiodes," *Applied Optics*, vol. 33, pp. 6902-6917, October 1994.

Scanning for a Satellite Radar Wind Sounder (RAWS)

R.K Moore, B. Beh, and S. Song
University of Kansas, Radar Systems and Remote Sensing Laboratory
2291 Irving Hill Road, Lawrence, KS 66046-2969 USA
TEL: 913/864-4835 , FAX: 913/864-7789 , E-MAIL: graham@ardneh.rsl.ukans.edu

Abstract—The Radar Wind Sounder (RAWS) is a proposed satellite-borne radar capable of measuring wind aloft using Doppler shifts of hydrometeors. Previous studies showed the sensor can retrieve wind vectors at various levels in the atmosphere while also measuring rain rates and ocean-surface winds. Here we present the method of retrieving wind-aloft information from a conically scanned antenna. The approach combines the radial velocities measured at many points within a region into a least-squares algorithm to obtain a mean wind for the region.

INTRODUCTION

Analysis and forecasting using numerical weather models would improve greatly if world wide wind information were available. Lasers on satellites were proposed for this purpose, and the Laser Wind Sounder (LAWS) was an original component of the Earth Observation System (EOS) [1]. However, gaps would exist in coverage as lasers can only profile winds in clear air or light clouds. Accordingly, we proposed a radar sensor to complement the laser sensor by profiling winds in the cloudy and rain areas [2,3]. Both systems measure Doppler shift, from aerosols for lasers and from hydrometers for radars.

Our previous studies showed that the optimal frequency for single-channel coverage is 35 GHz and, 24 GHz and 94 GHz for dual channels [4]. Using these frequencies, RAWS can cover most cloud types with the original proposed power (3 kW peak), and miss the thin clouds with reduced power [5]. In clear air or light clouds, the contributions from the vertical components of wind vectors are small and can therefore be ignored in the calculation of the wind vectors. In precipitating systems, the vertical components can be estimated from the raindrop fall speed, based on the rain-echo intensity [6].

This paper considers the derivation of the horizontal wind vectors and the accuracy achievable by integrating multiple measurements of radial velocities. The approach considered is to measure radial velocities at many points within a region, combining the results in a least-squares algorithm to obtain a mean wind for the region.

SCAN PATTERN AND MEASURED POINTS DISTRIBUTION

Fig. 1 shows the measured points distribution by a conically scan antenna using 256 pulses per point. The figure only displays half of the swath. The asterisks are the forward looks and the circles are the aft looks. Note that the measurements closer to the edge area are much more dense than that in the center area. These measured points are grouped to form cells of 66 km square. The exact dimensions of the cells were chosen based on the assumed scan rate to allow equal numbers of measurements in each cell within a region.

DERIVATION OF WIND VECTORS FROM THE MEASURED DOPPLER VELOCITY

The wind vector can be expressed by

$$\overline{U_w} = U_{wx}\overline{X} + U_{xy}\overline{Y} + U_{wz}\overline{Z} \tag{1}$$

where U_{wz} can be derived from the rain fall speed [6] and will be ignored in the simulation. The radial velocities from the measured points within a cell are given by

$$U_{ri} = U_{wx}\sin\theta\cos\phi_i + U_{wy}\sin\theta\sin\phi_i \qquad i = 1,2,...,N \tag{2}$$

Applying a least-squares method to (2) we obtained [7]

$$\begin{pmatrix} U_{wx} \\ U_{wy} \end{pmatrix} = \Delta \begin{pmatrix} \sum \sin^2\phi_i & -\sum \sin\phi_i\cos\phi_i \\ -\sum \sin\phi_i\cos\phi_i & \sum \cos^2\phi_i \end{pmatrix} \begin{pmatrix} \sum U_{di}\cos\phi_i \\ \sum U_{di}\sin\phi_i \end{pmatrix} \tag{3}$$

where

$$\Delta = \frac{1}{\sin\theta\sum \sin^2\phi_i - \left(\sum \sin\phi_i\cos\phi_i\right)^2} \tag{4}$$

The standard deviation of the average velocity for a covariance estimator is [8]

$$\Delta V_d = \lambda\left[\left[32\pi^2 M\rho^2(T_s)T_s^2\right]^{-1}\left[\left[\left(1-\rho^2(T_s)\right)\lambda\right]\frac{1}{\left[4\sigma_s T\Pi^{1/2}\right]} + N^2/S^2 + 2(N/S)\right]\right]^{1/2} \tag{5}$$

where M is the number of pulses per measured point, T_s is the interval between pulses in a pulse-pair, T is the pulse-pair repetition time, σ_s^2 is the variance of the power spectral densities of received echoes, and N/S is the inverse of signal-to-noise ratio. $\rho(T_s)$ is the correlation function [5]

$$\varrho(mT_s) = \exp\left[-8\left(\frac{\pi\sigma_s m T_s}{\lambda}\right)^2\right] \tag{6}$$

where m=1 and λ is the RF wavelength. σ_s is bounded by [5]

0-7803-3068-4/96$5.00©1996 IEEE

$$\sigma_x \le \frac{\lambda}{4\pi T_s} \quad (7)$$

to prevent ΔV_d from increasing exponentially and also to keep the samples correlated.

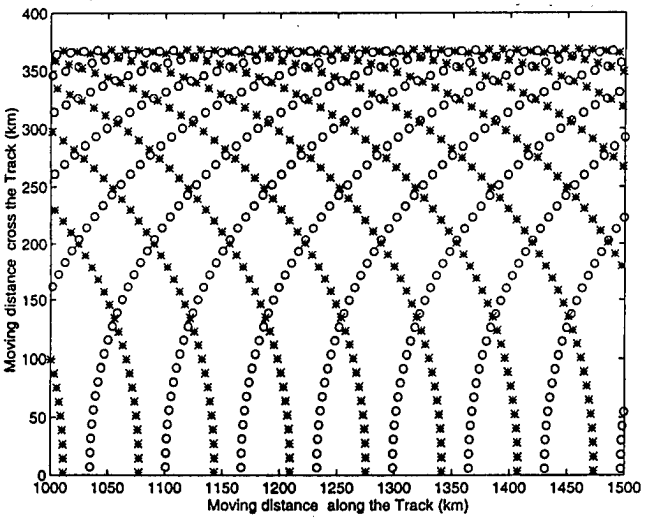


Fig. 1 Conically scanned measured point distributions on the ground.

Using (3) and (5), along with the measurement errors (assuming Gaussian), we developed an algorithm to simulate the errors in the measured wind vectors. The simulations assumed 256 pulses per point and an SNR of 10 dB. The cell sizes are 66 km x 66 km in areas close to the edge (bands # 1,2,7,8) and 132 km x 132 km at areas around the center (bands # 3,4,5,6). Our preliminary simulations showed that we need a larger cell for the center areas to keep the errors below the specifications [7].

Figs. 2 to 6 depict the rms errors obtained from the simulations. Here we only present the results for wind speed at 5 m/and 14 m/s, as we found that both the magnitude and direction errors tend to decrease as the wind speeds increase [7]. At 5 m/s, the direction errors at the center bands are slightly above 20° for 24-GHz cases and below 20° for the 35-GHz cases. The magnitude errors are less than 2 m/s for all the cases except the 24-GHz with wind direction at 90°. At 14 m/s, both the direction and magnitude errors are below 20° and 2 m/s in all cases except the 24-GHz case with wind direction at 90°, where the magnitude error is slightly above 2 m/s at the center bands.

CONCLUSIONS AND RECOMMENDATIONS

The simulation results indicate that this approach to analyzing RAWS data can provide measurements of wind aloft with adequate accuracy for use in global atmospheric models. However, our simulations assumed the cells to be covered entirely by hydrometeors, which is seldom the case in reality, as the areas involved are relatively large. Using RAWS alone may degrade the measurement accuracy when the cells are only partially covered with cloud. Hence, we recommend the combination of measurements from both the lidar and the radar. The lidars proposed use a conical scan pattern similar to that of the radar, but with a different scan rate. The measurement errors would then differ from those of the radar, but we would expect the results to be similar. When vertical components are significant in rain, we can estimate the vertical speed from the relation between rain rate and fall speed [6]. Thus the combined radar and laser sensors would have the capability to measure winds at most altitudes even in rainy areas.

REFERENCES

[1] R. J. Curran, Ed., *Earth Observation System Instrument Panel Report: LAWSLaserAtmosphericWindSounder*, vol.IIg, NASA, Wash.DC, 1987.

[2] W. Xin, *A Satellite-Based Radar Wind Sounder*, Ph.D. Dissertation, Univ. of Kansas, 1990.

[3] R. K. Moore, M. Stuart, W. Xin, and T. Propp, "A satellite-borne radar wind sensor (RAWS)," *Digest IGARSS'92*, Houston, pp. 999-1001, 1992.

[4] M. A. Stuart and R. K. Moore, "Satellite-based radar wind sounder (RAWS) optimal frequency study," *Digest IGARSS'93*, Tokyo, Japan, pp. 215 -217, 1993.

[5] M. A. Stuart, *Radar Sensitivity and Antenna Scan Pattern Study for a Satellite-Based Radar Wind Sounder (RAWS)*, M.S. Thesis, Univ. of Kansas, 1992.

[6] S. R. Pallikala and R. K. Moore, "Use of radar wind sensor to determine vertical drop speed for RAWS," RSL Technical Report 10240-1, Radar Systems & Remote Sensing Laboratory, Univ. of Kansas, May 1994.

[7] S. Song, B. Beh, and R. K. Moore, "Scan patterns and accuracy of a radar wind sensor (RAWS)," RSL Technical Report 11170-2, Radar Systems & Remote Sensing Laboratory, Univ. of Kansas, Nov. 1995.

[8] R. J. Doviak and D. S. Zrnic, *Doppler Radar and Weather Observations*, Academic Press, New York, 1984.

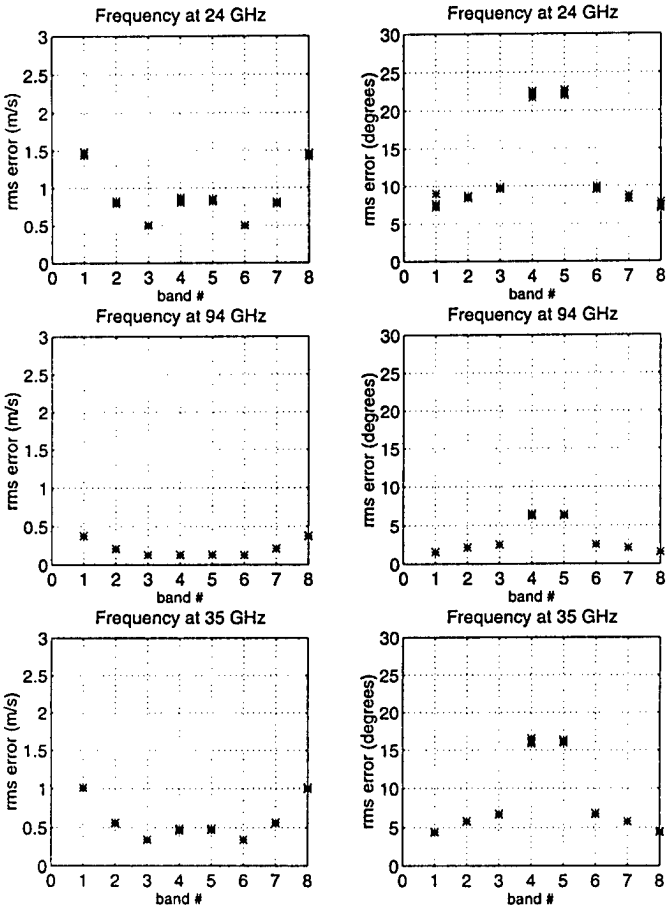


Fig. 2 RMS errors of wind vectors assuming true wind of 5 m/s at 0°.

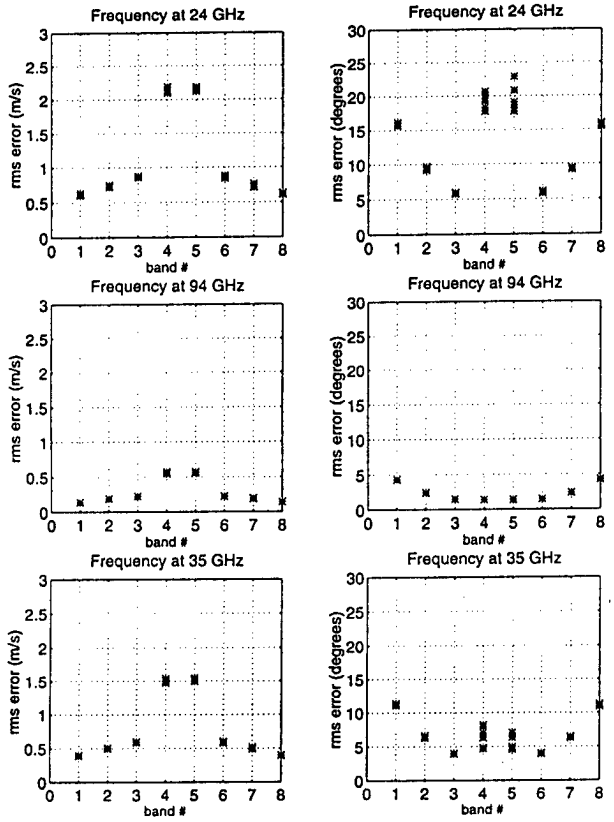


Fig. 3 RMS errors of wind vectors assuming true wind at 5 m/s at 90°.

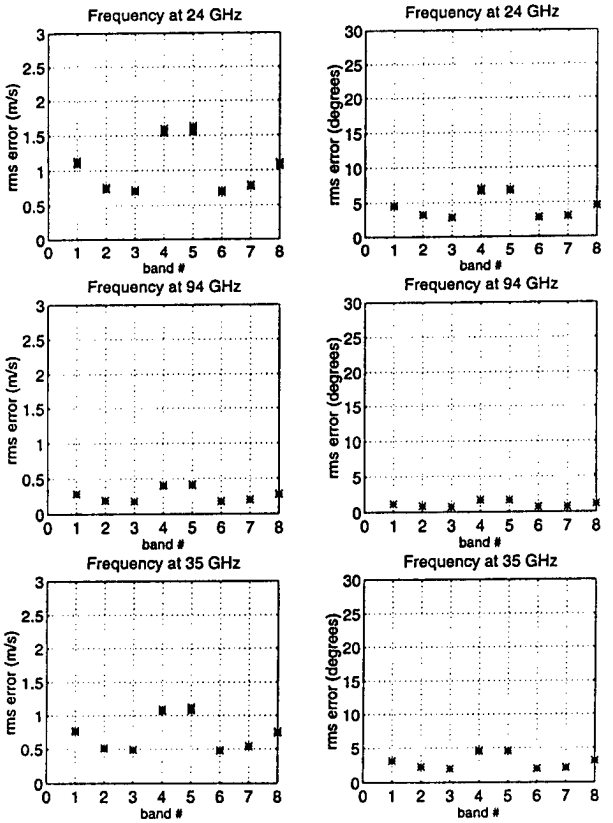


Fig. 5 RMS errors of wind vectors assuming true wind of 14 m/s at 45°.

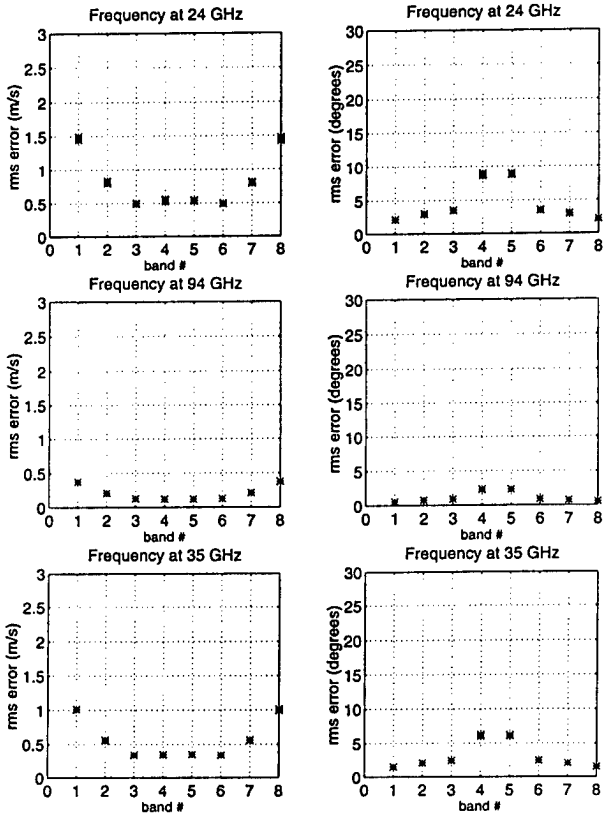


Fig. 4 RMS errors of wind vectors assuming true wind of 14 m's at 0°.

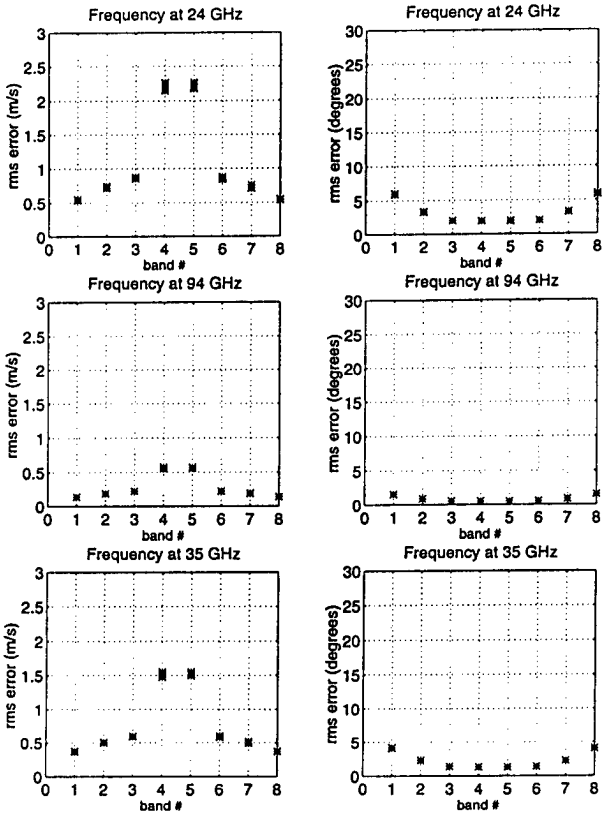


Fig. 6 RMS errors of wind vectors assuming true wind of 14 m/s at 90°.

Feasibility Study of a Compact Low Cost Correlation LIDAR Using a Pseudo Noise Modulated Diode Laser and an APD in the Current Mode

Bernhard O. Bundschuh*, Dirk Schneider, Markus Grindel****
***Fachhochschule Merseburg**
Geusaer Straße 88, D-06217 Merseburg, Germany
E-Mail: BUBE@MAILSERV.HRZ.TH-MERSEBURG.DE

****Universität Siegen**
Hölderlinstraße 3, D-57068 Siegen, Germany

Abstract -- LIDAR, a well known tool for remote sensing of the atmosphere, has not yet migrated into a large commercial market. Currently it is not affordable for most potential users such as small companies and environmental authorities. The simulation study was performed in order to check the feasibility of a low cost system that overcomes the main hindrances of the wide spread use of this powerful environmental sensing technology. The new system should be able to measure profiles of aerosols and molecules within a few seconds to several minutes depending on the required spatial resolution and the background light conditions.

INTRODUCTION

Conventional LIDARs contain three basic components that make them expensive, a sophisticated impulse laser that provides high peak power, a large receiver telescope, a highly sensitive photo detector usually a photon counting photo multiplier tube (PMT). Our new approach is based on the usage of a semiconductor diode laser, an avalanche photo diode (APD) in the current mode and a compact receiver telescope. In order to check the feasibility of such a low cost system a simulation study [1] was performed using a mixture of self written software and public domain programs.

PRINCIPLE OF OPERATION

The atmosphere is modeled as a linear, shift invariant (LSI) system. The laser transmitter provides the input signal s(t) while the photo receiver detects the output signal g(t). The impulse response h(t) is determined by the spatial distribution of scattering and transmission properties.

$$g(t) = h(t) * s(t) = \int_{-\infty}^{\infty} s(\tau) h(t-\tau) d\tau \qquad (1)$$

Stimulating the system with a delta function δ(t) we obtain h(t) at the output. Impulse LIDARs approximate this ideal test signal using very short high power laser pulses, a main reason for high system costs. Impulses of long duration enhance sensitivity but lead to poor spatial resolution and vice versa. Cross correlation provides an elegant solution of this dilemma. Fig. 1 shows the principle of operation.

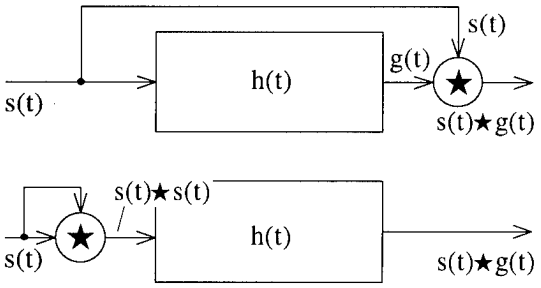


Fig. 1, System identification by cross correlation

It is allowed to exchange cross correlation and convolution in the case of a LSI system. This is equivalent to a stimulation of the system by the auto correlation function (ACF) of s(t). Since the ACF of a periodic pseudo noise (PN) sequence closely approximates the delta function δ(t) such sequences are well suited for system identification applications. They are easy to generate by means of feed back shift registers as indicated in fig. 3. Fig. 2 shows one period of such a signal.

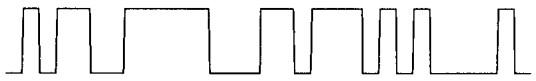


Fig. 2, PN sequence (1 period)

Since the laser energy is uniformly spread over time the required laser peak power is within the range of continuous wave (CW) diode lasers even in the case of a compact receiver telescope and an APD detector in the current mode.

LASER TRANSMITTER

The laser transmitter is simply modeled as a one pole low pass filter with an edge frequency of 100 MHz followed by an ideal voltage to optical power converter [2]. The maximum CW laser power was assumed to be 200 mW. The size of the emitting area is 1 µm x 3 µm. The corresponding divergence angles are 30° respectively 10°. The full width of half max (FWHM) of the spectrum is 2 nm. These data correspond to the SDL 5430 laser diode series.

0-7803-3068-4/96$5.00©1996 IEEE

ATMOSPHERE

The wavelength dependent atmospheric impulse response is determined by the spatial distribution of scattering and transmission. Background illumination significantly contributes to the receiver noise especially in daytime applications. The atmosphere was subdivided into 20 layers of 500 m thickness leading to a maximum range of 10 km. Taking into account the velocity of light an impulse response of the atmosphere can be calculated [3]. Aerosol detection is conveniently simulated using the LOWTRAN7 software, which provides a wavenumber resolution of 20 cm^{-1}. In order to obtain the aerosol phase function we slightly modified the source code [3]. Molecular scattering is a slowly varying parameter but there are extremely narrow absorption lines. Therefore transmission by molecules was simulated [3] using FASCODE3, which provides extremely fine wavelength resolution. Proper detection of aerosols should be performed at wavelengths without significant molecular absorption.

Background illumination was simulated using LOWTRAN7. For daytime operation we used day 93 of the year at 10 AM Greenwich time with 51° north and 8° east (central region of Germany in a late spring morning). For night time operation we used a moon phase angle of 90° [3].

IMAGING SYSTEM

The imaging system was simulated using modified ray tracing software, which was originally developed for the simulation of optical contour sensing [3, 4]. The diameter of the well corrected transmitter lens (e.g. achromatic lens) is 5 cm. The focal length is 8 cm. The receiver telescope was assumed to be build using a 25 cm parabolic reflector with a focal length of 80 cm. In order to suppress background light a 2 nm optical bandpass filter matched to the FWHM of the laser spectrum was assumed.

PHOTO RECEIVER

The receiver contains a silicon APD HAMAMATSU S6045-02. The quantum efficiency at $\lambda = 830$ nm is 75%. The amplification was set to $M \cong 100$. The excess noise factor is $F(M) = M^x$ ($x \cong 0.3$). The dark current is about 100 pA ($\cong 0.2$ pA primary, $\cong 80$ pA secondary) [2]. The diameter is 0.5 mm so that proper focusing is no problem. The transimpedance amplifier was modeled as a three pole low pass filter of Butterworth type. The edge frequency is matched to the clock frequency of the PN generator [2].

Shot noise results from signal current, dark current and photo current generated by background light. These contributions are modeled using Poisson distributed random numbers [2].

The amplification M is a stochastic quantity. We found out [2], that the probability density function of M, $f_M(M)$ is well approximated by a log normal distribution:

$$f_M(M) = \frac{1}{\sigma\sqrt{2\cdot\pi}}\ \frac{1}{M}\ \exp\left(-\frac{(\ln M - m)^2}{2\cdot\sigma^2}\right) \qquad (2)$$

$$m = \ln\left(\frac{\overline{M}}{\sqrt{\overline{M}^x/n+1}}\right) \qquad \sigma = \sqrt{\ln\left(\overline{M}^x/n+1\right)}$$

$\overline{M}$ is the mean gain. n is the number of electrons prior to amplification. Using an APD in the current mode strongly reduces the complexity of the envisaged LIDAR system. No PMT or photon counting receiver [5, 6] is needed.

Thermal noise contributions of the transimpedance and the amplifier noise are modeled using Gaussian distributed random numbers [2].

CORRELATION UNIT

Averaging is required in order to obtain significant test results. Therefore the correlation function for all lags must be determined simultaneously. In fig. 3 a delaying shift register, a number of EXORs and integrators form the correlation unit. Programmable ICs enable an economic realization. Different to [5, 6] no broadband signals must be digitized and processed on a computer. This leads to finer spatial resolution. The PN-sequences can be much longer (2^{15}-1 chips). This leads to proper offset suppression [2, 5, 6].

RESULTS OF SIMULATION

Fig. 4 shows a simulated aerosol detection [2] at $\lambda = 830$ nm. The U.S. 1976 standard atmosphere with a viewing range of 23 km (rural atmosphere) was assumed. The viewing direction was vertical. 4a shows the impulse response of the atmosphere. 4b shows the simulated test result for nighttime measurement. The clock frequency is 25 MHz leading to a spatial resolution of 6 m. The measurement time is 10 seconds. Thermal noise in the transimpedance amplifier is the dominating source of error. 4c shows the simulated test result for daytime measurement. The receiver bandwidth respectively the clock frequency is 5 MHz leading to a spatial resolution of 30 m. The measurement time is 50 seconds. Shot noise caused by background illumination is the dominating source of error.

CONCLUSION

The simulation confirms the feasibility of the envisaged concept for daytime and nighttime applications. This enables the development of an economic LIDAR, which should match a variety of standard applications, e.g. surveillance of particular industrial facilities and companies. Considering the fast development of diode lasers (e.g. DBR lasers) there seems to be virtually no limitation for future applications.

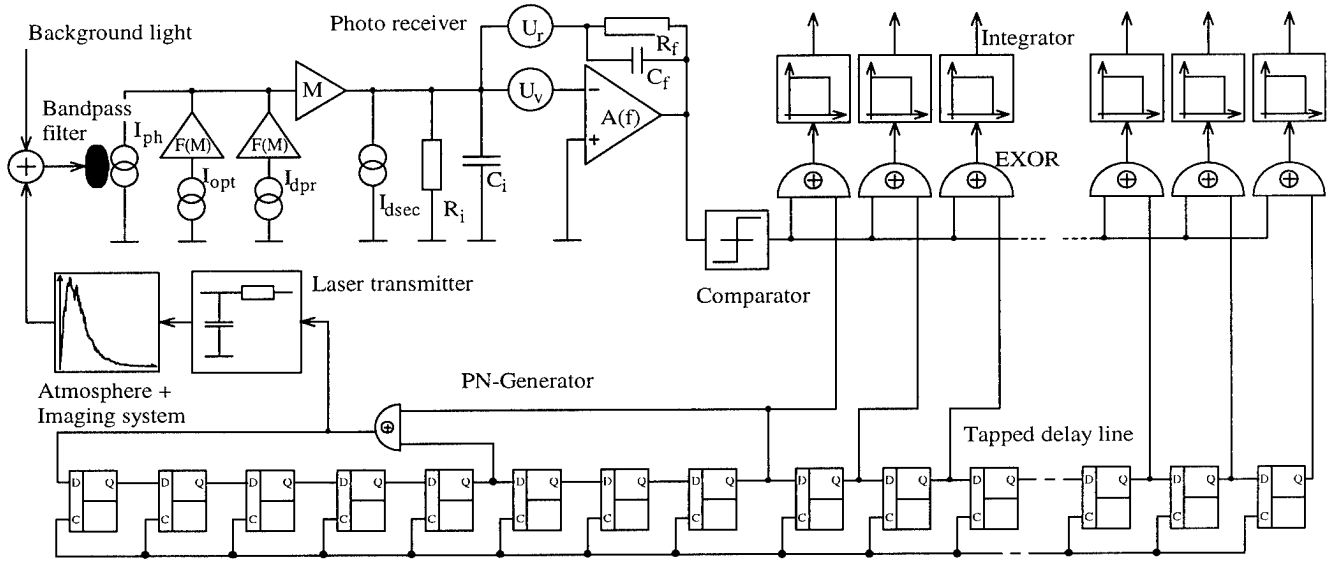


Fig. 3, Simulation model

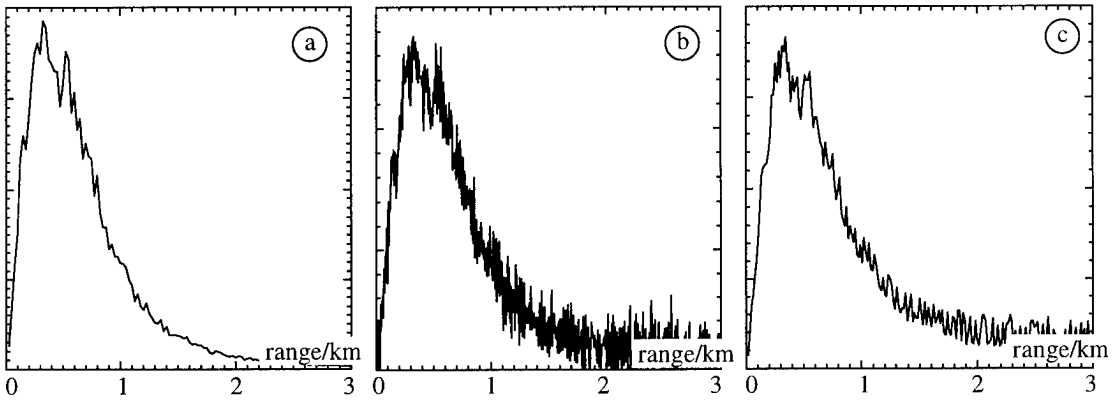


Fig. 4, Simulated aerosol detection

ACKNOWLEDGMENTS

First we would like to thank Otmar Loffeld and Ferdinand Klaus, University of Siegen, Germany, for the support of the computer simulations. Annette Rinke and Edo Becker from AWI Potsdam, Germany, as well as J. H. Chetwynd, Airforce Geophysics Laboratory, Hanscom AFB, MA, generously supported the atmospheric simulations. A special acknowledgment is due to 'Wandel&Goltermann-Stiftung', Eningen, Germany, for funding of this work.

REFERENCES

[1] B. Bundschuh, "Untersuchung und Simulation der Einsatz- und Realisierungsmöglichkeiten eines 'Low-Cost-LIDAR-Systems' zur Atmosphärenvermessung", feasibility study, funded by 'Wandel&Goltermann-Stiftung' 1994/95'

[2] D. Schneider, "Entwicklung eines Simulationsmodells zur Untersuchung eines Korrelationsverfahrens für die atmosphärische Rückstreumessung", master thesis, July 1995

[3] M. Grindel, "Untersuchung und Simulation des Transmissions- und Streuverhaltens der Atmosphäre in Abhängigkeit von der optischen Wellenlänge", master thesis, July 1995

[4] B. Bundschuh, "Laseroptische 3D-Konturerfassung, Modellierung und systemtheoretische Beschreibung eines Sensorsystems", Vieweg, Braunschweig, 1991

[5] N. Takeuchi, N. Sugitomo, H. Babe, K. Sakurai, "Random Modulation CW-Lidar", Applied Optics, Vol. 22, No. 9, May 1983

[6] N. Takeuchi, H. Babe, K. Sakurai, T. Ueno, "Random Modulation CW-Lidar", Applied Optics, Vol. 25, No 1, May 1986

Remote Sensing Spectrometry of a Temperate Deciduous Forest - A Modeling Approach -

Demarez V., Gastellu-Etchegorry J.P., Zagolski F., Mougin E., Marty G.

Centre d'Etude Spatiale de la Biosphère (UPS/CNRS/CNES)
18, Avenue Edouard Belin - BP 31055 - Toulouse (France)
Tel: 61-55-85-36 (+33); Fax: 61-55-85-00 (+33);
Email: demarez@cesbio.cnes.fr

Dufrêne E., Le Dantec V.

Laboratoire d'Ecologie Végétale
(L.E.V, ORSAY)
75000 Paris (France).

Abstract

This work evaluates the potential of remote sensing visible and near infrared spectrometry for studying the dynamics of a temperate deciduous forest. It is conducted with the airborne Reflective Optics Spectrometric Imaging System (ROSIS) in the frame of the European Multisensors Airborne Campaign (EMAC-94). A modeling approach, *i.e.* coupled canopy and leaf reflectance models, is used for assessing the sensitivity of forest parameters and associated relationships to experimental (illumination and viewing conditions) and biophysical (soil reflectance, forest structure) factors.

Introduction

Until now a number of empirical studies has been carried out for analyzing forest chemistry (chlorophyll, lignin, etc.) and structure parameters (leaf area index: LAI, tree density) with remote sensing spectrometry. Results are quite variable depending on the test site and forest conditions ([1], [2]). The difficulty to make definite statements stresses the importance of realistic modeling approaches to study the robustness of regression relationships that are usually found empirically between forest parameters and reflectance data.

Study area: the Fontainebleau forest, near Paris, is a deciduous forest (23,000ha) mainly composed of oaks (Quercus petraea, Quercus pedonculata), beeches (Fagus sylvatica), and pines (Pinus sylvestris). It is managed by the French National Office of Forestry. Fifty one stands along a 16 km transect were intensively checked (Table 1) in the field for a number of parameters (LAI, chlorophyll concentration, tree density, tree dimensions, etc.).

	May 10; 1994	July 10, 1994
Chlorophyll concentration (µg/cm²)	R: 10.6*-*33.1 m: 21.9 σ: 5.5	R: 45.2*-*87 m: 68.6 σ:12.4
LAI	R: 1.1*-*7.6 m: 3.9 σ: 1.9	R: 1.2*-*8.3 m: 4.6 σ: 2.2

Table 1: Range (R), mean (m) and standard deviation (σ) of chlorophyll and LAI of stands that were overflown.

Remote sensing data: the ROSIS spectrometer works in the visible and near-infrared region with an IFOV of 0.56 mrad and a FOV of ±8°. It is operated by the Institute of Optoelectronics (DLR, Germany) and the Institute of Physics (GKSS, Germany). It was flown at 10,000 m altitude. DLR provided calibrated and roll corrected data. Their spectral and spatial characteristics are in Table 2.

Pass (1994)	Mode	Spectral sampling	Δx	Stands overflown
(1): May 10 visibility:10km	Spectral Nadir (81 bands)	430-550 nm: 12nm 554-830 nm: 4nm	16m	36
(2): July 10 visibility:12km	Spatial Nadir (32 bands)	430-550 nm: 12nm 554-830 nm: 4nm	5.6m	24
(3): July 10 visibility:12km	Spatial 20° forward (32 bands)	430-550 nm: 12nm 554-830 nm: 4nm	5.6m	26

Table 2: Main characteristics of ROSIS acquisitions.

The models

Leaf optical properties with variable chlorophyll concentrations. were simulated with the PROSPECT model [3]. This model uses only three input parameters: leaf chlorophyll (C_{ab}) and water (C_w) concentrations and a leaf mesophyll structure parameter (N).

Canopy reflectance was simulated with the DART [4] model (Discrete Anisotropic Radiative Transfer). The latter simulates remote sensing images of heterogeneous 3D scenes with leaves, grass, trunks, water and soil elements.

Atmospheric corrections

Raw ROSIS reflectances (ρ*) were atmospherically corrected with input parameters from the 6S model [5], a mid-latitude summer atmosphere and atmospheric profiles:

$$\rho_c = \frac{\rho^* - T_g(\theta_s,\theta_v,z).\rho_a(z)}{T_g(\theta_s,\theta_v,z).T(\theta_s).T(\theta_v,z)+S(z).(\rho^*- T_g(\theta_s,\theta_v,z).\rho_a)}$$

$\rho_a(z)$: atmospheric reflectance, S(z): spherical albedo of the atmosphere, $T_g(\theta_s,\theta_v,z)$: transmittance (gaseous absorption), $T(\theta_s)$ and $T(\theta_v,z)$: transmittance (total scattering and aerosol absorption) with sun zenith angle (θ_s), view zenith angle (θ_v) and aircraft altitude (z).

Fig 1 and 2 show raw and atmospherically corrected mean spectra of various forest stands, on May 10. Raw reflectances are very low (≈3-4%) in the blue region, which is impossible; *e.g.* with a 100 km visibility the 6S model indicates that $\rho_a(\lambda=480nm)$ is 7%. In fact the visibility was 10km, *i.e.* $\rho_a(\lambda=480nm)\approx 15\%$. This explains that corrected reflectances are negative in the blue region; calibration coefficients may not be correct in that region.

0-7803-3068-4/96$5.00©1996 IEEE

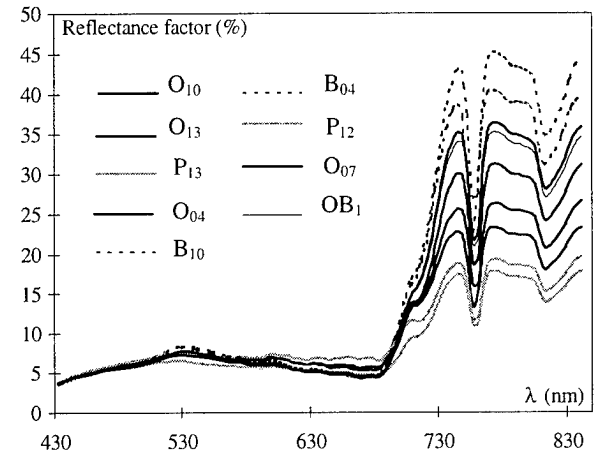


Figure 1: Raw ROSIS reflectances of forest stands (May 10, 1994). O: oak , B: beech , P: pine, OB: oak and beech. The index indicates the number of test sites. Atmospheric features (O_2: 762nm, H_2O: 720 and 820nm) appear.

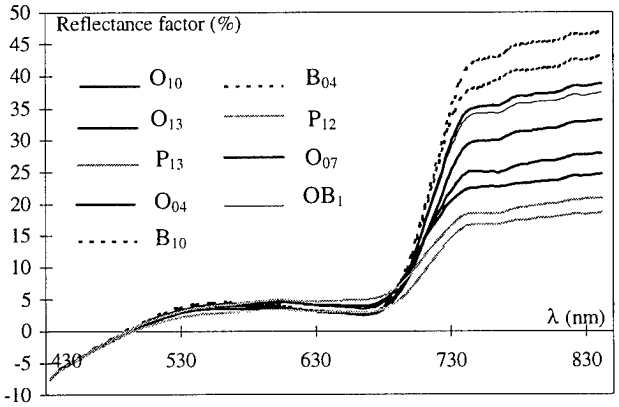


Figure 2: Atmospherically corrected ROSIS spectra of Fig. 1. The O_2 absorption feature at 760nm was corrected assuming $T_g(O_2)=0.69$, *i.e.* 8 nm spectral resolution.

Statistical analysis

Significant differences between species spectra were assessed with a one-factor analysis of variance: the Tuckey's method, *i.e.* pairwise comparisons on means differences. Stands spectra were gathered into four groups: oaks, beeches, pines and mixed (oaks and beeches). For both passes 1 (May 10; $\theta_v=0°$) and 3 (July 10; $\theta_v=+20°$) spectra of pines, oaks and beeches differ significantly in the near-infrared (730-845 nm) region. Viewing direction appeared to be a discriminating factor because spectra of the vertical acquisition on July 10 could not be differentiated.

So, in the 730-800nm region, the variability of species spectra seems to be explained mainly by canopy structure. Indeed, on July, at maximum vegetation extent, the nadir observation did not allow us to detect significant differences between the three species whereas these spectra were differentiated with the 20° off-nadir viewing configuration, *i.e.* a configuration more suitable for structure detection.

The existence of relationships between ROSIS reflectance and chlorophyll concentration (Chl, µg/cm²) was investigated with a two terms (Tab. 3) stepwise regression:

$$Chl = b_0 + b_1.\rho_{\lambda 1} + b_2.\rho_{\lambda 2}$$

Wavelength selection	r^2	Constant	Coefficients	σ	Number of spectra
λ_1=527 λ_2=563	88.1	b_0=100.5	b_1=-2545 b_2=1675	9.6	29
λ_1=703 λ_2=563	87.8	b_0=30.8	b_1=-815 b_2=1432	9.7	29
λ_1=479 λ_2=655	86.5	b_0=158.8	b_1=-3145 b_2=607	10.2	29

Table 3: Coefficients of best stepwise regression of ROSIS spectra against chlorophyll concentration (µg/cm²).

Reflectances are highly correlated: $r^2 \in [81\text{-}100]$ in the visible [433-681]. This explains why we find many "good" regression relationships whereas no wavelength is more significant than others.

We investigated also the existence of a relationship between chlorophyll concentration and the red-edge shape, through the computation of the inflection point (λ_i) in the 710-750nm region. λ_i was defined as the root of the second derivative of a Lagrange interpolation polynomial computed with 5 points in the red edge region. For both dates, no correlation was found between λ_i and chlorophyll concentration (Fig. 3). Moreover, the normalized difference vegetation index (NDVI) was not related to chlorophyll concentration (r^2=0.068, Fig. 4).

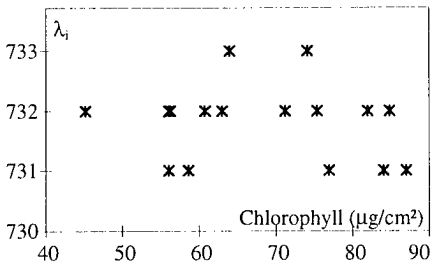


Figure 3: λ_i vs. chlorophyll concentration (µg/cm²), with ROSIS corrected data of July, 10.

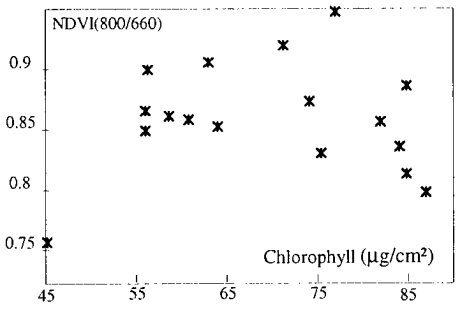


Figure 4: NDVI vs. chlorophyll concentration, with ROSIS data of July 10.

Model simulations

Only preliminary results are presented hereafter. In a first step we tested the capability of the DART model to simulate actual remotely acquired images. Simulations were first conducted for site B_{13}. A good agreement was found using a 35% filling coefficient of crowns (Fig. 5).

Moreover a sensitivity study was conducted in order to quantify the effect of variations of leaf chlorophyll concentration on visible canopy reflectance. Canopy reflectance of site B_{13} was simulated with varying chlorophyll concentrations [10-35µg/cm²] and actual concentration of 20.31µg/cm². Simulations were conducted with two models (SAIL [6] and DART) for LAI=7.6. Input parameters are mentioned in Table 4. DART and ROSIS simulations show a similar trend (*i.e.* lower canopy reflectance with higher chlorophyll concentrations) but the SAIL model overestimates reflectances because it assimilates canopy to homogeneous horizontal layers (shadows are neglected and soil influence is not well taken into account). ROSIS data do not allow us to verify this tendency because all the overflown stands have different LAI. Presently, ROSIS images of all sites are being simulated. The objective is to assess the influence of LAI, structure and chlorophyll concentration in canopy reflectances. Indeed, these reflectances appear to be nearly constant for all spectral bands in the visible domain. Fig. 5 shows reflectances for λ=550nm.

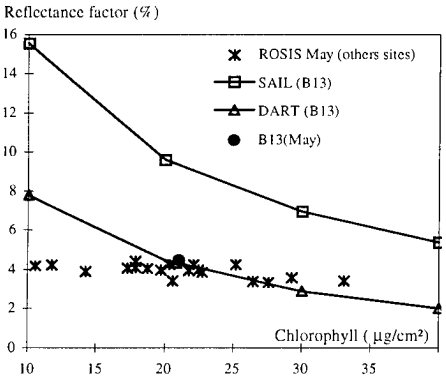


Figure 5:

Comparison of DART and SAIL simulations of site B_{10} (LAI=7, Chl=20.3µg/cm²). ROSIS data are for all stands (LAI=1.05-7.6)

Structural parameters	Optical & experimental parameters
LAI = 7.6	$\rho_{understory}$: 0.15, ω_{leaf} : 60 to 15%
Tree Height: 16m ± 0.8m	SKYL = 0.23
Tree density : 3563 trees/ha	$\theta_s = 53°$, $\varphi_s = 103°$
Crown diameter : 1.5m	$\theta_v = 0°$

Table 4: DART input parameters for simulating B_{13} stand. LAI is the only structural parameter used with SAIL.

Conclusion

Due to experimental constraints, our study area was overflown at two dates only and moreover with a partial coverage only. So, our work is limited by the small range of canopy parameters (chlorophyll, structure). In order to minimize this constraint, we are complementing the empirical analysis of ROSIS data with a physically based approach (*i.e.*, DART and PROSPECT) that allows us to simulate actual remotely acquired images (Fig. 6). Study of forest parameters will be conducted with the images.

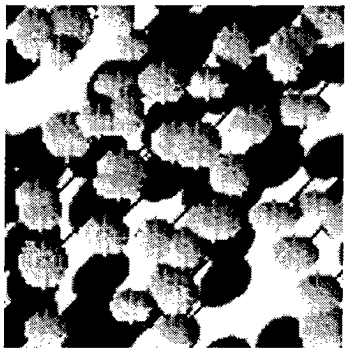


Figure 6:

DART simulated image of a 3-D heterogeneous tree cover.

Acknowledgments: we thank very much the European Space Agency (ESA), the French National Office of Forestry (ONF), the French Ecosystem Committee 'Forêts tempérées', the French Space Center (CNES), the National Program of Remote Sensing (PNTS), and the Program of Environment (SEAH) for their collaboration and support.

References

[1] Peterson D.L. et al, 1988, Remote sensing of forest canopy and leaf biochemical contents, Rem. Sens. Env. 24:85-108.

[2] Gastellu-Etchegorry J.P., Zagolski F., Mougin E., Marty G., Giordano G., 1995, An assessment of canopy chemistry with AVIRIS - A case study in the Landes forest, France. Int. J. Rem. Sens., 16(3): 487-501.

[3] Jacquemoud S., Ustin S.L., Schmuck, G., Andreoli G., Hosgood B, 1996, Estimating leaf biochemistry using the PROSPECT leaf optical properties model, Rem. Sens. Env.

[4] Gastellu-Etchegorry J.P., Demarez V., Pinel V. and Zagolski F, 1996, Modeling radiative transfer in heterogeneous 3D vegetation canopies, Rem. Sens. Env., in press.

[5] Vermote E., D. Tanré, J.L. Deuzé, J.J. Morcette, 1996, 2nd simulation of the satellite signal in solar spectrum: an overview, IEEE Trans. Geos. Rem. Sens., submitted.

[6] Verhoef W., 1984, Light scattering by leaf layers with application to canopy reflectance modeling: the SAIL model, Remote Sens. Environ. 16:125-141.

A Revised Measurement Methodology for Spectral Optical Properties of Conifer Needles

Elizabeth M. Middleton[1], Stephen S. Chan[2], Mark A. Mesarch[3], and Elizabeth A. Walter-Shea[3]

[1] Laboratory for Terrestrial Physics (Code 923), Goddard Space Flight Center, National Aeronautics and Space Administration (NASA), Greenbelt, MD 20771. Phone: 301-286-8344; Facsimile: 301-286-0239.
[2] Science Systems and Applications, Inc., 5900 Princess Garden Parkway, Lanham, MD 20706. Phone: 301-286-2386.
[3] Department of Agricultural Meteorology, University of Nebraska (UN-L), Lincoln, NE 68583. Phone: 420-472-1553; Facsimile: 420-472-6614.

Abstract-- A procedure for determination of conifer needle spectral optical properties (transmittance, T_λ; reflectance, R_λ; λ = wavelength) was developed to support field measurements acquired in the Boreal Ecosystem-Atmosphere Study (BOREAS). This was a revision of a protocol [1] which uses an indirect and labor-intensive step (involving painting of needles) to estimate the inter-needle light transmittance gaps, or gap fraction (GF), in each sample. Our procedure uses a direct image capture method to calculate GF, enabling measurements on both dorsal and ventral surfaces of all samples, and is 3-4 times faster than [1]. However, for either method T_λ underestimates often result, including negative T_λ in the visible (VIS) spectrum, especially when GF is large (>25%). We performed controlled experiments to evaluate the general effect of GF, and errors in GF estimation, on the calculated T_λ and R_λ spectra. T_λ was found to be inversely related to GF, with larger coefficients associated with VIS than near-infrared (NIR) λ. Consequently, GF overestimates also yielded T_λ underestimates. Using these results, we developed a correction algorithm for our BOREAS measurements. "Corrected" estimates of the fraction of absorbed photosynthetically active radiation (APAR) were ~80-84% for jack pine and 75-78% for black spruce. Correction reduced the Simple Ratio (SR = VIS/NIR) by 40-60% in most cases. SR calculated from corrected T_λ spectra were significantly higher than those determined from R_λ spectra.

INTRODUCTION

Accurate estimates of leaf spectral optical properties for reflectance (R_λ, λ=wavelength), transmittance (T_λ), and absorptance (A_λ) are critical for relating radiative transfer properties of leaves to their phenological stage and physiological state. These optical properties provide the critical link between remotely acquired optical observations at canopy or landscape scales and leaf-level mass and energy exchange processes. A rigorous method is available for obtaining R_λ and T_λ spectra of broadleaf species using a small integrating sphere mounted on a spectroradiometer [1]: a leaf holder and attached sample is placed in a port of the sphere, covering the entire aperture (~1.65 cm^2) with a single flat layer of leaf material.

Obtaining comparable measurements on conifer needles is much more difficult. Needles typically do not conform to a uniform and flat projection; they exhibit a species-specific cross-sectional shape, with thickness varying across the needle's width, as well as a characteristic 3-dimensional shape [2]. Additionally, the widths (mm) and lengths (mm to cm) of needles of many species are relatively small, requiring the inclusion of multiple needles per sample to provide adequate material for measurements. In the course of compositing a single layer of needles, inter-needle gaps are unavoidable, producing a variable gap fraction (GF) per sample.

Originally, we utilized the equations and methodology for obtaining conifer needle R_λ and T_λ advocated by [1], including the use of a large gap fraction (>25%) per sample. Their protocol for indirectly accounting for GF requires painting of one side of each needle sample set, a labor-intensive and time-consuming step that limits measurements to either dorsal or ventral surfaces. We replaced that procedure with a direct GF estimate using a digital computer image capture and analysis system. Combined with streamlined, specialized software for data acquisition and processing steps, our revised protocol is 3-4 times faster than theirs, enabling the acquisition of R_λ and T_λ for ~30 sample sets (both dorsal and ventral surfaces) per day. However, with either the indirect or direct GF methods, large GFs contribute to large underestimates of T_λ, especially in the visible spectrum where negative transmittances routinely result. Also, R_λ may be overestimated with large GF.

Another revision [3] of the Daughtry method was recently presented which eliminates the GF effect by placing 4 needles in fixed, individual slots across a sample holder. However, calculations are more complicated, and the T_λ estimate obtained is for the needle core (typically the thickest region) and therefore underestimates T_λ for the whole needle, as verified in comparisons made with the two methods (unpublished data).

In this paper, we evaluated the influence of GF on optical properties of conifer needles calculated with the published equations [1]. We developed a revised methodology to account for the influence of GF on spectral optical properties. We applied the findings to our measurements [4] for jack pine (*Pinus banksiana* Lamb.) and black spruce (*Picea mariana* Mill.) made in Saskatchewan, Canada as participants in the 1994 Boreal Ecosystem-Atmosphere Study (BOREAS)[5].

METHODS

Our revised methodology for the acquisition of spectral measurements integrates a Needle Image Analysis System (NIAS, described below) with the standard hardware comprised of a spectroradiometer (SE-590, Spectron Engineering, Denver,

0-7803-3068-4/96$5.00©1996 IEEE

CO), an integrating sphere (LI-1800, LI-COR, Inc., Lincoln, NE), and one of two light sources (LI-1800-12 & LI-9918-011; LI-COR, Inc.) designed to produce either round or slitted illumination beams, respectively. These were paired with custom-made sample holders having either circular (for pine needles) or slitted (spruce needles) apertures (Fig. 1). The NIAS includes a B/W CCD video camera, a monochrome frame-grabber board, an IBM PC compatible laptop unit with docking station, a light table, and a video monitor display with full 640 x 480 square pixel spatial resolution (pixel = 1.11 x 10^{-4} mm^2) and 256 gray levels. NIAS was used to determine gap fraction per sample, the ratio of needle gap area to that of the total illuminated area within the aperture (round or slitted) of a precision reference template placed on a light table and viewed from above by camera. Software for image capture was "Computer Eyes/RT" (Digital Vision, Inc., Dedham, MA) and for processing was "Mocha" (Jandel Scientific, San Rafael, CA). Appropriate calibration procedures were used: a) for the template, each sample; b) for the stray light/dark current scans per measurement set; and c) for the wavelength stability of the radiometer and its spectral radiance coefficients, each field campaign. Custom software was developed by M.A. Mesarch (UN-L) to label, organize, document, and preprocess the spectral data acquired for T_λ and R_λ of dorsal and ventral surfaces of each sample. We collected T_λ and R_λ with large GF (0.25-0.60) during the early summer 1994 BOREAS field campaign, IFC-1. We restricted GF to $\leq$0.15 for the mid-summer and fall campaigns (IFCs-2 &3) to minimize the GF effect on our measurements.

We eliminated several potential factors that might produce T_λ underestimates, including a mismatch between the size and position of the illumination beam and the sample template, differences in reflectivity of the sphere coating and the reference plug, and software errors. After BOREAS, separate laboratory tests were performed by the UN-L and the NASA participants to evaluate the influence of GF on the measured optical properties of conifer needles. The UN-L team performed sensitivity analyses on the influence of GF estimation errors (for select GF) on the calculated optical properties [1], using processed Ektachrome slide film (with T_λ and R_λ characteristics similar to green vegetation) cut to resemble conifer needles. The NASA team performed experiments to determine the general effect of increasing GF on the calculated T_λ and R_λ of locally available mature pine needles (e.g., *Pinus virginiana* Mill.). The UN-L team also examined the impact of GF estimation errors, for select GF (e.g., 0.56 and 0.06), on their BOREAS measurements. Together, we utilized the results of the UN-L sensitivity analyses and the NASA GF experiment to develop a correction algorithm for our BOREAS data [4], obtaining improved seasonal estimates of spectral T_λ, R_λ, and A_λ for jack pine and black spruce needles. From A_λ spectra, the fraction of absorbed photosynthetically active radiation (APAR, 400-700 nm) was determined. A spectral vegetation index based on near-infrared (NIR) and visible (VIS) observations was computed for values at 820 nm and 670 nm from T_λ and R_λ spectra. This was the Simple Ratio (SR= NIR/VIS).

RESULTS

The UN-L sensitivity analyses revealed that an overestimate of GF produced an underestimate of T_λ, often resulting in negative T_λ in the VIS region. The absolute and relative errors in VIS & NIR optical properties that resulted from errors in determinations of GF (Table 1) are unacceptably high for a 10% error in GF determination at relatively large GF (0.30-0.60). For that GF range, relative errors in T_λ associated with a 10-20% error in GF were >20% (VIS) and 15-20% (NIR); comparable relative errors for R_λ were 9-12% (VIS) and 9-16% (NIR). Even for relatively small GF (0.05-0.15), the relative errors in T_λ (Fig. 2) associated with a 10-20% error in GF were ~16-20% (VIS) and ~5% (NIR), but comparable errors in R_λ were only 2-3%. Errors in T_λ and R_λ due to GF errors were slightly larger when acquired with the smaller, slitted holders.

The general effect of increasing gap fraction (<50%) on the measured T_λ of mature pine needles was a monotonic decrease with increasing GF, as shown for needles similar in thickness to the boreal species (Fig. 3). The spectral regions associated with the greatest absorption (e.g., chlorophyll) were most affected: negative T_λ were calculated in the visible λ for virtually all GF, for these needles. The measured T_λ ($T_\lambda x$) is linearly related to GF, as shown for select λ in Figure 4A, for which the 'y intercept' represents the true (GF=0) value ($T_\lambda o$) and c_λ is the regression coefficient:

$$T_\lambda x = T_\lambda o - c_\lambda * GF . \quad \{1\}$$

When applied over the full VIS & NIR spectrum, a correction spectrum (c_λ*GF) per GF is produced (Fig. 4B), essentially the estimated spectral bias in the measurement due to GF distortions. Different slopes (c_λ) and correction factors were needed for thick and thin needles (data not shown). For all needles, those spectral regions that are relatively transparent (e.g., NIR) are less affected by GF, as evidenced by a lower slope of the linear relationship (and smaller correction factor). When this information was applied to T_λ for BOREAS measurements of jack pine and black spruce (Fig. 5 A, B), improved T_λ spectra were obtained.

The measured R_λ were not affected by GF for this particular needle set. [However, a 10% overestimate was observed in all λ at GF>0.15 for another species; and, we observed a linear increase for R_λ as a function of GF for another set comprised of thinner needles. Data not shown]. R_λ and T_λ spectra were used to calculate A_λ as [1 - R_λ - T_λ]. Table 2 gives APAR and SR determined from the original and corrected BOREAS spectra for jack pine and black spruce in IFCs-1&3. The corrected APAR estimates (78-80%) for early summer were 8-11% *lower* than those for uncorrected needle spectra. The SR for corrected spectra were also significantly different, and in most cases were 40-60% lower. Corrected SR calculated from T_λ spectra were significantly higher that those calculated from R_λ spectra.

Table 1. Per cent absolute (Abs.) and relative (Rel.) errors for Transmittance (T_λ) and Reflectance (R_λ) in the VIS (400-700 nm) and NIR (700-1000 nm) spectra that result from errors in the estimation of Gap Fraction (GF).

GF Range	Relative GF Error	Optical Property	Error Type	Spectrum VIS	NIR
1. Round Aperture					
0.05-0.15	10%	T_λ	Abs.	1.3	1.3
			Rel.	16.0	4.6
		R_λ	Abs.	<0.5	1.0
			Rel.	<3.0	2.0
0.0 5-0.15	20%	T_λ	Abs.	2.0	2.0
			Rel.	>20.0	5.0
		R_λ	Abs.	<0.5	1.3
			Rel.	<3.0	2.5
0.30-0.60	10%	T_λ	Abs.	6.5	5.5
			Rel.	>20.0	14.5
		R_λ	Abs.	1.5	4.5
			Rel.	8.5	8.5
0.30-0.60	20%	T_λ	Abs.	10.0	8.0
			Rel.	>20.0	20.0
		R_λ	Abs.	2.0	7.0
			Rel.	11.7	15.5
0.40-0.80	10%	T_λ	Abs.	15.0	14.0
			Rel.	>20.0	>20.0
		R_λ	Abs.	7.5	12.5
			Rel.	>20.0	20.0
0.40-0.80	30%	T_λ	Abs.	>20.0	25.0
			Rel.	>20.0	>20.0
		R_λ	Abs.	15.0	22.0
			Rel.	>20.0	>20.0
2. Slitted Aperture					
0.05-0.15	15%	T_λ	Abs.	1.5	1.8
			Rel.	20.0	5.8
		R_λ	Abs.	<1.0	1.3
			Rel.	<6.0	2.5
0.05-0.15	30%	T_λ	Abs.	4.0	2.5
			Rel.	>20.0	7.7
		R_λ	Abs.	1.5	2.0
			Rel.	8.0	4.0

DISCUSSION

We revised the Daughtry et al. [1] protocol because we needed a flexible method that was easy to implement for a large sample size in a portable, field laboratory. Also, we could not assume a fixed low (<2%) in the red chlorophyll absorptance region for our needles, as was done by [1], because of the expected seasonal change in the visible spectra of boreal species.

Table 2. Optical Parameters [APAR, SR_R^*, and SR_T^*] derived from uncorrected and corrected A_λ, R_λ, and T_λ spectra for jack pine (JP) and black spruce (BS), from BOREAS 1994 IFCs-1 & 3 (early summer and fall).

Species/IFC	Parameter	Uncorrected	Corrected
JP/ IFC-1	APAR (%)	91.3	80.0
	SR_R	5.3	N/A
	SR_T	14.0	8.8
JP/ IFC-3	APAR (%)	86.4	84.1
	SR_R	6.7	N/A
	SR_T	21.4	9.3
BS/ IFC-1	APAR (%)	86.8	78.2
	SR_R	4.5	N/A
	SR_T	7.8	9.8
BS/ IFC-3	APAR (%)	74.6	75.3
	SR_R	3.8	N/A
	SR_T	8.4	5.0

* SR_R and SR_T were calculated from Reflectance and Transmittance spectra, respectively.

Our results clearly indicate that transmittances are underestimated when light gaps are present in the sample holder's aperture. T_λ is linearly reduced as a function of increased GF, with greater impact in the visible spectrum. Even at small GF, a correction is beneficial. The errors in T_λ resulting from 10-20% errors in the estimation of GF (based on the sensitivity analyses) represent a special case of this general result, with overestimates of GF resulting in underestimates of T_λ. By working with needles of similar thickness to the boreal species, we were able to transfer the results of our controlled experiments to our field data, with good success. However, different slopes for T_λ vs. GF were observed for a range of needle thicknesses; and overestimates of R_λ at large GF were apparently sample-dependent.

T_λ is controlled by the optical density of the needle interior and R_λ is controlled by needle surface features. Therefore, it is preferable to develop the regression coefficients for T_λ (and R_λ, if needed) vs. GF from the same needle type, species, age and condition as are examined in the field measurements. We currently plan to include this procedure in our protocol for each species examined in each field campaign. The importance of employing these corrections is highlighted by the adjusted APAR and SR values (Table 2): the uncorrected APAR (or SR) estimates were ~10% (or <50%) too large when measurements were made with GF ≈ 0.40. Whereas estimates of APAR were similar in corrected/uncorrected spectra collected with a small GF (~0.08), the associated SR for uncorrected spectra were 44-60% too large. Consequently, the expected relationship between APAR and SR [6] was confounded without application of the corrections.

ACKNOWLEDGMENTS

We thank Mr. Scott Mitchell (SSAI) for assisting with data processing.

REFERENCES

[1] C.S.T. Daughtry, L.L. Biehl, and K.J. Ranson, "A new technique to measure the spectral properties of conifer needles," *Rem. Sens. Environ.*, vol. 27, pp. 81-91, 1989.

[2] D.G. Brand, "Estimating the surface area of spruce and pine foliage from displaced volume and length," *Can. J. For. Res.*, vol. 17, pp. 1305-1308, 1987.

[3] J.W. Harron and J.R. Miller, "An alternative methodology for reflectance and transmittance measurements for conifer needles," *Proceed., Canadian Rem. Sens. Symposium*, pp. 654-661, June 1995.

[4] E.M. Middleton and E.A. Walter-Shea, "Optical prope. of canopy elements in the boreal forest," *Proceed. 1995 International Geoscience and Remote Sensing Symposiu. (IGARSS'95)*, Library of Congress No. 95-75916, Firenze, Italy, pp. 789-793, July 1995.

[5] P.J. Sellers, et al., "The Boreal Ecosystem-Atmosphere Study (BOREAS): An overview and early results from the 1994 field year," *Bull. Amer. Meteorol. Soc.*, vol. 76, pp. 1549-1577, 1995.

[6] P.J. Sellers, J.A. Berry, G.J. Collatz, C.B. Field, and F.G. Hall, "Canopy reflectance, photosynthesis, and transpiration. III. A reanalysis using improved leaf models and a new canopy integration scheme," *Rem. Sens. Environ.*, vol. 42, pp. 1-30, 1992.

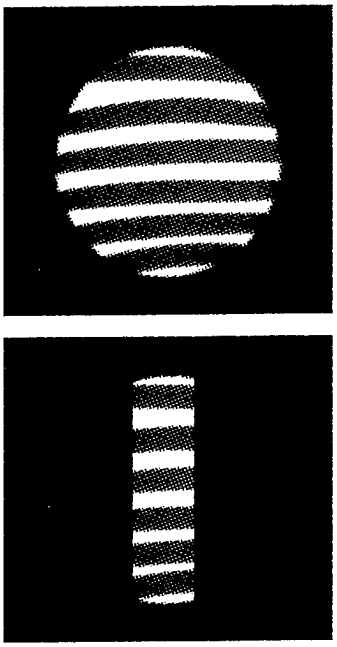


Figure 1. The sample holders are shown: A) jack pine needles, with the round aperture; and B) black spruce needles, with the slitted aperture. Light sources with round and oval beams, respectively, and used with these two sample holder types.

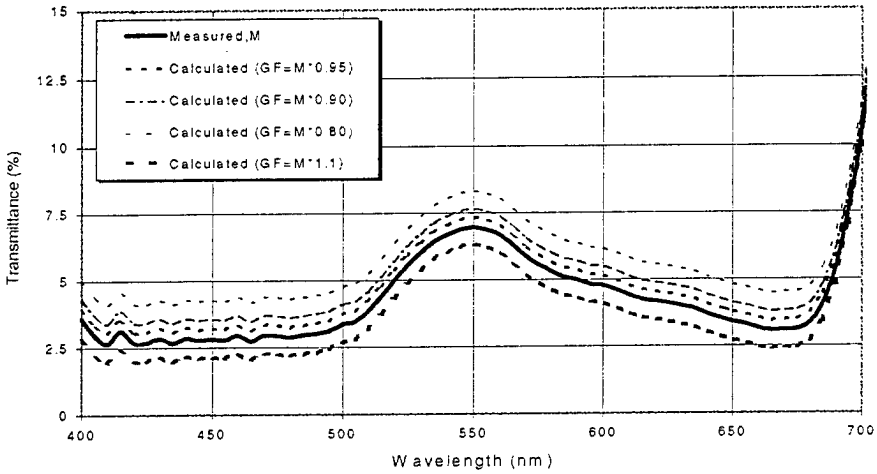


Figure 2. Shown are the changes in the calculated value for T_λ that result from uncertainty in the accuracy of the GF determination. Measurements were originally made on jack pine needles using a relatively small GF (0.06), and recalculated using GF underestimates of 5, 10, and 20% and an overestimate of 10%.

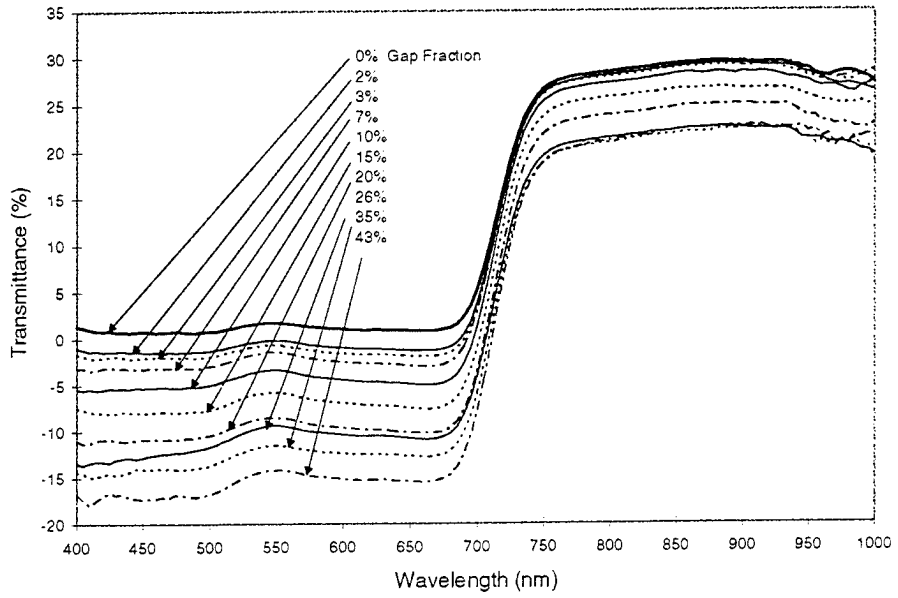
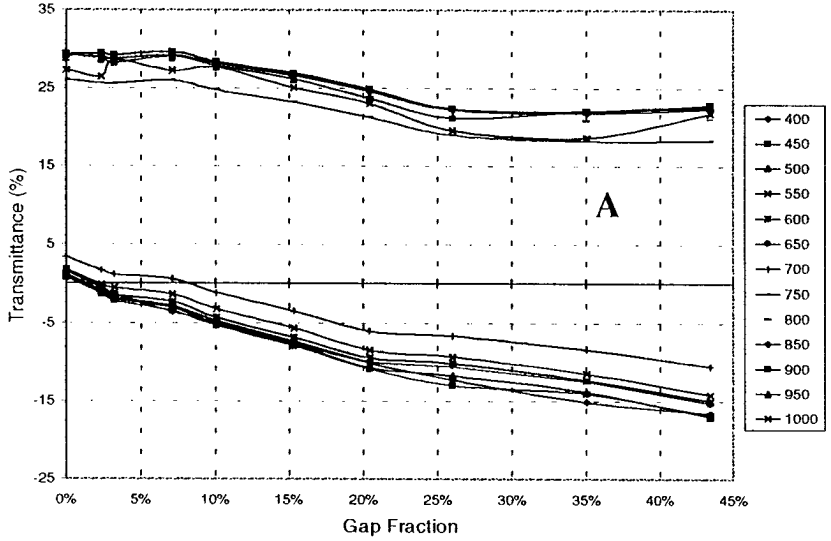


Figure 3. The measured transmittance ($T_\lambda x$) spectra obtained over a range of GF (<50%) for mature pine needles is shown. $T_\lambda x$ for dorsal and ventral surfaces were averged here and in subsequent figures.



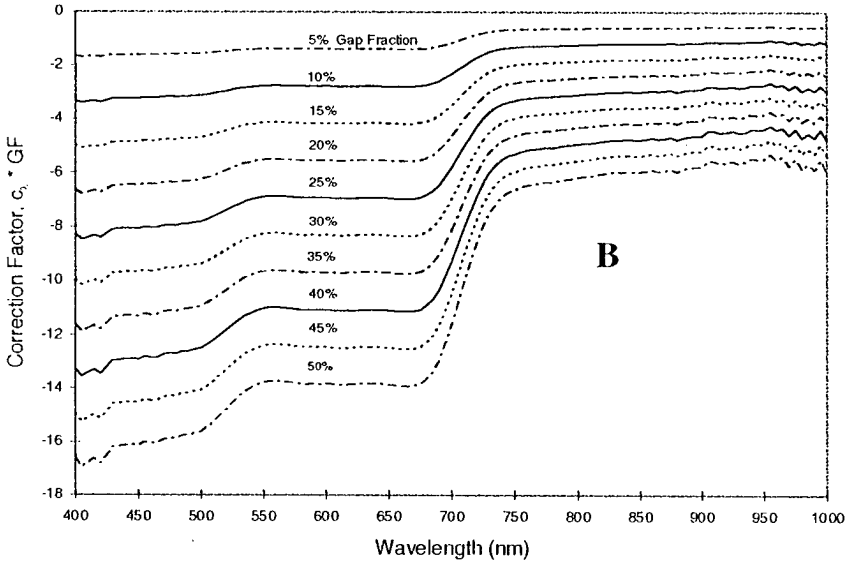
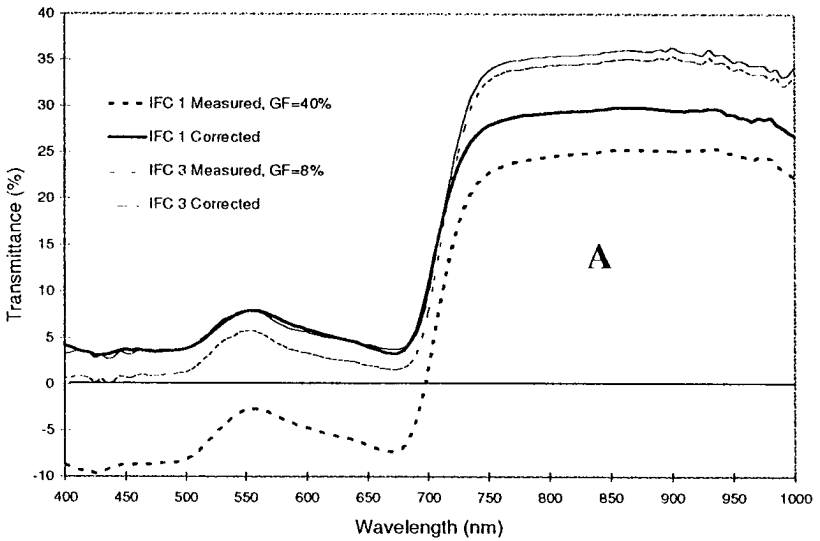


Figure 4. Two steps is the correction of GF on $T_\lambda x$ are shown: A) the inverse linear relationship of $T_\lambda x$ with GF, for select λ; and B) the correction factor, c_λ*GF, as a function of λ, for a range of GF (<50%).



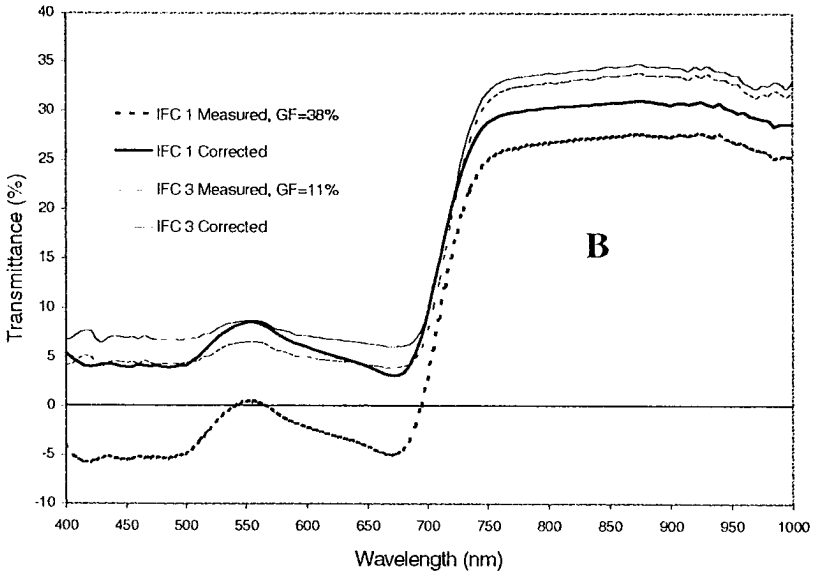


Figure 5. Seasonal T_λ spectra before and after correction: A) jack pine; and B) black Spruce.

Airborne Imaging Spectrometry in National Forest Inventory

Kai Mäkisara, Erkki Tomppo
Finnish Forest Research Institute (METLA)
Unioninkatu 40 A, FIN-00170 Helsinki, Finland
Tel: +358-0-85705334. Fax: +358-0-625308. Email: Kai.Makisara@metla.fi

Abstract - - This paper describes the first steps in our work towards using an airborne imaging spectrometer (AISA) as a source of information in an operational, large area forest inventory system. The necessary properties of algorithms for this kind of task are discussed, including handling of the atmospheric effects. An algorithm for automatic selection of spectral channels for estimation of forest parameters is presented and it is applied to AISA data from Southern Finland.

INTRODUCTION

The National Forest Inventory of Finland (NFI) has produced large-area forest resource information for over 70 years for management planning of Finnish forestry and forest industries [1]. The results of NFI are quantitative and qualitative estimates of different forest parameters. Examples of these parameters are the volume of wood divided into different groups by forest type, tree species, and wood quality. The NFI system currently uses a systematic grid of field plots over the whole country, satellite images (Landsat TM and Spot), and digital map data.

The most serious problem in the current system is that clouds often prevent obtaining satellite images from the same growing season when the ground measurements have been made. The users would also like to get more up-to-date information than we can nowadays provide. These reasons have prompted us to examine airborne optical instruments. An airborne imaging spectrometer, the AISA instrument [2], was designed and built in Finland during the recent years and Metla has acquired the first pre-series AISA instrument in 1995.

Processing data from large forest areas poses some restrictions to the algorithms being used. It is not possible to make ground measurements simultaneously with the flights except at a very small number of sites. This means that the atmospheric correction methods being used must be based almost solely on the airborne data. Another alternative being studied is to use spectral features that are invariant to changes in the atmospheric conditions. The problem is complicated even more by the desire to be able to fly during cloudy weather.

Another requirement comes from the large amount of data collected by this kind of a system. The AISA spectrometer collects 500 kilobytes of data per second. The algorithms used in analysing this data must not be too complex. Geolocating of the data has limited accuracy without excessive operator workload. This means that, even if most individual trees can be seen in the data, tree-level analysis can be done only locally.

Two test flights have been performed during Summer 1995 with our AISA instrument to test the instrument and to collect data for algorithm development. Both flight were successful and showed that the instrument and the preprocessing software for the data operate well. Preliminary plans for the use of the instrument in NFI have been made. Before making more detailed plans, the limits of accuracy in estimation of the forest parameters have to be found out. The first experiments to clarify this concentrated on the efficiency of spatially averaged spectral data and simple texture features. Forest stand data was used in the experiments instead of sample plot data to get better statistical accuracy with limited flight effort.

THE ROLE OF AISA IN NFI

The role of the AISA instrument in the NFI system must be based on the characteristics of AISA data. The main characteristics of the AISA spectrometer are:

- can collect a large number of programmable spectral channels in the wavelength range 450 – 900 nm,
- has fairly good spatial resolution (pixel dimensions typically 1 – 3 m), and
- can cover larger areas than field crews but smaller than satellite images.

In the current NFI system the field plots are used for computation of large area averages. The satellite images and the digital map data (e.g., arable land, built areas, roads, digital elevation model when applicable) are used to generalise the field plot data so that averages for smaller regions can be computed.

In this framework we can readily see two possible application possibilities. Firstly, the AISA data can be used to update the field plot data between the times the field crews visit the plots (five to ten years). The second possibility is to use AISA to introduce a new component into the system. One possibility is to use a sparse, line-wise sampling over the country. Both of these methods augment the use of field measurements. It is not reasonable to expect that any airborne or satellite data can completely replace field measurements.

The study was funded partly by the Technology Development Centre (TEKES).

0-7803-3068-4/96$5.00©1996 IEEE

Table 1: The forest parameters available in the forest stand data together with the mean values of the continuous-valued parameters in the test data. The codes are used in Table 3.

Parameter	Code	Mean	Unit
Land use class	luc		class
Subclass of forestry land	scl		class
Site fertility class	sfc		class
Soil type	st		class
Development class	dc		class
Age	age	52.6	years
Stem volume	stv	14.9	m^2
Stem diameter	std	15.9	cm
Average tree height	hgt	13.3	m
Growth in m^3	gro	5.9	m^3/ha
Volume of pine	vp	29.0	m^3/ha
Volume of pine saw log	vps	10.1	m^3/ha
Volume of spruce	vs	92.3	m^3/ha
Volume of spruce saw log	vss	49.3	m^3/ha
Volume of deciduous trees	vd	20.7	m^3/ha
Vol. of deciduous tree saw log	vds	3.0	m^3/ha
Total volume	vol	142.0	m^3/ha
Total volume of saw log	vos	62.4	m^3/ha

EXPERIMENTS WITH CHANNEL SELECTION

The Material

The test area was located in Southern Finland near Mäntsälä. Forest stand data was available for this area, provided by the Uusimaa-Häme Forestry Board and updated by Metla during years 1994 – 1995. The recently clear cut areas were taken out based on examination of the AISA data. The final ground data consisted of 137 stands. The available forest parameters are shown in Table 1.

Two test flights were carried out with the AISA spectrometer during Summer 1995, providing over five gigabytes of raw data. Three different altitudes (1000 m, 1600 m, and 2000 m) were used resulting in on-ground pixel dimensions between 1 m and 2.5 m. Several different programming configurations were tested, including both spatial and spectral mode configurations. The number of channels selected for the spatial mode configurations varied between 20 and 41. The data used in this paper was collected on July 11 at about 1 PM from 2000 m altitude. The spectral configuration consisted of 41 channels (see Fig. 1 and Table 2 for the assignment). The integration time was 50 milliseconds.

Two flight lines were used to cover the test area and the data was rectified onto the forest stand map. Rectification was done with the software from VTT [3], with small modifications from Metla. A differential GPS system was used to locate the instrument (aircraft) during flight. The software used this data together with ground control points shown by the operator. Based

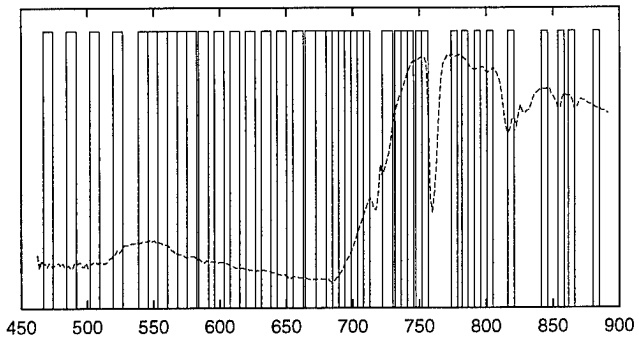


Figure 1: The 41 channels used in this study along with a typical spectrum from vegetation sampled in the spectral mode of the AISA spectrometer.

Table 2: The placement of the spectral channels in this experiment.

	nm		nm		nm
1	466.6 - 473.9	15	631.1 - 638.4	29	736.3 - 741.0
2	484.2 - 491.5	16	642.8 - 650.2	30	741.0 - 745.7
3	501.8 - 509.2	17	654.9 - 662.7	31	747.2 - 751.9
4	519.4 - 526.8	18	664.3 - 672.1	32	751.9 - 756.6
5	538.5 - 545.9	19	672.1 - 680.0	33	773.9 - 778.5
6	545.9 - 553.2	20	679.6 - 684.6	34	781.7 - 786.4
7	553.2 - 560.6	21	684.6 - 689.3	35	791.1 - 795.8
8	560.6 - 567.9	22	689.3 - 694.0	36	800.5 - 805.2
9	567.9 - 575.3	23	694.0 - 698.7	37	816.1 - 820.8
10	575.3 - 582.6	24	698.7 - 703.4	38	841.1 - 845.8
11	584.1 - 591.4	25	703.4 - 708.1	39	853.7 - 858.4
12	595.8 - 603.2	26	708.1 - 712.1	40	861.5 - 866.2
13	607.6 - 614.9	27	722.2 - 730.0	41	880.3 - 885.0
14	619.3 - 626.7	28	731.6 - 736.3		

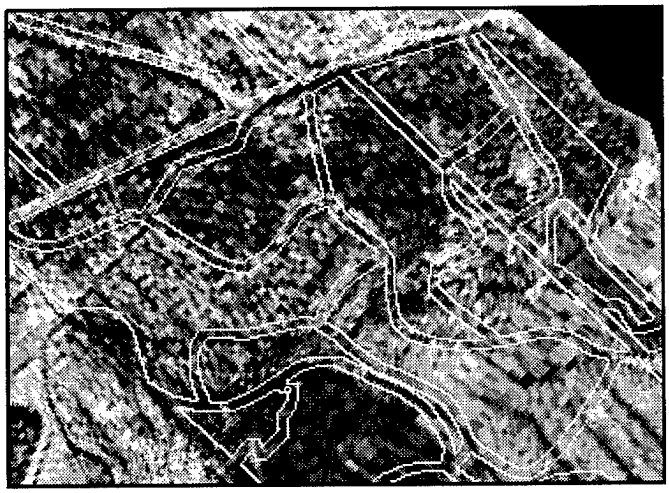


Figure 2: A sample of the image data together with the forest stand boundaries. Wavelength band 708.1 - 712.1 nm.

on visual inspection, the rectification errors seemed to be below five meters. To remove from the results the inaccuracy caused by the rectification errors, a two-pixel (four meter) guard zone was used around the forest stand boundaries. An example of the rectified image data together with the forest stand boundaries and guard zones is seen in Fig. 2.

The radiometric correction of the data is done simultaneously with geometric correction by the software from VTT. The radiometric correction transforms the digital numbers into units of radiance as "seen" by the instrument. Atmospheric correction of the data has been studied but no algorithm has yet been selected for operational use.

To compare the results with a commonly known method, the same experiments were performed also using Landsat TM-data (channels 1 – 6).

The Methods

The purpose of these experiments was to find the best channel combinations for estimation/classification of the different forest parameters shown in Table 1. Both learning and test material were from the same flight minimising the effects of changes in atmosphere and illumination.

Two kinds of features were used in order to utilise both the spectral and spatial aspects of the data. The spectral aspects were represented by 25 by 25 pixel averages for each spectral channel. The averages were computed by using only pixels within the stand containing the center point of the window. The spatial aspects were represented by local standard deviations within a similar window. The data from feature analysis consisted of 2920 pixels.

An automatic algorithm was used for finding the best channel combinations and the best channel set size. The fidelity criterion was minimisation of the RMS error for the continuous-valued parameters and minimisation of the number of incorrect classifications for the classed variables. The algorithm consisted of the following steps:

1. Recursive adding of a new channel to the set until the maximum size is reached or the error starts to increase.
2. Substitution of the channels one by one until no changes occur. Adding channels is attempted if the set size is below the maximum.
3. Substitution with wider channels up to a predefined maximum width until no changes occur. Adding channels attempted if below maximum set size. Wider channels are formed by summing adjacent original channels.
4. The contribution of each channel was determined by dropping the channel out of the channel set.

The search algorithm does not guarantee that the global optimum is found but, on the other hand, no assumptions have to be made about the data.

This kind of algorithm is practicable with current computers if the test material is not too large and the classification or estimation algorithm is simple enough. The *K-nearest neighbour* (K-NN) classifier or estimator with K = 4 was used in this study.

The K-nearest neighbour classification algorithm is as follows. The feature space distance $d_{i,p}$ is computed between the pixel p to be classified and each pixel i in the training material, and the set of smallest distances $\{d_{(1),p} \leq .... \leq d_{(K),p}\}$ is determined. The Euclidean distance was used in this study. If more set members come from one class than from any other class, this class is the classification result. In case of a tie, the class corresponding to $d_{(1),p}$ is selected.

Estimation with the K-nearest neighbour method is performed in the following way. Define

$$w_{(i),p} = \frac{1}{d_{(i),p}} / \sum_{i=1}^{K} \frac{1}{d_{(i),p}} \qquad (1)$$

The estimate $\hat{m}_p$ of the variable M for the pixel p is defined by

$$\hat{m}_p = \sum_{j=1}^{K} w_{(j),p} \cdot m_{(j),p} \ , \qquad (2)$$

where $m_{(j),p}$, $j = 1, ..., K$, are the values of the variable M in the K closest pixels to the pixel p in the feature space [1].

Three trials were made for each channel combination. Two thirds of the stands were used as learning data and one third was used as test data in each trial.

Classification or estimation is performed separately for each feature vector. The final estimate within a stand is computed as median of the estimates for the pixels within the stand. The classification results are decided using the majority rule.

The Results

Selection of the best channel combinations has been tested with the AISA data. Table 3 summarises the results obtained with set size of up to six channels and maximum width of three sampled channels. To put the results into a perspective, one should note that the typical error of the total volume in operative stand-level field inventory is about 30 m^3/ha [4].

The results show that AISA data gives in all cases but one (subclass of forestry land) better accuracy than TM data. The best channel combinations for the different parameters are different, as was expected. The optimal number of channels was nearly always smaller than six. It is surprising that summed channels are not selected more often. The reason may be that the radiometric accuracy of the AISA data is quite good and summing adjacent channels does not increase the accuracy significantly.

The behaviour of the error versus the number of spectral channels was tested by selecting fixed number of channels into the set. Table 4 shows the result for the total volume. The error does not seem to change significantly when channels are added. In this case the estimation error with exactly six chan-

Table 3: Results from the experiment were the best combination of up to six channels of width up to three channels was determined. The channels are presented in the order of decreasing importance determined by step 4 of the optimisation algorithm. The channels with suffix s denote the standard deviations of the corresponding channels. The last two columns give the estimation error or percentage of incorrect classifications for the AISA data and the reference error using TM data.

Code	Channels	AISA	TM
luc	25 52	1.6	2.1
scl	30s 16s 25 8 5 4	26.2	24.1
sfc	23 2s 22s 3s	52.2	52.7
st	25s 17 18	54.3	76.3
dc	22 16s-17s 12s	74.0	89.0
age	33-34 24s 17s-18s 29 4 22s-23s	24.1	27.7
stv	6 1 20s 2s	4.5	7.1
std	7 31s 39s 40s 36s-37s	7.0	8.2
hgt	6 24s 1s	5.1	6.2
gro	18s-19s 5 4s 2 4 3s	2.4	3.5
vp	32s 30 41 22s 37 2s	27.8	36.4
vps	33s 28 33-34	16.0	20.1
vs	26 1 19 4s-5s 1s-2s 3-4	36.9	71.6
vss	26 24s 21 24 1	30.6	47.7
vd	28 13 14s 16s	21.9	31.7
vds	6s-8s 36s	6.7	8.5
vol	9 39-40	42.4	71.9
vos	35 27s 30s	36.2	52.3

nels is slightly smaller than the optimum found previously for two channels.

Feature vectors normalised to unit norm were also tested as feature sets invariant to changes in the illumination level. The results for two forest parameters are shown in Table 5. The number of channels in the optimal set is larger when using normalised vectors but the estimation error was at the same level as without normalisation. This is a coarse method for atmospheric correction, but the results prove that good results can be obtained even without absolute calibration of the data.

CONCLUSIONS

The studies show that the imaging spectrometer data gives in most cases much better accuracy than Landsat TM data in estimation of forest parameters. The optimal performance for each task was reached with a very small number of channels and summed channels were chosen rarely. The good results with AISA can thus not be attributed to the use of a large number of channels simultaneously but to the radiometric accuracy and the possibility to fine-tune the channel placement. Different channel combinations were optimal for different tasks. The ability to sample a large number of channels simultaneously gives the opportunity to collect optimal information for several tasks simultaneously.

Table 4: Results from the experiment where different number of channels were optimised for estimation of the total volume.

Number of channels	Channels	RMS error
1	8	44.7
2	9 39-40	42.4
3	32 8 6	42.2
4	32 39-40 10 7-8	42.2
5	8 32 40-41 6 38-39	42.6
6	32 8 10 9 41 39-40	42.1

Table 5: The best channel assignments for two forest parameters when normalised vectors were used.

Code	Channels	Error
vp	41 18 1 20 4 2	26.9
vol	5 1 18s 13s 3s 21s	45.9

The normalised feature vectors gave good results. This means that handling the atmospheric correction can be based on using relative spectral features. However, the features should take into account what is known about the relative changes in different spectral bands in varying atmospheric conditions.

This channel selection study was only the first step in our search for the most efficient features from AISA data. The next step will be studying of different functions of the sampled spectral channels and utilisation of the spatial features tuned towards analysis of the forests.

REFERENCES

[1] E. Tomppo, "Satellite image-based national forest inventory of Finland," International Archives of Photogrammetry and Remote Sensing, vol. 28, pp. 419–424, 1991.

[2] K. Mäkisara, M. Meinander, M. Rantasuo, J. Okkonen, M. Aikio, K. Sipola, P. Pylkkö, and B. Braam, "Airborne imaging spectrometer for applications (AISA)," In International Geoscience and Remote Sensing Symposium Digest, pp. 479–481, 1993.

[3] K. Mäkisara, J.-P. Kärnä, and A. Lohi, "A system for geometric and radiometric correction of airborne imaging spectrometer data," In International Geoscience and Remote Sensing Symposium Digest, pp 851–853, 1994.

[4] R. Päivinen, A. Pussinen, and E. Tomppo, "Assessment of boreal forest stands using field assessment and remote sensing," In Proceedings of the International Symposium "Operationalization of Remote Sensing", 1993.

An Approach for Obtaining Best Estimates of Spectral Optical Depths and Calibration Intercepts From Solar Radiometer Data Corrupted by Temporal Variations

Wayne H. Erxleben and John A. Reagan *
Department of Electrical and Computer Engineering
The University of Arizona, Tucson, AZ 85721
Phone: (520) 621-4297 / FAX: (520) 621-8076 / email: erxleben@ece.arizona.edu

Abstract—Calibration of solar radiometers is generally accomplished by the Langley plot method; however, slight temporal variations in optical depth can significantly bias zero-airmass intercepts thus derived. This paper presents signal processing techniques for improving the Langley analysis under temporally varying conditions, as well as better characterizing the variability itself. These techniques include spectral analysis of the data to identify systematic atmospheric variations and distinguish them from measurement noise, and exploitation of the correlation between measurements at different wavelengths and on different days. The processing is applied to data from an automated 10-channel radiometer.

1. BACKGROUND

The response of a solar radiometer to direct sunlight of wavelength λ, seen at time t through an atmosphere of airmass $m(t)$ and optical depth $\tau(\lambda,t)$, on a day with earth-sun distance R, is given by Beer's Law:

$$V(\lambda,t) = (R_0/R)^2\, V_0(\lambda) e^{-m(t)\tau(\lambda,t)} \qquad (1)$$

where $V_0(\lambda)$ is the instrument's response to the irradiance at the top of the atmosphere (zero airmass) for the mean earth-sun distance R_0. If $V_0(\lambda)$ is known, optical depths can be found as

$$\tau(\lambda,t) = -\frac{1}{m(t)} \ln \frac{V(\lambda,t)}{V^*_{0,j}(\lambda)} \qquad (2)$$

where $V^*_{0,j}(\lambda) = (R_0/R)^2 V_0(\lambda)$ for day j. $V^*_{0,j}(\lambda)$ is usually found by the Langley method, in which a line is fit to a plot of $\ln V(\lambda,t)$ *vs.* $m(t)$. If $\tau(\lambda,t)$ is constant over time, it will equal the negative slope of the line, and the vertical-axis intercept (*i.e.*, $m(t) = 0$) will be $\ln V^*_{0,j}(\lambda)$. Temporal variations of the apparent $\tau(\lambda,t)$ due to zero-mean white measurement noise should average out, and the calculated $V^*_{0,j}(\lambda)$ will still be valid. Systematic variations, however, reflecting actual atmospheric changes during the 2- to 3-hour measurement period, can yield inaccurate zero-airmass intercepts. To minimize this inaccuracy, measurements are made at clean, high-altitude sites, and the resulting intercepts averaged for several "good" days, with "good" defined rather subjectively.

Our goal in this paper is to remove some of the subjectivity from the calibration process, and to broaden the class of days which are useful for calibration. We utilize new signal processing techniques which exploit the correlation between curves of optical depth *vs.* time for different wavelengths on the same day (Section 3), and between curves of intercept *vs.* wavelength for different days (Section 4). Before using these techniques, however, we attempt (Section 2) to remove measurement noise so that the curves we correlate represent only true atmospheric variations, using a filter derived by spectral analysis.

*This work was sponsored by NASA Global Change Research Fellowship No. NGT-30215

2. SPECTRAL ANALYSIS OF OPTICAL DEPTHS

Under the old Langley-plot assumption of constant optical depth, all temporal variations were considered noise to be removed. A more modern viewpoint is that both the noise and the underlying signal have random variations, but can be distinguished by their spectral densities. It is well known that many natural processes exhibit fractal, or scale-invariant, characteristics [1]. Specifically, many one-dimensional (temporal or spatial) series generated by natural phenomena have power spectra of the form

$$S_x(\omega) \sim \frac{\sigma_x^2}{|\omega|^\gamma} \qquad (3)$$

where γ typically varies between -1 and 3. We assume that the temporal variations of optical depth can be well modelled as having such a power spectrum.

For such signals, known as $1/f$ processes, Wornell [2] has shown that orthonormal-basis discrete wavelet transforms act as Karhunen-Loève-type expansions, in the sense that the wavelet coefficients are nearly uncorrelated. When a $1/f$ signal $x(t)$ is corrupted by additive stationary white Gaussian noise $w(t)$, a set of wavelet coefficients of $r(t) = x(t) + w(t)$, denoted

$$\{r_n^m : n = 1,2,3,\ldots,2^{m-1}; m = 1,2,3,\ldots,M\}, \qquad (4)$$

has for any fixed scale m a variance of the form

$$\sigma_m^2 = \sigma^2 \beta^{-m} + \sigma_w^2 \qquad (5)$$

where $\beta = 2^\gamma$. An algorithm is developed in [2] for finding maximum likelihood estimates of β, σ^2, and σ_w^2. Furthermore, a Wiener-type smoothing filter can be effected by multiplying the wavelet coefficients r_n^m by the factor $\sigma^2\beta^{-m}/\sigma_m^2$ and then performing the inverse wavelet transform to obtain the optimal estimate of $x(t)$.

We have applied this technique to eight sets of Langley-derived residual optical depths (*i.e.*, zero-mean signals found by subtracting the mean from the instantaneous optical depths) from Tucson in April 1995. Included were four morning runs and four afternoons, with subjective Langley-plot day-quality assessments ranging from

0-7803-3068-4/96$5.00©1996 IEEE

TABLE 1: SPECTRAL PARAMETERS FOR APRIL 22, 1995.

Wavelength	β	σ^2	σ_w^2	γ
380 nm	3.08	2.61×10^{-2}	7.92×10^{-7}	1.62
400 nm	3.14	2.44×10^{-2}	1.80×10^{-6}	1.65
440 nm	3.27	2.09×10^{-2}	1.24×10^{-6}	1.71
520 nm	2.59	2.28×10^{-3}	1.09×10^{-6}	1.37
670 nm	2.56	7.05×10^{-4}	5.17×10^{-7}	1.36
780 nm	2.37	7.08×10^{-4}	1.20×10^{-6}	1.24
870 nm	2.74	8.25×10^{-4}	1.31×10^{-6}	1.45
1030 nm	1.94	2.35×10^{-4}	1.08×10^{-6}	0.96

"good" to "poor." Three of the data sets had been collected at a rate of one measurement every 10 seconds. Truncating the number of measurements to a power of 2 (as required for the algorithm) gave us 1024 data points. The other five records contained only one measurement per minute, so we had to limit their length to 128 points. (This still covered the desired airmass range but limited the high-frequency resolution.)

This technique's effectiveness is largely independent of the specific choice of wavelet basis; we selected the 6th order Daubechies basis [3]. The resulting β's for the high-data-rate days generally fell in a range of $1.8 < \beta < 4.0$, as shown in Table 1. Fig. 1 shows a typical residual optical depth curve before and after optimal smoothing.

3. EXPLOITING OPTICAL DEPTH CORRELATIONS BETWEEN WAVELENGTHS

Forgan [4] has developed a technique for calibrating multi-channel radiometers which uses the calibration at a reference wavelength (assumed correct) to derive the calibration at a second wavelength. The assumption inherent in this method is that the same form of temporal variation applies, with appropriate scaling, to the aerosol optical depths at all wavelengths, so that for any two wavelengths λ_1 and λ_2, the ratio

$$\frac{\tau_a(\lambda_1, t)}{\tau_a(\lambda_2, t)} = \Psi_{2,1} \tag{6}$$

is a constant, independent of t. This assumption, while not always obeyed in reality, is often a reasonable approximation and is certainly more general than the assumption inherent in the Langley model.

The method is similar to the Langley plot method, but the Rayleigh and gaseous optical depths (τ_R and τ_g) are absorbed into the ordinate, and the aerosol optical depth (τ_a) at the reference wavelength is absorbed into the abscissa. Thus, if the reference wavelength is λ_{i^*}, the equation of the "Forgan plot" for wavelength λ_i is

$$\ln V(\lambda_i, t) + m_R(t)\tau_R(\lambda_i, t) + m_g(t)\tau_g(\lambda_i, t) = \ln V_{0,j}^*(\lambda_i) - \Psi_{i^*,i}[m_a(t)\tau_a(\lambda_{i^*}, t)] \tag{7}$$

and we fit a straight line to the data points to get the slope $\Psi_{i^*,i}$ and the intercept $\ln V_{0,j}^*(\lambda_i)$.

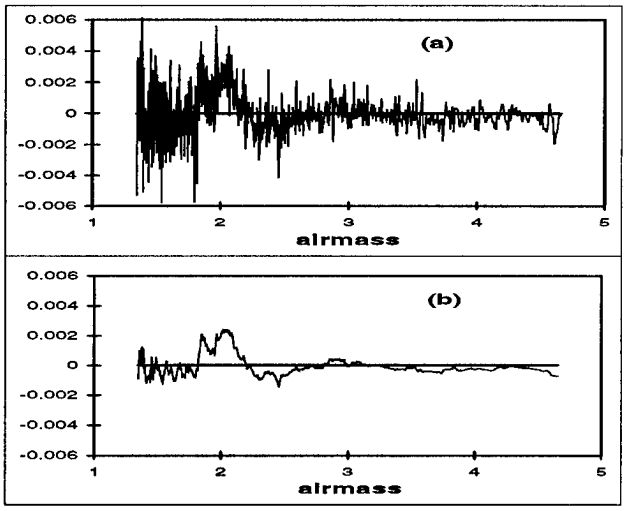


Fig. 1: Residual optical depths at 870 nm on April 22, 1995. (a) Before smoothing; (b) After smoothing.

Significant gaseous absorption occurs at several of our wavelengths. Since our present interest is primarily aerosols, we omitted from our analysis the two channels of our 10-channel instrument which exhibit the strongest absorption: 610 nm (ozone) and 940 nm (water vapor). For the other absorbing wavelengths, τ_g is small enough that nominal levels of ozone and NO_2 can be used.

Since we are trying to simultaneously calibrate all channels of our radiometer, we do not have an *a priori* well-calibrated reference channel. Rather, we have performed the Forgan analysis using *every* wavelength as a reference channel, the initial $\tau_a(\lambda_{i^*}, t)$ estimates being those found by Langley analysis. A weighted average of the results was then computed. Weights $\mu_{i^*,i}$ were assigned to each pair of channels, based on the relative correlation between their residual optical depth curves.

At any given wavelength on any given day, the Forgan plot intercepts found using the various other channels as references typically agree within 0.5%. Undoubtably this success is partly due to the removal of uncorrelated noise from the optical depth signals. Indeed, visual inspection of the filtered residuals shows nearly identical plots for some pairs of channels. Unfortunately, the discrepancy between results for different days is nearly as large as it is with ordinary Langley analysis. In the next section, we introduce a technique to handle this phenomenon.

4. EXPLOITING INTERCEPT CORRELATIONS BETWEEN DAYS

It has often been observed that the day-to-day variations of the computed $V_{0,j}(\lambda)$ (normalized to the mean earth-sun distance) are similar at all wavelengths. Thus, although plots of intercept *vs.* wavelength should be identical on every day, a reasonable first approximation is that they have similar shapes on every day. This suggests a

way to correct erroneous intercepts that may be found for a few wavelengths on a few days.

The plot of $V_{0,j^*}(\lambda)$ *vs.* λ for some day j^* can be approximated by a scaled version of the plot from a different day j. The scaling factor $C_{j^*,j}$ is adjusted to give the best fit in a least squares sense, *i.e.* to minimize the error

$$\epsilon_{j^*,j} = \frac{1}{N_\lambda} \sum_{i=1}^{N_\lambda} \left[\frac{V_{0,j^*}(\lambda_i) - C_{j^*,j} V_{0,j}(\lambda_i)}{V_{0,j^*}(\lambda_i)} \right]^2 \qquad (8)$$

where N_λ is the number of wavelengths (in our case, 8). We find that

$$C_{j^*,j} = \left[\sum_{i=1}^{N_\lambda} \frac{V_{0,j}(\lambda_i)}{V_{0,j^*}(\lambda_i)} \right] \Bigg/ \left[\sum_{i=1}^{N_\lambda} \frac{V_{0,j}^2(\lambda_i)}{V_{0,j^*}^2(\lambda_i)} \right] \qquad (9)$$

We did this for each day j^* and took a weighted average of the approximations found from all the other days j in the set. (Again, we used eight days from April 1995.) The weights α_j were based on both the subjective day-quality factors previously used in averaging Langley plot results, and on the sum of all the $\mu_{i^*,i}$ assigned to day j in the previous section, as a general indicator of how well-correlated the measurements were for that day.

Note that this procedure does not compute a single set of intercepts for the instrument, but rather removes the effect of a faulty channel on one or a few of the days. The resulting approximated curves all have very nearly the same shape, but are shifted up and down relative to each other. One still must do another step of averaging over days to derive the desired product, a single set of calibration intercepts.

5. OVERALL PROCESSING SCHEME

The processing scheme illustrated in Figure 2 combines the three techniques described in this paper. The blocks shown as "Langley plot" and "Beer's law" are nearly inverse transformations to each other; if results from a Langley plot are plugged into Beer's law without modification in the "intercept/optical depth" domain, the original data are returned. (The same is not necessarily true going from the "intercept/optical depth" domain to the "measurement" domain and back.) Our scheme executes this pair of transformations twice per iteration. The first time, the optical depths are modified by optimally filtering before transforming back. The second time, the intercepts are replaced using the methods of the previous two sections.

Although Figure 2 suggests that this entire scheme can be iterated, it appears to reach a point of diminishing returns after just two iterations. By the second round of spectral estimation, some of the β's are significantly larger than the first time (sometimes $> 2^3$), and the σ_w^2's tend to be at least 2 orders of magnitude smaller, indicating that very little noise remains to be removed in further iterations. The $\mu_{i^*,i}$ weights only change a few percent from the first iteration to the second, and the intercept

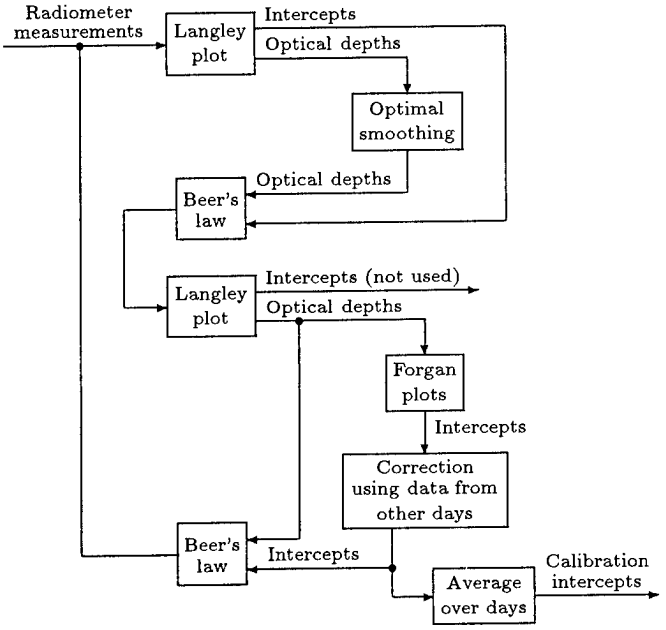


Fig. 2: Radiometer calibration scheme incorporating all techniques described in this paper.

vs. wavelength curves for all days have visually identical shapes after two iterations.

6. CONCLUSIONS AND FUTURE WORK

The general theme that the techniques in this paper have in common is that the quantities of interest in solar radiometry are not all independent, but exhibit correlations which we can exploit during data processing in order to improve our estimation of those quantities. Indeed, most calibration schemes assume some such correlations, and adjust certain parameters to minimize a measure of how well the estimated quantities obey those assumptions. The trick is to find the "right" measure, or the right balance between a number of measures which may not be consistent. Correlation coefficients between residual optical depth curves seem to be useful measures; further analysis of the spectral and fractal properties of optical depth variations may provide additional ones. The addition of a solar aureole channel to our instrument will also provide more information with which to enhance the procedures discussed herein.

REFERENCES

[1] B. B. Mandelbrot, *The Fractal Geometry of Nature.* New York: W. H. Freeman, 1982.

[2] G. W. Wornell, *Signal Processing With Fractals: A Wavelet-Based Approach.* Upper Saddle River, NJ: Prentice Hall, 1996.

[3] I. Daubechies, *Ten Lectures on Wavelets.* Philadelphia: SIAM, 1992.

[4] B. W. Forgan, "General method for calibrating Sun photometers," *Applied Optics*, vol. 33, pp. 4841–4850, July 1994.

Estimation of Abundances in Two-Component Mineral Mixtures Using Mid-Infrared Laser Reflectance Ratios

Ram M. Narayanan, Kristin K. Warner, and Robert F. Diffendal, Jr.*

Department of Electrical Engineering and Center for Electro-Optics
University of Nebraska, Lincoln, NE 68588-0511, USA
T: 402.472.5141 F: 402.472.4732 EMail: eerdrmn@engvms.unl.edu

* Conservation & Survey Div., University of Nebraska, Lincoln, NE 68588-0517

Abstract— The mid-infrared spectral region (8-14 μm wavelength) is emerging as a viable geologic remote sensing tool due to the presence of reststrahlen bands for minerals such as silicates and carbonates. An experimental study was carried out to characterize the mid-infrared laser reflectance of mineral mixtures, and to explore the potential of laser remote sensing systems to estimate mineral abundances in two-component mixtures. An empirical model was developed to establish a relationship between laser reflectance ratios at judiciously selected wavelengths and percentage of one of the minerals in the mixture. It was found that the abundances can be estimated to within2% using this technique. This method shows promise for remote estimation of mineral abundances in applications such as planetary remote sensing since the use of reflectance ratios obviates the need for absolute calibration.

INTRODUCTION

Laser reflectance sensors operating in the backscatter mode are ideally suited for remote sensing applications over conventional spectroradiometers due to their higher signal-to-noise ratios and ease of data acquisition. Although pure and uncontaminated minerals possess unique reflectance features, rocks usually occur as mixtures containing two or more constituents in their natural environment. There is a need, therefore, to develop techniques not only to identify specific minerals, but also to estimate their relative abundances in mineral mixtures. A recent study was performed using passive reflectance values of various mineral mixtures [1]. The objective of our study was to explore the potential of laser remote sensing for remote estimation of mineral abundances in mixtures, and to compare our results with the passive measurements.

In this paper, we describe the University of Nebraska's unique mid-infrared laser reflectance sensor that has been used both in the laboratory and the field for data collection from a variety of surfaces. This sensor was used to collect calibrated reflectance data in the laboratory from two-component mineral mixtures (quartz/albite, quartz/microcline, quartz/hornblende) under various relative abundances, including each mineral by itself. We also develop a simple empirical model based on the relationship between laser reflectance ratios at judiciously selected wavelengths and percentage of one of the minerals in the mixture.

EXPERIMENTAL SETUP

The laser reflectance sensor used in the experiments is described in detail in [2], and its block diagram is shown in Fig. 1. It consists of a line-tunable laser that operates in the 9-11 μm wavelength range with an output power of about 5 W. The receiver consists of a lens-detector combination, followed by a matched preamplifier and a lock-in amplifier. Both co-polarized as well as cross-polarized backscattered energy can be measured. The entire optical system is packaged in a box of approximate dimensions 104 cm x 38 cm x 22 cm.

Reflectance measurements were made at 12 wavelengths as indicated in Table I. Incidence angles used were 0 and 30 degrees. Both co-polarized and cross-polarized backscatter measurements were made. The mineral samples used were quartz, albite, hornblende, and microcline. These samples were the same as those investigated in [1]. The samples were powdered and prepared as far as possible to conform to that in [1]. The particle sizes were in the range 75-250 μm range, in order to ensure that the powder reflectance closely mimicked that of the naturally rough rock surface. Two-component mineral mixtures were formed using quartz as one constituent in all of them. Component percentages (by volume) investigated were 0/100, 25/75, 50/50, 75/25, and 100/0. The samples were placed in a 15-cm diameter Petri dish. Speckle averaging was performed by averaging 50 measurements of the reflectivity as the mineral sample was rotated during the measurement. Calibration was accomplished using a Labsphere Reflectance Standard of 94% reflectivity.

EMPIRICAL MODEL

The model assumes that the reflectance ratio, i.e., the ratio of the mineral-mixture reflectances at any two wavelengths is a volume-weighted function of its constituents. The functional form of the first-order model is given by

$$R_{12} = \frac{\rho(\lambda_1)}{\rho(\lambda_2)} = A_0 + A_1 x \qquad (1)$$

where R_{12} is the reflectance ratio, $\rho(\lambda_i)$ is the reflectance at wavelength λ_i, x is the percentage of mineral 1, and A_0 and A_1 are empirically derived constants. For the second-order model, we add a quadratic term whose coefficient is A_2. This model is

$$R_{12} = \frac{\rho(\lambda_1)}{\rho(\lambda_2)} = A_0 + A_1 x + A_2 x^2 \qquad (2)$$

0-7803-3068-4/96$5.00©1996 IEEE

The constants $A_0 - A_2$ are obtained by best-fits to measured data. The choice of wavelengths λ_1 and λ_2 is crucial in obtaining optimal fits to data. Ideally, the wavelengths must be chosen so as to provide a large slope between the reflectance ratio and the mineral abundance.

RESULTS AND DISCUSSION

From the large data set acquired, it was determined that the relationship between mineral abundances and reflectance ratios at judiciously selected wavelengths could be fitted by both the first-order and the second-order models described above. As expected, the second-order model fit had lower RMS error. Furthermore, it was determined that ratios derived from the co-polarized reflectance values at 30 degree incidence angle gave the minimum errors.

The spectral characteristics of quartz-microcline mixtures is shown in Fig. 2. Since 100% quartz has a peak near 9.283 μm where microcline has a trough, and 100% microcline has a peak near 10.319 μm where quartz has a trough, it was conjectured that this ratio would be useful in estimating the abundance of microcline in a qaurtz-microcline mixture. Fig. 3 shows the relationship between the reflectance ratio and microcline abundance and compares the data with the model fits. As expected, the second-order fit is seen to be better. It was observed that the error between the fit and the data was 0.95% for the first-order and 0.23% for the second-order fits.

Similar results were obtained for quartz/albite and quartz/ hornblende mixtures, and these results are shown in Table II.

CONCLUSIONS

Our study indicates that laser reflectance ratios in the mid-infrared can be used as a tool for remote estimation of mineral abundances in two-component mixtures. This shows its potential in planetary remote sensing applications wherein absolute calibration is not feasible. More work is needed to characterize other mineral mixtures, and also multi-component mixtures.

ACKNOWLEDGMENT

We appreciate the assistance provided by Brian D. Guenther during the measurements and data analysis.

REFERENCES

[1] J.L.Thomson and J.W.Salisbury, "The mid-infrared reflectance of mineral mixtures (7-14 μm)", Remote Sensing of Environment, vol. 45, pp. 1-13, July 1993.

[2] R.M.Narayanan and S.E.Green, "Field measurements of natural and artificial targets using a mid-infrared laser reflectance sensor", IEEE Photonics Technology Letters, vol. 6, pp. 1023-1026, August 1994.

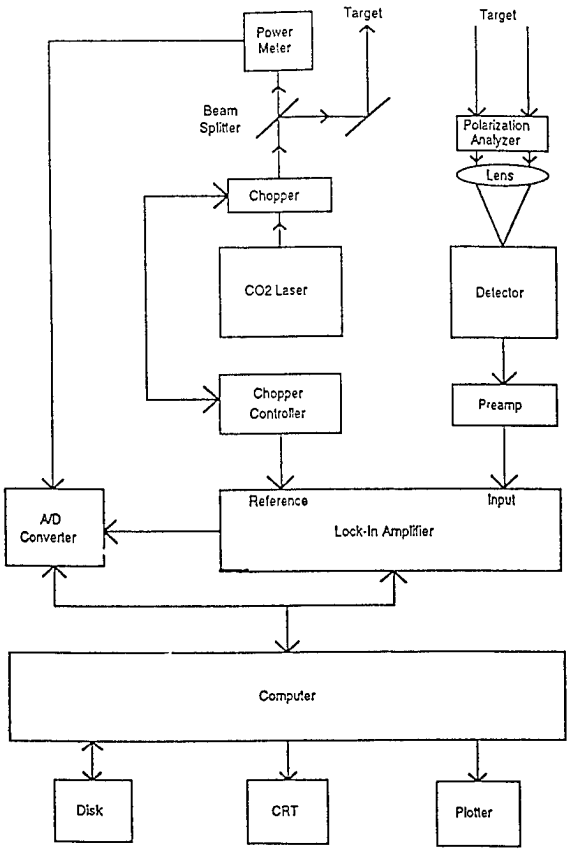


Figure 1: Block diagram of the mid-infrared laser reflectance sensor

TABLE I

WAVELENGTHS USED(μm)
9.2010
9.2500
9.2825
9.5195
9.5690
9.6395
10.1825
10.2470
10.3190
10.4945
10.5915
10.6325

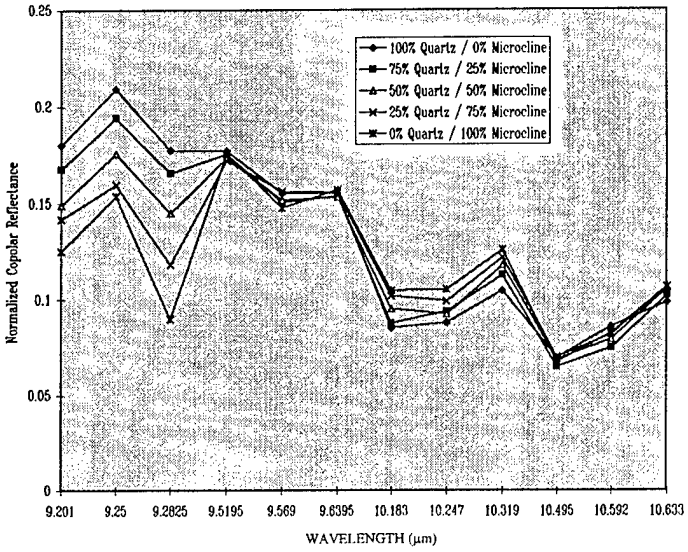


Figure 2: Laser reflectance characteristics of quartz/microcline mixture at various abundances

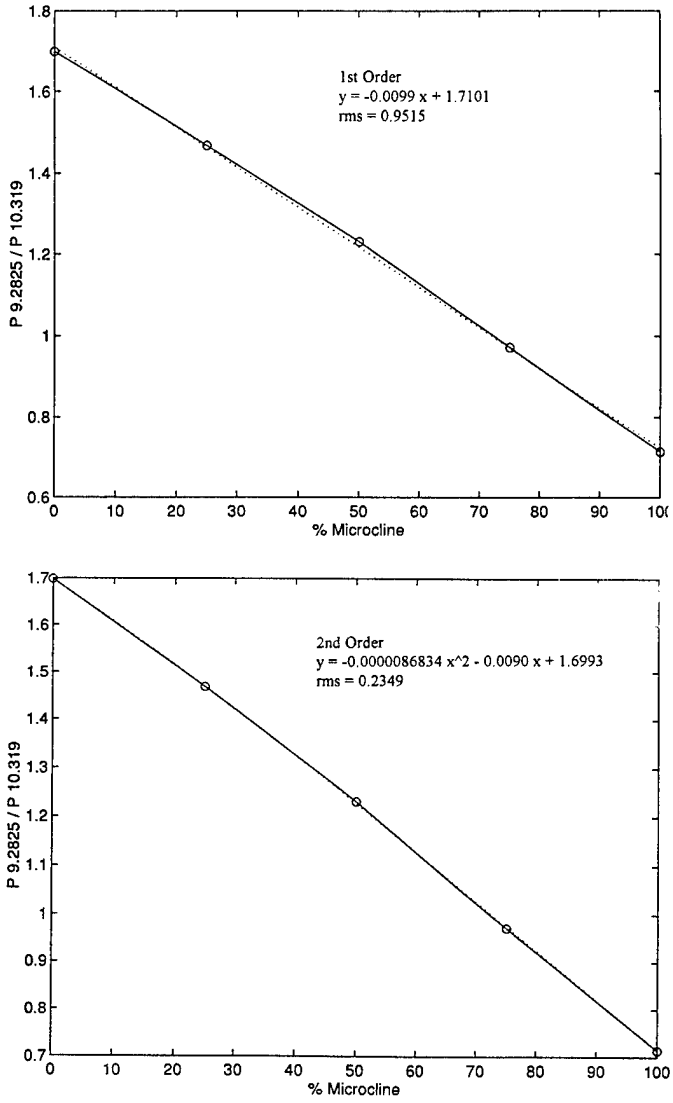


Figure 3: First and second order model fits to measured reflectance ratios for quartz/microcline mixture

TABLE II

RMS ERRORS IN ABUNDANCE ESTIMATION

MIXTURE	WAVELENGTH RATIO	ORDER	RMS ERROR
QUARTZ/ MICROCLINE	9.2825/10.319	FIRST	0.95%
		SECOND	0.23%
QUARTZ/ ALBITE	9.2825/10.495	FIRST	2.58%
		SECOND	0.95%
QUARTZ/ HORNBLENDE	9.2825/10.183	FIRST	2.44%
		SECOND	1.84%

Near Lossless Transform Coding of Multispectral Images.

Andrew G. Tescher, John T. Reagan and J. A. Saghri
Lockheed Martin Corporation
Palo Alto Advanced Technology Center
3251 Hanover Street
Palo Alto, CA 94304-1191
415-424-2165 tescher@lmsc.lockheed.com

ABSTRACT

We have extended the previously developed adaptive transform coding based multispectral algorithm for the lossless / virtually lossless case. Preliminary results are encouraging compared with traditional lossless implementation. The primary technical challenge is to compensate for the quantization errors introduced in processing the high dynamic range eigen images.

INTRODUCTION

The requirement for accurate exploitation of multispectral images introduces the demanding, yet accepted, constraint of not permitting the usual small degradation associated with lossy techniques. Since the sensor-relevant platforms are in space and the image collection is expensive and not easily repeatable, the use of conventional lossless techniques are the implementation choice of the user community. The lossless implementation introduces a severe limitation on compression performance. In particular, a compression ratio of approximately 2:1 is typical performance for a lossless system. Most algorithms operating on individual spectral planes do not significantly outperform this basic limit. In fact, the compression ratio associated with a lossless compression system is more dependent on the quality of the source image - which in turn determined by the appropriate sensor system - than the algorithm itself.

It is reasonable to assume that one approach to achieve additional compression performance is to include the spectral direction as part of the overall algorithm design. In an earlier study, the authors considered a lossy adaptive multispectral system designated "Terrain-Adaptive Transform Coding Algorithm," TATCA [1]. This system has proven to be effective with a wide variety of multispectral imagery. In this paper, we are discussing the extension of this algorithm to the lossless and near lossless application.

0-7803-3068-4/96$5.00©1996 IEEE

BACKGROUND

The TATCA algorithm uses an adaptive Karhunen-Loeve transformation over modest regions (terrains) of the image. The typical region is over 64 by 64 pixels. The decorrelated "eigen" images become the subsequent inputs to the coding algorithm. For the previously implemented lossy compression algorithm, the baseline JPEG was utilized. The basic processing steps of the algorithm are shown in fig. 1.

EXTENSION OF THE ALGORITHM TO THE "LOSSLESS" CASE

Extension of the algorithm to the lossless case introduces several challenging implementation issues which are the subject of the current study. The original TATCA system was lossy; the primary component of the introduced error was the result of the JPEG processing step. It appears reasonable to assume that by replacing the lossy component by its lossless equivalent, the system becomes lossless. In principle, Karhunen-Loeve transformation introduces no error. This transformation is implemented by a well behaved orthogonal matrix operation which has a well defined inverse. The spectrally decorrelated "eigen" images are produced by the forward transform. The application of the inverse transform on the eigen images should produce the original multispectral image set exactly. Clearly, if this is the case, a lossless algorithm operating on the eigen image set will produce an overall lossless algorithm. Furthermore, since the entire compression process is based on the spectral as well as spatial redundancy, the compression efficiency should be superior to algorithm which utilize only the intra-image redundancy.

In a practical implementation, the eigen images require quantization. The required amplitude quantization process introduces a certain error component which, while insignificant for the lossy case, becomes the dominant source of error in what would have been a truly lossless implementation.

Without the introduction of modifications to the described process or allowing for subsequent compensation, the revised TATCA system with lossless component becomes "virtually" lossless but not lossless. To achieve a completely lossless implementation the following approaches may be pursued:

1. *Systematic eigen image plane optimization.*

   In the subsequent examples, similarly to the lossy implementation, we have requantized the eigen images to 8 bpp. While this approach produces excellent results for the lossy system, it is not optimum for the lossless case. An exhaustive optimization procedure to identify the proper quantization procedure for the individual eigen images subject to the constraint to simultaneously minimize, both the quantization error impact and the compression rate is a formidable challenge. It has not, however, been addressed in our current study.

2. *Compensation for eigen image quantization.*

   An alternate, also suboptimal approach, is to compensate for the negligible, but finite, error introduced by the eigen image requantization. It is assumed that the bandwidth required to produce a truly lossless representation from the virtually lossless case is reasonable. Again, the experimental details are the subject of future studies.

EXPERIMENTAL RESULTS

We have performed various experiment using the TIROS 5 band multispectral imagery. The purpose is to demonstrate the benefit of utilizing the additional spectral decorrelation compared with processing the individual spectral planes. Fig 2 illustrates the impact of spectral decorrelation by showing the five original images and the five eigen planes. Although only five planes are utilized, the first eigen image dominates the set. The additional planes showing decreasing "energy" content.

The experiments with the lossless systems are demonstrated in fig 3. The first two bars refer to generic lossless techniques (GNU gzip, UNIX compress) and the third bar indicates the "standard" lossless JPEG implementation. The last bar represents implementation of the adaptive multispectral compression algorithm utilizing the lossless JPEG. No correction was made for the eigen image quantization. It should be further noted that compression factor relates to the spectral components for the first three cases. For the multispectral case, the result refers to the eigen images. The overall result is, however, the same whether the averaging is over the spectral components or the eigen images.

One can make the following qualitative assessments: The lossless JPEG outperforms the generic techniques for each spectral component. The overall efficiency of the multispectral technique produces over 20% additional efficiency improvement. Note, the first two eigen images require additional bits, which are more than compensated by relevant efficiency in processing the remaining three eigen images. Fig.3 illustrates the quantitative details.

CONCLUSIONS

Preliminary experiments demonstrate the benefits of utilizing true multispectral processing to optimize the lossless compression efficiency. The extension of the previously developed TATCA system to the lossless / virtually lossless case, although beneficial, requires several additional processing considerations. More detailed implementation scenarios are the subjects of ongoing studies and will be reported in future publications.

REFERENCES

[1] J. A. Saghri, A. G. Tescher and J. T. Reagan, "Practical Transform Coding of Multispectral Imagery," IEEE Signal Processing Magazine, pages 32-43 (1995).

[2] N. D. Memon, K. Sayood and S. S. Magliveras, "Simple Method for Enhancing the Performance of Lossy Plus Lossless Image Compression Schemes," J. of Electronic Imaging, pages 245-251 (1993).

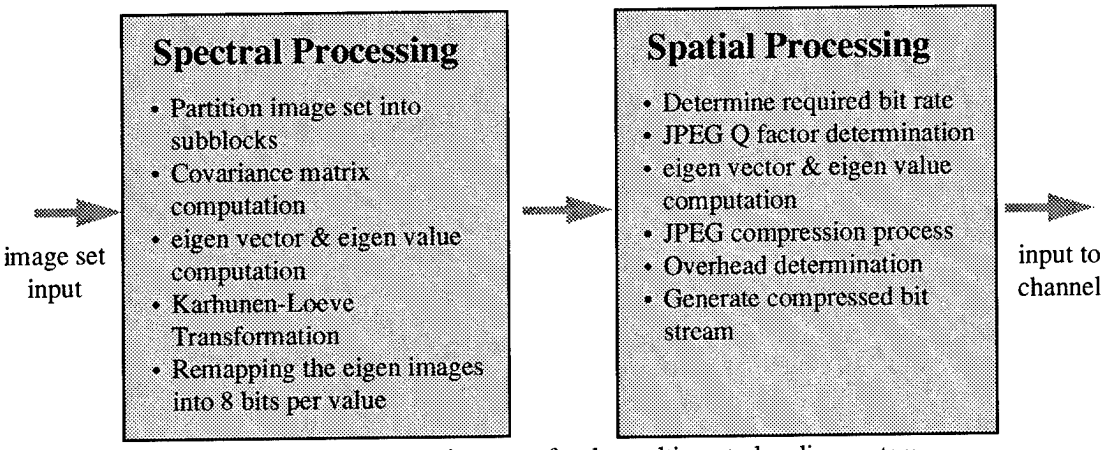


Figure 1. Basic processing steps for the multispectral coding system

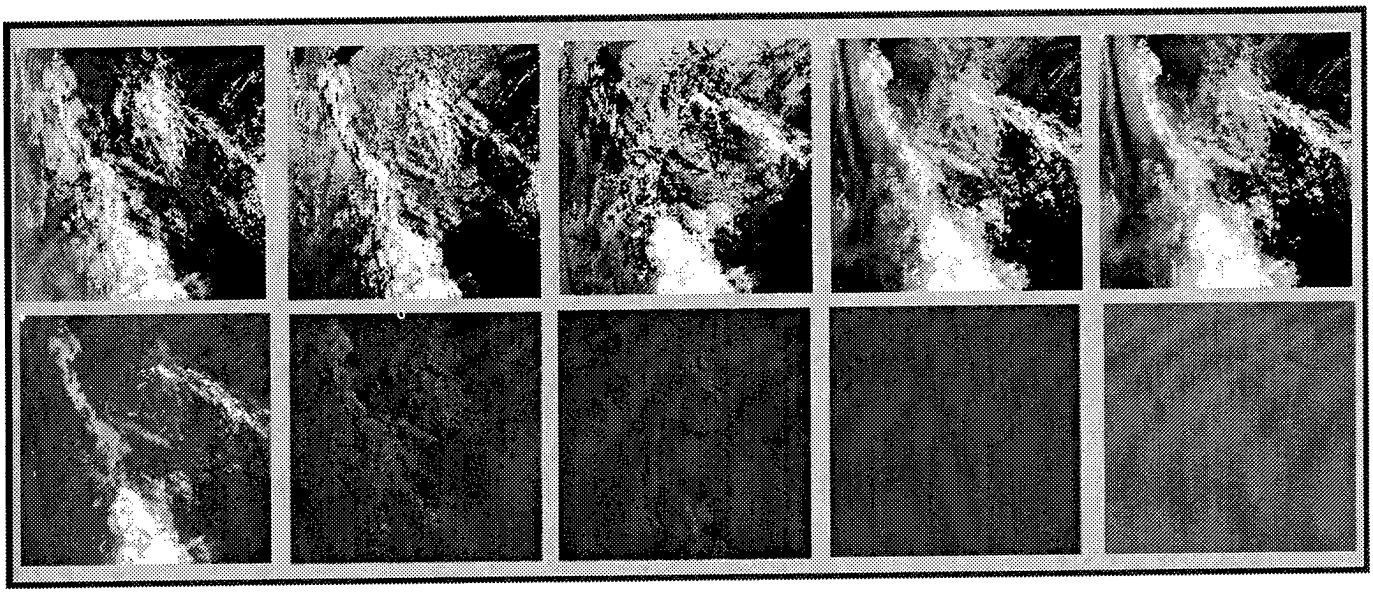


Figure 2. Original TIROS 5-Band, 8-bpp images and the spectrally decorrelated eigen images

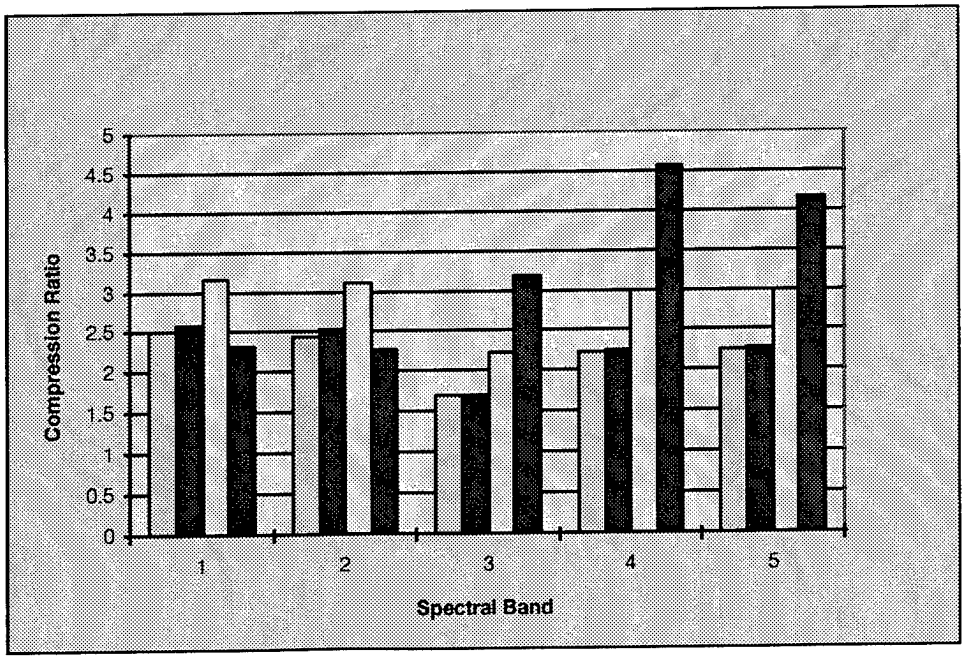


Figure 3. Comparison of Lossless Codecs of 5 band 8 bpp images

Progressive Model-Based VQ for Image Data Archival and Distribution

Mareboyana Manohar
Department of Computer Science, Bowie State University, Bowie, MD 20715
email: manohar@cosc.bsu.umd.edu
James C. Tilton
Information Sciences and Technology Branch, Code 935, NASA/Goddard Space Flight Center
Greenbelt, MD 20771, email: tilton@chrpisis.gsfc.nasa.gov

Abstract -- Vector Quantization (VQ) based lossy compression techniques are ideally suited for image archival and distribution applications due to their asymmetrical computational properties. The practical use of VQ is however limited due to complications arising from design and maintenance of codebooks. Model-Based VQ (MVQ) is a variant of VQ with the computational properties of VQ but without complications from explicit handling of codebooks. In MVQ, error models combined with a Human Visual System (HVS) model are used to generate an implicit model codebook. The decoder generates same codebook using the model parameters thus eliminating the need for training algorithm, transmitting and maintaining the codebooks. This algorithm was tested on several NASA images and results were published [1-2]. In this paper we describe Progressive MVQ along the lines of Progressive VQ [3] and evaluate its performance on NASA images.

INTRODUCTION

Vector Quantization (VQ) is an attractive lossy compression technique for image data archival and distribution due to its asymmetrical computational property. It has the least computational burden on the user compared to some symmetrical techniques such as JPEG/DCT[4].

The performance of the VQ depends heavily on the codebooks employed. The codebook generation is generally a computationally intensive. The codebooks generated on a training set provide optimal performance on the training set whilethe performance is suboptimal for images outside the set The rate-distortion performance of the VQ compression technique also depends on the codebook size. Large codebooks are required for better performance[2]. Large codebooks pose some practical problems of generating them and maintaining the copies with decoders. Data users would see this as unwelcome burden. This codebook management problem is a significant detraction from making VQ approaches a viable option for data archival and distribution.

We have developed a Model-Based VQ (MVQ) [1-2] which eliminates the need for codebook training and management. There is a slight computational overhead compared to VQ both in coding and decoding which is independent of the size of the input image being coded/decoded. We have reported in our earlier work [2] the performance characteristics of MVQ.

0-7803-3068-4/96$5.00©1996 IEEE

In this paper, we propose a technique of using the MVQ for progressively compressing the image data into multiple levels for effective data distributions. In the following sections we describe briefly the MVQ technique, and how MVQ can be used in progressive mode and present some results on progressive compression using MVQ.

MODEL-BASED VQ

In MVQ, the image to be compressed is decomposed into nonoverlapping blocks (4x4). Block means are computed and losslessly compressed using standard algorithms such as JPEG, or Ziv-Lempel. The block means are subtracted from the block generating mean removed residuals. Assuming the mean removed error fits Laplacian distribution, MVQ generates errors using uniform random number generator and converts them to Laplacian by logarithmic mapping [1-2]. The mean of the Laplacian distribution, λ $(=\sigma_e/\sqrt{2})$ is computed from the block residuals. The model generated errors are independent and identically distributed (i. i. d). But the source errors are not independent. Therefore, the model generated errors are grouped together into vectors (the size of the block) and appropriate correlations are imposed on model generated error residuals by using Human Visual Systems (HVS). One way to impose HVS properties on codebook vectors generated by Laplacian model is to DCT transform the vectors, weight the result with HVS DCT weight matrix, and inverse DCT transform the result to get back the vectors that have the correlations corresponding to HVS. The weight matrix is employed is given in [1. The compression (CR) from MVQ is given by

$$CR = \frac{k * b}{b + \log_2(n_c)} \qquad (1)$$

where b is number of bits per pixel in the original image data, k is the vector (block) size and n_c is number of model codes generated. Equation (1) is a conservative estimate of CR, because it does not account for lossless compression of block means. The MVQ decoder generates the same codevectors that encoder used by using the parameter, λ contained in the encoded data file. The decoder gets the residue vector corresponding to every index of the encoded vector (X_i) and adds to the corresponding block mean (μ_i) to obtain the

reconstructed vector ($X_i^{'}$) . Distortion, D between the input image and reconstructed image can be expressed in terms of Mean Squared Error (MSE) and is given by

$$D = \sum_i \left\| X_i - X_i^{'} \right\| \qquad (2)$$

where $\| \|$ is Euclidean norm between the vectors input vector, X_i and reconstructed vector, $X_i^{'}$. The compression ratio is directly proportional to the vector size, k and inversely proportional to the logarithm of number of model codevectors.

PROGRESSIVE MVQ

Progressive compression refers to a form of image data compression in which the first part of the compressed file (that is either transmitted to a remote site or stored locally) can be used to reconstruct an approximate representation of the image. The remaining portions of the compressed file contribute increasingly detailed information to the reconstruction of the image until the image is losslessly reconstructed when the entire compressed file is received over the network or read from local storage.

Progressive compression is usually accomplished by decomposing the original image file into a hierarchy, in which the highest level is the initial data rendition. The lower levels of the hierarchy comprise details that are missing in the upper levels. The data rendition at the highest level of hierarchy, called browse data, should be accurate so that it is possible to make a decision concerning whether or not the data is useful for the specific application. If the decision is negative, the cost of the decision is the cost of obtaining the browse data. If the decision is positive, there are two options: i) the users can either get the successive detail data from the hierarchy and buildup the data by adding details to initial browse data until the data precision is adequate and then terminate the transmission, ii) or the users can get the remaining data set from the hierarchy to reconstruct the data in lossless mode. VQ can be used in progressive compression mode by using VQ compression on successive residuals as described in [3].

The block schematic of progressive MVQ is shown in Fig.1. The first stage of MVQ creates block mean file, In.bmn.C (C indicates compressed file using appropriate lossless compression technique). The successive MVQcode and MVQdecode compress/decompress residual images for which block means are zeros. In the figure MVQ progressive compression decomposes the input image into four levels, although, in principle, any number of levels can be used. To reconstruct the input image without loss, the last residual has to be losslessly compressed. Image reconstruction from these data is exactly the reverse process. Every successive data is used to refine reconstructed image until, either the quality of the reconstructed image is satisfactory or the reconstructed image exactly same as the input image.

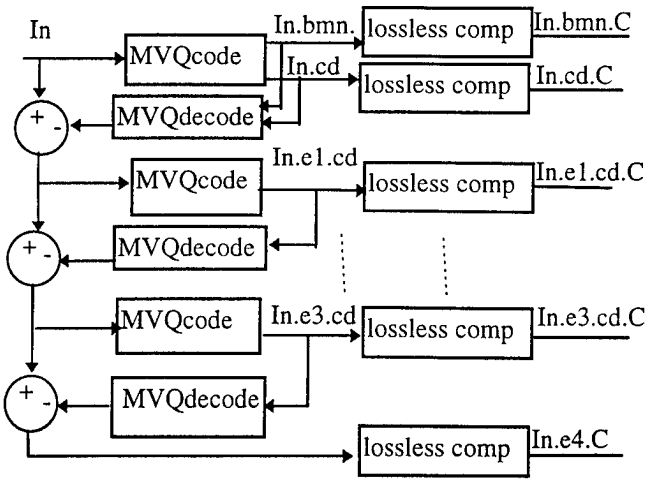


Fig. 1. Block schematic of Progressive MVQ compression

RESULTS AND DISCUSSIONS

Progressive MVQ compression and decompression were tested on remote sensed image of Washington, D. C. (Fig. 4a). This image is compresses to a compression ratio of 1.458 by using Ziv-Lempel lossless compression technique. By using image specific lossless compression techniques some improvement in compression ratio can be obtained. The rate distortion characteristics are studied with codebook size as parameter (Fig. 2). We can obtain lossless reconstruction of the input image by adding the losslessly compressed last residual data to the previous rendition. This can be obtained for various levels of decomposition. The number of levels of decomposition in our experiments varied from 1 to 4. Level 1 corresponds to straight lossless compression ratio of 1.458using Ziv-Lempel on Fig. 4a. The 2 level decomposition corresponds to MVQ compressed data of the input image and losslessly compressing the difference between the input image and reconstructed image. In Fig. 3, the effective lossless compression ratio vs. number of levels of decomposition with internal codebook size as a parameter are plotted. We see that overall lossless compression ratio is slightly better than straight lossless compression for level 1 and decreases for levels greater than 1. The results are not as dramatic as in the case of progressive VQ as reported in [3]. This may be attributed to the optimality of the trained codebook for the class of images in the case of progressive VQ compared to model generated codebook in the case of progressive MVQ. The results of the reconstruction from four level decomposition on Washington, D. C. image are shown in Figure 4(b-d). In this figure, a 256x154 subimage extracted from the center of original 512x512 image is shown. One can notice the progressive refinement of the reconstructed image and lastly the image shown in Fig. 4d is exact reconstruction of Fig. 4a.

ACKNOWLEDGMENT

This research effort is supported by NASA Grant NAG-5-2829 through an RTOP from Mission to Planet Earth.

REFERENCES

[1] M. Manohar and J. C. Tilton, "Model-Based VQ for Image Data Archival, Retrieval and Distribution," Visual Information Processing IV, Proc. of the SPIE International Conference, Orlando, FL, April 17-18, 1995, pp. 190-196.

[2] M. Manohar and Tilton, "A comparison of Model-Based VQ Compression with other VQ approaches", 1995 Science Information Management and Data Compression Workshop, October 26-27, 1995.

[3] M. Manohar and J. C. Tilton, "Progressive Vector Quantization on Massively Parallel SIMD Machine with Application to Multispectral Image Data.

[4] W. Pennebaker and J. Mitchell, JPEG Still Image Data Compression Standard, pp. 29-64, Van Nostrand, 1993.

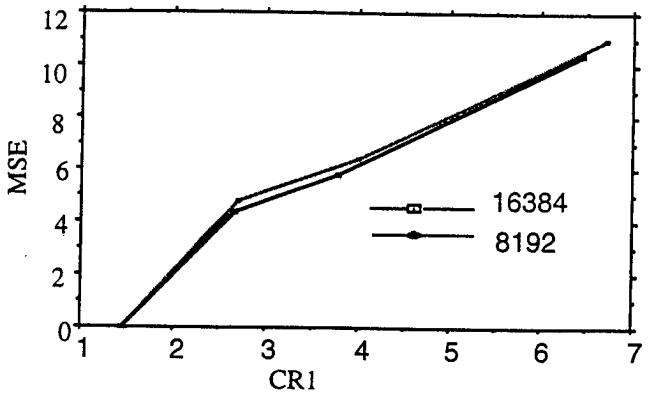


Figure 2. Rate-distortion performance of Progressive MVQ for codevectors 16384, and 8192

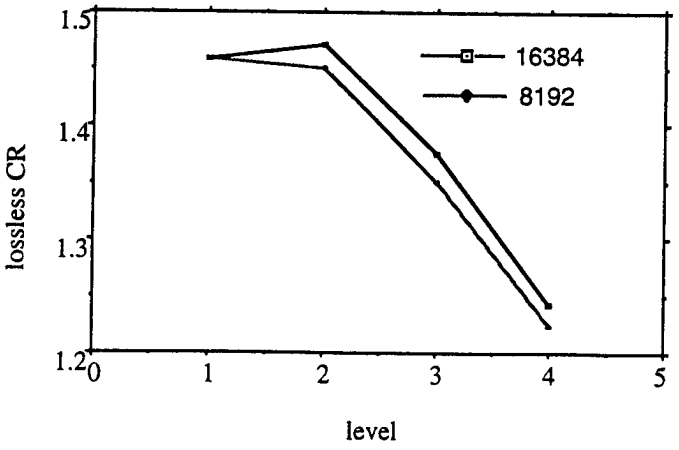


Figure 3: Lossless compression Vs. number of levels of decomposition



Figure 4. a) Washington, D. C. image, b) First level reconstructed image (CR = 6.5), c) Second level reconstructed image by adding details (CR = 3.78), d) Losslessly reconstructed by adding all the details (CR = 1.458)

Effect of Compression on Physical Parameters Derived from Polar Ice Radiances

K. M. St.Germain[1] and K. Sayood[2]

[1]Department of Electrical Engineering and Center for Electro-Optics
University of Nebraska-Lincoln, Lincoln, NE 68588-0511, USA
Tel: 402-472-9604 Fax: 402-472-4732 Email: kst.germain@unl.edu

[2]Information Technologies Research Institute
Marmara Research Center, TUBITAK
PK 21, Gebze 41470, Kocaeli - Turkey

Abstract— This study presents a comparison of the results of three different compression schemes when applied to remotely sensed arctic radiance images. Images obtained via Special Sensor Microwave/ Imager (SSM/I) are compressed using three different compression schemes at varying levels of compression and are evaluated using the ice concentration and ice type derived from the radiance values as metrics. The results show that the DRIQ compression scheme consistently performed better than the MRVQ and DCAVQ algorithms.

I. Introduction

Image compression schemes have generally been designed with the assumption that the reconstructed image will be viewed by a human observer. As such, distortions that are not perceptually discernible are considered acceptable. However, in a scientific environment the criterion for acceptability or unacceptability of the reconstruction are substantially different [1]. In remote sensing the obtained image is generally processed to extract parameters of interest. Remotely sensed microwave emission images of the Arctic are used to obtain a number of different parameters including ice concentration and ice type. In this study we look at some of the issues that need to be addressed when designing compression algorithms for images of polar ice and evaluate the effects of several compression algorithms on the extracted products. Our performance metrics are therefore the errors introduced in the ice concentration and ice type estimates, as derived by the NASA Team Algorithm.

In the following section we describe the datasets, data products and error tolerance. Section III contains a description of the compression algorithms. The results are evaluated in Section IV.

II. Arctic Remote Sensing

On average, polar sea ice covers only about 7% of the ocean surface, but it's impact on the global climate is tremendous. By changing the earth's surface albedo and restricting fluxes of energy between the ocean and the atmosphere, the polar sea ice is a critical component of the global climate modeling effort.

Monitoring polar sea ice on a global scale is accomplished by satellite borne remote sensing systems. Passive microwave sensors such as the Scanning Multichannel Microwave Radiometer (SMMR) and more recently the Special Sensor Microwave/Imager (SSM/I) have proven to be very effective in monitoring ice extent, concentration, and "type." Ice concentration refers to the fractional ice cover within an image pixel. The ice type typically distinguishes between ice in two categories: "first year" ice and "multi-year" ice. Multi-year ice is sea ice that has survived at least one summer melt season, circling in the Arctic Ocean. The seasonal temperature cycling causes the surviving ice to desalinate, thus making its radiometric properties distinguishable from those of first year ice.

Several algorithms have been proposed to estimate ice concentration and type from SMMR and SSM/I radiances. The most commonly used algorithm, and the one we use in this study, is the NASA Team Algorithm [2], [3]. The technique relies on the microwave polarization and spectral characteristics of open water and the two ice types through the spectral gradient ratio and the polarization ratio. The spectral gradient ratio measures the spectral difference between the 19 GHz and 37 GHz vertically polarized emission, while the polarization ratio measures the polarization of the 19 GHz emission. Generally speaking, the polarization ratio is strongly dependent on ice concentration and the gradient ratio is strongly dependent on the ice type.

The precision of the estimates of ice concentration are estimated to be in the range of 5% to 9%. The multi-year ice concentrations are less robust, with error bars on the order of 13% to 25%. The standard deviation of ice concentrations in midwinter ranges form ± 2 % to ± 4 %. This may also server as an estimate of the upper limit on the ice concentration precision [4].

III. Compression Algorithms

We use three different compression schemes at different levels of compression. The compression schemes are a differentially encoded scheme with recursively indexed quantization (DRIQ) [5], a distortion constrained adaptive vector quantizer (DCAVQ) and a mean removed vector quantizer (MRVQ). The first two algorithms were designed using a per pixel distortion constraint, while the third algorithm uses an average squared error distortion

K. Sayood is on leave from the Department of Electrical Engineering, University of Nebraska-Lincoln.

0-7803-3068-4/96$5.00©1996 IEEE

constraint. This distinction is important in that unlike images destined for human perception the individual pixel values in scientific images can have a significant effect on the extracted parameters and hence on the performance.

In the differentially encoded scheme the value of the pixel to be encoded is predicted using the previous reconstructed pixels. The prediction is subtracted and the prediction error is quantized using the recursively indexed quantizer (RIQ). The recursively indexed quantizer is effectively an infinite level uniform quantizer with the thresholds being the mid-points of output levels. The quantizer with infinitely-many output levels with uniform spacing Δ yields granular distortion only. The magnitude of the distortion is bounded by $\Delta/2$. The quantizer levels are encoded using recursive indexing.

Recursive indexing is a mapping of a countable set to a collection of sequences of symbols from another set of finite size [6]. Given a countable set $A = \{a_0, a_1, \ldots\}$ and a finite set $B = \{b_0, b_1, \ldots, b_{M-1}\}$ of size M, the recursive indexing of A by B is a mapping I of A to the collection of all sequences of symbols from B such that

$$I(a_i) = \underbrace{b_{M-1}b_{M-1}\ldots b_{M-1}}_{q \text{ times}} b_r \text{ if } i = q(M-1)+r \quad (1)$$

where q and r are the quotient and remainder of i when divided by $M-1$. Recursive indexing is a one-to-one mapping, a symbol-to-variable length, M-ary, prefix-free code and therefore uniquely and instantaneously decodable.

The image pixels for the SSM/I data are given as 16 bits per pixel. This rather large dynamic range makes it hard to use many of the standard VQ approaches as in order to adequately represent this range we need impractically large codebooks. Consider compressing the input with a compression ratio of 8:1. For a 16 bit input this means that we need to represent the input using two bits per pixel. For a 16 dimensional VQ this results in a codebook size of $2^{16\times 2} = 4,294,967,296$. To get around this problem we used two different approaches. In the first we used an adaptive vector quantizer which adaptively builds its codebook. The second approach was to use a mean removed vector quantizer in which the bit resources are divided between a vector quantizer and an encoder for coding the mean.

The DCAVQ is a vector quantizer with two distinct codebooks C_1 and C_2. The codebook C_1 consists of 16 dimensional vectors and the second for 4 dimensional vectors. The image is divided into 4×4 blocks. Each block is first quantized using C_1. The difference between the input block and the reconstructed block is compared against a threshold on a pixel by pixel basis. If all pixels pass the threshold test the label of the vector is stored or transmitted. If not, the block is subdivided into four 2×2 blocks which are then encoded using C_2. After encoding the reconstructions are again subjected to the threshold test. If all four vectors pass the threshold test the corresponding labels are stored or transmitted and the 16 dimensional vector constructed by concatenating the four dimensional reconstructions is added to the codebook C_1. If C_1 has already reached a prespecified maximum size the vector that has been least used is deleted from C_1. A counter is kept for each vector in the codebook. At each encoding step the count for the vector in the codebook which is used is incremented by one and the count for all vectors in the codebook that have not been used is decremented by one. When a vector needs to be deleted from the codebook the vector with the lowest count is discarded. If any of the four dimensional vectors fails the threshold test the individual pixels are quantized using a recursively indexed quantizer. When this happens the codebook C_2 is updated in a manner similar to the update procedure described for C_1 described above. blocks.

In the mean removed vector quantizer [7] we again divide the image into 4×4 blocks. For each block we first remove the mean which is then losslessly encoded. The residual is then quantized using a vector quantizer.

IV. Results

The results obtained using the DRIQ algorithm for rates of 5 bits per pixel and 2.5 bits perpixel are shown in Table I. The data show that the DRIQ algorithm with a compression rate of 5 bits per pixel yields errors on the order of 2 to 3 %. The November 27 error rate is a bit higher because the original data set had an unusually high number of missing (zero) data points. Through the compression/decompression process some of these pixels seem to have "contaminated" neighboring pixels, thereby raising the overall RMS difference in retrieved products by a factor of two. The performance is, of course, not as robust at the 2.5 bits per pixel compression rate, particularly for the multiyear ice concentration. Although the product retrieval images are noticeably noisy, the important trends are preserved even at this compression rate.

The results obtained from using the MRVQ algorithm are shown in Table II. These results for the same compression rates range from 18 to 25 % at the 5 bits per pixel rate, and from 21 to 32 % at the 2.5 bits per pixel rate. The products derived after data compres-

	16 Oct	27 Nov	23 Dec
5 b/p			
Total Ice Conc.	3.5 %	5.1%	3.5 %
Multi-Year Conc.	2.3 %	4.3 %	2.5 %
2.5 b/p			
Total Ice Conc.	7.2 %	10.2%	6.8 %
Multi-Year Conc.	8.1 %	11.2 %	8.2 %

TABLE I

RMS DIFFERENCE BETWEEN PRODUCTS DERIVED FROM UNCOMPRESSED IMAGES AND IMAGES COMPRESSED USING THE DRIQ ALGORITHM.

	27 Nov	23 Dec
5 b/p		
Total Ice Conc.	22.3%	18.5 %
Multi-Year Conc.	24.6 %	19.6 %
2.5 b/p		
Total Ice Conc.	27.9%	21.0 %
Multi-Year Conc.	31.3 %	24.3 %

TABLE II
RMS DIFFERENCE BETWEEN PRODUCTS DERIVED FROM UNCOMPRESSED IMAGES AND IMAGES COMPRESSED USING THE MRVQ ALGORITHM.

	27 Nov	23 Dec
5 b/p		
Total Ice Conc.	5.7%	4.4 %
Multi-Year Conc.	5.4 %	4.6 %
2.5 b/p		
Total Ice Conc.	13.9%	10.2 %
Multi-Year Conc.	16.9 %	14.3 %

TABLE III
RMS DIFFERENCE BETWEEN PRODUCTS DERIVED FROM UNCOMPRESSED IMAGES AND IMAGES COMPRESSED USING THE DCAVQ ALGORITHM.

sion/decompression by the MRVQ algorithm are not usable.

Finally, the results obtained using the DCAVQ algorithm are shown in Table III. As with the results from the DRIQ algorithm, the RMS error is lower for the Dec 23 data set than for the Nov 27 data set. The DCAVQ algorithm performs nearly as well as the DRIQ algorithm at the 5 bits per pixel rate. It's performance deteriorates, however, at the 2.5 bits per pixel compression rate. This is most noticeable for the most complete data set (Dec 23).

V. Conclusion

The DRIQ algorithm appears to outperform the MRVQ and DCAVQ algorithms in the application studied here. The DRIQ compression/decompression scheme contributes error that is reasonable with regard to the currently accepted level of uncertainty for Arctic ice concentration and ice type estimates. Even at the highest compression rate, the important trends are preserved by the DRIQ algorithm. Although the DCAVQ algorithm performed well at the lower compression rate, it struggled to preserve the trends at the highest compression rate.

Note that the results are substantially better for compression schemes which have a per pixel distortion constraint, that is DRIQ and DCAVQ, than for the compression scheme that attempts to minimize the mean squared error, namely the MRVQ scheme. This indicates the need for the development of compression schemes for scientific data based on per sample distortion constraints rather than the average distortion constraints typically used when designing compression schemes for data which is to be perceived by humans.

Acknowledgments

The data for this study was provided by the National Snow and Ice Data Center, Cooperative Institute for Research in Environmental Sciences (CIRES), University of Colorado, Boulder, Colorado.

References

[1] K. Sayood. Data Compression in Remote Sensing Applications. *IEEE Geoscience and Remote Sensing Newsletter*, (84):pp. 7–15, September 1992.

[2] Cavalieri, D.J., *et. al.* NASA Sea Ice Validation Program for the DMSP SSM/I: Final Report, NASA Technical Memorandum 104559, National Aeronautics and Space Administration, Washington, DC, pp. 126, 1992.

[3] Swift, C.T., D.J. Cavalieri, An algorithm to measure sea ice concentration with microwave radiometers, *EOS, Transactions*, American Geophysical Union, 66(49), 1087-1099, Washington DC, 1985.

[4] Carsey, F.D. Ed., Microwave Remote Sensing of Sea Ice, American Geophysical Union, Geophysical Monograph 68, Chapters 3 and 10, 1992.

[5] K. Sayood and S. Na. Recursively Indexed Differential Pulse Code Modulation. In *Proceedings IEEE/DIMACS Joint Workshop on Coding and Quantization.* IEEE, October 1992.

[6] K. Sayood and S. Na. Recursively Indexed Quantization of Memoryless Sources. *IEEE Transactions on Information Theory*, IT-38, November 1992.

[7] A. Gersho and R.M. Gray. *Vector Quantization and Signal Compression.* Kluwer Academic Publishers, 1991.

Lossless Seismic Data Compression using Adaptive Linear Prediction

Giridhar Mandyam and Neeraj Magotra

Department of Electrical and Computer Engineering
The University of New Mexico
Albuquerque, NM 87131

Wes McCoy

Motorola Incorporated
5401 North Beach Street
Fort Worth, TX 76137

ABSTRACT

This paper presents a comparison of adaptive linear predictors as applied to the area of lossless compression of seismic waveform data. Three methods are explored: the normalize least-mean square (NLMS) algorithm, the gradient adaptive lattice (GAL) algorithm, and the recursive least squares lattice (RLSL) algorithm. When compared to standard linear prediction techniques, all three of these methods require little overhead, are more computationally efficient, and can be implemented using floating point techniques. With respect to a standard seismic database, the RLSL filter outperforms the other two methods in nearly all cases tested.

1. INTRODUCTION

Lossless compression of data is extremely important in cases where immense amounts of data are present and the integrity of this data must be preserved. One finds such an instance in the case of seismic data, since not only large amounts of seismic data are collected by many different organizations, but this data must fully retain its information for accurate analysis. For instance, vast quantities of seismic data are collected and processed for monitoring purposes related to the Comprehensive Test Ban Treaty.

Usually, lossless compression is achieved in two stages: the first stage is a *decorrelator* which exploits redundancy between neighboring samples in a data sequence, and the second stage is an *entropy coder* which takes advantage of the decreased variance of the data. In this paper, we will be concerned with the first stage. Normally, *linear prediction* is used for decorrelation. Given a sample sequence of length K, $ix(n)$ $(0 \leq n \leq K-1)$, one can design a linear predictor of order M by using M predictor coefficients $\{b_i\}$ to find an estimate $\hat{ix}(n)$ for each sample in $ix(n)$:

$$\hat{ix}(n) = \sum_{i=0}^{M-1} b_i ix(n-i-1) \qquad (1)$$

Obviously, M should be much less than K to achieve compression, because $\{b_i\}$ must be included with the compressed data. The estimate $\hat{ix}(n)$ is not the same as the original value; therefore a residue sequence is formed to allow exact recovery of $ix(n)$:

$$ir(n) = ix(n) - \hat{ix}(n) \qquad (2)$$

If the predictor coefficients are chosen properly, the entropy of $ir(n)$ should be less than the entropy of $ix(n)$. Choosing the coefficients $\{b_i\}$ involves solving the *Wiener-Hopf* equations:

$$\begin{aligned} R_{0,0}b_0 + R_{0,1}b_1 + \cdots + R_{0,M-1}b_{M-1} &= R_{M,0} \qquad (3)\\ R_{1,0}b_0 + R_{1,1}b_1 + \cdots + R_{1,M-1}b_{M-1} &= R_{M,1}\\ &\vdots\\ R_{M-1,0}b_0 + R_{M-1,1}b_1 + \cdots + R_{M-1,M-1}b_{M-1} &= R_{M,M-1} \end{aligned}$$

where $R_{i,j}$ is the average over n of the product $ix(n)ix(n+(i-j))$. This can be represented as the matrix-vector product

$$\mathbf{Rb} = \mathbf{p} \qquad (4)$$

where $\mathbf{R}$ is the M by M matrix defined in (3), $\mathbf{b}$ is the M by 1 vector of predictor coefficients, and $\mathbf{p}$ is the M by 1 vector in (3).

While the method of linear prediction is effective, it suffers from the problem of finding a solution to the Wiener-Hopf equations in (3), which becomes increasingly computationally expensive with larger data block sizes. Adaptive FIR filters have been proposed and used successfully as a way of solving this problem [2]. With a fixed filter size, M, there is a variety of stochastic gradient methods to adapt the filter.

2. ADAPTIVE FILTERS

Adaptive filters encompass many classic stochastic gradient techniques, such as the LMS or RLS algorithms. One common method is discussed here, the normalized least mean square algorithm (NLMS) [3]. With the sample sequence index denoted by n, the set of predictor coefficients $\{b_i\}$ in (1) is now time-varying, and is represented by the

0-7803-3068-4/96$5.00©1996 IEEE

column vector $\mathbf{b}(n) = [b_0(n) \cdots b_{M-1}(n)]^{\mathbf{T}}$, where $[]^{\mathbf{T}}$ is the transpose operator. If the input to the filter is the vector $\mathbf{ix}(n) = [ix(n-1) \cdots ix(n-M)]^{\mathbf{T}}$, then a time-varying residue [4] is given by

$$ir(n) = ix(n) - NINT\{\mathbf{b}^{\mathbf{T}}(n)\mathbf{ix}(n)\} \quad (5)$$

If two fixed parameters, a smoothing parameter β and a convergence parameter u, are specified, then $\mathbf{b}(n)$ is computed iteratively as follows:

$$\mathbf{b}(n+1) = \mathbf{b}(n) + \mu(n) ir(n) \mathbf{ix}(n) \quad (6)$$

$$\mu(n) = \frac{u}{\sigma_M^2(n)} \quad (7)$$

$$\sigma_M^2(n) = \beta\sigma_M^2(n-1) + (1-\beta)(ir^2(n-1)) \quad (8)$$

In order to reverse the algorithm without loss [4], the following equation may be used along with (6)-(8):

$$ix(n) = ir(n) + NINT\{\mathbf{b}^{\mathbf{T}}(n)\mathbf{ix}(n)\} \quad (9)$$

Therefore, one needs the initial predictor coefficients $\mathbf{b}(0)$, the initial data vector $\mathbf{ix}(0)$, and the error sequence $ir(n)$ to reconstruct the original $ix(n)$ sequence exactly. Moreover, in this approach, the coefficients $\mathbf{b}(n)$ and the data vectors $\mathbf{ix}(n)$ do not have to be transmitted at all after start-up. We note that the functions used in encoding must be repeated exactly in decoding. Therefore all quantities used in (6)-(8), that is, u, β, $\mathbf{b}(0)$, and $\mathbf{ix}(0)$, must be stored in the compressed data frame exactly as they are used in the encoding process, so that they may be used in the same way in the decoding process. We also note that here it is not necessary to break the data up into frames as was the case with the linear predictor method described previously, and that in general this method requires less overhead than the linear predictor method.

3. LATTICE FILTERS

Although the NLMS adaptive filter is effective, it sometimes displays slow convergence, resulting in a residue sequence of high-variance. This has lead to the use of a class of adaptive filters known as *lattice filters*. Although the implementation of lattice filters is more involved than that of the NLMS algorithm, faster convergence usually makes up for the increased complexity. A simple M-stage adaptive lattice filter is shown in Figure 1; this filter is known as the *gradient adaptive symmetric lattice* (GAL) filter. The update equations for this filter are [4]

$$b_i(n) = b_{i-1}(n-1) + k_i(n) f_{i-1}(n) \quad (10)$$

$$f_i(n) = f_{i-1}(n) + k_i(n) b_{i-1}(n-1) \quad (11)$$

$$k_i(n) = k_i(n-1) + \alpha \frac{f_i(n-1)b_{i-1}(n-2) + f_{i-1}(n-1)b_i(n-1)}{\sigma_{i-1}^2(n-1)} \quad (12)$$

$$\sigma_{i-1}^2(n-1) = \beta\sigma_{i-1}^2(n-2) + (1-\beta)(f_{i-1}^2(n-1) + b_{i-1}^2(n-2)) \quad (13)$$

$$f_M(n) = ix(n) + NINT\{\sum_{i=0}^{M-1} b_i(n-1)k_i(n-1)\} \quad (14)$$

where α is a convergence parameter, β is a smoothing parameter, $f_i(n)$ is the *forward prediction error*, and $b_i(n)$ is the *backward prediction error*. The recovery equation is [4]

$$ix(n) = f_M(n) - NINT\{\sum_{i=0}^{M-1} b_i(n-1)k_i(n-1)\} \quad (15)$$

An improvement on the GAL is the recursive least-squares lattice (RLSL) filter [3]. The Mth-order forward and backward prediction error coefficients, $\eta_M(n)$ and $\psi_M(n)$ respectively, are given by:

$$\eta_M(n) = \eta_{M-1}(n) + \Gamma_{f,M}(n-1)\psi_{M-1}(n-1) \quad (16)$$

$$\psi_M(n) = \psi_{M-1}(n-1) + \Gamma_{b,M}(n-1)\eta_{M-1}(n) \quad (17)$$

$$\Gamma_{f,M}(n) = -\frac{\Delta_{M-1}(n)}{B_{M-1}(n-1)} \quad (18)$$

$$\Gamma_{b,M}(n) = -\frac{\Delta_{M-1}(n)}{F_{M-1}(n)} \quad (19)$$

$$\Delta_{M-1}(n) = \lambda\Delta_{M-1}(n-1) + \gamma_{M-1}(n-1)\psi_{M-1}(n-1)\eta_{M-1}(n) \quad (20)$$

$$F_{M-1}(n) = \lambda F_{M-1}(n-1) + \gamma_{M-1}(n-1)\eta_{M-1}^2(n) \quad (21)$$

$$B_{M-1}(n) = \lambda B_{M-1}(n-1) + \gamma_{M-1}(n)\psi_{M-1}^2(n) \quad (22)$$

$$\gamma_M(n) = \gamma_{M-1}(n) - \frac{\gamma_{M-1}^2(n)\psi_{M-1}^2(n)}{B_{M-1}(n)} \quad (23)$$

The parameter λ is a fixed constant arbitrarily close to, but not equaling 1. The error residuals are computed as [4]

$$ir(n) = ix(n) + NINT\{\sum_{i=1}^{M} \Gamma_{f,i}(n-1)\psi_{i-1}(n-1)\} \quad (24)$$

4. SIMULATIONS

The three methods described above were compared with respect to several seismic data files quantized to 32 bits per sample) which were provided by the United States Geological Survey (USGS). The stations where this data was collected and the corresponding sampling rates are given in Table 1.

The RLSL performed better than the GAL or the NLMS algorithms. The seismic waveforms given in were each subjected to all three methods; the residue variances are given in Table 2. As can be seen, the RLSL outperformed the NLMS and GAL algorithms in nearly every case, with the residue variances reducing to lower values. The residue files associated with the RLSL filter were then subjected to the modified arithmetic coding method given in [5], with the resulting compression ratios (denoted by CR) given in Table 3. The results are promising, with the minimum compression ratio still exceeding two to one compression.

File	Location	Latitude	Longitude	Sampling Rate
anmbhz89	Albuquerque, NM	34.95	-106.5	20sps
anmbhz92	Albuquerque, NM	34.95	-106.5	20sps
anmehz92	Albuquerque, NM	34.95	-106.5	100sps
anmlhz92	Albuquerque, NM	34.95	-106.5	1sps
kipehz13	Kipapa, Hawaii	21.42	-158	100sps
kipehz20	Kipapa, Hawaii	21.42	-158	100sps
rarbhz92	Rarotonga, Cook Islands	-21.21	-159.8	20 sps
rarlhz92	Rarotonga, Cook Islands	-21.21	-159.8	1 sps

Table 1: Seismic Data Base

File	Input	NLMS	GAL	RLSL
anmbhz89	$1.87e^{9}$	$3.85e^{4}$	$6.81e^{1}$	$2.07e^{1}$
anmbhz92	$3.18e^{2}$	$2.26e^{1}$	$1.06e^{1}$	$9.24e^{0}$
anmehz92	$7.84e^{4}$	$2.17e^{4}$	$2.28e^{4}$	$1.82e^{4}$
anmlhz92	$4.44e^{5}$	$9.40e^{4}$	$7.61e^{4}$	$4.54e^{4}$
kipehz13	$2.45e^{3}$	$6.74e^{0}$	$8.22e^{0}$	$5.67e^{0}$
kipehz20	$1.52e^{4}$	$9.56e^{1}$	$7.17e^{1}$	$4.45e^{1}$
rarbhz92	$1.02e^{7}$	$2.05e^{3}$	$4.36e^{2}$	$2.71e^{2}$
rarlhz92	$1.76e^{8}$	$1.42e^{7}$	$2.21e^{7}$	$2.34e^{7}$

Table 2: Residue Variances

File	Input Size (bytes)	Output Size (bytes)	CR
anmbhz89	268000	40945	7.82
anmbhz92	288000	41305	8.72
anmehz92	56000	14995	5.24
anmlhz92	344000	122919	3.37
kipehz13	248000	30883	9.17
kipehz20	244000	40789	6.57
rarbhz92	288000	62025	5.20
rarlhz92	344000	153561	2.46

Table 3: Compression Results

5. CONCLUSIONS

Three adaptive linear prediction techniques have been applied to the area of lossless seismic waveform data compression. The RLSL filter in general outperformed the other two methods. This is encouraging, since the RLSL has practically no coefficient transmission overhead, and the data does not require blocking. Further analysis should be done into the statistical nature of the residuals for each respective adaptive filter, as suitable entropy coders can then be designed to achieved maximal compression.

6. REFERENCES

[1] Stearns, S.D., Tan, L.-Z., and Magotra, N. "Lossless Compression of Waveform Data for Efficient Storage and Transmission." *IEEE Transactions on Geoscience and Remote Sensing.* Vol. 31. No. 3. May, 1993. pp. 645-654.

[2] Widrow, Bernard and Stearns, Samuel D. *Adaptive Signal Processing.* Englewood Cliffs, NJ: Prentice-Hall, Inc., 1985.

[3] Haykin, Simon. *Adaptive Filter Theory.* Englewood Cliffs, NJ: Prentice-Hall, Inc., 1991.

[4] McCoy, J.W, Magotra, N., and Stearns, S. "Lossless Predictive Coding." *37th IEEE Midwest Symposium on Circuits and Systems.* Lafayette, LA. August, 1994.

[5] Stearns, Samuel D. "Arithmetic Coding in Lossless Waveform Compression." *IEEE Transactions on Signal Processing.* Vol. 43. No. 8. August, 1995. pp. 1874-1879.

[6] McCoy, J.W. *Lossless Waveform Data Compression.* Ph.D. Thesis. The University of New Mexico. 1995.

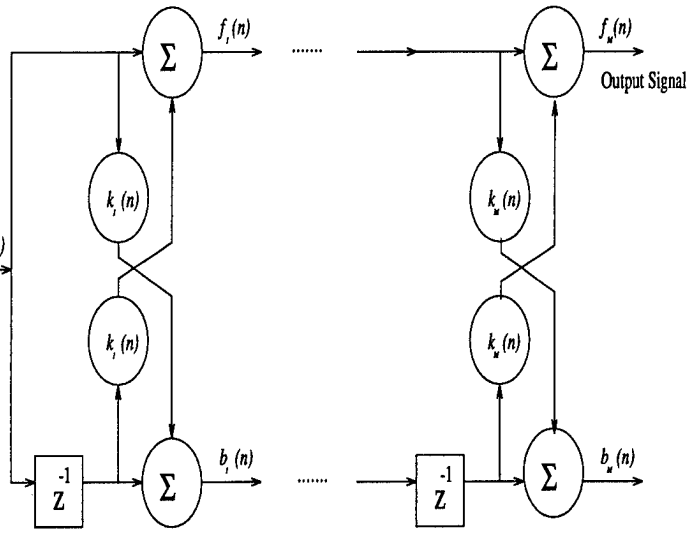


Figure 1: Gradient Adaptive Lattice (GAL) Filter

Performance of An Enhanced DCT Compression System for Space Applications

Pen-Shu Yeh*, Warner H. Miller* and Steve Hou+
*Goddard Space Flight Center, Code 738.3 Greenbelt, MD 20771
+The Aerospace Corporation, 2350 E. El Sequndo Blvd., El Sequndo, CA 90245
T: 301.286.4477 F:301.286.1751 EMail:psyeh@psy.gsfc.nasa.gov

Abstract -- A low bit-rate data compression system utilizing a hybrid transform has been implemented for space applications. This hybrid transform reduces blocking distortion inherent in a 2D DCT and has smaller distortion measurement.The system also employs a developed adaptive entropy coder to reduce overhead associated with Huffman code tables. The performance of the system will be given along with its comparison with a JPEG compression system.

INTRODUCTION

Low bit rate lossy video data compression has been used in many industrial applications including distribution of video on tapes and compact disc, and transmission of diagnostic imagery over low rate communication channels. The goal of this technique is to cram as much information into the storage medium or transmission channel as possible within the limitation of available hardware. The development of various low bit rate compression techniques accumulated enough momentum in the 80's that an industrial standards activity was initiated and finally in the early 90's, the JPEG standard was approved [1].

The baseline JPEG standard for still image transmission has several functional parts shown in Fig.1. A format conversion unit takes 8 lines of input data and converts it into 8x8 pixel blocks. A 2D DCT is used to transform the block into frequency components, these components are further quantized into integers. A zig-zag ordering is used to serialize these integers before the run-length and component magnitudes are coded by an entropy coder using either arithmetic code or Huffman code. JPEG gives excellent image quality in general for a compression ratio around and below 10:1. At higher compression ratio, the blocky distortion becomes vivid and objectionable to many applications.

Much effort has been focused on techniques that reduce blocky distortion. The promising ones are wavelet, subband, etc. However, for space applications there are several constraints:

- •The definition of a square frame may not exist. Except for square format CCD, many space sensors give long scanlines of several thousand pixels in multiple spectral bands which operate in a push broom mode, the storage and formatting of these data into square image required by some techniques would demand too much onboard resource.
- •Noise or interrupt in the space communication channel may induce error in the data stream. Error propagation at decompression should be minimized and the algorithm should self start at least at the start of a data packet.
- •For operational purpose, uploading of code tables should be kept at a minimum.
- •Scientific instruments require variable quantization from 8 to 16 bits.

In this paper, we present an enhanced JPEG system for space use. Like JPEG, this system requires data buffer on 8 scan lines and can interface easily with a packet data architecture. With proper choice of error control coding, the error propagation at decompression will be contained within a strip of 8 scanlines, yet this technique reduces blocky effect and simplifies implementation.

THE ENHANCED DCT SYSTEM FOR SPACE USE

The lapped orthogonal transform has been shown to exceed the DCT in both quantitative measurement and perceptual quality on signals. Its performance also compares favorably with wavelet technique [2]. A direct and efficient 2D implementation would require an additional large buffer to hold intermediate results than the baseline JPEG. Furthermore, the error propagation would extend beyond 8 scanlines. In our system, a modulated lapped transform (MLT) [2] is combined with a DCT to form the basis transformation. The MLT is applied along the scanline direction and the DCT in the other direction. The hybrid transform enhances the perfor-

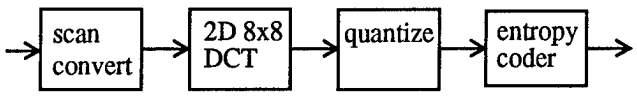


Fig. 1. JPEG functional modules

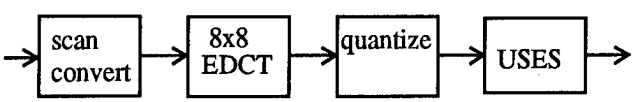


Fig. 2. Enhanced DCT system modules

0-7803-3068-4/96$5.00©1996 IEEE

mance of the more conventional DCT, and is termed the Enhanced DCT (EDCT) in Fig. 2.

In addition to the more compact transform, a second improvement comes from the use of an adaptive entropy coder, the universal source encoder for space (USES), which was developed for space use. The adaptive entropy coder is based on the Rice algorithm architecture [3][4], and has been shown equivalent to a set of Huffman codes, each optimal for a 1-bit entropy range. A major advantage of this algorithm is its fast adaptability to a wide range of data statistics, yet its implementation does not require lookup tables. This eliminates the need to either compute an local optimal Huffman code or to transmit one, as done in the baseline JPEG with Huffman code. With this adaptive technique, there will be no need to design, load and transmit the Huffman code. However, it does require a different run-length data format in order to achieve best system performance.

PERFORMANCE

The performance of the enhanced system is tested on many types of images. Two sets of results are presented. Both the EDCT and the JPEG baseline technique are applied to the same data set. A uniform quantization table has been used for the EDCT system. Quantitative measurement of mean square error (mse) is calculated on the decompressed image. The bit-rate (bits per pixel) vs. mse curves are shown in Fig. 3 and Fig. 4 for the images given in Fig. 5 and Fig. 6 respectively. The performance curve of EDCT in solid line, in general, lies below that of the JPEG, in dashed line at lower bit rate. Even at higher bit rate around 1 bit/pixel, when the quantitative measurement is similar in both cases, the perceptual quality is better for the EDCT technique.

STATUS OF DEVELOPMENT

The proposed technique has been simulated in software on various types of remote sensing data and is proposed as an experiment on the Lewis spacecraft. In the experiment, the EDCT technique will be used to compress multispectral data, using both 8x8 and 16x16 EDCT. As a comparison, a 16x16 DCT will be exercised as well.

A VLSI hardware chip is currently under development for execution of the EDCT module.

The adaptive entropy coder, USES, has been developed as a rad-hard VLSI chip. It is implemented as a lossless data compression module on the Lewis mission as a co-processor in the spacecraft computer. The USES algorithm has also been implemented on other missions in software.

CONCLUSION

The performance of the EDCT system exceeds that of JPEG at low bit rate. Even though at higher bit rate, the quantitative measurement of the two systems are similar, the constraint for space use makes the EDCT compression system a more suitable choice for space science missions.

REFERENCES

[1] William B. Pennebaker, Joan L. Michell, JPEG: Still Image Data Compression Standard, Van Nostrand Reinhold, New York, 1993.

[2] Henrique Marvar: The Lapped Orhogonal Transform and Its Applications, 1993.

[3] Rice, Robert F., Pen-Shu Yeh and Warner H. Miller, "Algorithms for High-Speed Universal Noiseless Coding," *Proc. of the AIAA Computing in Aerospace 9 Conference,* San Diego, CA, Oct. 19-21, 1993

[4] Yeh, Pen-Shu, Robert F. Rice and Warner H. Miller, "On the Optimality of a Universal Noiseless Coder," *Proc. of the AIAA Computing in Aerospace 9 Conference*, San Diego, CA, Oct. 19-21, 1993.

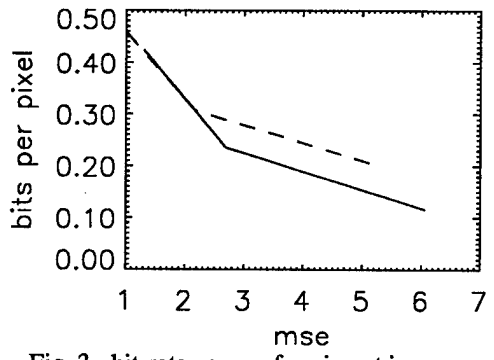


Fig. 3. bit-rate vs mse for airport image

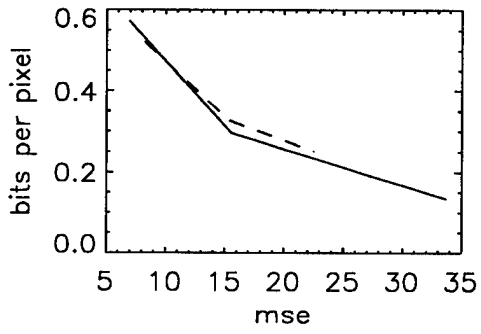
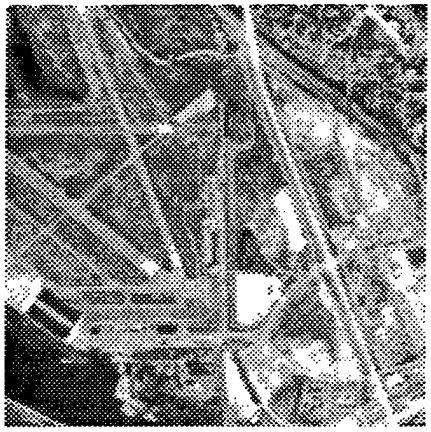
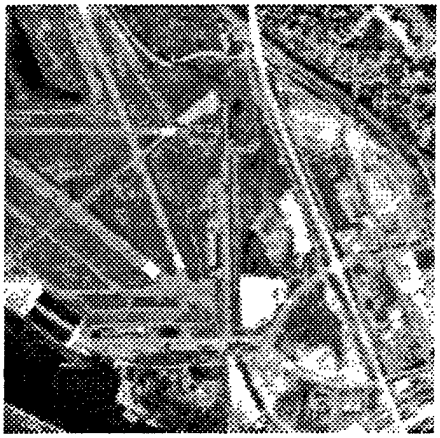


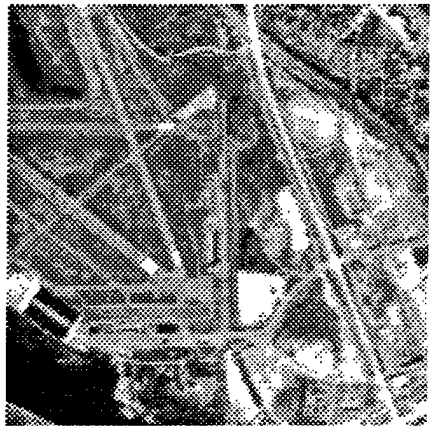
Fig.4. bit-rate vs mse for Advanced High Resolution Radiometer (AVHR) image



a. original

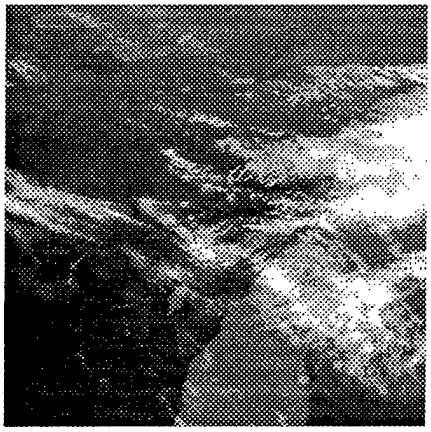


b. EDCT bit-rate 0.30 bits/pixel

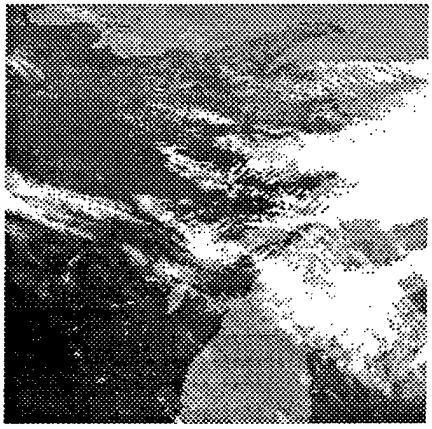


c. JPEG bit-rate 0.31 bits/pixel

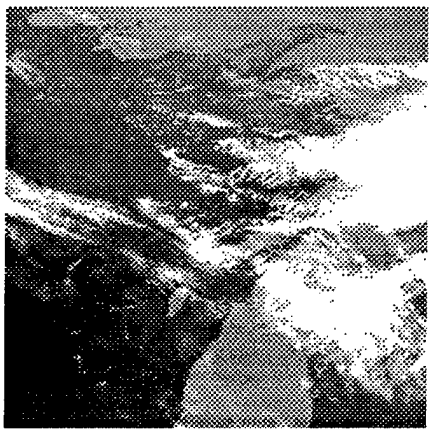
Fig. 5 airport image



a. original



b. EDCT bit-rate 0.30 bits/pixel



c. JPEG bit-rate 0.33 bits/pixel

Fig. 6 AVHR image

End-to-End System Consideration of the Galileo Image Compression System

K. Cheung K. Tong M. Belongie
Jet Propulsion Laboratory
Mail Stop 238-343, 4800 Oak Grove Drive, Pasadena, CA 91109
Tel: 818 -393-9480 Fax: 818-393-1717 Email: kmcheung@shannon.jpl.nasa.gov

May 29, 1996

Abstract[1]

In this article we describe the image compression scheme of the Galileo spacecraft and other downstream signal processing algorithms that enable efficient and robust transmission of data to Earth.

Introduction

We present a robust implementation of the Galileo image compression system. Due to the loss of the high gain antenna, the mission is replanned to incorporate advanced data compression, error correction, and other downlink communication functions to maximize data return. Most instrument data will be highly edited and compressed before downlink through a noisy and unpredictable channel. The data compression schemes share a common disadvantage, that channel errors in the compressed data tend to propagate in the reconstructed data. To ensure reliable communication we developed a Feedback Concatenated Decoder (FCD) for error-correction and error-detection, and a concealment strategy to prevent error propagation and realign the reconstructed data after decoder failure. We also developed a frame repair scheme that combats phase inversions and symbol insertion/deletion in the channel, and a frame merging scheme that prevent data loss due to station hand-over.

Image Compression

The Galileo image compression scheme is a block based lossy image compression algorithm which uses an 8x8 Integer Cosine Transform (ICT) [1]. The algorithm is similar in functionality to the baseline JPEG standard which converts a fixed length string into a variable length string. A major difference between the JPEG standard and the Galileo compression scheme is that the JPEG standard uses an 8x8 Discrete Cosine Transform (DCT). The Integer Cosine Transform (ICT) is an integer approximation of the DCT. ICT requires only integer arithmetic, making it much simpler to implement. Although the ICT has a much lower complexity, the rate-distortion performance is not sacrificed. This lower complexity of the ICT is necessary because the Galileo spacecraft uses late 1970's microprocessor technology.

[1]This work was performed at the Jet Propulsion Laboratory, California Institute of Technology, under contract with the National Aeronautics and Space Administration.

0-7803-3068-4/96$5.00©1996 IEEE

Error Correction

The Galileo error-correction coding scheme uses a (255,k) variable redundancy Reed-Solomon (RS) code as the outer code, and a (14,1/4) convolutional code as the inner code. The RS codewords are interleaved to depth 8 in a frame. The redundancy profile of the RS codes is (94, 10, 30, 10, 60, 10, 30, 10). The staggered redundancy profile was designed to facilitate the novel feedback concatenated decoding strategy [2]. This strategy allows multiple passes of channel symbols through the decoder. During each pass, the decoder uses the decoding information from the RS outer code to facilitate the Viterbi decoding of the inner code in a progressively refined manner. The FCD is implemented in software on a multiprocessor workstation. The code is expected to operate at bit signal-to-noise ratio (SNR) of 0.65 dB at a bit error rate of 10^{-7}. The FCD code selection and performance analysis are discussed in detail in [3].

If the FCD cannot decode the data, due to errors beyond its capability to correct, the FCD will invoke the "frame repair" utility and the "gap processing" utility. Gap processing involves using data from either side of good decoded data and attempts to fill in data that was missing (the gap) because of loss of synchronization or hardware glitches. The frame repair utility attempts to correct any symbol insertions, deletions or inversions due to transmission reception problem. The reprocessed data is then fed back to the FCD for another attempt at decoding.

Frame Repair

Sometimes a frame is received that has adequate SNR, but the frame markers at the beginning and end of it have too many or too few symbols in between them and/or have opposite phase. This indicates that some symbols were inserted or deleted and/or a phase inversion occurred, somewhere in the frame. (A phase inversion is an event where the symbols after it are detected with the opposite phase of the symbols before it. So, if the transmitted symbols were all +1, the received symbols, in the absence of noise, would be +1 up to the inversion, and -1 for all symbols after that, or at least until the next phase inversion.) Because a high redundancy Reed-Solomon codeword with too many errors is vastly more likely to not be decodable than to decode incorrectly, one can make guesses about where the errors are and safely assume that a guess is correct if it results in a decodable codeword. However, while guessing may be safe, it is not likely to be successful unless there is some reason for making a particular guess. The assumption in frame repair is that n bits were inserted or deleted, and/or a phase inversion occurred, at one particular but unknown location in the frame. The guessing involved is restricted to guessing this location. A guess is tested by creating a modified version of the received frame with the appropriate number of symbols inserted or deleted, and/or a phase inversion made, at the guessed location. The frame is then Viterbi decoded, the result is deinterleaved, and Reed-Solomon decoding is attempted on the resulting eight words. If the highest redundancy Reed-Solomon decoder succeeds, it is extremely likely that the guess was approximately correct. The reason the guess need not be exact is that the effect of an incorrect guess is that essentially all of the Reed-Solomon symbols in between the actual anomaly location and the guessed one are incorrect, but if the gap is small enough, the Reed-Solomon decoder can correct those additional errors. Once the location is approximately known, the guess can be refined by trying nearby locations and choosing the one that minimizes the number of errors the Reed-Solomon decoder corrects. Then the frame, modified to reflect the refined guess, is sent on to the FCD for redecoding. But how are the

guesses made in the first place? One rather simple minded method is to guess each of the 65536 symbol locations in the frame, one at a time. This, however, would take an unreasonable amount of time, because Viterbi decoding is slow. Slightly less simple-minded is to do a binary search, since you only need to get close enough to the correct location. Thus, you first guess the location halfway through the frame, then 1/4 of the way, then 3/4, then 1/8, and so on. This method, in fact, is used when everything fails, but it can still take a very long time unless you're lucky. Before resorting to this, some other educated guesses are made. If any of the following methods succeeds, meaning that the highest redundancy Reed-Solomon decoder succeeds, the guess is then refined and the modified frame is sent to the FCD, as explained above. If not, the next method is tried. First method: if a data rate change occured at some point during the frame, that location is guessed, since anomalies are known to be common when data rate changes occur. Second method: the end of the frame is tried as a guess, which means that the frame is Viterbi decoded as is. The branch metrics along the decoded path are saved, for use in the next step in case this method doesn't succeed. Third method: if insertions or deletions are known to have occurred, the branch metrics mentioned above are analyzed. Although the effect is subtle when SNR is low, the mean value of the metrics will be slightly higher after the location of the anomaly is reached than before it. This analysis results in an estimate of where this increase occurred, and this estimate is used as the next guess. Fourth method: if only a phase inversion is known to have occurred (i.e. the frame is the correct length, but the markers on either end have opposite phase) the transparency of the Galileo (14, 1/4) convolutional code means that the output of the Viterbi decoder, after a transient in the vicinity of the inversion, is the same as it would have been without an inversion, except with opposite sign. Thus, in this special case, one can make multiple guesses without having to Viterbi decode a whole frame each time. It is only necessary to invert all the Viterbi decoded symbols (from the original frame) after the guessed location and then attempt Reed-Solomon decoding. A binary search is used to make guesses throughout the frame, each of which can quickly be tested. Fifth method: the last resort is the binary search described previously. If this fails, frame repair is not accomplished.

Frame Merging

Because of the large frame size (65536 symbols) and low bit rates that Galileo will be using, a single frame will take close to half an hour to transmit at the lowest bit rate. The lowest bit rate is used near the beginning and end of a pass, when the SNR is lowest, and it is not unlikely that a frame that starts out with adequate SNR may not be completed before the signal is lost, or becomes noisy enough to render the whole frame undecodable. Because the ground stations have overlapping coverage, the next station may pick up the signal in the middle of the same frame. Thus, each of two stations may have an incomplete and/or too noisy version of the same frame. Because of the nature of the redecoding algorithm, a partial frame by itself is essentially useless. Since the best part of each frame is the worst part of the other, it seems obvious to try to paste them together somehow. If the SNR at the crossover point, where the falling SNR at the first station equals the rising SNR at the second, is high enough, one could make a good frame by just using the symbols from the first station up to that point and from the second station after that point. However, even if the SNR at the crossover point is significantly below the decoding threshold, by adding the

symbols from the two frames together, 3 dB could theoretically be gained in the vicinity of the crossover point, assuming the noise at the two stations is independent, a reasonable assumption. Farther from the crossover point, one could still combine symbols from the two frames, but with weights reflecting their relative SNR's. Note that this requires estimates of the SNR throughout both frames, and that the results can be expected to depend on the accuracy of these estimates. An additional problem arises, however: low SNR not only makes symbols noisy, it can also cause symbol insertions and deletions. One way this could be detected is if the frame markers both before and after a frame were detected, and the number of symbols in between was greater or less than 65536. Since frame markers can be detected at SNR's way below the threshold of decodability, this is not unlikely. Notice, however, that this does not give any information about where in the frame symbols were inserted or deleted. To try to find the approximate location of any insertions or deletions, dynamic programming is used. Basically, the idea is to try to maximize the correlation between the two frames, by deleting or inserting various symbols. This is possible whether or not the existence of insertions or deletions in one or both frames was detected via counting symbols between frame markers; the latter just reduces the number of possibilities that must be considered. The result of this algorithm is a small number of candidate merged frames, that must then be sent to the FCD to attempt decoding.

Error Containment

If all these attempts fail to correct the data, then the final step is to minimize error propagation. Because any corruption of data in a compressed data stream can cause magnified errors due to propagation, safeguards were introduced into the compresseddata stream to minimize these effects.

First, images are compressed independently by rows of 8, with a synchronization marker inserted at the beginning, so any bit errors during data transmission can be isolated.

Second, the decompression algorithm includes provisions for detection of errors so that error containment mode will be activated.

These two safeguards are used together in the following manner: if an error is detected during decompression, the decompression algorithm will start a search for the synchronization marker. This marker is 32-bits wide which consists of 2 fields. A 7-bit sequencing field and a 25-bit fixed pattern field. The 7-bit field will identify where the 8-rows of data belongs relative to the whole image and the 25-bit field is used for synchronization. Using these safeguards, error propagation can at most be isolated to 16-rows of image data.

References

[1] W. Cham, "Development of Integer Cosine Transform by the Principle of Dyadic Symmetry," *IEE Proceedings*, Vol. 136, Pt. I, No. 4, August 1989.

[2] E. Paaske, "Improved Decoding for a Concatenated Coding System Recommended by CCSDS," *IEEE Transaction of Communications*, Vol. COM-38, August 1990.

[3] S. Dolinar and M. Belongie, "Enhanced Decoding for the Galileo Low-Gain Antenna Mission," *Proceedings 1994 IEEE International Symposium on Information Theory*, Trondheim, Norway, June 27 - July 1, 1994.

A Bounded Distortion Compression Scheme for Hyper-spectral Image Data

Nasir D. Memon

Computer Science Dept.
Northern Illinois University
De Kalb, IL 60115

1. INTRODUCTION

The large number of spectral bands in hyper-spectral images lead to an enormous amount of data. In order to manage the large data requirements, some form of data compression is required. Recent studies on AVIRIS data have indicated that the presence of sensor noise limits the amount of compression that can be obtained by any lossless compression scheme [6]. This is supported by the fact that the best results reported in the literature on compression of AVIRIS data seem to be in the range of 5 - 6 bits per pixel [4, 7]. Increased compression can be obtained with lossy compression techniques [2, 8]. Lossy schemes have been shown to provide very high compression ratios with little or no loss in *visual fidelity*. Lossy compression, however, may not be desirable in many circumstances due to the uncertainty of the effects caused by lossy compression on subsequent scientific analysis that is performed with the image data. One compromise then is to use a *bounded distortion* (or *nearly-lossless*) technique which guarantees that each pixel in the reconstructed image is within ϵ counts of the original.

In this paper, we propose a new approach for compression of hyper-spectral images that can provide a bound on the distortion introduced. The technique involves an adaptive re-ordering of the spectral components of each pixel. This re-ordering adaptively exploits, on a pixel-by-pixel basis, the presence of inter-band correlations by clustering together the bands that have similar intensity values. The re-ordered components are then approximated by a piece-wise linear function to a given specified tolerance ϵ. Entropy coded parameters of this piece-wise linear approximation are transmitted to the receiver.

The proposed approach takes advantage of spatial and spectral correlations in hyper-spectral data sets, potentially leading to improved compression over standard nearly lossless techniques that encode the image spatially one band at a time. Preliminary results demonstrating the effectiveness of the approach are presented.

2. SPECTRAL RE-ORDERING AND LINEAR PREDICTION

Recent studies indicate that correlations in a multi-spectral data set are highest along the spectral dimension [10]. For hyper-spectral data sets it is also known [5] that for homogeneous ground features, intensity values in different bands are related by a multiplicative factor of the form

$$I[i,j,r] = \alpha_{rs} I[i,j,s] + \beta_{rs}$$

where $I[i,j,k]$ is the intensity value at spatial location (i,j) in band k. However, it has been observed in [3] that in hyper-spectral data, bands which are spectrally far apart can be highly correlated. Hence the question of *band selection* arises. That is, which band(s) are the best to use for predicting intensity values in a given band. In [9], it was shown that significant compression benefits can be obtained by re-ordering the bands of multi-spectral images, prior to prediction. The problem of computing an optimal ordering was formulated in a graph theoretic setting, admitting an $O(N^2)$ solution for an N-band image.

Although significant improvements were reported, one major limitation of this approach is the fact that it is two-pass. An optimal ordering and corresponding prediction coefficients are first computed by making an entire pass through the data set. Another limitation of the approach is that it re-orders entire bands. That is, it makes the assumption that spectral relationships do not vary spatially. The optimal spectral ordering and prediction co-efficients may change spatially depending on the composition of the objects being imaged. This latter fact is taken into account in by Rao and Bhargava [5], who also re-order spectral bands in order to optimize inter-band prediction. However, since the optimal prediction co-efficients and spectral ordering changes spatially, they partition the image into blocks, and compute optimal predictors on a block-by-block basis. The predictor coefficients are then transmitted as overhead. Large blocks are required to keep the overhead reasonably small and this leads to poorer prediction performance as compared

0-7803-3068-4/96$5.00©1996 IEEE

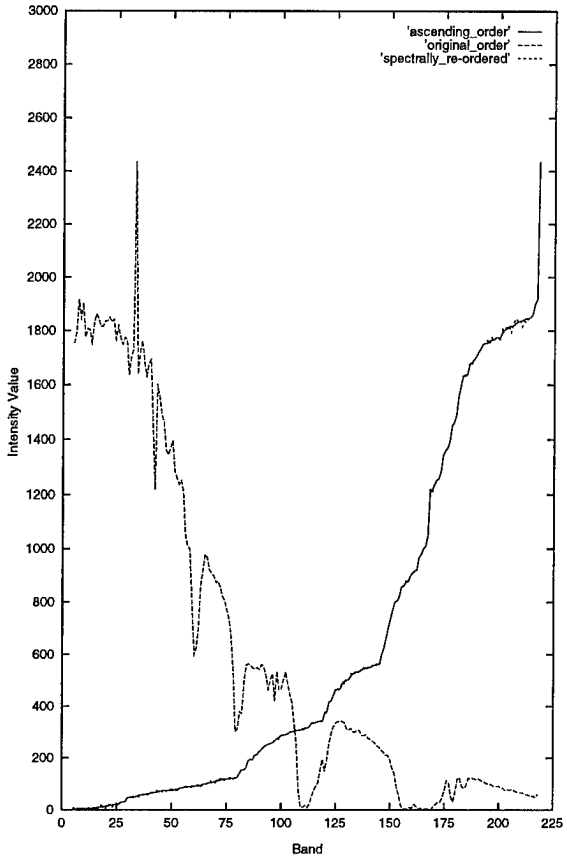


Figure 1: The spectral components of a pixel before and after re-ordering

to that obtained with a smaller block. Furthermore, they also found that using the previous band for prediction gives results that are very close to those obtained after computing an optimal ordering.

In this paper, we propose a new approach, applicable to nearly-lossless compression of hyper-spectral images. According to this approach, an adaptive re-ordering of the spectral components of each pixel is performed prior to prediction and encoding. This re-ordering exploits, on a pixel-by-pixel basis, the presence of inter-band correlations for prediction. Furthermore, the proposed approach takes advantage of spatial correlations, and does not introduce any coding overhead to transmit the order of the spectral bands. This is accomplished by using the assumption that two spatially adjacent pixels are expected to have similar spectral relationships. We thus have a simple technique to exploit spectral and spatial correlations in hyper-spectral data sets.

Given a composite pixel X from an n band image, $X = (x_1, x_2, \ldots, x_n)$, let σ be a permutation on n points that sorts the components of X in ascending order and let the resulting vector be $\hat{X} = (\hat{x_1}, \hat{x_2}, \ldots, \hat{x_n})$ where,

$$\hat{x_1} = x_{\sigma(1)} \leq \hat{x_2} = x_{\sigma(2)} \leq \cdots \leq \hat{x_n} = x_{\sigma(N)}$$

It is clear intuitively that the vector $\hat{X}$ is more amenable to approximation by a linear model as compared to the original vector X. Furthermore, the sorting step brings closer spectral components that might have been widely separated in the original data although they are highly correlated with one another and have similar intensities.

In figure 1 we plot the spectral components of a random pixel selected from an AVIRIS image. The dotted plot is the components in original order and the solid line plots the components re-arranged in ascending order. It can be clearly seen from this figure that that the re-ordered vector $\hat{X}$ can be better approximated by a linear model using a given number of parameters as compared to the original vector X. For example, if we wish to approximate $\hat{X}$ with a piecewise linear function, we would expect to do so with fewer segments as compared to the piecewise approximation of the original vector X. The problem with this approach is the fact that the sorting permutation is different for different pixels. The overhead incurred by explicitly transmitting the sorting permutation for each pixel turns out to be prohibitively high. Hence, we employ *predictive ordering*, that is, a prediction is performed for the sorting permutation based on previously reconstructed pixels and the current pixel X is reordered according to this predicted permutation. If X and Y are spatially adjacent pixels of a hyper-spectral image, then the permutation that sorts X into ascending order, usually serves as a good approximation of the permutation that sorts Y. For example in figure 1 we also show the pixel plot after re-ordering with respect to the sorting permutation σ of a neighboring pixel. The resulting plot of spectral components is almost in ascending order and is difficult to distinguish from the plot of components given in ascending order. In the next section we describe a technique for effectively modeling the predictively ordered vector.

3. A BOUNDED DISTORTION COMPRESSION TECHNIQUE

As noted before, once a vector has been reordered we can approximate it well by a piecewise linear function. In recent work, Bhaskaran et. al. [1] have given an optimal algorithm for waveform approximation with a piecewise linear function at a specified error tolerance ϵ. This gives us a simple and effective bounded distortion compression technique for multi-spectral image data. Specifically, given a distortion bound ϵ and a multi-spectral image in band-pixel-interleaved raster order, we do a predictive re-ordering of the current pixel, getting an almost sorted vector. A piecewise linear approximation of the

	Re-ordering			No re-ordering		
% Loss	0.25	0.5	1.0	0.25	0.50	1.0
No. pts.	80	53	32	128	100	71
Max Diff.	11	21	41	11	22	42
Min Diff.	-11	-21	-41	-11	-21	-41
Avg Diff.	0.24	0.89	0.93	-0.37	-0.88	-0.51
Abs. Diff.	5.41	9.71	16.9	6.39	11.88	20.50
Est. rate	2.98	2.18	1.47	5.02	4.19	3.23

Table 1: Results of piece-wise linear approximation with and without predictive re-ordering

vector is transmitted after entropy coding of the parameters. There are various options available for predicting the sorting permutation of the current pixel and for entropy coding model parameters. In this work we obtained the sorting permutation by arranging the average intensity values of the vertical, horizontal and left-diagonal reconstructed neighbors of the current pixel in ascending order.

In Table 1 we show some preliminary results obtained with the simple approach described above. The results were obtained from a portion of an AVIRIS image of the Cuprite Mining District, Cuprite, Nevada. The image contained 200 samples, 200 lines, and 224 spectral bands. Piece-wise linear approximation was performed with and without predictive ordering. The distortion ϵ was set to $0.25, 0.5$ and 1.0% of the dynamic range of the pixel being approximated. It can be seen that the number of segments needed to approximate a pixel in the spectral dimension reduces dramatically if a predictive ordering step is carried out prior to approximation. The bit rate estimates shown in Table 1 were obtained by taking the zero-order entropy of the difference values of successive x co-ordinates of the piece-wise linear function obtained. To this we added the zero-order entropy of the prediction error for the y co-ordinates using a simple and fixed linear predictor. It should be noted that these bit-rates are very conservative and further reduction can be obtained by more sophisticated error modeling techniques prior to entropy coding. Furthermore, the sub-optimal algorithm mentioned in [1] was used for obtaining a piece-wise linear approximation. A 25-50% reduction in the number of line segments can be obtained by using the optimal algorithm which is considerably more complex. Our intention here is to show the improvements that can be obtained by predictive re-ordering.

4. CONCLUSIONS AND FUTURE WORK

We have presented in this paper a new approach for nearly lossless compression of multi-spectral image data that exploits both spectral and spatial correlations in a simple and adaptive manner. What we have described in this paper is just one choice of predictor, re-ordering and encoding. A number of alternatives can be used. Implementation results with a few different choices schemes are currently under investigation and will will be described in the full version of the paper. Also, we need to make more detailed comparisons of compression performances obtained with other lossy and nearly-lossless schemes given in the literature.

5. REFERENCES

[1] V. Bhaskaran, B. K. Natrajan, and K. Konstantinides. Optimal piecewise-linear compression of images. In *Proceedings of DCC*, pp 168–177. IEEE Computer Society Press, 1993.

[2] S. Gupta and A. Gersho. Feature predictive vector quantization of multispectral images. *IEEE Transactions on Geoscience and Remote Sensing*, 30:491–501, May 1992.

[3] R. N. Hoffman and D. W. Johnson. Application of EOF's to multispectral imagery: Data compression and noise detection for aviris. *IEEE Transactions on Geosciences and Remote Sensing*, 32(1):25–34, 1994.

[4] N. D. Memon, K. Sayood, and S. S. Magliveras. Lossless compression of multispectral image data. *IEEE Transactions on Geosciences and Remote Sensing*, 32(2):282–289, March 1994.

[5] A. K. Rao and S. Bhargava. Multispectral data compression using inter-band prediction. In *Proceedings of the Industry Workshop on DataCompression.* Snowbird, Utah, 1994.

[6] R. E. Roger and J. F. Arnold. Reversible image compression bounded by noise. *IEEE Transactions on Geoscience and Remote Sensing*, 32(1):19–24, 1994.

[7] R. E. Roger and M. C. Cavenor. Loosless compression of AVIRIS images. Preprint: Submitted to IEEE Transactions on Geoscience and Remote Sensing, 1995.

[8] J. A. Saghri, A. G. Tescher, and J. T. Reagan. Practical transform coding for multispectral imagery. *IEEE Signal processing Magazine*, 12(1):32–43, 1995.

[9] S. R. Tate. Band ordering in lossless compression of multispectral images. In *Proceedings of the Data Compression Conference*, pages 311–320. IEEE Computer Society, 1994.

[10] V. V. Vaughn and T. S. Wilkinson. System considerations for multispectral image compression designs. *IEEE Signal Processing Magazine*, 12(1):19–31, 1995.

Lossless Image Compression Based on a Generalized Recursive Interpolative DPCM

B. Aiazzi*, P. S. Alba*, L. Alparone°, S. Baronti*

* Istituto di Ricerca sulle Onde Elettromagnetiche "Nello Carrara" - CNR, via Panciatichi, 64, I-50127 Firenze, Italy
Phone: +39-55-4235-275; Facsimile: +39-55-410893; E-mail: baronti@iroe.fi.cnr.it
° Dipartimento di Ingegneria Elettronica, University of Florence, via S. Marta, 3, I-50139 Firenze, Italy
Phone: +39-55-4796-372; Fax: +39-55-494569; E-mail: alparone@cosimo.ing.unifi.it

Abstract -- It is shown that the *generalized recursive interpolation* algorithm (GRINT) proposed is the most effective hierarchical technique for reversible compression of images that typically occur in remote sensing. The main advantage of the novel scheme with respect to other noncausal DPCM schemes is that interpolation is performed from all error-free values, thereby reducing the variance of residuals. Tests on LandSat, NOAA/AVHRR, MeteoSat, and SPOT images show that GRINT outperforms established hierarchical techniques, and also lossless JPEG and optimum DPCM when dealing with SPOT data, with the further advantage that GRINT makes error-free tokens available at any resolution, thereby expediting remote browsing on large image data-bases.

INTRODUCTION

Data transmission and archiving are crucial topics in Remote Sensing, where the evolution of technology makes multi-temporal data available at increasing spatial, spectral, and radiometric resolution. Consequently, the need of efficient data compression algorithms is becoming more and more pressing.

Compression efficiency can be high with acceptable visual quality when standard techniques, such as JPEG [1], are utilized; however, only in those applications where reconstruction errors are tolerated. When lossless coding is mandatory, compression ratios greater than *2* or *3* can hardly be obtained [2], due to the intrinsic noisiness of sensors imaging at high spatial and/or spectral resolution.

The two stages of lossless compression are decorrelation and entropy coding [3]. Differential pulse code modulation (DPCM) techniques are usually efficient in decorrelating image data [4]. Moreover, a noncausal version of DPCM can be implemented in a hierarchical way [5],[6], thus producing high-quality intermediate versions (tokens) of the input images at increasing spatial resolutions. Data retrieval and transmission can be achieved in a progressive fashion, either by stopping the process at the requested resolution level, or by recognizing that the image being retrieved is no longer of interest. However, for lossless schemes progressiveness is usually achieved with a small performance penalty with respect to reference DPCM (i.e., 4-pel optimum causal auto-regressive prediction [4]), mostly due to accumulated aliasing.

In this work we suggest a modified version of the Hierarchical INTerpolation (HINT) algorithm [5], employing a separable generalized interpolation [6], instead of a nonseparable bilinear interpolation, for image expansion.

The original image is first recursively decimated by *2* alternately along either rows or columns, thus creating a gray-level *binary pyramid* (i.e., a pyramid whose number of pixels halves at every layer). First the top of the pyramid is DPCM encoded; then the difference between pairs of top-to-bottom successive pyramid layers -the half-resolution ones being 1-D interpolated to match the sizes of their underlying versions- is entropy coded and stored, in order to retrieve the image.

Performance are evaluated by comparing GRINT with S-Transform [7], and HINT which are recognized as the most effective algorithms for lossless progressive image coding. Optimum 4-pel regression DPCM and lossless JPEG [1] are also considered for completeness of comparisons [8], although they are not progressive. GRINT and all the above mentioned algorithms are non-redundant, since the number of differential data to encode equals exactly the number of image pixels.

GENERALIZED RECURSIVE INTERPOLATION

Let $\{G(m,n),\ m = 0,...,M - 1;\ n = 0,...,N - 1\}$, $M = p \times 2^K$, and $N = q \times 2^K$, be an integer-valued image, p, q, and $K \in \mathbb{N}$. The set of *down-sampled* images $\{G_k,\ k = 0,1,..,2K\}$

$$G_k(m,n) = G\left(2^{\lfloor (k+\delta_m)/2 \rfloor} \cdot m,\ 2^{\lfloor (k+\delta_n)/2 \rfloor} \cdot n\right) \qquad (1)$$

for $m = 0,...,M/2^{\lfloor (k+\delta m)/2 \rfloor} - 1$, $n = 0,...,N/2^{\lfloor (k+\delta n)/2 \rfloor} - 1$ constitutes a *binary* pyramid, i.e., a pyramid whose number of pixels halves between successive levels; k denotes pyramid level and $2K$ the $p \times q$ top or *root*; δ_m, $\delta_n \in \{0,1\}$, with $\delta_m + \delta_n = 1$ define the direction along which samples are decimated first. Figure 1 shows that two pyramids exist, depending on whether $(\delta_m,\delta_n) = (1,0)$ or $(0,1)$, whose even-order levels coincide.

0-7803-3068-4/96$5.00©1996 IEEE

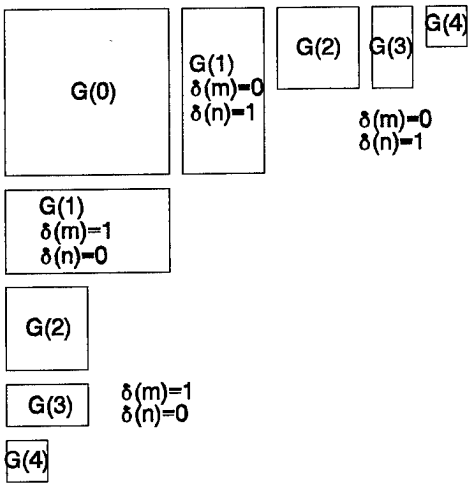


Figure 1. Example of binary pyramids with alternate decimation by 2; *m*-axis top-to-bottom, *n*-axis left-to-right.

The *Generalized Recursive INTerpolation* (GRINT) is defined as $H_{2K}(m,n) = G_{2K}(m,n)$, and for $k = 0,1,..,2K - 1$ as:

$$H_k(m,n) \triangleq G_k(m,n) - \left[\sum_{i=-L}^{L} \sum_{\substack{j=-L \\ (m+i(\delta_m \oplus k)) \bmod \left(2^{\delta_m \oplus k}\right) = 0 \\ (n+j(\delta_n \oplus k)) \bmod \left(2^{\delta_n \oplus k}\right) = 0}}^{L} e(i)e(j) G_{k+1}\left(\frac{m+i\cdot(\delta_m \oplus k)}{2^{\delta_m \oplus k}}, \frac{n+j\cdot(\delta_n \oplus k)}{2^{\delta_n \oplus k}} \right) \right] \quad (2)$$

where $m = 0,...,M/2^{\lfloor (k+\delta m)/2 \rfloor} - 1$, $n = 0,...,N/2^{\lfloor (k+\delta n)/2 \rfloor} - 1$, while $[\bullet]$ and $\oplus$ denote roundoff to integer and *modulo-2* addition, respectively. If a *half-band* filter [6] is used for interpolation, then it stems that $H_k(m,n) = 0$, $k = 0,...K - 1$, and either of m or n even, as interpolation preserves the values of the original decimated samples, thus yielding null errors.

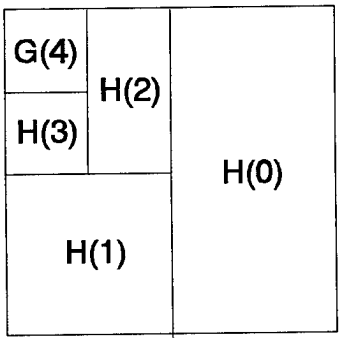


Figure 2. Base-band and interpolation errors from GRINT accommodated in subband-like regions: $K = 2$, $(\delta_m,\delta_n) = (0,1)$.

Figure 2 shows that, since one half of interpolation errors is identically zero, the transformation is *non-expansive*, viz., the number of decorrelated data equals the number of image pixels.

A *7-tap* half-band filter ($L = 3$) was chosen for interpolation

$$e(0)=1;\ e(\pm1)=b;\ e(\pm2)=0;\ e(\pm3)=0.5-b \quad (3)$$

b is an adjustable parameter determining the shape of the frequency response, which is plotted in Figure 3. The values $b = 0.5$, and $b = 0.5625$ yield *linear* and *cubic* interpolation, respectively. Such a parameter should be tuned to the detail content of the images to be coded. As a tendency images with sharp edges benefit from little selective frequency responses (e.g., $b = 0.475$), while a higher value of b is better for smooth images, although frequency overshoot, which starts with $b > 0.5625$, actually prevents from using $b > 0.625$.

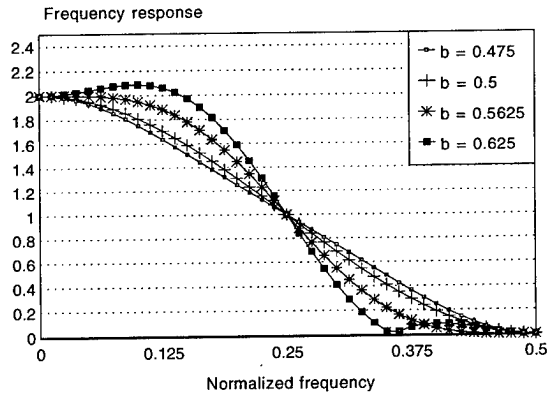


Figure 3. Frequency response of the parametric kernel (3) for half-band interpolation at different values of b.

S-TRANSFORM

The S-Transform [7], is a multiresolution orthogonal transformation based on the Walsh-Hadamard Transform (WHT) [4], having the attractive feature of an algorithm consisting only of sums and differences. A singular property of the WHT coefficients, possessing all the same parity when coming from integer samples, has been exploited for lossless coding, to yield integer coefficients and saving extra bits:

$$S_{k,m,n} = \left\lfloor \frac{G_{k,m,n} + G_{k,m,n+1} + G_{k,m+1,n+1} + G_{k,m+1,n}}{4} \right\rfloor \quad (4a)$$

$$S_{k,m+1,n} = \left\lfloor \frac{G_{k,m,n} + G_{k,m,n+1} - G_{k,m+1,n+1} - G_{k,m+1,n}}{2} \right\rfloor \quad (4b)$$

$$S_{k,m,n+1} = \left\lfloor \frac{G_{k,m,n} - G_{k,m,n+1} - G_{k,m+1,n-1} + G_{k,m+1,n}}{2} \right\rfloor \quad (4c)$$

$$S_{k,m+1,n+1} = G_{k,m,n} - G_{k,m,n+1} + G_{k,m+1,n+1} - G_{k,m+1,n} \quad (4d)$$

for $k = 0,1,...,K - 1$; $m = 0,2,...,M/2^k - 2$; $n = 0,2,...,N/2^k - 2$, with $G_{0,m,n} \triangleq G(m,n)$ (i.e., the $M \times N$ image) and $G_{k+1,m,n} \triangleq S_{k,m,n}$.

Besides saving two bits (by dividing by *4*) in the base-band coefficients $S_{k,m,n}$ (4a), also the co-diagonal terms (4(b-c)) may be divided by *2* without affecting reversibility.

The low-frequency coefficients $S_{k,m,n}$, are thus further decomposed according to (4(a-d)), in order to yield a *wavelet* space-frequency representation [9], in which spatial details are accommodated into dyadic *subband-like* regions depending on their spatial frequencies. Hence, S-Transform may be regarded as a *zero-order* wavelet transform, based on such a polynomial approximation of the finite-support wavelet function.

CODING RESULTS AND COMPARISONS

A test set of remote sensing *8-bit* images comprises Meteosat (visible band) and NOAA/AVHRR (Band *3*), Landsat Thematic Mapper (TM) (Band *5*), and Panchromatic SPOT. Figure 4 shows performances of GRINT compared with HINT, S-Transform, JPEG, and DPCM with 4-pel auto-regressive (AR) prediction [4],[8]. Zeroth order entropy of decorrelation residuals has been calculated for all the algorithms, including lossless JPEG.

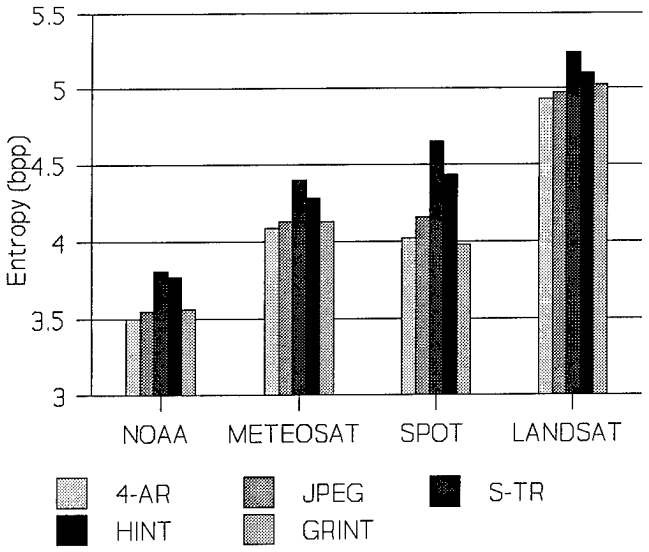


Figure 4. Entropy of the residuals, in bit/pel, from the four types of image: GRINT compared with S-transform, HINT, JPEG, and 4-pel regression DPCM.

All progressive algorithms work with $K = 3$, i.e., *7* levels of decomposition for GRINT, *4* for both HINT and S-Transform. A further parameter which must be set for GRINT is the pair (δ_m, δ_n) which drives the order of interpolation. The first stage (e.g., that originating *H(3)* in Fig. 2) should better be performed along the direction of minimum correlation. In fact, interpolation errors will be larger in average but one half in number. The last stage which involves the largest number of residuals will therefore be along the maximum correlation axis.

CONCLUSIONS

A novel algorithm for multiresolution image decorrelation has been introduced and assessed on a test set of remotely sensed images. It is based on a recursive 1-D parametric interpolation by two performed from all error-free values following a pyramid whose number of pixels doubles at each stage. The choice of the maximum correlation direction along which samples from the base-band are interpolated first provide a saving of about *0.1 bit/pel*. Lossless coding capability is greater than that of other hierarchical schemes, comparable with JPEG, and slightly poorer than optimum regression DPCM, except for PAN-SPOT images, for which GRINT outperforms the other methods. Since multi-band (i.e., *inter-frame*) decorrelation is usually employed for Landsat TM [8] and multispectral image data, interest for *intra-frame* decorrelation will be mainly addressed to SPOT data.

REFERENCES

[1] W. B. Pennebaker, and J. L. Mitchell, *JPEG: Still Image Compression Standard*, New York, NY: Van Nostrand Reinhold, 1993.

[2] R. E. Roger, J. F. Arnold: "Reversible Image Compression Bounded by Noise", *IEEE Trans. Geosci. Remote Sensing*, Vol. 32, No. 1, pp. 19-24, Jan. 94.

[3] R. B. Arps, and T. K. Truong, "Comparison of International Standards for Lossless Still Image Compression", *Proc. of the IEEE*, Vol. 82, No. 6, pp. 889-899, Jun. 1994.

[4] A. N. Netravali, and B. G. Haskell: *Digital Picture-Representation and Compression*. Applications of Communications Theory Series. New York, NY: Plenum Press, 1988.

[5] P. Roos, M. A. Viergever, M. C. A. Van Duke, and J. H. Peters, "Reversible Intraframe Compression of Medical Images", *IEEE Trans. Medical Imaging*, Vol. 7, No. 4, pp. 328-336, Dec. 1988.

[6] B. Aiazzi, L. Alparone, and S. Baronti, "A Reduced Laplacian Pyramid for Lossless and Progressive Image Communication", *IEEE Trans. Communications*, Vol. 44, No. 1, pp. 18-22, Jan. 1996.

[7] S. Wong, L. Zaremba, D. Gooden, and H. K. Huang, "Radiologic Image Compression - A Review", *Proc. of the IEEE*, Vol. 83, No. 2, pp. 194-219, Feb. 1995.

[8] J. Wang, K. Zhang, "Spectral and Spatial Decorrelation of Landsat-TM Data for Lossless Compression", *IEEE Trans. Geosci. Remote Sensing*, Vol. 33, No. 5, pp. 1277-1285, Sep. 1995.

[9] M. Antonini, M. Barlaud, P. Mathieu, and I. Daubechies, "Image Coding Using Wavelet Transform", *IEEE Trans. Image Processing*, Vol. 1, No. 2, pp. 205-220, Apr. 1992.

Image Sequence Compression Using Adaptive Wavelet Packet

S Sarita
Software Engineer
D 11/12, C V Raman Nagar, Bangalore - 560 093, INDIA
P Nagabhushan
Professor, Dept. of Computer Science and Engineering
SJCE, Mysore - 570 006, INDIA

Abstract -- Segmentation-based motion compensation is used in combination with Adaptive wavelet packet transform for compressing image sequences. Motion compensation and estimation are performed at both encoder and decoder so that the region shape information need not be transmitted and only the changed vectors are transmitted. This is very useful in low bit-rate applications. Also the adaptive wavelet packet transform used promises a very faithful representation of the images.

INTRODUCTION

Image sequence coding has become a necessity in areas like teleconferencing, broadcast television and multimedia applications. Image sequence compression is achieved by the removal of temporal and spatial redundancies. The most widely used schemes make use of motion compensation to decorrelate the data along the temporal direction and block-matching algorithms for motion estimation [5]. The spatial redundancy is removed using any transform like the Discrete cosine transform/ Wavelet transform in combination with a quantizer. The block-based methods however lead to block artifacts, especially in low bit-rate applications. Segmentation-based techniques have proven to be useful in avoiding the block effects [6]. This paper proposes to use a segmentation-based motion compensation algorithm in combination with the adaptive wavelet packet transform for image sequence coding.

THE CODING ALGORITHM

The proposed algorithm uses a combination of motion-compensated prediction scheme and adaptive wavelet packet transform coding. Motion-compensation based prediction involves moving object detection, motion estimation and compensation. Let f_n denote the current frame. Its prediction $\tilde{f}_n$ is obtained by motion-compensation of the previously reconstructed frame $\hat{f}_{n-1}$. The previously reconstructed frame $\hat{f}_{n-1}$ is segmented into a number of regions, and the moving regions are determined by detecting changes between successive frames. The segmented reconstructed frame $\hat{f}_{n-1}$, along with the motion vectors of every moving region give a motion-compensated frame. The differential error signals e_n are then calculated by subtracting the predicted frame from the original. and encoded using adaptive wavelet packet transform.

MOVING OBJECT DETECTION

Moving object detection consists of segmentation, change detection and merging of small regions. The previously reconstructed image frame $\hat{f}_{n-1}$ is segmented, compared with $\hat{f}_{n-2}$ for detecting the changed regions and visually insignificant changed segments are merged. For segmentation, the image pixels are scanned in one pass from left to right and top to bottom. Assuming the very first pixel scanned as the first segment, at each pixel the average gray levels of all image segments neighboring that pixel are compared. Segments are merged if their differences in average gray levels do not exceed a threshold T_s

$$T_s = wT_p \tag{1}$$

where w is a weighing factor such that 0<w<1

and $T_p = \begin{cases} t_w & t_w \le t_{\max} \\ t_{\max} & t_w > t_{\max} \end{cases}$

$$t_w = (m|G/2 - p| + d) \tag{2}$$

where p is the average gray level of 8 pixels neighboring the current pixel, G is the number of gray levels in the image, and m & d are the parameters to control the number of segments created in the image, t_{max} is the upper limit of T_p. Similarly, the current pixel's intensity value is compared with the average intensity values of the neighboring segments and merged with the closest segment in which their intensity differences does not exceed T_p.Otherwise, a new segment is started. The segmented

0-7803-3068-4/96$5.00©1996 IEEE

reconstructed frame $\hat{f}_{n-1}$ is compared with $\hat{f}_{n-2}$ for detecting changes. The pixels that have a large difference than the threshold value are detected as changed region elements. The number of changed regions in each segment are counted and if the ratio of this number with the total number of pixels in the segment exceeds a threshold value, it is considered a changed segment. Small regions which are visually insignificant are merged with the neighboring changed segment, which closely matches its average intensity value.

MOTION ESTIMATION AND COMPENSATION

Motion between frames does not change significantly from frame to frame in most applications. Therefore, assuming that motion within a few frames remains constant along its trajectory is valid for most parts of the image. Based on this assumption, a prediction of motion vectors for the current frame can be obtained from those of the previous frame. Let $f_n(r)$ denote the intensity values of the current frame, where r = (x,y) is the spatial location and n is the frame number. First $\hat{f}_{n-1}$ is segmented and changes are detected. For every changed region R_i, i = 1,2,...c (c is the number of changed regions), motion vector V_i is obtained by searching the corresponding match region in $\hat{f}_{n-2}$ using minimum mean absolute difference criteria. However, if constant motion is assumed between successive frames, the predicted motion vectors for the current frame will be the same as that of the previous frame, which is untrue for occluded or newly uncovered regions. Thus motion correction is obtained using the current frame f_n and previous reconstructed frame $\hat{f}_{n-1}$ at the encoder. The new motion vectors are calculated for all moving regions of $\hat{f}_{n-1}$. The predicted motion vector for each region is replaced by the newly calculated value, if the difference between the old and new values exceeds a threshold value. Only the new motion vectors are coded and transmitted to the decoder. The motion vectors which are not sent to the receiver can be obtained from $\hat{f}_{n-1}$ and $\hat{f}_{n-2}$, at the receiver end. This ensures that only a small portion of the motion vectors are transmitted, thus reducing the overhead for motion information. The predicted current frame is estimated by $\tilde{f}_n(r+\tilde{V}_i) = \tilde{f}_{n-1}(r)$ $r \in R_i$ i=1...m, for changed regions or $\tilde{f}_n(r) = \tilde{f}_{n-1}(r)$ for unchanged regions. The differential image $e_n(r) = f_n(r) - \tilde{f}_n(r)$ is then generated for transmission.

TRANSFORM CODING

The differential image is further encoded using the adaptive wavelet packet transform suggested by [3]. Adaptive wavelet packets are signal dependent. That is, for a given image, the best set of basis functions is determined from a library of possible bases. Hence the first task is to construct a general set of discrete-time orthonormal bases for application to compression.

Construction Of Discrete-Time Bases

The complete set of basis functions for a given signal x is constructed such that

$$X = \Sigma \langle x, \phi_k \rangle \phi_k \qquad (3)$$

where $\langle x, \phi_k \rangle$ denotes the inner product, and the set of basis functions which are orthonormal, are give2n by

$$\langle \phi_k, \phi_l \rangle = \delta_{k-l} \qquad (4)$$

Basis functions must have overlaps between adjacent, but different wavelet packet decomposition's to avoid discontinuities at boundaries. Such time-varying bases which retain orthogonality as well , are achieved using time-varying orthogonal tree structures. The method is based on the construction of transition and boundary filters, which allow the construction of arbitrary tilings. Using a two-channel filter bank, that is a pair of analysis filters $H_0(z)$ and $H_1(z)$,with $H_0(z)$ of even length and $H_1(z) = z^{2k-1}H_0(-z^{-1})$ the given image is split. These filters form an orthogonal filter set and the details of the construction of boundary and t ısition filters is given in [3]. Once the time-varying orthogonal trees are constructed, then, for a given image, the best set of basis functions for that particular image is determined using the "best basis and quantizer" algorithm.

Since our aim is compression, we make use of the rate-distortion criteria. The rate "R" is the number of bits required to represent the image and the distortion "D" is the squared error between the original image and its approximation using R bits. Every combination of basis and quantization choice represents a single operating point and is chosen by the the "best basis and quantizer" algorithm described below. For a given quality factor λ the following steps are carried out:

Step1: Generate the Wavelet packet coefficients and quantizer set dependent (R,D) values for the complete tree for each binary subset of the image to be coded.

Step 2: For a fixed λ, determine the best basis/ quantizer for each of the binary subset by minimizing the Lagrangian cost function $J = D + \lambda R$.

Step 3: All (R,D) points are converted to their associated Lagrangian costs

Step 4 : Each internal Wavelet packet tree is populated with the minimum Lagrangian cost to get the best quantizer at each node

Step 5: Full depth tree is pruned into that subtree which has minimum sum-of-leaves-cost to determine the best basis

Step 6: Global splitting tree is populated with minimum Lagrangian costs obtained from step 2 for each binary segment

Step 7: The splitting tree is pruned to get the best binary split tree

SIMULATIONS AND RESULTS

The methodology adopted in this paper was simulated for the "Canadian flag". Fig 1 shows a comparison of SNR versus the frame number for the above mentioned image sequence. It clearly indicates that a better SNR is achieved.

CONCLUSION

The segmentation-based motion compensation algorithm used here avoids the block effects that are persistent with the block-matching methods. Also the scheme is so designed that 1) The region shape information need not be transmitted as the segmentation of the reconstructed image is performed at both the encoder and the decoder; 2) Since motion vector prediction is performed at both encoder and decoder, and only the changed vectors are transmitted, a significant amount of overhead for motion information is reduced; 3) The Adaptive wavelet packet transform used represents the images more faithfully. A better SNR is obtained as demonstrated by results, even at very low bit-rates.

REFERENCES

[1] O. Rioul and M.Vetterli, "Wavelets and signal processing", IEEE Signal Proc. Mag, pp 14-38, Oct. 1991.

[2] M. Ohta and S. Nogaki., "Hybrid picture coding with Wavelet Transform and Overlapped Motion-compensated Interframe Prediction Coding",IEEE Trans on Sig. Processing, V 41, N 12, pp 3416-3424, 1993.

[3] C.Herley, J.Kovacevic, K.Ramachandran, and M.Vetterli, "Tilings of the Time-Frequency Plane : Construction of Arbitrary Orthogonal Bases and Fast Tiling Algorithms", IEEE Trans. on Sig. Proc., V 41, N 12, pp 3341-3359, 1993.

[4] I.Daubechis., "Orthonormal bases of Compactly Supported Wavelets", Comm. on Pure and App. Math., V XLI, pp 909-996,1988

[5] Le Gall D J., "The MPEG Video Compression Algorithm ", Signal Processing - Image Comm., V 4 , pp 1129-140, 1992.

[6] E.Salari and S Lin, "Low-bit-rate segmentation based image sequence coding", Optical Eng., V 34 , N 3 , pp 829-832, March 1995.

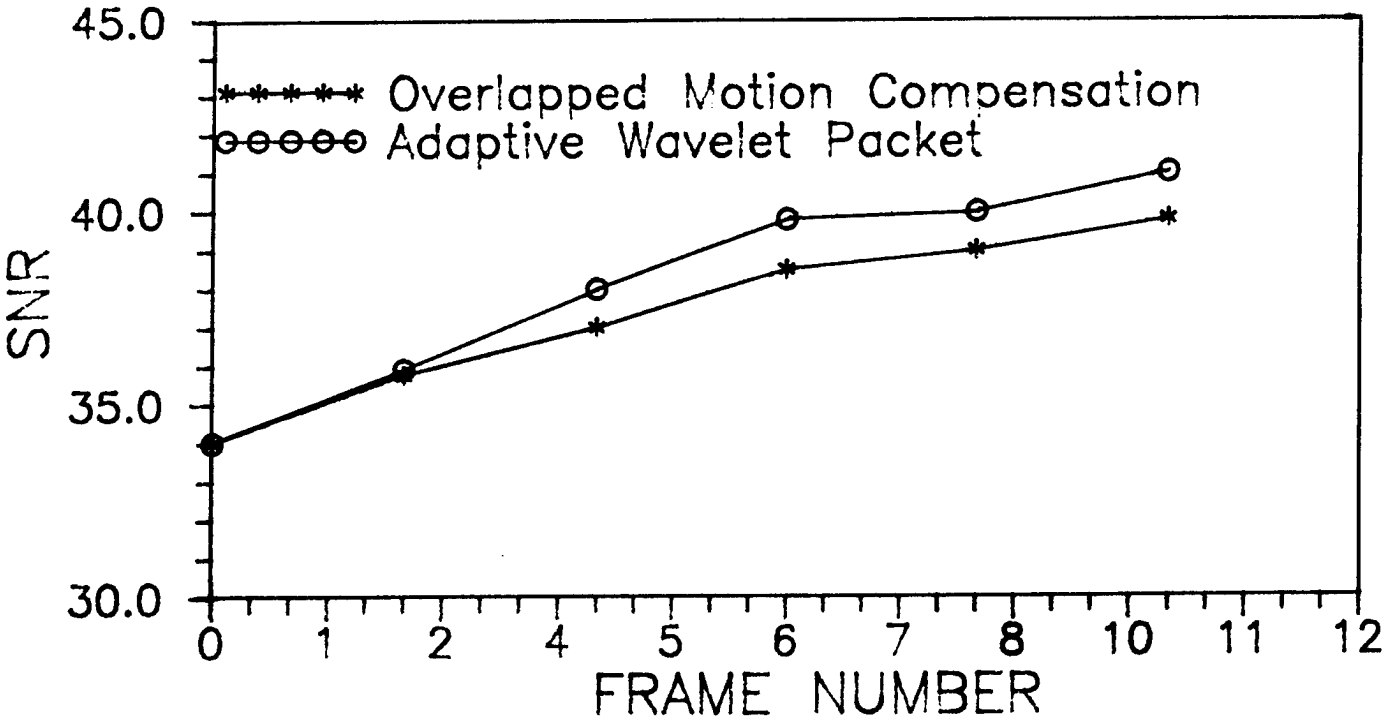


Fig. 1: Comparison of SNR vs Frame Number for the "Canadian Flag"

USING ATM NETWORKS FOR PROCESSING GLOBAL EARTH DATA*

Barbara L. Kess bkess@cse.unl.edu
Phillip R. Romig III romig@cse.unl.edu
Stephen E. Reichenbach reich@cse.unl.edu
Ashok Samal samal@cse.unl.edu

Department of Computer Science & Engineering
University of Nebraska, Lincoln
Lincoln, NE 68588-0115

ABSTRACT

Current workstation technology provides an unprecedented amount of computational power to researchers at an affordable cost, making it feasible to use workstations rather than expensive supercomputers to perform scientific analysis of large data sets, such as the Global Land 1-Km AVHRR data. In addition to this, inexpensive high speed ATM networks have the potential to improve the overall computational efficiency of workstations by using several workstations in a distributed environment.

This research studies the practicality of using distributed workstations interconnected with a 155 Mb ATM network for analysis and compression of the Global Land 1-Km AVHRR data versus sequential computing on one of the workstations. Performance comparisons are given for three algorithms associated with the compression of these data. Based on the test results, a discussion is given regarding the practicality of using a distributed system to enhance performance when processing global earth data.

1. INTRODUCTION

The proliferation of powerful inexpensive workstations, or desktop computers, is making it feasible for users in the remote sensing community to use workstations for data analysis of large data sets, whereas previously they had to arrange for time on supercomputers which are often expensive and inconvenient to use. Even though computing power is increasingly affordable, processing large data sets, such as the Global Land 1-Km AVHRR data [1], still poses significant problems in terms of processing time and disk resources. One possible solution is to process large data sets in a distributed environment, in which several workstations are interconnected via a Local Area Network (LAN) and simultaneously working on the same problem. Previous to current technological developments, this was not a viable alternative for processing global earth data because the speed of LAN technology was too slow to efficiently distribute large data sets such as the global AVHRR data. However, the introduction of new high speed network technology may change this and allow for efficient computing on global earth data over a network of distributed workstations. In this paper the performance of several algorithms for compression and analysis of Global Land 1-Km AVHRR data is reported using one workstation versus a distributed systems with one server and eight clients. A discussion compares the characteristics of problems that are well suited for the upcoming generation of distributed systems to problems that are still solved more efficiently in a monolithic environment.

2. MODELING DISTRIBUTED PERFORMANCE

One goal of this research is to model the performance of distributed algorithms for the analysis and compression of the Global Land 1-Km AVHRR data set, to determine in advance whether an algorithm merits the time and expense involved in converting it from a sequential to a distributed program. To do this a simplified model for runtime performance is used. Given an algorithm that reads in N data elements, performs operations on them, and then stores M data elements back onto the disk, the algorithm is divided into two parts: a sequential part which contains start up and shutdown overhead and any other operations that are not done in parallel, and a parallel part which contains all operations that may be executed in parallel. The time spent executing code which is not parallelizable is labeled T_s and the time spent executing code which is parallelizable is labeled T_p. The times required to read and write one data element to and from the disk are labeled as D_r and D_w, respectively. An equation for modeling the runtime of the sequential algorithm is given as

$$R_s = (D_r * N) + T_s + T_p + (D_w * M). \quad (1)$$

When modeling the distributed case, it is necessary to add the time required to transfer the data to and from the clients. Given a network which can transfer one data element in ω seconds, the time required to transfer the data to the clients is $\omega * N$, and the time required to transfer the results back to

*Support was provided in part by NASA Graduate Student Researchers Program grants NGT-51293 and NGT-595-204 and the Center for Communication and Information Sciences (CCIS) at the University of Nebraska.

0-7803-3068-4/96$5.00©1996 IEEE

the server is $\omega * M$. If P is the number of clients, then the distributed runtime is modeled as

$$R_d = (D_r*N)+(\omega*N)+T_s+\frac{T_p}{P}+(\omega*M)+(D_w*M). \quad (2)$$

The speedup gained by distribution is the ratio, $S = R_s/R_d$. This means that two conditions must hold in order for distribution to provide a speedup. First, the network transfer time ($\omega * N$) must be small. This paper assumes that the transfer time is indeed small when using a high-speed ATM network. The second condition is

$$(D_r * N) + (D_w * M) + T_s << T_p \quad (3)$$

If the left side of this inequality is not significantly less than T_p, then the speedup ratio, S, will tend towards one. If T_p is larger than the other terms then the speedup will approach P. Assuming that the network transfer time is small, performance prediction is based on the above inequality.

3. DESCRIPTION OF THE ALGORITHMS

Performance comparisons are given for three algorithms used by Kess, Steinwand and Reichenbach [2] to analyze and compress Global Land 1-Km AVHRR data. The algorithms vary in their computational complexity and although none of the algorithms has a high computational complexity, they are representative of typical algorithms used to analyze and compress large data sets. One of the merits of a good data compression algorithm is low computational complexity, making it unrealistic to report results from highly complex algorithms as representative of whether distributed systems can improve the speed of data compression algorithms for large data sets. The data used in the tests are the NDVI band of the April 1-10, 1992 data set, which contains 694,417,757 samples of 8-bit data. The first algorithm computes the histogram, the second computes the entropy of the residual image that results from each of the eight lossless JPEG [3] linear predictors, and the third algorithm compresses the data.

Computing the histogram is easily parallelized. In the distributed implementation each client receives a portion of the image, tallies the counts for the histogram, and sends the final results back to the server. The server sums the results from all of the clients and writes the final histogram to a file. This is a very simple program and the computation required for both T_s and T_p is very small. This means that the disk read time, $D_r * N$, will dominate the speedup ratio, S, and as a result S is expected to approach one. Thus, the distributed histogram is expected to perform only slightly better than the sequential algorithm.

The second algorithm finds the entropy of the residuals created from using each of the JPEG linear predictors for lossless compression. This algorithm was used by Kess *et al.* to determine which of the eight linear predictors in the lossless JPEG compression standard performs the best on the Global Land 1-Km AVHRR data. In the distributed version each client computes the residuals for a portion of the image. Each client sends eight histograms back to the server. As the server receives results from the client, it adds the histograms together. After all of the results are received, the server computes the entropy of each histogram and writes the results to an output file. The sequential time, T_s, is expected to be larger than T_s is for the histogram algorithm, but still small. The total processing time for tasks performed by the clients, T_p, is expected to be significantly larger than T_p for the histogram, and in fact it should dominate the sequential processing time, T_s, the disk read time, D_r*N, and the disk write time, D_w*M given in Inequality refpred. Hence, the entropy program is expected to give a speedup that is significantly greater than one.

The third program compresses the land data with the method used by Kess *et al.* This compression program divides the image into subimages and compresses each subimage independently of the others. Approximately 80% of the image is composed of solid regions for the water, interrupted areas in the Goode's Homolosine map projection, and land where there is no data. These areas are compressed by Kess *et al.* with a quadtree algorithm and the results from this compression are not reported. The land compression algorithm reads in all of the subimages and only compresses the data values that represent land. There are approximately 135 million land samples in the image. The compression algorithm for the land computes a residual image using the JPEG lossless linear predictor with the lowest entropy from the JPEG entropy tests, and then uses adaptive Huffman coding to compress the residual image.

This algorithm, like the others, is also easy to distribute because the compression is performed independently on subwindows of the image and the data file is preprocessed so that the subwindows are stored contiguously in the data file. The number of operations for each data element is the highest of all three programs, but these operations are only performed on the 20% of the data that represents land values. Thus, the expected total parallel processing time, T_p, is less than the JPEG entropy process. The sequential time, T_s, and the disk read time, $D_r * N$, are similar to the other two algorithms. However, the disk write time, $D_w * M$ is significantly larger because the server writes the compressed data to a file. Thus, the speedup is expected to be greater than one, but not as large as the JPEG entropy speedup.

4. THE DISTRIBUTED SYSTEM

Results are reported using a homogeneous workstation cluster consisting of eight Hewlett Packard 9000/715s and a server HP 9000/735. All the machines are connected by an ATM network running *classical* TCP/IP over ATM[4]. PVM[5] was used for message passing and synchronization. Results are given for two different methods of distributing data to the pro-

Computing Technique	Program Execution Times		
	Histo-gram	JPEG Entropy	Land Compress
Sequential	8:17	25:25	20:10
Distributed			
Centralized Data	12:50	19:00	16:43
Distributed Data	6:34	12:06	15:51

Table 1: Runtimes in Minutes:Seconds

cessors. The first method uses a Network File System (NFS) in which the file system is centralized and the entire image is stored on a single disk that is connected to the system via a 20MB/s Fast/Wide SCSI III interface. The second method makes use of local disk drives to perform a simplified type of data striping. In this method the image is divided into equal size subimages and one subimage is placed on the local disk of each client in the distributed system.

5. RESULTS

Table 1 presents the sequential and distributed results for each of the three algorithms discussed in this paper. The distributed results are presented for centralized data and data distributed to the local disks of each client. The sequential tests were performed on the 735 which is a faster machine than the 715's used as clients for the distributed tests. Because of this the reported runtimes for the sequential algorithms are slightly faster than if they were executed on the clients. However, none of the 715s had enough local disk space to run the sequential algorithm without using the network and thereby incurring a network transfer penalty for the execution time. Although executing the sequential algorithms on the faster processor decreases the speedup ratios, the processor speed inaccuracy is not as large as the extra network transfer time incurred by running the sequential algorithm on a client processor.

The speedup ratios for the distributed algorithms were 0.64 for the histogram, 1.33 for JPEG Entropy and 1.2 for the compression algorithm. By distributing the data these values improved to 1.2, 2.1, and 1.2 respectively. The model did not accurately predict a slow down for the distributed histogram with centralized data. This is because the model does not incorporate the overhead required for distribution. The results for the distributed histogram with distributed data improved because the disk read time was less.

It is interesting to note the speedup improvement when the data is stored locally on the client disks rather than on the centralized server. There are at least two advantages for using a decentralized file system. One advantage is that a decentralized file system processes the data without using large, fast and expensive disks, and the other advantage is it achieves the best speed of all the methods tested. This speed of the decentralized file system is also impressive because the local disks are 5MB/s SCSI disks, which is much slower than the 20MB/s FW SCSI III central disk.

6. CONCLUSION

Clearly, distributed processing of global AVHRR data is beneficial in some cases. It takes time to modify existing programs to run in a distributed environment, which is an important consideration before deciding to distribute an algorithm. If programs are originally written for distribution, then the programming time is not an issue. The simple model given in section 2 provides a starting point for analysis of distributed versus sequential processing. A modification is needed to incorporate the overhead required for distribution. While the model is mathematically straightforward, quantifying prediction values for the terms in the model is difficult.

The results suggest that distributed computing with distributed data has more benefits for large data sets than distributed computing with centralized data. Decentralized data storage can use slower and smaller disks than centralized data storage and still achieve better runtime performance. One implication of this is that large data sets could be stored in a distributed format for faster retrieval from permanent storage devices. For example, compressed browse images could be stored on a local disk for easy browse retrieval and compressed full resolution data could be permanently stored in distributed archival locations for distributed retrieval.

7. REFERENCES

[1] J. Eidenshink and J. Faundeen. The 1-Km AVHRR Global Land Data Set: First stages in implementation. *International Journal of Remote Sensing*, 15(17):3443–3462, 1994.

[2] B. Kess, D. Steinwand, and S. Reichenbach. Compression of the Global Land1-Km AVHRR Data Set. *International Journal of Remote Sensing*, To appear.

[3] W. Pennebaker and J. Mitchell. *JPEG Still Image Data Compression Standard.* Van Nostrand Reinhold, 1993.

[4] M. Laubach. Classical IP and arp over ATM (update). `ftp:\\ftp.com21.com`, August 1995.

[5] A. Geist, A. Beguelin, J. Dongarra, W. Jiang, R. Mancheck, and V. Sunderam. *PVM, Parallel Virtual Machine.* MIT Press, 1994.

Applications of Passive Microwave Observations of Surface Soil Moisture

Thomas Schmugge
USDA/ARS Hydrology Laboratory
Beltsville, MD 20705, USA
Tel:301-504-8554, FAX:301-504-8931, E-mail: schmugge@hydrolab.arsusda.gov

Abstract -- In large scale field experiments over the past 10 years, long wavelength microwave radiometers have been used to map surface soil moisture with considerable success. These experiments, which include FIFE (87 & 89), Monsoon 90, Washita 92 and 94, and HAPEX-Sahel, covered a wide range of climatic regimes. The results from all of them have shown that the microwave emission at the 21-cm wavelength is a strong function of surface (0 to 5-cm) soil moisture. The salient results from these experiments will be presented and compared. The use of the surface soil moisture data to determine geophysical parameters such as evaporative fraction, soil evaporation and soil hydraulic properties will be discussed.

INTRODUCTION

After more than 20 years of research on the use passive microwave radiometers[1] for soil moisture sensing the basic capabilities are well understood. The soil emissivity at microwave wavelengths, about 1 to 30 cm, is a strong function of its moisture content because of the large dielectric contrast between dry soil and water. The resulting emissivity for soil changes from about 0.95 for dry soil to about 0.6 for wet soils at a rate of about 0.01/% moisture content. The rate is a function of the soil texture, being greater for lighter sandy soils and smaller for heavier clayey soils. The rate will also be reduced by surface features such as roughness and vegetation cover. The observed emissivity is determined by the moisture content in a thin layer at the surface on the order of a few tenths of a wavelength thick. Therefore it has been found that the longer wavelengths (> 10 cm) are more effective for moisture sensing both the depth of penetration and the ability to penetrate a vegetated canopy[2,3]. Knowledge of this surface layer moisture content is very important for determining the energy balance at the soil surface and its rate of change can be used to infer information about the hydraulic properties of the soil. In this short paper we will describe briefly describe some results obtained by microwave radiometers in field experiments during the past ten years and their applications to range of problems.

LARGE SCALE FIELD EXPERIMENTS

Microwave radiometers operating at the 21-cm wavelength were used to map surface soil moisture in large scale field experiments and to study its utility for determining such things as surface fluxes and soil hydraulic properties. Here we will discuss the results from four recent experiments: the First International Satellite Land Surface Climatology Project (ISLSCP) Field Experiment (FIFE) conducted in central Kansas in 1987-89[4]; MONSOON'90 conducted during the summer of 1990 over and arid watershed in south central Arizona in the US[5]; WASHITA 92 conducted over the Little Washita watershed in central Oklahoma in 1992[6] and the Hydrological and Atmospheric Pilot Experiment in the Sahel (HAPEX-Sahel) experiment conducted in Niger West Africa in 1992[7,8].

The radiometric measurements were made with L-band (frequency = 1.42 GHz; wavelength = 21-cm) microwave radiometers. They were the PushBroom Microwave Radiometer (PBMR)[9] and the Electrically Scanned Thinned Array Radiometer (ESTAR)[10] and were flown aboard the NASA C-130 aircraft. While they have very different antenna systems they have similar operating characteristics. Both receive horizontally polarized radiation with a 16° resolution. The PBMR has 4 beams and a ±32°swath while ESTAR has 10 beams with a ±45°swath.

FIFE

The test area for FIFE was about 15x15 km and primarily tall grass prairie. It contains the Konza Prairie Research Natural Area and surrounding grasslands. Microwave brightness temperature maps were obtained for a 7 X 15 km area by flying 12 parallel east-west flight lines at an altitude of 600m. This was done for a total of 12 days during 4 Intensive Field Campaigns (IFC's) between 28 May and 20 October 1987. With these microwave brightness temperature maps for the FIFE site it was possible to determine the surface soil moisture over a wide area. The results were in excellent agreement with the ground measurements[11]. The RMS difference between the estimated and measured values of soil moisture was 4.5% over the range from 10% to over 40% with a 1.8% bias. We believe that the latter came from the fact that the aircraft and ground measurements were made at different times of day.

In an analysis of the FIFE-89 data for the surface area averaged fluxes. Sellers et al.[12], found that the remotely sensed surface soil moisture from the PBMR is very important for parameterizing the soil resistance to evaporation and for estimating the soil profile moisture content.

MONSOON'90

The test site for MONSOON'90 was the Walnut Gulch research watershed near Tombstone, Arizona [5]. The purpose here was to

0-7803-3068-4/96$5.00©1996 IEEE

observe the moisture fluxes in an arid climate during a drydown and the role of remote sensing in determining these fluxes. There were a series of 6 flights with the PBMR between 31 July and 9 August at an altitude of 600 m. Seven flight lines were flown to map an area of about 5 x20 km. The results showed a high correlation between the PBMR observations and ground measurements of soil moisture. The brightness temperature maps faithfully represented the rainfall variability indicated by the high density rain gage network[13]. In this experiment the PBMR observations of the surface moisture state were successfully used to set the initial conditions for a rainfall runoff model[14].

WASHITA 92

The Little Washita watershed was selected for this experiment because of the extensive hydrologic research that has been conducted there in the past (32 years of data collection); the ongoing data collection by the Agricultural Research Service; and the complementary nature of the region to previously conducted large scale remote sensing experiments e.g. Monsoon 90 and FIFE. The watershed is located is southwest Oklahoma in Great Plains region of the United States and covers an area of 603 km^2. The climate is classified as sub-humid with an average annual rainfall of 75 cm. There are a total of 42 continuous recording rain gages distributed at a 5 km spacing over the watershed. The topography of the region is moderately rolling. Soils include a wide range of textures with large regions of both coarse and fine textures. Land cover is dominated by rangeland and pasture (63%) with significant areas of winter wheat and other crops concentrated in the floodplain and western portions of the watershed. Data collection was performed during the period of June 10 to June 18, 1992. This followed a period of very heavy rains. While, there was considerable spatial variability during the individual rain events, the integrated totals over the various gages over the site were rather uniform. As a result the initial conditions encountered at the beginning of the experiments were mostly saturated soils with some standing water. No rainfall occurred during the experimental period, thus allowing the observation of drying conditions.

In this experiment the ESTAR was flown on a set of high altitude mapping flight lines at a nominal altitude of 2200 m. This pattern was designed to provide contiguous coverage of the 40 x 15 km test area with a resolution of about 600m. These data were used to produce soil moisture maps of the area[6]. Rodriguez-Iturbe[15] used these maps to study the statistical structure of soil moisture fields. They found a power law relationship between the variance and pixel area with the variance decreasing as the area increased. The slope of the relationship increased as the soil dried. With the same data Dubayah et al.[16] found that multiscaling, i.e. the log-log linearity of statistical moments as functions of scale, can be used to infer spatial variability at scales other than that of the measurements. For example they showed how a coarse remotely sensed field of soil moisture could be used estimate variability at finer grid scales. By studying the temporal changes of the surface soil moisture Mattikalli et al. [17] have shown that there is a direct relationship between changes in soil moisture and soil texture. As a result it may be possible to estimate the saturated hydraulic conductivity on a large area basis.

HAPEX-Sahel

HAPEX-Sahel [7,8] is an international land-surface- atmosphere observation program that was undertaken in western Niger, in the west African Sahel region. The overall aims were to improve our understanding of the role of the Sahel on the general circulation, in particular the effects of the large interannual fluctuations of land surface conditions in this region and, in turn, to seek relationships between the general circulation and the persistent droughts that have affected the Sahel during the last 25 years. The field program obtained measurements of atmospheric, surface and certain sub-surface processes in a 1deg x1deg area that incorporates many of the major land surface types found throughout the Sahel. In order to obtain data for this large area, an extensive measurement program was undertaken including field, aircraft, and satellite remote sensing measurements, mainly between mid 1990 and late 1992. An intensive operations period (IOP) was undertaken for 8 weeks from mid to late growing season of 1992.

The aim of HAPEX-Sahel was to make simultaneous measurements of relevant variables at the micro and meso scales. The heterogeneity of surface types and seasonal variation in the region are much greater than in the areas studied in any previous measurement campaign of this type. To address this aspect of the problem an extensive remote sensing program was used to extend the field measurements to the entire region, i.e to the meso-scale. This aircraft program included the PBMR on the C-130 aircraft for soil moisture observations. Because of the timing of the IOP during the monsoon season a wide range of surface moisture conditions were observed from extremely dry to rather wet. Chanzy et al.[18] have found excellent correlations between the ground measurements of soil moisture and the PBMR data at both the East and West central sites using ground observations made by two different groups. The rapidly drying surface soil also enabled us to make certain inferences about the soil hydraulic properties. Hollenbeck et al. [19] compared the brightness temperature values on two successive flight on 2 and 4 September 1992 using a normalized difference to obtain maps of relative soil hydraulic properties which matched the existing soils maps.

DISCUSSION

In all of the large scale experiments a wide range of soil moisture conditions was observed and in each case a good correlation between the microwave response and soil moisture was found. These results were for a range of vegetation conditions from sparse vegetation in the MONSOON'90 and HAPEX-Sahel experiments to a rather heavy grass cover in the FIFE experiment. In none of these cases did the vegetation preclude making a useful assessment of soil moisture conditions with the microwave radiometer data. The temporal variations of soil moisture observed in these experiments have been used in flux studies and

in making estimates of soil hydraulic properties on an areal basis. Maps of the microwave brightness temperature were produced in all these experiments. They have made possible new studies of the spatial variability and structure of soil moisture fields. These maps have provided just a small sample of what could be done if such a radiometer on a satellite platform were doing the mapping on a global basis.

REFERENCES

[1] Schmugge T., P. Gloersen, T. T. Wilheit, and F. Geiger, 1974. "Remote Sensing of Soil Moisture with Microwave Radiometers," Jour. Geophys. Res., 79(2), pp. 317-323.

[2] Jackson, T. J. and T. J. Schmugge, 1989. Passive Microwave Remote Sensing System for Soil Moisture. IEEE Trans. Geoscience and Remote Sensing, March 1989, GE-27:225-235.

[3] Schmugge, T.J. and Jackson, T.J., 1994. Mapping Surface Soil Moisture with Microwave Radiometers. Meteorology and Atmospheric Physics, 54, pp 213-223.

[4] Sellers, P.J., F.G. Hall, G. Asrar, D.E. Strebel and R.E. Murphy, (1992) An Overview of the First International Satellite Land Surface Climatology (ISLSCP) Field Experiment (FIFE), J. Geophys. Res., 97, pp 18,345-18371.

[5] Kustas. W.P., et al., 1991. An Interdisciplinary Study of the Energy and Water Fluxes in the Atmosphere-biosphere System over Semiarid Rangelands: Description and Some Preliminary Results. Bull Am Meteorol Soc., vol. 72, pp 1683-1705.

[6] Jackson, T.J., LeVine, D.M., Swift, C.T., Schmugge, T., and Schiebe, F.R., 1995. Large Area Mapping of Soil Moisture Using the ESTAR Passive Microwave Radiometer. Remote Sens. Environ., 54, pp 27-37.

[7] Goutorbe J-P., et al., 1993. HAPEX-*Sahel: A Large Scale Observational Study of Land Atmosphere Interactions in the Semi-Arid Tropics. Annales Geophysicae, 12, pp 53-64.

[8] Prince, S.D., et al., 1995. The Hydrology Atmosphere Pilot Experiment in the Sahel (HAPEX-II-Sahel). Remote Sens. Environ., 51, pp 215-234.

[9] Harrington, R. and R.W. Lawrence, 1985. An Airborne Multiple Beam 1.4 GHz PushBroom Microwave Radiometer. Proc IGARSS85, 7-9 October, 1985, Amherst MA. pp 601-606.

[10] Le Vine, D.M., A.J. Griffis, C.T. Swift, and T.J. Jackson 1994. ESTAR: A Synthetic aperture Microwave Radiometer for Remote Sensing applications. Proc IEEE, 82, pp 1787-1801.

[11] Wang, J. R., T. J. Schmugge, J. C. Shiue, and E. T. Engman, 1990. The L-band PBMR measurements of surface soil moisture in FIFE. IEEE Trans. Geoscience and Electronics, GE-28:906-914.

[12] Sellers, P.J. et al., 1995. Effect of Spatial Variability in Topography, Vegetation Cover and Soil Moisture on Area-averaged Fluxes: A Case Study using the FIFE 1989 Data. J Geophys. Res., 100, pp 25,607 - 25,629.

[13] Schmugge, T.J., Jackson, T.J., Kustas, W.P., Roberts, R., Parry, R., Goodrich, D., Amer, S. and Weltz, M.A., 1994. PBMR Observations of Surface Soil Moisture in Monsoon 90. Water Resources Research, 30, pp 1321-1327.

[14] Goodrich, D.C., Schmugge, T.J., Jackson, T.J., Unkrich, C.L., Keefer, T.O., Parry, R., and Amer, S., 1994. Runoff Simulation Sensitivity Measurements to Remotely Sensed Initial Soil Water Content. Water Resources Research, 30, pp 1393-1405.

[15] Rodriguez-Iturbe, I., Vogel, G.K., Rigon, R., Entekhabi, D., Castelli, F. And Rinaldo, A., 1995. On the spatial organization of soil moisture fields. Geophysical Research Letters, 22, pp 2757-2760.

[16] Dubayah, R., Wood, E.F., and Lavallée, D. 1996. The Spatial Scaling Properties of Remotely Sensed and Modeled Near-surface Soil Moisture State for the Little Washita Basin. To be published in Scaling of Remote Sensing Data for GIS, ed.: D. Quattrochi and M. Goodchild, Lewis Publishers.

[17] Mattikalli, N.M., E.T. Engman, L.R. Ahuja, and T.J. Jackson, 1995. Estimating Soil Properties from Microwave Measurements of Soil Moisture. Proc. SPIE Conf.. on Remote Sensing for Agriculture, Forestry, and Natural Resources. 26-28 September 1995, Paris France. Vol 2585, pp 89-101.

[18] Chanzy, A., Schmugge, T.J., Calvet, J.-C., Kerr, Y., van Oevelen, P., Grosjean, O., and Wang, J.R., 1996. Airborne microwave radiometry on a semi-arid area during HAPEX-Sahel. To be published Journal of Hydrology.

[19] Hollenbeck, K.J., Schmugge, T.J., Hornberger, G.M. and Wang, J.R., 1996. Identifying soil hydraulic heterogeneity by detection of relative change in passive microwave remote sensing observations. Water Resources Research, vol. 32, pp 139-148.

Spatial and Temporal Trends in Land Surface Moisture and Temperature Observable Using Data from the Nimbus-7 Microwave Radiometer

Eni G. Njoku and Brian W. Rague

Jet Propulsion Laboratory, M/S 300-233
California Institute of Technology
4800 Oak Grove Drive, Pasadena, CA 91109
Tel: (818) 354-3693
Fax: (818) 354-9476
Email: njoku@lor.jpl.nasa.gov

Abstract -- Nimbus-7 SMMR brightness temperatures have been reprocessed in a form that simplifies the data handling associated with estimation and analysis of global land parameter fields. Spatial and temporal analyses of the brightness temperatures indicate their sensitivities to land surface and atmospheric conditions, and show trends linked to changing surface moisture, temperature, and vegetation patterns. An estimation algorithm is used, calibrated to sites in arid regions and forests, to obtain preliminary estimates of the land parameters for a given geographic region. Focusing on semiarid areas where the potential for observing moisture variability using the SMMR channels is greatest, the estimates are compared with model output data. Results of the study are helpful in evaluating the potential of future L-band spaceborne radiometer measurements, which would have greatly increased capability for surface moisture estimation if available.

INTRODUCTION

The need for routine space-based measurements of surface soil moisture, surface temperature, and vegetation biomass has been firmly established [1], [2]. Measurements of these parameters are valuable for initializing and calibrating weather and climate models, and for forecasting and monitoring floods and droughts. Microwave radiometry has shown potential for such measurements, but sensors optimized for measuring these parameters are not yet available in space.

Data from the Nimbus-7 Scanning Multichannel Microwave Radiometer (SMMR) have been used in land parameter studies, but have elicited limited interest in practical applications. The frequency range (6.6 to 37 GHz) is higher than desired for good sensitivity to surface soil moisture in the presence of roughness and vegetation. The spatial resolution (ranging from ~150 km at 6.6 GHz to ~30 km at 37 GHz) limits applications mainly to climate and large-scale monitoring. The natural heterogeneity of land surfaces leads to retrievals over SMMR footprints of spatially-averaged parameters that may require care to interpret and to relate to parameters of climate and hydrologic models [3]. Nevertheless, the SMMR data cover a near-decadal time period (1978 to 1987) which is of benefit in studying climatological trends. Furthermore, the SMMR has similar low-frequency channels to those planned for EOS-era microwave radiometers (MIMR and AMSR). Analyses of SMMR data are thus useful for developing improved processing algorithms for these sensors, and for creating a radiometric climatology for interpreting future measurements.

In this paper the retrievability of land parameters using SMMR data is investigated. First, the results of a theoretical sensitivity analysis are presented. A principal component analysis is then applied to the SMMR data over the African continent to illustrate spatial patterns and temporal trends in the radiometric data. Finally, retrievals are carried out for a localized region in the Sahel, indicating the feasibility of using SMMR data to study seasonal trends of soil moisture, vegetation, and temperature in semiarid regions. The sensitivity study indicates that the use of lower frequencies than available on the SMMR, i.e. 1.4 as opposed to 6.6 Ghz, will result in greatly enhanced capability to follow soil moisture trends in the presence of moderate vegetation, thereby extending the global coverage area of soil moisture retrievability.

SENSITIVITY

The retrievability of soil, vegetation, and atmospheric parameters from spaceborne radiometer data is determined to a large extent by the sensitivity of brightness temperature to these parameters at optimum frequencies, polarizations, and viewing angles. A microwave model is used here to assess these sensitivities. The model can be expressed as:

$$T_B = \Phi \{ \bar{x} \} \quad (1)$$

where, T_B is the brightness temperature, $\Phi\{\}$ is the radiative transfer model function, and $\bar{x}$ is a vector of parameters describing the sensor configuration, media characteristics, and geophysical variables. The model function is based on models described previously in [4]. Normalized sensitivities, S_i, are computed as:

0-7803-3068-4/96$5.00©1996 IEEE

$$S_i = \left| X_i \left(\frac{\partial \Phi}{\partial x_i} \right)_{\bar{x} = \bar{x}_o} \right| \qquad (2)$$

where, X_i are the typical dynamic ranges or uncertainties of the parameters x_i, and $\bar{x}_o$ are the values of $\bar{x}$ at which the partial derivatives are evaluated (baseline values). Since the model is nonlinear in some parameters, the sensitivities will depend on $\bar{x}_o$. Table 1 shows the results of sensitivity calculations at three frequencies—1.4, 2.6, and 6.6 GHz (L, S, and C bands). The 1.4 GHz frequency is considered optimal for soil moisture sensing, while 6.6 GHz is the lowest frequency available from the SMMR. The sensitivities have been computed for a viewing angle of $\theta = 50°$ and for circularly-polarized reception. Circularly-polarized radiation is invariant to Faraday rotation through the ionosphere which may prove to be a significant source of error for linearly-polarized reception at 1.4 GHz. The parameters for which sensitivities are shown in Table 1 are: soil moisture, m_v (g cm^{-3}); soil temperature, T_{se} (C); soil clay fractional content, s; vegetation water content, w_c (kg m^{-2}); atmospheric precipitable water, q_v (mm); surface air temperature, T_{as} (C); near-surface atmospheric temperature gradient, dT_a (C); and Faraday rotation angle at 1.4 GHz, ϕ_f (deg).

As expected, the sensitivity to soil moisture is dominant at L-band, while sensitivity to vegetation becomes dominant at C-band (~4-5 times as sensitive as L-band). The sensitivity to soil parameters is fairly uniform over the frequency range. Sensitivity to atmospheric parameters increases with frequency but is relatively negligible. Sensitivity to Faraday rotaion is zero since circular polarized reception has been assumed. These sensitivity results are for a baseline of $w_c = 0$ (bare soil) and will vary as w_c changes. The magnitudes of the normalized sensitivities also depend of course on the assumed values of X_i.

Table 1: Normalized sensitivities at L, S, and C-bands (1.4, 2.6, and 6.6 Ghz), $\theta = 50°$, circular polarization, and for given parameter ranges and baseline values. (Parameter units are given in the text.)

Parameter	Range (X_i)	Baseline (x_{oi})	Sensitivities, S_i (K) (L)	(S)	(C)
m_v	0.32	0.15	80.3	80.1	77.8
T_{se}	40	20	35.1	34.5	30.4
s	0.4	0.3	10.0	10.2	10.1
w_c	1.5	0	27.4	50.1	119.7
q_v	5	2.5	0.02	0.07	0.74
T_{as}	30	15	0.37	0.39	0.53
dT_a	10	13.5	0.12	0.13	0.18
ϕ_f	40	20	0	0	0

DATA SETS

The SMMR data used here have been extracted from the SMMR Pathfinder brightness temperature data set [5]. The data were gridded to a monthly 1° x 1° lat-lon scale for the African continent region. The results shown here are for the year 1980. Subsequent analyses will cover the full SMMR time period. Comparisons with the SMMR retrievals have been made using data from the ISLSCP Initiative I CD-ROM [6]. These data are also gridded at monthly 1° x 1° lat-lon resolution.

PRINCIPAL COMPONENT ANALYSIS

A principal component analysis (PCA) was performed to identify the spatial and temporal modes of variability in the SMMR brightness temperature data at different space-time scales. PCA is commonly used as a technique for reducing the dimensionality of a data set, for culling signal from noise, and for viewing the dominant modes of 'smooth' variability in the data [7]. Fig 1 shows the PCA for the 6.6 GHz polarization ratio, $PR_{6.6}$, defined as the difference divided by the sum of the vertical and horizontal brightness temperatures at 6.6 GHz. Forming this ratio minimizes the dependence on surface temperature so that the dominant dependence is on soil moisture and vegetation variability [8]. The annual mean field is shown in Fig.1(c). The two dominant spatial modes (i.e. principal components, e_1 and e_2) with maximum time variability are shown in Figs.1(a), (b). The amplitude vectors for the first four modes (e_1 to e_4) are shown in Fig.1(d). The amplitude vectors are time-series indicating the time-variability of each mode (which, summed, constitute the time variability of the $PR_{6.6}$ field). The amplitude vectors e_1 and e_2 show annual cycles offset in phase. The principal components illustrate the brightness temperature variability in the broad savanna/Sahel belt north of the equator and at other isolated locations, in particular at: 15°N, 5°W; 8°N, 30°E; 13°S, 23°E. These locations correspond to regions of seasonal flooding of the Niger, White Nile, and Zambezi rivers, respectively, with opposite phases in the northern and southern hemispheres. Additional analysis is required to fully understand these localized phenomena.

RETRIEVALS

It is expected that retrievals of soil moisture using SMMR will only be successful in regions of low vegetation, due to the high sensitivity to vegetation at frequencies of 6.6 GHz and above. A location close to the site of the 1992 HAPEX-Sahel experiment, centered at 12.75°N, 4.25°E, was chosen for testing the parameter retrievability. Four SMMR channels: 6.6 and 10.7 GHz, V and H polarizations, were used in an iterative least-squares estimation procedure to retrieve three geophysical parameters—surface soil moisture, m_v, vegetation water content, w_c, and surface temperature, T_{se}. Fig.2(a)-(c) shows results of the monthly retrievals for the year 1980. The results show clearly the cycles of surface

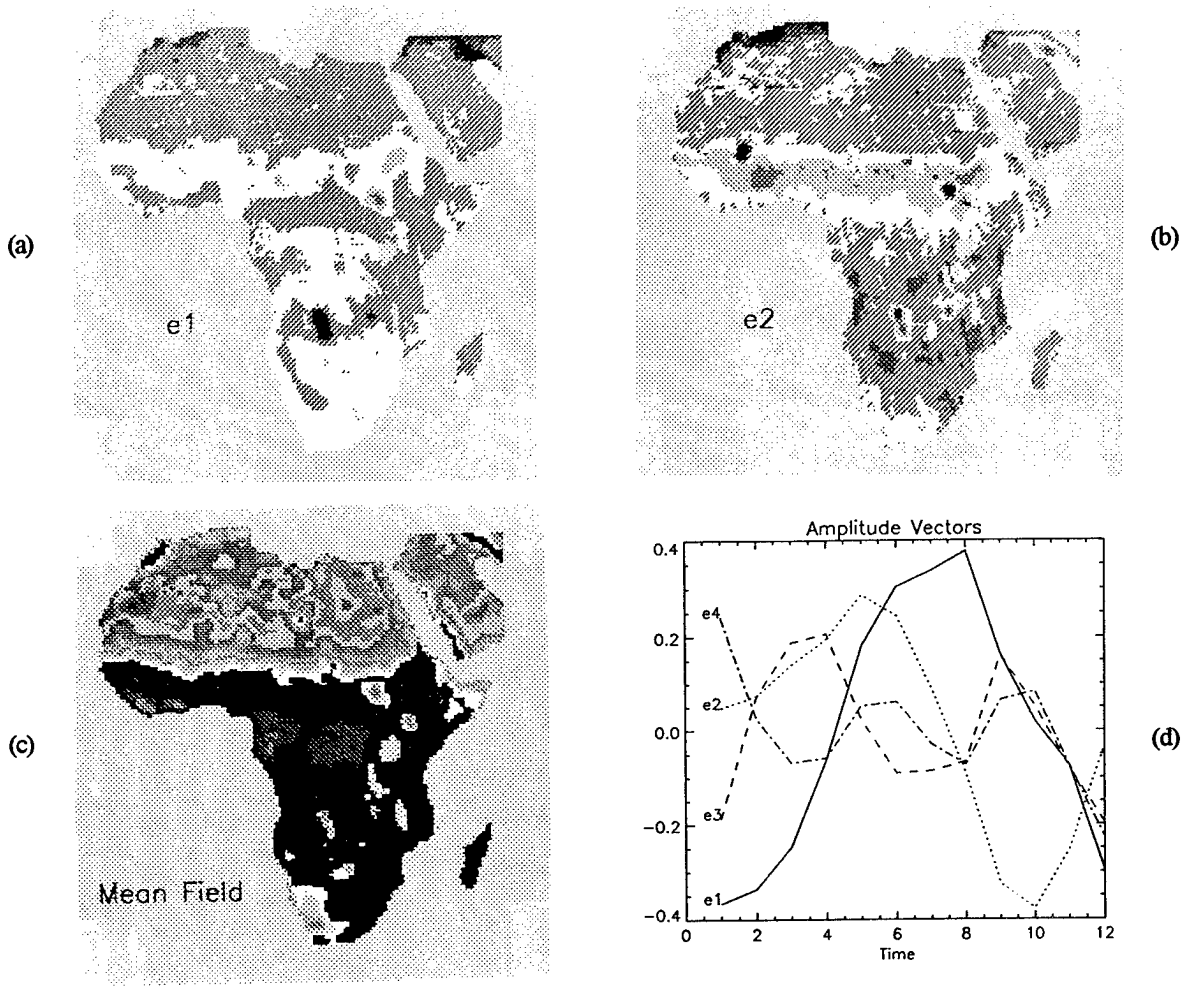


Fig.1 Illustrative results of principal component analysis over Africa using monthly, gridded SMMR brightness temperature polarization ratio data from 1980 at 6.6 Ghz. (a) and (b) First and second principal components, respectively. (c) Annual mean field. (d) Amplitude vectors for the first four principal components; time is in months of the year (1980).

moisture and vegetation growth/senescence related to the annual precipitation cycle in the region. The earlier phasing of the peak moisture relative to the peak vegetation is clearly evident. Also evident is a dip in the surface temperature in July-August that may be related to the period of precipitation maximum. Fig.2(d)-(f) shows values of surface wetness, normalized difference vegetation index (NDVI), and noon surface temperature, extracted from the ISLSCP CD-ROM [6]. Although these data are for the year 1987 the temporal trends agree well with the SMMR retrievals. The ISLSCP surface wetness and temperature data are outputs from the ECMWF numerical weather forecast model. The NDVI data are derived from the NOAA/AVHRR satellite instrument.

The SMMR retrieval algorithm was 'calibrated' at two end points representing desert and tropical forest. It is encouraging to note that the expected trends in soil moisture, vegetation water content, and surface temperature are indeed observed in the retrievals. Further analysis is required to achieve more confidence in the validity of the retrievals.

CONCLUSION

The SMMR data set provides a radiometric climatology that can be analyzed for trends and anomalies in land surface parameters (soil moisture, vegetation status, temperature). These parameters can also be retrieved quantitatively from the SMMR data in low-vegetation regions. The fraction of global land cover for which SMMR retrievals are feasible may be limited. However, the ability to discriminate soil moisture trends using SMMR data at 6.6 and 10.7 GHz bodes well for possible future spaceborne missions using 1.4 GHz which has five times less sensitivity to the perturbing influence of vegetation.

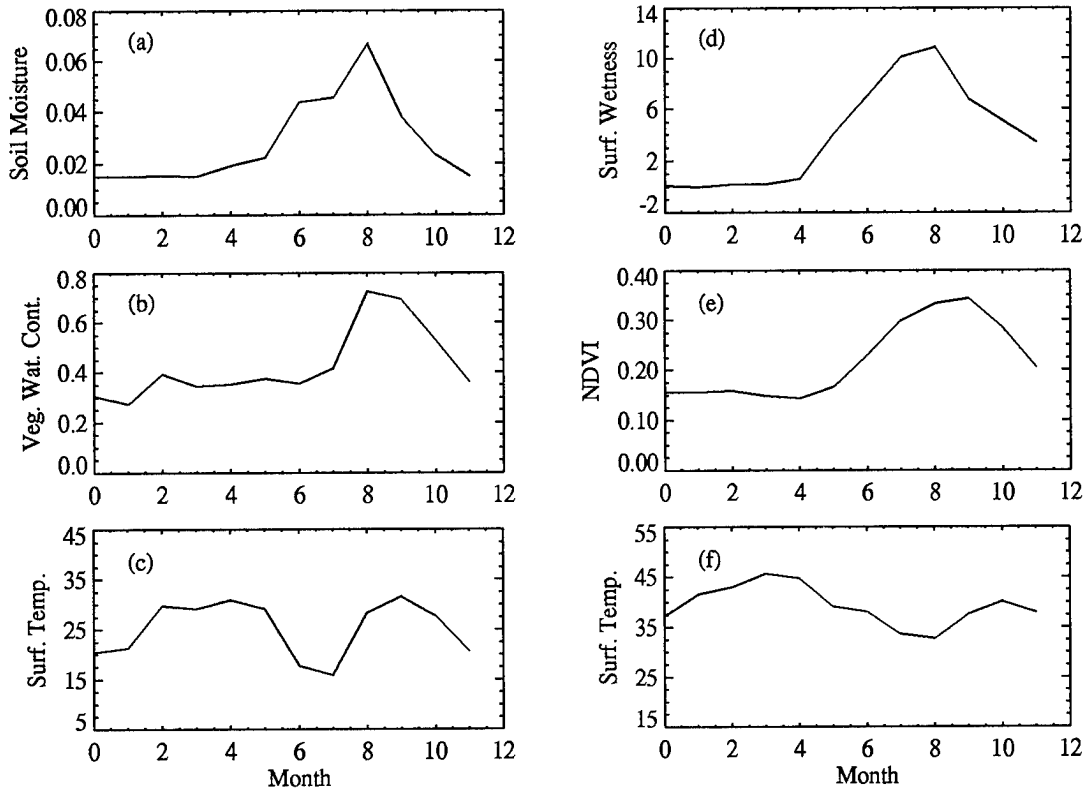


Fig.2 Comparison of trends from SMMR noontime land parameter retrievals with those from ISLSCP data for a 1°x1° lat-lon grid cell centered at 12.75°N, 4.25°E in the African Sahel. (a), (b), (c) SMMR monthly retrievals of soil moisture, m_v, vegetation water content, w_c, and surface temperature, T_{se}, respectively for 1980. (d), (e), (f) ISLSCP data of surface wetness, NDVI, and noontime surface temperature, respectively, for 1987.

ACKNOWLEDGMENTS

This paper represents one phase of research carried out at the Jet Propulsion Laboratory, California Institute of Technology, under contract to the National Aeronautics and Space Administration.

REFERENCES

[1] National Research Council, "A decade of international climate research: The first ten years of the World Climate Research Program," National Academy Press, Washington, DC, 1992, 59pp.

[2] M.-Y.Wei, Ed., "Soil Moisture: Report of a Workshop Held in Tiburon, California, 25-27 January 1994, NASA Conference Publication 3319, National Aeronautics and Space Administration, Washington, DC, 1995, 78pp.

[3] E.G.Njoku, S.J.Hook, and A.Chehbouni, "Effects of surface heterogeneity on thermal remote sensing of land parameters," Proceedings of the Workshop on Scaling-Up Hydrological Variables Using Remote Sensing, Institute of Hydrology, Wallingford, UK, 10-12 June 1996 (submitted).

[4] E.G.Njoku and D.Entekhabi, "Passive microwave remote sensing of soil moisture," J. Hydrology (in press), 1996.

[5] E.G.Njoku, B.Rague, and K.Fleming, "The Nimbus-7 SMMR Pathfinder Brightness Temperature Data Set," 1995. Available from the Hydrologic Cycle Distributed Active Archive Center, NASA Marshall Space Flight Center, Huntsville, AL. http:/wwwdaac.msfc.nasa.gov.

[6] B.W.Meeson and 7 others, "ISLSCP Initiative I–Global Data Sets for Land-Atmosphere Models, 1987-1988, Volumes 1–5. Published on CD by the National Aeronautics and Space Administration (USA_NASA_GDAAC_ISLSCP_001–USA_NASA_GDAAC_ISLSCP_001, 1995.

[7] R.W.Preisendorfer, "Principal Component Analysis in Meteorology and Oceanography," New York: Elsevier, 1988.

[8] Y.H.Kerr and E.G.Njoku, "A semi-empirical model for interpreting microwave emission from semiarid land surfaces as seen from space," IEEE Trans. Geosci. Rem. Sens., vol. 28, pp. 384-393, 1990.

Application of Microwave Remotely Sensed Surface Soil Moisture for Estimation of Sub-surface Soil Hydraulic Properties

Edwin T. Engman, and Nandish M. Mattikalli
NASA Goddard Space Flight Center, Laboratory for Hydrospheric Processes
Hydrological Sciences Branch, Code 974, Greenbelt, MD 20771, USA
Tel: (301) 286-5480 Fax: (301) 286-1758
E-mail: tengman@neptune.gsfc.nasa.gov

Laj R. Ahuja
USDA Agricultural Research Service, Great Plains Systems Research
301 South Howes, PO Box E, Fort Collins, CO 80522, USA

Thomas J. Jackson
USDA Agricultural Research Service, Hydrology Laboratory
Beltsville, MD 20705, USA

Abstract -- Multi-temporal microwave remote sensing techniques have been employed to obtain information on surface soil moisture dynamics during June 10-18, 1992 in the Little Washita watershed, Oklahoma. Analysis of remotely sensed data in conjunction with soils map revealed that changes in brightness temperature and soil moisture hold a direct relationship with soil texture. Areas identified by loam/ silt loam are characterized by higher changes of total soil moisture and those of sand/ sandy loam soils by remarkably lower amounts of change. Detailed study yielded valuable information on soil physical properties (soil texture) and saturated hydraulic conductivity (K_{sat}). Root Zone Water Quality Model has been employed to simulate soil water redistribution during the dry down period, and therefore to estimate profile soil properties. Results provided good relationships between surface soil moisture dynamics and profile K_{sat} values. It follows that temporal variability of surface soil moisture can be used as indicators of both surface and sub-surface soil properties. These findings have potential application of microwave remote sensing of soil moisture to obtain quick estimates of spatial distributions of soil properties for parameterization of mesoscale hydrologic and general circulation models.

INTRODUCTION

Information on surface soil moisture is important to hydrologic research for partitioning rainfall into runoff and infiltration components as well as separating incoming radiation into latent and sensible heat [8]. Hydrologically, soil is an important reservoir of fresh water, and owing to the action of which non continuous precipitation is transformed into continuous discharge as stream base flow and recharge to ground water. Quantity of water resources available in a drainage basin is therefore greatly influenced by soil hydrology. Microwave remotely sensed data have a great potential for providing areal estimates of soil moisture [5]. Passive microwave remote sensing employs measurements of thermal emission from soil at longer microwave wavelengths (> 10 cm) to determine moisture content in the surface layer. It relies on the fact that emissivity at these wavelengths is a function of dielectric constant of the soil-water mixture and thus soil moisture. Relationship between microwave emission of natural surfaces and their inherent moisture content has been studied and well documented in the literature [5,7,8]. Studies involving truck and aircraft measurements not only demonstrated this basic relationship but have also helped to quantify effects of various surface parameters such as soil texture, roughness and vegetation that distort and confound the basic relationship [7].

This paper demonstrates that temporal measurements of brightness temperature and surface soil moisture obtained from microwave remote sensing can be employed to estimate soil hydraulic properties. This research suggests that two-day initial drainage of soil is related to an important soil property viz. saturated hydraulic conductivity (K_{sat}).

STUDY AREA AND DATA DESCRIPTION

The Little Washita watershed occupies an area of 610 km^2 in the southern part of the Great Plains in southwest Oklahoma. The watershed has long term hydrologic monitoring facility. Climate of the region is classified as moist and subhumid with an average annual rainfall of about 750 mm [2]. A research experiment (Washita'92) was a carried out in the watershed during June 10-18, 1992. During the experiment, land cover in the watershed was dominated by pasture and senesced or harvested winter wheat [4]. The forest cover within the watershed is very sparse and constitutes a small proportion of the watershed. As part of the Washita'92, multitemporal airborne microwave data were collected using the Electronically Steered Thinned Array Radiometer (ESTAR) [4]. ESTAR is a synthetic aperture, passive microwave radiometer which operates at L band (21 cm wavelength, or 1.4 GHz frequency) [7]. Spatial resolution of the ESTAR data collected during Washita'92 is 200 m.

In addition to the aircraft measurements, a large number of ground soil moisture measurements (more than 700

0-7803-3068-4/96$5.00©1996 IEEE

gravimetric samples per day) were carried out. These ground truth data have been used to support and validate microwave remotely sensed data. Profile soil moisture was measured at thirteen sites using a Resonant Frequency Capacitance (RFC) probe [4]. The study area experienced heavy rainfall (more than 30 mm) on June 5, 1992, and moderate rainfall continued till June 9, 1992. However, there was no rainfall in the watershed for the entire duration of the Washita'92 experiment [4]. Therefore, hydrologic conditions in the watershed were ideal because it was possible to follow a drying period from very wet (about 30%) to dry (about 10%) over a period of nine days (fig. 1).

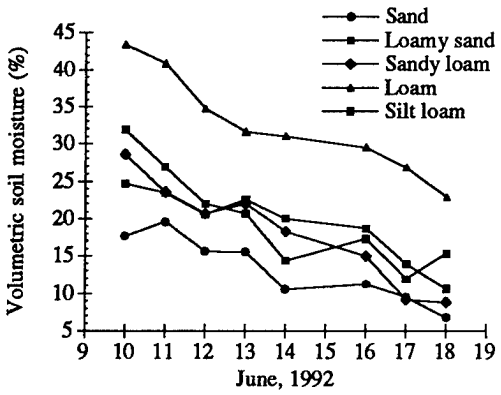


Fig. 1. Temporal variations of surface soil moisture for various soil texture types typically found in Little Washita watershed. Different soil types have distinct characteristics of soil moisture contents and the associated temporal changes, which therefore, can be used as indicators of soil texture.

TEMPORAL CHANGES OF BRIGHTNESS TEMPERATURE AND SOIL MOISTURE

Data collected from ESTAR were converted into brightness temperature values [7]. Daily maps of brightness temperature portrayed significant spatial and temporal variations. On June 10, 1992, the watershed was characterized by regions of low temperatures on the eastern and western parts separated by a region of comparatively higher temperatures . On the last day, temperatures increased all over the watershed with enhanced spatial variation. Surface soil moisture information was generated from brightness temperature after correction, where possible, for vegetation effects, and validated using field measurements [7]. Over a large corn field, which represented the densest vegetation cover encountered during the experiment (canopy height of 2.1 m), excellent match was obtained between predicted and measured soil moisture, with an average absolute error of less than 1.5% [6]. On June 10, 1992, wet and dry soils had a volumetric moisture contents of about 35% and 15%, respectively. Therefore, at the start of the experiment, surface soil was at near saturated condition in the eastern and western part of the watershed. Dry down pattern of the soil was captured clearly in the soil moisture maps. These observations of temporal surface soil moisture are interesting from hydrologic perspective to establish relationship between changes in soil moisture and soil texture.

Spatial and temporal variations of soil moisture observed during Washita'92 were mainly attributed to drainage and redistribution of water content. Hydro-meteorological parameters could be considered spatially constant because of their small variation across the area. Drainage is mainly controlled by physical property viz. soil texture, and hydrologic property viz. K_{sat}. A careful study of spatial distribution of both brightness temperature and soil moisture revealed that distribution follows the pattern of soil texture. This observation is obvious in fig. 1 which shows the temporal variation of soil moisture for five different soil types. An analysis was carried out within a GIS framework to correlate soil moisture change and soil texture [8]. This demonstrated that silt loam and loam soils are characterized by higher changes of total moisture content, whereas sandy loam and sandy soils are associated with lower changes. These characteristics may be related to hydraulic properties of the soil. Sandy soils with higher hydraulic conductivity drained quickly, whereas loamy soils having lower hydraulic conductivity did not drain before the start of the experiment on June 10, 1992 [8]. This is an important observation in that it suggests that remotely sensed soil moisture information can be employed to identify soil types and to estimate soil hydraulic properties.

ESTIMATION OF SOIL HYDRAULIC PROPERTIES

In a recent study, statistically significant relationships have been established between changes in moisture content of the surface soil, 2 days after a thorough wetting, and average K_{sat} of the soil profile [1]. Such relationships are valuable to obtain estimates of an average K_{sat} from remotely sensed soil moisture observations made at 2-day temporal resolution. Study was conducted to establish such relationships for the field conditions of Washita'92. A state-of-the-art physically based soil hydrology model viz. the Root Zone Water Quality Model (RZWQM) [3] and a GIS have been employed to carryout soil moisture simulation studies to estimate profile K_{sat}. Details of the modeling procedure have been reported elsewhere [8]. Approximate profile soil hydraulic properties obtained from soil series maps and soil texture data were optimized and validated using field measurements. Results of model simulations were employed to calculate the harmonic-mean K_{sat} for each site. Figs. 2(a)-(b) show relationships between two-day initial surface drainage (0-5 cm depth) and profile harmonic-mean K_{sat} for 5 cm and 60 cm depths, respectively. The least squared linear regression equations presented in fig. 2 suggest that profile harmonic-mean K_{sat} bears good positive relationship with two-day changes in surface soil moisture (with correlation coefficients of 0.77 and 0.68 for 5 cm and 60 cm depths, respectively). The results are in close agreement with that reported by literature [1].

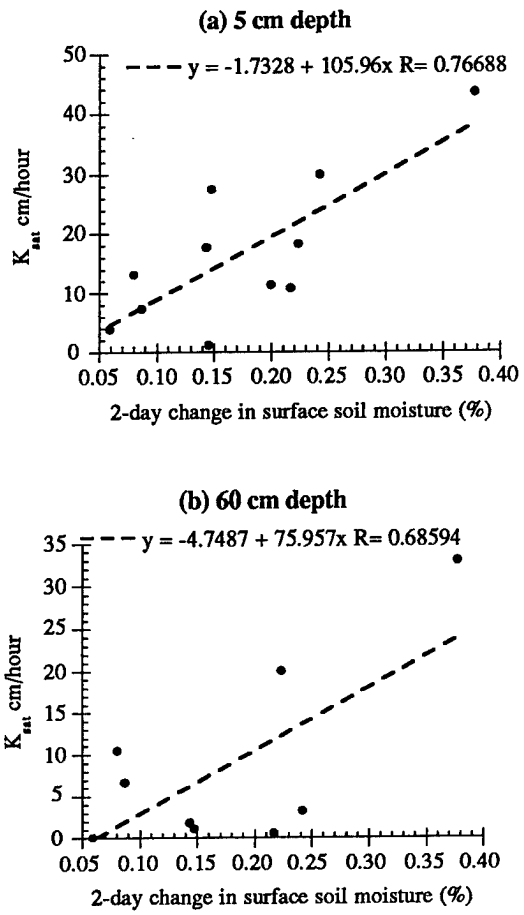


Fig. 2. Relationships between profile harmonic-mean K_{sat} derived from hydrologic model simulations and two-day initial changes in surface soil moisture obtainable from microwave remote sensing.

CONCLUSIONS

Microwave remote sensing was employed to obtain spatial and multi-temporal soil moisture data for the Little Washita watershed, Oklahoma. Spatial and temporal pattern observed in both brightness temperature and soil moisture closely followed pattern of soil texture. Various soil types exhibited distinct patterns of soil moisture contents and drainage which suggested that remotely sensed soil moisture contents and their temporal changes could be employed to identify soil type and to estimate soil hydraulic properties. A methodology was developed to employ remotely sensed data to estimate profile K_{sat} using a hydrologic model and GIS. Relationships were established between profile harmonic-mean K_{sat} and two-day soil moisture change. Results demonstrated that temporal changes in surface soil moisture observed from remote sensing can be used to estimate soil hydraulic properties. The findings have a significant potential to obtain quick estimates of spatial distribution of K_{sat} from remotely sensed soil moisture data. Long term potential applications of these results are derivation of soil properties on a regional and continental scale from space borne remote sensing platforms for input into mesoscale and general circulation models.

ACKNOWLEDGMENTS

Nandish M. Mattikalli held a National Research Council-NASA GSFC Research Associateship. The support was provided by the Science Division of NASA's Office of Mission to Planet Earth.

REFERENCES

[1] L. R. Ahuja, O. Wendroth, and D. R. Nielsen, "Relationship between initial drainage of surface soil and average profile saturated conductivity," Soil Sci. Soc. Am. J., vol. 57, pp. 19-25, 1993.

[2] P. B. Allen, and J. W. Naney, Hydrology of the Little Washita River watershed, Oklahoma: data and analysis. USDA/ARS-90, 74 p., 1991.

[3] D. G. Decoursey, and K. W. Rojas, "A Root Zone Water Quality Model (RZWQM)," Proc. of Symp. on Towards a Sustainable Agri. for Great Plains, Jan. 19-20, Fort Collins, CO., 1990.

[4] T. J. Jackson, and F. R. Schiebe (eds.), Hydrology data report: Washita'92. USDA-Agri. Res. Ser., Nat. Agri. Water Quality Lab., NAWQL 93-1, Durant, OK, 1993.

[5] T. J. Jackson, D. M. Le Vine, A. J. Griffis, D. C. Goodrich, T. J. Schmugge, C. T. Swift, and P. E. O'Neill, "Soil moisture and rainfall estimation over a semiarid environment with the ESTAR microwave radiometer," I.E.E.E. Trans. Geosci. and Rem. Sensing, vol. 31, pp. 836-841, 1993.

[6] T. J. Jackson, D. M. Le Vine, A. Griffis, D. C. Goodrich, T. J. Schmugge, C. T. Swift, P. E. O'Neill, R. R. Roberts and R. Parry, "Soil moisture verification study of the ESTAR microwave radiometer: Walnut Gulch, AZ 1991", Proc. IGARSS'92, Houston, TX, vol. I, pp. 486-488, 1992.

[7] T. J. Jackson, D. M. Le Vine, C. T. Swift, T. J. Schmugge, and F. R. Schiebe, "Large area mapping of soil moisture using the ESTAR passive microwave radiometer in Washita'92," Rem. Sen. Environ., vol. 53, pp. 27-37, 1995.

[8] N. M. Mattikalli, E. T. Engman, L. R. Ahuja, and T. J. Jackson, "Estimation of sub-surface soil hydraulic properties from surface soil moisture data obtained from remote sensing," In: E. T. Engman, G. Guyot, C. M. Marino (ed.), Remote sensing for agriculture, forestry, and natural resources, SPIE vol. 2585, pp. 89-101, 1995.

[9] W. J. Rawls, and D. L. Brakensiek, "Estimation of soil water retention and hydraulic properties", In: H. J. Morel-Seytoux (ed.), Unsaturated flow in hydrologic modeling-theory and practice. Kluwer Academic Pub, pp. 275-300, 1989.

Investigation of the Accuracy of Soil Moisture Inversion Using Microwave Data and Its Impact on Watershed Hydrological Modeling

P.E. O'Neill, A.Y. Hsu
Hydrological Sciences Branch/974, Laboratory for Hydrospheric Processes,
NASA/Goddard Space Flight Center, Greenbelt, MD 20771 USA,
Tel: 301-286-8273, Fax: 301-286-1758, E-mail: peggy@hydro2.gsfc.nasa.gov

T.J. Jackson
USDA/ARS Hydrology Laboratory, 104 Bldg 007 BARC-West, Beltsville, MD 20705 USA
Tel: 301-504-8511, Fax: 301-504-8931, E-mail: tjackson@hydrolab.arsusda.gov

E.F. Wood, M. Zion
Department of Civil Engineering, Princeton University, Princeton, NJ 08544 USA
Tel: 609-258-4675, Fax: 609-258-1270, E-mail: efwood@pucc.princeton.edu

INTRODUCTION

During 1992 and 1994 NASA/GSFC, USDA, and Princeton University conducted hydrology field experiments in the Little Washita River watershed near Chickasha, Oklahoma with a goal of characterizing the spatial and temporal variability of soil moisture using microwave sensors from ground, aircraft, and space platforms. A major objective of these activities included the subsequent incorporation of the microwave-derived soil moisture patterns in models of larger scale water balance and partial area hydrology. While work is continuing to improve the accuracy of microwave soil moisture inversion algorithms for both bare and vegetated soils, the impact of errors in estimated soil moisture on hydrological modeling of the watershed has yet to be addressed.

In this study a coupled water and energy balance model operating within a topographic framework was used to predict surface soil moisture fields for the Little Washita watershed for an eight-day period in June, 1992 which covered a wide range of soil moisture conditions. The model was first driven by meteorological forcing data, and the model-generated soil moisture fields are compared in space and time to those produced for the watershed by the airborne passive microwave ESTAR sensor for the same time period. In a second analysis, the model was initialized by the remote sensing data, and subsequent model predictions of soil moisture are compared to measured values.

WASHITA '92 EXPERIMENT

The Little Washita River watershed is situated in southwest Oklahoma in the Great Plains region of the United States and covers an area of approximately 600 km^2. Extensive data collection for the Washita '92 experiment occurred during the period of June 10 through June 18, 1992 following several weeks of heavy rain. Surface cover in the watershed was predominantly pasture, rangeland, and senesced or harvested winter wheat, with some agricultural crops (corn, alfalfa) and urban and woodland areas. Eight days of passive microwave measurements from the airborne ESTAR 1.4 GHz radiometer were acquired along with supporting ground truth data as the soil dried out from saturation level [1]. ESTAR data were processed to produce calibrated brightness temperature maps on a 200-m grid for the northern two-thirds of the Little Washita watershed. Using a soil moisture retrieval algorithm which incorporated information about soil texture and surface cover, these brightness temperatures were then converted into estimates of soil moisture for the 0-5 cm surface layer for each flight day [2]. The ESTAR-derived soil moisture maps were used in this study both for assessing the accuracy of the hydrological model results and for model initialization.

HYDROLOGICAL MODELING

Surface soil moisture fields for the Little Washita watershed for June 10-18, 1992 were generated by a semi-distributed coupled water and energy balance hydrological model. The model uses spatially distributed topographic and soils data to develop a statistical distribution of hydrological response to meteorological forcings. The model assumes that subsurface moisture flows are driven by topographic gradients as described by the soil-topographic index, and uses Brooks-Corey equations to relate soil moisture, matrix potential, and unsaturated hydraulic conductivity. The unsaturated soil column is divided into two layers: a 5-cm thin upper layer and a deeper transmission zone; vegetation roots can be distributed between both layers. For modeling purposes, a modeling element (pixel) can be divided into bare soil and vegetated areas (fractional coverage), with the latter

0-7803-3068-4/96$5.00©1996 IEEE

including canopy interception storage in the flux calculations. The model is described in [3].

Meteorological forcings used in the model include available energy (net radiation minus ground heat flux), air temperature, relative humidity, and wind; there was no precipitation during the experimental period. Radiation and meteorological data were measured at three sites and averaged across the watershed. The data were reported every 30 minutes and used at that time step for the simulations in this study. The data are described in [1].

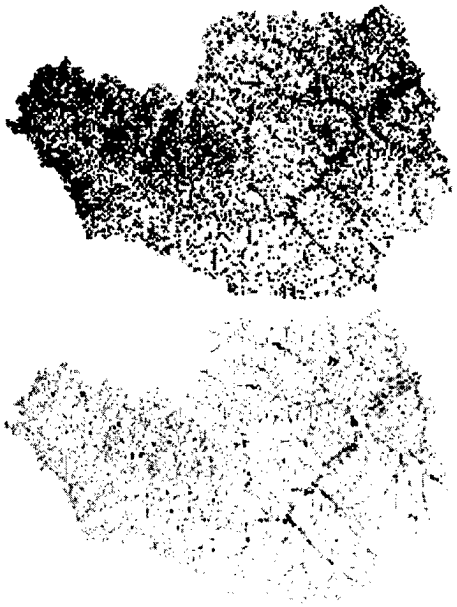
RESULTS

Calibration of hydrological models has usually been carried out on the basis of streamflow recession analysis. Following this procedure, the hydrological model described above was run for the Little Washita for the period June 10-18, 1992. The 0-5 cm soil moisture fields generated by the model for the wet day of June 10 are shown in Fig. 1(a), where darker tones represent wetter areas. The model outputs were compared to ESTAR-derived soil moisture values whose accuracy was validated using ground measurements of soil moisture from a number of test fields in [2].

In general, the hydrological model initialized with streamflow data on June 10 produced surface soil moisture fields that were too wet on June 10 and remained wetter than the ESTAR soil moisture throughout the drydown period. Fig. 2(a)-2(b) show difference images on a wet and dry day created by subtracting ESTAR soil moisture from the model soil moisture; black indicates areas of no data (no ESTAR flightlines), bad data (RFI noise), or manmade structures (turnpike running diagonally across the watershed). Both difference images as well as the histogram in Fig. 2(c) clearly demonstrate the overall model bias to wetter values. This result is not surprising given that the baseflow component of the water budget is often a minor factor, especially during summer months, and may be an inappropriate state variable if calibration of the surface parameterization for infiltration and evaporation is desired.

In the second set of model runs, the hydrological model was initialized using the ESTAR soil moisture from June 10. This was accomplished by adjusting the basin average soil moisture from the model to match the basin average soil moisture from ESTAR. Implicit in this approach is the assumption that pixels with the same soil topographic index respond the same way hydrologically. Model soil moisture fields on June 10 resulting from the remote sensing initialization are shown in Fig. 1(b). Compared with Fig. 1(a), it is obvious that the model can now resolve small farm ponds and saturated areas in ways that were impossible with the streamflow initialization. Difference values in Fig. 2(d) - 2(f) indicate that the model soil moisture fields now match

(a)



(b)

Fig. 1. Model soil moisture fields on June 10 from initialization with (a) June 10 baseflow and (b) June 10 ESTAR.

the observed surface soil moisture from ESTAR much more closely throughout the drydown period with less bias. Furthermore, the spatial distribution of surface wetness which implies spatially different rates of drying can be related to differences in soil hydraulic properties. Thus, in addition to producing better overall simulations of the hydrological response of the watershed, model initializaton with the microwave-derived soil moisture could also be used to provide more accurate values of hydraulic parameters for the dominant soil texture classes in the area.

REFERENCES

1. Jackson, T. and F. Schiebe, eds., 1993, "Hydrology Data Report: Washita '92," NAWQL 93-1, USDA/ARS National Agricultural Water Quality Lab., Durant, OK.

2. Jackson, T., D. Le Vine, C. Swift, T. Schmugge, and F. Schiebe, 1995, "Large area mapping of soil moisture using the ESTAR passive microwave radiometer in Washita '92," Remote Sensing of Environment, 53, pp. 27-37.

3. Famiglietti, J. and E. Wood, "Multi-scale modeling of spatially-variable water and energy balance processes," Water Resources Research, 30 (11), 3061-3078, Nov., 1994.

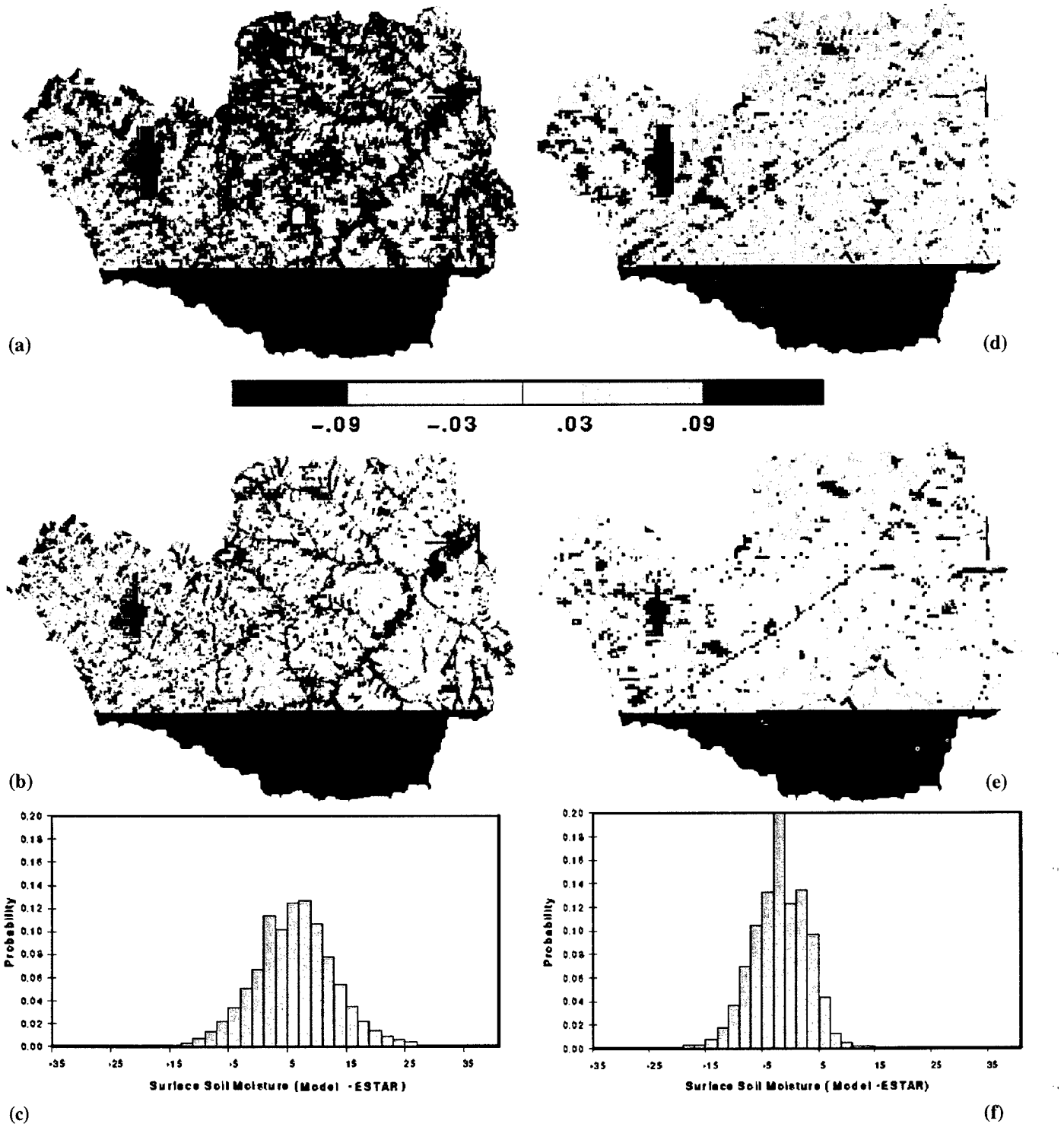


Fig. 2. Difference images of 0–5 cm surface soil moisture created by subtracting ESTAR soil moisture from hydrological model soil moisture using (a) model initialized w/June 10 baseflow for June 10 (wet day); (b) model w/June 10 baseflow for June 16 (dry); (d) model initialized w/June 10 ESTAR for June 10 (wet); (e) model w/June 10 ESTAR for June 16 (dry). Histogram distributions on June 16 for (c) model w/baseflow and (f) model w/ESTAR.

SIR-C/X-SAR As a Bridge to Soil Moisture Estimation Using Current and Future Operational Satellite Radars

Thomas J. Jackson*
USDA ARS Hydrology Lab, 104 Bldg. 007 BARC-W, Beltsville, MD 20705
(301) 504-8511 fax (301) 504-8931 tjackson@hydrolab.arsusda.gov

Tang Ling Li
Chinese Remote Sensing Satellite Ground Station, Beijing, China

Eric F. Wood
Dept. of Civil Engineering, Princeton University, Princeton, NJ 08544

Ann Hsu
SSAI, Lanham, MD 20706

Peggy E. O'Neill and Edwin T. Engman
NASA Goddard Space Flight Center, Laboratory for Hydrospheric Processes,
Hydrological Sciences Branch, Greenbelt, MD 20771

ABSTRACT

The Shuttle Imaging Radar experiments in 1994 (SIR-C/X-SAR) involved simultaneous data acquisition at a variety of frequencies and polarizations that included those of all existing and near future satellite SAR systems. As part of SIR-C/X-SAR a soil moisture experiment was conducted in the Little Washita watershed located in Oklahoma. Hydrologic conditions during the April mission started from a mostly wet soil condition with no additional rain for the duration of the mission. A data set of georegistered SIR-C and X-SAR data and ground observations has been prepared for distribution. Daily changes in incidence angle were normalized using published results for various land cover types. These normalized data were then related to soil moisture for satellite configurations representative of ERS-1 and 2, Radarsat, JERS-1, and other planned missions. Initial results show that for rangeland regions the empirical angular correction performs well and that some single frequency-polarization combinations can be used for estimating soil moisture if additional land cover/vegetation factors are considered.

INTRODUCTION

Operational satellite synthetic aperture radar (SAR) systems have been available for several years, and a number of studies have been conducted to evaluate the potential of these data for surface soil moisture estimation. For the most part these studies have been of limited success and no robust procedure for soil moisture has emerged. Possible reasons for the lack of progress in this area include the difficulty of algorithm development and verification with limited temporal coverage, the available system designs, and the inherent limited information content of a single frequency and polarization system. The Shuttle Imaging Radar experiments in 1994 (SIR-C/X-SAR) involved simultaneous data acquisition at a variety of frequencies and polarizations that included those of all existing and near future satellite SAR systems. As part of SIR-C/X-SAR a soil moisture experiment was conducted in the Little Washita watershed located in Oklahoma. Ground based soil moisture sampling was conducted concurrent with the SIR-C/X-SAR observations for a number of sites which were representative of the region (dominated by rangeland). In addition to providing a suite of radar observations, the hydrologic conditions during the 8 day April mission were started with wet soil conditions with no additional rain for the duration of the mission. Thus within a relatively short time period, a wide range of soil moisture conditions were observed with minimal change in other physical parameters such as biomass. The objective of this paoer is an assessment of the utility of the SIR/C-X/SAR data in the development and assessment of different approaches to soil moisture estimation based on existing satellite radar sensors.

THE WASHITA94 SIR-C/X-SAR DATA BASE ON CD

One of the major issues addressed was the assembly and integration of a wide variety of data collected as part of Washita94, including the SIR-C/X-SAR observations. All of the data directly related to the two SIR-C/X-SAR missions (April and October) have been assembled on a CD for distribution. Data are arranged in the following directories:

0-7803-3068-4/96$5.00©1996 IEEE

1. Descriptions of the ground test sites
2. Average soil moisture for each site
3. Site location maps
4. False color composite images collected 4/6/94 of most test sites using the NS001 multispectral sensor on the C-130 aircraft
5. Landsat Thematic Mapper data from 4/12/94.
6. ERS-1 satellite radar data from 4/15/94
7. SIC-C data from April (dB)
8. SIC-C data from October (dB)
9. X-SAR data from April (dB)
10. Truck based radar observations (C and L band, all polarizations and a range of angles)

Sites and Ground Sampling.

The majority of the 24 test sites used in Washita94 were selected to provide representative spatially distributed soil moisture information. Four of these sites were used solely for transect soil moisture studies and two sites were sampled occasionally by investigators for specific reasons. In addition, some changes in the sites used were made during the different experimental periods. Data included for each site are site coding, soil texture, bulk density, vegetation parameters (wet and dry biomass), and surface roughness.

The primary purpose for collecting ground observations of surface soil moisture was to provide calibration and verification data for the microwave remote sensing instruments. Sites were selected in an attempt to include a representative sampling of the various soil textures and land cover conditions. In addition, it was desirable to have these sites spatially distributed over the 600 sq. km. study area (in case of spatially distributed rainfall events) and also to have some clustered for radar analysis. For most of the sites, the primary goal was to determine the field average soil moisture. Gravimetric soil moisture sampling was used to characterize the 0-5 cm layer. These data were converted to volumetric soil moisture using the bulk density observations at each site. Some limited sampling of the 0-1 cm layer was also performed.

Other Satellite Data.

A Landsat Thematic Mapper image was acquired April 12, 1994. This image was georegistered to topographic maps and then the primary study area was extracted. This image served as the base for georegistering the radar data sets. The data are in individual TIF grayscale files for each channel. Processed files contain 934 lines by 1467 pixels at a resolution of 30 m.

A single ERS-1 image (SGF product) was available for April 15, 1994 and was corrected for antenna pattern using an algorithm provided by the Canadian Centre for Remote Sensing. The ERS-1 image was georegistered to the TM image using control points, resampled to a 30 m resolution, and stored as described above for the Landsat data.

SIR-C and X-SAR Data.

The original SIR-C and X-SAR data sets (Table 1) as processed and calibrated by NASA JPL were were the basis for the data sets generated here. NASA JPL software was modified to output the data as a backscattering coefficient with the same scale used on all dates. The use of one scale for all the images should facilitate day to day comparisons. These data sets were then processed as described above. Coverage on each day varies greatly due to the different modes, angles and orientation.

Table 1. Summary of Washita94 SIR-C and X-SAR Data Sets

Date	Pass(1)	Incidence Angle at Center (deg.)	Polarizations	X-SAR
4/11/94	a	28.0	hh hv vv	y
4/12/94	a	42.3	hh hv vv	y
4/13/94	a	50.1	hh hv vv	y
4/14/94	a	56.3	hh hv	y
4/14/94	d	48.3	hh hv	y
4/15/94	a	60.2	hh hv vv	n
4/15/94	d	42.4	hh hv vv	y
4/16/94	d	36.2	hh hv vv	y
4/17/94	d	30.9	hh hv vv	n
4/18/94	d	26.5	hh hv vv	y
10/02/94	a	28.4	hh hv vv	n
10/03/94	a	41.3	hh hv vv	n
10/04/94	a	49.9	hh hv vv	n
10/05/94	d	47.2	hh hv vv	n
10/06/94	d	40.1	hh hv vv	n
10/10/94	d	34.4	hh hv vv	n

(1) a=ascending and d=descending

ANGULAR ADJUSTMENTS OF SIR-C AND X-SAR DATA

A major problem in utilizing the SIR-C and X-SAR data for generating data sets comparable to those collected by operational satellites is the change in angle that occurs each day during the missions . We utilize the extensive results published by Ulaby and Dobson [1] as a means of correcting for these changes. This publication summarizes numerous data bases and describes the backscattering coefficient (σ°) as a function of land cover, band (frequency), and polarization. For each of these categories, using the data sets available, the authors have fit a nonlinear function that predicts σ° as a function of angle (θ) and have summarized the parameters for each function. These relationships are used here to examine the angular sensitivity of σ° for specific land cover types found in the study area. As an example, Figure 1 shows the predicted relationships for grasses for all of the SIR-C/X-SAR frequencies. Key points of this figure include the relatively low sensitivity to θ of σ° above 30° (compared to that at low values of θ and the overall consistency of the pattern regardless of the frequency-polarization chosen.

For the purposes of the current investigation, the results of these angular studies mean that (for a first pass analysis) at larger viewing angles we can compare the various SIR-C/X-SAR

data passes on a day to day basis with minimal concern for angular changes. This allows us to focus on the soil moisture changes. These results also suggest that it is possible to develop a quantitative angular adjustment technique. Utilizing the angular functions, we can specify a particular viewing angle representative of a satellite configuration and compute the differences between σ^o at this angle and the angle of observation of each SIR-C/X-SAR pass. This results in a correction factor for each land cover-frequency-polarization-pass combination. By applying these correction factors to the SIR-C/X-SAR observations we simulate the observations that might be made by a particular operational satellite utilizing a particular viewing angle. In Figure 2 the observations made over one of the rangeland sites on all passes have been plotted along with the predicted relationship (assuming that angular change is the only significant variable). The angular model tracks the observed data pattern fairly well. Unfortunately, if much of the observed variation can be explained by angular change then it may be difficult to isolate soil moisture effects.

The correction approach described above was used to evaluate the ERS-1 configuration (C-VV-23°) for estimating soil moisture over grasslands. These results are shown in Figure 3. The soil moisture-σ^o relationship based on a linear regression had a standard error of estimate of 0.055 for soil moisture which is typical of results published elsewhere [2-5].

SUMMARY

The development and evaluation of operational satellite radar sensors for soil moisture estimation has been quite limited. Part of the problem has been the lack of adequate temporal coverage compounded by uncontrollable changing site conditions. Data collected during the Washita94 SIR-C/X-SAR experiments were ideally suited for soil moisture studies due to a wide range of moisture conditions within the short mission duration. These data have been processed and integrated into a data set available for distribution. A procedure is suggested here for utilizing this data set to evaluate the potential of various satellite configurations in estimating soil moisture for the range of conditions encountered in the Washita94 investigation.

REFERENCES

[1] F. T. Ulaby and M. C. Dobson, "Handbook of radar scattering statistics for terrain," Artech House, MA, 357p., 1989.

[2] M. O. Benallegue, O., Taconet, D. Vidal-Madjar, and M. Normand, M., "The use of radar backscattering signals for measuring soil moisture and surface roughness," Remote Sensing of Environment, 53:61-68, 1995.

[3] A. Cognard, C. Loumagne, M. Normand, P. Olivier, C. Ottle, D. Vidal-Madjar, S. Louahala, and A. Vidal, "Evaluation of the ERS-1/synthetic aperture radar capacity to estimate surface soil moisture: two-year results over the Naizin watershed," Water Resources Research 31:975-982, 1995.

[4] J. M. Sabburg, "Evaluation of an Australian ERS-1 SAR scene pertaining to soil moisture measurement," Proc. of the Int. Geoscience and Remote Sensing Symposium 1994, IEEE 0-7803-1497-2/94:1424-1426, 1994.

[5] F. Von Ponce and M. Tapkenhinrichs, "Analysis of soil physical parameters and their influence on ERS-1 backscatter," Proc. of the Int. Geoscience and Remote Sensing Symposium 1994, IEEE 0-7803-1497-2/94:1432-1434, 1994.

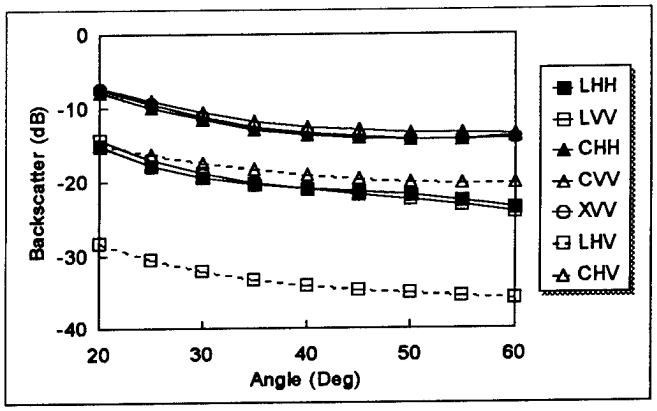


Figure 1. Predicted angular response of backscattering coefficient as a function of viewing angle for grass based on [1].

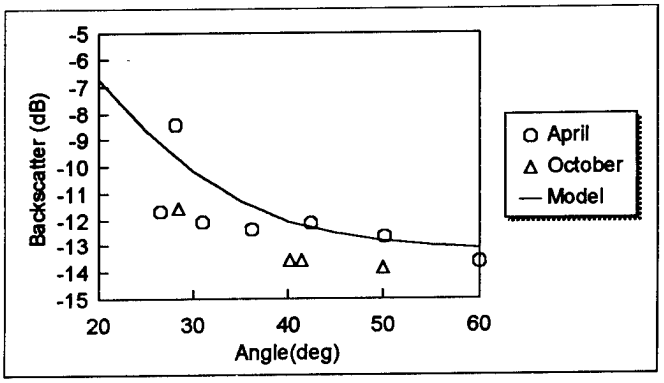


Figure 2. Observed and predicted values of the backscattering coefficient for all SIR-C C band vv passes of field 23.

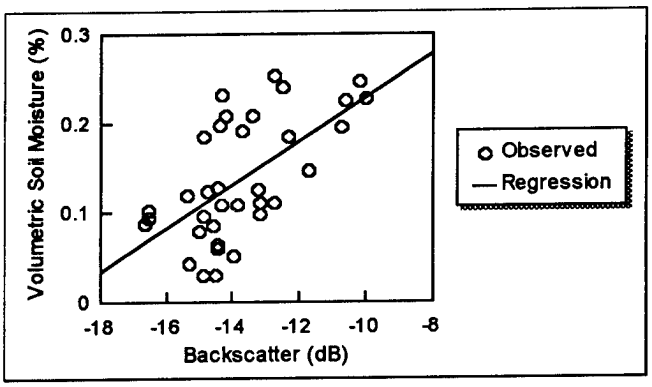


Figure 3. Observed C band vv SIR-C observations of soil moisture and backscattering coefficient for all grassland sites.

BACKSCATTERING OVER BARE SOILS: MEASUREMENTS AND SIMULATIONS USING SIRC/XSAR AND ERASME 1994 DATA OVER ORGEVAL

M. Zribi[1], O. Taconet[1], S. Le Hégarat-Mascle[1], D. Vidal-Madjar[1],
C. Emblanch[2], C. Loumagne[2] and M. Normand[2]
1 CETP/ CNRS, 10-12 avenue de l'Europe, 78140 Velizy(France)
phone 33 1 3925 4901, Fax 33 1 3925 4922, E-mail: zribi@cetp.ipsl.fr
2 CEMAGREF, Antony-Hydrologie, BP121-F. 92185 Antony Cedex(France)

ABSTRACT

During the 1994 SIRC/XSAR mission (Shuttle Imaging Radar C/X- Synthetic Aperture Radar), a part of the scientific activities was devoted to hydrology applications. In April 94, as the ground condition stayed very wet over the Orgeval watershed (France), the SAR imagery was used to assess the sensitivity of radar on the single problem of soil roughness over bare soils. To complement the Shuttle Radar data the helicoper-borne scatterometer ERASME was used. As a result, incidence angles ranging from 25 to 50 degrees are available in C and X bands. Principal results are the followings. The difference in backscatter response due to direction angles (perpendicular and parallel to the row direction) remain large over fields with moderate periodicity and height root mean square. The comparison between radar data and numerical simulations from a theoritical model (IEM) and a semi-empirical algorithm (Oh et al, 1994) shows adequacies and limits. The IEM model reproduces well radar scatter over smooth surfaces. The Oh algorithm agrees with the backscatter response over rough surfaces at medium incidence angle.

INTRODUCTION

In the first part of this paper, the "SIRC/XSAR Orgeval 1994" Campaign is presented, including the field surface parameters and radar measurements. It was conducted in collaboration between the CEMAGREF/ Antony (Centre d'Etude du Machinisme Agricole, du Génie Rural, et des Eaux et Forêts) and the CETP/CNRS (Centre d'Etude des Environnements Terrestre et Planétaires).

In the second part, the main results are presented.

THE SIRC/XSAR ORGEVAL'1994 EXPERIMENT

The Orgeval site extends on 8 by 8 km^2, East of Paris (France). The soil texture is relatively constant: clay, 17%, limon, 78%, sand 5%. In April 1994, the single vegetation canopy was winter wheat (20 cm high) covering 40% of the area. The remaining part are bare fields, classified in three types: sowing of peas eroded by rain resulting in a smooth crusted top layer, sowing of peas and flax corresponding to smooth surface with numerous clods, and different ploughed soil pratices for future cultures. As result of a heavy rainy winter, during the 5 day SAR survey, soil moisture remains high and constant over the watershed (about 0.35 cm3/cm3) and soil roughnesses and practices were the remaining factors of the radar variability.

A global survey was done by elaborating crop map and photographies of soil surfaces over 50 bare fields. Ten fields representative of the crop practices (4 of wheat, 2 of peas, 3 of corn, 1 of ploughed soil) were intensively caracterized. Soil moisture and density measurements, heights profiles by pin-profilers were done. For analysis of the radar backscatter from soils, the statistical parameters of the surface geometry have to be estimated, taking into account two spatial scales of roughness, the small scale random roughness (clods) and the larger scale periodic roughness (rows). They were derived from height profiles measurements parallel and perpendicular to the row direction by pin-profiler (2 meter length), following the method developped by Rakatoarivony et al. [1]. It is based on a description of the surface proposed for plowed fields by Shin and Kong [2]: a randomly perturbed quasi periodic surface. The parameters of the small scale are rms height s and length of correlation l, and of the large scale are periodicity P, width of the narrow frequency band L, rms heights S. The small scale correlation function is modelled by an exponential function. Field roughness parameters are given in Table 1. Over smooth sowing surfaces, retrieved periodicities are not significant, as they are close of the pin-profiler Shannon frequency (1meter). Row periodicity is not measurable, even if the furrow line is visible to the eye, as the line is broken in clods.

The radar measurements were done by two sensors. The CETP helicopter-borne FMCW scatterometer ERASME operates in C and X bands (5.35 and 9.65 GHz) with a wide range of incident angles (here from 25°to 50°). The pixel size after averaging is 10m x 20m. Relative calibration within 1 dB upon cross section is achieved within an aperture range of $\pm$7° around the antenna axis. A more detailed description of the radar and its calibration is given in Benallegue et al. [3].

The SIRC/XSARs images angles range from 44° to 57° (14 to 18 April 1994). Simultaneous flights of ERASME were done looking in the SIRC/XSAR direction and over some fields perpendicular and parallel to the rows directions. Differences in calibration between the two sources of radar data were evaluated over natural targets and are smaller than 2dB.

0-7803-3068-4/96$5.00©1996 IEEE

and within the absolute calibration accuracy level for both SIRC/XSAR.

COMPARISON WITH MEASURED AND SIMULATED RADAR DATA

1- Influence of direction toward rows

Present empirical models developped on radar measurements to infer soil moisture and surface roughness are essentially built for isotropic surfaces (Oh et al. [4]). Nevertheless, they circumvent the difficulty of the radar sensitivity to view angle with row direction over agricultural surfaces. Most observations were done on pronounced ridges (built for irrigation) which explains important azimutal effect on backscatter. Figure 1 shows that, on the Orgeval site with moderate periodicity and r.m.s. heights (Table 1) significant enhancement scattering (up to 5dB with an average of 2 dB) can be observed between parallel and perpendicular directions rows both in C and X bands from ERASME data. The Integral Equation Model of Fung et al. [5] offers the possibility to evaluate this directional effect by taking account of the surface anisotropy. The cross section calculation is done for the two bands (C, X) and the surface parameters representative of the three soil classes over the region : W3 for very smooth sowings, W2 for cloddy sowings and PL9 for ploughed fields. The surfaces fall within the IEM validity range. It is seen, that over sowing, simulated direction effect remains weak (1dB) and for plough tillage increases up to 5 dB (Figure 2). The directional sensitivity may be underestimated. An explanation could be the inadequacy of the soil description, especially for smooth surfaces where the row periodicity retrieval is not significant.

2- Comparison between simulated and measured radar data

IEM simulations were calculated, taking directely for each band and for the three sets of surfaces, the fitted roughness parameters and the dielectric constant derived from the Hallikainen et al. [6] formula for the given soil moisture and texture. Some results are shown in Figures 3 and 4. Very good agreement is observed between the model simulations and the radar measurements in absolute level (within 2 dB) and across the entire tested angular range, in L band (from 44 to 57 degrees) over all the smooth surfaces (ks=0.14 and 0.18), and in C band (from 25 to 57 degrees) only over the smoothest ones, corresponding to crusted top layer (ks=0.61). But for roughest conditions (ks> 0.8), IEM simulations tend to become flat and no more sensitive to incidence angles. The discrepancy can reach ±10 dB.

Based on experimental observations and theoretical and numerical solutions, a semi-empirical model was developped by Oh et al. [4] for the backscattering coefficients, in terms of surface dielectric constant and two surface rouhness parameter (rms height and length of correlation). Over the angular range of 25 to 57 degree, the Oh formulation reproduces well the absolute level and angular decrease in XVV band, within ±2dB, where IEM predictions fail. But a large shift appears between experimental data and calculations in C and L bands, with a systematic underestimation of the algorithm (5dB) (Figures 3 and 4).

CONCLUSION

The comparison between measured radar data and simulated ones, from a theoritical retrodiffusion model (Integral Equation Model of Fung et al.[5] and a semi-empirical algorithm (Oh et al. [4] opens some questions:

- the adequacy of the surface representation (centered over an harmonic component with a narrow spatial frequency band random component) for simulating the dirctional sensitivity of radar with rows directions over smooth surfaces,
- the derivation of theoritical solutions over rough surfaces,
- the importance of validated semi-empirical algorithms over various data sets of different training sources (radar and natural conditions).

REFERENCES

[1] Rakotoarivony, L., Taconet, O., Vidal-Madjar, D., and Benallegue, M. (1996), Radar backscattering over agricultural bare soils,*J. of Electromagnetic Waves and Applications*, Vol. 10 , 2:187-210.

[2] Shin, R. T., and Kong, J. A. (1984), Scattering of electromagnetic waves from a randomly perturbed quasi-periodic surface, *J. App. Phys.*, Vol. 56, 1:10-21.

[3] Benallegue, M., Taconet, O., Vidal-Madjar, D., Baudin, F., Lancelin, P. , and Laurent, G. , (1994), Evaluation of calibration method for an helicopter-borne microwave scatterometer devoted to land use, *INT. J. Remote Sensing*, Vol. 15 , 3:645-656.

[4] Oh, Y, Sarabandi, K., and Ulaby, F. T.(1994), An inversion algorithm to retrieve soil moisture and surface roughness from polarimetric radar observation, *Proc. of the Int. Geoscience and Remote Sensing Symp., IGARSS'94,* held in Pasadena, CA-USA, August 8-12.

[5] Fung, A. K., Zongqian Li, and Chen, K. S. (199), Backscattering from a randomly rough dielectric surface, *IEEE Transaction on Geoscience and Remote sensing,* Vol. 30, 2:356-369.

[6] Hallikainen, M. T., Ulaby, F. T., Dobson, M. C., El-Rayes, M.A. , and Wu, L. K. (1985) Microwave dielectric behaviour of wet soil - part I: empirical models and experimental observations, *IEEE Transaction on Geoscience and Remote sensing,* Vol. 23, 1:25-46.

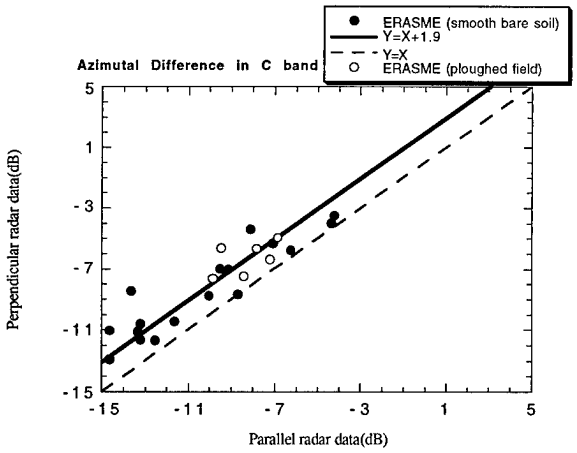


Figure 1: Directional sensitivity of backscatter versus furrows. Data are from ERASME scatterometer.

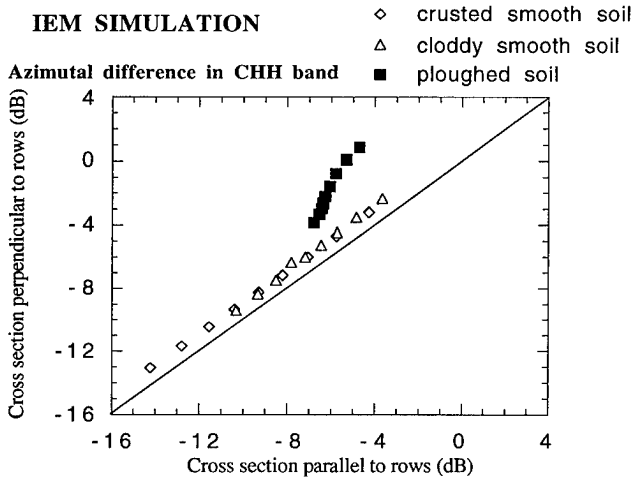


Figure 2: Simulated directional effect from Integral Equation Model. Effects are evaluated for three surfaces, crusted eroded soil, cloddy sowing soil and ploughed soil.

	Roughness Parameters(cm)				
Field	s	l	S	L	P
PL1	2.7	6.1	0	0	0
W2	0.7	5.9	0.97	34.7	99.6
W3	0.5	12.6	0.73	143.4	197.3
W4	0.9	2.5	0.83	42.4	104.5

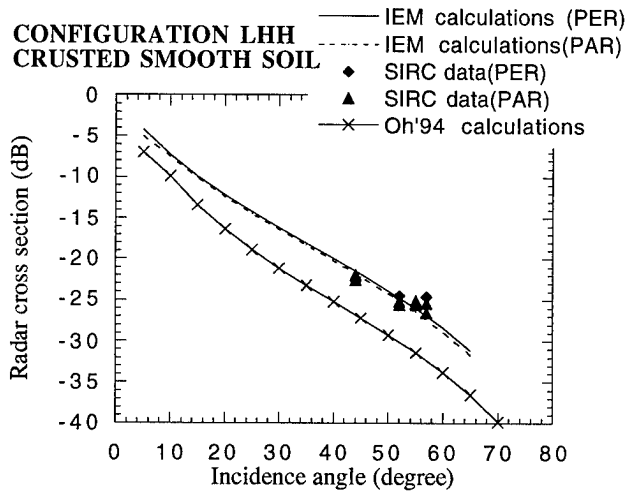


Figure 3: Comparisons between radar cross sections and simulations from IEM model and Oh algorithm for one surface roughness (eroded crusted soil) and perpendicular and parallel direction toward rows in L band.

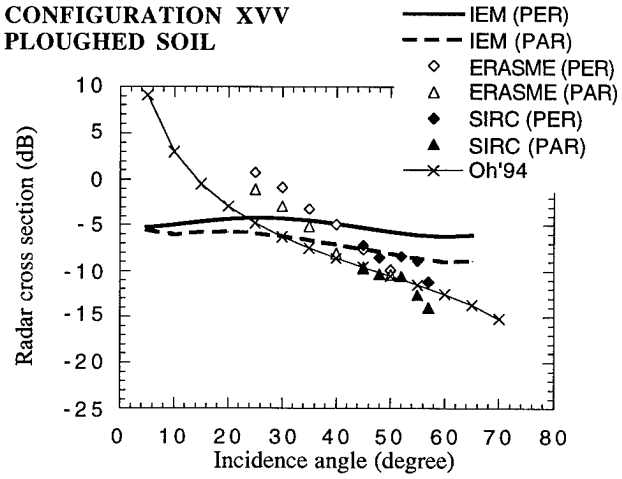


Figure 4: Same results in X band for ploughed field.

PL6	3.8	7.3	0.94	128.9	94.3
PL7	2.5	8.1	1.73	147.0	45.2
P8	1.3	3.5	1.44	93.7	43.0
PL9	1.0	8.1	1.63	115.3	40.2
P10	0.6	5.7	0.3	172.1	120.7

Table 2: Roughness parameters of test fields (W: Wheat, P: Peas, Pl: Ploughed fields)

Polarimetric Backscattering Measurements of Herbaceous Vegetation : A Sensitivity Study for Soil Moisture Retrieval

Tsenchieh Chiu, Kamal Sarabandi, and Fawwaz T. Ulaby
Department of Electrical Engineering and Computer Science
The University of Michigan, Ann Arbor, MI 48109-2122
Tel:(313) 936-1575, Fax:(313) 747-2106
Email: tcchiu@engin.umich.edu

Abstract – In this paper, the feasibility of soil moisture retrieval from radar backscatter data acquired from surfaces covered with short, dense, and herbaceous vegetation such as soybean is studied. For this purpose, a series of polarimetric measurements were performed on a soybean field at L-, C-, and X-band frequencies over a wide range of incidence angles. In these experiments the University of Michigan polarimetric scatterometer systems were used. The backscatter measurements were conducted for two extreme vegetation conditions : (1) in the middle of the season for a fully grown soybean condition when vegetation biomass is maximum, and (2) toward the end of the season when the leaves were fallen and the plants were drier. For each vegetation condition backscatter measurements were also conducted under different soil moisture conditions to examine the sensitivity of radar backscatter to soil moisture. Simultaneous with the radar measurements, a complete set of ground truth data, including the moisture content, size and number density of leaves, stems, and pods were also collected. The dielectric constant of leaves and stems were also measured at C- and X-band immediately after radar measurements.

EXPERIMENTAL PROCEDURE

Scatterometer

The University of Michigan's LCX POLARSCAT [1] was designed with the capability to measure the scattering matrix of point or distributed targets with center frequencies at 1.25, 4.75, and 9.5 GHz, respectively. The scatterometer consists of a vector network analyzer (NWA) (HP 8753A), a personal computer (PC), an amplifying and pulsing circuit for hardware range gating, a relay actuator, and L-, C-, and X-band RF circuits and antennas. These antennas are dual-polarized with orthogonal mode transducers (OMT) used for simultaneous transmission of V- and H-polarized signals and reception of both V- and H-components of the backscattered signal. The PC is used to control the NWA through the HP-IB interface bus to acquire the measured data automatically. To achieve good statistical representation of the measured backscatter for the distributed targets, a large number of spatially independent samples are required. In this measurement, more than 70 independent samples are collected at incidence angles of 20^0, 30^0, 40^0, 50^0, 60^0, and 70^0. To achieve good range resolution and to increase the number of independent samples, this measurement were performed over bandwidths of 0.3 GHz for L-band and 0.5 GHz for C- and X-band. Assuming the backscattering coefficients are constant and that the backscattered fields decorrelate as a function of frequency, the number of independent samples were increased to more than 500. The deterministic background noise was measured by pointing the antennas toward sky and then subtracted from target backscatter data coherently to improve the signal to noise ratio. The polarimetric response of a conducting sphere was measured to achieve calibration of the radar system [2].

Soil Moisture Measurement

The dielectric constant of the soil surface was measured by using a C-band field-portable dielectric probe [3]. The probe consists of a reflectometer assembly with a coaxial probe tip and a signal processing assembly with a calculator. The relative dielectric constant (ϵ_r) was used to estimate the moisture contents (m_v) by inverting a semi-empirical model [4] which give ϵ_r in terms of m_v. The imaginary part of ϵ_r was not used to estimate m_v because of measurement errors [5]. The mean m_v was then used to estimate ϵ_r at the other frequencies.

Dielectric Constant Measurement of Soybean Leaves and Stems

Two dielectric measurement techniques [6, 7] were used to measure the dielectric constant of leaves and stems, respectively. These measurement were performed over two frequency bands, namely 4-6 GHz using a WR-187 waveguide sample holder, and 8-12 GHz using a WR-90 waveguide sample holder. Most of the stems with larger diameter and high moisture content could not be measured at x-band because of their high reflection coefficients which lower the dielectric measurement accuracy.

MEASUREMENTS

In order to understand the scattering behavior of soybean plants and evaluate the sensitivity of radar backscatter to soil moisture, backscatter measurements were conducted for two extreme vegetation conditions: (1) in the middle of the season for a fully grown soybean condition when vegetation biomass is maximum (see Fig. 1a), and (2) toward the end of the season when the leaves were fallen and the plants were drier(see Fig. 1b). For each vegetation condition backscatter measurements

0-7803-3068-4/96$5.00©1996 IEEE

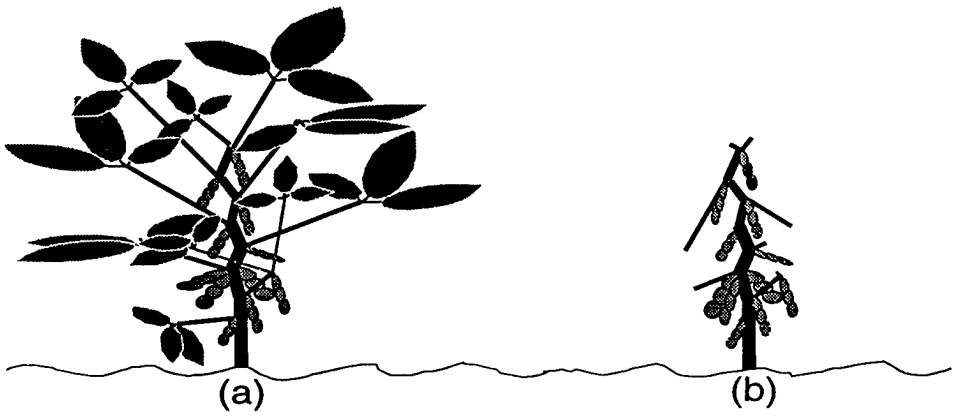


Figure 1: Two vegetation conditions: a fully grown plant and a dry plant at the end of the season.

were also conducted under different soil moisture conditions to examine the sensitivity of radar backscatter to soil moisture.

Fig. 2 and 3 show the radar backscatter of fully grown soybean plants in both dry and wet soil conditions at L-band and C-band, respectively. The dielectric constant of soil for the dry and wet conditions were measured by the C-band probe and are , respectively, given by $\epsilon_r = 3.1 - i0.73$ and $\epsilon_r = 8.2 - i1.66$. for the wet soil, the backscattering coefficients at L-band increase 2 to 3 dB, while the backscattering coefficients at C-band for the most incidence angles remained the same. This result shows that the sensitivity to soil moisture for surfaces covered with dense short vegetation canopies like soybean exists only at low frequencies. The sensitivity of radar backscatter to soil moisture at L-band can also be inferred from the polarimetric behavior of the radar backscatter. At L-band σ^0_{hh} is higher than σ^0_{vv} which indicates a strong ground bounce scattering mechanism which is a function of the ground reflectivity. The C-band data shows that $\sigma^0_{vv} > \sigma^0_{hh}$ which indicates that the extinction for h-polarized wave is higher than that for v-polarized wave.

Fig. 4 and 5 show the radar backscatter of dry soybean plants for both dry and wet soil conditions at L-band and C-band, respectively. The measured dielectric constant of soil for the dry and wet conditions are $\epsilon_r = 2.3 - i0.89$ and $\epsilon_r = 9.1 - i2.3$, respectively. for the wet soil, At the end of the season, the soybean plants became dry and mostly only the main stems and pods remained(see Fig. 1b). At this time stems of soybean plants were very dry and their structure changed from a solid cylinder to a hollow cylinder. In this case scattering from and attenuation in the vegetation layer decreased significantly. Because leaves and most of the stems were absent ,the radar backscatter at lower incidence angles decrease significantly as compared to the case of fully grown plant. For the dry plant condition both L-band And C-band backscattering coefficients show sensitivity to soil moisture. Also for the dry plant condition $\sigma^0_{vv} > \sigma^0_{hh}$ (unlike the previous case) which is the expected behavior of a bare soil surface.

REFERENCES

[1] M.A. Tassoudji, K. Sarabandi, and F.T. Ulaby, "Design consideration and implementation of the LCX polarimetric scatterometer (POLARSCAT)," Rep. 022486-T-2, Radiation Laboratory, The University of Michigan, June 1989.

[2] K. Sarabandi, and F.T. Ulaby, "A convenient technique for polarimetric calibration of radar systems," *IEEE Trans. Geosci. Remote Sensing*, vol. 28, pp. 1022-1033, 1990.

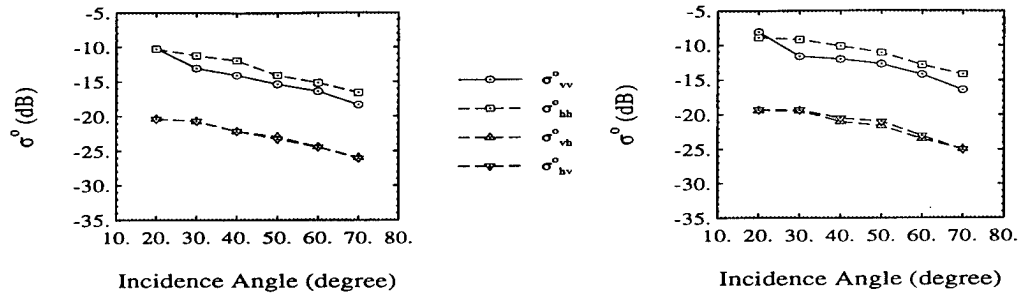
[3] D.R.Brunfeldt, "Theory and design of a field-portable dielectric measurement system," *IEEE Int. Geosci. Remote Sensing Symp. (IGARSS) Digest* vol. 1, pp. 559-563, 1987.

[4] M.T. Hallikainen, F.T. Ulaby, M.C. Dobson, M.A. El-Rayes, and L. Wu, "Microwave dielectric behavior of wet soil - Part I: Empirical models and experimental observations," *IEEE Trans. Geosci. Remote Sensing*, vol. GE-23, pp. 25-34, 1985.

[5] T.J. Jackson, "Laboratory evaluation of a field-portable dielectric/soil-moisture probe," *IEEE Trans. Geosci. Remote Sensing*, vol. 28, pp. 241-245, Mar. 1990.

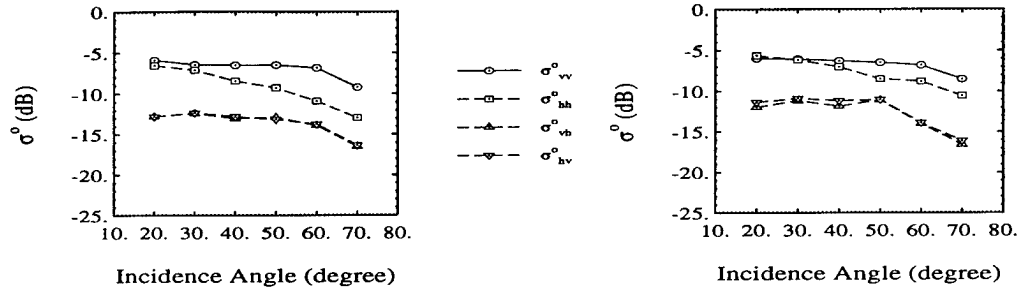
[6] K. Sarabandi, and F.T. Ulaby, "Technique for measuring the dielectric constant of thin materials," *IEEE Trans. Instrum. Meas*, vol. 37, no. 4, pp. 631-636, Dec. 1988.

[7] K. Sarabandi, "A technique for dielectric measurement of cylindrical objects in a rectangular waveguide," *IEEE Trans. Instrum. Meas*, vol. 43, no. 6, pp. 793-798, Dec. 1994.



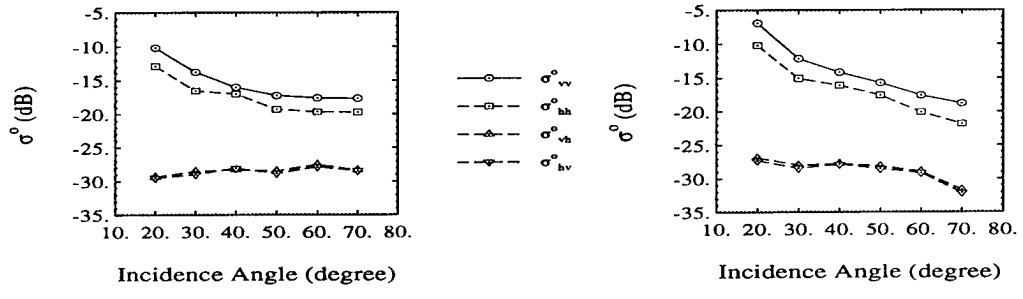
(a) (b)

Figure 2: Measurement results of fully grown soybean plants in (a) dry and (b) wet soil conditions at L-band.



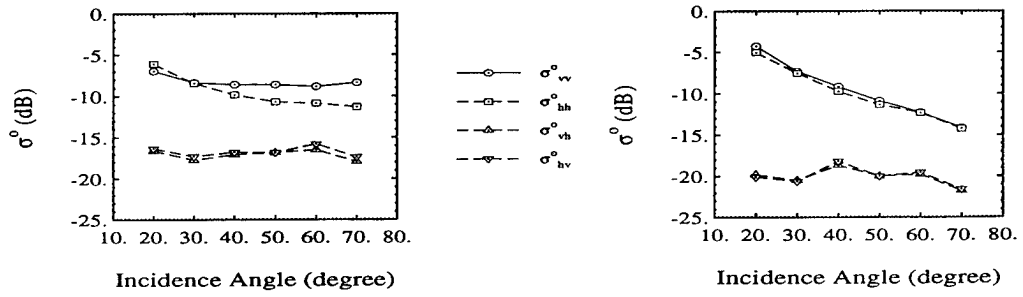
(a) (b)

Figure 3: Measurement results of fully grown soybean plants in (a) dry and (b) wet soil conditions at C-band.



(a) (b)

Figure 4: Measurement results of dry soybean plants in (a) dry and (b) wet soil conditions at L-band.



(a) (b)

Figure 5: Measurement results of dry soybean plants in (a) dry and (b) wet soil conditions at C-band.

Comparison of Spatial Statistics of SAR-Derived and In-Situ Soil Moisture Estimates

P. P. Hirsave*, R. M. Narayanan*, B. T. Tracy**, B. L. Gwilliam**, R. L. Bolus**, T. Pangburn**, H. L. McKim**

*Department of Electrical Engineering and Center for Electro-Optics
209N WSEC, University of Nebraska, Lincoln, NE 68588-0511, USA
T: 402.472.5141 F: 402.472.4732 EMail: rnarayanan@unl.edu

**U. S. Army CRREL
RS/GIS Center, 72 Lyme Road, Hanover, NH 03755-1290, USA

Abstract— The technology of using spaceborne SAR systems for soil moisture estimation has been refined over the last few years. In order to reduce the confounding effects of surface roughness on soil moisture inversion, multifrequency SAR systems have shown promise. The Shuttle Imaging Radar (SIR-C) has an onboard SAR system operating at L, C, and X bands for high resolution imaging of the earth's surface. Over the early part of October 1994, the SIR-C SAR collected radar reflectance data from two sites near Concord, New Hampshire. SIR-C data were collected on four consecutive days and concurrent ground truth measurements were also made of the actual soil moisture distribution at the test sites. The objective of the study was to evaluate the radar system's ability not only to estimate soil moisture, but also to characterize its spatial variability. The University of Nebraska has developed inversion algorithms to estimate soil moisture from SIR-C data. The spatial statistics of the in-situ measurements were used to refine the soil moisture inversion algorithm. The SIR-C derived and the in-situ soil moisture estimates compared well not only for the mean soil moisture of each pixel, but also for the spatial statistical parameters, such as correlation lengths and the gradients of soil moisture.

Introduction

It is well known now that microwave sensors can be successfully used for soil moisture estimation. There are several methods that have been developed for retrieving soil moisture and surface parameters from radar backscatter. The increased interest in using radars for remote sensing on satellite platforms is because of its all-weather round the clock monitoring capabilities. In the early days of remote sensing many of the advantages offered by radars were masked by their high power requirements and poor spatial resolution. The advances in SAR technology have made high resolution imagery an attractive possibility.

Availability of SIR-C/X-SAR data by NASA has further enhanced the use of SAR signatures for remote sensing. The primary advantage of SAR on satellite platforms as opposed to optical and sensors is year-round coverage independent of weather and illumination conditions. Further it has been seen that SAR systems are superior in performance than passive sensors in maritime traffic monitoring, soil moisture estimation and monitoring hurricanes.

Soil performs the storage function in hydrological cycle's interaction with the land surface. The monitoring of the energy and moisture fluxes is recognized important for application ranging from study of the biosphere processes at local scales (10's of m) to modeling of atmospheric behavior at regional/global scales. The measurements of soil moisture using microwave sensors is based on large contrast between the dielectric properties of dry soil (about 2.5) and water (about 80). However the radar backscatter also varies significantly with the changes in surface parameters. Hence the relationship between backscatter and soil moisture is not clearly one-to-one. Various methods exist for soil moisture inversion. Empirical techniques [1] and statistical methods [2], [3] are the most noteworthy. However empirical techniques inherently imply more computation and availability of HH, HV and VV data for a single frequency. The statistical inversion technique despite being linear offers accurate estimates of the soil moisture. An improvement is to consider the use of neural networks to include non-linear effects.

Soil moisture algorithms using SIR-C data

Here a linear inversion technique formerly reported by Njoku and Kong [4] and later adopted to active microwave remote sensing of soil moisture by [3] is described. Of all the methods described earlier this technique is more suitable for the case in which the dataset consists of multiband, multi-look angle and multi-polarization signatures. The results obtained with this method are used for comparison with neural network inversion. Finally we refine the implementation of the above two techniques knowing the spatial statistics of the in-situ measurements. The general form of the statistical inversion discussed by Njoku and Kong [4], can be expressed as

$$\hat{\mathrm{P}} = Dd \tag{1}$$

where $\hat{\mathrm{P}} = (P_1, P_2, ..., P_m)$ is the estimated parameters vector and $d = (d_1, d_2, ..., d_n)$ is the data vector. D is the matrix (m X n) containing the inversion coefficients. For the inversion of surface parameters, $\hat{\mathrm{P}}$= (s, m_v, l) and d contains the multi-band data. Here s is the standard deviation of surface height, m_v is the volumetric soil moisture and l is the surface correlation length. To make the data

The partial support of this work by the U.S. Army CRREL under Contract #DACA89-95-K-0018 is gratefully acknowledged.

0-7803-3068-4/96$5.00©1996 IEEE

vectors more resolvable and to account for the non-linear inter-dependency between system and surface parameters, the original dataset is augmented with non-linear terms to obtain the data vector d. The D matrix is derived as

$$D = C(P,d)C^{-1}(P,d) \quad (2)$$

where $C(x,y) =< xy^T >$. For a three frequency approach [3]:

$$d = (1, d_1, d_2, d_3, d_1d_1, d_1d_2, d_1d_3, d_2d_2, d_2d_3, d_3d_3) \quad (3)$$

where d_1, d_2, d_3 are the radar signatures at three different frequencies. A model dataset over the whole range of surface parameters ($m_v < 50$, $l < .5m$, $s < .05m$) and at the frequencies of investigation is generated using various models [5][6]. SIR-C/X-SAR data at L, C and X bands were considered, hence the 3-frequency approach was taken. We train for the given data set to obtain the required D matrix. Once the D matrix is obtained by training the dataset, we estimate the soil moisture by the procedure described above. The result of our simulation study is shown in Fig. 1 and we note that the average absolute error is 7.35%.

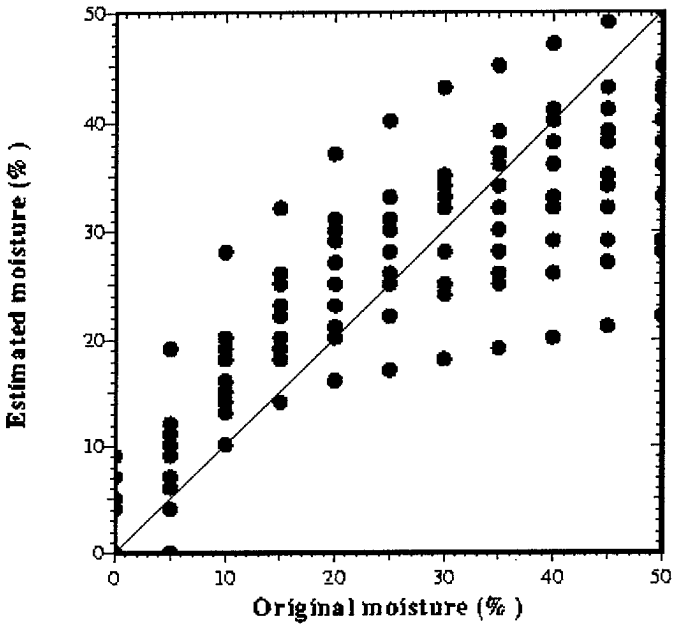


Fig. 1. Plot of estimated vs assumed soil moisture using Statistical inversion technique.

The need for a neural network approach is essentially to look for non-linear boundaries. The statistical technique although fairly successful and mathematically rigorous does not seek out non-linear boundaries. This is one of its main drawbacks. In the neural network approach we use the perceptron, which is the basic unit of the neural network and is used for separating linearly separable patterns [7]. We have a single neuron with adjustable weights. The perceptron by itself fails to classify non-linear boundaries and hence is not very useful. However the decision boundaries of a perceptron can be made non-linear either by cascading perceptrons to form a multi layer feed-forward network or by including a pre-processor to augment the input data vector with non-linear terms [8]. A perceptron learns to recognize patterns through prior learning. The error correction rules alter the weights to correct the error in the output response to the current pattern. Its seen that the Least Mean Square rule is useful here. The mean square error surface for a perceptron is a quadratic surface with a global minimum. With each iteration the weights can be altered such that the error moves in the direction of the negative gradient of the error surface. Finally the well known Back-Propagation rule is used to obtain the required estimate of soil moisture. This rule uses the instantaneous sum of squared errors as the cost function to train the weights of the network. A three layer network with three neurons in each hidden layer is incorporated. The absolute backscatter values were used as the input to the network. The coefficients of the network were computed and the final estimate for soil moisture is shown in Fig. 2 with an average absolute error of 5.87%.

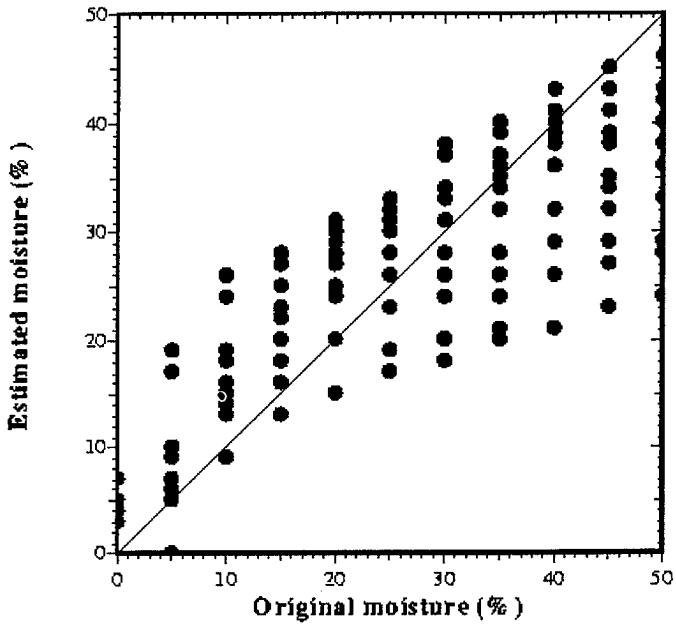


Fig. 2. Plot of estimated vs assumed soil moisture using Neural network inversion technique.

Results

The L, C and X-band data from the SIR-C/X-SAR were obtained over Concord in New Hampshire. The data were collected over a period of four consecutive days over the test site. Concurrent ground truth measurements were also made of the actual soil moisture distribution for comparison with the inversion algorithms. The SIR-C/X-SAR data obtained is at 12.5 m resolution and the concurrent ground truth measurement at 15 m intervals. Soil moisture inversion from SIR-C/X-SAR data using neural network technique is currently being pursued.

Conclusions

The spatial statistics of in-situ measurements are being used to refine the soil moisture inversion algorithms. The SIR-C/X-SAR data derived estimates and the concurrent ground truth soil moisture are expected to compare favorably not only for the mean soil moisture for each pixel, but also for the spatial statistical parameters, such as correlation lengths and the gradient of soil moisture. Further study is underway to refine the soil moisture inversion algorithms.

References

[1] Y. Oh, K. Sarabandi, and F. T. Ulaby, "An empirical model and an inversion technique for radar scattering from bare soil surfaces," *IEEE Transactions on Geoscience and Remote Sensing, Vol. 30, No. 2,* pp. 370-381, March 1992.

[2] R. M. Narayanan, J. R. Horner, and K. M. St. Germain, "Inversion algorithms based on non-linear model functions for soil moisture and surface roughness estimation from remotely sensed radar reflectances," in *ASPRS/ACS Annual Convention and Exposition,* pp. 471-483, 1994.

[3] K. S. Rao, S. Raju, and J. R. Wang, "Estimation of soil moisture and surface roughness parameters from backscatter coefficients," *IEEE Transactions on Geoscience and Remote Sensing, Vol. 31,* pp. 1094-1098, September 1993.

[4] E. G. Njoku and J. A. Kong, "Theory of passive microwave remote sensing of near surface soilmoisture," *J. Geophys. Res., 82,* pp. 3108-3118, 1977.

[5] F. T. Ulaby, R. K. Moore, and A. K. Fung, *Microwave Remote Sensing-Active and Passive - Vol I, II.* Addison-Wesley Publishing Company, Reading, MA, 1978.

[6] F. T. Ulaby, R. K. Moore, and A. K. Fung, *Microwave Remote Sensing-Active and Passive - Vol III.* Artech House, Inc., Dedham, MA, 1978.

[7] S. Haykin, *Neural Networks.* Macmillan College Publishing Company, Inc., New York, 1994.

[8] C. Lau, ed., *Neural Networks.* IEEE., New York, 1992.

Soil Moisture and Temperature Determination by Recursive Assimilation of Multifrequency Observations Using Simplified Models of Soil Heat and Moisture Flow and Emission

J. F. Galantowicz and D. Entekhabi
Dept. of Civil and Environmental Engineering
Massachusetts Institute of Technology, 48-333
Cambridge, MA 02139, USA
Telephone: +1–617–253–7145, Facsimile: +1–617–253–7475
Email: johng@mit.edu

ABSTRACT

Although the sensitivity of radiobrightness to soil moisture content has been well established, direct inversion of remote sensing measurements is impeded by variable surface cover (vegetation and snow), surface roughness, and soil temperature and moisture profiles. During interstorm periods, soil moisture and temperature conditions change dynamically under atmospheric and radiative forcing. A model of these dynamics may be used to encapsulate a priori soil information and constrain the inversion solution. A soil and land-atmosphere model driven by local meteorology or forecasts can propagate soil conditions between times at which remote sensing measurements are available. The predictions of the model soil would facilitate incorporation of imperfect measurements from multiple sources through comparisons of the modeled and observed states.

This paper presents the results of an assimilation study using simple models of the coupled heat and moisture transport in soil and microwave emission. Simple models enable the full utilization of available microwave and thermal infrared measurements through recursive application of Kalman filtering. Comparisons are made between soil emission models based on coherent wave radiative transfer, classical radiative transfer (CRT), a first order approximation to CRT, and a gray body. Data from the BARC (Beltsville Agricultural Research Center) 1994 experiment–including micrometeorology, soil conditions, and L-band (1.4 GHz) radiobrightness–drive the model. We test the sensitivity of the model to temporal radiometric measurement availability ranging from hourly to daily and show that a simplified emission parameterization is adequate.

0-7803-3068-4/96$5.00©1996 IEEE

Radar Backscatter Components from Ponderosa Pine Forests

Yong Wang and Frank W. Davis*

Department of Geography, East Carolina University, Greenville, NC 27858
E-mail: gewang@ecuvm.cis.ecu.edu, Tel (919) 328-1043, and Fax (919) 328-6054

*Institute for Computational Earth System Science, University of California, Santa Barbara, CA 93106

ABSTRACT

We used a signal decomposition method to study scattering mechanisms in pine forests near Mt. Shasta, CA. Signal decomposition was applied to two sets of the JPL multi-frequency airborne synthetic aperture radar (AIRSAR) backscatter data acquired during a wet spring (1991) and a dry summer (1989) conditions. The scattering mechanisms decomposed were scattering power with an odd number of reflections, scattering power with an even number of reflections, and diffused scattering power.

INTRODUCTION

Recent progress on radar target theory makes it possible to decompose polarimetric SAR backscatter into a scattering power with an odd number of reflections (shortened as SP-I), a scattering power with an even number of reflections (shortened as SP-II), and a diffused scattering power (SP-III) ([1-2]). The decomposition method is based on the decomposition of the backscatter covariance matrix from targets.

A single SAR image pixel is typically comprised of many scatterers. The backscatter covariance matrix can be thought of as the average of the covariance matrices of individual scatterers within the pixel. Because the scattering properties derived from the averaged covariance matrix are significantly different from those derived from the covariance matrix of each individual scatterer, it is difficult to understand the scattering properties derived from the averaged covariance matrix. Thus, this decomposition method helps simplify the scattering mechanisms by decomposing the covariance matrix. Cloude's and van Zyl's work lay theoretic ground for the decomposition method, but its potential application in forested environment needs further to explore. Thus, our objective is to apply this decomposition method to the multi-frequency AIRSAR data 1) to understand the decomposed scattering powers from ponderosa pine forests under dry and wet ground conditions and 2) to evaluate the potential of using the decomposed scattering powers in forests.

APPROACH

The approaches are 1) to decompose the backscatter covariance matrix of pine forests from the AIRSAR data, and 2) to analyze the decomposed results, coupled with collected ground data.

For a SAR, the backscatter covariance matrix, **U**, for azimuthly symmetric and reciprocal targets is

$$\mathbf{U} = \begin{bmatrix} < s_{hh}\, s_{hh}^{*} > & 0 & < s_{hh}\, s_{vv}^{*} > \\ 0 & 2 < s_{hv}\, s_{hv}^{*} > & 0 \\ < s_{vv}\, s_{hh}^{*} > & 0 & < s_{vv}\, s_{vv}^{*} > \end{bmatrix} \quad (1)$$

Cloude and van Zyl ([1-2]) showed that the **U** can be decomposed as

$$\mathbf{U} = \lambda_1 K_1 (K_1^{*})' + \lambda_2 K_2 (K_2^{*})' + \lambda_3 K_3 (K_3^{*})' \quad (2)$$

λ_i (i = 1, 2, and 3) are eigenvalues of **U**. K_i (i = 1, 2, and 3) are eigenvectors of **U**, and

$$K_i = [\, k_{i1} \;\; k_{i2} \;\; k_{i3} \,]' \quad (3)$$

Because k_{11} / k_{12} ratio is always negative ([2]), the K_1 and K_2 represent scattering mechanisms with an 180° phase shift. Further analysis shows that:

i) if the real part of $k_{11} \geq 0$ and the real part of $k_{21} \leq 0$, then
$\lambda_1 K_1 (K_1^{*})'$ represents SP-I return, and
$\lambda_2 K_2 (K_2^{*})'$ represents SP-II return.

ii) if the real part of $k_{11} < 0$ and the real part of $k_{21} > 0$, then
$\lambda_1 K_1 (K_1^{*})'$ represents SP-II return, and
$\lambda_2 K_2 (K_2^{*})'$ represents SP-I return.

iii) $\lambda_3 K_3 (K_3^{*})'$ represents SP-III return.

Using Eq. (2) and conditions i), ii), and iii), we can decompose the SAR backscatter data into three types of scattering powers. It should be noted that the decomposed diffused scattering power, $\lambda_3 K_3 (K_3^{*})'$, is simply twice of HV or VH backscatter ([2]).

RESULT

We have analyzed two sets of the AIRSAR data from ponderosa pine forests, Mt. Shasta, CA. The forests has been used to study the radar backscatter from forested environment for years ([3-4]). The first dataset was acquired on 6 September 1989 after a dry summer. An estimated volumetric soil moisture was less than 5%. The second dataset was obtained on 1 May 1991. The ground was wet due to a heavy rain and the melting of snow. An estimated volumetric soil moisture was 48%. All SAR data were processed and calibrated by the

0-7803-3068-4/96$5.00©1996 IEEE

JPL, and provided to us ([4]).

Under a dry ground condition

At C-band, open field and clear-cut area show the strongest SP-I power. The forested area is also dominated by the SP-I return. There are some SP-II and SP-III returns scattered within the forested area, but these two types of scatterings are small. These results show that at C-band the SP-I dominates in the forests.

At L-band, the image is still dominanted by the SP-I. However, in the forested area there is more SP-II return at L-band than C-band. The increase of SP-II may be a result of the increase of trunk-ground interactions at L-band. As the wavelength increases to P-band, there is even more SP-II within the forests than at L-band; more trunk-ground interactions within the forests at P-band than L-band (and C-band). These results are consistent with those from the analysis of the HH-VV phase differences of the SAR data and the modeled backscatter from the forests ([4]).

Under a wet ground condition

There is not much variation in the scattering powers from the open field and clear cut area when the ground condition changes from dry to wet. The SP-I dominates under both ground conditions. However, at the same wavelength, more SP-II return from the forested area is observed at the wet ground condition than at the dry ground condition. Based on our canopy backscatter model simulation, this increase of the SP-II comes from the increase of the trunk-ground term as the ground condition changes from dry to wet.

Scattering power normalized by the total power

We select five ponderosa pine stands where ground data were collected to quantify our analysis. The density of the stands is from 24 trees/ha to 775 trees/ha. Mean tree diameter at breast height ranges from 0.78 m to 0.28 m, tree height from 25.1 m to 18.5 m, and mean basal area (cm^2/m^2) from 13.4 to 75.6. Because radar incidence angles to the stands range from 25° to over 40°, the variation of the incidence angle could potentially affect the analysis. To minimize its effect, we have normalized the three types of scattering powers by the total power. The normalization is done on the pixel by pixel basis.

Under the dry ground condition: With an increase of the stand mean basal area, 1) normalized SP-I decreases from 0.74 to 0.58 at C-band and from 0.55 to 0.35 at P-band, 2) normalized SP-II increases slightly at C-band, varies between 0.19 to 0.24 at L-band, and increases from 0.22 to around 0.40 at P-band, and 3) normalized SP-III may increase slightly at C-band and L-band, and varies slightly between 0.24 and 0.22 at P-band (Fig. 1).

Under the wet ground condition: As the basal area increases, 1) the SP-I decreases at C-, L-, and P-band, 2) the SP-II varies slightly at C-band and L-band, and increased from 0.32 to 0.47 at P-band, and 3) the SP-III increases from 0.10 to 0.23 at C-band and from 0.11 to 0.24 at L-band, and varies between 0.16 and 0.17 at P-band (Fig. 1).

Model simulations showed that, as the basal area increases, the increase of the normalized SP-II at P-band is a result from the increase of the trunk-ground scattering.

REMARK

By studying decomposed scattering powers from ponderosa pine forests, we noted that at P-band, as the basal area increased, the increase of the SP-II return was about 9 dB, whereas the increase of the total power was around 5 dB. This enlarged dynamic range of the SAR data could provide a better potential in retrieving the biophysical parameters of forests because the decomposed data were more sensitive to the change of the parameters. This is a task we will pursue in the future.

ACKNOWLEDGMENT

The AIRSAR data were obtained from the SIR-C/X-SAR project funded by NASA through JPL (contract # 958468), and this research was also funded by this project.

REFERENCE

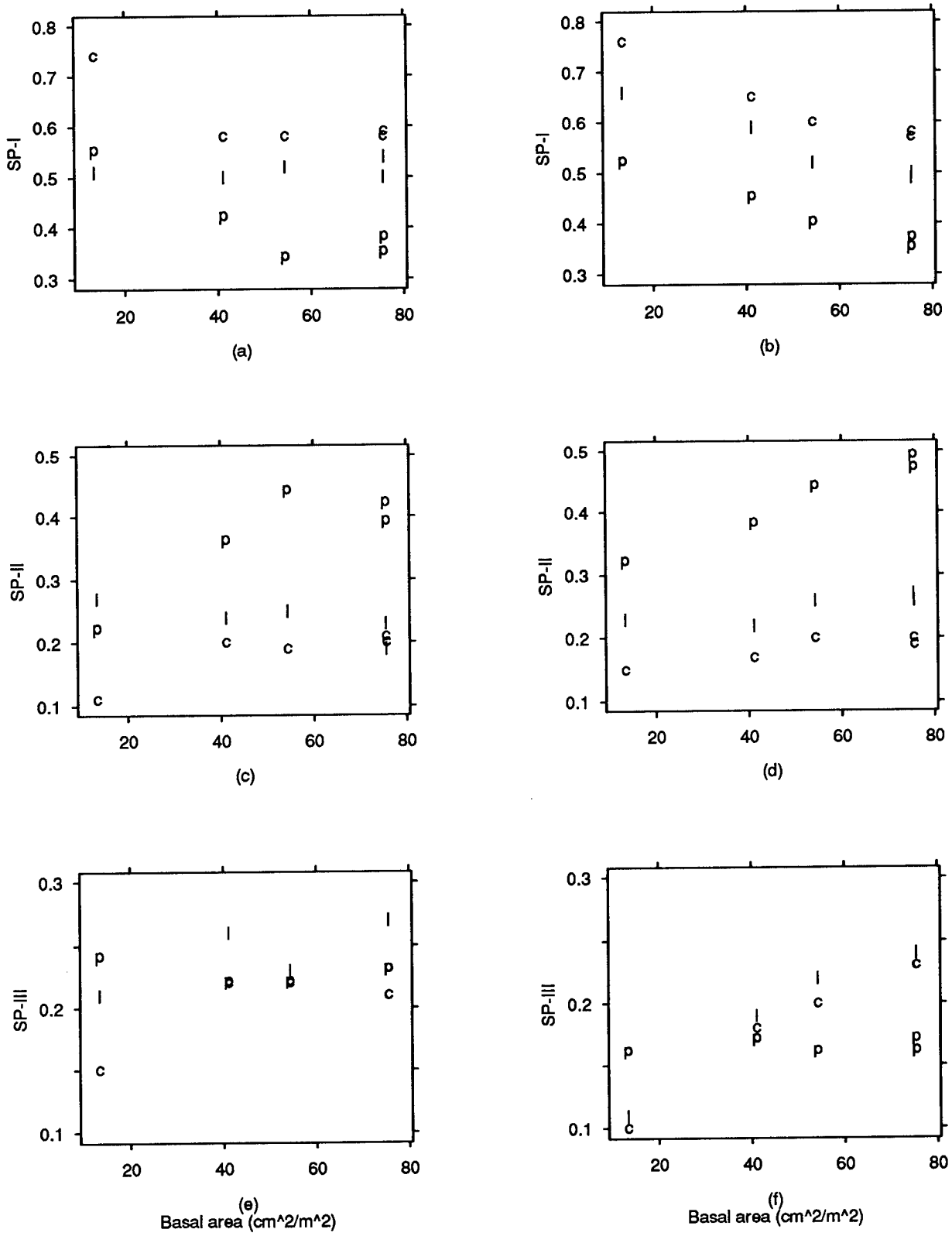
[1] S. R. Cloude, Uniqueness of target decomposition theorems in radar polarimetry, in *Direct and Inverse Methods in Radar Polarimetry, Part I,* (ed. by W. M. Boerner et al.) Kluwer Academic Publishers, Dordrecht, The Netherlands, pp. 267-296, 1992.

[2] J. J. van Zyl, Application of Cloude's target decomposition theorem to polarimetric imaging radar data, *Proceedings of the Third Spaceborne Imaging Radar Symposium,* held at the Jet Propulsion Laboratory, Pasadena, California, Jan. 18-21, 1994, pp. 207-216, 1994.

[3] G. Sun, D. S. Simonett, and A. H. Strahler, A radar backscattering model for discontinuous coniferous forests, *I.E.E.E. Transactions on Geoscience and Remote Sensing,* **29**, 639-650, 1991.

[4] Y. Wang, F. W. Davis, and J. M. Melack, Simulated and observed backscatter at P-, L-, and C- bands from ponderosa pine stands, *I.E.E.E. Transactions on Geoscience and Remote Sensing,* **31**, 871-879, 1993.

Fig. 1. Scattering power of three scattering types normalized by total power at C-, L-, and P-bands 5 ponderosa pine stands, Mt. Shasta, CA. Left: dry ground condition. Right: wet ground condition.



The Suitability of Multifrequency, Multipolarimetric and Multitemporal Radar Data for Forest Monitoring

Anton Haas, Bernhard Förster, Ulrich Ammer
Institute for Landuse Planning and Nature Conservation
University of Munich, Hohenbachernstr. 22, D-85354 Freising, Germany
Tel.:++49-8161-71-4662, Fax.:++49+8161-71-4671
e-mail: toni@abies.lnn.forst.uni-muenchen.de

Abstract -- From the two SIR-C/X-SAR Missions in April and October 1994 for the Oberpfaffenhofen supersite southwest of Munich/Germany numerous data sets with different aquisition modes are at disposal.
All used datasets were calibrated, so that the backscatter coefficient in dB (Dezibel) - values can be compared directly. The SIR-C data were geometrically adapted to the geocoded X-SAR data via image to image registration. Field observations and aerial photographs have been made for Ground Truth data. The analytical evaluation of the aerial photographs has been a very important step during the investigation of the information content. Results from visual comparisons and signature analysis have shown, that neither tree species nor stand composition influence radar signals markedly, but structural characters like altitude differences of trees and shrubs as well as vegetation density or gaps do. We conclude that in our case the highest spatial resolution is more important than the full polarimetric resolution.

INTRODUCTION

The aim of the evaluation is Forest Monitoring using SIR-C/X-SAR data. Of special interest are questions like, from what size on are non-wooded areas in forests recognized, where is the limit in stocking degree among forest and non-forest, which biomass classes can be discriminated and wether differences in state of foliage of the two seasons as well as further structures can be detected.

METHODS

Study Area and SAR Data

The forested surfaces of the supertestsite Oberpfaffenhofen are mainly located on moraines which contain an elevation difference of about 100 m maximum. The most important tree species are spruce (Picea abies), beech (Fagus silvatica) and pine (Pinus silvestris). First of all the area is -in addition to small monocultures- characterized by mixture in species, age-classes and management. The resulting diversity of structure has been accelerated by storm damage and bark beetle infestation of the last few years.

Overall 13 X-SAR and 6 SIR-C datasets from both missions were included in the presented work up to now. The used X-SAR data were available as GTC (Geocoded Terrain Corrected)-products. The SIR-C data exists in SLC (Single Look Complex)-products and in MLC (Multi Look Complex). The X-SAR data have one fixed polarization VV (Vertically transmitted, Vertically received). From the SIR-C data were either dual-pol or quad-pol datasets -depending on the recording modus- derived. Quadpol data allow the calculation of every polarization direction (linear, circular and elliptical), but show a lower spatial resolution at the same time. With dual-pol data on the other hand only certain polarization configurations (e.g. TP [Total Power], HH [Horizontally transmitted, Horizontally received], HV [Vertivally received]) are possible, but they show higher spatial resolution. The nominal resolution of the X-SAR GTC data is 25m * 25m, the pixel spacing is 12.5m * 12.5m. In order to create images with relatively square pixels and to get a similar spatial resolution like the already processed X-SAR data, the SIR-C data were processed with 1 look in range and 3 look in azimuth [2].

Image to Image Registration

The X-SAR data were available as GTC - products. The 6 datasets form April and the 7 datasets from October could be combined directly to one multitemporal dataset. A subset of 15 km * 15 km within the Testsite Oberpfaffenhofen has been choosen. The SIR-C data had to be geometrically adapted to the geocoded X-SAR data via image to image registration. This was performed with the aid of Ground Control Points and polynomial transformations. Here often the problem aroused finding enough qualified Ground Control Points in the corresponding datasets. Because variations of the elevations were not taken into account within this method, the procedure owns clear inaccuracies and is therefore restricted to small area. In this way a multifrequent, multipolarized and multitemporal dataset has been created.

Evaluation of the Aerial Photographs

Aerial photographs for forest inventory have been used for a long time. In our case the bird's eye view delivers the best

0-7803-3068-4/96$5.00©1996 IEEE

synoptical overview of the forest condition and documents it for comparisons with the radar data and temporal comparisons in the future. The aerial photographs were taken in late April 94. Field observations have been made during both missions. In addition to visual comparisons with the radar images, the photos were used for detailed analyses, depending on existing technical equipment.

We were able to use a stereoplotter for a detailed analyses of the aerial photographs. For that purpose Ground Control Points with the aid of a GPS (Globle Positioning System) - receiver have been measured so that the aerial photos could be geocoded absolutely. Now different measurements -for example stand heights or the size of deforested or storm damaged areas- could be carried out. From that step digital thematic maps result, which were linked to the radar data via corresponding coordinates and used as training and verification areas. Thus a method has been developed allowing an objective selection and exact location of the objects of investigation and classes of characters within the radar data independent of the display of a color composit shown on a screen.

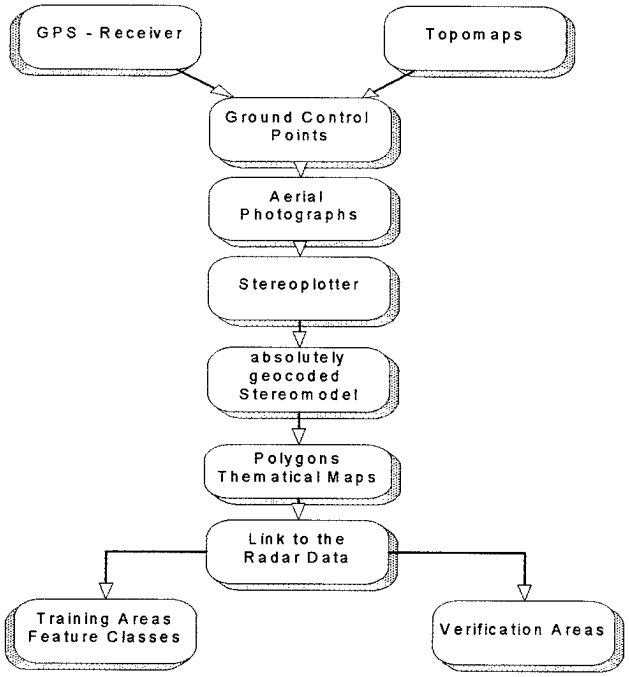


Figure 1: Flowchart evaluation of aerial photographs

Visual Interpretation

X-SAR

This short wavelength provides less information for the object forest. Wooded and agricultured areas could not be differentiated in a proper way. Multitemporal applications did not improve the information content clearly.

SIR-C

By combination of the three frequencies and the different polarizations the content of information was significantly enhenced. Forest and nonforest areas could be separated well within coherent woodland. Between forest and build-up areas some intersections appear. Especially the cross-pol combination of C and L band was found to be a good combination for forest application. We noticed as the most important feature the different spatial resolution of Quad-pol (mode x16) and Dual-pol (mode x11) data. Dual-pol data allow the recognition of non-wooded areas within forests smaller than 1 ha (hectare), which cannot be detected by quadpol data anymore. We found that the benefits of the higher spatial resolution are much more important than the disadvantage of the restricted polarimetric capacity. Nevertheless circular polarizations with the Quad-pol data were tested, but there could not be found any advantage in comparison to the linear polarizations. So Dual-pol data were evaluated higher and used preferentially for this heterogeneous investigation area.

Signature Analysis

Since the used data were calibrated, it was possible to calculate the backscatter coefficient in dB values [1]. This is a great advantage of active imaging radar systems. Now the mean dB values of many different training areas, subclasses and combined classes were compared. A good visualization for that are signature diagrams in form of dB-values as a function of frequency and polarization. It is important to take the variance of the means into consideration. It has been found, that if the means indicate for example in L-HV a possible separation of interesting features, the variance of the means was often significantly higher. For detailed analyses and scattergrams and histograms of single combinations were very helpful.

In our study we made several test with different training areas, subclasses and combined classes (similar to different classification levels) and found out, that typical forest parameters like tree species or stand composition do not influence the radar image clearly. Structural features like altitude differences of trees and shrubs as well as vegetation density or gaps within forested areas were found to be a more decisive factor in the backscatter coefficient.

The results of the signature analysis are:

- Even for a raw landuse classification there are big intersactions of the signatures, especially between forest and build-up
- Forest and agricultural areas can be separated clearly
- The mean backscatter coefficient of deciduous and conifer differs only slightly
- Deforested areas or storm damaged areas in general show in the L-Band obvious lower sigma0 values, so that they could be distinguished from wooded areas, but they overlap with wetland areas.

- Training areas of wooded surfaces containing gaps with a size of up to about 2500 qm (square meters) could not be separated from wooded areas without any gap.
- Training areas of wooded surfaces containing gaps with a size of about 2500 up to 10000 qm show in certain combinations (for instance L-HV) lower sigma0 values, but separation is difficult.
- Seasonal differences -covered with leaves or not- were hard to deduce from the data.
- there seems to exist a limit of biomass, wich indicates the change of forest and nonforest areas in the image. This limit is not found yet exactly, but is assigned to be correlated to the stand height of trees of about 5 m.

The next step is the application of a suitable speckle reduction (see for example fig.2 and fig.3). Then a classification will be performed.

CONCLUSIONS

Multipolarimetric multifrequency SIR-C/X-SAR data proved to be a valuable tool for forest monitoring. In the centre of attention is the observation of increase or decrease of woodland. In such a heterogeneous testsite like the study area the best spatial resolution is more important than the full polarimetric resolution.
To confirm detailed analysis it is necessary to investigate SIR-C **GTC** products.

FUTURE WORKS

The study has been taken place on the supersite Oberpfaffenhofen, because there were several SIR-C/X-SAR data available. We intent to transfer our experience to a more expanded and typical forested area and wish to investigate the National Park „Bavarian Forest". The attempt of a corregistration of the SIR-C data to the geocoded X-SAR data was without any success, caused by the effect of topography. Top priority for us is to get SIR-C **GTC** products.

ACKNOLEDGEMENT

The authors thank the staff of DFD of the DLR for support.
The work was funded by the German Space Agency (DARA), contract number 50 QS 900049.

REFERENCES

[1] Zink, M.: Results of X-SAR Calibration, International Geoscience and Remote Sensing Symposium (IGARSS'95), July 10 - 14, 1995, Florence, Italy, Vol.1, pp. 590-592

[2] Werle, D.: RADAR REMOTE SENSING FOR APPLICATION IN FORESTRY, December 1989, CCRS, Ottawa

[3] Chapman, B.: SIR-C Data Compression Software User Guide. Jet Propulsion Laboratory Internal Note JPL D- 11427, Revision 2.0, June 1994

[4] Lee, J.S.,Jurkevich, I., Dewaele, P., Wambacq, P., Oosterlinck, A.: Speckle Filtering of Synthetic Apertur Radar Images: A Review. Remote Sensing Reviews, Vol.8, 1994, pp.313-340

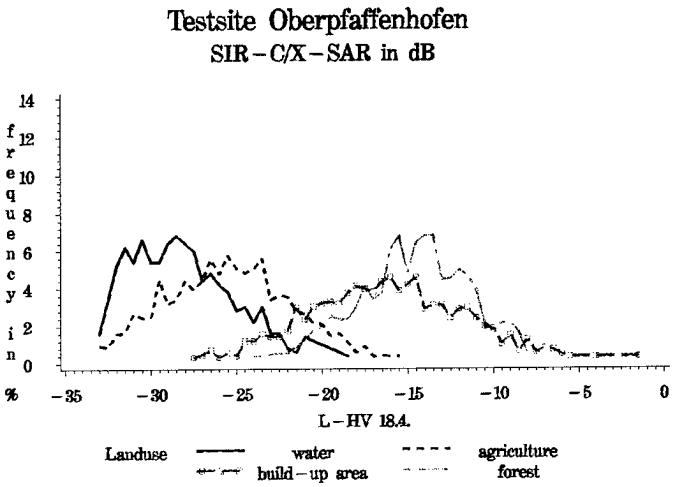


Figure 2: Histogram of unfiltered raw classes

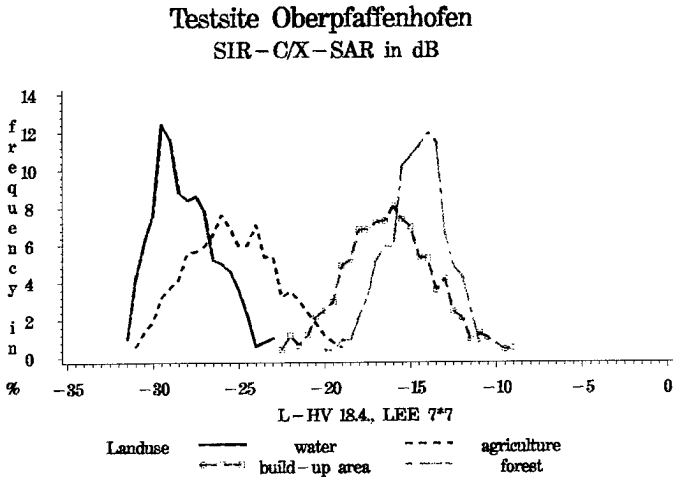


Figure 3: Histogram of filtered raw classes (LEE filter, 7*7)

Sensitivity of Modeled C-band Backscatter from Loblolly Pine Forests to Surface Soil Roughness and Moisture

Yong Wang, John L. Day*, and Frank W. Davis*

Department of Geography, East Carolina University, Greenville, NC 27858
Tel (919) 328-1043, Fax (919) 328-6054, and E-mail: gewang@ecuvm.cis.ecu.edu
*Institute for Computational Earth System Science, University of California, Santa Barbara, CA 93106

ABSTRACT

We investigated effects of surface-related scattering on C-band radar backscatter in loblolly pine forests at Duke Forest, North Carolina. Five loblolly pine stands, aged from 8 to over 60 years old, were used. Stand density ranged from 589 trees/ha to 5505 trees/ha, and mean tree trunk diameter at breast height (dbh) was between 0.10 m and 0.27 m. We used the ratio of the modeled total backscatter to modeled canopy scattering (T/C) to evaluate the importance of ground surface-related scattering. C-band backscatter at 20°, 30°, and 40° incidence angles (θ_0) was simulated for the stands. C-HH and C-VV backscatter showed modest sensitivity to the surface-related scattering in the young stand (8 years old) at θ_0 of 20° and 30°, and in a mid-aged stand (25 years old) at θ_0 of 20°. C-HV backscatter was somewhat sensitive to surface scattering in the young stand at θ_0 = 20°. In the other cases, C-band backscatter was not sensitive. The changes in C-band T/C ratios due to surface scattering occurred only in the young and mid-aged stands. As incidence angle increased, the maxima of T/C ratios decreased for all stands, a consequence of the larger relative contribution of canopy scattering to total backscatter at large θ_0 than at small θ_0.

INTRODUCTION

Backscatter models have been developed (e.g. [1-2]) in order to understand the complex nature of backscattering from forests. Much effort has been invested in collecting ground data to parameterize the models and to validate the models by comparison of model simulations to synthetic aperture radar (SAR) backscatter data. The canopy backscatter models require many input parameters, and collecting data to estimate the parameters is difficult, time consuming and labor intensive. One often needs to ask whether the available (limited) forest and SAR data and existing canopy backscatter models can be used to help 1) understand backscattering from forests, 2) guide ground truthing so as to concentrate on critical parameters that are realistically measurable, and 3) retrieve forest parameters from backscatter data. With these questions in mind, we have designed a model sensitivity analysis to investigate 1) under what ground conditions (i.e., surface roughness and soil moisture) can we ignore surface related scattering in our attempts to understand backscatter from forests and retrieve canopy parameters from radar returns? 2) when do surface related scatterings make a difference? and 3) how does sensitivity to surface conditions depend on radar incidence angle?

APPROACHES

The approaches are to 1) model the backscattering from forests by using collected ground and stand data, 2) separate modeled total backscatter into canopy scattering and non-canopy scattering (surface-related scattering), and 3) compute the ratio of modeled total backscatter to canopy scattering in order to appraise the importance of canopy scattering in the total backscatter.

Based on our canopy backscatter model, we can divide modeled total backscatter into two classes of scattering: non-canopy related-scattering and direct canopy scattering (see [3] for a schematic diagram of the model). The non-canopy related-scattering consists of trunk-ground interactions, canopy-ground interactions, and surface backscatter. Because these scattering mechanisms involve ground surface scattering, they are affected by surface conditions such as roughness and moisture. Canopy scattering does not include surface interactions. Thus, it is not directly affected by surface conditions.

To determine the importance of the canopy scattering (vs. non-canopy scattering) we calculate ratio of the modeled total backscatter to canopy scattering (T/C). If a T/C ratio is 1.0 (0 dB), the total backscatter is equal to the canopy scattering. There will be no non-canopy related-scattering in the total backscatter. The surface-related scattering has no effect on the total backscatter. If the ratio is 2.0 (3 dB), the total backscatter is twice the canopy scattering (or 3 dB higher than the canopy scattering). In this case, the total backscatter would consist of 50% canopy scattering and 50% of non-canopy scattering. Table 1 gives some typical values for the T/C ratio (in dB scale) and the corresponding canopy scattering percentages.

RESULTS

The effects of roughness and moisture on modeled backscatter can be shown by plotting T/C ratios as contour lines in the plane formed by surface rms roughness height and volumetric soil moisture content. Before creating the contours, we use the range of the rms roughness heights and soil

0-7803-3068-4/96$5.00©1996 IEEE

moisture measured at the Duke Forest as the basis for setting up a 2-D roughness-moisture region for modeling. The region is 0.8 cm to 4.2 cm for the rms height and 5% to 45% for soil moisture. To create the contour lines in the 2-D region, we have simulated the T/C ratios over a 50x50 grid equally distributed across the region. The roughness and moisture vary at each location on the grid. 2500 simulations were done to obtain T/C ratio data covering the roughness-moisture modeling region. To study the effects of roughness and moisture on forest backscatter, other non-surface-related model inputs (e.g. dbh, stand density, etc.) are held constant. We also hold correlation length constant at 28.2 cm (the mean value for pine stands in the study area, measured in April 1994) to simplify our analysis and presentation.

Threshold

A small T/C ratio indicates that canopy scattering dominates the total backscatter and surface-related scattering is unimportant. In other words, one can establish a threshold such as T/C = 1 dB as a criterion for importance of surface effects, an indicator of whether or not total backscatter may be considered sensitive to surface conditions. If the T/C ratio is less than the threshold, surface-related scattering can be ignored. When the T/C ratio is 1 dB the total backscatter is only 1 dB higher than the canopy scattering. The canopy scattering contributes 79% and the surface-related scattering 21% to the total backscatter (Table 1).

Sensitivity of Backscatter to Roughness and Moisture

Modeled contour lines of T/C ratios (in dB scale) from a young loblolly pine stand D68 are shown in Fig. 1. The radar incidence angle is 30°. T/C ratios vary from 0.5 dB to 1.3 dB at C-HH and C-VV, and from 0.5 dB to 0.6 dB at C-HV for the tested roughness-moisture region. If we use a threshold of T/C = 1 dB, the modeled total backscatter is not sensitive to the surface roughness when the moisture is ≤ 22% at C-HH and C-VV (Fig. 1a,c). Within the tested moisture-roughness region, the C-HV backscatter is not sensitive to the surface-related scattering (Fig. 1b). (The vibration in some contours is an artifact caused by the contour routine of our graphics package.)

Minima and maxima of C-band T/C ratios from the five loblolly pine stands for the tested roughness-moisture region are summarized in Table 2. In Table 2, we use,

i) roman font if the maximum T/C ratio is ≤ 1 dB, and

ii) *italic font* if the minimum T/C ratio is < 1 dB and maximum T/C ratio is > 1 dB.

We refer to i) as an insensitive case, in which the total backscatter is not sensitive to surface-related scatterings, and ii) as an intermediate case. C-HH and C-VV backscatter have a moderate degree of sensitivity to surface-related scattering for a young stand D68 at θ_0 of 20° and 30°, and a mid-aged stand D51 at θ_0 of 20°. C-HV backscatter has intermediate sensitivity to the surface-related scattering for the young stand at θ_0 = 20°. In the other cases, backscatter is not sensitive to surface scattering (Table 2). Therefore, it is not necessary to measure surface roughness and moisture in these stands for purposes of modeling forest backscatter at C-band.

To understand variation of the T/C ratios, we simulate C-band scattering from the stands at θ_0 = 30° (Fig. 2). Because the relation of modeled surface scattering, canopy volume scattering, and total backscatter is similar at C-HH, C-HV, an C-VV, only modeled C-HH results are shown. Surface rms roughness height of 2.5 cm (mean of 0.8 cm and 4.2 cm) and soil volumetric moisture content of 25% (mean of 5% and 45%) are used in the simulation. Canopy scattering (curve c) dominates total backscatter from the stands. There is some contribution from surface scattering (curve s) to the total backscatter (curve t); its contribution is smaller for the mature stands (Fig. 2). Because scattering from the trunk-ground and canopy-ground terms is less than −40 dB, their curves are not shown in the figure. The variation of T/C ratios over the range of surface conditions in the young stand and mid-aged stands is due to surface backscatter.

Table 1. Values of typical T/C ratio and percentage of the canopy scattering in the total backscatter

T/C ratio (dB)	0	0.5	1	2	3	10
% of canopy scattering	100	89	79	63	50	10

Table 2. Simulated minima and maxima of T/C ratios (dB) for ranges of soil moisture content (5% – 45%) and surface rms roughness height (0.8 cm – 4.2 cm) for loblolly stands

Stand	θ_0	C–HH	C–HV	C–VV
D68 (8 yr. old)	20°	*0.6–3.0*	*0.1–1.1*	*0.6–3.1*
	30°	*0.2–1.4*	0.0–0.6	*0.2–1.4*
	40°	0.2–1.0	0.0–0.4	0.2–1.0
D51 (25 yr. old)	20°	*0.2–1.2*	0.0–0.2	*0.2–1.3*
	30°	0.1–0.5	0.0–0.1	0.1–0.4
	40°	0.0–0.2	0.0–0.1	0.0–0.2
D14 (23 yr. old)	20°	0.0–0.2	0.0–0.1	0.0–0.2
	30°	0.0–0.1	0.0–0.0	0.0–0.1
	40°	0.0–0.0	0.0–0.0	0.0–0.0
D44 (60+ yr. old)	20°	0.0–0.2	0.0–0.0	0.0–0.2
	30°	0.0–0.1	0.0–0.0	0.0–0.1
	40°	0.0–0.0	0.0–0.0	0.0–0.0
D7 (60+ yr. old)	20°	0.0–0.1	0.0–0.0	0.0–0.1
	30°	0.0–0.0	0.0–0.0	0.0–0.0
	40°	0.0–0.0	0.0–0.0	0.0–0.0

Scattering Mechanisms Causing Variation of T/C Ratio

Comparing modeled scattering (Fig. 2), we have noted that the change of C-band T/C ratios is caused by surface scattering, and this occurs only in young and mid-aged stands. We attribute the finding to the surface roughness. For a surface with a roughness rms height of 2.5 cm, the surface is very rough at C-band. When a surface is rough the direct surface backscattering may be strong but surface specular scattering may not be. Therefore, direct surface backscatter could be strong, whereas scattering mechanisms involving specular scattering (eg., the trunk-ground and canopy-ground terms) could be weak. Surface scattering is greater in the young stand and (perhaps) mid-aged stands than in the mature stands. This may be a result of more canopy attenuation in mature stands than in the young and mid-aged stands.

ACKNOWLEDGMENTS

This work was supported by the NASA SIR-C/X-SAR project through the JPL (contract # 958468).

REFERENCES

[1] Ulaby, F. T., Sarabandi, K., McDonald, K. C., Whitt, M., and Dobson, M. C., Michigan Microwave Canopy Scattering Model (MIMICS), *Int. J. Remote Sens.*, 11:1223-1253, 1990.

[2] Sun, G., Simonett, D. S., and Strahler, A. H., A radar backscattering model for discontinuous coniferous forests, *IEEE Trans. on Geosci. Remote Sens.*, 29:639-650, 1991.

[3] Wang, Y., Davis, F. W., Melack, J. M., Kasischke, E. S., and Christensen, N. L., Jr., The effects of changes in forest biomass on radar backscatter from forest canopies, *Int. J. Remote Sens.*, 3:503-513, 1995.

Fig. 2. Modeled C-band backscatter at 30° incidence angle from 5 loblolly pine stands (roughness height = 2.5 cm, moisture content = 25%).

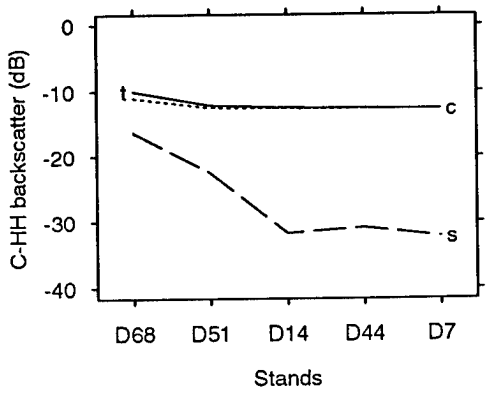
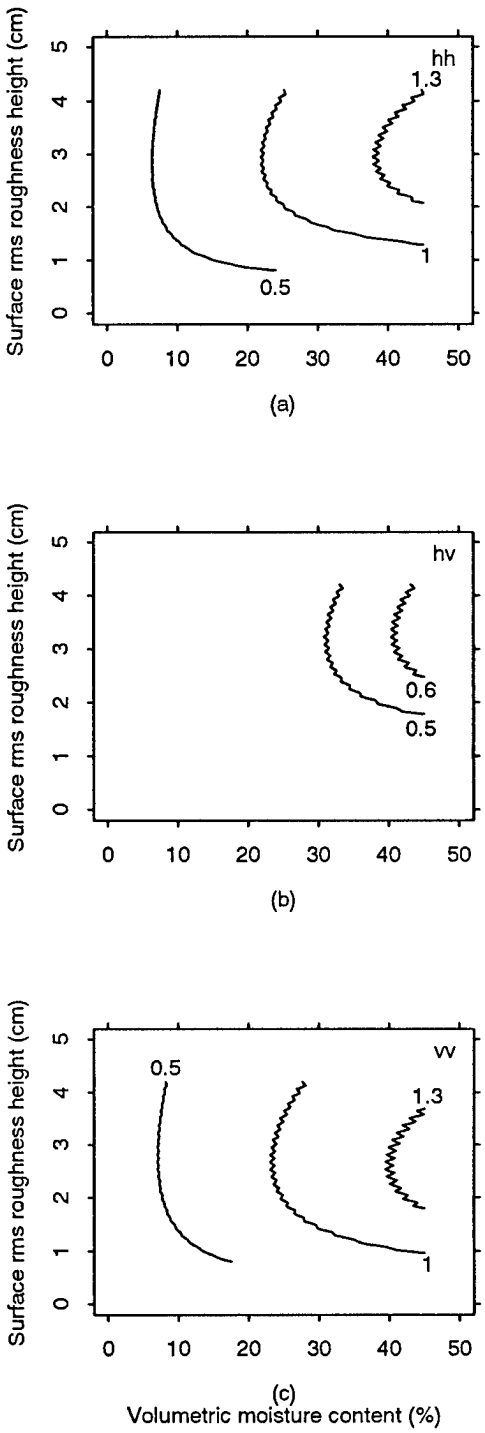


Fig. 1. Modeled C-band total backscatter to canopy scattering ratio (dB, contour line) at 30° incidence angle from a young loblolly pine stand D68.



Multifrequency and Polarimetric Analysis of Forests with SIR-C/X-SAR Data

F. M. Seifert, H. Kietzmann, M. Zink
Deutsche Forschungsanstalt für Luft- und Raumfahrt (DLR)
Institut für Hochfrequenztechnik, P.O. Box 11 16, D-82230 Weßling, Germany
Phone: +49-8153-28-2352, FAX: +49-8153-28-1449, E-mail: Frank-Martin.Seifert@dlr.de

Abstract – The potential of multifrequency and polarimetric data to monitor deciduous and coniferous forests is presented. A remarkable increase of the backscatter can be noticed from spring to autumn for both forest types. Backscatter derived from data reasonably agrees with model calculations. Correlation coefficient, co-polarized phase differences and backscattering coefficients show no significance for species discrimination. A dominance of volume scattering from the crown is verified by decomposition model calculations for all three frequencies.

INTRODUCTION

In April and October 1994 the Space Shuttle Endeavour flew the SIR-C/X-SAR missions, where the Earth was observed for the first time with three radar frequencies simultaneously from space – L- and C-band with full polarimetric capabilities and X-band in VV-polarization. During each of the two Space Radar Lab (SRL) missions the super test site Oberpfaffenhofen was imaged twice fully polarimetric – on April 11 and October 2 (data take 30) under 26^o and on April 13 and October 4 (DT 62) under 42^o incidence angle. Mature beech and spruce forests in Bavaria [1] were under observation. Seasonal changes of backscatter, comparison of SIR-C/X-SAR data and MIMICS results, correlation coefficient, co-polar phase and backscatter differences for species distinctiveness and a decomposition model for scattering discrimination are the topics of the paper.

SEASONAL CHANGES

The life processes of a tree undergo seasonal and diurnal cycles which will reflect in changing backscatter behavior. Foliage growth and loss patterns are different for deciduous and coniferous trees. Beech exhibits a pronounced annual cycle whereas spruce keeps needles up to seven years and replaces only a fraction of the total needle biomass annually. The most extensive growth of leaf or needle biomass occurs in late spring after bud break. Therefore it can be expected that the spruce forest exhibits only a low seasonal backscatter variation compared to a high variability of the beech forest.

Backscatter of these four data takes is compared in table 1. For DT 30 a seasonal difference Δ_{S-A} (spring - autumn) of -3 dB in L-band and -5 dB in C-band can be noticed in all polarizations for the beech forest (table 1a). DT 62 shows no such significant differences, which is quite remarkable because on 13 April the whole test site was covered with a wet snow layer.

Beech	**L-Band**			**C-Band**			**X-Band**
σ^o [dB]	HH	VV	HV	HH	VV	HV	VV
11.4.94	-8.9	-11.7	-14.7	-10.8	-11.4	-17.2	-8.4
2.10.94	-6.2	-8.4	-11.0	-6.2	-4.6	-12.6	-7.2
Δ_{S-A}	-2.7	-3.3	-3.7	-4.6	-6.8	-4.6	-1.2
13.4.94	-7.2	-7.6	-12.3	-6.1	-7.2	-10.6	-9.1
4.10.94	-6.9	-5.9	-10.3	-7.8	-8.7	-15.0	-8.4
Δ_{S-A}	-0.3	-1.7	-2.0	1.7	1.5	4.4	-0.7

Table 1a: Seasonal σ^o changes of the beech forest between the two space radar lab missions (SRL-1/-2)

Spruce	**L-Band**			**C-Band**			**X-Band**
σ^o [dB]	HH	VV	HV	HH	VV	HV	VV
11.4.94	-6.2	-9.8	-14.0	-10.0	-11.1	-13.1	-9.5
2.10.94	-5.7	-6.9	-11.3	-6.4	-5.6	-12.2	-9.3
Δ_{S-A}	-0.5	-2.9	-2.7	-3.6	-5.5	-0.9	-0.2
13.4.94	-6.1	-7.2	-10.6	-8.0	-8.0	-13.6	-10.0
4.10.94	-5.4	-6.7	-10.6	-7.7	-8.3	-14.7	-10.4
Δ_{S-A}	-0.7	-0.5	$\pm$0.0	-0.3	0.3	1.1	0.4

Table 1b: Seasonal σ^o changes of the spruce forest between SRL-1 and SRL-2

The spruce forest shows seasonal differences for DT 30 of -3 dB for the co-polar signals with the exception of L-HH with only -0.5 dB (table 1b). In DT 62 again no significant difference can be found between spring with a snow layer and autumn.

SIR-C/X-SAR DATA AND MIMICS RESULTS

The Michigan Microwave Scattering Model (MIMICS) for continuous canopies is a semi-empirical backscatter

0-7803-3068-4/96$5.00©1996 IEEE

model where the tree canopy is devided in three layers: the crown layer, the trunk layer and the underlaying ground [2]. MIMICS is a first order scattering model with full polarimetric capabilities, valid for frequencies from 0.5 GHz to 10 GHz and incidence angles between 10 and 60 degrees, and therefore covering the whole range of SIR-C/X-SAR data.

Geometric and dielectric properties were sampled during an extensive ground truth campaign in autumn. These parameters are necessary inputs for the model calculation which are compared with SAR data in table 2.

Beech	**L-Band**			**C-Band**			**X-Band**
σ^o [dB]	HH	VV	HV	HH	VV	HV	VV
2.10.94	-6.2	-8.4	-11.0	-6.2	-4.6	-12.6	-7.2
MIMICS	-6.5	-8.6	-14.7	-8.9	-9.1	-26.8	-8.7
Δ_{D-M}	0.3	0.2	3.7	2.7	4.5	14.2	1.5
4.10.94	-6.9	-5.9	-10.3	-7.8	-8.7	-15.0	-8.4
MIMICS	-8.3	-9.0	-15.0	-6.3	-9.3	-27.1	-9.3
Δ_{D-M}	1.4	3.1	4.7	-1.5	0.6	12.1	0.9

Table 2a: Comparison of modeled and measured backscatter from beech forest

Spruce	**L-Band**			**C-Band**			**X-Band**
σ^o [dB]	HH	VV	HV	HH	VV	HV	VV
2.10.94	-5.7	-6.9	-11.3	-6.4	-5.6	-12.2	-9.3
MIMICS	-6.4	-8.3	-11.7	-8.6	-9.5	-15.6	-7.4
Δ_{D-M}	0.7	1.4	0.4	2.2	2.9	3.4	-1.9
4.10.94	-5.4	-6.7	-10.6	-7.7	-8.3	-14.7	-10.4
MIMICS	-8.0	-12.4	-14.4	-11.5	-11.9	-17.9	-10.6
Δ_{D-M}	2.6	5.7	3.8	3.8	3.6	3.2	0.2

Table 2b: Comparison of modeled and measured backscatter from spruce forest

Co-polarized components for both stands derived from data reasonably agree with the model calculation where HH is normally a little bit higher than the VV component. The predicted RCS of the beech for HV-polarization in C-band is 13 dB below the measured data. This is most likely from an underestimation of multiple scattering from branches in the model.

CORRELATION COEFFICIENT

The correlation coefficient indicates the measure of similarity of backscatter signals in the different polarization modes. It estimates the relation between the deterministic and statistical scattering behavior of the observed object.

The correlation coefficient ρ_{hv} of the two co-polarised signals is in L-band 0.28 $\pm$0.05 for both species. In C-band the correlation is higher 0.55 $\pm$0.15 indicating a surface scattering character of the forest for this shorter wavelength, i.e. the dominant scatters are small twigs, leaves for the beech and the needles for the spruce. The correlation coefficient ρ_{vx} reaches its highest values on the 13 April – the "godsend" snow data take. This effect of the wet snow is stronger in C-band than in L-band.

CO-POLAR PHASE DIFFERENCE

From the co-polar phase difference Φ_{HH-VV} (table 3) the main scattering mechanism can be deducted: $\Phi_{HH-VV} = 0^o$ for pure single-bounce scattering and $\Phi_{HH-VV} = 180^o$ for double-bounce scattering.

Φ_{HH-VV}	**Beech**		**Spruce**	
	L-band	C-band	L-band	C-band
11.4.94, $\theta = 26^o$	-19.6^o	23.8^o	-32.8^o	2.7^o
13.4.94, $\theta = 42^o$	-62.0^o	-10.5^o	-30.9^o	15.9^o
2.10.94, $\theta = 26^o$	-53.9^o	4.9^o	-39.6^o	7.4^o
4.10.94, $\theta = 42^o$	31.0^o	13.1^o	-6.2^o	6.5^o

Table 3: Mean value of co-polar phase difference Φ_{HH-VV} in degrees

For both species the mean value of Φ_{HH-VV} is around 0^o in C-band whereas in L-band Φ_{HH-VV} reaches absolute higher values. That indicates a higher double-bounce contribution from trunk-ground scattering in the lower frequencies.

DISTINCTIVENESS OF SPECIES

In table 4 no significant difference between the backscatter of beech and spruce (Δ_{B-S}) can be noticed. All differences in C-band are within the accuracy of the sensor and as well most differences in L-band.

Δ_{B-S}	**L-Band**			**C-Band**			**X-Band**
σ^o [dB]	HH	VV	HV	HH	VV	HV	VV
11.4.94	-2.7	-1.9	-0.7	-0.8	-0.4	-0.1	1.1
13.4.94	-1.2	-0.4	-1.7	1.2	0.1	0.4	0.9
2.10.94	-0.4	-1.5	0.3	0.3	0.9	-0.4	2.1
4.10.94	-1.4	0.9	0.4	$\pm$0.0	-0.3	-0.4	2.0

Table 4: Difference of measured backscatter: Beech – Spruce

Therefore the low measured beech-spruce backscatter differences for all polarization states can be attributed to a similar backscatter behavior of the beech forest after bud break and immediately before defoliation in autumn related to the backscattering of the spruce forest. Hence a distinctiveness of species from two seasonal data sets seems not feasable. At least a third data set is necessary during summer when the beech foliage is fully developed. However in X-band a difference of 2 dB occurs in autumn and 1 dB in spring. This can be an effect of differences in the surface scattering of needles and leaves.

DECOMPOSITION MODEL

For forested areas different microwave frequencies provide information about different layers of the canopy [3]. X- and C-Band signals primarily interact with the crown layer – the X-band with the crown surface and the C-band with the tree canopy volume. L-band penetrates the crown and interacts primarily with main branches, trunks and ground. Canopy architecture strongly affects the contribution from different scattering mechanisms like surface, volume and double-bounce scattering [4].

Model calculations with MIMICS show that for co-polarization the crown provides the main contribution to the backscatter in all three frequencies. Additionally the trunk-ground and ground-trunk interaction is a significant component for HH-polarization at L-band. The crown is the only source for the backscatter in cross-polarization.

Freeman and Durden developed a three-component scattering model to describe polarimetric SAR data [5]. A combination of three basic scattering mechanisms –

1. volume scatter from a cloud of randomly oriented dipoles (vol)
2. even-bounce scatter from a pair of orthogonal surfaces with different dielectric constants (dbl)
3. Bragg scatter from a moderately rough surface (surf)

– is fitted to polarimetric SAR data.

For volume scattering the assumption of very thin cylinder-like scatterers with a uniform orientation distribution one can deduct that the cross-pol term power is a third of the co-pol term power. Thus the model determines the volume scatter from the HV term. The model assumes pure volume scattering if the difference between the lower co-pol term and the cross-term is lower than 4.8 dB.

For C-band (table 5) the beech forest exhibits a greater volume component in spring (80%) than in autumn (65%) whereas the spruce forest has always a volume component about 75% (with the exception of the snow data take). In the beech forest the longer propagation path through the crown for 42^o incidence angle results in an increasing volume term. For both species are double-bounce effects almost neglectable.

C-band	Beech			Spruce		
[%]	dbl	surf	vol	dbl	surf	vol
11.4.94, $\theta = 26^o$	4.5	16.1	79.4	0.2	27.7	72.1
13.4.94, $\theta = 42^o$	0.2	16.4	83.4	1.2	12.1	86.7
2.10.94, $\theta = 26^o$	0.1	37.2	62.7	0.4	22.6	77.0
4.10.94, $\theta = 42^o$	0.7	30.5	68.8	4.6	24.8	70.6

Table 5: Decomposition results of beech and spruce in C-band

The dominance of volume scattering from the crown is predicted by MIMICS for all frequencies and veryfied by decomposing the polarimetric SAR data.

FUTURE WORK

This work is part of a long term investigation on beech and spruce forests in Central Europe with spaceborne (ERS, Radarsat) and airborne (ESAR) radar sensors. A permanent data logging station has been installed for the ground truth data collection, including measurements of trunk dielectric constants, xylem fluxes and microclimate. The overall aim is to retrieve forest vitality parameters from remotely sensed SAR data.

ACKNOWLEDGMENTS

We would like to thank Professor F. Ulaby and Dr. L. Pierce from the University of Michigan for providing us with the MIMICS software and Dr. A. Freeman from JPL for the program of the three-component scattering model.

REFERENCES

[1] Seifert, F. M., H. Kietzmann, M. Zink, "Forest Monitoring with SIR-C/X-SAR", *in Proc. EUSAR'96*, Königswinter, March 1996, in press.

[2] Ulaby, F. T., K. Sarabandi, K. C. McDonald, M. Whitt, M. C. Dobson, "Michigan Microwave Scattering Model", *Int. Journal of Remote Sensing*, Vol. 11, No.7, pp. 1223-1253, 1990.

[3] D. H. Hoekman, J. J. van der Sanden and M. A. M. Vissers, "MAESTRO-1 Flevoland/Speulderbos: Analysis results of multiband polarimetric SAR data of forests and agricultural crops", *in Proc. of MAESTRO-1/AGRISCATT Workshop*, ESTEC, Noordwijk, The Netherlands, ESA WPP-31, pp. 53-58, May 1992.

[4] A. Freeman, S. Durden, R. Zimmermann, "Mapping sub-tropical vegetation using multi-frequency, multi-polarization SAR data", *in Proc. IGARSS'92*, Houston, Texas, May 1992, pp. 1686-1689.

[5] A. Freeman, S. Durden, "A three-component scattering model to describe polarimetric SAR data", *in Proc. of SPIE Vol. 1748 Radar Polarimetry*, pp. 213-224, 1992.

Optimization of a Scanning Radar Altimeter for Forest Inventory; a Simulation Method

Juha Hyyppä[1] and Martti Hallikainen
Helsinki University of Technology, Laboratory of Space Technology
Otakaari 5 A, FIN-02150 Espoo, FINLAND
[1]Phone: 358-0-4514775 (after 12 Oct. 1996, 358-9-4514775)
[1]Fax: 358-0-4512898 (after 12 Oct. 1996, 358-9-4512898)
[1]Email: Hyyppa@ava.hut.fi

Abstract - Evaluating the accuracy of a scanning radar altimer for forest inventory is problematic, as no feasible radars exist, and the ground truth data collected by conventional means is often not accurate enough. In this paper, a simulation method [1] for optimizing the technical parameters of a scanning radar altimeter and evaluating the radar's accuracy for forest inventory is described. The method is based on statistical information of boreal forest stands, radar-derived stand profiles and simulation.

INTRODUCTION

The possibility of applying ranging radars for forest canopy inventory has been extensively studied since the mid 1980s [2,3,4,5]. Bernard et al. [2] reported the first radar-derived stand profiles using a helicopter-borne ranging 5.35 GHz dual-polarization scatterometer, ERASME (Etude Radar des Sols et de la Mer) and suggested that the shape of the backscattering signal correlates with important mean stand characteristics, such as tree height and density. Later, Hyyppä [1] showed that the ranging radar is a powerful tool for determining the mean and dominant tree height, total basal area, stem volume, height of the crown base and classification of categorical variables of compartments, such as development classes, land classes, bog types and fertility classes. In earlier studies non-imaging (non-scanning) radars have been used. However, imaging radar systems, i.e. scanning radar altimeters, offer better means to meet the cost and accuracy requirements of operational forest inventories.

A scanning radar altimeter is a good alternative for topographic terrain survey in cases where conventional techniques are too inaccurate, laborious, and/or time-consuming. Potential applications include tree height, stem volume and biomass measurements for forest inventories, topographic terrain survey of forest areas, determination of volumes of hills, gravel pits, chip or coal piles, tracing of roads, railways, pipe and cable routes.

*The authors are grateful to the **Academy of Finland, Jenny and Antti Wihuri Foundation and Alfred Kordelin Foundation** for financial support.*

0-7803-3068-4/96$5.00©1996 IEEE

In 1988 Pulliainen and Hyyppä [6] suggested the use of a scanning ranging altimeter for stem volume assessment. Evaluating the accuracy of the instrument in forest inventory is, however, very problematic, as no feasible radars exist and, on the other hand, the ground truth data collected by conventional means is often not accurate enough. The accuracy of field inventories is typically 15 %.

In this paper, a simulation method for optimizing the technical parameters of the scanning radar altimeter and evaluating the radar's accuracy for forest inventory is described.

METHOD

The method combines statistical information of boreal forest stands, radar-derived stand profiles and simulation. A simulated forest was created by using both the statistical information of stand characteristics and 'true' compartmentalized forest inventory data to obtain a representative forest area with stand characteristics exactly known. The response of the radar from the forest was simulated by using true radar-derived stand profiles obtained by non-imaging ranging scatterometer, HUTSCAT (Helsinki University of Technology Scatterometer).

SCANNING RADAR ALTIMETER

The scanning radar altimeter (Fig. 1) produces three-dimensional image of the target by scanning the antenna beam in the across-track direction [7]. A high spatial resolution can be achieved by synthetic aperture techniques in the flight direction, and in the across-track direction with a narrow beam produced by a large antenna. A high range resolution can be obtained by transmitting linear frequency-modulated pulses, and by using deramp compression in the receiver.

SIMULATION OF FOREST AREA

The 'true' field inventory data of the 1300-ha test site (Teijo) located 130 km west of Helsinki was obtained from the Finnish Forest and Park Service. The compartmentalized

data included estimates for the stem volume [m^3/ha], basal area [m^2/ha], mean height [m], number of tree stems [pc/ha] and tree species. In addition over thousand trees were carefully measured to obtain the statistical information of stand characteristics.

In the simulation, the forest was constructed tree by tree resulting in one possible realization of a true forest with exactly known characteristics. The simulation consisted of two procedures, the creation of an individual tree and the creation of a compartment, described in speudo code below.

Simulation of an individual tree

A tree (location, diameter, height and stem volume) was simulated as follows. In all simulations, a random function, rand, was used to create normally distributed random numbers between -1 and 1.

The location was simulated by using a table to identify compartment number of the respective x and y coordinates, and using information of centre points of each compartment.

Repeat

$x \leftarrow f(x\_coord\_of\_centre\_of\_compartment, rand)$

$y \leftarrow f(y\_coord\_of\_centre\_of\_compartment, rand)$

Until location [x,y] belongs to compartment

The diameter (at breast height), d, was simulated by using the median tree diameter of the corresponding compartment taking into account the statistical diameter variation (based on tree measurements) within the compartment.

$$d \leftarrow d\_of\_a\_median\_tree + variation \times rand$$

The height, h, was simulated by using a regression model as a function of d. The model was developed using the diameter and height statistics obtained from Teijo tree measurements.

$$h \leftarrow f(d, rand)$$

The stem volume of a tree, v, was calculated using formulae developed for Finnish forests [8]. The equations are based on diameters at a fixed height and tree height.

$$v \leftarrow exp(\alpha_1 + \alpha_2 ln(d) + \alpha_3 d + \alpha_4 ln(h) + \alpha_5 ln(h-\alpha_6))$$

where α_i is spesific for each tree species.

Simulation of a compartment

A compartment was simulated by invoking the procedure of an individual tree according to the number of the tree stems in a compartment. The 'true' compartmentalized data consisted of five strata; therefore, in simulation each strata was created individually.

A strata was simulated by using median tree diameter, tree species, number of tree stems, stem volume per hectare, basal area per hectare, mean tree height and size of the compartment.

Repeat
  simulate a tree
  put tree information into stack
  calculate total volume, total basal area and
    mean height
  increment number of simulated stems
  if all stems have been simulated
    check that volume, basal area and mean
      height do not deviate more than
      30 % of the 'true' data
    if error
      clear the stack and variables
Until all stems are simulated and no error exists
Record the data of simulated trees
Record the averaged data of the strata

SIMULATION OF 3-D IMAGES

The Teijo test site was measured with an FM-CW helicopter-borne 8-channel ranging scatterometer, HUTSCAT (Helsinki University of Technology SCATterometer). Because HUTSCAT is a non-imaging instrument, the Teijo forest area was divided into 18 strips with 150 metres spacing. The incidence angles were 3^o (C-band) and 23^o (C- and X-band) off nadir. To localize HUTSCAT data (which includes time), GPS-coordinates and the corresponding time were recorded at one second intervals. About 70000 radar profiles were obtained at both incidence angles covering 200 of the total of 500 compartments.

The three-dimensional image of the forest was simulated by using the 70 000 radar-derived stand profiles and the earlier knowledge [1] on mean and dominant tree heights which could be obtained with 1.2 metres accuracy from 5-metres antenna footprint. For the simulation purposes, the stand profiles were stored into the database according to the antenna footprint (spatial resolution), tree species and radar-derived tree height. In the simulation, profiles, which corresponded to simulated tree height and tree species, were randomly picked up from the database. Different spatial resolutions were obtained by averaging corresponding radar profiles. Range resolution degradation was performed by averaging corresponding range cells.

INTEGRATION AND OPTIMIZATION

The tree height was calculated from the averaged stand profile corresponding to the resolution pixel. The stem volume estimate was obtained as a function of height for each

resolution pixel. The sum of stem volume estimates was divided by the size of the compartment to get radar-derived compartmentalized estimates, which were regressed against simulated compartmentalized values. After determination of optimal spatial and range resolutions, the technical radar parameters were calculated.

ACKNOWLEDGEMENT

The authors are grateful to Finnish Forest and Park Service, especially Asko Saatsi, for providing the field inventory data.

REFERENCES

[1] J. Hyyppä, Development and feasibility of airborne ranging radar for forest assessment, Dr. Techn. thesis, Helsinki University of Technology, 112 p, 1993.

[2] R. Bernard, M. Frezal, and D. Vidal-Madjar, "Nadir looking airborne radar and possible applications to forestry", *Remote Sensing of Environment*, No. 21, pp. 297-309, 1987.

[3] D.E. Pitts, G.D. Badhwar, and E. Reyna, "The use of a helicopter mounted ranging scatterometer for estimation of extinction and scattering properties of forest canopies, part II: experimental results for high-density aspen", *IEEE Transaction on Geoscience and Remote Sensing*, Vol. 26, No. 2, pp. 144-151, 1988.

[4] M. Hallikainen, T. Tares, J. Hyyppä, E. Somersalo, P. Ahola, M. Toikka, and J. Pulliainen, "Helicopter-borne measurements of radar backscatter from forests", *International Journal of Remote Sensing*, Vol. 11, No. 7, pp. 1179-1191, 1990.

[5] J. Hyyppä, and M. Hallikainen, "A helicopter-borne 8-channel ranging scatterometer for remote sensing, Part II: Forest inventory", *IEEE Transaction on Geoscience and Remote Sensing*, Vol. 31, No. 1, pp. 170-179, 1993.

[6] J. Pulliainen, J. Hyyppä, and M. Hallikainen, Future trends in active microwave satellite remote sensing, XIV National Convention on Radio Science, Abstract of papers, Helsinki University of Technology, Laboratory of Electromagnetism, Report 32, 1988.

[7] C. Elachi, *Spaceborne radar remote sensing: applications and techniques*, IEEE Press, New York, 255 p.

[8] J. Laasasenaho, Taper curve and volume functions for pine, spruce and birch, *Communicationes Instituti Forestalis Fenniae* 108, Helsinki, 74 p.

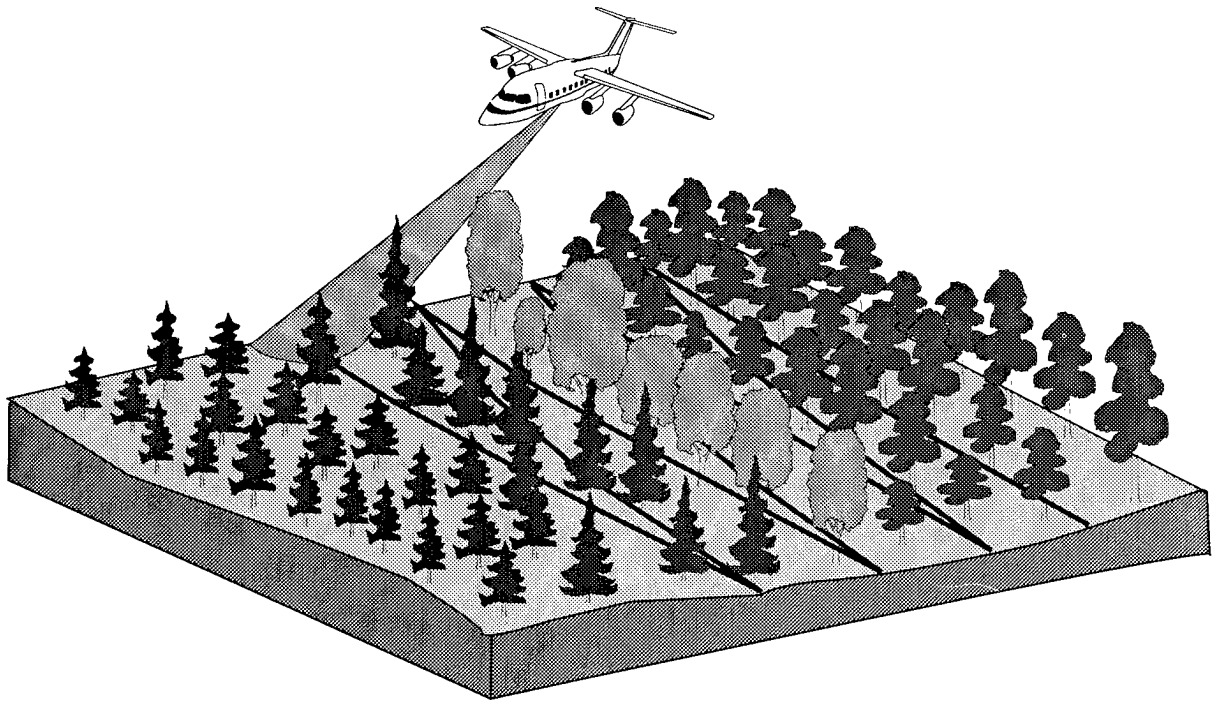


Figure 1. A scanning radar altimeter, which applies real aperture techniques.

Temporal Stability of Northern Forest Biophysical Retrievals Using SIR-C/X-SAR

M. Craig Dobson, Leland E. Pierce, Kathleen M. Bergen and Fawwaz T. Ulaby

Radiation Laboratory, EECS Dept., The University of Michigan
Ann Arbor, Michigan 48109-2122 USA
Tel.: (313) 747-1799, Fax.: (313) 747-2106, Email: dobson@eecs.umich.edu

ABSTRACT

A semi-empirical approach for retrieval of forest biophysical properties (basal area, height, woody stem biomass and crown biomass) has been previously demonstrated for forests in Northern Michigan using SIR-C/X-SAR data. This technique uses a multi-step process that incorporates (1) a land-cover classification to specify forest structural type, (2) estimates of SAR-derived basal area, height and canopy biomass from class-specific empirical algorithms using multifrequency and polarimetric SIR-C/X-SAR data (3) in conjunction with readily available ancillary information to convert volume to dry mass in the analysis of SIR-C/X-SAR data.

This paper examines the temporal stability of the retrieval process. At issue is the sensitivity of the algorithms to scene dynamics such as ground-cover conditions (i.e., snow-cover and soil moisture) and phenological control of plant water status. We examine four SIR-C/X-SAR scenes all acquired at approximately 30° angle of incidence over the Raco Supersite in Northern Michigan. These SAR scenes represent four distinct conditions with respect to dielectric attributes at the test site. Two scenes from SRL-1 in April 1994, represent early spring tree physiology with thawed tree stems and sap movement in some species and without deciduous leaf-cover; the scenes are differentiated by the thickness and wetness conditions of the snowpack (dry and wet). Two additional scenes, from SRL-2 in October 1994, represent early senescence of deciduous species, and are differentiated by near-surface soil moisture conditions (i.e., before and after heavy precipitation). The vegetation is not frozen during any of the SAR observations. The results show that the date-to-date differences in the algorithm coefficients are related to dielectric effects of the surface (soil and snow-cover). The net effects are shown to be strongest for areas of low biomass conditions, wherein SAR sensitivity of surface properties is strongest due to limited extinction by the overlying vegetation.

0-7803-3068-4/96$5.00©1996 IEEE

Regional Stability of an ERS/JERS-1 Classifer

Josef M. Kellndorfer, M. Craig Dobson, Fawwaz T. Ulaby

The University of Michigan, Radiation Lab
Ann Arbor, MI 48109-2122 USA
FAX: +1-313-747-2106 email: josefk@eecs.umich.edu

ABSTRACT

The potential of combined ERS/JERS-1 SAR images for land cover classification was demonstrated for the Raco test site (Michigan) in recent papers and articles. Our goal is to develop a classification algorithm which is stable in terms of applicability in different geographical regions. Unlike optical remote sensing techniques, radar remote sensing can provide calibrated data where the image signal is solely determined by the physical (structural) and electrical properties of the targets on the Earth's surface and near subsurface. Hence, a classifier based on radar signatures of object classes should be applicable on new calibrated images without the need to train the classifier again.

This article discusses the design and applicability of a classification algorithm, which is based on calibrated radar signatures measured from ERS-1 (C-band, vv polarized) and JERS-1 (L-band, hh polarized) SAR image data. The applicability is compared in two different test sites, Raco, Michigan and the Cedar Creek LTER site, Minnesota. It was found, that classes separate very well, when certain boundary conditions like comparable seasonality or soil moisture conditions are observed.

Keywords: JERS-1/ERS Classifier, Calibration, Radar Signatures, Regional Stability.

1. INTRODUCTION

The potential use of combined ERS-1 and JERS-1 SAR image data for land cover classification has been demonstrated by the University of Michigan group in recent papers and articles [1, 2]. The "key" was found to be the combination of two complementary frequencies (C- and L-Band) and polarizations (hh and vv). Since radar remote sensors can be absolutely calibrated to a very high degree of radiometric stability over time and space, the idea of developing a single classifier based on calibrated data is apparent. In theory, structurally and electrically similar objects, no matter where they appear on earth, should have similar radar signatures, provided their backscattering values (σ^0) were derived from calibrated images.

A total of seven out of 14 image pairs from test sites in various ecological regions in North and South America have been received so far. A prototype classifier was developed for the University of Michigan test site in Raco, Michigan, also known as a SIR-C/X-SAR supersite for ecological mapping. All other test sites in the project are located within a network of Long Term Ecological Research Sites (LTER). This paper describes the results found when analyzing the first two test sites in the project "Regional Scale Land Cover Classification Using Existing Orbital Imaging Radar".

2. SCENE SELECTION

It is well known that seasonal changes (e.g. defoliation), moisture changes, and changes in temperature (frozen/non-frozen) affect radar backscatter to a considerable extent, which makes radar remote sensing a useful tool for many applications. However, in the case of a unique classifier design with intended multi-site application, it is necessary to select ERS/JERS-1 images which have comparable environmental conditions on the dates of image acquisition. Preferably summer scenes with non-frozen, "leaf on" and dry conditions should be selected. If scene availability leads to the necessity to select scenes outside these boundary conditions, the migration of the backscatter values might still allow correct identification of the class [2]. However, chances for misclassification increase and adjustments to the classifier might be necessary.

The two compared test sites used in this study are Raco, Michigan, and Cedar Creek, Minnesota. Both sites are located in similar ecological regions. The regions contain numerous lakes, scattered grasslands, wetlands, agricultural areas and forests: northern hardwoods, aspen, upland conifers, and lowland conifers. The dates of acquisition for Raco were 17th of August 1992 (ERS-1) and 7th of August 1992 (JERS-1). The Cedar Creek scenes were acquired on 10th of September 1994 (ERS-1) and 9th of September 1994 JERS-1). All four scenes were acquired under dry summer/late summer conditions, since there was no rainfall on and during five days before the datatakes.

Although it should make no difference, it was decided to order all scenes from the same processing facilities in order to avoid problems with different processor gains, as encountered in some cases in the past. In the project, all ERS-1 scenes were/will be processed by the German Processing and Archiving Facility (D-PAF). All JERS-1 scenes were/will be processed

0-7803-3068-4/96$5.00©1996 IEEE

by NASDA. The products ordered are *Precision Image* (ERS-1) and *Level 2.1* (JERS-1). Both product types are 3-look Ground Range images with 12.5m × 12.5m pixel spacing in range and azimuth.

3. PREPROCESSING STEPS

Three basic requirements in order to apply a single JERS-1/ERS based classifier on multiple scene pairs need to be fullfilled:

1. Accurate Geocoding of the Image Pairs
2. Absolute Calibration of each Image
3. Constant Radiometric Upgrading and Conversion

Geocoding

To enable classification of the combined ERS/JERS-1 data accurate geocoding of each scene is a prerequesite. In cooperation with the Vexcel Corp. a geocoding software for ERS-1 and JERS-1 SAR images has been developed. With this software package distortions in range and azimuth due to terrain can be corrected with the use of Digital Elevation Models. In addition layover and shadow masks as well as a map of the local angle of incidence can be generated. Several ERS/JERS-1 composites have been generated so far, and the average error of mislocation is smaller than 50m. For further reference see [3, 4].

Calibration

A very critical preprocessing step is the radiometric calibration of each ERS-1 and JERS-1 scene. Both sensors are reported to have a radiometric stability on the order of about half a dB [7, 9], whereas several corrections need to be made:
ERS-1: a calibration constant of -58.24 dB is given for all received scenes. Variations are found in the image replica power to range from -0.2 to -0.9 dB. Usually the image replica power is given in the header of the ERS-1 PRI data. However, some values needed to be screened from an database at D-PAF [10]. By taking into account the calibration constant, the correction term for the image replica power and the correction term for the local angle of incidence, the ERS-1 PRI digital numbers (=Amplitudes) can be converted to σ^0 after the formula given in [4, 7].
JERS-1: Unlike the PRI data, NASDA's Level 2.1 data are delivered with the local incidence angle already corrected. However, this is only done for an earth ellipsoid model [11]. To apply the correction for the local angle of incidence derived from the DEM during the geocoding procedure, the ellipsoid correction needs to be "uncorrected" and the DEM-derived correction term can be applied [4]. For the conversion of the values in the Level 2.1 product a set of three different conversion factors is given by NASDA. Depending on the acquisition and processing date the correct factor can be choosen. In the case of the Raco and Cedar Creek scenes the factors were -66.42 dB and -68.5 dB.

Radiometric Upgrading and Conversion

After the system inherent calibration was performed, the last preprocessing step is the radiometric upgrading of the SAR

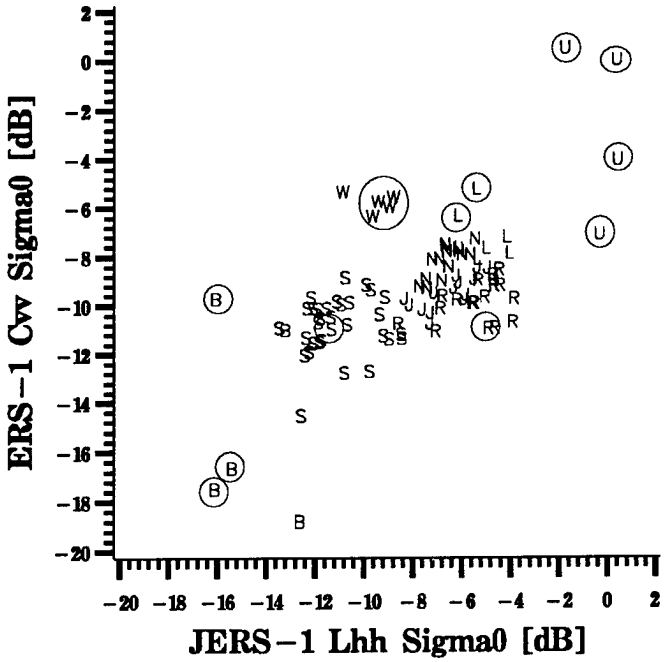


Figure 1: Scatterplot of ERS-1/JERS-1 backscatter values. Values in circles are measured in the Cedar Creek image composite, all others are measured in the Raco image composite. Legend: B = Bare/Flat surfaces, S = Short Vegetation, W = Wetland, N = Northern Hardwoods, J/R = Jack/Red Pine, L = Lowland Conifers/Forested Wetland, U = Urban/Built Up.

imagery. In order to increase the effective number of looks to reduce the fading noise, the SAR scenes need to be filtered. It was found that at least a 5x5 average filter on 25m resolution data was necessary to reduce the noise and increase the classification accuracy from 70% (3x3 Filter) to 90% in the Raco scene [2]. However, an averaging filter is a low pass filter and has the disadvantage of loss of detail (e.g edges). A very promising new filter was designed by [5] and will be used in the ongoing project.

After the filter process, data are converted from 16 bit to 8 bit resolution by mapping -25 dB to +0.5 dB from 0 to 255. This allows very simple conversion of the digital number back into the dB-domain and makes the interactive interpretative work on the image processing system easier.

4. CLASSIFIER DESIGN AND COMPARISON OF RADAR SIGNATURES

To evaluate the applicability of a single JERS-1/ERS-1 classifier, a two step process was performed. The radar signatures measured from 80 forest test stands in the Raco test site plus several other training areas from different classes were compared with training plots in the Cedar Creek site. Signatures measured in the Cedar Creek image composite were identified

by visual interpretation of the image during a site visit. Figure 1 shows the signatures found in both the Raco and Cedar Creek scene pairs. The combined signatures were used as decision rules in a Maximum Likelihood Classifier, where clustering of the groups is carried out a posteriori by using the a priori knowledge of which cluster belongs to which class.

Interpretation of Figure 1: Urban/Built Up: Urban areas were only measured in the Cedar Creek scene, since no larger built up areas could be found in the Raco scene pair. High backscatter in both JERS-1 and ERS-1 (around 0 dB) is found. Low ERS-1 backscatter identify either no identification of urban area or misregistration errors lead to confused signatures. However, if one instrument identifies urban, it is sufficient for separation from other classes. Bare/Flat Surfaces: Similar behavior as for urban on the "low" side of the scatterplot. Generally JERS-1 is identifying flat/bare surfaces better, since it is less sensitive to roughness due to the longer wavelength. This is especially useful for the identification of water bodies, where ERS-1's C-Band is very sensitive to water roughness. Short Vegetation: Separates well from tall vegetation in L-Band and is very confused with tall vegetation in C-Band. The short vegetation signatures in the plot are mainly derived from hayfields and very young forest plantations after clearcutting. No agricultural fields with standing crop were measured. Other groups report for corn fields ERS-1 backscatter values from -8 dB (dry soil) to -6 dB (wet soil) [6]. Wetland: Backscatter in ERS-1 around -7 to -6 dB . Shows confusion here only with some lowland conifers. However, in conjunction with JERS-1 (backscatter around -9 dB) this class separates well. Tall Vegetation: Range for tall vegetation is related to biomass (relates to "structural roughness"). Neither instrument alone could separate between the three classes, but the combination of the sensors allows separability between the excurrent and decurrent forms. However, the dynamic range is small and inaccuracies in calibration of the data will have the strongest effects on separation of different structural forest classes. Overall: Identical classes in both test sites are found to be in the same neighborhood in the scatter plot.

The addition of radar signatures measured in Cedar Creek and added to the classifier solely based on the Raco rules improved the Raco scene classification, e.g. in better idenification of wetlands. In the ongoing project it is expected to fill in gaps in the scatterplot and therefore refine the clusters for the classifier.

5. CONCLUSIONS

It was pointed out, that careful scene selection and accurate preprocessing of JERS-1 and ERS-1 data can provide radiometrically comparable SAR image composites. It was demonstrated, that for two regions a single land cover classifier design, based on structural classes is possible and applicable. Twelve more test sites from different ecological regions will be investigated.

6. REFERENCES

[1] Dobson, M.C., L.E. Pierce, F.T. Ulaby, "Konwledge-Based Land-Cover Classification Using ERS-1/JERS-1 SAR composites" *IEEE Trans. Geosci. and Remote Sensing*, Vol. 34, No. 1, Jan. 1996, 83–99.

[2] Kellndorfer, J.M., L.E. Pierce, M.C. Dobson, F.T. Ulaby, "Temporal Stability of an ERS-1/JERS-1 SAR Classifier," *1995 International Geoscience and Remote Sensing Symposium (IGARSS'95)*, pp 910–912, July 1995, Florence, Italy.

[3] Pierce, L.E., J.M. Kellndorfer, F.T. Ulaby, "Practical SAR Orthorectification" *1996 International Geoscience and Remote Sensing Symposium (IGARSS'96)*, May 1996, Lincoln, Nebraska, USA.

[4] Kellndorfer, J.M., M.C. Dobson, F.T. Ulaby, "Geocoding for Classification of ERS/JERS-1 SAR Composites," *1996 International Geoscience and Remote Sensing Symposium (IGARSS'96)*, May 1996, Lincoln, Nebraska, USA.

[5] Hagg, W., M. Sties, "Efficient Speckle Filtering of SAR Images" *1994 International Geoscience and Remote Sensing Symposium (IGARSS'94)*, pp 2140–2142, August 1994, Pasadena, California, USA.

[6] Mauser, W., M.Rombach, H. Bach, R. Stolz, A. Demircan, J. Kellndorfer, "The Use of ERS-1 Data for Spatial Surface-Moisture Determination" *Proceedings of the First ERS-1 Pilot Project Workshop*, pp 61-73, June 1994, Toledo, Spain. (ESA SP-365, October 1994).

[7] Laur, H., P. Meadows, J.I. Sanchez, E. Dwyer, "ERS-1 SAR Radiometric Calibration" *Proceedings of the CEOS SAR Calibration Workshop*, pp 257-281,Nordwijk. (ESA WPP-048).

[8] Shimada, M., "User's Guide to NASDA's SAR Products" Earth Observation Center, NASDA, March 1993. (NASDA HE93014)

[9] Chapman, B., M. Alves, A. Freeman, "Validation and Calibration of J-ERS-1 SAR Imagery" Jet Propulsion Laboratory, California Institute of Technology, Online on the World Wide Web: http://southport.jpl.nasa.gov/users/bc.jers/cal.html

[10] Schaettler, B., Personal communication, D-PAF, Oberpfaffenhofen, Germany

[11] Shimada, M., Personal communication, NASDA, EOC, Tokyo, Japan.

Radar Modeling of Forest Spatial Structure

Guoqing Sun[1], K. Jon Ranson[2]

[1]Science Systems and Applications, Inc. 5900 Princess Garden Parkway, Suite 300, Lanham, MD, 20706, USA.
Phone: (301)286-2485, Fax: (301)286-1757, E-mail: guoqing@aspen.gsfc.nasa.gov

[2]Biospheric Sciences Branch, Code 923, Goddard Space Flight Center, Greenbelt, MD 20771, USA.
Phone: (301)286-4041, Fax: (301)286-1757, E-mail: jon@taiga.gsfc.nasa.gov

Abstract -- The understanding of ecosystem processes and the impacts of natural and anthropogenic induced change upon them requires developing techniques to monitor possible changes in the structure, composition, and function of ecosystems. In this research we used a 3-D radar backscatter model and spatial data analysis to study the relationships between forest patterns caused by logging and spatial properties of radar images. The simulated results compared favorably with AIRSAR data from an area of managed forests.

INTRODUCTION

Forest management practices, such as thinning, strip or clear cutting, changes the canopy structure at different scales. Radar backscattering is sensitive to vegetation water content, its arrangement within the 3-D canopy structure as leaves, branches, trunks, and the underlying surface characteristics. Gaps between trees influence the relative intensity of backscattering components from a forest stand and the texture of radar images. The ability to characterize forest spatial properties in terms of horizontal and vertical structure would be useful for initializing forest ecosystem models and understanding the processes contributing to forest development. Many methods have been used for the analysis of spatial pattern, such as the two-term local quadrat variance (TTLQV) [1,2], fractal geometry [3], lacunarity [4-5], and variogram [6]. In this research we use a 3-D radar backscatter model [7] and variogram analysis to study the relationships between forest patterns caused by logging and spatial properties of radar images. Model results are compared to AIRSAR data of a managed forest in Maine, USA.

AIRSAR DATA

The two AIRSAR images used in this study were acquired on October 7, 1994 with less than one hour apart. Fig. 1 shows two L-band total power images. The illumination directions of the two images are different: the left image (cm4457) is from the left while the right image (cm4458) is from the top. Backscattering coefficients (L-band HH) from four target areas of uncut forest and three strip cuts with different orientations extracted from AIRSAR images are listed in Table 1.

For the images used in this study, the strip cuts slightly reduced backscattering as shown in Table 1. The most reduction is in the case when radar illumination was parallel to strip cuts so more bare forest floor could be seen. Simulated images show a similar trend as discussed below.

Table 1. LHH backscattering coefficients (dB) of four forest targets: No Cut (undisturbed forests) and strip cuts of different orientations relative to radar beam.

Strip cut direction	CM4457	CM4458	MODEL
No Cut	-5.97	-6.10	-6.00
Diagonal	-5.15	-6.50	-7.97
Parallel	-7.00	-6.84	-8.28
Perpendicular	-6.12	-6.60	-7.43

BACKSCATTER MODELING

In a 3-ha 70-year old stand of northern forest within International Paper's Northern Experiment Forest, located near Howland, Maine, USA, the Cartesian stem location, diameter at breast height (dbh), tree species and relative canopy position were measured for each stem (> 3 cm dbh). A total of 7807 trees were recorded in this stand. This 200m x 150m stem map data was used to construct a 3-D model of the stand. Strip cut patterns similar to those observed elsewhere in the forest area were imposed on the 3-D model of the stand. The patterns were developed by alternating 9.15m wide swaths of trees with 15.25m wide bare areas (all trees removed) which is a typical strip cut pattern in our study area. The process was repeated for strip cuts oriented at different azimuth angles with respect to the radar range direction. The L-band radar backscattering images of pixel spacing from 1 m and 8 m were simulated. Modeled backscatter coefficients for the four patterns are compared to AIRSAR data in Table 1. Fig. 2 shows the simulated images.

SPATIAL ANALYSIS

Variogram has been called a structure function in probability, and has been used in studying spatial structure of a random

0-7803-3068-4/96$5.00©1996 IEEE

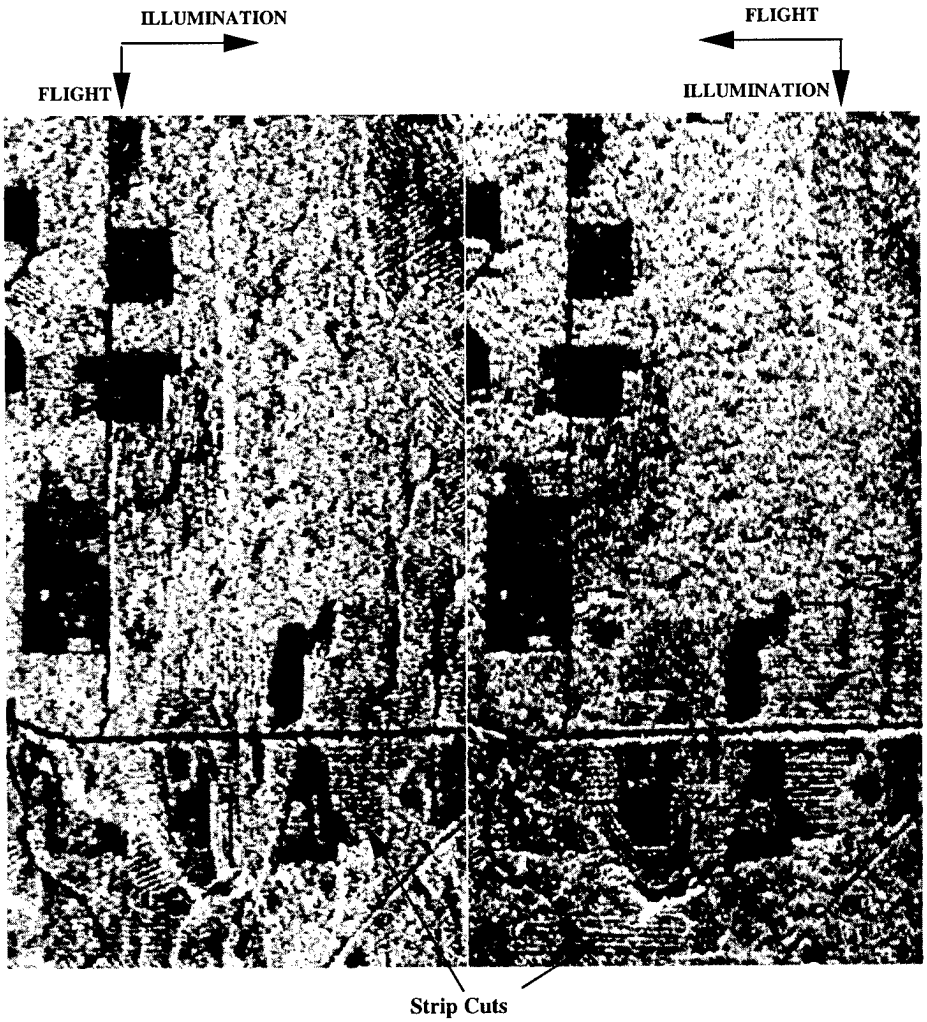


Fig. 1. AIRSAR images of a managed forest near Howland, Maine, acquired Oct. 7, 1994.

process at several scales simultaneously [7]. When the variogram can be fitted into a power model ($2\gamma(h)=c+b*h^{\lambda}$), the $0<\lambda<2$ is a fractal Brownian motion with parameter $H=\lambda/2$. Fig. 3 shows variograms along the range direction of simulated and AIRSAR images (cm4457). Simulated images with 1-meter pixel size show that the four forest types have distinct variograms: while the strip cuts along azimuth direction shows a wave pattern, the rest show a power pattern with different λ's. At 8-meter pixel size, for both simulated and AIRSAR images, the strip cuts at diagonal and azimuth directions show obvious wave patterns. For simulated images the lags of pixels between peaks are 3 pixels for perpendicular cuts and 4 pixels for diagonal cuts, corresponding to the strip cut widths of 24 and 32 meters in the radar looking directions. AIRSAR data shows 6 pixels between peaks for diagonal cuts. Undisturbed forests and strip cuts along the range direction show a rational quadratic semivariogram.

SUMMARY

Both simulated and AIRSAR images show spatial patterns related to different strip cuts. AIRSAR images were found to have similar spatial features as simulated images at similar pixel spacing.

Questions of scale in spatial statistics combine both the issues of level of aggregation of the observations and the extent of the observations. If the data behave in a self-similar way across a number of scales, such as fractals, parameters estimated at one scale are relevant to inference for the process at a smaller, unobserved scale. Simulated images at various pixel spacing can be used to investigate this capability and aid image interpretation.

REFERENCES

[1] J. F. Weishampel, G. Sun, K. Jon Ranson, K. D. LeJeune,

and H. H. Shugart, "Forest textural properties from simulated microwave backscatter: the influence of spatial resolution," Remote Sensing of Environment, Vol. 47, 1994, pp.120-131.
[2] M. O. Hill, "The intensity of spatial pattern in plant communities," J. Ecol., Vol. 61, 1973, pp.225-235.
[3] M. W. Palmer, "Fractal geometry: a tool for describing spatial patterns of plant communities," Vegetatio, Vol. 75, 1988, pp. 91-102.
[4] R. E. Plotnik, R. H. Gardner and R. V. O'Neill, "Lacunarity indices as measures of landscape texture," Lanscape Ecology, Vol. 8, No. 3, 1993, pp. 201-211.
[5] G. M. Henebry and H. J. H. Kux, "Lacunarity as a texture measure for SAR imagery," Int. J. Remote Sensing, Vol. 16, No. 3, 1995, pp. 565-571.
[6] Guoqing Sun and K. Jon Ranson, "A three-dimensional radar backscatter model of forest canopies," IEEE Transactions on Geoscience and Remote Sensing, Vol. 33, No. 2, 1995, pp. 372-382.
[7] Noel A. C. Cressie, Statistics For Spatial Data, John Willey & Sons, Inc., Revised Edition, 1993.

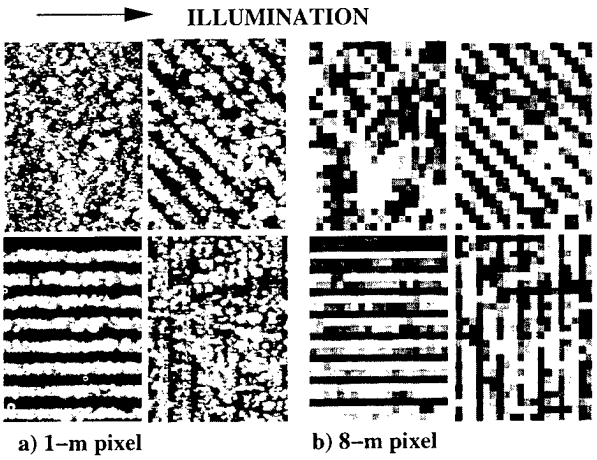


Fig. 2. Simulated SAR images: up–left – undisturbed; up–right – diagonal cuts, low–left – parallel cuts, low–right – perpendicular cuts.

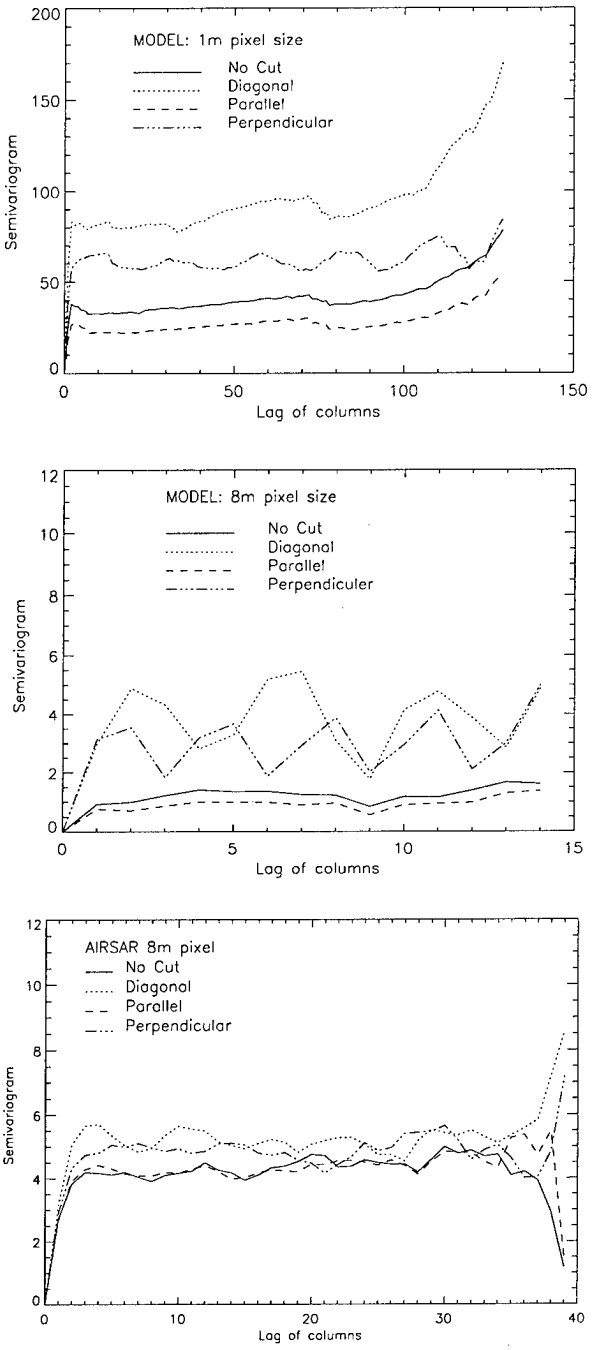


Fig. 3. Variograms of simulated and AIRSAR images for uncut forest and strip cuts of different orientations relative to the radar beam.

Knowledge Based System for Weather Information Processing and Forecasting

Khalid J. Siddiqui, Steve M. Nugen*
Dept. of Computer Science, SUNY at Fredonia, Fredonia, NY 14063
*Hughes Information Technology Corporation, 1620 Wilshire Drive, Bellevue, NE 68005

Abstract: Using physical observations from the satellite imagery and the meteorological information a Knowledge Based Weather Information processing and forecasting System (KB/WIS) is designed. The characteristic features extracted from the weather images are used to represent various weather patterns. The system is statistically trained to characterize, interpret, and forecast weather patterns. The system proposed is a composite of five components, namely: Image Acquisition, Image Preprocessing and Enhancement, Feature Extraction and Selection, Weather Knowledge Base, and Weather INference Engine (WINE). Complete architecture of the KB/WIS system including its application and algorithms is described.

INTRODUCTION

Acted on by the combined effects of earth's motions and the energy exchanges that continually occur between the atmosphere and the earth's surface and between the atmosphere and space, our planet's formless and invisible envelope of air reacts by producing an infinite variety of weather patterns. The methods available for weather information processing and forecasting can be roughly grouped into five approaches: analog, synoptic, numerical, statistical, and time-based dynamic forecasting methods. These methods can be used for various short-range to long-range weather forecasting [1].

Analog approaches match current conditions with records of similar past weather events with the idea that the succession of events in the past will be paralleled by current conditions. Synoptic methods are based on careful studies of the historic (synoptic) weather charts over a period of years, from which a set of empirical rules are established to forecast. Numerical methods use mathematical models to predict the evolution of physical processes in the atmosphere by the determinations of the conservation of mass, energy and momentum. The recent such techniques employ multi-level baroclinic models and include variables pertaining to pressure, wind directions and temperature as primary weather characteristics whereas the fronts are regarded as secondary features. Thanks to fast computers and large vector processors, vast amounts of computations which these models require has become possible to allow the preparation of a forecast map sufficiently ahead of the weather changes. Statistical techniques are now used to predict actual weather conditions. One such technique is Model Output Statistics (MOS) developed by the US National Weather Service. To predict for specific locations between the variables of interest a series of regression models are also developed [1]. Weather elements so predicted include daily maximum/minimum temperature, 12-hour probability of precipitation of occurrences and precipitation amount, probability of frozen precipitation, thunderstorm occurrence, cloud cover, surface winds, etc. Dynamic methods are being attempted at various weather centers using longer integrations of medium-range models [1]. It should be, however, noted that the object of weather forecasting is not only to project the location and possible intensification of existing pressure system, but also to identify probable sites for the formation of the storm or severe weather centers.

The weather information processing procedures discussed above require human operator for interpretation and characterization which is cumbersome, labor-intensive and inefficient process. These methods often lead to inaccurate results. Though computer assisted forecasting using advanced mathematical models for the analysis of data has made greater strides, real-world weather situations often defy such modeling. Other advanced methods, such as pattern recognition and image/signal processing combined with the skill and experience of human offer solutions to a large range of problems with much less investment of highly skilled personal and expensive computing resources [2]. Additionally, the solutions provided by such systems will be more reliable and robust as compared to their human counterpart or semi automated systems which must be operated by the trained personnel. Using a PC-based environment we developed knowledge based pattern recognition methods to model the weather patterns. Using these patterns the system learns to interpret and forecast the weather. The weather features from their maps (images) are automatically extracted to uniquely define different weather patterns.

OVERALL SYSTEM DESIGN

The KB/WIS system is a composite of five components (see Fig. 1, Fig. 2). 1) **Data acquisition** subsystem (DAS) performs three functions: data acquisition, data mapping and calibration, and image formation. It provides tools for image and multispectral data acquisition in various satellite formats including TIROS, DMSP, GOES, GMS, and METEOSAT. It also includes the modules for low level smoothing and quality enhancement. A GUI-based user-interface helps user to acquire, display, and edit images/spectra and clean them as desired. 2) **Image Preprocessing and Enhancement** subsystem (IP/ES) performs data ingest, conditioning, editing, and correction (noise elimination and enhancement to improve image to noise ratio; smoothing; rectification of atmospheric effects and radiometric/

0-7803-3068-4/96$5.00©1996 IEEE

geometric distortion; correction for skew, scan time, orientation, and registration; normalization, etc.). Several routines to overlay, zoom, scale, rotate and loop (with direction controls) images providing functions for color/hue controls, resolution/ brightness controls, etc., are available. High-level image processing and manipulation modules for both the point (pixel) operations and vector operations are developed to aid feature extraction. These modules are used to automatically process the image to correctly detect and delineate the desirable regions (clouds, image foreground/background, objects, geophysical boundaries, etc.) and other components of interest in digital images of weather maps: temperature, pressure, and moisture. Functions for image/ region thresholding of grayscale; region growing/elimination; grayscale histogram construction; and regional enhancements using histogram equalization, edge detection, and filtering are also provided. These method adopted from [3]. 3) **Feature Extraction and Selection:** This module constitutes a set of algorithms to extract the features from various image regions. The number of features extracted may be too many to warrant efficient classification. Feature optimization modules to analyze and synthesize the extracted information are also developed [4]. This analysis determines the information contents each feature carries. The objective is to determine the most optimal parameters that could possibly be used for automatic classification of weather patterns. Using the optimal features each weather pattern is represented through a vector of selected features. Using clustering algorithms and discriminant analysis [5] visual tools are developed to allow the user to perform subjective analysis of features. 4) **Weather Knowledge Base (WKB):** Using the selected features a set of samples describing three pattern classes representing three major factors, i.e., wind, cloud, and water which contribute most to weather formation are constructed. These weather patterns are used as reference patterns and are stored in the knowledge base WKB. Additional meteorological knowledge in the form of rules that a meteorologist may apply in identifying the weather patterns is also stored in WKB. For efficient retrieval and processing the knowledge base is organized as a tree of associated weather patterns (TAP). Structural proximity among weather patterns is used to determine the association between weather classes. This organization helps in classifying a large set of weather classes using their own features without sacrificing the performance. In addition, the user will be able to analyze all weather patterns affecting a region as a hierarchy of candidate weather classes. 5) **Weather INference Engine (WINE):** Using the concept learning algorithm [5] WINE is trained to interpret the reference weather patterns which were organized as TAP. A set of pattern recognition algorithms [5] which use the optimal features, classify and discriminate weather patterns, determine their identity, and hence interpret the oncoming weather. WINE automatically suggests a very small but definitive set of possible solutions along with level of confidence attached to each alternative.

METHODOLOGY AND PROCEDURES

To demonstrate the potential of the KB/WIS presently a minimal subset of the system design was adopted. The methodology specifically used is described in this section. The DAS system reads the satellite data. Since the data from various satellites is received from 5/6 channels, it was mapped and calibrated. To create the multispectral weather images, the channels were scaled to one another. For example, to create a visible image from the TIROS two visible channels were calibrated so that for a particular pixel value (0-255 grayvalues), albedo values are the same. The DMSP data was inverted to occupy the same dynamic range as the visible data. The GOES infrared data was replicated to the equivalent visible resolution being input. The image formation is performed using histogram scaling which creates a colored visual image (RBG). To construct an image in the visual bands, for each pixel value two intensities (gun values) were evaluated. The gun values were computed based on the respective input image biases with respect to relative pixel values of both input images. The IP/ES performs histogram equalization to smooth and enhance the quality of the image displays.

Feature extraction is performed first by segmenting the image. The rules for segmentation are described in terms of HSI (hue, saturation, intensity) color space [3] by transforming from the RGB (Red, Green, Blue) color space. The intensity is described as, $I = R + G + B$, hue is described as,

$$H = \begin{cases} \theta & b \le g \\ 360 - \theta & b > g \end{cases}$$

and the saturation is described as,

$S = [\ 1\text{-}3\ \mathrm{Min}\ (r, g, b) / (r+g+b)]$

where, Min () is a function which selects the minimum of r,g, and b; and r, g, and b are defined as

$r = \frac{R}{I}, g = \frac{G}{I}, b = \frac{B}{I}$ and θ is given by,

$$\theta = \cos^{-1}\left[\frac{2r - g - b}{\sqrt{6\{(r-1/3)^2 + (g-1/3)^2 + (b-1/3)^2\}}}\right].$$

For different satellites different bands were considered as R, G, and B. The RGB data for corresponding bands of respective satellites was transformed into HSI space. The advantages of dealing with data in HSI space is that it compensates for the dynamic range fluctuations of the scanned data and that it is useful for describing rules to extract objects from image data. Once the image is transformed, the components carrying weather information are extracted.

For example, compared to the resolution of images from the individual satellites, the areas covering large water regions will be large. Selecting the band that transmits the most of the water related information, simple thresholding at some intensity of the selected band can detect the water regions. However, because of the HSI space, the dynamic range fluctuations of scanned data did not affect the water regions identification.

Weather Modeling: Since weather varies with time and location, weather forecasting and effects analysis must be constantly reappraised to retain its usefulness. To describe a weather model several parameters with associated level of confidence in 5 component areas were selected. These include, 1) meteorological event to be forecasted, 2) climate, 3) current ground truth, 4) the size of the forecast region, 5) the lead time and forecast period.

Major meteorological parameters are based on atmospheric and oceanographic observations (see Table I). In addition geographic, solar, geophysical and terrestrial parameters such as latitude/longitude, topographic/terrain data, etc., also play important role. The model, however, should be adjusted to the regional characteristics.

Considering above parameters as weather characterizing features each experimental weather class, i.e., water, land, and cloud was represented as a vector of selected features. To determine the potential of the system the inference engine, WINE was trained on minimum distance classifier using Mahalanobis distance. WINE correctly recognized all three pattern classes.

DISCUSSION AND CONCLUSION

A weather image analysis, and interpretation system is designed. Preliminary result in correctly recognizing the major classes of water, land and cloud show the potential of the system. Upon completion, the system will implement full scale computer-enhanced decision making using methods from image/spectral processing, pattern recognition, statistical decision theory, and knowledge engineering. The system increases the reliability, accuracy and consistency of identification and interpretation of weather images. Many benefits of this system can be mentioned including: 1) Accurate image acquisition, ingest, storage, and dissemination of data using a smaller set of the most representative features. 2) Provide rapid and robust data processing. 3) Presents a comprehensive, yet user-friendly, hybrid decision-making facility combining meteorologist's expertise and exhaustive computer synthesis of physical observations. The design of the system is highly modular and application independent and enhancements to the KB/WIS system will be possible. In addition the system will be able to adapt to other weather processing applications e.g., identification of geographical locations; vegetation/crop analysis and estimation; object spotting; monitoring of environmental events processing and interpretation; dynamic object tracking and classification, etc., may be investigated in future.

REFERENCES

[1] F.K. Lutgens, and E.J. Tarbuck, The Atmosphere, 6th Edn., Prentice Hall, Englewood Cliffs, NJ, 1995.

[2] K.J. Siddiqui, "Feature Selection in the Classification of Time-Variant Patterns, Ph.D. Thesis, Dept. of Computer Science, Concordia Univ., Montreal, Canada 1994.

[3] K.R. Castleman, Digital Image Processing,, Prentice-Hall, Englewood Cliffs, NJ, 1996.

[4] K.J. Siddiqui, Y.-H. Liu , D.R. Hay, and C.Y. Suen,"Optimal waveform feature selection using a pseudo-similarity method. Journal of Acoustic Emission, Vol. 9, No. 1, pp. 9-16, 1991.

[5] K. Fukunaga, "Statistical Pattern Recognition," Academic Press, New York, 1990.

Table I

Atmospheric	Oceanographic
Moisture: precipitation (type, rate), regional thresholds, estimates, humidity, dew point, variations	sea surface: topology, waves, vertical profile, salinity, near/ off shore currents, tides, color, bio-luminescence
Clouds: type, overage, ceiling, visibility	sea ice :cover, thickness, iceberg
Pressure: profile, variations	bathymetry
Temperature: vertical profile, heat flux , location values	Temperature: vertical profile
Winds: gust, sand/dust, aerosols, insulation	turbidity
Albedo	
Severe Weather parameters	
Climatic values for above	

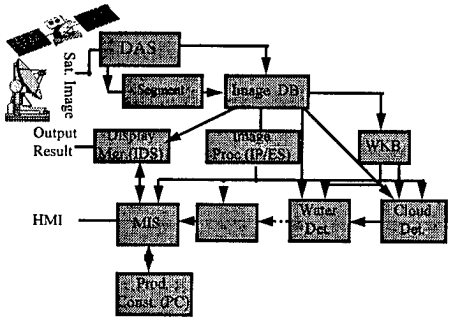


Fig. 1: Conceptual Structure of KB/WIS

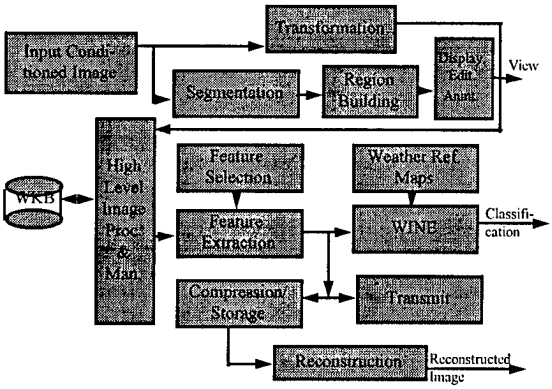


Fig. 2: Functional Design of KB/WIS

A Database Program to Archive and Analyze Current Weather Data

Steven H. Parkin and John P. Refling
Parkin-Refling & Associates
67-642 Club House Road
Desert Hot Springs, CA 92241
Telephone/Fax (619) 329-2774
E-mail: sparkin@imag-alchemy.com

INTRODUCTION

Statistically accurate weather projections have strategic implications for a broad cross section of worldwide consumers, including military and commercial institutions. Current weather-prediction algorithms depend on accurately collecting, testing, and storing a wide variety of weather data from more than 5,000 stations located throughout the world. Several commercial programs have been developed to collect and sample the variety of input data streams (airways, synoptic, metar, and plain-language bulletins) and then parse (place) the data into a series of fields, usually in a text file format, which limits the ability to reorganize and further manipulate the data. While these programs typically read the input stream and parse the data according to a predetermined format, they lack the robustness of a relational database. Also, because many of the data streams are sent via satellite to a distant location for processing, sunspot and other noise sources influence data transmission and present a potential threat to the consistency of the data. Therefore, we developed a C/C++ data-stream identification and parsing program that is coupled with and integrated into a relational database program for further sorting, testing, analysis, and reorganization of the data.

Algorithms such as the Krick predication algorithms, based on local daily temperature and precipitation parameters and on weekly mean temperature and precipitation, have been used since D-Day in World War II. In general, the prediction algorithms we examined depend on the accurate identification of various temperature and precipitation parameters for specific stations. Thus, to be useful, the database program needed to correctly test and analyze the parsed data on a station-by-station basis. We developed a C/C++ data-stream identification and switching program that correctly selects the proper data stream (e.g., airways) and parses the data into the series of fields required for the corresponding prediction criteria. The C/C++ front-end program is integrated into a Microsoft Access database program to store, sort, test, analyze, and further process the data and then provide the optimum results for a particular station. Increasingly precise quality-control checks and protocols were designed and programmed into the Access portion to identify and eliminate questionable data. The flow chart (Fig. 1) shows the general flow of information within the combined program. When fully implemented, the total program provides an essentially unattended data-processing function, which could be used to eliminate the numerous transcription and other errors that typically occur when various prediction algorithms are implemented manually.

METHODS AND MATERIALS

The C/C++ portion of the program was initially developed using Microsoft (MS) C v7.0 and Visual C++ v1.0. Further refinements were programmed in Visual C++ v1.5, v1.52, and v4.0. The database portions were programmed using MS Access v2.0 and MS Visual Basic v3.0. The initial work was coded on IBM-compatible 80486 clones, which, over the development cycle, included DX-50, DX2-66, DX4-100 and DX4-120 CPUs. The programs have also been run on a series of Pentium CPUs, varying in speed from 75 MHz to 133 MHz. We are currently modifying the programs to Windows 95 using MS Access for Windows 95, which includes changing the compilation of the C/C++ program from 16 bits to 32 bits. The programs have been tested on a variety of networks, including Novell NetWare v3.11, MS Windows for Workgroups v3.11, Windows 95, and Windows NT.

DISCUSSION

Because the actual date and time information embedded in the data stream is removed for airways, synoptic, and metar data when sent via various satellite processing programs, an unambiguous date and time stamp must be re-encoded onto the data stream. Since the data we used in the predication algorithms were in "remote local time," the potential pitfalls of converting GMT (Zulu) time to remote local time needed careful consideration. Ultimately, we used 32-bit CRC tables to track date- and time-stamp integrity.

Both human error in the preparation of the data stream for transmission and subtle changes in the programming of the data stream format cause deviations from the expected or nominal data format. Dealing with these contingencies requires both identifying the deviation and developing a more robust program to deal with the enormous number of potential errors. As an example, we cite the "SFO anomaly," where, following an insubstantial airways code change, SFO began reporting the minimum temperature as ...NN/ instead

0-7803-3068-4/96$5.00©1996 IEEE

of ...NN. Since the program was not designed to decode minimum temperature strings ending in a "/," none of the reported minimum temperatures for SFO were captured until this deviation in format was corrected.

Random sunspot or other noise in the incoming satellite data stream was the source of lost data until the C/C++ program could be made sufficiently robust to bypass the "garbage" and pass only data that matched the correct format. The import data format restrictions inherent in the selected database program drive this consideration.

Because of the extended data buffers found in the programs used to process and store the incoming satellite data, the possibility of substantial duplication was addressed. We designed the database portion of the program with a series of queries to eliminate these duplicate data. The CRC updates that occur when the initial date and time stamping is performed in the C/C++ front-end also help to alleviate duplication.

The testing and analyzing, or quality control, portions of the database program include evaluating a variety of temperature fluctuations by identifying the temperature variations at a given station during successive hours. This presented a major programming obstacle, since at this point in the program the data resided in a series of database tables, not in ASCII text files, and thus were not amenable to conventional programming techniques. This problem was finally resolved by an extensive series of queries and unique variations in the use of data access objects (DAO). This particular difficulty is inherent in the approach we chose to process the data (i.e., a relational database for the testing and analyzing portions of the program) and might be better addressed in the C/C++ front-end in later modifications.

Plain-language bulletins pose a series of difficulties in programming because the potential for variation from the prescribed format is always present. We had to refine the programs that parse the plain-language bulletins many times as we became painfully aware of subtle and random variations in the format of a particular bulletin. These changes negated the use of traditional programming constructs, since many of the record elements vary in length by as few as one and as many as 60 characters in one report to the next. We ultimately dealt with this problem using a "brute force" approach, in that we finally wound up using a large (and ever increasing) number of "select case" structures. Also, because some plain-language bulletins reverse the position of required parameters in the AM and PM reports, a number of select-case structures were again required to parse the data successfully. We found it essential that the programs used to parse and process plain-language bulletins be extremely robust.

While obvious to the experienced meteorologist, unit consistency was a problem when we ultimately attempted to obtain the best data for a specific station. Since the airways and plain-language bulletins are typically in inch/degree Fahrenheit units and metar and synoptic data in meter/degree Celsius units, the potential for incorrectly converted units was always present.

Since the potential users of our program are typically meteorologists or support personnel, who may not yet be computer literate, the user interface needed to be simple and intuitive. As a significant element of our database program, we designed what we think is an extremely intuitive user interface. The operator is guided through the steps via the metaphor of pushing a series of buttons that perform one or a series of functions (running programs, opening queries, etc.) without further involvement. A series of timers, available in MS Access Basic or Visual Basic, were programmed to perform the various program steps repetitively on an unattended basis.

Finally, the database portion of the program was designed to provide a variety of output formats. This was essential if the final data were to undergo further specific, perhaps proprietary, tests or be further prepared for data warehousing.

Although the various quality-control protocols devised and programmed to test and analyze the data increase data reliability, an experienced meteorologist should review all the processed data, since no computer program can currently eliminate every potential pitfall in all possible cases.

CONCLUSION

We have developed a computer program that can identify a specific incoming satellite data stream; restore the date and time stamp; select the correct parsing algorithm; parse the data; import the data into a relational database; sort, test, analyze, and manipulate the data according to a predetermined weather-prediction algorithm; and, finally, format the data for further processing or for data warehousing.

ACKNOWLEDGMENTS

The authors wish to thank Linda M. Parkin for her invaluable help in preparing the documentation for this project and her insight into helping us say things clearly and concisely.

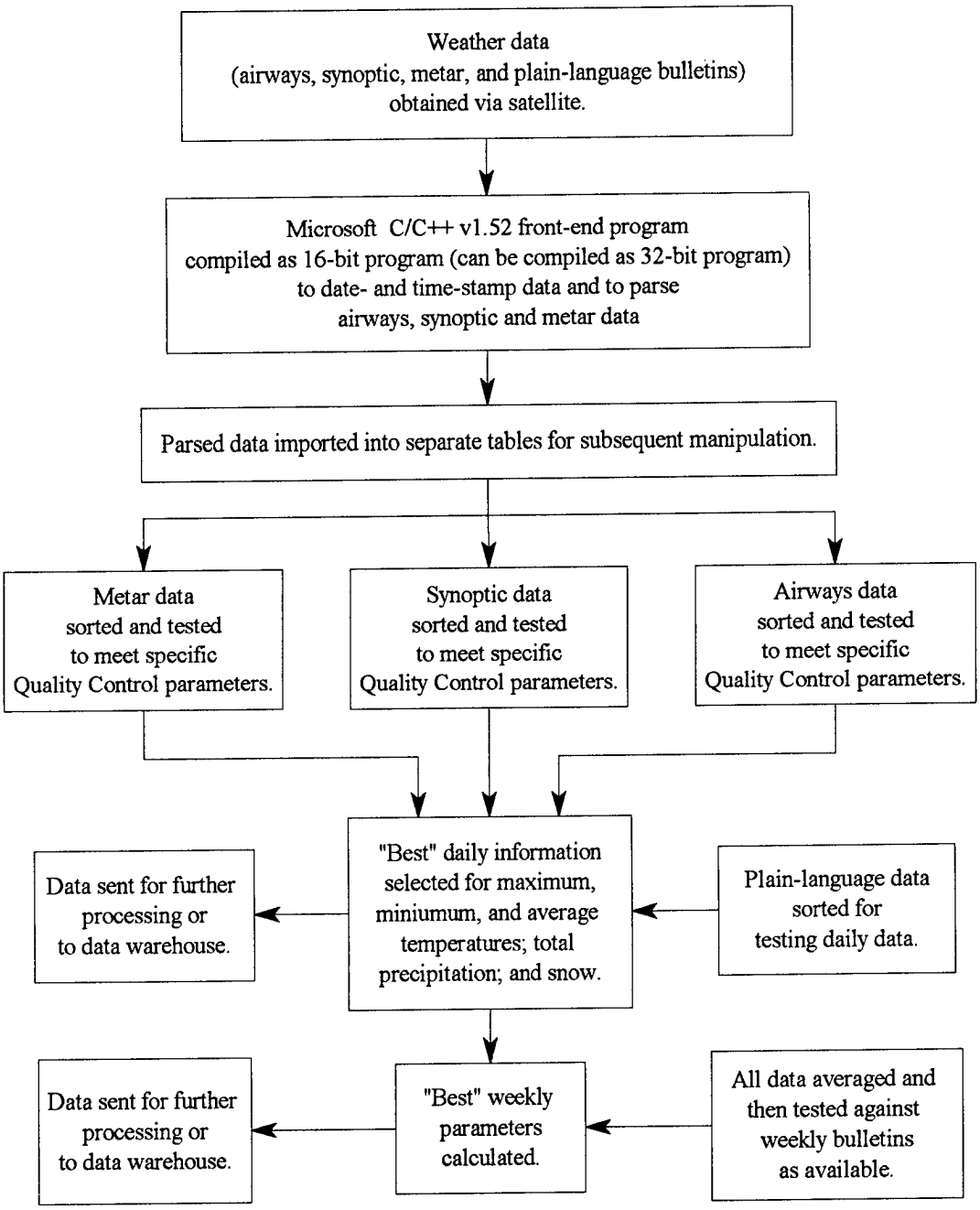


Fig. 1. Generalized data flow in combined C/C++ and Access database program

Neural Network-Based Cloud Detection/ Classification using Textural and Spectral Features[+]

Mahmood R. Azimi-Sadjadi*, Mukhtiar A. Shaikh*, Bin Tian* , Kenneth E. Eis**, and Donald Reinke**
*Electrical Engineering Department **Cooperative Institute for Research in the Atmosphere
Colorado State University, Fort Collins, CO 80523
Tel: (970) 491-7956 Fax: (970) 491-2249 E-mail:azimi@lance.colostate.edu

Abstract

An efficient and robust neural network-based scheme is introduced in this paper to perform automatic cloud detection and classification. An unsupervised Kohonen neural network was used to classify the cloud contents of a 8x8 blocks in an image into ten different cloud classes. Inputs to the network consisted of textural features of each block obtained using an efficient feature extraction scheme namely the Wavelet Transform (WT). This scheme not only reduces the dimensionality of the data but also extracts useful features of the data. To improve the detection rate and reduce the false positive rate, especially for low clouds and thin high clouds, a multi-channel fusion system was constructed to combine the results of different optical bands. An alternative approach for automatic cloud detection/ classification based on multi-spectral features was also studied to analyze and compare the effectiveness of multi-spectral-based scheme vs textural-based scheme. The results using high resolution GOES 8 data show the promise of the Kohonen neural network when used in conjunction with WT as feature extractor for cloud detection/ classification.

I. Introduction

Highly efficient and robust cloud detection/ classification schemes are needed for automatic processing of the huge amount of satellite cloud imagery data (over 25 GB/day from each GOES satellite). In recent years, considerable research has been focused on this area resulting in the development of two major classes of cloud detection/ classification methods: spectral-based and textural-based algorithms. The first class utilizes the information on the cloud radiances in different spectral bands. Some of the most commonly used methods in this category include threshold-based techniques and clustering approach. The second category uses textural-based methods to classify the data based on the characteristics of spatial distribution of gray levels corresponding to a region/block within the image. Most of the textural-based cloud detection/ classification methods, in the past used statistical measures to characterize the textural features such as Gray-level Co-occurrence Matrix (GLCM), Gray-level Difference Matrix (GLDM), Gray-level Difference Vector (GLDV) and Sum And Difference Histogram (SADH) [1], [2]. Recently, new emerging texture analysis schemes such as the Gabor Transform and the Wavelet Transform [4] have been developed which not only extract the salient features of the data efficiently but also reduce the dimensionality of the data to a manageable size.

The application of neural networks to cloud detection/ classification problems has been proved to be very effective. Owing to the fact that the characteristics of clouds are highly variable and difficult to classify using the traditional approaches, neural network classifiers through their adaptive learning nature offer attractive and computationally very efficient alternatives. Various feature extraction methods have been used in the past with different neural network paradigms [5]-[7]. The supervised back-propagation network is probably the most widely used paradigm [5], [6] even though for these networks the detection/ classification relies on the availability of ground truth. However, in most of the situations the ground truth may not be available. Consequently, an unsupervised Kohonen neural network-based system is more appropriate for this problem.

The proposed cloud processing approach consists of several stages. Wavelet transform is first applied to the blocks of images to extract textural, intensity and shape dependent features of the cloud image data. Once the appropriate features are extracted, detection/ classification for each data block is done using an unsupervised Kohonen neural network [8] which performs mapping of these features into one of the different possible categories or classes. The network is trained on both the visible and IR data. Detection/ classification tasks are performed separately for each type of data. The final decision for cloud typing is then made by fusing the results of these channels. An alternative approach using spectral-based features is also proposed. The results on actual GOES 8 satellite data are presented.

II. Detection/ Classification Based on Textural Features

The cloud data analyzed in this study was obtained from the GOES 8 satellite that carries a five channel sensor. This study was carried out exploiting the data of two channels namely channel 1 (visible) and channel 4 (IR). Images shown in Figures 1(a),1(b) chosen for this study were acquired on May 1, 1995 at 16:45 UTC using these channels. These

[+] This work is supported by DOD under contract # DAAH04 94 G0420.

0-7803-3068-4/96$5.00©1996 IEEE

images with spatial resolution of 512x512 pixels cover mid-west and most of the eastern part of the US extending from the Rocky Mountains to the Atlantic coast. This scene is of particular interest because of the presence of a variety of cloud types especially thin cirrus in the left middle part, high cirrus in the right middle part and stratoform and cumuloform clouds in the center part and over the water.

The feature extraction scheme using WT was applied to these images. Images were divided into small blocks of size 8x8 (32km x 32km) in order to extract the " local" textural features within each block. A two-level wavelet decomposition was carried out on each data block using a 16-tap Daubechies filter [3]. In this hierarchy, a two-level decomposition resulted in 7 sub-images. The total number of coefficients in all decomposition levels is exactly equal to the number of pixels in an original image (e.g 64 for a block of size 8x8). In order to reduce the dimensionality for efficient neural network training and to pick the best wavelet coefficients, energy and entropy measures corresponding to each wavelet sub-image were calculated. It was found that substantial amount of energy/entropy was packed only in the second level low-pass approximation sub-images. Due to down sampling at each decomposition level, the size of each block is reduced by a factor of four. As a result, at level two there are only 4 coefficients in the low-pass approximation sub-image. These were used for training and testing of the neural network detector/ classifier.

Features corresponding to different blocks were studied by applying them to an unsupervised Kohonen neural network [8] which performs automatic detection/ classification of the feature sets. Ten output neurons were specified for this detection/ classification problem in order to accommodate all possible cloud types. The network was trained using one-fifth of the total number of blocks of the image taken randomly from the original image. After training is completed, each weight vector represents the centroid of a particular decision region created in the space of pattern data. Once the clusters were established, the network was tested on the whole image. The goal of this testing process was to discriminate the input into ten distinct pre-specified number of classes.

After processing the visible and IR data separately, the resultant images both for IR and visible data were fused together using a simple OR operation in order to reduce the amount of misdetection and false positive. The results in Figure 2 show the fused image in which the blocks detected as cloud in both channels are kept. The cloud areas which are misdetected in the visible case or in IR case alone are now detected using combined channels.

To explore the behavior of the individual outputs of the classifier, the information carried by each of the output units was studied. The color coded images are formed by assigning a fixed color to all the blocks classified by each output unit. The classification results corresponding to the ten output classes both for the visible and the IR cases are indicated by the different colors/ grey-levels in Figures 3(a), (b), respectively. It is clear from these results that the network was successful in classifying the cloud data into different classes. In the visible case, the network had little success in discriminating the low clouds over the water and the land except at the tip of Florida. For the IR case, the network did not have any problem in discriminating between the water, low-clouds over the water and land which is different from the spectral-based threshold technique in which it is difficult to distinguish low clouds in the IR as compared to distinguish them in the visible channel. In this case, the low stratoform clouds over the land in the middle of the image were also well differentiated from other low-clouds within the same scene. The thin cirrus on the left middle part and high cirrus on the right middle part of the image were easily categorized.

III. Cloud Detection/ Classification Based on Multi-Spectral Features

In this group, another approach for automatic cloud detection/ classification based on multi-spectral features in all the five channels was studied. This study was designed to examine the effectiveness of multi-spectral feature-based scheme for cloud analysis in contrast to the textural-based method. In this analysis, multi-spectral features are used to perform the classification of the clouds. Using an unsupervised neural network, the five channel data are incorporated to form one image with substantially smaller grey level resolution while keeping the global textural features unchanged. Each grey level in the generated image shows a different cloud class. An unsupervised Kohonen neural network was used as a classifier with input vector consisting of five values of the corresponding pixels in the five channels. The number of output classes for the neural network was specified to be 10. The neural network was trained and tested using the same set of images data as in the previous method, and the result is shown in Figure 4. An important observation is that the global textural information is retained in the image even though the image lost some local textural details as a result of reduced grey level resolution. It can be seen that the network successfully classified the land, water, and different types of clouds. However, it exhibited some difficulties in discriminating low-level and medium-level clouds in the middle of the image. Additionally, in some areas the class labels of adjacent pixels changed abruptly hence resulting in the appearance of noise pixels. This "noise" is clearly associated with the more random cumulus cloud type, as seen in the corresponding visible image in Fig. 1(a). Overall, the simulation results of the spectral feature-based method are promising. Further improvement may be achieved by combining the spectral and the textural features.

IV. CONCLUSIONS

This paper presents the results of the study on cloud detection and classification for IR and visible images using WT feature extraction scheme in conjunction with Kohonen neural network. The results in this research indicated that the performance of the system is highly dependent on input variations, both in terms of intensity and texture. This approach provides better classification capability in many difficult situations such as cirrus clouds, low clouds and high intensity background. This fact is demonstrated in the processed images. For example, the image in Figure 1(b) has big portions of cirrus clouds on the lower left and upper right corners and low-level clouds over water which are difficult to identify using the traditional approaches but were successfully detected by the neural network.

REFERENCES

[1] R. M. Welch, K. S Kuo, S. K. Sengupta, and D. W. Chen, "Cloud field classification based upon high spatial resolution textural feature, I. Gray -level cooccurrence matrix approach", Journal of Geophysical research, Vol. 93, pp 12,663-12681, October 20, 1988.

[2] Z. Gu and C. Duncan, "Texture and spectral features as an aid to cloud classification," in Proc. IGARSS'88 Symp.2, pp1193-1194, 1988

[3] Ingrid Daubechies, " Ten Lectures of Ingrid Duabechies" June 1990.

[4] Stephane G. Mallat ."A Theory for Multi resolution Signal Decomposition: The Wavelet Representation". IEEE Transactions On Pattern Analysis and Machine Intelligence, Vol. 11. No. 7, pp 674-693, July 1989.

[5] I.G. Smotroff, T.P. Howells, and S. Lehar, "Meteorological classification of satellite imagery using neural network data fusion" in proceedings of IJCNN, San Diego, CA, pp.II-23-II-28.

[6] Jonathan Lee, et al. "A Neural Network Approach to Cloud Classification", IEEE Transactions on Geoscience and Remote Sensing, vol.28, No 5., Sept. 1990, pp846-855

[7] Ren-Jean Liou, et al " Detection and Classification of Cloud Data From Geostationary Satellite Using Artificial Neural Networks" Proceedings of 1994 IEEE International Conference on NN, pp. 4327-4332 Orlando, FL, 1994.

[8] Kohonen, T., "The self-organizing map." Proc. of IEEE78, pp1464-1480, 1990.

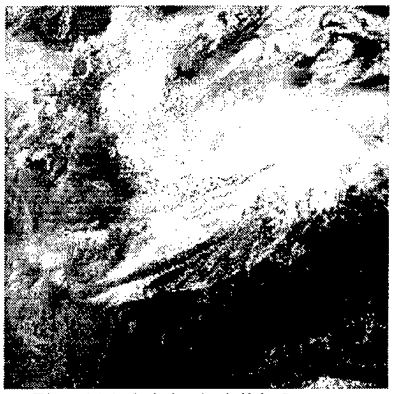


Fig. 1(a) Original visible Image.

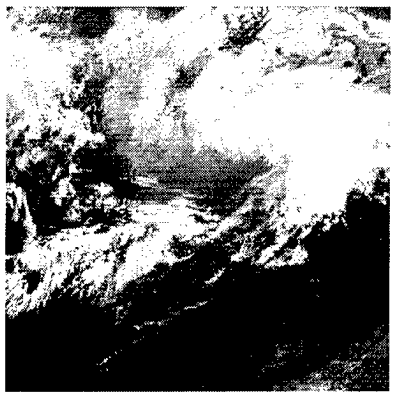


Fig. 1(b) Original IR Image.

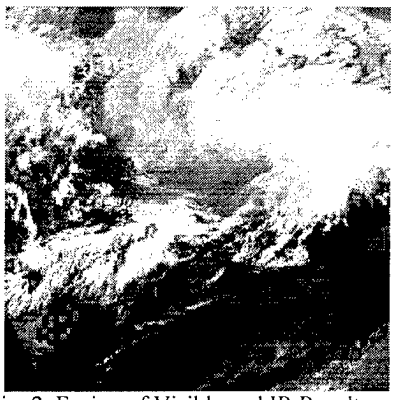


Fig. 2. Fusion of Visible and IR Results



Fig. 3(a) Classification based on the Textural Features (Visible).

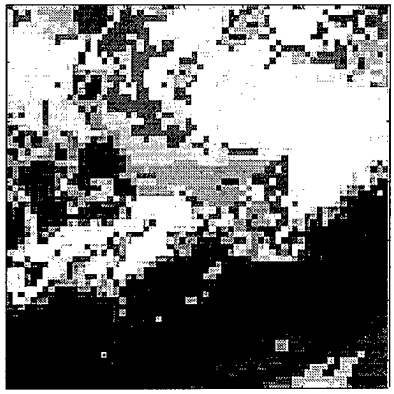


Fig. 3(b) Classification based on the Textural Features (IR).

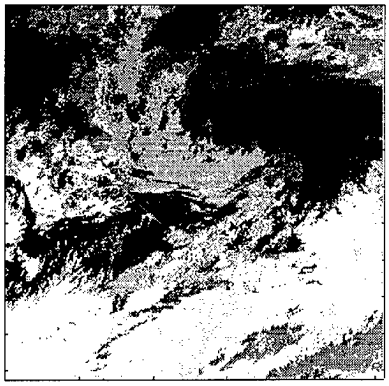


Fig 4. Classification based on Spectral Features.

An FFT-Based Algorithm for Computation of Gabor Transform with its Application to Cloud Detection/Classification*

Bin Tian[1], Mahmood. R. Azimi-Sadjadi[1] , Mukhtiar A. Shaikh[1] and Tom Vonder-Haar[2]

[1]Dept. of Electrical Engineering, Colorado State University (CSU), Fort Collins, CO 80523, USA
[2]Cooperative Institute for Research in the Atmosphere, CSU, Fort Collins, CO 80523, USA

Email: btian@lamar.colostate.edu. Tel: (970)-491-7956 Fax: (970)-491-2249

Abstract

In this paper an efficient algorithm for the computation of 2-D discrete Gabor transform is introduced. Under the assumption of non-overlapping windows, which is satisfied in many practical cases, the 2-D Gabor coefficients can be calculated through an FFT-based scheme. Combining with the Kohonen self-organized map, this method is used in a real-world problem dealing with cloud detection/ classification. Simulation results are also provided which show the promise of the proposed method.

I. Introduction

Highly efficient and robust cloud detection/ classification schemes are needed for automatic processing of the satellite cloud image data. Gabor transform has been found to be one of the most effective tools for textural feature extraction and is widely used in cloud detection/classification field [1],[2]. It has optimal " time-localization" property and complies well with the mammalian visual receptive process [1]. Experimental results reveal that the 2-D Gabor elementary functions can nicely mimic the simple cell of mammalian visual receptive field [1]. However, one of the drawbacks of Gabor transform, especially for real-time cloud detection/classification application, is the difficulty in computing the coefficients. This is primarily due to the fact that the Gabor elementary functions are non-orthogonal. An analytic solution for 1-D signals via bi-orthogonal (auxiliary) functions was first proposed by Bastiaans [3] and was further extended to the 2-D case by Porat and Zeevi [2]. Wexler [4] and Wang [5] utilized Bastiaans' idea in the discrete domain and provided a simpler approach. Nonetheless, there is still the need to solve a set of linear equations in order to get the bi-orthogonal functions, hence making the algorithm computationally demanding. Another class of approaches is proposed which use neural networks. Daugman [1] proposed an LMS-based learning neural network to extract the Gabor transform coefficients. In [6] Ibrahim and Azimi-Sadjadi used a RLS-based learning algorithm for a single-layer network to compute the Gabor coefficients directly from the data. However, most of these methods are not suitable for real-time applications as they require considerable time to update the weights.

In most of the applications of the Gabor transform , the signal or image is divided into blocks that are processed separately. Assuming non-overlapping blocks, a new approach is developed in this paper which allows for calculation of the Gabor transform coefficients using an efficient FFT-based algorithm without the need to solve any equation as with the auxiliary function schemes [4]. This new method is proven theoretically to yield the same result as the auxiliary function methods but with more efficiency and real-time implementation capability.

The rest of the paper is organized as follows: Section II provides a review of the Gabor transform. The implementation using FFT-based algorithm is also discussed in this section. In Section III, the effectiveness of the proposed approach is examined for the textural feature extraction for cloud detection /classification tasks. Simulation results are also presented in this section.

II. Discrete Gabor Transform and its Fast Implementation using an FFT Algorithm.

II.1 1-D Gabor Transform

The basic idea of Gabor transform is to expand a signal, $f(x)$, $x \in [0, L-1]$, into a set of shifted and modulated Gaussian window functions,

$$\hat{f}(x) = \sum_{m=0}^{M-1} \sum_{n=0}^{N-1} a_{mn}\, G_{mn}(x) \qquad x = 0,1,\ldots,L-1 \qquad (1)$$

where $\hat{f}(x)$ is the reconstructed signal, equal to or approximately equal to $f(x)$ in some optimal sense and $G_{mn}(x)$ are the Gabor elementary functions defined as

$$G_{mn}(x) = g(x - mD)\, \exp(j2\pi nx / N)$$

where $g(x)$ is the Gaussian window function with an effective width W, i.e.

$$g(x) = (\sqrt{2} / \alpha)^{1/2} \exp[-\pi(x - W/2)^2 / \alpha^2] \qquad x \in [0, W-1]$$
$$= 0 \qquad \text{otherwise} \qquad (2)$$

* This work is supported by DOD under contract # DAAH04 94 G0420.

0-7803-3068-4/96$5.00©1996 IEEE

α decides the shape of the Gaussian window and D defines the spatial distance between two adjacent windows. Moreover M=L/D is the number of windows that are needed to cover the whole signal while N decides the lowest frequency of the sinusoids that modulates the Gaussian window or in other words it controls the analysis resolution in the frequency domain. When $D=N$, which is originally advocated by Gabor, (1) is also called the critical sampling Gabor transform, while for $D<N$, (1) is called over-sampling Gabor transform.

It is easy to show that the set of Gabor elementary functions $G_{mn}(x)$ are non-orthogonal to each other, hence leading to difficulties in computing the coefficients. One way to solve this problem is to apply the idea of Bastiaan's auxiliary function. For a given window function, g(x), suppose there exists a biorthogonal function r(x), so that the Gabor expansion coefficients can be derived by the following equation:

$$a_{mn} = \sum_{x=0}^{L-1} f(x) r^*(x - mD) \exp(-j2\pi nx / N) \qquad (3)$$

Substituting (3) into (1) and using discrete Poisson-sum formula [4], it can be shown that r(x) is determined by

$$\sum_{x=0}^{L-1} r^*(x) g(x + mN) \exp(-j2\pi nx / N) = \delta_m \delta_n$$

m=0,1,... M-1. n=0,1, ... N-1 (4)

There are totally MN equations and L variables in the above equation. In mostly used critical sampling Gabor transform, N=D, in which case the above equation will have a unique set of solutions. The signal f(x) can then be reconstructed from the Gabor expansion coefficients using (1) without any distortion. The case N>D, i.e. the oversampling , leads to an overdetermined case and the solution could only be achieved in optimal MSE sense. The effective window length, W, will also affect the analysis results of the Gabor transform. The best frequency resolution will be achieved when W=N, where N decides the lowest frequency that modulates the Gaussian window. Consequently, critical sampling Gabor transform using non-overlapping window is preferred if both the distortion-less reconstruction and excellent frequency resolution are required as in many practical applications.

For critical sampling Gabor transform using non-overlapping windows, where W=D=N, we can define a signal $f_m(x)$ in each window, i.e.

$$f_m(x) = f(x) \quad , \quad x \in [mN, (m+1)N - 1]$$
$$= 0 \quad , \quad otherwise$$

Thus, we can write

$$f(x) = \sum_{m=0}^{M-1} f_m(x). \qquad (5)$$

From (1), we can get

$$f(x) = \sum_{m=0}^{M-1} \left[\sum_{n=0}^{N-1} a_{mn} \exp(j2\pi nx / N) \right] g(x - mN) \qquad (6)$$

Since non-overlapping window is used, $g(x - mN) \neq 0$ when $x \in [mN, (m+1)N - 1]$ and zero outside this window. Thus , comparing (5) and (6), it is easy to show that

$$f_m(x) = \left[\sum_{n=0}^{N-1} a_{mn} \exp(j2\pi nx / N) \right] g(x - mN)$$

The coefficients a_{mn} can then be obtained using

$$a_{mn} = \frac{1}{N} \sum_{x=mN}^{(m+1)N-1} \frac{f_m(x)}{g(x - mN)} \exp(-j2\pi nx / N) \qquad (7)$$

which may be computed using an efficient FFT algorithm. It can be shown that this approach provides the same results as with the auxiliary function methods [8].

II.2 Fast Implementation of 2-D Discrete Gabor Transform using FFT algorithm.

The 1-D Gabor transform definition can easily be extended to the 2-D case. For a given image f(x,y), x=0,1... L_x , y=0,1... L_y , the 2-D Gabor transform is defined as

$$\hat{f}(x,y) = \sum_{n_x=0}^{N_x-1} \sum_{n_y=0}^{N_y-1} \sum_{m_x=0}^{M_{x-1}} \sum_{m_y=0}^{M_y-1} a_{m_x n_x m_y n_y} G_{m_x n_x m_y n_y}(x,y) \qquad (8)$$

where the 2-D Gabor elementary functions are

$$G_{m_x n_x m_y n_y}(x,y) = g(x - m_x D_x, y - m_y D_y) \exp\left[j2\pi \left(\frac{n_x x}{N_x} + \frac{n_y y}{N_y} \right) \right]$$

The definition of all the other variables and functions are the same as in the 1-D case, except that the subscripts x and y are added to represent x and y coordinates.

For critical sampling discrete 2-D Gabor transform using non-overlapping windows, i.e., $N_x=D_x=W_x$, $N_y=D_y=W_y$, we can also employ 2-D FFT for computing the Gabor transform coefficients similar to the 1-D case. In this case we can get

$$a_{m_x n_x m_y n_y} = \frac{1}{N_x N_y} \sum_{x=m_x N_x}^{(m_x+1)N_x-1} \sum_{y=m_y N_y}^{(m_y+1)N_y-1} \frac{H(x,y)}{g(x - m_x N_x, y - m_y N_y)} \exp\left[-j2\pi \left(\frac{n_x x}{N_x} + \frac{n_y y}{N_y} \right) \right] \qquad (9)$$

III. Simulation Results.

The effectiveness of the proposed algorithm is examined for real-time textural feature extraction from satellite data. The cloud image (see Fig. 1) analyzed in this study was obtained from the GOES 8 satellite which transmits a high resolution image of a part of the earth every 30 minutes. To process such an overwhelming volume of data, obviously fast processing schemes are needed. Gabor transform coefficients were first computed for this image. These were then applied to an unsupervised Kohonen neural network [9] for automatic cloud detection/ classification. In order to find the coefficients, the entire image was divided into small blocks of size 8x8. Using the proposed non-overlapping Gabor transform, the total number of Gabor coefficients are equal to the number of pixels in the image. However, due to symmetry only half of the coefficient will be sufficient for the image representation. In order to reduce the dimensionality of input data for the neural network only

those coefficients which contained most of the image energy were used. Ten output neurons were used for this detection/classification problem in order to accommodate different possible classes. The network was trained using randomly chosen blocks covering different areas of interest in the image. After training was completed, the network was tested on the whole image. Fig. 2 shows the regions detected as cloud and no-cloud. Figs. 3(a)-(b) show the classification results for some of the output classes. The network has well discriminated between land, water and clouds. The results indicate the promise of this scheme for cloud detection and classification when used as a fast feature extraction method.

References

[1] *J.Daugman, "Complete Discrete 2-D Gabor transform by Neural Networks for Image Analysis and Compression",IEEE Trans. on ASSP, vol. ASSP36, No. 7, pp. 1169-1179,July, 1988.*

[2] *M.Porat and Y. Y. Zeevi, "The Generalized Gabor Scheme of Image Representation in Biological and Machine Vision", IEEE Trans. Pattern Anal. Machine Intell., vo.10, pp 452-467, July 1988.*

[3] *M.Bastiaans, "Gabor's Expansion of a Signal into Gaussian Elementary Signals," Opt. Eng., vol. 20, no. 4, pp594-598, July 1981.*

[4] *J. Wexler and S. Raz, "Discrete Gabor Expansions", Signal Proc., Vol 21, No. 3, pp207-220, Nov., 1990.*

[5] *L. Wang, C.T. Chen and W.C. Lin, "An Efficient Algorithm to Compute the Complete Set of Discrete Gabor Coefficients", IEEE Trans. on Image Proc. , Vol 3, No 1. , pp 87-92, Jan., 1994.*

[6] *A. E. Ibrahim and M. R. Azimi-Sadjadi, et al., "A Fast Learning Algorithm for Gabor Transformation ", to appear in IEEE Trans. on Image Processing, Jan. 1996.*

[7] *M.Bastiaans, "Gabor's Expansion of a Signal into Gaussian Elementary Signals," Opt. Eng., vol. 20, no. 4, pp594-598, July 1981.*

[8] *B. Tian and M. R. Azimi-Sadjadi, "An Efficient FFT-based Algorithm for Discrete Gabor Transformation", submitted to IEEE Trans. on Image Processing, unpublished .*

[9] *T. Kohonen, "The self-organizing map.", Proc. of IEEE 78, pp 1464-1480, 1990.*

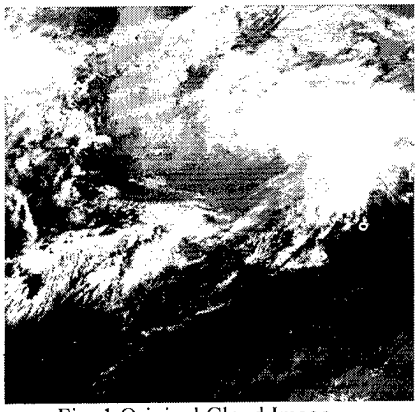


Fig. 1 Original Cloud Image

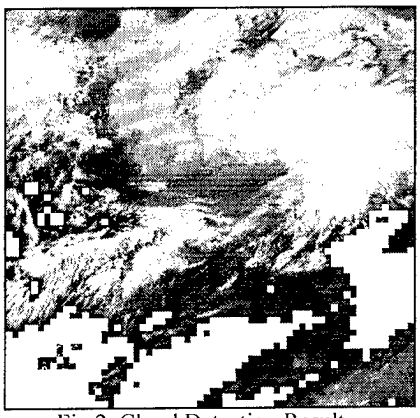


Fig 2. Cloud Detection Result
Bright White = No cloud Regions)

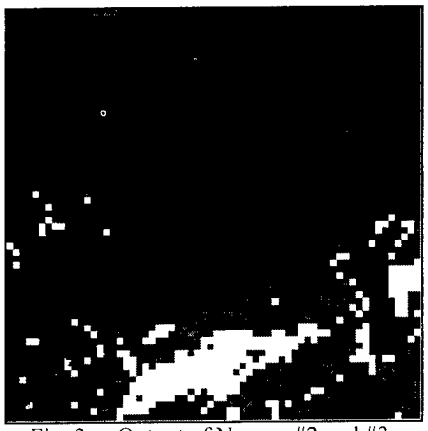


Fig. 3-a Output of Neuron #2 and #3
(Class 2 : White = Water Regions
Class 3 : Gray = Low-level Clouds)

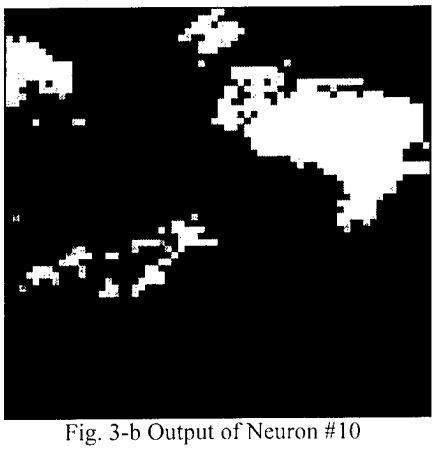


Fig. 3-b Output of Neuron #10
(White = High-level Cirrus)

A Prototype Sea Ice Mapping System using a Geographical Information System and Expert Knowledge.

R.N.Williams and J.Hartnett.

Department of Applied Computing and Mathematics, University of Tasmania, PO Box 1214, Launceston, Tasmania, Australia, 7250

Phone: 61 (03) 243480 Fax: 61 (03) 243368
Email: R.Williams@appcomp.utas.edu.au

Abstract -- An operational sea ice mapping system is being developed which will assist meteorologists at the Casey Antarctic Base to create sea ice maps, from NOAA AVHRR imagery received at the base itself. The system will take AVHRR imagery initially processed via the McIdas meteorological system, and initiate an interactive procedure which assists the expert interpreter to produce a sea ice map from the imagery.

A prototype system, called ICEMAPPER, has been developed. It is based on an existing geographical information system and uses production rules, incorporating expert knowledge derived both from the scientific literature and from local sea ice interpreters, to provide an initial classification. If the expert is satisfied with the map produced it can be printed out. If not, thresholds used in the production rules can be altered interactively and the map recreated.

INTRODUCTION

The Australian Bureau of Meteorology supports shipping operations undertaken by the Australian Antarctic Division into the bases at Mawson, Davis and Casey. A small meteorological centre has recently been established at the Casey base itself. One important part of the meteorological service is the provision of sea ice maps and reports which enable ships to be navigated safely into and out of the bases.

These maps are currently produced manually at the Bureau of Meteorology office in Hobart, from AVHRR images received from the NOAA10 and NOAA11 polar orbiting satellites. The data is obtained from the satellite on an operational basis and initially processed using the McIdas meteorological system. Any of the five wavelength bands, two visible and three infra-red, can be displayed on the workstation screen. The expert image interpreter observes the bands of interest and uses them to identify regions of various types of sea ice on the image. The regions are classified, using a scheme defined by the World Meteorological Organisation, into the following classes :-

open water - which is ocean free of sea ice.
very open ice - ice concentration of 1 to 2 eights.
open ice - ice concentration of 3 to 4 eights.
close ice - ice concentration of 5 to 6 eights.
very close ice - ice concentration of about 7 eights.
compact ice - ice concentration of 8 eights.
cloud - regions obscured by clouds.

Once the regions have been identified, the interpreter draws an ice chart by hand, writes interpretive comments on the chart and then faxes the chart down to the Antarctic base and onto relevant ships in the area.

The aim of the work reported in this paper is to design and construct an operational system which can partially automate this process. A prototype (called ICEMAPPER) has been developed using an expert-moderated approach in which the five wavelength bands of a NOAA image are converted into albedo and brightness temperature images and a sea ice interpretive knowledgebase analyses the resulting data to produce an appropriate ice map. The knowledgebase consists of production rules which can classify each pixel into one of the classes described above by comparing various albedo and temperature values, and differences between values, with a number of specified radiometric thresholds. It uses this knowledge, derived from human image interpreters and from the scientific literature [1-6], to produce an initial classification.

If the expert using the system is satisfied with the sea ice map produced, it can be saved and printed out. If the map produced is not sufficiently accurate, the expert can alter the thresholds being used in the production rules as these are believed to change during the year and under different

0-7803-3068-4/96$5.00©1996 IEEE

climatic conditions. The map can then be redrawn using the altered thresholds and, if satisfactory, printed out. This process can be repeated several times if necessary, although the aim is to obtain a satisfactory map after a relatively small number of iterations on most occasions.

The expert also has the ability to record those thresholds which produced a satisfactory map. The aim of doing this is to obtain further knowledge about how the thresholds vary according to time of day, time of year and under different climatic conditions. This knowledge would be incorporated into a future version of the system thus improving its performance.

PROGRAM DESIGN AND IMPLEMENTATION

The ICEMAPPER program developed from an earlier project which aimed to produce a spatial expert system for the automatic analysis of AVHRR images. The knowledge needed to produce the sea ice maps was obtained from two expert image interpreters over an eight month period, and supplemented by information gleaned from the research literature. It was encoded as production rules and incorporated into an expert system shell, which was then integrated with a geographical information system in order to handle the spatial data involved.

This spatial expert system enabled us to acquire the sea ice knowledge, convert it into production rule form and incorporate into a working program for validation. It was a very useful research tool but to be effective in an operational setting it required two modifications. Firstly, in order to achieve the execution speed required, the production rules were recoded in C (as is often done when an expert system moves from an experimental to an operational phase). Secondly, the desire to produce a fully automated analysis system proved unrealistic at this stage, so the system needed to allow the possibility for expert intervention, when required, to produce a satisfactory final product. A graphical user interface was added to enable the expert to modify the production rules (by altering thresholds) and to undertake repeated attempts at producing a satisfactory sea ice map.

The ICEMAPPER system design has now been completed and substantially implemented. All of its modules are accessible via mouse operations from a single pull-down main menu. They include the following :-

(1) Import a McIdas Image - enables a five band multispectral AVHRR image, in McIdas format, to be imported into the image analysis system. It reads in the header information and also splits the image into its five separate spectral bands.

(2) Navigate an Image - will use satellite navigation data to navigate the image and to underlay it with an accurate coastline map provided by the Antarctic Division. (A considerable amount of background work has been completed in relation to this module but the module has not yet been implemented).

(3) Calibrate the Image - uses appropriate radiometric calibration formulae to convert bands 1 and 2 to albedo values (corrected for solar zenith angle) and bands 3, 4 and 5 to brightness temperatures. (All background work has been completed for the development of this module but implementation has yet to be completed.)

(4) Create an Ice Map - uses the sea ice interpretative knowledge, in this case coded as production rules written in C, to attempt a classification of the image (once it has been imported, navigated and calibrated). The result of this is an ice map of the region depicted by the multispectral image, in which the regions of open water as well as different sea ice concentrations, ranging from very open ice to compact ice, are displayed in various colours. Regions obscured by low and high cloud and the superimposed coastline are also shown on the ice map.

(5) Display Multispectral Bands and Ice Map - can display any of the multispectral bands used to create the ice map as well as the ice map itself. The most important function of this module is to allow the expert to look at appropriate bands and to look at the ice map to see whether it agrees with the expert's own manual interpretation of the data.

(6) Modify Thresholds for Production Rules - allows the expert to alter the thresholds for the production rules in the knowledgebase if the ice map produced by the default thresholds is deemed inadequate. It is known that the thresholds needed in the knowledge base may alter under unusual climatic conditions, thus rendering the ice map inaccurate. This module provides a number of point-and-click dialogue boxes which enable the expert to alter the thresholds easily, prior to recreating the ice map.

(7) Save/Print Multispectral Bands and Ice Maps - once the expert is satisfied with the ice map produced, it can be saved as a GIF file and subsequently printed out on a colour printer. Proposed additions to this module will enable the map to be recreated in black-and-white form (using shading patterns rather than colours to display the various regions) so that the map can be transmitted by fax.

(8) Record Details - on occasions when the thresholds have been altered and an accurate ice map produced, it is important to record the altered thresholds and as many other potentially relevant details as possible (eg, time of day, season, local meteorological conditions etc.) so that at a later date these records can be analysed in order to relate variations in the thresholds to changes in these other variables. The aim is to enhance the knowledgebase in the future so that this particular situation can be accommodated without the need for expert intervention.

TESTING AND EVALUATION

The current prototype system has been tested experimentally on five test images. In four of these images it created ice maps regarded as acceptable by the expert using the default thresholds. However, on the fifth image, substantial alterations were needed to the thresholds and even then an acceptable map could not be obtained. We are currently investigating what conditions were responsible for this situation. It is possible that the erroneous result occurred due to our current temporary implementations of the navigation and calibration modules. On the other hand it may reflect unusual climatic conditions of the type that can potentially affect the production rule thresholds needed to accurately classify the sea ice regions and further investigation could give us our first extra piece of knowledge on the relationships between the thresholds and other variables.

It is hoped that a fully-implemented version of the system will be ready for operational use by late 1996. The aim is to operate it under close supervision for about a year to assess its performance before considering whether to use it as a long-term operational tool.

CONCLUSIONS

We have determined that for the majority of the small selection of test images tested, the system produces acceptable ice maps. However more extensive testing is required before we can be confident of the accuracy of the system. Feedback from experts intending to use the system indicates that the semi-automatic mode of operation will be flexible enough to provide significant assistance, but without taking over the decision-making process. Due to the ramifications of a wrong analysis, it is necessary that the human expert still has the final say over the product produced.

It is intended that eventually this system will operate as a stand-alone system that can be set up and used, on a permanent basis, in the Antarctic Meteorological Centre at Casey.

ACKNOWLEDGMENTS

We wish to thank Mr Steve Pendlebury (Bureau of Meteorology, Hobart), Dr Robert Massom (Antarctic CRC, Hobart) and Mr Neal Young (also from the Antarctic CRC) as well as Dr Beth Ebert (Bureau of Meteorology, Melbourne) for contributing sea ice interpretive knowledge to the ICEMAPPER system. Also Justin Baker (Bureau of Meteorology, Melbourne) provided us with very valuable information on McIdas file formats. The work reported in this paper was supported by a research grant from the Antarctic Science Advisory Committee.

REFERENCES

[1] G. Zibordi and G.Meloni, "Classification of Antarctic surfaces using AVHRR data: a multispectral approach." Antarctic Science, vol.3, pp. 333-338, 1991.

[2] G.Zibordi and M.L.Van Woert, "Antarctic sea ice mapping using the AVHRR". Remote Sensing of the Environment, vol. 45, pp. 155-163, 1993

[3] E.Ebert, private communication, April 1992.

[4] T.Yamanouchi and S.Kawaguchi, "Cloud distribution in the Antarctic from AVHRR data and radiation measurements at the surface", Inernational Journal of Remote Sensing, vol.13, no.1, pp. 111-127, 1992.

[5] K.Kidwell, NOAA Polar Orbiter Users Guide, NOAA-NESDIS, Washington, 1991.

[6] R.Massom and J.Comiso, "The classification of Arctic sea ice types and the determination of surface temperature using advanced very high resolution radiometer data.", Journal of Geophyical Research, vol.99, no.C3, pp.5201-5218, 1994.

Combined Use of Radar and Satellite Information for Precipitation Estimation in Hungary*

I. Csiszár and J. Kerényi

Hungarian Meteorological Service
Satellite Research Laboratory
H-1675 Budapest P.O. Box 39., Hungary
Tel: /+36 1/290-0163, fax: -7387.
e-mail: csiszar@met.hu

Abstract -- Radar and satellite measurements can be used for the detailed description of the properties of precipitating clouds. Radars primarily detect the existing raindrops. From the satellite radiances, however, one can derive such additional physical characteristics of the cloudiness that can provide information on the further development of the precipitation systems. In this study we used digitized data from a 3 and 10 cm MRL-5 radar and satellite data from the Advanced Very High Resolution Radiometer (AVHRR) on board the polar orbiting NOAA satellites. From the AVHRR radiances we derived cloud-top temperature, optical thickness and effective cloud droplet size. We also determined a cloud-class flag using thresholding and clustering classification techniques. The radar and satellite images were transformed into the same geographic projection format and displayed simultaneously for qualitative evaluation. In addition, an empirical relationship was established between coincident ground precipitation measurements, radar data and satellite cloud parameters using data from a two-year period over Hungary.

INTRODUCTION

The multispcetral radiance measurements of AVHRR on board the polar orbiting NOAA satellites allow the retrieval of various physical properties of cloudiness. From these parameters cloud top temperature (T_c) alone has been proven to be a weak indicator of ground precipitation. However, as it has been pointed out in [1], cloud optical thickness and effective droplet radius can be successfully applied in the identification of the area of precipitation especially in case of low clouds. These data can be also used as complementary information for the quantitative estimation of precipitation from radar measurements. Also, satellite data are free from the loss of information that characterizes radar observations due to the weakening of the radar signal on precipitation elements. Thus satellite data alone may be useful tools in areas that are far from the radar instrument. In this study we present the results of a project aimed at the investigation of the relationship between satellite-derived cloud parameters, radar data and ground precipitation measurements.

INPUT DATA AND METHODOLOGY

We investigated simultaneous satellite, radar and precipitation measurements from summers 1994 and 1995 in the 250 km radius range of the Szentgotthárd-Farkasfa operational MRL-5 weather radar of the Hungarian Meteorological Service (HMS) in the western part of Hungary. First we collected instantaneous precipitation measurements provided by the Hungarian raingauge network for the times of the afternoon overpasses of NOAA-11 and NOAA-14 satellites archived at the HRPT (High Resolution Picture Transmission) receiving station of HMS Satellite Research Laboratory. As instantaneous measurements we took 5 minute sums of automatic raingauge readings and then converted them into the more conventional hourly sum units.

Cloud optical depth (τ) and effective radius (r_e) were derived from the AVHRR LAC (Local Area Coverage) visible (channel 1) and near-infrared (channel 3) reflectivities. The actual retrieved values of optical depth and effective radius were selected from a precalculated look-up table by taking the τ and r_e values corresponding to the reflectivities that were closest to the observed reflectivities at the given sun-satellite geometry. The look-up table contains reflectivities for a wide range of optical depths, effective radii and sun-satellite geometries. Here the synthetic reflectivities were calculated my the Mie scattering program MIEV0 [2] and the discrete-ordinate model DISORT [3]. We performed optical thickness retrievals only for the pixels that were identified as cloud-covered by a cloud detection scheme based on threshold values of all the 5 AVHRR channels [4]. Also, effective radii were retrieved only for pixels where the optical depth value was higher than 10. As in was shown in [5], such clouds are opaque for the 3.7 μm radiation and only absorption and reflection processes have to be taken in account. For the removal of the thermal emission component from the channel 3 radiance we used AVHRR channel 4 infrared window brightness temperatures. The satellite images were geographically transformed into the format of the 2 km resolution radar images containing 256x256 pixels.

For the comparison of satellite and radar imagery we selected the closest possible 3 or 10 cm PPI (Plan Position

*Supported by Hungarian Scientific Research Fund (No. F015961)

0-7803-3068-4/96$5.00©1996 IEEE

Indicator) radar observations. The time difference between the satellite overpasses and the corresponding radar observations was not allowed to exceed 10 minutes.

RESULTS AND DISCUSSION

The extinction of radar signal in precipitation at the 3 cm wavelength in strong and hence reliable data can be expected only within a 50 km radius area of the radar instrument. Thus here we concentrated on the 10 cm observations that provided a better opportunity for comparison over a larger area. Fig.1 and Fig.2 show collocated cloud optical depth, cloud effective radius and 10 cm radar echo fields on 19 July 1994.

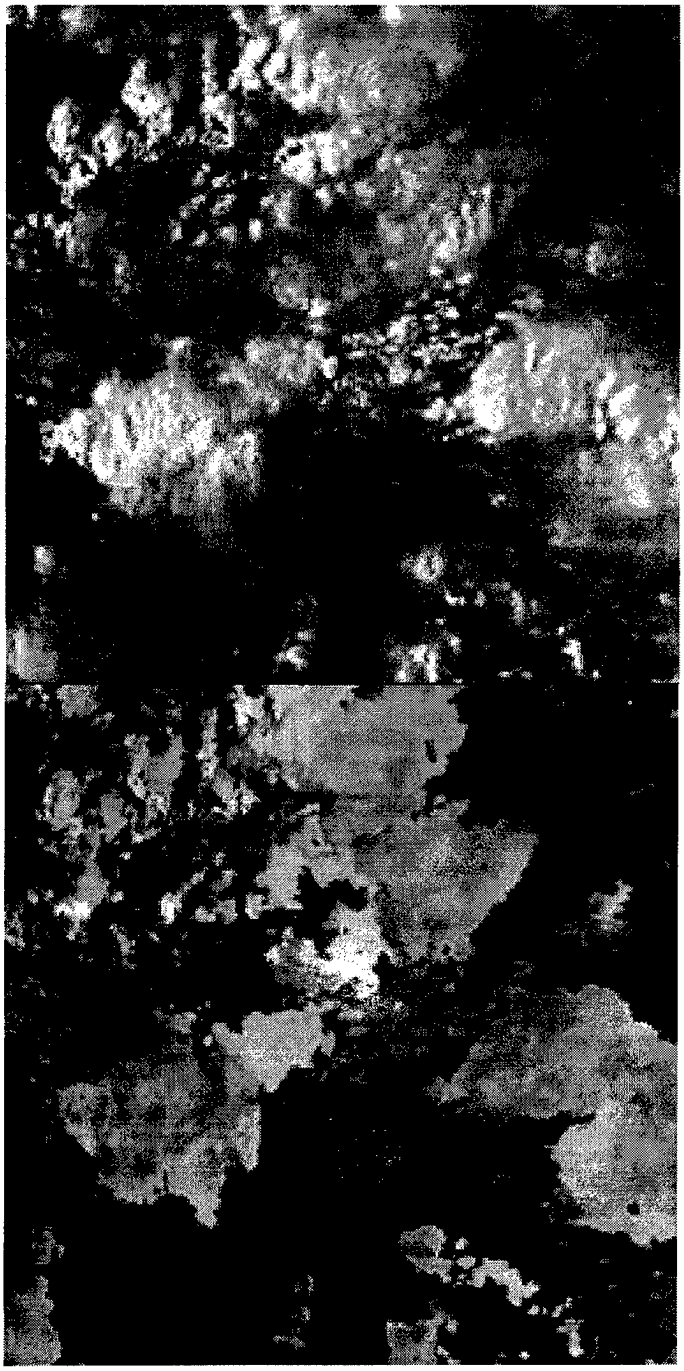


Fig.1 The cloud optical depth and cloud effective radius fields on 19 July 1994.



Fig.2. The radar echo field on 19 July 1994

It can be observed that the areas of precipitation can be identified with high values of cloud optical depth. By the investigation of various similar scenes it has been found that values higher than 15 of cloud optical depth mark well the areas of precipitation. On the other hand, the relationship between effective droplet radii and radar echoes is weaker. This is due to the fact that precipitating clouds may often be overlain by thin cloud layers with effective radii significantly different from those of the lower cloud.

We also investigated the quantitative relationship between satellite cloud parameters and radar reflectivity factor (Z). For this goal we separated high- and low level clouds by the 245K isotherm. We neglected mixed pixels only partly containing precipitation by considering only those pixels that were surrounded by pixels having radar logZ values higher than 1.65. We investigated the statistical relationship between cloud parameters and radar echoes. For high clouds a weak, rather qualitative relationship between τ and logZ could be observed. This relationship was stronger for low clouds, where high values of r_e also proved to be good indicators of precipitation. However, in both cases the correlation between the cloud parameters and logZ values was below 0.3, which cannot be explained only by the temporal and spatial collocation inaccuracy. It rather suggests that cloud parameters and radar data provide relatively independent pieces of information about precipitation clouds and thus there is a potential in their combined use to improve the accuracy of precipitation estimates.

We derived an empirical relationship between satellite cloud parameters and ground precipitation based on data from 15 days in 1994 and 1995. Here we added as predictor to τ, r_e and T_c the product of τ and r_e that is proportional to cloud liquid water path [5]:

$$LWP=2/3*\tau*r_e \quad (1)$$

if r_e and LWP are expressed in μm and g/m^2 respectively.

The regression equation to estimate the I instantaneous ground precipitation amount expressed in [mm/hour] from satellite cloud parameters is

$$I=-0.071*\tau*r_e+0.735*\tau+ 1.212*r_e-0.122*T_c+23.333 \quad (2)$$

This equation estimates the ground precipitation by a correlation accuracy of 0.51 that is comparable to the accuracy of precipitation estimation from radar data found earlier. This underlines the potential of using satellite cloud parameters for precipitation estimation.

Our final goal is the derivation of a regression equation for precipitation estimation from the satellite and radar data. This time, however, the low number of available coincident satellite, radar and raingauge data made a statistical comparison impossible. This was mainly due to the lack of radar information at many locations far from the radar instrument where raingauge measurements indicated precipitation.

CONCLUSION AND PLANS FOR THE FUTURE

In this paper the potential for the combined use of radar and satellite information for quantitative estimation of precipitation has been investigated. It has been found that satellite-derived cloud parameters alone can be applied for precipitation estimation with an accuracy that is comparable to the accuracy of the radar estimates. As cloud parameters have proven to be statistically weakly dependent from radar echoes, we expect their synergy to improve the accuracy of precipitation estimates. Also, we plan to simultaneously use of 3 and 10 cm radar information, since they are sensitive to low and high precipitation intensities respectively. However, for the derivation of a statistically significant empirical formula a larger dataset of coincident satellite, radar and ground observations is needed. So far the compilation of such a dataset has been hampered by the low temporal resolution of the NOAA satellite overpass. This problem, however can be overcome by the future use of the new generation geostationary meteorological satellites that, carrying imagers having similar spectral characteristics to AVHRR allow the retrieval of cloud optical depth and effective radius with high temporal resolution.

ACKNOWLEDGMENTS

We wish to thank Gy. Gyarmati and J. Nagy for providing radar imagery and assitance in radar data processing. Also, we thank the authors of MIEV0 and DISORT for making the software available.

REFERENCES

[1] D.Rosenfeld and G.Gutman,"Retrieving microphysical properties near the tops of potential rain clouds by multispectral analysis of AVHRR data.", Atmos.Res., 34, 1995, pp.259-283.

[2] W.J. Wiscombe, "Mie scattering calculations: advances in technique and fast, vector-speed computer codes." NCAR Technical Note TN-140+STR, 1979, National Center for Atmospheric Research, Boulder, Colorado.

[3] K.Stamnes, S.C.Tsay, W.Wiscombe and K.Jayawera,"A numerically stable algorithm for discrete-ordinate-method radiative transfer in multiple scattering and emitting layered media.", Appl.Opt. 27, 1988, pp.2502-2512.

[4] J.Kerényi, I.G.Szenyán, M.Putsay and F.Wantuch,"Cloud detection based on a threshold technique for NOAA/AVHRR images for the Carpathian Basin.",in proceedings of the 1995 Meteorological Satellite Data Users' Conference, Winchester, UK 4th-8th September 1995.,pp.565-569.

[5] T.Y.Nakajima and T.Nakajima,"Wide-area determination of cloud microphysical properties from NOAA AVHRR measurements for FIRE and ASTEX.", J. Atmos. Sci., 52, 1995, pp.4043-4059.

[6] A.Slingo,"Sensitivity of the Earth's radiation budget to changes in low clouds.", Nature, 343, 1990, pp.49-51.

The AEOLIS Program: Prospects for Future Low-Cost, Space-Borne Vector Wind Sensors

Michael L. Van Woert
Office of Naval Research, Code 322HL, 800 N. Quincy St. 22217
T:(703)696-4720 F:(703)696-2710 Email: vanwoem@onrhq.onr.navy.mil

Abstract -- The ocean surface wind speed and direction play important roles in meteorology, oceanography, climatology, and operational weather forecasting. Currently, global ocean vector wind measurements are derived from costly active microwave radars, such as the ERS-1 scatterometer and the soon to be launched NASA scatterometer (NSCAT). Recent work in the former Soviet Union [1] and analysis of Special Sensor Microwave/Imager data [2] both reveal wind direction signals in passive microwave data. To determine the limits of passive microwave vector wind remote sensing, the All-weather, Earth-observing, Ocean, Land, Ice Sensor (AEOLIS) program was established [3]. This program consists of laboratory and theoretical studies augmented by analysis of existing space-based data sets and an aggressive aircraft instrument development program. Preliminary results show detectable wind direction signals over the observed wind speed range of 2 to 9 m/s. In this paper, and the papers that follow, the state-of-the-art knowledge about this relatively new, passive microwave, vector-wind remote sensing technology is presented.

INTRODUCTION

Operational and climatological applications in meteorology and oceanography require accurate observations of surface wind speed and direction (vector wind) over the global oceans. Oceanic surface wind data of high quality and high temporal and spatial resolution are required to understand and predict the large-scale air-sea interactions that significantly influence our climate. Such observations are needed to drive ocean circulation and surface wave models; calculate surface fluxes of heat, moisture, and momentum; provide initial conditions and verification data for atmospheric models; and calculate surface climatologies.

Ocean wind-speed and direction are also important to Naval and civilian operations, yet are poorly observed over most of the world's ocean. The United States Navy lists: tactical weather forecasting, prediction of acoustic conditions for submarine and anti-submarine warfare, prediction of sea and surf conditions for amphibious warfare, mine warfare, underway replenishment, swimmer operations, and search and rescue operations as environmental products critical for tactical operations. Knowledge of the ocean surface wind speed and direction are critical elements in the calculation of these parameters. The operational wind requirements are listed in Table 1.

Only satellite-borne sensors are capable of providing global wind data coverage with high spatial resolution and frequent sampling. Scatterometers, satellite altimeters and multi-channel passive microwave radiometers can be used to estimate scalar wind speed under all but the worst weather conditions. Spanning more than 20 years of operation, passive microwave sensors provide one of the longest global records of remotely sensed data (Fig. 1). Currently, the Special Sensor Microwave Imager (SSM/I), is flown operationally on the Defense Meteorological Satellite Program (DMSP) Block 5D-2 satellites, and is used routinely to produce global maps of scalar wind speed, atmospheric water vapor, and cloud liquid water. To date, however, these instruments have been unable to measure wind direction.

Table 1: Operational ocean-surface, wind requirements.

Parameter	Speed	Direction
Resolution	25 km	25 km
Accuracy	> of 10% or 2m/s	± 20°
Precision	1 m/s	±10°
Range	0-50 m/s	360°<12 hours
Refresh	<12 hours	<12 hours

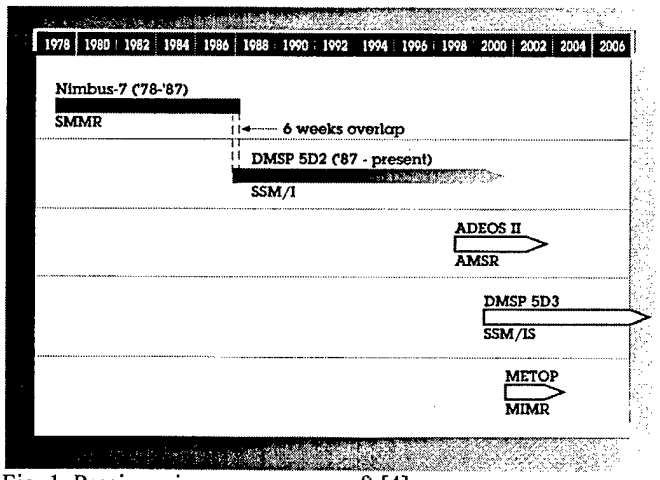


Fig. 1. Passive microwave spacecraft [4].

Satellite-borne scatterometers, such as those carried by the European Remote-sensing Satellites (ERS), the European Meteorological Operational (METOP) satellites and the Japanese ADvanced Earth Observing Satellites (ADEOS) are the only sensors currently capable of acquiring global, high-resolution, wind speed and direction data [5]. These data have already proven to be extremely valuable in atmospheric and oceanic modeling studies. Fortunately, international plans call for scatterometers to fly on research satellites well into the next decade (Fig. 2) providing continued high-quality, vector-wind data for research studies.

Presently, the National Polar-orbiting Operational Environmental Satellite System (NPOESS) Integrated Program

0-7803-3068-4/96$5.00©1996 IEEE

Office (IPO) is planning for the next generation of operational wind sensors (beyond ~2005). Both scatterometers and passive microwave sensors need to be seriously considered and their relative merits - cost, power, weight, and accuracy's compared.

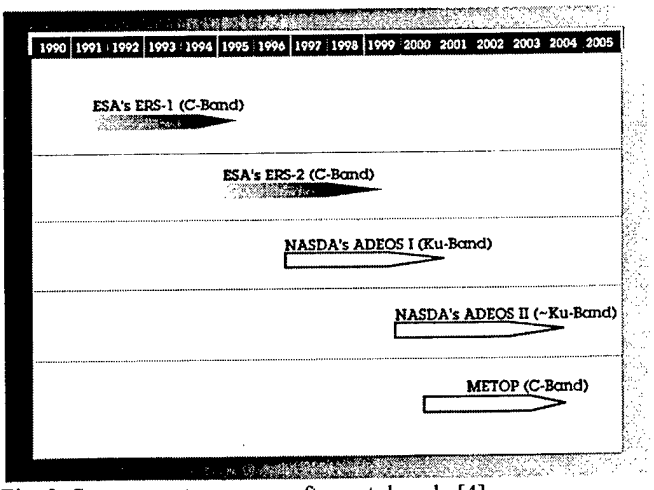


Fig. 2. Scatterometer spacecraft: next decade [4].

THREE RECENT TECHNOLOGY ADVANCES

Three advances have been made in recent years that make it possible, for the first time, to extract vector wind signals from passive microwave data. Wentz [2] has shown that wind direction signals exist in monthly-averaged vertical and horizontal SSM/I brightness temperatures. Key to this success is the realization that near-simultaneous passive microwave data, when collected from different viewing directions, contains wind direction information. The second major technological advance in passive microwave vector wind sensing is the recognition that the third, and possibly the fourth, members of the Stokes vector (i.e. the real and imaginary parts of the cross-correlation between the vertical and horizontal electric field components) are sensitive to wind direction [6]. In contrast with scatterometers, the combination of the vertical and horizontal brightness temperatures and the third Stoke parameter are potentially capable of retrieving an unambiguous wind direction. Finally, the third major advance in passive microwave vector-wind remote sensing is in the area of data assimilation. Atlas and colleagues [7] have adapted methodologies developed for scatterometer ambiguity removal for use in assigning wind direction estimates to SSM/I-derived wind speeds. Comparison against insitu data indicate an accuracy of ±20° to ±25°, which approaches the current operational wind direction requirement.

TECHNICAL OBJECTIVES

Before an optimal spacecraft-borne sensor design can be developed, a number of critical questions need to be addressed. For example:

1) What is the basic physical mechanism responsible for the wind direction sensitivity in the passive microwave data? Bragg scattering, geometric optics, and foam are three possibilities.

2) What are the sensitivities of the passive microwave vector wind measurement to highly-evolved sea states and two-scale composite seas? Non-locally generated long-waves are a known source of uncertainty for scatterometer wind retrievals. To what extent are passive microwave techniques also susceptible to long-wave induced uncertainties?

3) What is the range of environmental parameters under which wind direction can be measured? How does rain, water vapor, temperature, salinity, etc. affect the measurement of wind direction?

4) Does robust vector wind measurement require that the ocean surface be observed near-simultaneously from multiple directions (e.g. fore-aft scanning) or is the addition of a polarimetric channel sufficient for wind direction measurement?

5) What is the optimal incidence angle for measuring the vector wind field using passive microwave radiometers? The current operational SSM/I scans at an angle of 53°. Should this incidence angle be adopted, or is there an alternative incidence angle that would result in improved system performance?

6) What are the optimal frequencies for observing wind direction variations? Preliminary results indicate that 19 and 37 GHz sensors are both capable of measuring wind direction during periods of moderate winds. Is this a robust result? Can lower frequency (e.g. ~10 GHz) radiometers extend the range of valid wind speed and direction sensing to higher wind speed regimes and regions of more adverse environmental conditions?

7) Can a radiometer with sufficient stability be designed to reliably measure the small brightness temperature variations associated with wind direction? What is the optimum hardware implementation for measuring the Stokes vector with the required accuracy?

8) What does a preliminary wind direction retrieval algorithm look like? What wind direction ambiguities exist in the data and what are the best methods of ameliorating their effects?

9) How do we assimilate high-resolution, asynoptic, wind vectors into atmospheric numerical models so as to produce improved weather forecasts and analyses.

To address these questions and explore the limits of passive microwave vector wind remote sensing, the All-weather, Earth-observing, Ocean, Land, Ice Sensor (AEOLIS) program was established [3]. This program consists of laboratory and theoretical studies augmented by analysis of existing space-based data sets and an aggressive aircraft instrument development program.

FUTURE PLANS

Data collected by instrumented aircraft are critical for addressing many of these questions. Aircraft flights during 1996 will take place in the Gulf of Mexico. Plans are still evolving for this field program, but the intent is to acquire radiometer data under poorly understood low wind speed regimes. *In situ* wind vector data for these flights will be acquired from the NOAA operational meteorological buoys

Flights during 1997 will be coordinated with the post-launch validation campaigns for NSCAT, which will be launched on ADEOS in August 1996 (Fig. 2). These multi-radiometer aircraft flights are nominally planned for January in the Labrador Sea to provide radiometer data during high wind events with highly evolved sea states (Question 2). *In situ* data for this experiment will consist of a moored meteorological buoy, drifting pressure, temperature, and wind speed sensors, and detailed, high-resolution atmospheric numerical model analyses. These *in situ* measurements are being collected under the auspices of the Office of Naval Research, Deep Convection Accelerated Research Initiative, and the NASA NSCAT calibration-validation program.

SPACECRAFT DEMONSTRATION OPPORTUNITIES

Several national spacecraft programs are under development that represent potential opportunities to test passive microwave remote sensing of ocean surface vector winds. The NASA New Millennium Program (NMP) has been announced. It focuses on technology development and therefore, is a prime candidate for the development of a microwave, vector wind sensor. The NASA Earth System Science Pathfinder (ESSP) program will be announced later this summer and is chartered with providing low-cost missions focused on high priority Earth system science research. Again, a passive microwave wind sensor would fit comfortably within this program and would fill critical research and operational needs. Within the Department of Defense, the Advanced Technology Demonstration (ATD) program and the Space Test Program (STP) also represent viable avenues for developing a spacecraft-borne demonstration of this technology.

CONCLUSIONS

A spacecraft-borne demonstration of this exciting new microwave technology is justified and should be undertaken before the end of this decade [3]. Furthermore, it should overlap in time with active microwave sensors to allow the results from the two sensors to be compared. Research completed to date [3] suggest that these next generation radiometers should include:

1) a) newly developed polarimetric circuitry and b) scan techniques that permit the same footprint on the ocean surface to be viewed near-simultaneously from at least two different directions. Both of these modifications add information that is currently unavailable from the SSM/I, information that is essential for an improved signal-to-noise ratio for wind direction retrievals.

2) Research with aircraft and satellite data further indicate that future sensors should scan at incidence angles between 50° and 65° to insure adequate spatial coverage without compromising radiometer wind direction sensitivity (i.e. maintaining a strong signal-to-noise ratio).

3) Research also shows that the sensor should include two polarimetric radiometers with frequencies in the 18 to 37 GHz range, and an ~22 GHz non-polarimetric radiometer. This will permit wind speed and direction to be retrieved and to correct these retrievals for atmospheric moisture effects.

4) The data processing system should build on the long-term investment in civilian and military computer weather model development by merging the satellite data with computer-generated wind products using data assimilation techniques.

REFERENCES

[1] Etkin, V.S., M.D. Raev, M.G. Bulatov, Yu.A. Militsky, A.V. Smirnov, V.Yu. Raizer, Yu.A.Trokhimovsky, V.G. Irisov, A.V. Kuzmin, K.Ts. Litovchenko, E.A. Bespalova, E.I. Skvortsov: M.N. Pospelov, and A.I. Smirnov, *Radiohydrophysical Aerospace Research of Ocean, Report-1749*, Academy of Sciences, USSR, Space Research Institute, 1991.

[2] Wentz, F. J., "Measurement of oceanic wind vectors using satellite microwave radiometers", IEEE Trans. Geosci. Remote Sensing, Vol. 30, pp. 960-972, 1992.

[3] Van Woert, M.L.et al., "Ocean Winds from Space...the Next Generation", Office of Naval Research, Report No. 32296-13, Arlington, VA 58 pp., 1996.

[4] Patzert, W. and M. L. Van Woert, "Ocean and land space missions during 1990 & beyond", unpublished manuscript, Jet Propulsion Laboratory, Pasadena, CA, 1996.

[5] Naderi, F.M., M.H. Freilich, and D.G. Long, "Spaceborne Radar Measurement of Wind Velocity Over the Ocean -- An Overview of the NSCAT Scatterometer System", Proceedings of the IEEE, Vol. 79, pp. 850-866, 1991.

[6] Yueh, S. H., R. Kwok, F. K. Li, S. V. Nghiem, W. J. Wilson, and J. A. Kong, "Polarimetric passive remote sensing of ocean wind vectors", Radio Science, pp. 799-814, July-August, 1994.

[7] Atlas, R., S. C. Bloom, R. N. Hoffman, J. V. Ardizzone, and G. Brin, "Space-Based Surface Wind Vectors to Aid Understanding of Air-Sea Interactions", EOS, Trans. Amer. Geophys. Un., Vol. 72, pp. 201-208, 1991.

Polarimetric Scanning Radiometer for Airborne Microwave Imaging Studies

Jeffrey R. Piepmeier and A. J. Gasiewski
School of Electrical and Computer Engineering
Georgia Institute of Technology, Atlanta, GA 30332-0250
(404) 894-2984; (404) 894-2934; FAX (404) 894-4641
gt2930b@prism.gatech.edu ; ag14@prism.gatech.edu

Abstract – A multiband microwave polarimetric scanning radiometer (PSR) has been constructed for airborne observations from the NASA DC-8 airborne platform. The primary application of the PSR is the development of optimal spaceborne hardware configurations and retrieval algorithms for passive wind-vector sensing over the ocean surface. Four radiometers, operating at 10.7, 18.7, 37, and 89 GHz, each measure the first three modifed Stokes' parameters (T_v, T_h, and T_U). A gimballed mechanism allows observations at any incident angle within a cone of $\sim 70^o$ half-angle around nadir. The PSR's four radiometers and two-axis scanning capability will provide unique polarimetric data for microwave emission studies of both ocean and land surfaces, as well as atmospheric clouds and precipitation.

1. INTRODUCTION

Airborne remote sensing instruments can provide critical data needed for spaceborne sensor and retrieval algorithm development. Given the recent mandates for low-cost Earth probes, airborne measurements have become all the more important to such development. Indeed, for only a small fraction of the cost of a comparable spaceborne system, an airborne sensor can provide a wealth of data for determining the optimal configuration of spaceborne hardware and geophysical estimation algorithms. We describe here a new instrument for passsive microwave remote sensing from airborne platforms which provides several unique capabilities. The Polarimetric Scanning Radiometer (PSR) was developed to provide wideband spectral coverage with tri-polarimetric (three Stokes' parameter) capability using a variety of scan modes. The primary application of the PSR is the development of optimal hardware configurations and retrieval algorithms for passive wind-vector sensing over the ocean surface. Additional applications include high-resolution polarimetric imaging of clouds, convective precipitation, sea ice, and (to a lesser degree) soil moisture.

2. INSTRUMENT DESCRIPTION

The PSR consists of four gimbal-mounted radiometers operating at 10.7, 18.7, 37, and 89 GHz (Figure 1). Each radiometer measures the first three modified Stokes' parameters ($T_v = \langle |E_v|^2 \rangle$, $T_h = \langle |E_h|^2 \rangle$, and $T_U = 2Re\langle E_v E_h^* \rangle$). Analog detection hardware is used to measure the orthogonal brightness temperatures, T_v and T_h. A recently developed three-level digital correlator operating at 1 GS/s has been implemented for the measurement of T_U. This combination of receiver/detector technology allows precise calibration using only two (hot and cold) non-polarized calibration standards.

A dual-band feedhorn antenna with integrated lens provides 3-dB beamwidths of 8^o and 2.3^o at 10.7 and 37 GHz, respectively. The antenna uses a corrugated scalar feedhorn along with a grooved rexolite lens. Orthomode couplers are used to obtain the orthogonally-polarized signals. Two similar single-band lens/feedhorn antennas operating at 18.7 and 89 GHz have 3-dB beamwidths of 8^o and 2.3^o, respectively. These beamwidths correspond to nadir spot sizes from 200 to 700 meters when operated at a nominal altitude of 5 km. Polarization isolation within the principal planes is typically better than 30 dB. While conventional double sideband superheterodyne radiometers are used for the 37 and 89 GHz channels, single sideband receivers with HEMT front-end amplifiers are used for the 10.7 and 18.7 GHz channels. Other important radiometric specifications are provided in Table 1. The block diagram for the typical PSR radiometer is shown in Figure 2.

The digital correlators are comprised of three basic components: (1) high-speed analog-to-digital converters (ADC), (2) three-level multipliers, and (3) ripple accumulators. The baseband radiometer signals are sampled and quantitized into three levels at 10^9 samples per second. Following discretization, the signal samples are multiplied and the resulting products are accumulated in a 24-bit ripple counter. The accumulated value is converted into an estimated analog correlation coefficient using methods presented in [1]. With the appropriate threshold levels, the three level correlator achieves a sensitivity of ~ 0.81 relative to a perfect analog correlator [2].

The correlators use discrete high-speed ECL components to achieve a fast sampling rate and wide bandwidth. The high-speed ECL signals exhibit transition times of

This work was supported by ONR grant N00014-95-1-0426, NASA grant NAGW 4191, and the Georgia Institute of Technology.

0-7803-3068-4/96$5.00©1996 IEEE

$\lesssim$ 250 ps; therefore, the digital signals have spectral content $\gtrsim$ 4 GHz. The circuit is fabricated on low-loss woven PTFE double-sided copper-clad circuit board. All high-speed components (both passive and active) are surface mount devices. Microstrip transmission lines with terminating resistors form signal interconnections. The use of such microwave digital design techniques eliminates ringing and minimizes transition time, thus maximizing the correlator bandwidth. When sampled at the Nyquist rate, each correlator measures an IF band of width 500 MHz. The use of several correlators along with IF subband splitting hardware provides a total IF channel bandwidth equal to a multiple of the bandwidth for a single correlator.

The PSR gimbal structure allows the radiometer antennas to be scanned in-flight using two independent degrees of freedom (azimuth and elevation). The mechanism permits a number of scanning modes, including conical, cross-track, and spot-light modes. These scan modes may include any observation angle within a cone of $\sim 70^o$ half-angle around nadir. (A fence is located in front of the instrument to reduce wind loading; this fence limits the direct forward view to $\sim 53^o$ from nadir.) A programmable controller operates two sealed, low-temperature stepper motors with position feedback obtained using two 12-bit optical encoders providing 0.088^o pointing knowledge.

Electrical power is supplied to the instruments in the drum via slip-rings, thus allowing continuous rotation of the radiometer drum in both axes. Maximum motor torque is $\sim$ 75 N·m (100 ft·lbf), providing a minimum scan rate of one line every three seconds. Passive motor brakes are used to prevent windmilling in the event of power loss.

Calibration of the PSR is accomplished by viewing two unpolarized blackbody standards, one at ambient temperature ($\sim$ 250 K) and one heated to $\sim$ 310 K. Each standard consists of absorber material fastened to a metal heat sink and contained within a closed-cell styrofoam insulating jacket. Using the digital correlator, only two such calibration standards (hot and cold) are needed to calibrate both the total power channels (T_v and T_h) and the cross-correlating channel (T_U). Blackbody temperatures are measured at eight locations on each standard using RTD sensors embedded in the absorbing material. The scanhead drum, slip rings, and calibration loads are purged in-flight with dry nitrogen to protecting the radiometers, electronics, and other sensitive materials from water vapor and condensation.

Radiometric data is collected by a computer located within the scanning drum. This remote system communicates with the main computer via a 10-base-2 local area network. The main computer system, used for interactive experiment control and data logging, is located in the cabin of the aircraft. Temperature data from the calibration standards is stored in a RAM cache and transferred via an RS232 interface for storage by the data acquisition system. Data from the various sources are time-stamped using time generators synchronized to IRIG-B signals, thus facilitating precise temporal registration. A video camera is located within the scanhead and co-boresighted with the radiometer antennas.

3. APPLICATIONS

Dual-polarized radiometer data from the DMSP SSM/I instrument has been shown to be useful for the measurement of the oceanic wind vector [3]. Recently, the utility of T_U was experimentally observed by [4, 5]. Specifically, azimuthal brightness variations of T_U were shown to be similar in amplitude to those of T_v and T_h, but in phase quadrature. T_U appears to be relatively insensitive to unpolarized emissions from clouds. The paucity of available polarimetric data, however, has hindered the development of an optimal passive wind-vector sensor. The PSR is unique in that it is the first aircraft instrument designed to both verify and help improve passive wind vector sensing techniques applicable to spaceborne observation systems. Importantly, images of the upwelling Stokes parameters can be made over a wide microwave frequency range (X- to W-band) with channels comparable to the SSM/I, SSM/I-S, and EOS MIMR sensors, and over a wide range of surface incident angles. Thus, the conically scanned imagery from the PSR will be critical to both the developement of wind vector retrieval algorithms and the optimal configuration for a spaceborne wind vector sensor.

Since the launch of the first SSM/I in 1987, this instrument has been used to map convective precipitation rate, cloud liquid water, ice content, and integrated water vapor, along with sea surface parameters. Improvements in global equatorial coverage could be obtained using a slightly wider cone-angle than provided by the SSM/I. The requirement of global equatorial coverage at the SSM/I altitude of 833 km in turn requires a greater surface incident angle ($\sim 63^o$). Underflights of the SSM/I using the PSR will be useful in assessing the impact of such an increase in the angle of incidence on the accuracy of the above retrieved parameters. In addition, the PSR will be useful as a post-launch underflight sensor for calibration and validation purposes.

4. SUMMARY

PSR components are currently being assembled at the Georgia Institute of Technology, with initial flights being

planned for May-June, 1996. A second set of lights focussing on passive wind vector sensing is being planned for January 1997 over the Labrador Sea area. With its multispectral polarimetric measurement capabilities the PSR will provide important data necessary for the development of passive wind-vector sensing techniques. Future deployments of the PSR are being planned in conjunction with the NASA Tropical Rainfall Measurement Mission (TRMM) and with calibration/validation studies in support of the National Polar-Orbitting Operational Environmental Satellite System (NPOESS).

Acknowledgements: The authors would like to thank R. Davidson, J. Baloun, and M. Tucker of the Raytheon Corporation; C. Campbell, E. Panning, D. Kunkee, E. Thayer, and S. Sharpe of the Georgia Institute of Technology for valuable contributions to the design of the PSR; and Dr. M. Van Woert of the U.S. Office of Naval Research for his support.

REFERENCES

[1] S. R. Kulkarni and C. Heiles, "How to obtain the true correlation from a 3-level digital correlator", *The Astronomical Journal*, vol. 85, no. 10, pp. 1413–1420, October 1980.

[2] B. F. C. Cooper, "Correlators with two-bit quantization", *Aust. J. Phys.*, vol. 23, pp. 521–527, 1970.

[3] F. J. Wentz, "Measurement of oceanic wind vector using satellite microwave radiometers", *IEEE Trans. Geosci. Remote Sensing.*, vol. 30, no. 5, pp. 960–972, September 1992.

[4] S. Yueh, W. Wilson, F. Li, S. Nghiem, and W. Ricketts, "Polarimetric measurements of sea surface brightness temperatures using an aircraft K-band radiometer", *IEEE Trans. Geosci. Remote Sensing.*, vol. 33, no. 1, pp. 85–92, January 1995.

[5] A. J. Gasiewski and D. B. Kunkee, "Polarized microwave emission from water waves", *Radio Sci.*, vol. 29, no. 6, pp. 1449–1466, December 1994.

Table 1. Radiometer specifications

Band	X	Ku	K	W
Frequency (GHz)	10.4-10.8	18.4-19.0	36-38	86-92
Receiver type	SSB/HEMT	SSB/HEMT	DSB/LO	DSB/LO
IF bandwidth (MHz)	400	500	1000	2000
Receiver temp. (K)	250	350	550	800
Sensitivity (K) for 10 ms integration	0.24	0.29	0.27	0.24
3-dB beamwidth	8^o	8^o	2.3^o	2.3^o
3-dB spot size (km) at 5 km altitude:				
nadir	0.70	0.70	0.20	0.20
53^o incidence	1.1 X1.9	1.1 X1.9	0.32 X0.55	0.32 X0.55

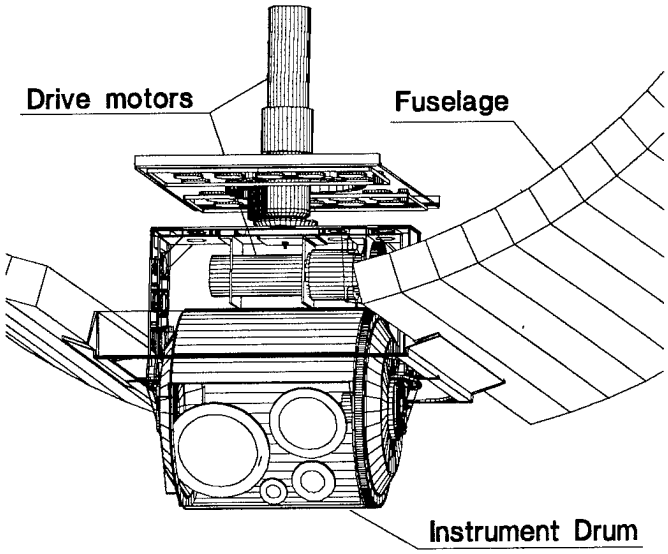


Figure 1: Three-dimensional CAD rendering of PSR illustrating instrument drum and gimbal mount. Support structure has been removed for clarity.

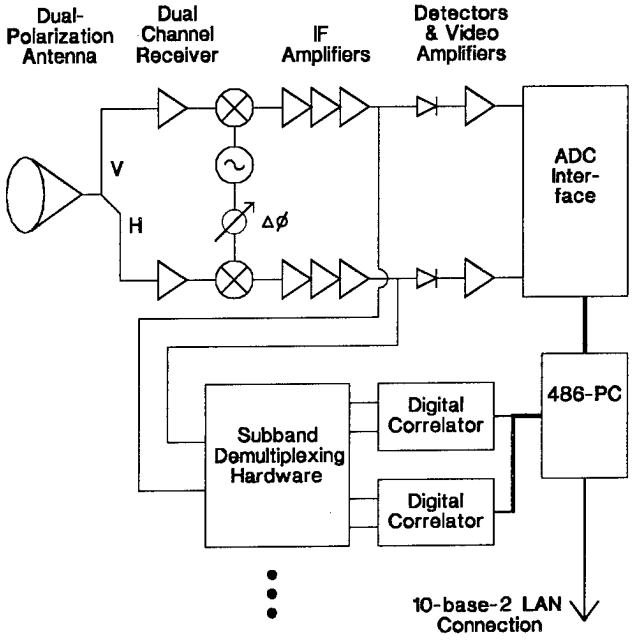


Figure 2: Block diagram of the typical PSR radiometer.

Ocean Surface Wind Direction Retrievals Using Microwave Polarimetric Radiometer Data

Peter W. Gaiser[1], Paul Chang[2] and Li Li[2]

[1] Naval Research Laboratory, Washington DC 20375-5351; (202)767-8253; (202)767-9194 FAX; gaiser@vaximg.nrl.navy.mil; Corresponding Author

[2] NOAA/NESDIS/Office of Research and Applications, Washington DC 20233; (301)763-8231; (301)763-8020 FAX; pchang@orbit.nesdis.noaa.gov

Abstract–This paper presents ocean surface wind direction retrievals using polarimetric radiometer data collected during the WINDRAD'94 experiment. The results suggest that unambiguous direction retrievals are realizable with passive microwave polarimeters.

INTRODUCTION

The global ocean surface wind speed and direction is essential information for short-term weather forecasts and warnings, climatology and oceanography studies in both the civilian and military sectors. Historically, spaceborne scatterometers such as SASS [1] aboard SeaSat and the Active Microwave Instrument (AMI) aboard the European Environmental Remote-Sensing Satellites (ERS-1 and ERS-2) have provided global ocean surface wind vector information. Passive microwave sensors, such as the Special Sensor Microwave/Imager (SSM/I), [2],[3] aboard the Defense Meteorological Satellite Platforms (DMSP), also provide information about the ocean surface winds, but the current sensor designs of SSM/I and the future SSMIS only allow for wind speed measurements.

The SSM/I and SSMIS sensors both measure the magnitude of the vertically and horizontally polarized brightness temperatures, T_V and T_H. T_V ad T_H are both even functions of the relative wind direction, which is defined as the angle between the radiometer look angle and the wind direction. Since T_V and T_H are both even functions, the wind direction cannot be determined unambiguously using the current SSM/I or SSMIS measurement scheme. Research results by [3], [4] have shown that the direction can be extracted from SSM/I data by using different sensor look angles (ascending and descending passes). Unfortunately, this method does not meet operational requirements. Recent research results [5], [6], have also demonstrated that usable direction information is obtained by measuring the correlation between T_v and T_h. Measurement of the correlation between T_v and T_h yields the third and fourth parameter of the Stokes' vector, **F**, where **F** is defined by [7]

0-7803-3068-4/96$5.00©1996 IEEE

$$\mathbf{F}=\begin{bmatrix}I\\Q\\U\\V\end{bmatrix}=\begin{bmatrix}T_v+T_h\\T_v-T_h\\T_p-T_m\\T_l-T_r\end{bmatrix}=\begin{bmatrix}\langle E_h E_h^*\rangle+\langle E_v E_v^*\rangle\\\langle E_v E_v^*\rangle-\langle E_h E_h^*\rangle\\2\,\mathrm{Re}\langle E_v E_h^*\rangle\\2\,\mathrm{Im}\langle E_v E_h^*\rangle\end{bmatrix}$$

Both U and V have been shown to behave in a similar fashion [6], [8], where U has the more robust signal. U and V are odd functions of the relative wind direction, which is opposite that of T_v and T_h. Together T_v, T_h and U provide enough information to unambiguously solve for the wind speed and direction.

Several recent aircraft experiments have investigated the ocean surface microwave scattering and emission characteristics, and how these apply to wind vector retrievals [9], [10]. The brightness temperature variations with azimuth angle are clearly evident, where the peak-to-peak brightness temperature modulation appears to vary from about 3-5 K at moderate wind speeds to less than 1 K at low wind speeds. T_v reaches its peak value at about the upwind direction, and T_h is at a maximum in the cross-wind directions. The measured brightness temperatures also appear to exhibit a similar upwind/downwind asymmetry that has been measured by scatterometers.

EXPERIMENT AND DATA ANALYSIS

The JPL WINDRAD system consists of two polarimetric radiometers operating at 19 and 37 GHz, which are two of the SSM/I frequencies. These radiometers, which were installed on the NASA DC-8 aircraft, measure T_v, T_h and U. U is measured indirectly by measuring the ±45° linear polarizations. The 19 GHz radiometer can be configured to measure V. However, this was done for only three data sets and this study does not include that data. The radiometer data were averaged over approximately 32 samples to obtain sensitivities of 0.028 Kelvin for the T_v and T_h data, and 0.04 Kelvin for the U and V data. The WINDRAD'94 experiment was jointly conducted by JPL and NRL in 1994 off the California and Oregon coast. Circles flights were flown over several NOAA National Data Buoy Center (NDBC) buoys for comparisons with in situ data. Each flight was flown at three bank angles to acquire data at 45°, 55° and 65° incidence

angles. The selected NDBC buoys reported the wind speed and direction only once per hour; several other ocean surface parameters such as sea surface temperature, near surface air temperature, and significant wave height were also reported hourly. Polarimetric radiometer data was collected at wind speeds from 2 m/s to 10 m/s under clear and cloudy skies.

Fig 1. plots T_v, T_h and U at 19 and 37 GHz measured at 55° incidence as a function of relative wind direction to illustrate the typical azimuth modulation observed in the WINDRAD'94 data. These measurements are consistent with other experimental data and theoretical predictions [3], [10]. For example, T_v reaches a maximum at the upwind direction, and T_h reaches a maximum in the crosswind directions. U displays maximums/minimums around 45° azimuth.

RESULTS

Several wind vector retrieval algorithms were developed using a neural network approach with the WINDRAD'94 data set. The retrieval algorithms were evaluated as a function of frequency, incidence angle and in situ data. The scatter plots in Figs. 2,3,4 and 5 show the direction retrieval performance of the one-look neural network algorithm using T_v, T_h and U at 19 and 37 GHz measured at 45°, 55° and 65° incidence.

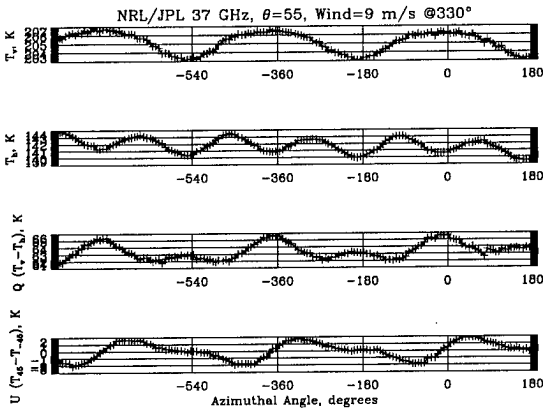


Fig 1. Sample 37 GHz polarimetric radiometer data set at 55°.

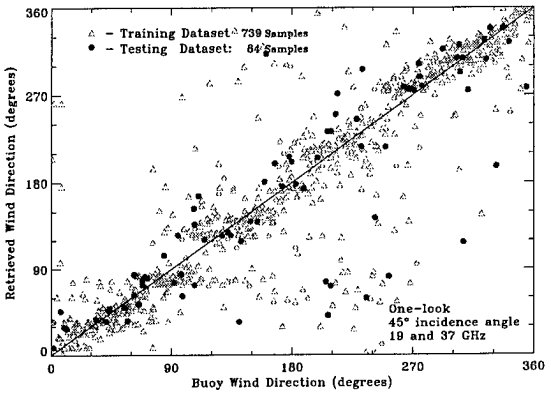


Fig. 2. Single-look retrieval of wind direction at 45° with wind speeds of 3-10 m/s..

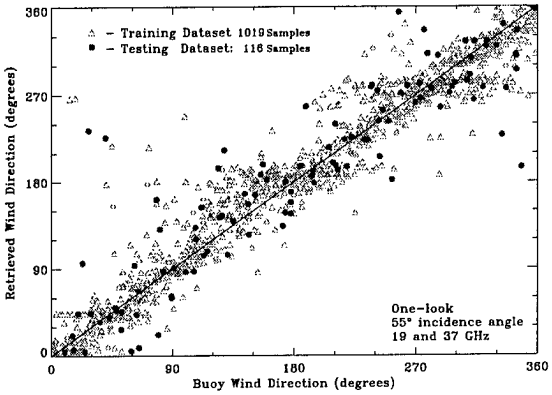


Fig. 3. Single-look retrieval of wind direction at 55° with wind speeds of 3-10 m/s.

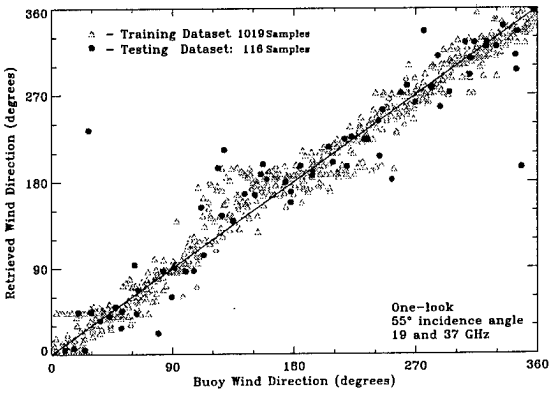


Fig. 4. Single-look retrieval of wind direction at 55° with wind speeds of 6-10 m/s.

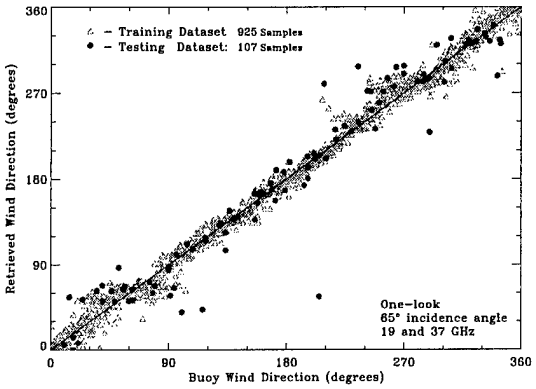


Fig. 5. Single-look retrieval of wind direction at 65° with wind speeds of 6-10 m/s.

Note that much of the scatter or error in the direction retrieval is due to the lower wind speed data (< 3 m/s), which is seen in Figs. 3 and 4 where wind direction retrievals are plotted for the same retrieval algorithm with and without the low wind speed data, respectively.

The RMS errors for the wind retrievals are listed in Table 1. Please note that the RMS errors are not meaningful as an absolute measure of retrieval accuracy since the WINDRAD'94 data set is very limited, but rather the listed errors are to be used as an aid in comparing the different measurement configurations considered in this study using the WINDRAD'94 data set.

The NDBC buoys also reported other in situ parameters which included sea surface temperature, air temperature and significant wave height. Including these parameters in the neural network algorithm resulted in marginal wind retrieval improvements which can most notably be seen at the lower wind speeds.

CONCLUSIONS AND RECOMMENDATIONS

This study has demonstrated that unambiguous wind direction retrievals are possible using a passive sensor. However, several issues remain that warrant further study to assure that user requirements will be fully satisfied. In particular, the WINDRAD'94 lacks high wind speed data (>15 m/s) and data in presence of varying concentrations of water vapor and cloud liquid water. Knowledge of the wind retrieval performance under these limiting conditions is essential to gauge the full utility of these data to the operational community.

REFERENCES

[1] W. L. Grantham, E.M. Bracalente, W. L. Jones, and J.W. Johnson, "The SeaSat-A satellite scatterometer", *IEEE J. Oceanic Eng.*, vol. 2, no. 2, 1977.

[2] J.P. Hollinger, "DMSP Special Sensor Microwave/Imager calibration/validation," Tech. Rep., Naval Research Laboratory, 1989.

[3] F.J. Wentz, "Measurement of oceanic wind vector using satellite microwave radiometers", *IEEE Trans. Geosci. and Rem. Sens.*, vol 30, no 5, 1992.

[4] M. Van Woert et al., "All -Weather Earth-Observing Ocean, Land and Ice Sensor Report", Tech. Rep., in press, 1996.

[5] L. Tsang, "Polarimetric passive remote sensing of random discrete scatterers and rough surfaces", *J. Electromag. Waves App.*, no. 5, pp. 41-59, 1991.

[6] S.H. Yueh et al., "Polarimetric thermal emission from periodic water surfaces", *Radio Sci.*, no. 29(1), 1994.

[7] L. Tsang, J.A. Kong and R.H. Shin, *Theory of Microwave Remote Sensing*, John Wiley & Sons, 1985.

[8] L.Li, C.H. Chan, and L.Tsang, "Numerical simulation of conical diffractions of tapered electromagnetic wave from random surfaces and applications to passive remote sensing", *Radio Sci.*, no. 29(3), 1994.

[9] V.S. Etkin et al., " Radiophysical aerospace research of ocean", Rep-Pr-1749, 1991.

[10] S.H. Yueh et al., "Polarimetric measurements of sea surface brightness temperatures using an aircraft K-band radiometer", *IEEE Trans. Geosci. and Rem. Sens.*, no. 33(1), 1995.

Table 1. RMS Error of Wind Direction Retrievals

Incidence Angle	19/37 GHz (u=3-10 m/s)	19/37 GHz (u=6-10 m/s)	19/37 with Buoy Data
45°	57.7°	29.9°	—
55°	42.3°	35.9°	—
65°	—	25.5°	21.9°

Polarimetric Observation of Ocean Internal Waves by Microwave Radiometers during the Coastal Ocean Probing Experiment

Vladimir G. Irisov
Cooperative Institute for Research in Environmental Sciences (CIRES),
University of Colorado at Boulder
NOAA/ERL/Environmental Technology Laboratory
325 Broadway, Boulder CO 80303-3328
ph. (303)-497-6549, fax (303)-497-3577, e-mail: virisov@etl.noaa.gov

Yuri G. Trokhimovski
National Research Council Resident Associate
NOAA/ERL/Environmental Technology Laboratory
325 Broadway, Boulder CO 80303-3328

Abstract -- One of the main objectives of the Coastal Ocean Probing Experiment was to observe internal wave (IW) manifestations by using microwave radiometers mounted on a blimp. IW parameters were simultaneously measured directly by R/V *FLIP* and by Ka-band and X-band doppler radar from the shore. Comparison with *in situ* data permits us to determine IW speed and the phase of surface roughness modulation with respect to near-surface currents.

INTRODUCTION

The variation of the brightness temperature measured by microwave radiometers is related mainly to a change in the sea surface roughness. An internal wave (IW) in the ocean produces a variable current near the surface which modulates the surface wave spectrum. This is the reason for the sensitivity of microwave radiometers and radars to internal ocean processes. Nevertheless, despite an intensive study of this phenomenon [1-3] some aspects, important for the understanding of air-sea interaction, are not clear.

INTERNAL WAVE OBSERVATIONS

The Coastal Ocean Probing Experiment (COPE) was conducted off the Oregon coast during September-October 1995. An airship (blimp) was used as a platform for a microwave dual-frequency radiometer (23 GHz (v.p.) and 31 GHz (h.p.)), a microwave polarimeter (37 GHz), two IR radiometers and a video camera, all of which were installed on the port side of the blimp. The sensitivity was about 0.1 K at 1 s. integration time for the dual-frequency radiometer and 0.05 K at 1 s. integration time for the polarimeter. The antenna half-power beam widths were about 3.6° and 6° for the dual-frequency and polarimetric radiometers, respectively. Along with the ETL instrumentation, an X-band radar, altimeter, and IR imager operated by Applied Physics Laboratory, University of Washington, were installed on the blimp. The air and sea temperatures, wind speed and direction, momentum fluxes, ocean currents, etc. were measured from the R/V *FLIP* at a fixed point about 24 km from the shoreline. The depth at the *FLIP* site was about 150 m. Simultaneously, IW manifestations were observed by ETL Ka-band and X-band doppler radars at vertical, horizontal, and cross polarizations from the shore. The area is characterized by strong IW, generated more or less periodically by a tide on the edge of the shelf and propagating mainly toward the shore. Sometimes a packet of IW can be clearly seen as regular strips of rough and smooth water on the ocean surface.

One of the strongest waves was registered on September 25, 1995. Fig. 1 shows the trajectory of the blimp flight, and the square denotes the position of R/V *FLIP*. Arrows indicate wind direction and the directions of the blimp flight. The wind was about 5 m/s along the internal waves that propagated from the west to the east. Several passes were made across the IW. Intersections of the slick areas are indicated by the sequences of crosses and diamonds. The local reduction of the sea-surface roughness leads to a decrease of the brightness temperature at all viewing angles for horizontal polarization and at the angles less than 55° from nadir for vertical polarization, so that the marked points correspond to minima of the microwave brightness temperature.

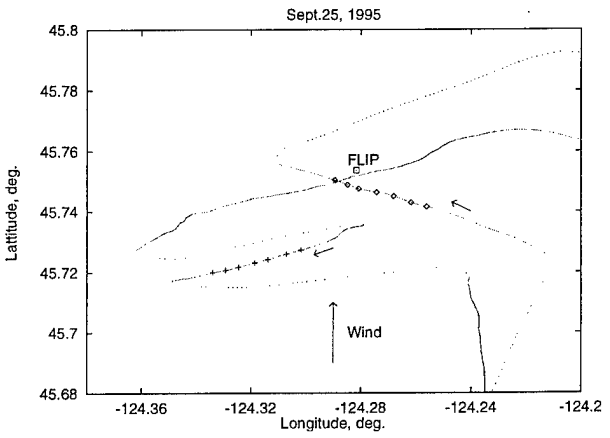
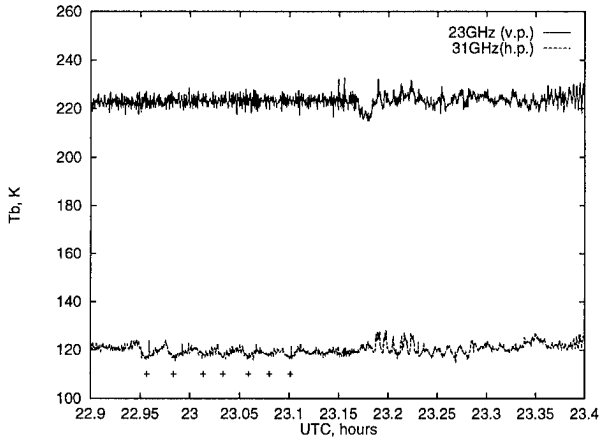
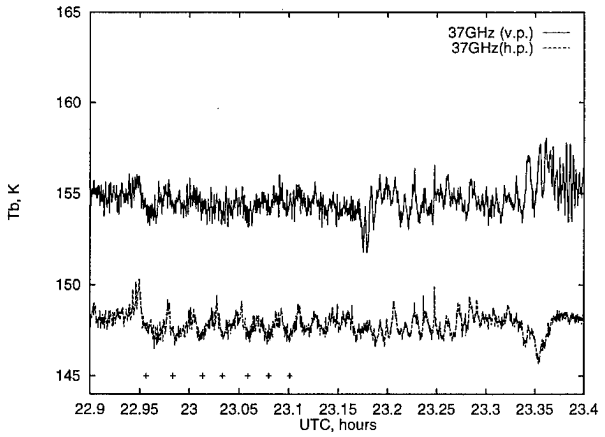


Fig.1. The blimp flight trajectory, wind direction and *FLIP* position during IW observation.

0-7803-3068-4/96$5.00©1996 IEEE

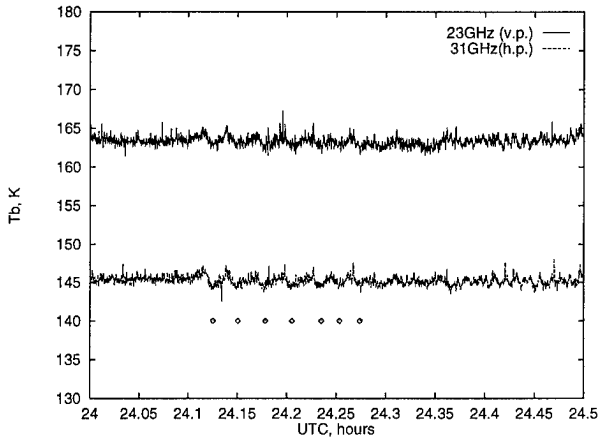


a)

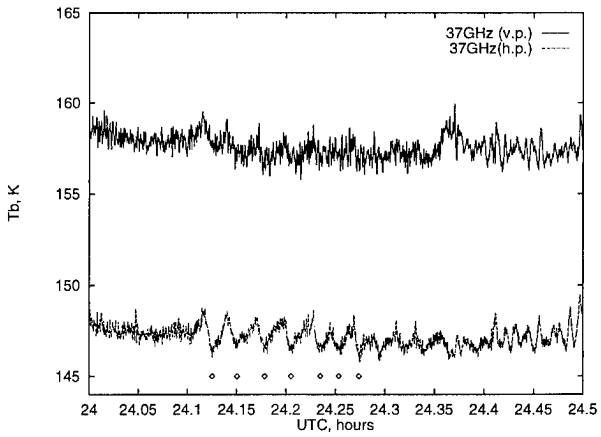


b)

Fig.2. The brightness temperature variations related with modulation of the surface roughness by IW, measured by the dual-frequency radiometer (a) and by the polarimeter (b).



a)



b)

Fig.3. The same as Fig.2 during another cross of IW packet. Diamonds correspond to the points on Fig.1.

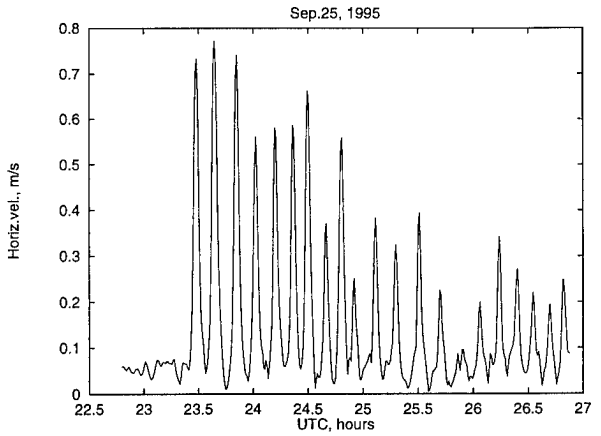


Fig.4. Horizontal current measured form the *FLIP* near-surface.

The radiometric signal variations related to IW surface manifestations are presented in Fig. 2. Fig. 2a shows the brightness temperature measured by the dual-frequency radiometer and Fig. 2b the brightness temperature measured by the 37 GHz polarimeter at vertical and horizontal polarizations. Observation angles were about 62° for the dual-frequency radiometer and 17° for the polarimeter. Here, the crosses indicate the slick positions, which are shown in Fig.1.

During another pass the same IW were registered in a different position (Fig. 1). In this case the observation angle was 16° for the 23/31 GHz radiometer and 22° for the 37 GHz radiometer (Fig. 3). From these data it is easy to estimate the speed of IW as about 0.82 m/s. This is a very large value, so the waves are probably strongly non-linear solitons. It is interesting that during the first pass the 23 GHz channel at vertical polarization (Fig. 2a) almost does not reveal any variations, contrary to all other channels, but during the second pass (Fig.3a) it shows the same dependencies as the others. We attribute it to insensitivity of the microwave radiation at vertical polarization to the surface roughness at observation angles about 55° from nadir [4].

Simultaneously with the blimp observations the IW parameters were measured directly from the *FLIP*. Fig. 4 shows

the value of the horizontal current near the sea surface versus time. Note again an extremely high amplitude of the variations which is also an indication of strong non-linearity of the waves.

Finally, using the fact that blimp and *FLIP* measurements are close in time and space, we made an attempt to relate surface roughness modulations with the phase of the currents. Our estimation shows that the slick areas, marked on Fig. 1 - 3 as crosses and diamonds, are very close to the maxima of the horizontal currents. Very probably, the relative position of the currents and surface roughness modulation strongly depends upon the mutual orientation of the wind direction and propagation of the waves.

CONCLUSION

The COPE experiment is characterized by very detailed *in situ* measurements of the main physical parameters of the atmosphere and ocean. Unfortunately, the case when wind blows along the IW is more difficult for modeling than the two-dimensional problem. Nevertheless, the analysis of well calibrated radiometric and radar data along with accurate *in situ* measurements are very important for understanding the IW evolution, surface wave modulation, and interaction between the atmosphere and the upper ocean.

ACKNOWLEDGMENTS

This work was supported by Advanced Sensor Applications Program, U.S. Department of Defense.

REFERENCES

[1] J.R.Apel, J.R.Holbrook, J.Tsai and A.K.Liu, "The Sulu Sea Internal Soliton Experiment," *J. Phys. Oceanogr.*, **15**, pp.1625-1651, 1985.

[2] G.C.Hogan, R.D.Chapman, G.Watson and D.R.Thompson, "Observations of Ship-Generated Internal Waves in SAR Images from Loch Linnhe, Scotland, and Comparison with Theory and *In Situ* Internal Wave Measurements," *IEEE Trans. Geosci. Remote Sensing,* (in press).

[3] Yu.G.Trokhimovsky, V.Yakovlev, R.D.Chapman and D.R.Thompson, "The Coherence of Wind and Radar Data Obtained during the Joint US-Russia Internal Wave Experiment," *IGARS Symp. Proc.*, Pasadena CA, pp.802-804, 1994.

[4] Y.G.Trokhimovski and V.G.Irisov, "Wind speed and direction measurement using microwave polarimetric radiometers", NOAA Tech. Memo. ERL ETL-250, 1995, 35 p.

BROADBAND PHENOMENA IN OCEANIC PASSIVE WIND DIRECTION SIGNATURES: THE SENSITIVITY TO WAVE ASYMMETRY, FOAM, AND ATMOSPHERIC PROFILE

D. B. Kunkee

The Aerospace Coporation
PO Box 92957 - M4-927
Los Angeles, CA 90009-2957
Tel: (404) 336-1125, Fax: (310) 336-6914
email: David.Kunkee@aero.org

A. J. Gasiewski

Georgia Institute of Technology
School of Electrical Engineering
Atlanta, GA 30332-0250
Tel: (404) 894-2934, Fax: (404) 894-4641
email: ag14@prism.gatech.edu

ABSTRACT

An inherently broadband asymmetric-wave geometrical optics (AWGO) model of the upwelling thermal radiation over the ocean was used to investigate the contributions of wave asymmetry, foam, and the downwelling (background) radiation profile to the passive oceanic wind direction signature. Signatures at K- and K_a-band (19 and 37 GHz) were calculated using a Monte-Carlo ocean surface simulation. The investigation showed that at angles near the SSM/I observing angle, T_h and T_U are sensitive but T_v is insensitive to wave asymmetry. However, T_v was found to be sensitive and T_U insensitive to the placement of foam on the waves. Sensitivity to the background radiation profile was investigated by varying the atmospheric temperature and humidity profiles. For changes of $\gtrsim 33\%$ in atmospheric water vapor from a global mean value, only slight variation (~ 0.2 K) in the upwind/downwind brightness temperature difference for either polarization resulted.

1. INTRODUCTION

A potentially less expensive alternative to measuring wind-direction by scatterometry is to use passive radiometry. The optimal design of a spaceborne passive wind-vector sensor, however, would benefit from a better understanding of the physical nature of the upwelling brightness temperature signature than has yet been presented. In this paper we use an Asymmetric-Wave Geometrical Optics (AWGO) model to investigate anisotropic broadband ocean surface phenomena. The model incorporates two physical mechanisms that are particularly relevant to the passive problem: ocean foam and gravity-wave anisotropy. The model is based on Monte Carlo ocean surface simulations and a broadband geometrical optics (GO) radiation model for the upwelling Stokes parameters. The combined GO and MC model is corroborated by the observed SSM/I brightness temperature signatures at 19 and 37 GHz over the open ocean for moderate sea states [1]. Details about the model formulation can be found in Gasiewski and Kunkee [2, 3].

Using the AWGO model, perturbations to the amounts of ocean foam and wave asymmetry show that both of these features have a major impact on the upwelling wind direction signatures. Unfortunately the amount of ocean-wave asymmetry at wavelengths applicable to a GO emission model is somewhat poorly characterized by existing statistical ocean models. Although the total foam coverage as a function of wind speed is well established (e.g. [4]), there is a paucity of information on the distribution of foam over gravity (long) ocean waves. Therefore, it is useful to investigate the sensitivities of the upwelling polarimetric signatures to both ocean-wave asymmetry and foam distribution for future model refinement and airborne studies.

The upwelling brightness temperature over the open ocean consists of surface emission and downwelling energy that is reflected into the observation direction. Indeed, previous studies of emission from wave-covered water surfaces at W-band have shown the importance of the background radiation profile in modelling upwelling brightness temperature anisotropies [2]. The level of downwelling radiation at 19 and 37 GHz (K- and K_a-band) is lower compared to W-band, however, this downwelling radiation remains important at these lower frequencies. Although no seasonal or latitudinal variation of observed passive signatures has yet to be shown, any sensitivity to the downwelling component, and hence, the atmospheric water vapor profile suggested by the AWGO model may be useful for future studies.

2. GEOMETRICAL OPTICS MODEL

The use of a GO emission model is supported by consideration of the applicability of the Kirchoff approximation (KA) to water wave scattering. The widely accepted criterion of Beckmann and Spizzichino, [5] bounds the minimum radius of curvature of the surface; the region of validity is given as $2kr_c\cos\theta \gg 1$ where r_c is the minimum local radius of curvature of the surface, k is the electrical wavenumber, and θ is the local angle of incidence.

The Beckman criterion can be applied to a wind-driven ocean surface by calculating the root-mean-square (rms) curvature $\sigma_X(w) = \sqrt{\langle X^2 \rangle}$ from the curvature spectrum $X(\overline{K}, w)$ by:

$$\sigma_X(w) = \left[\int_{-\infty}^{\infty} \int_{-\infty}^{\infty} X(\overline{K}, w) d^2\overline{K} \right]^{1/2} \quad (1)$$

where $\overline{K}$ is the surface wave vector ($|\overline{K}| = K$), $X = \nabla^2 z(x, y)$

[1]This work was supported by NASA grants NAG 5-1490 and NAGW 4191.

0-7803-3068-4/96$5.00©1996 IEEE

is the surface curvature, and $z(x, y)$ is the surface height function. Calculations of $\sigma_X(w)$ using the curvature spectrum given by Apel, [6] are shown in Fig. 1 (bold solid line, uppermost curve) for wind speeds $0 \leq w \leq 24$ m/sec. Included are curves showing the electromagnetic frequency f_B at which $2k\cos\theta_s = 3\sigma_X$ for various observation angles θ_s, that is, $f_B = (3\pi/4)c\sigma_X/\cos\theta_s$ where c is the velocity of light. At this frequency the Beckman criterion using $r_c \geq \sigma_X^{-1}$ holds by at least a factor of three. For a surface for which the curvature is a Gaussian-distributed random variable this condition will hold over 68.3% of the surface. Alternately, we may interpret f_B as the frequency at which the Beckman criterion will be satisfied with equality, but over more than 99.7% of the surface. Under these conditions the KA (and hence, GO) is applicable. Using Fig. 1 it can be seen that such GO conditions occur for all wind speeds considered ($0 \leq w \leq 24$ m/sec) for the 89-GHz SSM/I channel ($\theta_s = 53.1°$) and nearly so for the 37-GHz SSM/I channel. (GO conditions occur for the SSM/I 37-GHz channel for all wind speeds below ~ 12 m/sec.) For the 19-GHz SSM/I channel the Beckman criterion is satisfied with equality over $\sim 80\%$ of the surface. In this case, the theoretical justification for GO modelling of the SSM/I 19 GHz channels (especially at high wind speeds) is marginal. However, at reduced viewing angles (e.g. 30°) GO is applicable at 19 GHz.

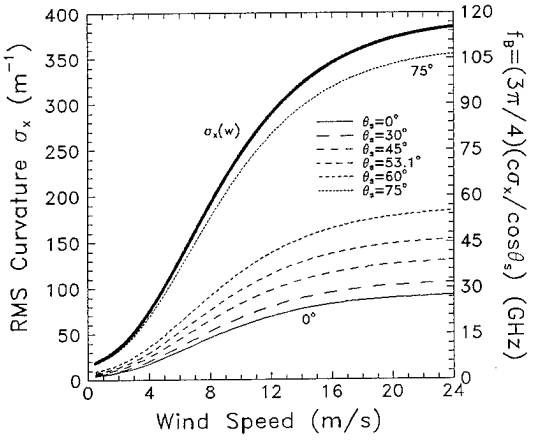


Figure 1. The RMS curvature of a wind-driven ocean surface versus wind speed (in bold). The right-hand ordinate shows the frequency at which $2k(\cos\theta_s)/\sigma_X(w) = 3$.

3. SENSITIVITY TO WAVE ASYMMETRY AND FOAM

The AWGO model was used to determine the sensitivity of the first three Stokes parameters, (T_v, T_h and T_U) to wave asymmetry and foam. Azimuthal wind-direction signatures at 19 GHz and an observation angle of 30° were calculated from simulated wind-driven sea surfaces under the following conditions (Fig. 2): (1) all foam concentrated on the leeward side of breaking waves and (2) foam distributed over the leeward and windward slopes of the breaking waves. The total foam coverage was the same in both studies. Similarly, calculations were performed for five levels of wave asymmetry; starting with a symmetric wave-train (no asymmetry) to the full value of asymmetry prescribed by Cox and Munk [7]. The atmospheric profile assumed 50% surface relative humidity (SRH) and a 2 km scale height with a temperature profile interpreted to 34°N. latitude in July.

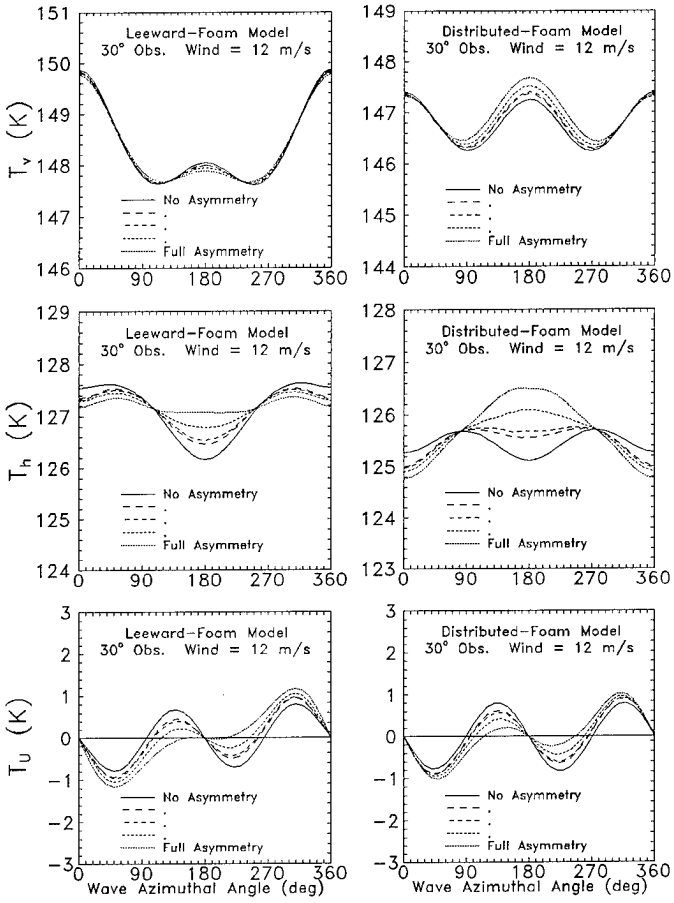


Figure 2. Polarimetric brightness temperature vs. wave angle at 19 GHz. Five level of asymmetry and two-models for incorporating ocean foam were used to indicate the sensitivity of the wind-direction signatures to wave-asymmetry and foam.

The above brightness temperature signatures can be described by using the azimuthal Fourier amplitudes, $B_{\alpha n}$ and phases, $\Phi_{\alpha n}$, defined by:

$$T_{\alpha n}(\theta_s) = \sum_{n=0}^{\infty} B_{\alpha n}(\theta_s)\cos\left[n\phi_s + \Phi_{\alpha n}(\theta_s)\right] - \langle T_\alpha(\theta_s)\rangle \quad (2)$$

where $\langle T_\alpha\rangle$ is the mean (azimuthal) brightness, α is the polarization, n is the azimuthal harmonic and ϕ_s is the azimuthal observation angle with respect to the water wave vector (wave azimuthal angle). For an upwind observation $\phi_s = 0°$.

The above sensitivity study showed that at the 30° observing angle, T_h and T_U are sensitive but T_v is relatively insensitive to wave asymmetry. The characteristics of the azimuthal variation in T_v changed only slightly when the amount of wave-asymmetry was adjusted over the full range using either foam model. However, the Fourier harmonics ($B_{\alpha n}$ of T_h and T_U were largely affected by the amount of wave asymmetry. In particular, T_U appears to be an excellent indicator of wave asymmetry due to the variation in its zero-crossing point near 90° and 270° wave azimuthal angle.

The vertically-polarized brightness temperature was found to be very sensitive to the distribution of ocean-foam on the surface. The T_v brightness temperature at $\sim 180°$ is significantly lower when the leeward-side foam model is used. Similarly, for T_h, a brightness temperature depression is also noted at $\sim 180°$ but the effect is not as great. The T_U brightness temperature was found to be very insensitive to placement of foam. This was expected due to the T_U insensitivity to baseline brightness temperatures in general (e.g. variations in T_v and T_h).

4. SENSITIVITY TO THE ATMOSPHERIC WATER VAPOR PROFILE

Due to spatial and temporal variability of the atmospheric water vapor profile, the sensitivity of the wind direction signatures to a change in the water vapor profile was investigated. In particular, the upwelling signature at $w = 8$ m/s and 53° observation was simulated using a mean global atmospheric water porfile and compared to the similar signature calculated using the U.S. standard 50% SRH profile with a temperature profile iterated to 34°N. latitude for July. The pressure and temperature profile for the mean global atmosphere was derived from the Air Research and Development Command (ARDC) model atmosphere [8]. The mean global water vapor profile was based on the annual zonal-mean cross sections of the specific humidity [9], however, the SRH was increased slightly from the suggested 77.5% to 80% (1.7 km scale height) because the relative humidity is higher, in general, over the oceans than over the land. This increase is supported by maps of the global distribution of surface specific humidity.

The differences between the above two atmospheric profiles can be summarized by the temperature and water vapor density at the surface. For the U.S. standard atmosphere in this investigation, the temperature at the surface was 301.71 K compared with 288.16 K for the mean global profile. Similarly, the water vapor densities at the surface are 15.6 g/m^3 and 10.6 g/m^3 (respectively). This has the effect of reducing the downwelling background brightness temperature at zenith from 27.18 K to 23.31 K.

The signatures calculated using each atmospheric profile are shown in Fig. 3. The reduction of atmospheric water vapor reduced the upwind/downwind asymmetry (B_{a1}) in both the T_v and T_h signatures. The effect on the peak-to-peak azimuthal variation of T_v and T_h was also small; however, the study suggests that some spatial or seasonal variation in the wind-direction signatures exist. Although no spatial or seasonal variation of the wind direction signature was noted in the SSM/I observations, the atmospheric sensitivity shown here does not appear to be large enough to indicate an inconsistency with the SSM/I observations.

5. CONCLUSION

Based on a study of the curvature spectrum of a wind-driven ocean surface, and application of the primary Beckmann criterion, the use of a GO emission model to simulate upwelling brightness temperatures over the ocean is justified at 37 GHz for wind speeds $\lesssim$12 m/s and 53° observation from nadir. At 19 GHz, and similar conditions, use of a GO model was shown to be marginal. However, when the observation angle (from nadir) is reduced, the study suggests that the GO approximation is improved.

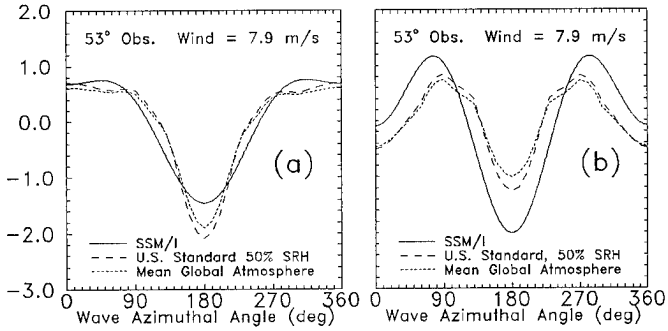


Figure 3. Monte-Carlo simulation of the 37-GHz T_v and T_h perturbations: (1) using the U.S. standard atmosphere (34° N latitude, July, and 50% SRH) and (2) the estimated mean global atmosphere over the ocean. The simulations are compared to the SSM/I observations by Wentz, [1]: (a) ΔT_v (b) ΔT_h.

The AWGO sensitivity studies suggest that at 30° observation, T_h and T_U are sensitive but T_v is less sensitive to wave asymmetry. However, T_v was found to be sensitive and T_U insensitive to the placement of foam on the waves. The study will help identify the optimum uses of T_v, T_h and T_U for remote sensing of ocean surface wind-direction and also may aid airborne studies of polarimetric signatures. Corroboration of the above results with observed wind-direction signatures is also limited by the paucity of information on the distribution of foam over wind-driven ocean waves. Although the AWGO modelled signatures are affected by the atmospheric water vapor profile, the model suggests that this dependence is not significant at the SSM/I observing angle of 53°.

6. REFERENCES

[1] Wentz, F., "Measurement of oceanic wind vector using satellite microwave radiometers," *IEEE Trans. Geosci. Remote Sensing*, 30(5), 960-972, 1992.

[2] Gasiewski, A. J., and D. B. Kunkee, "Polarized microwave emission from water waves," *Radio Sci. 29*(6), pp. 1449-66, December, 1994.

[3] Kunkee, D. B., and A. J. Gasiewski, "Simulation of passive microwave wind direction signatures over the ocean using and asymmetric-wave geometrical optics model," unpublished, February, 1996.

[4] Bondur, V. G., and E. A. Sharkov, "Statistical properties of whitecaps on a rough sea," *Oceanology, 22*(3), pp. 274-279, 1982.

[5] Beckmann, P., and A. Spizzichino, The Scattering of Electromagnetic Waves From Rough Surfaces, London: Pergamon Press, 1963.

[6] Apel, J. R., "An improved model of the ocean surface wave vector spectrum and its effect on radar backscatter," *J. Geophys. Res. 99*(C8), pp. 16269-16291, August 15, 1994.

[7] Cox, C., and W. Munk, "Measurement of the sea surface from photographs of the sun's glitter," *J. Opt. Soc. America*, 44(11), 838-850, 1954.

[8] Goody, R. M., Atmospheric Radiation: Theoretical Basis, New York: Oxford University Press, 1964.

[9] Piexoto, J. P., and A. H. Oort, Physics of Climate, pp. 278-283, New York: American Institute of Physics, 1992.

Modelling of Wind Direction Signals in Polarimetric Sea Surface Brightness Temperatures

Simon H. Yueh, William J. Wilson, and Fuk K. Li

Jet Propulsion Laboratory, MS 300-235
California Institute of Technology
4800 Oak Grove Drive, Pasadena, CA 91109, USA
Tel: 818-354-3012, Fax: 818-393-5285
E-mail: simon@malibu.jpl.nasa.gov

Abstract – A preliminary geophysical model function, relating the sea surface brightness temperatures to ocean surface wind speed and direction, was developed using the data acquired at 45°, 55°, and 65° incidence angles by Jet Propulsion Laboratory's (JPL) aircraft 19- and 37-GHz polarimetric radiometers in 1994 and 1995. Radiometric temperatures from all polarization channels under cloud-free conditions showed clear dependence on surface wind direction. When there were stratus or scattered clouds, T_v and T_h were significantly influenced by the radiation from cloud water, but the polarimetric channel U was found to be insensitive to clouds. The Fourier harmonic coefficients of the wind direction signals were derived from experimental data and related to the wind speed and direction, incidence angle and frequency. In general, all harmonic coefficients increase from low to moderate wind speeds, except the $\sin 2\phi$ component of U at 65° incidence, which peaked at low winds with a peak-to-peak amplitude of 0.6 to 1 Kelvin at about 3 m/s winds. At moderate wind speeds, 45° incidence angle exhibits larger second harmonic signals, but smaller first harmonic signals, than higher incidence angles. Wind direction signals were similar in 19 and 37 GHz channels, but the 37 GHz channel showed a slightly stronger wind direction sensitivity than the 19 GHz channel. The results suggest promising applications of passive microwave radiometers to ocean wind vector measurements.

INTRODUCTION

There has been an increasing interest in the application of passive microwave radiometers for ocean wind vector measurements [1]-[9]. Aircraft radiometer measurements performed at near normal incidence angles [1, 7], the SSM/I data at 53° incidence angle [2], and the aircraft polarimetric radiometer measurements acquired at 30° to 50° [8] have found the dependence of sea surface brightness temperature on wind direction over a large range of incidence angles. However, these experimental data are insufficient for designing a spaceborne sensor for ocean wind sensing. To obtain a better understanding of the frequency dependence, a Ka-band (37 GHz) polarimetric radiometer was built and integrated with the K-band (19 GHz) radiometer used in the 1993 WINDRAD experiments [8]. The dual-frequency system was integrated with the NASA DC-8 and flown in July-August 1994 and March-May and September 1995 over ocean buoys to obtain more extensive measurements from 45° to 65° incidence angles.

MICROWAVE POLARIMETRIC RADIOMETRY

Electromagnetic waves emitted from natural media due to random thermal motion of electric charges are in general partially polarized. To fully characterize the polarization state of a partially polarized thermal radiation requires four Stokes parameters I, Q, U, and V. I=$T_v + T_h$ represents the total radiated energy and Q=$T_v - T_h$ the polarization balance. T_v and T_h are the brightness temperatures of vertical and horizontal polarizations, while U and V characterize the correlation between these two orthogonal polarizations. A typical approach for U and V measurements is to carry out the power measurements at 45°-linear, −45°-linear, left-hand-circular, and right-hand-circular polarizations. By denoting the brightness temperature measurements at these four polarizations as T_{45}, T_{-45}, T_L, and T_R, U and V can be derived from these four brightness measurements as $U = T_{45} - T_{-45}$ and $V = T_L - T_R$.

For wind-generated sea surfaces, the surface spectrum is expected to be symmetric with respect to the wind direction (ϕ_w). Denote the azimuthal observation angle of radiometer look direction with ϕ_r and the relative azimuth angle with $\phi = \phi_w - \phi_r$. Yueh et al. [10] derived from Maxwell's equations using reflection symmetry that T_v and T_h are even functions of ϕ and U and V are odd functions of ϕ. Hence, expanded to the second harmonic of ϕ,

$$T_v \simeq T_{v0} + T_{v1}\cos\phi + T_{v2}\cos 2\phi \quad (1)$$

$$T_h \simeq T_{h0} + T_{h1}\cos\phi + T_{h2}\cos 2\phi \quad (2)$$

$$U \simeq U_1 \sin\phi + U_2 \sin 2\phi \quad (3)$$

$$V \simeq V_1 \sin\phi + V_2 \sin 2\phi \quad (4)$$

All coefficients are functions of surface wind speed, incidence angle, and frequency. There are also indications that the sea surface spectrum is influenced by the presence of large waves and the atmospheric boundary layer stability. Since sea surface brightness temperatures are influenced by the surface scattering, it is therefore possible that the harmonic coefficients are also functions of surface temperatures and significant wave height.

This work was performed under a contract with the National Aeronautics and Space Administration at the Jet Propulsion Laboratory, California Institute of Technology.

0-7803-3068-4/96$5.00©1996 IEEE

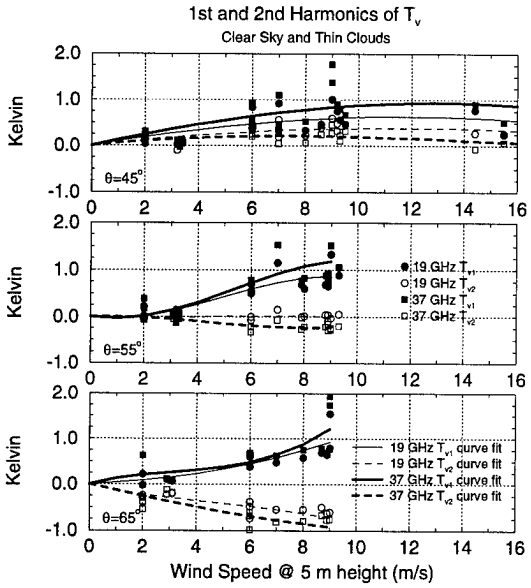


Figure 1. T_{v1} and T_{v2} from 19.35 and 37 GHz JPL wind radiometer channels versus wind speed at 5 m elevation. (a) $\theta = 45°$, (b) $\theta = 55°$, and (c) $\theta = 65°$.

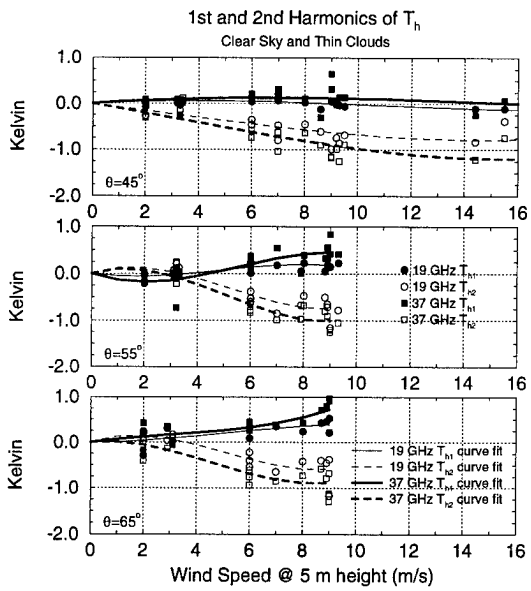


Figure 2. T_{h1} and T_{h2} from 19.35 and 37 GHz JPL wind radiometer channels versus wind speed at 5 m elevation. (a) $\theta = 45°$, (b) $\theta = 55°$, and (c) $\theta = 65°$.

PRELIMINARY GEOPHYSICAL MODEL

A dual-frequency polarimetric radiometer system operating at 19 GHz (K band) and 37 GHz (Ka band) has been built and installed on the NASA DC-8 aircraft for ocean wind measurements. This dual-frequency system was an upgrade of the 19 GHz polarimetric radiometer used in the first WINDRAD experiment in November 1993 [8], A series of aircraft flights were carried out in 1994 and 1995 to acquire polarimetric sea surface brightness temperatures with the dual-frequency polarimetric radiometer system. Circle flights were performed over the National Data Buoy Center (NDBC) moored buoys deployed off the US west coast, which provided ocean wind speed and direction measurements. A set of flights were performed near the Hurricane Juliette in September 1995, and the ground truth was obtained by the dropsonde launched from the DC-8. The K- and Ka-band antenna horns were mounted on the DC-8 windows at a fixed angle. The DC-8 was banked at three different angles to measure the data at the nominal incidence angles of 45°, 55°, and 65°, and performed circle flights to acquire data from all azimuth angles with respect to the surface wind direction. There were clear wind direction signals in all polarization channels under clear sky conditions. When there were stratus or scattered clouds, the radiation from clouds would obscure the wind direction signals in T_v and T_h, but had no significant influence on the azimuthal modulations in U.

The Fourier coefficients shown in Eqs. (1) to (3) were calculated with a minimum mean square error fit to the data. Figures 1 to 4 illustrate the harmonic coefficients for the data acquired for clear skies and thin clouds. In general, all harmonic coefficients had an increasing trend from low to moderate wind speeds, except U_2 at 65° incidence, which peaked at about 3 m/s winds. These figures show a few Kelvin peak-to-peak signals in $Q = T_v - T_h$ and U channels at moderate wind speeds, but only a few tenths of one Kelvin at 2 to 3 m/s winds. The harmonic coefficient, which is most sensitive to the wind direction at low winds, is U_2 at 65° incidence. It is unclear why U_2 at 65° peaked at about 3 m/s wind speed, but low wind measurements from 1994 and 1995 confirmed the repeatability of this signal.

The signatures of 19 and 37 GHz data are very similar for all incidence angles. This was observed in all data collected throughout the flight experiments. This could be due to the nature of sea surfaces, which are known to have a wavenumber spectrum closely following a power law, and are thus nearly self-similar at various scales like a fractal surface. Hence, although 19 and 37 GHz thermal emissions interact with different parts of the spectrum, the length scales of surface dominating the scattering would appear similar at these two frequencies, if normalized by the electromagnetic wavelength. However, the 37 GHz channel was shown to be more sensitive to the wind direction than the 19 GHz channel. We do, however, expect that the 19 GHz channel to be less sensitive to atmospheric effects than the 37 GHz channel.

SUMMARY

A preliminary geophysical model function for the sea surface brightness temperatures in incidence angle range of 45° to 65° was developed using the data from a series of dual-frequency airborne radiometer flights in 1994 and 1995. Dependence of the wind direction signals in polarimetric brightness temperatures on frequency, incidence angle, and wind speed were discussed. Further flight experiments to acquire data at high wind (above 15 m/s) are necessary for a more complete evaluation of the wind speed dependence of wind direction signals. The effects of other atmospheric and oceanic variables, such as air and sea surface temperatures (SST) and significant wave height also need to be quantified to understand the lim-

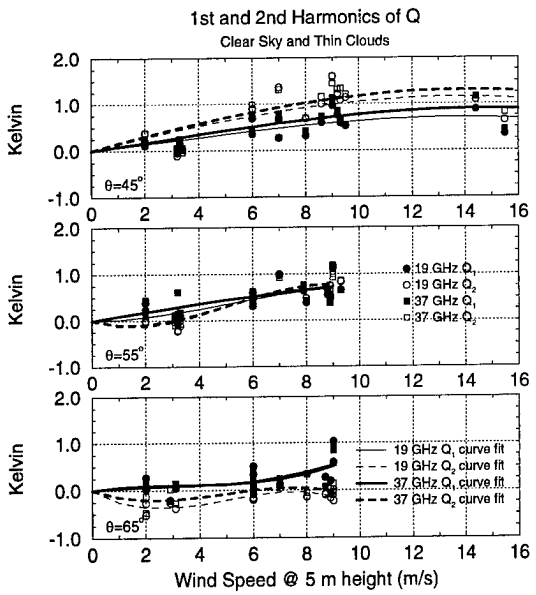


Figure 3. Q_1 and Q_2 from 19.35 and 37 GHz JPL wind radiometer channels versus wind speed at 5 m elevation. $Q = T_v - T_h$. (a) $\theta = 45°$, (b) $\theta = 55°$, and (c) $\theta = 65°$.

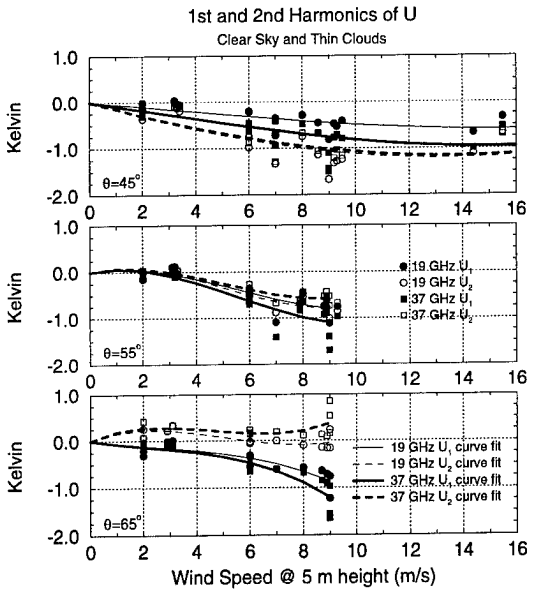


Figure 4. U_1 and U_2 from 19.35 and 37 GHz JPL wind radiometer channels versus wind speed at 5 m elevation. $U = T_{45} - T_{-45}$. (a) $\theta = 45°$, (b) $\theta = 55°$, and (c) $\theta = 65°$.

itation of passive microwave radiometry and to develop techniques to reduce these effects.

ACKNOWLEDGMENTS

The authors would like to thank Steven Dinardo, Amarit Kitiyakara, David Orozco, David Huynh, and Son V. Nghiem of JPL for their technical help, and John Reller, Christi Scofield, Chris Miller and the DC-8 aircraft flight crew of the NASA Ames Research Center for assistance in aircraft flight planning and experiments.

REFERENCES

[1] Etkin, V.S., M.D. Raev, M.G. Bulatov, Yu.A. Militsky, A.V. Smirnov, V.Yu. Raizer, Yu.A. Trokhimovsky, V.G. Irisov, A.V. Kuzmin, K.Ts. Litovchenko, E.A. Bespalova, E.I. Skvortsov, M.N. Pospelov, and A.I. Smirnov, *Radiohydrophysical Aerospace Research of Ocean*, Report Пр-1749, Academy of Sciences, Space Research Institute, Moscow, USSR, 1991.

[2] Wentz, F. J., "Measurement of oceanic wind vector using satellite microwave radiometers," *IEEE Trans. Geosci. Remote Sensing*, Vol. 30, No. 5, 960-972, Sep., 1992.

[3] Nghiem, S. V., M. E. Veysoglu, R. T. Shin, J. A. Kong, K. O'Neill, and A. Lohanick, "Polarimetric passive remote sensing of a periodic soil surface: microwave measurements and analysis" *J. Electromagnetic Waves and Appl.*, Vol. 5, No. 9, 997-1005, 1991.

[4] Johnson, J. T., J. A. Kong, R. T. Shin, D. H. Staelin, K. O'Neill and A. W. Lohanick, "Third stokes parameter emission from a periodic water surface," *IEEE Trans. Geosci. Remote Sensing*, Vol. 31, No. 5, 1066-1080, September 1993.

[5] Yueh, S. H., S. V. Nghiem, R. Kwok, W. J. Wilson, F. K. Li,J. T. Johnson, and J. A. Kong, "Polarimetric thermal emission from periodic water surfaces," *Radio Science*, January-February, 1994.

[6] Gasiewski, A. J., and Kunkee, "Polarized microwave emission from water-waves," *Radio Science*, Vol. 29, No. 6, 1449-1466, November-December, 1994.

[7] Dzura, M. S., V. S. Etkin, A. S. Khrupin, M. N. Pospelov, and M. D. Raev, "Radiometers-polarimeters: principles of design and applications for sea surface microwave emission polarimetry," Proceedings of International Geoscience and Remote Sensing Symposium, Houston, 1992.

[8] Yueh, S. H., W. J. Wilson, F. K. Li, W. B. Ricketts, and S. V. Nghiem, "Polarimetric measurements of sea surface brightness temperatures using an aircraft K-band radiometer," *IEEE Trans. Geosci. Remote Sensing*, Vol. 33, No. 1, 85-92, 1995.

[9] Yueh, S. H., W. J. Wilson, F. K. Li, S. V. Nghiem, and W. B. Ricketts, "Polarimetric brightness temperatures of sea surfaces measured with aircraft K- and Ka-band radiometers," submitted for publication in *IEEE Trans. Geosci. Remote Sensing*, January 1995.

[10] Yueh, S. H., R. Kwok, and S. V. Nghiem, "Polarimetric scattering and emission properties of targets with reflection symmetry," *Radio Science*, Vol. 29, No. 6, 1409-1420, November-December, 1994.

The Atmosphere Influence on Sea-Surface Polarized Microwave Emission

Michael N. Pospelov

Space Research Institute, Russian Academy of Sciences
Profsoyuznaya Str. 84/32, Moscow 117810, Russia
Phone: (7-095)-333-5078; Fax: (7-095)-333-1056; EMail: kub@asp.iki.rssi.ru

ABSTRACT

The atmosphere influence on sea-surface emission is discussed in the context of passive microwave polarimetry application for surface wind vector retrieval. Two aspects of the problem are considered. First, the atmosphere stability affects sea surface roughness and therefore its emissivity. This dependence restricts the accuracy of wind speed retrieval algorithm. A feasible way of algorithm correction is proposed. The second issue addressed is atmospheric attenuation of microwaves. A simplified radiative transfer equation is used to estimate this effect, and to correct wind retrieval algorithm for atmospheric attenuation.

INTRODUCTION

The sea surface thermal microwave emission depends on several factors, such as water temperature, salinity, foam cover, wind-generated waves. The atmosphere affects sea surface emissivity because the ocean-atmosphere interaction influences on surface geometry. That is why sea surface emission may be used in remote sensing as an indicator of atmospheric processes, say near-surface wind.

The near-surface wind generates short surface waves (ripples). These waves modify sea surface roughness causing brightness temperature dependence on wind speed. Further still the angular anisotropy of the ripples leads to azimuthal dependence of brightness temperature. At nadir view angle this angular dependence manifests itself in polarizational anisotropy of thermal emission: sea surface brightness temperature reaches its maximum when polarization plane coincides with wind vector, and it is minimal for orthogonal vector. This effect may be used successfully for surface wind speed and direction remote determination. The algorithm of wind vector retrieval from passive microwave polarimeter data was briefly described in [1].

This paper is addressed to the atmosphere influence on an accuracy of wind vector retrieval algorithm. First, the dependence of the algorithm parameters on atmosphere boundary layer stability is discussed. A transition from stable stratification to unstable affects radically the air-sea interaction conditions. The damping of the ripples under stable stratification conditions causes the wind speed to be underestimated. To improve the accuracy of wind retrieval algorithm, this effect should be taken into account. And second, atmospheric attenuation of microwaves should be considered as well. The absorption along the path from sea surface to a sensor leads to depolarization of surface self-emission. This causes the retrieved wind speed to be underestimated under cloudy conditions.

The experimental results presented hereafter were obtained in frames of Joint US/Russia experiment JUSREX [2]. The JUSREX was conducted in July 1992 on the continental shelf off the east coast of the USA approximately 60 nmi south of the eastern end of Long Island. One Russian and two US remote sensing aircrafts participated in the experiment. Russian research vessel "Ac. Ioffe" collected oceanographic, meteorological and remote sensor data.

This paper discusses the data obtained with Ka-band (37 GHz) radiometer-polarimeter. The polarimeter measured brightness temperature at four linear polarizations: -45°, 0°, 45°, and 90° about the flight direction. Fluctuation sensitivity of the instrument was 0.15K for 1s integration time. A type of antenna used was a corrugated conical horn.

During the experiment, winds were generally light to moderate, ranging from a few meters per second up to about 12m/s. The atmospheric boundary layer stratification varied between slightly stable and slightly unstable.

THE INFLUENCE OF ATMOSPHERIC STABILITY ON POLARIZATION ANISOTROPY

JUSREX has given us a good opportunity to examine the atmospheric stability influence on polarizational anisotropy. The results of this study were reported in [3]. Here we briefly outline the principal results, and propose a correction for wind retrieval algorithm.

The polarimeters aboard TU-134CX were used for surface wind vector retrieval. When the aircraft flew close to "Ac. Ioffe," this remotely measured wind speed (V_{radio})

The work was supported by the Russian Foundation for Basic Research, grant No. 95-02-03681-a

0-7803-3068-4/96$5.00©1996 IEEE

could be compared with true surface wind speed. We have selected the data when the distance between the aircraft flight pass and "Ac. Ioffe" was less than 15km. The total amount of such points reaches 22. Before the comparison, polarimeter data were averaged over 40s interval (that corresponds approximately to 6km flight pass) to reduce random errors. Surface wind speed was recalculated from the anemometer height 30m into reference height 10m. This recalculated wind speed is denoted by V_{meteo}.

In Fig.1 the value of polarizational anisotropy ΔT_a is plotted versus surface wind speed V_{meteo} separately for stable and unstable stratification of atmosphere boundary layer. Solid line is square approximation:

$$\Delta T = A \cdot V_{radio}^2; \qquad A = 19.06 \cdot 10^{-3} \qquad (1)$$

that we used for wind speed retrieval from polarizational measurements. Two clusters of points differ considerably. The RMS difference between true surface wind speed V_{meteo} and remotely retrieved from (1) V_{radio} for these 22 experimental points is as large as 2.8m/s.

To correct the algorithm, one may establish different coefficients for unstable and stable (or neutral) stratification. This algorithm with empiric coefficients will look as:

$$V = A \cdot \sqrt{\Delta T_a}; \qquad A = \begin{cases} 5.85 & \text{if } z/L < 0 \\ 12.8 & \text{if } z/L \geq 0 \end{cases} \qquad (2)$$

where negative parameter z/L describes unstable stratification, and vice versa. Such a simple correction allowed RMS difference reducing to 1.33m/s. Separate approximations (2) are shown in Fig.1 with dashed lines.

Obvious weakness of algorithm (2) is a drop of retrieved speed in areas of transition from stable to unstable stratification. To avoid this, a bit more complicated correction may be suggested. In Fig.2 [3] the value $\ln(V_{radio}/V_{meteo})$ is plotted versus stability parameter z/L. Evidently, in the transition region $-0.25 < z/L < 0.25$ the dependence in semi-log axes can be described linearly. To improve the accuracy of surface wind speed retrieval, this correlation should be taken into account. Thus (1) was modified as:

$$V_{radio} = A \cdot (\Delta T)^B \cdot \exp(C \cdot z/L) \qquad (3)$$

where coefficients were derived from the data presented in Fig.2, namely:

$$B = 0.37; \quad \begin{cases} A = 6.81; \ C = 0 & \text{if} \quad z/L < -0.25 \\ A = 9.83; \ C = 0.89 & \text{if} \quad -0.25 \leq z/L \leq 0.25 \\ A = 12.62; \ C = 0 & \text{if} \quad z/L > 0.25 \end{cases} \qquad (4)$$

The resulting RMS difference was 0.86m/s. Of course, the statistics of presented experiment are insufficient to derive the coefficients at reasonable accuracy, especially

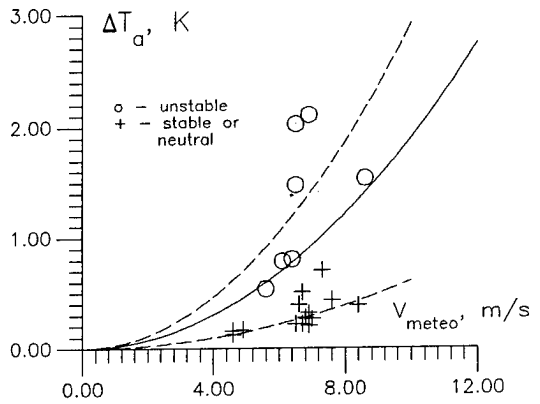


Figure 1 The dependence of polarizational anisotropy ΔT_a on surface wind speed

for extremely stable or unstable conditions. However, a tendency of retrieval algorithm improvement, if atmospheric stability is accounted for, is obvious.

THE WIND ALGORITHM CORRECTION FOR ATMOSPHERIC ABSORPTION

For wind retrieval short centimeter and millimeter waves are usually applied because at these bands wind-induced polarizational anisotropy ranges up to several Kelvins. On the other hand, atmospheric absorption for these waves is significant as well. This leads to depolarization of sea surface self-emission. The effect may be estimated using the radiative transfer equation.

Sea surface brightness temperature T_x received by a radiometer from a height H in linear polarization X at an angle Θ from nadir will be:

$$T_x = T_s \cdot (1 - R_x) \frac{\exp(-\tau(H))}{\cos\Theta} + T_{up} + T_{down} \cdot R_x \frac{\exp(-\tau(H))}{\cos\Theta} \qquad (5)$$

here T_s – surface temperature; T_{up} – upwelling brightness temperature of atmosphere layer between a surface and a radiometer; T_{down} – downwelling brightness temperature

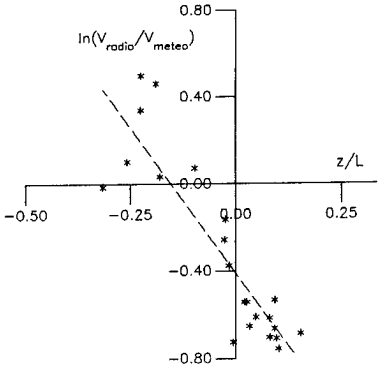


Figure 2 The dependence of discrepancy function $\ln(V_{radio}/V_{meteo})$ on stability parameter z/L

of the total atmosphere; $R_x=R_{x0}+R_{xw}$ - surface scattering coefficient at polarization X into the upper hemisphere; R_{x0} - Fresnel coefficient; R_{xw} - the scattering coefficient perturbation due to the wind; $\tau(H)$ - the absorption of atmosphere layer of the height H. The brightness difference at two orthogonal polarizations will be:

$$\Delta T_a = T_x - T_y = T_s\left(\frac{T_{down}}{T_s} - 1\right)(\Delta R_0 + \Delta R_w)\frac{\exp(-\tau(H))}{\cos\theta} \quad (6)$$

The atmospheric attenuation decreases ΔT_a as it causes both τ and T_{down} to increase. A simple correction procedure may be supposed under the following assumption: atmosphere effective temperature to be constant and equal to T_s. In [4] it was shown that such a simplification results in brightness error of a few Kelvins for frequencies far from vapor and O_2 absorption lines. Thus for nadir view angle a correction may be achieved by multiplying measured ΔT_a to coefficient $RT_s/(T_{sB}T_x)$. We used this correction for our nadir measurements during the JUSREX; as a rule, it was not essential. Really, in great majority of meteorological situations nadir measurements have no need in correction at all. To the contrary, for off-nadir angles such a correction is important.

Fig.3 illustrates this influence. The additive contribution from atmosphere to ΔT_a (V and H polarizations are taken) at Ka-band is plotted for various cloud conditions. Absorption data for this illustrative example were taken from [5]. Dashed line is the value ΔT_a=0.4K that corresponds to the wind speed 7m/s. Obviously, for sounding angles over 10° from nadir the contribution of atmosphere exceeds that of wind, under assumption the latter to be approximately constant at these angles (see Fig.4 in [6]). Moreover, the calculations [7] have proved the anisotropy versus wind speed dependence to decrease in this range of view angles. Consequently, for off-nadir sounding the correction for atmosphere influence is essential.

CONCLUSIONS

The atmosphere conditions affect the accuracy of wind speed retrieval algorithm. First, short gravity capillary waves are sensitive to the stability of atmosphere boundary layer. The discrimination between two states of atmosphere (stable - unstable) allows to improve theaccuracy of wind retrieval approximately twice. For this discrimination any additional information may be applied, say radar images of sea surface. If the information on stability parameter z/L were available the accuracy might be improved further more. This makes the problem of stability parameter remote determination ever more important. Second, the atmospheric absorption of microwaves should be accounted to improve the accuracy of wind algorithm, especially for off-nadir sounding.

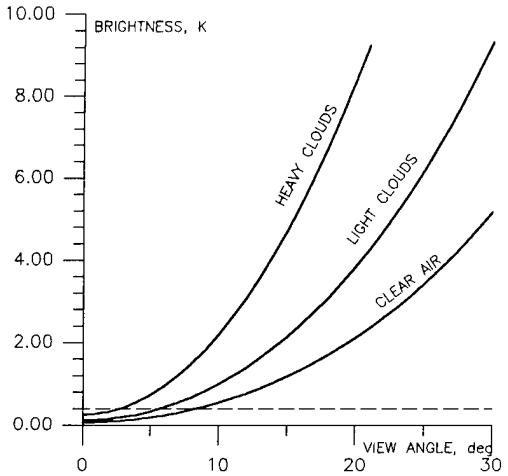


Figure 3 The atmosphere contribution to the polarization contrast

REFERENCES

[1] V.S.Etkin, A.V.Kuzmin, M.N.Pospelov, A.I.Smirnov, and V.V.Yakovlev, "The Determination of Sea Surface Wind and Temperature With Airborne Radiometric Data (Joint US/Russia Internal Waves Remote Sensing Experiment)," *IGARSS'93 Proc.*, pp.1622-1624

[2] R.F.Gasparovic and V.S.Etkin, "An Overview of the Joint US/Russia Internal Wave Remote Sensing Experiment," *IGARSS'94 Proc.*, pp.741-743

[3] M.N.Pospelov, "Surface Wind Speed Retrieval Using Passive Microwave Polarimetry: The Dependence on Atmospheric Stability," *IGARSS'95 Proc.*, pp.1773-1775

[4] A.Guissard and P.Sobieski, "A Simplified Radiative Transfer Equation for Application in Ocean Microwave Remote Sensing," *Radio Science*, 1994, v.29, No.4, pp.881-894

[5] S.D.Slobin, "Microwave Noise Temperature and Attenuation of Clouds: Statistics of These Effects at Various Sites in the United States, Alaska, and Hawaii," *Radio Science*, 1982, v.17, No.6, pp.1443-1454

[6] S.H.Yueh, R.Kwok, F.K.Li, S.V.Nghiem, W.J.Wilson, and J.A.Kong, "Polarimetric Passive Remote Sensing of Ocean Wind Vectors," *Radio Science*, 1994, v.29, No.4, pp.799-814

[7] A.J.Gasiewski and D.B.Kunkee, "Polarized Microwave Emission from Water Waves," *Radio Science*, 1994, v.29, No.6, pp.1449-1466

Oceanic Wind Vector Determination Using a Dual-Frequency Microwave Airborne Radiometer - Theory and Experiment

Mark D. Jacobson[1], William J. Emery[2], and Edgeworth R. Westwater[3]

[1]NOAA/ERL/ETL, R/E/ET1, 325 Broadway, Boulder, CO 80303-3328 USA, Voice: (303)497-6497, FAX: (303)497-3577, email: mjacobson@etl.noaa.gov

[2]CCAR Box 431, University of Colorado, Boulder, CO 80309 USA, Voice: (303)492-8591, FAX: (303)492-2825, email: Emery@orbit.colorado.edu

[3]CIRES, University of Colorado, Boulder, CO 80309 USA, Voice: (303)497-6527, FAX: (303)497-3577, email: ewestwater@etl.noaa.gov

I. INTRODUCTION

The near ocean surface wind vector is an important measurement for local and global climatic and oceanographic studies. A direct result of this wind is that it creates a rough ocean surface consisting of a variety of waves and foam. Recently, passive ocean-viewing microwave radiometers are producing promising results for measuring the near-surface wind vector by measuring the thermal emission from the combined rough surface and atmosphere. The brightness temperature variations of the rough ocean surface provide the necessary information for determining the near ocean surface wind speed and direction.

Microwave radiometers have been measuring ocean wind speeds for many years [1] based on the ocean surface brightness temperature variations. In contrast, the ocean wind direction measurements have only recently been obtained by microwave radiometers [2]. These recent wind direction measurements showed that ocean brightness temperature variations with respect to azimuth angle (wind direction) varied by a few kelvin. All these radiometers measured the azimuthal dependence of vertically- and horizontally-polarized ocean brightness temperatures. However, [2] showed that brightness temperature measurements at other polarization states (four Stokes parameters) are also sensitive to near surface ocean wind direction.

Nevertheless, this paper focuses on a nonpolarimetric aircraft-based dual-frequency dual-polarized microwave radiometer that was developed at the Environmental Technology Laboratory (ETL) of the National Oceanic and Atmospheric Administration (NOAA) [3]. The lower frequency at 23.87 GHz is horizontally-polarized with respect to the aircraft's flight direction and the 31.65 GHz frequency is vertically-polarized to that direction. This radiometer was one of several instruments deployed in ETL's first Advanced Sensor Applications Program (ASAP) experiment. This experiment was named the San Clemente Ocean Probing Experiment (SCOPE) [4]. The main purpose of the airborne microwave radiometer was to determine if it could measure azimuthal-dependent brightness temperature variations from a rough ocean surface, and thus infer the near-surface wind vector. Furthermore, in order to gain a better understanding on the potential of the NOAA dual-frequency radiometer for near-surface wind vector determination, the SCOPE radiometer measurements are compared with a new combined atmospheric and two-scale ocean surface model.

0-7803-3068-4/96$5.00©1996 IEEE

II. THEORETICAL FORMULATION

The brightness, i.e., brightness temperature, observed by an airborne radiometer viewing the ocean at an angle θ relative to the nadir direction is given by

$$B(T_{ap}(f,\theta,\phi,p)) = B(T_{up}(f,\theta,\phi)) + \Upsilon_{up}(0,s(h_a)) \times \left[B(T_{bs}(f,\theta,\phi,p)) + B(T_{rf}(f,\theta,\phi,p))\right] \quad (1)$$

where

$$\Upsilon_{up}(0,s(h_a)) = e^{-\tau(0,s(h_a))}, \quad (2)$$

h_a is the vertical line-of-sight aircraft height above the ocean surface, $s(h_a)$ is the refracted ray path length from the ocean surface to the aircraft height h_a, θ is the angle relative to the nadir direction, ϕ is the azimuth angle, f is the frequency, τ is the total atmospheric optical thickness, p is the polarization, $B(T_{up})$ is the upward atmospheric brightness,

$B(T_{bs})$ is the ocean surface brightness, and $B(T_{rf})$ is the ocean surface-reflected brightness.

The last two brightness factors, $B(T_{bs})$ and $B(T_{rf})$, are functions of the surface reflectivity $r_a(\theta, \phi)$ for the given incident polarization a. This is evaluated by integrating the bistatic scattering coefficients $\gamma_{ba}(\theta, \phi; \theta', \phi')$ over all scattering angles in the upper hemisphere and summing the results of both orthogonal scattering polarizations [5]

$$r_a(\theta, \phi) = \frac{1}{4\pi} \sum_{b=1}^{2} \int_0^{\frac{\pi}{2}} d\theta' \sin\theta' \int_0^{2\pi} d\phi' \gamma_{ba}(\theta, \phi; \theta', \phi') \quad (3)$$

where (θ, ϕ) and (θ', ϕ') represent the incident and the scattered directions, respectively, and a and b represent the polarizations of the incident and the scattered waves, respectively.

For this research, we obtain

$$\gamma_{ba}(\theta, \phi, \theta_s, \phi_s) \approx \langle \gamma^1_{ba}(\theta, \phi, \theta_s, \phi_s) \rangle = \int_{-\infty}^{\infty} \gamma^1_{ba}(\theta', \phi', \theta_s', \phi_s') \, P(Z_x) \sqrt{1 + Z_x^2} \, dZ_x \quad (4)$$

where θ and ϕ are the incident angles; θ_s and ϕ_s are the scattering angles; θ' and ϕ' are the local incident angles, θ'_s and ϕ'_s are the local scattering angles; Z_x is the surface slope; and $P(Z_x)$ is a one-dimensional surface slope distribution of the large-scale waves [6].

We evaluate (4) by the method of steepest descent. The result yields a total power reflectivity of

$$r_a(\theta, \phi) \approx A^+ \frac{r_a^+(\theta, \phi)}{2} + A^- \frac{r_a^-(\theta, \phi)}{2} \quad (5)$$

where

$$r_a^{\pm}(\theta, \phi) = \left[\frac{1}{4\pi} \sum_{b=1}^{2} \int_0^{\frac{\pi}{2}} d\theta' \sin\theta' \int_0^{2\pi} d\phi' \gamma^1_{ba}(\theta, \phi; \theta', \phi') \right]_{\theta_n = \pm \tan^{-1}(m)} \quad (6)$$

$$A^{\pm} = A_0 \left(1 + \frac{3m^2}{2} \right) + A_2 \pm A_1 \sqrt{\frac{2}{\pi}} \quad (7)$$

where A_0 - A_2 and the rms slope m are given by the slick surface measurements in [6].

The small-scale features are chosen to have a sinusoidal corrugated profile. The extended boundary condition (EBC) method [5] is used to calculate the brightness temperature from a tilted periodic surface for an arbitrarily linearly-polarized electric field. An attractive feature of the EBC method is that it allows for the small-scale features to be similar to the incident electromagnetic wavelength. This feature is necessary when describing the capillary-ultragravity wave region. In addition, the pure water model in [7] with an additional standard salt term is used to calculate the complex permittivity of sea water.

III. A COMPARISON OF EXPERIMENTAL AND THEORETICAL RESULTS

Several instruments were deployed at various locations during SCOPE. In particular, the NOAA King Air aircraft, the moored Scripps FLoating Instrument Platform (FLIP), the NOAA R/V Titan, and San Nicolas Island served as platforms for the remote sensing and *in-situ* instruments pertinent to this research.

Flight tracks for the NOAA aircraft were done at specified way points with the radiometer's antenna system [Jacobson et al., 1994] fixed in the downward-viewing mode. At each of the way points, the aircraft performed 360° banked turns at a roll angle of approximately 32°. Sixteen way points were accomplished around Titan and FLIP. These points provided the necessary instrument measurements to compare measured and calculated brightness temperatures.

The predominately horizontally-polarized 23.87 GHz channel was used to obtain an empirical wind speed algorithm. This was accomplished by measuring the corrected 23.87 GHz brightness temperature variations (peak-to-valley), ΔT_{b24} (K), from thirteen circle flights around Titan and FLIP. These measurements are regressed against the Titan and FLIP sonic anemometer wind-speed measurements. The wind speed (W in m/s) algorithm is given by

$$W = 1.8 \, \Delta T_{b24} - 0.15 \, . \quad (8)$$

During the course of the experiment Titan observed the highest winds at about 2000 UTC on 17 September 1993; the surface winds were 7.8 m/s at 275.8° with clear sky conditions. This way point is chosen to compare with the theoretical model because of the high winds, the cloudless sky conditions, and the four circle flights.

In order to enhance the comparison between experimental and theoretical results, the following process is used. First,

the mean theoretical brightness temperatures for each 360° circle are computed. Then, these brightness temperatures are subtracted from their respective mean measured brightness temperatures. This is given as

$$T_{bmd} = T_{bmm} - T_{bmt} \qquad (9)$$

where T_{bmd} is the mean brightness temperature difference, T_{bmm} is the mean measured brightness temperature in, and T_{bmt} is the mean theoretical brightness temperature in; the above temperatures are in K. The measured three-dimensional antenna patterns were incorporated into this model.

Next, the T_{bmd} is then subtracted from the above theoretical brightness temperatures. Last, these adjusted brightness temperatures are overlayed with the measured brightness temperatures. The experimental and theoretical 23.87 and 31.65 GHz brightness temperature results agreed best when the small-scale wave height and wavelength were approximately 0.5 mm and 0.5 cm, respectively, i.e., the capillary wave region, see Fig. 1.

V. CONCLUSION

For wind speeds less than 12 m/s, we expect that the inferred wind vector from the NOAA microwave radiometer can give wind speed to an accuracy better than 2 m/s (4 m/s for the model) and wind direction to within 15° accuracy. Furthermore, the upwind and downwind directions can be distinguished from each other.

ACKNOWLEDGMENTS

We thank the following ETL staff: Jack B. Snider, Anthony Francavilla, Duane A. Hazen, Bill Madsen, Janelle Reynolds, Leonard S. Fedor, Chris Fairall, and Jim Churnside. We also thank NOAA's AOC staff: Brad Patten, Tom Gates, and Randy. This document has been generated as part of a joint NOAA/DOD-Advanced Sensor Applications Program.

REFERENCES

[1] J. P. Hollinger, "Passive microwave measurements of sea surface roughness," *IEEE Trans. Geosci. Electron.*, vol. 9, pp. 165-169, 1971.

[2] S. H. Yueh, W. J. Wilson, F. K. Li, S. V. Nghiem, and W. B. Ricketts, "Polarimetric measurements of sea surface brightness temperatures using an aircraft K-band radiometer," *IEEE Trans. Geosci. Remote Sens.*, vol. 33, pp. 85-92, 1995.

[3] M. D. Jacobson, L. S. Fedor, D. A. Hazen, W. B. Madsen, M. H. Francis, and D. P. Kremer, "A dual frequency mm-wave radiometer antenna for airborne remote sensing of atmosphere and ocean," *Microwave J.*, vol. 37, No. 9, pp. 24-38, 1994.

[4] R. A. Kropfli, and S. F. Clifford, "The San Clemente Ocean Probing Experiment: a study of air-sea interaction with remote and in situ sensors," *Proc. IGARS Symp., Pasadena, California*, pp. 2407-2409, 1994.

[5] J. T. Johnson, J. A. Kong, R. T. Shin, D. H. Staelin, K. O'Neill, and A. W. Lohanick, "Third Stokes parameter emission from a periodic water surface," *IEEE Trans. Geosci. Remote Sens.*, vol. 31, pp. 1066-1080, 1993.

[6] C. Cox and W. Munk, "Measurement of the roughness of the sea surface from photographs of the Sun's glitter," *J. Opt. Soc. Am.*, vol. 44, pp. 838-850, 1954.

[7] H. J. Liebe, G. A. Hufford, and T. Manabe, "A model for the complex permittivity of water at frequencies below 1 THz," *Int. J. Infr. Milli. Waves*, vol. 12, pp. 659-675, 1991.

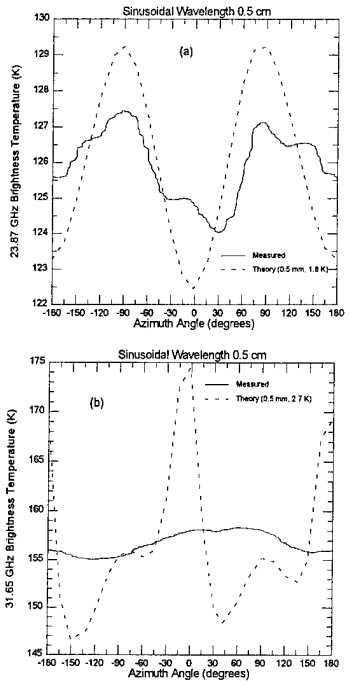


Fig. 1. The measured and computed brightness temperatures at (a) 23.87 and (b) 31.65 GHz versus azimuth angle. The wave height and T_{bmd} values are given by the first and second entries in the parenthesis, respectively. The upwind, downwind, and crosswind directions correspond to 0°, ±180°, and ±90°, respectively.

A PC-based Remote Sensing System for Detection and Classification of Oceanic Fronts

F. Askari[1], E. Malaret[2], D. Lyzenga[3], M. Collins[4], T.Donato[1], A. Skoelv[5], T. Jenserud[5], and C. Brownsword[6].

[1] Remote Sensing Division, Naval Research Laboratory, Washington, D.C. 20375

[2]ACT Corp. VA,[3]ERIM, MI,[4] Acoustics Division NRL,[5]NDRE, Norway; and [6]DRA, England.

Phone 202 767 2095, Fax 202 767 3303, Email: askari@nrlfs1.nrl.navy.mil

ABSTRACT

This paper describes a PC-based multilayered data integration and classification system that is under development for monitoring coastal oceanographic processes. For data integration and sensor fusion, we have developed a multilayered "hypercube" that includes data from satellite ERS-1, multi-frequency airborne SAR imagery, AVHRR imagery, in situ measurements of temperature, salinity and the calculated sound speed. Here, we show examples from a number of the systems applications that include: georeferencing, sensor fusion, pattern classification and automatic frontal detection, geophysical parameter extraction, objective interpolation, and prediction of acoustic propagation loss within the water column.

INTRODUCTION

Detection and characterization of oceanic fronts is important for predicting the transport of heat and mass in the coastal ocean as well as exploiting the fisheries potential and primary food production. Oceanic fronts are regions where dynamical, biological and chemical properties change abruptly. Passive and active remote sensing devices readily map the surface manifestation of the fronts in terms of the changes in sea surface temperature (SST), ocean color, and the small-scale surface roughness. Radar imagery can readily detect surface manifestation of SST fronts, velocity fronts, and wind fronts. With the recent advances in sensor technology, it is now possible to detect and characterize these fronts rapidly and generate enhanced products for environmental assessment and prediction. With the improved sensor technology, however, the amount of information has also dramatically increased. An operational coastal monitoring system requires access to a multitude of information from different sensors and platforms. This is a multi-dimensional problem that can be tackled using a multilayered hypercube that contains georeferenced uniformly-spaced data that is common to all the remotely sensed imagery.

To construct the hypercube, we use the data from the Rocky Road campaign which was a joint oceanographic exercise conducted between the Norway, U.K. and the U.S. in October, 1993 in Vesfjoden Norway. In the Rocky Road campaign, a detailed hydrographic survey of the Vestfjord area in the coastal region was conducted over a three day period. To facilitate the in situ measurements, the DELAUNY objective interpolation algorithm was used to convert the irregularly spaced ship tracks into regularly-spaced values of SST, salinity and sound speed for any point inside the hypercube. Computer memory is the only factor that limits the number of layers in the hypercube. The programming tools developed here were formulated using the commercially available PROVIEW image processing and programming environment. This is a highly versatile PC-based language, that operates under the MS Windows 3x and NT, as a 32 bit application and permits easy transportability to other PC-based computers that are available worldwide.

0-7803-3068-4/96$5.00©1996 IEEE

formulated using the commercially available PROVIEW image processing and programming environment. This is a highly versatile PC-based language, that operates under the MS Windows 3x and NT, as a 32 bit application. and permits easy transportability to other PC-based computers that are available worldwide.

RESULTS

We use two-dimensional matched-filter and pattern recognition algorithms complimented with satellite AVHRR imagery to automatically detect in SAR imagery frontal features that include wind fronts, SST, and current velocity fronts The basis for automatic detection is the fact that in radar imagery, SST and wind fronts manifest themselves as step-changes in surface roughness, while velocity fronts often appear as narrow isolated bright or dark bands of surface roughness. Wind fronts can also be distinguished from SST fronts using the combination of AVHRR and SAR imagery. Wind fronts, in general produce a flat response in the AVHRR-derived SST field, and a corresponding step-change in the radar backscatter field. SST fronts, on the other hand produce step-changes in both the SST and backscatter fields. Therefore, by modulating the radar imagery with the step-changes in the temperature field one can easily distinguish between the two fronts. Velocity fronts have distinct surface shapes and signatures that vary according to their dynamical properties, ie, shear and convergence. The horizontal shapes and curvatures of the fronts are combined with the radar look direction to make inferences about the dominance of shear or convergence along the front. It is shown that based

on the radar azimuth angle (θ), the modulations for shear front are proportional to the Sin θ Cos θ, while the modulations for converging fronts are proportional to $Cos^2\theta$. As such with respect to the radar look direction, the modulations for a shear front can change from dark to bright, whereas the modulations for a converging front will always remain bright.

For the acoustic component of the coastal prediction system we used a Parabolic Equation (PE) acoustic propagation loss model [1] that was developed at NRL. In its present configuration, the model predicts the propagation loss as a function of frequency using the range-dependent sound speed, surface roughness and bottom depth. For the Rocky Road region, we showed that for high acoustic frequencies (>1000 Hz), the SAR-derived rough-surface boundary increased the amount of acoustic energy that was scattered to the deeper layers. Finally, we implemented three of the most widely used scatterometer models on our PC-based system to derive wind speeds and friction velocities from calibrated SAR imagery.

REFERENCE

1. Collins M.D., S.A. Chin-Bing, Journal Acoustic. Soc Am., 87 (3) pp 1104-1109, 1990.

A LIGHTWEIGHT SPECTRASAT CONCEPT FOR GLOBAL OCEAN WAVE MONITORING

R. C. Beal, D. Y. Kusnierkiewicz, J. L. MacArthur, F. M. Monaldo, S. F. Oden
The Johns Hopkins University Applied Physics Laboratory, Laurel, Maryland USA 20723
Tel: 301-953-5009 / Fax: 301-953-5548 / email: r.beal@jhuapl.edu

ABSTRACT

For more than two decades, spaceborne SAR has been advocated as a practical means of monitoring directional ocean wave spectra. Seasat, ERS-1 and -2, JERS-1, Almaz, the Shuttle Imaging Radars A, B, and C, and most recently Radarsat have all carried SARs that have been or are being used to monitor the spatial evolution of wind-driven waves, with the hope (or promise) of improving storm prognosis. Yet it has been well known for more than a decade that all the higher altitude platforms (Seasat, ERS-1 and -2, JERS-1, and Radarsat) suffer serious imaging problems caused by the moving ocean scatterers, which effectively act to filter along-track waves shorter than about 300 m wavelength. Nevertheless, substantial effort has been expended toward the problem of understanding the SAR transfer function, and toward optimally assimilating the SAR wave estimates into operational wave forecast models. Unfortunately, these efforts at assimilation are unlikely to yield their intended results (i.e., improved wave forecasts) without a much lower altitude operational SAR platform.

1. INTRINSIC LIMITATIONS OF SAR

The SAR azimuth wavelength limit is approximately

$$\lambda_{az} \cong K \frac{R}{V} \sqrt{H_S} \ ,$$

where $K \sim 1\ m^{1/2}/s$, R/V is the range-to-velocity ratio of the SAR platform, and H_s is the significant wave height [1, 2]. Figure 1 illustrates the severity of the azimuth limit by comparing estimated wavenumber cutoffs for both 300 km and 800 km altitude SARs as a function of sea state. Both SARs are assumed to have equal (stationary target) resolutions of 35 m, and therefore both are able to resolve at least 70 m waves in all directions, in the limit of very low sea states. For actual (moving) azimuth-travelling waves, however, the high altitude SAR is limited to only 3/8 of the wavenumber of the low altitude SAR. This limit is a problem, of course, only if it eliminates or distorts actual wave systems. For wave heights below about 1 m, the problem is not severe, but for wave heights above about 2 m, the probability of severe wave distortion or filtering becomes high with the high altitude SARs.

To further illustrate the problem, Fig 2 shows a WAM wave model hindcast of wavenumber distribution during the SIR-C Southern Ocean experiments conducted in April and October 1994. Both SAR-measured and WAM modeled distributions were nearly identical [3], suggesting that both the SAR and WAM yielded unbiased estimates of the (20-day) wave climate. Also shown on the figure are azimuth wavenumber cuttoffs for an 800 km altitude, calculated from the above equation for a range of sea states. For wave heights of interest (i.e., >2 m), high altitude SARs effectively eliminate the azimuth-travelling waves. To alleviate this problem, a dedicated low altitude SAR satellite was suggested nearly a decade ago [4, 5].

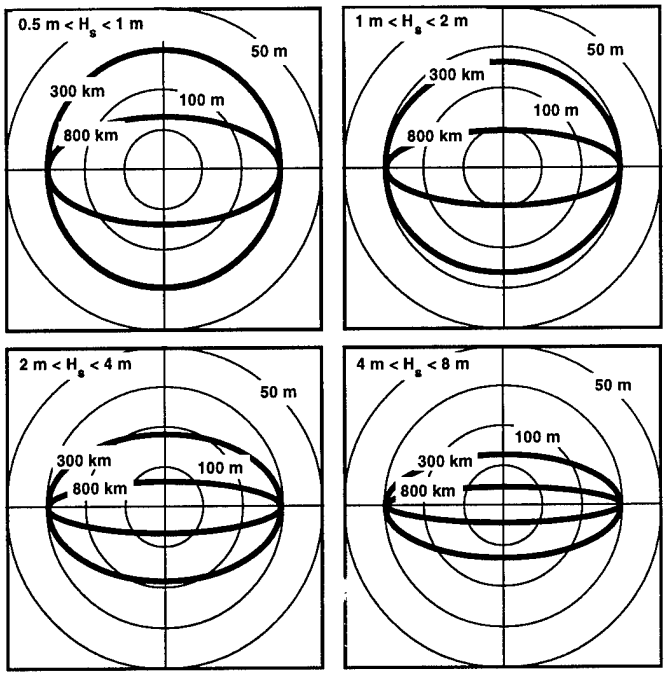


Figure 1. Comparision of azimith wavenumber response for SARs orbiting at 300 km and 800 km over a range of sea states. Both SARs are assumed to have 35 m resolution for stationary scenes. Spacecraft velocity vector is vertical.

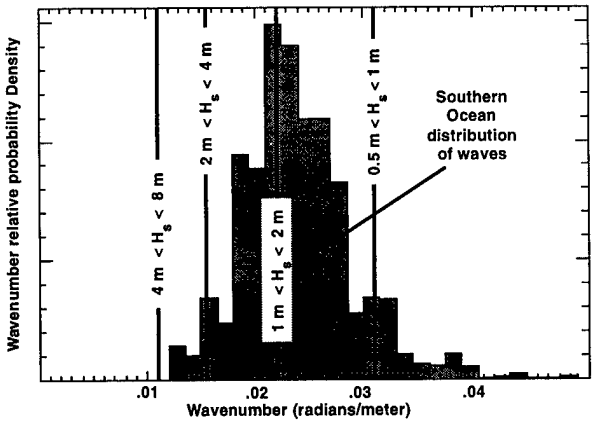


Figure 2. Effect of azimuth wavenumber cut-off vs H_s for high altitude SAR, overlaid on WAM model Southern Ocean wavenumber distribution for two 10-day intervals in 1994 [3]. Low altitude SAR cut-off (not shown) would be 8/3 that of high altitude SAR for same H_s. All wavenumbers to right of vertical lines are filtered by the SAR.

0-7803-3068-4/96$5.00©1996 IEEE

2. AN IMPROVED LOW ALTITUDE SAR DESIGN

It is commonly assumed that a long-life, low altitude (~300 km) SAR platform would be impractical because of its increased drag. Indeed, drag is a major consideration [4,5]. However, by minimizing the frontal cross section, and by optimizing the SAR antenna and instrument specifically for the directional ocean wave spectra problem, a lightweight SAR spacecraft having a five-year (propellent) lifetime is quite feasible.

Such a lightweight SAR spacecraft, in which the frontal cross section is only ~1 m^2, is shown in Fig 3. It includes a 1 m x 3 m combined SAR/altimeter antenna, near-nadir (20°) SAR geometry, C_{HH} transmission, a swath width of 10 km, and a nadir-return receiver for absolute waveheight calibration via standard altimetry. For a transmitter power of 20 w peak, 10% duty cycle, 10 MHz bandwidth, 300 km altitude, minimum ocean radar backscatter σ_0 of −10 dB, and allowing for 5 dB of loss, an SNR of +10 dB can be achieved with the 1 m x 3 m antenna.

The resulting instrument suite can provide estimates of absolute directional energy spectra every 50 km along-track over a range of ocean wavelengths from about 100 m to 600 m (or periods from about 8 s to 20 s) in all directions. With real-time on-board SAR processing and rapid data dissemination over the world wide web, demonstrated during the 1994 SIR-C Southern Ocean experiment [2, 6], and using a dawn/dusk sun-synchronous orbit, wave forecast models around the world could receive updates twice a day from the single satellite.

Table 1 shows a weight and power budget partitioned by major spacecraft subsystem. Estimates for many of the subsystems are extrapolated directly from actual achieved weights on the small scientific satellite NEAR (Near Earth Asteroid Rendezvous), the first of the low cost, low weight NASA Discovery series designed by JHU/APL and launched on 17 Feb 1996. The SAR/altimeter antenna weight is based on the use of a low mass aluminum truss structure having a density <20 kg/m^2, combined with distributed MMIC transmit/receive modules.

The spacecraft has been designed with several advanced features, including a 32-bit RISC processor integrating command and data handling (C&DH), attitude control, and power management. The communications system resides on a single card, which includes a GPS receiver for navigation. Spacecraft weight and power margins are robust: >200 kg and >100 W. The payload has been configured to be compatible with a Taurus launch vehicle, capable of placing 950 kg into a circular sun synchronous orbit of 96.7° inclination at 300 km altitude. Approximately 600 Mbits of data, with overhead, are accumulated in 12 hrs.

The spacecraft block diagram is shown in Fig 4. The SAR instrument, processor, and spacecraft subsystems are based on a card cage architecture. All subsystem and instrument electronics are redundant. The altimeter/SAR processor uses 14 cards, housed in a single card cage, which is then duplicated. The redundant spacecraft subsystems are contained in one 14-slot card cage.

In addition to two C&DH cards and the solid state memory card, one card is required for the interface with the attitude system electronics. Another provides a (standard) 1553 serial bus interface between the SAR/altimeter cages and the spacecraft subsystem card cage. One card is devoted to DC/DC converters to provide all the required regulated voltages.

Finally, the RF communications system, a GPS-Linked Transponder (GLT), is contained on a single card. The GLT consists of a GPS receiver for navigation, and an S-Band re-

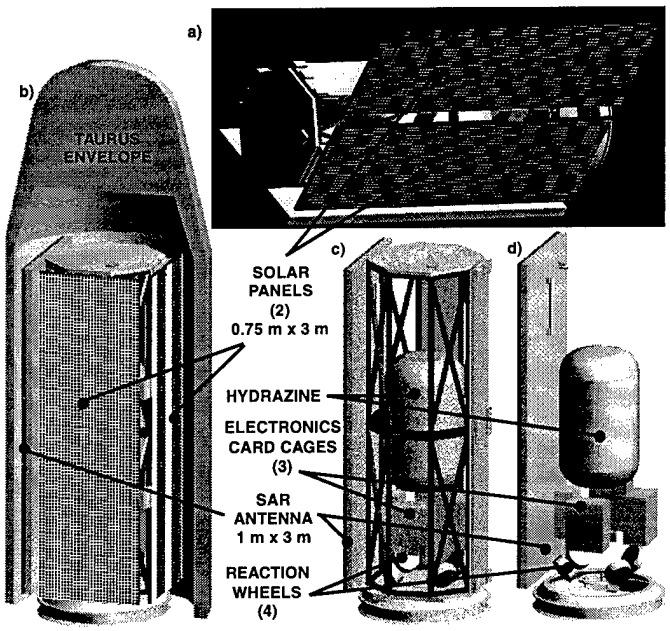


Figure 3. Lightweight Spectrasat design showing a) orbital configuration, b) Taurus-compatible launch configuration, c) partially exposed launch configuration, d) fully exposed launch configuration.

Table 1: Spacecraft Weight/Power Estimates

Subsystem	Weight / Power kg / watts	
SAR/Altimeter Antenna Panels (1 m x 3 m @ 20 kg/m^2)	60	
SAR/Altimeter Instrument (C-band, 2 W average power)	10	35
SAR/Altimeter Processor (real-time, based on SIR-C design)	30	30
Hydrazine Propellent (for 5 year life)	285	
Propulsion System	45	50
Solar Panels, hinges, batteries, misc.	50	
Attitude Determination and Control	20	100
Command and Data Handling	5	25
GPS System, RF Communications	5	25
Card Cages	50	
Thermal Blankets, Heaters	20	50
Harness	30	15
Structure	145	
Total estimated weight and power:	750	330
Total Weight and Power Budget:	**950**	**430**
Contingency:	200	100

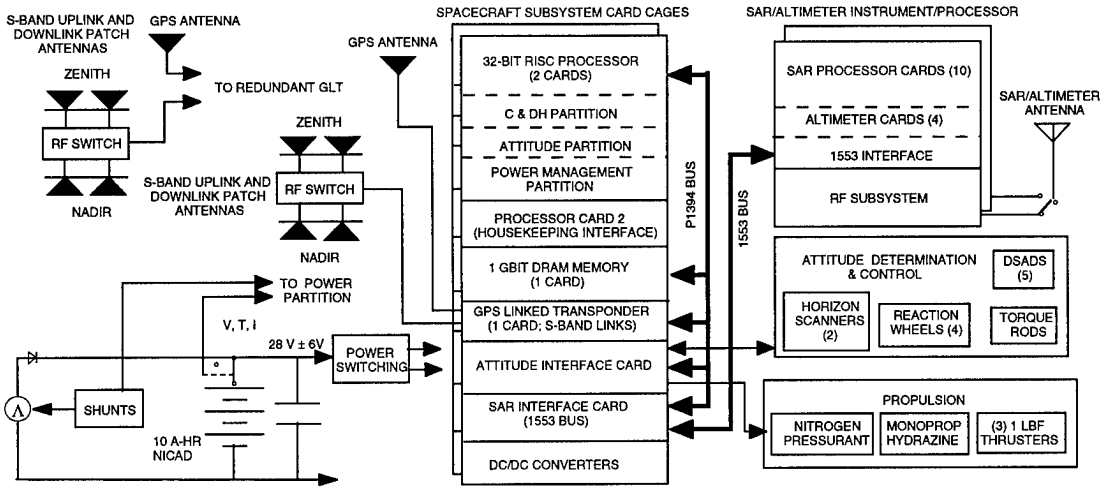


Figure 4: Spectrasat block diagram

ceiver and transmitter. A 1 W solid state power amplifier on the card can provide sufficient downlink margin to accommodate rates in excess of 4 Mb/s, more than adequate for dumping the recorder contents in one 5 min pass. Lightweight patch antennas are located on both zenith and nadir viewing sides of the spacecraft to ensure communications regardless of spacecraft orientation. Similarly, zenith viewing patch antennas are used for receiving GPS signals.

The spacecraft is three-axis stabilized using reaction wheels, and electromagnetic torque rods for momentum dumping. A horizon scanner and digital solar attitude detectors provide spacecraft attitude knowledge to 0.1° for each axis.

The propulsion system is an unregulated step repressurized hydrazine system using nitrogen pressurant. Three thrusters provide the required thrust for drag compensation and orbit maintenance. Approximately 285 kg of fuel are required for the 5 yr mission. The fuel is contained in a single tank of diameter 0.7 m and length 1.0 m, chosen to present a minimum frontal cross section. The fuel capacity of the tank exceeds 310 kg. The expulsion mechanism is by way of surface tension, viable since all thrusting is along the velocity vector.

The spacecraft power system uses a silicon solar array of area 4 m^2, capable of providing about 430 W. A 10 amp-hr nickel cadmium battery is used primarily to support launch loads, but remains on-line to support orbital passage through the Earth's umbra. Provisions have been made for switching the battery off-line, if required, during the life of the mission.

3. CONCLUSIONS

Existing and planned SAR spacecraft, having many diverse purposes, are not well suited for ocean wave monitoring. Their high altitudes severely limit ocean wave imaging in the along-track direction. This limitation applies equally to ERS-2, Radarsat 1, and follow-on missions orbiting at ~800 km.

To solve the problem, a low altitude, dedicated SAR platform is required. By optimizing the SAR and spacecraft specifically for the ocean monitoring problem, and keeping the frontal cross-section down to ~1 m^2, a light weight Taurus-compatible, 5-year lifetime mission, orbiting at an altitude of only 300 km, appears quite feasible. A single satellite would be sufficient to provide twice-daily updates to wave forecast models around the world, without any of the severe limitations of presently orbiting and planned SAR systems.

4. REFERENCES

[1] R.C. Beal, D.G. Tilley and F.M. Monaldo, Large and Small Scale Spatial Evolution of Digitally Processed Ocean Wave Spectra from Seasat Synthetic Aperture Radar, *J. Geophy. Res.* **88**, 1761-1778 (1983).

[2] F.M.Monaldo and R.C.Beal, Real-Time Observations of Southern Ocean Wave Fields from the Shuttle Imaging Radar, *IEEE Trans. Geoscience and Remote Sensing* **33**, 942-949 (1995).

[3] Monaldo, F.M., Comparisions of Wavenumbers, Propagation Directions, and SWHs by the Real-Time SAR Processor with Wave Model Estimated during the SIR-C Experiment, *Proc. IGARSS 96*, Lincoln, Nebraska (1996).

[4] R.C.Beal, Spectrasat: A Hybrid ROWS/SAR Approach to Monitor Ocean Waves from Space, *Johns Hopkins APL Digest* **8**, 107-115 (1987).

[5] Kilgus, C.C., and W.E. Frain, A Spectrasat System Design based on the Geosat Experiment, *Johns Hopkins APL Digest* **8**, 133-137 (1987).

[6] Beal, R. C., S. F. Oden, J. L. MacArthur, and F. M. Monaldo, Real-Time Ocean Wave Monitoring: A Thirty Year Quest Achieved, *Johns Hopkins APL Tech Digest*, **15**, 237-241 (1994).

ACKNOWLEDGEMENTS

The authors gratefully acknowledge the support of their colleagues at JHU/APL in the spacecraft design: Mark Harold, mechanical configuration; Mike McCullough and Larry Mosher, propulsion System; Will Devereaux, GLT communications system.

Using the CCRS Along Track InSAR to Measure and Interpret Ocean Surface Currents

John W. M. Campbell, A. Laurence Gray, John Hughes Clarke[1], Jim Gower[2], and Karim E. Mattar
Canada Centre For Remote Sensing, 588 Booth St., Ottawa, Ontario, Canada
Tel: (613) 998-9060, Fax: (613) 993-5022, Email: jcampbel@ccrs.emr.ca

[1] Ocean Mapping Group, Dept. Geodesy and Geomatics Eng., UNB, PO Box 4400, Fredericton, NB, Canada
[2] Institute of Ocean Sciences, 9860 W. Saanich Road, PO Box 600 Sydney, B.C., Canada

Abstract -- In 1993 the Canada Centre for Remote Sensing modified its CV-580 C(HH)-band airborne cross-track interferometric SAR (InSAR) to operate in an along track interferometric mode using a switchable microstrip antenna mounted on the right side of the aircraft. Subsequently this instrument has been used to measure ocean surface velocities in missions over the Bay of Fundy, the Grand Banks, and in Active Pass. The resulting velocity images can be used to provide information about surface current vectors, bottom topography, or ocean wave heave spectra. Ground truthing of the bottom topography was provided during a Bay of Fundy mission by a side scan sonar on the Canadian Hydrographic Services vessel, "NSC Frederick G. Creed", whereas validation of the surface current measurements has come mostly from current models. The results of these experiments suggest that, under the right conditions, the CCRS along track InSAR can produce a self-consistent surface current vector map and can detect bottom topography changes of 3 to 4 m at depths up to 30 or 40 m.

INTRODUCTION

It has been apparent for many years that ocean surface features such as fronts, wave trains and wakes were visible in SAR imagery. The most common explanation of ocean backscatter is Bragg scattering from short wavelength ($\Lambda = n\lambda / (2\sin\Theta)$, where Θ is the radar incidence angle, $\lambda = 5.656$ cm is the radar wavelength and n is a positive integer) waves on the surface of the water. These waves are strongly affected by such physical processes as wind stress, surfactant density and the strain caused by current velocity modulations. The precise relationship between the radar cross section (RCS) of the ocean and the relevant geophysical parameters is difficult to define, however, and different models have been suggested [1,2].

Along track InSAR provides a more direct way of observing the properties of the ocean than conventional SAR imagery. The phase difference between the radar images received by two antennas separated along the flight path of the aircraft is used to directly measure the mean radial velocity of the scatterers in each target pixel. This information can be used to study wave spectra [3], ocean currents [4,5] and ship wakes [6]. In this paper, the focus is on the CCRS results with ocean currents. Results are considered both in terms of mapping the currents directly and in terms of using current modulations as an indicator of bottom topography modulations.

0-7803-3068-4/96$5.00©1996 IEEE

SYSTEM INFORMATION

The structure and operation of the CCRS C/X-band SAR has been described in detail previously [7]. The InSAR system utilizes a microstrip antenna on the right hand side of the aircraft which can be divided into two separate sub-antennas with phase centres separated by $d = 0.46$ meters along the aircraft. The main C-band antenna, located underneath the aircraft, transmits and the returned signal is received and recorded separately from each of the microstrip antennas. The microstrip antennas have asymmetric azimuth weighting functions which results in each antenna having a main lobe squint of approximately 1.1^0 in opposite directions. To compensate for this, the antennas are mounted with a dihedral having an included angle of approximately 2^0. This results in two-way transmit-receive sidelobes of better than -40 dB. Phase calibration is necessary to achieve accurate estimates of radial velocity. Currently this is achieved by using a large flat object with zero radial motion across the swath (i.e. a few kilometers of coastal terrain) to define the absolute zero phase as a function of incidence angle.

After correcting for sub-pixel misregistrations caused by electronic path lengths and antenna geometry, the complex SAR image from one sub-antenna is multiplied by the complex conjugate of the image from the other antenna to produce an interferogram. The magnitude of each pixel in the interferogram is a measure of the target's radar backscatter and its phase, Φ, is a measure of the target's radial velocity. This is because the doppler processed image from the second antenna represents the same spatial scene as that from the first antenna, but with a temporal offset corresponding to the time taken for the aircraft (and thus the phase centre of the antenna) to travel the distance between the two antennas, $t = d / 2V$, where V is the aircraft velocity and the factor of two comes from the fact that the main antenna transmits for both InSAR receive antennas. In that time a target with radial velocity, v, will have moved a distance vt and thus its phase will have changed by $4\pi\, v\, t / \lambda$. The radial velocity of a given target pixel is thus given by $v = V\lambda\, \Phi / 2\, d\pi$. In initial tests in 1994, the InSAR proved capable of measuring velocities of bright point targets with an accuracy of 5 to 10 cm/s [8].

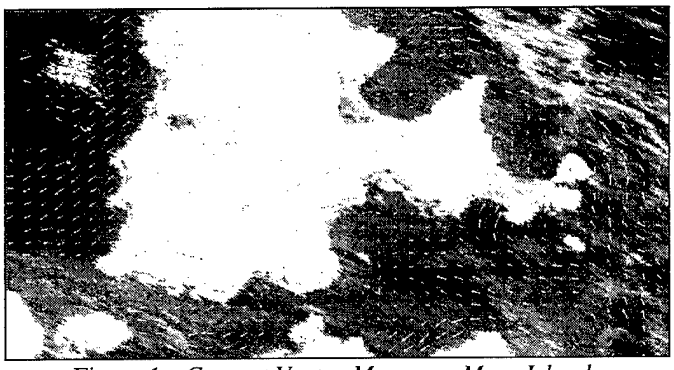


Figure 1 - *Current Vector Map near Macs Island*

SURFACE CURRENT FIELDS

On June 24, 1995 the CCRS Along Track InSAR imaged Letete Passage at the entrance to Passamaquoddy Bay, N.B. The radial velocities from two interferograms derived from passes with approximately perpendicular aircraft tracks were registered and combined to produce a directional velocity vector map. Figure 1 shows these velocity vectors for 60 m by 60 m averaged areas superimposed on a SAR magnitude image. This image was obtained under difficult conditions imposed by the close proximity of bright land targets to the narrow channels of water, and by the low wind speeds on the morning of the data acquisition. Despite this, the current vectors (magnitude range is from 0 m/s to 1.6 m/s) agree with predictions for a flood tide as water passes from the Bay of Fundy through Letete Passage (upper right) and Little Letete Passage (lower left) into Passamaquoddy Bay. That the current turns directly into or forms eddies inside the small bays, is consistent with a rising tide. The shear current down the left side of Macs Island fits the model for the strong current through Letete Passage, following the coastline after it rounds the northern tip of the island until it joins with the lesser current coming through Little Letete Passage. The bright object in the top left of the image is a fish farm.

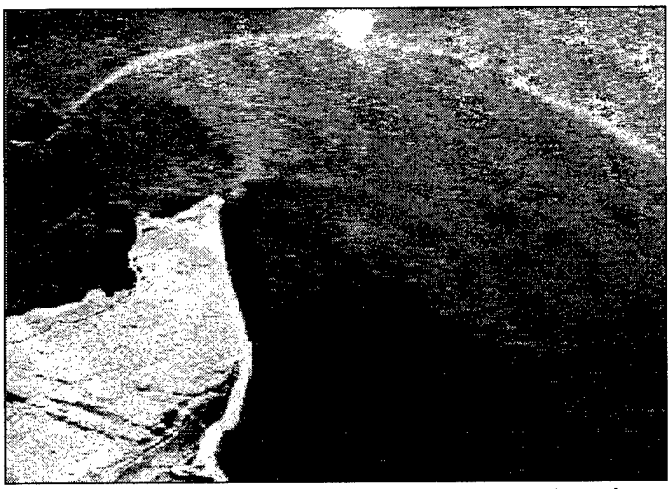


Figure 2 - *SAR Magnitude and Velocity in Bay of Fundy*

BOTTOM TOPOGRAPHIC MODULATIONS

On June 2, 1994 the InSAR flew a long flight line over the Minas Channel in the Bay of Fundy, approximately two hours after low tide. The water depths were low while the currents were large, so this was an ideal time to investigate the ability of the InSAR to detect bottom topographic modulations through their effects on surface velocity. A sample of the features observed is shown in Figure 2, which is a combined SAR magnitude and velocity image. The dark water at the bottom of the image is moving up along the coastline until it encounters the main Fundy current which is traveling to the left. This creates the bright arc near the top of the image, as the two currents come together. Of even more importance, however, is the feature in the bottom right characterized by a series of bright and dark lines along the border of the dark water mass. This feature, which is visible as both a SAR magnitude and velocity modulation, corresponds to a dunefield in Advocate Bay. The dunefield does not appear on any Hydrographic charts and had not been previously surveyed, but local fishermen have verified its existence, and a Canadian Hydrographic Services (CHS) survey is now planned to include this area in 1996.

More quantitative results are shown in Figure 3, which features a larger dune field near Cape Split in the Bay of Fundy. This dune field was the subject of a CHS sonar study by the vessel "NSC Frederick G. Creed" simultaneous with the airborne mission. The three transects through the SAR magnitude image of the dunefield in Fig. 3(a) are used to plot depth (from the side scan sonar), SAR intensity modulation and radial surface velocity versus distance. Only one component of the surface velocity is being measured, so it is difficult to directly model the velocity as a function of depth, but in each transect there is a strong correlation between changes in depth, changes in SAR intensity and changes in surface velocity. Depth modulations of as little as 3 to 4 m at a mean depth of 20 to 30 m produce intensity modulations of up to 5 dB and velocity modulations of up to 0.5 m/s. The maximum ratio of absolute depth to depth modulation which produces observable results in this dunefield is approximately 15.

CONCLUSIONS

The CCRS airborne along track InSAR can produce high resolution, geocoded, calibrated velocity images which can be combined to produce current vector maps for currents which are stable over the time between two passes (approximately twenty minutes) or used individually to detect oceanographic features, including bottom topographic modulations. Since there is currently no simple way of producing high resolution current maps over large areas, this may be a useful tool for examining the current patterns near river deltas, harbours, and other key areas or in environmental monitoring and impact analysis where knowledge of current flow patterns can be very important. The along track InSAR can detect the velocity

modulations caused by subsurface features at depths up to 40 m or more, provided the ocean backscatter is high enough to produce acceptable phase noise levels and the absolute depth to depth modulation ratio is less than 15. Ship based sonar surveys produce more detailed maps of subsurface features than airborne InSAR surveys and they do not have a minimum wind stress or ambient current requirement, but they are very time consuming (approximately 12 hours of sonar imaging time was required for the Scots Bay area versus less than 1 minute for the InSAR image). The ability of the InSAR to detect hydrographic features of interest over large areas has been clearly established, but more data analysis (preferably involving full current vector maps over sonar surveyed areas) before along track InSAR can serve as anything other than a preliminary sensor which is used to queue hydrographic survey vessels to the appropriate areas.

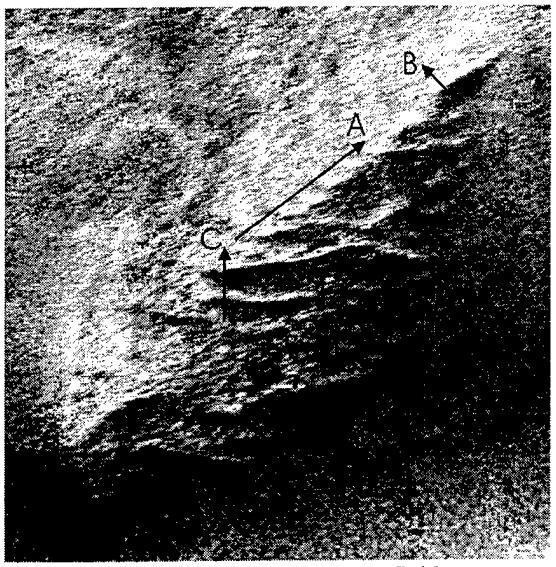


Fig 3(a) - Scots Bay Dunefield

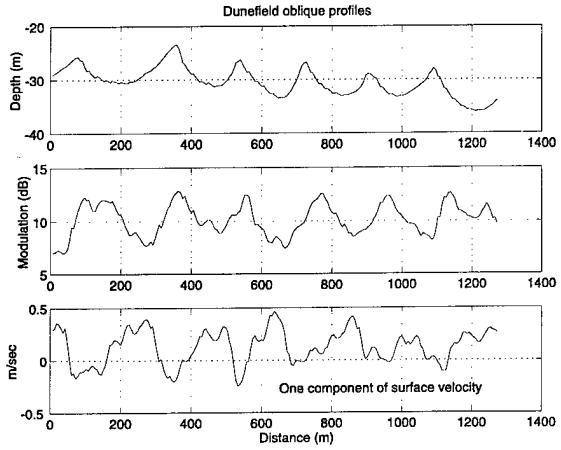
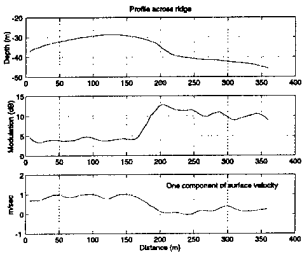
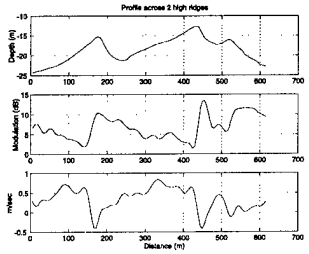


Fig 3(b) - Transect A


Fig 3(c) - Transect B


Fig 3(d) - Transect C

ACKNOWLEDGMENTS

The authors would like to thank Marco van der Kooij for his contributions to the 1994 Bay of Fundy mission and to the initial analysis of the data from this experiment. The crew and sensor operators on the CCRS CV-580 and the "NSC Frederick G. Creed" are also gratefully acknowledged.

REFERENCES

[1] Alpers, W. R., D. B. Ross and C. L. Rufenach, "The detectability of ocean surface waves by real and synthetic aperture radars", *J. Geophys. Res.*, 86, 6481-6498, 1981

[2] Hasselmann, K., R. K. Raney, W. Plant, W. Alpers, R. Shuchman, D. Lyzenga, C. Rufenach and M. Tucker, "Theory of Synthetic Aperture Radar Ocean Imaging: A MARSEN View", *J. Geophys. Res.*, 90, 4659-4686, 1985

[3] Vachon, P. W., C. Bjerkelund, J. Buckley, J. Campbell, F. W. Dobson, A. L. Gray, H. Johnsen and R. Lalbeharry, "Validation of SAR Ocean Wave Measurements: ERS-1 and CV-580 Cross Spectra and CV-580 Along-track InSAR", *Proc. of IGARSS '96*, 1996

[4] Goldstein, R. M. and H. A. Zebker, "Interferometric radar measurement of ocean surface currents", *Nature*, 328, 707-709, 1987

[5] Shemer, L., M. Marom and D. Markman, "Estimates of Currents in the Nearshore Ocean Region Using Interferometric Synthetic Aperture Radar", *J. Geophys. Res.*, 98, 7001-7010, 1993

[6] Orwig, L. P. and D. N. Held, "Interferometric Ocean Surface Mapping and Moving Object Relocation with a Norden Systems K_u-Band SAR", *Proc. of IGARSS `92*, 1598-1600, 1992

[7] Livingstone, C. E., A. L. Gray, R. K. Hawkins, P. Vachon, T. I. Lukowski and M. Lalonde, "The CCRS Airborne SAR Systems: Radar for Remote Sensing Research", *Canadian J. of Remote Sensing*, 21, 468-491, 1995

[8] Gray, A. Laurence, Marco W. A. van der Kooij, Karim E. Mattar and Peter J. Farris-Manning, "Progress in the Development of the CCRS Along-Track Interferometer", *Proc. of IGARSS `94*, 2285-2287, 1994

Comparison of Wave Parameters Measured from the SIR-C On-Board Processor with WAM Predictions in the Southern Ocean

Frank M. Monaldo
The Johns Hopkins University Applied Physics Laboratory
Johns Hopkins Road, Laurel, MD 20723-6099 U.S.A
Tel: (301) 953-5000, Fax: (301) 953-5548, email: Frank_Monaldo@jhuapl.edu *

ABSTRACT

During the SIR-C (Shuttle Imaging Radar) mission in 1994, an APL-built on-board processor computed image spectra from the synthetic aperture radar (SAR) C-band signal. The image spectra, acquired for the purpose of estimating two-dimensional ocean wave energy spectra, were transmitted to the ground in real time. In this paper, we compare the dominate wavelength, propagation direction and significant wave height (SWH) estimated from processor spectra (with additional post processing) with nearly co-located estimates from the WAM (WAve Model) global wave model, as implemented by the U.S. Navy Fleet Numerical Meteorology and Oceanography Center (FNMOC). We demonstrate that despite significant scatter, there are no systematic biases between SAR and WAM estimates of wavenumber and propagation direction. The SAR tends to underestimate SWH at SWHs greater than 4 m. This discrepancy is removed with a simple linear adjustment.

1 INTRODUCTION

In 1978, the United States launched *Seasat*, which provided synthetic aperture radar (SAR) ocean imagery from space for the first time. One of the purposes of the SAR was to measure two-dimensional ocean wave spectra. Several passes, where coincident environmental information was available, were studied intensively [1] [2]. Although the waves imaged by the *Seasat* L-band SAR showed reasonable spatial variations in wavelength and direction, there was a pronounced loss in response to azimuth-traveling waves.

In October 1984, the SIR-B (Shuttle Imaging Radar) mission provided additional SAR imagery. Off the southern coast of Chile, independent estimates of ocean wave spectra from aircraft radars were compared in detail with spectra from five passes of SIR-B imagery. Besides showing close correspondence with independent measurements of the spectrum, SIR-B imagery exhibited far broader response to azimuth-traveling waves than did *Seasat* [3].

The reduction in azimuth response is a consequence of ocean surface motion. A SAR relies on Doppler information from the return radar signal to achieve fine-scale azimuth resolution. The motion of the ocean adds noise to this Doppler information, degrades azimuth resolution and makes azimuth-traveling waves more difficult to image. The effect is proportional to the range-to-velocity ratio of the SAR platform. The minimum detectable azimuth wavelength, $\lambda_{\min}$, can be estimated by

$$\lambda_{\min} = [1\ \mathrm{m}^{\frac{1}{2}}/\mathrm{s}]\frac{R}{V}H_s^{\frac{1}{2}} \quad (1)$$

where R is the range from the SAR platform to the imaged area, V is the velocity of the platform and H_s is ocean significant wave height (SWH) [1].

Since the SIR-B mission flew on the shuttle *Challenger* at about a 230 km altitude and *Seasat* flew at 800 km, SIR-B image spectra had nearly four times better azimuth wavenumber response. In 1991, another SAR was launched on *ERS-1* at an 800 km altitude. The high-altitude mission suffered the same limitations in the measurement of azimuth-traveling waves that *Seasat* did.

The SIR-C mission, flown in April and October 1994, as part of the Space Radar Laboratory (SRL), offered a new opportunity to acquire spectra from a low-altitude orbit. However, obtaining the large number of spectra required for statistical comparisons over large ocean areas would not have been possible using traditional image processing strategies.

To alleviate this problem, the Johns Hopkins University Applied Physics Laboratory designed and fabricated an on-board, real-time processor [4]. These real-time spectra (over 100,000 in all) plus additional post processing form the basis for the comparisons shown here.

During the flights, the U.S. Navy Fleet Numerical Meteorology and Oceanography Center (FNMOC) was running its implementation of the WAM (WAve Model) wave model. These spectra were archived for later comparisons. In this paper, we compare estimates of wavenumber, propagation direction and SWH from the SAR spectra with nearly temporally and spatially coincident WAM spectra.

2 SAR IMAGERY SPECTRA TO OCEAN WAVE SPECTRA

In general, the relationship between the ocean wave height-variance spectrum, $S_h(\vec{k})$, and the SAR image intensity-variance spectrum, $S_{sar}(\vec{k})$, where $\vec{k}$ is vector wavenumber,

*This work was supported by funding from the National Aeronautics and Space Administration and the Naval Research Laboratory (Stennis Space Center).

0-7803-3068-4/96$5.00©1996 IEEE

is nonlinear and difficult to invert [5] [6]. For the case of a SAR with a low R/V ratio ($\leq$ 60 s), a quasi-linear approximation may be invoked, so that

$$S_{\rm sar}(\vec{k}) = \gamma^2(\vec{k}) \exp\left(-\frac{k_a^2}{2k_\sigma^2}\right) R_{\rm sar}^2(\vec{k}) S_{\rm h}(\vec{k}) \,. \qquad (2)$$

The γ^2 function describes the coherence between wave height and radar cross section. For situations with no cross section nonlinearities and no noise, $\gamma^2 = 1$.

The motion of the ocean surface, to first order, simply degrades azimuth resolution. The Gaussian term in Equation 2 represents the loss of resolution at large azimuth wavenumbers, k_a. The value k_σ defines the azimuth falloff. This value is dependent upon both the sea state and R/V. The higher the sea state and the higher the value of R/V, the smaller the k_σ and the greater the loss in azimuth resolution.

The function $R_{\rm sar}$ is the SAR modulation transfer function. This function describes how ocean height variations map into cross section variations — the wave imaging mechanisms [7]. Using a simplified version of the $R_{\rm sar}$ found in [8], we inverted (2) to estimate wave height spectra from the processor image spectra.

3 WAM SPECTRA

WAM is a third-generation wave model for the global prediction of wave height spectra from an input wind field. FNMOC runs an operational implementation of the WAM for the U.S. Navy [9]. FNMOC archived the WAM estimates of the two-dimensional spectra for the April and October periods corresponding to the SIR-C flights.

The WAM spectra and the wavenumber propagation direction and SWH were extracted on a 4° × 4° spatial grid, and in twelve hours time steps. These parameters form the basis for comparison with the SIR-C processor-derived wave spectra.

4 COMPARISON

To compare SIR-C and WAM wave parameters, we averaged 20 adjacent along-track spectra from the on-board processor. We then post processed these spectra to estimate the height-variance spectra and determine the peak wavenumbers, propagation angles, and SWHs associated with the processor spectra. The closest WAM spectra in space and time were selected for comparison. If the WAM had only a single dominant peak and the SAR-derived spectrum had a single dominant system, then we associated the wavenumber, propagation direction and SWH from each of these spectra for comparison.

Figure 1 is a plot showing the comparison between WAM estimates of dominant wavenumber and associated SAR-derived estimates. The correlation coefficient between the wavenumber estimates is low, 0.23. However, the distributions of observed wavenumbers are nearly identical. We conclude that the SAR

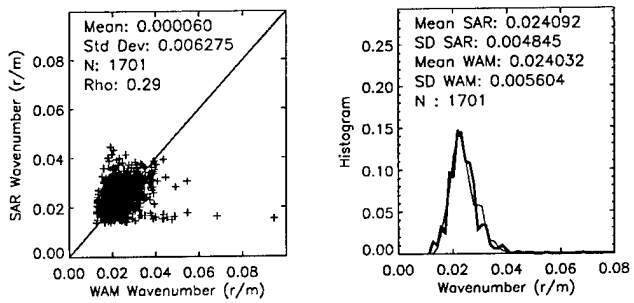


Figure 1. Comparison of SAR and WAM wavenumbers . The thick line in this histogram refers to the WAM distribution.

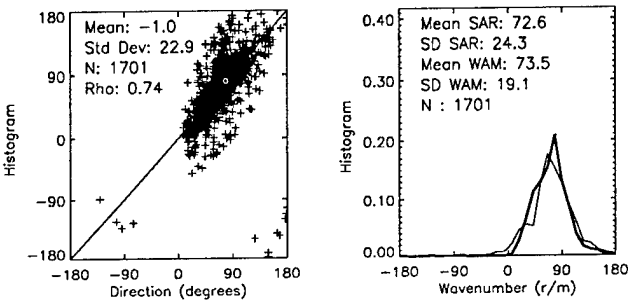


Figure 2. Comparison of SAR and WAM propagation angles. The thick line in this histogram refers to the WAM distribution.

produces an unbiased estimate of wavenumber that matches the model predicted wavenumber distributions. Observed point-by-point differences with the WAM estimates may be associated with spatial and temporal differences in spectra location, local errors in the input wind field or model inadequacies.

Figure 2 is a plot comparing propagation direction estimates from the SIR-C SAR and WAM wave spectra. The spectrum-by-spectrum correlation of 0.74 is excellent. The RMS difference between the SAR and WAM direction estimates is about 23° and the largest mean difference −1°. We conclude that a properly corrected, a low-R/V SAR produces unbiased errors in propagation direction.

When we attempted a spectrum-by-spectrum comparison of SWH, we found that the SAR underestimated SWH at SWHs greater than 4 m. By making a simple linear adjustment to the SAR SWH estimates, we eliminated this systematic error. Figure 3 shows the spectrum-by-spectrum comparisons between WAM and SAR SWH estimates after adjustment.

5 CONCLUSIONS

The processor-computed spectra from the SIR-C shuttle missions offered the first opportunity to acquire a large number of SAR image spectra over a large variety of sea states for statistical

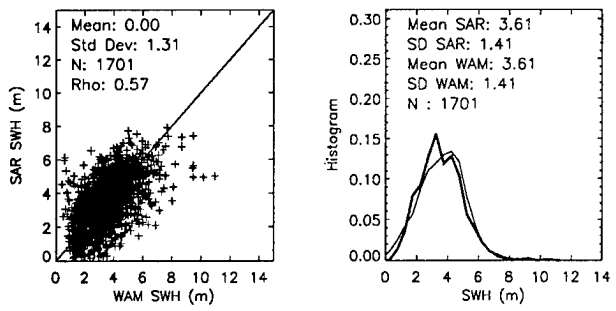


Figure 3. Comparison of SAR and WAM SWH. The thick line in this histogram refers to the WAM distribution.

comparisons with other estimates.

With modest additional processing, image spectra from a low-R/V SAR can be used to estimate wave height-variance spectra. There appears to be no systematic differences in the WAM and SAR estimates of wavenumber and propagation direction. The distribution of wavenumber and propagation direction over the Southern Ocean estimated from the SAR agree closely with WAM distributions. Some of the scatter in the spectrum-by-spectrum comparisons is associated with temporal and spatial differences between the SAR and WAM estimates. In addition, we believe that much of the scatter may be caused by errors in the input wind field and wave model errors.

It is interesting that the spectrum-by-spectrum correlation is far better for propagation direction than for wavenumber. If we assume that the model input wind field geographically positions the storms correctly, the correspondence of the WAM estimates with the SAR measurements of propagation direction is not surprising. If there are errors in either the timing of the storms or their intensities, random errors would occur in the WAM wavenumber estimates. These random errors are observed in the data. However, if the errors in timing and intensity in the input wind field are random, the total distribution of WAM wavenumbers and propagation angles should not be affected. This is consistent with the comparisons presented here.

In addition, after a linear adjustment in SAR-estimates SWH, there is less systematic disagreement in the spectrum-by-spectrum comparison of SWH. The RMS residual differences were about 1.3 m.

We have employed other, more complex, models of the SAR modulation transfer functions and the results for those models are very similar to those presented here.

REFERENCES

[1] Beal, R. C., D. G. Tilley and F. M. Monaldo, "Large- and small-scale spatial evolution of digitally processed ocean wave spectra from Seasat synthetic aperture radar," J. Geophys. Res., vol. 8, pp. 1761–1778, 1983.

[2] Beal, R. C., T. W. Gerling, D. E. Irvine, F. M. Monaldo, and D. G. Tilley, "Spatial variation of ocean wave directional spectra from the Seasat synthetic aperture radar," J. Geophys. Res., vol. 91, pp. 2433–2449, 1986.

[3] Beal, R. C., F. M. Monaldo, D. G. Tilley, D. E. Irvine, E. J. Walsh, F. C. Jackson, D. W. Hancock III, D. E. Hines, R. N. Swift, F. I. Gonzalez, D. R. Lyzenga, and L. F. Zambresky, A Comparison of SIR-B directional ocean wave spectra with aircraft scanning radar spectra," Science, vol. 232, pp. 1531–1535, 1986.

[4] Beal, R. C., S. F. Oden, J. L. MacArthur, and F. M. Monaldo, "Real-time ocean wave monitoring from space: A thirty-year quest achieved," Johns Hopkins Tech. Digest, vol. 15, pp. 237–241, 1994.

[5] Hasselmann, K., and S. Hasselmann, "On the nonlinear mapping of an ocean wave spectrum into a synthetic aperture radar image spectrum and its inversion," J. Geophys. Res., vol. 96, pp. 10,713–10,729, 1991.

[6] Jensen, J. R., "The Fourier transformation and the power spectral density of SAR imagery of the ocean surface," Proc. International Geoscience and Remote Sensing Symposium, vol. 2, Espoo, Finland, pp. 447–450, 1991.

[7] Alpers, W. R., D. B. Ross and C. L. Rufenach, "On the detectability of ocean surface waves by real and synthetic aperture rada " J. Geophys. Res., vol. 86, pp. 6481–6498, 1981.

[8] Monaldo, F. M., and D. R. Lyzenga, "On the estimation of wave slope- and height-variance spectra from SAR imagery," IEEE Trans. Geosci. Remote Sensing, vol. GE-24, pp. 543–551, 1986.

[9] Wittman, P. A. and R. M. Clancy, "Implementation and validation of global third-generation wave model and Fleet Numerical Oceanography Center," Ocean Wave Measurement and Analysis, Proc. of the Second International Symposium, American Society of Civil Engineers, New Orleans, 1993.

Estimation of Thermocline Depths From SAR Imagery and a Two Layer Density Model

David L. Porter and Donald R. Thompson
The Johns Hopkins University
Applied Physics Laboratory
Johns Hopkins Road
Laurel, MD 20723 USA
(410) 792-5000; fax: (410) 792-5548
email: David_Porter@jhuapl.edu

Abstract -- Imagery from the ERS-1 Synthetic Aperture Radar (SAR) collected on July 18, 1992 was used to estimate the depth of the seasonal thermocline in the New York Bight. It was assumed that the internal wave packets observed in the SAR imagery were tidally generated at the shelf break and that the temporal spacing between the packets was 12.42 hours i.e. one M_2 tidal cycle. The wave speed of a packet was estimated by measuring the distance from the leading crest in one packet to the leading crest in the previous one and dividing by the tidal period. For each packet pair, nine separate measurements, evenly spaced along the wave crest, were used to obtain a mean separation between the packets. The mean of the observed internal wave speeds for the southern packet was 0.79 m/s with a deviation about the mean of 11%. The depth of the thermocline was computed from the wave speed derived from a simple two-layer fluid model for these internal wave dynamics. The densities were obtained from a joint Russian-United States internal wave experiment that was concurrent with the SAR overpass. The computed mean depth of the seasonal thermocline is 22 m. The average depth of the seasonal thermocline observed during the summer season from historical data was on the order of 20 m, which agrees with the estimated thermocline depth from the SAR imagery.

0-7803-3068-4/96$5.00©1996 IEEE

1 INTRODUCTION

During the spring and summer, when the thermocline on the continental shelf is fully developed, the entire Mid-Atlantic Bight is replete with internal waves. Figure 1 shows the surface manifestation of these internal waves as imaged on July 18, 1992 from the C-band Synthetic Aperture Radar (SAR) on the European spacecraft ERS-1 during the Joint US/Russia Internal Wave Experiment [Gasparovic et al., 1993.] The center of this image is at 39°37'20"N, 72°35'40"W and is 100 km on the sides. Note that there are no internal waves in the lower right hand portion of the image, and only rather weak indications of their existence in the upper left portion [Porter et al., 1996.] Moving from the lower right hand corner of the image diagonally to the upper left hand corner, internal wave generation, propagation, and dissipation can be observed. There are four strong packets of waves in the center of the image. This image shows that wave genesis and dissipation takes place over a distance of roughly 100 km across the continental shelf. It is the generally accepted hypothesis that the interaction of the internal tides with the sharply-sloped bathymetry at the shelf break is the dominant generation mechanism for the internal waves visible in Figures 1 [Zheng et al., 1993].

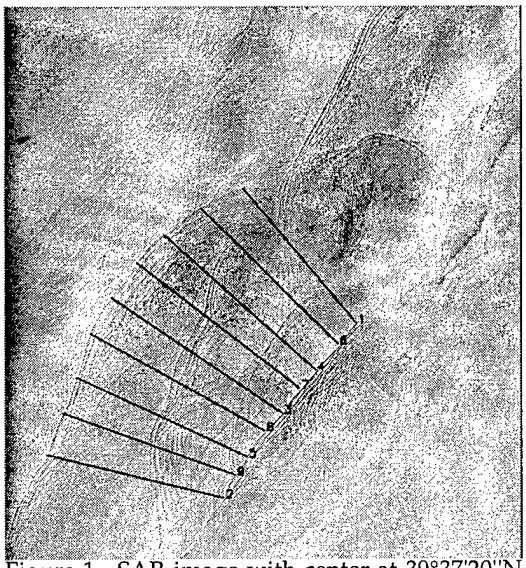


Figure 1. SAR image with center at 39°37'20"N, 72°35'40"W. The sides of the image are 100 km in length. The image is oriented 8.5° west of North. Shown are two internal wave packets, where the first crest in each packet was connected to the previous packet.

2 ANALYSIS

In Figure 1 nine lines have been drawn connecting two internal wave packets that may have been generated 12.42 hours apart. The lines are labeled with numbers that correspond to the number shown in Table 1. The average distance is 35.7 m with a standard deviation of 11%. This gives a speed of wave propagation of 0.79 m/s.

TABLE 1. Wave number and distance [km] between lead crests in the two packets.

Line Number	Distance [km]
1	32.1
2	33.9
3	38.2
4	37.4
5	34.9
6	35.5
7	38.0
8	37.0
9	34.0
AVERAGE	35.7

If we assume that the water column on the continental shelf can be represented by two layers of constant density, then the phase speed of the wave is given by:

$$c_p = \sqrt{g\left(\frac{\rho_2 - \rho_1}{\rho_2}\right)\frac{hH}{h+H}}$$

where,

$\rho_1 = 1.0224$ gm / cm^3

$\rho_2 = 1.0253$ gm / cm^3

g = gravitational acceleration

h = depth of pycnocline

H = depth from pycnocline to bottom.

The densities ρ_1 and ρ_2 were measured during the joint Russian-United States internal wave experiment [Porter, et al., 1993.] Using the average depth of the water column in this area, we have plotted c_p as a function of h in Figure 2.

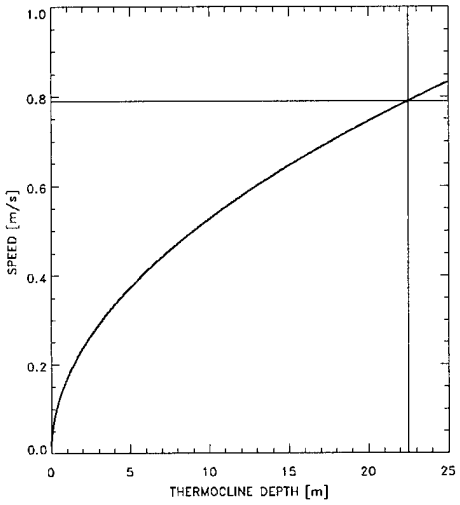


Figure 2. This is the wave speed as a function of the thermocline depth. Note the horizontal line, that represents the observed speed of the wave, i.e. 0.79 m/s. The point where this intersects the line then has a vertical line showing that the depth required for this speed is approximately 22.5 m.

Observations over the past decade conducted by the National Ocean and Atmospheric Administration in this region of the water is shown in Figure 3. Note the evolution of the pycnocline in time as the season progress. In winter we see a vertically mixed column of water. At the onset of spring in May we see the thermocline beginning to be developed then

in summer we see a very well defined pycnocline. This persists until early fall when the storms mix the thermocline and it begins to erode.

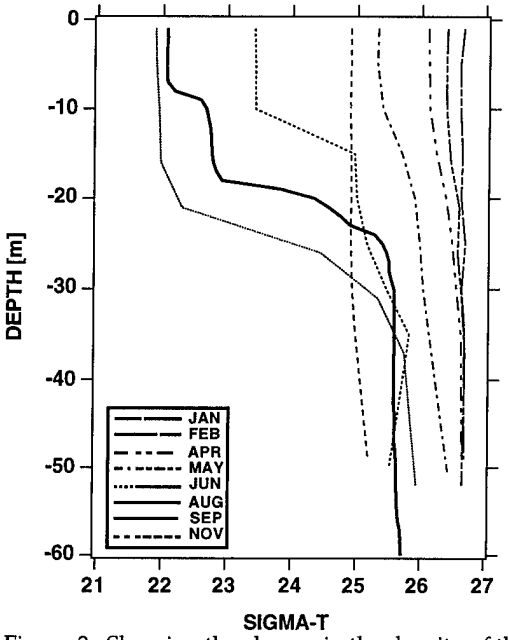


Figure 3. Showing the change in the density of the water column during the seasonal cycle. This observation was made at 40°58'N and 71°10'W.

Note that in August (this is the closest in time to the July SAR image) the depth of the thermocline is about 20m. This compares well with the estimated depth of the thermocline from the SAR observation of 22 m.

3 CONCLUSIONS

Preliminary results from using SAR images to estimate oceanographic parameters on the continental shelf of the world's oceans have been promising. By employing a two layer model, an estimate of the thermocline depth was made that agreed well with seasonal observation made in the same area. Future work will research internal wave breaking and its role in mixing on the shelf.

4 REFERENCES

Gasparovic, R. F., R. D. Chapman, F. M. Monaldo, D. L Porter, and R. E. Sterner, Joint U.S./Russia internal wave remote sensing experiment: Interim results *JHU/APL Technical Report S1R-93U-011*, May 1993.

Porter, D. L., R. D. Chapman, and R. F. Gasparovic, "Comparisons of Internal Waves as Observed by a Towed CTD and RADAR," *JHU/APL Technical Report S1R-93U-010*, September 1993.

Porter, D. L., H.H. Pao and D.R. Thompson, "Continental Shelf Parameters Inferred from SAR Internal Wave Observations," *EOS*, p. OS83, January 16, 1996.

Zheng, Quanan, Xiao-Hai Yan, and Vic Klemas, Statistical and dynamical analysis of internal waves on the continental shelf of the middle Atlantic bight from space shuttle photographs, *J. Geophys. Res.*, **98**, 48495-8504, 1993.

Validation of SAR Ocean Wave Measurements: ERS-1 and CV-580 Cross Spectra, and CV-580 Along-track InSAR

P.W. Vachon, C. Bjerkelund, J. Buckley[1], J. Campbell, F.W. Dobson[2], A.L. Gray, H. Johnsen[3], R. Lalbeharry[4]

Canada Centre for Remote Sensing, 588 Booth St., Ottawa, Ont. K1A 0Y7 CANADA
Phone: (613) 998-9060 Fax: (613) 993-5022 E-mail: vachon@ccrs.emr.ca

[1]Royal Military College of Canada, Kingston, Ont. K7K 5L0 CANADA
[2]Bedford Institute of Oceanography, Dartmouth, N.S. B2Y 4A2 CANADA
[3]NORUT Information Technology, N-9005 Tromso, NORWAY
[4]Atmospheric Environment Service, Downsview, Ont. M3H 5T4 CANADA

Abstract – In Dec., 1994 a field program, now known as Sea Truth and Remote Sensing (STARS'94), was carried out over the Grand Banks of Newfoundland. The field program has provided data which offers the opportunity to validate synthetic aperture radar (SAR) measurements of the ocean wave spectrum. We present validation of SAR spectral inversions, starting from the inter-look cross spectrum, for ERS-1 SAR and the CCRS CV-580 SAR. We also present a direct measurement of the heave spectrum using the along-track interferometry (ATInSAR) mode of the CCRS SAR.

INTRODUCTION

In this paper, we validate SAR as a sensor of ocean waves based on the cross spectrum between individual looks [1]. The cross spectrum eliminates noise contributions to the SAR image spectrum and often resolves the wave propagation direction. Furthermore, it may be inverted to a wave height spectrum using an iterative inversion scheme to account for the nonlinear velocity bunching imaging mechanism.

The ERS-1 [2] and CCRS CV-580 airborne SAR [3] data acquired during STARS'94 are summarized in Fig. 1 and Tables 1 and 2. The airborne SAR data, acquired with a small range-to-velocity ratio R/V, have less imaging nonlinearity than the ERS-1 SAR data and are a useful validation standard in their own right [4]. We also obtained Directional Wave Rider (DWR) heave spectra, Minimet (MM) wind data, and wave model hindcasts from the 3rd generation Canadian Spectral Ocean Wave Model (CSOWM) [5].

Table 1: Summary of STARS'94 SAR data.

date 1994	LP	time UTC	lk	trk [deg]	mode
Dec. 3		14:32	R	195	ERS-1
	44	15:05	L	137	dual pol.
	55	15:23	R	317	ATInSAR
	62	16:10	R	47	ATInSAR
Dec. 4		01:50	R	345	ERS-1
	44	02:13	L	137	dual pol.
Dec. 5	44	23:30	L	130	dual pol.

0-7803-3068-4/96$5.00©1996 IEEE

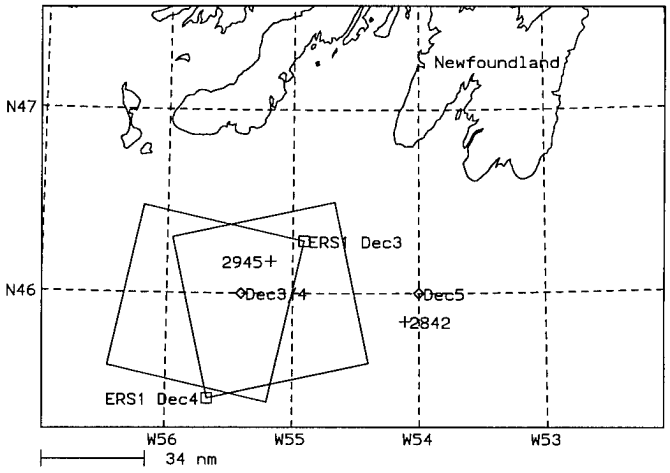


Figure 1: Map of Grand Banks of Newfoundland study site. CSS *Parizeau* location on Dec. 3/4, and 5, and key CSOWM grid points (+) (labelled by number) are indicated.

The CCRS SAR was operated in its C-band HH ATInSAR mode [6] for several passes on each date of STARS'94. In this case, images are collected from antennas whose phase centres are separated along track by 0.46 m, corresponding to separations in acquisition time on the order of 4 ms. An interferogram may be formed between the fore and aft images, whose phase is a direct measure of the wave orbital velocity [7].

RESULTS

Fig. 2 shows time-series of MM and model wind speed and direction. Figs. 3, 4, and 5 show the heave spectra from Dec. 3, 4, and 5, respectively. The SAR image cross spectra were calculated as follows: 7 individual looks were extracted in azimuth and detected; image cross spectra were formed between look pairs 1/4, 2/5, 3/6, and 4/7; and the four cross spectra were averaged together and smoothed. The resulting SAR image cross spectra were inverted using the algorithm described by Engen and Johnsen [1]. The real and imaginary parts of the

Table 2: Derived RAR MTF and H_s values.

data	mode	R/V [s]	θ [°]	ϕ [rad]	M	H_s [m]
Dec. 3	ERS	114.7	21.9	1.88	13.4	1.2
	HH	25.3	55.2	1.15	5.3	2.0
	VV			1.15	5.5	2.0
Dec. 4	ERS	114.6	21.8	0.79	13.1	1.3
	HH	36.3	66.9	0.12	14.0	2.5
	VV			0.13	8.3	2.0
Dec. 5	HH	38.5	53.3	0.83	8.5	1.7
	VV			0.31	7.7	1.7

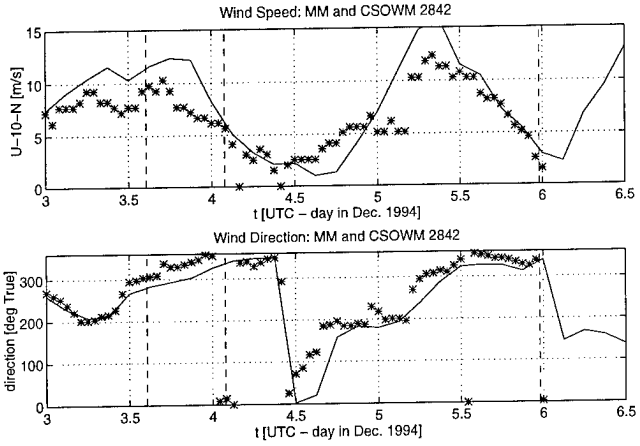


Figure 2: Wind time-series from STARS'94. $*$: data. Solid line: model. Vertical lines: SAR pass times.

cross spectrum were weighted so that they contributed equally to the inversion cost-function. The real aperture radar (RAR) modulation transfer function (MTF) magnitude M and phase ϕ were estimated for each case using an empirical method [8]. The measured values for the RAR MTF and the waveheights of the inverted spectra are summarized in Table 2.

For the CV-580 spectra, the RAR MTF is not always dependent on polarization. The RAR MTF for ERS-1 differs due to its smaller incidence angle. The inverted CV-580 spectra are consistent between polarizations. The ERS-1 spectra have underestimated the waveheight due to their large azimuth cutoff.

The ATInSAR spectrum shown in the lower left corner of Fig. 3 is also based on image cross spectrum techniques. Seven individual complex looks were extracted from the fore and aft channels, individual look interferograms were formed, and the velocity was extracted from the phase. The cross spectra between pairs of velocity images were then calculated and averaged, and the resulting directionally resolved velocity spectrum was mapped directly into a heave spectrum based on the acquisition geometery. For Dec. 3, we have crossing passes available in ATInSAR mode. Rather than trying to account for the az-

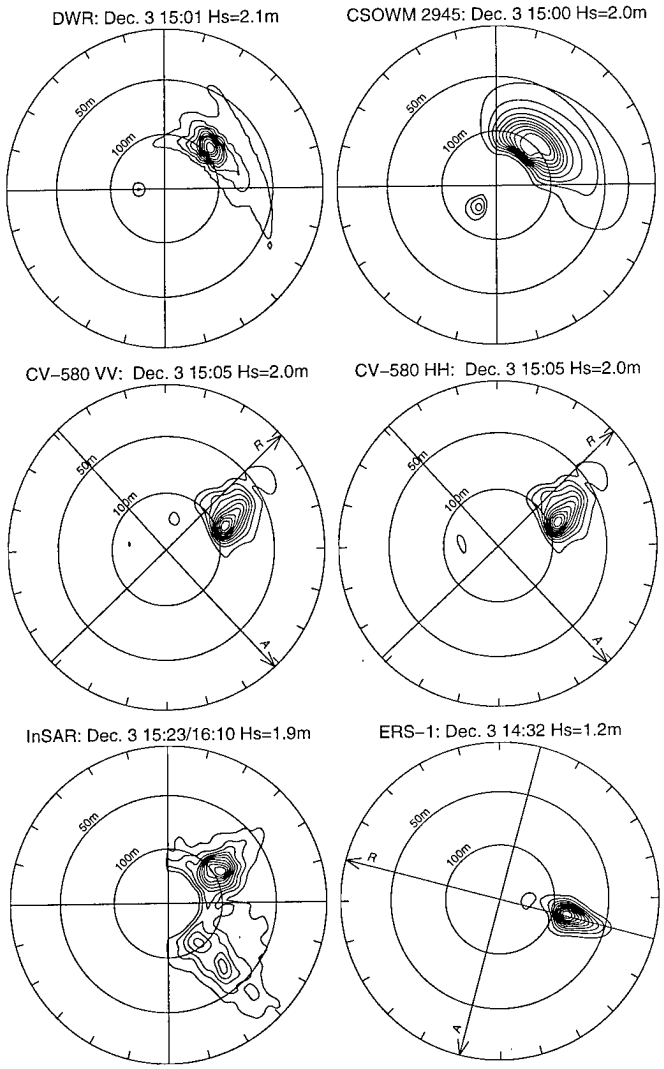


Figure 3: Heave spectra: Dec. 3.

imuth cutoff with an inversion process for each pass, we have blended the derived heave spectra from the crossing passes to produce a composite spectrum which reduces azimuth cutoff.

The ATInSAR heave spectrum has a distinct bi-modal nature, which differs from the other SAR-derived spectra. However, the bi-modal spectrum is consistent with the wind backing following the passage of two fronts around the ERS-1 pass time (showing in Fig. 2, which is east of the ATInSAR measurement site). There is good agreement between the ATInSAR waveheight and that from the other sources.

CONCLUSIONS

The cross spectrum between individual looks, for both the ERS-1 and the CV-580 SARs, is a useful starting point for SAR wave spectral inversion. The inverted ERS-1 and CV-580

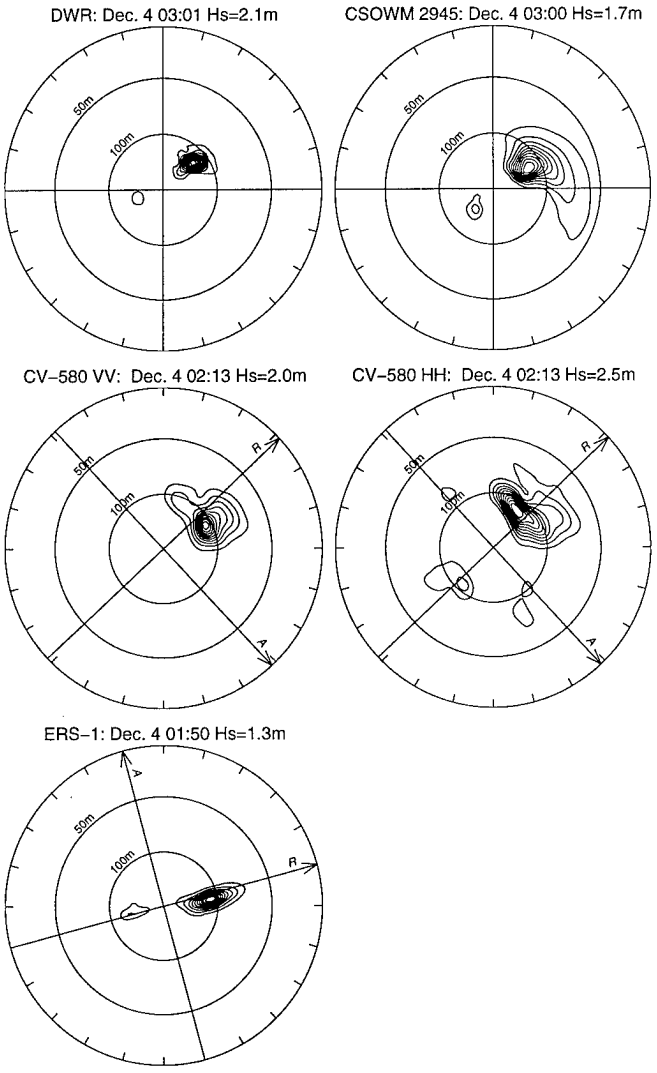


Figure 4: Heave spectra: Dec. 4.

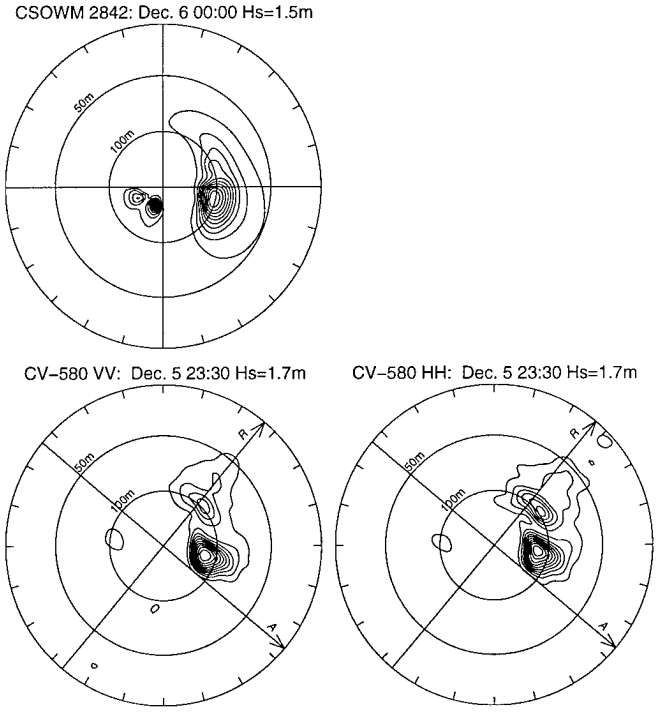


Figure 5: Heave spectra: Dec. 5.

SAR spectra, based upon empirical estimates of the RAR MTF, show reasonable agreement with buoy and model spectra. A directionally-resolved ATInSAR-derived heave spectrum is in reasonable agreement with the noted validation data, without the need for any inversion processing.

REFERENCES

[1] G. Engen and H. Johnsen. SAR-ocean wave inversion using image cross spectra. *IEEE Trans. Geoscience Rem. Sens.*, 33(4):1047–1056, 1995.

[2] E.P.W. Attema. The active microwave instrucment on-board the ERS-1 satellite. *Proc. IEEE*, 79(6):791–799, 1991.

[3] C.E. Livingstone, A.L. Gray, R.K. Hawkins, P.W. Vachon, T.I. Lukowski, and M. LaLonde. The CCRS airborne SAR systems: Radar for remote sensing research. *Can. J. Rem. Sens.*, 21(4):468–491, 1995.

[4] P.W. Vachon, H.E. Krogstad, and J.S. Paterson. Airborne and spaceborne synthetic aperture radar observations of ocean waves. *Atmosphere-Ocean*, 32(1):83–112, 1994.

[5] M.L. Khandekar, R. Lalbeharry, and V. Cardone. The performance of the Canadian Spectral Ocean Wave Model (CSOWM) during the Grand Banks ERS-1 SAR wave spectra validation experiment. *Atmosphere-Ocean*, 32(1):31–60, 1994.

[6] A.L. Gray, K.E. Mattar, and M.W.A. van der Kooij. Cross-track and along-track airborne inteferometric SAR at CCRS. In *Proc. 17th Canadian Symposium on Remote Sensing, 13–15 June 1995, Saskatoon, Saskatchewan, Canada*, pages 232–237, 1995.

[7] R.M. Goldstein, F. Li, J. Smith, R. Pinkel, and T.P. Barnett. Remote sensing of ocean waves: The surface wave process program experiment. *J. Geophys. Res.*, 99(C4):7945–7950, 1994.

[8] S. Jacobsen and K.A. Høgda. Estimation of the real aperture radar modulation transfer function directly from synthetic aperture radar ocean wave image spectra without a priori knowledge of the ocean wave height spectrum. *J. Geophys. Res.*, 99(C7):14,291–14,302, 1994.

COAST WATCH -95: ERS-1/2 SAR Applications of Mesoscale Upper Ocean and Atmospheric Boundary Layer Processes off the Coast of Norway

O. M. Johannessen[1], J. A. Johannessen[2], A. D. Jenkins[3], K. Davidson[4], D. R. Lyzenga[5], R. Shuchman[5], P. Samuel[3], H. A. Espedal[3], J. Knulst[6], E. Dano[7], and M. Reistad[8]

[1]Nansen Environmental and Remote Sensing Center, Edvard Griegs vei 3a,
N-5037 Solheimsviken, Bergen, Norway; and
Geophysical Institute, University of Bergen, Norway.
+47-55 29 72 88, Fax +47-55 20 00 50, Ola.Johannessen@nrsc.no
[2]ESA-ESTEC, Keplerlaan 1, NL-2200 AG Noordwijk, The Netherlands.
[3]Nansen Environmental and Remote Sensing Center, Bergen, Norway
[4]Naval Postgraduate School, Monterey, CA, U.S.A.
[5]Environmental Research Institute of Michigan, Ann Arbor, MI, U.S.A.
[6]Institute for Water and Air Research, Aneboda, S-36030 Lammhult, Sweden.
[7]Dept of Naval Architecture & Marine Engineering, University of Michigan, Ann Arbor, MI, U.S.A.
[8]The Norwegian Meteorological Institute, Allégt. 70, Bergen, Norway

ABSTRACT

The ERS SAR sensors have demonstrated their capability for imaging ocean waves, internal waves, underwater topography, eddies, fronts, natural slicks, oil slicks, and atmospheric features in the marine boundary layer such as wind.

In order to quantify the mesoscale upper ocean and atmospheric boundary layer processes, a tandem ERS-1/2 ESA AO experiment was carried out off the south-western coast of Norway during the month of September 1995. A unique integrated data set was collected, including extensive SAR coverage in the ERS-1/2 tandem mode, an extensive set of oceanographic and meteorological variables from the R/V Håkon Mosby of the University of Bergen, metocean parameters from state-of-the-art metocean buoys, and natural slick sampling with two radio-controlled "mini research vessels".

Analysis from this very comprehensive integrated experiment is reported, quantifying coastal jets, ocean fronts, natural slicks, wind velocity, wind fronts and rain showers from SAR imaging.

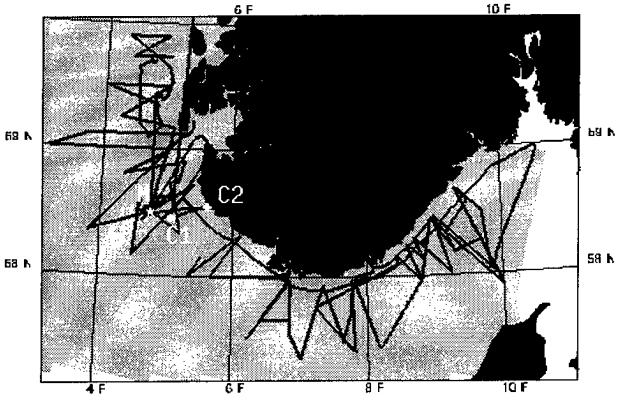


Figure 1: The experimental area, showing SAR coverage in grey, location of moorings (M = metocean buoy, C1/C2 = current meter moorings), and ship track. The field cruise took place from 11 September to 1 October 1995.

1. INTRODUCTION

The synthetic aperture radar (SAR) capability of the ERS-1 and ERS-2 satellites for imaging geophysical phenomena near the sea surface has been demonstrated in many studies [1–11]. The phenomena include ocean waves, internal waves, underwater topography, oceanic eddies and fronts, natural slicks and oil slicks, and atmospheric features in the marine boundary layer such as wind and atmospheric gravity waves.

In order to quantify these mesoscale upper ocean and atmospheric boundary layer processes, a tandem ERS-1/2 ESA AO experiment was carried out in the Skagerrak, off the south-west coast of Norway, during September 1995. The data collected comprises a unique integrated data set, with SAR coverage in the ERS-1/2 tandem mode, ship-borne oceanographic meteorological, and active/passive microwave observations, meteorological and oceanographic observations from a ship and

0-7803-3068-4/96$5.00©1996 IEEE

moored instruments, and *in situ* sampling of natural surface slicks. Fig. 1 shows the experimental area, the positions of the moorings, the ship track, and the ERS-1/2 SAR coverage (including both descending and ascending orbits).

2. OBSERVATIONS

2.1. Remote Sensing

The ERS SAR coverage shown in Fig. 1 shows that ample use was made of the tandem ERS-1/2 SAR coverage at 24-hour separation, and also ascending/descending ERS passes at ~11–13-hour separation. There was also substantial cloud-free coverage by ERS ATSR and NOAA AVHRR infra-red sensors, giving good information on the surface ocean thermal structure.

2.2. Ship-borne instrumentation

The University of Bergen research vessel R/V *Håkon Mosby* was employed in the field programme, to make *in situ* metorological and oceanographic measurements, and to deploy and retrieve current meter moorings, a metocean buoy, and a "mini research vessel" for surface microlayer sampling. The ship was directed to locations of interest using analyses of SAR and infra-red (AVHRR/ATSR) satellite images which were processed by Tromsø Satellite Station, analysed at the shore operations centre in Bergen, transmitted to the ship by facsimile and subsequently downloaded to the shipboard computer system by digital satellite transmission. The Norwegian Meteorological Institute also provided a special operational forecast service, for meteorology and sea state.

Meteorology An Aanderaa weather station provided wind, pressure, air temperature and humidity observations from the *Håkon Mosby*. The Naval Postgraduate School (NPS) weather station duplicated these observations, with additional observations of turbulent wind components using an ultrasonic anemometer, turbulent humidity fluctuations using an Ophir hygrometer. Surface-layer aerosol particle size distribution in the range 0.3–200 μm was measured continuously, and regular rawindsonde launches were performed.

Ship-borne radar/radiometer *In situ* measurements were made by an ERIM/University of Michigan consortium represented by Eric Dano and Dave Lyzenga, using a rail-mounted system consisting of a C-band dual-polarized Doppler radar, C-band radiometer and video camera. The measurements collected during the experiment include the following situations: box patterns, near the NPS buoy, and during typical wind-wave situations; transects of current fronts, temperature fronts, and surfactant regions; periods of low wind, and of high wind; breaking waves, atmospheric fronts, and rain showers. Radiometer data were collected on five occasions, on September 17, 18 and 20, for a total period of approximately 10 hours.

Oceanographic measurements The sea surface temperature (SST) was recorded continuously, with supplementary SST observations being made with a thermistor suspended from the ship so that it skimmed the water surface. Temperature and salinity measurements down to 200 m depth were made using a SeaSoar towed CTD.

2.3. Moored Instruments and Instruments Deployed from the Research Vessel

Metocean buoy The NPS metocean buoy measured two-dimensional wave spectra using a Hippy Datawell sensor. It also measured pressure, vector wind, air and sea temperature, humidity, turbulent fluctuations in wind, temperature and humidity, and aerosol particle size distribution.

Current measurements Two sub-surface current meter moorings were deployed, with Aanderaa current meters at 25 m, 50 m and 100 m depth and at 25 m above the sea bottom.

Mini research vessel A remotely-controlled platform "INTERFACE II" was deployed on September 13, 15 and 18. It is approximately 1 m long and is equipped with a rotating teflon drum to take direct samples of the surface microlayer. It was also equipped with air and sea temperature sensors and a K-band radar.

3. RESULTS

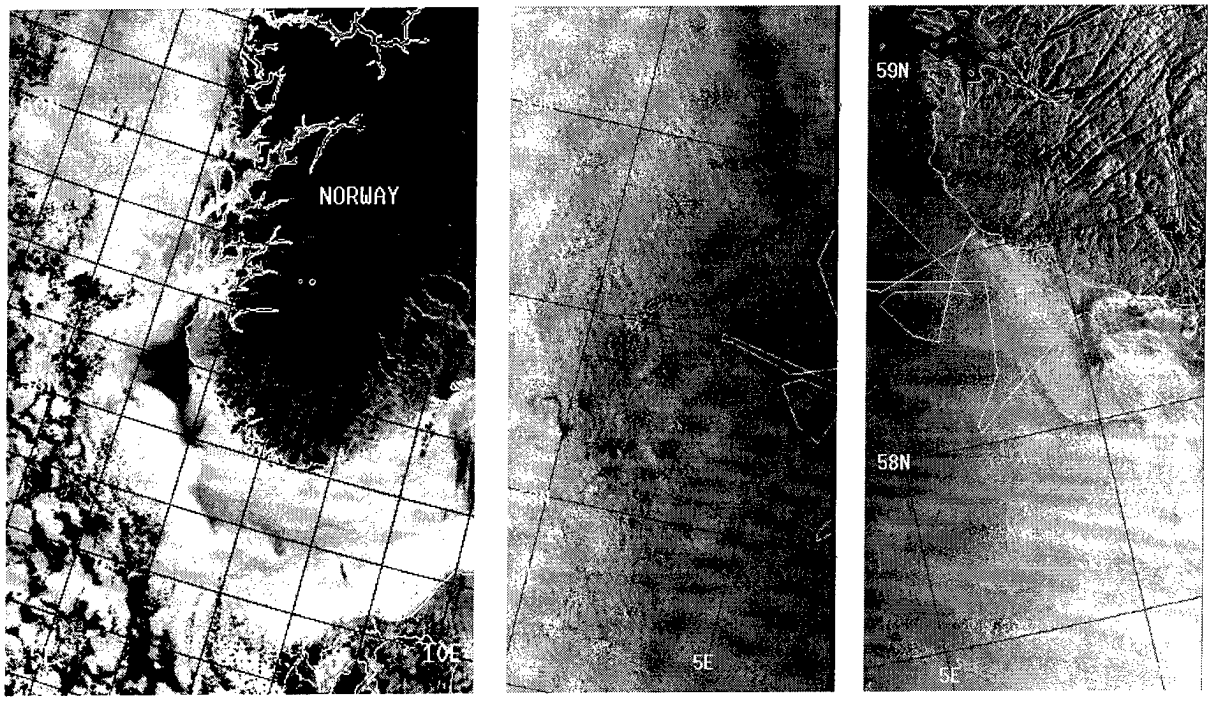
3.1. Ocean Fronts and Coastal Jets

Coastal upwelling was induced by north-westerly winds during the latter part of the field program. A good example is shown in the AVHRR image in Fig. 2: from the ship the sea-surface temperature was measured as ~8°C inside the dark region and ~12°C outside it. The air temperature was ~8°C at the time of observation. SAR images obtained near the same time are shown to the right of the AVHRR image. A remarkable feature of the left-hand SAR images is that it shows the western edge of the dark feature shown in the AVHRR image, i.e. the radar backscatter pattern reflects the sea temperature. This is likely to be a result of the increased atmospheric stability as the air flows over the colder water, reducing the wind stress and thus the growth of short wind-waves. The wind was light (2–3 m s^{-1}) at the SAR observation time, so a change of stability can have a large effect on short wind-wave generation.

The warmer water to the east of the dark AVHRR feature is moving westwards along the coast as a coastal jet: typical current speeds measured by the ship-borne ADCP were 60 cm s^{-1}, and sharp changes in the current were measured when the ship moved across the wavelike (frontal) boundaries shown in the the right-hand SAR image in Fig. 2.

3.2. Surface Slicks

There were unfortunately no ERS SAR images obtained at times when slick samples were taken by the "mini research vessel". However, the air and sea temperature measurements shown in Fig. 3, as the vessel was driven through a natural slick, are of considerable interest. They show that the water



Original ERS SAR data © ESA/TSS 1995. Image analysis NERSC

Figure 2: *Left:* NOAA 1 AVHRR image, 1995 September 30, 12:30 UTC, indicating sea surface temperature. Cold regions appear dark.
Right: ERS-2 SAR image, 10:41 UTC, with ship track indicated.
Centre: ERS-1 SAR image, 21:37 UTC.

temperature is higher in the presence of a slick, presumably as a result of reduced wave-induced mixing and thus greater stratification of the water column. Analysis of slick material indicates that they were composed predominantly of natural surfactant materials from marine organisms, rather than from terrestrial sources as seen in slicks in fjord regions [11]. More foam was also present in the slicks observed offshore, presumably as a result of increased wave action.

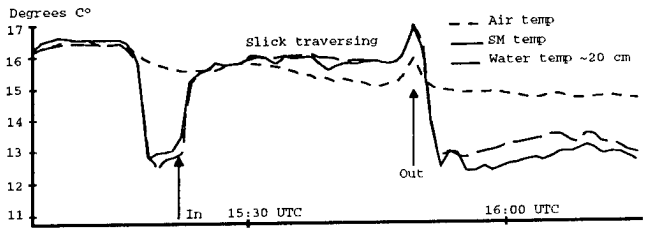


Figure 3: Air, and water (SM = surface microlayer, and 20 cm depth) temperatures measured from the mini research vessel on 1995 September 18.

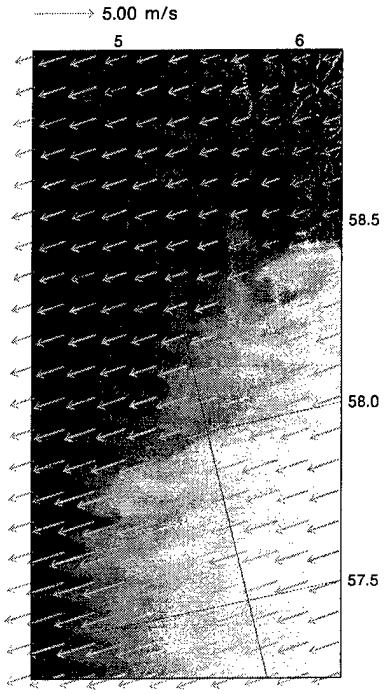
3.3. Wind Velocity, Atmospheric Fronts and Rain Showers

Fig. 4 shows a SAR image from September 14, and the wind computed from the CMOD4 algorithm. Wind vectors are computed using σ_0 averaged over 100×100 pixels and assuming a constant wind direction along the streaks seen in the lower part of the image. The wind speeds shown are somewhat less than predicted in the Norwegian Meteorological Institute 24-hour forecast for the same period.

Fig. 5, a SAR image from 1995 September 27, 10:36 UTC, shows a frontal line advancing from the west, with cellular rain-shower features. In the calmer region towards the top of the image, oceanic frontal features can still be seen.

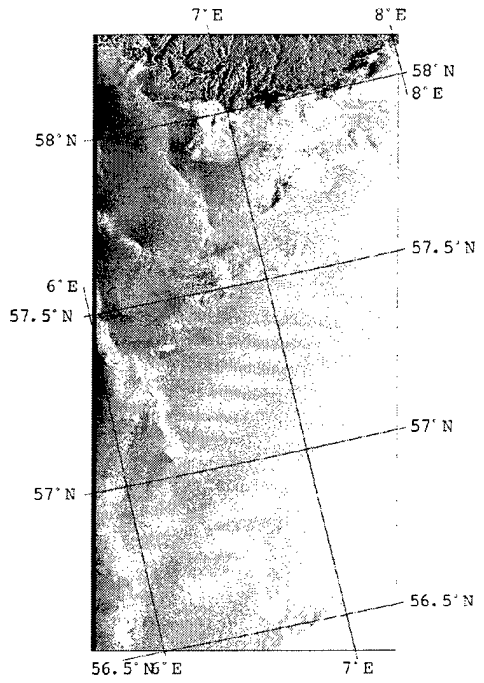
4. ACKNOWLEDGMENTS

The work described was carried out under the Strategic Programme for SAR remote sensing at NERSC, funded by the Norwegian Research Council. Ship time was provided by the University of Bergen, and ERS-1/2 data were provided under the European Space Agency AO Programme.



Original data © ESA/TSS 1995. Image analysis NERSC.

Figure 4: SAR image from 1995 September 14, showing wind streaks and wind speed computed using the CMOD4 algorithm.



Original data © ESA/TSS 1995. Image analysis NERSC.

Figure 5: ERS-2 SAR image from 1995 September 27, 10:36 UTC, showing rain cells in an atmospheric frontal zone.

5. REFERENCES

[1] J. A. Johannessen, L. P. Røed, and T. Wahl, "Eddies detected in ERS-1 SAR images and simulated in reduced gravity model," Int. J. Remote Sensing, vol. 14, pp. 2203–2213, 1993.

[2] J. Vogelzang, G. J. Wensink, M. W. A. van der Kooij, and R. van Swol, "Mapping of sea bottom topography with ERS-1 C-band SAR," In ESA [10], pp. 945–948.

[3] W. Alpers and B. Brümmer, "Atmospheric boundary layer rolls observed by synthetic aperture radar aboard the ERS-1 satellite," J. Geophys. Res., vol. 99, pp. 12 613—12 621, 1994.

[4] M. Bao, C. Brüning, and W. Alpers, "A generalized nonlinear ocean wave—SAR spectral integral transform and its application to ERS-1 SAR ocean wave imaging," In ESA [10].

[5] H. Hovland-Espedal, J. A. Johannessen, and G. Digranes, "Slick detection in SAR images," In Proc. IGARSS'94, Pasadena, California, August 8–12, vol. 4, pp. 2038–2040, Pisacataway, New Jersey: IEEE, 1994.

[6] J. A. Johannesen, G. Digranes, H. Espedal, O. M. Johannesen, P. Samuel, D. Browne, and Paris Vachon, SAR Ocean Feature Catalogue. Noordwijk, The Netherlands: ESA Publications Division, esa-SP-1174, 1994.

[7] R. A. Shuchman, J. A. Johannessen, C. Rufenach, and C. Wackerman, "Determination of wind speed and direction using ERS-1 data during NORCSEX'91," In Proc. Second ERS-1 Symposium, Hamburg, 1993 October, ESA SP-361, 1994.

[8] P. W. Vachon, O. M. Johannessen, and J. A. Johannessen, "An ERS-1 synthetic aperture radar image of atmospheric lee waves," J. Geophys. Res., vol. 99, No. C11, pp. 22 483—22 490, 1994.

[9] C. S. Nilsson and P. C. Tildesley, "Imaging of oceanic features by ERS 1 synthetic aperture radar," J. Geophys. Res., vol. 100, No. C1, pp. 953–967, 1995.

[10] Proc. Second ERS-1 Symposium, Space at the Service of Our Environment, Hamburg, 1993 October. Noordwijk, The Netherlands: ESA Publications Division, ESA SP-361, 1994.

[11] H. A. Espedal, O. M. Johannessen, and J. C. Knulst, "Natural films in coastal waters," Proc., IGARSS'95, Florence, Italy, 1995 July 10–14, pp. 2106–2108. Pisacataway, NJ: IEEE, 1995.

Ocean Surface Slope Measurement Using Polarimetric SAR

J.S. Lee and D. L. Schuler
Remote Sensing Division
Code 7263, Naval Research Laboratory, Washington DC 20375-5351, USA
Tel/Fax: +[1] (202) 767-2004/5599, E-mail:lee@imsy1.nrl.navy.mil

Abstract - A new technique has been developed to measure ocean surface slopes by polarimetric SAR. This technique has the potential of estimating surface slope in the along-track direction at an accuracy of a fraction of a degree. Experimental results using NASA/JPL AIRSAR P-, L-, C-band data from the Gulf Stream'90 Experiment showed a sudden slope change at a converging current front. The effect of velocity bunching on this measurement technique is also investigated.

INTRODUCTION

The topographic effect of ocean surface features, such as current fronts, eddies, and surface waves can be measured with radar altimeters to an accuracy of a few centimeters. The conventional altimeter provides only a surface topographic profile along the radar flight path. Although a scanning altimeter or a cross-track interferometric SAR can measure topography over 2-D land surfaces, their application to ocean surfaces is limited by the required accuracy. In this paper, we propose a new technique that uses polarimetric SAR to measure the slope in the along-track direction over a 2-D ocean surface. With a given topographic profile in the cross-track direction, this technique may have the potential to derive 2-D topography by integration.

The capability of SAR for the imaging of ocean waves, currents, surfactants, slicks, etc. has been studied in great detail (*Hasselman et al*, 1985, *Alpers et al*, 1981). However, few studies have been devoted to the understanding of polarimetric aspects of the SAR response to waves, currents and other ocean surface features. Polarimetric SAR simultaneously collects the backscattered responses from HH, HV, VH and VV polarizations, from which a Mueller matrix can be formed. From the Mueller matrix, the inherent scattering mechanism can be revealed by the polarization signature (*van Zyl*, 1987). *Schuler et al* (1993) have shown that, based on the stochastic surface tilts suggested by *Cox and Munk* (1954), the polarimetric SAR response of an ambient ocean surface agrees with the tilted-Bragg model (*Valenzuela,* 1968).

For idealized Bragg scattering, the peak value of the co-polarization signature plot occurs at a polarization orientation angle of 90°, and an ellipticity angle of 0°(i.e., at VV polarization). However, a tilted surface in the azimuth direction introduces HV and VH components, and causes a shift of the location of the maximum response away from the orientation angle of 90°. The amount of shift correlates with the slope of the tilted surface. This phenomenon has been utilized to develop slope measurements of mountainous desert terrain and forested areas [1] (*Schuler, Lee and De Grandi*, 1996). For topographic measurements, the inhomogeneities of forest and desert areas often introduce various dominant scattering mechanisms. Algorithms for the slope measurement have to be carefully devised to account for this variation. For ocean surfaces, however, the dominant scattering mechanism for incident angles between 25° to 65° has been adequately represented by a composite surface (tilted-Bragg) model for the backscatterer (*Valenzuela*, 1968). Consequently, the estimation of ocean surface slope is expected to produce more consistent results.

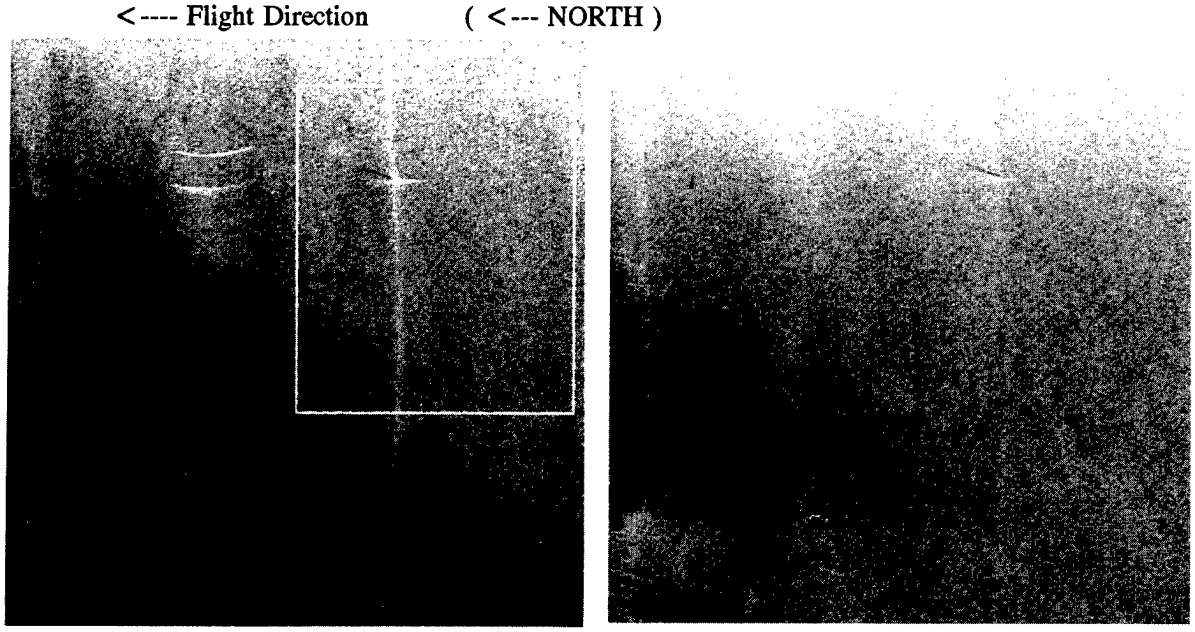
This slope measurement technique is applied to the P-, L-, C-band polarimetric SAR images of a current front with converging flows. The orientation angle displacement in the co-polarization signature is computed for each pixel. The results for P- and L-Band show a sudden 1.3° slope change at the front. The C-band results are not acceptable because of a higher noise level, The effect of velocity bunching on this measurement technique has been investigated. The limitations of this technique are discussed.

POLARIMETRIC SAR MEASUREMENTS

During the 1990 Gulf Stream Experiment, the NASA/JPL AIRSAR imaged the north edge of the Gulf stream supersite near the coast of Virginia (36.5°N, 72.0°W) (*Valenzuela*, 1991). Simultaneous shipboard measurements of currents, temperature, salinity, etc. were also made by R/V Cape Henlopen. Two relatively bright lines in the SAR imagery delineated a filament of cool, fresh water that was entrained by the Gulf Stream as it passed near the continental shelf. The vertical bright line seen in Fig. 1 corresponds to a surface front having relatively weak current shear, but a convergence velocity (measured at 7-m depth) of about 20 cm/s. Nearly coincident interferometric SAR measurements confirm the weak shear and show a surface convergence of 20-25 cm/s. Ocean waves were driven by southwesterly 8 m/s winds. A detailed discussion of the environmental setting and in-situ measurements is given by *Marmorino et al* [2].

The typical image covers an area of 12.4 km in azimuth and 9 km in slant range. The incidence angle

0-7803-3068-4/96$5.00©1996 IEEE



(A) P-Band, HV Polarization (B) P-Band, VV Polarization

Fig. 1 The P-Band HV and VV radar responses of a Gulf Stream converging front. The R/V Cape Helopen was crossing the front. The HV response ($\approx$ 2 dB) is much higher than VV.

varies across the image from 10 to 65 degrees. Flight paths of the AIRSAR crossed the convergent front several times, providing valuable data for analysis. A north-south pass was investigated (AIRSAR data: CM3597), and it was found that the cross-pol (HV) signatures of the front are much higher than co-pol responses (VV and HH), and that P-Band HV has the highest signal-to-background ratio ($\approx$2 dB). The P-band HV and VV images are shown in Fig. 1, where the R/V Cape Henlopen is crossing the converging front. It is interesting to note that P-band VV has a very weak signature. The presence of strong signatures in HV polarization indicates that strong wave-current interactions are producing large surface tilts in the along-track direction.

OCEAN SURFACE SLOPE MEASUREMENT

For idealized Bragg scattering, the scattering matrix can be represented by

$$S_{Bragg}=\begin{bmatrix} a & 0 \\ 0 & b \end{bmatrix} \qquad (1)$$

where a and b are real, and $b>a$ (i.e., $\sigma_{vv}>\sigma_{hh}$). The HV and VH polarization responses are zero. The polarization signature was introduced by *van Zyl et al* (1987) to graphically represent the variation of scattering cross-section as a function of the ellipticity and orientation angles of the transmitted waves. Using the polarimetric SAR data (CM3597), for incidence angles between 20° and 65°, co-polarization signatures of all three bands display the same characteristics as Bragg scattering.

For Bragg scattering, maximum co-polarization signatures occur at an orientation angle $\psi=90°$, and ellipticity angle $\chi=0°$ (i.e., at VV-polarization). However, a tilted ocean surface in the azimuth direction introduces HV and VH components, and causes a shift of the location of the maximum response in the co-polarization signature away from $\psi=90°$. The amount of shift from $\psi=90°$ correlates with the slope of the tilted surface. Intuitively, the maximum co-pol response occurs when the vertical antenna is perpendicular to the ocean surface in the azimuth direction. The surface tilt causes the shift of the maximum response away from the vertical position. The amount of shift can be visualized as the rotation of the vertical-horizontal basis vectors to an angle where the vertical component is again perpendicular to the tilted surface. This phenomenon has been utilized by *Schuler et al.*[1] for slope measurements of non-forested mountainous desert terrain, where the Bragg scattering mechanism is also dominant.

This new slope measurement technique is applied to the same data of Fig. 1 in the boxed area (shown in Fig.1A) to measure the slope change across the converging currents. The ideal polarimetric SAR imaging alignment for the slope measurement is to have the front aligned in the range direction. The AIRSAR CM3597 image is one set of data that possesses this alignment. The P-Band polarimetric data is used to compute the orientation angle of the maximum co-pol response for each pixel. The result for the lower right quarter of data is shown as an image in Fig. 2. This figure displays a sudden slope change at the convergent front of about 1°. The R/V Cape Henlopen is crossing the front in this image and its

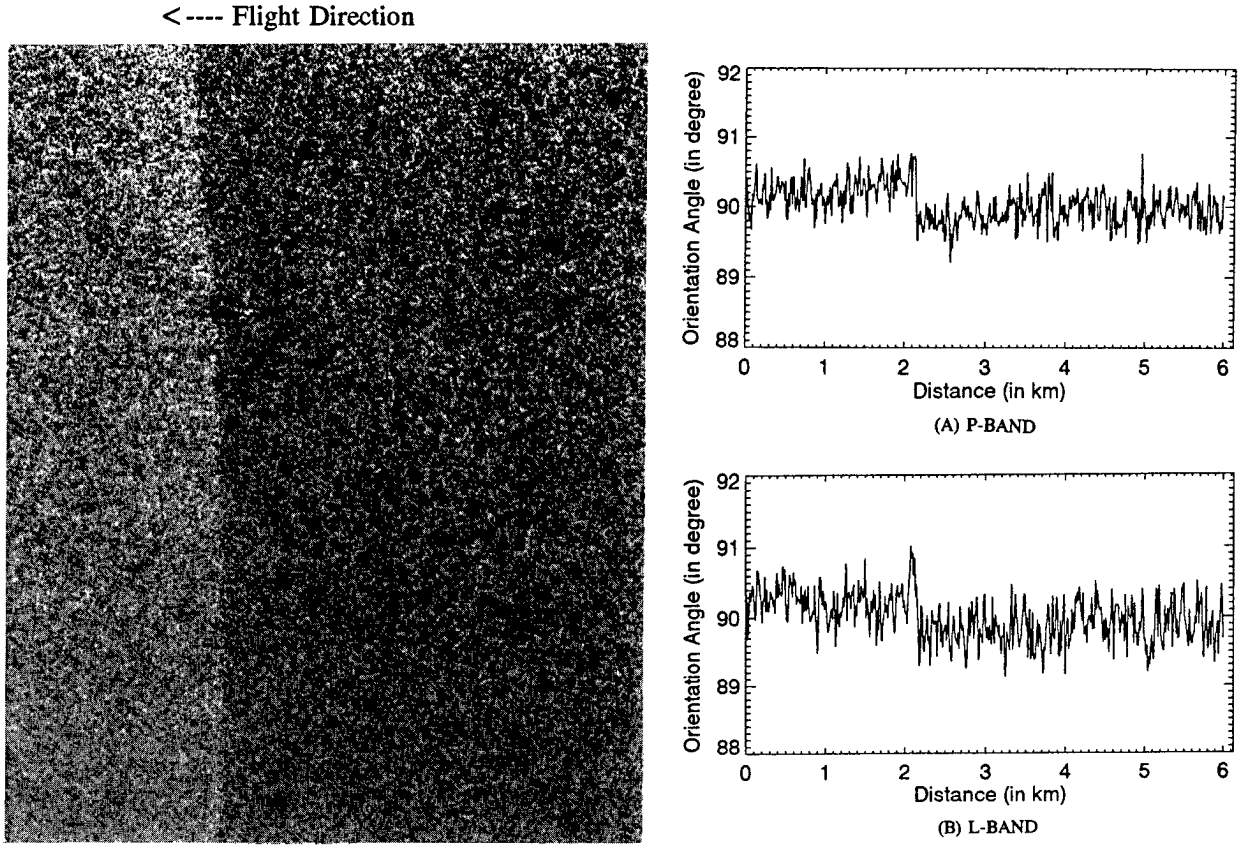


Fig.2 The P-band polarimetric SAR measured surface slopes around the convergent front is encoded as a gray-level image (on the left). Profiles of 50 line average for P-band and L-band at a position below the ship are also shown. The estimated slope at the front has an abrupt change from +0.8° to -0.5°.

wake can be seen as a contrasting dark streak. To quantify the slope change at the front, a 50-line average below the ship (at incidence angle=47°) is plotted in Fig. 2. Also shown (Fig. 2B) is the result when L-Band is used. The estimated slope at the front has an abrupt change from an average of +0.8° to -0.5°. C-Band with its shorter wavelength is more subject to local wave variations, the noise level is much too high for slope measurements.

REMARKS

The polarization orientation angle shift for a given surface tilt is incident angle and HH to VV ratio dependent. For a given incident angle and HH to VV ratio, a theoretically derived function relates the shift of orientation angle to the surface tilts. This function should be applied to map the polarimetric SAR orientation angle shifts into surface tilts.

The velocity bunching affects the accuracy of this slope measurement technique. We have estimated this effect using polarimetric SAR imagery with azimuth traveling waves. The velocity bunching effects are very apparent. However, no appreciable slope change is detected which corresponds to the wave pattern. This is due to the fact that the velocity bunching causes the resolution cells with opposite slopes to merge together. The summation of positive and negative slopes neutralizes the effect of orientation angle shift, and reduces the effectiveness of this new polarimetric technique.

ACKNOWLEDGMENTS

We thank Dr. J. van Zyl of JPL and the NASA/JPL AIRSAR team for providing polarimetric SAR data. We also thank Dr. G. Valenzuela and Dr. G.O. Marimorino for their contributions in organizing the Gulf Stream Experiment.

REFERENCES

[1] D. L. Schuler, J.S. Lee and G. De Grandi, "The Measurement of Topography Using Polarimetric SAR Images" IEEE Trans. Geoscience and Remote Sensing, 1996 (in press).

[2] G.O. Marmorino, et al.,"Gulf Stream Surface Convergence Imaged by Synthetic Aperture Radar,"JGR,99(C9), 18315-18328, September 15, 1994.

Studying the Earth's Environment from Space - A Curriculum Workshop

LCDR M.A. Alfultis
US Coast Guard Academy (ds)
15 Mohegan Ave.
New London, CT 06320
Phone: (860)444-8633
FAX: (860)444-8627
E-Mail: alfultis@dcseq.uscga.edu

Abstract -- The two biggest challenges facing pre-college and undergraduate educators in bringing satellite data into their classroom is the lack of a theoretical background and the lack of time to tailor currently available curriculum materials to their particular classroom application. The proposed 5-day curriculum workshop will provide teachers the background to interpret a wide variety of satellite imagery and the time to develop some of their own classroom-ready materials. The first two days of the workshop will be dedicated to providing a background on the principles of remote sensing, types of sensors, their application, and some of the various ocean/atmospheric processes currently studied from spaceborne instruments. Application of the background material discussed during the first two days will be provided on the third day through hands-on computer exercises on satellite data enhancements and interpretation. Participants will explore the World Wide Web for currently available curriculum materials on the fourth day, and the final day will provide the participants the opportunity to develop classroom materials presented/discovered during the previous sessions. At the conclusion of the workshop, participants will have been exposed to how remote sensing is used to study various aspects of the earth's environment, and will have some classroom-ready materials.

THE PROBLEM

Satellite images of the earth's atmosphere, hydrosphere, lithosphere, and biosphere have proven to be valuable tools in illustrating the complexity of the earth's environmental systems. Satellites are used to monitor our rapidly changing weather, El Nino Southern Oscillations in the Pacific, ocean currents, land and oceanic vegetation, polar sea ice distribution, and stratospheric ozone. Students at all levels daily see applications of satellite data for short term decisions such as hazardous weather preparation and long term policy making such as global warming and stratospheric ozone depletion. Increased use of satellite technology in the classroom will increase student knowledge of the dynamical nature and complexity of the earth's environment, student awareness of social environmental issues, and student interest in careers in environmental science/engineering.

Educators find incorporating satellite data into their science curriculum difficult, however, due to:

1. the technical complexity of the data,
2. the computer hardware/software requirements to process the data,
3. little theoretical background on the ocean/atmosphere processes illustrated by the satellite data, and,
4. little time during the academic year available to develop curriculum.

The goal of this project is to make it easier for satellite data to be incorporated into pre-college and undergraduate science classrooms.

THE PROPOSED SOLUTION

The proposed 5-day curriculum workshop seeks to resolve some of these issues by:

1. providing educators with a background on the physical radiation principles which form the foundation for measuring geophysical, biological, and chemical processes from space.,
2. providing educators with a background on the various ocean/atmosphere processes currently studied from spaceborne instruments, and,
3. providing the educators some computer resources and time to develop some classroom ready materials.

Plans call for two of these workshops to be held. The first will be at the Satellites and Education Meeting in West Chester, Pennsylvania, in March 1997. The second will be held at the Coast Guard Academy in July 1997. The first two days of each workshop will be dedicated to providing a background on the principles of remote sensing, types of sensors, their application, and some of the various ocean/atmospheric processes currently studied from spaceborne instruments (stratospheric ozone, ocean circulation, El Nino, phytoplankton, and sea ice). All materials presented during these sessions will be available to the participants. Application of the background material discussed during the first two days will be provided on the third day through hands-on computer exercises on satellite data enhancements and interpretation. Participants will explore the World Wide Web (WWW) for currently available curriculum materials on the fourth day, and the final day will provide the participants the opportunity to develop classroom materials presented/discovered during the previous sessions. At the conclusion of the workshop, participants will have been exposed to how remote sensing is used to study various aspects of the earth's environment, and will have some classroom-ready materials. All materials developed during the workshops will be placed on the WWW for wider dissemination and evaluation/improvement.

0-7803-3068-4/96$5.00©1996 IEEE

Constructing Earth System Science Learning Through Multidisciplinary Studies of Global Change

Rosanne W. Fortner and Victor J. Mayer
The Ohio State University
Ohio Sea Grant Education, 2021 Coffey Rd., Columbus, OH 43210 USA
Phone 614-292-9826; Fax 614-292-7432; e-mail fortner.2@osu.edu

Abstract — A productive topic for introducing Earth Systems science in K-12 classrooms is global environmental change. Beginning with changes in the local environment, students are led to construct an understanding of how these changes affect all of Earth's subsystems, including humans and their activities. They follow the local changes into national or regional ones on a larger scale of space and time, and conclude at the higher grades with studies of global phenomena such as alterations in atmospheric composition, ocean circulation patterns, and biological diversity. Curriculum materials and teacher education programs offered through the Ohio Sea Grant Education Program at The Ohio State University focus on such topics of change, and use remotely sensed images, electronic networking and other modern technologies in a collaborative learning setting.

BACKGROUND

Earth Systems Education is a K-12th grade program of curriculum restructure in which teachers take responsibility for critical evaluation of their science curriculum, including content, classroom processes, learner outcomes and assessment, and strive to make changes that create a curriculum more responsive to human needs and future quality of life [1]. Earth Systems Education is based on integration of traditional science disciplines for a more comprehensive understanding of the interactions of Earth subsystems: the hydrosphere, lithosphere, atmosphere and biosphere. In studies of the Earth system, students find science relevant and exciting; learners seek information from varied sources and apply the processes and concepts of science as the bases for answering important questions.

Earth Systems Education efforts are guided by a Framework of seven Understandings developed by science teachers, science educators and scientists to represent fundamental desired results of all of science education (Fig. 1).

Since the most prevalent existing science instructional mode is almost entirely textbook focused and delivered by lecture, new systems-based efforts such as education about global change require specially designed materials and methods to break instruction out of such modes. With support from the National Science Foundation and the National Oceanic andAtmospheric Administration, two volumes of curriculum activities have been developed for secondary science classrooms. Activities for the Changing Earth System (ACES) [2] materials use innovative

1. Earth is unique, a planet of rare beauty and great value.
2. Human activities, collective and individual, conscious and inadvertent, affect planet Earth.
3. The development of scientific thinking and technology increases our ability to understand and utilize Earth and space.
4. The Earth system is comprised of the interacting subsystems of water, rock, ice, air and life.
5. Planet Earth is more than 4 billion years old, and its subsystems are continually evolving.
6. Earth is a small subsystem of a solar system within the vast and ancient universe.
7. There are many people with careers that involve study of the origin, processes, and evolution of Earth.

Fig.1. Framework of Earth Systems Understandings

field, laboratory and classroom techniques to address global change issues on a planetary scale. Great Lakes Instructional materials for the Changing Earth System (GLIMCES) [3] take similar issues into the ecoregional context of the Great Lakes of North America, where the manifestations of change are more specific and relevant to a binational audience.

GLOBAL CHANGE IN EARTH SYSTEMS EDUCATION

Once almost entirely confined to scientific journals, complex scientific research and data interpretations have found their way into everyone's daily life, thanks largely to the mass media. People have come to expect that when they read or listen to news reports, they are likely to be informed of the results of one scientific study or another. Earth Systems Education, with its mission of science literacy, sees this as a teachable moment. Science has relevance to people in the forms in which it is presented by the media, but those media often raise as many questions as they answer. Using global change as an interesting, sometimes controversial, science topic that has implications for everyone, gives teachers entré for instructional experiences that lead to interdisciplinary science understandings.

Earth Systems Understanding (ESU) #1 is illustrated through the value of Earth's resources that potentially will be altered by global change. The shifting of climate patterns, with resulting

0-7803-3068-4/96$5.00©1996 IEEE

changes in agricultural belts, forest composition, animal ranges, and other ecosystem responses,is a simple example that can anticipate parallel economic changes. Where will the corn belt be in the next century? Will Canada's national symbol, the sugar maple, still be able to grow there?

If students achieve ESU #2, they understand that human induced environmental changes are the basis of many global problems. Population growth and resource consumption put pressure on natural systems that can result in irreversible changes in the Earth system.

ESU #3 is the basis of good science process. It relates to how scientists have learned about global change by using their tools and observations to assemble datasets. Analyzing and comparing the trends can reveal the relationships that are key to understanding Earth processes and changes. With ESU #4 students are reminded that everything is connected to everything else, and when one component of the Earth system changes there are likely to be changes in the other components as well. In a greenhouse warming scenario, for example, changes in atmospheric composition result in a warmer climate, which can cause melting of polar ice (cryosphere), rising of sea level (hydrosphere) related to thermal expansion, increasing coastal erosion (lithosphere) and destruction of wetlands (biosphere).

According to ESUs #5 and 6, the Earth system as we know it is part of the solar system, and Earth features such as the atmosphere, landforms, oceans and living things are the product of dynamic changes that are ongoing. If change is natural, then, how do scientists decide whether global change is human induced or part of a normal cycle for the Earth system?

Finally, in a study of global change students can encounter the work of many types of scientists, demonstrative of the kinds of careers in Earth system monitoring, data analysis, ecosystem assessment, remote sensing, communication, and such. To introduce students to the excitement of seeking answers to complex questions with such direct implications for Earth's future can help to draw new talent into growing fields of science.

EXAMPLES OF MULTIDISCIPLINARY STUDIES

Topics within the materials include some designed to address all the interacting Earth subsystems. They are specifically not classified as being biological, meteorological, or other disciplinary topics, but instead begin with such questions as "How will we get enough fresh water for a warmer world?" "What is meant by the Earth's energy budget?" and "After the maples, then what?"

An example of an ACES activity is "Do volcanic eruptions have an impact on global climate and atmospheric conditions?" Some significant volcanic eruptions since 1883 are plotted on a world map using geographic coordinates, and the Volcanic Explosivity Index for each is entered on a graph of time versus global atmospheric temperature. Students compare the three data sets to determine the relationships. For example, which volcanic eruptions appeared to coincide with global temperature anomalies? Are the geographic locations of the volcanoes associated with their apparent temperature effects? Were there periods of high volcanic activity associated with major climatic events?

Global changes are sometimes signaled by changes in living things, and indicator species such as the miner's canary may be studied to help us detect such changes as well as forecast their potential impacts. The Christmas Bird Count conducted throughout North America is one data source readily available to schools for such studies, and time series satellite imagery can provide similar information about vegetation changes. For aquatic environments, a set of activities built around "The Downeaster Alexa," a 1989 song by Billy Joel, invites students to study the decline of the commercial fishery for striped bass off New England. Datasets from NOAA, fishery management regulations from the northeastern U.S., and climate model predictions from a scientific journal article are used as the basis for students to decide "What causes the decline of a fishery?" The information, however, is not only a study in science, but also in the culture of the striped bass fishery. Students hea· the poignant tale of hard life in the Joel song, and begin to 1) appreciate the value of science in addressing human concerns, and 2) identify the interconnections between human activity and size of wildlife populations.

The Global Climate Game makes an excellent culminating activity for studies of global change. Teams of students move a single playing piece around a game board, making collective decisions in response to issues that will affect the amount of CO2 in the atmosphere. For each decision, environmental points are awarded, and amounts of CO2 increase result. With the object of the game being to have the least effect on global change, student teams soon realize that making wise choices in personal lifestyles will have the most positive effects, but they also find that not everyone in the team may agree with those choices. Since the game, as in life, reminds them that "we're all in this together," they evaluate costs and benefits of options without seeing them as simply good or bad.

STRUCTURE OF GLOBAL CHANGE INSTRUCTIONAL MATERIALS

If learning is to be relevant to students it must fit into their existing cognitive frameworks; that is, it must relate to situations or ideas they have encountered, and preferably have implications for them directly. Such abstract and complex concepts as global change must be especially structured to meet these needs, or no amount of teaching will result in lasting learn-

ing. Therefore, materials about global change and the Earth system follow the methods of what educators call the Learning Cycle [4].

Instruction begins with *engaging* the student's attention, through an exciting activity, or through direct relationship to something the student already knows. For global change, this implies here-and-now studies. Sometimes these can be facilitated by the mass media: video clips on hurricanes, stories about endangered species found in the area, or discussions of recent weather extremes and why they happen.

The next phase is to facilitate students' *exploring* the idea. Earth Systems Education uses activities that bring the concept of data collection, interactions, and change into the student's experience. Studies of global climate may begin with data collection on local weather, especially emphasizing variations that are normal and examining in detail those extremes (blizzards, floods, etc.) that are memorable to students. As data are analyzed for trends and compared with past records available from local meteorologists, the lesson proceeds into *concept development.* At this stage new terms can be introduced and further complexity built, since we are assured that students at least have the same instructional background upon which to build the concept.

As students grow in understanding of the concept of climate change, they can begin *elaborating* on it through additional learning experiences. Studies of weather may generate interest in student projects such as ice formation on the Great Lakes and its implications for shipping, sea level rise and its impact on coastal developments, presence of new species of birds at the feeder and the questions that arise about why they have not been seen in the area before.

The elaboration phase may thus lead to new opportunities for engagement of student interest. It may also lead to *application* of information to new situations. If there are new birds at the feeder, will they compete with the "native" birds? Are there new fish in the river too? What would happen if the new species outcompeted the natives for food and nesting/spawning sites?

Completing the cycle is the phase of *assessing* student understanding. Students may do this themselves at various phases by deciding they do not have enough information to effectively answer questions. This is an important admission, and if accommodated by flexible instructional modes it can lead to independent learning and real accomplishment of science process. In Earth Systems Education, assessment of student progress by the teacher is typically not by testing but by demonstration of competency in performance. Portfolio assessment allows students to assemble the pieces that best reflect their own understanding and the extent to which they have elaborated and applied their learning. Other assessment products might include peer teaching tools by which student groups teach each other about the explorations they have completed. In addition to providing information about subject matter mastery, such products encourage the development of effective communication skills.

DELIVERY OF CURRICULUM INNOVATIONS

Since interdisciplinary problem-based learning is not standard practice in most K-12 schools, teacher education programs reinforce the need for new methods of classroom leadership. Earth Systems Education efforts have reached out to classrooms all over North America, to several South American countries, and most recently the Pacific Rim. Workshops for educators involve participants in cooperative learning and provide assistance in developing collaborative investigations. Sources are provided for remotely sensed images and interdisciplinary data sets; programs for electronic networking are introduced and facilitated. Ohio Sea Grant, the continuing sponsor of innovations such as GLIMCES, markets and distributes the curriculum materials and supports the efforts to remain responsive to changing needs in Earth system science education. A catalog of the materials described here, and others useful for Earth Systems Education, is available from the authors.

ACKNOWLEDGMENTS

The authors are grateful to the teacher-authors and scientist-reviewers of the curriculum materials described here, and especially to the editors of the volumes: Dr. Tony P. Murphy, Dr. Dan Jax, Don Torma, Heidi Miller and Amy Sheaffer. The editorial and design support of the Ohio Sea Grant Program was invaluable in production.

REFERENCES

[1] V.J. Mayer and R.W. Fortner, Science is a Study of Earth. Columbus: Ohio State University, 1995, Ch. 1.

[2] Activities for the Changing Earth System. Columbus: Earth Systems Education Program, Ohio State University, 1993.

[3] Great Lakes Instructional Materials for the Changing Earth System. Columbus: Ohio Sea Grant, 1996.

[4] J.R. Carpenter, "Constructivism and Learning Cycle-Based instruction." Unpublished manuscript.

A CD-ROM Study Package on Current Forest Issues for Use in Secondary School Science Classes

Susan Hassol
John Katzenberger
Aspen Global Change Institute
100 East Francis
Aspen CO 81611
USA
970 925 7376 ofc. 970 925 7097 fax
johnk@agci.org & shassol@agci.org

Compton J. Tucker
NASA/Goddard Space Flight Center
Code 923
Greenbelt MD 20771
USA
301 286 7122 ofc 301 286 1775 fax
compton@kratmos.gsfc.nasa.gov

ABSTRACT

With the proliferation of personal computers and CD-ROM devices in secondary school classrooms there is the opportunity to make available scientific study packages of current environmental issues using CD-ROM media. The Aspen Global Change Institute and scientists from NASA's Goddard Space Flight Center are developing an integrated package of selected Landsat satellite data sets emphasizing tropical forests, publicly available image analysis software for PCs, ancillary information such as photographs, and specific lesson plans, all on a CD-ROM titled "The Changing Forest," for use in secondary school science classes. Emphasis will be placed on simplicity and ease of use, coupled to specific lesson plans developed around environmental issues and concepts for which satellite data provide a unique information source. Themes are introduced that include the extent, rate, fragmentation and edge effect associated with deforestation and remote sensing technologies in land cover assessment. Selected CD-ROM content and interactive strategies to engage the student user are discussed.

INTRODUCTION

How much of the Earth's surface is covered in forest? What are natural rates of change in forest cover and what are rates of deforestation from human activity in different regions of the world? Questions such as these have become increasingly important since concern over deforestation has gained public attention globally. In an international opinion poll about the environment, 60 percent of those surveyed in developing countries and 64 percent in industrialized countries found loss of rainforests to be a "major problem" [1]. There is a timeliness associated with forest issues and an educational opportunity that spans basic science and policy. Skole and Tucker found that deforestation in the Brazilian Amazon increased nearly three-fold from 78,000 sq. km. in 1978 to approximately 230,000 sq. km. in 1988. Taking into account the isolated forest fragments and forest edge effects the total affected forest habitat increased from an estimated 208,000 to 588,000 sq. km. during the same period [2].

Forest issues are interdisciplinary and are conducive to exploration in an inquiry-based education project. The Changing Forest CD-ROM project, a collaboration of the NASA Goddard Space Flight Center and the Aspen Global Change Institute[1], takes advantage of the digital capacity of CD-ROMs, the growing availability of CD-ROM technology in the classroom [3] and the significant amount of digital data available for determining global vegetative cover, such as for Amazonia [4].

The following statement, "Forests world wide have been and are being threatened by uncontrolled degradation and conversion to other types of land use, influenced by increasing human needs; agricultural expansion; and environmentally harmful mismanagement" [5] came not from a forest conservation group, but rather one signed by 178 governments at the United Nations Conference on Environment and Development (UNCED), June 1992, in Rio de Janeiro. UNCED also produced a "Statement of Forest Principles" that identified a critical need for "reliable and accurate information on forests and forest ecosystems" [6]. This need for accurate forest information is a recognition of the limitations found in estimates made by more traditional methods, such as ground and limited aerial surveys. This is particularly true in attempting to detect change over time.

Since 1972, beginning with Landsat 1, the ability to map global vegetative patterns from space became possible, but a comprehensive use of this data is only becoming realized in recent work. For example, utilizing Landsat satellite imagery, Skole and Tucker developed and applied a technique to the Brazilian Amazon Basin which is useful in detecting

[1] Compton J. Tucker, of the Laboratory for Terrestrial Physics, NASA Goddard Space Flight Center, Greenbelt, Maryland is project PI for the Forest CD-ROM Project, with Gene Feldman and Blanche Meeson, also from Goddard as co-PIs, along with Susan Hassol and John Katzenberger, of the Aspen Global Change Institute, Aspen, Colorado.

0-7803-3068-4/96$5.00©1996 IEEE

change in total forest cover, habitat fragmentation, and edge effects. This study was based on 210 Landsat Thematic Mapper scenes that were processed into a "seamless" dataset for the entire Brazilian Amazon [7]. This same methodology is being applied to countries neighboring Brazil, as well as in Southeast Asia, and tropical Africa [8]. This methodology provides a means for improving global land cover maps and is the basis for The Changing Forest CD-ROM project, which will provide the opportunity for students to work with actual data from the Amazon Basin and explore related scientific, economic, political, and social issues.

The Changing Forest CD-ROM will integrate the Amazon dataset with oblique aerial photographs taken during low altitude small-aircraft flights over the study area, on-the-ground photographs of unique flora and fauna, sounds of the rain forest, and "Quicktime" video clips of field scientists at work. In addition to the digital data, photographs, and motion pictures, the CD-ROM will contain a subset of the Aspen Global Change Institute's database on forest topics. The database, EarthPulse Notes[2], contains searchable summaries of recent research articles on a wide variety of forest research issues. The research article summaries included in the CD-ROM will be selected to provide the user with insights into the process of science. In addition, they serve as interesting examples of the range of subject matter of interest to the research community. By becoming familiar with some of this current research, students' ability to formulate their own investigations will be enhanced.

CD-ROM DESIGN AND APPROACH

Navigation - 5 Paths

The Changing Forest CD-ROM design is intended to engage students through 5 paths of exploration. Each is linked to the others and back to the main menu. The paths are all within the context of the project's unifying theme, "the changing forest," and provide additional links to data, image processing software, a glossary, resources, sounds, photographs, video clips, and summaries of recent scientific research. The "Games and Activities" path includes activities for both inside and outside the classroom and investigations on the computer that include image processing and simulations. An inviting forest scene guides the user to icons of the five paths for exploring The Changing Forest:

- People of the Forest
- Human-Disturbed Forest
- Games & Activities
- Forest Policy and Management
- Naturally-Disturbed Forest

The aim of the navigation approach is to appeal to different student learning styles and to allow users to construct new understandings of forest attributes and processes over repeated explorations with the CD-ROM. For example, if a student clicks on "People of the Forest," a new page emerges with additional choices such as indigenous peoples, modern settlers, field scientists from within and outside the country, and historical sketches. To help unify the experience, students will create portfolios to record their interactions with The Changing Forest CD-ROM. A simple database that contains a running record of their own work from each episode will be maintained by the students.

7 Themes

Initial work on The Changing Forest CD-ROM project identified seven key forest themes which integrate social, scientific and technological elements. Each of the seven themes has an associated set of approximately 10 questions that serve as the basis for student investigations that can be worked on individually, as a whole class, or in small groups. Examples of a few of the questions accompanying each theme follow.

1. Humans change the way land is used and consequently change land cover, such as forest cover.
   - What types of changes do humans make in the landscape and why?
   - How has the extent, rate, and tools used, changed through history?
   - Where on Earth is the change most rapid, and slowest?
   - What are some ecosystem effects?

2. The rate and extent of these changes such as deforestation can be significant compared to natural rates of change.
   - What natural changes occur in land cover?
   - What are the extent and rate of change for various natural disturbances?
   - What are some beneficial effects of natural disturbance?

3. Remote sensing is a powerful tool in assessing land cover change.
   - How is remote sensing used in land cover assessment?
   - What regions of the Earth are well documented, and poorly documented?
   - What are the advantages and limitations of remote sensing?

4. Ground verification of remotely sensed data is critical.
   - Why is it necessary to verify remotely sensed data?
   - How much ground work is necessary?
   - What can be known without it?

5. The ratio of forest edge to forest area can significantly affect the impact deforestation has on ecosystems.
   - What is the ecological significance of forest edge?
   - How does the ratio of forest edge to forest vary with different patterns of deforestation?
   - What are some examples of species that thrive at the forest edge?

[2] An on-line version of AGCIs global change database, EarthPulse Notes, is located at http://www.gcrio.org/agci-home.html

6. Change in forest cover affects the atmosphere.
   - What role do forests play in the global carbon cycle?
   - How do emissions from biomass burning effect climate, and the ozone layer?
   - What is the magnitude of human change to the carbon cycle versus the Earth's natural cycle?

7. Visual representation of land surface data can effectively inform decisionmakers.
   - How does the visual display of quantitative information effect how it is perceived?
   - What are some examples of forest cover maps that have been used effectively in the development of policy?
   - What types of visual representation work best for different types of data?

Linking Students to Current Research: Three Examples

Consistent with the goal of developing understanding and ability in the practice of scientific inquiry, students will be able to access summaries of selected research articles on contemporary forest research topics on the CD-ROM. These summaries are used as an introduction to the more difficult source articles, providing interesting content, as well as a model for the design of student investigations. Research examples will be chosen based on their relevance to the 7 themes. For example, in a paper by Ralph Cicerone in *Science,* "Fires, Atmospheric Chemistry and the Ozone Layer," links are made to theme number 6, "Change in forest cover affects the atmosphere." This article explores the constituents of biomass burning and their transformations and effects in the troposphere and stratosphere. The main component of the discussion is how methyl bromide emitted from biomass burning may release as much as 30% of atmospheric methyl bromide, a chemical that may account for as much as 25% of stratospheric ozone destruction [9].

Another example is the paper by Scott Robinson *et al.*, in *Science,* "Regional Forest Fragmentation and the Nesting Success of Migratory Birds" which explores the hypothesis that forest fragmentation is a major cause of the observed decline in neotropical migratory bird species. The authors conclude that conservation strategies should include large unfragmented nesting areas [10]. This paper links to theme numbers 1 and 7.

A third example is a paper by John Maurice in *New Scientist*, "Fever in the Urban Jungle," which discusses the juxtaposition of vector borne diseases such as malaria and yellow fever, forest settlement practices, and human health in the tropics [11]. This discussion relates to several of the 7 themes, particularly theme number 3, since remote sensing is increasingly being used by organizations such as the World Health Organization to better understand vector habitats and human settlement patterns.

SUMMARY

The Changing Forest CD-ROM under development by NASA Goddard Space Flight Center and the Aspen Global Change Institute is designed to provide an interactive set of learning experiences for secondary school students. The project aims to engage students in an exploration of forest change, a global environmental change of major concern to people in both industrialized and developing countries. Students will gain access to satellite and other sources of data, tools such as PC-based image processing software, and a database of current research articles on forest topics. Students can navigate the CD-ROM through 5 pathways of exploration and will document their work with individual portfolios.

REFERENCES

[1] D. E. Bloom, "International Public Opinion on the Environment," *Science*, Vol. 269, 21 July 1995, p. 356.

[2] D. Skole, C. J. Tucker, "Tropical Deforestation and Habitat Fragmentation in the Amazon: Satellite Data from 1978 to 1988," *Science*, Vol. 260, 25 June 1993, p. 1909.

[3] QED National Education Database, Datasheet: "New Technologies School Trends," 1995.

[4] W. J. Emery, C. J. Tucker, "Changes in Global Vegetation Patterns — Update and Methodology," *Elements of Change 1995,* S. Hassol, J. Katzenberger, Eds. (AGCI, Aspen CO, in press).

[5] United Nations Conference on Environment and Development, *Earth Summit Agenda 21* (UN Dept. of Public Information, New York NY, 1992) p. 90.

[6] United Nations Conference on Environment and Development, *Earth Summit Agenda 21* (UN Dept. of Public Information, New York NY, 1992) p. 292.

[7] D. Skole, C. J. Tucker, "Tropical Deforestation and Habitat Fragmentation in the Amazon: Satellite Data from 1978 to 1988," *Science*, Vol. 260, 25 June 1993, p. 1906.

[8] W. J. Emery, C. J. Tucker, "Changes in Global Vegetation Patterns — Update and Methodology," *Elements of Change 1995,* S. Hassol, J. Katzenberger, Eds. (AGCI, Aspen CO, in press).

[9] R. Cicerone, "Fires, Atmospheric Chemistry, and the Ozone Layer," *Science*, Vol. 263, 4 Mar. 1994, p. 1243.

[10] S. K. Robinson, F. R. Thompson III, T. M. Donovan, D. R. Whitehead, J. Faaborg, "Regional Forest Fragmentation and the Nesting Success of Migratory Birds," *Science*, Vol. 267, 31 March 1995, pp. 1987-89.

[11] J. Maurice, "Fever in the Urban Jungle," *New Scientist*, 16 Oct. 1993, pp. 25-28.

Our Role in the Earth System: One K-12 School District's Science Education Initiative

P.D. Lindgren: Norfolk Public Schools & AMS Project Atmosphere

510 Pasewalk Avenue, Norfolk, Nebraska, U.S.A. 68701
Phone: (402)644-2584, Fax: (402) 644-2519
Email: lindgren@pluggers.esu8.k12.ne.us

1. Background

The community of Norfolk is located in the heart of the Elkhorn Valley in northeast Nebraska with the Sand Hills lying to the west and farmland to the east. The surrounding land is gently rolling. A city of 23,000, Norfolk is an economic growth center for an area encompassing six counties. Norfolk is one of the few mid-size cities in Nebraska off the Omaha/Lincoln interstate corridor which has continued to sustain population growth over the last decade. Its public school district includes nine elementary schools, a middle school, a junior high, and a senior high. The district serves over 4,400 students.

2. District Mission and Responsibilities

An enormous responsibility has been given to the Norfolk Public Schools. As a part of Nebraska's public school system, Norfolk's schools are required by law to:

- Offer each individual the opportunity to develop competence in the basic skills of communications, computation, and knowledge of basic facts concerning the environment, history and society:
- Offer each individual the opportunity to develop higher order thinking and problem solving skills by means of adequate preparation in mathematics, science, the social sciences, and foreign languages and through appropriate and progressive use of technology [1].

This responsibility is also seen as an opportunity by the public school teachers of Norfolk, whose mission is "to equip all students to succeed in a complex changing world." The project *Our Role in the Earth System* is a concerted effort to better fulfill our responsibilities and mission. Our project is especially focused upon communication, higher order thinking skills, problem solving, the environment, science, and technology.

3. Project Goals

Through this project we endeavor to develop in young people an awareness of their actions' significance within the earth system. In addition, we intend to develop students' ability to investigate global issues from a systemic point of view: identifying key component parts, identifying significant interactions between those components, gathering diverse types of information from various sources, exchanging information and collaborating intelligently about its significance with a variety of people, synthesizing that information into a defensible conclusion, and effectively communicating their conclusion and evidence to a broad audience.

4. Infrastructure and Funding

The implementation of this science-technology project is entirely dependent upon an infusion of computer and network technologies. When the infrastructure installation is complete each of our district's schools will have frame-relay network connections through either T1 or 56kb leased telephone lines. These frame-relay connections then tie into an education network that spans the state and that ultimately leads to the global Internet. Each region in the state has an Educational Service Unit that serves as a site for training, Internet traffic routing, and electronic mail services.

In addition to the network and Internet equipment, each district school has also received computers, scanners, printers, digital cameras, and various software packages. Our senior high also purchased a series of computer interfaced probes for quantitative investigations. One computer in each school building will be set up as a World Wide Web server to provide easy access to teacher and student created materials (HTML web pages). A multi-platform training lab was also created to conduct the technology training for the project.

Initial and on-going funding for our project is provided as a joint effort between the Norfolk Public School district and the Nebraska Excellence in Education Commission. The NEEC accepts competitive proposals from Nebraska school districts for innovative educational projects. The NEEC selects a small number of proposals for funding with the expectation that the school district will contribute materials and finances to the project as well.

5. Implementation Process

All district science teachers in grades 4 through 12 have received initial training in team dynamics, problem-solving, electronic mail, World Wide Web information access, multimedia authoring, system dynamics modeling, World Wide Web page writing, World Wide Web server

0-7803-3068-4/96$5.00©1996 IEEE

setup, and World Wide Web server management.

These 52 teachers were then divided into 3 teams. Each team has at least 2 high school level teachers, one teacher from each level grades 7-9, and elementary teachers from either the 4th, 5th, or 6th grade. These diverse teams were created as a support community. The secondary level teachers are expected to serve as resources for the elementary teachers who have not had as much formal training in science.

After being divided into the 3 teams, selected teachers brainstormed global issues as potential topics for student investigation. From this extensive list each team prioritized and selected the topics they wished to have their students research. The teams decided upon the following complementary topics: World Water Supply, World Food Supply, and Waste Management Practices. Each team is now constructing curriculum activities that focus upon investigating the issues and problems related to their selected topic. Activities being designed are intended to promote interaction within each team between students of the different age levels and subject areas. The activities will be designed to integrate science concepts already present in classroom curriculum into a comprehensive examination of a single problem. Teachers will receive release time for this curriculum development and stipends for summer curriculum work.

To facilitate the successful integration of technology into student work, a peer-mentor training program has been initiated. Students have submitted applications for these positions. Selected students will receive pre-training (summer 1996) on the various technologies essential to the project. These students will then act as peer resources for class activities when student project work begins in the fall of 1996.

When the students of each multi-age team are presented with their respective problems, they will be guided through an investigative and problem-solving process. Each grade level of student will examine and investigate the problem from a perspective most suited to the class they are taking. For example: eighth grade students (who spend a large part of the year examining the atmosphere of earth) might examine the world food supply issue from a meteorological point of view. That is, how do weather and climate play a role in the quantity and distribution of food worldwide? Using remote sensing imagery and data obtained through the Internet and experimental observations, students will investigate and become experts within their own unique perspective. Students will provide their specific expertise on the issue to other team members through electronic mail and by posting materials to their World Wide Web server.

Final products of student research, experimentation, and collaboration will include interactive multimedia presentations created with multi-media authoring software. Refined World Wide Web based *micropedias* will summarize and highlight the results of the student work. These *micropedias* will show the connections between the various components of the earth system that are significant to the global issue of concern. Electronic mail addresses will be posted on each web page to facilitate interactive reviews of student work. Interactive computer models of systems will also be created to simulate various parts and processes within the earth system.

6. Invitation to Collaborate

Our project is nearing the end of the infrastructure installation and teacher training phases. In the fall of 1996 student teams will begin to examine the chosen topics and begin the collaborative research process. An invitation to collaborate with our students is extended to any interested scientist. Contacts via electronic mail are preferred (lindgren@pluggers.esu8.k12.ne.us). Updates on our project's progress can be accessed through our district's web server at: http://jrhigh.nps.esu8.k12.ne.us.

7. Conclusion

In the early 60's the first satellite images of earth were sent to earth. This marked the beginning of a revolution in the way we perceive our planet. Even those crude, early pictures began to help us see the earth as a single entity--a complex system whose seemingly infinite number of parts and sub-systems are inexorably entwined and interdependent.

On the eve of the 21st century, the global scientific community is positioning itself to further refine its understanding of the earth system. NASA's Mission to Planet Earth will be carried out by the spacecraft of the Earth Observing System. This armada of earth-orbiting satellites will use high-resolution sensors to monitor ozone concentration, cloud cover, pollutants, solar radiation budget, and other critical environmental attributes.

Of the thousands of young people that will graduate from Nebraska's schools before the next millennium, each individual's future actions has the potential to dramatically impact the overall conditions for life on this small planet. This impact might be made as a scientist, an industrialist, a poet, a novelist, a government official, or a consumer.

Will these individuals contribute to the demise of a significant component in our atmosphere? Will these individuals discover a method of preventing some form of dangerous climate change? Will these individuals become the government officials whose policy leadership decides the fate of some endangered species? Will these individuals write the best-selling novels or Pulitzer Prize-winning poems that begin to sensitize a generation to an attitude of concern for their planet? Will these individuals write the anthems that inspire others to wonder at the complexity and interdepen-

dence of life on planet earth? Will each of these individuals have the knowledge, skills, attitudes, and aspirations that are needed for them to fulfill these roles? As we endeavor to implement *Our Role in the Earth System* we hope to make substantial progress toward these goals in the lives of Norfolk Public Schools students.

8. References

[1] Revised Statutes of the State of Nebraska: Section 79-4, 140.01

Earth System Science Education: A Continuing Collaboration

Donald R. Johnson, Martin Ruzek, Michael Kalb
Universities Space Research Association
7501 Forbes Blvd., Suite 206, Seabrook, MD 20701-2253
301-805-8396 FAX 301-805-8466
donj@ssec.wisc.edu, ruzek@usra.edu , mkalb@gvsp.usra.edu

Abstract - Since 1991 the Universities Space Research Association (USRA) has led the Cooperative University-based Earth System Science Education Program (ESSE) under NASA sponsorship to develop courses and curricula in Earth System Science at the undergraduate level. At that time twenty-two universities were selected to participate in the Program with an aim to advance interdisciplinary views of the Earth as a system in the classroom. The courses offered at the survey and senior levels provide a scientifically based appreciation of topical issues in global change, and engage advanced students and faculty from different disciplines in addressing Earth Science and Global Change issues. Over 4000 students were enrolled and over 100 faculty and staff were involved in teaching survey and senior level courses during the 1993/94 academic year.

As the Program evolved, the need became apparent for a shared repository of educational resources for Earth System Science which would be beneficial to all participants, as well as to the broader Global Change science community. In 1994 the program established a server on the Internet with a World Wide Web Home Page (http://www.usra.edu/esse) designed to foster the collaborative development of educational materials and to assist the organization of relevant source material already available on the Web. The content and organization of the server is being updated continuously with input from the participants. In addition, a moderated listserver has been established to encourage communication among faculty participants, students and NASA researchers. Response from a survey of the original participants indicates that the program has been successful in developing Earth System Science Education and a forum for the discussion of courses, curricula and learning modules.

In August of 1995 an additional twenty-two colleges and universities were selected to continue the Program through the end of the decade, building upon the success and experiences of the original program participants. In addition to the continued maintenance of the server content, the program is exploring ways to further increase its impact upon undergraduate Earth Systems Science Education. A prototype Journal of Earth System Science Education is being established with the goal of providing peer review, publication and recognition for the authors of quality learning modules. The ESSE Program is also preparing to team with other Earth Science Education initiatives such as Project ALERT (Augmented Learning Environment for Renewable Teaching), and possibly the education component of the Inter-American Institute (IAI) for Global Change Research.

BACKGROUND AND CURRENT STATUS

Since the late 1980s, Earth System Science has captured the attention and respect of the scientific community as an overarching concept under which disciplinary researchers work together to attack the increasingly complex interdisciplinary problems which are facing society [1]. Popular literature and the press have also embraced the concept of the Earth as a system, bringing the concepts and problems of ozone depletion, global warming and population increase to younger and more attentive audiences [2].

Since 1991, the Earth System Science Education Program (ESSE), funded by NASA's Office of Mission to Planet Earth, has supported the development of undergraduate courses focused on aspects of Earth System Science. In addition, the Program has encouraged collaboration and communication between NASA researchers and educators through its exchange program. Twenty-two institutions were originally chosen to participate in the ESSE Program, and their overall success led to the selection in 1995 of an additional twenty-two schools to carry the program through the year 2000. Proposals from smaller colleges and universities were especially encouraged in an effort to broaden the base of ESSE schools, resulting in a richer mixture of academic programs including aspects of the human dimensions of global change (Table 1). The ESSE background and program concept are further described in Johnson et al, 1995 [3]. This paper will focus on progress and plans for the Program since selection of the new ESSE participants.

THE ESSE WEB SERVER

A continuing emphasis of the Program is the development of a World Wide Web server capability to foster communications and collaboration among the ESSE participants and others interested in the Program. The WWW server (http://www.usra.edu/esse) is a repository for information concerning courses, curricula material, data and electronic modules relating to Earth System Science and Global Change education. The site is under continuous development, and several new features have been added to improve its usability:

• Each participating institution is referenced by image map to a home page listing the principal participant, collaborators, courses offered and links to the participants own WWW sites.

0-7803-3068-4/96$5.00©1996 IEEE

• A feature called "ESSE Notes" has been established, distributing news, relevant WWW sites, reviews and other items of interest every few days.

• A listserver for the ESSE participants and others interested in the program has been established, with nearly 150 participants. Discussion topics include book announcements, comments on textbooks and student intern opportunities. Instructions for participation are included on the ESSE Home Page.

• Documented electronic learning modules, developed by ESSE participants and others, are being collected.

• A list of over 650 WWW resources of relevance to Earth System Science educators continues to be maintained.

• An archive of ESSE Program documents (briefing charts, articles etc.) and information as well as a calendar of ESSE related events has been established.

Overall response to the server has been positive, and suggestions for improvement are always welcomed. Plans for the coming year include implementing an improved search engine, design of a more elegant and easily navigable graphical user interface and the continued collection of documented learning modules and Earth System Science course syllabi.

Table 1
ESSE Participating Universities (1995 - 2000)

University	*Principal Participant*
Bryn Mawr College	Mark Johnsson
Cal State Univ - Monterey Bay	Susan Alexander
Carleton College	Will Hollingsworth
Clark Atlanta University	Denise Stephenson-Hawk
Coastal Carolina University	Craig Gilman
Cornell University	Bryan Isacks
Florida Institute of Technology	George A. Maul
Georgia Institute of Technology	Dana Hartley
Michigan State University	Stuart Gage
North Carolina State University	Robert Bereman
San Diego State University and Cal State Univ - Long Beach	Eric Frost Elizabeth Ambos
South Dakota School of Mines	Ronald Welch
Union College	Sharon Locke
University of Colorado	James White
Univ. of Ill. at Urbana Champaign	Walter Robinson
Univ. of Maryland at College Park	Owen Thompson
University of Massachusettes	William McCoy
University of Michigan	Timothy Killeen
Univ. of N. Carolina at Chapel Hill	Douglas Crawford-Brown
University of Oklahoma	John Snow
West Chester University	Richard Busch
Westminster College of Salt Lake City	Robert Ford

PARTNERS AND PLANS

ESSE continues to foster partnerships and collaborations with individuals and organizations engaged in Earth System Science education.

Project ALERT

Representatives from the California State University system have established a partnership with the technological expertise in imaging and information systems at NASA's Jet Propulsion Laboratory and others to help impact science literacy and education in the geosciences and space sciences. Called Project ALERT (Augmented Learning Environment for Renewable Teaching), the focus of the effort is twofold: (1) university students who will be the future teachers in K-12 education, and, (2) teachers already in the classroom. The California State Universities represent one of the largest educational systems in the nation, and train the majority of teachers in California. By focusing on the science and science methods classes that are the primary science education for teachers, ALERT aims to better prepare future science teachers with knowledge, techniques, and resources to vitalize Earth and space science education. A powerful aspect of this project is that the subject matter includes cutting-edge, active science for interactive learning and discovery. Data from space missions, observation of the Earth, and active science programs augment the classroom learning environment and show why science is important to society as a whole. By using such information to enhance the teachers' ability to teach and to promote problem solving and critical thinking skills, ALERT will distinctly impact science literacy [4]. The principal architects of Project ALERT are represented in the ESSE team, and efforts to coordinate and share resources have been initiated.

The Inter-American Institute for Global Change (IAI)

An outcome of the 1992 United Nations Conference on Environment and Development (UNCED) in Rio de Janeiro was an agreement establishing the Inter American Institute for Global Change Research signed by sixteen countries of the Americas. The IAI will focus its efforts on increasing our understanding of global change related phenomena and the societal implications of such phenomena while augmenting the overall scientific capacity of the region [5]. One of the IAI's goals is the establishment of training and education programs coordinated with an IAI science agenda that is consistent with other international global change research programs. The ESSE Program has proposed to organize a university-based collaborative effort to develop Earth System Science and Global Change educational resources in the context of the IAI science agenda. The ESSE Program would be used as a model for the development of similar collaborative efforts within the IAI member countries; however, tailored to the specific technical capabilities and scientific interests of the participants. In addition, the existing scientific, technical and support resources of the

ESSE program would be available to share with the ESSE-IAI team to facilitate an immediate, effective initiation of the proposed program. A planning meeting to better define the project goals and implementation will be organized in mid-1996 pending selection of the project by the IAI.

The Journal of Earth System Science Education (JESSE)

ESSE participants have recognized the need for a reputable review process for classroom educational resources dealing with Earth System and Global Change science. Such a peer review mechanism will enable standards of content and presentation quality to be set, and should encourage the development of these materials by offering the authors a means of peer reviewed publication that may be beneficial during university consideration of achievements. A working group has been set up to discuss the appropriate editorial and review procedures, content and format for an electronic Journal of Earth System Science Education. The mission of the Journal is to set high standards of quality, encourage the development of pedagogical tools and techniques, and facilitate the exchange and wide access to educational materials and information associated with Earth System Science Education. The electronic publication process and progress of other e-journals (such as the American Geophysical Union's "Earth Interactions") are being reviewed. It is anticipated that the resulting recommended procedures will be in place to allow general solicitation of materials for publication in early 1997.

A Virtual Earth System Science Laboratory (VESSL)

Shared experiences and communication of ideas are essential for understanding of the multi- and interdisciplinary problems being addressed. This is especially important for both multi- and interdisciplinary education and research in Earth System Science and Global Change. ESSE hopes to develop a prototype of a Virtual Earth System Science Laboratory (VESSL) to enable communication and collaboration among traditionally distant users through utilizing Internet tools which allow students and teachers to interact, perform classroom exercises and explore Earth System Science data and phenomena. Tools such as VRML, IRC and CU-SeeMe will be explored, first to deliver a short series of question and answer lectures to a distributed interdisciplinary audience. If such an exercise proves fruitful, the technology will be extended to deliver a series of Earth system laboratory exercises conducted by lab partners from different institutions. The ESSE participants have expressed a willingness to participate in such an exercise to enrich the interdisciplinary content of their courses. Initial testing of the concept is hoped to begin in Fall of 1996.

Summer Workshop

The first meeting to include the new group of ESSE universities was hosted at the University of California - Santa Barbara in November, 1995. This organizational meeting included a workshop introducing the concepts of remote sensing science and geographic information systems. The aim of the workshop was to familiarize program participants (including their teaching assistants) with these concepts so that they could be better integrated into the classroom. Discussions during and following the meeting led to the suggestion that the next meeting be devoted to definition and development of a series of Earth system teaching modules by a group of teams during a week-long hands-on session. Accordingly, plans are being drafted for a workshop to be held in the Summer of 1996. Workshop participants will divide beforehand into groups focused on an interdisciplinary topic dealing with some aspect of the Earth system (e.g. water as a resource, the industrial metabolism of energy and resources, the agricultural cycle of nutrients and carbon, etc.) Each group will be tasked to define and develop over the coming summer a supplemental teaching module explaining their topic, using Internet technologies, STELLA models or other multimedia presentation tools. These documented learning modules will then be shared via the ESSE server. Summary lectures on such topics as systems theory, pedagogy and active learning techniques, and human dimension aspects of global change will be delivered throughout the week.

SUMMARY

The ESSE Program has progressed over the past five years, encouraging the study of the Earth as a system and fostering a collaborative learning environment. Network technology developments are now enabling an extension of the original program goals by offering innovative and effective ways to deliver course materials and a means to develop truly interdisciplinary approaches for Earth System Science and Global Change education problems. Collaboration with other educators and programs will continue to be an important part of ESSE, as well as the testing and adoption of new tools and methods for effectively delivering Earth System Science and Global Change concepts to the classroom.

ACKNOWLEDGMENTS

This effort is supported by a grant from NASA's Office of Mission to Planet Earth (NAGW-4831).

REFERENCES

[1] "Earth System Science - An Overview" Report of the Earth System Science Committee NASA Advisory Council, May, 1986

[2] "The Forgiving Air", R. C. J. Somerville, 1996, University of California Press

[3] "Earth System Science Education: An Internet-based Electronic Curriculum" Johnson, Ruzek and Kalb, 1995 IGARSS'95 pp 572-574

[4] Project ALERT WWW Home Page http://stargate.jpl.nasa.gov/alert/

[5] The Inter-American Institute WWW Home Page http://www.nsf.gov/stratare/egch/iaidescr.htm#iai

The OMSI/NSF Young Scholars Research Participation Program

Jeffry Gottfried
Oregon Museum of Science and Industry
1945 SE Water Ave., Portland OR 97214
503-797-4579/FAX: 503-797-4568

Abstract: Since 1989, 120 promising high school science students from throughout the U.S. have engaged in an intensive six-week residential summer program of research in geology, archaeology, or ecology as participants in the OMSI-NSF Young Scholars Research Participation Program, conducted by the Oregon Museum of Science and Industry with funding from the National Science Foundation (Grant #ESI-9452688) . Based upon a demonstrated interest in science, an essay, recommendations from teachers and others, Young Scholars are selected from a pool of applicants nationwide. OMSI Young Scholars conduct research as members of a research team and as individuals and write a research paper, under the guidance of a research leader, an instructor, and logistic specialist.

THE NEED

Blue-ribbon panels of scientists and science educators have called for changes in the way that science is taught to pre-college students (1,2). Scientific inquiry, research and hands-on projects, integration of technology and math in science, and exposure to science careers are among the recommendations. They also stress the importance of recruiting and involving women and minority students, typically underrepresented in the sciences. The National Research Council's "National Science Education Standards" calls for the creation of "learning communities" that "reflect intellectual rigor of scientific inquiry and the attitudes and values conducive to science learning." (3) They call for learning environments that provide students with time, space and resources, technology and human support for extended student investigations. The OMSI Young Scholars Research Particpation Program is an attempt to create such a community and environment.

THE PROGRAM

The OMSI-NSF Young Scholars Research Participation Program is a six-week, total immersion in scientific research, career exploration and teamwork. Promising high school science students engage in field work and data analysis as a members of research teams under the supervision of researchers from universities, government agencies and/or private industry and science educators from OMSI.

Since 1988, research teams have included Geology/Paleontology, Freshwater Ecology, High Desert Ecology, and Archeology. Each team consists of ten Young Scholars from throughout the U.S., one Lead Researcher from a university or government agency, one Instructor, typically an OMSI science educator or high school teacher, a Logistics Specialist, typically a camping/outdoor skills instructor from an OMSI science camp and one or two outstanding past Young Scholars who work as research assistants and role models for the new cadre of Young Scholars. Cooperating agencies and universities include the National Science Foundation, USDA Forest Service, Bureau of Land Management, National Park Service, University of Oregon, Oregon State University, Portland State University, and Oregon Graduate Institute For Science and Technology.

The Geology/Paleontology Research Team, in one form or another, has existed continuously for approximately 45 years. Since becoming an NSF Young Scholars program, research projects have included work on paleobotany, the Triassic-Jurassic extinction event, and paleosols and climate change. The Aquatic Ecology Research Team conducts studies of watersheds, habitat management and anadromous fish. The High Desert Ecology Research Team studies soils, plant ecology and grazing practices in the high desert of Central Oregon. The Archeology Research Team records and interprets American Indian petroglyphs and pictographs in Central and Eastern Oregon.

Researchers have been recruited for the program, based upon the accessibility of their research to students and ability to communicate well with youth. Researchers engage in the research that they would otherwise be doing and are assisted by a Young Scholars team. Additional scientists and guest speakers visit the teams for two to five days to share their particular expertise and to expose Young Scholars to a greater variety of people and career possibiliites.

0-7803-3068-4/96$5.00©1996 IEEE

Research teams are in-residence at OMSI's Hancock Field Station, at Forest Service installations or at field locations throughout Oregon, whatever is most appropriate for the summer's research agenda. The six weeks each summer is much closer to mounting three research expeditions than conducting three science classes.

In addition to assisting research leaders with their on-going work, Young Scholars are each required to complete a research project of their own and present it at a seminar held on the last day of the program. In most cases, Young Scholars choose research topics that are subsets of the overall research goal of the team. Of the 120 Young Scholars chosen for the program, 117 successfully completed research papers and presented their work at a seminar.

In addition to learning about the particular science subject matter of their research effort, Young Scholars also discuss and debate the ethics of science and learn methods of scientific research. They interact with scientists, science educators, and graduate students at many stages of their education and professional development. In this way, they learn about and experience first-hand the life of a scientist during the busy summer field research season. They also learn about the training and coursework and college preparation that is necessary in order to pursue science as a career and have the experience of defining a project, collecting and organizing data, interpreting it and actually writing a research paper and presenting it at a seminar attended by parents, teachers, team mates and members of the scientific community.

INTEGRATING TECHNOLOGY

As a science and technology museum, OMSI strives to integrate both science and technology in its educational programs. The Young Scholars Program is no exception and has undergone a remarkable evolution in this regard.

In response to our first NSF review in 1990 that called for increased communication between research teams that were separated by as much as 200 miles from one another following an initial three day orientation, OMSI installed a telecommunications network using First Class software. The network was soon followed by Internet accounts and Apple Quick take cameras for recording and communicating data and research activities. This relatively simple system operating from a Macintosh computer revoutionized communication and information retrieval for Young Scholars resulting in profound change in the program. It added a whole new dimension to summer research since telecommunications was for some the medium and others the message of their research.

On a daily basis, Young Scholars down-loaded images of their work and shared them with members of other teams hundreds of miles away along with personal correspondence that allowed each team to appreciate and benefit from the other's experiences. Images of fossils, petroglyphs and aquatic insects were transmitted daily over the system along with news of the day. Since 1995, a past Young Scholar has compiled news from the field and created a World Wide Web Page so that parents, friends, teachers and anyone who cares to can follow the progress of the teams over the course of the summer.

The next breakthrough came when it was discovered that many university libraries could be accessed via telecommunications and that literature searches could begin from the field and researchers who could not find the time to visit with teams in the field were quite willing to correspond with Young Scholars and consult in research activities. The Archeology Research Team accessed an international rock art list-server.

Other technology has also added tremendous value to the work of the OMSI Young Scholars teams and to the education of their members. Since 1992, teams working with the US Forest Service have had use of a global position system (GPS) for mapping and wilderness orientation and route-finding. It is amusing now to hold our new GPS in the palm of my hand and to recall the 20 pound backpack and parabolic dish-mounted helmet that constituted the system that the Forest Service made available to us in 1992! Using GPS, teams are able to accurately locate and map sigificant cultural sites, fossiliferous outcrops or watershed features.

Stream-flow meters, recording thermometers, solar path-finders and other technological advances have allowed Young Scholars to experience a technological education in the context of solving research questions. One of the most fascinating examples of high tech applications is that of a scientific photographer, who instructs Archeology Team members in photographing petoglyphs at night using controlled polarized light, which reveals details of the rock art not perceptible to the naked eye.

OUTCOMES

The OMSI-NSF Young Scholars Researh Participation Program has resulted in a number of success stories including scientific discoveries that have been of great value to research leaders. For example, in 1993, a Young Scholar found the fossil skull of a Shatasausus, a Jurassic marine reptile, in the Wallowa Mountains of Eastern Oregon. This species had previously been found only in China. A 1994 Young Scholar, discovered three species of rare and threatened amphibians in a National Forest stream that was scheduled to be de-watered as a part of a hydro-electric diversion. Professional environmental consultants had previously not reported any of these species. The list of discoveries and could go on and on and can be found in the publications of Lead Researchers.

Young Scholars have benefited personally through admission to colleges of their choice, scholarships and, once in college, to a "leg up on the competition" in research skills. Success stories of Young Scholars are particularly poignant when the students are from underserved groups and/or poverty backgrounds. While OMSI cannot take full credit for the success of its Young Scholars. It is significant to note that every successful Young Scholar during their senior year receives written recommendtions to colleges and scholarship committees and personal counseling and guidance in college applications and financial assistance. OMSI is also instrumental in finding summer positions for past Young Scholars in labs and university or govenmental field research.

The program has been especially successful in recruiting, mentoring and promoting the success of low-income students and students from under-served communities. Due to the prestigious nature of the program and the fact that it is totally free to those that are accepted, very bright students from low-income backgrounds are among the applicants. It is in these youth that the strength of OMSI's mentoring and efforts to promote Young Scholars network can best be seen. At this time, the 10-15% of past Young Scholars from low-income and poverty backgrounds are succeeding and excelling at prestigious universities with full scholarships, due in part to OMSI "matchmaking" and recommendations.

Feedback from universities indicates that OMSI Young Scholars enter college with a skill-set that exceeds their peers. They can think and plan on their own, ask good research questions. They can do science and not just say or write the correct answers to questions (4). When the ExonValdez Oil spill occured in Alaska, a past OMSI Young Scholar, then a sophomore at Univesity of Alaska, dropped out of school for a semester and successfully competed as a sub-contract on a portion of the impact statement. His standing to bid on the contract was due to his experience as a member of the Aquatic Ecology Research Team and his work as a Research Assistant during the following summer. College recruiters impressed with the performance of past Young Scholars call and visit OMSI each year in order to actively recruit current graduates.

Thanks to the Internet, it is easier than ever to communicate with past Young Scholars and keep up with their progress. The news is most heartening. This winter, we learned of the first award of a graduate school fellowship to a past OMSI Young Scholar!

REFERENCES

(1) F. James Rutherford, Science For All Americans, New York:Oxford,1990, pp.185-201.

(2) AAAS, Project 2061 Update, 1992, pp. 24-25.

(3) National Research Council, National Science Education Standards, 1994, Washington,DC: National Academy Press (11-9)-(11-25).

(4) Personal Communication, Dr. William Orr, Professor of Geology, University of Oregon, 1994.

Alaska SAR Facility Education Outreach

Donna Sandberg and Frank Carsey
Alaska SAR Facility Science Division, Geophysical Institute,
University of Alaska Fairbanks, PO Box 757320, Fairbanks, Alaska 99775-7320
Phone: 907-474-6390, Fax: 907-474-6441, Email: donna@dino.gi.alaska.edu

ABSTRACT

The goal of the Alaska SAR Facility (ASF) Education Outreach is to use ASF data (and/or a family of data sets), technology, and resident expertise for education. Feedback from local teachers and the local school district has enabled us to develop our first cirriculum element prototype module on glaciers: "From a Snowflake to a Surge." This element, which currently resides on a CD-ROM and is still in Beta form, has been targeted for 4-6th grades and reviewed by a panel of local teachers and officials.

INTRODUCTION

The National Research Council recently published the *National Science Education Standards* which "empowers teachers, school administrators, parents, and community leaders to make decisions about curriculum, professional development, content, assessment, science programs, and educational systems."[1] The National Science Teachers Association (NSTA) is a leader in efforts to implement these new science education standards and states, "Each of the guidelines will give teachers options for adapting their instructional programs to move toward the vision of the Standards."[2] These efforts, in fact, free teachers and school administrators to work more closely and creatively with research-oriented facilities like ours. Albert Einstein said, " Restricting the body of knowledge to a small group deadens the philosophical spirit of a people and leads to spiritual poverty."[3] The field of science education is in an exciting time of renewal and change.

As there is a growing nationwide effort to develop education outreaches and to improve the quality of science education in general, we have been asked to discuss the Alaska SAR Facility (ASF) Education Outreach and the relative success of our ideas in implementing this plan. We plan to develop K-12 educational modules using SAR data; initially, modules will be focused on Alaskan interests. However, since we have been asked to focus on "big" (i.e. interesting to children) topics, the material should be relevant throughout the country.

STATUS OF SCIENCE EDUCATION

There are various reform movements defining styles which describe how science should be taught. Some of these include the Science/Technology/Society (STS) model, the Scope/Sequence/and Coordination (SSC) effort and the constructivist model. Remote sensing is not specifically included or excluded in any of the reforms or the styles. Most current reforms have such general, open-ended guidelines that the way in which a district/teacher goes about meeting the curriculum, etc., is open to considerable individual interpretation. One of the big themes in the AAAS "Project 2061" is change. Most reforms also mention earth systems at some point, so any remote sensing of the earth might apply to that goal. One of the major undercurrents in science education is that technology be used as a tool of science. This is where remote sensing fits particularly well and may find its niche.

Science education student performance standards for the State of Alaska were adopted in 1994. The state considers these standards to be an important first step in restructuring our education system. Alaska wants its students to learn, not just put in time. The Fairbanks North Star Borough School District (FNSBSD) has recently adopted a K-12 *Science Curriculum Guide* for its local school district (5/16/95). Our ASF Education Outreach is one of the early projects responsive to this guide. The *Science Curriculum Guide* is similar to the reforms mentioned above, containing various grade-level science focuses. Statewide general science education curriculum requirements are being written and will be released this spring in a document entitled *Frameworks*.

We hope remote sensing will become an integral part of this development. We want to equip teachers to teach students about earth sciences and earth science technologies, including remote sensing topics. We hope that by developing interactive, portable modules which can be taken to the classroom, we will be able to get students excited about doing real science utilizing remote sensing.

1 Shelly Fisher, President, National Science Teachers Association (NSTA), cited from the NSTA Web page http://www.nsta.org.
2 ibid. NSTA, http://www.nsta.org.
3 Earthwatch, Center for Field Research, http://gaia.earthwatch.org/www/cfr.html.

0-7803-3068-4/96$5.00©1996 IEEE

WHO WE ARE

The Alaska SAR Facility (ASF) is a National Aeronautics and Space Administration (NASA)-funded satellite receiving ground station and scientific research program located at the University of Alaska Fairbanks. The aspects of our mission statement relevant to the Education Outreach are:

- We exist to advance polar research and earth sciences by supporting scientific and operational application of remote sensing data to better understand the earth as a system.
- We acquire, process, distribute and archive remote sensing data in support of research, operational applications, and education.
- We contribute to education at the university, primary, secondary and community levels through student involvement, lectures, curriculum development, electronic information exchange and tours.

Research resulting from the use of SAR data, and ASF SAR data in particular, has begun to flow into many thematic areas: hydrology, glaciology, forestry, land cover, oceanography, volcanology, geomorphology, geology, topography, air-sea-ice interaction, and interferometry (a relatively new science). Algorithms, tools, and data sets have been developed by researchers. Theses and dissertations based on SAR research have been successfully defended. Remote sensing, particularly SAR remote sensing, is an important aspect of earth system science.

HISTORY

We decided to examine the use of the wealth of resources within the Geophysical Institute and ASF for K–12 education. Our first fact-finding meeting with the Fairbanks North Star Borough School District (FNSBSD) became a brain-storming session concerning subjects for curriculum elements teachers would find useful. The FNSBSD asked us to target our efforts toward middle school grades 4–6. We were also asked to tackle "big" subjects like glaciers, volcanoes, forest fires, floods, oil spills: topics which would stimulate children's interest. Specifically, we were asked to develop "something" on the subject of glaciers.

We have experimented with several software authoring environments such as Digital Chisel and HyperStudio. Our first module, created with Digital Chisel, received excellent reviews from teachers. In that environment, we were able to input sounds, imagery, and videos. Unfortunately, imperfections in earlier versions of that software necessitated a migration to HyperCard to finalize the prototype. Although HyperCard was also able to incorporate sounds, imagery, and videos, its use involved more intensive scripting. Teachers were again pleased with our preliminary results, which we placed on a CD-ROM.

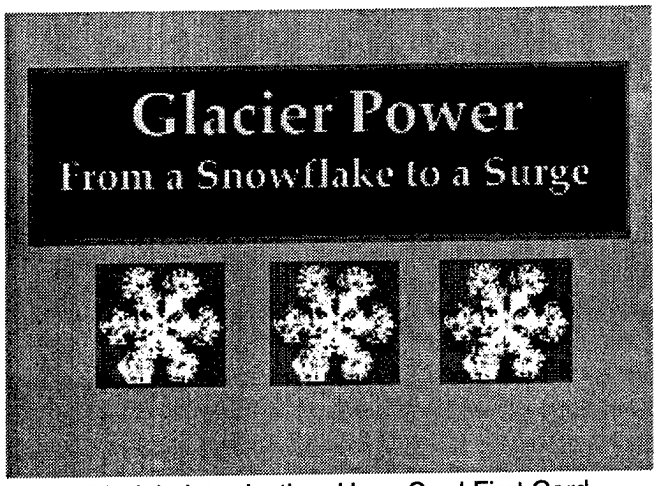


Fig. 1 Module Introduction–HyperCard First Card

Our prototype, "Glacier Power: From a Snowflake to a Surge," incorporated expert input from local glaciologists and was reviewed by a formal panel of teachers and school district officials, including curriculum implementation coordinators.

Feedback from this panel enabled us to continue development. The panel's specific recommendations for hands-on materials and more intensive interactive capability are currently being developed. A guidebook for teachers and an activity book for students are presently being written. We are also authoring most of the documentation in html mark-up language. One of the key elements of our efforts is our intent to place many of the resources for each module on our Internet home pages. This will give both teachers and children further experience using the Internet as a science/technological tool. We will have a great variety of links, including sound, imagery, video segments, and activities, to maintain children's interest. Also, feedback and assessment for the student activities will be provided via web links. We plan a follow-up workshop/review for further assessment.

Since much of Alaska's population lives in remote areas, incorporating our modules on Internet sites is important. We would like to implement a plan to include interested students from this population which consists primarily of native Alaskans, both Eskimo and Indian. The Alaskan school system is diverse in its technological capabilities (from schools with satellite links to schools without computers). We want our modules to be portable and to carry technology with them in order to cover the whole spectrum and meet the needs of individual schools.

We also plan to equip teachers to teach about earth sciences and earth science technologies, including remote sensing topics, and have been working with the University of Alaska Education Department to implement this plan. One of our team

members is currently writing curriculum for an accredited continuing education course(s) in remote sensing. The class(s) will equip teachers to use remote sensing as an earth science tool as well as introduce any curriculum elements we generate. The Remote Sensing Research Group within the University of Alaska Fairbanks is currently also generating a core curriculum in the field of remote sensing.

THE TEAM

The ASF Education Outreach team leader develops the outreach with guidance from the ASF Chief Scientist and from members of the ASF Education Outreach Advisory Group, which is organized into focus teams to address issues such as Internet development, curriculum development, continuing education, and other areas of interest to the education outreach as a whole. Since the development of the World Wide Web, that aspect of the education outreach will be critical, and that focus team will evolve into a semi-permanent working group.

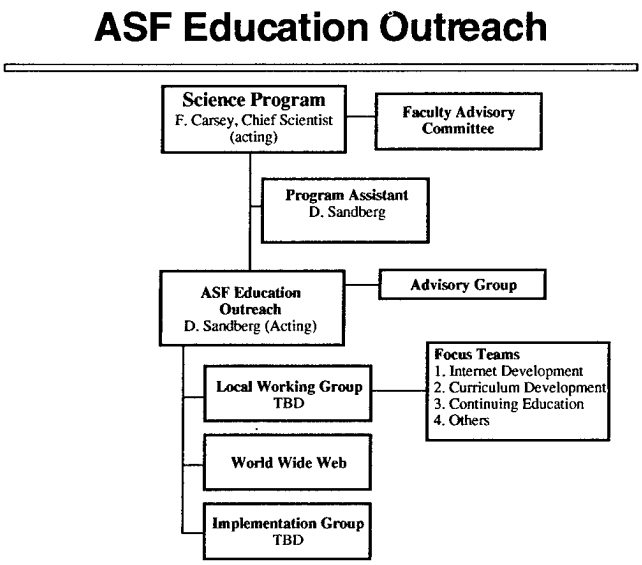


Fig. 2 ASF Education Outreach Organization Chart

Fig. 3 Education Outreach Matrix

Advisory Group	Working Group
Scientists	Scientists
Professional/Technical	Professional/Technical
UAF Education Dept.	Teachers
Curriculum Experts	Students
K-12 Teachers	
University Teachers	
School District Officials	
UA Museum	
Focus Team	**Implementation Team**
Professional/Technical	Professional/Technical
Scientists	Scientists
Teachers	Teachers
Students	Students

The Implementation Group will consist of people who become instrumental in delivering the product of the ASF Education Outreach to educators, classrooms, and students. We will train teams to take our material to Alaskan villages. Some of the benefits reaped by village teachers and students will include further familiarization with technology, as well as instruction in earth science.

OTHER IMPORTANT LINKS

The FNSBSD is also involved with an NSF-funded *Partners in Science Program* which exists to "further math and science learning in grades K-12 in the Fairbanks North Star Borough School District, in two rural Alaskan school districts (Iditarod and Gateway), and among isolated home-schoolers. This project links practicing scientists from higher education, government, and industry with teachers and students, using the latest information networking technology. It will be instrumental in igniting a redefinition of technology's place in the education process in the targeted school districts." We have recently agreed to supplement the *Partners in Science Program* and have suggested a cooperative project with the Iditarod School District. This project will enable students to assist calibration engineers and scientists in the set-up of corner reflectors. The ASF uses corner reflectors to callibrate signals from the satellites we serve. A corner reflector will appear as a bright white pixel in a satellite synthetic aperture radar image. Within the *Partners in Science Program*, one of our scientists has also teamed up with a local 4th grade classroom. Students email questions to "their scientist." We are developing an Internet home page for this scientist to use and plan to develop pages for each of our scientists who become involved with education.

SUMMARY

We are a new, developing project within a larger entity, the NASA-funded Alaska SAR Facility. We are making progress towards our goal of contributing to education and have an exciting group of people to interact and create with. We continue to work with officials, curriculum experts, and teachers to perfect our work and ensure its quality. Our team members are developing guidebooks for students and teachers as well as CD-ROMs. Much of the material will be accessible on the Internet.

Observations of Sea Ice Physical Properties during the Sea Ice Electromagnetics Initiative

A.J. Gow and D.K. Perovich
USACRREL
72 Lyme Road
Hanover NH 03755
603-646-4256 phone
603-646-4644 fax
perovich@hanover-crrel.army.mil

Abstract - An Office of Naval Research sponsored sea ice electromagnetics research initiative has been directed towards relating the observed variability in sea ice electromagnetic signatures to changes in sea ice physical properties, and then using this information to develop forward and inverse models. In this paper we present an overview of laboratory and field observations made of sea ice physical properties during the past three years. This description included a statistical characterization of the ice microstructure. We shall present these observations in the context of tracing the development of sea ice. The laboratory studies included *in situ* measurements of the physical and electromagnetic properties of young ice sheets grown under both quiescent and active conditions.

INTRODUCTION

The ONR sponsored sea ice electromagnetics initiative has been directed towards relating the observed variability in sea ice electromagnetic signatures to changes in sea ice physical properties, and then using this information to develop forward and inverse models. Sea ice is a complex material with an intricate and highly variable structure, and a detailed description of the ice physical properties has been an integral component of this effort. This description includes vertical profiles of ice salinity, temperature, brine volume, density and crystal structure. In this paper we present an overview of laboratory and field observations made of sea ice physical properties during the past three years.

Measurements entailed the use of a large pond at CRREL to fabricate a variety of saline ice types, ranging from first-year ice simulants to thermally modified ice sheets where physical and structural properties closely mimicked arctic second-year ice. Snow-covered ice sheets in addition to rubbled and pancake ice sheets were successfully fabricated in conjunction with active and passive microwave imaging. Experiments were extended to first-year and multi-year ice at Barrow, Alaska for intercomparison with the pond-grown ice sheets. The effect of an aligned c-axis structure, prodominant in the ice at Barrow, but absent in pond-grown ice at CRREL, was clearly reflected in a number of electromagnetic measurements. In addition to this qualitative description of the ice, we formulated a statistical characterization of the ice microstructure, including inclusion size distributions and spatial correlation functions of permittivity.

0-7803-3068-4/96$5.00©1996 IEEE

RESULTS

During the first year of operations of the new CRREL pond facility, known as the Geophysical Research Facility (GRF), measurements were confined to a single ice sheet grown under ambient meteorological conditions. The pond contained water with a bulk salinity of 29-30 $^{o}/_{oo}$ made up essentially of components closely simulating arctic ocean water. Ice growth was initiated during the evening of 18 January 1993. The water was allowed to nucleate spontaneously (without seeding) leading to the formation of coarse-grained columnar ice typical of that found in a quietly freezing arctic lead. Ice thickness increased slowly to 6 cm by 21 January and to 8.7 cm by 30 January. It reached a maximum thickness of 19.5 cm by 19 February. An ice characterization program that was applied to this and all subsequent saline ice sheets grown over the next two seasons included measurements of surface air and in situ water and ice temperatures, surface and bulk salinities, and documentation of crystalline structure/brine pocket characteristics on thin sections taken from samples cut from the growing ice sheet. The effects of a snow cover including brine wicking on microwave signatures were investigated along with surface roughness effects created by broadcasting ice chips onto the ice sheet surface. A series of salinity profiles over the extended period of growth of this ice sheet is shown in Fig. 1. C-shaped profiles, typical of young sea ice growth in the Arctic, characterize the earlier stages of growth of the pond ice; later profiles reflect the desalinating effects of periodic elevated air temperatures occurring during the latter stages of ice growth.

Experiments in January 1995 included the application, for the first time in the GRF, of a wave maker to fabricate a pancake ice sheet. In this instance the wave generator was fastened securely to the portable walkway spanning the pond. The wave maker consisted of a paddle attached to a variable speed motor. Turbulence created by the wave maker ensured the formation of a layer of frazil ice crystals on top of the pond. The continued effect of waves produced in this manner was to convert the semi-consolidated frazil ice layer into a field of pancakes with individual pans ranging in size from

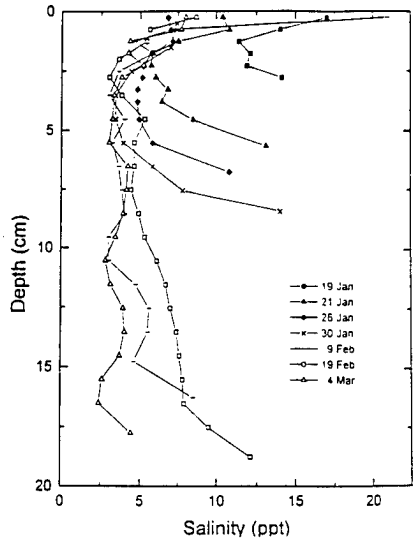


Fig. 1. Selected salinity profiles of a first-year ice simulatant grown in the CRREL pond.

10-50 cm in diameter and several centimeters thick. A vertical thin section slice of a pan showing the frazil platelet structure and salinity distribution within the pan is presented in Fig. 2. The shapes of the pan, with their raised rims, and the overall nature of their aggregation simulated very closely the same features observed in pancake fields in the Arctic.

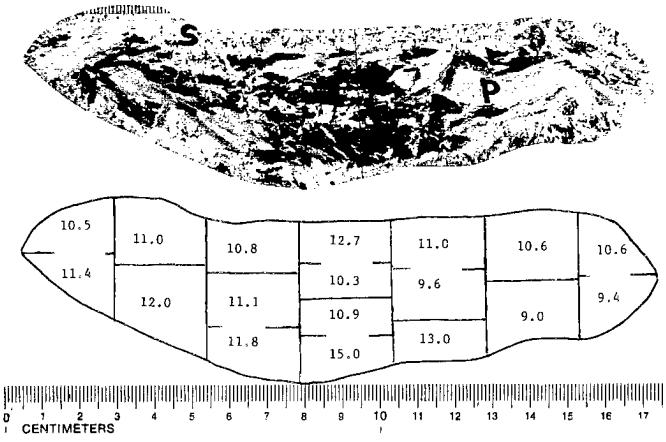


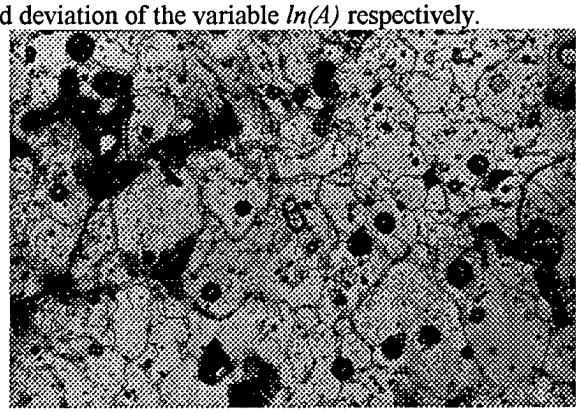
Fig. 2. Crystal structure and salinity distribution (o/oo) in a vertical slice of a pancake from pancake ice sheet simulant grown in the CRREL pond. Sequence of ice textures is slush (S) at top of pancake underlain by platy frazil (P).

We also determined statistical descriptions of the ice microstructure. One such description is the inclusion size distribution of brine pockets and air bubbles. Thin section photographs were digitized and analyzed using personal computer based image processing software [1,2]. Results from the top centimeter of pond-growth pancake ice are shown in Fig. 3. The granular nature of the ice, and the presence of both air bubbles and brine pockets are evident in the photograph. The air bubbles resulted from the agitated nature of the initial ice growth. There were roughly one-third as many air bubbles as brine pockets. Air bubbles were larger, with a mean area of the air bubbles approximately five times greater than the brine pockets (0.28 mm^2 vs 0.046 mm^2). As Fig. 3 demonstrates, the size distributions for the air bubbles and brine pockets are separated and easily distinguished.

In general, air bubbles are much larger than brine pockets, with mean major axis lengths on the order of millimeters for air bubbles and tenths of a millimeter for brine pockets. The inclusion shape also differs, as the brine pockets are more elongated than the air bubbles. The cumulative size distributions for both the air bubbles and brine pockets are well-fitted by a two-parameter lognormal distribution of the form:

$$CDF(A) = \frac{1}{2} erfc\left[\frac{-(\ln A - \mu)}{\sigma\sqrt{2}}\right]$$

where the two parameters, μ and σ, are the mean and standard deviation of the variable $ln(A)$ respectively.



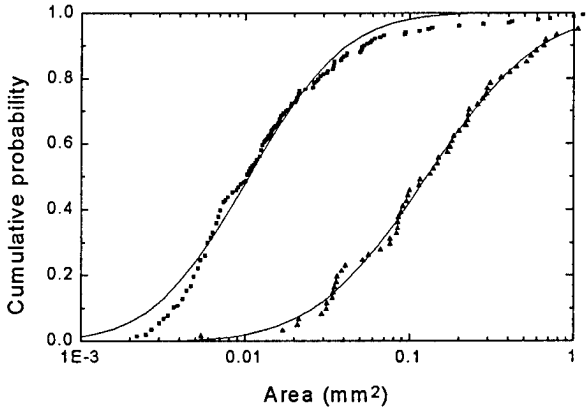


Fig. 3. Inclusion size distribution results for pancake ice. a) Horizontal thin section at a depth of 1 cm. b) Plot of observed (solid squares) and best-fit (curve) cumulative brine pocket (left) and air bubble (right) size distributions.

A field project was undertaken during April-May 1994 at Point Barrow, Alaska, to determine if conclusions from the laboratory experiments could be substantiated in the field. The work, centered around observations at two first-year ice sites, involved comprehensive investigations of the physical properties of the ice and the overlying snow conducted in conjunction with active and passive microwave imaging and other related remote sensing measurements.

Physical property characterizations of the ice sheets at both sites were based on cores drilled at selected locations within the remote sensing grids. Salinity profiles from the Chukchi Sea site, exhibiting c-shaped features so typical of Arctic first-year ice, are shown in Fig. 4.

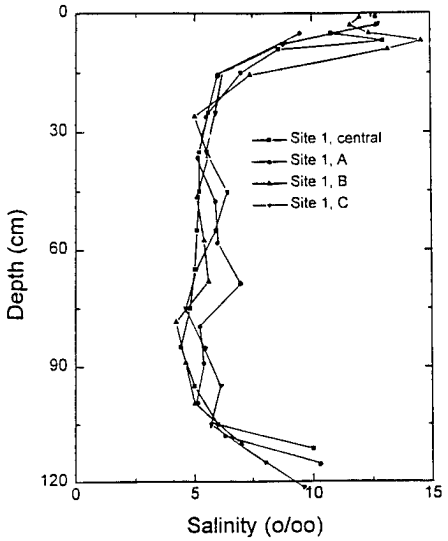
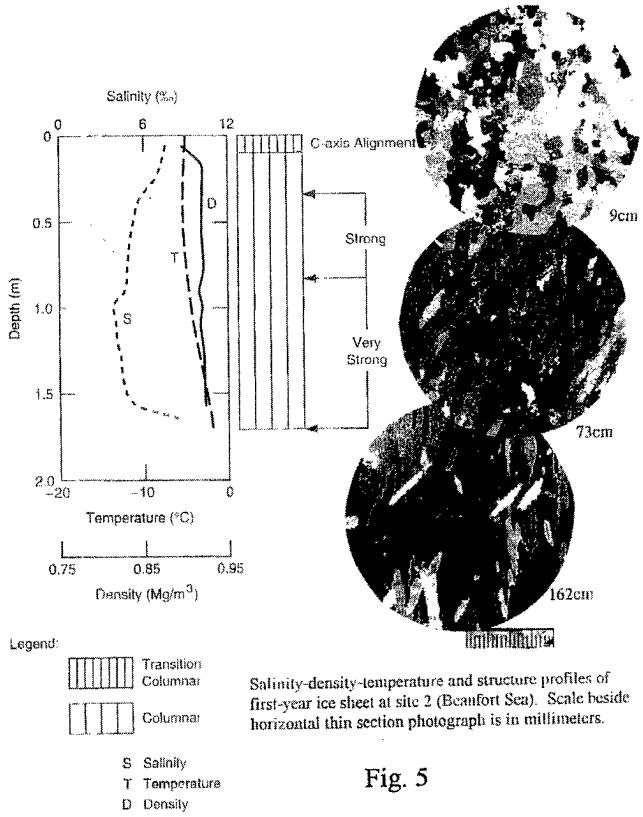


Fig. 4. Salinity profiles of first-year ice at Chukchi Sea site, Barrow Alaska.

At the second site, located in the Beaufort Sea, the ice measured 1.65-1.76 m thick and had formed during a single sustained episode of freezing. Except for a 5-10 cm thick layer of granular and transition type ice at the top of the sheet, the ice at this location consisted of elongated columnar crystals with c-axes moderately to very strongly aligned in the direction of the long shore current. A slight swing (10-15°) in the c-axis alignment in the lower layers of the ice is attributed to the effects of nearby pressure ridge formation causing a small deflection of the prevailing current direction, generally paralleling the shoreline. Bottom cores all contained abundant algae. A physical and structural property diagram is presented in Fig. 5. The salinity profile shows evidence of significant desalination at the top of the ice sheet attributable to the effects of sustained elevated surface air temperature that occurred prior to and during investigations at this site.



Salinity-density-temperature and structure profiles of first-year ice sheet at site 2 (Beaufort Sea). Scale beside horizontal thin section photograph is in millimeters.

Fig. 5

SUMMARY

A large pond at CRREL was used to fabricate a variety of saline ice types, including first-year ice simulants whose properties closely mimicked their Arctic sea ice counterparts. These experiments conducted in conjunction with active and passive microwave observations, were extended to first-year ice studies at Barrow Alaska for intercomparison with pond-grown ice sheets. Cumulative probability distributions of the size of air bubbles and brine pockets are well-fitted by a two-parameter lognormal distribution. Results indicated that air bubbles, in general, are roughly an order of magnitude larger than brine pockets and are less elongated.

ACKNOWLEDGMENTS

This work was funded by the Office of Naval Research under contract numbers N00014-95-MP3002 and N00014-95-MP-3019.

REFERENCES

[1] Perovich, D.K. and Gow, A.J., A statistical description of the microstructure of young sea ice, . *of Geophys. Res.* 96, 16,943-16,953, 1991.

[2] Perovich, D.K. and A.J. Gow, Towards a quantitative characterization of sea ice microstructure, *Dig., Intnl. Geosci. Rem. Sens. IGARRS '92, Vol 2*, 1249-1252, 1992.

Physical and Electrical Characteristics of Snow on Sea Ice; Implications for Forward Scattering Model Development

David. G. Barber, Sheldon D. Drobot, and John Iacozza

Centre for Earth Observation Science, Department of Geography,
University of Manitoba, Winnipeg, Manitoba, Canada, R3T 2N1.
Ph. (204) 474-6981. Fx. (204) 275-8281, dbarber@cc.umanitoba.ca

ABSTRACT -- In this work we quantify the vertical and seasonal characteristics of the geophysical and electrical properties of snow covers on landfast first-year and multiyear sea ice. Snow grain size, density, salinity, temperature and wetness were measured; the volume fractions of air, ice, brine, and the complex dielectric constant of the snow and sea ice were modelled over a cm vertical resolution spanning the seasonal periods from April to June. First-year sea ice snow covers (FYI'92 and FYI'93) showed that over the vertical dimension all variables depict a multilayer system. Deposition of a new snow cover (FYI'92) significantly altered the physical characteristics of the snow volume but not the dielectric properties. The basic vertical patterns observed in FYI'92 were also observed in FYI'93, except for the influence of the new snow layer of FYI'92. The pattern of physical and electrical characteristics for a multiyear sea ice snow cover were statistically different than an equivalent first-year ice case. Modelling of the snow grain area size characteristics can be done using a family of Chi-Square distributions with varying degrees of freedom.

INTRODUCTION

Snow is a complex crystalline material which forms from the condensation and sublimation of water vapour onto a nucleating material. Relative to snow on terrestrial surfaces, little is known about the precipitation or distribution of snow on sea ice. Climatologically, the snow cover on sea ice forms the interface volume which partitions the hydrosphere and atmosphere. The snow geophysics are directly linked with the physical properties of the underlying sea ice, as are the fluxes of energy and mass operating across this interface. Radiatively, snow (or lack of it) controls the surface radiation balance through its affect on shortwave and longwave exchanges. The combined snow and sea ice volume both affect and are affected by the forcing of the atmosphere and hydrosphere resulting in an integrated system which is modulated by feedback mechanisms amongst the components of the interface.

The objectives of this research are to investigate the microscale characteristics of a snow cover on first-year and multiyear sea ice. Specifically we address two research themes, from the perspective of microscale physical and electrical properties: i) What is the nature of the vertical heterogeneity of these types of snow covers?; and ii) can the vertical heterogeneity be modelled statitistically? These themes are important in the development of forward and inverse scattering model development as it relates to microwave and optical wavelength scattering over snow covered sea ice.

METHODS

Data used in this research were collected during the Seasonal Sea Ice Monitoring and Modelling Site (SIMMS) experiments in 1992 and 1993. Details of the experiment are available elsewhere [1]. Three case studies are analyzed: landfast first-year sea ice with a thick snow cover (FYI'92); landfast first-year sea ice with a thin snow cover (FYI'93); and a multiyear sea ice surface (refrozen melt pond) with a thick snow cover (MYI'93). Details of the methods used in sample collection are available elsewhere [2].

Assessment of the vertical structure of the snow cover was addressed by analyzing the observed and modelled variables under typical winter conditions. We selected temperatures of less than -10°C for all points within the volume (at 1330 hrs local time), as a winter criterion. Smoothed averages of salinity, density, permittivity and loss (ε' and ε''), and snow grain area were plotted as a function of depth for each of the cases studied (i.e., FYI'92, FYI'93 and MYI'93). Statistical groupings over the vertical dimension were computed using a *post hoc* difference of means test in a one way analysis of variance (Wilkinson, 1992). A bar chart was constructed to display the results of the statistical grouping analysis and is presented with the vertical smoothed profiles. A solid bar represents a statistically indistinguishable grouping (α = 0.05) over the depths associated with the bar. An analysis was conducted to test the similarity of the vertical distributions which were observed for each of the variables over the three sites tested. A Kolmogorov-Smirnov non-parametric test (Wilkinson, 1992) was used to assess whether the distributions could be considered to come from a single parent population (i.e., could be considered equivalent both in shape and magnitude).

A statistical analysis was conducted to determine the 'best fit' parametric distribution to snow grain sizes over the vertical dimension of the snow volume. A probability plot was computed using all snow grain areas within a particular vertical layer within the snow cover. This probability plot was then compared to all possible Chi-Square distributions with degrees of freedom between 0 and 10 (Fig 1). The best fit Chi-Square was selected based on a least-squares decision rule.

0-7803-3068-4/96$5.00©1996 IEEE

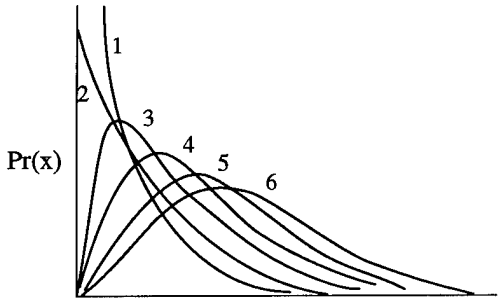


Fig. 1. Chi-Square probability density functions for 1 through 6 degrees of freedom.

RESULTS AND DISCUSSION

In a first-year sea ice snow cover, the salinity, density and grain size vertical profiles indicate the existence of a multilayer system (Figs 2 and 3). Each of the variables illustrate the existence of a high brine volume, low density, large grain size, basal layer. This layer gradually transforms into a typical snow cover through a transitional zone. Statistically the salinity variable illustrated a 4 layer system with the ice surface, 3 (2) cm basal, 6 (4) cm transitional, and the aggregate of 9 (6) to 30 (12) cm levels, being statistically separable at FYI'92 (Fig. 2) and FYI'93 (Fig. 3). Density and snow grain size illustrated a 5 layer system in 1992 and a 3 layer system in 1993. The differences are due to a low density snow precipitate being deposited over an older "original" snow layer in 1992 [2]. Assessment of the grain types [3] typical within each of the layers indicates good agreement in the basal and original snow layers between 1992 and 1993 (Figs 2 and 3). Dielectrically the snow cover consisted of a single group and the ice cover a second group in both 1992 and 1993.

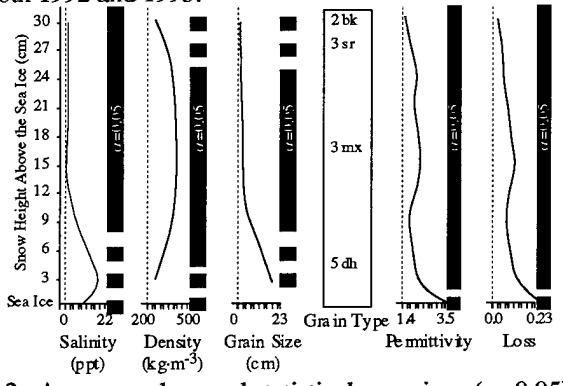


Fig. 2. Average values and statistical groupings (α=0.05) for Salinity, Density, Grain Size, Permittivity (ε'), and Loss (ε'') for the FYI'92 study site for temperatures below -10°C. Grain Type refers to the predominant grain structure within each of the main vertical groups. See text for description of the profiles, grain types and statistical groupings.

The vertical distributions of bulk salinity, between FYI'92 and FYI'93 under winter conditions, were found to be statistically indistinguishable (α=0.05) in the Kolmogorov-Smirnov analysis. This is because the new snow layer had a salinity of 0. The density and grain size distributions were however, distinguishable (α=0.05). This was due to low density and small grain sizes in the 27 to 30 cm levels. Comparison of the dielectric vertical profiles indicated that FYI'92 and FYI'93 profiles were indistinguishable in winter conditions. Although there was much more variability in the profiles of both ε' and ε'' in FYI'92 the within depth spread was sufficiently large to result in a non-significant difference.

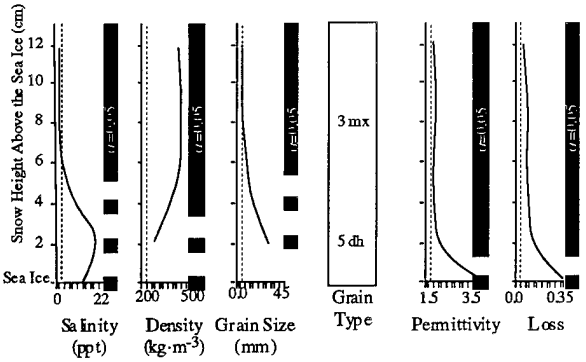


Fig. 3. Average values and statistical groupings (α=0.05) for Salinity, Density, Grain Size, Permittivity (ε'), and Loss (ε'') for the FYI'93 study site for temperatures below -10°C. Grain Type refers to the predominant grain structure within each of the main vertical groups. See text for description of the profiles, grain types and statistical groupings.

In a multiyear sea ice snow cover (MYI'93) the salinity, density and grain size vertical profiles indicated the existence of a single layer system (Fig 4). The vertical profile of snow grain size indicated an enlargement of grains in the 3 and 6 cm levels. Statistically, the density and grain size variability was sufficiently large that the general trends observed in the profiles did not create a statistically distinct class for either density or snow grain size. Dielectrically the snow cover consisted of a single group and the ice cover a second group in MYI'93 (Fig. 4).

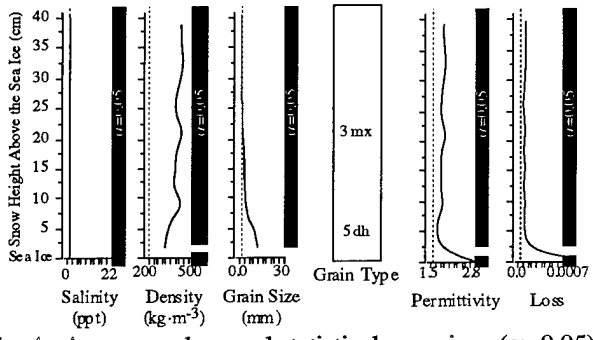


Fig. 4. Average values and statistical groupings (α=0.05) for Salinity, Density, Grain Size, Permittivity (ε'), and Loss (ε'') for the MYI'93 study site for temperatures below -10°C.

Results from the distribution fitting illustrate that the Chi-Square family of distributions are appropriate for estimating the grain size area distribution throughout the vertical dimension of the snow volume of both first-year and multiyear sea ice types. An illustration of the method (Figure

5) shows the modelled versus observed probabilities between a Chi-Square (df=6) and observed snow grain area at the 54 cm level at the SIMMS'92 MYI site.

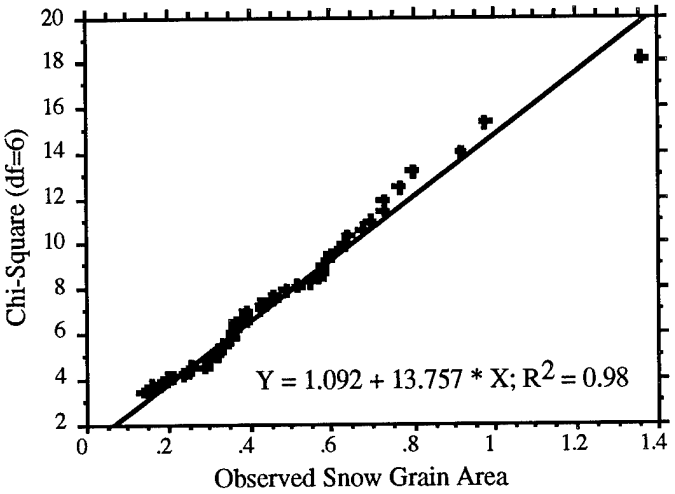


Fig. 5. Chi-Square distribution least squares fit with the observed snow grain area at the 54 cm level at the SIMMS'92 MYI site.

Optimal selection, based on the best least squares fit, resulted in a vertical distribution of Chi-square fits to the observed snow grain area estimates (Figs. 6 and 7). Results from this analysis show that the first-year and multiyear sea ice type snow covers require different Chi-Square distributions to model the vertical heterogeneity of snow grain sizes with depth.

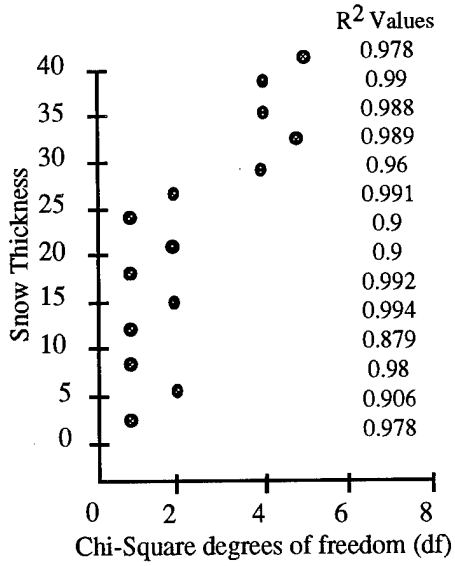


Fig. 6. Best fit Chi-Square distributions (degrees of freedom) per vertical snow layer on first-year sea ice (day 152).

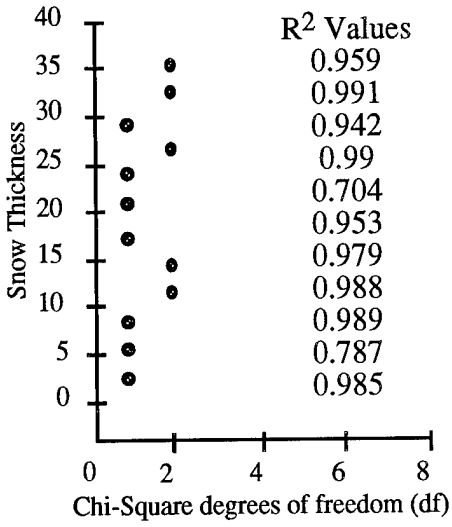


Fig. 7. Best fit Chi-Square distributions (degrees of freedom) per vertical snow layer (day 151) on multiyear sea ice.

LITERATURE CITED

[1] E.F. LeDrew and D.G. Barber, "The SIMMS program: A study of change and variability within the marine cryosphere," *Arctic*, vol. 47, no.3, pp 256-264, 1994.

[2] Barber, D.G., T.N. Papakyriakou, and E.F. LeDrew. 1994. On the Relationship between Energy Fluxes, Dielectric Properties, and Microwave Scattering over Snow Covered First-Year Sea Ice During the Spring Transition Period *Journal of Geophysical Research (Oceans)*. 99(C11): 22,401-22,411.

[3] Colbeck, S.C., E. Akitaya, R. Armstrong, H. Gubler, J. Lafeuille, K. Lied, D. McClung and E. Morris. The International Classification for Seasonal Snow on the Ground. Int. Comm. Snow and Ice (IAHS), World Data Center A for Glaciology, U. of Colorado, Boulder, CO, USA.

ACKNOWLEDGMENTS

Data used in this paper have been obtained from the collective efforts of the SIMMS'92 and 93 participants - thanks to each. This work was supported by an NSERC and Office of Naval Research Grant (N00014-94-1-03-86) to D. Barber. Thanks to the Polar Continental Shelf Project for the SIMMS logistical support and to E. LeDrew for discussions throughout this project.

Sea Ice Polarimetric Backscatter Signatures at C Band

S. V. Nghiem[1], R. Kwok[1], S. H. Yueh[1], J. A. Kong[2], A. J. Gow[3], D. K. Perovich[3], S. Martin[4], and R. Drucker[4]

[1]Jet Propulsion Laboratory, MS 300-235
California Institute of Technology
4800 Oak Grove Drive, Pasadena, CA 91109, USA
Tel: 818-354-2982, Fax: 818-393-5285
E-mail: nghiem@malibu.jpl.nasa.gov

[2]Department of Electrical Engineering and Computer Science
and Research Laboratory of Electronics
Massachusetts Institute of Technology
77 Massachusetts Avenue, Room 26-305
Cambridge, MA 02139, USA

[3]U.S. Army Cold Regions Research and Engineering Laboratory
72 Lyme Road
Hanover, NH 03755, USA

[4]University of Washington
School of Oceanography
Seattle, WA 98195, USA

Abstract – This paper presents C-band polarimetric backscatter signatures of sea ice measured during CRRELEX (Cold Regions Research and Engineering Laboratory Experiment) from 1993 to 1995. Observed radar backscatter of sea ice is related to sea ice physical characteristics. Complex scattering models for sea ice are developed and used to interpret measured radar data with sea ice physical parameters. These results for sea ice at C band are important for applications to remote sensing data acquired with many airborne and spaceborne C-band synthetic aperture radars.

INTRODUCTION

Sea ice has important effects on local and regional heat transfer processes between the atmosphere and ocean and on global climate due to feedback mechanisms in the climate system. In the remote sensing of the global environment, many radar systems have been used, such as the Jet Propulsion Laboratory (JPL) Aircraft SAR, the Spaceborne Imaging Radar, the European Remote Sensing Satellites (ERS-1 and ERS-2), and the Canadian Radar Satellite (RADARSAT); all operate at C band (see references [1, 2, 3]). For remote sensing of sea ice, it is thus pertinent to study C-band backscatter signatures of sea ice in relation to ice geophysical characteristics.

Experiments have been carried out at CRREL to measure polarimetric backscatter signatures from sea ice together with ice physical and morphological characteristics. The purposes are to investigate the electromagnetic scattering mechanism in saline ice, to relate the polarimetric backscatter to ice physical characteristics, and to develop and verify forward and inverse models for remote sensing of sea ice. Controlled laboratory conditions are used to avoid complicated variations in interrelated ice characteristics and environmental effects. The important feature in these experiments is that fully polarimetric data as functions of incident angles are obtained together with ice characterization data, not just for several isolated ice conditions but at all stages of the ice growth. These experimental data impose strict constraints on the determination of the dominant scattering mechanism. Full polarimetric data sets require a simultaneous explanation of all measured curves, while ice parameters, which cannot be treated independently, are interrelated and governed by physical processes during the ice growth.

In this paper, we present results from CRREL experiments conducted in 1993, 1994, and 1995. The C-band polarimetric scatterometer system, operation, sensitivity, and calibration has been described [4]. Specifically, we investigate the evolution of C-band polarimetric signatures of sea ice under constant growth and quiescent conditions, effects on sea ice backscatter due to diurnal thermal temperature cycling, and backscatter response to the frost flower formation of sea ice surface.

The research described in this paper was performed by the Center for Space Microelectronics Technology, Jet Propulsion Laboratory, California Institute of Technology, and was sponsored by the Office of Naval Research (ONR), through an agreement with the National Aeronautics and Space Administration. The research by the Massachusetts Institute of Technology was under ONR contracts N00014-89-J-1107 and N00014-92-J-4098, by the U. S. Army CRREL under ONR contracts N00014-95-MP-3002 and N00014-95-MP-3019, and by the University of Washington under ONR contract N00014-90-J-0161.

0-7803-3068-4/96$5.00©1996 IEEE

CRREL EXPERIMENTS 1993

In CRRELEX 1993, saline ice was grown under quiescent conditions at constant air and water temperatures to measure polarimetric signatures during ice growth. A constant growth rate was achieved and the interfaces of the ice sheet were unperturbed. Physical characteristics of the ice sheet including growth conditions, thickness and growth rate, temperatures and salinities, and internal and interfacial structures were measured. The results verify the similarity of the ice grown in this experiment with Arctic sea ice grown under similar environmental conditions. Polarimetric backscattering coefficients measured during the ice growth reveal a significant increase by 8-10 dB for the range of ice thickness from 3 cm to 11.2 cm. The C-band backscatter results are plotted in Figure 1. Since the interfacial surfaces were unchanged, the surface scattering mechanism cannot be the dominant factor to account for the 8-10 dB backscatter increase in this experiment. The backscatter increase correlates with the increase in thickness of the saline ice volume during the ice growth at all incident angles under consideration and the scattering mechanisms is related to brine scatterers in the ice sheet. The composite sea ice model including thermodynamic effects on the phase and morphological distributions of brine inclusions agrees with the observed backscatter variations caused by thermal effects.

CRREL EXPERIMENTS 1994

CRRELEX 1994 was carried out in January 1994 at the CRREL outdoor Geophysical Research Facility. The purpose was to investigate the effects on polarimetric scattering signatures of sea ice grown under diurnal temperature variations. An ice sheet was grown in 2.5 days to achieve a thickness of 10 cm. The C-band polarimetric scatterometer was used to obtain backscattering data interlaced with passive measurements in conjunction with ice-characterization measurements. The ice growth was initiated in the late morning of January 19, 1994 and the growth rate was slow due to high insolation and temperature. During the night, the air temperature dropped and the growth rate increased significantly. The air temperature changed drastically from about $-10°C$ to $-35°C$ between day and night. The next day, the temperature cycle was repeated and the growth rate varied in the same manner. Throughout the 2.5-day duration of the experiment, polarimetric backscatter data were measured at roughly every centimeter of ice growth together with ice characterization parameters. The results in Fig. 2 reveal a strong correlation between radar data and temperature variations during two diurnal thermal cycles. The backscatter decreases for a colder temperature and increases for a warmer temperature.

CRREL EXPERIMENTS 1995

In CRRELEX 1995, frost flowers were grown on saline ice. Frost flowers consisted of fragile saline ice crystals growing on the surface of young sea ice. The flower formation thermally modifies the characteristics of the ice sheet. The flower cover has been suggested to cause a backscatter enhancement observed in SAR images of young ice. The experiment was carried out in an indoor refrigerated facility at CRREL. The objective of this study is to determine effects of the frost flowers on C-band radar backscatter. More than 90% areal coverage of frost flowers was achieved at a controlled air temperature of $-28°C$. Polarimetric scatterometer data were measured throughout the experiment together with salinities and temperatures at various parts of the frost flowers. A video system was used to take time series images at normal incident angle to characterize the areal coverage of the flowers. Oblique images of the overall ice surface were obtained with a camera at the beginning of every set of scatterometer measurements. Closeup photographs of frost flowers were taken with a hand-held camera to show detail structures of the flowers at different growth stages. At the first stage of the ice growth, frost flowers appeared in a stellar dendrite form. Then, the flowers changed into needle crystals. Three sets of polarimetric data were measured: (1) for the full frost flower formation, (2) for the ice crystals removed leaving the slush patches underneath the flowers, and (3) for bare ice with all the flower formation removed. The experiment determined that the frost flower formation enhanced backscatter by 3-5 dB over the background ice layer as shown in Fig. 3.

SUMMARY

This paper presents results of C-band polarimetric backscatter signatures of sea ice obtained from CRREL experiments in 1993, 1994, and 1995. Measurements in CRRELEX 1993 show that backscatter increases by 8-10 dB for ice grown from 3 cm to 11.2 cm under a constant growth rate and quiescent conditions. Sea ice grown under diurnal thermal cycling in CRRELEX 1994 reveals a strong correlation between backscatter and temperature. CRRELEX 1995 indicates that frost flower formation causes a 3-5 dB enhancement in backscatter over the radar return from the background ice in this experiment. The experiments provide the data base for forward and inverse model development and verification to interpret sea ice remote sensing data. C-band polarimetric measurements were also made to study effects of ice warming, flooding, snow cover, surface roughness, and brine drainage channels.

REFERENCES

[1] S. V. Nghiem, R. Kwok, S. H. Yueh, and M. R. Drinkwater, Polarimetric signatures of sea ice, 2, Experimental observations, *J. Geophys. Res.*, vol. 100, no. C7, pp. 13681-13698, 1995.

[2] ESA, *The ERS-1 System*, European Space Agency Publication, ESA SP-1146, 1992.

[3] F. Carsey, *Science Requirements for RADARSAT/ERS-2 Modifications for the Alaska SAR Facility*, JPL D-10443, Jet Propulsion Laboratory, Pasadena, 1993.

[4] S. V. Nghiem, C-band polarimetric scatterometer: System, operation, sensitivity and calibration, *Sea Ice Electromagnetics Workshop*, Hanover, New Hampshire, September 14-16, 1993.

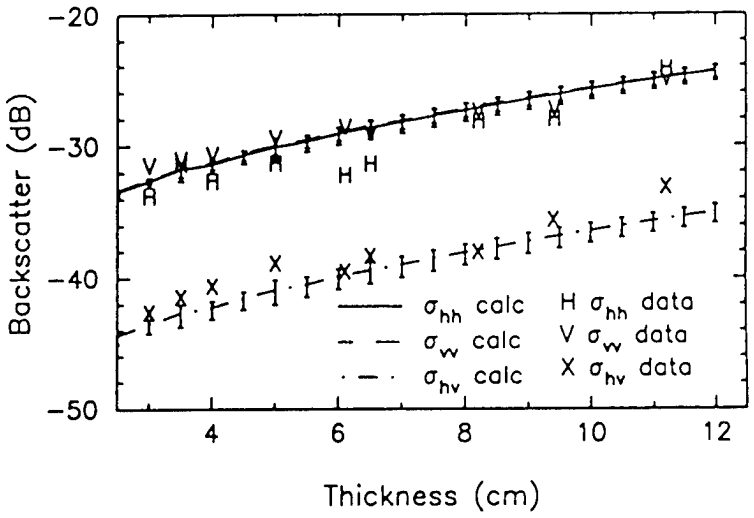


Figure 1. CRRELEX 1993 results for backscattering coefficients σ_{hh}, σ_{vv}, and σ_{hv} as functions of ice thickness at 25° incident angle. The symbols are for measured data and curves for theoretical calculations.

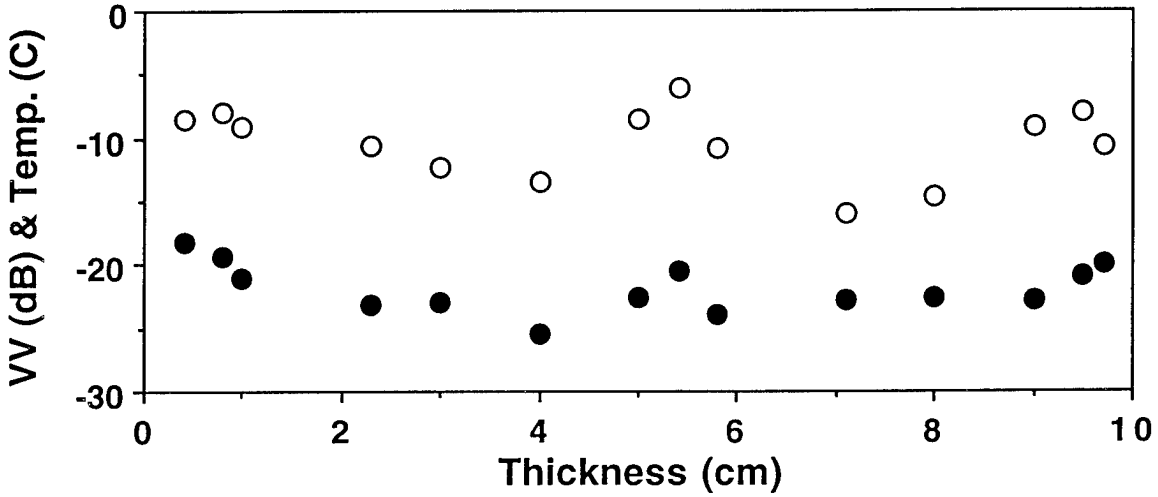


Figure 2. CRRELEX 1994 results show the correlation between backscatter at 25° incidence angle and ice temperature. The black circles are backscatter data for σ_{vv} in dB and the open circles are for average temperature in °C of the ice sheet.

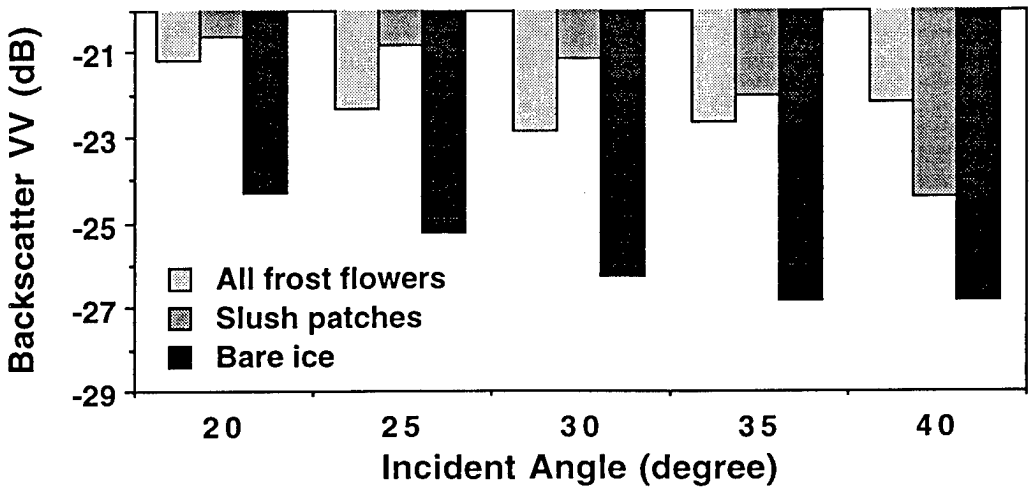


Figure 3. CRRELEX 1995 results of σ_{vv} for the full frost flower formation, for flower ice crystals removed, and for bare ice with all frost flowers removed.

Polarimetric Properties of Simulated Sea Ice With Special Focus on Property Retrieval and Important Scattering Processes

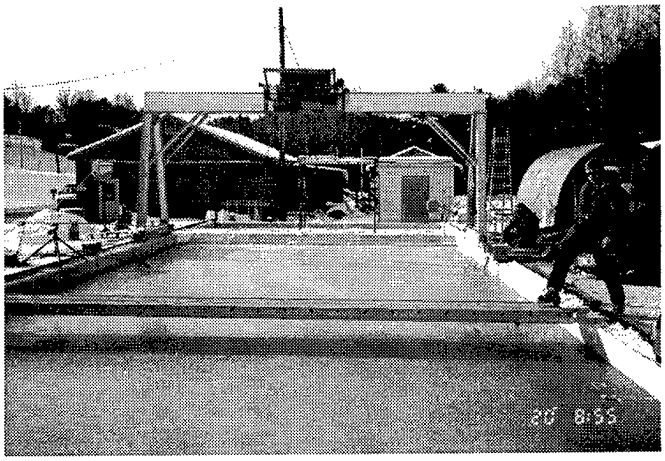
Robert G. Onstott
Center for Earth Sciences , Environmental Research Institute of Michigan
P.O. Box 134001, Ann Arbor, MI 48113-4001
Phone: (313) 994-1200 FAX: (313) 994-5824 Email: Onstott@ERIM.org

Abstract -- To improve the ability to retrieve geophysical properties using remote sensing sensors and model the electromagnetic properties of sea ice, an intensive, well-integrated multidisciplinary program is sponsored by the Office of Naval Research to study simulated and natural sea ice of a variety of forms. As part of this effort we have made polarimetric scattering measurements over a wide range of micro- and millimeter-wave frequencies (e.g. 0.5 to 95 GHz) and incidence angles (0° to 70° with fine angle resolution). An additional aspect of these measurements is that they have been made with fine temporal resolution to allow correlation with small changes in ice sheet properties, in the air-ice interface, and meteorological properties.

Results from this work are used to demonstrate how polarimetric radar data at a single frequency, or a suite of frequencies may be used to assess sea ice age, state, and thickness.

INTRODUCTION

The objective of this program is to improve the forward and inverse scattering modeling of a complex dielectric medium with embedded scatterers, i.e. sea ice. This is being accomplished in numerous ways. The electromagnetic properties of sea ice are characterized through the measurement of their active microwave scattering properties. Both monostatic and bistatic radar observations are made in the laboratory and field. Based on these data and the detailed documentation of physical, chemical, and electrical properties, the identification and quantification of the important scattering mechanisms is being refined. This is important in that this knowledge directs the development and evaluation of the theoretical models by insuring that these processes are addressed and incorporated into the models. Since forward scattering models are developed to describe specific ensemble of scattering processes, the above is important in determining which class of sea ice form and conditions a particular model is most applicable. Multiple case studies are being assembled for model testing and validation. These case studies also serve as a catalyst to stimulate interactions between the various disciplines so that rapid progress may be made in the development and validation of applicable scattering models. Efforts are conducted to quantify how much each layer and volume contribute to the total electromagnetic signature. This effort is guided by applying



forward scattering models to produce simulations and performing parameter studies. This effort provides additional evidence of model robustness and utility in diagnosing and quantifying the various EM processes (e.g. contribution of snow, brine accumulation at the snow-ice interface, surface roughness, low porosity in the upper ice layer, the sea water below a thin ice layer, etc.)

In this paper, the transformation of open water into young sea ice 30 cm thick is addressed. Fine temporal observations are conducted over a 40-hour period to document the rapid changes which take place as the ice thickens to 15 cm. Periodic measurements are then continued until an ice thickness of 30 cm is obtained. Forces which influence the electromagnetic properties of ice are also considered. These forces include solar radiation input, deposition of ice particles onto an ice surface, and the warming-cooling effects of the ambient air mass.

INSTRUMENTATION AND MEASUREMENTS

Active microwave and millimeter properties have been documented using an instrument called a radar polarimeter. We are operating in six bands which extend in frequencies from 0.5 to 95 GHz. Typical operating bandwidth is less than 2000 MHz. With this instrument, an array of antennas are used to illuminate the sea ice form under observations. The material reradiates a scattered field which is detected and compared with a sample of the original transmit signal in both amplitude and phase. This operation if performed for each orthogonal transmit and receive polarization. Linear polarization is used, and a complex matrix

0-7803-3068-4/96$5.00©1996 IEEE

is obtained to describe scattering at VV, VH, HV, and HH polarizations. The first letter denotes the transmit polarization, while the second denotes the received polarization. The heart of the system is the Hewlett-Packard vector network analyzer (HP-8510) and a very wideband synthesized frequency source (HP-8341). This sensor has two roles. The first is to obtain measurements of absolute scattering intensity as a function of frequency, polarization and angle; the second function is to record a data record which will allow the study of the contribution of surface and volume scattering. This recording allows the scattered field to be associated with a physical position along an axis between the radar transmit and receive antennas. Based on these data, the location of the source of the scattering signals may be determined. Scattered signals may originate from the snow volume, ice surface, ice interior, or combination of these elements. An abbreviated summary of sensor parameters and measurement types is presented in Table 1.

OBSERVATIONS CONDUCTED *IN SITU*

A number of investigations have been supported through this program during the period from 1993-1995. This has included work in laboratory outdoor and indoor tanks, and in the field at two different locations (e.g. Barrow, Alaska and Resolute Bay N.W.T.). A summary of the various data sets which have been acquired is provided in Table 2.

DISCUSSION

The coherent reflectivity (0°) is measured in 5 frequency bands which extend from 0.5 to 35 GHz, for small changes in ice thickness from 0 to 5 cm. Reflectivity is inverted to the magnitude of the dielectric constant and displayed in Figure 2. Since backscatter intensity is a strong function of the dielectric constant of the material radiated, knowledge of how reflectivity changes with ice form is important. In addition, inverse methods to exploit reflectivity observed over very wide bandwidths are under development. This figure is important in that it illustrates how the effective dielectric constant of newly formed ice changes as a function of ice thickness, ambient temperature, and solar conditions. It is also important to note that if the ice is thinner than about one wavelength, then the sea water layer below contributes to the effective dielectric constant, reflectivity, and radar backcatter. A documented temporal response provides insight as to the range of ice thickness values for which the radar signal is influenced by the sea water below and how solar illumination impacts the process of ice formation and backscatter. When solar radiation is near its peak, the ice sheet warms to a point where ice growth is shut off for a period of 5 hours, in this case. Internal ice property changes have also been documented. The brine volume profile is modified and results in a change in the bulk dielectric constant of the ice sheet. The bulk dielectric constant sensed at each frequency is different. The higher the frequency, the thinner the layer of the upper ice sheet layer which contributes. These modifications contribute and, at times, dominate the radar signature which is responding to changes associated with the thickening of the ice sheet.

Table 1. **Radar System Parameters**

Description	Monostatic	Bistatic
Type	Swept-Frequency	Swept-Frequency
Frequency Range (GHz)	0.4-1, 1-2, 5, 10, 35, 94	0.5-12.5 or 1-8
Frequency Bands	P, L, C, X, W	P to X
Wavelength (cm)	75-30, 30-15, 6, 3, 0.9, 0.3	75-2.4
Polarization	VV VH HH HV	HH
Incidence Angle	0° to 70°	20° to 50° with Δ5°
Scattered Angle	0° to -70°	20° to 50° with Δ5°
Azimuth Angle	0°	90° & 180°
Range (m)	$3.05/\cos(\theta_{inci})$	range = 2.5 (field) height = 3 (lab)

CONCLUSIONS

There are several implications to the above result. When during the day a scene is observed may be used to emphasize a particular target attribute. For example, the signatures of thick ice at night and solar noon are very similar, and much less variable than those of thin ice. The frequency selection may also be used to minimize or maximize the sensitivity to solar illumination. To monitor the change in ice thickness with minimal solar influence, a middle frequency will be optimal. To monitor the intensity of solar radiation that reaches the ground, either a very low or high frequency is optimal.

Also from these data, the effect of the depth of penetration is observable by examining the rate of decay in dielectric magnitude after t=0. Attaining a DC value below 4 indicates that a semi-infinite layer of lossy sea ice has been attained. High values indicate that the sea water below is contributing to the reflectivity response, that a surface brine layer has formed, or that the ice layer has warmed.

ACKNOWLEDGMENTS

This study is funded by the Office of Naval Research under Contract Number N00014-93-C005. Charles A. Luther is the Technical Monitor.

Table 2. **Summary of Experiments Performed andEmphasis Noted**

Form Experiment	Evolution OW -> GY	Snow on Sea Ice	Frost Flowers	Rough Surfaces	Special Experiments	Thick First Year Ice
CR'93 Outdoor	*	*		*	Horizontal Variability	
CR'93 Outdoor	*			*	σ° (Tair)	
CR'94 Outdoor	*	*	*	*	σ°(porosity)	
CR'94 Indoor	*		*		σ°(porosity, Tair)	
Barrow'94 Alaska		σ° .vs.H_{snow} Transects		Deformation	Bistatic ERS-1 SAR	1-2 m ice
CR'95 Outdoor	Frazil & Waves	*		Pancakes	Bistatic	
CR'95 Indoor					Particles and Solar Radiation	
SIMMS'95 Resolute Bay		σ°.vs.H_{snow} Transects			Energy Balance & EM Signature Study ERS-1 & CCRS SAR	Seaonal Sig.& Prop. Study. -> 3-D Maps

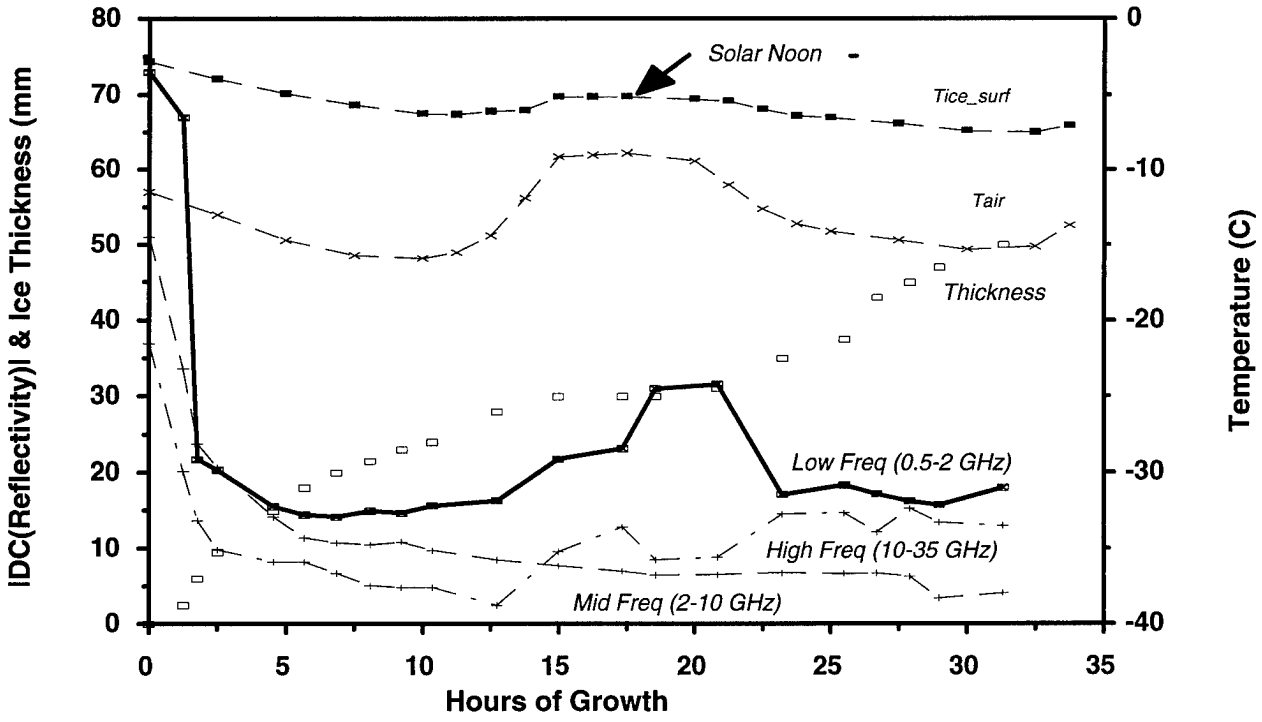


Fig. 1. The coherent reflectivity (0°) is measured in 5 frequency bands which extend from 0.5 to 35 Ghz for small changes in ice thickness from 0 to 5 cm and then inverted to dielectric constant.

Ultra-Wideband Radar Measurements Over Bare and Snow-Covered Saline Ice

S. Gogineni and P. Kanagaratnam
Radar Systems & Remote Sensing Laboratory
University of Kansas
2291 Irving Hill Rd., Lawrence, KS 66045-2969, USA
TEL: 913/864-7734 , FAX: 913/864-7789
E-mail: gogineni@rsl.ukans.edu

K. Jezek
Byrd Polar Research Center, 108 Scott Hall
The Ohio State University
1090 Carmack Road, Columbus, Ohio 43210 USA
TEL: 614/292-7973 , FAX: 614/292-4697
E-mail: jezek@iceberg.mps.ohio-state.edu

Abstract—We developed an ultra-wideband radar operating over frequencies from 500 MHz to 18 Ghz and used it in conjunction with a plane-wave illuminator to perform radar backscatter measurements over pancake, bare and snow-covered saline ice. The ice was grown in an outdoor pond at the U.S. Army Cold Regions Research and Engineering Laboratory, Hanover, NH. Data were acquired over incidence angles from 0° to 50° with VV and HH polarizations. Data were also collected on surface roughness, snow properties and ice structure.

The combination of wide bandwidth and plane-wave illumination allowed us uniquely to identify returns from air-snow and snow-ice interfaces. Returns from the snow-ice interface were about 10 dB higher than those from the snow-air interface. At 0° incidence scattering from bare saline ice varied little with frequency over the frequency range from 5 to 18 GHz, whereas scattering from pancake ice increased from about 16 dB at 5 GHz to 27 dB at 18 GHz. In contrast scattering from snow-covered ice decreased by about 10 dB over the same frequency range. For both bare and snow-covered saline ice, the scattering coefficient decreased by more than 40 dB with over the angular region from 0° and 30°. The rapid decay of the scattering coefficient is indicative of the presence of a coherent component near vertical and of the dominance of surface scattering over this angular region.

INTRODUCTION

During the 1994 and 1995 winter seasons we made radar backscatter measurements over simulated sea ice at the U.S. Army Cold Regions Research and Engineering Laboratory (CRREL), Hanover, NH. The main goal of our research was to determine primary scattering mechanisms by measuring both radar scattering signatures over a wide range of frequencies in conjunction with detailed observations of surface and volume characteristics of the ice under study. The radar measurements are a small part of a multidisciplinary investigation aimed at developing forward and inverse scattering models for interpreting remotely sensed data in terms of the geophysical parameters of sea ice [1].

We used an ultra-wideband radar consisting of an antenna operated in the near field to simulate plane waves to collect the backscatter data reported here. We used the concept of a compact antenna range to simulate plane waves [2]. We acquired radar data on smooth bare and snow-covered saline ice, and pancake ice. Contemporaneous measurements were made of surface roughness, salinity, temperature and internal structure of the ice as well as measurements of snow including thickness, grain size and density. We collected data over the frequency range from 500 MHz to 18 GHz and incidence angles from 0° to 50° with both VV and HH polarizations.

The results from our experiments show that scattering from bare saline ice is dominated by surface scatter at frequencies less than about 10 GHz and incidence angles less than 30°. We also observed that scattering from snow-covered saline ice is about 3 dB higher than that for bare saline ice at 30° at 5 GHz.

In this paper we provide a brief summary of the system used for data collection, the experiments and their results, and the conclusions based on these results.

SYSTEM AND EXPERIMENT DESCRIPTION

To accomplish our objective of identifying the primary scattering mechanisms, we needed a system with fine-range resolution to resolve signals from different depths of ice and provide exceptional angular resolution to estimate accurately the scattering response. We developed an ultra-wideband radar using an HP 8722C Vector Network Analyzer operated as a step-frequency radar and used a 42-inch offset parabola operated in the near field to simulate plane waves.

During the 1994 experiments we used a broadband (2 to 18 GHz) TEM horn as the feed and optimized its location to obtain plane-wave illumination at about six feet from the reflector. During 1995, we employed a bow-tie strip-slot line feed capable of operation over the frequencies between 500 MHz and 18 GHz. Nominally we operated the radar over a bandwidth of 16 GHz with a step size of 10 MHz. We calibrated the radar at the end of each data run with an 8-inch metal sphere.

In 1994 we collected radar data on bare saline ice and snow-covered saline ice with snow thickness of about 7 cm at incidence angles between 0° and 30° with VV polarization. During 1995, we collected data on bare saline ice and pancake ice over incidence angles between 0° and 50° with VV and HH polarizations. Pancake ice was simulated by using a

0-7803-3068-4/96$5.00©1996 IEEE

motor-driven paddle to produce wave action in an outdoor pond as frazil ice formation commenced. We also acquired data at 0° to obtain probability density functions by collecting more than 100 independent samples for separating coherent and incoherent scattering terms.

SIGNAL PROCESSING AND RESULTS

Frequency-domain data collected with the vector network analyzer are windowed and Fourier transformed to obtain time-domain or range-domain representation of the signal. Next this signal is range-gated to isolate ice returns from clutter and integrated over the illuminated area to compute total power return. Since the measurements were made using plane waves, the fields do not decay as a function of range. The scattering coefficient is determined from the power return as

$$\sigma^0 = \frac{P_r \sigma_c}{P_c A_{ill}} \quad \text{where}$$

P_r = power return from the ice
P_c = power return from the calibration target
A_{ill} = illuminated area
σ_c = radar cross section of the calibration target
σ^0 = scattering coefficient

Fig. 1 shows power return as a function of range for snow-covered saline ice at 0°. The first small peak at about 2 m is the signal reflected by the snow-air interface and the second peak at about 2.1 m is from the snow-ice interface. The return from the snow-ice interface is about seven times larger than that from the snow-air interface. The higher return is the result of higher dielectric discontinuity at the snow-ice interface. Using a resonant monopole antenna we measured the real part of the dielectric constant of snow and ice as 3.5 and 1.17, respectively. The corresponding reflection coefficients for snow-ice and snow-air interfaces are 0.266 and 0.0406. The range plot also shows the exceptional range resolution capability of our radar.

Figs. 2a and 2b show the angular response of the scattering coefficients for bare and snow-covered saline ice and pancake ice at C and Ku bands. For bare and snow-covered saline ice the scattering coefficient decreased by more than 40 dB when the incidence angle increased from 0° to 30°. The scattering coefficient decay with the incidence angle between 30° and 55° is fairly small because of the presence of volume scattering. At large incidence angles scattering from pancake ice is about 10 dB higher than that for bare ice.

Fig. 3 shows that σ^0 for VV polarization at 5.5 GHz is a function of incidence angle along with showing comparison data from field measurements made during the International Arctic Ocean Experiment (IAOE) for pancake ice. The backscatter measurements were on pancake ice growing in leads during the transit phase of IAOE. The average σ^0 from the IAOE data, along with maximum and minimum measurements (as extended bars), are shown in here. The average scattering for simulated pancake ice is about 5 dB lower than that observed during IAOE. The lower scattering may be the result of the formation of elongated pancakes in the laboratory because of less vigorous wave action.

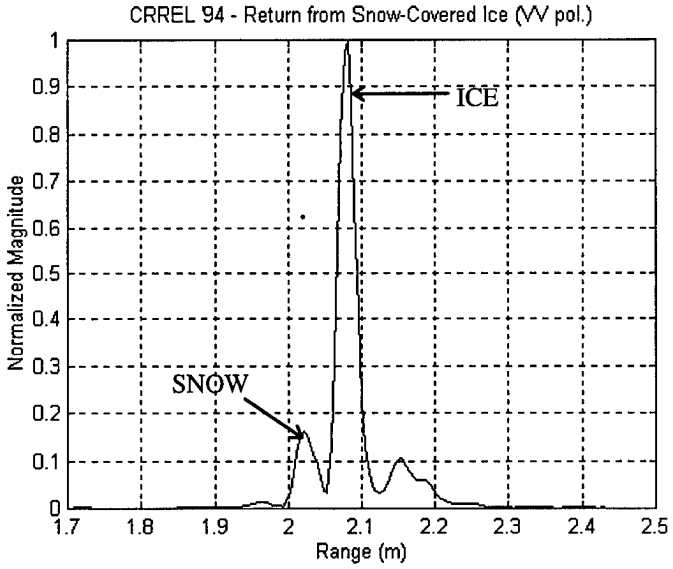
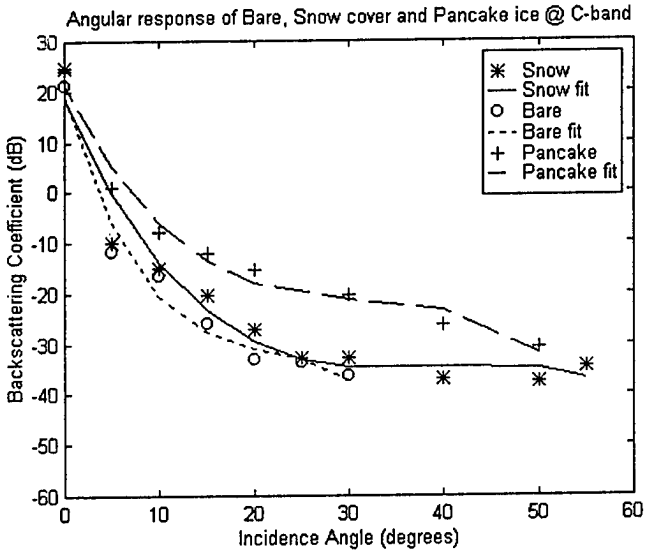


Fig. 1 Return from snow-covered ice at 0°.

Fig. 4 shows the frequency response of scattering from bare and snow-covered saline ice and pancake ice at 20°. The scattering coefficient generally increased with frequency for the three ice types with the increase being much higher for pancake ice. The slight decrease of scattering coefficient for bare and snow-covered ice at frequencies between 14 and 18 GHz is an artifact associated with filtering of data and antenna feed. Although we corrected for the droop introduced by the filter used for range gating, its effect cannot completely be eliminated.

CONCLUSIONS

The use of plane-wave illumination and wide bandwidth allowed us to determine experimentally the relative contributions to the backscattered signal and the scattering response of smooth surfaces. The results from our experiments indicate that the backscattered signal from saline ice is dominated by contributions from the ice surface at frequencies less than about 10 Ghz at incidence angles less than 30°.



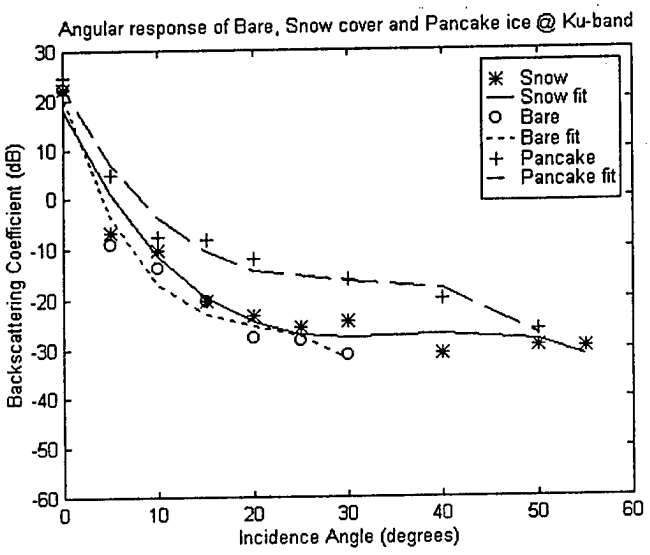


Fig. 2 Angular responses of bare, snow-covered, and pancake ice at (a) C band and (b) Ku band.

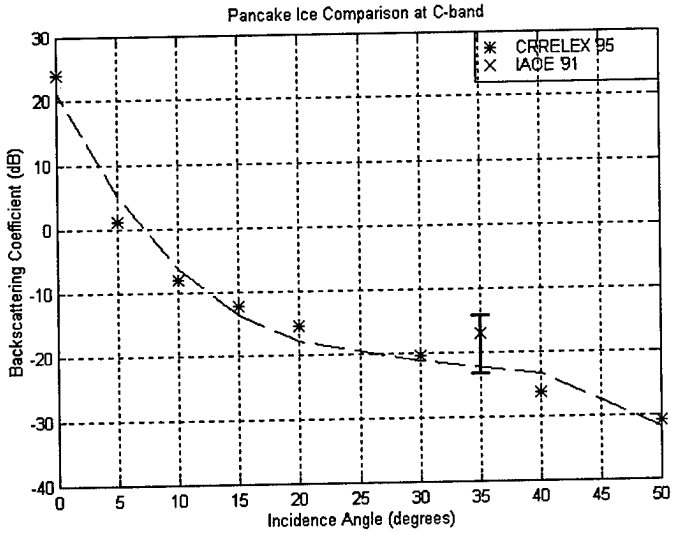


Fig. 3 Comparison between field and laboratory measurement of pancake ice.

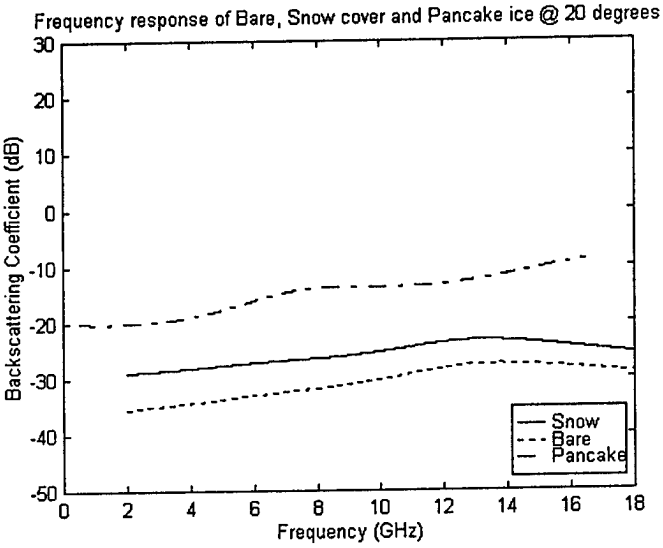


Fig. 4 Frequency response of bare, snow-covered, and pancake ice at 20°.

REFERENCES

[1] S. Gogineni, K. Jezek, L. Peters, J. Young, S. Beaven, and E. Nassar, "Application of plane waves for accurate measurement of microwave scattering from geophysical surfaces," *IEEE Trans. on Geoscience and Remote Sensing*, vol. 33, pp. 627-633, 1995.

[2] K. Jezek, P. Gogineni, L.Peters, J.Young, S. Beaven, E.Nassar, and I.Zabel, "Microwave scattering from saline ice using plane wave illumination," *IGARSS'94 Digest*, 8-12 Aug. JPL, Pasadena, CA, pp. 493-495, 1994.

Microwave and Thermal Infrared Emission from Young Sea Ice and Pancake Ice

T. C. Grenfell
Dept. of Atmospheric Sciences, Box 351640,
University of Washington, Seattle WA 98195-1640
Phone (206) 543-9411/ FAX (206) 543-0308/tcg@atmos.washington.edu

INTRODUCTION

The goals of this study are to observe the development of multifreqency microwave emissivity (e) of new and young sea ice grown under dynamic conditions, and to investigate the effects of ice growth and structural changes on its microwave signature. In particular, we are interested in three ice types, whose signatures are particularly difficult to investigate under normal field conditions.

Unconsolidated frazil ice and pancake ice, which occur when ice forms in a wave field under stormy conditions, are found in abundance in the marginal ice zones of the Arctic and Antarctic sea ice packs. They make up a significant portion of the area covered by the new and young ice.

Because new and young ice types are weaker than the surrounding thick ice and fracture first under conditions of high ice stress, a large percentage of the ridged ice consists of thin saline ice. As the ridges evolve, brine drains out of the elevated parts causing substantial changes in the permittivity distribution which can affect their microwave emissivities.

Previous studies [1,2,3,4] have shown that the microwave signatures of these ice types appear to be distinct in several respects, but the data from these experiments are sparse and the uncertainties are still relatively large. The differences between the microwave signatures of these ice types and those of first-year (FY) ice types grown under relatively calm conditions are important for interpreting satellite derived ice concentrations and ice type distributions. In this paper we present the results of our latest studies of the microwave emissivities of these ice types.

OBSERVATIONS

We carried out a series of surface-based multifrequency (6.7,10,18.7,37, and 90 GHz) passive microwave and thermal infrared (8-14μm) observations of frazil and pancake ice, 0-6 cm in thickness during January 1995 at the CRREL Geophysical Research Facility.

A sheet of young congelation was prepared in advance of the experiment to produce the proper environment for the pancake ice production. This ice was removed and was used to construct a simulated pressure ridge for subsequent study. Frazil and pancake ice growth was then initiated by creating a wave field using an oscillating paddle placed at one end of the pond. Ice growth continued for about 11 hours by which time pancakes had formed and began to evolve. After the wave field was stopped, the ice was cooled and the pancakes allowed to freeze solid onto a consolidated sheet. The ice thickness (z_{ice}) versus time is shown in Fig. 1.

Measurements at vertical and horizontal polarization (V-Pol and H-Pol) were made at the 5 microwave frequencies listed above. The infrared (IR) data were unpolarized. The development of the H-Pol brightness temperatures (T_B) is shown in Fig. 2 together with the surface and ambient air temperatures. During pancake growth, T_B values generally increased with ice growth, and at each thickness the values were greater for higher frequencies primarily due to the decrease in the real part of the permittivity with frequency. Near the end of the growth sequence, the ice compacted somewhat, and the surface experienced a flooding event resulting in a decrease in z_{ice} and T_B.

Representative emissivity spectra during various stages of the pancake growth are shown in Fig. 3. The ice growth was accompanied by a steady decrease in polarization ratio (PR) typical of new and young ice, consistent with our previous

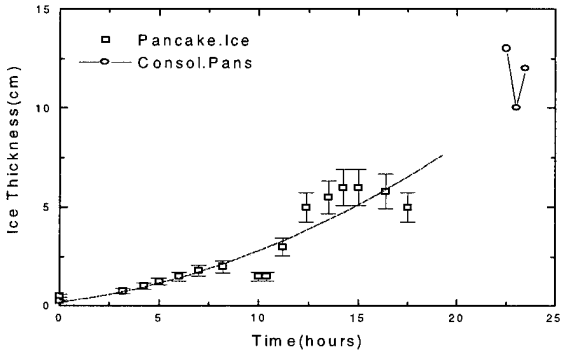


Fig. 1 Ice thickness versus time for the pancake growth. The solid line is a quadratic regression (r^2 = 0.86). The results for the consolidated pancakes were actually measured about 260 hours later but are plotted at 23 hours for convenience.

Acknowledgments - This work was supported by research grants N00014-89-J-1140, N00014-89-J-3132, and NAGW-2574 from the Office of Naval Research and NASA. We are grateful for helpful discussions with D.P.Winebrenner, A.J.Gow, and D.K.Perovich.

0-7803-3068-4/96$5.00©1996 IEEE

observations of pancake growth [1]. The spectral gradient (expressed by GR) also decreased with growth, most of the change occurred during the consolidation phase.

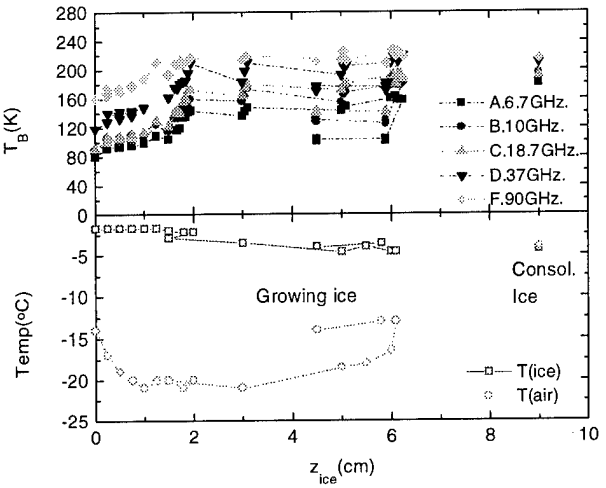


Fig 2. Brightness temperature for the indicated frequencies, surface and air temperature versus ice thickness. Nadir angle = 50°.

Measurements of the young pressure ridge were carried out before and after a warming event accompanied by rainfall. This made it possible to compare cases that closely represented a newly formed pressure ridge and a ridge that had undergone considerable brine drainage, meter scale structural alteration and crystal metamorphism. The spectra, shown in Fig. 4, indicate a decrease in GR after the melt/ freeze event due to increased volume scattering in the ice.

DISCUSSION

Fig. 5 shows a plot of e(18.7V) versus e(37V). The development very nearly along a direct line connecting the open water (OW) and first-year (FY) ice regions is quite different from the development of congelation ice [5] and suggests a gradual decrease in the amount of liquid water on the surface. The PR-GR plot (Fig.6) shows similar behavior except that the end point is at a value of approximately (0.1,0.0) where bare young ice has been observed [1,3].

The signature evolution of the pancake ice produced in 1995 was quite similar to the 1990 results. It showed significant differences from that of congelation ice but stabilized by the end of pancake growth at about the same emissivity and GR-PR values as young congelation ice.

While development of the signature of congelation ice can be characterized by progressive saturation from higher to lower frequencies representative of a distinct thickening sheet followed by modification of the surface properties due to natural desalination [*e.g.* 3, 4], the evolution of the signature of unconsolidated frazil and pancake ice is more nearly characterized by a linear mixture of ice and liquid water with the ice concentration rising smoothly.

The values for pressure ridges have V-Pol emissivities that are essentially the same as those of FY ice, but the ridges

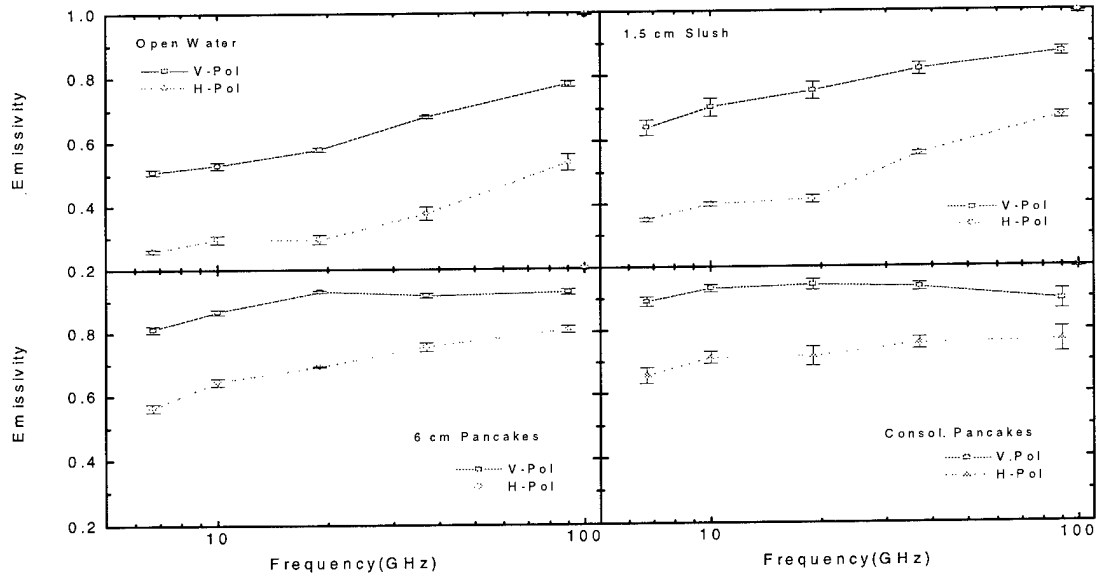


Fig. 3 Emissivity spectra for various stages during the growth of pancake ice. The nadir angle was 50°. The thermal infrared values are unpolarized and are plotted at 100 GHz.

show H-Pol values that are nearly equal to the V-Pol values so that the PR values are very small. Thus, to detect ridge signatures dual polarization data are needed. The IR emissivities obtained together with the microwave observations are shown in Figs. 4 and 5. For convenience they are plotted at 100 GHz. The values obtained ranged between 0.99 for open water/new ice to 0.999 for the frazil, pancake and ridged ice. The error made in interpreting the surface skin temperature assuming unit emissivity is therefore less than 3K.

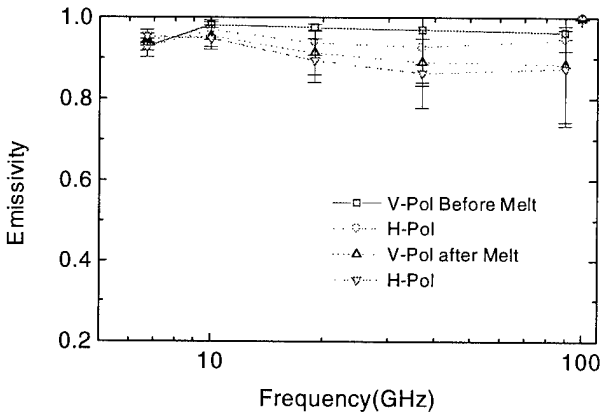


Fig. 4 Emissivity spectra at a nadir angle of 50° for the simulated pressure ridge just after formation and after a prolonged melt-freeze event.

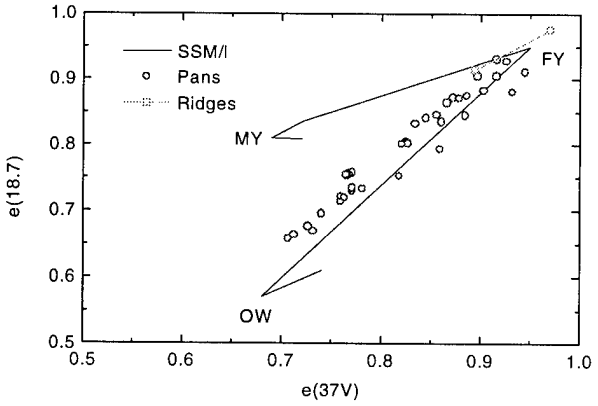


Fig. 5 18.7 vs. 37 GHz scatter plot for the pancake and ridge observations. The ridge points are connected by a line and the SSM/I line is from satellite data (adapted from [6]). Nadir angle = 50°.

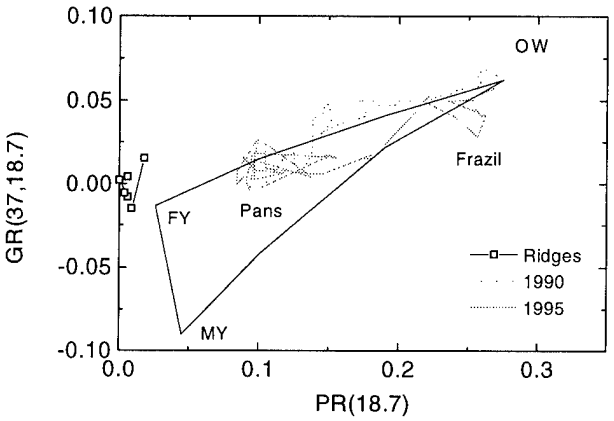


Fig. 6 PR-GR scatter plot for the pancake observations from 1995 (solid line) and from the 1990 experiment (dotted line) [1]. Observations of the presure ridges are shown as open boxes.

REFERENCES

[1] Grenfell, T. C., Wensnahan, M. R., and Winebrenner, D. P., Passive microwave signatures of simulated pancake ice and young pressure ridges, Remote Sensing Reviews, 9, pp.51-64, 1994.

[2] Eppler, D. T. *et al.*, Passive microwave signatures of sea ice, Chapter 8 in *Microwave Remote Sensing of Sea Ice*, F. Carsey ed., Amer. Geophys. Union, Washington D.C.,pp.47-68, 1992.

[3] Grenfell, T. C. *et al.*, Considerations for the remote sensing of thin sea ice, Chapter 14 in *Microwave Remote Sensing of Sea Ice*, F. Carsey ed., Amer. Geophys. Union, Washington D.C., pp.291-300, 1992.

[4] Swift, C. T. et al, Laboratory investigations of the electromagnetic properties of artificial sea ice, Chapter 14 in *Microwave Remote Sensing of Sea Ice*, F. Carsey ed., Amer. Geophys. Union, Washington D.C., pp.177-200, 1992.

[5] Grenfell, T. C. and Comiso J. C., Multifrequency passive microwave observations of first-year sea ice grown in a tank, IEEE Trans. Geosci. and Rem. Sens., GE-24, pp. 826-831, 1986.

[6] Comiso, J. C., Arctic multiyear ice classification and summer ice cover using passive microwave satellite data, *J. Geophys. Res., 95*, pp. 13,411-13,422, 1990.

Modeling of Ice Thickness Effect and Its Application to Data Interpretation

A.K. Fung[1] and R.G. Onstott[2]
[1]E.E. Dept.,Box 19016, University of Texas at Arlington, TX 76019
Tel: 817–273–3422, FAX 817-273-3443, eefung@uta.edu
[2]ΣRIM, Ann Arbor, Michigan

Abstract--A dense medium scattering model based on the standard radiative transfer formulation but with a scattering phase function for a group of scatterers as opposed to the conventional single scatterer phase function is developed to account for volume scattering from saline ice. Surface scattering due to air-ice and ice-water boundary is accounted for using the IEM surface scattering model. To avoid the coherent scattering effect only off nadir measurements are considered. Experimental measurements at CRREL during ice growth indicates that due possibly to some roughness of the bottom ice surface at the ice-water interface, backscattering from thin ice (less than 2 cm) is above -17 dB at 20 degrees incidence and 5.3 GHz. As ice grows in thickness towards 8 cm, backscattering between 20 to 40 degrees decreases with thickness to about -26 dB to -32 dB respectively. The purpose of this study is to investigate the cause of this decrease by examining the relative contributions from the ice volume and the two boundary surfaces. Preliminary study indicates that for thin ice the contribution of water under the ice sheet in the form of producing an effective impedance at the air-ice interface is the dominating factor. Reflectivity measurements confirm this idea. When the effective dielectric constant is used in the computation of backscattering from the air-ice interface, good agreement is obtained between model predictions and backscattering measurements. Results indicate that volume scattering is not a factor in this study.

INTRODUCTION

The problem under consideration is backscattering from a salinated ice layer above salted water. This layer is increasing in thickness as a function of time and backscattering, reflectivity and ice thickness measurements were taken at time intervals. Since the ice layer is an inhomogeneous dense medium with irregular boundaries we use a scattering model which accounts for boundary surface roughness and the inhomogeneities. Note that the classical radiative transfer formulation is for sparse media and the phase function is the product between the average of the magnitude squared of the scattering amplitude $\langle |S|^2 \rangle$ of a single scatterer multiplied by the number density n_0 [1]. This definition of the phase function is applicable to sparse media where independent scattering occurs. For the current problem the scatterers may scatter as a group in some correlated manner rather than independently. For this reason we shall give an effective number density for Gaussian correlated scatterers. We assume that the scatterers originally were positioned on a lattice structure with an average spacing of d and then they were randomly displaced from their central positions with a variance of σ^2 and a correlation distance of L.

0-7803-3068-4/96$5.00©1996 IEEE

BACKSCATTERING MODEL

The backscattering model follows the standard radiative transfer formulation as given in [1]. It has the form,

$$\cos\theta \frac{d\bar{I}}{dz} = -\kappa_e \bar{I} + \int \bar{P}\bar{I}\, d\Omega, \text{ where } \bar{P} = n_0 \langle |S|^2 \rangle \quad (1)$$

We want to generalize n_0 from a constant to a function depending on the correlation properties of the random positions of the scatterers. This effective number density n_{eff} was given in [2] as

$$n_{eff} = \frac{1-e^{-k_{si}^2\sigma^2}}{d^3} + \frac{e^{-k_{si}^2\sigma^2}}{d^3} \sum_{m=1}^{\infty} \frac{(k_{si}^2\sigma^2)^m}{m!}$$

$$\left[\left(\sqrt{\frac{\pi}{m}} \left(\frac{L}{d} \right) \right)^3 \exp\left(\frac{-k_{si}^2\sigma^2}{4m} \right) - a(k_x)a(k_y)a(k_z) \right] \quad (2)$$

where

$$a(k_r) = \sqrt{\frac{\pi}{m}} \left(\frac{L}{d} \right) \exp\left(\frac{-k_r^2 L^2}{4m} \right) \mathrm{Re}\left\{ \mathrm{erf}\left(\frac{(md/L) + jk_r L}{2\sqrt{m}} \right) \right\}$$

$$\hat{k}_s = k(\hat{x}\sin\theta_s\cos\phi_s + \hat{y}\sin\theta_s\sin\phi_s + \hat{z}\cos\theta_s)$$

$$\hat{k}_i = k(\hat{x}\sin\theta_i\cos\phi_i + \hat{y}\sin\theta_i\sin\phi_i + \hat{z}\cos\theta_i)$$

$$\hat{k}_s - \hat{k}_i = \hat{x}k_x + \hat{y}k_y + \hat{z}k_z \equiv \hat{k}_{si} \quad (3)$$

With this effective number density we can form a phase function using the Rayleigh scattering amplitude. A summary of a simplified surface-volume scattering model may be found in Chapter 2 of [3]. A brief account of this model is given below.

We approximate the total backscattering from an inhomogeneous irregular layer as the sum of scattering from the top surface defined by (4), volume scattering from the

inhomogeneous layer given by (5), bottom surface scattering with layer attenuation given by (6) and volume scattering interacting with bottom layer given by (7) as follows:

$$\sigma^0_{pp} = 4\pi\cos\theta[I_p(\theta)/I^i_p]$$
$$= \frac{k^2}{2}\exp(-2k_z^2\sigma^2)\sum_{n=1}^{\infty}|I^n_{pp}|^2\frac{W^{(n)}(-2k_x, 0)}{n!} \quad (4)$$

where $k_z = k\cos\theta$, $k_x = k\sin\theta$, and $pp = vv$ or hh ,

$$I^n_{pp} = (2k_z\sigma)^n f_{pp}\exp(-k_z^2\sigma^2)$$
$$+\frac{(k_z\sigma)^n[F_{pp}(-k_x, 0) + F_{pp}(k_x, 0)]}{2} \quad (5)$$

and the symbol $W^{(n)}(-2k_x, 0)$ is the Fourier transform of the nth power of the surface correlation coefficient. Other symbols are given in Appendix 2A of reference 3. The volume scattering term from the layer is

$$\sigma^0_{vpp} = 0.5(\kappa_s/\kappa_e)T_{1t}T_{t1}\cos\theta$$
$$[1-\exp(-2\kappa_e d/\cos\theta_t)]P_{pp}(\cos\theta_t, -\cos\theta_t; \pi) \quad (6)$$

where κ_s/κ_e is the albedo; P_{pp} is the phase function; $\kappa_e d$ is the optical depth of the layer; θ and θ_t are the angles of incidence and transmission from the medium above into the layer and T_{ij} is the transmissivity from medium j to i. The term representing scattering from the bottom boundary surface attenuated by the layer may be approximated as

$$\sigma^0_{gpp} = \cos\theta T_{1t}(\theta, \theta_t)T_{t1}(\theta_t, \theta)\sec\theta_t$$
$$\exp(-2\kappa_e d/\cos\theta_t)\sigma^0_{pp}(\theta_t) \quad (7)$$

where $\sigma^0_{pp}(\theta_t)$ has the same form as (4). It is the surface scattering coefficient for the lower boundary evaluated using parameters of the layer medium.The term representing interaction between layer inhomogeneities and the lower boundary is given by

$$\sigma^0_{vgpp} = (4\pi\cos\theta I^s)/I_0 = \cos\theta T_{t1}{}^2 R(\kappa_s/\kappa_e)$$
$$[P_{pp}(-\mu_t, -\mu_t, \phi_t - \phi_i) + P_{pp}(\mu_t, \mu_t, \phi_t - \phi_i)]$$
$$(\kappa_e d/\cos\theta_t)\exp(-2\kappa_e d/\mu_t) \quad (8)$$

where R is the reflectivity at the bottom boundary; $\mu_t = \cos\theta_t$, $\mu_i = \cos\theta$.

In the above relations σ_1, σ_2 are the rms heights of the top and bottom boundaries.

MODEL APPLICATIONS

The model described above is a first-order model in the sense that the interaction between the layer boundaries is limited to the first-order. If we apply the model as it is, we shall be applying a first-order model to do the analysis. We shall refer to this as the *first-order model* approach. Another way to use the model when the overall reflectivity is available or the effective dielectric constant at the air-ice interface including the combined effect of ice and water is calculated or measured is to use only (4) and (6) and in (4) we use the effective dielectric constant to calculate the discontinuity across the air-ice boundary. The effect of layer thickness is included in the effective dielectric constant calculation or measurement. We shall refer to this as the *effective dielectric* approach.

COMPARISONS WITH MEASUREMENTS

In Figure 1 we show comparisons between the *first-order model* described in the last section and backscattering measurements from a saline ice layer at 5.3 GHz and 40 degree incidence. The saline ice permittivity ε_{ice}, surface roughness parameters and its correlation function have been estimated to be 3.4-j0.2, a rms height of σ_1 = 0.05 cm, a correlation length of L_1 = 0.7 cm and an exponential correlation function respectively. As an inhomogeneous medium saline ice has a very low albedo because of its high salinity. We use an albedo of 0.0012 The corresponding lower boundary parameters are σ_2 = 0.053 cm and L_2 = 0.7 cm. The dielectric value for water is calculated from Stogryn's formula and is 51.3 -j 43.7. Results from Figure 1 show that (a) better agreement occurs at larger depth, if volume scattering is smaller and (b) the agreement is not good at smaller depths. Hence, this first-order result is not satisfactory.

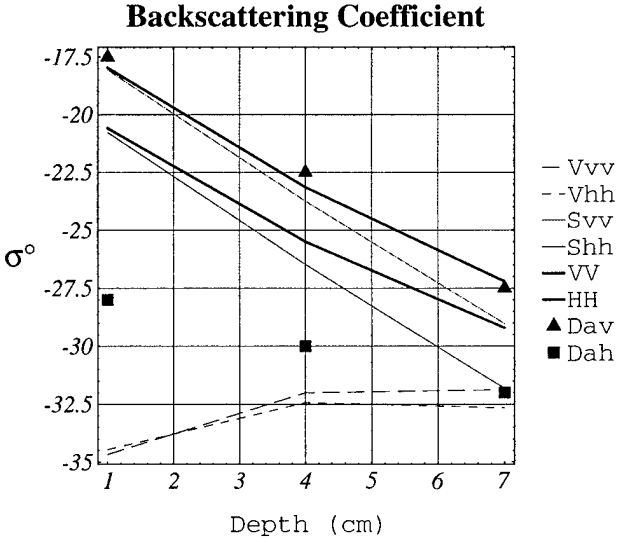


Figure 1 Comparison with measurements using the first-order backscattering model.

In Figure 2 we show another comparison using the effective dielectric model with the same data set. The concept used is impedance transformation in a multiple interface problem. Through measurements of reflectivity the multiple interface effect can be replaced by an effective impedance or dielectric constant seen by the incident wave at the first interface. As a result the problem is reduced to a single interface problem. In this study measurements of reflectivity have been taken as the ice layer reaches different depths. Since the ice layer is fairly smooth, there is some coherent effect resulting in some oscillation of the transformed impedance with depth, and, hence, some variation in the effective dielectric constant. The table below shows the measured and predicted values of the dielectric constants. It is clear that when the ice sheet is thick enough to fully attenuate any return from the water-ice interface, the reflectivity measured should be equal to that from ice alone. In this case the dielectric constant will also be that of the ice,i.e., around 3.4-j0.2.

Table 1: Measured and Predicted Dielectric Constant Magnitudes

Observation	*Thickness*	ε_m	ε_{th}
1	0	73	73
2	0.1	43,7	
3	0.3	37.9	
4	0.8	55.4	10.1
5	2.0	31.1	6.8
6	4.0	7.1	5.3
7	7.1	5.5	4.2

The use of the measured values of the effective dielectric constant results in curves shown in Figure 2 based on σ_1 = 0.075 cm and L_1 = 0.7 cm. Albedo is set equal to 0.0002. Much better agreement with measurements are seen.

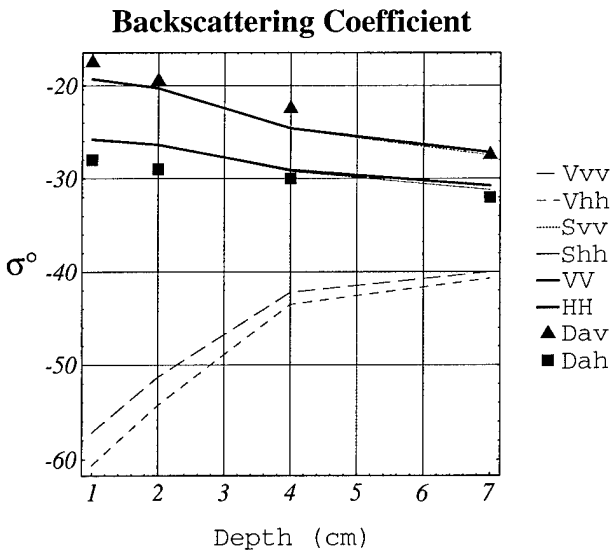


Figure 2 Comparison of data with model using the effective dielectric constant.

CONCLUSIONS

The measured data illustrate that the saline water below the ice sheet contributes to the backscatter and reflectivity response for thin ice forms at moderate wavelength. Sensing a composite of ice and saline water results in backscatter and reflectivity levels higher than that predicted for the ice sheet alone, because the combined dielectric constant of ice and water is larger than ice. This much larger dielectric constant leads to a large polarization difference between VV and HH when the ice is very thin. It is clear that when ice is very thin, the incident wave sees essentially water and the converse must be true when ice sheet is very thick.

This study was supported by the Office of Naval Research under grants, N00014-93-C and N00014-90-J-132.

REFERENCES

[1] Tsang,L.,Kong,J.A.,and R.Shin,Thoery of microwave remote sensing, John Wiley, pp. 129-131, 1985.

[2] Fung,A. Chuah, H.T., Tjuatja,S., and J.W. Bredow,Dense medium phase and amplitude correction theory for spatially and electrically dense media, IGARSS'95

[3] Fung, A.K. Microwave scattering and emission models and their applications, Artech House, Chapter 1, 1994

Inversion of Wideband Microwave Reflectivity to Estimate the Thickness of Arctic Lead-like Sea Ice

D. P. Winebrenner[1] and J. Sylvester[2]

1. Applied Physics Laboratory - University of Washington, 1013 NE 40th St., Seattle, WA 98195, (206)543-1393, (206)543-1393 fax, dpw@apl.washington.edu

2. Department of Mathematics, University of Washington, Seattle, WA 98195, (206)543-1158, sylvest@math.washington.edu

ABSTRACT

The inversion of coherent reflection data from lossy media in which waves are governed by the Helmholtz equation is problematic both mathematically and practically. Conventional layer stripping methods applied to this nonlinear inverse problem are unstable even in the lossless case, and instability is accentuated in the lossy case. We have recently stabilized layer stripping in the lossless case by enforcing causality with a nonlinear analog to the Hilbert transform. The analysis in this work has led to a nonlinear analog to the Payley-Wiener theorem in classical Fourier analysis. The classical theorem relates the width of the region of analyticity in the (complex) frequency (or wavenumber) domain to width in the (real) time (or spatial) domain. The nonlinear analog of this theorem, applied to reflection data, yields the thickness of the reflecting layer, albeit in a depth coordinate scaled by the travel time through the layer. We show by simulation that this method produces accurate thickness estimates even when applied to reflection from moderately lossy media. Application of this method to wideband, vertical incidence, microwave reflection data for sea ice, together with a "guess" for the average permittivity of the ice, yields an estimate of the sea ice thickness. We show via simulation that the thickness estimate is not very sensitive to the guess for average permittivity – the entire range of plausible values leads to a variation in thickness estimates of only about 10%.

1. INTRODUCTION

Thin Arctic sea ice exerts an influence on the ocean and atmosphere far out of proportion to its area on the Earth's surface, because of its dominant influence on the heat balance of the Arctic during winter [1]. ("Thin" sea ice typically refers to ice less than about 70 cm in thickness.) The location and distribution of such sea ice is also important in determining the cost and difficulty of various surface and subsurface operations in the Arctic basin and many coastal waters. Thus the remote estimation of sea ice thickness has long been a goal.

Existing microwave remote sensing methods for estimating sea ice thickness rely on the observation of processes at the upper surface of the ice (either the air/ice or snow/ice interface), which are hoped to serve as reliable proxies for ice thickness via one physical link or another. Increasing understanding of such links, however, shows them to be tenuous. For example, the development of frost flowers and rough slush on new ice surfaces, which is visible in backscatter at 5.3 GHz, fails to occur under some conditions of ice growth; thus there is no one-to-one relation between backscattered intensity, or even a given history of backscattered intensity, and new ice thickness. A method of sea ice estimation based on a direct signature response to ice thickness itself is therefore highly desirable.

We present here the first steps toward such a method based on observations of coherent, wide-band, microwave reflectivity observations at nadir. The method arose in the course of devising a new layer stripping method for the Helmholtz equation made stable by enforcement of causality [2]. but the method itself forgoes layer stripping and produces a direct estimate of reflecting layer (in this case, sea ice) thickness in units related to travel time. This travel time thickness must be converted to physical depth using an estimate of a depth-averaged refractive index supplied independently. In the following section, we present an overview of the derivation of the travel time thickness estimate in the special case when the material in the reflecting layer is lossless and there are no discontinuities in refractive index at the top or bottom of the layer. These idealizations obviously do not hold in the case sea ice, but section 3 shows that the formula derived in section 2 nonetheless yields accurate estimates of layer thickness when applied to synthetic data from a realistic, lossy model for sea ice. Moreover, the conversion from travel time to physical thickness is rather insensitive to the accuracy of a guess for the depth-averaged refractive index. Hence even a rough guess provides physical thickness estimates with accuracies of about 10%.

2. A PAYLEY-WIENER THEOREM FOR INVERSE SCATTERING

Consider a continuously stratified, non-magnetic dielectric layer sandwiched between free space (above) and a homogeneous dielectric beneath, with a plane wave of frequency ω vertically incident from above. Assume for now that the dielectric is lossless and that there is no discontinuity in permittivity at the top or bottom of the layer. Electromagnetic wave propagation is governed by the one-dimensional Helmholtz equation:

0-7803-3068-4/96$5.00©1996 IEEE

$$\frac{d^2u}{dy^2} + \omega^2 n^2(y)u = 0 \tag{1}$$

which we transform into travel time coordinates by introducing the new independent variable

$$x = \int_0^y n(s)ds.$$

Equation (1) becomes, with $' = \frac{d}{dx}$ and $\alpha(x) = \frac{n'(x)}{n(x)}$,

$$u'' + \alpha(x)u' + \omega^2 u = 0 \tag{2}$$

We consider the unique solution to (2) which has the asymptotics

$$u(x,\omega) \sim e^{-i\omega x}$$

as $x \to -\infty$. We assume that $n(x)$ varies only for $x < 0$ and $n \equiv 1$ for $x > 0$, hence $\alpha \equiv 0$ for $x > 0$ and, for $x > 0$, u has the representation

$$u(x,\omega) = \frac{1}{T(\omega)}\left(e^{-i\omega x} + R(\omega)e^{i\omega x}\right) \tag{3}$$

The formula 3 defines the reflection coefficient, $R(\omega)$. For $x < 0$, 3 is not available; however, if we notice that

$$R(\omega) = \frac{1 + \frac{u'(0,\omega)}{i\omega u(0,\omega)}}{1 - \frac{u'(0,\omega)}{i\omega u(0,\omega)}}, \tag{4}$$

then we may define the reflection coefficient for $x < 0$, by

$$r(x,\omega) = \frac{1 + \frac{u'(x,\omega)}{i\omega u(x,\omega)}}{1 - \frac{u'(x,\omega)}{i\omega u(x,\omega)}}, \tag{5}$$

It turns out that $r(x,\omega)$ satisfies — see [2] —

$$\begin{aligned} r' &= 2i\omega r + \tfrac{\alpha}{2}(1 - r^2) \\ & r(-\infty,\omega) = 0 \\ & r(0,\omega) = R(\omega). \end{aligned} \tag{6}$$

This over-posed Ricatti boundary value problem is utilized to produce a stable layer stripping algorithm in [2]. The r^2 term in (6) includes the effects of multiple reflections in the model. If we were to drop this term (we won't), we would be considering a system with only primary reflections.

For a system with only primary reflections it is easy to locate the top and the bottom of the variations in the medium. *Above the top, the index of refraction is constant and equal to the index of refraction of air; below the bottom, the index of refraction equals that of the water.* For a medium with only primary reflections, the inverse Fourier transform of the reflection coefficient — this is the time dependent reflection coefficient — is nonzero only between the first and last arrival times. The first arrival time is the travel time distance to the top, while the last arrival time gives the travel time distance to the bottom.

When we include the effects of multiple reflections, the meaning of the first arrival time doesn't change, but there is no longer a last arrival time; that is, the last primary reflection is obscured by multiple reflections.

The main point of this paper is that it is possible to ferret out this last arrival time by the simple expedient of considering the functions $\frac{1}{1-|R|^2}$ and/or $\frac{R}{1-|R|^2}$ instead of R. Specifically,

THEOREM 1:

$$\begin{aligned} \text{supp} \quad \left(\tfrac{1}{1-|R|^2}\right)^{\vee} &= [B-T, T-B] \\ \text{supp} \quad \left(\tfrac{R}{1-|R|^2}\right)^{\vee} &= [B-2T, -B] \end{aligned}$$

In the theorem above, $^{\vee}$ denotes the inverse Fourier transform,

$$f^{\vee}(t) = \int_{-\infty}^{\infty} \mathrm{e}^{2i\omega t} f(\omega)d\omega$$

and supp f is the support of the function, f, the closure of the set of points where f does not vanish.

A proof of the theorem will appear in [3]. For the moment, we will just point out that, with the notation, $n = \left(\frac{r}{1-|r|^2}\right)^{\vee}$ and $d = \left(\frac{1}{1-|r|^2}\right)^{\vee}$, $n(x,t)$ and $d(x,t)$ satisfy the system of hyperbolic partial diffferential equations:

$$\begin{aligned} \frac{\partial n}{\partial x} - \frac{\partial n}{\partial t} &= \alpha\left(\delta(t) + 2d\right) \\ \frac{\partial d}{\partial x} &= \alpha\left(n(x,t) + n(x,-t)\right) \end{aligned}$$

This hyperbolic system, has three wavespeeds, $0, \pm 1$ (notice that $n(x,-t)$ appears in the last equation). An analysis of the propagation for this system will, with a little work, yield the theorem.

3. NUMERICAL RESULTS

We consider now application of the theorem above to synthetic reflection data from a system like that described at the beginning of the previous section, except that the dielectric materials within and beneath the layer may now be lossy and discontinuities in dielectric properties occur at the upper and lower layer interfaces. These changes permit us to model more realistically a sea ice layer overlying sea water. The point of this section is that application of the theorem above to synthetic reflection data

from a realistic sea ice/sea water system yields accurate ice layer thickness estimates. We will account for this utility of the method outside its initial theoretical bounds of applicability in a forthcoming publication, but here we simply demonstrate the fact.

We assumed a parabolic profile of brine volume vs. depth roughly typical of thin Arctic sea ice and used the empirical equations of Vant [4] to estimate real and imaginary parts of the relative permittivity as a function of depth. One aspect of our forward model remains unrealistic at this stage: we have not accounted for the frequency dependence of real and imaginary parts of sea ice permittivity across the band in which we simulate reflection. Forthcoming work will address this.

We used a standard Runge-Kutta integration of a Riccatti equation similar to that above, together with a boundary condition specifying no reflection below the lower interface, to compute the solution of the forward problem. We computed the complex reflection coefficient, as a function of microwave frequency over a very wide frequency band reaching from 0.1 GHz to 10 GHz. The real and imaginary parts of the reflection coefficient are damped oscillatory functions of frequency due to interference between wave components transmitted into the ice and reflected from the ice/interface. The electromagnetic loss within the ice, however, is sufficiently high that the oscillations at the highest frequencies (above approximately 8 GHz for a 10 cm thick ice sheet) are completely damped out – thus the reflection coefficient approaches a constant limiting value in the upper part of the frequency band.

Figure 1 shows the real part of the inverse Fourier transform (approximated by a simple discrete inverse Fourier transform) of the quantity $1/(1-|R|^2)$, plotted as function of estimated physical depth by "guessing" a depth-averaged index of refraction (i.e., real part of the square root of permittivity, averaged over depth) of 2. (We judge this figure reasonable in the absence of any information except typical observations of sea ice permittivities, and we did not "tune" the figure. Note also that the imaginary part of the transform is theoretically zero and in practice consists only of numerical noise.) In the absence of jumps discontinuities in permittivity at the upper and lower interface, we would expect from section 2 to see the plotted quantity go to zero at the depth corresponding to the layer thickness. Because of the discontinuity at the ice/water interface, we in fact see what is evidently a smoothed impulse at that depth. Estimating the depth of the bottom of the layer by the depth at which the peak of the smoothed impulse occurs, we infer a physical layer depth of 10.7 cm, which differs from the true value by only 7%. Thus despite the considerable electromagnetic loss in the model from which synthetic data are generated, it appears that our result from theory for the lossless case continues to hold to a good approximation (which we will quantify in forthcoming work).

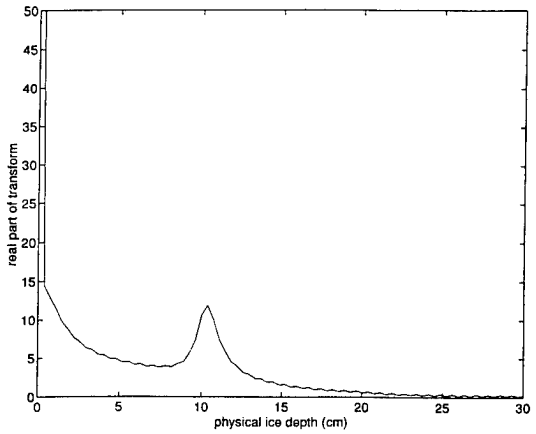


Figure 1. Real part of the inverse Fourier transform of $1/(1-|R|^2)$ versus estimated physical depth.

This fidelity recurs over a range of model ice thicknesses – it is no accident. Further simulation shows that while the upper frequency limit of data in the simulation can be decreased considerably for 10 cm thick ice, the quality of the thickness estimate is more strongly affected by the *lowest* frequency at which data are available. This aspect of the problem in particular deserves further investigation.

More immediately, we intend use the method outlined above in a trial inversion of wideband microwave reflectivity data acquired as part of the ONR-sponsored CRREL Experiment to compare ice thickness estimated via our method with directly measured thicknesses.

4. ACKNOWLEDGMENTS

This work was sponsored by the Office of Naval Research, grant N00014-96-1-0266.

5. REFERENCES

[1] Maykut, G.A., "The surface heat and mass flux", pp. 395-464 in *The Geophysics of Sea Ice*, N. Untersteiner, ed., NATO ASI Series B, Physics vol. 146, Plenum Press, New York, 1986.

[2] Sylvester, J., D. Winebrenner, and F. Gylys-Colwell, "Layer stripping for the Helmholtz equation", *SIAM Journal of Applied Mathematics*, to appear in 1996.

[3] Sylvester, J., and D. Winebrenner, "A Payley-Wiener theorem on supports and a sampling theorem for 1-D inverse scattering", in preparation.

[4] Vant, M.R., R.O. Ramseier, and V. Makios, "The complex dielectric constant of sea ice at frequencies in the range 0.1 - 40 GHz", *Journal of Applied Physics*, 49(3), pp. 1264-1280, 1978.

Thickness Retrieval Using Time Series Electromagnetic Measurements of Laboratory Grown Saline Ice

S.E. Shih, K.H. Ding, S.V. Nghiem†, C.C. Hsu, J.A. Kong, and A.K. Jordan‡
Research Laboratory of Electronics
Massachusetts Institute of Technology, Cambridge, MA 02139
†Jet Propulsion Laboratory
California Institute of Technology, Pasadena, CA 91109
‡Remote Sensing Division
Naval Research Laboratory, Washington, DC 20375

Abstract -- An electromagnetic inverse scattering theory using time-series measured data has been developed to retrieve the thickness of sea ice. The approach is based on a parametric estimation algorithm where the radiative transfer equation is used as the direct scattering model to calculate backscattering signatures from sea ice. The Levenberg-Marquardt optimization method is used as the inversion algorithm to retrieve the sea ice parameters iteratively. Additional information provided by the sea ice thermodynamics is applied to constrain the electromagnetic inverse problem to achieve more accurate reconstruction. This inversion algorithm is illustrated with experimental data from a thin saline ice sheet grown in a cold room at the U.S. Cold Regions Research and Engineering Laboratory in 1993. Based on this inversion method, the evolution of ice thickness is accurately reconstructed.

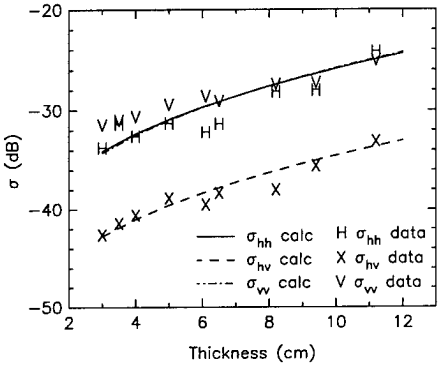


Figure 1: CRRELEX'93 measured backscattering coefficients and the corresponding simulation results.

INTRODUCTION

Sea ice thickness is an important parameter in the global climate modeling because of its role in the heat and mass balance processes involved in the interaction between the ice, ocean, and atmosphere. However, the ground field work in polar regions is quite difficult because of the vast spatial scales and the hostile climate. With the advance of space technology, spaceborne remote sensing has been applied in monitoring the polar regions. Therefore, it is necessary to develop a technique to accurately estimate the sea ice thickness from satellite electromagnetic measurements.

In the past few decades some sea ice direct scattering models have been developed and verified by various experimental measurements. To utilize these direct scattering models for sea ice thickness retrieval, parametric estimation is an appropriate approach because it offers great flexibility in the choice of the parameters to be reconstructed and data to be inverted. However, using parametric estimation approaches like least-squares optimization algorithm usually comes with non-unique solutions, and its performance degrades with noisy data. To reduce the effects of these uncertainties, more diverse data are necessary. Since a satellite repeats its orbit at a fixed time interval, it records a series of data for a fixed period. By using these time-series data, more measured data becomes available which will be useful for retrieving geophysical parameters. It is also helpful for resolving noise and non-uniqueness problems. Applying time-series measured data to sea ice inverse problem was proposed by Veysoglu *et al.* [1] in the passive microwave remote sensing of sea ice. In this paper, we develop an inversion algorithm which uses time-series active remote sensing data, and employ this algorithm to reconstruct the growth of a sheet of thin saline ice from CRRELEX'93 experiment.

EM MODEL AND COMPARISON WITH CRREL 93 EXPERIMENT

In order to investigate the electromagnetic scattering mechanisms involved in thin sea ice, and to relate the polarimetric backscatter signatures to ice physical parameters, a saline ice experiment was carried out by the Jet Propulsion Laboratory (JPL), the U.S. Army Cold Regions Research and Engineering Laboratory, and the Massachusetts Institute of Technology (MIT) in September 1993. Detailed descriptions of experimental set up and procedure are given by Nghiem *et al.* [2]. The measured polarimetric backscattering coefficients are shown in Figure 1. It is noted that there is a 8-10 dB increase in the backscatter through the whole ice growth stage. This large increase can not be explained by the increase of thickness only, it may also be contributed by the size increase of brine inclusions due to the desalination processes [2].

0-7803-3068-4/96$5.00©1996 IEEE

A two-layer scattering medium with flat interfaces (Figure 2) is considered here to interpret this set of backscatter data. For the ice sheet under consideration, the upper surface is smooth and lower surface does not significantly contribute to the total scattering [2]. The uppermost medium is air with permittivity ϵ_o, the layer of thickness d represents the sea ice and the lower half space is saline water with complex permittivity ϵ_2. Within the sea ice layer, the brine inclusions are modeled as vertically oriented ellipsoids of complex permittivity ϵ_s, they are randomly distributed in the pure ice background with complex permittivity ϵ_1. The model parameters like permittivities, brine volume fraction, and brine sizes are determined by the sea ice physical properties such as the salinity, density, and temperature which are also subject to dynamic change during ice growth.

In this paper, the radiative transfer theory is applied to calculate the electromagnetic scattering from sea ice. The propagation and scattering of specific intensities through a sea ice layer is described by the following equation,

$$\cos\theta \frac{d\overline{I}(\theta,\phi,z)}{dz} = -\overline{\overline{\kappa}}_e(\theta,\phi)\cdot\overline{I}(\theta,\phi,z) + \int_{4\pi} d\Omega' \overline{\overline{P}}(\theta,\phi;\theta',\phi')\cdot\overline{I}(\theta',\phi',z) \quad (1)$$

where $\overline{\overline{\kappa}}_e$ is the extinction matrix which accounts for the attenuation due to both scattering and absorption, and $\overline{\overline{P}}(\theta,\phi;\theta',\phi')$ is the phase matrix which describes how particles scatter radiation from the direction (θ',ϕ') into the direction (θ,ϕ). By solving (1), the backscattering cross section per unit area is given as

$$\sigma_{\beta\alpha}(\theta_i) = 4\pi\cos\theta_i \frac{I_{\beta s}(\theta_i,\phi_i+\pi)}{I_{\alpha i}(\theta_i,\phi_i)} \quad (2)$$

where (θ_i,ϕ_i) is the incident direction, α,β can be v for vertical or h for horizontal polarization, and the subscripts i and s denote the incident and scattered waves, respectively. In Figure 1, we also present the model simulations where the desalination process has been taken into account in determining the sea ice parameters at various stages of ice growth. It shows a good match for this two-layer model.

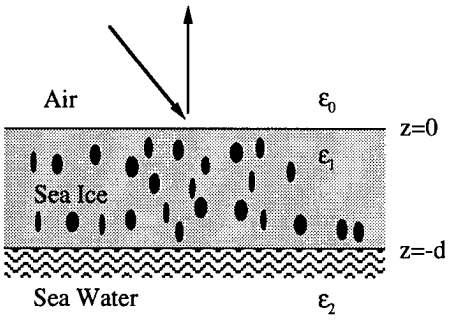


Figure 2: Sea ice model

LEAST-SQUARES METHOD

Given an electromagnetic model of sea ice, the model response at a specific time t_i, $i = 1,2,\cdots,n$, can be described by a nonlinear functional

$$y_i = y_i\left(\overline{z}(t_i),\overline{x}(t_i)\right) \quad (3)$$

where $\overline{z}$ denotes the set of known parameters such as radar parameters, and $\overline{x}$ denotes the set of unknown sea ice parameters. The corresponding remote sensing measurement at time t_i is denoted by Y_i.

The technique used in this paper to solve the sea ice inverse problems is one involving the least-squares parameter estimation [3]. Let $\overline{e}$ represent the discrepancy between the observation and the model response at the k-th iterative step,

$$\overline{e} = \overline{Y} - \overline{y}^{(k)}(\overline{z},\overline{x}^{(k)}) \quad (4)$$

where $\overline{x}^{(k)}$ are the estimated parameters at the k-th step. During the iteration, the process of adjusting parameters is critical for rapid convergence. The Levenberg-Marquardt algorithm [4] is applied to minimize the square of difference $\overline{e}\cdot\overline{e}^T$. The advantage of this method is that at beginning it behaves like the steepest descent method which is robust for poor starting values, then it approaches the Gauss-Newton method with a quadratic convergence rate.

SEA ICE GROWTH

Although time-series measurements supply more data to reduce the problems of uncertainty and noise, they also introduces more unknowns to the inverse problem. In order to reduce the more unknowns introduced by the proposed inversion scheme, the thermodynamics which governs the growth of sea ice is utilized to link the sea ice model responses at different growth stages.

For an ice sheet of thickness h under steady-state conditions, assuming no heat flow to the water underneath, the rate of heat flow through the ice is given as [5]

$$L\rho\frac{dh}{dt} = \frac{k_i}{h}(T_m - T_s) = e(T_s - T_a) \quad (5)$$

where T_a is the ambient (air) temperature, T_s is the ice surface temperature, and T_m is the ice melting temperature. k_i is the thermal conductivity of ice, e is the overall coefficient of surface heat transfer which accounts for the contributions from both convection and radiation. L is the latent heat of freezing, ρ is the density of the ice, and $\frac{dh}{dt}$ gives the ice growth rate. Assuming constant air temperature during the ice growth period, which is the case in CRRELEX'93, (5) can be solved to obtain

$$h = k_i\left[\frac{-1}{e} + \sqrt{\frac{1}{e^2} + \frac{2(T_m - T_a)}{k_i L\rho}t}\right] \quad (6)$$

which gives the time dependence of ice thickness growth. In general, (6) shows that ice thickness is proportional

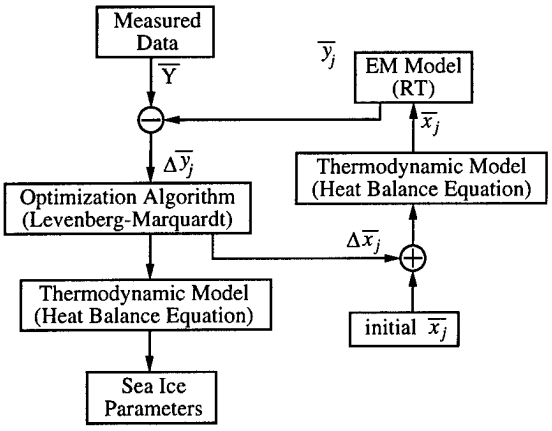


Figure 3: Block diagram of the inversion algorithm with time series measured data.

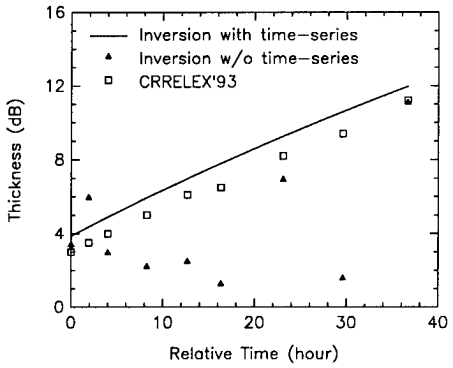


Figure 4: CRRELEX'93 thickness inversion with and without time-series data.

to the square-root of elapsed time. For the thin sea ice case as in CRRELEX'93, the contribution of conduction is smaller than the convection term due to small thickness h, and the ice growth is approximately linear [2].

INVERSION RESULTS AND DISCUSSION

The inversion algorithm using time-series measurements is summarized in Figure 3. The inversion steps begin with an initial guess of ice thickness at a specific time, the subsequent thicknesses at different growth stages are calculated from (6) according to the elapsed time between each measurements. This set of ice thicknesses is then substituted into our forward model which solves the radiative transfer equation and generates a simulated time-series backscatter which is to be compared with the real data. If the predicted results do not match the measurements, the input parameters are adjusted. The procedure is then repeated until the calculated results match the measured data. The saline ice experimental data shown in Figure 1 is applied to this time-series inversion algorithm. In Figure 4, the reconstructed results are compared with the measured ground truth. It is shown that the retrieved ice thickness agrees quite well with the measured ice growth. Another set of inversion results also presented in Figure 4, which uses individual radar measurements only, shows a large fluctuation in the retrieved thicknesses.

It is noted that, as shown in Figure 1, even our direct scattering model results follow the trend of measured data for the whole ice growth stage, the peak deviations between them can still be as large as 2dB which can be due to some measurement uncertainties. This may explain why the inversion was unsuccessful if we do not consider time-series data. Also, since the growth rate is a function of thickness, different initial guesses will produce different growth conditions in the subsequent time series and the backscatter response will be affected concomitantly. In order to minimize the least-squares objective function, the entire time-series simulation results must match the whole time-series measurements. Therefore, the range of possible retrieved thicknesses from an initial trial thickness is reduced and the retrieval is also more robust to noise at individual data points. Thus, better retrieval of thickness is achieved by using time-series measurements.

ACKNOWLEDGMENT

The research in this paper was partially supported by the Office of Naval Research. The research contribution described in in this paper was performed by the Center for Space Microelectronics Technology, Jet Propulsion Laboratory, California Institute of Technology, and was supported by the Office of Naval Research, through an agreement with the National Aeronautics and Space Administration.

REFERENCES

[1] M. E. Veysoglu, H. T. Ewe, A. K. Jordan, R. T. Shin, and J. A. Kong, "Inversion algorithms for remote sensing of sea ice," *Proc. IGARSS'94 Conf.*, pp. 626-628, 1994.

[2] S. V. Nghiem, R. Kwok, S. H. Yueh, A. J. Gow, D. K. Perovich, J. A. Kong, and C. C. Hsu, "Evolution in polarimetric signatures of thin saline ice under constant growth," submitted for publication, 1996.

[3] J. E. Dennis and R. B. Schnabel, *Numerical Methods for Unconstrained Optimization and Nonlinear Equations*, Englewood Cliffs: Prentice-Hall, 1983.

[4] D. W. Marquardt, "An algorithm for least-squares estimation of nonlinear parameters," *J. Soc. Indust. Appl. Math.*, vol. 11, pp. 431-441, 1963.

[5] C. M. Adams, Jr., D. N. French, and W. D. Kingery, "Solidification of sea ice," *J. Glaciol.*, vol. 3, pp.745-761, 1960.

Vexcel Corporations' SAR Processing Ground Station: An Overview

Matt Compton and Richard E. Carande
Vexcel Corporation
2477 55th St., Boulder, Colorado, USA
(303) 444-0094

ABSTRACT

We will present an overview of a portable ground station technology for SAR processing. This system provides complete SAR processing capabilities for multiple satellites in four modules: ingest processing, SAR processing, interferometric processing and orthoSAR processing. Data is first ingested via the P-DIF/120 interface. The P-DIF/120 is a highly programmable digital interface designed with run-time programmable logic. The P-DIF/120 hardware is configured at run-time to provide a specialized decoder for the specific data to be captured. Currently ERS-1,2, JERS-1 and RADARSAT are supported, but the highly programmable aspects of the P-DIF/120 make the addition of new formats an easy chore. This module provides frame synchronization, PRN decoding and user programmable data extraction. The raw data ingested by the PDIF/120 is then passed to the SAR processing subsystem which generates single look complex data and multilook images. The interferometric subsystem can take suitable single look complex data pairs and produce interferometrically derived elevation models. The orthoSAR module is also provided to geocode and orthorectify SAR results. All the subsystems are controlled from a user-friendly graphical user interface.

INTRODUCTION

End-to-end processing of spaceborne synthetic aperture radar (SAR) data to imagery has historically been performed at large institutions such as universities and government funded organizations. This has been due in part to the extensive resources which have been required to design, build and operate such a facility. Developing such a processing system requires in-house experts for development, maintenance and operations.

In this paper we present an overview of a SAR processing ground station which alleviates many of these difficulties, making development of new and more flexible ground stations possible. The keys to this capability are the programmable front-end ingest hardware, the use of commercially available and inexpensive computer hardware and software packages for SAR processing and an easy to use operator interface. This architecture is not only inexpensive to purchase and operate, but also offers considerable flexibility in terms of the satellites and processing algorithms which may be hosted. In the overview presented here, we include an interferometric/stereo processor and an orthorectification processor as example *add on* modules which are included in our ground station.

0-7803-3068-4/96$5.00©1996 IEEE

TOP LEVEL GROUND STATION

Figure 1 shows a schematic view of the Vexcel ground station. The general capabilities supported by the four subsystems shown are:

1) **Data Ingest Subsystem** This subsystem consists of interface, decoding and control software and hardware between a high speed data network and the SAR Processor computer. This system transcribe raw data from high-density tapes or live down-link to the SAR processor disk subsystem.

2) **SAR Processor Subsystem** This subsystems consists of software to process raw SAR data transcribed onto the SAR Processor disk subsystem. Output products include standard CEOS products in addtion to single-look complex data suitable for interferometry.

3) **Ortho-Rectification/Output Products subsystem** Software to orthorectify processed SAR imagery using elevation models if available. Geocoding may be carried out in the absence of an elevation model by using a smooth earth model. CEOS standard output products are created.

4) **Interferometric/Stereo subsystem** Subsystem to process suitable image pairs interferometrically or using stereo techniques. The use of ground control points with this software permits an elevation model to be created as well as a geometrically correct image product.

Control of the various subsystems is achieved via a graphic user interface (GUI). In the following sections we will describe the GUI and each of these subsystems.

THE GRAPHICAL USER INTERFACE

The entire operation of the ground processor is controlled by a series of graphical user interfaces. Each subsystem is composed of several low level programs of varying complexity and flexibility. Most ground station operations, however, do not require day-to-day modifications to the operations environment. The operators typically perform a limited series of operations. The GUI, which may be customized to each stations preferences, promotes fast and accurate ground station operations by limiting the choices available to the operator.

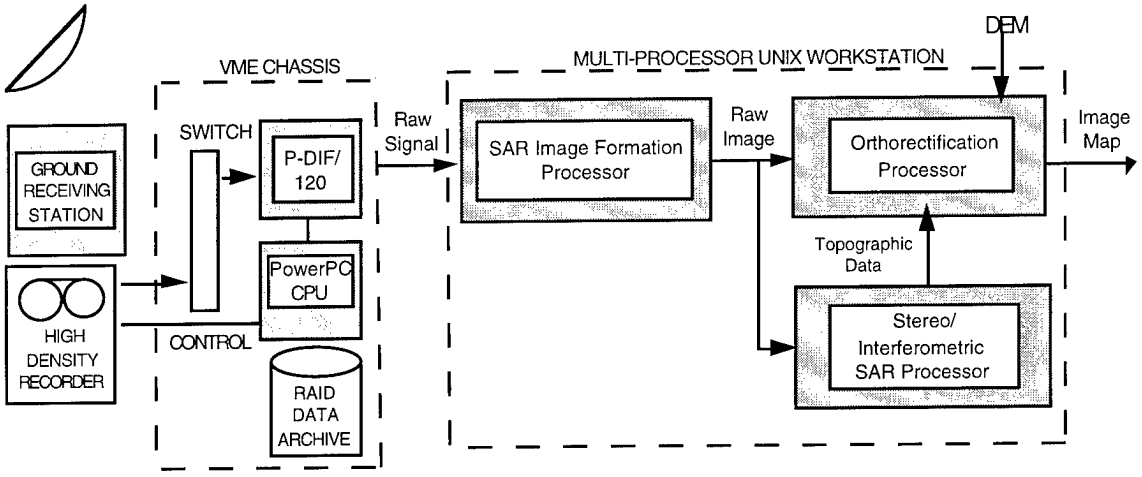


Figure 1. Functional diagram of the Vexcel SAR Processor Ground Station

The power of the underlying programs are still available to ground station personnel via the "expert mode," in which the GUIs are by-passed.

DATA INGEST SUBSYSTEM

The Data Ingest System of the Vexcel SAR Processing ground station is designed to allow data input from a variety of input sources and to provide hardware preprocessing for the workstation based SAR processor. The primary design goals of the Data Ingest System were that the system designed was to have extremely flexibility and low cost. To achieve these design goals, the Data Ingest System was created from off-the-shelf elements surrounding the P-DIF, a custom hardware data ingest solution.

The Data Ingest System resides in a VME chassis and contains three major elements as shown in Figure 2. The three primary components of the Data Ingest System include the MVME1601 VME bus master, the P-DIF/120 programmable data interface and a disk storage element. The Motorolla MVME1601 bus master is an off-the-shelf PowerPC based VME64 capable VME bus master that is primarily responsible for control of the Data Ingest System. The MVME1601 has the following responsibilities:

- Command and control of the P-DIF
- Data and status transfer from the P-DIF into local memory at transfer rates of up to 30 MBytes/sec burst.
- Transfer of data from the local memory to the Disk Storage Component
- Transfer of data from the Data Ingest System to the SAR Processor via fast ethernet
- Command and control of any station data recorders.

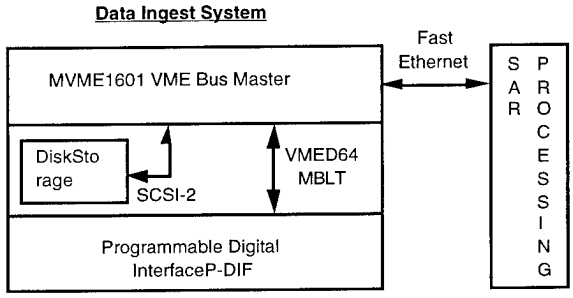


Figure 2 - Data Ingest Overview

Control of the MVME1601 is provided via a set of Graphical User Interfaces that are hosted on the SAR processing workstation.

The Disk Storage system is connected to the MVME1601 via a wide fast SCSI-2 connection allowing data transfer rates up to 15MBytes per second continuous. This system module may contain either a single disk or a RAID array depending on the requirements of the specific installation. If the Data Ingest System is used primarily as a front end for serial data recorders, a single fast disk will suffice for data storage. If the Data Ingest System is connected directly to the digital down link, a level 3 RAID system is utilized to provide the high levels of reliability required for data storage, and replaces the costly high speed digital tape storage system that has been utilized in previous designs.

The custom hardware P-DIF board set is the primary component of the Data Ingest System. The P-DIF is a programmable VME based data ingest and preprocessing unit for use with remote sensing satellites. The P-DIF concept centers around the use of SRAM based field programmable gate arrays (FPGAs). The use of a run-

time programmable gate array allows sensor specific hardware configurations to be downloaded at run time.

The P-DIF design allows very specific hardware implementations to be designed for specific sensor platforms. As an example, the P-DIF could be configured to capture ERS-1 data, PRN decode that data and extract the relevant data. If the decision was then made to process RADARSAT data, a new hardware description would be downloaded to the P-DIF, and within 30 seconds would be ready to perform the same functions on RADARSAT data. The use of run time programmable hardware also allows the P-DIF the capability to process future formats unanticipated by the system designer simply by compiling new hardware descriptions for future sensors as they appear.

The P-DIF allows serial data capture rates of up to 120 Mbps serial or 15MBytes/sec byte parallel. The captured data is then aligned to a specific framesync with data lock being contingent on several user programmable parameters such as number of bit errors in the sync and amount of bit slip allowed. This data is then PRN decoded and the specified fields extracted as status and data into onboard memory double buffers. This data is then available to the MVME1601 VME master via a VME64 MBLT transfer mode.

The configuration and operations of the data ingest subsystem is controlled completely via the graphical user interface. Operators must enter satellite specification, and start and stop time for data transfers.

SAR/INTERFEROMETRIC PROCESSOR SUBSYSTEM AND STEREO PROCESSOR SUBSYSTEM

Once the data ingest subsystem has provided the data on the SAR processor disks, processing of the data may proceed. We have selected a commercially available SAR processor, from Gamma, AG, Remote Sensing, to act as the raw phase history processor.

Gamma's Modular SAR Processor (MSP) is used to produce single look complex imagery and multi-look imagery. MSP is closely linked to another Gamma product called the Interferometric SAR Processor (ISP). The ISP performs the interferometric processing required to take two single look complex SAR images produced by MSP and determine a digital elevation model using interferometric techniques.

The sophistication of the MSP is hidden via the GUI. For processing a raw data set captured through the ingest subsystem, the operator must choose the appropriate orbit and frame number and select the output product to be created. The GUI will then operate the MSP with the appropriate commands to form the requested imagery. Vexcel developed software will produce the CEOS output products. Operation of the ISP is similarly streamlined. However, the nature of interferometric processing does require some operator intervention for ground control entry and other dynamic inputs.

In addition to implementing interferometric techniques for elevation determination, we have also developed software for deriving elevations from stereo SAR imagery. With the recent successful launch of RADARSAT, the availability of stereo radar data over large regions will significantly increase in the near future. RADARSAT is the only operating spaceborne SAR with the beam articulation necessary to routinely acquire SAR data in appropriate stereo geometries. We are currently modifying existing auto-matching and stereo range-Doppler solution software for RADARSAT application. This will be included as a ground station option.

ORTHORECTIFICATION SUBSYSTEM

If an existing elevation model of the terrain imaged by the SAR is available, the ground station also provides software which will correct the SAR imagery for terrain effects. The orthorectification subsystem offers three options: geocode, terrain correction/geocode, terrain correction/geocode with ephemeris adjustment. The later option requires an operator to provide ground control via an interactive display environment.

CONCLUSION

The SAR processor ground station described here provides an inexpensive and flexible solution to developing and operating a SAR ground station with limited resources. Careful design of a GUI permits user friendly operations of the sophisticated underlying software with little training. A programmable front end makes the same hardware useful for a number of satellite systems with no hardware modifications. The use of commercially available and tested software assures consistent results.

Azimuth and Range Scaling for SAR and ScanSAR Processing

Alberto Moreira, Rolf Scheiber and Josef Mittermayer
Deutsche Forschungsanstalt für Luft- und Raumfahrt (DLR)
Institut für Hochfrequenztechnik
82234 Oberpfaffenhofen, Germany
T: +49-8153-28-2360, EMail: alberto.moreira@dlr.de

Abstract - This paper presents new range and azimuth scaling functions which can be introduced into the processing of SAR and ScanSAR data for automatic geometric scaling in range and azimuth directions. These new phase functions have been implemented into the extended chirp scaling algorithm for air- and spaceborne SAR data processing. Several examples using the scaling functions are presented and results of the data processing are shown to verify the validity of the proposed algorithms.

I. INTRODUCTION

SAR processing requires normally an interpolation for the correction of the range cell migration. It consists of two components (linear and quadratic term), which must be corrected in order to perform an accurate azimuth compression. Since both terms are varying as a function of the range distance, the migration correction must be updated for each range position.

The interpolation for range cell migration correction (RCMC) can be circumvented by means of the chirp scaling operation [1]. The chirp scaling principle is based on the fact that the positioning of the impulse response function after compression is determined by its phase center position before compression. Since a linear scaling is required for RCMC, a linear frequency modulated function can be used to shift the phase center of the range chirps, whereby the amount of the shift is proportional to the distance to a reference range r_{ref}. In the case of SAR processing, the chirp scaling correction is applied in the range-Doppler domain, since the targets at a given range distance will have the same RCM trajectory independent of their azimuth position.

In this paper, the chirp scaling principle has been further exploited for several other applications. In addition to the traditional range chirp scaling, which equalizes the range cell migration in the processing, the following applications have been investigated:

- Range scaling. It performs a geometric scaling of the image in the range direction and is incorporated within the range chirp scaling operation. It can be used for automatic range co-registration of interferometric image pairs obtained in a multi-pass scheme. The range scaling can also be used to modify the sampling interval in the final image.

- Azimuth chirp scaling. Its principle is similar to the range chirp scaling but additional operations are required to accommodate the hyperbolic phase history in the azimuth direction. It can also be used for automatic azimuth co-registration of interferometric image pairs obtained in a multi-pass scheme with different PRF's and/or velocities as well as to selected the final sampling interval in a stripmap SAR image.

- Azimuth scaling. It is used to select the final azimuth sampling interval of ScanSAR or Spotlight data. In opposite to the azimuth chirp scaling, the basic scaling is applied in the range-Doppler domain due to the burst operation of ScanSAR and Spotlight imaging modes.

In section II of this paper, the scaling in the range direction (range chirp and range scaling) is presented. Section III shows the theory of the azimuth (chirp) scaling for stripmap and ScanSAR/Spotlight case. Several results of data processing are presented in section IV for demonstration of the geometric scaling in the final image. Section V concludes the paper.

II. SCALING OF THE RANGE SIGNAL

The basic idea is to combine the scaling of the image in the range dimension with the RCM equalization operation (range chirp scaling) of a chirp scaling processor into a single operation. This is possible since both operations represent a linear scaling of the range signal. This implies that their combination can be performed within one single step and is in fact also a chirp scaling operation but with a modified scaling factor:

$$a_{scl}(f_a) = \frac{1 + a(f_a)}{\alpha_{rg}} - 1 \qquad (1)$$

where $a(f_a)$ is the traditional chirp scaling factor known from [1] and α_{rg} is the desired scaling of the processed image in range dimension. For $\alpha_{rg} = 1$ no scaling occurs and $a_{scl}(f_a) = a(f_a)$. The full derivation of a_{scl} is given in [2]. Also the full derivations of the phase functions H_1,H_2,H_3 and H_4 (see fig. 1) are given there. Here we will concentrate on some essential discussions:

- Since the new chirp scaling factor a_{scl} is used instead of a within the first phase function H_1, this impacts all other phase functions.

- The second phase function H_2 performs RCM correction with the traditional chirp scaling factor a, since the natural curvature of the azimuth signal was not changed by the range and range chirp scaling operation, but for the compression of the range signal a modified rate according to a_{scl} must be considered.

- The phase correction H_3 which must be applied after

0-7803-3068-4/96$5.00©1996 IEEE

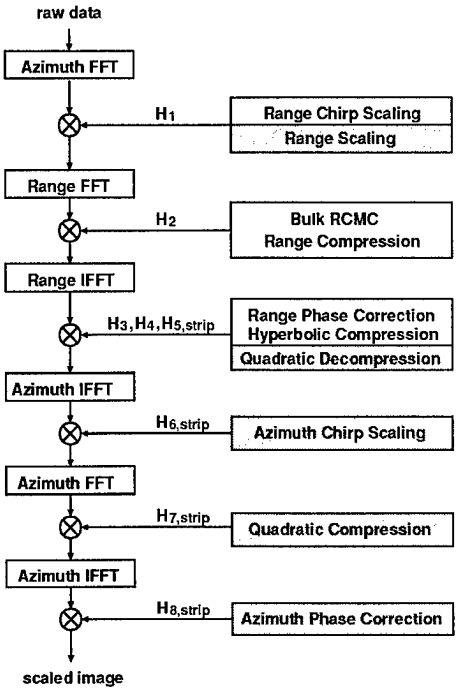


Figure 1: Signal flow of the Extended Chirp Scaling algorithm for processing of one block of stripmap data with modified/additional functions for the range and azimuth chirp scaling.

range compression in the range-Doppler domain is dependent on a_{scl} and a and is given explicitely by:

$$H_3 = exp\left[j4\pi \cdot \frac{k(f_a; r_{ref}) \cdot a_{scl} \cdot (1+a)^2}{c^2 \cdot (1+a_{scl})} \cdot (r_0 - r_{ref})^2\right], \quad (2)$$

where k is the modified chirp rate from [1] and r_0 the range distance.

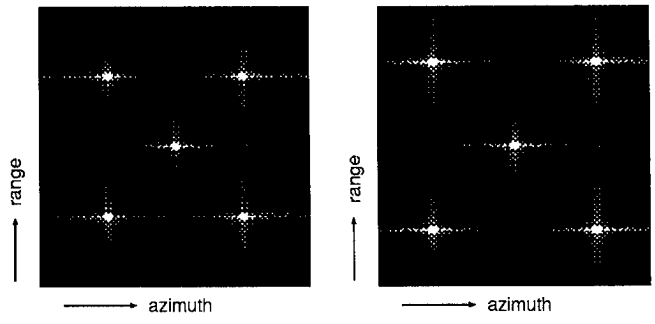
Finally, special care must be given to the update of H_4 with range since at this step of the processing the image is already scaled in the range dimension.

Using this approach the co-registration of interferometric image pairs in the range dimension during processing is possible without any additional computation load. For wavenumber processors a similar approach with some additional computations was already presented in [3]. Another application of range scaling is the processing of highly squinted data [2]. Any desired resampling of the image in the range dimension can also be achieved by using this approach.

III. SCALING OF THE AZIMUTH SIGNAL

Stripmap case

The chirp scaling principle is also adaptable for scaling the azimuth dimension of stripmap SAR data. In order to obtain a very precise scaling, the natural hyperbolic phase history must be substituted by its quadratic approximation. The grey boxes of the signal flow in fig. 1 show



(a) (b)

Figure 2: Simulated response of 5 point targets of stripmap SAR data processed with the extended chirp scaling algorithm: no scaling (a), phase preserved scaling of 20% in range and azimuth dimension (b)

that three additional phase multiplies and two FFT operations are needed to obtain a precisely scaled image in azimuth. The function $H_{5,strip}$ performs the decompression of the focused azimuth response in the range-Doppler domain and can be applied together with the phase correction function in range H_3 and the hyperbolic compression function H_4. It should be updated with range as follows:

$$H_{5,strip}(f_a; r_0) = exp[j \cdot \pi / k_a(r_0) \cdot f_a^2], \quad (3)$$

where f_a is the azimuth frequency. At this stage the natural modulation of the azimuth signal is substituted by a quadratic modulation of rate k_a allowing the use of the chirp scaling principle:

$$H_{6,strip}(f_a; r_0) = exp[j \cdot \pi \cdot a_{az} \cdot k_a(r_0) \cdot (t - t_{ref})^2] \quad (4)$$

The azimuth chirp scaling factor $a_{az} = 1/\alpha_{az} - 1$ is zero for $\alpha_{az} = 1$. The quadratic compression with modified modulation rate and the phase correction follow immediately:

$$H_{7,strip}(f_a; r_0) = exp\left[j \cdot \pi \cdot \frac{f_a^2}{k_a(r_0) \cdot (1+a_{az})}\right], \quad (5)$$

$$H_{8,strip}(f_a; r_0) = exp\left[j \cdot \pi \cdot \frac{a_{az} \cdot k_a(r_0) \cdot a_{az}}{1+a_{az}} \cdot (t - t_{ref})^2\right] \quad (6)$$

The best choice for the reference position t_{ref} is the azimuth block center. Relative to this position the azimuth chirp scaling will be performed.

This approach is exact and phase preserving, but the additional computation load is not negligible. In cases where the amount of scaling is small (e.g. ERS-1), the azimuth chirp scaling can be performed at the beginning of the processing without substituting the hyperbolic phase by its quadratic approximation. For this case the additional computation load reduces to two phase multiplications [4].

ScanSAR case

For ScanSAR processing we have introduced subaperture processing into the extended chirp scaling algorithm

combined with an improved SPECAN approach [2].

The azimuth processing starts in the range-Doppler-domain after range processing, RCMC and radiometric correction by applying the new azimuth scaling function:

$$H_{5,scan}(f_a; r_o) = exp\left[j \cdot 2 \cdot \pi \cdot (t_c(r_{scl}) - t_c(r_o)) \cdot f_a\right] \cdot$$

$$exp\left[\frac{j \cdot 4 \cdot \pi \cdot r_o}{\lambda} \cdot (\beta(f_a) - 1)\right] \cdot exp\left[\frac{j \cdot \pi}{k_{a,scl}} \cdot f_a^2\right], \qquad (7)$$

where $k_{a,scl}$ is the linear Doppler rate at the properly selected scaling range r_{scl}. The first factor is essential for avoiding time shifts before deramping, which would lead to wrap around effects. The azimuth scaling function improves the SPECAN approach by eliminating the hyperbolic azimuth phase history (second factor in eq. 7) and introducing a quadratic one (third factor). Since the quadratic modulation is constant over range, no azimuth interpolation is required. The scaling factor is selected depending on the chosen scaling range. In order to avoid wrap around effects during the final FFTs an additional azimuth time extension is applied before the first azimuth FFT.

The deramping is performed in the time domain according to:

$$H_{6,scan}(t; r_o) = exp\left[j \cdot \pi \cdot k_{a,scl} \cdot t^2\right] \cdot$$

$$exp\left[j \cdot 2 \cdot \pi \cdot k_{a,scl} \cdot (t_c(r_{scl}) - t_c(r_o)) \cdot t\right]. \qquad (8)$$

Because of the azimuth scaling all azimuth signals are multiplied with the same inverted quadratic phase function for the scaling range (first exponential term in eq. 8). The second term is related to the first term of $H_{5,scan}$ and introduces an azimuth time shift in order to relocate the targets according to their Doppler zero position. The final step of the azimuth processing is an azimuth FFT, which compresses the azimuth signals.

IV. SIMULATION RESULTS

Five simulated point targets were used to verify the performance of the scaling approachs in strip mode.

In fig. 2a the processing was performed with a normal chirp scaling approach and the targets appear at their natural position. In fig. 2b the processing steps were like in fig.1 including a range scaling with $\alpha_{rg} = 1.2$ and an azimuth chirp scaling of $\alpha_{az} = 1.2$. The reference range r_{ref} and the reference time in azimuth t_{ref} used for the processing are according to the target in the image center. Thus the image appears as scaled by 20 percent in both directions, leaving the position of the middle target unchanged. The phase of the targets remains unmodified in any case.

For the ScanSAR case the extended chirp scaling algorithm has been implemented including the described azimuth scaling approach. Fig 3 shows the results of the processing of 6 simulated point targets. A group of 3 point targets is located in near range, while the second

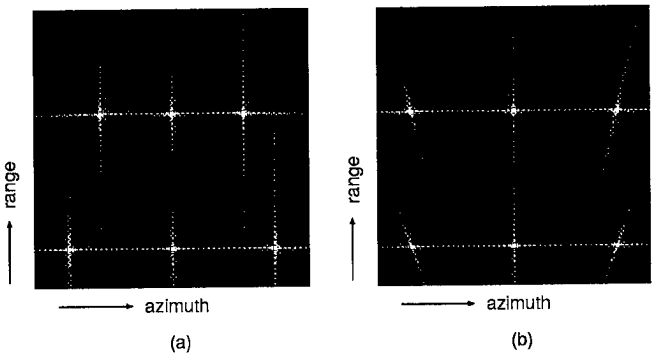


Figure 3: Simulated point targets of a burst of ScanSAR mode data processed with the extended chirp scaling algorithm without (a) and with (b) azimuth scaling

group of three point targets is located in far range. Due to the decrease of the Doppler rate as a function of range, the far range point targets are compressed in the azimuth direction and the near range point targets are distanced, if the azimuth scaling is not used (see fig. 3.a). This effect can be corrected by means of the azimuth scaling, as shown in fig. 3.b. In this case, the reference sampling distance in azimuth has been fixed to that of the near range point targets, so that their scaling remains constant.

V. DISCUSSION

In addition to the presented applications for the range and azimuth (chirp) scaling, the same principle can be used in connection with subaperture processing of airborne SAR data with strong motion errors. By means of the azimuth chirp scaling, the velocity variations can be compensated in each subaperture by scaling the azimuth signal to the same reference velocity. By means of the range scaling, the deviations from the linear flight path in line of sight direction can be precisely corrected instead of using a simple linear shift. These extensions of the range and azimuth scaling will be subject of future research.

VI. REFERENCES

[1] Raney, R.K. Runge, H., Bamler, R., Cumming, I., and Wong, F.:"Precision SAR Processing without Interpolation for Range Cell Migration Correction", IEEE Trans. Geosc. Remote Sensing, vol.32, no.4, 1994

[2] Moreira, A., Mittermayer, J. and Scheiber, R.:"Extended Chirp Scaling Algorithm for Air- and Spaceborne SAR Data Processing in Stripmap and ScanSAR Imaging Modes",IEEE Trans. Geosc. Remote Sensing,in press

[3] Fornaro, G., Franceschetti, G., Marzouk, E.S.:"A New Approach for Image Registration in Interferometric Processing", Proc. of IGARSS 1994, pp. 1983-1985

[4] Fernandes, D., Waller, G., Moreira, J.R.:"Registration of SAR Images Using the Chirp Scaling Algorithm", Proc. of IGARSS, 1996.

High Precision Processing of SIR-C ScanSAR Data

J. Mittermayer, A.Moreira, G. Davidson, R. Bamler, Y.L. Desnos[+]
Deutsche Forschungsanstalt für Luft- und Raumfahrt (DLR)
82234 Oberpfaffenhofen, Germany
T: +49-8153-28-2360, E-Mail: josefm@atlas.op.dlr.de

[+]ESA/ESTEC - ENVISAT Project
P.O.BOX 229
2200 AG Noordwijk, The Netherlands

Abstract - This paper presents the results of a study carried out for the ENVISAT Expert Support Laboratories group set up by the European Space Agency. The objectives of this study are the identification and investigation of relevant problems related to the processing of ScanSAR data. Data of the SIR-C sensor in the ScanSAR mode of operation were used for processing. The results and experience gained in this analysis might be used when relevant for the ground processing development of the ASAR instrument on board the ENVISAT platform.

I. INTRODUCTION

ESA is preparing a future Earth Observation Mission called ENVISAT embarking a set of key instruments for environmental monitoring from Space. Among these instruments an Advanced Synthetic Aperture Radar operating at C-band has been selected for the ENVISAT payload ensuring continuity with ERS-1 and ERS-2 SARs and featuring enhanced capability in terms of coverage, range of incidence angles, polarisation, modes of operation. This enhanced capability is provided by significant differences when compared to AMI in the instrument design: a full active array antenna equipped with distributed Transmit/Receive modules which provides distinct transmit and receive beams, a digital waveform generation for pulse "chirp" generation, a Block Adaptive Quantisation scheme, a ScanSAR mode of operation by beam scanning in elevation. In the framework of an ENVISAT Expert Support Laboratories group set up by the European Space Agency, the DLR has been appointed to support several critical aspects of the ENVISAT ASAR product quality and algorithm development. The present study is focusing on algorithm prototyping and image radiometric quality based on real ScanSAR data acquired during the SIR-C/ XSAR mission.

The main points which were investigated are 1) the processing algorithm accuracy to allow a phase-preserving processing, 2) the processing parameters strategy including the trade-off between radiometric and geometric resolution and 3) the improvement of algorithms for the estimation of the Doppler centroid and roll angle which is a crucial point for the radiometric correction of ScanSAR images.

The extended chirp scaling algorithm used for the processing combines the accuracy of the chirp scaling algorithm [5] with the efficiency of the SPECAN approach. Due to the use of the SPECAN approach, an azimuth scaling function is introduced into the processing in order to avoid the required azimuth interpolation for geometric correction. The azimuth scaling removes the change of the Doppler rate as a function of range and introduces a constant Doppler rate which leads to the desired sampling space in azimuth.

For Doppler centroid estimation a new approach for the ScanSAR imaging mode is proposed, which is applicable when at least three azimuth looks are available. For the roll angle estimation, standard techniques are used which are based on the signal ratio in the overlapping region between subswaths.

Section II of this paper describes the extended chirp scaling algorithm for the data processing in ScanSAR mode. The roll angle and Doppler centroid estimations are shown in section III and IV, respectively. Section V concludes the paper with some discussions concerning the problems involved in the processing of the data.

II. SCANSAR PROCESSING

The extended chirp scaling algorithm (ECS) [3] in combination with an improved SPECAN approach is used for processing the SIR-C ScanSAR data. In [4] a detailed description of this method is given. The block diagram in Fig.1 shows the main steps in the processing.

At the beginning of the processing the bursts are multiplied by a weighting function for the azimuth sidelobe suppression. The first phase function H_1 performs the chirp scaling operation which carries out the equalisation of all range migration trajectories in the range-Doppler domain.

The range compression and the range cell migration correction are performed in the wavenumber domain by applying the phase function H_2. When transforming the signal back to the range-Doppler domain, a residual phase correc-

0-7803-3068-4/96$5.00©1996 IEEE

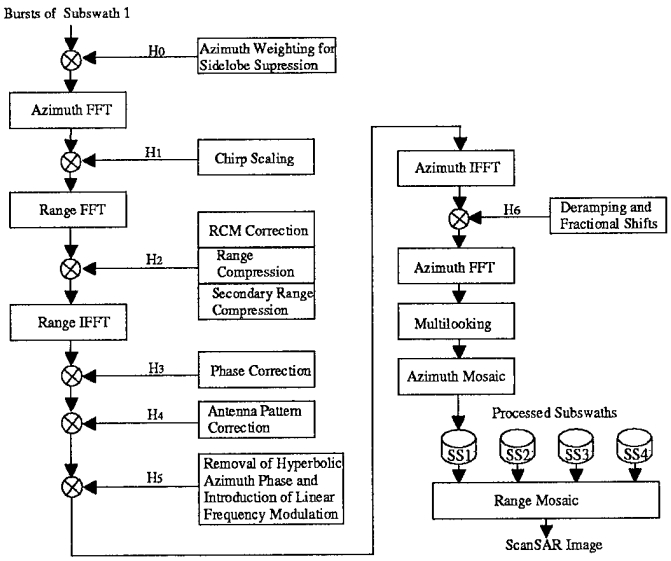


Fig.1: *The extended chirp scaling algorithm for ScanSAR.*

tion H_3 is applied which compensates a slowly varying range-dependent azimuth phase.

After the two-dimensional radiometric correction H_4 the azimuth scaling is performed as follows:

$$H_5(f_a;r_o)=\exp\left[j2\pi\left(t_c(r_{scl})-t_c(r_o)\right)f_a\right]\cdot \qquad (1)$$
$$\cdot\exp\left[\frac{j4\pi r_o}{\lambda}\left(\sqrt{1-\left(\frac{\lambda f_a}{2V}\right)^2}-1\right)\right]\exp\left[\frac{j\pi}{k_{a,scl}}f_a^2\right],$$

where r_o is the slant range of a point target, f_a is the azimuth frequency and t_c is the time between Doppler zero and Doppler centroid. The effective velocity and the wavelength are denoted by V and λ, respectively. The second term of the azimuth scaling function in (1) removes the hyperbolic azimuth phase history, which varies over range while the third term introduces a constant linear frequency modulation, which is independent on range. The introduced Doppler rate $k_{a,scl}$ corresponds to a linear frequency modulation at the scaling range r_{scl}. The first exponential term is needed to avoid wrap around of the azimuth bursts in time domain.

The next step is the compensation of the linear frequency modulation by the deramping function H_6 in the time domain.

$$H_6(t;r_o)=\exp\left[j\pi\,k_{a,scl}f_a^2\right]\exp\left[j2\pi\,k_{a,scl}\left(t_c(r_{scl})-t_c(r_o)\right)t\right] \qquad (3)$$

The first term performs the deramping while the second term causes a shift in the azimuth time t, which compensates the time shift in H_5. Thus the final azimuth FFTs compress the azimuth signal at Doppler zero geometry.

An azimuth time extension T_1 is required before the first azimuth FFT to avoid wrap around effects in the burst signal after the deramping:

$$T_1=T_a\left|1-\frac{r_{scl}}{r_o}\right|-T_s\left(1-\frac{r_{scl}}{r_o}\right), \qquad (2)$$

where T_a is the full synthetic aperture time while T_s corresponds to the burst duration. The maximum value of T_1 must be selected for the time extension.

III. ROLL ANGLE ESTIMATION

Methods for roll angle estimation in the ScanSAR mode use the overlap regions between the subwaths, e.g. [2]. The difference of the logarithms of the subswaths intensities in the overlapping regions is calculated. After a linear fit the elevation angle corresponding to the zero difference is estimated, which corresponds to the position where the antenna gains in the overlapping areas are equal. The range antenna patterns and the terrain height have to be known.

In the scene we processed there are no overlap regions with equal intensities and so we estimated the position which corresponds to a certain intensity difference (not neccessarily zero). The obtained accuracy of the roll angle estimated in the three overlap regions is about 0.3°. However, the accuracy of the look angle estimation should be below 0.05° for a good radiometric correction. There are several reasons for the degraded accuracy: 1) the signal to noise level in two overlapping regions is too low; 2) the profiles in some overlapping regions are too flat; 3) the available antenna patterns are not accurately known.

Better results of the look angle estimation will be possible if the antenna patterns are precisely measured over homogeneous areas.

IV. DOPPLER CENTROID ESTIMATION

Radiometric correction of the azimuth antenna pattern in ScanSAR images requires accurate Doppler centroid estimation. Since conventional Doppler centroid estimators are not suitable because of the scene dependence of the azimuth spectrum, algorithms for ScanSAR Doppler centroid have been proposed which use the log of the ratio of overlapping portions of burst intensity images corresponding to the same scene [2]. Also, the accuracy can be improved by a least squares fit of estimates over many bursts and range bins.

Doppler centroid estimation methods for ScanSAR were investigated by simulation, where it was observed that the ratio of images approach suffered degradation when parts of burst images had low signal to noise ratio. In this case the log ratio is close to zero because the average of additive noise

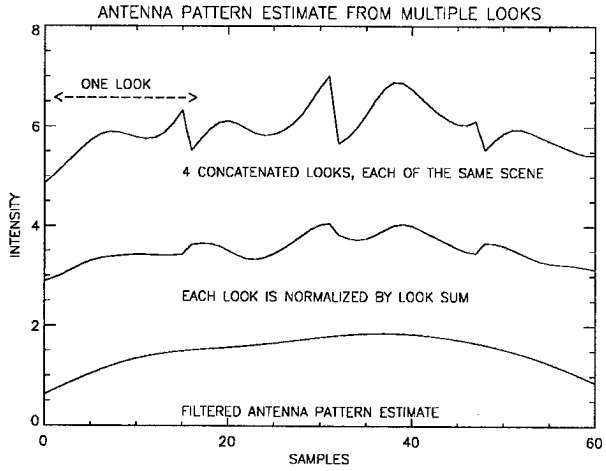


Fig.2: *Antenna pattern estimate.*

power in each image is the same regardless of the antenna pattern, causing errors in the Doppler centroid esti-mate.

In this work we investigate an alternate approach to Doppler centroid estimation for ScanSAR, which can be used when at least three looks are available. The idea is to use the different looks of the same scene, which are weighted by different parts of the antenna pattern, to construct an estimate of the antenna pattern itself. Burst intensity images are averaged over a number of range bins, then looks are extracted and concatenated as shown in the first graph of Fig. 2. An estimate of the scene intensity is obtained by look summation, which is used to normalize each look as shown in the second graph of the figure. In the concatenated looks the scene intensity is periodic, so the normalized looks are then filtered with a lowpass filter with cutoff frequency equal to the inverse of the length of a look, with the result shown in the last graph of the figure. This estimated antenna pattern is used to estimate the Doppler centroid by correlation. In addition, an average of antenna pattern estimates can be used directly for the radiometric correction.

Burst images were simulated assuming a scene with a 20 dB drop in intensity and an average SNR of 20 dB. Assuming a system with 3 looks, the average Doppler centroid error in the ratio of images approach was 36 Hz, compared with 8 Hz for the new method. Finally, both methods were used to estimate Doppler centroid of 4-look SIR-C ScanSAR data. Estimates from each of the bursts were fit to a bilinear function in range and azimuth, and the standard deviation of the estimate from a single burst is measured from the difference from the fitted function. The standard deviation with the ratio of images method was 123 Hz, and with the new method was 103 Hz. The results indicate that the new method can be used for Doppler centroid estimation, is slightly more accurate than the ratio of overlapping images approach, and is less sensitive to scene contrast. The required accuracy of 25 Hz for the Doppler estimation for precise radiometric correction can be achieved by averaging the estimates of ca. 16 adjacent bursts.

V. DISCUSSION

The proposed algorithm for ScanSAR image formation is suitable for high precision phase preserving processing. For the processing of the data, two different strategies can be used: 1) Processing the available bandwidth (ca. 85 % of PRF) which leads to different number of looks in each subswath (i.e. far range subswaths have greater number of looks), 2) Processing with a constant number of looks, which does not lead to a constant radiometric resolution in the full image due to the variation of the signal-to-noise ratio in each subswath. Together with the look weighting strategy [1], the processing with variable look number can be used in order to achieve a constant radiometric resolution in the ScanSAR image. Due to the variation of the transmitted pulse length and the variation of the burst length the ASAR system achieves also a relatively constant geometric resolution.

Fig.3 shows the result of the image processing of SIR-C ScanSAR data using the extended chirp scaling algorithm. This image shows the region of Chickasha, Oklahoma, USA acquired during the second SIR-C flight (data take DT 82.1). Image dimensions are 236 × 252 km in ground range and azimuth, respectively.

The main difficulties for the radiometric correction are the estimation of Doppler centroid and roll angle. Sections III and IV showed that the Doppler centroid estimation is not a critical point if a large number of azimuth looks is used in the scanning strategy. However, the estimation of the roll angle requires a very precise knowledge of the elevation antenna patterns which should be obtained by in-flight calibration (e.g. over large homogeneous regions like rain forest). The overlap of the elevation antenna patterns of adjacent subswaths should be as symmetrical as possible in order to increase the accuracy of the estimation algorithm.

VI. ACKNOWLEDGMENT

The authors would like to thank A. Freeman and C.Y. Chang from NASA/JPL for providing the SIR-C ScanSAR data set and the program to calculate the SIR-C antenna patterns.

VII. REFERENCES

[1] Bamler R.: "Optimum look weighting for burst mode and ScanSAR processing". IEEE Trans. on Geosc. and Remote Sensing, Vol.33, No.3, May 1995.

[2] Bamler, "Roll angle estimation in SIR-C ScanSAR processing," JPL, Interoffice Memo IOM 3340-94-030, March 16, 1994

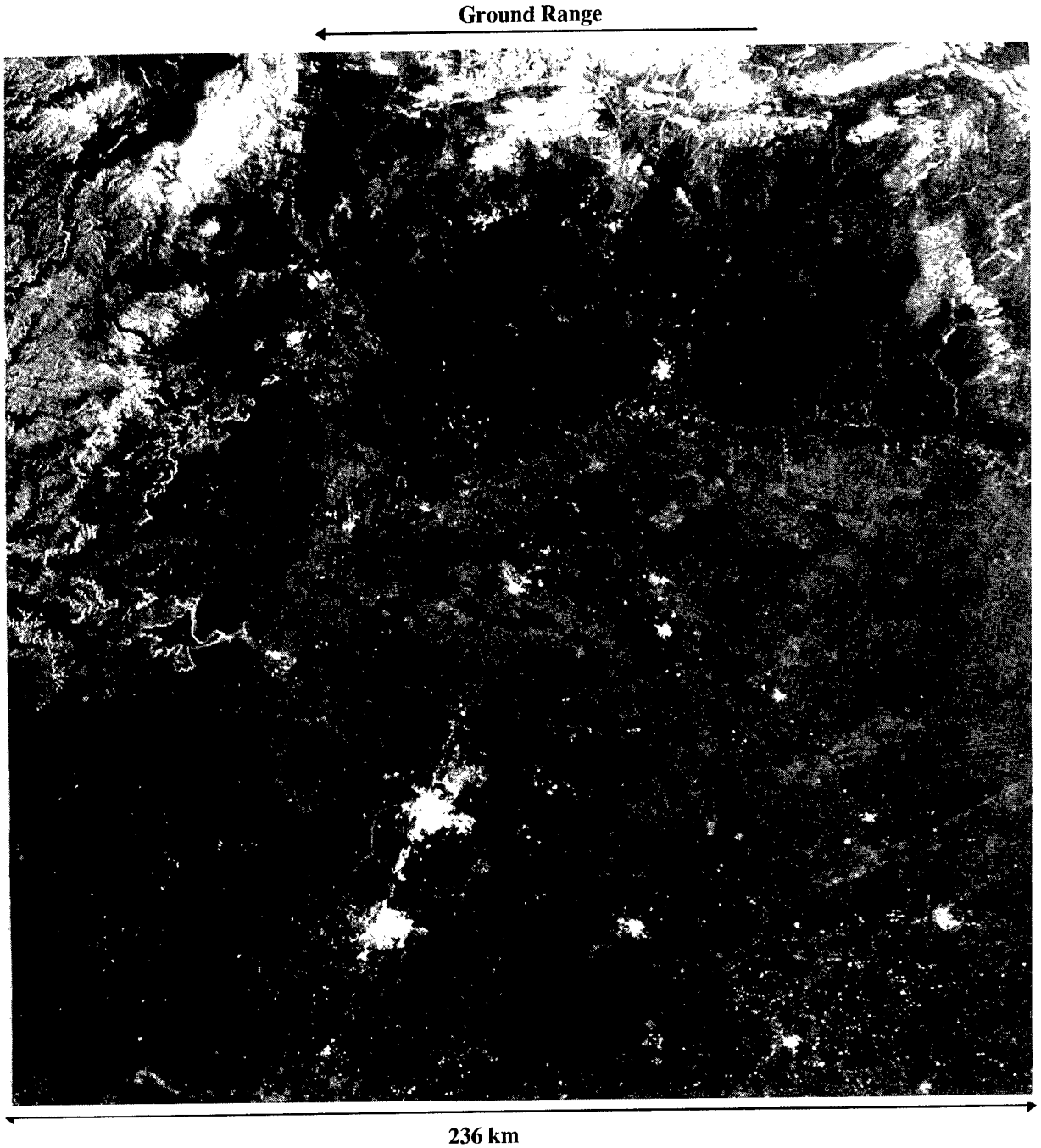


Fig.3: *Processed SIR-C ScanSAR image using the ECS algorithm with azimuth scaling.*

[3] Moreira,A. and Huang, Y.: "Airborne SAR Processing of Highly Squinted Data Using a Chirp Scaling Algorithm with Integrated Motion Compensation", IEEE Trans. on Geosci. and Remote Sensing, Vol. 32, No.5, September 1994.

[4] Moreira, A., J. Mittermayer, R. Scheiber: "Extended Chirp Scaling Algorithm for Air- and Spaceborne SAR Data Processing in Stripmap and ScanSAR Imaging Modes", IEEE Trans. on Geosc. and Remote Sensig, 1995, in press.

[5] Raney, R.K., H. Runge, R. Bamler, I. Cumming, and F. Wong: "Precision SAR Processing without Interpolation for Range Cell Migration Correction", IEEE Trans. on Geosci. and Remote Sensing, Vol. 32, No. 4, July 1994.

A Comparison of the Range-Doppler and Chirp Scaling Algorithms with reference to RADARSAT

W. Hughes[1], K. Gault[1], G.J. Princz[2]

[1] Atlantis Scientific Systems Group Inc., 1827 Woodward Drive, Ottawa, Canada, K2C 0P9
[2] Canada Centre for Remote Sensing, 588 Booth Street, Ottawa, Canada, K1V 0Y7

Abstract

The Range-Doppler algorithm has long been a popular method for the digital processing of SAR data from spaceborne platforms. The success of this algorithm is due in part to its conceptual simplicity, and in part to a number of approximations which reduce the computational complexity of the method. However, the widespread use of these same approximations has given the Range-Doppler algorithm the (mostly undeserved) reputation of producing inferior image quality, especially with regard to phase. In recent years, the Chirp-Scaling algorithm has been proposed as an alternative to Range-Doppler. The Chirp-Scaling algorithm avoids the complicated and computationally expensive interpolations used by the Range-Doppler algorithm and is more naturally phase preserving. RADARSAT (single beam) data, in view of its moderate squint and multiple PRF Doppler Centroid excursion across an image, is a good test case for both algorithms. Atlantis, with the support of the Canada Centre for Remote Sensing, has developed a desk top software processor which implements both the Range-Doppler and Chirp-Scaling algorithms. In this paper, a comparison is made between the performance of the two algorithms with reference to the RADARSAT sensor. As well, issues of implementation and computational complexity are discussed.

1. Introduction

The Range-Doppler algorithm was the original algorithm used in digital processing of SAR data from spaceborne platforms. The algorithm provides a dramatic increase in processing speed over a simple time domain correlation approach by simultaneously focusing in azimuth, all targets a given slant range. As well, the algorithm naturally accommodates several approximations, which further decrease the processing time while retaining adequate focus quality. However, the phase fidelity of an image degrades long before the focus. Hence processors that provide good focus can nonetheless be inadequate for applications requiring precise phase information (e.g. interferometry). A carefully designed Range-Doppler processor can be phase preserving, but because of the need for care the Range-Doppler algorithm cannot be said to be naturally phase preserving. In the late 1980's, wavenumber domain algorithms, which are naturally phase preserving, were introduced. However, these new algorithms shared with the Range-Doppler algorithm the need for computationally expensive, and potentially inaccurate, interpolations. This problem was addressed by the introduction of the Chirp-Scaling algorithm [1] [3] [6], which eliminates the need for such interpolations.

Atlantis Scientific has developed a commercial desktop software SAR processor capable of processing data from a number of sensors including RADARSAT. (This work was supported by the Canada Centre for Remote Sensing.) The processor implements both the Range-Doppler and Chirp-Scaling algorithms. RADARSAT is not yaw steered to reduce the Doppler centroid, and has modes combining high range compression bandwidth with high incidence angle. Thus RADARSAT data is a good test of a processor's ability to deal with moderate squint. As well, the large Doppler centroid excursion in RADARSAT data (up to 2.3 PRF's) provides a good test of a processor's ability to deal with Doppler centroid variation across a scene.

2. Range-Doppler

The basic problem with (correlation) SAR processing is that, in the time/time domain, the range migration curves of targets at the same ranges are not coincident, and the range migration curves of targets at different ranges intersect. This, combined with the fact that focusing parameters are range dependent, means that processing in the time/time domain can only be done one pixel at a time, an intolerable computational burden. The Range-Doppler algorithm uses the fact that, in the time/frequency domain, the range migration curves of targets at the same range are coincident and, the range migration curves of targets at different ranges do not intersect. In the Range-Doppler algorithm, after compres-

0-7803-3068-4/96$5.00©1996 IEEE

sion in the range direction, the signal data is converted to the time/frequency domain. The return for all targets at a given range is extracted along the appropriate range migration curve and compressed using standard FFT convolution techniques.

The Range-Doppler algorithm has two basic drawbacks. One is that the extraction of the spectra along the range migration curves requires interpolation. As the range migration curves are not parallel, this interpolation cannot be achieved by fast convolution methods. Thus, the interpolation is slow, and the short interpolation kernels used to reduce the computational burden can introduce errors into the processing.

The second drawback is the fact that the return from a point target is not perfectly concentrated on the range migration curve in the time/frequency domain, but spread by an amount that depends on the Doppler frequency. This spreading leads to a degradation in range focus. It can be compensated for by convolution with a frequency dependent reference function, a process know as secondary range compression [4] This convolution can be achieved at insignificant computational cost by modifying the form of the filter used in range compression. However, this processing takes place in the time/time domain where no frequency information is available. Thus, a single reference function is used to approximate the set of frequency dependent functions. This approximation can lead to degradation of focus and loss of phase preservation. (Alternatively, secondary range compression can be accomplished in the time/frequency domain by modifying the form of the interpolation kernel used to extract the spectra. Unfortunately, this approach leads to an non-trivial increase in computational cost.)

3. Chirp-Scaling

In the Chirp-Scaling algorithm, range compression is done in the time/frequency domain, rather than in the time/time domain. The algorithm relies on the fact that small changes to the phase of the data can cause a shift in the location of the compressed pulse with negligible loss of focus. Shifts are applied in such a way that the resulting range migration curves from scatterers at different ranges are parallel. This approach allows the range migration to be corrected using fast convolution techniques (which are, in practice, combined with the range compression step). Again, the secondary range compression and primary range compression steps can be combined. However, as this is done in the time/frequency domain, there is no need to ignore the frequency dependence of the secondary range compression reference function.

4. Implementation Issues

Because there is no need for explicit interpolation, the Chirp-Scaling algorithm is more elegant than the Range-Doppler algorithm. However, although the absence of an interpolator simplifies the implementation with respect to the Range-Doppler algorithm, there are a number of factors which complicate the implementation.

1. Chirp-Scaling requires three corner turns (data transposes) while the Range-Doppler requires only one. Furthermore, in Chirp-Scaling the second corner turn occurs before range compression but after the azimuth FFT and thus, involves a larger quantity of data. In our implementation, intermediate results are stored in buffers. These buffers are stored in memory, if sufficient memory is available. Otherwise the buffers are stored on disk in a format which can be accessed relatively easily either by rows or by columns. The type of buffer used and the mechanics of the disk access (if needed) are hidden from the higher levels of the program.

2. During range compression, all samples must correspond to the same *absolute* Doppler frequency. However, the number of such samples is limited by the change in Doppler centroid with range, the PRF and the processed azimuth bandwidth. For RADARSAT, this number will be smaller than the number of samples in a data line, which means that range compression must be accomplished in sections (range blocking). The most straightforward method to accommodate the changes in Doppler centroid is to store the azimuth FFT'd data in buffers that are greater than one FFT in width, providing a frequency excursion of greater than one PRF (see e.g. [5] pp.1034–1035). In our implementation we avoid this cost of extra space at the cost of extra data transfers and some added bookkeeping.

3. Range resampling and slant to ground range conversion can be conveniently incorporated into the Range-Doppler algorithm, but not the Chirp scaling algorithm. In our implementation range resampling and slant to ground range conversion are not incorporated into the Range-Doppler algorithm. Instead, a separate resampling module is provided. This module can be applied to the output from either method.

5. Image Quality

The major contribution to the difference in image quality between the two algorithms (assuming that an adequate interpolation length is used in the Range-Doppler algorithm) is the fact that in the Range-Doppler algorithm, the frequency dependence of the secondary range compression correction is ignored. The approximate phase error in the transfer function due to the use of a frequency independent secondary range compression function is

$$r \cdot \frac{c}{4} \cdot \frac{\omega^2}{\omega_0^3} \cdot (k_x^2 - k_{x_0}^2) \qquad (1)$$

with r the slant range, ω_0 the angular frequency of the carrier, ω the instantaneous angular frequency of the

pulse modulation, k_x the azimuth wavenumber, and k_{x_0} the azimuth wavenumber corresponding to the Doppler centroid ([2] p 712). The maximum phase correction error increases quadratically with range compression bandwidth and linearly with Doppler centroid. Thus, the worst RADARSAT case is a fine beam mode near the equator where the squint is highest. The worst case phase errors at the edge of the processed bandwidth will be about .20 radians for the fine beam modes, .04 radians for the standard beam modes, and .025 radians for the wide beam modes. This suggests that the differences in image quality between the two algorithms should be small or negligible for the wide and standard modes, while the phase preservation of the Range-Doppler method may be somewhat inferior to the Chirp-Scaling method for the fine beam modes.

6. Summary

Both the Range-Doppler (with frequency independent secondary range compression) and the Chirp-Scaling algorithms seem reasonable approaches to the precision processing of RADARSAT data. The Chirp-Scaling algorithm is slightly more complex in implementation, but promises slightly better image quality in some extreme cases.

References

[1] Bamler R.; Runge H.: A Novel High Precision SAR Focusing Algorithm Based on Chirp Scaling IGARSS 92, May 1992

[2] Bamler R.: A Comparison of Range-Doppler and Wavenumber Domain SAR Focusing Algorithms IEEE Trans. Geosci. Remote Sensing, July 1992.

[3] Cumming I.; Wong F.; Raney K.: A SAR Processing Algorithm with no Interpolation. IGARRS 92, May 1992

[4] Jin M.; Wu C.: A SAR Correlation Algorithm which Accommodates Large-Range Migration. IEEE Trans. Geosci. Remote Sensing **GE-22** (Nov. 1984), 592–597.

[5] Moreira A.: Airborne SAR Processing of Highly Squinted Data Using a Chirp Scaling Approach with Integrated Motion Compensation IEEE Trans. Geosci Remote Sensing, September 1994

[6] Raney R. K.; Runge R.:; Bamler R.; Cumming I.; Wong F.;: Precision SAR Processing Using Chirp Scaling IEEE Trans. Geosci Remote Sensing, September July 1994

Comparison of Medium Resolution Algorithms for Spacecraft On-Board SAR Image Generation

Ana Vidal, Josep Rosello

European Space Agency (ESA), Spacecraft Control & Data Systems Division
ESTEC-WSP, Postbus 299, 2200 AG Noordwijk, The Netherlands
Tel: +31-71-565-5409/4058, Fax: +31-71-565-4295
ana@wd.estec.esa.nl, josep@wd.estec.esa.nl

Abstract--Traditionally, Spacecraft Synthetic Aperture Radar (SAR) processing has been performed on ground. This is mainly due to the huge amount of computation, high reliability and resources that SAR processors require. However, new space-qualified technology will offer an adequate scenario for producing medium resolution SAR images. In this framework, this paper presents a comparative study among the most appropriate algorithms for on-board implementation. A feasibility assessment and a quality analysis of the identified processors for on-board SAR medium resolution imagery are provided.

INTRODUCTION

Spaceborne Synthetic Aperture Radar (SAR) plays an important role for Earth Observation, since it provides all-weather global coverage. However, SAR images are not directly available because data processing usually takes place on ground. A new space qualified Digital Signal Processor (DSP) that will become available for ESA will provide the possibility of medium resolution on-board image generation. It will offer important savings in down-link data rate and will enable direct delivery to potential users. Medium resolution imagery is based on processing a decimated image without loss of quality if multilooking is also carried out. Consequently, the final data volume is lowered and further reduction is possible by image compression.

This paper identifies and assesses different processing techniques. The proposed algorithms have been implemented in high level language and their performances have been evaluated in terms of image quality and computation costs. It is concluded that a compromise among resolution, radiometric quality and computing cost must be adopted according to the available resources.

BASIC THEORY

Some simplifications have been made along this paper and must be considered in order to extrapolate the results. A quadratic approximation for the Doppler phase history and the transmitted waveform has been adopted. SAR processors need a Doppler parameter estimator that has not been taken into account. If the range decimation is large enough for the amount of range migration to be less than a final range bin, then the range curvature does not need correction. This is the approach we have followed, which is usually valid for a C or X band radar. It allows us to carry out a Range-Doppler processor in which azimuth and range decorrelation can be isolated and simplified compared to conventional algorithms.

System Impulse Response

Under the aforementioned assumptions, the phase of the system impulse response h has two independent contributions coming from the Doppler history and from the delayed transmitted chirp and it is given by

$$h(s,t) = CA(s)exp(j\Phi_a(s) + j\pi Kt^2), \quad (1)$$

$$\Phi_a(s) \cong -4\pi R_c/\lambda + \pi f_r (s-s_c)^2 + 2\pi f_{Dc}(s-s_c), \quad (2)$$

where t is time, s is slow time [1], C is a constant, $A(s)$ is the antenna gain, R_c is the slant range distance in the broad side angle, s_c is the beam center offset time, λ is the radar wavelength, f_{Dc} is the Doppler Centroid Frequency, f_r is the Doppler frequency modulation (FM) rate and K is the transmitted chirp FM rate.

A SAR processor must decorrelate the system contribution from the raw data in order to reconstruct the radar cross section. This can be achieved by different techniques and the most significant ones are described below.

MEDIUM RESOLUTION SAR TECHNIQUES

Fast Frequency Convolution

Fast Frequency Convolution (FFC) is one of the most widely used methods and it is a good reference for comparison. It performs one-dimensional Fast Fourier Transform (FFT), reference multiplication and inverse FFT (IFFT) in smaller sub-lines that correspond to different looks.

The FFT data length must be at least as large as the corresponding reference templates and as large as possible for efficiency reasons. Therefore, FFC involves the use of large

A. Vidal is under a Research Fellowship funded by the 'Ministerio de Educación y Ciencia' from Spain.

0-7803-3068-4/96$5.00©1996 IEEE

corner-turn memory blocks. This requirement can be relieved by filtering and down-sampling the incoming data, but this operation is also very time consuming and does not bring much benefit apart from reducing the initial size of the FFT's as it is shown in following sections.

Unfocused Processing

The unfocused azimuth processing relies on a coherent integration of the unfocused synthetic aperture. The aperture length is limited by the maximum phase error tolerated by the system [1]. If it is bounded by $\pi/4$, then the best available azimuth resolution δx is fixed and equal to $\sqrt{R\lambda/2}$, letting R be the slant range distance. The resolution restriction is the principal disadvantage of this simple method, in which the azimuth lines that form the unfocused aperture are merely weighted and added. The weighting window consists of a band pass filter centered on f_{Dc}. Azimuth multilooking may also be realized by a filter bank consisting of different Doppler bands. Nevertheless, increasing phase errors in looks located far from f_{Dc} restrain this strategy. Range processing is applied by means of the previously explained FFC method after azimuth compression in order to save computation time. Since azimuth processing takes place before range down-sampling, the range migration phenomenon is more critical.

Spectral Analysis

An efficient method for quadratic chirp compression is the deramping and spectral analysis technique described in [1]-[2]. It first performs a multiplication by the reference chirp isolating target positions at different frequency tones. An efficient spectral estimator like FFT is then applied in order to get the target position. This method allows efficient look extraction, since data is processed in bursts and the total amount of processed data depends on the preferred radiometric quality.

This technique can be applied to azimuth and range processing, since both are modeled by quadratic chirp waveforms. However, the main drawback of this approach in the case of azimuth processing is the system dependence on f_r which varies along the satellite orbit. For a fixed choice of FFT length, the output data rate and the inter-look pixel mismatch depend on f_r. This problem can be solved by resampling, which is not considered in the study.

COMPARATIVE STUDY

The SAR processing techniques mentioned above have been tested over ERS-1 real data and a simulated point target. The selected raw data set represents an area of 70 by 70 Km acquired over the Flevoland test site. Five algorithms have been isolated for comparison: Standard FFC in range and azimuth (FFC), FFC with a pre-filtering stage (Pre-FFC), unfocused processing plus range FFC (Unf), range FFC plus azimuth Specan (Spe), Specan in range and azimuth (Spe2D).

In order to perform a proper comparison, the same number of looks and close decimation ratios have been selected. Ratios of 32~41.5 (8 looks) in azimuth (azi) and 6.7~8 (3 looks) in range (rng) have been used for Table I and Table II. The resulting multilook image has a pixel spacing in the order on 160 m in azimuth and projected slant range (fan-shape interpolation is not considered). A data volume reduction by a factor 640 over raw data is achieved without considering image compression.

Table I shows some resulting image quality parameters. The Equivalent Number of Looks (ENL) measured over uniform sea regions in Flevoland evaluates the multilook effectiveness. The Integrated Side Lobe Ratio (ISRL, ESA ERS-1 method) and the Spatial Resolution in pixels (SR) have been obtained following [3] over an ERS-1 simulated point target.

The FFC algorithm produces better image quality and the Pre-FFC presents the poorest results. Nevertheless, all of them show a similar high quality that is due to the much coarser grid produced by the decimation compared to the high resolution case.

The computational assessment is the most important factor in the selection of the most suitable algorithm for on-board purposes. The five algorithms have been implemented in ANSI C on a SUN SPARC 10 and the resulting processing times are given in Table I. This allows us to make an estimation of the real time cost in terms of computation and memory requirements. Some parallel floating point computing is available for the ADSP 21020 DSP. Therefore, the processing time can be estimated by the number of real multiplications per input point needed to implement the algorithms (final square root operation is not considered). Table II shows these relevant parameters. The number of DSP's has been evaluated considering two main assumptions. The first one is that incoming data lines have 4096 samples with a PRF equal to 1678 Hz and the second one is that the

Table I. Simulation results

Parameters	FFC	Pre-FFC	Unf	Spe	Spe2D
Ratio azi/rng	32/8	40/8	39/8	41.5/8	41.5/6.7
ENL	24	21.5	23.7	23.2	23.2
ISLR (dB)	-16.5	-15.4	-17.3	-17.3	-16.2
SR azi (pix) SR rng (pix)	1.20 1.21	1.29 1.27	1.25 1.26	1.21 1.26	1.21 1.23
Time (s)	763	403	570	140	101

Table II. Estimated computational costs

Parameters	FFC	Pre-FFC	Unf	Spe	Spe2D
#Mul/input	74	33	47	15	6
#DSP	20	9	13	4	2
Memory req.*	high	high	low	low	low

* high represents more than 16 Mbyte, low less than 1 Mbyte

DSP uses a 25 MHz clock rate.

The same number of looks in azimuth and range has been extracted by all the algorithms for the calculation of Table II (24 looks). Nevertheless, each algorithm is specially efficient under different conditions. More particularly, the unfocused method is not very convenient for azimuth multilooking, which turns it into a very time-consuming procedure.

In a more general analysis, a comparison of the algorithm performances over a broad range of resolutions is illustrated. As the maximum number of available looks is different for each algorithm (pre-filtering stages decrease multilook capability), two scenarios are compared: the first one with single look processing and the other with maximum number of looks.

In the first case, Fig. 1 shows that Specan-based techniques are the least time-consuming and FFC is the most expensive method. That is due to the total spectrum computation that FFC produces independently of the desired number of looks. On the contrary, Specan-based techniques carry out a much more efficient multilook extraction as said previously.

For the second scheme, Fig. 2 describes the expected computational load when maximum number of looks are processed (optimum quality). Early down-sampling stages reducing the available number of looks cause the Pre-FFC and unfocused methods to be the least adequate. In contrast, Specan techniques provide a very good trade-off between computation requirements and multilook achievement.

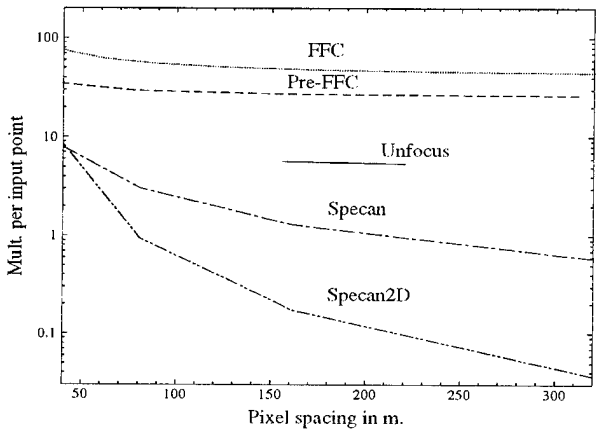


Fig. 1. Multiplications per input point (one look)

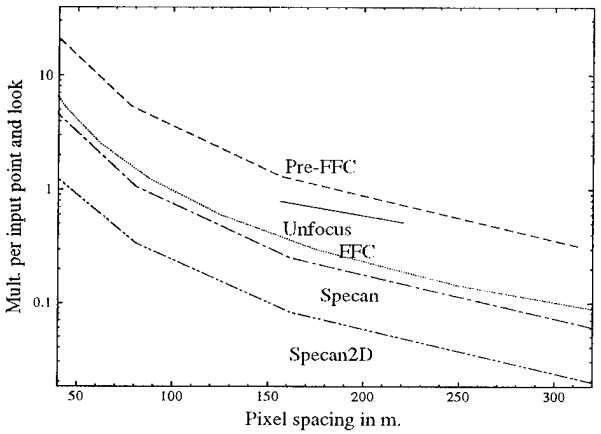


Fig. 2. Multiplications per look and input (maximum looks)

CONCLUSIONS

The main purpose of this paper has been to identify and evaluate several algorithms for on-board medium resolution imagery. It appears that FFC techniques are very accurate, but they require high computation efforts and a large amount of memory. On the contrary, unfocused processing offers a very simple method when restricted resources are available, although it presents main limitations on resolution and multilooking. Finally, Specan-based techniques offer the best compromise between quality and computational load. They do not require large storage, need fewer number of operations and offer acceptable image quality. Specan in both dimensions turns out to be the most suitable choice for on-board imagery and it is also appropriate for multi-swath data processing.

It is concluded that on-board SAR medium resolution image generation, producing an important data rate reduction and direct image distribution, will be feasible with the new technology developed by ESA. The next step in the development of an on-board SAR system will be the definition of an architecture based on four DSP's and the implementation of the selected algorithm.

REFERENCES

[1] J. C. Curlander and R. N. McDonough, Synthetic Aperture Radar Systems and Signal Processing, 1st. ed. New York: Wiley, 1991, pp. 154-209, 487-496.

[2] M. Sack, M. R. Ito and I. G. Cumming, "Application of efficient linear FM matched filtering algorithms to synthetic aperture radar processing", IEE Proc. Pt. F, vol. 132, No. 1, pp. 45-57, February 1985.

[3] A. Martínez, J. L. Marchand, "Implementation and Quality Analysis of a CSA SAR Processor", in Proc. IGARSS'93 vol. 3, pp 1179-1181, August 1993.

Interferometric Analysis of Multifrequency and Multipolarization SAR Data

K. P. Papathanassiou and J. R. Moreira

Deutsche Forschungsanstalt für Luft- und Raumfahrt (DLR)
Institut für Hochfrequenztechnik, P.O. Box 11 16, D-82230 Weßling, Germany
Phone: +49-8153-28-2367, FAX: +49-8153-28-1449, E-mail: Kostas.Papathanassiou@dlr.de

Abstract - - This paper gives a first insight into the evaluation of multifrequency and multipolarisation data in repeat-pass SAR interferometry. A method for "coherence synthesis" i.e. for the calculation of the interferometric coherence for any possible combination of the polarimetric state of the transmitting and the receiving antennas between the two passes is presented. First results of the application of this technique indicate the potential of the application of polarimetric techniques in interferometry.

INTRODUCTION

The phase of a radar signal received from a resolution cell can be composed of two different parts. The first one is of a deterministic nature, which results from the distance between the center of the resolution cell and the antenna, and is proportional to the ratio of the distance to the wavelength. The second part is a statistical contribution, which results from the interaction of the transmitted signal with the scatterer inside the resolution cell, and has the effect of a random phase shift. Illuminating the same area with two antennas from different spatial locations and, therefore different look angles leads, to the assumption that the statistical phase shift is about the same for both received signals. Their phase difference is deterministic and corresponds to the path difference of both signals. This phase difference is called interferometric phase.

INTERFEROMETRIC COHERENCE

The interferometric coherence corresponds to the normalized mean complex product of both complex signals s^1 und s^2 and is defined as:

$$\gamma = \frac{< s^1 s^{2^*} >}{\sqrt{< s^1 s^{1^*} >< s^2 s^{2^*} >}} \qquad (1)$$

where $< ... >$ means the expectation value and * is the complex conjugation operator. The absolute value of the interferometric coherence varies between 0 and 1. The coherence is a maximum ($\gamma = 1$) if both signals are identical, and vanish ($\gamma = 0$) if the signals do not correlate. The decorrelation of the signals is caused by several factors:

- The different look angles for both signals correspond to different parts of the range reflectivity spectra of the scatterer. The bigger the difference of the look angles, the smaller the common part of the reflectivity spectra in both signals and ergo their coherence [1],[2]. The same effect occurs in the azimuth direction where different squint angles coresponds to different azimuth Doppler spectra.
- Additive noise in either signal, e.g. thermal noise or receiver noise, leads to a reduction of the coherence.
- Processing artifacts and defocusing contribute to both systematic and random errors.
- Volume scattering effects introduce a "randomness" in the phase and reduce the coherence.

If the two signals are not received at the same time but at different times during two nearly exact repeating passes over the same area the following additional temporal decorrelation effects decrease the coherence:

- changing of the scattering geometry within the resolution cell during the time between the two acquisitions,
- changing of the physical properties of the scattering mechanisms during the time between the two acquisitions,
- changing of the behaviour of the propagation medium (atmospheric effects).

The amount of temporal decorrelation describes processes occurring on size scales on the order of the signal wavelength with a time resolution defined by the repeat time interval. This sensitivity of the coherence for changes in the characteristics of the scattering mechanisms in time can be used for the understanding and the detection of a wide variety of scattering and penetration processes.

COHERENCE MAPS

For these investigations, data from the Space Shuttle-borne SIR-C/X-SAR radar system which was flown twice in 1994 are used. SIR-C/X-SAR provided for first time imaging in three different frequencies (L-, C-, and X-band) and multipolarization (in L- and C-band). Data from the Tien Shan test site acquired on October 8 and 9, 1994 (data takes 122.20 and 154.20) were provided by NASA/JPL as single-look complex SAR images. The image area is near the southeastern edge of lake Baikal in Russia (latitude: 52.16°, longitude: 106.67°). Fig. 1. shows the C-band SAR image of this region in HH polarisation..

Before forming the interferogram the complex image pair was separately filtered: a) spectral-shift range filtering was applied in order to minimize baseline-induced decorrelation and b) filtering to a common Doppler band in the azimuth direction was applied to eliminate decorrelation due to the Doppler centroid difference between the two images. After coregistration using the maximum spectrum method, the interferogram was formed by multiplying the first image with the complex conjugate of the second, and then filtered using an average window size of

0-7803-3068-4/96$5.00©1996 IEEE

5 (in range) and 7 (in azimuth) in order to reduce the phase noise. The coherence images are evaluated from equation (1) using an average window of 5 resolution cells in range and 5 in azimuth. Fig. 2. shows the coherence maps in C-band using HH-polarization for both images. Fig. 3. shows a coherence map in the L-band generated also from images having HH-polarization. Fig. 4. shows the coherence map in the L-band obtained by using HV-polarization for both images. Finally Fig. 5. shows a coherence map in L-band obtained by using HH-polarization for the first image and VV-polarization for the second image. The areas of high coherence observed in the interferograms generated from the combination of HH- and VV-polarization stem from the fact that the scattering centers producing these areas, though different in the two polarizations, are correlated (hence coherent) to each other over the time between the two observations. This first results demonstrate very clear the strong dependency of the coherence on the polarisation.

COHERENCE SYNTHESIS

For polarimetric radar systems we obtain a measured 2x2 complex scattering matrix $[\mathcal{S}]$ for each resolution element. The knowledge of the scattering matrix in one polarization basis permits the calculation of the corresponding scattering matrix for any other orthogonal (X,Y)-polarisation basis.

$$[\mathcal{S}]_{XY} = [\mathcal{U}]^T [\mathcal{S}]_{HV} [\mathcal{U}] \qquad (2)$$

where $[\mathcal{U}]^T$ is the transposition of $[\mathcal{U}]$. $[\mathcal{U}]$ is a complex 2x2 unitary transformation matrix defined by:

$$[\mathcal{U}] = \frac{1}{\sqrt{1+\rho\rho^*}} \begin{bmatrix} exp(j\psi_A) & -\rho^* \, exp(j\psi_B) \\ \rho \, exp(j\psi_A) & exp(j\psi_B) \end{bmatrix} \qquad (3)$$

ρ is defined as the polarization ratio and can be expressed in terms of the orientation angle χ (which varies from $-90°$ to $90°$) and the ellipticity angle ϕ (which varies from $-45°$ to $45°$) of the polarization ellipse as follows:

$$\rho = \frac{\cos 2\phi \; sin 2\chi + j \sin 2\phi}{1 + \cos 2\phi \; \cos 2\chi} \qquad (4)$$

The phases ψ_A and ψ_B represent the absolute-zero phases of the new polarimetric basis. Their absolute knowledge is not important because it is not characteristic for the polarization state of the wave. But from the interferometric point of view it is important to use the same phases for the transformation of both scattering matrices. For the present investigation we set $\psi_A = \psi_B = 0$. Hence, the unitary transformation matrix $[U]$ is expressed in terms of the complex polarization ratio ρ.

The possibility of transforming the scattering matrix in any orthogonal polarimetric basis thus permits the calculation of the interferometric coherence for any possible polarimetric combination of the transmitting and receiving antennas between the two interferometric passes. Analogous to the "polarization synthesis" technique, that permits the calculation of received power for any possible combination of the polarimetric state of the transmitting and receiving antennas. Thus we can speak here about "interferometric coherence synthesis". Fig. 6. shows a "synthesized" coherence map in L-band produced from an interferogram which is generated from images having left-hand circular polarization. The "coherence synthesis" gives the possibility to apply polarimetric techniques in the interferometric analysis. This would improve the classification of different scattering mechanisms as well as the determination of the optimal polarisation which gives the highest coherence and hence the most accurate phase for DEM generation. Analysis on the available SIR-C data shows strong effects but allows no clear interpretation due to residual uncertainties in the polarimetric callibration. Proper calibration of the data is required to fully exploit the potential of polarimetric repeat pass interferometric data.

CONCLUSIONS

The coherence analysis of the polarimetric data shows some problems, which are still unclear. We suppose that these problems are due to the insufficient accuracy of the polarimetric calibration. Further studies about the dependence of the coherence on the polarization and frequency and on a more exact treatment of the scattering mechanisms are being carried out. We see the great potential of full-polarimetric and multi-frequency repeat pass interferometry as these first results have shown. Full-polarimetric and two frequency repeat-pass interferometric radar systems can be optimally developped to be a accurate and powerfull tool for land classification and DEM generation. First results with multifrequency interferometric data have demonstrate an accurate generation of DEMs and classification maps using both L- and X-band frequencies.

REFERENCES

[1] C. Prati, F. Rocca, "Use of the Spectral Shift in SAR Interferometry", *Proc. of the First ERS-1 Symposium*, Cannes, pp. 691-696, November 1993.

[2] F. Gatelli, A. Monti-Guarnieri, F. Pasquali, C. Prati, F. Rocca, "The Wavenumber Shift in SAR Interferometry", *IEEE Trans. on Geoscience and Remote Sensing*, Vol. 32, No. 4, pp. 855-863, Juli 1994.

[3] C. Prati, F. Rocca, "Focusing SAR Data with Time-Varying Doppler Centroid", *IEEE Trans. on Geoscience and Remote Sensing*, Vol. 30, No. 3, pp. 550-559, May 1992.

[4] M. Schwäbisch, D. Geudtner, "Improvement of Phase and coherence Map Quality Using Azimuth Prefiltering: Examples from ERS-1 and X-SAR", *Proc. of IGARSS'95*, Firence, pp. 205-207, 1995.

[5] A. Gabriel, R. Goldstein, "Crossed Orbit Interferometry: Theory and Experimental Results from SIR-B", *International Journal of Remote Sensing*, vol. 9, No. 5, pp. 857-872, 1988. A. Gabriel, R. Goldstein, "Crossed Orbit Interferometry: Theory and Experimental Results from SIR-B", *International Journal of Remote Sensing*, vol. 9, No. 5, pp. 857-872, 1988.



Fig. 1. C-band SAR Image (HH-polarisation)

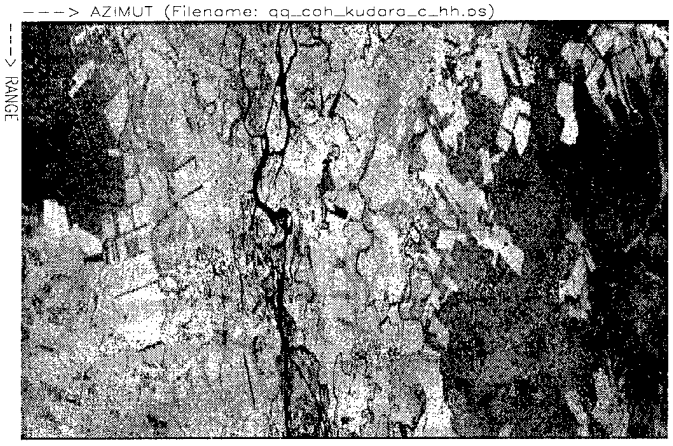


Fig. 2. C-band coherence map (Image 1: HH Image 2: HH)

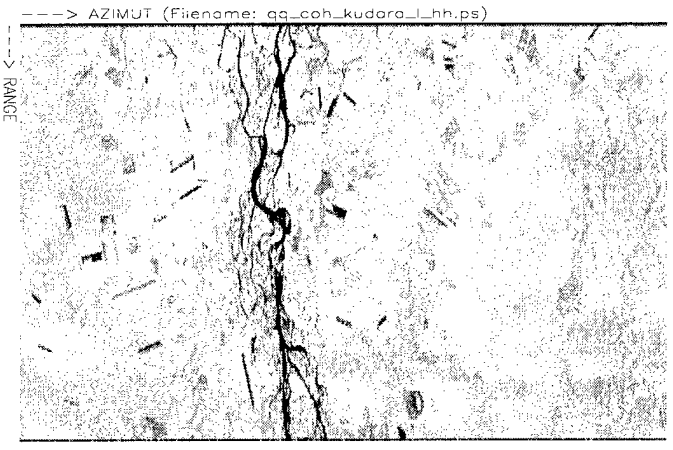


Fig. 3. L-band coherence map (Image 1: HH, Image 2: HH)



Fig. 4. L-band coherence map (Image 1: HV Image 2: HV)



Fig. 5. L-band coherence map (Image 1: HH Image 2: VV)

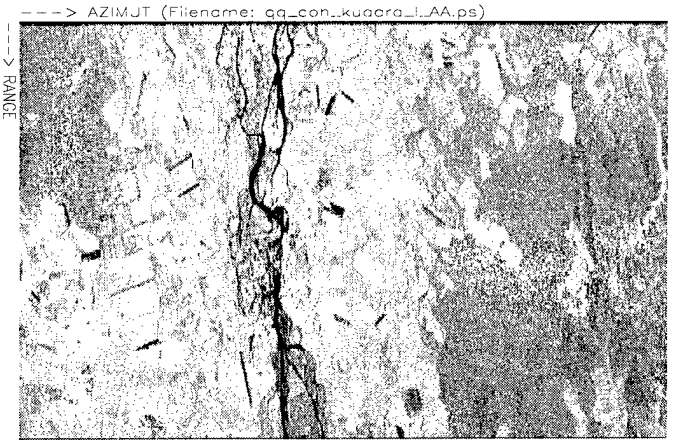


Fig. 6. L-band coherence map (Image 1: ○○ Image 2: ○○)

Autofocus of Wide Azimuth Angle SAR Images by Contrast Optimisation

F. Berizzi, G. Corsini, M.Diani, M. Veltroni

Department of Information Engineering, University of Pisa
Via Diotisalvi 2, I-56126 Pisa, Italy - Phone: +39-50-568511,
Fax: +39-50-568522, E-mail: gcorsini@iet.unipi.it

Abstract - In this paper, we address the problem of focusing Synthetic Aperture Radar (SAR) images for wide azimuth angle of observation. In these applications a second order polynomial approximation does not accurately fit the phase term due to the platform motion. Therefore, image focusing requires higher order polynomial approximation. We propose a simple and effective autofocusing method based on the contrast optimisation of the image. We also present and discuss simulation results to illustrate the effectiveness of the method.

INTRODUCTION

Synthetic Aperture Radar (SAR) imaging requires the estimate of the platform motion parameters to determine the phase term necessary for the azimuth compression. The commonly used approach is to model the phase term due to the motion as a second order polynomial depending on two parameters f_{DC} and f_r [1]. These parameters represent the Doppler spectrum centroid and the Doppler frequency rate, respectively; f_{DC} can be estimated according to different methods such as clutterlock techniques (CDE) and Sign Doppler Estimation (SDE), while f_r can be evaluated by means of autofocus techniques such as subaperture correlation method. In the case of wide observation angle , as can occur in Spot-light SAR, or in Strip-map SAR when a wide azimuth antenna beamwidth is used, a second order polynomial approximation does not accurately fit the phase term due to the motion. In these applications (Wide Azimuth Angle SAR imaging), it is necessary to consider higher order polynomial approximations.

In this paper, the typical Spot-light SAR geometry is considered [2],[3]. During data collection, the sensor steers its antenna beam to continuosly illuminate the surface patch being imaged. Hence, real antenna beamwidth does not limit the variation of the aspect angle as in Strip-map SAR; so that, finer azimuth resolution is achievable. However, as the variation of aspect angle increases, a second order polynomial fitting does not accurately approximate the phase term due to the motion and higher order polynomials must be considered. Because of the trajectory symmetry the phase term due to the motion is approximated as a polynomial where only the even order terms are retained.

In the sequel, the effects of the fourth order term on the pulse response of the imaging system are investigated and a criterion is proposed to determine the maximum allowable phase error. Then, a method for the image focusing based on the estimation of the coefficients of the second and fourth order phase terms is proposed. The method makes use of an imaging system response model depending on two coefficients α, β. The estimates of α and β are obtained by maximising a measure of the focusing efficiency: the contrast of the image.

0-7803-3068-4/96$5.00©1996 IEEE

SPOT- LIGHT SAR SIGNAL MODEL

A Spot-light SAR receives energy backscattered from a multitude of scatterers in the illuminated area A (Fig.1). The Fourier Transform of the received signal complex envelope $S_R(t_n,f)$ can be expressed by [2]:

$$S_R(t_n,f)=S_T(f)\int_A f(\underline{x})e^{-j2\pi(f+f_0)\frac{2|\underline{R}(\underline{x},t_n)|}{c}}d\underline{x}\ rect\left(\frac{t_n}{T_{obs}}\right) \quad (1)$$

where $S_T(f)$ is the complex envelope of the transmitted signal; $t_n=nT_R$ (T_R is the pulse repetition interval) is the time at which the n-th pulse is transmitted (slow time); $|\underline{R}(\underline{x},t_n)|$ is the distance from the antenna phase centre (APC) to the scatterer located at the point $\underline{x}$ in the system of coordinates shown in Fig. 1; $f(\underline{x})$ is a complex function related to the backscattering coefficient of the illuminated surface.

By introducing the following approximation:

$$|\underline{R}(\underline{x},t_n)|\cong|\underline{R}(\underline{O},t_n)|+\underline{x}\bullet\frac{\underline{R}(\underline{O},t_n)}{|\underline{R}(\underline{O},t_n)|} \quad (2)$$

where $|\underline{R}(\underline{O},t_n)|$ is the distance from the APC to the origin $\underline{O}$ of the system of coordinates fixed on the scene, we have:

$$S_R(t_n,f)=S_T(f)e^{-j2\pi(f+f_0)\frac{2|\underline{R}(\underline{O},t_n)|}{c}}\int_A f(\underline{x})e^{-j2\pi\underline{x}\bullet\underline{X}}d\underline{x}\ rect(t_n/T_{obs}) \quad (3)$$

where $\underline{X}\equiv(X_1,X_2)=\frac{2(f_0+f)}{c}\ \frac{\underline{R}(\underline{O},t_n)}{|\underline{R}(\underline{O},t_n)|}$.

Equation (3) highlights that $S_R(t_n,f)$ can be related to the Fourier Transform of $f(\underline{x})$. So that, a smoothed version of $f(\underline{x})$ (SAR image) can be obtained by removing the phase

term due to the motion of the APC and by taking the inverse Fourier Transform of the result. In the sequel, we will not account for the problem of the range curvature will be considered in the definition of the imaging algorithm.
For the sake of simplicity, let us consider an ideal point scatterer located in the origin $\underline{O}$, and assume that a cosinusoidal signal is transmitted. In this case, we have $f(\underline{x})=\delta(\underline{x})$, $S_T(f)=\delta(f)$ and (3) becomes:

$$S_R(t_n,f)=\delta(f)\,e^{-j2\pi f_0\frac{2|\underline{R}(\underline{O},t_n)|}{c}}\,rect\left(t_n/T_{obs}\right) \quad (4)$$

To estimate the distance $|\underline{R}(\underline{O},t_n)|$, we consider its Taylor's approximation where only the even order terms are retained because of the trajectory symmetry:

$$|\underline{R}(\underline{O},t_n)|=R_0+\alpha t_n^2+\beta t_n^4+\Theta(t_n^6) \quad (5)$$

where $\alpha=v^2/2R_0\,;\beta=-v^4/8R_0^3$

To investigate the effects of the fourth order term in (5), let us refer to the plot of Fig.2. It shows the SAR images obtained for different values of the maximum phase variation $\Delta=\pi f_0 v^4 T_{obs}^4/\left(64cR_0^3\right)$ when α is exactly known. In the plot, the amplitude is scketched as a function of $x_1/\Delta x_1$, where Δx_1 is the azimuth resolution given by $\Delta x_1=2X_{obs}/\lambda R_0$ [4]. Note that, as Δ increases, the main lobe widens and its amplitude decreases so that the spatial resolution gets worse. The effects of the fourth order term can be neglected if the maximum phase variation is less than $\pi/2$.
So, when the system is designed to obtain very high azimuth resolution, as in Spot-light SAR with wide variation of the aspect angle, the fourth order term must be removed.

FULL-FOCUSING OF SAR IMAGES

To remove the phase term due to the motion of the APC with respect to the centre of the illuminated area, we propose an iterative procedure based on the following steps:
i) trying to compensate the phase by multiplying $S_R(t_n,f)$ by the term $\exp\left(j4\pi(f+f_0)(\alpha t_n^2+\beta t_n^4)/c\right)$, where α and β are the first guess of the second and the fourth order coefficients respectively;
ii) constructing a trial image $I(x_1,x_2,\alpha,\beta)$ by means of the Inverse Fourier Transform;
iii) calculating a functional of the image that represents the degree of focus of the image;
iv) adjusting α and β and repeating the steps i) - iii) until the degree of focus is maximum.
We have chosen the contrast of the image as the functional representing the degree of focus.
The contrast is defined as the coefficient of variation of the image intensity, i.e. the ratio between the standard deviation and the mean of the image intensity:

$$C(\alpha,\beta)=\frac{\sqrt{E\left\{\left(I^2(x_1,x_2,\alpha,\beta)-E\left[I^2(x_1,x_2,\alpha,\beta)\right]\right)^2\right\}}}{E\left[I^2(x_1,x_2,\alpha,\beta)\right]}. \quad (6)$$

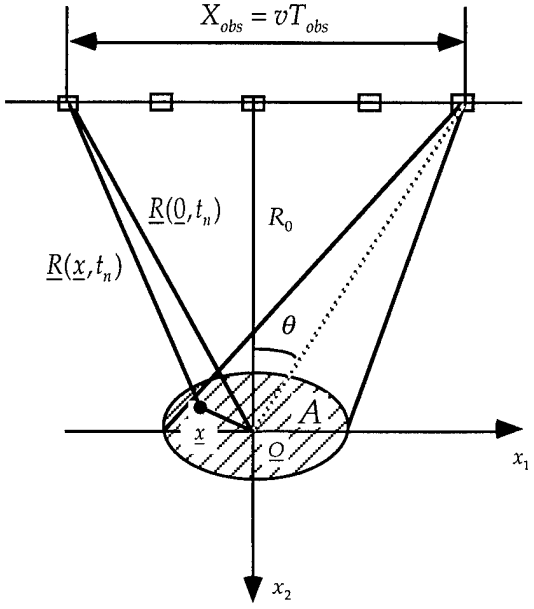


Fig. 1 *Spot-light SAR - Geometry of the system.*

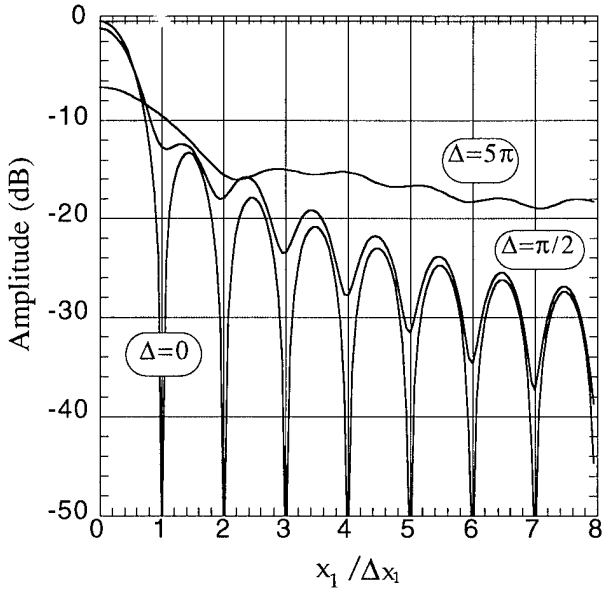


Fig. 2 *Fourier Transform of* $\exp\left(j2\pi kt_n^4\right)$ *rect*(t_n/T_{obs}) *for different values of* Δ.

Fig.3 shows the plot of the contrast of the image as a function of α and β. The location of the absolute maximum of $C(\alpha,\beta)$ can be easily estimated. The function does not present any other relative maxima and then iterative

procedure can be successfully applied to locate the absolute maximum. Extensive simulation trials show that the contrast presents one well distinguishable absolute maximum if a dominant scatterer is imaged by the radar.

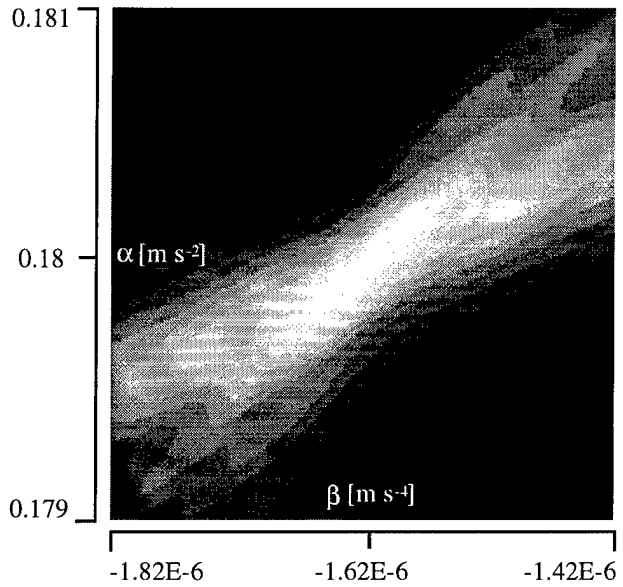


Fig. 3 *Contrast of the image as a function of the second and fourth order coefficients. The grey level (from 0 to 15) represents the normalised contrast of the SAR image.*

NUMERICAL RESULTS

An example of simulation results is shown in this section to demonstrate the effectiveness of the proposed technique .
The example discussed refers to a set of data relevant to an airborne Spot-light SAR. The height of platform flight is 10 Km, the wavelength λ is 6 cm and a total variation of the aspect angle is about 8°. In this condition, the theoretical cross-range resolution is about 0.25m and the values of α and β are respectively 0.18 m/s^2 and -1.62 10^{-6} m/s^4.The contrast shown in Fig. 3 refers to this operating condition. It is easy to recognise that $C(\alpha,\beta)$ has the absolute maximum in correspondence of the aforementioned values of α and β. The function has been calculated for discrete values of α and β and the sampling rate has been chosen by fixing the maximum allowable phase error. We fixed a maximum phase error of $\pi/2$ both for the second order and the fourth order phase term. Fig.4 represents the SAR image obtained by compensating the second order phase term and the fully-focused one reconstructed by using the autofocusing method . Note that the amplitude of the full-focused image is about 5 dB higher and the width of the main lobe is roughly halved. So, the spatial resolution is significantly improved and a better quality of the final image is obtained.

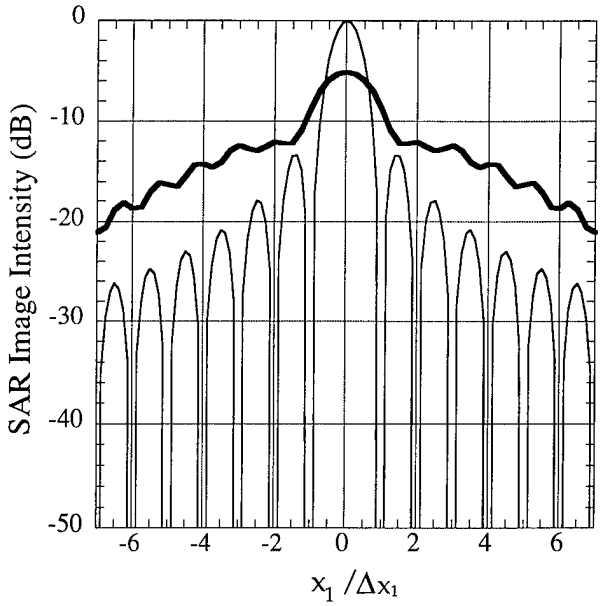


Fig. 4 *SAR image obtained by compensating the second order motion phase term (marked line) compared with the fully-focused image obtained by using autofocusing method (thin line).*

CONCLUSIONS

In this paper, we have proposed a simple and effective method to focus Wide Azimuth Angle SAR images. The method is based on the maximisation of the contrast that we have chosen as a measure of the degree of image focus. The contrast depends on two parameters representing the coefficients of the second and fourth order terms of the polynomial that approximates the phase due to the APC's motion. Simulation results show the effectiveness of the method when a dominant scatterer is present inside the illuminated scene. In detail, the compensation of the fourth order term allows a significant improvement of the spatial resolution and an enhancement of the image quality due to contrast optimisation.

REFERENCES

[1] J.P. Curlander, R.N. MC Donough, "Synthetic Aperture Radar," John Wiley and Sons Inc., New York., 1991.

[2] W. G. Carrara, R. S. Goodman, R. M. Majewski, "Spotlight Synthetic Aperture Radar, "Artech House, London, 1995.

[3] D. Munson, "Tomographic Formulation of Spotlight-mode Synthetic Aperture Radar", Proceedings of the IEEE, Vol. 71, no. 8, August 1983, p. 917-925.

[4] D.A. Ausherman, A. Kosma, J. L. Walker, H.M. Jones, E.C. Poggio, "Development in radar imaging," IEEE Trans. on Aereospace and Electronic System, Vol. AES-26, no. 4, July 1984, p.363-400.

High Frequency Phase Errors in SAR Imagery and Implications for Autofocus

Nick Marechal
The Aerospace Corporation
Radar and Signals Systems Department
2350 E. El Segundo Bl.
El Segundo, CA 90245-4691
E-mail:marechal@seal.aero.org

ABSTRACT

The subject of this paper is the characterization of high frequency phase errors in synthetic aperture radar (SAR) imagery formed using the polar format processing approach and the implications for autofocus. A mathematical model for the phase error is reviewed which illustrates the dependency of the phase error on range wavenumber as well as azimuth wavenumber. In the case of a single sinusoidal phase error, it is shown that the resulting paired echoes have a characteristic two-dimensional (2D) appearance. This implies that for sufficiently high phase error frequencies the associated autofocus problem is 2D, that is the phase error is a function of range and azimuth wavenumbers. Radars operating at long wavelengths and fine resolution, such as a 1 meter resolution L-band system, are the most likely candidates to produce imagery having 2D phase error.

INTRODUCTION

A key ingredient to the formation of a synthetic aperture radar (SAR) image is the time for the transmitted signal to propagate to the illuminated scatterers and back to the sensor as a function of the pulse reception time. In general one has, with some level of fidelity, *a priori* knowledge of that two-way travel time based on radar motion measurements and electromagnetic propagation models. However, the accuracy of the two-way travel time data may not be perfect leaving unmodeled "phase errors" which in turn degrades the contrast or focus of the image. The phase error can be decomposed into low order polynomial type functions and higher frequency sinusoidal components, each having a different effect on the appearance of the image. For example a travel time bias error leads to a quadratic phase error which broadens the main lobe and raises the "near in" sidelobes of the azimuth (i.e., cross range) impulse response response of the SAR, which when focused has a $\sin(y)/y$ characteristic. In this paper, the effects of high frequency phase errors on the appearance of the radar image and the implications to phase error estimation and removal (i.e., autofocus) are studied. High frequency errors can emerge for example from unmodeled antenna jitter or a turbulent ionosphere. The amplitude of those errors may be only a small fraction of the wavelength corresponding to the radar transmit center frequency.

SAR image formation using polar format processing as described by Walker [1], Brown [2], Ausherman, et al. [3] is assumed in this paper. That technique was developed as a solution to the range cell migration problem associated with SAR image formation. It is based on the fundamental observation that *the range compressed, Fourier transformed and motion compensated data, corresponding to reception of a single pulse, is the 3D Fourier transform of the reflectivity density evaluated in the radar line of sight direction $\vec{u}$ over the wavenumber segment* $\mid k - 4\pi/\lambda \mid \leq \pi/\Delta x$, [1-2]. The wavelength $\lambda = c/f_0$ is defined in terms of the transmit center frequency f_0 and the speed of light c, while Δx denotes the range resolution. The classical image model for a single sinusoidal phase error in SAR data is one in which paired impulse response echoes (and their harmonics) appear and the phase error is a function of azimuth wavenumber alone. In the case of polar format processed SAR data the classical model applies so long as the number of phase error cycles does not exceed approximately twice the ratio of the transmit center frequency to the transmit bandwidth as will be reviewed here. Otherwise the phase error is effectively a function of azimuth *and range* wavenumber. The 2D dispersion of the echo energy was first communicated in an unpublished

0-7803-3068-4/96$5.00©1996 IEEE

report by Melzer [4], with antenna jitter the assumed error source. In that report, the peak of the dispersed echo amplitude is computed as a function of the sinusoidal antenna jitter frequency. That analysis is in contrast to the classical theory in which the (relative) peak echo amplitude is given by the simple formula $(4\pi/\lambda)(a/2)$ where a is the amplitude of the sinusoidal motion projected onto the radar line-of-sight direction. In [4] the term "relief" is used in reference to the reduced peak echo amplitude associated with the echo energy dispersion. With that terminology the point is made in [4] that the relief increases (i.e. the peak echo amplitude decreases) with the sinusoidal phase error frequency.

Over the last several years there has been increasing interest in nonparametric phase error estimation. The phase gradient autofocus algorithm (PGA) Eichel, Ghiglia, and Jakowatz [5], Eichel, Jakowatz [6] is perhaps the best known nonparametric approach. PGA was introduced in 1989 as a technique to remove phase error as a function of azimuth wavenumber. Subsequent to the first PGA papers, Ghiglia and Mastin [7] pointed out that 2D phase error problems exist in optics and astronomy and "anticipated" that a 2D PGA approach would be needed for SAR as well. Indeed, if for example the range impulse response has elevated sidelobes due to an imperfect radar waveform generator one is motivated to perform a 2D focus. One of the main points made in this paper is that a 2D focus is needed for sufficiently high frequency sinusoidal (slow time) phase errors, unless the phase error is estimated and removed prior to the polar to rectangular interpolation step of polar format processing. Furthermore, autofocus algorithm testing on radar imagery which has been injected with simulated phase errors depending on azimuth wavenumber alone can give the mistaken impression that a 1D error estimator will remove errors whose bandwidth is limited only by the image azimuth width, [8]. A theoretical 1 meter resolution, L-band example is presented here in which it is observed that 65 and 130 cycle phase error sinusoids cause the mainlobe width of the corresponding impulse response *echoes* to be on the order of 10 and 20 resolution widths in each coordinate direction, respectively. This example is in contrast to the classical theory in which the echo main lobe widths do not exceed approximately 2 resolution units. It is also apparent from the model that there is less 2D energy dispersion in imagery generated with a radar operating at a higher radar frequency (e.g., Ku band) and thus there may be little need to use a 2D autofocus on imagery generated from data collected by a radar operating at a higher radar frequency. To this author's knowledge these points have not been made elsewhere in the literature.

In the sections that follow, the high frequency phase error model is reviewed and is used to 1) establish a rationale for deciding when a 2D focusing approach is needed, based on the maximum phase error bandwidth which is to be removed for a given radar transmit wavelength and range resolution and 2) introduce the concept of an *ad hoc* "bow tie" image domain filter (as opposed to a filter which is unity over a subimage rectangle) to be used as part of the sampling associated with the 2D PGA approach. The intent of the bow tie filter is to reject the noise (principally radar receiver noise and unwanted clutter), where the signal corresponding to the phase error is small.

Finally, there is some reason to expect that the energy dispersion effect is not limited to the case of imagery formed using the polar format processing technique. In polar format processing the phase of a point scatterer at the center of the scene imaged is matched as part of the motion compensation which acts as the range cell migration corrector as well [3]. That other image formation approaches ideally correct for range cell migration and match the phase of a point scatterer implies that a phase error would be subject to signal processing which is similar to the polar format technique. Thus there is the potential for the occurrence of echo energy dispersion using other image formation techniques. This is an area for future investigation.

PHASE ERROR MODELING

In this section we review the equations which lead to a phase error model, as a prelude to the next section. As mentioned in the introduction polar format image formation processing is assumed. The phase error is shown to be a function of both range and azimuth wavenumbers, and one observes that the phase error sensitivity to range wavenumber increases with the number of phase error cycles over the synthetic aperture.

Time Dependent Phase

To begin, let $\vec{u}(t)$ be the unit vector which points from the antenna to the center of the scene imaged for a given pulse at "slow time" t. Let the interval $[-T/2, T/2]$ denote the coherent integration period (i.e., the time to form the synthetic aperture) and define the following "slant plane" unit basis vectors:

$$\vec{u}_x = \vec{u}(0) \tag{1}$$

$$\vec{u}_z = \frac{\vec{u}_x \times \vec{v}}{\|\vec{u}_x \times \vec{v}\|} \tag{2}$$

$$\vec{u}_y = \vec{u}_z \times \vec{u}_x \tag{3}$$

where $\vec{v}$ is the velocity of the SAR at $t = 0$, and $\vec{u}_x$, $\vec{u}_y$, $\vec{u}_z$ are the unit range, azimuth and slant plane normal vectors, respectively. The center of the scene imaged is taken to be the origin of the coordinate system spanned by the basis vectors defined above. It has been shown [3] that the wave number vector $\vec{k}$ sampled by the SAR on a pulse-to-pulse basis is given by

$$\vec{k} = k\,\vec{u}(t) \tag{4}$$

where the scalar k varies over the wavenumber segment $\mid k - 4\pi/\lambda \mid \leq \pi/\Delta x$, Δx is the range resolution of the radar, and t is the time the pulse is received. In preparation for the following analysis define the wavenumber components of $\vec{k}$

$$\frac{4\pi}{\lambda} + k_x = \vec{k}\cdot\vec{u}_x \tag{5}$$

$$k_y = \vec{k}\cdot\vec{u}_y \tag{6}$$

$$k_z = \vec{k}\cdot\vec{u}_z\ . \tag{7}$$

With the definitions above, a general expression for the phase error ε due to a range error $\Delta r(t)$ (equivalent to an unmodeled two-way travel time error) is given by

$$\varepsilon = -\|\vec{k}\|\,\Delta r \tag{8}$$

$$= -\sqrt{(\frac{4\pi}{\lambda}+k_x)^2 + k_y^2 + k_z^2}\ \Delta r \tag{9}$$

$$\simeq -\left[\frac{4\pi}{\lambda} + k_x + \frac{1}{2}\frac{k_y^2+k_z^2}{\frac{4\pi}{\lambda}+k_x}\right]\ \Delta r. \tag{10}$$

Within the brackets of equation (10) there are various terms involving the wavenumbers which have significance when the range error $\Delta r(t)$ is in some sense large. For example, the presence of the k_x term shows that a range bias error will cause the image to be translated in the range direction by an amount equal to the bias. The quotient term containing k_y^2 in the numerator will be a source of image defocus. Nominally, the SAR line of sight vector $\vec{u}(t)$ is contained in the slant plane for every t during the coherent integration period, in which case $k_z = \vec{u}_z \cdot \vec{u}(t) = 0$.

For the purpose of analytical modeling of sinusoidal range errors which are on the order of a wavelength λ, the following approximation to the phase error is used

$$\varepsilon \simeq -\frac{4\pi}{\lambda}\,\Delta r(t)\ . \tag{11}$$

However, for numerical work on a computer the equation (9) can be used without approximation. The next step is to model time as a function of range and azimuth wavenumbers k_x and k_y.

Time as a Function of Wavenumber

A necessary step in the derivation of the high frequency phase error model is to express (slow) time t as a function of the wavenumbers k_x and k_y. That this part of the derivation is necessary is attributed to the polar format processing approach to image formation which is assumed in this paper. Let θ represent the polar or "viewing" angle associated with the line of sight vector $\vec{u}(t)$ in the slant plane defined by the range and azimuth unit vectors $\vec{u}_x$ and $\vec{u}_y$, respectively. Then equations (12-13) below hold by definition and the subsequent equations (14-16) follow from small angle and geometric series approximations

$$\theta = \arctan\left(\frac{\vec{u}(t)\cdot\vec{u}_y}{\vec{u}(t)\cdot\vec{u}_x}\right) \tag{12}$$

$$= \arctan\left(\frac{k_y}{\frac{4\pi}{\lambda}+k_x}\right) \tag{13}$$

$$\simeq \frac{k_y}{\frac{4\pi}{\lambda}+k_x} \tag{14}$$

$$= \frac{\lambda}{4\pi}\,\frac{k_y}{1+\frac{\lambda}{4\pi}k_x} \tag{15}$$

$$= \frac{\lambda}{4\pi}k_y\left[1 - \frac{\lambda}{4\pi}k_x + \cdots\right]\ . \tag{16}$$

To facilitate analytic modeling, assume that the view angle $\theta = \alpha\, t$ with a constant angular rate α. Then $t = \theta/\alpha$, and with the expression for θ given above one obtains time t as a function of the range and azimuth wavenumbers k_x and k_y. One will find it useful to express the angular rate α in terms of the coherent integration time T, azimuth resolution Δy and transmit wavelength λ as follows. The relation between azimuth resolution and the total change in view angle β is given by $\beta = \lambda/2\Delta y$ so that $\alpha = \beta/T = \lambda/2\,T\,\Delta y$. Thus the relation for (slow) time as a function of range and azimuth wavenumbers, resolution, transmit wavelength and integration time can be expressed as

$$t(k_x, k_y) \simeq \frac{T}{2\pi}\,\Delta y\, k_y\left[1 - \frac{\lambda}{4\pi}k_x\right]\ . \tag{17}$$

At this point it is worth mentioning that the extent to which the classical 1D paired echo theory and the 2D theory presented here are different is attributed to the term containing the product $k_x\,k_y$ in equation (17). The wavenumber-time relation will be used in the next section where the image of the phase error is studied in detail.

PHASE ERROR IMAGE

The "image" of a point scatterer at the center of the im-

age scene is given as the (inverse) 2D Fourier transform of the complex exponential of the phase $\varepsilon(\, t(k_x, k_y)\,)$. Denote the (inverse) 2D Fourier transform of a function g by

$$\mathcal{F}[g] = \int\int e^{\,i(x\,k_x + y\,k_y)}\; g(k_x, k_y)\; dk_y\; dk_x. \qquad (18)$$

Then the image of a point scatterer in the presence of a phase error ε is given as

$$\begin{aligned} image &= \mathcal{F}\left[h_x h_y e^{i\varepsilon}\right] && (19)\\ &\simeq \mathcal{F}\left[h_x h_y\,(1 + i\varepsilon)\right] && (20)\\ &= \mathcal{F}\left[h_x h_y\right] + i\mathcal{F}\left[h_x h_y \varepsilon\right] && (21) \end{aligned}$$

where h_x and h_y are the range and azimuth SAR frequency response functions which include the finite bandwidth and weightings (e.g., Hanning). Equations (20-21) are a first order approximation to the image model (19). The finite bandwidth is defined by the the wavenumber limits, $|\, k_x \,| \leq \pi/\Delta x$ and $|\, k_y \,| \leq \pi/\Delta y$, with Δx and Δy the range and azimuth resolutions, respectively. The first term on the right side of (21) is by definition the image of a point scatterer in the absence of phase error, while the second term represents *the weighted 2D Fourier transform of the phase error.* Other higher order terms involving $\varepsilon^2, \ldots$ account for harmonics (echoes corresponding to integer multiples of the sinusoidal phase error frequency). As an example the Fourier transform (19) is computed and displayed in Figure 1 for a hypothetical 1 meter resolution, L-band (i.e., λ =.25 meters) SAR, with 65 cycles of sinusoidal phase error whose amplitude is $3\lambda/100$. Observe that the echo energy is dispersed, or spread, over a rectangular region. Figure 2 is obtained from the image of Figure 1 as an azimuth pixel sampling of the image at the range pixel corresponding to the range impulse response peak. Notice that the echoes are approximately 18 dB down from the peak of the azimuth impulse response and that the harmonics are more than 40 dB down. In general the harmonics are unlikely to be observable against a clutter background for small phase error levels.

2D Paired Echoes

In the previous section an expression for (slow) time as a function of range and azimuth wavenumbers was derived (17). Once the phase error has been expressed as a function of wavenumber, the Fourier transform (19) is computed to observe the effect of the phase error on the image as in the example presented in Figure 1. In this section the first order approximation (20-21) to (19) is used to further study sinusoidal phase errors as they emerge in the image domain.

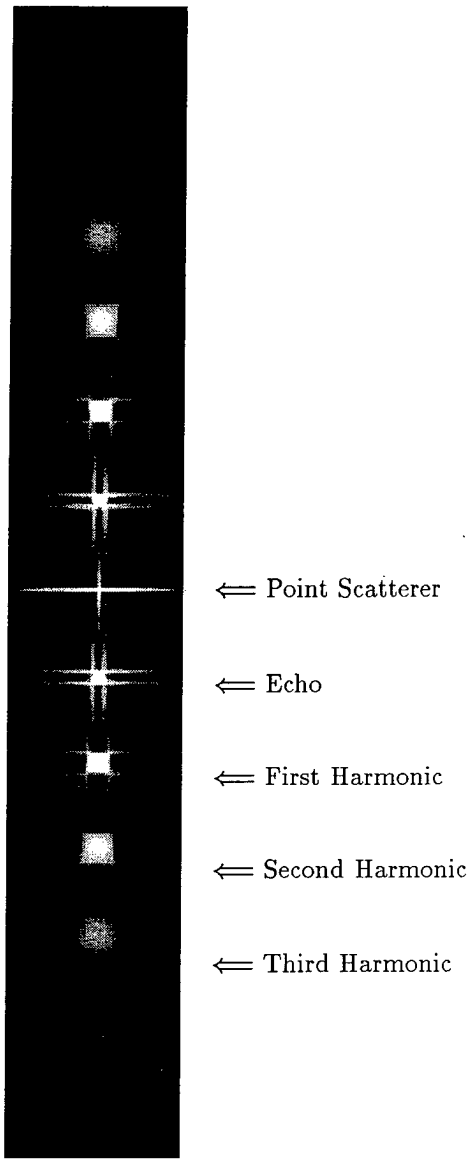


Figure 1. The image of a point scatterer with a 65 cycle sinusoidal phase error whose amplitude is $3\lambda/100$ with λ = .25 meters and 1 meter resolution.

In general the range error $\Delta r(t)$ has a Fourier series representation

$$\Delta r(t) = \sum a_n\, \cos(2\pi\nu_n t + \xi_n) \qquad (22)$$

where ν_n is the sinusoidal phase error frequency in units of Hertz. It is sufficient to consider a single sinusoidal term from the expansion above and deduce its image domain characteristics, as the general case involving all of the terms in the series is obtained by superposition, pro-

vided that the harmonic terms are negligible as discussed above.

Consider the complex exponential form of a single sinusoidal phase error from equation (22). Then equation (11) for the phase error is

$$\varepsilon(t) \simeq -\frac{4\pi}{\lambda}\,\frac{a}{2}\left[e^{i(2\pi\nu t+\xi)} + e^{-i(2\pi\nu t+\xi)}\right]. \qquad (23)$$

From the equations (19) and (23) it is apparent that one always has a symmetric pair of echoes, one for each complex sinusoid. In Figures 2 and 3 we observe that 65 and 130 cycle phase error sinusoids cause the width of the corresponding impulse response *echoes* to be on the order of 10 and 20 resolution units, respectively. This an example of the 2D echo energy dispersion discussed in the introduction. Next the 2D Fourier transform of one of the complex sinusoids (23) is studied in detail to further develop an analytic characterization of the echo energy dispersion.

Given that time t is a function of range and azimuth wavenumbers, either echo image is given by

$$echo\ \ image = -i\frac{4\pi}{\lambda}\,\frac{a}{2}\,e^{\pm i\xi}\mathcal{F}\left[h_x h_y\, e^{\pm i2\pi\nu t}\right]. \qquad (24)$$

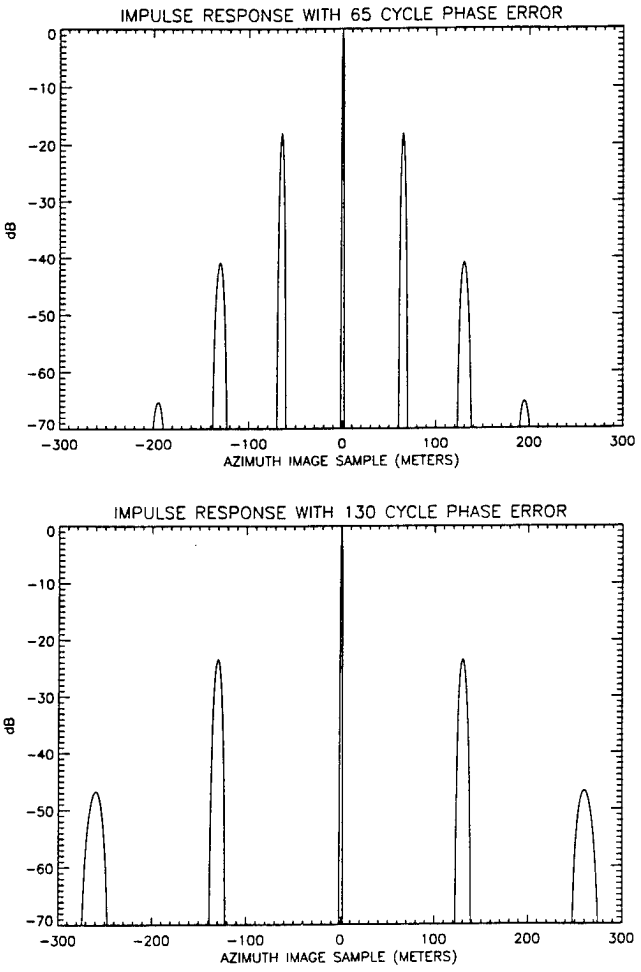
As in the classical paired echo theory, one observes that the echo brightness relative to the point scatterer is proportional to the ratio of the phase error amplitude a to the wavelength λ. Consider the argument of the complex exponential which is integrated as part of Fourier transform (24) and the approximation for time as a function of wavenumber (17)

$$2\pi\nu t(k_x,k_y) \simeq T\nu\Delta y\,k_y\left[1-\frac{\lambda}{4\pi}\,k_x\right] \qquad (25)$$

$$= y_\nu k_y - \frac{\lambda}{4\pi}\,y_\nu\,k_x\,k_y \qquad (26)$$

and $y_\nu = T\nu\Delta y$. The first phase term on the right side of equation (26) is linear and therefore determines the azimuth pixel location of the echo; it is displaced $y_\nu = T\nu\Delta y$ distance units from the point scatterer's azimuth location (or $T\nu$ azimuth resolution units Δy). The second term in (26), involving $k_x\,k_y$, accounts for the echo energy dispersion which is shown below.

The range and azimuth dimensions of a rectangle which contain the bulk of the dispersed echo energy will be determined as the intersection of two rectangles each centered on the echo of interest whose sides are parallel to the the coordinate axes. One rectangle will be shown to have range and azimuth dimensions X and A, respectively, with $X < A$. The other rectangle will have azimuth and range dimensions dimensions Y and R, respectively, with $Y < R$. Then the intersection of the two rectangles is also rectangle centered on the echo with dimensions $X \times Y$. The argument involves interchanging the order of the two integrations associated with the 2D Fourier transform (24).



Figures 2 and 3. Figure 2 (top) is obtained from the point scatterer image of Figure 1 as an azimuth pixel sampling of the image at the range pixel corresponding to the range impulse response peak. That simulated image was generated with a 65 cycle sinusoidal phase error whose amplitude is $3\lambda/100$ with $\lambda = .25$ meters and 1 meter resolution. Figure 3 (bottom) is obtained similarly with 130 phase error cycles.

Performing the first integration with respect to range wavenumber k_x causes an azimuth wavenumber dependency in that the range impulse response peak location is displaced by $\lambda\, y_\nu\, k_y\, /4\pi$. The maximum displacement of the range impulse response peak occurs at the azimuth wavenumber limits $\pm\pi/\Delta y$. Thus the range dimension X of the rectangle containing the dispersed energy is twice the maximum displacement

$$X = 2\, y_\nu \frac{\pi}{\Delta y} \frac{\lambda}{4\pi} = T\nu \frac{\lambda}{2}\,. \tag{27}$$

This relation is derived using the definition of the echo azimuth location $y_\nu = T\nu\Delta y$, with T the coherent integration time and ν the sinusoidal phase error frequency. Conceptually, the 2D Fourier transform calculation is completed by the second integration which is with respect to azimuth wavenumber. At this point one concludes that the echo energy is dispersed over a rectangle whose range dimension is X as defined in (27) and whose azimuth dimension is bounded from above by the azimuth width A of the image.

The dimensions of the second rectangle are determined by first integrating the 2D Fourier transform (24) with respect to azimuth wavenumber. Then the azimuth dimension Y of the rectangle containing the dispersed echo energy is twice the maximum displacement of the azimuth impulse response peak

$$Y = 2\, y_\nu \frac{\pi}{\Delta x} \frac{\lambda}{4\pi} = T\nu \frac{\Delta y}{\Delta x} \frac{\lambda}{2}\,. \tag{28}$$

One concludes that the echo energy is dispersed over a second rectangle whose azimuth dimension is Y as defined in (28) and whose range dimension is bounded from above by the range width R of the image.

It has therefore been shown that the bulk of the dispersed echo energy is contained in the rectangle whose dimensions are $X \times Y$. The range and azimuth dimensions of the echo in resolution units are given as

$$\frac{X}{\Delta x} = T\nu \frac{\lambda}{2\Delta x} \tag{29}$$

and

$$\frac{Y}{\Delta y} = T\nu \frac{\lambda}{2\Delta x}\,, \tag{30}$$

respectively. Thus the sides of the rectangle containing the echo energy, measured in resolution units, are equal [4]. As an example consider the same hypothetical L-band, 1 meter resolution system in which $\lambda/2\Delta x = 1/8$. Then 65 cycles of sinusoidal phase error causes the energy to disperse over a rectangle whose dimensions are $X/\Delta x = Y/\Delta y = 65/8 \simeq 8$ resolution units. Refering to Figure 2 one visually estimates that the echo energy is spread over 7 to 10 pixels which is in good agreement with the analytical result (30). It is also interesting to note that not only does the azimuth position of the echo imply the number of phase error cycles, $T\nu$, but so does either dimension of the of the 2D echo (rectangle), if it is fully observable through the clutter.

AUTOFOCUS AND IMAGE FILTERING

The echo energy dispersion model derived in the previous section motivates one to ask the question: What is the maximum phase error frequency which an autofocus algorithm can be expected to remove given that the error estimate is a function of azimuth wavenumber alone (i.e., no echo energy dispersion is modeled)? A reasonable criteria is that the echo energy corresponding to the maximum phase error frequency, ν_{max}, should not disperse by more than 2 range resolution units. Refering to (29), that occurs when the number of cycles, $T\nu_{max}$, of sinusoidal phase satisfies the following inequality

$$\frac{X}{\Delta x} = T\nu_{max} \frac{\lambda}{2\Delta x} \geq 2\,. \tag{31}$$

A rearrangement of terms gives the following expression for the maximum number of phase error cycles over the synthetic aperture

$$max\ cycles \leq \frac{4\Delta x}{\lambda}\,. \tag{32}$$

For a hypothetical L-band, 1 meter resolution system in which $\Delta x/\lambda = 4$ the maximum number of cycles is 16, which for a 10 second integration period implies ν_{max} =1.6 Hz maximum phase error frequency. To contrast the L-band example, with the case of a 0.3 meter resolution, Ku band ($\lambda = .02$ meters) system, one computes $\Delta x/\lambda = 15$ which according to (32) implies a 60 cycle upper bound.

2D Image Filtering

In the case where the number of cycles of phase error exceeds criterion (32) the autofocus problem is 2D, that is the phase error estimate depends on both azimuth and range wavenumbers as previously shown. In that case a 2D PGA approach [7] is appropriate. In the broadest sense, 2D PGA involves the sampling of many subimage rectangles centered on the best targets (e.g., locally the brightest), and a subsequent weighted averaging of many realizations of the phase gradient (as a function of wavenumber) derived from those samples.

The dimensions of the sampled rectangle of image data determines the bandwidth of the phase error estimate, because the image domain is essentially the spectral domain of the phase error, as can be observed from (19-21). If one has an *a priori* upper bound on the number of phase error cycles, then it is natural to set the azimuth width of the rectangle equal to twice that number of cycles plus $Y/\Delta y$ as defined in (30). The range dimension of the rectangle is set equal to $X/\Delta x$ as defined in (29). The incentive for minimizing the passband of the "rectangular filter" is to reduce the noise power admitted into the subsequent PGA estimation process.

Further noise suppression is achieved by "down weighting " that part of the subimage rectangle which contains very little of the phase error spectrum. Based on (19-21) and the Fourier series (22) for the range error, the power spectral density function of the signal $h_x h_y \exp(i\varepsilon)$ is approximated as

$$\mathrm{E}\left[\left|\mathcal{F}\left[h_x h_y e^{i\varepsilon}\right]\right|^2\right] \simeq \left|\mathcal{F}\left[h_x h_y\right]\right|^2 + \left(\frac{2\pi}{\lambda}\right)^2 \sum_{|m|\geq 1} \mathrm{E}\left[a_m^2\right] \left|\mathcal{F}\left[h_x h_y\, e^{i2\pi\,\nu_m\, t}\right]\right|^2 \qquad (33)$$

where E[w] denotes the expectation of the random variable w, and it is assumed that the phase shifts ξ_m appearing in (22) are uniformly distributed on $[-\pi, \pi]$ and are pairwise uncorrelated. Based on equation (33) and the preceding analysis regarding the dispersion of echo energy, one concludes that the bulk of the phase error energy is contained in a "bow tie" shaped region. Then an *ad hoc* approach to suppress unwanted clutter and receiver noise from the estimate is to define a filter which is unity on the interior of the bow tie and is zero elsewhere. Figure 4 is an example of such a filter (with some smoothing applied). In that case the bow tie region is defined according to

$$|\,x\,| \leq \mathrm{int}\left[\frac{\lambda}{4\Delta x}\;|\,y\,|\right] + \frac{1}{2}\,, \qquad (34)$$

where x and y are the number of range and azimuth resolution cells, respectively, and int[w] means truncate to the largest integer less than w. This leads to a filter which is one range cell wide at its center, where the dispersion is negligible, and spreads out in range as a function of azimuth just enough to admit the majority of the phase error spectral energy. The integrated noise power within the sampled subimage rectangle is reduced approximately by a factor of 2 with the bow tie filter.

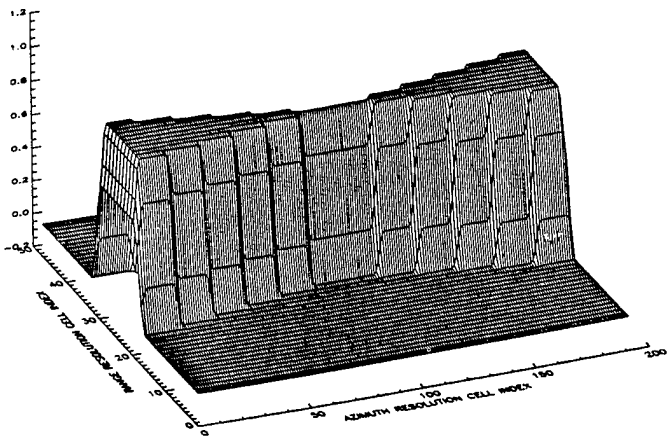


Figure 4. The bow tie filter reduces the clutter and receiver noise power in regions where the phase error power spectrum is known to be small.

CONCLUSIONS

For sufficiently high frequency (slow time dependent) phase errors the SAR autofocus problem is 2D, that is the phase error is estimated as a function of range as well as azimuth wavenumber. Whether or not one needs to be concerned about 2D phase error depends on: 1) the bandwidth of the phase error to be removed, and 2) the ratio of the range resolution to the transmit wavelength for the specific SAR system considered. In particular small wavelength systems (e.g., Ku band) are the least susceptible to the 2D phenomenon. Long wavelength systems (e.g., L band) are the most susceptible and are most likely to need a 2D autofocus. If a given autofocus problem is 2D, then there is an established 2D PGA approach for estimating the phase error as a function of range as well as azimuth wavenumber. Finally, when a 2D PGA algorithm is used for the purpose of removing high frequency phase errors (depending on slow time alone), it was proposed that a "bow tie" filter be used to reduce the noise power of the data within each of the sampled subimage rectangles by a factor of two.

ACKNOWLEDGEMENTS

This author expresses thanks to his colleagues Richard Dickinson and Samuel D. Gasster for helpful discussions and suggestions during the preparation of this paper. Appreciation is also expressed to The Aerospace Corporation for supporting this research.

REFERENCES

1. J. L. Walker, "Range doppler imaging of rotating objects," IEEE Trans. on Aero. and Elect. Syst., vol. AES-16, pp. 23-52, January 1980.

2. W. M. Brown, "Walker model for radar sensing of rigid target fields," IEEE Trans. on Aero. and Elect. Syst., vol. AES-16, pp. 104-107, January 1980.

3. D. A. Ausherman, A. Kozma, J. L. Walker, H. M. Jones, E. C. Poggio,"Developments in radar imaging," IEEE Trans. on Aero. and Elect. Syst., vol. AES-20, no. 4, pp. 363-399, July 1984.

4. S. Melzer,"Spotlight synthetic aperture radar systems analysis," Aerospace Technical Operating Report, TOR-0081 (6527-30), September 1981. Refer to Appendix A concerning paired echoes.

5. P. H. Eichel, D. C. Ghiglia, C. V. Jakowatz Jr.," Speckle processing method for synthetic-aperture radar phase correction," Optics Letters, vol. 14, no. 1, pp. 1-3, January 1, 1989.

6. P. H. Eichel, C. V. Jakowatz Jr.,"Phase-gradient algorithm as an optimal estimator of the phase derivative," Optics Letters, vol. 14, no. 1, pp. 1101-1103, October 15, 1989.

7. D. C. Ghiglia, G. A. Mastin," Two-dimensional phase correction of synthetic-aperture radar imagery," Optics Letters, vol. 14, no. 20, pp. 1104-1106, October 15, 1989.

8. D. E. Wahl, P. H. Eichel, D. C. Ghiglia, C. V. Jakowatz Jr.," Phase gradient autofocus-A robust tool for high resolution SAR phase correction," IEEE Trans. on Aero. and Elect. Syst., vol. AES-30, no. 3, pp. 827-835, July 1994.

9. M. Soumekh, J. Choi,"Phase and amplitude phase restoration in sythetic aperture radar imaging," IEEE Trans. on Image Processing, vol. 1, no. 2, pp. 229-242, April 1992.

Phase Errors Compensation in SAR Imaging

Tommaso Isernia[1-2], **Vito Pascazio**[3], **Rocco Pierri**[4], **Gilda Schirinzi**[2]

[1]Dipartimento di Ingegneria Elettronica, Università di Napoli *Federico II*
via Claudio, 21 - 80125 Napoli - Italy, ☎ +(39)-81-7683512 fax +(39)-81-5934448, E-mail: isernia@die003.dis.unina.it
[2]Istituto di Ricerca per l'Elettromagnetismo e i Componenti Elettronici, Consiglio Nazionale delle Ricerche
Via Diocleziano 328, 80124 Napoli, Italy, ☎ +(39)-81-5707999 fax +(39)-81-5705734, E-mail: schiri@irece1.irece.na.cnr.it
[3]Istituto di Teoria e Tecnica delle Onde Elettromagnetiche, Istituto Universitario Navale
Via A. Acton 38, 80133 Napoli, Italy, ☎ +(39)-81-5513976 fax +(39)-81-5512884, E-mail: pascazio@nava1.uninav.it
[4]Dipartimento di Ingegneria dell'Informazione, Seconda Università di Napoli
via Roma, 29 - 81031 Aversa - Italy, ☎ +39-(0)81-5044035, fax +39-(0)81-5045804, E-mail: pierri@uxing2.sunap.unina.it

Abstract -- The problem of SAR imaging when only phase corrupted raw data are available is addressed. Results on real data, when polynomial phase errors are used, are also presented. The presented method is able to compensate for both 1D and 2D phase errors.

INTRODUCTION

SAR imaging problem amounts to find a finite resolution estimate of the ground reflectivity function. It is known that unwanted deviations of the platform carrying the SAR antenna from the nominal trajectory, or turbulence effects affecting the propagation in the troposphere, or phase instability in the receiver apparatus, can induce o,ly phase errors [1] on the received SAR signal, so heavily affecting the accurate focusing of the final images. Conventional processing of these phase corrupted data provides defocused or blurred images.

We present a new method to accurately reconstruct a Synthetic Aperture Radar (SAR) complex image starting from phase errors affected raw received data, based on the inversion of the non linear relationship between the raw data square amplitude distribution and the unknown complex reflectivity of the scenario [2]. As the unknown complex reflectivity is found by minimizing a proper functional, the resulting problem is a non quadratic optimization problem, so that, in the general case, the functional can exhibit, in addition to the desired global minimum that provides the required solution, local minima providing false solutions (traps). However, starting from the knowledge of phase corrupted received raw data, we can determine by a linear inversion a useful initial guess for the iterative procedure. In fact, conventional processing of these phase corrupted data provides defocused or blurred images, which belong, under common conditions, to the attraction region of the global minimum, so that the occurrence of local minima is avoided. Note that, even assuming lack of local minima, ill-conditioning problems must be dealt with.

Numerical results on real data show that the focusing of the recovered images is very accurate, even if the corrupted initial image is significantly different from the ideal one.

THEORY

We consider the problem of an extended object of complex-amplitude reflectance, imaged with a coherent imaging system with known point spread function (PSF). In the following, we will make reference to SAR systems. Results will anyway serve as a basis for other coherent imaging systems.

The complex signal received by the SAR antenna can be expressed [3] by equation:

$$h(x',r') = \iint \gamma(x,r)\; g(x'-x, r'-r; x, r)\; dx\, dr, \qquad (1)$$

where (x,r) and (x',r') are the azimuth and range co-ordinates on the ground and on board, respectively, γ is the complex reflectivity coefficient of the imaged scene, and g is the system space-variant PSF (SVPSF), depending on the electronic, geometrical, and kinematic parameters of the SAR system, whose Fourier transform (the system transfer function needed for the image computing) can be analytically evaluated [3]. If the scene dimension is sufficiently small [3], the space variance of g can be neglected, and the imaging system acts like a linear filter with a space-invariant PSF (SIPSF); in this case Eqn. (1) reduces to a convolution:

$$h(x,r) = [\gamma \otimes g](x,r) = \mathcal{G}\gamma, \qquad (2)$$

where $\otimes$ indicates two dimensional convolution, and $\mathcal{G}$ is the linear operator linking the ground reflectivity function to the received data. In the following, for the sake of simplicity, we consider the SIPSF case. The extension of the treatment to the SVPSF case is straightforward and requires only a marginal increase in computational complexity [3].

In this ideal case, SAR imaging is a *linear* inverse problem and consists in inverting Eqns. (1) (or (2)) in order to find the unknown object function. Unfortunately, phase errors on the received signal, due, for instance, to unwanted deviation of the platform carrying the SAR antenna from the nominal trajectory, or to turbulence effects affecting the propagation in the troposphere, or to phase instability in the receiver apparatus, can greatly affect the accurate focusing of the final image. In particular, it can be shown that if the motion instability of the flying platform is not very large [1], only the phase of the received signal is affected, so that the phase perturbed received signal is given by:

$$h_m(x',r') = h(x',r')\; \exp[j\vartheta(x',r')], \qquad (3)$$

where ϑ represents the phase term induced by motion instability and/or turbulence effects. According to Eqn. (3) the amplitudes of the ideal received signal h and of the phase corrupted received signal h_m are the same, while their

0-7803-3068-4/96$5.00©1996 IEEE

phases are different. Also note that by virtue of the $\exp[j\vartheta(x',r')]$, h and h_m have got different bandwidths. For this reason, the magnitude information present in the phase error affected received data can be hopefully exploited to develop alternative image focusing techniques. To this end, define $\mathcal{B}$ the operator performing the square amplitude of $\mathcal{G}\gamma$

$$\mathcal{B}\gamma = (\mathcal{G}\gamma)(\mathcal{G}\gamma)^* = |\mathcal{G}\gamma|^2, \tag{4}$$

where * denotes complex conjugation. The SAR imaging problem can be stated as finding $\tilde{\gamma}$, a *finite resolution* estimate of γ, belonging to a finite dimension functional space Γ, satisfying

$$\mathcal{B}\gamma = |h|^2 = |h_m|^2. \tag{5}$$

It has to be noted that the link between the unknown function γ and the data $|h_m|^2$ is non linear, in other words, no linear transfer function exists between the image intensity and any property (complex amplitude or intensity) of the object.

As h is essentially bandlimited, and the full knowledge of $h = \mathcal{G}\gamma$ would allow conventional SAR processing, problem (5) is analogous to a PR problem for a bandlimited function (h) from its intensity distribution ($|h_m|^2$). However, a solution to (5) could not exist at all, so that the problem is intrinsically ill-posed. This implies that the inversion has to be performed in a generalised sense, that is, by finding the global minimum of a proper functional. If the best fitting concept is used, then the problem can be recast as finding $\tilde{\gamma}$ such that

$$\tilde{\gamma} = \arg \min_{\gamma \in \Gamma} \phi(\gamma), \qquad \phi(\gamma) = \left\| \mathcal{B}\gamma - |h_m|^2 \right\|^2, \tag{6}$$

wherein $\|\cdot\|$ denotes the quadratic norm in the space of the data.

THE SOLUTION ALGORITHM

The sampling of raw data is usually accomplished according to its bandwidth, whose upper bound is given by the known bandwidth of the system unit response g (see Eqn. (2)). However, the phase error affected raw data h_m hve a larger bandwidth so that its reliable sampling implies a finer grid in order to avoid aliasing effects. By virtue of (4) and (5), the available data have twice the bandwidth of phase error free raw data $h = \mathcal{G}\gamma$. Now, define $|h_m|^2$ the discretised versions of $|h_m|^2$. Moreover, let $\hat{\gamma}$ be a pointwise representation of $\gamma \in \Gamma$, sampled, as usual, at the same rate as h. $\hat{\gamma}$ will have a finite number $M \times N$ of complex samples, where M and N are the extensions along the two dimensions of the image. On the other hand, the system PSF g is essentially a band-limited function of finite extension and can be accordingly approximated by $P \times Q$ discrete complex samples. Consequently, $|h_m|^2$, the data of the inverse problem, can be represented in a space of real dimension $2(M+P) \times 2(N+Q)$.

As a consequence of the above, the entire problem can be accurately approximated in finite dimensional spaces.

Then, the discretised problem amounts to finding $\hat{\gamma}$ such that

$$\phi(\hat{\gamma}) = \sum_{l=1}^{2(M+P)} \sum_{s=1}^{2(N+Q)} \left(\boldsymbol{B}\,\hat{\gamma}\big|_{ls} - \left|\hat{h}_m(l,s)\right|^2 \right)^2, \tag{7}$$

where $\boldsymbol{B}$ is the discretized version of $\mathcal{B}$, is globally minimised with respect to $\hat{\gamma}$.

Thanks to the chosen formulation, several consequences relevant to an accurate minimisation of ϕ can be drawn. First, thanks to the quadratic nature of $\mathcal{B}$, whenever the ratio between the essential dimension of the space of data (related to the bandwidth of $|h|^2$) and the essential dimension of the unknowns (related to the bandwidth of $\tilde{\gamma}$) is sufficiently large, it can be argued [4] that local minima problems can be overcome, so that normal *local* (non random) minimisation schemes can be herein utilised with global effectiveness. In the present case, by virtue of the convolution operation involved in $\mathcal{G}\gamma$, the above mentioned ratio assumes a quite large value so that the occurrence of local minima is not very likely.

Moreover, partial information about the phase is available in our case. In fact, the ideal complex received signal is known but for the multiplicative phase term $\exp(j\vartheta)$. Starting from the knowledge of phase corrupted received raw data h_m, we can determine the initial guess of the iterative procedure by the linear inversion of (2):

$$\hat{\gamma}^{(0)} = \boldsymbol{G}^{-1}\hat{h}_m, \tag{8}$$

where $\boldsymbol{G}^{-1}$ is the inverse of the discretized version of $\mathcal{G}$. Processing (8) will provide defocused or blurred images, which, on the basis of the experiments presented in the following Section, will belong, under common conditions, to the attraction region of the global minimum of (7), so that the occurrence of local minima is avoided.

The above mentioned considerations have a twofold effect. On the one hand, the first allows us to deal with a large attraction region of the global minimum (representing the desired focused image). On the other hand, the latter allows us to increase the possibility that the initial guess will be in this attraction region, so further increasing the possibility of the success of the method.

Finally, improved accuracy can be obtained in the neighbourhood of the solution by modifying the functional ϕ through the introduction of weights enhancing the low data values [4], i.e., through the minimisation of the functional

$$\psi(\hat{\gamma}) = \sum_{l=1}^{2(M+P)} \sum_{s=1}^{2(N+Q)} \frac{1}{\left|\hat{h}_m(l,s)\right|^2} \left(\boldsymbol{B}\,\hat{\gamma}\big|_{ls} - \left|\hat{h}_m(l,s)\right|^2 \right)^2. \tag{9}$$

When values $\left|\hat{h}_m(l,s)\right|^2$ are lower than a threshold μ, they are replaced by μ, a fixed amount depending on the numerical precision of the used computer, in the corresponding denominators.

For the minimisation of (7), resort can be made to an iterative scheme of the kind

$$\hat{\gamma}^{(k+1)} = \hat{\gamma}^{(k)} + \lambda_k \underline{\underline{A}}_k \nabla\phi_k, \tag{10}$$

wherein k and $(k+1)$ denote respectively the k-th and $(k+1)$-th iteration, $\nabla\phi$ is related to the gradient of ϕ, and

$\underline{\underline{A}}_k$ is a matrix depending from the adopted minimization scheme. The quadratic nature of $\boldsymbol{B}$ allows the step λ_k to be chosen analytically by solving a third degree equation [4], so that the whole minimisation procedure can be efficiently realised. Also note both $\boldsymbol{B}$ and $\nabla\phi$ can be efficiently computed through FFT and zero padding operations.

Only slight modifications occur when (9) is used in place of (7).

SAR IMAGING EXPERIMENTS AND CONCLUSIONS

Typical numerical results on actual data are now presented. The numerical experiment has been performed by sequentially minimising functional (7) and (9). In agreement with the arguments in [4], this choise exhibited the best performance from the point of view of the reconstructions.

Experiments have been performed on raw data of the German airborne Experimental-SAR (E-SAR). A zoom of a small part of an image of 1550×768 samples, obtained by processing the available actual data is shown in Fig. 1.a. Since the system impulse response function is represented by 450×256 samples, 2048×1024 raw data samples and 4096×2048 intensity data samples, are required.

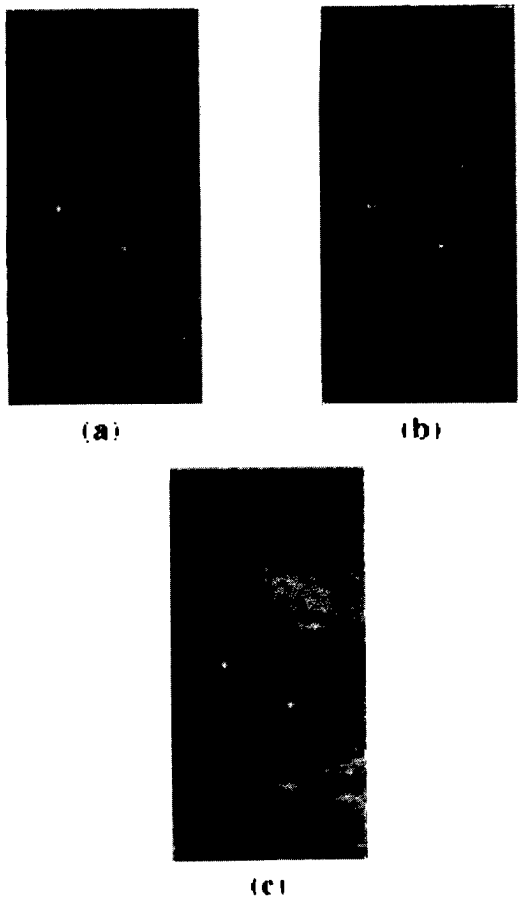


Fig.1: Zoom of a particular of an E-SAR image:
(a) uncorrupted image; (b) defocused image;
(c) reconstructed image.

We consider a one-dimensional (1D) 10-th order polynomial-like phase error, whose maximum value is 10 rad.. This kind of phase error might be expected in the azimuth direction as a result of unwanted deviations from the nominal straight trajectory of the platform carrying the SAR antenna. The same part of the image shown in Fig. 1.a, obtained by corrupting the raw data with the above polynomial phase error is shown in Fig. 1.b. The image recovered by applying the presented method is presented in Fig. 1.c. The focusing of the recovered image of Fig. 1.c is very accurate.

To better show the good quality of the reconstruction, the slice cuts of the image of a single point scatterer are presented in Fig. 2, where ideal, defocused, and reconstructed point target are represented with solid, dashed, and dotted lines, respectively. The defocusing effect produced by the polynomial phase error along the azimuth direction is evident; the reconstruction obtained applying the presented method is almost perfect. As far as the phase is concerned, it has to be noted that the method allows the recover of complex images, thus well compensating the errors also on the image phase, that is even more sensitive than the amplitude to the presence of phase errors on the data. The lack of compensation of these effects can be very critical for those applications requiring an accurate knowledge of the phase (as for instance in interferometric applications).

Note the presented approach is capable of compensating for different kinds of phase errors, both 1D and 2D, unlike other techniques that are based on the assumption that the phase errors depend only on the azimuth co-ordinate.

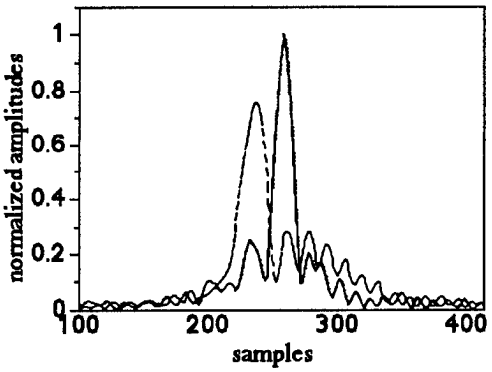


Fig. 2: Slice cuts of a point target image; uncorrupted image; (solid line); defocused image (dashed line); reconstructed image (dotted line)

REFERENCES

[1] T. Isernia, V. Pascazio, R. Pierri, G. Schirinzi, "Image Reconstruction from Fourier Transform Magnitude with Application to SAR Imaging", in print on *J. Opt. Soc. Am. A.*, May 1996.

[2] T. Isernia, V. Pascazio, R. Pierri, G. Schirinzi, "Synthetic Aperture Radar Imaging from Phase Corrupted Data", in print on *Proc. IEE, Radar, Sonar and Navigation.*

[3] G. Franceschetti, R. Lanari, V. Pascazio, G. Schirinzi, "WASAR: a Wide Angle SAR Processor", *Proc. IEE Part F*, **139**, pp. 107-114, 1992.

[4] T. Isernia, G. Leone, R. Pierri, "Phase Retrieval of Radiated Fields", *Inverse Problems*, **11**, pp. 183-203, 1995.

Cirrus Cloud Detection by Micro Pulse Lidar: Algorithm Development and Testing

A. E. Galbraith*, J. A. Reagan*, J. D. Spinhirne**

* Electrical and Computer Engineering, University of Arizona, Tucson, AZ 85721
(520) 621-4768, (520) 621-8076 (fax) , amyg@ece.arizona.edu

** NASA Goddard Space Flight Center, Code 912, Greenbelt, MD 20771
(301) 286-9099, jspin@virl.gsfc.nasa.gov

Abstract -- Micro pulse lidar (MPL) recently has been developed for profiling cloud and aerosol structure over long time periods. MPL offers advantages over previous lidars by providing more horizontal data due to a high pulse repetition rate and long data collection times. The lidar operates at low energy levels (~1 μJ), requiring a more statistical approach for obtaining relevant cloud properties such as cloud base height. Due to the high volume of time versus height backscatter data, an automated algorithm is required. This paper presents an automated algorithm for cirrus cloud detection and develops a simulated cloud model used to test the algorithm. The increased amount of information along the time axis allows one to take advantage of horizontal correlations in the data. Local running standard deviations are taken both vertically and horizontally to determine threshold criteria for cloud boundaries. Image processing techniques are incorporated in the algorithm developed to improve confidence levels in detected cloud boundaries.

INTRODUCTION

Lidar sensing techniques have progressed significantly in the several decades since its inception. Originally, lidar systems were large and lacked eye safety due to high laser pulse energy. However, recent technological advances have led to the development of compact, eye-safe, and relatively inexpensive lidar systems. Eye safety is achieved by reducing the pulse energy, and acceptable signal-to-noise (SNR) ratios are attained by averaging over tens of thousands of pulses, using high pulse repetition rate lasers.

Cirrus clouds are an important factor in global climate studies due to their role in the earth's radiation budget. In particular, global monitoring of clouds is necessary for a more complete understanding of these processes. Lidar systems are ideal for global cloud monitoring, especially thin cirrus, due to their ability to profile the vertical structure and height of clouds. Micro pulse lidar (MPL), developed by Spinhirne at NASA Goddard, is a new type of lidar that uses photon counting detection [1]. Using micro-Joule pulse energies and kilohertz pulse repetition rates, it can profile significant cloud and aerosol features in the atmosphere within a time span of a minute or less. A pulse energy of 1 to 8 μJ is used with a 2500 Hz pulse repetition rate. The data is in the form of a time versus range image, with each pixel representing average backscatter in photoelectrons per microsecond in a 300 meter range bin for an averaging time of one minute. The MPL system is capable of collecting data with higher resolution range bins, but the present software sets a 300 meter bin limit. Each column in the image is one range profile and each row is one time profile.

The first MPL system has been operating since 1992, and has demonstrated full time operation for more than a year. An improved MPL system, MPL-2, has been in operation during the past year at the DOE Atmospheric Radiation Measurement (ARM) Cloud and Radiation Testbed (CART) site in Oklahoma, and has supplied the data used for the work reported in this paper.

A specialized approach is required to process the data from an MPL system. To consistently provide accurate results, a cloud detection algorithm must be automated to handle a high volume of data, it must use the additional information available through horizontal correlations to improve performance, and it must incorporate knowledge of the physical and geometrical characteristics of the expected signal. This paper outlines an automated algorithm for cirrus cloud detection using statistical and image processing methods. A cloud model is developed to simulate the expected received lidar signal. The symposium presentation of the paper will present results of testing the algorithm with simulated and actual lidar data.

LIDAR RELATIONS

The received lidar signal $n(r)$ for one transmitted laser pulse due to atmospheric backscattering from a range bin of length Δr centered at a distance r is given by

$$n(r) = \frac{\lambda \eta_\lambda}{hc} \times \frac{E_0 A_R \, \Delta r \, \beta(r) T^2(r)}{r^2} \quad \frac{PhE}{range\ bin} , \qquad (1)$$

where E_0 is the laser pulse energy centered on wavelength λ, η_λ is the detector quantum efficiency, h is Planck's constant, c is the speed of light, A_R is the effective receiver aperture, $\beta(r)$ is the atmospheric unit volume backscattering coefficient ($m^{-1}sr^{-1}$), and

This work supported in part by NASA Goddard Space Flight Center under contract NCC-05-77.

0-7803-3068-4/96$5.00©1996 IEEE

$T^2(r)$ is the atmospheric round-trip transmittance to range r for wavelength λ. The extinction coefficient $\sigma(r)$ is related to round-trip transmittance by

$$T^2(r) = \exp\left[-2\int_0^r \sigma(r')dr'\right] \quad . \tag{2}$$

The backscatter and extinction coefficients may be expressed as the sum of Rayleigh and aerosol components, given by

$$\alpha(r) = \alpha_R(r) + \alpha_a(r) \tag{3}$$

$$\beta(r) = \beta_R(r) + \beta_a(r) \tag{4}$$

where subscripts denote Rayleigh and aerosol, respectively.

CLOUD MODEL

In order to evaluate the performance of cloud detection algorithms, it is necessary to simulate the lidar signal under the expected conditions of operation. This includes a determination of background values under normal operating conditions for both day and night, defining a cloud model that closely approximates the geometrical and physical properties of cirrus clouds, and inclusion of an accurate noise model.

At the MPL operating wavelength of 523 nm, $\beta(r) \approx \beta_R(r)$ and $\sigma(r) \approx \sigma_R(r)$ may be assumed for clear air conditions in the upper troposphere above ~5 km. Simulations were done which confirmed that predicted and actual signal values closely follow Rayleigh levels between 5 and 10 km [2]. Therefore, a background model close to Rayleigh levels is used in the cloud model for algorithm testing.

A cloud model must consider both physical and geometrical characteristics of cirrus clouds. One defining feature is the magnitude of the return at the cloud peak, or signal increase above clear air levels. Prediction of the average increase above Rayleigh for a cloud boundary was done by analyzing one minute averaged MPL-2 data over several weeks. The increase above Rayleigh for high thin cirrus above 5 km is roughly a factor of 3 to 10 for these data. Another important parameter in the cloud model is the geometrical shape of the cloud (i.e. the sharpness of the transition from clear air to cloud and back again). Several cloud models have been used in the literature [3][4], and appear nearly gaussian in form. For simplicity, a step function model is used as a first approximation, then modified step and gaussian-like models are used to test the algorithm under more realistic conditions. However, the step function model may prove to more accurately simulate the 300 meter data due to its low resolution.

It also is necessary to include an accurate noise model to account for the rapidly degrading signal-to-noise ratio with increasing range. This is done by applying a gaussian noise with zero mean and fixed variance to every range bin in the non-range corrected signal. Suitable noise levels, or desired variances of the random gaussian noise, are determined by using actual MPL data to derive expected signal-to-noise ratios at each range bin. The observed signal to noise ratio at range bin k in height profile j is estimated by

$$SNR_{j,k} = \frac{\overline{n_{j,k}}}{\sigma_{j,k}} \tag{5}$$

where the numerator is the mean of the backscattered lidar signal and the denominator is the standard deviation of the signal. The mean and standard deviation are computed over many samples, typically a total of fifteen time bins. This sample size gives reasonable certainty to the estimates of the mean and standard deviation for a given range bin in the image.

Once the simulated lidar signal has been defined, the algorithm may be quantitatively tested. The SNR required to detect cloud boundaries will be investigated by testing the algorithm with each cloud model defined by expected signal and noise levels determined from MPL-2 data sets.

CLOUD DETECTION ALGORITHM

Previous cloud detection algorithms have taken advantage of the high spatial resolution of data from a particular system [5][6]. When high resolution is available (under 75 m range bin size), differential zero-crossing methods may be applied, which simply look for zero crossings in the slope of the lidar backscatter profile, $dn(r)/dr$. These same algorithms cannot be applied directly to MPL data because a cirrus layer can be relatively small compared to the 300 m range bin size, and the thickness of a cirrus cloud can be as small as one pixel even at a 75 m resolution. The low resolution will require the algorithm to make a cloud boundary decision from one pixel to the next. Therefore, the SNR of a given pixel must be high enough to compare consecutive pixels in a height profile and determine if a boundary has been crossed. A simulation of the expected performance of the system predicts daytime SNR's of ~ 10 to 30, and nighttime SNR's of ~ 40 or greater, for one minute averaging to heights of 10 km [2]. These simulations matched well with computed SNR's for a sample day of data where signal levels were essentially Rayleigh. These SNR's are acceptable for a decision algorithm that uses statistics between individual range bins for cloud detection.

The algorithm may be improved further by using a new adaptive horizontal approach. An adaptive algorithm can take advantage of the horizontal information available in the lidar image. In regions of the image where clouds are slowly changing, the correlation between two height profiles is high. By taking cross-correlations of profiles, several consecutive profiles with high correlation define a region that may be averaged to give a higher SNR or used as a sub-area for a statistically based edge detection test. The degree of correlation required between two

consecutive pulses must allow for some variability in the cloud structure yet be high enough so as to find all transitions between cloud and clear air regions. A similar adaptive approach has been used to find average cloud base heights using temporal averaging that varies to coincide with cloud time duration [4]. However, this approach was used only to average previously determined cloud base heights, while the proposed algorithm takes advantage of the correlations to improve the performance of the edge detection technique used to find the cloud boundaries.

Using the added advantage of determining highly correlated regions, we can define steps for a cloud boundary detection algorithm as follows. First, highly correlated sequences of consecutive profiles are grouped into subareas for edge detection using the process described above. The time indices of each subarea are recorded for use with the edge detection tests. Second, a running horizontal standard deviation is computed for each time profile in the image. We expect that the standard deviation will be small in a clear air region and inside a cloud, but will be much larger at a cloud boundary. Each jump in the horizontal standard deviation is used as a flag to set the condition of being in a cloud or non-cloud region, and a segmentation map is created which indicates a "cloud" or "no cloud" status for each pixel in the image. Third, the resulting correlated regions and segmentation map are used with edge detection to determine if a cloud boundary has been found.

The edge detection is done as a majority decision process based on a series of statistical tests that have proved useful for noisy image applications [7]. Tests include simple thresholding (a cloud must be greater in intensity than background), homogeneity of means and variances, and modality tests. Important features of this edge detection technique are that the tests are not gradient (derivative-based) operators and each individual test can have "yes," "no," and "no decision" outcomes. The final result is based on a majority vote of individual outcomes, and each test is done on small subareas of the image. This edge detection approach may be applied to the cloud boundary problem by defining a subarea based on the highly correlated regions found earlier. Cloud edges may be found by incrementing vertically through each correlated region and doing the edge detection on a two range-bin high by m time-bin wide subarea, where m is the number of consecutive correlated profiles in the current correlated region. If the majority of edge finding tests indicate a boundary, the segmentation map is used to determine if a cloud base or top has been found by comparing the number of "cloud" and "no cloud" pixels on the edge boundary. The reliability of the segmentation map must be analyzed to determine if further refinement to this step of the algorithm is required.

A data flow diagram of the algorithm is shown in Fig. 1. The overall approach of using horizontal correlations and several statistical tests in parallel to determine a final outcome should result in a reliable automated algorithm for cloud boundary detection.

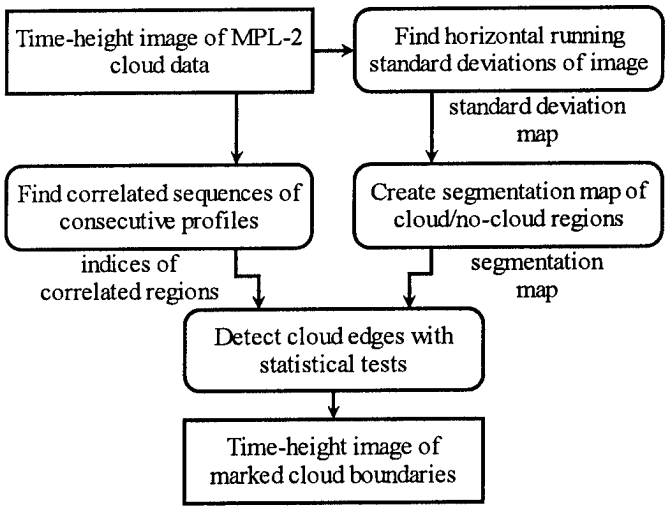


Figure 1. Data Flow Diagram of Cloud Detection Algorithm

FUTURE WORK

Work continues on algorithm development and testing. Additional results from this work including images of MPL lidar data with detected cloud boundaries will be given in the symposium presentation of this paper.

REFERENCES

[1] J.D. Spinhirne, "Micro pulse lidar," *IEEE Trans. Geosci. Remote Sensing*, vol. 31, pp. 48-55, Jan. 1993.

[2] J. A. Reagan, A. E. Galbraith, and J. D. Spinhirne, "Micro Pulse Lidar Daytime Performance: Simulations and Observations ," *Proc. IGARSS '96*, May 1996.

[3] S. A. Young, "Analysis of lidar backscatter profiles in optically thin clouds," *Applied Optics*, vol.34, pp.7019-7031, Oct. 1995.

[4] S. Elouragini, "Useful algorithms to derive the optical properties of clouds from a back-scatter lidar return," *Journal of Modern Optics*, vol. 42, pp. 1439-1446, Oct. 1995.

[5] Pal, Steinbrecht, and Carswell, "Automated method for determination of cloud-base height and vertical extent," *Applied Optics*, vol. 31, pp. 1488-1494, Apr. 1992.

[6] C. M. Platt et al., "The Experimental Cloud Lidar Pilot Study (ECLIPS) for Cloud-Radiation Research," *Bull. Am. Meteorol. Soc.*, vol. 75, pp. 1635-1654, Sept. 1994.

[7] M. Suk and S. Hong, "An Edge Extraction Technique for Noisy Images," *Computer Vision, Graphics, and Image Processing*, vol. 25, pp. 24-45, 1984.

Cloud Masking With Satellite Infrared Images Over Polar Oceans

Norbert Schlueter and Thorsten Markus*
Institute of Environmental Physics, University of Bremen, 28334 Bremen, Germany
Tel.:+49-421-218-2584, Fax:+49-421-218-4555
E-mail: schlue@diana.physik.uni-bremen.de
*Now at NASA Goddard Space Flight Center, Code 971, Greenbelt, MD

Abstract–
The classification of infrared images over polar regions is a difficult task. The algorithm presented in this paper uses the texture features of segments. The classification is done by a neural network. The results are promising. About 90% of the pixels are correctly identified.

Introduction

The importance of clouds in radiative processes, local heat budgets, and the transport of energy is widely recognized In order to study their influence on a global scale or regionally at locations, which are difficult to access, satellite measurements in the visible and infrared spectral range are commonly used. However, in the polar regions the land and sea ice can have the same albedo as the cloud tops and also, because of frequent temperature inversions, the same temperature. Most algorithms applied over the polar regions use combinations of visible and infrared channels [3]. Operational application is therefore restricted to times of solar illumination, so that no measurements are possible during the polar night. The purpose of this study is to develop a cloud masking algorithm which only uses of the infrared channels. This algorithm is based on texture analysis with a neural network. The texture features are calculated for areas which should have the same surface characteristics (open water, ice, clouds) identified with a segmentation procedure.

Data

In this study we use the infrared data of the Operational Linescan System (OLS) onboard the Defense Meteorological Satellite Program (DMSP) satellites. These satellites also carry the passive microwave sensor Special Sensor Microwave Imager (SSM/I). The temporal and spatial coincidence makes the OLS especially suitable for error analysis of SSM/I data because of cloud contamination or multi-sensor approaches. The OLS has two channels, where one is in the visible range (0.4–0.7 μm) and the other in the thermal infrared (10.5–12.6 μm). The resolution is either 0.6 or 2.7 km throughout the entire swath. During daylight the visible channel has an resolution of 0.6 km and the infrared of 2.7 km, during nighttime the resolutions are exchanged.

0-7803-3068-4/96$5.00©1996 IEEE

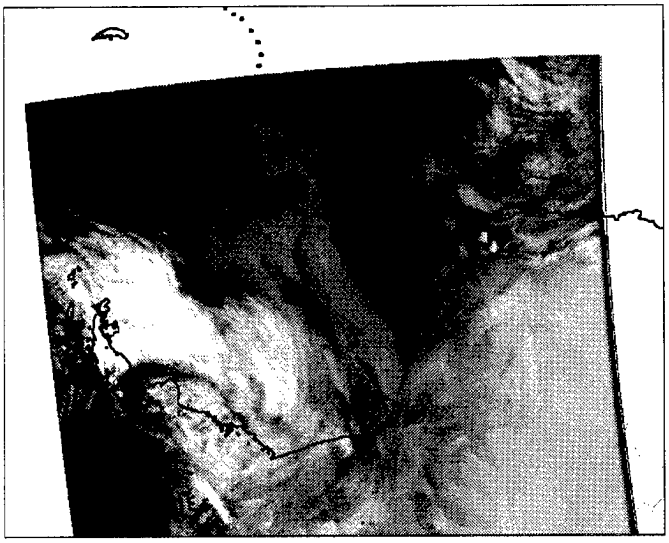


Figure 1: OLS infrared image of November 4, 1992.

Algorithm

Because using only temperature measurements can lead to ambiguities, the idea of this algorithm is to use additionally texture analysis. Calculations of texture features inside windows with a fixed size, shifted over the image, leads to blurring at the boundaries between clouds and surface. Therefore a special segmentation procedure is first applied and the texture features are calculated for each segment. The classification process (open water, sea ice, low and high clouds) is done by a neural network with the texture features as inputs.

In the following, the algorithm is introduced thorough an OLS-infrared image of November 4, 1992 (Fig.1).

Segmentation

The goal of the segmentation procedure is to gather pixels to regions. These regions have a minimal number of pixels and should include only pixels of the same class. From arbitrary starting points the routine enlarges the area of the respective



Figure 2: Segmented image of Fig.1. The gray tones are randomly chosen.

segment by comparing the pixel in question with the average of the previously included pixel. If the difference is small, the pixel is included. Therefore the average can change continuously.

The procedure is divided into two parts. During the first step only pixels with cold temperature are considered. To account for the high variability in temperature and fractal structure of cold high clouds the image is smoothed before. During the second step the pixels with higher temperature are considered. Because sea ice, open water and low and medium level clouds can have similar temperature, it is more difficult to segmentize them. Therefore the sobel-operator (an edge detection operator) of the image is processed, reinforced by a factor and the resulting image is added to the original image This procedure emphasizes the boundaries between different classes and the variability within heteorogenous regions like sea ice and some kinds of clouds.

The threshold for the difference is increased during several loops whereas the mininum number of pixel and the factor of the sobel operator image is decreased. After the fourth loop the image is smoothed. Therefore during the first few loops homogenous areas are segmented and later the heterogenous. The result of this procedure is a mask in which all pixels are associated with a segment. To avoid unsegmented pixels the image is treated with a morphological operation (dilation) afterwards. This is easy to understand for sea ice, where the warmer leads can be exclude during the segmentation. Using a dilation they are combined with the ice pixels and the segments show the full characteristic texture of sea ice. Fig. 2 shows the segmented image.

Texture

Texture features are statistical values which describe the spatial distribution of the gray level values in an image. In this algorithm they are calculated with the sum and difference histogram (SADH) approach [1]. The histogram of the sum and difference images based upon the original image and a displaced image are the basis for the texture features. The algorithm uses the following features defined by Chen [1]: *Mean, Standard Deviation, Contrast, Angular Second Moment (ASM), Correlation, Entropy, Local Homogeneity, Cluster Shade, Cluster Prominence.* All texture features are normalized in this algorithm in order to guarantee the comparability in the classification with neural networks.

Classification

Each segment should be classified into one of six classes (low, medium, high level cloud, sea ice, open water, land ice) using the calculated nine texture features. Therefore we have a nine dimensional cluster analysis problem. Two kinds of neural network are appropriate for this task: the Learning Vector Quantization (LVQ) and the Self Organizing Map (SOM). The software packages SOM-PAK and LVQ-PAK including a manual are freely available on the internet .

Both algorithms are described by Kohonen [2]. The *Self Organizing Map (SOM)* is an unsupervised learning algorithm. The goal is to cluster or categorize the input data. The input vectors $\vec{x_i}$ are projected on a two dimensional map, which has a topography. The output neurons are represented by codebook vectors $\vec{m}$. The algorithm uses competitive learning. The winner is the neuron with the largest output which is a measure for the similarity of the input vector and the codebook vectors. During the training phase not only the winner codebook vector but also these in the neigborhood are dragged to the input vectors.

$$\vec{m}_i(t+1) = \vec{m}_i(t) + h_{ci}(t)[\vec{x}(t) - \vec{m}_i(t)] \qquad (1)$$

The function $h_{ci}(t)$ describes the size of the neighborhood and the learning parameter. This causes the sensitivity of regions of the output map to similar input vectors.

In Fig. 3 the clustering of the input data from different classes is visualized.

Whereas the SOM is an unsupervised learning algorithm which considers the labelling of the input vectors only after the training, the *Learing Vector Quantization (LVQ)* is a supervised version. Labelled training input data are used and the updating of the codebook vectors depends on the classification. For a correct classification

$$\vec{m}_c(t+1) = \vec{m}_c(t) + \alpha_c(t)[\vec{x}(t) - \vec{m}_c(t)] \qquad (2)$$

is used, otherwise

$$\vec{m}_c(t+1) = \vec{m}_c(t) - \alpha_c(t)[\vec{x}(t) - \vec{m}_c(t)] \qquad (3)$$

The function $\alpha_c(t)$ describes the learning parameter.

RESULTS

The training set was prepared with several images from November 1992, because both the infrared and the visible channels are available. This makes the 'manual' classification

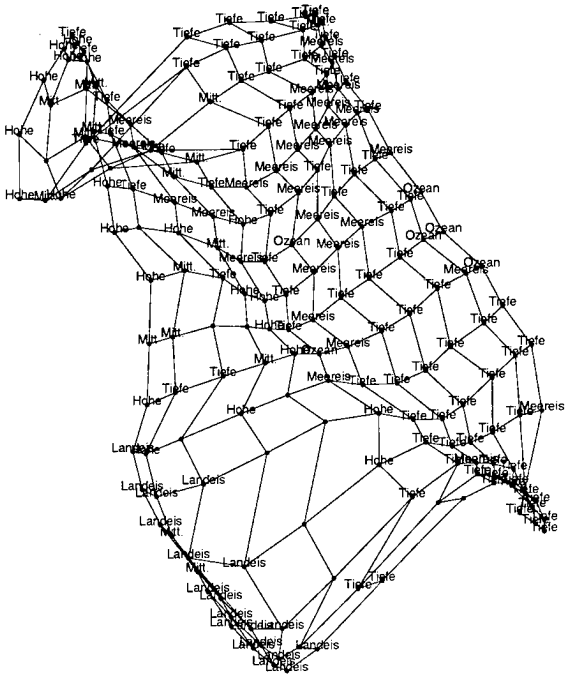


Figure 3: Visualization of the clustering using the self-organizing map (Sammon map). The german labelling means: *Hohe, Mitt., Tiefe*: High, medium and low level clouds, *Meereis*: sea ice, *Landeis*: land ice, *Ozean*: open water.

Table 1: Percentage of correctly classified segments of the training set and of unknown images. The + indicates the additional contingency check. The brackets present the standard deviation.

	training	unknown
SOM	87.9 (4.7)	81.5 (3.2)
SOM+	90.4 (4.4)	85.0 (3.7)
LVQ	92.5 (4.3)	83.6 (4.6)
LVQ+	95.6 (2.9)	89.1 (2.8)

of the segments possible, which are used as the desired output. Fig.4 shows the finally classified data set from Fig.1.

Table 1 shows the percentage of the correctly classified pixels for the training set and for unknown images. The indications SOM+ and LVQ+ stand for an additional contingency test, which uses SSM/I ice concentration analyses. It happens that clouds over the ocean have the same texture features like sea ice with leads. Therefore, if the ice concentration is zero all segments classified as sea ice are changed to clouds.

The results show that this algorithm generally gives very good estimates of cloud covered areas. As expected the images of the training set are better classified than the unknown images. The percentage of correctly classified pixels is higher for the LVQ than for the SOM. The reason is the knowledge of the desired output is taken into consideration during the training phase [2].

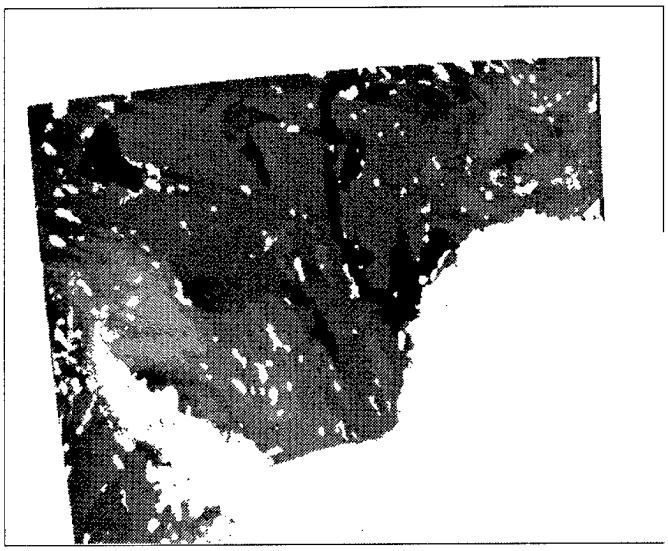


Figure 4: Classification of the image presented in Fig.1. Black regions are open water, dark gray are sea ice, and all brighter colored areas are clouds, where the brightness visualizes the temperature.

Conclusion

The results presented here show that the method developed to detect clouds by only using infrared data works with an accuracy of about 90%. The approach of using texture features of different segments of an infrared image as inputs to a neural network seems to be very promising. Of course the application on different seasons and regions has to be studied, but on the other hand, neural networks are especially suited to be applied on different situations, because during the training phase they adjust to the new problem.

References

[1] Chen, D.W., S.K. Sengupta and R.M. Welch, *Cloud field classification based upon high spatial resolution textural features. Part 2: Simplified vector approaches*, Journal of Geophysical Research Vol.94, No. D12, 14749-14765, 1989

[2] Kohonen, T., *The Self-Organizing Map*, Proceedings of the IEEE, Vol. 78, No.9, September 1990

[3] Steffen 1993 Steffen, K., R. Bindschadler, G. Casassa, J. Comiso, D. Eppler, F. Fetterer, J. Hawkins, J. Key, D. Rothrock, R. Thomas, R. Weaver und R. Welch, *Snow and ice applications of AVHRR in polar regions: report of a workshop held in Boulder*, Colorado, 20 May 1992, Annals of Glaciology 17, 1993,1-16

The Estimation of Aerosol Models by the Reflectance Analysis of the Airborne POLDER Data

A.Yamazaki, K.Ueda, Y.Kawata and T.Kusaka

Environmental Information Research Laboratory
Kanazawa Institute of Technology
Ogigaoka7-1, Nonoichi, Ishikawa 921, Japan
Tel: 81-762-48-1100, Fax: 81-762-48-7753
E-mail: yamazaki@infor.kanazawa-it.ac.jp

abstract: In this paper we have made the theoretical analysis of the reflectance data measured by the airborne POLDER sensor over the Mediterranean Sea in 1991. Several basic aerosol size distribution models, namely, a lognormal size distribution function, a modified gamma size distribution function, and a power law size distribution function by Junge were considered here under the assumption of an atmosphere-ocean system with an anisotropic Cos-Munk reflecting sea surface model. We present several aerosol models satisfied observed reflectance data when appropriate wind speed is assumed.

INTRODUCTION

The POLDER (POLarization and Directionality of Earth Reflectances) sensor, now under development at CNES, France, is one of Announcement Opotunity sensors for a Japanese satellite ADEOS scheduled for launch in 1996. Several airborne POLDER campaigns have been conducted by CNES and Laboratoire d'Optique Atmospherique (LOA), University of Science and Technology of Lille (USTL) since 1990. In this paper we analyzed the subset of the Medimar campaign data measured by airborne POLDER sensor sets and tried to develop a possible method for estimating aerosol models. The Medimar is the name of the sea truth measurements conducted over the Mediterranean sea in 1991 by using the Airborne POLDER. The solar zenith angle and the flight altitude of the airborne POLDER at the time of the observation were θ_0=38° and about 4700m, respectively.

0-7803-3068-4/96$5.00©1996 IEEE

BASIC FORMULATION

Consider an atmosphere-ocean system, the theoretical reflectance can be computed by the doubling and adding method. Let us consider an incident solar flux, $\pi\bar{F}_0 = \pi[F \quad 0 \quad 0 \quad 0]^t$ per unit area normal to the direction of propagation, illuminates a plane parallel atmosphere with the optical thickness of τ from the direction of (μ_0, ϕ_0), where symbols μ_0 and ϕ_0 are the cosine of the solar zenith angle and the solar azimuthal angle, respectively. In the above a superscript t represents the vector transposition, The upwelling Stokes vector $\bar{I}(\tau, \mu, \mu_0, \phi - \phi_0) = [I \quad Q \quad U \quad V]^t$ at the top of the atmosphere in the direction of (μ_0, ϕ_0) can be expressed by Eq.(1) in terms of the reflection matrix of the atmosphere-ocean system $\bar{R}_{at+sea}$.

$$\bar{I}(\tau, \mu, \mu_0, \phi - \phi_0) = \mu_0 \bar{R}_{at+sea}(\tau, \mu, \mu_0, \phi - \phi_0)\bar{F}_0 \qquad (1).$$

As for the components of the Stokes vector, I is the intensity, Q, U, and V are related to the linear polarization, the plane of polarization, and the circular polarization, respectively. By using adding method [1], $\bar{R}_{at+sea}$ can be expressed in terms of the reflection and transmission matrices of the atmosphere, $\bar{R}_{at}$ and $\bar{T}_{at}$, and the reflection matrix of the sea surface $\bar{R}_{sea}$. For a given atmospheric model, it is possible to compute $\bar{R}_{at}$ and $\bar{T}_{at}$ by the doubling and adding method [1].

Assuming that sea surface slopes follow an

anisotropic Gaussian distribution with respect to the surface wind and its direction [2], then the probability density function of the sea surface slope $P_{ws}(Z_c, Z_u)$ is given by

$$P_{ws}(Z_c, Z_u) = \frac{1}{2\pi\sigma_c\sigma_u}\exp\left(-\frac{\xi^2+\eta^2}{2}\right) \times\left[1-\tfrac{1}{2}c_{21}\left(\xi^2-1\right)\eta-\tfrac{1}{6}c_{03}\left(\eta^3-3\eta\right) +\tfrac{1}{24}c_{40}\left(\xi^4-6\xi^2+3\right) +\tfrac{1}{4}c_{22}\left(\xi^2-1\right)\left(\eta^2-1\right) +\tfrac{1}{24}c_{04}\left(\eta^4-6\eta^2+3\right)+\cdots\right]$$

$$\xi = Z_c/\sigma_c \quad , \quad \eta = Z_u/\sigma_u \qquad (2).$$

where ξ, η are the standardized slope components and Z_c, Z_u are the slope components along the crosswind and upwind directions, respectively. Furthermore, σ_c, σ_u are the root mean squares of Z_c, Z_u, respectively. The explicit forms for σ_c, σ_u and c_{ij} are given by Cox and Munk[2]. Then, according to the formulation by Takashima [3] with some modifications of his original form, the sea surface reflection matrix $\overline{R}_{sea}$ can be given approximately by Eq.(3).

$$\overline{R}_{sea}(\mu,\mu',\phi-\phi') = \frac{\pi P_{ws}}{4\mu\mu'\cos^4\beta}\overline{R}_c(\delta)\overline{R}_s(2\omega)\overline{R}_c(\gamma) \qquad (3).$$

where $\overline{R}_c$ is the rotation matrix and δ, γ are the rotation angles defining the reflection matrix with respect to the local meridian plane as a common reference for the Stokes vector and $\overline{R}_s$ is the specular reflection matrix and ω is the incident angle and reflection angle at the facet [3].

ANALYSIS OF AIRBORNE POLDER DATA

In this study the atmosphere is divided into two layers at an altitude of the airplane, i.e., 4700m and each divided layer consist of aerosols and gaseous molecules. We used values of the total observed aerosol optical thickness τ = 0.120[4] at 0.85μm. Values of the optical thickness and turbidity factors for each of two layers were chosen so as to agree with those computed for a Midlatitude Spring-Summer atmosphere by LOWTRAN 6 [5] at an aircraft altitude (4700m). We have computed the theoretical reflectance for 7 aerosol size distribution functions, namely, Haze M given by modified gamma function, Water-Soluble, Oceanic and Maritime given by lognormal distribution functions, Junge type given by power law distribution functions with ν = 3.5, 4.0 and 4.5. Furthermore, we considered 9 different refractive indices (m = 1.33, 1.33-i0.01, 1.33-i0.05 : m= 1.5, 1.50-i0.01, 1.50-i0.05: m= 1.75, 1.75-i0.01, and 1.75-i0.05) for Haze-M and Junge models, and specific refractive indices, m=1.52-i1.17$\times10^{-2}$, m=1.372-i1.03$\times10^{-6}$, m=1.38-i5.86$\times10^{-4}$, for Water-Soluble, Oceanic and Maritime, respectively[6]. We also considered 15 wind speeds (from V=8.0m/s to V=15.0m/s with an increment of 0.5m/s). The refractive indices of m=1.33, 1.5, and 1.75 correspond to those of water, dust, and soot aerosols, respectively. 135 cases for Haze-M and Junge model, and 15 cases for Water-Soluble, Oceanic and Maritime were examined whether the corresponding theoretical reflectance curves can satisfy the observed reflectance data or not. In this examination the surface wind direction of W_d = 220° was fixed. Here, the wind direction is measured counter clockwisely from the sun direction. The observed wind direction was given as NNW (330°: measured clockwisely from the north [4]), which is equivalent to W_d = 220° in our notation. As for the observed reflectance data, the mean values of it with a error bar (obtained from 24 successive Medimar scenes data between Scene Number 1 and 24) are used for the reference data in the comparisons. We adopted a simple rule that the theoretically computed reflectance values should be at least within the range of observed error bars at all viewing zenith angles. The error bar range is equal to $\pm3\sigma$, where σ is the standard deviation of the observed values at each viewing zenith angle. We found that Haze M, Oceanic and Maritime can not satisfy the above constraint for any combination of the refractive indices and wind speed. We found that Water-Soluble and Junge type size distribution functions can satisfy the observed reflectance data when an appropriate wind speed is assumed (Table). The case of Junge type function with ν=3.5 and m=1.5-i0.01 (the aerosol model A) is presented here in detail, because of two reasons: (1) an Ångström coefficient α=1.5 obtained from the aerosol optical thickness measurements [4] suggests ν=3.5, according to Ångström's law, namely, $\nu=\alpha+2$ (2) The refractive index of typical aerosols, like dust and water soluble particles, is m=1.5. The surface wind speed does not change the shape of the reflectance curve in the back

scattering direction, but it affects that in the sun glitter direction (at the viewing zenith angle between -30° to -50°). We can estimate a range of wind speed from the sun glitter portion of reflectance curve in the case of aerosol model A. The range of the wind speed was thus estimated to be 10.5m/s≤V≤13.5m/s from Fig., whereas the observed one is V=14.4m/s.

CONCLUSIONS

We came to conclusions by this study as follows:

1) We found Water-Soluble model and several Junge type aerosol models, A - F which can satisfy the observed reflectance data at 0.85μm in the principal plane by examining various combinations of aerosol optical parameters and wind speeds.

2) It was possible to estimate the surface wind speed by examining the reflectance surge in the glitter direction at 0.85μm.

3) The polarization data analysis should be made in the next study.

We thank Prof. Herman and Dr. Deschamps at LOA, and Dr. Bréon at Laboratoire de Modelisation du Climat et de l'Environment, France for kindly providing the Medimar POLDER data. We also wish to extend our sincere appreciation to Dr. Bréon at LMCE, Dr. Takashima at NASDA, Dr. Masuda at Meteorological Research Institute, Japan who kindly provide their valuable comments and suggestions, and to the referees for their constructive comments.

REFERENCES

[1] J.E. Hansen, and L. Travis, "Light Scattering in Planetary Atmospheres," Space Sci. Review, vol. 16, pp. 527-610, 1974.

[2] C. Cox, and W. Munk, "Measurement of the Roughness of the Sea Surface from Photographs of the Sun's Glitter," J,Opt.Soc.Amer. vol. 44, pp. 838-850, 1954.

[3] T. Takashima, "Polarization Effect on Radiative Transfer in Planetary Composite Atmospheres with Interacting Interface," Earth, Moon, and Planets, vol. 33, pp. 59-97, 1985.

[4] F.M. Bréon, and P.Y. Deschamps, "Optical and Physical Parameter Retrieval from POLDER Measurements over the Ocean Using an Analytical Model," Remote Sensing. Environ, vol. 43, pp. 193-207, 1993.

[5] F.X. Kneizys, et al., "Atmospheric Transmittance/ Radiation : Computer Code LOWTRAN 6," Air Force Geophys. Lab., AFGL-TR-83-0187, Mass., USA, 1983.

[6] Radiation Commission, IAMAP(1986), "A preliminary cloudless standard atmosphere for radiation computation," WCP-112, WMO/TD No.24. (World Meteorological Organization, Geneva)

Table: Estimated ranges of optical and physical parameters.

	Junge ν=3.5 (model A)	Junge ν=4.0 (model B)	Junge ν=4.0 (model C)	Junge ν=4.5 (model D)	Junge ν=4.5 (model E)	Water Soluble (model F)
refractive index (m)	1.50-i0.01	1.33	1.75-i0.05	1.33	1.75-i0.05	1.52-i1.17 ×10^{-2}
8.0 m/s						
8.5 m/s						
9.0 m/s						
9.5 m/s						
10.0 m/s				o	o	
10.5 m/s	o	o		o	o	
11.0 m/s	o	o		o	o	
11.5 m/s	o	o	o	o	o	
12.0 m/s	o		o	o	o	o
12.5 m/s	o		o	o	o	o
13.0 m/s	o					o
13.5 m/s	o					o
14.0 m/s						
14.5 m/s						
15.0 m/s						

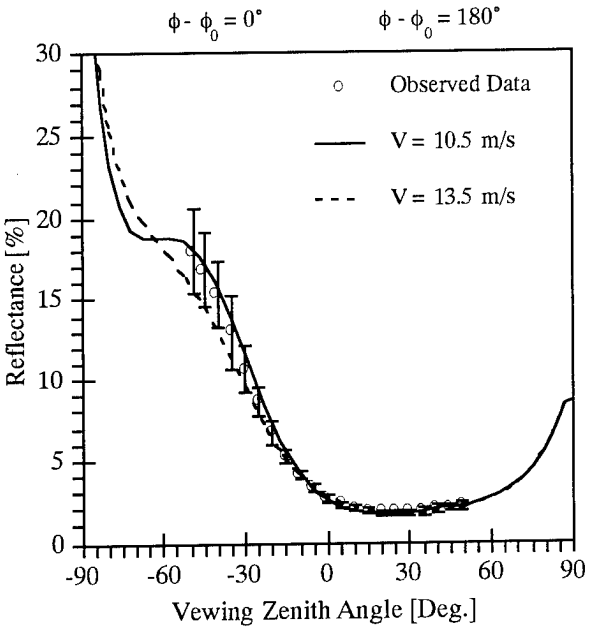


Fig.: The theoretical results based on the Junge type function with ν=3.5 and m=1.5-i0.01.

Particle Size Distributions and Extinction Determined By a Unique Bistatic Lidar Technique

T. D. Stevens and C. R. Philbrick
(tds102@psu.edu, crp3@psu.edu)

The Pennsylvania State University
PSU/ARL Lidar Laboratory
University Park, PA 16802
(814) 863-0851

INTRODUCTION

A study has been conducted to investigate the application of a unique bistatic lidar receiver to remotely determine properties of the lower tropospheric aerosols, particularly optical extinction, mean radius and size distribution width. The motivation for this study is to advance our understanding of aerosols near the ground with a possible long term goal of calculating extinction at any wavelength. Single ended remote sensing instruments, whether using lasers, radars, or microwaves, have difficulties determining absolute extinction along a propagation path. This is due to the large variations in the ratio of the forward scattering to the backward scattering between different particles (scattering phase function). The bistatic linear array receiver was developed to provide necessary information on the scattering phase function of the aerosols.

The bistatic remote receiver utilizes a linear photodiode array to image the radiation scattered from any high power CW or pulsed laser system. By observing the angular scattering variation along a horizontal path, additional information contained in the scattering angle phase function can be obtained. A technique has been developed to estimate particle size and distribution widths (of spherical scatters) by comparing two transmitted E-field components, one parallel and one perpendicular to the scattering plane. Polarizers are used on the receiver to measure the cross polarization to determine the amount of multiple scattering and nonsphericity of the particles in the scattering volume.

The first studies of this measurement technique have been conducted in a marine/coastal environment during the CASE I (Coastal Aerosol Scattering Experiment) program at the NASA flight center on Wallops Island, VA during September 1995. The atmospheric conditions during this measurement program correspond to cases of high relative humidity where the use of a spherical model to describe the scatterers would be reasonable. Results, which can be represented by trimodal lognormal size distributions, were obtained from both clear and hazy/misty nights. Extinction calculated from the size distributions is compared with extinction from the Raman lidar at two different wavelengths. On calm evenings with high humidity and decreasing temperature, the inversions also show increasing particle sizes consistent with radiation fog formation. The results show remarkable agreement with a tri-modal aerosol distribution used in a spherical scattering model (Mie theory).

INSTRUMENTATION AND EXPERIMENT

The linear photodiode bistatic lidar receiver is different from past bistatic lidars, which generally have the same goal of obtaining scattered radiation from the particles at angles other than 180°. Past experiments have used single or multiple polarizations, from a scanning laser beam to reconstruct a scattering phase function from tropospheric aerosols [1,2,3]. However, the measurement technique presented in this paper does not scan or attempt to reconstruct a scattering phase function of the particles. Instead, a ratio is obtained from the image of the scattering of two orthogonal polarization components with respect to angle, one in the scattering plane and one perpendicular to the scattering plane along a horizontal path, as shown in Fig.1. The use of a ratio cancels the effects of

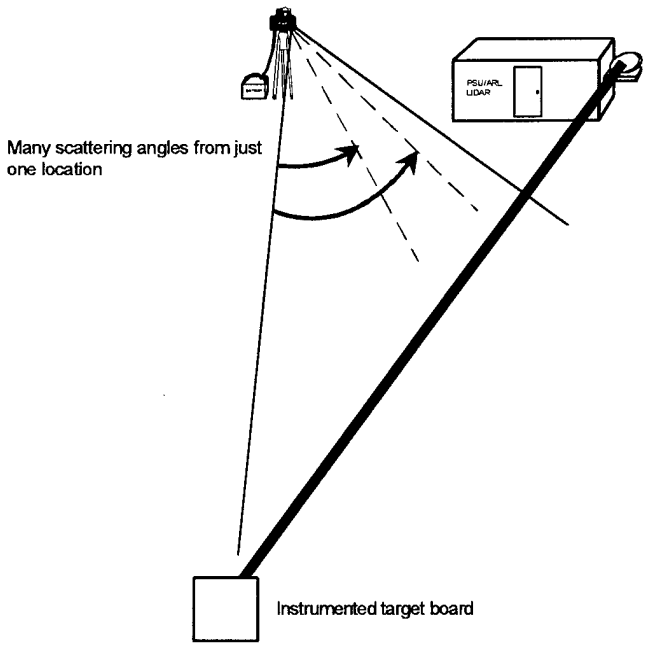


Figure 1. By operating in the horizontal mode, the bistatic lidar is able to collect radiation from many scattering angles, between 155° and 180°, from just one location.

0-7803-3068-4/96$5.00©1996 IEEE

many problems, including nonlinearities across the field of view of the receiver and extinction differences due to different path lengths for each scattering angle. Fig.1 demonstrates the ability of the bistatic receiver to simultaneously image the backscattered radiation from an angle range of 155° to 180°. The assumption of a uniform horizontal path is verified with horizontal extinction profiles from the monostatic Raman lidar during each data set [4,5]. Although this polarization ratio contains the information needed to characterize the scatterers, a model is needed to relate this ratio to the desired parameters, such as extinction, and particle size distribution.

One of the goals of this research was to determine how well Mie theory, with a lognormal distribution of scatterers would describe actual aerosol data, in a humid coastal/marine environment. A program was written using several subroutines including BHMIE from [6], that modeled the ratio of the two polarization components from the bistatic lidar with a trimodal lognormal distribution of spherical scatterers. It was discovered that in order to accurately model the return from a clear night, the molecular scattering component had to be added to the aerosol distribution. Fig.2 shows a sample lognormal particle size distribution including the addition of 2.54×10^{25} molecules per m^3, at a radius of 0.198 nm.

The first tests of this measurement technique were conducted in September 1995, during the CASE I (Coastal Aerosol Scattering Experiment) on Wallops Island Virginia. This location was chosen for its humid and misty, coastal/marine environment, and for an unobstructed 3.28 km horizontal path over a salt marsh. The Penn State LAMP (Laser Atmospheric Measurement Program) monostatic lidar, [7], was operated on both a horizontal path and a vertical path. When operating on a horizontal path the LAMP lidar collected rotational Raman temperature profiles, vibrational Raman water vapor profiles, vibrational Raman nitrogen profiles, and aerosol/molecular scattering profiles at the fundamental laser wavelength of 532 nm.

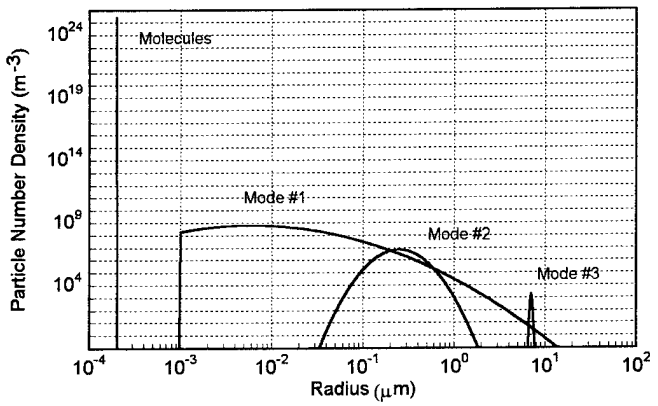


Figure 2. A plot of a trimodal lognormal particle size distribution using the bistatic lidar model. The addition of 2.54×10^{25} molecules per m^3 is shown at the "equivalent Mie radius" of 0.198 nm.

The bistatic receiver and the laser were separated by 15.24 m which imaged the scattering path between 35 m and 175 m, and corresponded to scattering angles between 155° and 175°. The distance from 175 m to 3.28 km corresponds to an angle range of 175° to 180°, so one must use care when analyzing data from this range, because the horizontal path is more likely to be uniform over 140 m than over 3 km.

DATA ANALYSIS AND RESULTS

Data were collected under a range of conditions, from dry and clear to damp and misty, during the Wallops CASE I program. However, the most interesting data were collected on September 14, 1995, a calm, damp and hazy evening. Fig.3b shows a plot from 11:00 pm to 3:00 am of the temperature and relative humidity versus time. The wind speed is indicated in miles per hour next to each temperature data point. Here we can see the relative humidity remains constant at about 90% until about 1:30 am, while the temperature slowly dropped from 23°C to 22°C. After 1:30 am the wind speed increased to 5 mph and brought with it a warmer and drier air mass. The temperature decrease of 1°C does not seem like a large change, but from

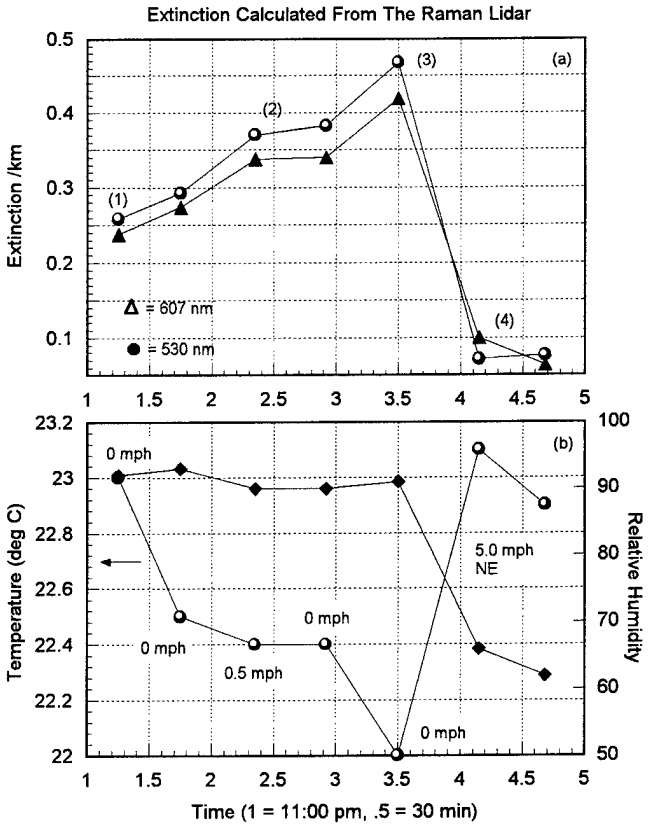


Figure 3. (b) A plot of the temperature and relative humidity versus time from the lidar weather station on the night of September 14, 1995. (a) Corresponding plots of extinction coefficients from the Raman lidar at 607 and 530 nm, at the same times as the temperature and relative humidity plots (b).

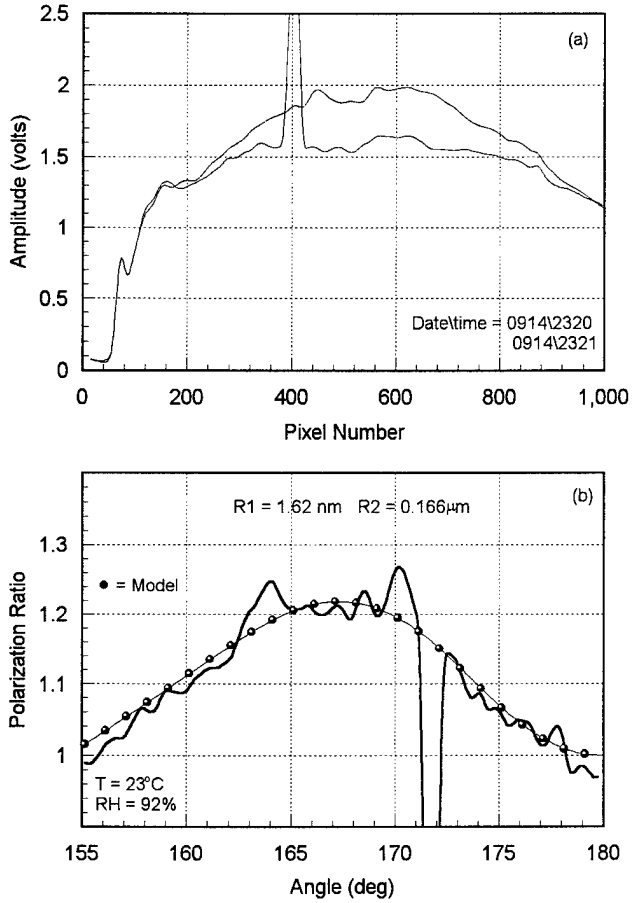


Figure 4. (a) A plot of the two electric field components measured with the bistatic lidar on September 14, 1995. (b) The ratio of the two polarization components in (a) shown with the best first order fit from the model.

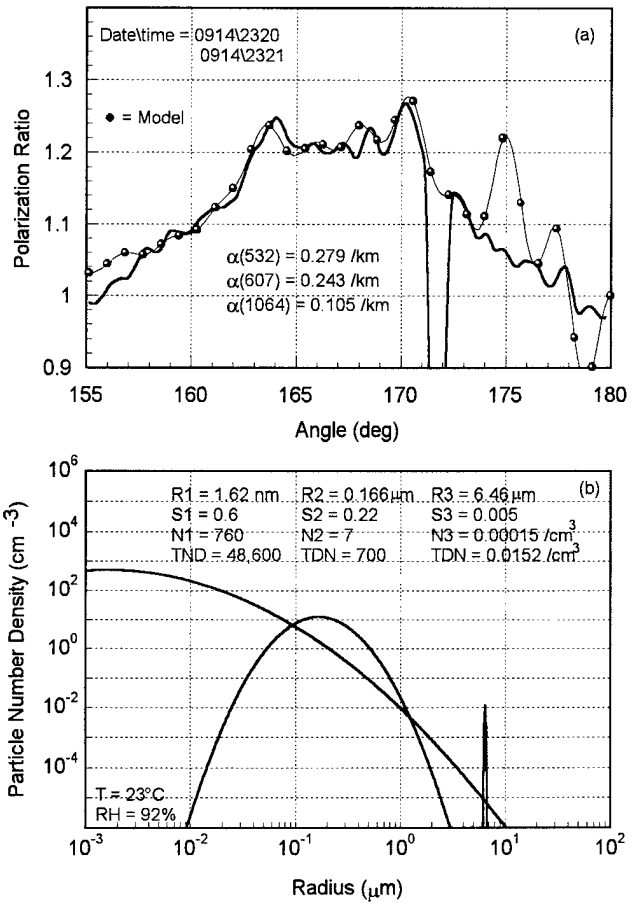


Figure 5. (a) A good trimodal fit of the model (dotted line) to the data showing a nearly monodispersed radiation fog forming. (b) The lognormal distributions, with an index of refraction of 1.38, used to fit the model to the data in (a).

Fig.3a, it is apparently large enough to cause significant changesin the average extinction coefficient calculated from the Raman 607 and 530 nm lidar channels. Prior investigations [4,5] present the analysis for determining absolute extinction from a Raman lidar return.

Fig.4a shows a plot of the unprocessed data for two polarization components measured with the bistatic lidar early in the evening at 11:20 pm, corresponding to the first data point in Fig.3. Because the two polarization components are separated in time by one minute, spikes in the data, like the one at pixel number 400, can occur when an insect flies through the laser beam. Fig.4b shows the ratio of the two components in Fig.4a with a solid dark line, accompanied by the best first order fit of the model. The first order fit with two aerosol modes is found by adjusting the six lognormal distribution parameters, with a fixed index of refraction (n=1.38), until the sum of the differences between the model and the data is minimized. On a clear night, with only a single mode of small aerosols, the number density of the molecules can be used as the absolute reference to tie off the number density of the aerosol distribution. On this night however, the second mode of the aerosol distribution, not the molecules, is dominating the scattering. The extinction calculated from the Raman lidar, shown as the first point in Fig.3a is used to normalize the number densities of the first two modes of the distribution. The presence of the high frequency ripples versus angle in Fig.4b is an indication that a third larger particle mode is contributing to the scattering. This last mode was extremely difficult to find because the standard third modes described in the literature did not improve the fit. Finally, very narrow distributions were tried, and an excellent match was found with a particle radius of 6.46 μm, and a distribution width of only $\log\sigma = .005$, as shown in Fig.5. Nearly monodispersed particle distributions like these are often called radiation fog, and generally form from the condensation of water vapor molecules onto the surface of particles as the temperature drops on calm, humid nights. The trimodal lognormal distribution that best matches this data set is shown in Fig.5, with TND referring to the total particle number density for that mode.

Because this evening was calm with zero wind speed, it can be assumed that the particle number density will not significantly change throughout the course of the night. If the particle

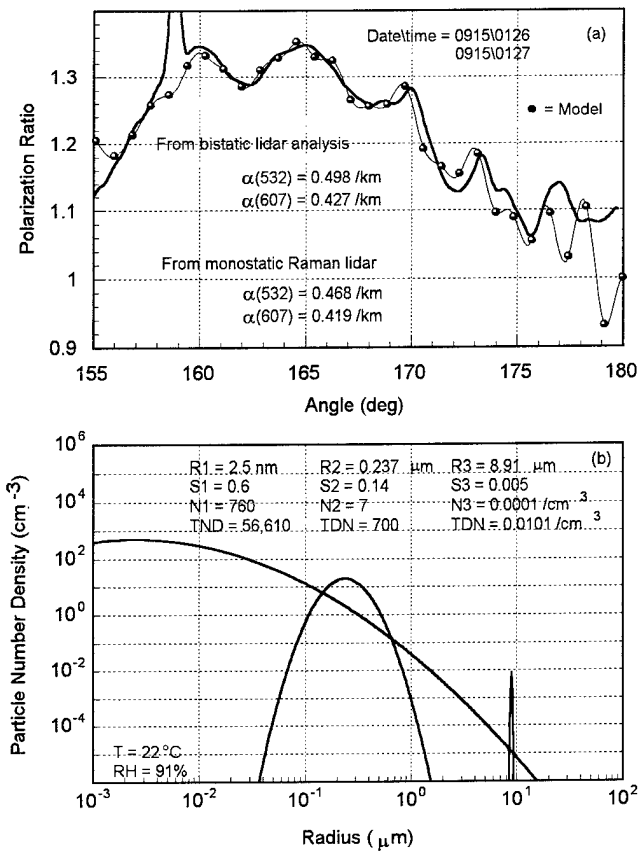


Figure 6. (a) A most convincing example of this bistatic lidar measurement technique, showing the best fit of the spherical model, using the distribution from (b), with the data. The radiation fog mean radius has grown from 6.46 μm to 8.91 μm in only 2.5 hours.

number density does not change, then only the radius and distribution width of the three aerosol modes should be altered to fit the model to each consecutive data set. Five bistatic lidar data sets were inverted for particle size distributions which show the increasing radius of each particle as the temperature dropped and the extinction increased. The last data set to be inverted for a trimodal lognormal particle size distribution corresponds to point 3 in Fig.3a and is shown in Fig.6.

Probably the most convincing example of this measurement technique is shown in Fig.6a, with the best fit of the model, and the corresponding trimodal distribution in Fig.6b. The temperature decreased while the extinction increased one last time before the wind brought a new air mass and different scatterers in the area. The second mode of the distribution is seen to narrow its distribution width as it grows from a radius of 0.166 μm to 0.237 μm. At the same time the third mode increases from a radius ot 6.46 μm to 8.91 μm. This data set is most striking because the model follows almost every contour in the data between 155° and 180° as seen in Fig.6a. Not only does the model fit the data almost perfectly after increasing only the mode radii, but the calculated extinction coefficients are also

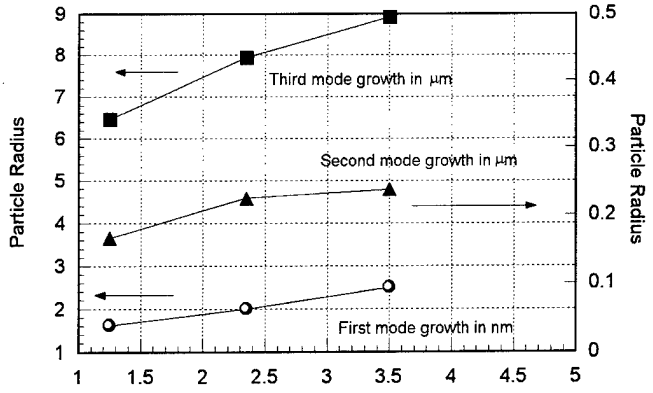


Figure 7. A summary of the growth of the particles through the night, as determined from inverting the data from the bistatic lidar.

the same as those measured by the Raman lidar, see extinction data in Fig.6a. Fig.7 summarizes the growth of the three modes throughout the evening before a new air mass entered the measurement area and the conditions changed from cold and humid, to warm and dry.

ACKNOWLEDGMENTS

Special appreciation for the support of this work goes to Dr. Juergen Richter of NCCOSC NraD, and to Dr. Geary Schwemmer of NASA GSFC. The efforts of Dr. Balsiger, Savy Mathur, Mike O'Brien, Dr. Ruf, Dr. Kunz, Dr. Aydin, Dr. Lyask, and Dr. Bohren have contributed much to the success of this project.

REFERENCES

[1] J.A.Reagan, and B.M.Herman, "Bistatic lidar investigations of atmospheric aerosols," Proc. Conf. Radar Mereorol., 14th, p.275, 1970.

[2] P.C.S.Devara, and P.Ernest Raj, "A bistatic lidar for aerosol studies," IETE Tech. Rev. Vol. 4, p.412, 1987.

[3] K.Parameswaran, K.D.Rose, and B.V.Krishna Murthy, "Aerosol characteristics from bistatic lidar observations," J. Geophys. Res. Vol. 89, No. D22, p.2541, 1984.

[4] T.D.Stevens, and C.R.Philbrick, "Atmospheric extinction from Raman lidar and a bistatic remote receiver," Proc. Conf. IEEE topical Symp. CO-MEAS, p.170, 1995.

[5] C.R.Philbrick, "Raman lidar measurements of atmospheric properties," Proc. of Atm. Prop. and Remote Sensing III, SPIE 2222, p.922, 1994

[6] C.F.Bohren, and D.R.Huffman, Absorption and Scattering of Light by Small Particles, Wiley-Interscience, New York, 1983.

[7] C.R.Philbrick, D.B.Lysak, T.D.Stevens, P.A.T.Haris and Y.-C.Rau. "Atmospheric measurements using the LAMP lidar during the LADIMAS campaign," Proc. of the 11th ESA Symp. ESA-SP-355, p.223, 1994.

Remote Sensing of the Marine Atmospheric Boundary Layer and Ocean Surface Winds: Observations From the LITE Correlative Flights

Stephen P. Palm
Science Systems and Applications Inc.
Code 912, Goddard Space Flight Center
Greenbelt, Maryland 20771
spp@virl.gsfc.nasa.gov

Geary Schwemmer
Laboratory For Atmospheres
Code 912, Goddard Space Flight Center
Greenbelt, Maryland 20771

Doug Vandemark and Don Hines
Laboratory For Hydrospheric Processes
Code 972 Wallops Flight Facility
Wallops, Virginia 23337
dug@aol7.wff.nasa.gov

S. H. Melfi
University of Maryland, Baltimore County
5401 Wilkens Avenue
Baltimore, Maryland 21228

Introduction

The Planetary Boundary Layer (PBL) is the lowest 1 km or so of the troposphere which directly interacts with the underlying surface. The fluxes of heat, moisture and momentum within the PBL are very important to weather forecasting and are in part determined by the mean wind speed and characteristics of the surface. Over the ocean, where the surface remains homogeneous over relatively large distances, the structure and height of the PBL are probably good indicators of the magnitude of the surface fluxes. This implies that changes in PBL height or convective intensity might be correlated with surface wind. In this paper we present simultaneous measurements of the height and convective structure of the PBL and surface (10 meter) wind speed derived from airborne lidar and microwave scatterometer instruments, respectively. We use these data to investigate the response of the PBL to changes in the wind speed over scales ranging from hundreds of kilometers (synoptic scale) to less than 10 km (micro scale). This data set provides a unique simultaneous measurement of the wind field and boundary layer structure over large distances and is likely the only one of its kind.

Experiment Description

During the Fall of 1994, we participated in the Lidar In-space Technology Experiment (LITE) aircraft correlative measurement program which was designed to collect coincident lidar measurements along the shuttle flight track for LITE data validation and correlation. While the main objective of the mission was to acquire lidar data from the ground to the mid stratosphere for comparison with the shuttle lidar, other instruments were flown to investigate the PBL and its interaction with the ocean. Specifically, we were interested in studying how the PBL responded to changes in sea surface temperature and surface wind speed. A total of 5 flights were performed over the tropical and sub-tropical Atlantic Ocean, each flight acquiring between 5 and 7 hours of data covering on average about 2500 km. The instrumentation consisted of the Large Aperture Scanning Airborne Lidar (LASAL) system [1], the Radar Ocean Wave Spectrometer (ROWS) system [2], the NASA/JPL Sea Surface Temperature Radiometer (SSTR) [3] and the University of Massachusetts Ku-band (KUSCAT) scatterometer [4]. The LASAL system provided us with a high resolution (5 meters horizontal and 15 meters vertical) picture of the height and convective structure of the PBL along the aircraft flight path. The LASAL data were used to derive the PBL height. The scatterometers enabled us to obtain (10 meter) wind speed and direction with a horizontal resolution of about 2 km. The SSTR, which is a six channel radiometer, can correct for the effects of water vapor absorption and thus retrieve the sea surface temperature to an accuracy of about 0.2 degrees centigrade. These data are available only where clouds do not interfere with the SST measurement.

Synoptic Scale Interactions

The height of the PBL is mainly controlled by the entrainment rate, the synoptic scale vertical velocity field and the strength of the capping inversion. The entrainment rate is directly related to the surface flux of heat and moisture at the surface. Over the tropical and sub-tropical oceans, the sensible heat flux is small while the latent heat flux accounts for about 90 percent of the total heat transfer. A good estimate of the flux of latent heat (E) over a homogeneous ocean surface can be obtained from the well known bulk aerodynamic formula shown below.

$$E = L_v C_e U \rho (q_s - q)$$

Where L_v is the latent heat of vaporization, ρ the air density, C_e the transfer coefficient for latent heat (which is a function of wind speed and stability), q_s the saturation

0-7803-3068-4/96$5.00©1996 IEEE

specific humidity associated with the SST, q the actual specific humidity and U is the mean wind speed. U and q are usually measured at a standard reference level of 10 meters. This equation demonstrates the importance of the wind speed in determining the latent (or sensible) heat flux provided that the SST and the moisture content of the air close to the surface are relatively constant. This is usually the case over large stretches of the tropical ocean, but wind speed can vary substantially. Fig. 1 shows data from the first LITE underflight from Wallops Island, Va. to Barbados, which occurred on September 11, 1994. The solid line on the lower half of the plot represents the height of the PBL as derived from LASAL data. The two dashed lines above and below the PBL height are the top and bottom of the entrainment zone, respectively. The entrainment zone is computed from the PBL height data in 10 km long, overlapping segments. For each segment the

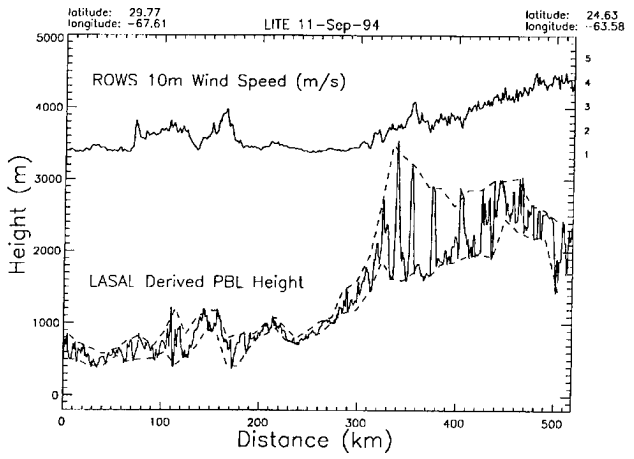


Fig. 1 The 10 meter wind speed (upper line) PBL height, entrainment zone depth (dashed) as a function of distance along the flight path for September 11, 1994.

bottom of the entrainment zone is defined as that height, above which the top of the PBL occurs 95 percent of the time. Likewise the top of the entrainment zone is that level below which the PBL top occurs 95 percent of the time.

Plotted at the top of the figure (right axis) is the wind speed at 10 meters as derived from ROWS (solid line). Our flight path took us across the trade wind belt which is generally between 15 and 25 degrees north. This is vividly seen to be between 280 and 500 kilometers in the figure. The wind speed increases from a very light 1.5 m/s to a moderate 4.5 m/s while the height of the PBL and depth of the entrainment zone increase markedly. It is interesting to note that the PBL depth and wind speed both increase by a factor of 3. This suggests a well obeyed relationship between the two in this case. While it is possible that the increase in PBL depth could be due to other processes, such as an increase in SST or a change in the magnitude or direction of the vertical motion, it is not likely. In fact, data from the SSTR do not show a substantial gradient of SST in this region and the ECMWF initial analysis shows widespread sinking motion in the area. We feel confident that the response seen in the PBL is mainly due to an increase in moisture flux caused by an increase in wind speed.

On September 17, we flew from Capetown, South Africa to Ascension Island and apparently encountered what could be described as the doldrums. The data are displayed in Fig. 2 and plainly show a relatively large area with wind speeds less than 3 m/s. Concurrent with the decline in wind speed is a reduction in PBL height as well as entrainment zone depth. On this day, the PBL exhibited a well defined two layer structure, which is quite common over the ocean. The lower layer, referred to as the well mixed layer, is actively connected to the surface and is capped by a relatively weak inversion which separates it from the layer above. This upper layer is a "residual" layer, which has advected into the area from a region where the mixed layer had grown to this height (possibly a continental PBL). The residual layer does not respond to changing conditions at the surface. It is the lower layer which most readily responds to variations in surface wind speed (or SST).

A glance at the ECMWF surface analysis for this day indicates that we crossed the axis of a high pressure ridge, flying about 400 km east of the center of the high. This would explain the light wind speeds and may be a partial explanation for the shallow PBL depths. Areas of enhanced sinking motion often are associated with high pressure systems and may be at least partially responsible for the very thin PBL in this area. However, the correlation of the wind speed with the PBL depth is so large, it is likely that we are also seeing smaller latent heat fluxes producing shallower PBL and entrainment zone depths.

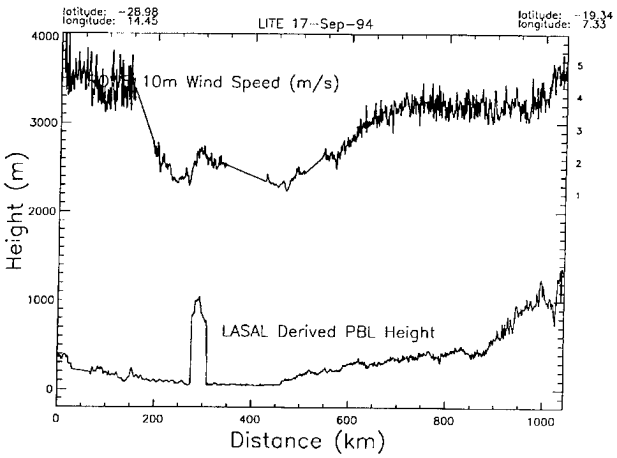


Fig. 2 Same as Fig. 1, except for data acquired on September 17, 1994.

Micro Scale Interactions

In addition to the large scale influences exerted on the PBL by the mean wind flow, we also encountered many examples of meso scale and micro scale interactions that were quite interesting. Fig. 3 is comprised of data from September 11th and shows the data from Fig. 2 between about 60 and 220 km. We see some remarkable correlations between PBL height and the wind speed on scales ranging from 10 to 40 km. Note in particular the wind speed minimum at about 120 km and the corresponding minimum in PBL depth at about 110 km. Also the general shape of the wind speed trace and the PBL depth are very similar for the entire region between 110 and 170, with highly correlated peaks occurring at roughly 130 and 150 km. Close inspection reveals that the correlations between the PBL height and wind speed appear to be phase shifted with the wind speed lagging the PBL height changes. This may be due to the fact that in an idealized convective cell, the highest PBL height would be expected to occur above the center of the updraft, while it is reasonable to assume that the highest surface wind speed would occur some distance from the central core of the updraft. Note as well that the PBL entrainment zone depth (or the amount of variance of the PBL top) is highly correlated with the variance of the wind speed.

On September 17, there was an isolated convective structure about 30 to 40 km wide which exhibited a strong correlation with the wind field. This can be seen centered at about 290 km in Fig. 2, where the PBL height jumps to almost 1.0 km from surrounding values of 200 meters or less. It should be noted that the capping inversion atop the shallow mixed layer in this region was very weak (as indicated by dropsonde) and that the residual layer

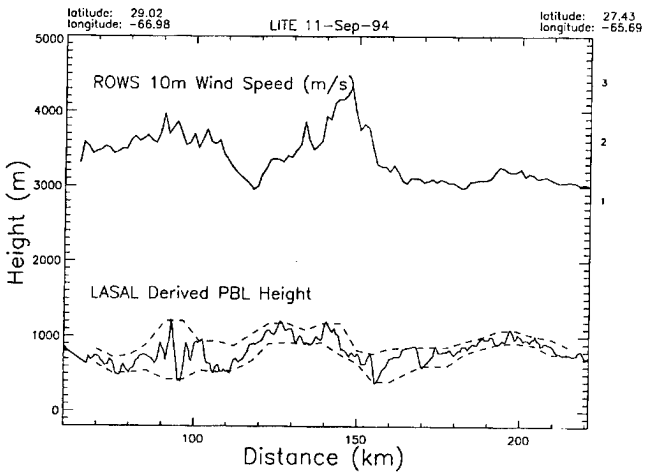


Fig. 3 A blowup of the region between 60 and 220 Km in Fig. 1 showing micro and mesoscale correlations of the PBL height and surface wind speed.

(between 200 and 1000 m) was nearly adiabatic. This means that a convective cell need not be extremely energetic to break through the lower inversion, and if it did so it would continue to rise until it hit the inversion capping the residual layer at 1.0 km. The wind speed increases from 1 to 2.5 m/s in the region of enhanced convection, but does not appear to fall off as quickly on the other side.

Summary

We have presented simultaneous measurements of the 10 meter wind speed and the depth of the boundary layer over the ocean in an attempt to understand how the wind field affects PBL structure, height and moisture flux. It is apparent that the wind field is closely coupled with the height and convective structure of the PBL at scales ranging from tens to hundreds of kilometers. This indicates that areas of relatively high PBL depth are associated with larger surface wind speeds and necessarily higher surface fluxes. The close relationship of the wind speed and PBL depth suggests that it may be possible to predict one given a measurement of the other. Such formulations already exist in the literature and the data presented here could be used to test their validity.

References

[1] S. Palm, S. H. Melfi, and D. L. Carter, "New Airborne Scanning Lidar System: Applications for Atmospheric Remote Sensing," *Appl. Opt.*, Vol. 33, No. 24, 1994, pp. 5674-5681.

[2] D. Vandemark, F. C. Jackson, E. J. Walsh, and B. Chapron, "Airborne Radar Measurements of Ocean Wave Spectra and Wind Speed During the Grand Banks ERS-1 SAR Wave Experiment," *Atmos.-Ocean.*, 32, 1994, 143-178.

[3] D. Hagan, "The Profile of Upwelling 11 Micron Radiance Through the Atmospheric Boundary Layer Overlying the Ocean," *J. Geophys. Res.*, 93, 1988, 5294-5302.

[4] J. Carswell, S. Carson, R. McIntosh, F. Li, G. Neumann, D. McGlaughlin, J. Wilkerson, P. Black, and S. Nghiem, "Airborne Scatterometers: Investigating Ocean Backscatter under Low- and High-Wind Conditions," *Proc. IEEE*, Vol. 82, 1994, pp. 1835-1860.

Remote Measurement of Coastal Marine Atmospheric Boundary Layer (MABL) Features

M. S. Jordan, C. H. Wash, and K. L. Davidson
Department of Meteorology
Naval Postgraduate School
589 Dyer Rd., Room 254
Monterey, CA 93943-5114, USA
T: 408.656.2295 F: 408.656.3061
EMail: wash@nps.navy.mil

SUMMARY

Coastal region marine atmospheric boundary layer (MABL) properties derived from satellite data are compared with coastal in situ aircraft-measured conditions. A multispectral approach using visible and IR data is being tested to estimate indirectly important variables such as depth of the MABL. In situ data were obtained from aircraft, ship mounted systems and from shoreline stations. In examined cases, remotely sensed information yields reasonable assessments of the height of the top of the boundary layer as well as of conditions immediately above the surface. Remote data describe high resolution horizontal/temporal variations, important in the coastal regions, but not described by point measured data.

INTRODUCTION

Coastal region MABL structures vary dramatically over short distances, 10-20 km. The height of the MABL is a feature of interest in several applications. For example, it is the location of elevated trapping layers affecting radio/radar waves. It is also the upper limit for mixing volume of pollution arising from shoreline activities. The depth of the MABL may be quite variable in coastal regions because it is influenced by both synoptic scale meteorological and local coastal circulations. In either case, horizontal variations occur in both the height of the MABL and strength of the capping inversion.

Currently, MABL depth is measured by radiosonde or aircraft vertical profiles. Neither method is sufficient for measurements over a large area. Remote sensing approaches based on passive sensors offer the potential to estimate variations of the MABL, such as its depth and relative moisture content, over a large region at one time.

Data collection and analyses have been funded in research programs managed by the Naval Command Control and Ocean Surveillance Center RTD&E Division (NRaD), Code 54, San Diego, CA.

In this paper we present results from examinations of multi-channel advanced very high resolution radiometer (AVHRR). This method is referred to as the multispectral approach. This approach uses visible and IR data to indirectly estimate important variables such as surface moisture and sea-surface temperature, as well as the depth of the MABL.

MULTISPECTRAL METHOD

The multispectral method is based on the radiative properties of aerosols and water vapor. Approaches for estimating aerosol optical depth have been developed, [1] and [2]. The method for estimating MABL depth and moisture properties relies on previously developed techniques for estimating aerosol optical depth and total column water vapor. The approach uses the red-visible radiance measurements of the NOAA AVHRR (channel 1) and the direct relationship between this radiance and optical depth. Satellite measurements of water vapor variations are also employed. Estimates of the total column water vapor, following Dalu [3], are derived from the split window brightness temperatures of the NOAA AVHRR (channels 4 and 5). Since both estimates are derived from the same sensor, the boundary layer estimates can be derived from a single satellite data source.

The method is based on three assumptions about the MABL: 1) The MABL is well-mixed, 2) aerosol optical depth variations are due to particles in the MABL, and 3) the percentage of column water vapor in the MABL can be estimated.

Satellite estimates of optical depth and column water vapor are both related to the MABL height and moisture. An iteration method was devised to solve for the MABL height and surface relative humidity for clear regions in a satellite pass using the AVHRR data, [4] and [5]. Sensitivity estimates using a model atmosphere indicated the method is reliable when the MABL satisfies the assumptions of the technique, [5].

0-7803-3068-4/96$5.00©1996 IEEE

RESULTS

The multispectral approach has been successfully applied to MABL analyses over Persian Gulf, Northern California and Southern California coastal waters. In this paper we will present a validation of the technique using case study during the Variability of Coastal Atmospheric Refractivity (VOCAR) experiment, off the southern California coast, in August-September 1993. The first VOCAR results are contained in the thesis by Walsh [6] and conference presentations at the last two IGARSS meetings.

To use the VOCAR period to test the technique, an estimate of the percentage of the water vapor in the MABL was used. This is an important improvement to the technique for climatological regions where significant water vapor is found above the marine inversion.

The case presented here, from the VOCAR period, was chosen because it was a clear day in the VOCAR region and radiosondes were launched within 30 minutes of the satellite pass time at seven locations (one ship, two island, 4 coastal locations). In addition, aircraft data are now available providing low level temperature and moisture profiles between the coast and San Nicolas (NSI) and San Clemente (NUC) islands with 2 hours of the satellite overpass.

In this case, there is significant mid-tropospheric water vapor. We computed the percentage of water vapor density in the MABL, compared with the total from the surface to 400 mb, for all radiosonde locations. The percentage, which is representative of the MABL throughout the region, is 14% for this case. This case indicates that the multispectral technique will work when significant amounts of mid-tropospheric water vapor is present.

Fig. 1 shows the multispectral MABL depth analysis for the 23:47 UT 26 August 1993 (4:47 pm local) NOAA AVHRR satellite pass. The dark areas indicate that the pixels were over land, are clouds, or the iterative method did not converge at that point. The raob observations are indicated by yellow dots on the image while aircraft profiles are denoted by white dots.

Fig. 1 shows the slope of the MABL, from shallow values to the west (75 m) to deeper values along the eastern portion of the coastal region (225 to 275 m). The thicker MABL region is associated with warmer sea surface temperatures (SST) along the California coast from Point Vincente (PVN) to North Island (NZY) near San Diego. The range of SST is from 23 to 24 C in the warmer area to 16 to 18 C south of Point Arguello (PDR) along the eastern edge of the California Current.

Evidence to confirm these coastal SST and MABL structures are found in the radiosonde and aircraft data. The only overwater raob is from the R/V Point Sur (PSUR) and its measured depth of 148 m compares favorably with the shallow 127 m satellite estimate.

A comparison of aircraft temperature and moisture profiles from the Point Mugu aircraft with the satellite assessment is presented in Table 1 and Figs. 2 and 3. The aircraft flew a vertical saw-tooth flight track between 75 m and 825 m penetrating the mixed layer. Nine measurements from aircraft descents and ascents along flight legs between San Clemente Island and south of Camp Pendleton (CPN) and between San Nicolas Island (NSI) and Point Vincente (PVN) are used. Of particular interest is the aircraft leg of the distinct gradient in MABL height and SST west of San Diego. Several aircraft soundings in the lee of San Nicolas Island have been excluded from the analysis as the MABL appears influenced by local island effects.

The aircraft soundings do confirm the slope of the MABL depth indicated by the satellite data. The satellite data does underestimate the depth by 36 m but the RMS differences are less that 42 m. The aircraft temperature of the mixed layer fall within 1 C of the satellite estimated SSTs. Scatterplots of aircraft vs satellite MABL depth (Fig. 2) and temperature (Fig. 3) confirm the good correlation between the two datasets.

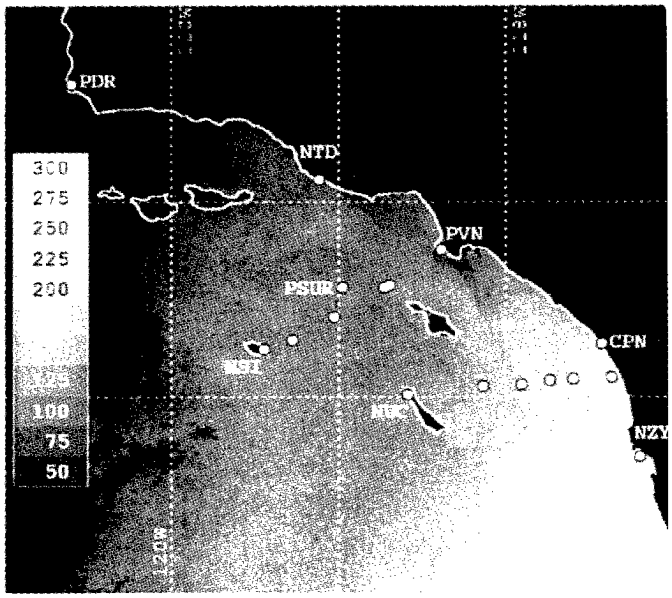


Fig. 1. Multispectral MABL depth (m) for 23:47 UT 26 August 1993 NOAA AVHRR satellite pass. VOCAR radiosonde observations are devoted by yellow dots and aircraft profiles are given by white dots. The dark areas indicate the pixels were over land, are clouds, or the iterative method did not converge at that point.

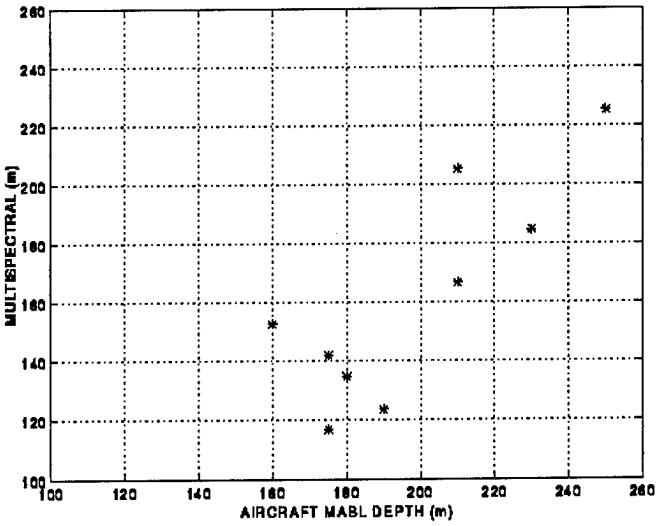


Fig. 2. Scatterplot of aircraft-measured and multispectral satellite estimates of MABL depths (m).

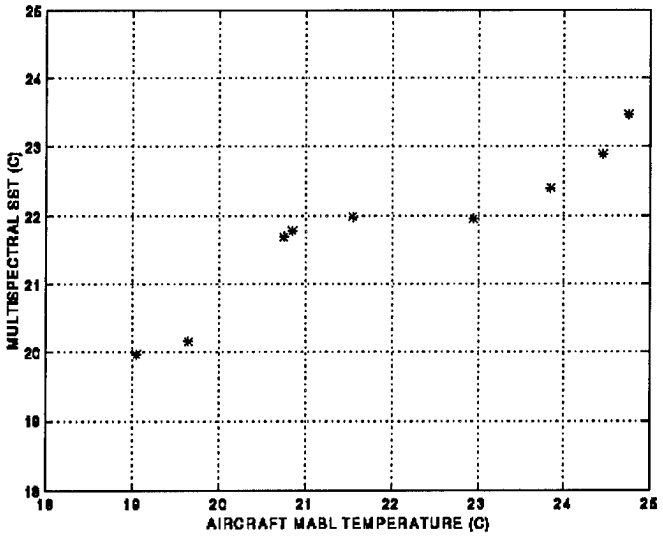


Fig. 3. Scatterplot of aircraft-measured MABL temperatures and satellite estimates of SST (C).

Table 1.
Comparison of Aircraft versus Satellite Retrieval Statistics

MABL HEIGHT

BIAS	36.6 m
RMS differences	41.7 m
Correlation Cofficient	.825

MABL TEMPERATURE VS NOAA SST

BIAS	0.16 C
RMS differences	1.06 C
Correlation Cofficient	.931

CONCLUSIONS

We have described the validation of remotely sensed estimates of mixed layer structure at and above the ocean surface in coastal regions using aircraft data during VOCAR. Presentation at the conference and future work will include more cases from the VOCAR period and other experiments.

ACKNOWLEDGMENTS

We thanks the NPS staff who contributed to the in situ VOCAR data collection and analyses (K. Jones, P. Frederickson, T. Neta). Special thanks goes to C. Skupniewicz, NPS, for his assistance in using the multispectral process code, and P. Jones, NPS, for her clerical assistance. Roger Helvey of Pacific Missile Test Center, Point Mugu provided the aircraft data and was of great assistance in its interpretation and use.

REFERENCES

[1] M. Griggs, "Satellite Measurements of Tropospheric Aerosols," Adv. Space. Res., vol. 2, pp. 109-118, 1983.

[2] P.A. Durkee, D.R. Jensen, E.E. Hindman and T.H. VonderHaar, "The Relationship Between Marine Aerosol Particles and Satellite-Detected Radiance," J. Geophys. Res., vol. 91, pp. 4063-4072, 1986.

[3] G. Dalu, "Satellite Remote Sensing of Atmospheric Water Vapor," Intl. J. Remote Sensing, vol. 7, 1089-1097, 1986.

[4] R.J. Kren, "Estimation of Marine Boundary Layer Depth and Relative Humidity with Multispectral Satellite Measurements," Masters Thesis, Naval Postgraduate School, Monterey, CA, 73 pp., June 1987.

[5] S.P. Smolinski, "Marine boundary layer depth and relative humidity estimates using multispectral satellite measurements," Masters Thesis, Naval Postgraduate School, Monterey, CA, 70 pp., March 1988.

[6] D.J. Walsh, "Multispectral NOAA Marine Atmospheric Boundary Layer (MABL) Estimates During VOCAR," Masters Thesis, Naval Postgraduate School, Monterey, CA, 106 pp., June 1994.

Estimation of the Ocean/Atmosphere Boundary Layer Height of Water Vapor from Space

Christopher S. Ruf and Shawn E. Beus
Communications and Space Sciences Laboratory
The Pennsylvania State University
121 Electrical Engineering East
University Park, PA 16802 USA
tel. 814-865-2363, FAX 814-865-7065, email ruf@rufece.psu.edu

Abstract -- A new retrieval technique has been developed which resolves some of the vertical structure of lower tropospheric water vapor over oceans from space. The relationship is demonstrated by comparisons between direct measurements of the water vapor profile, by radiosondes, and coincident estimates of the horizontal turbulence structure of Integrated Water Vapor, using the TOPEX Microwave Radiometer (TMR). Correlation is highest between the turbulence structure and the lower, boundary layer, component of the water vapor profile. The relationship is next applied to a two year time series of TMR data at Wake Island in the tropical Pacific. Both TMR and the Wake Island radiosondes indicate a periodic variation in the water vapor height which is consistent with the Madden and Julian Oscillation (MJO).

INTRODUCTION

Estimation from space of the vertically integrated water vapor burden (IWV) in the atmosphere over open ocean has reached a mature and operational level [1]. Measurements by a microwave radiometer of the upwelling brightness temperature near the 22 GHz water vapor line are used. Use of the relatively weak 22 GHz line results in robust estimates of IWV that are largely insensitive to variations in cloud cover, sea surface roughness and temperature, and the height distribution of the water vapor [2]. Global maps of IWV are routinely produced by satellite radiometers, including the SSM/I on board the DMSP platforms, the TMR on board the TOPEX/Poseidon satellite, and the microwave radiometers on board ERS-1 and ERS-2. The ability to infer some additional information about the vertical distribution of the water vapor from the global IWV images would add significantly to their value.

A relationship has been determined between the spatial correlation structure of the horizontal variations in IWV and the vertical distribution of the water vapor profile. The relationship can be explained by first considering the point-to-point correlation structure of the three dimensional water vapor density field. The structure function for this field is given by

$$D_\rho(s) = \left\langle \left[\rho(\vec{r}) - \rho(\vec{r}+\vec{s})\right]^2 \right\rangle \quad (1)$$

where s is the magnitude of the separation between points, $\rho(\vec{r})$ is the water vapor density at $\vec{r}$, and the expectation is over all realizations of the random function $\rho(\vec{r})$. If the separation, s, is assumed to lie within the inner and outer scales of isotropic turbulence, then Kolmogorov turbulence theory predicts a relationship of the form

$$D_\rho(s) = C_\rho s^\alpha \quad (2)$$

where C_ρ, the structure constant of the turbulence, scales according to the magnitude of the water vapor variability and α, the power law exponent, is a measure of the rate at which the water vapor distribution decorrelates with separation distance [3]. For the case of isotropic turbulence in three dimensions, α=2/3 [3]. If the separation, s, is larger than the outer scale (typically in the tens of meters), then (2) will not be strictly obeyed. For example, D_ρ will become independent of s at separations so widely spaced that the water vapor is essentially uncorrelated. Eqn. (2) can be considered a local model for the behavior of the correlation structure in different regions of the separation, with α considered a region dependent variable. For separations between the inner and outer scales of isotropic turbulence, α=2/3. For very large separations, α=0. In between these two extremes, we expect α to decay from 2/3 to 0.

Measurements of IWV are related to $\rho(\vec{r})$ by

$$IWV(\vec{x}) = \int_0^\infty \rho(\vec{r} = (\vec{x}, z))dz \quad (3)$$

where $\vec{x}$ denotes the two dimensions of horizontal variability of the IWV field and z is the height. The spatial correlation structure function for the IWV field is defined, in the same manner as the three dimensional field, as

$$D_{IWV}(s) = \left\langle \left[IWV(\vec{x}) - IWV(\vec{x}+\vec{s})\right]^2 \right\rangle. \quad (4)$$

0-7803-3068-4/96$5.00©1996 IEEE

If the separation, s, lies within the inner and outer scales of isotropic turbulence for the water vapor field, then Kolmogorov theory predicts a relationship of the form

$$D_{IWV}(s) = C_{IWV} s^{\beta} \quad (5)$$

where the power law exponent is given by $\beta=5/3$ [3]. We can locally fit the actual behavior of D_{IWV} to (5) for separations beyond the outer scale. We expect β to roll off from 5/3 to 0 as s increases to very large separations.

The behavior of β as a function of separation is also influenced by the finite vertical extent of the water vapor distribution. Even for the case of isotropic turbulence on all horizontal scales, separations which are an appreciable fraction of the vertical extent of the bulk of the water vapor will result in two dimensional structure functions for which β is reduced below 5/3. This aspect of the dependence of β on separation has been recognized and studied by several investigators [4, 5]. Armstrong and Sramek [4] estimate the dependence of β on separation directly from sets of phase differences between radio interferometer pairs with the Very Large Array in Socorro, New Mexico. They note a range of values $0.84<\beta<1.95$ for separations in the range 1-10 km. Treuhaft and Lanyi [5] corroborate this behavior with numerical simulations which predict a smooth, monotonic transition of β from 5/3 to 2/3 as the separation is varied from much less than to much greater than the height of a slab of water vapor which is isotropically turbulent on all scales in the horizontal direction. Note that their model does not incorporate the additional roll off of β with separation due to the finite outer scale in the horizontal direction.

TMR AND RAOB DATA PROCESSING

The IWV data used in this study were measured by the TMR [2]. TMR measures the brightness temperature in the nadir direction at 18, 21, and 37 GHz and estimates the path delay, PD, due to water vapor. Because the PD is nearly linearly proportional to the IWV [6], we use its turbulence structure to estimate the power law dependence, β, of the water vapor distribution. TMR data are recorded every 5.8 km along the satellite ground track. In our study here, we determine the structure function, D_{IWV} (s), by using sequential measurements of PD within a specified interval and approximating the expectation operator in (4) by an average over the data in that interval.

An estimate of the power law dependence, β, is made using a log/log linear regression of the structure function versus separation. We include only estimates of D_{IWV} (s) over the range $11.6<s<29.0$ km in our regression fit. This range has been found to produce a good correlation between β and coincident estimates of the water vapor scale height, as measured by the radiosondes.

Coincident radiosonde measurements were assembled as part of the TMR flight validation program [2]. Radiosondes provide a direct measure of the vertical profile of absolute humidity. One measure of the characteristic height of the water vapor, which we use here, is the fractional height, H(f). H(f) is defined as the height below which some fraction, f, of the total water vapor burden lies.

The flight validation program for TMR involves daily collection of radiosonde data from 24 island launch sites which lie within 50 km of the satellite ground track [2]. We have selected the subset of radiosonde launches which occurred within 100 min of a satellite overpass. Corresponding TMR data are selected which lie within a specified radius of the radiosonde launch site. This radius is determined independently for each overpass so that the standard deviation of path delay samples within the radius remains approximately the same. This controls for large changes in the statistics of the vapor field over the ensemble of data from which the turbulence structure is estimated. The average value for the radius was 500 km and results in a path delay standard deviation of ~2.0 cm.

TMR/RADIOSONDE INTERCOMPARISON

Scatter plots of H(f) versus the turbulence parameter β are shown in Figure 1. Fractional heights are shown with f = 10% and 50%. In both cases, the general trend is as expected. Higher rates of decorrelation with separation (higher values for β) generally correspond to lower characteristic heights of the water vapor profile. The correspondence appears stronger for the 10% fractional height. We conjecture that this may be due to the stronger correspondence between the lower fractional height and the thickness of the water vapor in the ocean/atmosphere boundary layer. This boundary layer water vapor is better mixed and, hence, more representative of three dimensional isotropic turbulence than are the higher regions of the profile.

A second comparison between the radiosonde height and β is possible by examining a continuous time series of the two values at a common location. The TMR-derived estimates of β are based on an ensemble of data from an entire orbit cycle (9.9 days), using all satellite ground tracks with closest approach points within 150 km of the launch site. The radiosonde heights, which are generally available twice daily, have been smoothed by a triangular running average of $\pm$10 days to approximate the effective time average imposed by the TMR processing. A sample of the results is shown in Figure 2 for the Wake Island

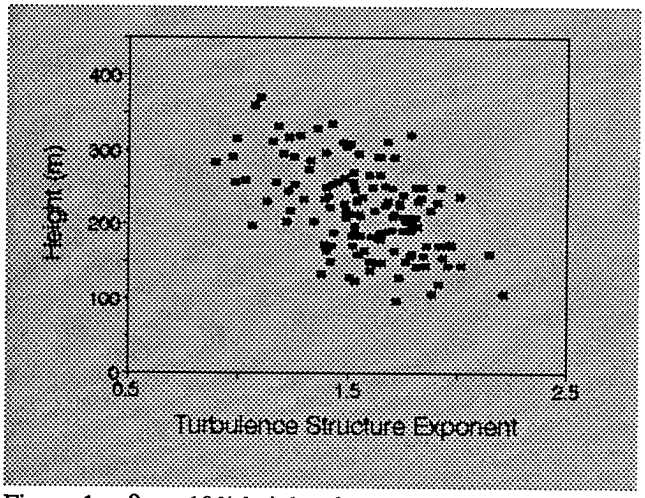


Figure 1a. β vs. 10% height of water vapor profile.

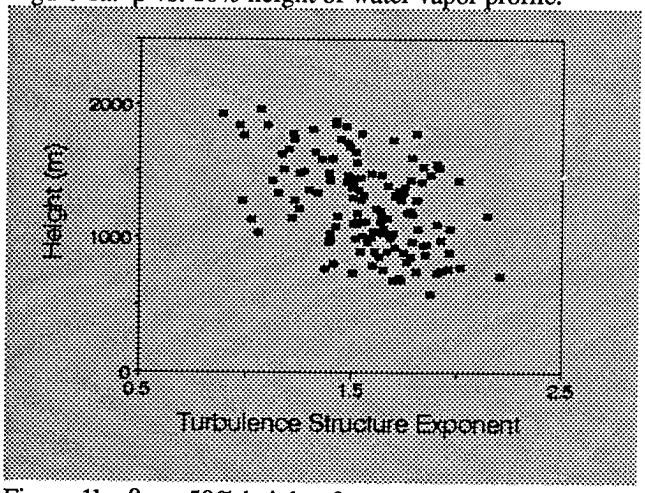


Figure 1b. β vs. 50% height of water vapor profile.

radiosonde station (latitude 19.28 North, longitude 166.65 East). Both radiosonde height and β time series' display an oscillating behavior which is consistent with the MJO period of 40-50 days [7]. The phase coherence between the two time series' suggests that they are responding to correlated characteristics of the water vapor profile. In addition to the similar MJO signatures, both time series' also have a similar response to the seasonal variation in the height of the water vapor profile. Higher levels are noted during the 1994 and 1995 summers in both the radiosonde height and the turbulence scale height which can be inferred from β.

REFERENCES

[1] J.C. Alishouse, S.A. Snyder, J. Vongsathorn, and R.R. Ferraro, "Determination of oceanic total precipitable water from SSM/I," IEEE Trans. Geosci. Remote Sens., 28(5), 811-816, 1990.

[2] C.S. Ruf, S.J. Keihm, B. Subramanya, and M.A. Janssen, "TOPEX/POSEIDON Microwave Radiometer Performance and In-flight Calibration," J. of Geophys. Res., 99(C12), 24915-24926, 1994.

[3] V.I. Tatarskii, Wave propagation in a turbulent medium, Dover, New York, 1961.

[4] J.W. Armstrong and R.A. Sramek, "Observations of tropospheric phase scintillations at 5 GHz on vertical paths," Radio Science, 17(6), 1579-1586, 1982.

[5] R.N. Treuhaft and G.E. Lanyi, "The effect of the dynamic troposphere on radio interferometric measurements," Radio Science, 22(2), 251-265, 1987.

[6] G. Elgered, "Tropospheric radio path delay from ground-based microwave radiometry," in Atmospheric Remote Sensing by Microwave Radiometry, M.A. Janssen, Ed., New York: Wiley, ch. 5, 1993.

[7] R.A. Madden and P.R. Julian, "Description of global-scale circulation cells in the tropics with a 40-50 day period," J. Atmos. Sci., 29, 1109-1123, 1972.

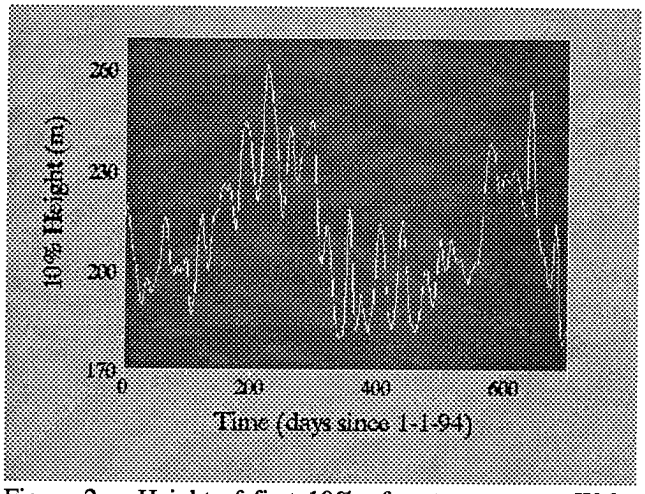


Figure 2a. Height of first 10% of water vapor at Wake Island - derived from RaOb profiles.

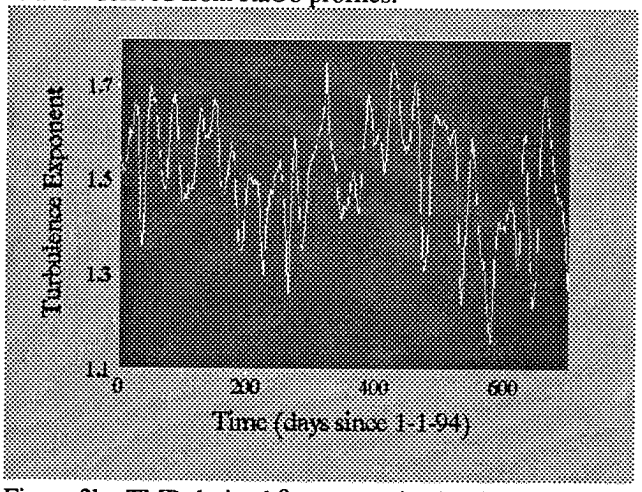


Figure 2b. TMR derived β at same site (Wake Island).

Rain Measurement with SIR-C/X-SAR

R. K. Moore, A. Mogili, Y. Fang, B. Beh, A. Ahamad
University of Kansas, Radar Systems and Remote Sensing Laboratory
2291 Irving Hill Road, Lawrence KS 66045-2969 USA
TEL: 913/864-4736 , FAX: 913/864-7789 , E-mail: rmoore@eecs.ukans.edu

Abstract—Rain measurements by ground-based radar are unavailable in many parts of the world, especially the oceans. Because many SARs will be flying in space, we (a group headed by Dr. F. Li of JPL) performed an experiment using the SIR-C/X-SAR radars to test the ability of spaceborne SARs to measure rain rates. SAR resolution in rain is degraded by Doppler shifts due to turbulent motion of the rain (Atlas and Moore, 1987). The wide vertical beam required to achieve SAR ground coverage means that one must accept a path-integrated estimate of the rain rate. We used two approaches to rain measurement using the SIR-C/X-SAR radars pointed well off vertical. Over the western Pacific Ocean, we used the strength of the rain echo to estimate rain rate using an appropriate Z-R relation, as do ground-based radars. To separate rain echo from surface echo, one must estimate the surface contribution to the signal. Over the Amazon rain forest where the shadows are obvious we used the reduction of signal in the shadow due to attenuation through a rain storm.

THE EXPERIMENT

SIR-C was a multi-polarized SAR with frequencies in L band and C band while the X-band X-SAR used only vertical (VV) polarization. The SRL-1 mission was in April 1994, and the SRL-2 mission in September-October 1994. We obtained storm images from both in both the southwest Pacific and in Brazil.

We could only turn the radars on a few times, with requests needed about 20 hours in advance for the southwest Pacific passes. The Brazil passes were scheduled for other purposes. For rain forecasts, the JPL team used cloud IR images from the GMS satellite and the Kansas team obtained forecasts of precipitation from the Australian Bureau of Meteorology at 6-hour intervals. Forecast maps from the Singapore Meteorological Service were also used.

THE PACIFIC OCEAN EXPERIMENT

Methodology

Users of ground-based weather radars get rain rates by inverting the radar equation for volume scatter. The volume scattering coefficient relates to the quantity Z, the mean sum of (drop sizes)6 /m3 in mm6 /m3 by

$$\eta = 10^{-10}\frac{\pi^6}{\lambda^4}|K_w|^2 Z \qquad (1)$$

where $|K_w|^2$ is a function of the refractive index of water, temperature and wavelength, and η is the volume-scattering coefficient. For practical purposes, at the wavelengths and temperatures here, we may consider it to be 0.93.

Many relations have been reported between Z and rain rate R [1,2]. We elected to use two relations: $Z = 300R1.5$ and $Z = 170R1.47$ from [3], based on drop-size distribution for convective cells measured in the area of our experiment during TOGA-COARE.

To determine the scattering volume we had to assume a height for the rain column and the rms turbulent velocity needed to get the along-track resolution. The thickness of the cell is the range resolution. The width of the shell must be determined from the assumed rms turbulent velocity. Using the analysis of [4], this width (the azimuth resolution) is

$$r_a = \frac{2u_t R}{u} \qquad (2)$$

where u_t is the rms turbulent velocity assumed for the rain drops and u is the spacecraft speed. Our analysis applies only when the entire range shell is within the storm. We ignored other cases in our calculations.

This result can only be used when is small enough to be ignored. If we must consider the attenuation to the bottom of the storm, one must correct the volume V of a range shell for the differential attenuation suffered by different parts of the shell. Of the numerous values of extinction coefficient K_{er} in the literature, we used [5]

K_{er}=0.002R dB/km or 0.00023R Np/km at C band (λ=5.7 cm)
(3)
K_{er}=0.008R1.1 dB/km or $0.00092R^{1.1}$ Np/km at X band (λ=3.2 cm).

These expressions require the rain rate, which is initially unknown, so an iterative procedure is necessary.

Since both rain echo and surface echo are random signals, we may get the rain echo by subtracting an estimate of the surface echo. We could use the surface echo from rain-free regions nearby, but this ignores both the effect of higher winds in a convective cell and of raindrops striking the water [5,6]. We estimated the wind in the convective cells to be 15 m/s (may be high), and obtained the scattering coefficient from the CMOD4 model [7] for C band and the SASS model [8] for X band, assuming cross-wind conditions.

Observations

Pass 13.4 of the Shuttle Radar Lab (SRL) was near Ontong Java Atoll in the South Pacific with an angle of incidence of 48°. The center of the images is at 6° S 159° E. Fig. 1

0-7803-3068-4/96$5.00©1996 IEEE

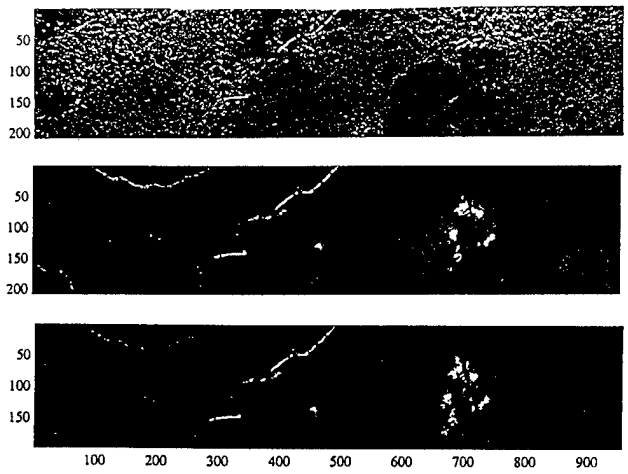


Fig. 1 L-, C-, and X-band images for pass 13.4 at 6° S 159° E. The bright curved lines present in all images are from Ontong Java Atoll. Rain cells are apparent to the east of the atoll in the C- and X-band images.

shows 100-km-long L-, C-, and X-band images of the area. The outline of a part of Ontong Java Atoll shows in all images and we see rain cells in the C-band and X-band images. We analyzed the strong storm cell that shows roughly between 710 and 790 on the horizontal axis. Dark spots on the L-band image occur near the brightest regions on the C- and X-band images, suggestg echo rain drops hitting the surface as reported by Atlas [9].

We assumed the storm height to be 4.5 km, and a reasonable value of 3.5 m/s as the rms turbulent velocity in the storm. Clearly the assumptions used affect the rain estimates.

We computed rain rates for three storms during the first mission and one during the second mission, but we report here results of only one set of measurements. Each storm was a relatively small cell, obviously convective from its size.

Tables 1 and 2 show the measured apparent rain signal in dBZ, ordered by signal strength in different parts of the storm echo. The corrected values shown (dBZ1 for $Z=300R^{1.5}$ and dBZ2 for $Z=170R^{1.44}$) come from removing the surface echo using attenuation of the surface echo for each of the Z-R relations. The rain rates (R1, R2) are based on the two Z-R relations. Finally, we show a modified dBZ and a *corrected* rain rate (R1C, R2C) based on the correction for attenuation of part of the rain echo.

The rain rate using the expression of [3] is nearly double that for $Z=300R^{1.5}$. We believe that the higher rate is likely to be a better estimate because it is based on convective storms in the same part of the world. Unfortunately, no surface measurements are available to verify this. Auki, Malaita, Solomon Islands weather station reported thunderstorms in the vicinity.

The C-band dBZ values often are larger than those at X band without the attenuation correction. However, the attenuation-correction seems to overcorrect the X-band values. This could be due to overestimating the attenuation rate using (3), to non-uniform density of the rain, or to some other problem.

dBZ	dBZ1	Mod dBZ1	R1 mm/hr	R1C mm/hr	dbZ2	Mod dBZ2	R2 mm/hr	R2C mm/hr
46.8	45.5	45.7	24.2	24.7	45.6	45.9	41.6	43.2
46.9	45.7	45.9	24.8	25.5	45.8	46.1	42.8	44.7
47.4	46.3	46.5	27	28.0	46.3	46.6	46.7	48.6
47.7	46.7	46.9	29.1	29.8	46.8	47.1	50.4	52.9
48.1	47.2	47.4	31.2	32.2	47.3	47.6	54.1	57.5
48.3	47.5	47.7	32.6	33.8	47.5	47.9	56.6	59.5

Table 1 C-band rain reflectivity and rain rates, SRL-1. Location 5°S 159°E.

dBZ is rain reflectivity with no corrections. dBZ1 is value corrected for surface echo, assuming attenuation for rain rate R1 obtained w/ $Z = 300R^{1.5}$. Mod dBZ1 is value of dBZ1 corrected using effect of attenuation on rain echo. R1C is R1 value corrected using effect of attenuation on rain echo. dBZ2 is value corrected for surface echo, assuming attenuation for rain rate R2 obtained with $Z=170R^{1.44}$. Mod dBZ2 is value of dBZ2 corrected using effect of attenuation on rain echo. R2C is R2 value corrected using effect of attenuation on rain echo.

dBZ	dBZ1	Mod dBZ1	R1 mm/hr	R1C mm/hr	dbZ2	Mod dBZ2	R2 mm/hr	R2C mm/hr
44.7	43.8	44.4	18.5	20.4	43.9	45.0	31.8	37.6
46.3	45.7	46.6	25.1	28.3	46	47.5	43.4	56.3
47.4	47	48.0	30.2	35.6	47.1	48.9	52.5	70.7
48.1	47.7	48.9	33.9	40.4	47.8	49.9	59.1	82.1
48.3	48	49.2	35.3	42.7	48.1	50.3	61.7	87.3
48.7	48.7	50.1	39.5	48.6	48.8	51.2	69.3	101.9

Table 2 X-band rain reflectivity and rain rates, SRL-1. Location 5°S 159°E. Legend same as Table 1.

THE AMAZON RAIN FOREST EXPERIMENT

Methodology

Meneghini [10,11] proposed a surface-reference technique (SRT) to estimate the path-averaged rain rate from the direct measurement of total rain attenuation, using the difference between signals from the surface in rain and outside the rain area. We used this method to estimate rain rate from rain shadows on images of the Amazon rain forest. Surface echoes in the shadow are given by $\sigma^0 A$, where A is the attenuation factor. If we know the path length through the rain volume between radar and surface target, we can get K_{er}, the attenuation coefficient in dB/km. Inverting the usual K_{er}-R law gives the average rain rate.

This technique does not use any rain-echo information. The surface-reference technique depends on comparing echoes in the shadow that are reduced by the integrated rain attenuation with echoes outside the shadow region. We used a simple

model to characterize the radar signal returns for the rain cell. Assumptions for the model are: 1) the rain is in a rectangular cylinder with height of h and width of w; 2) the σ^0 of the surface clutter is assumed to be constant; 3) the volume scattering from the rain is much smaller than the surface echo.

The model has two cases: 1) rain cell is long enough for a complete ray from top to ground within the rain, a low but widespread rain cell; and 2) a higher but smaller rain cell, in which the ray from the top of the rain passes out the back of the cell and therefore has less attenuation.

Fig. 2 shows the simulated range-profile signal for the model. The profile for the ground returns contains three segments. In the first segment, the surface return decreases with range with a slope proportional to the attenuation factor. In the second segment the attenuated path length remains constant, as does the ground return. In the third segment the return increases with the increasing range until the radar beam misses the rain.

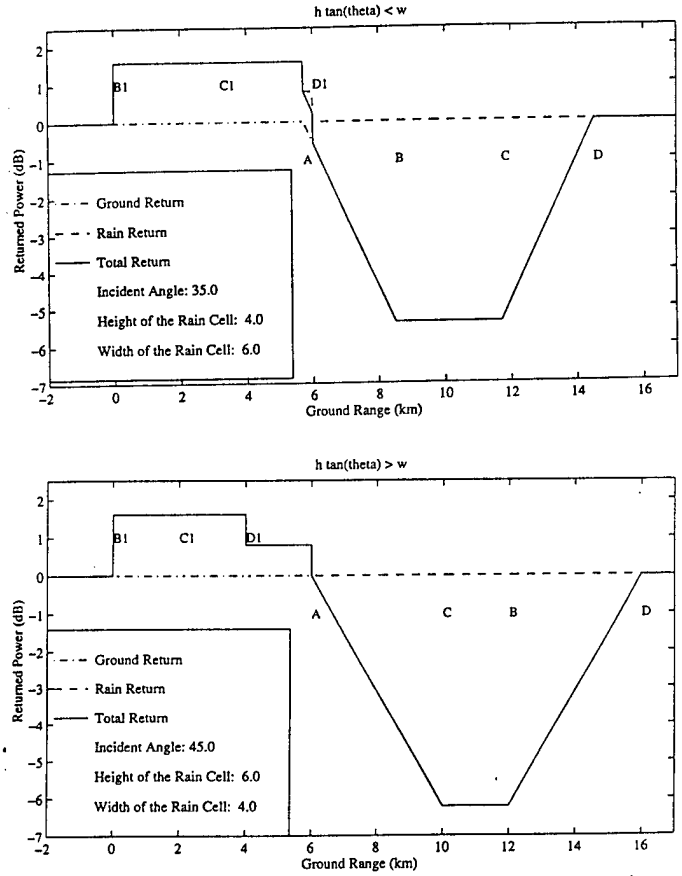


Fig. 2 Profiles of expected signals in presence of rain cell. Note that for case 1, the path length within the rain cell CC' is equal to BB' whereas for case 2, CC' = BB'-BC. This is an uncertainty in path length determination.

The Doppler frequency shift from rain drop motion can shift the rain echo away from the shadow by as much as 1 km. Note the shift for the rain cell shown in the upper right corner of Fig. 3. The rain shadows usually appear to have a fan shape. This may be because of the irregular shape of the rain cell, but the very long synthetic aperture of a spaceborne SAR can also contribute when the signal from only one end of the synthetic aperture passes through the rain.

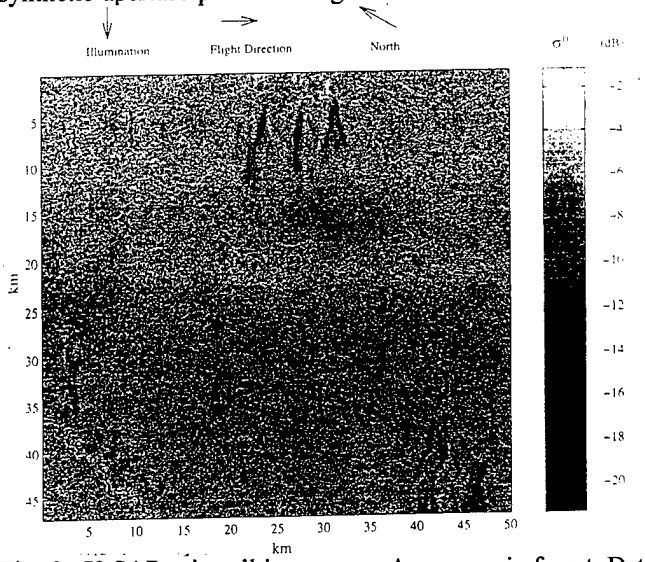


Fig. 3 X-SAR rain cell image over Amazon rain forest. Data take ID 103.60

Since the image pixels for the rain cell and its shadow are not necessarily well aligned, we cannot get the correct range profile of the signal return for the rain by plotting the signal returns on the same range line. To determine the right σ^0 value at a certain range, we pick portions with the strongest return along the track when the range is within the rain, while we pick portions with the weakest returns beyond the rain (inside the rain shadow).

Observation

Here we used the image from pass 103.60 taken by SIR-C/X-SAR at 43° incidence over the Amazon rain forest region during SRL-2. The overall results are stated in Table 3. The surface-reference technique (attenuation method) gives excellent results compared with the backscatter method used over the ocean. Both X- and C-band data give reasonable and similar results. The rain rates obtained from the C-Band image are less than from the X-Band image; but with the uncertainties in the K_{er} relations, these differences are not large.

CONCLUSIONS

Spaceborne SAR could provide information about rain rates in suitable areas of the world, but the errors in the rain rates retrieved can be large because of the many assumptions needed. However, the ground-mapping SARs are far from optimum for the purpose. A special-purpose SAR for rain [4]

would not have these limitations, but would be expensive for this application.

Our two approaches used Z-R relations for ocean and measurement of attenuation through rain cells for land. We presented examples of use of both methods for the SIR-C/X-SAR radars flown on the Shuttle in 1994. Retrieved rain rates over the Southwest Pacific were more variable because they required so many assumptions. Rain rates retrieved over the Amazon rain forest were less variable because we needed to make fewer assumptions.

Frequency Band	a	b	Attenuation (two way in dB)	Path Length within raincell (km)	rain rate (mm/hr)
X	0.008	1.1	5.4	6.5	83 cell 1
C	0.002	1	2.0	6.5	77 cell 1
X	0.008	1.1	5.5	6.1	89 cell 2
C	0.002	1	2.0	6.1	82 cell 2
X	0.008	1.1	7	5.5	128 cell 3
C	0.002	1	2.4	5.5	109 cell 3

Table 3 Rain rates in the Amazon rain forest.

We estimated rain rates over the ocean in the range of 20 to 140 mm/hr using a Z-R relation based on drop-size distributions measured in convective storms in the same general area. Rain cells over the Amazon basin show bright echoes at X band and strong shadows at both X band and C band. Rates of 77 to 109 mm/hr were estimated using the attenuation method. These seem reasonable for tropical convective storms. We believe this first attempt at using off-nadir SAR rain echoes and shadows to determine the rain shows that the methods used have potential to expand our climatology of rain by use of spaceborne SARs.

ACKNOWLEDGMENTS

This work was supported by NASA through JPL contract 958522. The work was done cooperatively with the group at JPL, including Fuk Li, Steve Durden, and Ziad Haddad.

REFERENCES

[1] R. Wexler and D. Atlas,"Radar reflectivity and attenuation of rain,"*J.Appl.Meteor.*, vol.2, pp. 276-280, 1963.

[2] L. J. Battan, *Radar Observation of the Atmosphere,* Chicago, Univ. Chicago Press, 1973, 324 pp.

[3] A. Tokay, D. A. Short, and O. W. Thiele, "Convective vs. stratiform rain over Kapingamarangi Atoll during TOGA-COARE: Evidence from raindrop spectra," *J. App. Meteor.*, in press.

[4] D. Atlas and R. K. Moore, "The measurement of precipitation with synthetic aperture radar," *J. Atmos. & Oceanic Tech.* vol. 4, pp. 368-376, 1987.

[5] R. K. Moore, Y. S. Yu, A. K. Fung, D. Kaneko, G. J. Dome, and R. E. Werp, "Preliminary study of rain effects on radar scattering from water surfaces," *IEEE Comm. in J. Oceanic Eng.*, vol. OE-4, pp. 31-32, 1979.

[6] L. F. Blivens and G. Norcross, "Effects of rainfall on scatterometer derived wind fields," *Digest IGARSS'88,* vol. 1, pp. 565-566, 1988.

[7] W. H. Gemmill, P. Woiceshyn, C. A. Peters, and V. M. Gerald, "A Preliminary Evaluation of Scatterometer Wind Transfer Functions for ERS-1 Data," *NMC/OPC Tech. Note. 20746,* Camp Springs MD, Ocean Product Center, 1994.

[8] L. C. Schroeder, et al., "The relationship between wind vector and normalized radar cross-section used to derive Seasat-A satellite scatterometer winds," *J. Geophys. Res.*, vol. 87, pp. 3318-3386, 1982.

[9] D. Atlas, "Footprints of storms on the sea: A view from spaceborne synthetic aperture radar," *J. Geophys. Res.*, vol. 99, pp. 7961-7969, 1994.

[10] R. Meneghini and D. Atlas, "Determination of rain rate from a spaceborne radar using measurement of total attenuation," *IEEE Trans. on Geosci. & Rem. Sens.*, vol. 21, pp. 34-43, 1983.

[11] R. Meneghini, J. A. Jones, and L. H. Gesell, "Analysis of a dual-wavelength surface reference radar technique," *IEEE Trans. Geosc. & Rem. Sens.*, vol. 25, pp. 456-471, 1987.

Artifact Correction and Absolute Radiometric Calibration Techniques Employed in the Landsat 7 Image Assessment System

Wayne C. Boncyk
U. S. Geological Survey
EROS Data Center, Sioux Falls, SD 57198
605-594-6020 fax:605-594-6529 boncyk@edcsgw4.cr.usgs.gov

Brian L. Markham
NASA/GSFC
Code 923, Greenbelt, MD 20771
301-286-5240 fax:301-286-1757 markham@highwire.gsfc.nasa.gov

John L. Barker
NASA/GSFC
Code 925, Greenbelt, MD 20771
301-286-9498 fax:301-286-1757 jbarker@highwire.gsfc.nasa.gov

Dennis Helder
South Dakota State University
EERC, Brookings, SD 57007
605-688-4184 fax:605-688-5880 helderd@mg.sdstate.edu

Abstract -- The Landsat-7 Image Assessment System (IAS), part of the Landsat-7 Ground System, will calibrate and evaluate the radiometric and geometric performance of the Enhanced Thematic Mapper Plus (ETM+) instrument. The IAS incorporates new instrument radiometric artifact correction and absolute radiometric calibration techniques which overcome some limitations to calibration accuracy inherent in historical calibration methods. Knowledge of ETM+ instrument characteristics gleaned from analysis of archival Thematic Mapper in-flight data and from ETM+ prelaunch tests allow the determination and quantification of the sources of instrument artifacts. This a priori knowledge will be utilized in IAS algorithms designed to minimize the effects of the noise sources before calibration, in both ETM+ image and calibration data. Gain and Bias estimates for each ETM+ detector that are derived from onboard calibrators are tracked with Ground based measurements, and with prelaunch measurements of instrument gains and biases as part of a Combined Radiometric Model (CRaM), to yield improved estimates of absolute gain and bias per channel. Trends in these instrument parameters are observed and recorded, allowing for the development of analytic models of detector gain and bias as functions of time and instrument state. IAS radiometric calibration methodology, utilizing precalibration artifact correction in conjunction with CRaM gain and bias determination, provides a more consistent absolute calibration of the ETM+ than that possible with historical TM calibration approaches.

0-7803-3068-4/96$5.00©1996 IEEE

HISTORICAL PERSPECTIVE

The Thematic Mapper (TM) instruments flown on Landsats 4 and 5 were designed to provide image data to an overall absolute radiometric calibration accuracy of 10 per cent, and a band to band accuracy of better than 2 per cent [1]. The TM only has one onboard calibration reference source, the Internal Calibrator (IC) comprised of three halogen lamps for reflective band calibration and a heated black body for emissive band calibration. Thus, TM absolute radiometric calibration has been a daunting task. Within-band relative calibration has also proven somewhat difficult, as uncertainties in the position of the IC shutter and in the knowledge of cal pulse intensity as a function of position along the shutter flag have led to errors in the determination of each detector's response to input radiance.

Further complicating TM calibration has been the presence of various sources of instrument, spacecraft and transmission noise that have introduced radiometric "artifacts" such as Scan Correlated Shift (SCS), Memory Effect (ME), and Coherent Noise (CN), amongst others, into TM imagery. These artifacts place further limits on the radiometric quality of TM imagery.

Two approaches have traditionally employed to calibrate TM imagery. The method developed at NASA/GSFC uses a least squares regression technique on data provided from the IC to find a nominal gain and offset for each detector, based on cal data provided with the scene [2]. A variant of this approach has offsets determined scan by scan.

Resultant image Digital Numbers (DN) are rescaled to provide optimal band average dynamic range. These rescaled values are then subjected to a histogram normalization process to minimize residual detector-to-detector uncertainties (reducing residual image striping). Normalized DN are finally related to absolute spectral radiance.

The CCRS method can be thought of as the inverse of the NASA technique [3]. Detector offsets are removed on a scan by scan basis. Then within each band, matching of detector response histograms from the scene being processed is used to relate all other detector responses to that of a preselected "reference" detector. The result is a set of detector differential gains and offsets employed to relatively correct the image. Response of the reference detector to IC lamp radiance is then employed to effect subsequent absolute calibration.

While each historical technique appears to have been adequate to provide TM data calibrated to the original specification, both posess characteristics that make them less than optimal. Initially, these calibrations are essentially scene based. That is, gains and offsets are determined only from calibrator data available from the scene currently being processed. Uncertainties in estimates of these parameters result in variations in calibration from scene to scene, often resulting in obvious discontinuities along scene boundaries in mosaics of adjacent path-rows. Studies of TM data suggest that detector gains are actually quite stable over long intervals; variance in true gains is much smaller than the uncertainty in gain estimates derived from a single scene's calibrator data, using historical techniques.

Next, image artifacts have not been adequately addressed. Only Banding and Striping have been handled with any degree of success, using histogram normalization techniques. However, histogram normalization "corrects" image striping at the expense of absolute calibration knowledge. Further, artifacts like ME, SCS, and CN, which occur in both image and calibrator data, are typically not corrected at all. Although small when measured as a percentage of full dynamic range (in TM data ME error is typically 4 DN worst-case, SCS error is on the order of 1 DN and CN is less than 1 DN), these errors can be significant when attempting to use data from a low contrast image, or (as happens with many user applications) when using data over relatively uniform spatial domains where the range of radiance in some bands is as small as 20 DN or less.

IAS CALIBRATION METHODOLOGY

The ETM+ requirement for absolute radiometric calibration of 5 per cent is even more stringent than that levied on TM. The need for better calibration, coupled with the need to eliminate image artifacts from calibrated data, have determined the following calibration technique.

Artifact Correction

The IAS radiometrically calibrates ETM+ imagery in a manner which differs fundamentally from historical techniques in two respects. Initially, artifacts are removed from both image and IC data whenever possible *in advance of calibration.* ME, SCS, CN, etc., are sources of error in measurements of cal data as well as imagery. Upon inspection of TM - IC data, the effects of SCS, CN and ME on shutter samples are evident.

Key to the design philosophy of IAS is the assumption that many of the artifacts present in TM data will exist in ETM+ as well. This assumption is justified since the ETM+ instrument design borrows significantly from TM heritage. IAS models of ME, SCS, CN and other artifacts are analytical, based upon information derived from TM analysis and from ETM+ prelaunch test results. The results of those models are used within Pre-1R Correction algorithms to remove the artifacts which are known to compromise absolute radiometric calibration. The models are not initially static; they may be "tuned" to allow for ETM+ idiosyncracies that are not discovered until on orbit data have been processed.

First consider ME. This is a response of each detector's analog signal conditioning electronics to changes in detector output that result from changes in input radiance. In TM the ME is a third order response, but is dominated by a first order RC "undershoot" resulting from feedback in the detector preamps, having a time constant on the order of 1000-1100 minor frames (pixels). ME has been observed from the outset in TM data, but empirical characterizations of the data sets have historically failed to note that every phenomenon from "forward-reverse scan banding" to "bright target recovery" to "scan line droop" is principally due to ME.

In anticipation of similar effects in ETM+, the magnitudes and time constants of the ETM+ analog chain will be modeled. The IAS ME characterization algorithm investigates how closely the instrument response actually follows the model, and will allow corrections to be made to the initial model as appropriate. The model is employed together with an estimate of each detector channel's initial state at each minor frame to determine the magnitude of the ME correction to be applied to that pixel.

Next consider SCS. Analysis of Landsat 4 and 5 TM data have shown that the shift is a change in detector offset correlated to the beginning of a new scan and that the amount of shift in offset is quantized. L4 generally exhibits four discrete shift states, L5 TM only two. The net magnitude of the shifts is essentially constant, and the shift state of any scan line may be determined from investigation of IC offset level for that scan, after ME has been accounted for.

The SCS characterization algorithm within IAS is employed to determine the number and magnitude of shift states, if any, present in ETM+ data. SCS correction will introduce compensating offsets to be applied to all minor frames within scans, on a line by line basis.

The effects of CN are present throughout an image, but are most apparent in regions of uniform input. CN in IC shutter data is shown in Fig.1 as a "herringbone" pattern in the otherwise relatively uniform shutter offset. In TM the noise period is approximately 20 minor frames. The artifact affects individual detector channels differently, but results in either positive or negative spikes in the data that are correlated to SCS state. This suggests the CN mechanism is related to that causing SCS.

The IAS CN characterization algorithm measures the period, frequency, magnitude, and phase of CN both within the IC shutter region and within the near-uniform radiance scenes provided by ETM+ Full Aperture Calibration. This information is correlated to SCS state. CN correction determines the proper correction to be applied to a given scan line based on SCS state and after phase-locking to the noise present in the cal shutter region of a scan's IC data, applies an appropriate magnitude correction to affected minor frames in the given scan.

Absolute Radiometric Calibration and the CRaM

After those instrument artifacts that can be corrected pre-calibration are removed to the greatest extent possible, the image minor frame raw radiances (in DN) must be related to absolute values of spectral radiance. In essence this process is the same for ETM+ as for TM: a linear transfer function relating input minor frame measurements in DN to absolute values of spectral radiance is determined for each detector, for each band. The transfer function is specified in terms of instrument bias or offset (the zero input radiance value in DN) and gain. Gains and offsets are derived from calibration data. ETM+ differs from TM in that in addition to the calibration reference provided by the IC, periodic views of the Full Aperture Solar Calibrator (FASC) and Partial Aperture Solar Calibrator (PASC) are available. Further correlation of measured at-aperture radiance to ground target irradiance and reflectivity is available through Ground Look Calibrations.

The IAS calibration process differs from that employed for TM. It makes optimal use of all calibration data available by: 1) using gains and offsets derived from prelaunch calibration measurements, 2) determining gains (integrated per scene as well as line by line) and offsets (line by line) from all IC data processed, relating these parameters to instrument state (temperatures, time since "on", position in orbit, accumulated "on" time and accumulated life), 3) similarly determining gains and offsets from PASC data, 4) determining gains from FASC data, and 5) determining Ground Look derived gains and offsets. These parameters are trended, and a statistical determination of the random uncertainty in each individual parameter measurement is made. Outlier rejection criteria are determined from trend data.

Those measurements not rejected as outliers are used to develop analytic models of the behavior of each detector to individual calibration sources. These models allow both the determination of systematic differences between calibration sources and the prediction of future behavior on an individual detector to cal source basis.

Finally, individual cal source models are integrated in the Combined Radiometric Model (CRaM), using rules determined by observation of the on orbit response of the instrument to each cal source, correlated with Ground Looks. These are employed to weight the available sources of gain and offset to allow calculation of a "current" integrated gain and offset for each detector. It is anticipated that these results will be well behaved, and can be modeled as well. Thus the output of the CRaM is a model of detector gains and offsets as functions of time and instrument state.

CONCLUSIONS

CRaM ensures that an "optimal" calibration model for each detector is maintained throughout the life of ETM+, allowing the effects of instrument change to be eliminated from long-term scientific applications of ETM+ data. Additionally, it allows determination of gain and offset on an individual scan basis, affording the best possible calibration of any image scan and virtually eliminating observed scene to scene differences in calibration. When gain and offset corrections supplied by CraM models are employed as part of an overall IAS calibration strategy including the elimination of instrument artifacts pre-calibration, significant improvements in radiometry over historical methods are the result.

REFERENCES

[1] Hughes Aircraft Space and Communications Group, NASA Contract NAS 5-24200 Final Report - Thematic Mapper, prepared for Goddard Space Flight Center, June 1978, p. 2-53.

[2] J. Barker, R. Abrams, D. Ball, and K. Leung, "Radiometric Calibration and Processing Procedure for Reflective Bands on Landsat-4 Protoflight Thematic Mapper," NASA Conf. Pub. 2355 - Proc. of the Landsat-4 Science Characterization Early Results Symposium, vol. II, pp. II 47- II 86, Feb 22-24, 1983.

[3] T. Butlin and J. Murphy, "Early Processing of Thematic Mapper Data by the Canada Centre for Remote Sensing," Proc. of the 17th International Symposium on Remote Sensing of Environment, pp. 1383-1392 May 9-13, 1983.

Landsat-7 Enhanced Thematic Mapper Plus In-Flight Radiometric Calibration

Brian L. Markham
Code 923, NASA/GSFC
Greenbelt, MD 20771
(301)286-5240 (Voice)
(301)286-0239 (FAX)
Email: markham@highwire.gsfc.nasa.gov

Wayne C. Boncyk
USGS/ EROS Data Center
Sioux Falls, SD 57198
(605)594-6020 (Voice)
(605)594-6529 (FAX)
Email: boncyk@edcsgw4.cr.usgs.gov

John L. Barker
Code 923, NASA/GSFC
Greenbelt, MD 20771
(301)286-9498 (Voice)
(301)286-0239 (FAX)
Email: jbarker@highwire.gsfc.nasa.gov

Ed Kaita
Science Systems and Applications, Inc
Code 923, NASA/GSFC
Greenbelt, MD 20771
(301) 286-5597 (Voice)
(301) 286-0239 (FAX)
Email: kaita@ltpmail.gsfc.nasa.gov

Dennis L. Helder
Department of Electrical Engineering
South Dakota State University
Brookings, SD 57007
(605)688-4184 (Voice)
(605)688-5880 (FAX)
Email: helderd@mg.sdstate.edu

Abstract-- The Enhanced Thematic Mapper Plus (ETM+) for the Landsat-7 satellite is currently in the assembly and integration stage with the satellite due for launch in 1998. The ETM+ is a derivative of the earlier Thematic Mappers (TM's) flown on Landsats 4 and 5. Chief among changes designed to improve radiometric calibration accuracy is the Full Aperture Solar Calibrator (FASC), a diffuse reflecting plate that can be deployed in front of the ETM+ aperture. With knowledge of the reflectance and illumination geometry of this calibrator, an absolute radiometric calibration of the ETM+ can be performed in flight by reference to the sun. Also incorporated on the ETM+ is a Partial Aperture Solar Calibrator (PASC) which can perform more frequent, but less complete calibrations of the ETM+. These two calibration devices, along with an Internal Calibrator similar to the one on the earlier TM's, constitute the on-board calibration capability. Ground Look calibrations will supplement the on -board measurements.

INTRODUCTION

The Landsat-7 mission is to provide continuity with the 20 year record of Landsat imagery starting in 1972 with Landsat-1 and the Multispectral Scanner (MSS). It provides wide area coverage (~185 km swath) on a 16 day repeat cycle with modestly high (15-60 m depending on band) spatial resolution[1]. The sensor on Landsat-7, the Enhanced Thematic Mapper Plus (ETM+) is similar to the Thematic Mappers on Landsats 4 and 5 and the Enhanced Thematic Mapper built for Landsat 6. This sensor is currently being assembled and integrated at Santa Barbara Remote Sensing (SBRS) under contract to NASA. One of the requirements of the Landsat-7 mission is radiometric calibration of the ETM+ data to an uncertainty of less than 5% in at-aperture radiance. This requirement, which is more stringent than in the past for the Landsat program, is being met by some improvements in the design and new calibration hardware, e.g., improved bandpass filters and full and partial aperture calibrators, a planned program of ground look calibrations and changes in the radiometric calibration ground processing. This paper addresses the new full aperture calibrator, its pre-launch characterization and in-orbit usage. A companion paper [2] addresses the radiometric processing changes. This paper is an update to [3].

FULL APERTURE SOLAR CALIBRATOR (FASC)

Design

The Full Aperture Solar Calibrator (FASC) is a white painted panel that can be deployed in front of the ETM+ aperture and diffusely reflect solar radiation into the full aperture of the instrument. The active surface of the FASC is painted with the classic formulation of YB71, an inorganic flat white paint

0-7803-3068-4/96$5.00©1996 IEEE

designed for spacecraft thermal control. This paint was selected for its near Lambertian properties, high reflectance, and apparent stability in a space environment. A painted surface was selected over a sintered halon design, primarily due to weight as the panel active area is 20" in diameter.

The mechanical design of the FASC has changed since last presented [3] and now consists of a one piece panel that rotates into position beneath the aperture, as opposed to a folding door apparatus. This design was selected for decreased complexity and improved reliability. The design being built (Fig. 1) stores the panel away from the aperture beneath a stow cover, which protects the calibration surface from UV radiation and limits its exposure to contaminants. When a calibration is to occur the panel is rotated into position in front of the aperture.

When in the calibrate position the angle between the sensor nadir vector and the panel normal is specified to be 23.5° An angle greater than 24° would allow earth shine to illuminate the panel when it is in use. In use the panel can be illuminated by the sun from 90° zenith angle (sunrise on panel) to about 67° zenith angle, above which the instrument begins to shade the panel.

Calibration Equation

In orbit, radiometric calibration is provided using the FASC per (1).

$$L_\lambda(\lambda) = \frac{R(\theta_v, \theta_s, \phi, \lambda) f \cos(\theta_s) E_{\lambda,s}(\lambda)}{\pi d^2} \qquad (1)$$

Where:

$L_\lambda(\lambda)$ is the spectral radiance for spectral band λ

$R(\theta_v, \theta_s, \phi, \lambda)$ is the bi-directional reflectance factor (BRF) for the panel for spectral band λ

f is the reflectance enhancement factor (~1.01)

θ_v is the ETM+ view zenith angle to the panel (~23.5°)

θ_s is the solar zenith angle on the panel

ϕ is the relative azimuth angle

$E_{\lambda,s}(\lambda)$ is the solar spectral irradiance is spectral band λ

d is the earth-sun distance in astronomical units

Pre- Launch Characterization

In order to use the FASC for radiometric calibration its reflectance and geometric properties need to be characterized. The reflectance characterization is currently underway. The plan consists of primarily measuring the witness samples painted and kept with the actual panels. Measurements are

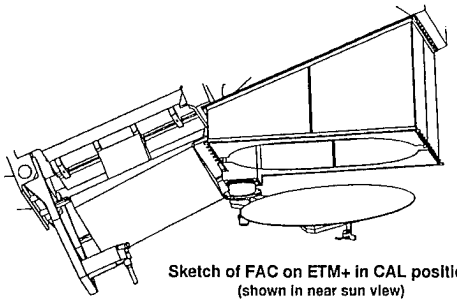


Figure1. Drawing of ETM+ FASC in calibration position

being made by Hughes Electroptical Systems (EOS) at two laser wavelengths, primarily to monitor the samples as a function of time. The NASA/GSFC BRDF facility is characterizing the samples across the spectral range of the silicon channels and Surface Optics is characterizing the BRDF in all the channels using ETM+ filter witness samples. To date measurements have been made on the witness samples made with the qualification panel (non-flight test panel). The qualification panel itself is planned to be measured by GSFC for uniformity in March 1996. The flight panels are planned to be painted in April 1996.

The visible to near-infrared reflectance of the FASC qualification witness sample is shown in Figure 2 for the nominal calibration condition. The material has a high reflectance, peaking at about 95% in ETM+ bands 3 (630-690 nm) and 4 (775-900 nm), falling to about 94% in band 2 (525-600 nm) and 92% in band 1 (450-515 nm). The variation in reflectance with relative azimuth angle of the sample is shown in figure 3 for 490 nm. The FASC is used at relative azimuth angles of 18° to 35°, depending on the time of year. The data show a slow monotonic decrease in reflectance as one goes away from the forescatter direction (0°). No variation with view zenith angle is discernible across the narrow range measured. The variation in reflectance as a function of illumination zenith angle is illustrated in figure 4. At the ETM+ view angle of the panel (23.5°) the reflectance decreases with increasing illumination zenith angle from 65° to 75°.

The stability of the YB71 paint with exposure to UV light has been rechecked using samples from the batch of paint to be used for the ETM+ flight parts. On exposure to 5 equivalent sun hours, roughly the equivalent of the lifetime exposure of the panel, no change was observed at 660 nm or 900 nm. At 400 nm, which is below the shortest ETM+ wavelength, about a 2% decrease in reflectance was observed. This change may be related to carbonization of contaminants on the samples as opposed to degradation of the material. Contamination is a major concern for the FASC. Although in flight the FASC is protected from the bulk of the satellite outgassing by its stow cover, and analyses have indicated that

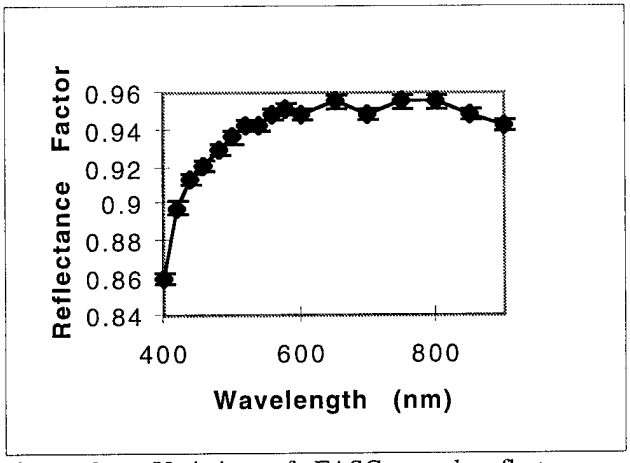


Figure 2. Variation of FASC panel reflectance with wavelength. FASC qualification witness reflectance measured at GSFC, 1/96. $\theta_s = 70°$, $\theta_v = 23.5°$, $\phi = 30°$

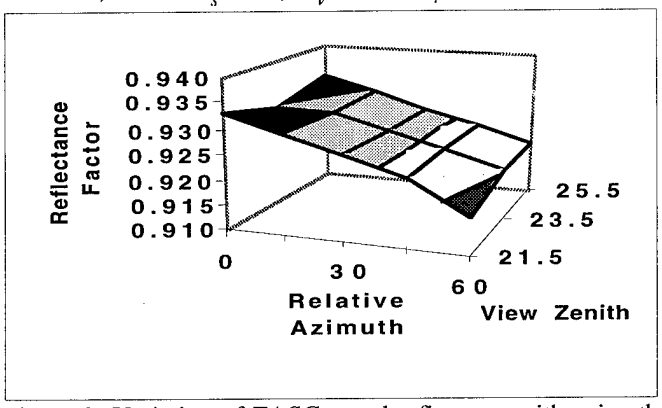


Figure 3. Variation of FASC panel reflectance with azimuth and view angle. FASC qualification witness reflectance measured at GSFC, 1/96, 490 nm (center of ETM+ band 1).

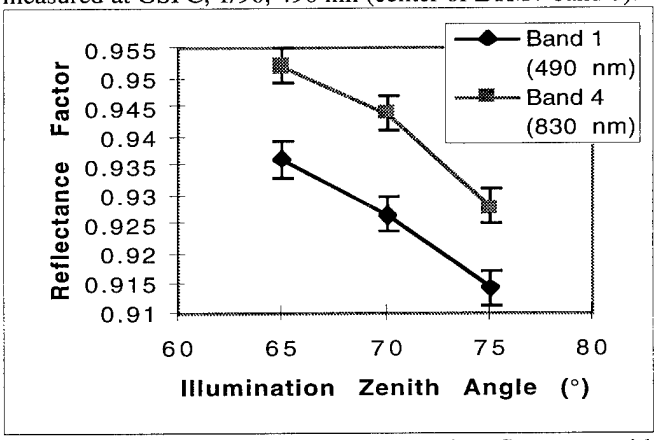


Figure 4. Variation of FASC panel reflectance with illumination angle at ETM+ view angle (23.5°). FASC qualification witness reflectance measured at GSFC, 1/96

in flight contamination should be small, some contamination will occur during integration, test and launch. The reflectance of witness samples will be measured throughout the integration and test program, though without UV exposure these tests are not expected to show degradation due to certain contaminants. Several options are being considered in order to reduce the contamination of the flight panel and/or its impact. The currently preferred option is to change out the flight panel with its spare shortly before launch so that as clean as possible panel is available in flight: this poses some risk as the panel is not easily accessible once the sensor is integrated onto the satellite. Also, a delay in the initial deployment to some 90 days after launch is being considered to allow the satellite and perhaps panel contaminants to outgas prior to solar exposure. Ways to examine the tendency of contaminants to come off the panel in vacuum are being studied.

Another concern in using the FASC is stray light, that is, light which reflects off other parts of the sensor or satellite and illuminates the panel. This will contaminate the calibration. A stray light analysis of the instrument conducted by SBRS suggests that light reflected off the external instrument structure is negligible. Stray light from internal reflections off of the optical surfaces is estimated to be about 1% of the incident light on the FASC, hence the 1.01 reflectance enhancement factor in (1).

In-Orbit Usage

Current plans call for the FASC to be deployed approximately monthly after an initial outgassing interval. Deployment will occur shortly after the satellite exits eclipse near the north pole. Data will be acquired for about 3 minutes of the FASC (roughly 8 scene equivalents), as the sun angle on the panel goes from about 78° to 67°. The at-aperture radiances will be determined per (1). A regression of instrument response after removing the bias with the at-aperture radiances will provide an absolute calibration of the instrument.

ACKNOWLEDGMENTS

The ETM+ sensor is being built by SBRS under contract and direction from the Landsat project at GSFC. Funding for this work was provided from the Landsat project. Measurements described herein have been made by the GSFC BRDF facility under the direction of J. Butler and the GSFC contamination engineering group represented by S. Straka.

REFERENCES

[1] J. Irons, D. Williams, and B. Markham, "Landsat-7 and Beyond," IGARSS'96 [this issue]
[2] W. Boncyk, B. Markham, J. Barker and D. Helder, "Artifact Correction and Absolute Radiometric Calibration Techniques Employed in the Landsat-7 Image Assessment System", IGARSS'96 (this issue)
[3] B. Markham, S. Ahmad, J. Irons, and D. Williams, "Radiometric Calibration of the Landsat-7 Enhanced Thematic Mapper Plus," Proc. IGARSS'94, Pasadena, CA, August 1994, 3pp.

Short Term Calibration of Landsat TM: Recent Findings and Suggested Techniques

Dennis Helder
South Dakota State University
PO Box 2220, Brookings, SD 57007
605-688-4184/605-688-5880(fax)/helderd@mg.sdstate.edu

John L. Barker
NASA/GSFC Code 925
Greenbelt, MD 20771

Wayne C. Boncyk
EROS Data Center
Sioux Falls, SD 57198

Brian L. Markham
NASA/GSFC Code 923
Greenbelt, MD 20771

Abstract -- Landsat Thematic Mapper (TM) data has traditionally been radiometrically calibrated on an individual scene basis. While this may be adequate for many applications, particularly single date applications, there are many cases where more advanced techniques are necessary. With emphasis today on global change, multi-temporal analysis is common place. Thus, forms of radiometric calibration are required that discriminate temporal change from changes in instrument response. To address this issue, a project is underway to evaluate TM calibration at several different time scales: short term, intermediate term, and lifetime. This paper will present some of the short term results. Short term is defined as within a single orbit. Continuous swaths of night data have been collected and the individual scenes, along with calibration files, stitched together. Analysis of the calibration files has revealed a number of interesting characteristics about detector gain and bias as well as instrument anomalies such as memory effect and scan correlated shift. Detector bias is a rapidly varying parameter that requires evaluation and correction as frequently as every scan. Detector gain varies significantly within an orbit in the primary focal plane in a predictable manner. Scan correlated shift has been accurately quantified and its effects may easily be removed from the data. Memory effect is in the process of being characterized and an algorithm is being developed to remove it. Line droop has been shown to simply be due to memory effect. Results from these investigations are being used in the development of radiometric correction algorithms for the Landsat 7 Image Assessment System.

TM CALIBRATION ARCHIVE SYSTEM

For more than 10 years, data have been collected from the Thematic Mapper instruments on-board Landsat 4 and 5. Early in the lifetime of these instruments significant efforts were undertaken to ensure that the data were well calibrated radiometrically [1-3]. However, over the passage of time these activities diminished significantly. As a result, the ability to extract information from these data has been reduced. Fortunately, the imagery in the archive is maintained with all of the internal calibration information that was obtained at the time of scene acquisition. These calibration data can be used to characterize the instruments on several different time scales and can be correlated with ground-based calibration campaign results.

To accomplish the goal of extracting pertinent calibration data from the TM archive, the TM Calibration Archive System (TMCAS)was developed [4]. This system consists of the software and hardware necessary to ingest data from 8mm tapes, archive calibration data at several levels, calculate various calibration parameters, and also has tools for plotting and statistical analysis.

Calibration of TM will be analyzed at three different time scales. The shortest time scale considered is a single orbit. The intent here was to understand what changes take place during a cycle where the instrument is turned on, acquires data continuously, and then turned off. At the other extreme, calibration data will be extracted over the lifetime of the instruments. Obviously, this allows determination of any long term trends in detector response. Lastly, an intermediate time period will be analyzed corresponding to the interval required for one outgassing cycle.

Over 600 scenes of TM data will be analyzed during the course of this project. Current efforts has been directed toward analysis of data obtained from contiguous single orbits. The rest of this paper will concentrate on the characterization of well-known TM anomalies, anomalies present in single orbit data, and recommendations for calibration based on these results.

SINGLE ORBIT ANALYSIS

Initial analysis of single orbit data sets from Landsat 5 has revealed several interesting anomalies [4]. Scene content has a significant effect on data recorded during the calibration interval. This can be observed by comparing data acquired during daytime descending orbital passes to data acquired during ascending, night orbital passes. Data collected during night has less variability. Additionally, daytime data has more variability on forward scans than on reverse scans. It is hypothesized that these differences are due to memory effect. Differences based on scan direction also exist in the calibration pulse magnitude recorded by the detectors. This observation is independent of day or night acquisitions and may be due to slight alignment differences in the calibration arm assembly on forward and reverse scans. Differences in calibration

0-7803-3068-4/96$5.00©1996 IEEE

lamp response based on odd versus even detector number appear to be due to the staggered detector arrays as they are assembled on the focal plane. Lastly, there is what appears to be a linear decrease in response of the detectors to the calibration pulse as a function of time. The decrease is independent of scan direction and present only in the primary focal plane. The cause of the phenomenon is unknown. As it appears to be a function of instrument 'on' time, it can have a significant impact in multi temporal studies.

SCAN CORRELATED SHIFT

Scan correlated shift (SCS) is a well-known TM phenomenon that was characterized in [5]. SCS is a shift in detector bias level that occurs between scans at irregular intervals. Detectors are either in a high or low bias state. When a shift occurs, all detectors in the instrument will change state at the same time. However, the lower and upper bias levels vary throughout the detectors and the amplitude of the shift varies as well. All detectors are not in phase. That is, when some detectors are at the high SCS level, others will be at the low SCS level. An example of SCS is shown in Fig. 1. The plot shows Band 3 Detector 1 shutter averages for all scans in a contiguous swath of data extending over 21 scenes obtained on December 25, 1984. SCS is readily apparent as two distinct levels at approximately 2.55 and 3.04 DN.

Characterization of SCS was originally done using only one scene of data for Landsat 4 and one for Landsat 5 [5]. In order to more accurately characterize SCS, and to understand its behavior as a function of time, an analysis of Landsat 5 data collected during ascending (night) orbital intervals was undertaken. Two data sets have been analyzed to date: Dec 25, 1984, path 23, rows 214-234; and Oct 21, 1985, path 116, rows 199-225. Night data were chosen because scene content affects calibration data through detector memory effect. Data similar to that shown in Fig. 1 was used to estimate SCS levels. Because of the large amount of data used, estimates of SCS are considered to be quite accurate--on the order 0.01 digital numbers (DN). Those detectors exhibiting the largest SCS amplitude are from Bands 2 and 3 with values ranging from 0.68 to 0.83.

It is interesting to note that the same six detectors exhibit the largest SCS amplitude in both data sets. However, the ranking and amplitudes have changed appreciably. Maximum and average changes in SCS amplitude by band are listed below.

SCS Amplitude Change

Band	Maximum	Average
1	- 0.13	-0.010
2	0.05	0.008
3	- 0.27	-0.179
4	0.17	0.006
5	0.17	-0.004
7	0.18	-0.011

Change within an orbit is negligible and evidence suggests that SCS levels change little as a function of time.

When the data collected for this analysis is compared with that obtained in [5], several interesting observations can be made. First, the phase relationship between detectors is consistent. This is true for the data in this study as well. Generally speaking, those detectors that have large SCS amplitudes are the same in both studies. Band 3 tends to have the largest values for SCS, while the values obtained in this study are larger still.

MEMORY EFFECT

Another well-known TM anomaly, memory effect (ME), has been reported on extensively (cf. [6]). It has most often been characterized as a decrease in detector sensitivity after observation of a bright target. It is most easily observed as light and dark bands over a dark target, such as water, that is adjacent to a bright target, such as clouds. Hypothesizing that ME is caused by time constants present in the instrument preamplifier circuitry, ME should also be observable during night scenes due to detector stimulation by calibration lamp pulses. To test this, consecutive reverse scans from Band 4, Detector 1 were averaged together while the instrument was in lamp state [111]. After smoothing, an exponential model was found to fit the data as shown in Fig. 2. These initial results support the hypothesis and show a time constant, $\tau = 1040$ minor frames.

Even with only this preliminary results, it is clear that ME will cause calibration data to be affected by scene data. This is particularly true for reverse scans. Reverse scan calibration pulses occur shortly after the end of scene data during that time when detector response from ME will be greatest. Forward scan calibration pulses occur on the order of one time constant after the end of scene and therefore would be less affected by ME. This suggests that only forward scan calibration data should be used for calculating detector gains.

LINE DROOP

One of the anomalies that has long been associated with Landsat TM has been line droop [5]. Traditional thinking suggests detector response changes as a function of position along scan lines. Analysis of night data, with zero radiance input to the detectors, served as a basis for this assertion. However, even during a night scene there is nonzero radiance input to the detectors. Calibration pulses occur at the end of every scan line that affect the response of the detectors. As a result, because of ME detector response is depressed immediately after a calibration pulse and then recovers during the interval of the following scan. One of the goals of this project was to determine if line droop actually existed or was simply another manifestation of ME.

Using a night scene of Landsat 5, average detector response was calculated at the beginning and at the end of each scan line for Bands 1,4, and 5 for three lamp states [000], [001], and [111]. For each lamp state, a minimum of 36 scan lines were used. The difference in the average at the beginning and end of

the scan line was calculated and tested for statistical significance. Lamp states [000], [001], and [111] were chosen to evaluate the influence of memory effect. During Lamp state [000] there should be no memory effect present. Lamp state [001] will introduce a small amount of ME, while lamp state [111] will produce the most significant ME during a night scene.

Results for Band 1 convincingly indicate that line droop is simply caused by ME. During lamp state [000], there is virtually no indication of line droop. Lamp state [001] indicates a significant difference in average value between start and end of scan for 11 of 16 detectors. Lastly, for Band 1 all detectors show differences between start and end of scan average values for lamp state [111]. Band 4 does not follow the model quite as perfectly as does Band 1. For lamp state [000], differences are quite small and random. During lamp state [001] the magnitude of the response was slightly larger, and for lamp state [111] the response was decidedly stronger and all detectors test positive for the effect. The data suggest the line droop is, at least primarily, another observation of memory effect. Lastly, Band 5 shows no significant indication of either line droop or ME.

The results from this analysis strongly suggest that line droop can be explained by memory effect. This is further substantiated by data obtained by averaging entire scan lines together as shown in Fig. 2. Note that the change along the scan line is roughly exponential in nature as a function of position. The change strongly indicates that the channels are responding to stimulus from the calibration pulse in a characterizable manner as described in the section on ME.

SUMMARY AND RECOMMENDATIONS

Results from this study indicate some preferred methods for calibrating Landsat TM. Because detector bias changes rapidly, it should be calculated for each scan. Detector gain appears to be a more stable quantity that slowly changes over an orbit but is affected by ME. Detector gain should be calculated using only forward scans and should be determined as a function of instrument 'on' time. Lastly, ME can significantly affect calibration, as well as scene, data. It is hoped that ME can be fully characterized through the approach described herein and a correction algorithm be developed.

REFERENCES

1. J.L Barker, "Characterization of Radiometric Calibration of Landsat-4 TM Reflective Bands," NASA Landsat-4 Scientific Characterization Early Results, Vol. 2, Pt. 1, pp. 373-474, January, 1985.
2. JL Barker, "Relative Radiometric Calibration of Landsat TM Reflective Bands," Proceedings of the Landsat-4 Science Characterization Early Results Symposium, Greenbelt, MD, NASA Conference Publication 2355, Vol. 55, No. 3, Feb. 22-24, 1983.
3. D. Fischel, "Validation of the Thematic Mapper Radiometric and Geometric Correction Algorithms," IEEE Transactions on Geoscience and Remote Sensing, Vol. GE-22, No. 3, pp. 237-242, May, 1984.
4. D. Helder, "A Radiometric Calibration Archive for Landsat TM," SPIE AeroSense, 1996, SPIE Proc. Vol. 2758.
5. M.D. Metzler and W.A. Malila, "Characterization and Comparison of Landsat-4 and Landsat-5 Thematic Mapper Data," Photogrammetric Engineering and Remote Sensing, Vol. 51, No. 9, pp. 1315-1330.
6. D. Helder et al., "A Technique for the Reduction of Banding in Landsat Thematic Mapper Images," Photogrammetric Engineering and Remote Sensing, Vol. 58, No. 10, pp. 1425-1431.

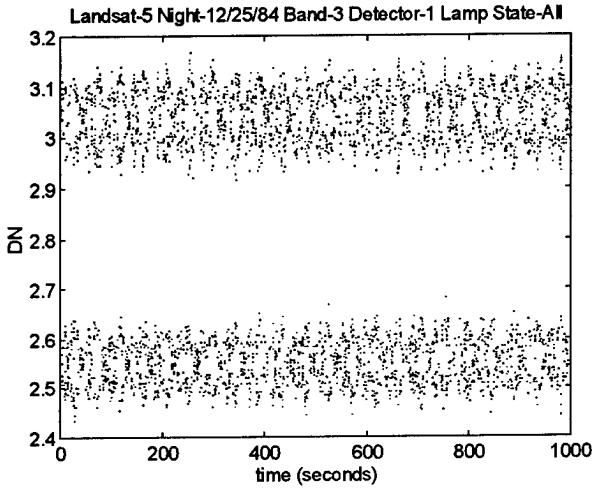


Fig. 1. SCS example using shutter data.

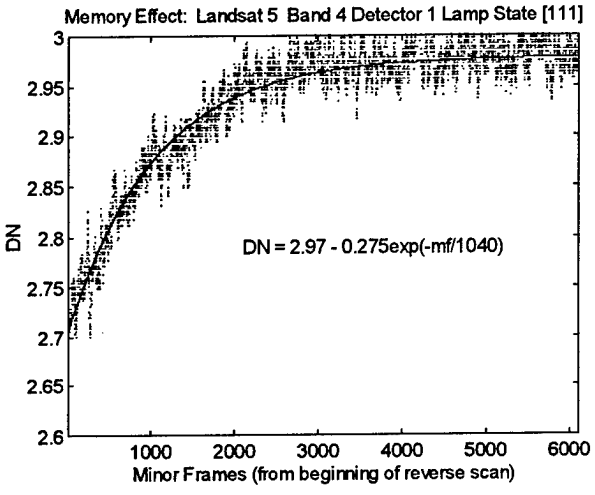


Fig. 2. Example of memory effect.

In-Flight Radiometric Calibration Plans for the Earth Observing System-Multi-angle Imaging SpectroRadiometer

Carol Bruegge, Robert Woodhouse, David Diner
Jet Propulsion Laboratory, California Institute of Technology
4800 Oakgrove Dr., MS 169-237, Pasadena, CA 91109
(818)354-4965/ (818)393-4619/ Carol.J.Bruegge@Jpl.Nasa.Gov

Abstract -- The Multi-angle Imaging SpectroRadiometer (MISR) will fly on the EOS-AM1 spacecraft, and provide global data sets with nine discrete view directions per scene. The instrument's radiometric scale is achieved by use of detector standards. On-orbit, photodiodes measure reflected light from solar-illuminated deployable Spectralon panels. The cameras simultaneously view the panels, providing the needed calibration data inputs. Other calibration methodologies include vicarious calibration and histogram equalization. Coefficients, as derived from the various methods, are weighted to produce a single determination of the gain and offset parameters. This process is repeated at monthly intervals to insure the calibration is maintained. Routine product generation makes use of these calibration coefficients, and also corrects for instrument-dependent errors in the radiance determination. These latter processing steps include corrections for camera out-of-band response, focal-plane scattering, and detector-to-detector non-uniformity of response. This paper reviews the MISR standard radiometric product and the in-flight radiometric calibration and characterization plans.

EXPERIMENT OVERVIEW

The Multi-angle Imaging Spectro-Radiometer (MISR) instrument is part of an Earth Observing System (EOS) payload to be launched in 1998. The purpose of MISR is to study the ecology and climate of the Earth through the acquisition of systematic, global multi-angle imagery in reflected sunlight. MISR will monitor top-of-atmosphere and surface reflectances on a global basis, and will characterize the shortwave radiative properties of aerosols, clouds, and surface scenes.

The MISR instrument consists of nine pushbroom cameras. It takes about 7 minutes of flight time to observe any given region at all nine view angles. The cameras are arranged with one camera pointing toward the nadir (designated An), one bank of four cameras pointing in the forward direction (designated Af, Bf, Cf, and Df in order of increasing off-nadir angle), and one bank of four cameras pointing in the aftward direction (designated Aa, Ba, Ca, and Da). Images are acquired with nominal view angles, relative to the surface reference ellipsoid, of 0°, ±26.1°, ±45.6°, ±60.0°, and ±70.5°. Each camera uses four Charge-Coupled Device (CCD) line arrays in a single focal plane. The line arrays consist of 1504 photoactive pixels. Each line array is filtered to provide one of four MISR spectral bands. The spectral band shapes are nominally gaussian, with bandcenters at 443, 555, 670, and 865 nm. MISR will acquire images in each of its channels with spatial sampling ranging from 275 m (250 m cross-track in the nadir) to 1.1 km (1.0 km cross-track in the nadir), depending on the on-board pixel averaging mode used prior to transmission of the data.

Each of MISR's photoactive pixel elements, when stimulated with incident radiation, responds with proportional output measured in digital counts. This response is measured during calibration, and reported as the best-fit gain and offset parameters. Gain is primarily a function of the optics transmittance (having a strong field-angle dependence), the filter transmittance, CCD quantum efficiency, the amplification of the electronics and the analog-to-digital conversion factor. Slight local deviations in response are due to filter pinholes or spatter sites, as well as CCD site defects. Pixel response may change with time, due to contaminant polymerization and radiation-induced effects to the lens and electronics. Because degradation is anticipated, the radiometric response is monitored routinely during the mission. The quantization and utilization of this response in MISR radiometric product generation is the primary objective of the MISR in-flight radiometric calibration program. Fig. 1 summarizes the program, as will be discussed in this paper.

Specifications require MISR to maintain absolute radiometric accuracy to within 3% (1σ confidence), for a 100% diffusely reflective scene, throughout the mission life. For a 5% scene, the requirement is to maintain 6% accuracy. Pixel-to-pixel relative calibration requirements are ±0.5% and ±1%, respectively, for these two scenes. Specifications also exist for nonuniform scenes, polarization sensitivity, and out-of-band rejection [1].

RADIOMETRIC PRODUCT GENERATION

During standard product generation, MISR will do a series of processing steps termed radiance scaling and

0-7803-3068-4/96$5.00©1996 IEEE

radiance conditioning. These make use of the sensor radiometric calibration and scene-specific data, respectively. Specifically, radiometric conditioning performs pixel-to-pixel nonuniformity of response corrections, point-spread-function (PSF) deconvolution, and spectral corrections. *Radiance scaling* and *radiance conditioning* are MISR unique terms, but refer to the usage of otherwise conventional processing methodologies.

Radiance Scaling

The inverse process to calibration is the determination of incident radiance for a given camera DN value. This process is termed radiance scaling.

For MISR, the best-fit to the radiometric (DN vs. L) transfer curve has been obtained by using a second-order polynomial:

$$G_2 L^2 + G_1 L + DN_o = DN - DN_v \ . \qquad (1)$$

where

- L is the sensor incident radiance [W m^{-2} sr^{-2} μm^{-1}],
- DN is the digital number,
- G_2, G_1, and DN_o are best fit parameters to the sensor radiative transfer curve, and
- DN_v is the video offset voltage, unique for each line of data, and measured by the overclock pixels for that line.

It is noted that prior to data transmission, the MISR system electronics square-root encode the output of the analog-to-digital converters. Some loss in resolution at the upper end of the dynamic range curve is sacrificed in favor of a reduced data rate. The DN values in (1) have had this square-root encoding reversed. Thus, the presence of a quadratic term in (1) is unrelated to this feature.

Preflight calibration has determined that, for the MISR cameras, the CCD response is nearly linear, and the second order coefficient is quite small. Inclusion of this term improves the radiance retrieval at the lowest end of the detector transfer curve.

Radiance Conditioning

Pixel non-uniformity correction ... is the process of adjusting for instrument on-board pixel-averaging. As many as four adjacent pixels may be averaged by the instrument prior to data transmission. The exact number will depend upon the selected camera configuration used during data acquisition. The process of pixel averaging introduces a radiometric error in the data, depending on the magnitude of the gain deviation among the pixels averaged, and the inhomogeneity of the scene. This error exists because the hardware design does not incorporate any adjustment for individual pixel response differences before the data are averaged.

Deviations in response across any four MISR pixels is typically 3%. Under these conditions the radiometric error would be less than 0.5% for extreme scene inhomogeneities, and no corrections are necessary. However, for each array there are a dozen or so pixels which violate this uniformity requirement.

The algorithm used in this correction first estimates the relative scene radiance incident on each pixel. MISR will be continually operated with the red channel of each camera supplying unaveraged data. The relative scene homogenity is assumed to be spectrally independent in this algorithm. With this information, and the pixel response coefficients, a radiance adjustment can be made.

PSF deconvolution ... is a process that allows the radiance product to maintain accuracy in the presence of high contrast scenes. During Engineering Model testing several unexpected focal plane scattering phenomena were characterized [2]. At that time it was determined that scattering from filter spatter sites was the cause of larger than anticipated out-of-band response. Additionally, reflections between the CCD and filter were observed. For the latter, a low-level scatter as far away as 30 pixels from the geometric image point was observed. In convolving this PSF with a "lake" scene, radiometric errors of 17% were predicted. The lake was 24x24 pixels in size, 5% in reflectance, and surrounded by a land background of 50% reflectance. The radiometry was compared using the center 8x8 pixels of the convolved and original targets. By using a maximum likelihood algorithm, a simple kernel of 1x6 pixels in dimension was used to restore the original target. This was done within a half-dozen iterations, producing a scene meeting the 2% radiometric error specification.

Spectral corrections ... are used to compute the band-weighted radiance that a nominal filter passband would have measured, while viewing a given scene. The correction is in two steps. First, the out-of-band response is subtracted using the preflight spectral calibration data. The MISR band data is used to approximate the scene spectral shape in this algorithm. Secondly, a passband of nominal center wavelength and bandwidth is assumed. The radiance retrieved from this idealized response function is computed. This correction allows MISR Level 2 (Science Products) to proceed without consideration of the individual spectral response functions for each of the 1504 detectors x 9 camera pixel elements.

Level 1B1 Radiance Product

The above processing steps are used to produce the MISR radiance product, termed the Level 1B1 Radiometric

Product. Processing occurs at the Distributed Active Archive Center (DAAC), and is done on every transmitted image. Image co-registration and geolocation occurs at the next level of processing and produces the Level 1B2 Georectified Radiance Product.

Ancillary Radiometric Product

The coefficients used in radiometric product generation are delivered to the DAAC in the form of the Ancillary Radiometric Product (ARP). Also included in the ARP is radiance uncertainty, spectral and instantaneous field-of-view (IFOV) information. The ARP is generated at the MISR Science Computing Facility (SCF). It is updated at monthly intervals, or as needed to maintain the calibration of the sensor.

IN-FLIGHT CALIBRATION

The Level 1B1 algorithm development, ARP generation, and product validation is the responsibility of the in-flight radiometric calibration and characterization (IFRCC) team, which resides at NASA/ Jet Propulsion Laboratory (JPL). The SCF processing facilities will be used to provide these deliverables, as well as routine characterization products and reports.

The in-flight calibration of MISR is provided by combining coefficients determined from multiple methodologies. A weighting scheme will facilitate this process. Uncertainty analyses for each method, frequency of data supplied for a given technique, and data quality indicators will be used in the weighting scheme. The methodologies involve the use of the On-Board Calibrator (OBC) hardware, an independent vicarious determination, and response prediction based on trending analysis and scene studies. Spatially and spectrally featureless targets are used to establish the calibration response.

On-Board Calibrator

The OBC consists of a wavelength set of High-Quantum Efficiency (HQE) trapped photodiodes, and five wavelength sets of radiation resistant PIN (p-i-n intrinsic layers) photodiodes. One PIN set is positioned on a goniometer, which scans through the along-track camera view angles. These detector standards are used to measure the radiance reflected from one of two Spectralon calibration panels.

Monthly, MISR will be commanded into Calibration Mode. During this time the instrument will collect data over oceans on the dark side of the orbit. These data will monitor dark current spatial variability. Then, over each pole, in turn, the Spectralon panels will be deployed to calibrate the aftward-viewing and nadir or forward-viewing and nadir cameras. These polar observations will collect light through a varying atmospheric path through the earth's limb to the Sun. Atmospheric attenuation will allow calibration of the MISR detectors through a range of illumination conditions. The detector standards will be used to measure the radiance as it changes with time.

Vicarious Calibration

Vicarious calibration techniques can utilize data from 1) high altitude sensor underflights, 2) surface radiance observations, or 3) surface reflectance observations. The preferred approach, Method 1, will utilize a MISR simulator (AirMISR) which will fly on the ER-2 aircraft. At 20 km altitude, AirMISR will need little atmospheric corrections to produce a measure of the top-of-atmosphere radiances. Method 2 utilizes a hemispherical scanning radiometer, PARABOLA III, to measure surface-reflected radiances and downwelling diffuse radiances. These are propagated from surface to top-of-atmosphere using a characterization of the atmospheric state and a radiative transfer code. Method 3 has the disadvantages of requiring a two-path radiance propagation (Sun-to-surface and surface to sensor), and therefore is the least desirable. It is, however, the simplest to implement, as PARABOLA data are referenced to a reflectance standard, and no radiometer calibration is required.

Relative Adjustments

Following OBC and vicarious coefficient weighting, the derived coefficients are next plotted in time against the other monthly determinations. A trend analysis on these data is done, and the smoothed parameters computed at the current point in time. This is done in order to avoid abrupt changes in the calibration coefficients. This trend analysis is believed to be more representative of the sensor response, which is known to be highly stable on short time scales, and otherwise expected to degrade slowly with time. In addition, histogram equalization is used [3], as necessary, to refine the pixel-to-pixel relative response values. Here, Earth-scene data are used to produce a histogram of measured radiance levels. Using a large number of observations, each pixel response is adjusted until the amplitude of the histogram is the same for each pixel. This is adjustment is made by using a sliding window approach, correcting pixel responses from first one spatial zone, then another. This step process allows

pixels to be compared which have the same viewing geometry, avoiding differences in atmospheric path and surface bidirectional reflectance.

IN-FLIGHT CHARACTERIZATION

Other IFRCC responsibilities include the characterization of the sensor during flight. Characterization is the measurement of the typical behavior of instrument properties which may affect the accuracy or quality of its response or derived data products. The in-flight characterization includes the determination of the radiometric errors for specific scene types, such as high contrast scenes, and a variety of scene spectral signature types. Noise analysis will include the determination of signal-to-noise ratio versus radiance input, and a check for the presence of coherent noise (that of a fixed frequency pattern). Spectral stability will be investigated, to the extent possible. Filter life-test studies, and correlation with Moderate Resolution Imaging Spectroradiometer (MODIS) filter stability determinations, are the best data sources.

CALIBRATION INTEGRITY

Calibration integrity is the process of validating and certifying the Level 1B1 product. Traceability of MISR data products is accomplished with the detector standards. These are used through the preflight, OBC, and vicarious determinations of the sensor calibration. Radiometric verification will be provided by cross-comparisons with MODIS and Système Probatoire d'Observation de la Terre (SPOT) sensors, as well as with the routine analysis of MISR imagery over desert sites.

The IFRCC team will also be responsible for the development of quality assessment indicators for the Level 1B1 data.

REFERENCES

[1] C.J. Bruegge, D.J. Diner, and V.G. Duval, "The MISR calibration program," J. of Atmos. and Oceanic Tech., EOS special issue, Vol. 13 (2), 286-299, 1996.

[2] R.P. Korechoff, D.J. Diner, D.J. Preston, C.J. Bruegge, "In Advanced and Next-Generation Satellites. Spectroradiometer focal-plane design considerations: lessons learned from MISR camera testing," EUROPTO/ SPIE Vol. 2538, pp. 104-116, 25-28 September, 1995

[3] M. P. Weitreb, R. Xie, J. H. Lienesch and D. S. Crosby, "Destriping GOES Images by Matching Empirical Distribution Functions," Remote Sensing of the Environment, 29, pp 185 - 195, 1989.

ACKNOWLEDGMENTS

The work described in this paper is being carried out by the Jet Propulsion Laboratory, California Institute of Technology, under contract with the National Aeronautics and Space Administration.

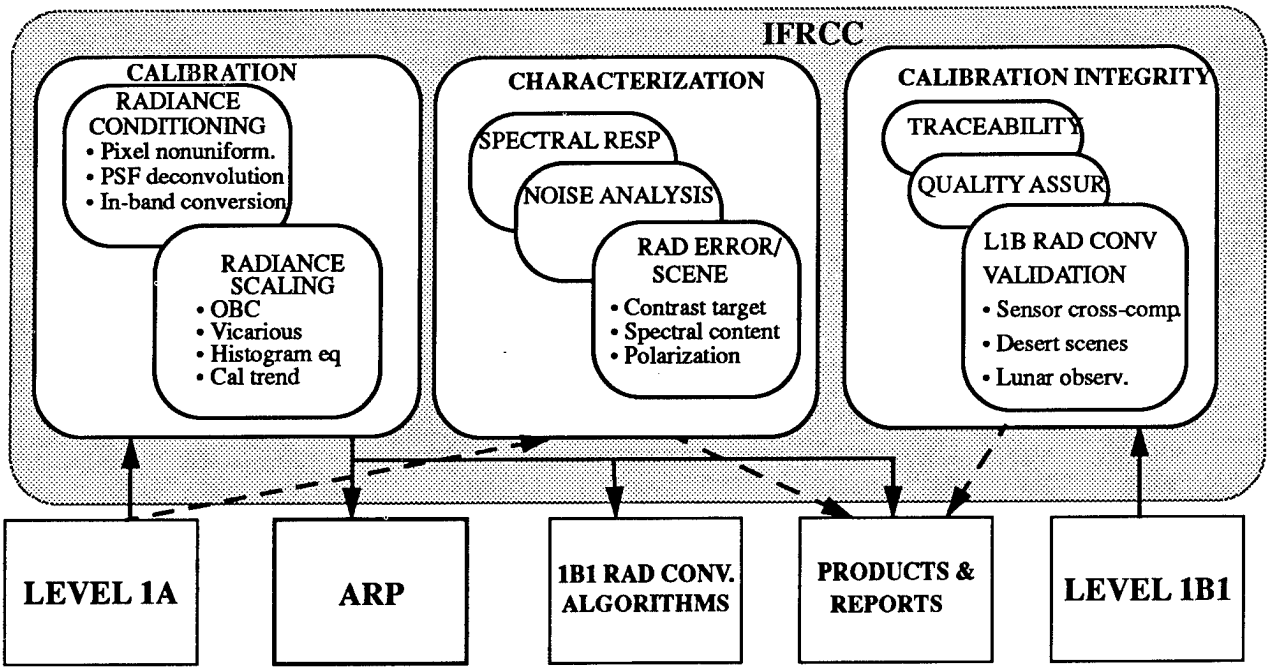


Fig. 1, IFRCC activities

Cross-Calibration of Two Small Footprint Sensors

Christine L. Gustafson-Bold and Kurtis J. Thome
Remote Sensing Group, Optical Sciences Center, University of Arizona
1600 North Country Club, Suite 100, Tucson AZ 85716-3116
Phone: 520-621-2158, Fax: 520-621-8292, Email: clg@gas.uug.arizona.edu

ABSTRACT

This paper presents a method for determining the calibration of a small footprint satellite sensor using another small footprint system. The work uses the System Pour l'Observation de la Terre (SPOT) 3 - High Resolution Visible (HRV) Sensor and Landsat 5 - Thematic Mapper (TM) to determine calibration coefficients for TM using HRV given the different look angles, bandpasses, crossing times and footprints. The cross-calibration results are referenced to the reflectance-based vicarious calibration results from October 8 and 9, 1994, from White Sands Missile Range, NM. Although the images are from two different days the atmospheric and reflectance data are very similar and both satellites had near-nadir views.

Bands 1, 2, and 3 of HRV, are used to calibrate bands 2, 3, and 4 of TM. The initial attempt of cross-calibration does not account for spectral differences. The calculated calibration coefficient for Chuck Site for TM is within 4% of the reflectance-based values. Several other sites are also used with dark areas providing the worst results. Other bright areas have errors ranging from 1 - 12%. Areas within the gypsum dunes have results within the 1-4% range. To determine misalignment effects, the TM image is moved relative to the HRV image. This produced changes of less than 1% for up to a 40 meter misalignment.

INTRODUCTION

This paper presents a method for calibrating Landsat Thematic Mapper (TM) using System Pour l'Observation de la Terre (SPOT) 3 - High Resolution Visible (HRV) Sensor. We want to cross-calibrate sensors for several reasons. One reason is the reflectance-based calibration is difficult to apply to large footprint sensors. Cross-calibration also leads to better comparisons of results from different sensors. Other reasons for cross-calibration are: different countries use different calibration methods, some sensors do not have onboard calibrators, and onboard calibrators are not consistent across sensors [1].

This is not the first attempt at a cross-calibration between two sensors. Teillet et al., presents three methods of calibration, two of which are cross-calibrations using TM to determine the gain coefficients for NOAA-9 or -10 Advanced Very High Resolution Radiometer (AVHRR)[2]. The first cross-calibration method uses ground-based data collected for TM on the same day and within a day or two of an AVHRR overpass. The second method uses the historical reflectance of the surface instead of field measurements, and creates a calibration coefficient based on the relationship between the average digital number (DN) of each satellite.

Teillet et al. assumes TM's calibration is known because the 30-m x 30-m footprint is a reasonable size for the reflectance-based calibration method. Bands 3 and 4 are used to calibrate channels 1 and 2 of AVHRR. Two data sets are used. The first is August 28, 1985, at White Sands Missile Range (WSMR) with a NOAA-9 AVHRR overpass four hours after a Landsat-5 TM overpass. The second set is from a February 10, 1988, overpass of TM with NOAA-10 AVHRR overpasses on February 8 and 9, 1988. The AVHRR sensors on NOAA-9 and -10 are used as the unknown sensor because the 1.1-km x 1.1-km footprint makes the reflectance-based calibration impractical. The estimates of the error in the cross-calibration method using the reflectance-based calibration of TM is 7% in channel 1 and 8% in channel 2 [2]. The primary sources of uncertainty are the atmospheric correction and the calibration of TM data. The difficulty with using these two sensors is the results cannot be verified to better than this because there is no independent calibration for AVHRR.

REFLECTANCE-BASED METHOD

The reflectance-based calibration method was developed by the Remote Sensing Group in the early 1980s to calibrate Landsat TM [1]. In this approach, the surface and atmosphere over a selected site are characterized at the time of sensor overpass.

The surface characterization is done by walking the site while carrying a radiometer attached to a backpack assembly. The radiometer measures the upwelling surface radiance which is ratioed to the upwelling radiance from a barium sulfate panel of known reflectance to determine the reflectance of the site. Carrying the radiometer makes this approach impractical for large footprint sensors.

We determine atmospheric transmittance using ten- and three-band solar radiometers. Data from the ten-band

This work is funded by NASA contract NAS5-31717

0-7803-3068-4/96$5.00©1996 IEEE

radiometer are used to determine atmospheric-spectral optical depths, and an inversion determines ozone optical depth and a Junge aerosol size distribution parameter. The three-band radiometer is used to determine columnar water vapor which is used to find band-integrated absorption [3].

The results of the surface and atmospheric measurements are inputs to a radiative transfer code which predicts at-sensor radiance. The predicted radiance is compared to reported DN to determine calibration coefficient. Site selection is important in the reflectance-based approach to reduce errors. We use the alkali flats of White Sands, where access is limited and surface characteristics remain fairly constant. The TM site is a 120-m x 480-m (or 4 x 16 pixels) rectangle oriented in the ground-track direction of the Landsat satellites. The SPOT site is a 320-m x 80-m (or 16 x 4 pixels) rectangle. The two sites are approximately at right angles and partially overlap. The different orientations arise from TM being a whiskbroom system while SPOT is a pushbroom system. The site's 1200-m elevation and the dry climate with low aerosol loading help reduce errors [4].

Uncertainties in this method have been studied and shown to be < 5% for typical White Sands conditions for band 1 of HRV and band 2 of TM [4]. The reflectance-based method has been used successfully for both SPOT [5] and TM [3].

CROSS-CALIBRATION METHOD

A block diagram of the method is shown in Fig. 1. Using selected ground control points (GCPs), the HRV image is twisted and resampled using nearest neighbor interpolation to coregister it to the TM image. The GCPs used are chosen based on permanence to allow comparisons with future work

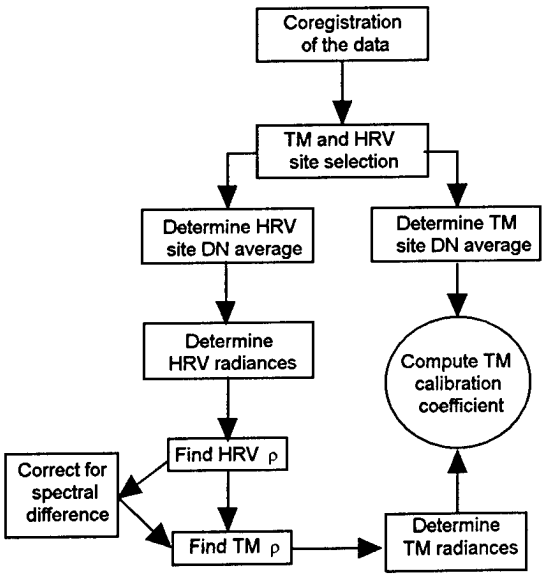


Figure 1: Finding TM Calibration Coefficient using HRV

Permanent targets include runway markers, large buildings, and curves in roads. Other surface features are adequate for day-to-day comparisons but are not for week-to-week comparison, such as tops of small dunes and surface water. For this work 9 GCPs were chosen (7 permanent and 2 semi-permanent).

Cross-calibration sites are of two types. The first is Chuck Site for which ground-based atmospheric and surface measurements exist. This should be where the best results will occur because we also have measured spectral reflectance. We can also check the cross-calibration results against those obtained using the reflectance-based method. The second type of site is a 90-m x 90-m TM area having no variability in DN.

Once a site is selected, the surface reflectance is found using HRV and the average DN for an 80-m x 80-m site. Using the calibration coefficient from the reflectance-based method, we convert the average DN to radiance. The radiance is atmospherically corrected to surface reflectance using ground-based atmospheric data and radiative transfer code output. The radiative transfer code output is used to derive a relationship between surface reflectance and at-sensor radiance. This is assumed to be linear over small intervals and reflectance is found through interpolation.

Once the HRV reflectance is found there are two ways to obtain the TM reflectance. One is to assume the spectral differences are so small they can be ignored and use the HRV reflectance. The other is to take spectral reflectance data of the site and make a spectral correction to the HRV reflectance to find the comparable TM band.

We convert TM reflectance to radiance by reversing the atmospheric correction scheme described above. The radiance versus reflectance curve for TM is developed using the atmospheric data from the day of the TM overpass. This radiance is compared to the average DN of the 90-m x 90-m site to determine the calibration coefficient.

DATA SET DESCRIPTION

The HRV and the TM sensors have many similarities. The center wavelengths for HRV bands 1, 2 and 3 are very similar to TM bands 2, 3, and 4 respectively (see Table 1). The footprints are very similar in size 20m x 20m (HRV) versus 30m x 30m (TM). The viewing geometry is also very similar for the two sensors (see Table 2). We have surface

Table 1: Band wavelength and bandpass comparisons in nm

Band		Center Wavelength		Bandpass	
HRV	TM	HRV	TM	HRV	TM
1	2	535.6	571	0.11	0.09
2	3	638	661	0.08	0.08
3	4	822	838.2	0.12	0.13

reflectance data from Chuck Site for TM on October 8, 1994, and for HRV on October 9, 1994, overpasses. Thus we can check the TM calibration coefficients determined from HRV with the calibration coefficients determined based on reflectance-based data from October 8, 1994.

RESULTS

We present results for four areas, Chuck Site, a dune area and two darker alkali flat areas. Table 3 presents the percent difference between the TM calibration coefficient obtained from the cross-calibration to SPOT and that obtained from the reflectance-based approach. Two sets of results are given for Chuck Site. The first is with no spectral correction and the second includes a spectral correction. The dune is a flat area between the dunes that is quite bright, about 20 DN brighter than Chuck Site. Both Chuck Site and the dunes give similar results. Most likely because of the similarity in spectral reflectance between the two areas. The last two areas appear very similar in the image and have average DN values of about 13 DN less than Chuck Site. The differences in their errors, we believe results from vegetation in the fourth area. Many more sites have been examined, but these four are representative.

ERRORS AND UNCERTAINTIES

The sources of uncertainties are spectral differences and the different overpass times. The non-coincident overpass times cause errors due to BRF effects, atmospheric differences, surface reflectance changes, and satellite view angles. The error in atmospheric correction is less than 5% [4], but because the atmospheric differences between the two days and because we use the same code for both cases the errors from atmospheric correction is negligible. The surface reflectance data for the two days agree to within the measurement uncertainties. The registration of the images has an uncertainty of less than 1% as found by shifting the images relative to each other and recomputing results. Measured BRF of the site indicate this effect to also be less than 1%. The largest error source is the spectral differences. This can be seen in Table 3. This error ranges from negligible to greater than 10%. Thus, careful site selection or evaluation is needed for this method to work.

Table 2: Satellite and Sun zenith's and azimuths at overpass

All at overpass	SPOT 3 HRV	Landsat 5 TM
Sensor Zenith	2.3	89.0
Sensor Azimuth	284.0	284.6
Solar Zenith	41.3	47.9
Solar Azimuth	159.4	138.8

Table 3: Presents the percent difference between the two methods for obtaining the TM calibration coefficient

Sites	HRV 1 - TM 2		HRV 2 - TM 3		HRV 3 - TM 4	
Chuck	4.3	0.26	0.9	0.42	0.1	0.2
Dune	4.2		1.2		1.1	
Dark 1	3.4		3.2		1.6	
Dark 2	13.9		12.7		7.0	

CONCLUSIONS

Cross-calibration works well for HRV and TM, which shows that cross-calibration is feasible. There are problems with vegetated areas for which a spectral reflectance correction would help alleviate. To do footprints of larger size a better method of image registration is needed. In the HRV to TM calibration the GCPs used were all very small or well defined pixels. This will not be the case for large footprint sensors. Future work will focus on studying this by creating large footprint images from these data sets.

ACKNOWLEDGMENTS

We wish to acknowledge the Atmospheric Sciences Laboratory at WSMR for the use of the site and data support. We also acknowledge P. Spyak, S. Biggar, J. Lamarr, C. Deschapelles, and C. Laumann for help in data collection.

REFERENCES

[1] Slater, Philip N., Stuart F. Biggar, James M. Palmer, and Kurtis J. Thome, "Unified approach to pre- and in-flight satellite sensor absolute radiometric calibration," in Proceedings of SPIE Vol. 2583, 1995, pp. 130-141.

[2] Telliet, P.M., P.N. Slater, T. Ding, R. P. Santer, R. D. Jackson, and M. S. Moran, "Three Methods for the Absolute Calibration of the NOAA AVHRR Sensors In-Flight," *Rem. Sens. Env.*, 31 (1990):105-120.

[3] Thome, K. J., S. F. Biggar, D. I. Gellman, and P.N. Slater, "Absolute-Radiometric Calibration of Landsat-5 Thematic Mapper and the Proposed Calibration of the Advanced Spaceborne Thermal Emission and Reflection Radiometer," in Proceedings IGARSS, 1994, vol. 4, pp. 2295-2297.

[4] Biggar, S. F., P.N. Slater, and D. I. Gellman, "Uncertainties in the in-flight calibration of sensors with reference to measured ground sites in the 0.4 to 1.1 mm range," *Rem. Sens. Env.*, 48 (1994), pp. 242-252.

[5] Gellman, David I., Stuart F. Biggar, Magdeleine C. Dinguirard, Patrice J. Henry, M. Susan Moran, Kurtis J. Thome, Philip N. Slater, "Review of SPOT-1 and -2 calibrations at White Sands from launch to the present," in Proceedings of SPIE Number 1938, 1993, pp. 13-20.

Evaluation of the Aerosol Scattering Phase Function from PGAMS Observation of Sky Path Radiance

Stephen Schiller
South Dakota State University
Physics Department, Brookings, SD 57007
P:605-688-5859/F:605-688-5878/Schilles@mg.sdstate.edu

Jeffery Luvall
Global Hydrology & Climate Center
NASA, Marshall Space Flight Center
977 Explorer Blvd., Huntsville, AL 35806
P:205-922-5886/F:205-922-5723/jluvall@msfc.nasa.gov

Abstract -- A knowledge of the spectral and geometrical distribution of sky path radiance at the time a remote sensing image of the earth's surface is acquired can greatly improve the application of atmospheric correction and vicarious calibration techniques. The focus of this investigation is to evaluate the sensitivity of the radiance exiting the bottom and top of the atmosphere to the representation of the aerosol single-scattering phase function for these applications. Hyperspectral almucantar sky path radiance measurements obtained with the Portable Ground-based Atmospheric Monitoring System (PGAMS) are compared to synthetic spectra generated by MODTRAN3.

INTRODUCTION

The objective in applying atmospheric corrections to remote sensing images is to transform at-sensor radiance to surface radiance and reflectance. The results of the transformation depend largely on the ability to estimate the radiance contribution produced by solar radiation scattered into the sensor's field of view by atmospheric aerosols. The accuracy one can achieve in estimating this path radiance component depends on the representation used for the aerosol single scattering phase function [1].

Typically the approach to developing a single scattering phase function is based upon seasonal average aerosol properties. Using these properties to define a particle size distribution and complex index of refraction, the phase function may be constructed by Mie theory [2]. Another effective tactic is achieved by adopting an asymmetry factor and employing the Henyey-Greenstein phase function [3]. Once generated, the single scattering phase function can be used in radiative transfer calculations to estimate the at-sensor path radiance contribution needed for atmospheric corrections routines.

The Moderate Resolution Atmospheric Radiance and Transmittance Model MODTRAN3 [4] encompasses both of these approaches in generating the aerosol single-scattering phase function and provides a very flexible and powerful platform for sky path radiance calculations. The capacity to deal with the complex problems of multiple scattering makes this code an excellent tool for generating synthetic spectra that can be compared to field observations. In this investigation, comparison will be made to hyperspectral observations obtained with the Portable Ground-based Atmospheric Monitoring System (PGAMS) [5]. The aim of this present work is to evaluate the sensitivity of the adopted aerosol single-scattering phase function in reproducing sky path radiance spectra obtained at different scattering angles.

OBSERVATIONS

The sky path radiance observations were collected using PGAMS in support of a field campaign dealing with the analysis of urban heat island development over Huntsville, Alabama on September 7, 1994. PGAMS obtains radiometric measurements using a Personal Spectrometer (PS) 2 diode-array field spectrometer built by Analytical Spectral Devices [6]. This instrument covers a range of 350 nm to 1050 nm, sampling in 1.4 nm steps, producing a linear response over a dynamic range greater than 3000:1.

A 1° field-of-view end-receptor is mounted on an alt-alt tracking system furnishing input to the spectrometer through a fiber optic bundle. Once set up in the field, the tracking system is calibrated to provide altitude and azimuth pointing of the end-receptor to an absolute accuracy, over the hemisphere of the sky, of better than 1°. Radiometric calibration of the end- receptor/spectrograph combination is made using a LI-COR optical radiation calibration unit. A NIST secondary standard lamp is used for absolute radiance calibration delivering an accuracy of better than 5% over the wavelength range of the spectrometer.

For this investigation, PGAMS recorded both direct solar irradiance and sky path radiance observations. The direct solar irradiance data was used in standard Langley plot analysis to monitor atmospheric transmittance and aerosol optical depth

0-7803-3068-4/96$5.00©1996 IEEE

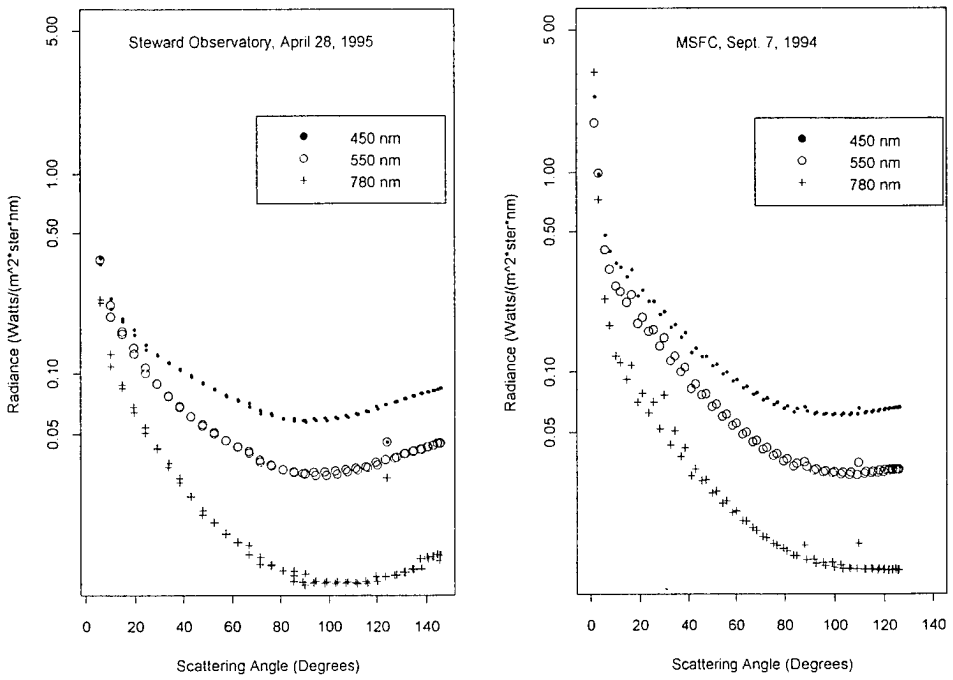


Fig. 1. Almucantar scans recorded at Steward Observatory, Arizona and Marshall Space Flight Center, Huntsville, Alabama. The scans were made at the sun's altitude of 15° and 27° respectively. Only the data for 3 of the 512 PGAMS channels are shown.

over visible and near-infrared wavelengths unaffected by the water vapor bands. The sky path radiance observations consisted of constant altitude scans with 5 degree azimuth steps over a full 360 degree azimuth circle. This resulted in a constant air mass data set in which the dominant radiance variation is due to changes in the "atmospheric" scattering phase function, the integrated scattering phase function from Rayleigh and aerosol single and multiple scattering processes. Fig. 1 presents scans obtained at the sun's altitude at two sites with significantly different aerosol loading. Note that a 360° azimuth scan records the phase function twice. Differences reflect variations in sky conditions and changes in the optical depth of the sun during the observation interval.

ANALYSIS AND DISCUSSION

Synthetic spectra were generated using MODTRAN3 for the purpose of trying to reproduce the observed "atmospheric" phase function and path radiance spectra focusing on the effects of the selected aerosol single scattering phase function. The data set recorded at MSFC, Huntsville, Alabama was employed. Calibration of MODTRAN3 to reflect the actual atmospheric conditions was done by using observations of direct solar irradiance obtained just a few minutes before the constant altitude scan. The sun photometry provided direct measurement of atmospheric transmittance. This was replicated with MODTRAN3 by selecting a spring/summer rural aerosol model and adjusting the visibility until the difference between the observed and synthetic spectra was minimized for wavelengths outside atmospheric water bands. The resulting fit is presented in Fig. 2. The MODTRAN spectrum is based on a solar zenith angle of 62.1° and a visibility of 48.0 km using the 1976 standard atmosphere. The excellent agreement may lead one to expect that accurate path radiance spectra would also result from this model.

Path radiance spectra were calculated with MODTRAN3 to generate an atmospheric scattering phase function for comparison. The initial results employed the aerosol single-scattering phase function based on Mie theory calculations. Because PGAMS was set up at a site dominated by large grassy fields, the vegetation a grass surface albedo was selected along with the 2 stream multiple scattering option. The slant path and solar zenith angles were set at 63° to match the observations and the path radiance was calculated over a range of azimuthal angles between 2° and 180°. The resulting phase function is presented in Fig 3 for wavelengths of 450 nm, 550 nm, and 780 nm. Good agreement is revealed at small scattering angles but in the back scattering realm large systematic differences are revealed.

Making use of the Henyey-Greenstein phase function instead of the fixed MIE scattering rural aerosol model can significantly improve the fit at large scattering angles by adjusting the asymmetry factor. Fig 3. shows the resulting phase function based on asymmetry factors of 0.70, 0.68, and 0.72 at the wavelengths of 450 nm, 550 nm, and 780 nm respectively. Corresponding surface albedos of 0.06, 0.09, and 0.20 were .

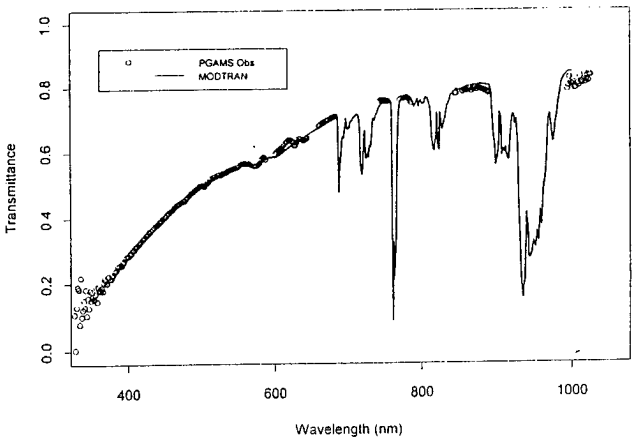


Fig. 2. MODTRAN3 fit to PGAMS transmittance spectra based on a solar zenith angle of 62.1° and a visibility of 48.0 km.

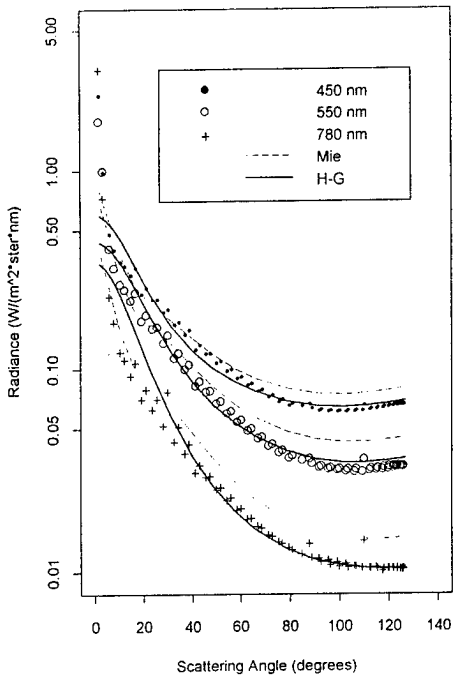


Fig. 3. PGAMS observed "atmospheric" scattering phase function compared to MODTRAN3 path radiance calculations for Mie and adjusted Henyey-Greenstein phase functions.

also utilized.

The improvements made at large scattering angles from the adjustments to the MODTRAN3 model based on fitting the observed phase function is shown in Fig. 4. This is a PGAMS path radiance spectrum recorded at a scattering angle of 120° along with the corresponding MODTRAN3 Mie and Henyey-Greenstein calculations. Even with hyperspectral sun photometry the Mie bottom of the atmosphere calculations are in error by 20 to 30%. Significantly less error is obtained with the adjusted Henyey-Greenstein calculations when the observed atmospheric phase function is also considered. This improvement in bottom of the atmosphere radiance calculations should also be reflect in the calculation of the top of the atmosphere radiances and the application of atmospheric corrections in remote sensing.

CONCLUSION

MODTRAN3 is a highly sophisticated radiative transfer code that is representative of the most effective models used for atmospheric correction and vicarious calibration applications in remote sensing. The results of this investigation reveal, even with such powerful codes, that path radiance spectra over a range of scattering angles from *in situ* observations are critical in accurately calculating radiances exiting the bottom and top of the atmosphere. This originates primarily from the sensitivity of the exiting radiances to the selected aerosol single-scattering phase function which can vary greatly, on a given day, from the seasonal average.

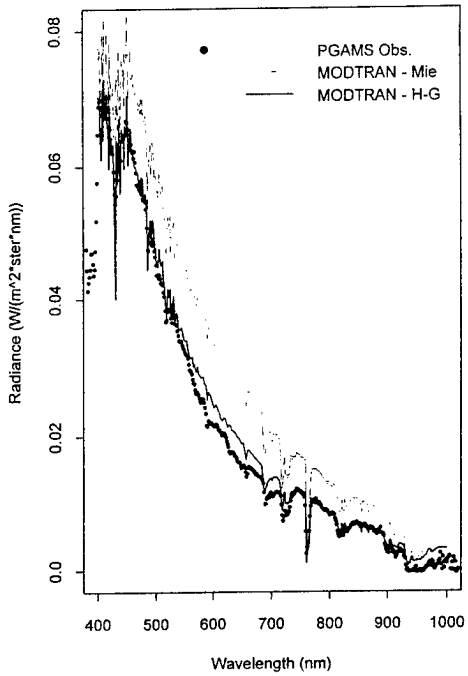


Fig. 4 PGAMS Sky path radiance spectra compared to MODTRAN3 spectra based on the Mie calculated single-scattering phase function for rural aerosols and the adjusted Henyey-Greenstein phase function (see text). The scattering angle is 120°

ACKNOWLEDGMENTS

S..S. would like to acknowledge support provided by the NASA/University JOint VEnture (JOVE) in Space Research and the South Dakota Space Grant Consortium. Additional support was provided by the National Science Foundation under Grant #OSR-9452894 and by the South Dakota Future Fund.. Acknowledgment is also made by J.L. and S.S. for supporting the development of PGAMS by the Marshall Space Flight Center Director's Discretionary Fund.

REFERENCES

[1] M.A. Box and C. Sendra,"Sensitivity of Exiting Radiances to Details of the Scattering Phase Function," J. Quant. Spectrosc. Radiat. Transfer, vol. 54, pp. 695-703, 1995.

[2] K.N. Liou, *An Introduction to Atmospheric Radiation,* Academic Press, New York, 1980.

[3] L.G. Henyey and J.L. Greenstein, "Diffuse Radiation in the Galaxy," Astrophys. J., vol.93, pp. 70-83, 1941.

[4] G.P. Anderson, et al., "MODTRAN3: Suitability as a Flux-Divergence Code", Proceedings of the Fourth Atmospheric Radiation Measurement (ARM) Science Team Meeting, Charleston, South Carolina, CONF-940277, pp. 75-80, April 1995.

[5] S. Schiller, and J. Luvall, "A portable ground-based atmospheric monitoring system (PGAMS) for the calibration and validation of atmospheric correction algorithms applied to satellite images,"SPIE, vol. 2231, pp. 191-198, 1994.

[6] B.L. Markham, D.L. Williams, J.R. Schafer, F. Wood, and M.S. Kim,"Radiometric Characterization of Diode-Array Field Spectroradiometers," Remote Sens. Environ., vol. 51, pp. 317-330, 1995.

RADARSAT CALIBRATION: The Operational System and Initial Results

S.K. Srivastava[1], T.I. Lukowski[2], R.K. Hawkins[2], C. Cloutier[3], L.D. Teany[2], N.W.Shepherd[4], R.B.Gray[5], A.P. Luscombe[6], and R. Banik[1]

[1] RADARSAT Program, Canadian Space Agency, 6767 Route de l'aeroport, St. Hubert, PQ, Canada, J3Y 8Y9
Phone: (514)926-5133 Fax: (514)926-5167 E-mail: srivastavas@sp-agency.ca

[2] Canada Centre for Remote Sensing, 588 Booth St.,Ottawa, ON, Canada, K1A 0Y7
Phone: (613)998-9060 Fax: (613)993-5022 E-mail: tom.lukowski@ccrs.nrcan.gc.ca

[3] Intermap Technologies, 2 Gurdwara Rd. , Nepean, ON, Canada, K2E 1A2
Phone: (613)998-9060 Fax: (613)993-5022 E-mail: caroline.cloutier@ccrs.nrcan.gc.ca
Under Contract to the Canada Centre for Remote Sensing

[4] N. W. Shepherd & Associates , 6632 Carp Road, RR#2 Kinburn, ON, Canada, K0A 2H0
Phone/Fax: (613)832-4462 E-mail: 72774.2232@compuserve.com
Under Contract to the Canadian Space Agency

[5] Brix Systems, 37 Belgrave Rd., Ottawa, ON, Canada, K1S 0L9
Phone/Fax: (613)230-5416 E-mail: robgray@brix.on.ca
Under Contract to the Canadian Space Agency

[6] SPAR Aerospace Ltd., 21025 Trans-Canada Highway, Ste Anne de Bellevue, PQ, Canada, H9X 3R2
Phone: (514)457-2150 Fax: (514)425-3041 E-mail: aluscomb@spar.ca
Under Contract to the Canadian Space Agency

ABSTRACT

The Canadian earth observation satellite, RADARSAT, was launched in late 1995. The aim of this space borne SAR program is to provide operationally calibrated products.

To enable calibration of RADARSAT data, the RADARSAT Image Data Calibration System has been developed. This includes RADARSAT Precision Transponders and two calibration workstations. Data from these point targets and diffuse target regions are being analyzed during the current testing phase. Results show that RADARSAT is meeting its performance specifications.

INTRODUCTION

The Canadian earth observation satellite, RADARSAT, was launched on November 4, 1995 and the first image produced on November 28, 1995 [1].The five year mission is to provide to users calibrated C-band HH polarized Synthetic Aperture Radar (SAR) data products, at various incidence angles, resolutions and swath coverages, using separate elevation beams. The SAR is also capable of operating in the ScanSAR mode by combining different elevation beams. Considerable emphasis in the RADARSAT Program has been placed on the provision of operationally calibrated products, which ensures that targets can be compared radiometrically within each scene and between scenes. Descriptions of this system are given in [2]. The Mission Management Office (MMO) in the Mission Control Centre (MCC) located at St. Hubert is responsible for the image quality management. The entire calibration process is centrally coordinated by the MMO. The SAR data are processed at the Canadian Data Processing Facility (CDPF) located at Gatineau, Quebec. In order to maintain end-to-end image quality for the mission life, routine external calibration using precision transponders and homogeneous targets (e.g. rain forest) is being carried out. The RADARSAT precision transponders (RPTs) developed under contract to CSA by MPB Technologies Inc. (Pointe Claire, Quebec)[1] are located at four sites in Canada (Ottawa, Ontario, Fredericton, New Brunswick, Prince Albert, Saskatchewan and Resolute Bay, Northwest Territories).

The calibration image data are analyzed off-line in the two calibration workstations, developed under contract to CSA by Array Systems Computing Inc. (North York, Ontario). One is located at the CDPF and the other at the MCC. Together they

[1] These devices are described in [3].

0-7803-3068-4/96$5.00©1996 IEEE

are used for measuring the image quality and to derive updates for calibration parameters. Resulting parameter updates are provided to the processor to generate calibrated products. Short term variations in the gain of the sensor electronics are tracked by the on board internal calibration system and these data are transmitted to the ground with the radar signal data. This allows the processor to automatically compensate for radar gain variations between external calibration periods, and thus maintain the required radiometric accuracy. The Image Data Calibration System has been described previously [4][5].

As of this writing, (March, 1996) both space and ground segments of the RADARSAT system are currently under the Commissioning Phase. Since November, image data have been acquired on a regular basis for different areas of the globe in both real time and on-board recorded configurations for most of the beams/modes. Functional testing of the system has been completed. Assessment of the image quality is being done by using images of the transponders (acquired when available) and distributed targets. Preliminary results of the image quality are being used for characterization and for adjustments, where required, of the sensor and the processor. Image quality assessment activity is continuing throughout the commissioning phase to complete the qualification of the products.

DATA ACQUISITION AND ANALYSIS

Imagery of the RPTs has been acquired in various modes and analyses performed on the IDCW to obtain preliminary values of image quality parameters. Specified [6] and measured values for parameters for SGX products [2] in each of the three frequency bandwidths are presented in Table 1.

In order to compare the inter-product radiometry of RADARSAT products, four products (SGX, SGF, SGC, and SLC) were produced from the same signal data (Beam S7, Ascending Pass, Orbit 1206, data of the Fredericton area). Averages were performed over the same diffuse target areas to obtain the mean β_o (Radar Brightness) values. These are tabulated in Table 2.

DISCUSSION AND CONCLUSIONS

Image quality parameters are better than the image quality specifications. Interproduct comparisons indicate the qsame radar brightness values. These and other initial results indicate that the RADARSAT System is meeting and exceeding its performance requirements.

More detailed results which will be available following declaration of RADARSAT Initial Operational Capability will be presented at IGARSS'96.

ACKNOWLEDGMENTS

The signal data have been processed to imagery and analyzed at the Canadian Data Processing Facility by the staff of RADARSAT International Inc. In particular, we thank W. Jefferies, D. Wilson, R. Periard, G. Fitzgerald, C. Fabi, and G. Robert.

REFERENCES

[1] J. McNally and L. Pilloud,`` First RADARSAT Synthetic Aperture Radar (SAR) Image - Cape Breton Island, Nova Scotia,'' Canadian Journal of Remote Sensing, vol. 21, no. 4, pp.531-533, December 1995.

[2] Special Issue: RADARSAT, Canadian Journal of Remote Sensing, vol. 19, no. 4, pp.277-395, November-December 1993.

[3] R.K. Hawkins, L.D. Teany, P. Daleman, M. Lalonde, S. Srivastava, N. Shepherd, S.Y.K. Tam, P. Nguyen, S.L. Foo, and B. Gibbs, ``External Calibration Transponders for RADARSAT,'' Proceedings of the CEOS Workshop on SAR Calibration, pp. 99-115, September, 1994.

[4] S.K. Srivastava, N.W. Shepherd, R.K. Hawkins, and T.I. Lukowski, ``Calibration for RADARSAT,'' Proceedings of IGARSS'94, pp. 1099-1101, August, 1994.

[5] S.K. Srivastava, N.W. Shepherd, T.I. Lukowski and R.K. Hawkins, `` Plans for RADARSAT Image Data Calibration,'' Presented at the 30th COSPAR Scientific Assembly, Hamburg, Germany, July, 1994.

[6] Canadian Space Agency, RADARSAT System Specification, Document no. RSCSA-SP0002, Rev. B, March 10, 1995.

[7] MacDonald Dettwiller and Associates, RADARSAT Canadian Data Processing Facility Product Specification, Document no. RZ-SP-50-5313, Rev. 5/1, Aug. 28, 1995.

[2] Detailed product descriptions are given in [7].

TABLE 1: Image Quality Parameter Test Measurements

Parameter	*Beam F2*	*Beam S2*	*Beam S7*
Date of Acquisition	Mar. 5, 1996	Mar. 9, 1996	Mar. 5, 1996
Orbit	1749	1799	1742
Chirp Bandwidth (MHz)	30.00	17.28	11.58
Impulse Response Width: Range (m) Spec	9.8	24.5	22.1
Impulse Response Width: Range (m)	8.07	21.13	19.07
Impulse Response Width: Azimuth (m) Spec	9.0	28.0	28.0
Impulse Response Width: Azimuth (m)	7.76	25.65	24.83
Peak Sidelobe Ratio: Range (dB) Spec	-18.0	-18.0	-18.0
Peak Sidelobe Ratio: Range (dB)	-19.23	-21.69	-22.22
Peak Sidelobe Ratio: Azimuth (dB) Spec	-18.0	-18.0	-18.0
Peak Sidelobe Ratio: Azimuth (dB)	-21.69	-21.58	-22.49
Absolute Location Error (m) Spec	750	750	750
Absolute Location Error: (m)	27.7	52.9	45.3

TABLE 2: Interproduct Comparison: Orbit 1206, Jan 27, 1996 22:29 UTC , Ascending Pass, Beam S7, Near Fredericton, NB

Product Type	*Mean β_o for Target Area 1 (dB)*	*Mean β_o for Target Area 2 (dB)*
Single Look Complex Product (SLC)	-12.40	-11.98
SAR Georeferenced Extra Fine Resolution Product (SGX)	-12.44	-11.98
SAR Georeferenced Fine Resolution Product (SGF)	-12.43	-11.98
SAR Georeferenced Coarse Resolution Product (SGC)	-12.40	-11.98

Calibrating the AVHRR Thermal Infrared Channels: Determining the Temperature of the Internal Calibration Target

D. A. Steyn–Ross*, Moira L. Steyn–Ross*, and S. Clift†
***Physics Department, University of Waikato**
***Hillcrest Road, Private Bag 3105, Hamilton, New Zealand**
***ph: +64-7-838-4026 / fax +64-7-838-4219 / email: asr@waikato.ac.nz**
†CSIRO Marine Laboratories, Hobart, Tasmania, Auatralia

Abstract -- Inflight calibration of the near and thermal infrared channels of the AVHRR (advanced very high resolution radiometer) proceeds by linearly interpolating between a pair of reference radiances: the zero-radiance of deep space, and the calculable radiance of a passive blackbody honeycomb target (internal calibration target, ICT) whose temperature is measured with a cluster of four embedded PRTs (platinum resistance thermometers) [1], [2]. Traditionally, the ICT temperature has been taken to be the equally-weighted average of the four PRT readings. We present evidence to show that equal weighting is not optimal, and describe how to compute revised weightings which improve calibration accuracies by ~0.13 K during times of rapid temperature change.

INTRODUCTION

There are three AVHRR models in present or prospective service. AVHRR/1 was the original four-channel radiometer design (channels 1 and 2 in the visible; ch.3 at 3.5 μm; ch.4 at 11 μm). AVHRR/2 has an additional infrared channel at 12 μm. The six-channel AVHRR/3 is scheduled to be launched in 1996. Recently released technical information from ITT [3] describes design improvements in the AVHRR/3 relative to the earlier /1 and /2 models. Of relevance to the inflight calibrations is the repositioning of the four PRT sensors to better sample the radiometer field of view when it is recording the radiance of the internal target. The sensors are placed at area-optimized positions which reduce the errors arising from temperature gradients across the surface of the ICT.

It follows that the present deployment of PRTs on AVHRR/1 and /2 is not optimal. This is clear from Fig. 1 where we see that PRT_3 is located just outside the annular region viewed by the radiometer. The old locations are at the vertices of a distorted rhombus, while the new positions are symetrically located at the corners of a square concentric with the view annulus. The temperature of the ICT is taken as the equally-weighted average of the four PRT readings, and for the symmetric deployment of AVHRR/3, this will be correct. For the older asymmetric PRT arrangement, the weighting factors should take account of the uneven sampling of the view annulus. We now proceed to compute a revised set of weights, and to evaluate the quantitative impact on calibration accuracies of such a change.

COMPUTING REVISED PRT WEIGHTS

We know the ICT temperature at the four PRT locations. If we can assume that the ICT temperature field is a linear function of position, then we can compute the temperature at any other surface position by linearly interpolating (or extrapolating) in the two surface dimensions x and y. In particular, we can map from the corners of a sub-optimal 'rhombus' to new grid positions at the corners of a square

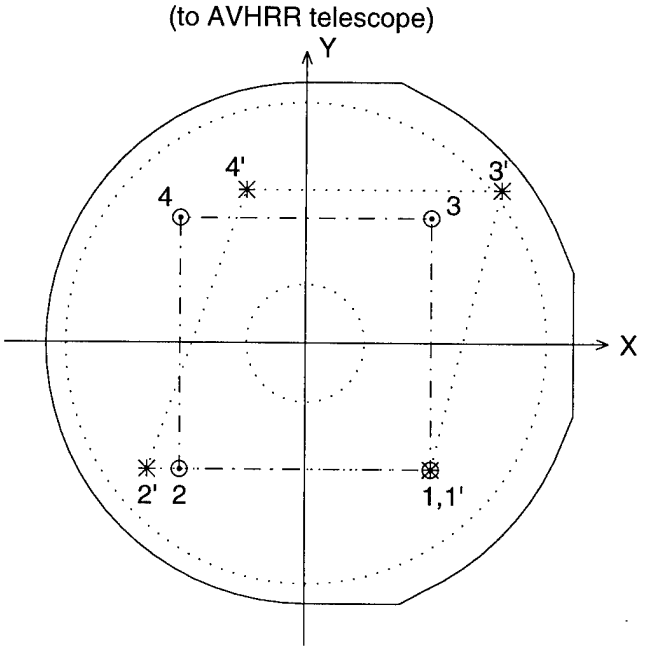


Fig. 1 AVHRR internal calibration target (ICT). The annular region between the two dotted circles indicates the field of view of the radiometer during the calibration cycle. The primed numerals show the placements of the four PRTs (platinum-resistance thermometers) for AVHRR models /1 and /2; the unprimed numerals show the revised PRT placements for AVHRR/3. The mirror scans the ICT from left to right in the $+X$-direction; the mirror rotation vector and the craft's velocity vector both point in the $-Y$-direction. [Source: Ref. 3]

0-7803-3068-4/96$5.00©1996 IEEE

whose vertices bisect the area of the radiometer view annulus. Referring to Fig. 1, we seek a set of weights which effectively map the temperature sensors from their present positions (A', B', C', D') to optimized virtual positions (A, B, C, D). The 'true' average temperature of the radiometer view annulus would then be given by the equally-weighted average of the temperatures computed at the four virtual sites.

Fig. 2 illustrates the interpolation scheme. Given temperatures at three positions A', B', C', what is the temperature at grid position A, assuming the two-dimensional temperature field is a linear function of position? The temperature at A can be expressed as a linear combination of the temperatures at intermediate points E and F:

$$T_A = \alpha T_E + (1 - \alpha)\, T_F \tag{1}$$

where the temperatures at E and F are in turn expressible as linear combinations of the temperatures at A', B' and C':

$$T_E = \beta T_{A'} + (1 - \beta)\, T_{B'} \tag{2}$$
$$T_F = \gamma T_{A'} + (1 - \gamma)\, T_{C'} \tag{3}$$

with weighting factors given by following ratios,

$$\alpha = \frac{AF}{EF}, \quad \beta = \frac{EB'}{A'B'}, \quad \gamma = \frac{FC'}{A'C'}. \tag{4}$$

Substituting (2) and (3) into (1) gives T_A as a linear combination of temperatures $T_{A'}$, $T_{B'}$, $T_{C'}$. This procedure is repeated for the remaining grid corners B, C, and D, to arrive at a final set of weighting factors to give the effective average temperature of the view annulus.

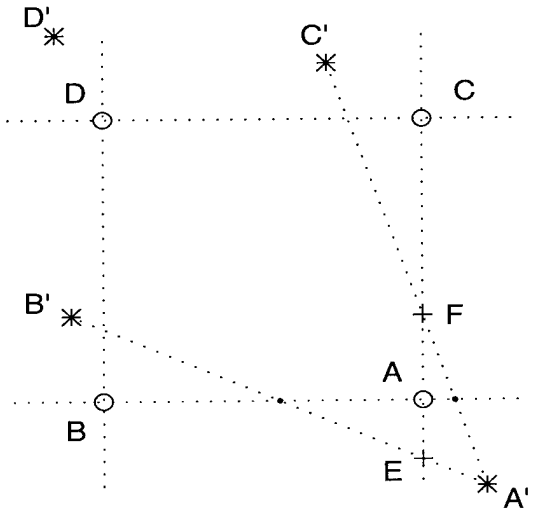


Fig. 2 Schematic illustrating a general bilinear mapping from arbitrary temperature sensor positions to virtual sensor positions at the vertices of a square. The mapping of $A' \rightarrow A$ uses nearest-neighbor information from B′ and C′, and ignores opposite neighbor D′.

Table 1: Locations of Actual and Optimal PRT positions for AVHRR/1 and /2 Calibration Target

	Actual		Optimal	
PRT	x (mm)	y (mm)	x (mm)	y (mm)
1	+54	-54	+54	-54
2	-68	-54	-54	-54
3	+84	+66	+54	+54
4	-25.6	+66	-54	+54

Table 1 lists the coordinates of the present PRT positions, and the revised coordinates for the virtual PRT positions. These values were measured directly from a diagram (drawn at 2:1 scale but without dimensions) published in [3]. We estimate that the Table 1 values have an accuracy of ±1.5 mm.

The optimal radial position for the PRTs would be that which bisects the radiometer view annulus into two snaller annuli of equal area. The PRTs should be separated by 90° with respect to the (x, y) origin to ensure the view annulus is evenly sampled by angle. Hence the optimal PRT locations form the vertices of a square defined in the fourth and fifth columns of Table 1.

The measured dimensions of the inner and outer radii of the view annulus are respectively R_1 = 25.4 mm, R_2 = 103.5 mm. The radius r which bisects this annulus is given by

$$\pi(R_2^2 - r^2) = \pi(r^2 - R_1^2)$$

$$r = \left[(R_2^2 + R_1^2)/2\right]^{1/2} = 74.05 \text{ mm}$$

which corresponds to a PRT_1 location of (x, y) = (52.36, –52.36) mm. Since this is very similar to the current PRT_1 location of (54, –54), the decision was made in the present work to leave the PRT_1 position unchanged (similarly, the y-coordinate for PRT_2 is left unchanged).

Applying the bilinear interpolation scheme of (1) through (4) to the values in Table 1, we arrive at the new PRT weighting factors listed in Table 2.

Comparing the default and revised weighting factors, we see that the most important change is the reduction in weight for PRT_3, with corresponding increases in the weights for PRT_1 and PRT_4. The reduction for PRT_3 is expected since it lies outside the view annulus; however, it samples regions of the ICT honeycomb which lie within the viewing region, thus its weight is small, but not zero.

Table 2: Revised vs Default Weights for Computing Average ICT Temperature for AVHRR/1 and /2

PRT	Revised	Default
1	0.3037	0.25
2	0.2463	0.25
3	0.1083	0.25
4	0.3417	0.25

Table 3: Zero-Lag Correlation Coefficients between IC4 and Each PRT for Pass Shown in Fig. 3

PRT	1	2	3	4
Night	0.38	0.38	0.37	0.41
Transition	-0.82	0.23	-0.92	-0.62
Day	0.57	0.91	0.25	1.01
Whole scene	1.14	2.43	-0.30	2.42

How important is this change to the formula for computing the ICT temperature? To answer this question, we re-examined a NOAA-11 pass recorded at the CSIRO Marine Laboratory in Tasmania, Australia in 1991. During this pass, the satellite crossed the terminator from night into day. During trannsition, the calibrations became unreliable because sunlight impinged directly on the internal calibration target, creating strong and transient temperature gradients. Fig. 3 shows the calibration trajectory for the four PRT temperature traces and for the channel-4 radiometric count recorded when the radiometer viewed the ICT. We see that PRT_3 responds to the sudden influx of solar irradiance more slowly than the other PRTs, and is the only PRT which fails to track the decreased radiance evident around line 4000 (this decrease is probably a shadow effect as spacecraft underparts partially block the sun).

Ideally the PRT and IC4 traces should all track in unison, with each apparent radiance change being matched with corresponding temperature change. To quantify the relative correlations between the PRT and radiometer records, we detrended each curve, inverted the IC4 trace (so that it has the same phase as the PRTs), and computed the zero-lag correlation coefficients between IC4 and each PRT in turn. The results appear in Table 3.

While none of the PRT traces correlates well with IC4 during transition, the correlation for PRT_3 is notably worse. This is particularly apparent for the portion of the pass following transition. These results provide further support for the proposition that the weighting for PRT_3 should be lowered.

In Fig. 4 we plot the correction which would apply to the ICT temperature if the area-optimized weights of Table 2 were to be used instead of the standard equal-weighting scheme. For the night portion, the correction is neglibible, while for the transition and day portion, the difference

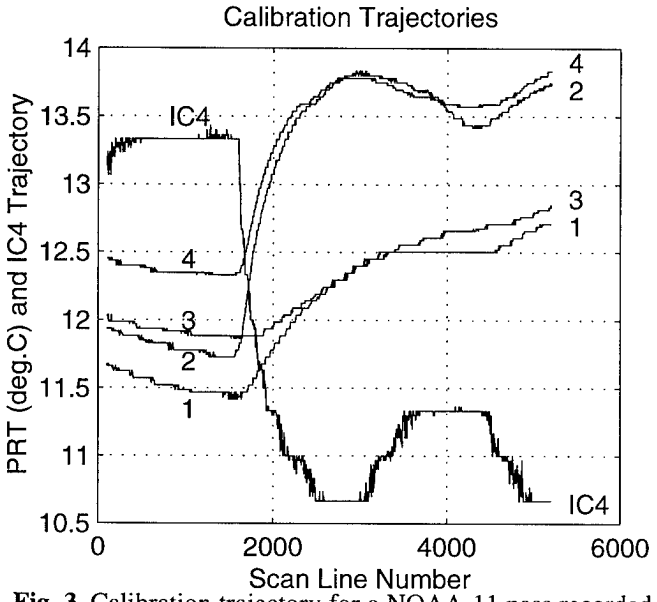


Fig. 3 Calibration trajectory for a NOAA-11 pass recorded at Hobart, Tasmania on Jan 2, 1991, 1531 UT. The spacecraft entered sunlight at scan line 1560. IC4 is the raw channel-4 radiometer count (scaled arbitrarily to fit the graph) when it views the ICT. The numbered curves show the temperature traces returned by the four platinum-resistance thermometers embedded in the ICT.

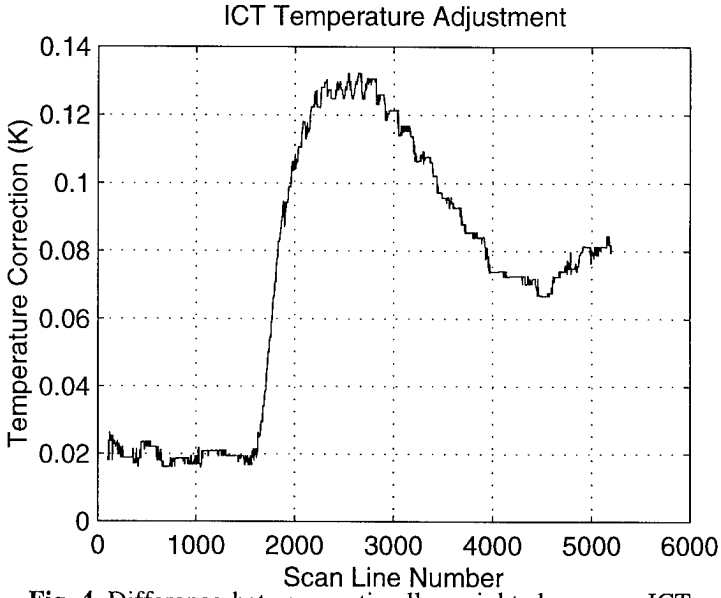


Fig. 4 Difference between optimally-weighted average ICT temperature and unweighted average temperature as a function of scan line number for the trajectories of Fig. 3. During the night portion (scan line < 1560), the difference is negligible. During terminator crossing, the difference can be significant, with a maximum value of +0.13 K.

between the two averages ranges from +0.07 to +0.13 K.

CONCLUSIONS

For the new model /3 AVHRR, the four PRTs which monitor the temperature of the internal calibration target have been moved to area-optimized positions to minimize the calibration errors arising from temperature gradients in the ICT. A similar improvement in calibration accuracy can be synthesized for the current AVHRR/2 and earlier /1 models by applying a bilinear transformation which maps the PRT locations to their idealized positions. The mapping is achieved by computing a new set of PRT weighting factors. The new weight for PRT_3 is smaller than the standard value because this PRT is located outside the view annulus of the radiometer.

ACKNOWLEDGMENT

We are grateful for several useful communications with Roy Galvin of ITT Aerospace/Communications Division.

REFERENCES

[1] Weinreb, M. P., G. Hamilton, S. Brown, R. J. Koczor, Nonlinearity corrections in calibration of advanced very high resolution radiometer infrared channels, *J. Geophys. Res., 95,* C5, 7381-7388, 1990.

[2] Steyn-Ross, D. A., M. L Steyn-Ross, and S. Clift, Radiance calibrations for advanced very high resolution radiometer infrared channels, *J. Geophys. Res., 97,* 5551-5568, 1992.

[3] ITT Aerospace/Communications Division, Technical Description for the advanced very high resolution radiometer AVHRR/3, vol. 1, contract NAS5-30384, Fort Wayne, Indianna, 1994.

A MODIFIED IEM MODEL FOR SCATTERING FROM SOIL SURFACES WITH APPLICATION TO SOIL MOISTURE SENSING

A.K. Fung[1], M.S. Dawson[1], K.S. Chen[2], A.Y. Hsu[3], E.T. Engman[3], P. O. O'Neill[3] and J. Wang[3]
[1]E.E. Dept.,Box 19016, University of Texas at Arlington, TX 76019
Tel: 817–273–3422, FAX 817-273-3443, eefung@uta.edu
[2]Center for Space and Remote Sensing Research
National Central University, Chung-Li, Taiwan
Tel: 886 3 425-7232, Fax: 886 3 425-4908
[3]Laboratory for Hydrospheric Processes,
NASA Goddard Space Flight Center, Greenbelt, MD USA

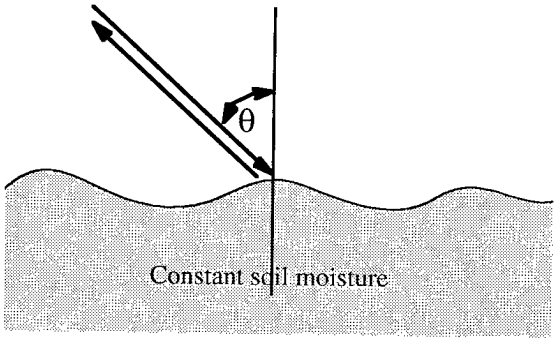
Abstract-- The IEM surface scattering model is generalized to include the possible existence of a dielectric profile such as observed in drying coditions after a rain. It is shown that for such a case, the generalized signal model including this improvement in reflectivity may give better agreement with backscatter measurements for some data sets. Hence, such a model may be applied either directly for estimating soil moisture or used to generate training patterns for statistical estimators.

INTRODUCTION

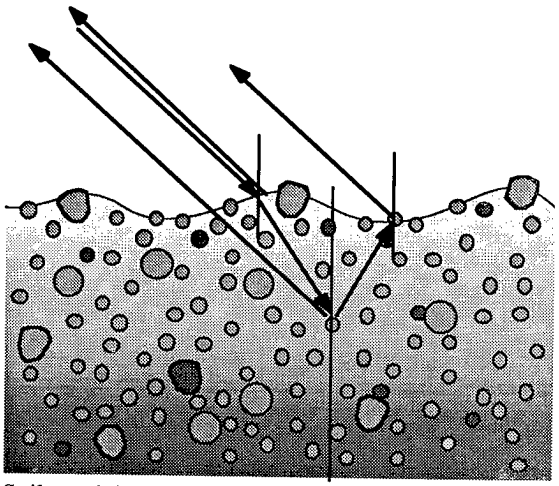
The quantitative estimation of soil moisture from radar measurements is usually obtained by employing an empirical relationship that maps the measured normalized backscatter coefficient σ° into volumetric soil moisture content m_v. Linear regression models between radar backscatter and measured soil moisture have been developed in many studies including [1-4]. More advanced empirical non-linear regression models such as those of Oh et al. [5,6], and Dubois et al. [7,8] have also been demonstrated for specific data sets.

In recent studies, advanced theoretical scattering models such as the IEM [9,10] have been used in conjunction with neural network and statistical based estimators for surface parameter retrieval [11-13] in an attempt to make soil moisture estimators more robust. In these estimators, a theoretical model is used to create a complete synthetic data-ground parameter training set for use in a robust statistical inversion technique such as those of Manry et al. [14]. The theoretical model can also be used to supplement or 'fill in' areas where measured data is not available. A main advantage in the use of the theoretical set over measured data is that we can exactly control the content and range of the set used in the construction of the inverse mapping. In addition, we can control the noise levels in each of the channels to be used so that the training set matches the statistics of the true measured data or the characteristics of the instrument.

One concern, however, is that the modeling of the soil using a closed-form signal model such as the IEM treats the soil as a homogeneous half-space. Whether or not this simplistic modeling is appropriate (or desirable) continues to be a point of discussion. It is known, for example, that soil surfaces dry up from the top down after rain. Thus it is desirable to incorporate a physical dielectric gradient into our theoretical modeling. An illustration of this drying effect and the modeling proposed is given in Figure 1.



a) Idealized soil model using a homogeneous half-space with rough surface.



b) Soil modeled as surface with scattering and volume effects and variable dielectric profile.

Figure 1. Two modeling representations for soil.

0-7803-3068-4/96$5.00©1996 IEEE

In this work, we extend the IEM model to incorporate a vertical soil moisture profile. The purpose of this paper is to incorporate such an effect by including a transition layer into the formula for the reflection coefficient. This reflection coefficient model along with an empirical permittivity model [15] is then combined with the existing IEM surface scattering model to serve as the model for backscattering from rough soil surfaces.

THE MODIFIED IEM MODEL

We consider the transitional dielectric layer given by [16] in which the permittivity as a function of depth, z, is

$$\varepsilon_r(z) = 1 + \varepsilon_{r_1} \frac{\exp(mz)}{1 + \exp(mz)}. \tag{1}$$

In the formulation of Brekhovskikh, note that $\varepsilon_{r_1} = \varepsilon_{r_\infty} - 1$, and $-N = \varepsilon_{r_1}$. The inputs to the model are the transition rate factor m and the dielectric constant at $z = \infty$ which is ε_{r_∞}. The real part of the dielectric will always start at $\varepsilon_{r_{-\infty}} = 1$ which is air and gradually change to ε_{r_∞} at a rate of m. An approximate value for m is generally about 12.

The standard Fresnel reflectivities are replaced by a modified set of relations which are given by

$$R_\perp = \frac{\Gamma(jS\cos\theta_0)}{\Gamma(-jS\cos\theta_0)} \frac{\Gamma\left[\left(\frac{-jS}{2}\right)\left(\cos\theta_0 + \sqrt{\cos^2\theta_0 + (\varepsilon_{r_\infty} - 1)}\right)\right]}{\Gamma\left[\left(\frac{jS}{2}\right)\left(\cos\theta_0 - \sqrt{\cos^2\theta_0 + (\varepsilon_{r_\infty} - 1)}\right)\right]}$$

$$\times \frac{\Gamma\left[1 - \left(\frac{jS}{2}\right)\left(\cos\theta_0 + \sqrt{\cos^2\theta_0 + (\varepsilon_{r_\infty} - 1)}\right)\right]}{\Gamma\left[1 + \left(\frac{jS}{2}\right)\left(\cos\theta_0 - \sqrt{\cos^2\theta_0 + (\varepsilon_{r_\infty} - 1)}\right)\right]} \tag{2}$$

and[1]

$$R_{//} = \frac{\Gamma(jS\cos\theta_0)}{\Gamma(-jS\cos\theta_0)} \frac{\Gamma\left[\left(\frac{-jS}{2}\right)\left(\cos\theta_0 + \frac{1}{\varepsilon_{r_\infty}}\sqrt{\cos^2\theta_0 + (\varepsilon_{r_\infty} - 1)}\right)\right]}{\Gamma\left[\left(\frac{jS}{2}\right)\left(\cos\theta_0 - \frac{1}{\varepsilon_{r_\infty}}\sqrt{\cos^2\theta_0 + (\varepsilon_{r_\infty} - 1)}\right)\right]}$$

$$\times \frac{\Gamma\left[1 - \left(\frac{jS}{2}\right)\left((\varepsilon_{r_\infty})^{1/3}\cos\theta_0 + \sqrt{\cos^2\theta_0 + (\varepsilon_{r_\infty} - 1)}\right)\right]}{\Gamma\left[1 + \left(\frac{jS}{2}\right)\left(\cos\theta_0 - \sqrt{\cos^2\theta_0 + (\varepsilon_{r_\infty} - 1)}\right)\right]} \tag{3}$$

where $S = 2k/m$. An example showing the differences in the reflectivities is shown in Figure 2.

1. This is an approximate relation which was not derived explicitly in Brekhovskikh.

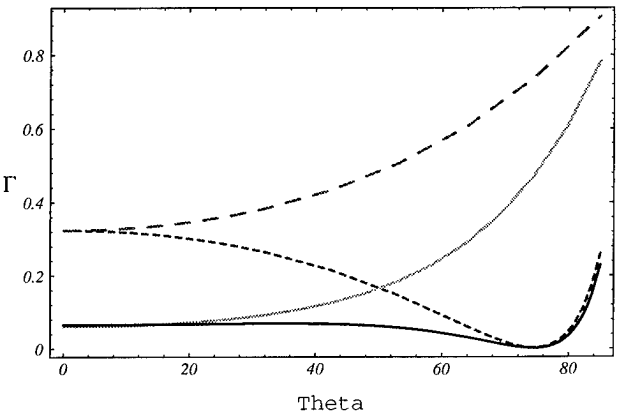


Figure 2. Comparison of standard Fresnel power reflection coefficients (dashed lines) with modified reflectivities.

ON THE APPLICATION OF THE MODIFIED IEM

The use of any retrieval algorithm clearly requires a good set of measured data upon which to validate the accuracy of the signal model used in the inversion algorithm. This signal model can be in one of many forms including empirical algorithms or a closed-form model such as the IEM. To date, a significant problem has been that there is a severe dearth of measurements with a *complete set of consistent ground truth.* In many existing sets encountered, the ground truth does not contain a soil moisture profile as required in our modified model. However, its needs can be demonstrated using a set of Washita data, where measurements were acquired over a period of time after rain. This is shown in Figure 3 where comparisons with data are made with and without using a dielectric profile.

By using one of the Washita data set taken from a bare soil surface to calibrate the reflection coefficient model, we can test the scattering model against other data sets acquired under similar conditions. This result will be shown during presentation.

REMARKS

Where angular measurements are available, these measurements can be used to determine the roughness parameters especially the surface correlation length through use of surface scattering model. This is believed to be a more effective way to ascertain this parameter because direct ground truth measurements are restricted by the length of the surface profile, the statistical homogeneity of the surface roughness, and the resolution of the profilometer. Hence, at a given frequency the directly measured value may not be the one seen by the radar. After the roughness parameters are determined either from ground truth or from angular measurements, the scattering model can be used to relate soil moisture to backscattering at various angles and frequency directly.

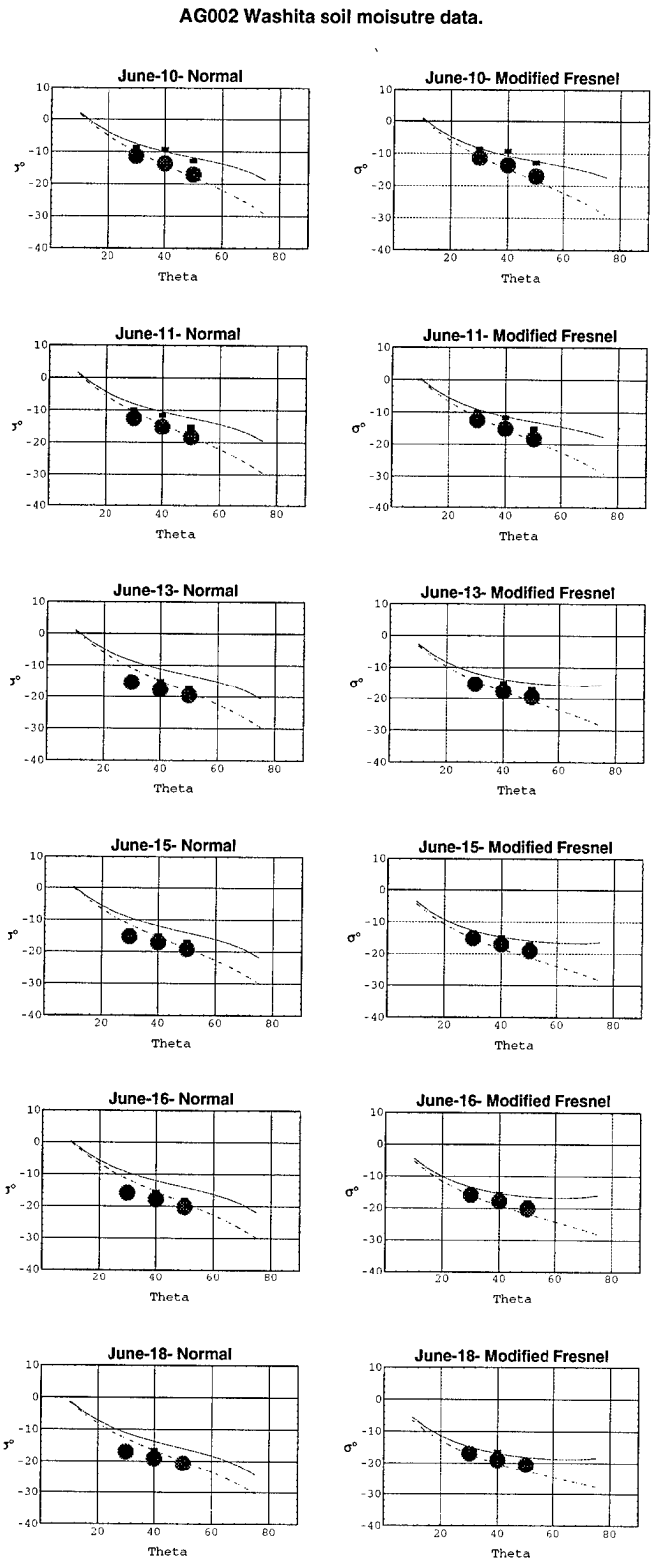


Figure 3. Illustration of the improved data fit with experimental data when the modified reflectivity is used in the IEM.

ACKNOWLEDGMENT

This work was supported by NASA SIR-C data analysis program funded through the Jet Propulsion Laboratory.

REFERENCES

[1] Ulaby, F.T., P. Batlivala, and M. Dobson, "Microwave Backscatter Dependence on Surface Roughness, Soil Moisture, and Soil Texture: Part I – Bare Soil," *IEEE Trans. on Geoscience and Remote Sensing*, Vol. GE-16, No. 4, Oct. 1978.

[2] Jackson, T.J., A. Chang, and T.J. Schmugge, "Aircraft Active Microwave Measurements for Estimating Soil Moisture," *Photogrammetric Engineering and Remote Sensing*, Vol. 47, pp. 810-805, June, 1981.

[3] Dobson, M.C., and F.T. Ulaby, "Active Microwave Soil Moisture Research," *IEEE Trans. on Geoscience and Remote Sensing*, GE-24, pp. 23-36, Jan. 1986.

[4] Pultz, T.J., R. Leconte, R.J. Brown, and B. Brisco, "Quantitative soil moisture extraction from airborne SAR data," *Canadian J. of Remote Sensing*, Vol. 16, pp. 56-62, 1990.

[5] Oh, Y., Sarabandi, K. and F. T. Ulaby, "An Empirical Model and an Inversion Technique for Radar Scattering from Bare Soil Surfaces", *IEEE Trans. Geoscience and Remote Sensing*, 1992, pp. 370-381.

[6] Oh, Y., K. Sarabandi, and F.T. Ulaby, "An Inversion Algorithm for Retrieving Soil Moisture and Surface Roughness From Polarimetric Radar Observations," *in Proc. of IGARSS 1994*, Vol. III, pp. 1582-1585.

[7] Dubois, P.C., J. van Zyl, and T. Engman, Measuring Soil Moisture with Imaging Radars, IEEE Trans. on Geoscience and Remote Sensing, Vol. 33, No. 4, July, 1995.

[8] Dubois, P.C., J. van Zyl, and T. Engman, Corrections to Measuring Soil Moisture with Imaging Radars, IEEE Trans. on Geoscience and Remote Sensing, Vol. 33, No. 6, Nov. 1995.

[9] Fung, A.K., Z. Li, and K.S. Chen, "Backscattering from a Randomly Rough Dielectric Surface," *IEEE Trans. Geo. and Remote Sensing*, Vol. 30, no. 2, March 1992.

[10] Fung, A.K., *Microwave Scattering and Emission Models and Their Applications*, Artech House, Norwood, MA, 1994.

[11] Dawson, M.S. and A.K. Fung, "Neural Networks and their Applications to Parameter Retrieval and Classification," *IEEE Geoscience and Remote Sensing Society Newsletter*, pp. 6-14, September, 1993.

[12] Dawson, M.S., A.K. Fung and M.T. Manry, "Surface Parameter Retrieval Using Fast Learning Neural Networks," *Remote Sensing Reviews*, Vol. 7, 1993, pp. 1–18.

[13] Dawson, M.S., A.K. Fung and M.T. Manry, "*A Robust Statistical-based Estimator for Soil Moisture Retrieval from Radar Measurements*" submitted for consideration in the forthcoming Special Issue of the IEEE Transactions on Geoscience and Remote Sensing, 1996.

[14] Manry, M.T., M.S. Dawson, S.J. Apollo, L.S. Allen, W.D. Lyle, W. Gong, and A.K. Fung, "Fast Training of Neural Networks for Remote Sensing", *Remote Sensing Reviews*, Vol. 9, pp. 77-96, 1994.

[15] Hallikainen, M.T., F.T. Ulaby, M.C. Dobson, M.A. El-Rayes, and L. WU, "Microwave Dielectric Behavior of Wet Soil - Part 1: Empirical Models and Experimental Observations," *IEEE Trans. on Geoscience and Remote Sensing*, Vol. GE-23, No. 1, pp. 25- 34, Jan. 1985.

[16] Brekhovskikh, L.M., *Waves in Layered Media*, Second Edition, Translated from the Russian by R.T. Beyer, Academic Press, New York, 1980.

Soil Moisture Retrieval Using the Danish L- & C-Band Polarimetric SAR

Jiankang Ji[1], Peter van der Keur[2], Anton Thomsen[3] and Henning Skriver[1]

[1]Danish Center for Remote Sensing, the Department of Electromagnetic Systems
Technical University of Denmark, Building 348, DK-2800 Lyngby, Denmark
Phone: +45 45 881444 Fax: +45 45 931634 E-mail: jjk@emi.dtu.dk

[2]Institute of Geography, University of Copenhagen
Østervoldgade 10, DK-1350 Copenhagen K, Denmark
Phone: +45 35322500 Fax: +45 35322501 E-mail: pvk@geogr.ku.dk

[3]Danish Institute of Plant and Soil Sciences
Research Center Foulum, DK-8830 Tjele, Denmark

ABSTRACT – Danish polarimetric SAR data have been applied to estimate soil moisture (SM). The preliminary results evaluated with the L- and C-band SAR data acquired at the Danish test site Foulum during a number of missions in 1994 and 1995 are presented. *In situ* data have been collected during the SAR missions and the variations of SM at field scale are discussed. The Integral Equation Method (IEM), the Dubois empirical model and the Oh polarized-ratio model have been used as algorithms to inverse SM from polarimetric SAR data under near bare field conditions. Comparisons between the inversions and the *in situ* measured data showed that the Dubois empirical model gave the best results for inversion of SM. The standard deviations between the inversed and the measured data at C-band are $s_{m_v} = 6.1\%$ for SM and $s_\sigma = 0.37cm$ for soil surface *rms* height, respectively. C-band data are better than L-band data for estimation of surface roughness.

INTRODUCTION

The principle of radar measuring soil moisture (SM) is that the backscattering coefficient varies strongly with the soil dielectric constant, and the latter depends on the SM content. Unfortunately, soil surface roughness and vegetation cover also have strong contributions to the backscattering coefficient. Thus, it is difficult to retrieve SM from single polarization radar data. A polarimetric SAR measures the full polarimetric signatures of targets and the ambiguity implied in backscattering coefficients from the contributions of SM, roughness and vegetation might be removed by evaluating the polarimetric signatures of backscattering coefficients, which makes SM retrieval from polarimetric SAR data possible.

The tool to infer SM from SAR data is backscattering models. It has been realized that the classical surface backscattering models have some limitations when applied to natural surfaces [1]. Therefore, the Integral Equation Model (IEM), valid in a large range of roughness conditions is currently widely used as a theory for soil scatter [1]. In addition, Dubois and Oh have developed two different empirical models [2, 3]. The empirical models are much simplified compared to the IEM. In this paper, the Danish L- and C-band polarimetric SAR data acquisitions and the *in situ* data collections are described. SM variations at field scale are illustrated. The Dubois model, the Oh model and the IEM have been applied for SM retrieval.

THE POLARIMETRIC SAR DATA

The Danish polarimetric SAR (EMISAR) was initially a C-band VV-polarized SAR first flown in 1989 and later in 1993 a fully polarimetric system. An L-band system with fully polarimetric capability was completed and tested early 1995. The EMISAR is developed by the Danish Center for Remote Sensing (DCRS) located at the Department of Electromagnetic Systems (EMI) of the Technical University of Denmark (DTU) [4].

The test site Foulum used for agriculture study is located in the northern part of Jutland, Denmark. Four different fields were selected as the test fields. There were four C-band acquisitions during 1994 and a number of L- and C-band acquisitions during 1995 over the test site, respectively. Polarimetric one-look images with spatial resolution of $2m$ by $2m$ are used in the study. One C-band scene acquired on April 28, 1994, a number of L- and C-band scenes acquired in 1995, for instance, on March 22 (L), March 24 (C), April 27 (C), May 1 (L), June 8 (L), and August 25 (L), are processed for SM retrieval. The incidence angles for all the four test fields are between $42° - 45°$.

FIELD EXPERIMENT DESCRIPTION

Corresponding to the EMISAR acquisitions from the beginning of March to the end of August both 1994 and 1995, extensive *in situ* data collections have taken place at the 4 test fields under conditions ranging from bare soil to fully vegetated. The vegetation types were winter wheat, spring barley, sugar beet and grass. All relevant parameters for interpretation of EMISAR images were measured

0-7803-3068-4/96$5.00©1996 IEEE

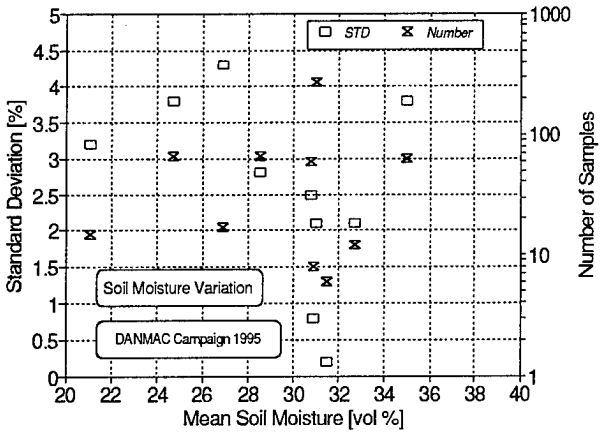


Figure 1: *In situ* SM vs. Standard Deviation (STD) and number of samples.

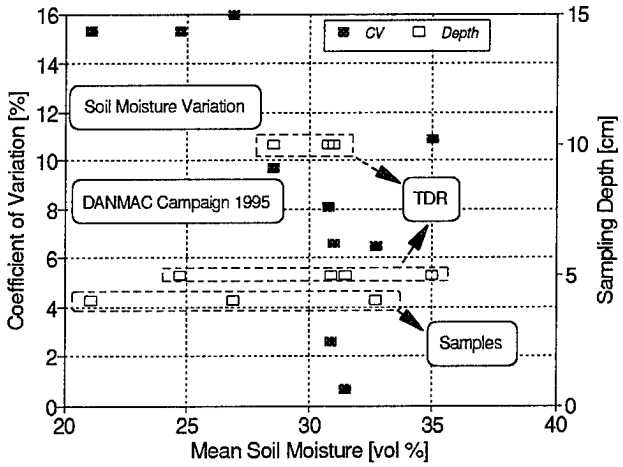


Figure 2: *In situ* SM vs. Coefficient of Variations (CV) and sampling depth.

in this period, including surface roughness, surface SM, Leaf Area Index (LAI) and other biophysical parameters such as vegetation water content, biomass and plant density and height.

Surface roughness was measured by a 2 meter long ruler and, later in the growing season, by a laser instrument, developed at the Research Center Foulum (RCF). SM was measured along transects for each 25 meter and in two grids, a 50 meter by 50 meter grid in the winter wheat field and a 150 meter by 150 meter grid in the spring barley field. Water content in the top 0-5cm and 0-10cm was determined by gravimetric sampling using 100cm^3 sampling rings (4cm in depth) and by Time Domain Reflectometry (TDR) with 5 and 10cm long probes. Leaf Area Index was monitored by the LAI2000 device (Licor). Biomass and water content in vegetation was sampled manually together with estimates of plant density and height. Climatological data were collected during the whole period from March to September. Furthermore, continuous TDR measurements of water content were made in a 60cm deep soil profile in the spring barley field.

SM VARIATIONS AT FIELD SCALE

In situ SM was measured at each sampling point with 6 samples for the TDR and 3 samples for the sampling rings, respectively. Mean values of the measured water contents are plotted against standard deviations and the number of samples in Fig. 1. Volumetric water content is calculated as the product of soil bulk density and gravimetric water content. Bulk density varies normally between 0.8 and 1.4g/cm^3, sometimes caused by sampling in and outside tractor wheel tracks. However, the standard deviation of the volumetric water content never exceeds 4.5%, which is in agreement with findings by Bell *et al.* [6].

The Coefficient of Variation (CV) in Fig. 2 is 16% or lower. Bell *et al.* [6] state that for mean SM higher than 20 vol.% CV is generally less than 15%, a value which is desirable for SM-brightness temperature correlations.

SM AND *rms* HEIGHT RETRIEVAL

The theoretical IEM, the Oh's polarized ratio model and the Dubois's co-polarized backscattering coefficient model have been applied to the fields under near bare soil conditions determined by Dubois's criteria $\sigma^\circ_{hv}/\sigma^\circ_{vv} < -11dB$ for both L- and C-band [2]. The roughness conditions of the fields fall into the validity regions of these models. Dobson's dielectric constant model has been used to convert between dielectric constant and SM [7].

Inversion with the IEM

The measured roughness data show that the hybrid Gauss-Exp function which is the product of Gaussian and exponential functions is a suitable form for autocorrelation function (ACF) [5], and there is approximately a linear relation between the correlation length l and the *rms* height σ for a natural soil surface. In the inversion with the IEM, the hybrid Gauss-Exp function is used for the ACF and l is replaced by the linear correspondence with σ. Results of the inversion from numerical fit of the IEM to the SAR data show that the IEM underestimates SM, and a *rms* error of 10.0% is obtained. This underestimation is equivalent to an overestimation of the backscattering coefficient. A recent study indicates that one reason may be that the surface roughness measured *in situ* does not resemble the roughness relevant for the radar backscattering. The radar signal is probably backscattered by a smoother subsurface layer.

Inversion with the Oh Model

Oh developed a polarized ratio model in 1992 and modified it in 1994 [3]. Unfortunately, only few of the EMISAR data could be inversed with both versions of the model, and the agreement was poor between the inversed and the measured SM. One reason might be that the model uses both co- and cross-polarized ratios. Cross-polarized ratio has a larger uncertainty compared to co-polarized backscatter because of the poorer signal-to-noise ratio.

Inversion with the Dubois Model

Figs. 3 shows the inversed SM and the *rms* height using the Dubois model. The *rms* errors between the inversed and the measured m_v are 7.6% (L-band, $N = 7$) and 6.1% (C-band, $N = 11$), and the *rms* errors for σ are $0.65cm$ (L-band, $N = 12$) and $0.37cm$ (C-band, $N = 12$), respectively. The Dubois model gave the best results of the three. There is no preference of L- or C-band for SM inversion, but for *rms* height inversion C-band gave the best results, and the *rms* error is very close to that of Dubois, $0.35cm$ [2]. The *rms* height results also show that the Dubois model seems to overestimate σ for $\sigma < 0.5cm$ and to underestimate σ for $\sigma > 0.5cm$.

The validity conditions of a model are important. Most of the theories and most of the SAR observations illustrate that the backscattering coefficient $\sigma^\circ_{hh}/\sigma^\circ_{vv} \leq 1$ for bare soil. Dubois *et al.* indicated that restricting the validity of the model to $k\sigma < 2.5$ and $\theta \geq 30^\circ$ will ensure that $\sigma^\circ_{hh}/\sigma^\circ_{vv} \leq 1$, where k is wavenumber, θ is incidence angle. Using this equation, we can study the validity conditions from the expressions of the Dubois model, which is $k\sigma \leq cos^5\theta sin^{\frac{20}{3}-1}\theta \cdot 10^{\frac{1}{3}(4+0.18\epsilon_r tan\theta)}$, where ϵ_r is the real part of the relative dielectric constant. It is obvious that the roughness conditions which the Dubois model can be applied to is related not only to the incidence angle, but also to the soil dielectric constant. For example, at $\theta = 35^\circ$ it is valid when $k\sigma \leq 2.4$ for wet soil ($\epsilon_r \geq 20.0$), but it is only valid when $k\sigma \leq 0.5$ for dry soil ($\epsilon_r \geq 4.0$). This reveals some differences of the validity of the Dubois model by keeping $\sigma^\circ_{hh}/\sigma^\circ_{vv} \leq 1$ as the criteria.

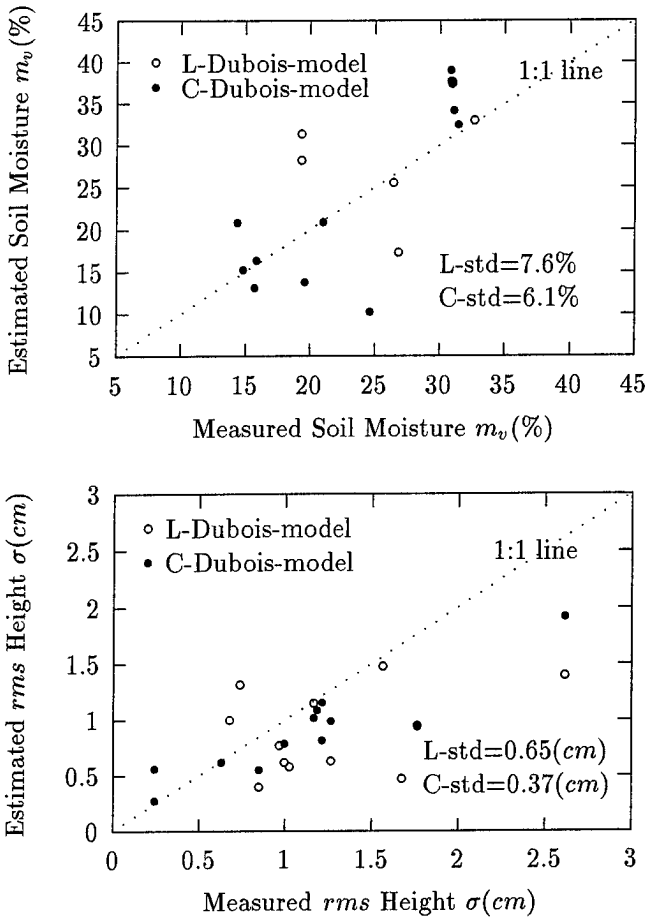


Figure 3: Inversion results using the Dubois model.

CONCLUDING REMARKS

Retrieval of SM with the polarimetric EMISAR data has been presented. The detailed grid measurements of the *in situ* SM data show that the standard deviation of SM at field scale is below 4.5%, which illustrates probably the best accuracy of the SAR measured SM. One can not expect that the accuracy of the SAR measured SM is better than the accuracy of the *in situ* measurement. The Dubois model for inversion of SM showed better results than both the Oh model and the IEM model. The L- and C-band data showed equivalent results for SM retrieval, whereas the C-band data was preferred for the *rms* height retrieval using the Dubois model. The validity condition of the Dubois model has been discussed under the restriction of $\sigma^\circ_{hh}/\sigma^\circ_{vv} \leq 1$.

On-going work is focused on two aspects. To improve *in situ* data quality by using a laser instrument to measure the roughness and by increasing the number of samples for SM measurement. To improve the inversion accuracy by modifying the existing models.

ACKNOWLEDGMENTS

This work and data acquisitions have been sponsored by the Danish Space Board and the Danish National Research Foundation. Development of the EMISAR system has been co-sponsored by the Thomas B. Thriges Foundation, the Danish Technical Research Council (STVF), the Royal Danish Air Force, the Technical University of Denmark and the EU's Joint Research Center (JRC).

References

[1] A.K. Fung, 1994, *Microwave Scattering and Emission Models and Their Applications*, Artech House, Boston.

[2] P.C. Dubois, J.V. Zyl, and T. Engman, 1995, Measuring Soil Moisture with Imaging Radars, *IEEE Trans. Geoscience and Remote Sensing*, Vol. GE-33, No.4, pp. 915-926.

[3] Yisok Oh, *et al.*, 1992, An Empirical Model and An Inversion Technique for Radar Scattering from Bare Soil Surfaces, *IEEE Trans. Geoscience and Remote Sensing*, Vol. GE-30, No.2, pp. 370-381.

[4] E.L. Christensen, J. Dall, N. Skou, K. Woelders, J. Granholm, and S.N. Madsen, 1996, EMISAR: C- and L-Band Polarimetric and Interferometric SAR, *This issue*

[5] J. Ji, A. Thomsen & H. Skriver, 1995, Estimating Soil Moisture Using the Danish Polarimetric SAR, *The Proceedings of IGARSS'95*, Vol.2, pp.942-944.

[6] K.R. Bell, *et al.* 1980, Analysis of Surface Moisture Variations Within Large-Fields Sites, *Water Resources Research*, Vol. 16, No.4, pp. 796-810.

[7] M.C. Dobson, et al., 1984, A Reexamination of Soil Textural Effects on Microwave Emission and Backscattering, *IEEE Trans. Geoscience and Remote Sensing*, Vol. GE-22, No. 6, pp. 530-536.

Remote Sensing of Soil Moisture Using EMAC/ESAR Data

Z. SU, P.A. TROCH, F.P. DE TROCH
Laboratory of Hydrology and Water Management
University of Ghent, Coupure Links 653, B-9000 Ghent, Belgium,
Tel.: 32-9-2646138 Fax.: 32-9-2646236, szhongbo@allserv.rug.ac.be

Abstract -- In this paper we present first results of surface soil moisture retrieval using data from the European Multisensor Airborne Campaign / Experimental Synthetic Aperture Radar (EMAC/ESAR) collected on April 9, 1994 in the Zwalm catchment, Belgium. We apply a theoretical backscattering model to investigate the sensitivity of EMAC/ESAR backscattering coefficients to surface parameters. By comparing the predicted backscattering coefficients to the observed ones, we can conclude that current measurement techniques for surface roughness parameters in remote sensing campaigns are not accurate enough for retrieving soil moisture using theoretical models. A method based on simultaneous retrieval of surface roughness parameters and soil moisture using multiple ESAR measurements is hence proposed. Promising results on retrieved soil moisture confirm the validity of the proposed method.

INTRODUCTION

This paper reports the first results of research towards soil moisture retrieval from active microwave measurements using ESAR, developed by the German Aerospace Research Establishment (DLR). This instrument, together with imaging spectrometer (ROSIS) and microwave radiometer were flown during EMAC'94 [2]. For EMAC'94 the ESAR was working in 4 frequencies (X, C, L, and P band) with vertical and horizontal co-polarization. Frequency and polarization are switchable during the flight. Cross-polarization is not available. For EMAC'94 the wide swath mode was flown (standard scene size: 6x6 km; geometric resolution: 4.5x4.5 m; operating altitude: 3600 m; incidence angle at center swath: 52°). The Zwalm catchment, Belgium, has been selected as a test site within the Vegetation and Soils thematic group of EMAC'94. ESAR flights over Zwalm were held on April 9, June 30 and August 19, 1994. One successful ROSIS flight was held on July 12, 1994 (cloud free conditions) in the Zwalm catchment. ROSIS images are used in this paper for identifying field boundaries within which ground truth samples for soil moisture, surface roughness and vegetation parameters were taken. In this paper only the ESAR data from April 9, 1994 will be considered.

GROUND TRUTH DATA COLLECTION

The Zwalm catchment is located about 20 km south of Ghent in Belgium. The total drainage area is 114 km^2. Several ESAR and ROSIS flights were held during the summer of 1994 over the catchment.

During the soil moisture remote sensing campaigns ground truth and SAR data acquisition took place in two subcatchments of the Zwalm, viz. Passemare and Sassegem. The ground truth data include soil moisture and soil bulk density at two depth (0-5cm and 5-10cm), soil surface roughness, vegetation height as well as meteorological variables measured at Bowen ratio stations and meteorological stations. Six trihedral corner reflectors were deployed [7] in Sassegem subcatchment for radiometric calibration purposes.

DATA PROCESSING

Data processing includes georeferencing of ROSIS and ESAR images, processing of ESAR data, processing of field data and extraction of backscattering coefficients for areas of interests. Processing of ESAR data consists of calculating of local incidence angle by employing flight geometry, geometrical relationship between georeferenced and original images and a digital terrain model of the subcatchment. Finally backscattering coefficients are extracted according to the delineated field boundaries and for the sampling locations along the transects, respectively. Field-averaged backscattering coefficients are calculated for each field.

SOIL MOISTURE RETRIEVAL FROM EMAC/ESAR DATA

a) Inversion algorithm based on the Integral Equation Model

In this paper, we use the Integral Equation Model (IEM) developed by *Fung et al.* [6] (see also [4]). The IEM is shown to unite the Kirchhoff and Small Perturbation models and therefore is applicable to a wide range of roughness conditions or frequencies. The complete version of IEM describes the backscattering behavior of a random rough surface with a much wider range of validity than the standard models.

An inversion procedure for soil moisture and surface roughness on the basis of the IEM using single frequency, single polarization backscattering coefficient was previously developed by [1]. This procedure is adopted here. Starting from a single radar backscattering coefficient soil moisture is determined by solving numerically the IEM equation under a given surface roughness condition. As the equation has only one independent variable, the problem is one-

0-7803-3068-4/96$5.00©1996 IEEE

dimensional, namely to find the root of the function. The Brent's algorithm [3] combining root bracketing, bisection, and inverse quadratic interpolation to converge from the neighbourhood of a zero crossing is used in this procedure. The above inversion procedure developed to derive soil moisture can also be used to derive the roughness parameters when the dielectric constant values are known.

b) The method of effective roughness parameters for retrieving soil moisture

Since the surface roughness parameters are usually not available for inversion of soil moisture, a method based on simultaneous inversion of surface roughness parameters and soil moisture is of great interest. For given SAR configurations there are three unknowns in this simultaneous inversion problem, namely soil dielectric constant ε, surface root mean square (rms) height σ and correlation length L for a given correlation function. To solve this inversion problem three input values would be necessary. These input values can be a combination of different frequency, different polarization, different incidence angle and/or temporal data sets. For the purpose of soil moisture retrieval the exact values of surface roughness parameters are of less concern as long as their effects on $\sigma°$ remain unchanged. Therefore we can use the surface rms slope (σ/L) and by doing so reducing the unknowns in the inversion to two. Consequently two inputs would be sufficient for the inversion. This is mainly of a practical concern in order to apply the method to operational application where only two inputs are available at the most (e.g. ERS-1/ERS-2 SAR). Such an approach may be called the method of effective parameters.

Using a set of measured surface roughness parameters and surface soil moisture values the IEM model predicted backscattering coefficients $\sigma°$ are compared to observed $\sigma°$ for two input data sets. Provided that the surface roughness parameters and soil moisture are correct the model prediction should approach the observed $\sigma°$. Due to inaccurate parameter estimation, the model predictions will deviate from the observed values. If the model predictions are consistent for both data sets, i.e. both under or over estimate $\sigma°$ or give similar values to the observed ones, the data sets can then be used for retrieval of soil moisture and roughness parameters in the sense of effective parameters.

Starting with one roughness parameter (either σ or L) and dielectric constant of a field the other roughness parameter (L or σ) can be inverted using one observed backscattering coefficient $\sigma°$. Using another backscattering coefficient $\sigma°$ from a different frequency or polarization as input as well as the inverted roughness parameter (L or σ) the dielectric constant of the field can then be inverted.

c) Soil moisture retrieval

As indicated in Fig.1, the IEM model predicts reasonably well the spatial variability in the averaged field backscattering coefficients for both C and L band, but underestimates considerably the backscattering coefficients for almost all fields at C band and L band. Based on the IEM model formulation and its successful validation with laboratory data sets [5], it is reasonable to assume that the deviation of the predicted backscattering coefficients compared to the observed ones is attributed to inadequate inputs such as roughness parameters and/or dielectric constants (i.e. soil moisture). Since the measurements of volumetric soil moisture using both gravimetric and TDR methods is accurate to a few percent at high soil moisture content (as is the case in this study) and given the low sensitivity of $\sigma°$ with respect to soil moisture variation [1], the observed deviation can be considered mainly due to roughness parameters. It therefore can be concluded that conventional measurements of field roughness are not accurate and such data introduce large errors in calculated backscattering coefficients and hence in soil moisture retrieval. Such roughness parameters cannot be blindly used in theoretical models such as IEM.

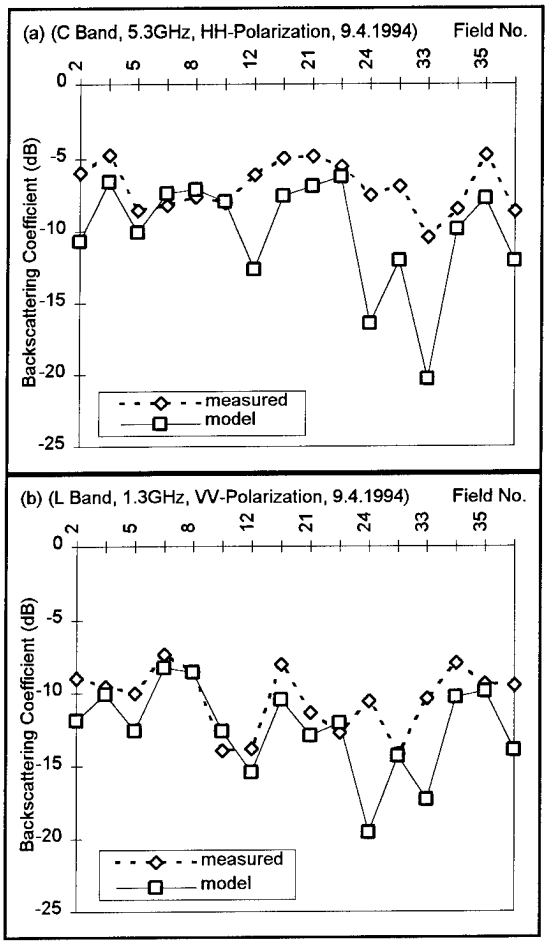


Fig.1. Comparison of observed and retrieved backscattering coefficients using non-calibrated IEM for different fields in Passemare subcatchment on 9 April 1994

Since the purpose here is to retrieve soil moisture from microwave observations using the above described inversion algorithm, it was decided to use one ESAR data set (C-band in this case) to invert for roughness parameters and use

another ESAR data (L-band) and the calibrated roughness parameters as model input for soil moisture retrieval. Both data sets are taken from the same date (9 April 1994).

The improved results, as shown in Fig.2, confirm the validity of the proposed approach. Some fields are left out of this analysis because the inverted roughness parameters are out of the validity range of the IEM.

Fig.3 compares the retrieved soil moisture values with the in situ measurements. This result indicates that reliable retrieval of soil moisture requires at least two independent radar observations. It is worth noticing that by switching bands in the sequence of analysis, similar results can be obtained. Both treatments can be considered equivalent, which indicates the robustness of the method.

Based on the above discussion it can be stated that the method proposed here proves to be a practical one to retrieve soil moisture using active microwave measurements.

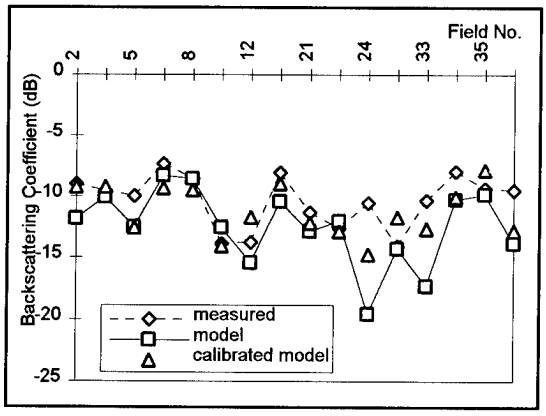


Fig.2. Comparison of observed and retrieved backscattering coefficients using both calibrated and non-calibrated roughness parameters for different fields in Passemare subcatchment on 9 April 1994

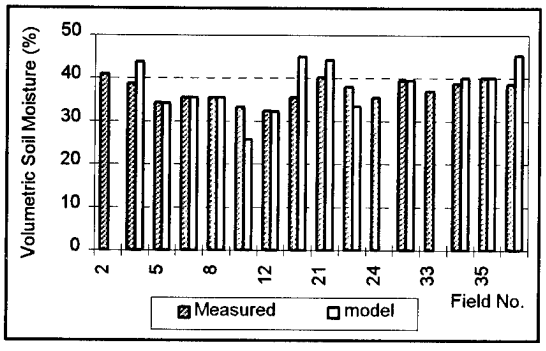


Fig.3. Retrieved volumetric soil moisture Mv (%) using 'effective roughness parameters' for different fields in Passemare subcatchment on 9 April 1994

CONCLUSIONS

Based on the foregoing discussion the following conclusions can be drawn:

(1) The IEM model can be used for field soil moisture retrieval using EMAC/ESAR data if accurate field data on roughness are provided.

(2) Conventional measurements of roughness are not accurate and such parameters introduce large errors in the predicted backscattering coefficients and hence in soil moisture retrieval. Such parameters cannot be blindly used in theoretical models such as IEM.

(3) A method of 'effective roughness parameters' is proposed in this study. Using the model calibrated roughness parameters, the retrieved soil moisture accuracy is better than 5% by volume.

(4) At least two independent radar observations are needed to retrieve soil moisture using active microwave data.

ACKNOWLEDGMENTS

This study was supported in part by ESA and the Belgian 'Federale Diensten voor Wetenschappelijke, Technische en Culturele Aangelegenheden' (DWTC) through grant n° T3/02/21 and by the EC Environment Research Programme under contract n° EV5V-CT94-0446, Climatology and Natural Hazards. We thank our colleagues D.S. Lin, L. Nachtergale and B. Cosyn for technical support and helpful discussions.

REFERENCES

[1] E. Altese, O. Bolognani, M. Mancini, and P.A. Troch, "Retrieving soil moisture over bare soil from ERS-1 SAR data, Sensitivity analysis based on a theoretical surface scattering model and field data", Water Resources Res., in press, 1996.

[2] E. Attema, M. Wooding, and J-C. Morin, "EMAC experimenters handbook, Programme for 1994", ESA, 1994.

[3] R.P. Brent, "Algorithms for minimization with derivatives", (Englewood Cliffs, N.J.: Prentice-Hall), 1973.

[4] A.K. Fung, "Microwave scattering and emission models and their applications", (Norwood, MA: Artech House), 1994.

[5] A.K. Fung and K.S. Chen, "A validation of the IEM surface scattering model", in Proc. IGARSS, Florence, 10-14 July 1995, pp. 933-935.

[6] A.K. Fung, Z. Li, and K.S. Chen, "Backscattering from a randomly rough dielectric surface", IEEE Trans. Geos. and Remote Sens., 30(2), 356-369, 1992.

[7] E. Robin and Ch. Craeye, "Prelimary report on calibration and data quality of the SAR measurements", Laboratoire de Telecommunications et Teledetection, Universite Catholique de Louvain, 1995.

Use Of Polarization Synthesis From Polarimetric SAR Data For Roughness Estimation Over Bare Fields

F. MATTIA (1), J.C. SOUYRIS (2), T. LE TOAN (2), G. DE CAROLIS (1), N. FLOURY (2), F. POSA (3),G. PASQUARIELLO (4)

(1) ITIS-CNR, c.p. aperta c/o Poste 75100 Matera, Italy; ph: +39 835 377 282, fax: +39 835 33 90 27, E-mail: mattia@asimt0.mt.asi.it

(2) CESBIO, BPI 2801, 31055 Toulouse Cedex, France; ph: +33 61 55 85 84, fax: +33 61 55 85 00, E-mail: souyris@cesbio.cnes.fr

(3) Politecnico di Bari, via Amendola 173, 70126 Bari, Italy; ph: +39 80 5443171, fax: +39 80 544 2434, E-mail: posa@axpba0.ba.infn.it

(4) IESI-CNR, via Amendola 166/5, 70126 Bari, Italy; ph: +39 80 548 1612, fax: +39 80 548 4311, E-mail:guido@ercole.ba.cnr.it

Abstract -- Polarimetric SAR data acquired during the first and second SIR-C/X SAR mission over bare soils located at Les Landes (France) and Matera (Italy) test areas, are exploited in order to investigate the antenna polarization effect on polarimetric surface roughness discriminators.
Among quantities under consideration, the copolarized correlation coefficient in circular polarization shows the best sensitivity to surface roughness.

INTRODUCTION

This paper addresses the use of polarimetric data acquired during the SIR-C/X SAR experiments to enhance/reduce the SAR sensitivity to surface roughness. For targets showing a high degree of coherence, the variation of the incident and/or received wave polarization is expected to be very sensitive to geometrical properties of the targets.
Over the past few years, the information content of backscattering polarimetric signatures has been assessed [1]. Surface roughness discriminators mainly based on HH, VV or HV data have been used in soil studies [2]. However, the polarization synthesis as well as the measurement of second order polarimetric SAR data statistics for retrieving geophysical information have been less studied.
In this work, the sensitivity to surface roughness of the copolarized correlation coefficient magnitude as well as of the cross- over co- polarized σ^0 ratio, both in linear and circular polarization, is investigated. Moreover, the experimental statistics of the copolarized correlation coefficient magnitude as a function of the polarization state is compared with the theoretical expressions derived by Goodman [3].
In the next section, the experimental data set is described, then the copolarized correlation coefficient as well as the σ^0 expressions in circular basis are given and, subsequently, the analysis of SAR data is presented. In the last section, results are summarized.

THE EXPERIMENTAL DATA

The SAR data analyzed in this paper are single look images acquired by the SIR-C/X-SAR over the Landes (France) and Matera (Italy) on April, 20 and on October, 4 1994, respectively. In both cases the acquisition mode was full polarimetric at *C* (5.304 GHz) and *L* (1.254 GHz) band and the orbit direction was ascending. The two sites were imaged at a central swath incidence angle of 26.44° and 45.8°, respectively.
During the SIR-C/X-SAR second mission, ground data measurements on bare soil surfaces, located in the Matera area, in terms of roughness profiles, moisture content and soil composition have been collected. The Matera test site is located in the South-East of Italy in the Basilicata region. It is a predominantly agricultural area mainly devoted to wheat cultivation. At the beginning of October 1994, fields were completely bare and only in some cases already tilled for the next winter wheat crop season. The selected fields have been clustered into three classes of roughness: *rough*, *medium rough* and *smooth* [4]. Soil moisture content was ranging between 0.10 and 0.20 g/cm^3.
The Landes data, acquired during the first SIR-C/X-SAR mission, have been used as an independent data set in order to validate the results obtained in the Matera area. Les Landes Forest is located in South-Western France. Ground data concerning six clear cuts fields, selected on the image, are available as photographs taken during the SIR-C/X-SAR first mission. From the visual analysis the clear cuts areas have been identified as very rough surfaces and therefore included in the *rough* class.

0-7803-3068-4/96$5.00©1996 IEEE

SAR DATA ANALYSIS

Correlation Coefficient expressed in a Circular Basis

Passing from a linear (h, v) polarimetric basis to a generic (p, q) orthonormal basis, the scattering matrix $\bar{S}(h,v)$ transforms in the following way [5]:

$$\bar{S}(p,q) = \bar{T}^{t}\bar{S}(h,v)\bar{T}$$

where $\bar{T} = (1+rr^{*})^{-1/2}\begin{pmatrix} 1 & -r^{*} \\ r & 1 \end{pmatrix}$ is a unitary matrix and $r = \frac{E_q}{E_p} = \frac{a_q}{a_p}e^{i\delta}\,(a_p^2 + a_q^2 = 1; \delta = \delta_p - \delta_q)$. In particular, considering a circular polarimetric basis (r, l) (i.e. $a_p = a_q$; $\delta = \pi/2$) and assuming a reciprocal azimuthally symmetric distributed medium (i.e. $S_{HV} = S_{VH}$ and $\langle S_{HH}S^{*}_{HV}\rangle = \langle S_{VV}S^{*}_{HV}\rangle = 0$, respectively) the σ^0 and copolarized correlation coefficient expressions are:

$$\left\langle |S_{RR}|^2 \right\rangle = \left\langle |S_{LL}|^2 \right\rangle = \frac{1}{4}\left[\left\langle |S_{HH}|^2 \right\rangle - 2\,\mathrm{Re}\left(\left\langle S_{HH}S^{*}_{VV}\right\rangle\right) + \left\langle |S_{VV}|^2 \right\rangle + 4\left\langle |S_{HV}|^2 \right\rangle\right]$$

$$\left\langle |S_{RL}|^2 \right\rangle = \left\langle |S_{LR}|^2 \right\rangle = \frac{1}{4}\left[\left\langle |S_{HH}|^2 \right\rangle + 2\,\mathrm{Re}\left(\left\langle S_{HH}S^{*}_{VV}\right\rangle\right) + \left\langle |S_{VV}|^2 \right\rangle\right]$$

$$|\rho_{RRLL}| = \frac{\left|\left\langle S_{RR}S_{LL}^{*}\right\rangle\right|}{\sqrt{\left\langle |S_{RR}|^2\right\rangle\left\langle |S_{LL}|^2\right\rangle}} = \frac{\left|\left[\left\langle |S_{HH}|^2 \right\rangle - 2\,\mathrm{Re}\left(\left\langle S_{HH}S^{*}_{VV}\right\rangle\right) + \left\langle |S_{VV}|^2 \right\rangle - 4\left\langle |S_{HV}|^2 \right\rangle\right]\right|}{\left[\left\langle |S_{HH}|^2 \right\rangle - 2\,\mathrm{Re}\left(\left\langle S_{HH}S^{*}_{VV}\right\rangle\right) + \left\langle |S_{VV}|^2 \right\rangle + 4\left\langle |S_{HV}|^2 \right\rangle\right]}$$

Polarimetric Discriminators as a Function of Roughness

For each one of the described roughness classes, the sensitivity of the $\sigma^0_{pq}/\sigma^0_{qq}$ ratio, both in circular and linear polarization, has been investigated, an almost insensitive behavior in the circular case and a good sensitivity in the linear polarization has found (fig. 1). It should be noted that, although *clear cuts* (Les Landes test site) and *rough* fields (Matera test site) have been clustered in the same class, the two sites were imaged at two very different incident angles: 26.44° and 45.8°, respectively. Considering Matera fields, $\sigma^0_{HV}/\sigma^0_{VV}$ is pretty well correlated with the roughness. However, it shows a degree of overlap between *medium rough* and *rough* classes. Moreover, $\sigma^0_{HV}/\sigma^0_{VV}$ is also very sensitive to the incidence angle, thus failing the separation between *clear cuts* and *medium rough* fields.

In [4], the data set has been studied with respect to the effect of surface roughness on co- and cross- polarized backscattering coefficients as well as on copolarized correlation coefficient, in the case of linear and circular polarization states. A higher sensitivity to surface roughness has been found at circular than at linear polarization. In fig. 2, the $|\rho_{RRLL}|$ dependence on roughness state is shown. Whatever the incident angle considered, roughness classes are well separated meaning a $|\rho_{RRLL}|$ negligible dependence on the imaging geometry. Moreover, the maximum $|\rho_{RRLL}|$ variability is much larger than the $\sigma^0_{HV}/\sigma^0_{VV}$ maximum spread.

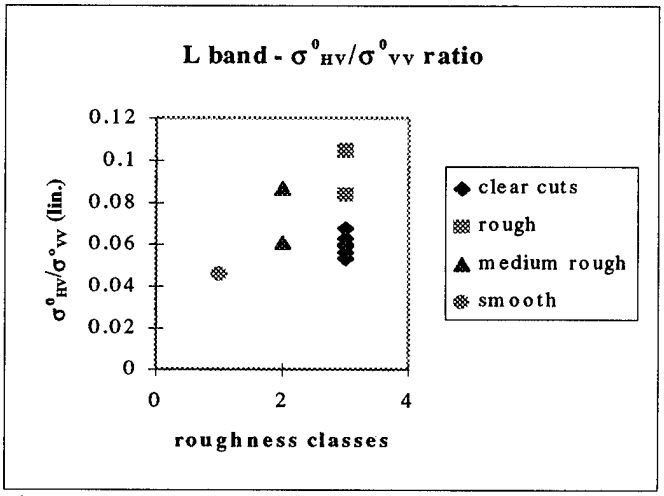


Figure 1: HV/VV backscattering ratio versus the roughness classes.

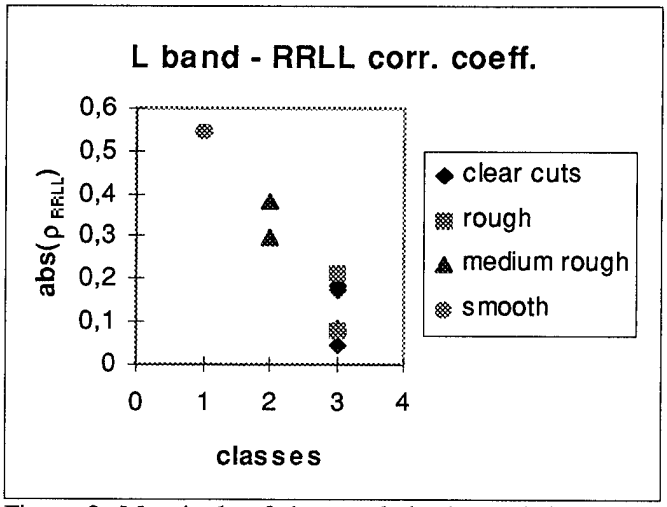


Figure 2: Magnitude of the copolarized correlation coefficient in circular polarization versus the roughness classes.

Distribution of the Correlation Coefficient Estimate

Under the assumption of circularly Gaussian distributed real and imaginary scattering matrix components, which holds whatever the polarization state is, Goodman [3] has derived the pdf of the copolarized correlation coefficient estimator:

$$\left|\hat{\rho}_{ppqq}\right| = \frac{\left|\sum_{k=1}^{n} S_{pp}(k) S_{qq}^{*}(k)\right|}{\sqrt{\sum_{k=1}^{n}\left|S_{pp}(k)\right|^{2} \sum_{k=1}^{n}\left|S_{qq}(k)\right|^{2}}}$$

where n is the number of independent samples.

In order to better understand the $|\rho_{RRLL}|$ behavior, the experimental statistics of both $|\hat{\rho}_{RRLL}|$ and $|\hat{\rho}_{HHVV}|$ have been measured over a number of 16 samples and compared with the Goodman's expression. In fig. 3 the results obtained at L band for the *smooth* case, the *medium rough* case and the *rough* case are shown, respectively.

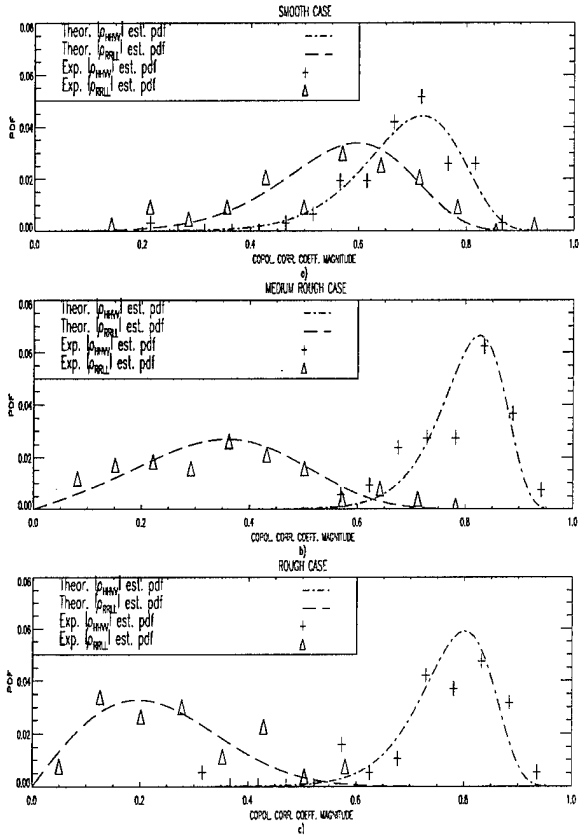


Figure 3: Theoretical and experimental copolarized correlation coefficients pdfs (n=16 independent samples) [3] of $|\hat{\rho}_{HHVV}|$ and $|\hat{\rho}_{RRLL}|$. a) *smooth* case, b) *medium rough* case, c) *rough* case.

It should be noted that the moisture content of these fields is almost constant. As can be seen, there is an overall good agreement between theoretical and experimental distributions and, moreover, the drastically different behavior between $|\hat{\rho}_{HHVV}|$ and $|\hat{\rho}_{RRLL}|$ is clearly shown. The $|\hat{\rho}_{HHVV}|$ distribution is peaked around an almost constant value irrespective of roughness. On the contrary, the peak of the $|\hat{\rho}_{RRLL}|$ distribution is shifting toward lower values as the roughness increases.

CONCLUSIONS

In this work the effect of antenna polarization on $\sigma^0_{pq}/\sigma^0_{qq}$ and $|\rho_{ppqq}|$ as polarimetric discriminators of surface roughness is investigated. In particular, the experimental analysis focuses on a comparison between their behavior in linear and circular polarization.

The data set consists of: 1) polarimetric SAR data acquired during the first and second SIR C/X SAR mission over Les Landes (France) and Matera (Italy) test areas; 2) ground data in terms of roughness profiles, moisture content and soil composition collected over selected bare fields.

Results show that the best separation between roughness classes is achieved by means of $|\rho_{RRLL}|$. Future work will be devoted to derive soil roughness maps based on $|\rho_{RRLL}|$ and to assess the moisture inversion problem.

REFERENCES

[1] F.T Ulaby, and C. Elachi, eds., Radar polarimetry for geoscience applications, Arthec House, 1990

[2] Y. Oh, K. Sarabandi, and F.T. Ulaby, "An empirical model and an inversion technique for radar scattering from bare soil surfaces," IEEE Trans. on Geo. and Rem. Sens., vol. 30, No. 2, March 1992

[3] N.R. Goodman, "Statistical analysis based on certain multivariate complex distribution (an introduction)," Ann. Math. Stats., 34, pp. 152-177, 1963

[4] F. Mattia, T. Le Toan, J.C. Souyris, G. De Carolis, P. Smacchia, D. Casarano, N. Floury, F. Posa, and G. Pasquariello, "The effect of surface roughness on multifrequency polarimetric SAR data," International Symposium on Retrieval of Bio- and Geophysical Parameters from SAR Data for Land Applications, 10-13 October 1995, Toulouse, France

[5] K. Tragl, "Polarimetric radar backscattering from reciprocal random targets," IEEE Trans. on Geo. and Rem. Sens., vol. 28, No. 5, Sept. 1990

Microwave Remote Sensing of Land Surfaces Soil Moisture at Global Hydrology and Climate Center

Shih-Tseng Steve Wu
NASA Global Hydrology and Climate Center
977 Explorer Boulevard, Huntsville, AL 35806
T: 205.922.5961, F: 205.922.5723, Email: steve.wu@msfc.nasa.gov

INTRODUCTION

The Global Hydrology and Climate Center (GHCC) consists of NASA Marshall Space Flight Center's ES41/Earth Systems Science Division, University Space Research Association and University of Alabama in Huntsville. A few researchers at GHCC and the microwave group of the Earth Systems Science Division, in particular, collaborated with Alabama A & M University in proposing hydrology, soil climatology and remote sensing studies by establishing a Minority University Research Center (MURC). The proposal was funded for FY95 to FY99 and we currently are in the first two years' planning and implementation phases. The microwave remote sensing of land surface soil moisture is one element of the research program.

SCIENTIFIC JUSTIFICATION

The work described herein is designed to address several of the specific recommendations of the workshop attendees of a NASA's Office of Mission to Planet Earth (MTPE) sponsored workshop in 1994 on soil moisture [1]. It is also consistent with the overall goals of MTPE Strategic Enterprise as it pertains to studies involving land-cover change, global productivity, and long-term climate variability. Recent study results indicated that both passive microwave and active microwave techniques have provided solid theoretical and experimental results that the top five cm of soil moisture can be measured from ground-based truck, aircraft and space platforms under a variety of environmental conditions and through a moderate vegetation cover [2, 3]. In view of these findings, Our work at GHCC will use past research findings as the starting point and will focus on a small-scale (plot-size) field experiment using truck-mounted radar and radiometer systems for the first two years.

TRUCK-MOUNTED RADAR AND RAIOMETER

Electromagnetic Techniques

Electromagnetic techniques make use of the dielectric properties of moist soil. A variety of sensors, responsive to either resistivity (the imaginary part of the dielectric constant) or polarization (the real part of the dielectric constant), or both, have been constructed. Some of these sensors are designed for *in situ* operation (i.e., implantable); others are to be operated remotely from either an airborne or a spaceborne platform.

Radiometer Systems

The S- and L-band Microwave Radiometer (SLMR) [3] is a dual frequency passive sensor system operating at S-band (2.65 GHz or 11.3 cm) and L-band (1.413 GHz or 21.2 cm). The radiometric sensitivity of each radiometer is 0.1 K for a one second integration time. Each linearly polarized microstrip patch antenna is configured as 4x4 phased array providing 20 degrees of beamwidth with a main beam efficiency of 97%. The antenna and receiver are packaged together in a thermally controlled enclosure for each frequency.

In addition to the SLMR radiometers provided by Dr. Tom Jackson of USDA-ARS Hydrology Lab. A C-band radiometer will be provided by Dr. Carl Swift of the University of Massachusetts to simulate C-band radiometer's brightness temperature, because both the Multifrequency Imaging Microwave Radiometer (MIMR) and Japanese Advanced Microwave Scanning Radiometer (AMSR) contained a C-band radiometer.

Mounting Frame and Boom Truck

The instrument platform (or mounting frame) to be mounted at the end of (manlift's) boom would be moved to vary incidence angle from 0° (nadir) to 180° (sky), while the boom itself would be rotated 360° in azimuth. The antennas are mounted to observe horizontal polarization. At the nominal operating height of 4 m with the specified field of view of radiometers (20°), the footprint size was 1.5 m at a viewing angle of 10° off nadir.

0-7803-3068-4/96$5.00©1996 IEEE

In addition to the two microwave radiometers, several other supporting instruments would also be mounted on the mounting frame. Pointing accuracy and target location for the microwave radiometers were achieved with a color video camera installed on the frame between the two antennas. The look angle of the instrument platform was determined by an inclinometer system.

Radiometer Calibration

Calibration of the radiometers is based on external reference targets. The external targets typically used are sky (~5 K) and absorber (~300 K). These are usually quite stable references, cover the entire range of instrument response, and are easy to obtain. These observations were made frequently at the beginning of the experiments to establish and verify the calibration and less often later in the summer. Another valuable calibration target is water. Water has well known brightness temperature (T_B) values as functions of temperature and angle. By varying the angle, reference T_B values between 50 K and 110 K can be obtained. Water calibration is more difficult to obtain frequently since it usually must be done at some location other than test sites; past experiments performed this calibration only a few times.

Truck Radar System

The truck radar system is a three(3) frequency active sensor system operating at X band (10.0 Ghz or 3 cm), C band (4.75 Ghz or 6.3 cm), and L band (1.6 Ghz or 18.75 cm). The system will be operated by Dr. Peggy O'Neil of NASA/GSFC's Hydrological Sciences Branch. The L band antenna consists of a 1.2 m parabolic dish, while smaller horn antennas are used for the C and X band radars. Antenna 3 dB beamwidths range from 9 - 12 degrees depending on frequency and polarization. Switching between frequencies and polarizations is accomplished by an HP3488A switching unit outfitted with SPDT coaxial switches.

Dr. Peggy O'Neill of NASA/GSFC will provide and in charge of truck radar system's field experiment during July 1996 [6].

FIELD DEPLOYMENT

To obtain an accurate and workable field experiment all proceedures and *in_situ* instruments, such as time domain reflectometers (TDR), and measurement requirements were included in the implementation plan. In the plan, three(3) plots, each plot with 100m by 20m in size, were selected within Alabama A&M University's agricultural research farm. Plot 1 comprises of one half each of a grass land and a cotton field; Plot 2 comprises of one half each of two bare soil fields with different surface roughness; Plot 3 comprises of one half each of a soy bean field and a corn field. *In_situ* instruments were placed in all three plots and data were collected concurrently with data acquisition of truck-mounted radar and radiometer systems. In the beginning, plots were irrigated thoroughly and using dry down period to control soil water content variations. Within two weeks' data acquisition window, microwave measurements will continue for seven days. All data sets were used to derive soil surface moisture and soil moisture and temperature profiles of each plot. This local scale (L.S.) soil moistures from all three plots were then input to the L.S. hydrology model. The model was then used to derive a larger area soil moisture database (e.g. 100m by 100m plot-size).

Window of measurements

The SLMR radiometers and the C-band radiometer will stay at the test bed during the month of July. GHCC will provide a boom truck and a mounting frame to be used as the field experiment platform. The C-band radiometer will use a fix mount type platform by which only one plot data will be collected.

The truck radar system is to be ready on the first week of July 1996 with two weeks of data acquisition time. In the beginning, plots were irrigated thoroughly and using dry down period to control soil water content variations. Within two weeks' data acquisition window, microwave measurements will continue for seven days.

In situ Instruments' Data Acquisition

Concurrent *in situ* soil data collection using a variety of implanted instruments will be made and to be continued within one months' data acquisition window.

SOIL MOISTURE PROFILING

Passive Techniques

The SLMR microwave radiometers measured multiparameter (frequency, polarization, look angle and time variations) brightness temperatures, T_b. These T_b and corresponding surface temperature, T_g, will be used to solve the inverse problem for soil moisture and temperature profiles [4]. The solution is based on combining a model of coherent wave radiative transfer and a model of coupled heat and moisture diffusion in porous media, and inputting T_b and T_g, to obtain the liquid volumetric water content and temperature profiles in a soil column. The physics-based algorithm as the solution without the use of empirical relations makes the retrieval theoretically sound and practically feasible.

We are in the process of obtaining a copy of source codes by which the measured brightness temperatures and surface

temperatures are used as inputs to obtain the plot-size soil moisture and temperature profiles. All three bands (L, S, and C band) brightness temperatures will be used when available. We will also include vegetation as well as bare soil in the solution of inverse problem.

Active Techniques

The radar systems measured multiparameter (frequency, polarization, look angle and time variations) backscattering coefficients. The backscattering coefficients and surface parameters (roughness, vegetation cover, etc.) will be used to solve the inverse problem for plot-size surface soil moisture[5]. Because the truck radar system is a three(3) frequency active sensor system operating at X band (10.0 Ghz or 3 cm), C band (4.75 Ghz or 6.3 cm), and L band (1.6 Ghz or 18.75 cm), the developed algorithm can be used to solve the inverse problem with space-based sensors (e.g., ERS-1,2; JERS-1; RADARSAT) data acquired over the same sites and same date. In this sense, the truck radars could be used as calibration instruments and the test plots as ground truths for the space-borne sensors.

SUMMARY

The plot-size microwave field measurement work is a team effort which includes not only multi-agency but also multi-discipline. Since we try to address several of the specific recommendations of the workshop attendees of a NASA's Office of Mission to Planet Earth (MTPE) sponsored workshop in 1994 on soil moisture [1], the results of plot-size experiment need to be progressively extended to a larger scale through hydrologic modeling. In this regard, research needs to be conducted to modify existing models [4, 5] or develop new models to effectively use remotely sensed soil moisture. There is need for research in understanding the role of surface soil moisture in basic hydrological, meteorological, and ecosystem processes.

ACKNOWLEDGMENTS

The SLMR radiometers were provided by Dr. Tom Jackson of USDA-ARS Hydrology Lab. and the C-band radiometer will be provided by Dr. Carl Swift of the University of Massachusetts. As a member of the External Advisory Team of Center for Hydrology, Soil Climatology, and Remote Sensing, Dr. Jackson provided timely and pertinent recommendations regarding test-plots and field experiments procedures during his site visit at AAMU Agricultural Research Station.

Dr. Peggy O'Neill of NASA/GSFC will provide and in charge of truck radar system's field experiment during July 1996.

As the field experiment program manager, Dr. Chip Laymon of USRA developed a research test-bed at AAMU Agricultural Research Station and the installation and operation of all field instruments at all test plots. The data collected from these instruments will be used to validate the inverted microwave measurements

REFERENCES

[1] Wei, M_Y., "Soil moisture: report of a workshop in Tiburon, California 25-27 January 1994," NASA Conference Publication 3319, NASA Headquarters.

[2] Engman, E. T. and N. Chauhan, "Status of microwave soil moisture measurements with remote sensing," Remote Sensing of Environment, 51, pp. 189-198, 1995.

[3] Jackson, T. J., P. E. O"Neill, and W. P. Kustas, "Passive microwave observation of diurnal soil moisture at 1.4 and 2.65 GHz," Proceedings of the hold IGARSS"95 Symposium, Firenze, Italy, 10-14 July 1995, vol. 1, pp.492-494, 1995.

[4] Entekhabi, D. Ч., H. Nakamura, and E. G. Njoku," Solving the inverse problem for soil moisture and temperature profiles by sequential assimilation of multifrequency remotely sensed observations," IEEE Trans. On Geo. Sci. and R. S., vol. 32, no. 2, pp. 438-448, March 1994.

[5] Oh, Y., K. Sarabandi, and F. T. Ulaby, "An empirical model and an inversion technique for radar scattering from bare soil surfaces," IEEE Trans. On Geo. Sci. and R. S., vol. 30, no. 2, pp. 370-381, March 1992.

[6] O'Neill, P. E., J. J. Petrella, and A. Y. Hsu,"Comparison of multifrequency truck radar and SIR-C backscatter for soil moisture estimation in Wasshita'94," Proceedings of the IGARSS"95 Symposium, Firenze, Italy, 10-14 July 1995, vol. 1, pp.368-370, 1995.

SOIL HYDRAULIC CHARACTERIZATION DERIVED FROM LANDSAT TM-5 DATA

Elena Bresci, Ignazio Becchi

Università degli Studi di Firenze, Facoltà di Ingegneria, sede di Prato, Piazza Ciardi, 25 - 50047 Prato, Italy
Tel: +39-574-602520. Fax: +39-574-602515
email:elenab@pinet.ing.unifi.it

ABSTRACT

The aim of this study is to test the utilization of Landsat TM-5 imagery in hydrological applications. The areas selected for the study are the Nievole river basin (47 km^2), a sub-catchment of the Arno river basin (Toscana, Italy) and the Fucecchio marsh (50 km^2, Toscana, Italy). A linear relationship has been found between satellite data and soil parameters obtained from pedological maps available for the marsh area, such as hydraulic conductivity (K, mm/h) and soil water content (WC, mm). An example of obtaining runoff Curve Number CN [1] is also presented. The same relation has been used for the hydraulic characterization of the Nievole river basin, marked by lack of pedologic maps. The procedure described in the article provides an accurate soil hydraulic characterization based on remote sensing for areas where soil maps are too expensive and time consuming to realize.

1. INTRODUCTION

Remote sensing from satellites can provide useful information for hydrologic applications, in particular in using distributed models [2]. Hydrological models of the distributed system type simulating the rainfall-runoff process allow to describe the hydrological processes taking into account the spatial variability of soil properties and the distribution of rainfall in time and space. The purpose of the present work, which is a part of the Arno project, a joint research project of the Department of Civil Engineering, University of Florence and the Group for Defence against Hydrogeological Catastrophes of the National Research Council (CNR), is to show the utility of Landsat TM-5 data on soil hydraulic characterization and, in particular, the high resolution in space that can be obtained. The crucial problem in using distributed models is that adequate data to describe quantitatively a hydrologic process with sufficient accuracy are seldom available, while a high resolution in space and/or time is always required. Many of the input parameters depend on catchment characteristics and they are conventionally estimated from maps often appearing inaccurate or obsolete. Regarding to hydraulic conductivity and soil water content values, they are derived from the available pedological maps for the study area. Satellite imagery opens the opportunities to have area measurements instead of point ones and a higher resolution in space and/or time comparing to the common methods. But remote sensing sensors do not measure hydrological data. They measure the electromagnetic signal emitted from bodies in certain spectral bands of the electromagnetic spectrum [3]. An indirect way, called "transfer function", for obtaining hydrologic information has to be found [4]. This study proposes a linear regression model as transfer function between real values of hydraulic conductivity, soil water content and CN values for the Fucecchio marsh derived from the available pedological maps and Landsat TM-5 data transformed into Reflectance Index Models (RIM). RIMs are defined as combination of Digital Number (DN) values for the same pixel in different wavelength bands.

A linear regression model is tested on the RIMs showing a significative correlation coefficient ($r \geq 0.8$) and the coefficients are calculated with the Least Mean Square Method for the Fucecchio marsh area. The same coefficients are used for deriving a grid map (30m×30m) representation of hydraulic parameters for the Nievole river basin for which no pedological maps at the requested scale 1:25,000 were available.

2. DATA DESCRIPTION

The areas selected for the study are the Fucecchio marsh and the Nievole river basin, located respectively (Fig.1) at South and North of Montecatini Terme. Both areas are inside the Pistoia district.

The Fucecchio marsh is one of the most important wetland in Italy and many studies with the aim of a soil characterization can be found in literature. We refer to a pedologic map 1:25,000 [5] offering a Soil Taxonomy classification [6], it has been digitized through the GIS ARC/INFO [7], saved in a vectorial format and then transformed in a grid format with cell size 30m by 30m. For each class, a range of variability for the hydraulic conductivity and soil water content is given. The Landsat scene is taken on September 24th, 1991 and covers all the Tuscany area.

0-7803-3068-4/96$5.00©1996 IEEE

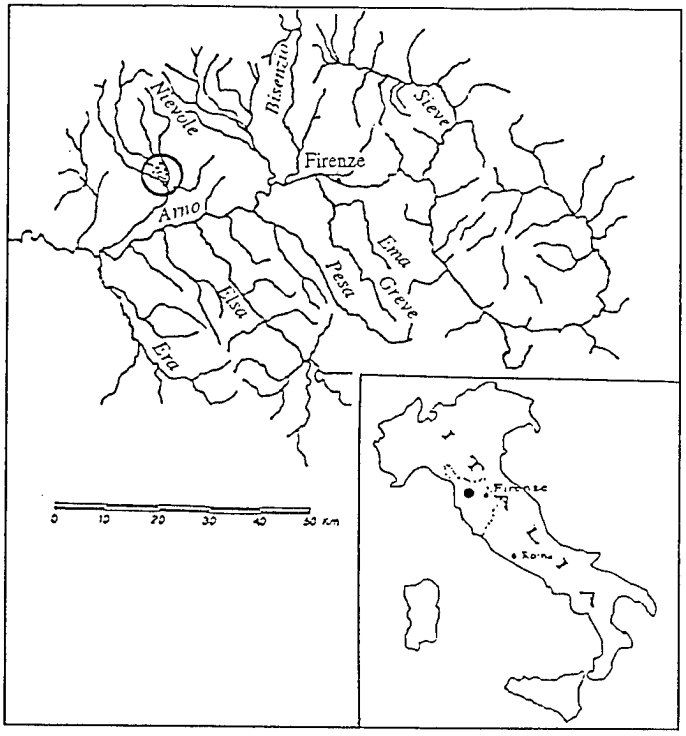


Fig. 1 - The study area

The total scene has been corrected for different solar illumination angles and georeferenced assigning Universal Transverse Mercator (UTM) map co-ordinates, then cut on the two different study areas.

As regards the georeference operation, maps from Militar Geographic Institute, scale 1:25,000 have been used for the exact location of the 100 Ground Control Points (GCPs) utilized for the linear transformation applied. The sensor Thematic Mapper (TM) mounted on-board the Landsat satellite, is able to detect and record the solar energy reflected from the earth's surface with a ground resolution of 30m by 30m in six wavelength intervals belonging to the visible and infra-red regions of the electromagnetic spectrum. It is expressed in terms of DN value which results from the quantisation of the amplified electronic signal generated by the detector through a simple linear relation of the radiance reaching the sensor. For each band, a binary number is produced, usually in the range of 0-256, so than 8 bits can be used to store one band value.

3. PROCEDURE

Different RIMs given by algebraic operations on the DNs corresponding to the same pixel are analyzed. For a better manipulation of DN values in different bands, such as rationing, summing, linear combinations, some routines are created in MATLAB [8] language for linking ERDAS [9] format files with Matlab format files. In such a way, it is possible to work on separate matrices whose elements are the DNs for each band. In Matlab format, each original pixel represented by an element in the matrix, keeps its geographical location. In fact, it may be obtained knowing the row and the column occupied in the matrix and the real geographical co-ordinates of the upper left element of the matrix (1,1).

The attention in the article has been focused on the hydraulic conductivity, but the same procedure has been used for soil water content and CN values. The abundance of reflectance data seems to be in contrast with the narrow range of variability for the hydraulic parameters obtained from pedologic maps. The central part of the marsh is occupied by very fine texture soils, such as Typic Hydraquents or Aquic Xerofluvents (TH1, TH2, TH3, AX1) with values around 0.4 mm/h, the surrounding parts are characterized by soils having values round 9-10 mm/h. These values show that all the area is almost impermeable and the range of variability is really small. Then, before the linear regression step, a method for reducing DN data has to be chosen.

Looking at the frequency histograms for each band and combinations of bands, the reduction to the mean value for all the pixels characterized by the same value of the hydraulic parameter under examination, seems to appear the best solution. Between all the RIMs available in literature [10], [11], the original DNs for some bands seems to have given the best results showing a correlation coefficient r greater than 0.8 (Table I). For the hydraulic conductivity, band 1 (0.45-0.52 μm) and band 5 (1.55-1.75 μm) have been chosen. A linear regression model is tested on the reduced DNs and the original hydraulic conductivity values derived from the pedological map for the Fucecchio marsh area. The coefficients are calculated with the Least Mean Square Method and the same coefficients are used for the Nievole river basin. For each grid cell, knowing the DN value in the band 1 the hydraulic conductivity can be calculated with the linear equation.

Table I - Correlation coefficients for the Fucecchio area

	K min	K max	WC min	WC max
Bands	DN*5*	DN*1*	DN*1*+DN*3*	DN*1*
Cor	-0.961	0.955	-0.819	-0.802

4. ANALYSIS OF RESULTS

A grid map, with a single value of the hydraulic conductivity can be obtained for both the study areas. A comparison analysis between the original pedological map and the new one has been done for a validation of the first results.

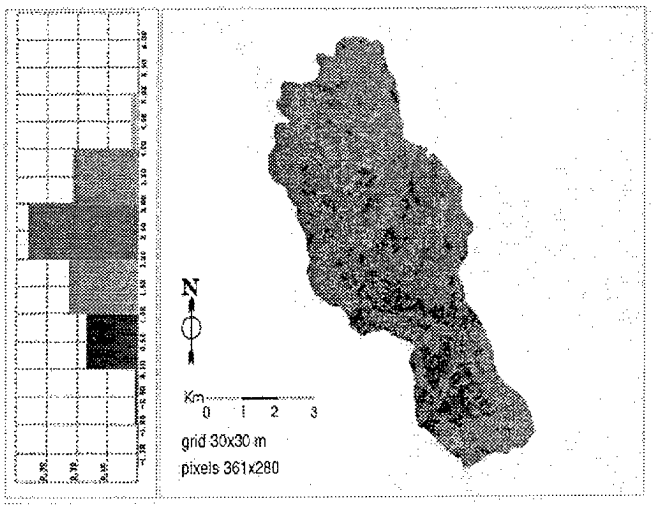


Fig.2 - Nievole river basin: hydraulic conductivity grid map (mm/h)

The central part of the marsh was characterized by values round 0.4 mm/h, from the application the range is 0.1-1 mm/h, more than 50 % of the total area has values between 0.1-10 mm/h. So, once verified that an acceptable correspondence between the original map values and the ones obtained from the linear regression has been obtained, the same coefficients can be used for the Nievole river basin. The results for the Nievole river basin are presented in a grid format in Fig. 2.

The procedure is able to answer to the following questions:

1-calculate the value of the hydraulic conductivity corresponding to a grid cell of known geographical co-ordinates;

2-individuate on the map areas characterized by a given range of variability for the hydraulic conductivity. This kind of application can be useful for an inventory of areas under high flood risks. Fig.2 shows that 20 % of the area is characterized by values in the range 0.1-1 mm/h corresponding to the urbanised area close to Montecatini Terme. More than 50 % is inside the 1-100 mm/h. The smallest values are close to the channel network to demonstrate the spatial variability of the hydraulic conductivity values satisfied.

5. CONCLUSIONS

The soil hydraulic characterization in general comes out from the available pedological maps for the study area. The reason for leaving out soils data from the approach is that soil maps are not available for some areas and direct field observations are sometimes too expensive and time consuming. The proposed technique using Landsat TM-5 data is able to integrate spatial variations on soil water movement estimating the hydraulic conductivity, soil water content and the CN. The obtained results give a preliminary positive answer to the possibility of using satellite data to characterize the hydrologic behaviour of those areas characterized by lack of pedologic maps.

ACKNOWLEDGMENTS

Substantial supports provided by Prof. Ing. G. Federici and PIN (Scientific Service of University of Florence in Prato) computation facilities are strongly acknowledged. Supports provided by CNR and Prof. Ing L. Ubertini are also sincerely acknowledged.

REFERENCES

[1] SCS-USDA, "National Engineering Handbook", Sect.4, Hydrology. Washington D.C., 1972.

[2] G.A. Schultz, E.C. Barret, "Advances on remote sensing for hydrology and water resources management". UNESCO, Techn. Doc. IHP, Project 5.1, Paris, 1989.

[3] G.A. Schultz, "Remote sensing in hydrology". Journal of hydrology, 100, pp. 239-265, 1988.

[4] A.M.J. Meijerink, H.A.M. de Brower, C.M. Mannaerts, C. Valenzuela, "Introduction to the use of Geographic Information System for practical hydrology". UNESCO ITC, Publ. Number 23.

[5] F. Crini, D. Magaldi, "Caratteri, distribuzione e processi genetici dei suoli del Padule di Fucecchio". Dipartimento di scienza del suolo e nutrizione della pianta".Università di Firenze, 1988.

[6] Soil Survey Staff, "Soil Taxonomy: a basic system of soils classification for making and interpreting soil surveys". Soil Conservation Service U.S. Department of Agriculture; Agriculture Handbook n. 436, U.S. Govt. Print Office, Washington D.C., 1975.

[7] ARC/INFO of Enviromental Systems Research Institute, Inc. (ESRI). Version 6.1.1, Redlands CA 92373 USA.

[8] MATLAB for MS Windows. Version 4.0, 1993.

[9] ERDAS Imagine of ERDAS Inc. Atlanta, georgia 30329-2137 USA, Version 8.1, 1994.

[10] A.M. Richardson, C.L. Wiegand, "Distinguishing vegetation from soil background information". Photogrammetric Engineering and Remote Sensing, 43, pp. 1551-1552, 1977.

[11] R.D. Jackson, P.J. Pinter, R.J. Reginato, S.B. Idso, "Hand-held radiometry". Agricultural Reviews and Manuals. ARM-W-191 USDA, 1980.

An Optical Reflectance Technique for Soil Moisture Measurement-Part I: Theory, Description, and Application

Belisle, W. R., A. Sharma, and T. L. Coleman
Center for Hydrology, Soil Climatology, and Remote Sensing,Alabama A&M University
P. O. Box 1208, Plant and Soil Science Department, Normal, Alabama 35762
(205)851-5462, fax(205)851-5429, Email: WBELISLE@ASNAAM.AAMU.EDU

ABSTRACT

Numerous techniques have been recently developed or modified for improved, *in-situ* soil moisture content determination. Examples of the devices used in these techniques include the time domain reflectometer, the soil moisture gauge, and the heat-pulse probe. This paper discusses the theory, description, and application of an optical reflectance technique for the *in-situ* measurement of soil moisture content. An encased, simple light source is proposed which produces a reflectance from a coated, porous membrane whose moisture content is a result of being in close contact with a moist section of soil. A photodiode and a photocell detector capable of sensing the 1.4 mm wavelength of light that is reflected by the moist porous membrane surface are used to quantify the moisture content. The device is approximately 125 cm^3 and can be pushed into the soil to desired depths. Reflectance measurement techniques such as this have been able to obtain soil moisture content measurements to an accuracy of better than 1%. The optical reflectance methodology presented here uses a simple technique that will allow the determination of soil moisture content by using a simple equation which is based on the fraction of reflected light power incident on the detector with a dry and moist porous membrane.

INTRODUCTION

Light reflectance on porous material surfaces such as soils is a topic that is well documented [5, 6, 7, 8, 9, 11, 13, 14, 15] . As light or electromagnetic radiation (EMR) moves in the form of various wavelengths from a source onto a material surface, the wavelengths may be 1) transmitted, 2) absorbed, 3) reflected or refracted by, 4) changed in length, or 5) a combination of the above [11, 16]. Such light may include wavelengths of 1.4 and 1.9 mm of the near infrared spectral region which shows a relatively high degree of absorbance in the presence of water [16].
Considering EMR reflectance on material surfaces, wavelengths may scatter upon striking the surface resulting in reflecting wavelengths moving in many directions.

The reflectance of EMR from surfaces may be affected by the surface porosity, surface and internal matrix structure, color, and composition as well as by the angle and nature of the emitting EMR source. The magnitude of the reflected EMR {or the measured bidirectional reflectance distribution function (BRDF) or reflectance factor [17, 18]} can be determined using a filtered sensor that is positioned geometrically with the EMR source and the material surface such that the reflected wavelengths are incident to the detector [12, 16]. The detected magnitude of the reflected EMR is dependent on the degrees of EMR reflectance, the amount of EMR absorbance, and the amount of EMR passing through the material surface. Increasing the EMR sorptive capacity of the reflecting surface decreases the magnitude of the reflected EMR that is incident to the detector. Since the reflecting surface of the material at increased moisture contents contain increased amounts of water, the absorption of EMR at 1.4 and 1.9 mm will increase and the magnitude of the reflected EMR is reduced [16].

Alessi and Prunty developed a fiber optics technique for determining soil water status based on the reduction in light transmission due to the presence of soil water [1]. Cary et al. reported similar findings for transmitted light through translucent porous materials [4]. The Cambria Corporation has recently developed an electro-optic technology called the EOS-100-W liquid detection sensor that also takes advantage of the absorption and transmission characteristics of water molecules at certain wavelengths [3]. The sensor is referred to as a single channel chemical spectrograph and has an accuracy of about five percent.

EMR reflectance interferences that are associated with the water that is held in or moving through porous materials have been identified and may be minimized for light reflection techniques. The principle of water moving through porous materials has been used in other devices that are used for evaluating soil moisture content. Tensiometers, for example, are composed of a de-aired tube of water that has a porous ceramic cup on one end and a pressure gauge or manometer on the other end [10]. The porous cup end is placed in unsaturated soils to desired depths and water is drawn from the tube by the soil until an equilibrium is reached. The soil moisture tension, and hence a comparable moisture content, is determined. The present study is concerned with the theory, description, and application of an in-situ moisture content measuring device that incorporates optical reflectance from porous material as a means of acquiring soil water status information.

IN-SITU OPTICAL REFLECTANCE SENSORS

The basis of the optical reflectance technique rests on the fact that the reflectance of light from moist soil surfaces shows strong adsorption bands at 1.4 and 1.9 mm as well as other wavelengths. The design of the optical reflectance sensor head is shown in Figure 1. The head is made of plexiglass or PVC pipe, and its dimensions are approximately 2.5 cm in diameter x 5 cm in height. This small volume contributes to the simplicity of the sensor head design as well

0-7803-3068-4/96$5.00©1996 IEEE

as to the ease with which the sensor may be used. The approximate volume of soil evaluated during a moisture content measurement is 10 to 100 cm^3. A porous ceramic membrane, similar to that used in conventional tensiometers, covers the bottom of the sensor head and seals the apparatus in an air-tight manner. The inner surface of the porous bottom is coated with a thin, clear material, such as glass, that minimally effects the light absorbance and reflectance wavelengths of water. Once the porous cover comes in contact with the moist soil and a short equilibrium time is allowed, the moisture content in the soil will be proportional to the moisture content in the porous membrane. The membrane helps to transport the moisture from the soil to the inner surface of the porous material which may then be exposed to the sensing light intensity. Under conditions of equilibrium, the amount of moisture per unit area of the inner membrane surface is independent of the nature of the soil.

The source of light in the sensor head is a simple flashlight lamp working with one or more 1.5 V batteries. The reflected light detector that is used

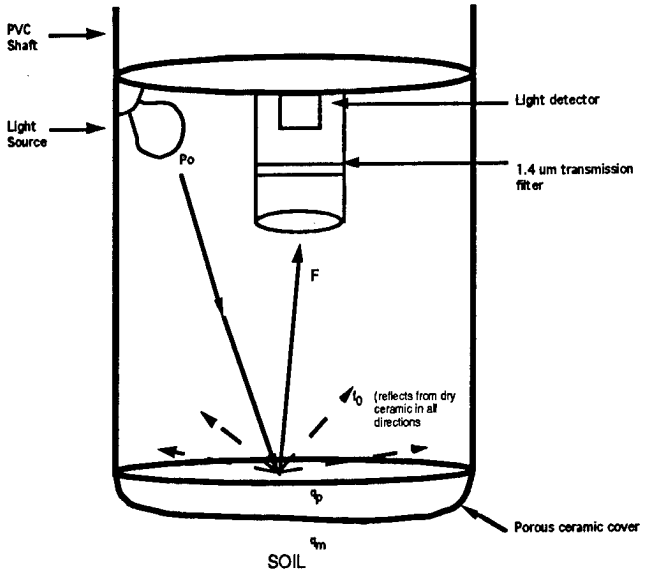


Figure 1. Optical reflectance sensor head schematic.

can be a photodiode or photocell sensitive to the 1.4 or 1.9 mm wavelength. A simple broad band glass filter or interference filter centered around the peak adsorption wavelength is used in front of the detector to allow only the wavelength of interest to pass through. Simple electronic circuitry is used to time average the detected signal which is compared to the reflectance measurement from the inner membrane surface when the sensor head is placed in a dry soil sample. Variations in the light reflectance of the moist membrane surface as compared to the reflectance from the dry membrane surface are attributed to changes in the moisture levels in the membrane and hence to the moisture content of the soil.

The complete *in-situ* optical reflectance sensor device is shown in Figure 2. The sensor is located at the end of a 2.5 cm diameter shaft made of PVC pipe with a length of 2 meters. The electronic circuitry and battery unit are located atop the PVC pipe (or within the upper portion of the pipe) in a manner such that the measured moisture content can be seen on a LED readout on the upper face of the aluminum handle. A cable located in the shaft connects the sensor to the electronic circuitry and LED readout. This small, light-weight optical reflectance sensor device may be easily pushed into the soil to a desired depth, in a manner similar to that of the conventional tensiometer, in order to indirectly measure soil moisture content.

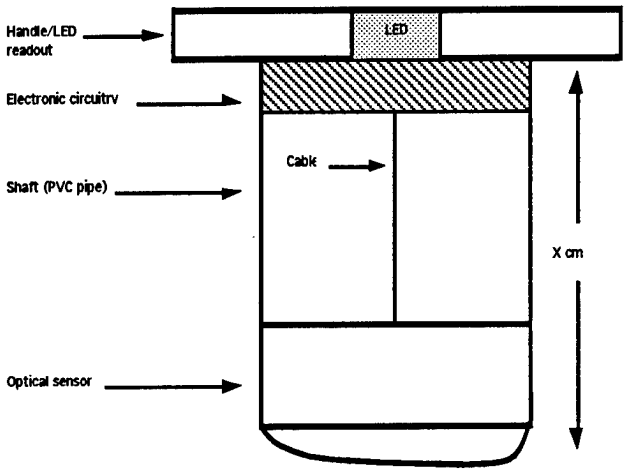


Figure 2. Complete *in-situ* optical reflectance sensor device.

THEORY

The reflected light energy from a power source, P_0, falling on the surface of a porous membrane is shown in Figure 1. Moisture present throughout the membrane absorbs light at 1.4 and 1.9 mm and hence reduces the magnitude of reflected light at these wavelengths. Placing the membrane in close contact with a moist soil causes the membrane to reach an equilibrium moisture content with the moist soil. Let q_p be the mass content of moisture per unit area of the porous membrane and let q_m be the mass content of moisture per unit volume of the soil. After equilibrium is reached, q_p is proportional to q_m. Therefore,

$$q_p = a q_m \qquad (1)$$

Assuming that the porous membrane is in good contact with the soil, the value of a depends only on the nature of the membrane and its ability to absorb and transport moisture. Specific membrane characteristics include thickness, composition, and porosity.

Let f_0 be the fraction of light power reflected by a membrane containing no moisture. The light power absorbed by the dry membrane is $P_0(1-f_0)$. If f is the fraction of light power reflected by a moist membrane, then $P_0 f < P_0 f_0$. This is due in part to the fact that water adsorbs light at 1.4 mm and

other wavelengths and causes less light to be reflected. The total light power absorbed by a moist membrane is $P_0(1-f)$. The additional absorption due only to the moisture on the membrane is

$$P_0(1-f)-P_0(1-f_0)=P_0(f_0-f) \quad (2)$$

If F is the fraction of reflected light power incident on the detector, then F is independent of the moisture content (which effects the magnitude of the reflected power) and depends only on the relative geometry of the source of light, membrane position, and the detector position. The light power seen by the detector with the dry and moist membrane are therefore $D_1=P_0f_0F$ and $D_2=P_0fF$, respectively. The change in the light due to the moisture is

$$(D_1-D_2)=P_0(f_0-f)F \quad (3)$$

Since $P_0(f_0-f)$ depends only on the moisture content per unit area of the porous membrane, we can write

$$P_0(f_0-f)=bq_p=(ba)q_m \quad (4)$$

where b is a constant of proportionality. The moisture content in the soil can therefore be described as

$$q_m=P_0(f_0-f)/ab=(D_1-D_2)/Fab=A(D_1-D_2) \quad (5)$$

where A=1/Fab.

Since F is a factor that depends on the relative geometry of the light source, membrane surface, and detector and a and b are constants of proportionality, the soil moisture content can be indirectly determined by measuring the detection signals D_1 with a dry membrane (initially) and calibrating the sensor by measuring D_2^{cal} with a known moisture content, q_m^{cal}. Therefore,

$$A=q_m^{cal}/(D_1-D_2^{cal}) \quad (6)$$

The sensor is then inserted below the soil surface and signal D_2 is measured after equilibrium has been reached. The moisture content is read as

$$q_m=A(D_1-D_2)=(q_m^{cal}/[D_1-D_2^{cal}])(D_1-D_2) \quad (7)$$

MATERIALS AND METHODS

The Quincy soil used for this study was collected from the Handford site in Richland, Washington and is a mixed mesic, Typic Torripsamment [19]. The soil was air dried, ground, and sieved through a 2 mm sieve. The soil properties of the Quincy soil were determined using standard methods [2] and are shown in Table 1. This sandy textured soil was chosen for the study because of the ease with which the moisture content of the Quincy soil can be varied without soil aggregation and clumping during the somewhat short time frames associated with measuring the light reflectance from moist soil surfaces.

Table 1. Soil properties of the Quincy soil.

	SOIL
Property	**Quincy**
pH	6.29
Particle density, gm/cm^3	2.84
Organic C, %	0.69
Particle size, %	
clay	11
silt	12
sand	77
Predominant clay	smectite
Porosity, cm^3/cm^3	
unpacked	49.65
packed	39.79
CEC, cmol/kg	5.99
Specific surface area, m^2/gm	54.11
Bulk density, gm/cm^3	
unpacked	1.43
packed	1.71

The apparatus used for this study is shown in Figure 3 and is an enlarged version of the optical reflectance sensor. Approximately 88 gm of the dry Quincy soil were placed in a dish and mounted on a small stand that was positioned in the center of the base of a cylindrically shaped container. An 8 cm x 8 cm x 0.64 cm Coors porous plate was placed on the soil surface for light reflectance measurements. All material surfaces associated with the apparatus (except the porous plate) were painted dull/non-glossy black in order to minimize light reflectance during the experiment. Two hollow tubes were positioned on the apparatus at approximately 90^0 with respect to each other and at approximately 45^0 with respect to the mounted porous plate. A 7 watt light bulb was position in a light-tight manner at the top of one tube and was the source of light falling on the porous plate. The second tube was positioned such that only the light image formed on the plate could be seen by a detector which was positioned in a light-tight manner at the top of the second tube. The detector was connected to a recorder that registered the amount of reflectance seen by the detector.

The apparatus described above was used to measure the light reflectance from the Coors porous plate that was in contact with air dried Quincy soil surface and at mass moisture contents ranging from 0.007 to 0.048. The moisture contents were achieved by spraying water onto the thin soil surface layer using a fine mist spraying water bottle and then allowing the moisture to distribute evenly throughout the soil. This technique appeared quite appropriate in that increasing the moisture content of this sandy textured soil containing a relatively low clay content resulted in no soil aggregation or

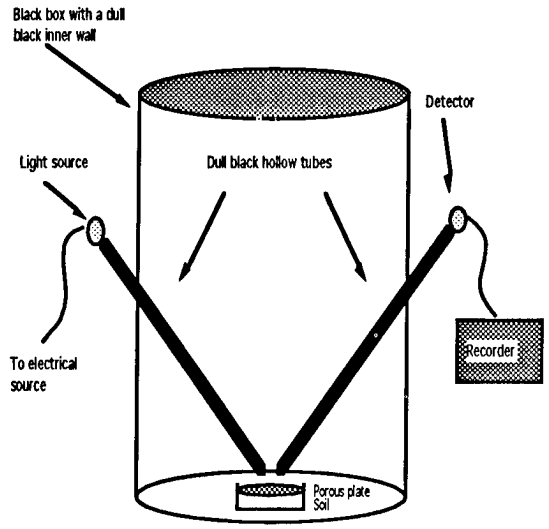


Figure 3. Experimental apparatus used to evaluate optical reflectance variation with varying soil moisture content.

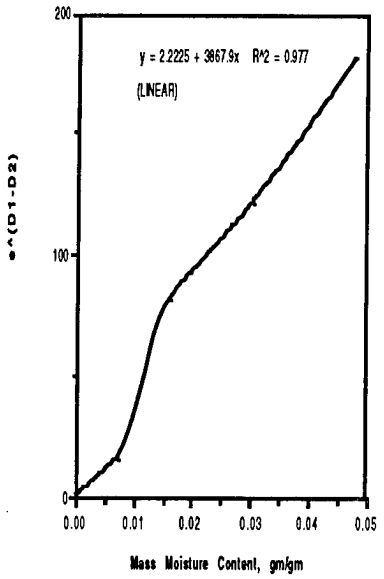


Figure 4. Results of the optical reflectance experiment plotted as mass moisture versus e^(D1-D2).

clumping as did a number of other soils tested for the experiment. Each soil sample was put in a petri dish with the porous plate in position and placed onto the stand inside of the apparatus and the light source and detector/recorder were switched on. The varying reflectance was measured and plotted against the varying soil moisture contents.

RESULTS AND DISCUSSION

The results of the experiment are depicted in Figure 4. Plotting the mass moisture content versus the anti ln (D_1-D_2) resulted in a good linear fit of the data with an R^2 value of 0.977. The mass moisture content varied slightly from 0.0071 to 0.048 gm/gm and may suggest that the Quincy soil had a low water holding capacity. In spite of the low degree of variation in the soil moisture content, mall incremental changes (1%) in the moisture content resulted in measurable variations in the light reflectance from the porous plate. The optical reflectance technique appears to be a viable addition to the existing *in-situ*, moisture measuring techniques available for moisture status evaluation. The theory upon which the technique is based is simple and its described operation is easy. Part II of this psaper will be concerned with the development of a hand-held soil moisture measuring device that is easy to use, accurate, and inexpensive. Additional concerns will include the device limitations, and comparisons to existing methodologies.

REFERENCES

[1] R. S. Alessi and L. Prunty, "Soil-water determination using fiber optics", Soil Science Society of America Journal, no. 50, p. 860-863, 1986.

[2] American Society of Agronomy, Methods of Soil Analysis, Part I and II, Madison, Wisconsin, 1965 and 1982.

[3] Cambria Corporation, EOS-100-W Liquid Detection Sensor, Seattle, Washington, 98107, 1995.

[4] J. W. Cary, J. F. McBride, and C. S. Simmons, "Electro-optic detection of liquid in translucent porous material", Soil Science Society of America Journal, vol. 53, no. 5, p. 1591-1595, 1989.

[5] H. Chen and C. R. N. Rao, "Polarization of light on reflection by some natural surfaces", Britain Journal of Applied Physics, no. 2(1), p. 1191-1203, 1968.

[6] J. E. Colwell, "Grass canopy bidirectional spectral reflectance", Proceeding of the 9th International Symprsium on Remote Sensing and the Enveronment, University of Michigan, Ann Arbor, 1974.

[7] K. L. Coulson, G. M. Bouricius, and E. L. Gray, "Optical reflection properties of natural surfaces", Journal of Geophysical Resorces, no. 70(18), p. 4601-4611, 1965.

[8] D. D. Egbert, and F. T. Ulaby, "Effect of angles of reflectivity, Photogrammetric Engineering and Remote Sensing", no. 38, p. 556-554, 1972.

[9] D. M. Gates, H. J. Keegan, J. C. Schleter, and V. R. Weidner, "Spectral properties of plants", Applied Optics, no. 4, p. 11-20, 1965.

[10] R. J. Hanks, and G. L. Ashcroft, Applied Physics, New York, p. 20-34, 1986.

[11] F. J. Janza, Interaction Mechanisms, Manual of Remote Sensing, American Society of Photogrammetry, Falls Church, Virginia, p. 75-179. 1975.

[12] D. S. Kimes, B. N. Holben, and C. J. Tucker, "Optimal directional view angles for remote sensing missions, Internation Journal of Remote Sensing", no. 5(6), p. 887-908, 1984.

[13] K. Y. Kondratyev, F. Mironova, and A. N. Otto, "Spectral albedo of natural surfaces", Pure Applied Geophysics, no. 59, p. 207-216, 1964.

[14] E. L. Krinov, "Spectral reflectance properties of natural surfaces", NRC Technology Translations, no. 439, p. 1-268, 1947.

15] R. B. MacDonald, M. E. Bauer, R. D. Allen, J. W. Clifton, J. D. Erickson, and D. A. Landgrebe, Results of the 1971 corn blight watch experiment, Proceeding of the 8th International Symprsium on Remote Sensing and the Environment, University of Michigan, Ann Arbor, 1972.

[16] M. A. Mulders, Remote Sensing in Soil Science, Elsevier, New York, p. 93-124.

[17] F. E. Nicodemus, "Reflectance nomenclature and directional reflectance emissivity", Applied Optics, no. 9(6), p. 1474-1475, 1982.

[18] B. F. Robinson and L. L. Biehl, Calibration procedures for measurement of reflectance factor in remote sensing field research, Proceeding of the Society of Photo-Optics Instrumentation and Engineering, no. 196, p. 16-26, 1979.

[19] United States Department of Agriculture, Soil Survey, Benton County Area, Washington, Washington Agricultural Experiment Station, p. 62-66, 1971.

Accuracy of Soil Moisture Determination by Means of Passive Microwave Remote Sensing Method. Modeling and Experiments.

Boris Liberman , Alexander Milshin
Institute of Radioengineering and Electronics, Russian Academy of Sciences, Moscow, Russia
Institute of Geoinformatics, Ltd, Friazino, Russia
141120 Friazino, Moscow reg., Vvedensky sq. 1
Tel. (007-095) 526-91-50/ Fax. (007-09656) 4-52-30/ Email: bml246@ire216.msk.su

ABSTRACT

Some results of passive microwave remote sensing application for the determination of surface (20 - 30 cm layer) soil moisture and general water content in 1 m layer are presented. Model estimation of accuracy dependence on different soil parameters, vegetation biomass, errors of calibration, etc. are given. Results of comparison between remote sensing data and contact data, obtained in different regions are analyzed. The algorithms for data processing were elaborated in Institute of Radioengineering and Electronics Russian Academy of Sciences, and developed in Institute of Geoinformatics, Ltd, software and microwave radiometers in centimeter and decimeter wavebands for experiments were elaborated in Institute of Geoinformatics, Ltd.

INTRODUCTION

Numerous results of theoretical and experimental investigations [1 - 5] shows, that the variations of next parameters have main influence on accuracy of passive microwave remote sensing application for soil moisture determination:- vegetation biomass; soil constants (bulk density; field capacity, wilting point);- calibration errors.

MODELING

The bulk density (BD) of grounds characterize the possibility of soils filling by water . The analyzing of more, then 20 soil types shows, that real natural variations of mentioned parameter from its mean value, which is known from soil maps and literature, does not exceed 10 %. Mentioned spatial bulk density dispersion leads to small (up to 0.025 g/cm3) increasing of remote sensing estimations of volumetric water content (Fig. 1a).

The land surface roughness, including relief variations, leads to small microwave radiation intensity variations, and, as a result, to insignificant increasing of remote sensing estimations of surface (0 - 30 cm layer) water content (up to 0.02 g/cm3).

From the other side the influence of ground surface processing degree (ploughing, harrowing, etc.) is accompanied by loosen of soil's upper layer, by increasing of porousness, decreasing of volumetric water W, which is equal to sharp variation of BD. In that case (Fig. 1b) the errors, which depends on difference in grounds processing increases up to 0.11 g/cm3.

As it's known from the literature the full range of bulk density (BD) natural variations for more, then 20 soil types, is about 0.24 g/cm3 (1.48 - 1.24).

The sensitivity of volumetric water mean value in 1 m layer to BD variations is about 1.92 [%]/[g/cm3]. It means, that natural variations of BD leads to remote sensing estimation errors about 0.5%.

The full range of wilting point (WP) is about 12.9 %. Sensitivity of volumetric water mean value in 1 m layer to WP variations is about 0.3 [%]/[%]. It means, that WP variations leads to maximum errors about 4 %. Usually mean value of WP is known with an absolute error of 2%. It leads to remote sensing error of soil moisture estimation about 1.2%.

Theoretical and experimental study of radiowaves

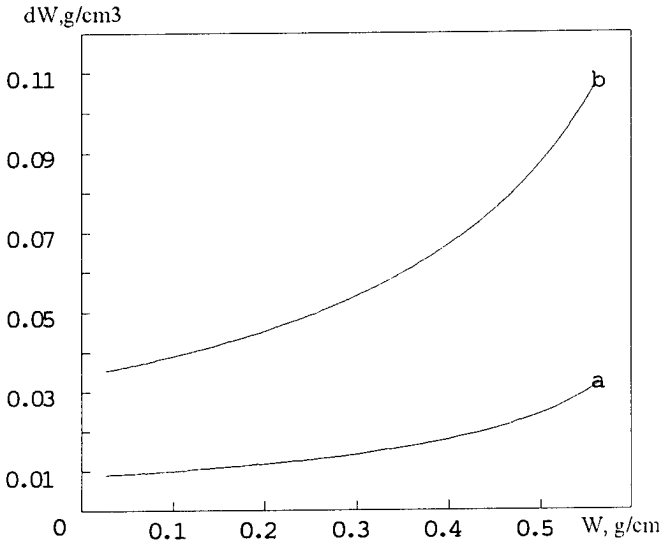


Fig.1 The Dependence of soil moisture remote sensing estimation errors from volumetric water content mean value in the presence of BD and state of earth surface variations. a) - dependence on natural BD variations; b) - dependence on grounds processing degree

0-7803-3068-4/96$5.00©1996 IEEE

propagation in the vegetation medium show, that main parameters, which it's necessary to take into account during remote sensing data processing are types and wet biomass of vegetation.

It's possible to get more or less correct information about the vegetation types from different sources (satellite images, physical maps, etc.). From the other side only mean values of vegetation biomass are known before data processing.

Its dispersion leads to soils brightness temperature estimation errors, and as a result, to errors of remote sensing water content estimations(RSWCE).

For example, on Fig. 2 the dependence of soil moisture remote sensing estimation errors from mean value of ground surface water content in the presence of vegetation biomass variations is given. It's seen, that accuracy of passive microwave remote sensing method depends not only on natural variations of vegetation biomass, but on mean value of water content in upper (0 - 30 cm) layer. In number of cases the W maximum error increases up to 0.15 g/cm3 In the same time sensitivity of RSWCE mean value in 1 m layer to transmissivity of the vegetation layer β, which depends on waverange and biomass, is about 0.49 [%]/0.1*β. As a result, the maximum variations of biomass ($\beta_{max.}$-$\beta_{min.}$ ~ 0.5) leads to 1 m water content relative error about 2.5 %.

Calculated sensitivity of soil moisture mean value variations in upper layer to its microwave radiation is 0.003

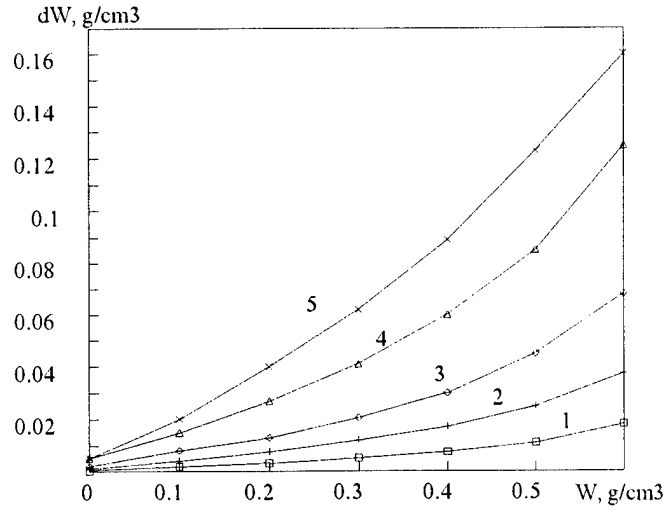


Fig. 2. The error of remote sensing estimation of upper layer soil moisture in a presence of vegetation biomass variations. Mean values of wet biomass: 1 - Q = 0.2; 2 - 0.5; 3 - 1.0; 4 - 2.0; 5 - 3.0 kg/m2.

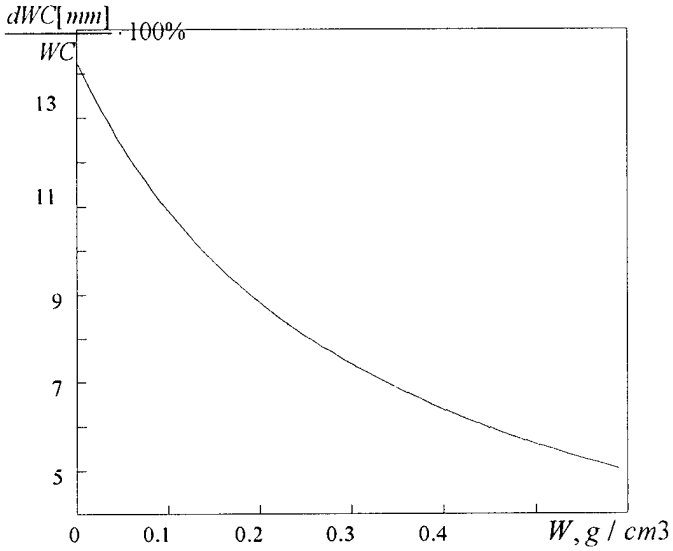


Fig. 3. Calculated general error of remote sensing estimation of water content 1n 1 m layer.

- 0.004 [g/cm3]/[K]. Real calibration errors, using relative calibration method on 2 repers (for example water and dry land or heavy forest), are about 1 - 2 K. In that case this component of RSWCE is equal to 0.006 - 0.008 g/cm3. The relative error for 1 m layer is about 1.2%.

As a result general calculated accuracy of method is about dW ~ 0.1 g/cm3 for upper layer and about dWC/WC ~ 15 % for 1 m layer.

Real variations of soil constants and vegetation biomass are really lower, then values, used for calculations. In that case the calculated mean value of RSWCE does not exceed 7 - 8 % (Fig. 3.).

EXPERIMENTS.

Experiments were conducted in different regions of former USSR and include measurements on the test sites, which were characterized by different soil types, vegetation biomass and water content variations. Brief characteristics o f used equipment are given in Table 1. All radiometers were nadir looking and were installed on the boards of light airplanes and helicopters. The flight high along the test sites was about 100 m. Each test trace was about 2 km long and includes a number of test regions for about 200 m distance from one to another. The scheme of test region is given on Fig. 4.

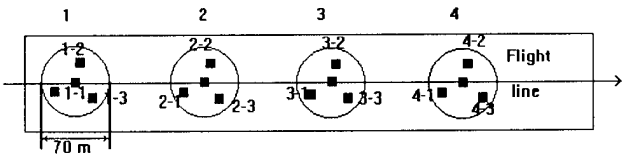


Fig.4. The scheme of test points location.

In each point there contact data were obtained from the surface and from 6 levels up to 1m depth.

The ranges of main parameters variations are given in Table 2.

Table 1.

Wavelength, cm	2.25, 6, 21, 27
Sensitivity, K	0.1
Spatial resolution, m	70

Table 2.

Biomass, kg/m2	Bulk density, g/cm3	Wilting point, %	Field capacity,%	Water content,%
0-5.72	1.12-1.74	0.48 -	11 -18	5 -20

Results of comparison between remote sensing and contact data are presented on Fig.5 and Fig. 6.

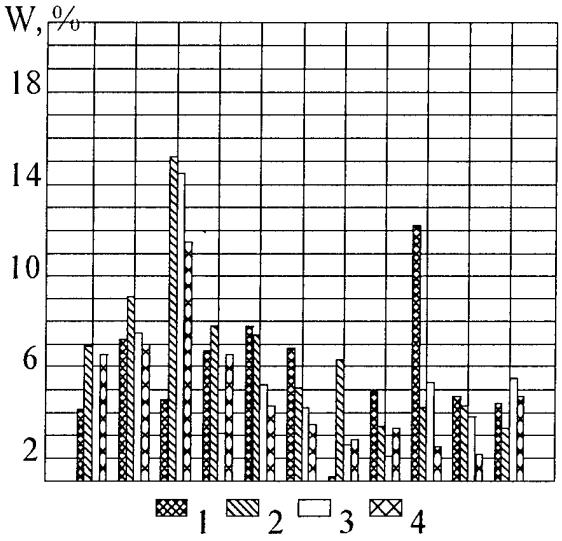


Fig. 5. The results of comparison between remote sensing and contact estimations of surface soil moisture. 1 - difference between mean values in 0 - 30 cm layer; 2 - natural dispersion of contact data in 0 - 2 cm layer; 3 - the same as 2 for 0 - 10 cm; 4 - the same as 2 for 0 - 30 cm.

CONCLUSION

The results of modeling and experiments show, that: - natural variations of soil parameters leads to decreasing of remote sensing method accuracy not more, then 3 - 5 %;

- artificial changing of ground surface (soil processing) may corresponds to larger values (2 - 3 times) of errors, if mentioned problem will be not taking into account during processing. Form of this procedure is very simple and it's possible to use visual information of remote sensing data, obtained in the other waveranges; - mean values of vegetation biomass can be used for determination of general water content in 1 m layer, but for determination of surface soil moisture it's necessary to use more detailed data;

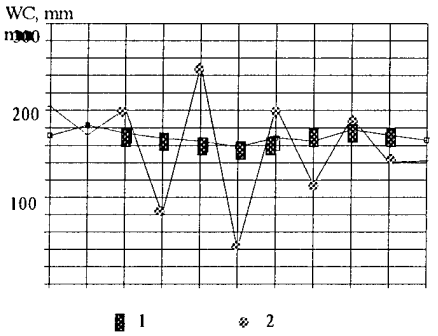


Fig 6. The example of comparison between remote sensing (1) and contact (2) data of general water content in 1 m layer along the test line in Belorussia region.

- accuracy of passive microwave remote sensing method is about 0.05 - 0.07 g/cm^3 in dependence of vegetation biomass variations;

- in numerous cases natural soil moisture variations in each remote sensing pixel are larger, then mean value of passive microwave remote sensing method accuracy.

REFERENCES

[1] A. M. Shutko, "Microwave radiometry of water surface and grounds,"Moscow, Publishing House Nauka, 1986, p.189, (English translation).

[2] E. A. Reutov, A. M. Shutko, "Microwave radiometry of water content of nonuniformly moistened soil with a surface transition layer," Soviet Journal of Remote Sensing, 1990, v. 6, pp. 72 - 79.

[3] T. J. Jackson, T. J. Schmugge, R. Parry, W. P. Kustas, J. C. Ritchie, A. M. Shutko, A. Haldin, E. Reutov, E. Novichihin, B. Liberman, et al, "Multifrequency passive microwave observations of soil moisture in an arid rangeland environment," Int. J. Remote Sensing, 1992, vol. 13, No. 3, pp. 573 - 580

[4] B. M. Liberman, A. A. Milshin, A. G. Grankov, A. A. Kovalev, V. S. Dragun, V. M. Kovalev, V. I. Melnik, "Some results and peculiarities of Remote Sensing methods application for the operative soil moisture determination of Belorussia region," Proc. of 2 Int. Symp. on Ecoinformatics Problems, (English translation), Moscow, 14 - 15 November, 1994, pp. 66 - 69.

[5] B. M. Liberman, A. G. Grankov, A. A. Milshin, A. E. Maximov, S.v.Braun, "Application of Microwave Remote Sensing Methods for Estimation of Grounds and Waters State in Southern Bavaria Region", Conf. Digest, BEMC-95, Malvern, 6 - 9 November, 1995, pp.33.1 - 33.4.

Microwave Dielectric Behavior of Wet Soils in Region of Transition Moisture

T.A.Belyaeva, Yu.M.Sosnovsky

Omsk Pedagogical State University
644099, Russia, Omsk,
Tuckhachevsky Embankment, 14
tel: (7-381-2) 243-795, fax: (7-381-2) 236-748
e-mail: fis@ lvt.ospi.omsk.su

Abstract – Remote sensing of different soils is made significantly easier if their dielectric characteristics are known [1,3]. One of the ways to determine this dielectric is to conduct laboratory studies to estimate the individual contribution of each factor responsible for it into the radio thermal emission of soils. The measurements of the permittivity of soils have shown that the variation of permittivity with moisture content depends on soils solinity. The moisture value at transition region was found to be higher for high solinity soils then for pure soils [4]. Pure sands and soils were studied. Measurements of permittivity samples were made in a waveguide at differ of frequencies in microwave range. The distilled water and the solution of salts were used for moisting of soil samples.

INTRODUCTION

The measurements of pure sand permittivity and different soils samples have been carried out at 7.6 and 18 GHz. The measurements of permittivity samples were made by the waveguide method. The temperature of specimen was near 20°C . The soil samples were of different textures. The moisture range was changed from 40 % to 1%. The distilled water and the solutions of $CaCl_2$ (concentration is 1.2 %) and KCl (concentrations are 1%,2 % and 3%) were used for moisting of soil samples. The density of soils samples with the same texture were identical. The permittivity soils samples as the function of moisture content were studied.

THE EXPERIMENTAL RESULTS

The measurements of permittivity of sand were made for different moisture contents. The distilled water and the solution of $CaCl_2$ (concentration is 1.2 %) were used for moisting of soil samples. The real part of the dielectric constant ε for sand as the function of volumetric moisture content **w** at a wavelength of 1.63 cm is presented in Fig.1.The studies of dependencies of sand real part permittivity from moisture content ε =f(w) have shown that permittivity of salin samples is smaller (for example see experimental result 2 on fig.1). The experimental result approaches well to linear dependencies because sand practucally has no bound water. As it is known, permittivity of saline solutions

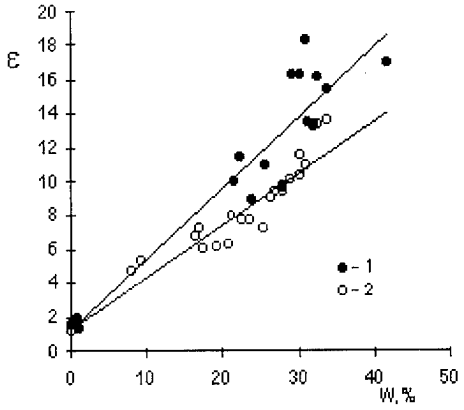


Fig.1 The real part of the dielectric constant for sand as function of volumetric moisture content at a wavelength of 1.63 cm.
1- sand was moistened by a distiling water,
2- sand was moistened by the solution of $CaCl_2$ (1,2% concentration).

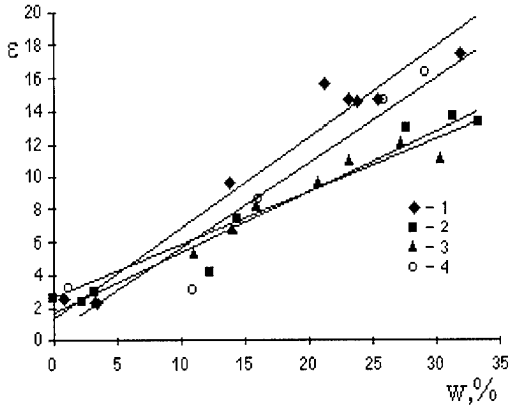


Fig.2 The real part of the dielectric constant for soil samples with code 2.4 as function of weight moisture content at a 7,6 GHz .
1- sample was moistened by a distiling water,2- sample was moistened by the solution of KCl (concentration is 1%),
3 - concentration is 2%, 4 - concentration is 3% .

0-7803-3068-4/96$5.00©1996 IEEE

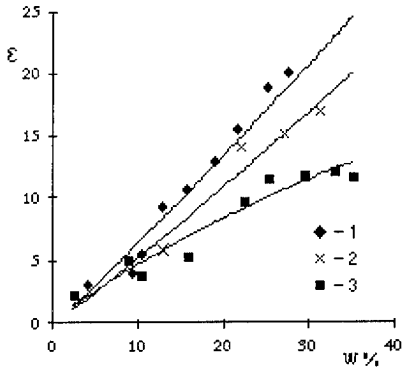


Fig.3 The real part of the dielectric constant for soil samples with code 4 as function of weight moisture content at a7,6 GHz. 1- sample was moistened by a distiling water,2- sample was moistened by the solution of KCl (concentration is1%), 3 - concentration is 2%.

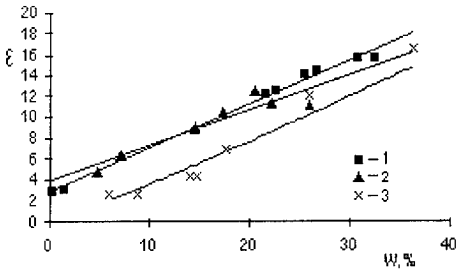


Fig.4 The real part of the dielectric constant for soil samples with code 5 as function of weight moisture content at a 7,6 GHz .1- sample was moistened by the solution of KCl (concentration is 1%), 2 - concentration is 2%, 3 - concentration is 3% .

is smaller than of distilled water therefore permittivity of soils is smaller too. The real part of permittivity of real soils as the function of weigh moisture is presented on fig.2,3 and 4. This measurements of permittivity have been carried out at 7.6 GHz (wavelength is 4 cm). The measurements showed decreasing permittivity of soils if samples were moistened with a solution of salt. The obtained experimental dependencies ε (w) aren't lineary . The value of transition moisture increases with the increasing of the level of salinity. On fig.5 the increase of transition moisture with increasing of soils salinity is shown.

The salt in soils increases the quantity of bound water.

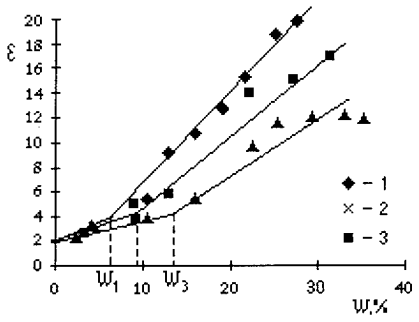


Fig.5 Move transition moisture with increasing of soils salinity (for example sample with code 4) after moisting by the solution of KCl at 7,6 GHz, 1 - sample was moistened by a distiling water,2- sample was moistened by the solution of KCl (concentration 1%), 3 - concentration is 2%.

We consider this fact to be important for modeling dielectric properties of saline soils [2].

SUMMARY

This paper presents laboratory studies of permittivity of sand and real soils dependence on moisture and salinity. The soils samples were moistened with two salt solutions of different concentrations.The obtained results showed real possibility of determining level salinity of soils and transition moisture value at frequency <18 GH.

REFERENCES.

[1] T.J.Jackson, P.E.O'Neill. Salinity effect on the microwave emission of soils. IEEE Trans. on Geosci . and Remote Sens. 1987. vol.GE-25, No.2 . Pp.214-220.

[2] J.R.Wang, T.J.Schmugge . An empirical model for the complex dielectric permittivity of soils as function of water content. IEEE Trans. on Geosci. and Remote Sens. 1980. vol.GE-18, No.4 . Pp.2188-2195.

[3] A.M.Shutko.UHF - radiometria vodnoy poverxnosty i pohvogruntov.M:Nayka.1986 . P.190 (in rassian).

[4].P.P.Bobrov at el. Issledovanie dielectriheckix haraktericticpohv v oblasty perehoda vlagi iz vobodnoy v svazannuy. Doclady academii nayk SSSR. 1989.Tom 304.N.5.Pp.1116-1119.(in rassian)

Simulation of Ocean Skin Temperature Modulation by Swell Waves

G. A. Wick, A. T. Jessup, and V. Hesany
Applied Physics Laboratory, College of Ocean and Fishery Sciences, University of Washington
1013 NE 40th Street, Seattle, WA 98105
phone: (206) 543-5942 fax: (206) 543-6785 e-mail: wickg@apl.washington.edu

Abstract -- The skin temperature of the ocean can be significantly modulated by the presence of swell waves. Experiments show that the magnitude of the modulation can be on the order of the bulk-skin temperature difference and that the phase is determined by the direction of the wind relative to the swell. A new model incorporating small-scale wave breaking, hydrodynamic modulation, and surface renewal theory is developed to simulate the modulation of the skin temperature. Comparisons with observations show that the model can accurately predict the mean skin temperature and both the amplitude and phase of the modulation.

INTRODUCTION

The existence of the bulk-skin temperature difference ΔT across the ocean thermal boundary layer (see reviews [1] and [2]) is important because of its effect on satellite-based measurements of sea surface temperature and relevance to air-sea exchange processes including heat and gas flux. Much time and effort has gone into attempting to model the behavior of ΔT (see [3] for a current summary of approaches). Recent results [4] showed that there is significant modulation of the ocean skin temperature (up to the order of ΔT) by swell waves and that the modulation is strongly affected by the direction of the wind relative to the swell. The results suggested that the combined effect and interaction of wind and waves may need to be considered in future modeling efforts. This work presents a model developed to simulate the observed modulation of the ocean skin temperature by swell. In the future, such results might be incorporated into more detailed and accurate models of ΔT.

We first summarize our experimental procedures and findings most significant to our modeling efforts. We then describe our new model for the observed temperature modulation and compare the predictions with our direct observations. The results suggest that small-scale wave breaking may have a dominant effect on the modulation of skin temperature and average values of ΔT.

EXPERIMENTAL OBSERVATIONS

We conducted two experiments aboard R/P *Flip* to measure the sea surface temperature and surface displacement. The first was in January 1992 in the deep ocean off southern California and the second was in September 1995 approximately 12 miles off the Oregon coast. The ocean skin temperature measurements were made with Heimann KT19 and Barnes PRT-5 infrared radiometers. The surface displacement was measured with wave gauges, radar altimeters, and laser altimeters. Spectral analysis was performed on the skin temperature and wave height time series to compute their coherence and the linear transfer function for the modulation of the skin temperature by the surface displacement. The key quantities for this work are the phase and amplitude of the transfer function. The phase Ψ indicates the location of the temperature maximum relative to the wave crest. We allowed $-180° < \Psi < 180°$ where $\Psi > 0$ on the forward face of the swell crest and $\Psi < 0$ on the rear face. The magnitude of the transfer function gives an estimate of the peak-to-peak temperature modulation at a given frequency. Full details of these calculations are given by Jessup and Hesany [4].

While the complete experimental results are described in [4], the main findings are illustrated in Fig. 1. The figure shows a one day time series from the first experiment of the squared coherence γ^2, the peak-to-peak temperature modulation T_0, and Ψ along with the wind speed at 25 m U_{25} and the angle between the wind and the swell direction ϕ_{SW}. Note first that the values of T_0 range between 0.1 and 0.3 K which is on the same order as ΔT which ranges between 0.1 and 0.6 K. The squared coherence and peak-to-peak modulation both tend to follow the wind speed. When the wind and swell are coming from the same direction (ϕ_{SW} near 0°) the phase is around 90°, which corresponds to the forward face of the swell crest on the downwind side. When the wind reverses and is opposite to the swell (ϕ_{SW} near 180°), however, the phase changes to near -90°. Though the dependence of T_0 and γ^2 on wind speed was not always as strong, the fact that the phase is near 90° when the wind and swell are aligned and near -90° when they are opposite persisted throughout the experiment.

Jessup and Hesany [4] discussed the possible mechanisms which could explain the observed skin temperature modulation associated with surface waves. They found that disruption of the skin layer by small-scale breaking due to shortwave/longwave interaction is consistent with the findings that the magnitude of the modulation is comparable to ΔT and that the phase is positive when the wind and swell are aligned. They also presented evidence suggesting that the phase of this hydrodynamic modulation can change from the front to rear face when the wind reverses. We now present a model which implements this mechanism and compare the predictions with the experimental observations.

NUMERICAL SIMULATIONS

Our model for the modulation of the ocean skin temperature by swell waves includes the effects of small-scale wave breaking as well as the modulation of the wind stress and heat flux over the wave form. Soloviev and Schlüssel [5] indirectly included the effects of wave breaking in a surface renewal model of ΔT by associating the time scale of renewal

0-7803-3068-4/96$5.00©1996 IEEE

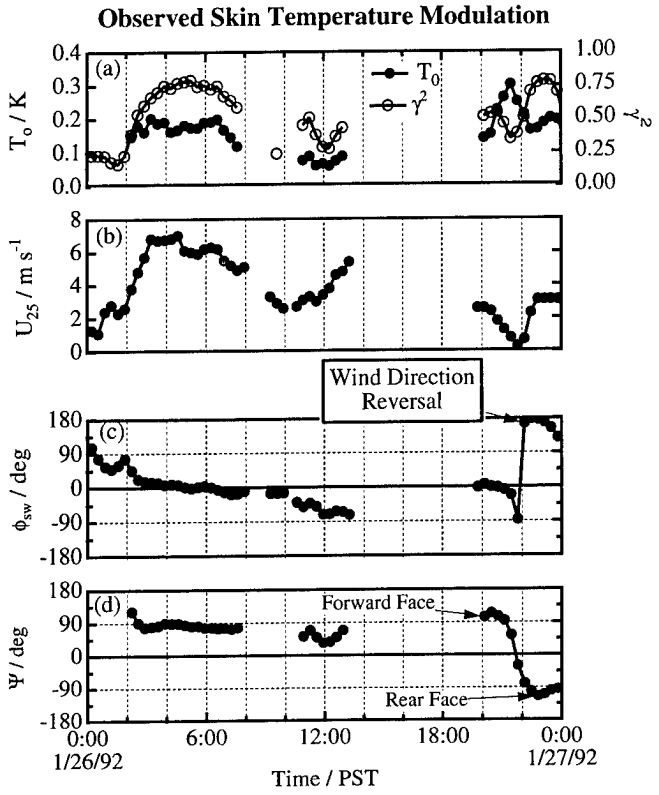


Figure 1. Time series of (a) peak-to-peak modulation T_0 and squared coherence γ^2, (b) wind speed U_{25}, (c) angle between wind and swell direction ϕ_{sw}, and (d) phase of transfer function Ψ. The squared coherence and magnitude closely follow the wind speed in the early morning hours, while the phase responds directly to wind direction relative to the swell.

events with wave phenomenon. Here we directly simulate breaking events at preferential points along the wave form and model the time evolution of ΔT and the skin temperature between these events. Assuming the temperature across the skin layer is governed by molecular diffusion, we follow [5] and take the value of ΔT at t seconds after a breaking or renewal event to be given by

$$\Delta T(t) = 2\pi^{-1/2}(t/\kappa)^{-1/2} q_0 \qquad (1)$$

where $q_0 = Q/\rho c_p$, Q is the net heat flux (positive out of the ocean), ρ is the water density, c_p is the specific heat of water at constant pressure, and κ is the thermal diffusivity of water. The net heat flux was computed from available meteorological quantities using standard bulk formulations. Variations of the net heat flux with the wave phase were modeled by taking the value of the wind speed used in the calculation of the heat flux to be modulated by the orbital velocity of the swell waves.

The remaining task is to determine when and where along the wave form disruption of the skin layer occurs. We assume that the skin layer remains intact and continues to cool until either a small-scale breaking event occurs or the surface is renewed through a convectively driven burst of fluid from below. Including the convective events provides for a limiting mean background ΔT in the absence of any wave breaking.

Following [5], we take the mean time between convective events to be proportional to $(\nu/\alpha g q_0)^{1/2}$ where ν is the kinematic viscosity of water, α is the coefficient of thermal expansion of water, and g is acceleration due to gravity and assume that the time between bursts follows a log-normal distribution. We determined the constant of proportionality by finding the mean time between bursts required to reproduce the mean ΔT observed during the lowest wind speed period of the 1992 experiment.

To simulate the location of small-scale breaking along the wave form we assume that the small-scale breaking is most likely to occur where there is the maximum hydrodynamic modulation of small waves by the larger swell. We generated a probability density function for the location of small-scale breaking to match the distribution of the hydrodynamic modulation. The distribution of hydrodynamic modulation was based on the model of Thompson and Gotwols [6]. An illustration of the modeled distribution of small-scale breaking along with the assumed wave form is shown in Fig. 2. The distribution suggests that small-scale breaking will most likely occur around a phase of 90°. The degree of enhancement occurring on the forward face was chosen to simulate the modulation of short, wind-generated gravity waves by swell waves. Alternative formulations for the hydrodynamic modulation can be easily substituted into our simulation.

To determine if there is small-scale breaking, we assume a probability that small-scale breaking occurs at some point along one wavelength of the swell wave. We select the probability so that the modeled average ΔT over several wavelengths matches the observed average ΔT. A 0.6 probability of small-scale breaking is required to predict the mean ΔT for the test period described below. A high fraction of small-scale breaking is not unreasonable considering this period corresponded to the peak observed coherence between the skin temperature and wave height. The probability is currently independent of the modeled hydrodynamic

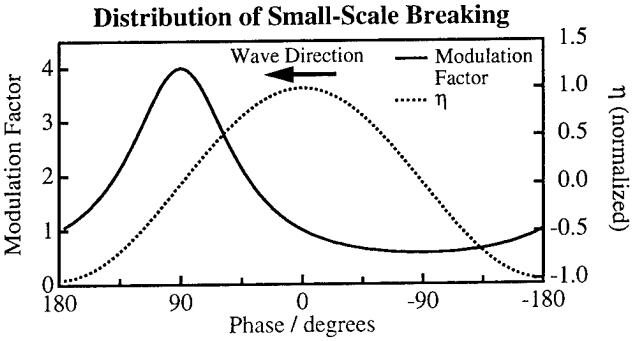


Figure 2. Schematic representation of the magnitude and location of the modeled distribution of small-scale breaking along the swell wave. The peak enhancement occurs on the front face of the wave.

modulation. In the future we hope to relate this probability to the fractional area of breaking observed with infrared imager data.

We independently simulate the evolution of ΔT for 100 different water parcels to get a better statistical sampling and allow for the fact that a radiometer views a large number of water parcels. Using the probability distributions for convective renewal and small-scale breaking described above, we simulate the location of skin layer disruption for each parcel. We then step through time computing ΔT from (1) for each parcel and take the average of all these values as our simulated ΔT. The skin temperature is computed from the simulated ΔT and measured bulk temperature.

We tested the simulation for a 60-second period from the first experiment occurring near 04:55 PST on January 26, 1992 (see Fig. 1). The average wind speed, net heat flux and ΔT during this period were 6.0 m s^{-1}, 107 W m^{-2}, and 0.26 K respectively. The wind and swell were aligned. The resulting simulated time series of skin temperature and wave height for the 60-second test period are shown with the observed values in Fig. 3. The observed swell waves vary in amplitude between 0.5 and 1.5 m. To simplify the simulation, we assumed the wave height to be given by a sinusoidal wave with an amplitude of 1.5 m. The simulated temperature fluctuations should, therefore, be compared with the three wavelengths where the actual amplitude was approximately 1.5 m. The simulated peak-to-peak modulation of about 0.08 K closely match the observed temperature fluctuations. The variability in the amplitude of our simulated temperature fluctuations shows the randomness inherent in our simulation procedure. The predicted phase of the modulation also closely matches the observations.

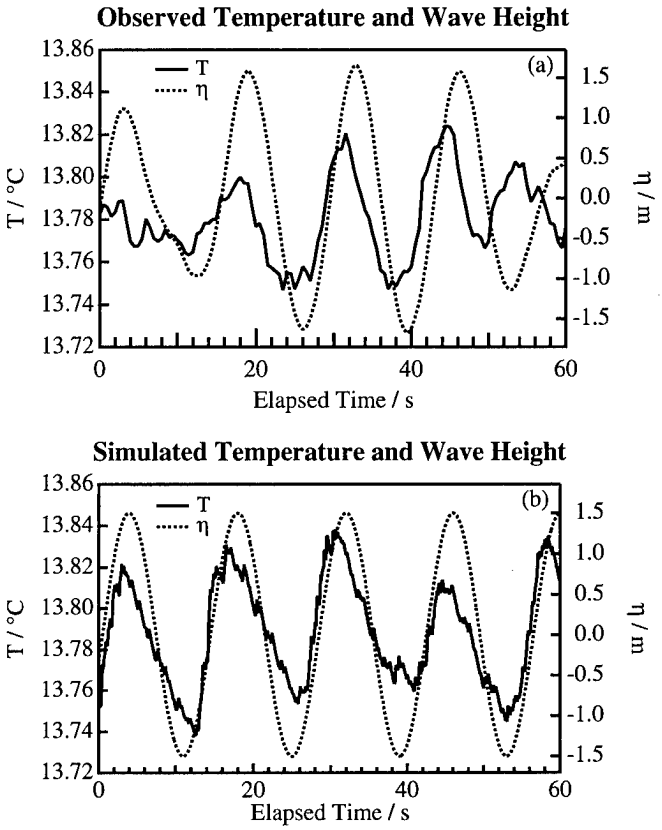


Figure 3. Observed (a) and simulated (b) skin temperature modulation with wave height. The simulation was run with an idealized wave height, but the measured wind speed and net heat flux. The simulation predicts the phase and magnitude of the peak-to peak fluctuations well.

CONCLUSIONS

Experimental findings suggest that disruption of the skin layer by small-scale breaking due to shortwave/longwave interaction could explain observed modulation of the ocean skin temperature by swell waves. To further test this hypothesis, a model of the ocean skin temperature incorporating small-scale breaking was developed and its predictions were compared with observations. By linking the location of small-scale breaking to regions of enhanced hydrodynamic modulation and taking the time evolution of the skin temperature to be governed by molecular diffusion, the model accurately predicted the mean skin temperature and the amplitude and phase of the temperature modulation. The results provide additional evidence that the mechanism of small-scale breaking may dominate the modulation of the ocean skin temperature by swell waves.

REFERENCES

[1] Katsaros, K. B., "The aqueous thermal boundary layer," Boundary-Layer Meteorol., vol. 18, pp. 107-127, 1980.

[2] Robinson, I. S., N. C. Wells, and H. Charnock, "The sea surface thermal boundary layer and its relevance to the measurement of sea surface temperature by airborne and spaceborne radiometers," Int. J. Remote Sens., vol. 5, pp. 19-45, 1984.

[3] Wick, G. A., W. J. Emery, L. H. Kantha, and P. Schlüssel, "The behavior of the bulk-skin sea surface temperature difference under varying wind speed and heat flux," J. Phys. Oceanogr., in press.

[4] Jessup, A. T. and V. Hesany, "Modulation of ocean skin temperature by swell waves," J. Geophys. Res., vol. 101, pp. 6501-6512, 1996.

[5] Soloviev, A. V. and P. Schlüssel, "Parameterization of the cool skin of the ocean and of the air-ocean gas transfer on the basis of modeling surface renewal," J. Phys. Oceanogr. vol. 10, pp. 1339-1346, 1994.

[6] Thompson, D. R. and B. L. Gotwols, "Comparisons of model predictions for radar backscatter amplitude probability density functions with measurements from SAXON," J. Geophys. Res., vol. 99, pp. 9725-9739, 1994.

Ocean Ripple Statistics Measured with a Scanning-Laser Glint Sensor

Joseph A. Shaw and James H. Churnside
NOAA Environmental Technology Laboratory
R/E/ET1
325 Broadway
Boulder, Colorado 80303
ph. (303) 497-6496, (303) 497-6744
Fax (303) 497-3577
jshaw@etl.noaa.gov, jchurnside@etl.noaa.gov

Abstract -- We describe a scanning-laser glint sensor that we have developed for field measurements of ocean slope statistics. In this method a narrow laser beam is scanned in a line and incidences of specularly backscattered light (glints) are counted and binned according to their slope angle. Slope probability density functions are calculated as normalized glint histograms. We report field measurements that show generally good agreement with previous results. The most significant difference we find is an enhancement of mean square slope during periods of negative air-sea temperature difference.

INTRODUCTION

Ocean ripples, or short wind waves, are the primary contributor to sea-surface slope. As such, they are of great importance in a variety of remote sensing measurements. Examples of measurements that require knowledge of ocean ripple statistics include active and passive microwave wind sensing [1-3], radiometric sea-surface temperature sensing [4], ocean color imagery [5], and laser backscatter analysis [6,7].

Very few field measurements of ripple statistics have been reported. The first significant field measurements were by Cox and Munk [8], who used photometric sun-glitter images to derive sea-surface slope statistics over a wind speed range of 1-14 m/s. In terms of completeness and simplicity of use, the Cox and Munk results still represent the standard model. However, their method required tedious data processing.

No other field measurements were reported until after interest was renewed by the the arrival of spaceborne scatterometers. Field measurements since 1977 [9-12] have been made mostly with refractive laser slope gauges that employ immersed lasers to determine slopes from the refraction of light as it passes through the water-air interface. Though these instruments work well, they require optics immersed in sea water, and they are limited in angular range fundamentally by total internal reflection and practically by the size of the receiving optics.

This document has been generated as part of a joint NOAA/DOD - Advanced Sensors Applications Program.

In this paper we describe a new reflective scanning-laser glint sensor that counts glints, or occurrences of specular backscatter, as a narrow laser beam is scanned over a wide angular range of the ocean surface. The instrument is conceptually simple, requires no immersed optics, and has the potential of measuring very large slopes with a small amount of data processing. We first describe the instrument and technique, then present slope measurements taken in the Pacific Ocean near the Oregon coast.

INSTRUMENT DESCRIPTION

The primary features of our reflective scanning-laser glint sensor are summarized in Table 1. A 10-mW HeNe laser is directed via two plane mirrors to the ocean surface. The primary scan mirror is mounted on the shaft of a dc motor, and rotates at a nominal rate of 2 revolutions per second, creating a linear scan across the ocean surface. A glint is counted in an angular bin when the backscattered power exceeds a threshold value chosen to be just above the receiver noise floor. The receiver signal is sampled at 0.1° intervals over a 150° range centered on nadir. An intermediate mirror is mounted on the shaft of a stepper motor to rotate in an axis orthogonal to the primary scan axis. The purpose of this mirror is to compensate for cross-scan sensor motion detected by an inclinometer. Sensor motion in the scan axis is compensated for by shifting the angular bin into which glints are counted.

Reflective markers (1° angular extent) near the beginning and end of the scan facilitate angular calibration to account for motor speed variations ($\leq 5\%$) from scan to scan. Motor speed variations during a single scan produce errors that are smaller than the final 1° resolution of our glint histograms.

A computer-controlled stepper motor allows remote steering of the optics module to a desired azimuth. To measure two-dimensional slope probability density functions, we alternate scan periods between along- and cross-wind azimuths. The receiver amplifier gain is also computer controlled, allowing the user to operate the instrument from a protected location while the instrument is deployed on a boom above the sea surface.

0-7803-3068-4/96$5.00©1996 IEEE

Table 1. Characteristics of the scanning-laser glint sensor

laser power, wavelength	10 mW, 632.8 nm
laser far-field divergence	1.18 mrad
optical filter bandwidth	10 nm
detector	UDT 455 photodiode
detector NEP@ 1kHz receiver bandwidth	$8x10^{-13}$ W
receiver field of view	25.4 mrad
receiver lens	F/4 singlet, 100-mm focus
scan-mirror rotation rate	2 rev/sec, adjustable
scan range	nadir ± 75°
glint sample rate	10 samples/degree

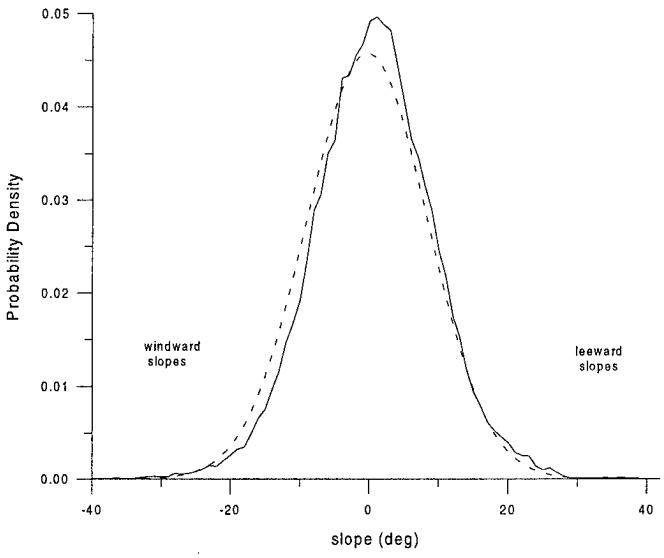


Figure 1. Along-wind slope probability density function.

OCEAN SLOPE MEASUREMENTS

The first field deployment of our system was during the Coastal Ocean Probing Experiment (COPE) near the Oregon coast during September 1995. The sensor was suspended from a boom on the Floating Instrument Platform (FLIP) operated by the Scripps Institution of Oceanography. The FLIP was moored 20 km from the Oregon coast, west of Tillamook at 45° 45.22' N latitude, 124° 16.9' W Longitude, in 150 m of water. All of our measurements were taken with winds blowing from the open sea, and are thus unaffected by the FLIP itself. The height of the optics module was approximately 6 m above the surface.

Figure 1 is a typical along-wind slope probability density function for a 20-minute averaging time (solid line), shown with a best-fit Gaussian (dashed line). These results are consistent with the Cox and Munk results [8] in that the shape is nearly Gaussian, but skewed toward leeward slopes for the along-wind case due to wave asymmetry. The cross-wind peaks show no significant skewness.

Figure 2 shows measured along-wind mean square slopes as a function of U_{10}, the anemometer wind speed at a 10-m height. The crosses correspond to near-neutral stability and the dots correspond to negative stability (air-sea temperature difference between -0.3 and -1°C). The dotted line is the linear regression for the Cox and Munk data, which were measured under conditions of neutral and positive stability. In our range of negative stability the mean square slope is increased by up to a factor of 2 over the Cox and Munk regression. This agrees with

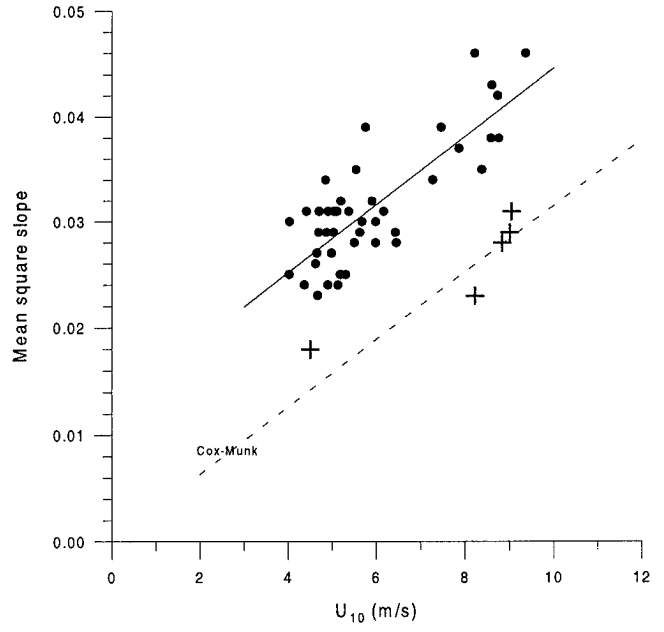


Figure 2. Sea surface along-wind mean square slope vs. wind speed. Dots are measurements with negative stability, crosses are measurements with near-neutral stability. The solid line is a linear regression for our negative-stability data, and the dotted line is the Cox and Munk along-wind regression (their data had near-neutral and positive stability).

predictions of ripple enhancement by negative stability and is similar to measurements of ripple suppression by positive stability [12,13]. We are preparing a more detailed publication showing the effects of negative stability on slope statistics [14].

CONCLUSIONS

We have described a new reflective scanning-laser glint sensor for measuring sea-surface slope statistics. This system can measure slopes over a large range, while being relatively simple to construct and operate. Deployment of this instrument in the Pacific Ocean produced results that agree well with previous studies. These data are the first published field measurements from the open ocean of mean square slopes that are enhanced significantly by conditions of negative stability. This instrument will be useful in further studies of ocean ripples, including swell and internal wave modulation of slope statistics and other related topics.

ACKNOWLEDGMENT

We gratefully acknowledge the assistance of Mark Jacobson who operated the instrument for part of the time on the FLIP.

REFERENCES

[1] A.K. Fung, Microwave Scattering and Emission Models and Their Applications. Boston: Artech House, 1994.

[2] S.H. Yueh, W.J. Wilson, F.K. Li, S.V. Nghiem, and W.B. Ricketts, "Polarimetric measurements of sea surface brightness temperatures using an aircraft K-band radiometer," IEEE Trans. Geosci. Remote Sens., vol. 33, pp. 85-92, January 1995.

[3] Y.G. Trokhimovski and V.G. Irisov, "Wind speed and direction measurement using microwave polarimetric radiometers," NOAA Tech. Memo ERL ETL-250, 1995, available from NTIS, 5285 Port Royal Road, Springfield, VA 22161.

[4] K. Yoshimori, K. Itoh, and Y. Ichioka, "Statistically corrected ocean thermography," Appl. Opt., vol. 33, pp. 7078-7087, 20 October, 1994.

[5] H.R. Gordon and M. Wang, "Surface-roughness considerations for atmospheric correction of ocean color sensors. II: The Rayleigh-scattering component," Appl. Opt., vol. 31, pp. 4247-4260, 20 July, 1992.

[6] J.A. Reagan and D.A. Zielinskie, "Spaceborne lidar remote sensing techniques aided by surface returns," Opt. Eng., vol. 30, pp. 96-102, January 1991.

[7] D.M. Winker, R.H. Couch, and M.P. McCormick, "An overview of LITE: NASA's Lidar In-space Technology Experiment," Proc. IEEE, vol. 84, pp. 164-180, Feb. 1996.

[8] C. Cox and W. Munk, "Measurement of the roughness of the sea surface from photographs of the sun's glitter," JOSA, vol. 44, pp. 838-850, November 1954.

[9] B.A. Hughes, H.L. Grant, and R.W. Chappell, "A fast response surface-wave slope meter and measured wind-wave moments," Deep Sea Res., vol. 24, pp. 1211-1223, 1977.

[10] S. Tang and O.H. Shemdin, "Measurement of high frequency waves using a wave follower," J. Geophys. Res., vol. 88, pp. 9382-9840, 20 November, 1983.

[11] S.P. Haimbach and J. Wu, "Field trials of an optical scanner for studying sea-surface fine structures," IEEE J. Ocean. Eng., vol. 10, pp. 451-453, October 1985.

[12] P.A. Hwang and O.H. Shemdin, "The dependence of sea surface slope on atmospheric stability and swell conditions," J. Geophys. Res., vol. 93, pp. 13903-13912, November 15, 1988.

[13] J. Wu, "Effects of atmospheric stability on ocean ripples: a comparison between optical and microwave measurements," J. Geophys. Res., vol. 96, pp. 7265-7269, 1991.

[14] J.A. Shaw and J.H. Churnside, "Laser glint measurements of sea-surface roughness enhanced by negative stability," unpublished (submitted to Appl. Opt., March 1996).

The Remote Technique of Sea Surface Waves by Optical Sensors

Victor I. Titov and Emma M. Zuykova
Institute of Applied Physics, Russian Academy of Sciences
46, Uljanova str., Nizhny Novgorod, 603600, Russia
Tel.: 7 8312 384528, Fax: 7 8312 365976
E-mail: titov@hydro.nnov.su

Abstract – The original optical sensors for remote sensing of surface waves in wide wavelength range in real time for natural (from ship or sea platform) or laboratory conditions are described. In the frame of twoscale approach of surface waves the theory of space-time spectral analysis of optical image of short waves is considered. It is shown that the dispersion of frequency fluctuations depends not only on the orbital velocity of the long wave but also on its height. The method for determination of long surface wave intensity is proposed.

The investigation of space-time structure of sea surface waves is important for better understanding of a variety of the ocean and atmosphere processes. It is typically difficult to carry out such investigations with point sensors such as wire probes or laser gauges of wave slopes. The optical methods based on the spectral analysis of surface wave image and radar methods are most suitable for such measurements of space-time characteristics of surface waves. The optical methods are easily adopted for various wavelengths from millimeters to tens of meters. This methods are used for definite illumination of water surface: under field conditions the illumination in clear sky or homoheneous cloudy conditions, under laboratory conditions the gradient spreading light source is used.

In experiments devoted to the investigation of two-dimensional space spectra of wave slopes [1], the light source was placed under water surface at the bottom of the water tank . The surface-wave image was recorded by a nadir-looking CCD-camera with a small time of exposure. At the same time, no studies have been performed on the space-time characteristics of short surface waves by means of the optical methods, including the one mentioned above. Apparently, this is because of difficulties in measuring high-frequency spectra of ripples due to limitations imposed by the repetition rate of a CCD-camera.

In IAP RAS it was developed some kinds of noncoherent optical devices for space-time analysis of surface wave images at wavelengths from few meters to few millimeters in real time [2,3] . These optical devices can be divided into groups aimed at the following real-time recordings:

- of 2D-space spectra of the surface wave slopes. For example, the spectra at wavelengths from about 7 cm to 1.5 m were recorded from a ship or a sea platform [4];
- of space-time spectra of sea waves as a function of the frequency for several wave numbers [2];
- of range-time-intensity (RTI) optical images of surface waves for wavelengths from 2m and more constructed from optical sections of sea surface like a side-looking radar images.

These RTI optical images permit to determine the kinematic and spectral characteristics of long sea waves [5]. These devices have high sensitivity, large dynamical and frequency range and can be used under laboratory and field conditions. The PC software was developed for recording data supplied by these devices on a hard disk and for imaging these data on TV monitor in real time. Some of this devices was used in the joint US-Russia experiment JUSREX-92, devoted to the investigation of effect of internal waves on sea waves [4,5].

This work was supported by the Russian Foundation of Basic Investigations, grant 96-02-18581a.

0-7803-3068-4/96$5.00©1996 IEEE

Consider the space-time spectra of surface wave image using the twoscale approach for surface waves. The analyzed short wave train is supposed to be on the large surface wave with more greater wavelength. The position y of image of short wave train from the optical axis in the focal plane of lens will be [6]:

$$y = F/(cos^2\beta tg\beta + Y cos^2\beta/(H-a)) - Ftg\beta,$$

where β - angle of observation, F - focal distance of lens, H - height of lens above sea level, Y - horizontal distance of short wave train from the lens, a - elevation of long wave in the place of location of short wave train. The instantaneous frequency of spectra of short waves that measured by the noncocherent spectrumanalyzer for $H >> a$ will be:

$$f = -(dY/dt + (da/dt)/tg\beta)/\lambda,$$

where λ is the short wave length.

The mean frequency of space-time spectra of surface waves depends on the phase velocity of short waves, the velocity of a surface current and surface wave drift. For example, on Fig.1 it is presented the measurements of wind drift velocity V of surface waves for various wind speed W. The wavelength of analyzed surface waves is pointed on the Figure. The observation direction was directed up-wind. The dashed curve is the experimental measurements from paper [7].

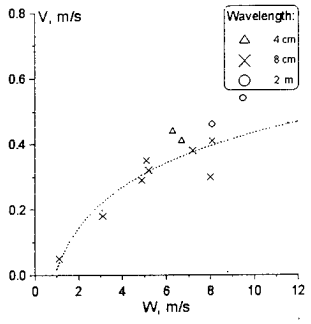


Fig.1. The wind drift velocity

The dispersion of frequency fluctuations σ_f^2 will be determined by the expression:

$$\sigma_f^2 = \frac{1}{\lambda^2}\left(\left\langle\left(\overrightarrow{v_0}\ \overrightarrow{j}\right)^2\right\rangle + \frac{1}{\tan^2\beta}\left\langle\left(\frac{\partial a}{\partial t}\right)^2\right\rangle\right),$$

where, $\overrightarrow{v_0}$ is the horizontal orbital velocity of a long wave, $\overrightarrow{j}$ is the unit horizontal vector in the observation direction. The contribution of the orbital velocity or of the long wave elevation to the space-time spectra of short waves depends on the observation angle. For the simple model of a harmonic long surface wave, the expression for σ_f^2 will be:

$$\sigma_f^2 = \frac{\sigma_a^2\omega_0^2}{2\lambda^2}\left(\left(\overrightarrow{k_0}\ \overrightarrow{j}/k_0\right)^2 + \frac{1}{\tan^2\beta}\right)$$

σ_a^2 is the dispersion of long wave elevations, ω_0^2 and $\overrightarrow{k_0}$ are the frequency and the wave vector of a long wave.

This proposed approach for space-time spectral analisys of sea image has been verified using the experimental spectra of sea surface images of cm waves derived during measurements from sea platform situated in Black Sea. On the Fig.2 it is presented the values of r.m.s. of long wave elevation h, evaluated using the expression for σ_f^2 for various conditions of observation.

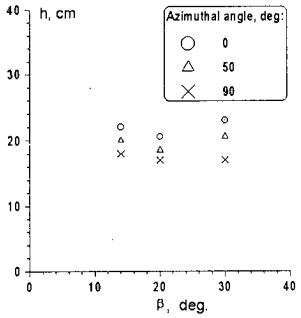


Fig.2. r.m.s. of long wave elevation.

The values of long wave elevation are close for various observation angles and azimutal angles of observation direction relative to direction of wind. So this developed expressions can be used for optical remote sensing of long surface waves using the space-time spectra of short waves.

REFERENCES

[1] Jane B., Riemer K. Two-dimensional Wave Number Spectra of Small-scale Water Surface Wave. Journ. Geoph. Res. v.95, N C7, p.11,531-11,546, 1990.

[2] E.M.Zuykova, A.G.Luchinin, and V.I.Titov.

Determination of the Characteristics of the Space-Time Spectra of Waves from an Optical Image of the Sea Surface. Izvestiya, Atmospheric and Oceanic Physics. 1985, v.21, N 10, p.833-837.

[3] V.I.Bakhanov et al. A Computer Ship Complex of Remote Sensing for Investigation of Ocean Subsurface Processes. Black Sea'92 Proceedings, Varna, Bulgaria, P.24-26, 1992.

[4] Bakhanov V.V. et al. Nonlocal Effects of Internal Waves on the Ocean Surface. IGARSS'94 Proceedings, Pasadena, USA, P.760, 1994.

[5] Titov V.I. et al. Investigation of Variations of Long Surface Wave Parameters by Optical Technique During JUSREX'92. IGARSS'94 Proceedings, Pasadena, USA, P.763,1994.

[6] Zuykova E.M., Titov V.I. Remote Sensing of Space-Time Characteristics of Gravity Waves by the Optical Methods. IAP RAS Proc. N 366, N.Novgorod, 15p., 1995.

[7] Perepelitcin O.V., Chernjavetc V.V. The Investigation of Surface Wind Drift in Sea. Izv. AS. Phisics of Atmosphere and Ocean. 1982, v.18, N 2, p.217-220.

A Coherent Scattering Model For Forest Canopies Based On Monte Carlo Simulation of Fractal Generated Trees

Yi-Cheng Lin and Kamal Sarabandi
Radiation Laboratory
Department of Electrical Engineering and Computer Science
The University of Michigan, Ann Arbor, MI 48109-2122
Tel :(313) 763-8162 FAX : (313) 747-2106
Email: yclin@umich.edu

Abstract – A coherent scattering model for tree canopies based on a Monte Carlo simulation of fractal generated trees is investigated in this study. In contrast to the incoherent models based on the radiative transfer theory, the present model is capable of preserving the relative phase of individual scatterer which give rise to the coherent effects and predicting the absolute phase of the backscattered field or equivalently the scattering phase center.

In the procedure for Monte Carlo simulation, first random generation of tree architectures is implemented by employing the Lindenmayer systems (L-systems), a convenient tool for creating fractal patterns of botanical structures. Since the generating code of tree structures is faithful in preserving the fine features of the simulated tree types, this study provides an efficient approach to examine the effects of tree structures on the radar backscatter. After generating a tree structure, the electromagnetic scattering problem is then treated by considering the tree structure as a cluster of scatterers comprised of cylinders (trunks and branches) and disks (leaves) with specified position, orientation, and size. The scattering solution is obtained by invoking the single scattering theory for a uniform plane wave illumination. In this solution scattering from individual tree components when illuminated by the mean field is computed and then added coherently. The mean field at a given point within the tree structure include the attenuation and phase change due to the scattering and absorption losses of vegetation particles. Finally, the backscattering coefficients are simulated at different frequencies based on the results of the Monte Carlo simulations obtained from a large number of independent trees.

INTRODUCTION

Radiative transfer theory [1] is the most widely used model for characterization of scattering from a forest canopy. When the medium consists of sparse scatterers that are small compared to the wavelength, RT theory can provide accurate statistics of radar backscatter including the phase difference of the scattering matrix elements. However, no information regarding the absolute phase can be extracted from a RT model. The other shortcoming of RT theory is its inability to account for the coherent effect that may exist between different scatterers or scattering mechanism. Moreover, recent investigations on scattering behavior of tree signatures have shown that both the backscattering and the attenuation are significantly influenced by tree architectures [2]. Therefore, a coherent scattering model seems crucial for the accurate estimation of radar behavior of forest canopies.

The purpose of this study is to develop an accurate coherent scattering model for tree canopies, which can preserve the effect of the tree structure on the radar response of forest canopies and can provide information about the absolute phase of the backscattered field. This model is comprised of three major components: (1) generation of tree structure, (2) evaluation of scattered fields, and (3) the Monte Carlo simulation. In the tree structure modeling, the L-systems [3] based on fractal theory, is employed to construct a tree-like structure as a tested target. The tree generating code is developed so that fine features of distinct tree structures can be preserved to any desired level of accuracy. In the scattering model, scattering from individual tree components when illuminated by the mean field is computed and then added coherently. The mean field at a given point within the tree structure, which accounts for the attenuation and phase change due to the scattering and absorption losses of vegetation particles, is calculated using Foldy's approximation [4]. Finally, a Monte Carlo simulation is performed on a large number of fractal generated trees to characterize the statistics of the backscattered signals.

RANDOM GENERATION OF TREES

Fractal theory is the most popular mathematical model used for relating the natural botanical structures to abstract geometries. Mandelbrot [5] defines the fractal as a set with Hausdorff-Besicovitch dimension strictly exceeding the topological dimension. In other words, the notion of fractal is defined only in the limit. However, in order to make the problem tractable, a finite curve can be considered an approximation of an infinite fractal as long as the significant properties of both are closely related. In the case of plant models, this distinctive feature is self-similarity which is kept through the derivation process.

The Lindenmayer systems (L-systems) is a versatile tool for plant pattern construction [3]. Its principal features lie on the easy generation of fractals and the realistic modeling of plant structures. The central concept of the L-systems is that of rewriting – a technique for defining a complex object using a set of simple patterns with rewriting rules or productions. Here,

0-7803-3068-4/96$5.00©1996 IEEE

we apply the L-systems to the development of branching structures.

The final stage of tree modeling is to integrate botanical knowledge of the architecture for the trees of interest, including the growth model, the pattern and orientation of leaves and branches, and the profile occupied by the entire tree given the age and number density. In this study, we focus on a real tree type, red maple, which is faithfully characterized and encoded, and then decoded by a computer based tree-generating code.

COHERENT SCATTERING MODEL

In this section, a coherent scattering model is developed to calculate the radar backscatter from the fractal generated trees. Once a tree is created, it is treated as a cluster of scatterers comprised of cylinders (trunks and branches) and disks (leaves) with specific position, orientation, and geometric shape and size. The entire tree is then illuminated by a plane wave, and the scattered field in the far zone is evaluated. To the first order scattering approximation, the backscatter from the entire tree is calculated from the coherent addition of the individual scattering terms. Hence, neglecting the multiple scattering among the scatterers, the total scattered field can be written as

$$\mathbf{E}^s = \frac{e^{ikr}}{r} \sum_{n=1}^{N} e^{i\phi_n} \mathbf{S}_n \cdot \mathbf{E}_o^i, \tag{1}$$

where N is the total number of the scatterers; $\mathbf{S}_n$ is the individual scattering matrix of the n-th scatterer and ϕ_n is the phase compensation accounting for the shifting of the phase reference from the local to the global phase reference, and is given by $\phi_n = (\hat{k}_i - \hat{k}_s) \cdot \mathbf{r_n}$, where $\mathbf{r_n}$ is the position vector of the n-th scatterer with measured in the global coordinate system.

In order to compute the scattering matrix of the n-th particle $\mathbf{S}_n$, consider the isolated particle above a ground plane. Ignoring the multiple scattering between the scatterer and its mirror image, the scattering matrix can be decomposed to four components : (1) direct component $\mathbf{S}_n^t$, (2) ground-scatterer component $\mathbf{S}_n^{tg}$, (3) scatterer-ground component $\mathbf{S}_n^{gt}$, and (4) ground-scatterer-ground component $\mathbf{S}_n^{gtg}$. Therefore, the individual scattering matrix $\mathbf{S}_n$ can be written as

$$\mathbf{S}_n = \mathbf{S}_n^t + \mathbf{S}_n^{gt} + \mathbf{S}_n^{tg} + \mathbf{S}_n^{gtg}, \tag{2}$$

where

$$\mathbf{S}_n^t = \mathbf{T}_n^i \cdot \mathbf{S}_n^0(-\hat{k}_i, \hat{k}_i) \cdot \mathbf{T}_n^i, \tag{3}$$

$$\mathbf{S}_n^{gt} = e^{i\tau_n} \mathbf{T}^t \cdot \mathbf{R} \cdot \mathbf{T}_n^r \cdot \mathbf{S}_n^0(-\hat{k}_r, \hat{k}_i) \cdot \mathbf{T}_n^i, \tag{4}$$

$$\mathbf{S}_n^{tg} = e^{i\tau_n} \mathbf{T}_n^i \cdot \mathbf{S}_n^0(-\hat{k}_i, \hat{k}_r) \cdot \mathbf{T}_n^r \cdot \mathbf{R} \cdot \mathbf{T}^t, \tag{5}$$

$$\mathbf{S}_n^{gtg} = e^{i2\tau_n} \mathbf{T}^t \cdot \mathbf{R} \cdot \mathbf{T}_n^r \cdot \mathbf{S}_n^0(-\hat{k}_r, \hat{k}_r) \cdot \mathbf{T}_n^r \cdot \mathbf{R} \cdot \mathbf{T}^t \tag{6}$$

with

$$k_r = k_i - 2\hat{n}_g(\hat{n}_g \cdot \hat{k}_i), \tag{7}$$

$$\tau_n = 2k_0(\mathbf{r_n} \cdot \hat{n}_g)(\hat{n}_g \cdot \hat{k}_r). \tag{8}$$

In the above expressions, $\hat{n}_g$ is the unit vector normal to the ground plane which in general can be tilted with respect to the global coordinate system. The optical lengths τ_n accounts for the extra path length. $\mathbf{S_n^0}$ is the scattering matrix of the n-th scatterer isolated in free space. $\mathbf{R}$ is the reflection matrix of the ground plane accounting for the reflection and polarization transformation due to the tilt ground plane. $\mathbf{T}_n^i$, $\mathbf{T}_n^r$, and $\mathbf{T}^t$ are the transmission matrix accounting for the different extinction portion within the random media as shown in the Fig. 2.

Forest stand can be represented by a layered structure according to its particle distribution statistics. The particle distribution as a function of height is needed for the calculation of extinction and can be obtained directly from the fractal model.

MONTE CARLO SIMULATION AND DISCUSSION

The radar backscatter from a distributed target is usually quantified in terms of the backscattering coefficient σ^0, define as the ratio of measured radar cross section to the illuminated area. To relate the total scattering matrix of a tree structure S to the backscattering coefficient σ^0, we assume no coherent correlation between trees, that is addition of powers instead of fields is needed to compute the backscatter from a number of trees. Hence σ^0 is proportional to the tree density D_t, i.e., $\sigma_{pq}^0 = 4\pi D_t < |S_{pq}|^2 >$.

A large number of fractal trees are created according to the prescribed tree features, such as leaf density, pdf of branch's orientation, and DBH distribution. Fig.1 shows a computer generated fractal tree based on the ground truth data collected at Raco Site, in Michigan's upper peninsula. In the traditional RT models, the forest canopies are simplified in terms of a two-layer structure. This treatment is not realistic in that location of the layer boundary between the crown and trunk layers is ambiguous and that the branches always have a non-uniform distribution in position, that is, the branches are located with larger diameter in lower region. Also the leaf density is usually higher in the upper layer of the canopy. In the present model, since the entire tree structure is well specified, it is easy to construct a multilayer model to characterize the vertical inhomogeneity of the tree structure. Fig. 1(b) shows the attenuation constants, α_m, profile of a seven layer canopy derived for the red maple forest stand. Using the Foldy's approximation, the expression for α_m is computed from :

$$\alpha_m = \frac{2\pi D_t}{k_0 d_m} Im\left(\sum_{n}^{layer-m} \mathbf{S}_n^0(\hat{k}, \hat{k}) \right) \tag{9}$$

where d_m is the thickness of the m-th layer; D_t is the tree density.

It is well known that the backscatter from forest canopies as a function of frequency is governed by various scattering

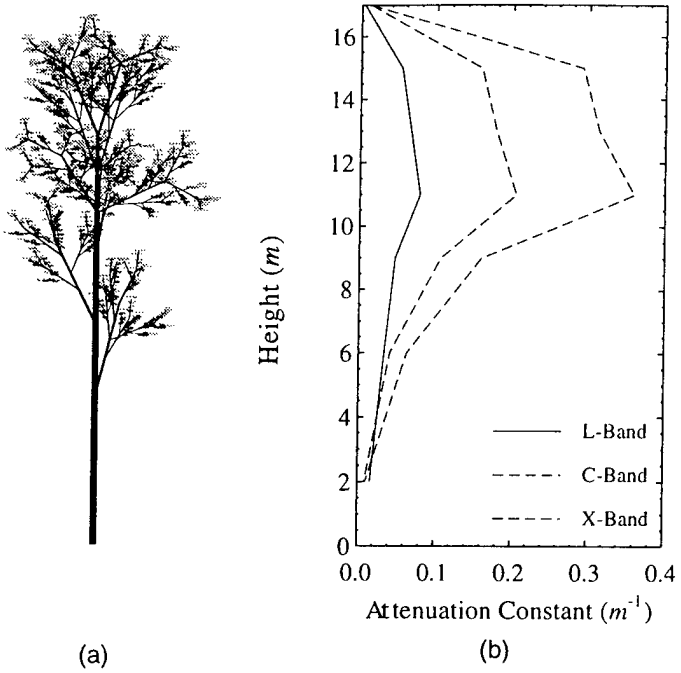


Figure 1: A red maple fractal generated tree (a) and its extinction profile (b).

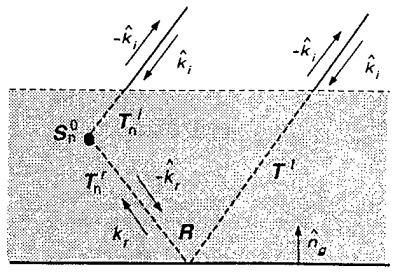


Figure 2: Extinction of a coherent wave in random media.

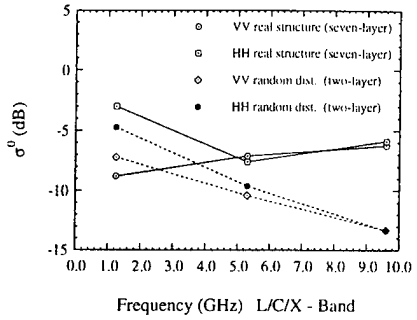


Figure 3: Comparison of the backscattering coefficients of the real structure andthe random distribution.

mechanisms. For instance, at lower frequencies the dominant backscatter term is the trunk-ground bounce, while at high frequencies the backscatter is mainly influenced by the direct scattering term from the crown layer. The difference between the backscatter from a forest stand using a multilayer model and a two-layer model is examined. In the two-layer model the forest is divided into a trunk layer (0-8 m) and a crown layer (8-17 m), and extinction parameters are averaged over the whole layer. Fig. 4 shows the results of this study where the backscattering coefficients are computed at different frequencies, L-band (1.25 GHz), C-band (5.3 GHz), and X-band (9,6 GHz). It is shown that at high frequencies the discrepancy between the two models increases.

REFERENCES

[1] F. T. Ulaby, K. Sarabandi, K. MacDonald, M. Whitt, and M. C. Dobson, "Michigan Microwave Canopy Scattering Model", *Int. J. Remote Sensing*, Vol. 11, NO. 7, pp. 1223-1253, 1990.

[2] M. L. Imhoff, "A theoretical analysis of the effect of forest structure on SAR backscatter and the remote sensing of biomass", *IEEE Trans. Geosci. Remote Sensing*, Vol. 33, No. 2, pp. 341-352, 1995.

[3] P. Prusinkiewicz and A. Lindenmayer, *The Algorithmic Beauty of Plants*, Spring-Verlag, New York, 1990.

[4] L. Tsang, J. A. Kong, and R. T. Shin, *Theory of Microwave Remote Sensing*, New York : Wiley Interscience, 1985.

[5] B. Mandelbrot, *Fractal Geometry of Nature*, New York, W. H. Freeman Company, 1983.

A Numerically Derived Electromagnetic Scattering Model for Grass Grain Heads

Paul Siqueira and Kamal Sarabandi
Radiation Laboratory
Electrical Engineering and Computer Science Department
University of Michigan, Ann Arbor, MI 48109-2122

Abstract

An easy to use semi-empirical model for the scattering from grass grain heads has been developed with the assistance of the T-Matrix method for determining scattered fields. It is shown that that physical grain model is significantly different than the more commonly employed dielectric cylinder model and that the derived empirical model can be used to efficiently replicate results obtained from the numerical analysis.

Introduction

The problem of electromagnetic scattering from vegetation covered surfaces has attained significant prominence in the past decade because of the advent of microwave remote sensors. In microwave remote sensing problems, the vegetation parameters such as height, vegetation biomass, moisture content, etc., may be the primary or secondary parameters to be retrieved from the measurements. In either case, an accurate electromagnetic scattering model for vegetation cover is necessary for a successful retrieval algorithm.

Vegetation components usually are modeled by simple, geometrical particles such as cylinders, disks, spheres and ellipsoids. Then, using the single scattering theory in conjunction with radiative transfer theory or an analytical wave approach, the backscattered power is predicted. In a number of situations where the vegetation particles do not appear as isolated individual particles, the single scattering formulation would fail. One such situation can be observed in wheat or barley plants when the cluster of grains appear atop of the plants in the middle of the growing season (Fig. 1). Recent, careful, backscatter measurements of a wheat field shows that at this level of maturity, the grain heads themselves overwhelmingly contribute to the backscatter response because this component of the radar's signal is unattenuated due to other components in the botanic layer. Therefore, an accurate scattering model for grain heads is needed to achieve an accurate backscatter prediction.

In most basic models, grain heads are usually approximated by a homogeneous finite cylinder, an approximation that has been shown to fail in predicting the backscatter measurements. In this paper, the electromagnetic scattering behavior of grain heads is studied using a rigorous numerical solution (Fig. 2). Here, the T-Matrix approach in conjunction with a physical

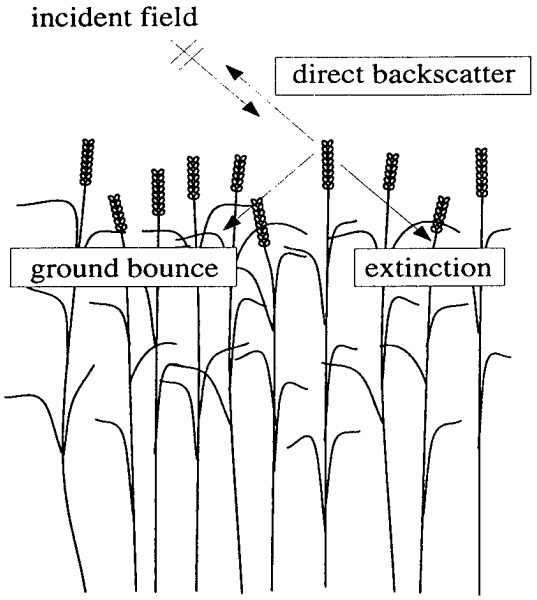


Figure 1: Wheat field model showing the three interactions of interest: (i) direct backscatter, (ii) ground bounce, and (iii) extinction. Because the signal interacts with the grain heads unattenuated, this contribution to the total backscattered field is the most significant one.

simulation for arranging the grains in a grain head cluster is employed to compute the backscatter, forward-scatter, and specular scatter fields. Empirical models based on the numerical simulations as a function of grain head dimensions, dielectric constant and incidence angle at L-, C-, and X-band frequencies are developed.

Deficiencies of the Dielectric Cylinder Model

The dashed lines in Fig. 3 illustrate the best fit dielectric cylinder to the numerically determined (solid line) scattering pattern of the grain head. The dielectric model is deficient for four fundamental reasons: (i) the dielectric cylinder model is based upon the solution for an infinite length cylinder, thus away from the broadside direction the model becomes inaccurate, (ii) a unique equivalent dielectric constant for the cylinder cannot be obtained due to the small number of grain particles that constitute the cylinder, (iii) the permittivity of the

0-7803-3068-4/96$5.00©1996 IEEE

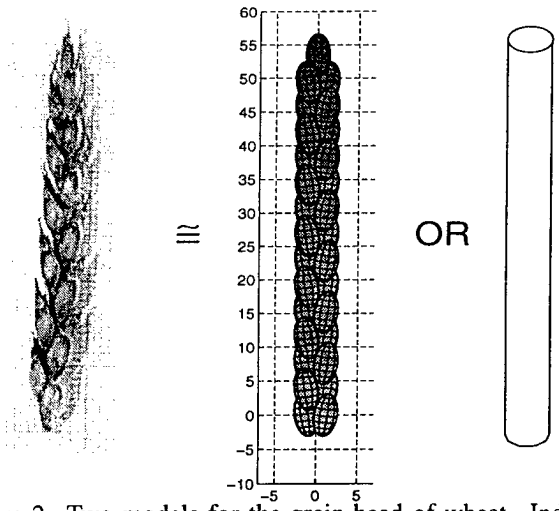


Figure 2: Two models for the grain head of wheat. Individual grains may contribute more strongly to the backscatter field than the "smooth" cylinder model most commonly employed.

grain head is anisotropic due to the vertical alignment of the individual grains (modeled here as ellipsoids), and (iv) the surface of the grain head is not smooth and thus it is expected that backscatter away from broadside incidence would be underestimated by the cylinder model.

Scattering Model

The electromagnetic scattering model presented in this paper is determined through a three-step process: (i) physical modeling of grain arrangement within the grain head (ii) T-Matrix solution of the specular, forward and back-scattered fields as a function of grain head height (6 to 8 cm), width (≈ 0.6 cm) and grain dielectric ($\mathrm{Re}(\epsilon) = 5$ to 25) at L, C and X-band and (iii) empirical modeling of the T-Matrix solutions.

The semi-empirical scattering formulae employed are based upon a simplified physical model of electromagnetic field interaction with a thin dielectric cylinder. This model is as follows:

$$
\begin{aligned}
E^{sca} &= LA[a_0 + a_2\cos(2\theta) + a_4\cos(4\theta)]E^{inc} \\
a_n &= e_{1n}P(\epsilon) + e_{2n}P^2(\epsilon) + e_{3n}P^3(\epsilon) \\
P(\epsilon) &= \begin{cases} (1-\epsilon) & \text{vv-pol} \\ (1-\epsilon)/(1+\epsilon) & \text{hh-pol} \end{cases}
\end{aligned}
$$

In the above set of equations, L and A are the grain head length and cross sectional area (in cm and cm^2) respectively, $P(\epsilon)$ is the polarizability tensor for a two-dimensional thin circular cylinder. The coefficients e_{mn} are in general functions of the frequency and polarization and are tabulated in Tables 1 - 6. For vertically polarized specular reflection, the incident field E^{inc} is multiplied by the vertical polarization reflection coefficient,

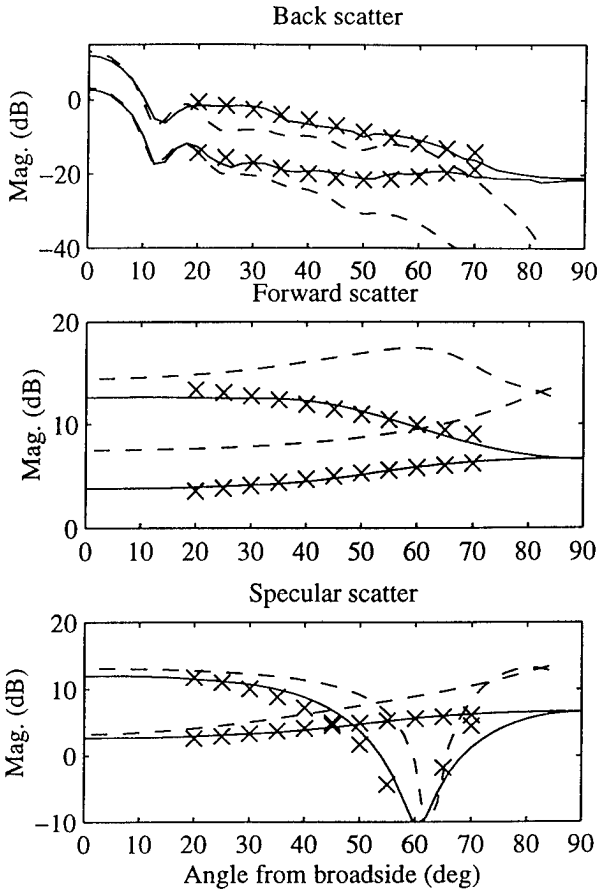


Figure 3: Sample scattered field patterns for the grain head (X-band, $\epsilon' = 15$, $\bar{L} = 71$ cm). Shown are results from the numerical model (solid lines), best fit dielectric cylinder model (dashed lines) and the empirical model (x's).

$R_{\|}$ given by

$$
R_{\|} = \frac{\sqrt{\epsilon_{\mathrm{brew}}}\cos\theta - \sqrt{1 - \sin^2\theta/\epsilon_{\mathrm{brew}}}}{\sqrt{\epsilon_{\mathrm{brew}}}\cos\theta + \sqrt{1 - \sin^2\theta/\epsilon_{\mathrm{brew}}}}
$$

where ϵ_{brew} is the permittivity related to the Brewster angle observed for vertically polarized incidence and is related to the permittivity of the wheat grains. A linear relation can be used to model this dependence as $\epsilon_{\mathrm{brew}} = b_0 + b_1(\epsilon - 1)$ where the coefficients b_0 and b_1 are given by

	L	C	X
b_0	1.86	1.60	1.97
b_1	0.10	0.14	0.066

It should be noted that while this model provides an excellent fit for $\mathrm{Re}(\epsilon)$ between 5 and 25, it does not approach the correct limiting value of $\epsilon_{\mathrm{brew}} = 1$ when $\epsilon = 1$. Thus the dielectric portion of this model should not be employed for grain permittivies

below 5 (at these permittivies, the grain heads would be uncharacteristically dry and would not be a common occurrence).

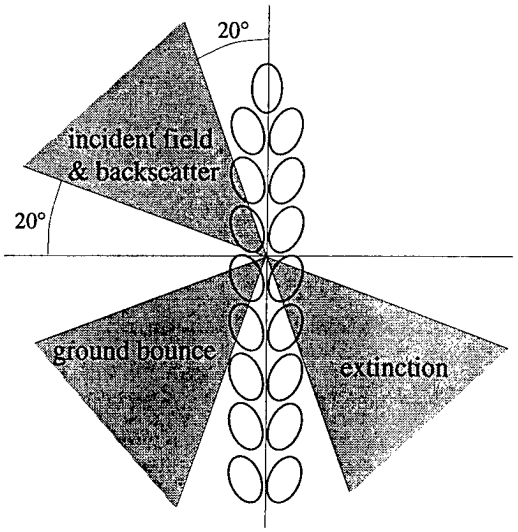


Figure 4: Illustration of the three scattering components of interest for the grain head and the validity regions ($20° < \theta < 70°$) of the empirical model.

Empirical Model Coefficients

Coefficients for the model given in Tables 1-6 were obtained by fitting the semi-empirical expression to the mean scattered fields evaluated by the T-matrix model for many realizations of the grain head. As a method of saving space, exponential components are given in parenthesis (i.e. $10^x \leftrightarrow (x)$)

Table 1: vv-forward scatter coeffs

freq	a_0	a_2
L	$e_{10} = 5.4(-4)$ $e_{20} = -3.0(-5)$ $e_{30} = 6.1(-7)$	$e_{12} = 1.7(-4)$ $e_{22} = -2.7(-6)$ $e_{32} = 0.0$
C	$e_{10} = 0.051$ $e_{20} = -1.1(-3)$ $e_{30} = 0.0$	$e_{12} = 0.026$ $e_{22} = -2.8(-4)$ $e_{32} = 0.0$
X	$e_{10} = 0.32$ $e_{20} = -0.018$ $e_{30} = 3.6(-4)$	$e_{12} = 0.10$ $e_{22} = -5.6(-3)$ $e_{32} = 1.0(-4)$

Table 2: hh-forward scatter coeffs

freq	a_0	a_2
L	$e_{10} = 1.4(-3)$ $e_{20} = 4.2(-4)$ $e_{30} = 0.0$	$e_{12} = 4.3(-7)$ $e_{22} = -5.6(-7)$ $e_{32} = 0.0$
C	$e_{10} = 0.15$ $e_{20} = 0.066$ $e_{30} = 0.0$	$e_{12} = 7.1(-3)$ $e_{22} = -0.022$ $e_{32} = 0.0$
X	$e_{10} = 0.63$ $e_{20} = 0.46$ $e_{30} = 0.0$	$e_{12} = 0.15$ $e_{22} = -0.40$ $e_{32} = 0.0$

Table 3: vv-backscatter coeffs

freq	a_0	a_2	a_4
L	$e_{10} = 4.2(-4)$ $e_{20} = -2.2(-5)$ $e_{30} = 4.5(-7)$	$e_{12} = 2.1(-4)$ $e_{22} = -3.9(-6)$ $e_{32} = 0.0$	0
C	$e_{10} = 7.6(-3)$ $e_{20} = -2.8(-5)$ $e_{30} = 0.0$	$e_{12} = 5.3(-3)$ $e_{22} = -5.3(-5)$ $e_{32} = 0.0$	0
X	$e_{10} = 0.030$ $e_{20} = -6.9(-4)$ $e_{30} = 0.0$	$e_{12} = 0.030$ $e_{22} = -8.7(-4)$ $e_{32} = 0.0$	$e_{14} = 0.023$ $e_{24} = -2.1(-3)$ $e_{34} = 4.7(-5)$

Table 4: hh-backscatter coeffs

freq	a_0	a_2	a_4
L	$e_{10} = 1.06(-3)$ $e_{20} = 3.0(-4)$ $e_{30} = 0.0$	$e_{12} = 3.1(-4)$ $e_{22} = 1.2(-4)$ $e_{32} = 0.0$	0
C	$e_{10} = 0.018$ $e_{20} = 8.1(-3)$ $e_{30} = 0.0$	$e_{12} = 0.14$ $e_{22} = -0.34$ $e_{32} = 0.21$	0
X	$e_{10} = 0.061$ $e_{20} = 0.028$ $e_{30} = 0.0$	$e_{12} = 0.039$ $e_{22} = -0.012$ $e_{32} = 0.0$	$e_{14} = 0.032$ $e_{24} = 4.4(-4)$ $e_{34} = 0.0$

Table 5: vv-specular scatter coeffs

freq	a_0	a_2
L	$e_{10} = 2.4(-3)$ $e_{20} = -1.7(-4)$ $e_{30} = 3.9(-6)$	$e_{12} = 1.6(-3)$ $e_{22} = -1.1(-4)$ $e_{32} = 2.5(-6)$
C	$e_{10} = 0.29$ $e_{20} = -0.018$ $e_{30} = 3.7(-4)$	$e_{12} = 0.20$ $e_{22} = -0.012$ $e_{32} = 2.1(-4)$
X	$e_{10} = 1.36$ $e_{20} = -0.091$ $e_{30} = 1.9(-3)$	$e_{12} = 0.81$ $e_{22} = -0.066$ $e_{32} = 1.4(-3)$

Table 6: hh-specular scatter coeffs

freq	a_0	a_2
L	$e_{10} = 1.4(-3)$ $e_{20} = 4.2(-4)$ $e_{30} = 0.0$	$e_{12} = -7.6(-7)$ $e_{22} = -1.2(-6)$ $e_{32} = 0.0$
C	$e_{10} = 0.15$ $e_{20} = 0.066$ $e_{30} = 0.0$	$e_{12} = 4.0(-3)$ $e_{22} = -0.024$ $e_{32} = 0.0$
X	$e_{10} = 0.58$ $e_{20} = 0.45$ $e_{30} = 0.0$	$e_{12} = 0.12$ $e_{22} = -0.42$ $e_{32} = 0.0$

References

[1] Y.M. Wang and W.C. Chew, "A Recursive T-Matrix Approach for the Solution of Electromagnetic Scattering by Many Spheres," IEEE Trans. Ant. Prop., 41(12), pp. 1633-1639, 1993.

Electromagnetic Scattering by Multiple Three-Dimensional Scatterers Buried under One-Dimensional Multi-Layered Media *

T. J. Cui† and W. Wiesbeck, Fellow, IEEE
Institut für Höchstfrequenztechnik und Elektronik, University of Karlsruhe,
Kaiserstr.12, 76128 Karlsruhe, Germany
(Telephon: +49 721/6086136, Telefax: +49 721/691865, E-mail: cui@iheaal.etec.uni-karlsruhe.de)

Abstract—**A general theory is presented for the electromagnetic scattering by multiple three-dimensional scatterers buried under one-dimensional multi-layered media. Closed-form formulations for the electric fields excited by an arbitrarily-oriented electric dipole under the layered media are investigated at first, from which electric field integral equations for the buried dielectric objects, conducting objects, and coupled electric field integral equations for multiple buried dielectric and conducting objects are then obtained.**

I. INTRODUCTION

The electromagnetic scattering and radiation by objects buried in one-dimensional medium have been investigated by many authors [1]-[3]. But most of them considered only two-dimensional case [1]-[2]. Michalski and Zheng [3] presented a general theory for the scattering by conducting objects buried in multiple layers, but it is not suitable for the mixed scattering problem of dielectric and conducting objects. For this reason, we have presented general theories for the TM wave and TE wave scattering by multiple dielectric and conducting cylinders buried under multi-layered media [4]-[5]. But we considered only the two-dimensional case.

In this paper, we investigate a general case – electromagnetic scattering by multiple three-dimensional dielectric objects and (or) conducting objects buried under the multi-layered media.

II. ELECTRIC FIELDS EXCITED BY AN ELECTRIC DIPOLE UNDER LAYERED MEDIA

See Fig.1, we consider a medium consisting of $n+1$ dielectric layers separated by n planar interfaces parallel to the xoy plane of a Cartesian coordinate system and located at $z = z_i, i = 1, 2, \ldots, n$. The relative permittivity of the ith layer is characterized by ϵ_i. The half spaces $z < 0$ and $z > z_n$ are homogeneous dielectric regions, whose relative permittivities are characterized by ϵ_b and ϵ_a. When the medium is lossy, ϵ_a, ϵ_b, and $\epsilon_i (i = 1, 2, \ldots, n)$ can be complex.

From the electromagnetic theory and Fourier transform theory, when an arbitrarily oriented electric dipole $I\vec{dl} = (\hat{x}I_x + \hat{y}I_y + \hat{z}I_z)dl$ is located at any point (x', y', z') under the layered media, its radiation electric fields can be formulated after a complicated derivation. In the region of $z < 0$,

$$E_{bu}(x,y,z) = -\frac{dl}{j4\pi\omega\epsilon_0\epsilon_b}\sum_{v=x,y,z}[W_{uv}(x-x', y-y', z-z') - \frac{j}{2\pi}F_{uv}(x-x', y-y', z+z')]I_v; \quad (1)$$

in the region of $z > z_n$,

$$E_{au}(x,y,z) = \frac{dl}{8\pi^2\omega\epsilon_0\epsilon_a}\sum_{v=x,y,z}Q_{uv}(x-x', y-y', z, z')I_v. \quad (2)$$

$$(u = x, y, z)$$

Here $W_{uv}(x,y,z)$ is defined as

$$W_{uu}(x,y,z) = \frac{\exp(-jk_bR)}{R^5}[u^2 f(k_bR) - R^2 g(k_bR)], \quad (3)$$

$$W_{uv}(x,y,z) = \frac{\exp(-jk_bR)}{R^5}uvf(k_bR), \quad (u \neq v) \quad (4)$$

in which $R = \sqrt{x^2+y^2+z^2}$, and $f(\cdot)$ and $g(\cdot)$ are functions

$$f(x) = x^2 - j3x - 3, \quad g(x) = x^2 - jx - 1; \quad (5)$$

and $F_{uv}(x,y,z)$ is Fourier integral defined as

$$F_{uv}(x,y,z) = \int_{-\infty}^{+\infty}\int_{-\infty}^{+\infty}\beta_b^{-1}\bar{F}_{uv}(k,\xi,\zeta)\cdot e^{j\beta_b z}e^{j(\xi x+\zeta y)}d\xi d\zeta, \quad (6)$$

in which, $\bar{F}_{uv}(k,\xi,\zeta)(u = x, y, z; v = x, y, z)$ are the following functions

$$\bar{F}_{xx}(k,\xi,\zeta) = (\zeta^2 + \beta_b^2)\vec{r_\perp} - \xi\beta_b\vec{r_{zx}}, \quad (7)$$

*This work is supported by the Alexander von Humboldt Foundation, Germany.

†T. J. Cui was with the Department of Electromagnetic Field Engineering, Xidian University, Xi'an 710071, P. R. China.

0-7803-3068-4/96$5.00©1996 IEEE

$$\bar{F}_{xy}(k,\xi,\zeta) = -\xi\zeta r_{\perp}^{\rightarrow} - \xi\beta_b r_{zy}^{\rightarrow}, \quad (8)$$

$$\bar{F}_{xz}(k,\xi,\zeta) = -\xi\beta_b r_{\parallel}^{\rightarrow}, \quad (9)$$

$$\bar{F}_{yx}(k,\xi,\zeta) = -\xi\zeta r_{\perp}^{\rightarrow} - \zeta\beta_b r_{zx}^{\rightarrow}, \quad (10)$$

$$\bar{F}_{yy}(k,\xi,\zeta) = (\xi^2+\beta_b^2) r_{\perp}^{\rightarrow} - \zeta\beta_b r_{zy}^{\rightarrow}, \quad (11)$$

$$\bar{F}_{yz}(k,\xi,\zeta) = -\zeta\beta_b r_{\parallel}^{\rightarrow}, \quad (12)$$

$$\bar{F}_{zx}(k,\xi,\zeta) = (\xi^2+\zeta^2) r_{zx}^{\rightarrow} - \xi\beta_b r_{\perp}^{\rightarrow}, \quad (13)$$

$$\bar{F}_{zy}(k,\xi,\zeta) = (\xi^2+\zeta^2) r_{zy}^{\rightarrow} - \zeta\beta_b r_{\perp}^{\rightarrow}, \quad (14)$$

$$\bar{F}_{zz}(k,\xi,\zeta) = (\xi^2+\zeta^2) r_{\parallel}^{\rightarrow}; \quad (15)$$

and $Q_{uv}(x-x', y-y', z, z')$ is also Fourier integral

$$Q_{uv}(x,y,z,z') = \int_{-\infty}^{+\infty}\int_{-\infty}^{+\infty} \beta_b^{-1} \bar{Q}_{uv}(k,\xi,\zeta) \cdot e^{-j(\beta_a z - \beta_b z')} e^{j(\xi x+\zeta y)} d\xi d\zeta, \quad (16)$$

and $\bar{Q}_{uv}(k,\xi,\zeta)(u=x,y,z; v=x,y,z)$ are defined as

$$\bar{Q}_{xx}(k,\xi,\zeta) = (\zeta^2+\beta_a^2) t_{\perp}^{\rightarrow} + \xi\beta_a t_{zx}^{\rightarrow}, \quad (17)$$

$$\bar{Q}_{xy}(k,\xi,\zeta) = -\xi\zeta t_{\perp}^{\rightarrow} + \xi\beta_a t_{zy}^{\rightarrow}, \quad (18)$$

$$\bar{Q}_{xz}(k,\xi,\zeta) = \xi\beta_a t_{\parallel}^{\rightarrow}, \quad (19)$$

$$\bar{Q}_{yx}(k,\xi,\zeta) = -\xi\zeta t_{\perp}^{\rightarrow} + \zeta\beta_a t_{zx}^{\rightarrow}, \quad (20)$$

$$\bar{Q}_{yy}(k,\xi,\zeta) = (\xi^2+\beta_a^2) t_{\perp}^{\rightarrow} + \zeta\beta_a t_{zy}^{\rightarrow}, \quad (21)$$

$$\bar{Q}_{yz}(k,\xi,\zeta) = \zeta\beta_a t_{\parallel}^{\rightarrow}, \quad (22)$$

$$\bar{Q}_{zx}(k,\xi,\zeta) = (\xi^2+\zeta^2) t_{zx}^{\rightarrow} + \xi\beta_a t_{\perp}^{\rightarrow}, \quad (23)$$

$$\bar{Q}_{zy}(k,\xi,\zeta) = (\xi^2+\zeta^2) t_{zy}^{\rightarrow} + \zeta\beta_a t_{\perp}^{\rightarrow}, \quad (24)$$

$$\bar{Q}_{zz}(k,\xi,\zeta) = (\xi^2+\zeta^2) t_{\parallel}^{\rightarrow}, \quad (25)$$

where $\beta_b = \sqrt{k^2\epsilon_b - \xi^2 - \zeta^2}$ and $\beta_a = \sqrt{k^2\epsilon_a - \xi^2 - \zeta^2}$ are the phase factors in Region b and a; and $r_{\perp}^{\rightarrow}$, $r_{\parallel}^{\rightarrow}$, $r_{zx}^{\rightarrow}$, $r_{zy}^{\rightarrow}$, $t_{\perp}^{\rightarrow}$, $t_{\parallel}^{\rightarrow}$, $t_{zx}^{\rightarrow}$ and $t_{zy}^{\rightarrow}$ are the reflection and transmission coefficients when the plane wave is incident from $\epsilon_b \rightarrow \epsilon_1 \rightarrow \cdots \rightarrow \epsilon_n \rightarrow \epsilon_a$. They are all functions of k, ξ, and ζ, which can be determined by boundary conditions.

III. ELECTRIC FIELD INTEGRAL EQUATIONS FOR BURIED DIELECTRIC OBJECTS

In this section, we consider the electromagnetic scattering problem for three-dimensional dielectric objects buried under the multi-layered media. See Fig.1, an arbitrarily shaped dielectric object with relative permittivity $\epsilon_r(x,y,z)$ and volume V is buried under the multi-layered media. An arbitrarily-polarized electromagnetic plane wave is incident to the interface $z = z_n$ from the upper space at a direction $\hat{t}_0$, as shown in Fig.1.

From the electromagnetic wave theory, the reflected electric field by the multi-layered media $\vec{E}_a^r(x,z)$, and the transmitted electric field through the multi-layered media $\vec{E}_a^t(x,z)$ can be easily obtained once the direction $\hat{t}_0$ and the polarization of the incident wave are given. From Fig.1, the transmitted electric field through the multi-layered media is just the incident electric field of the dielectric objects in Region b

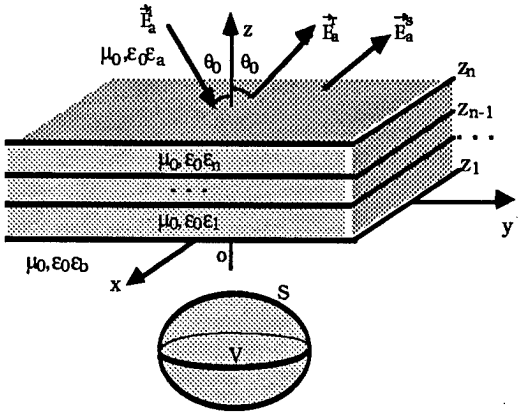


Figure 1: A scatterer buried under the multi-layered media

$$\vec{E}_b^i(x,y,z) = \vec{E}_a^t(x,y,z). \quad (26)$$

Under the illumination of the incident wave $\vec{E}_b^i(x,y,z)$, there will be internal electric field $\vec{E}_b(x,y,z)$ excited inside the dielectric object, which is the summation of scattered and incident electric fields

$$\vec{E}_b(x,y,z) = \vec{E}_b^s(x,y,z) + \vec{E}_b^i(x,y,z). \quad (27)$$

From the discussion in Section II, the scattered electric field generated by the dielectric object can be written as integral forms. Substituting the integrals into (27), we will obtain electric field integral equations for the internal electric fields inside the buried dielectric object

$$E_{bu}(x,y,z) + \frac{1}{4\pi}\int_V \left[\frac{\epsilon_r(x',y',z')}{\epsilon_b} - 1\right] \sum_{v=x,y,z} [W_{uv}(x-x', y-y', z-z') - \frac{j}{2\pi} F_{uv}(x-x', y-y', z+z')] E_{bv}(x',y',z') dx'dy'dz' = E_{bu}^i(x,y,z), \quad (28)$$

$$(u = x,y,z)$$

Then the scattered electric field in the upper space excited by the dielectric object is obtained

$$E_{au}^s(x,y,z) = \frac{j}{8\pi^2\epsilon_a}\int_V [\epsilon_r(x',y',z') - \epsilon_b] \sum_{v=x,y,z} Q_{uv}(x-x', y-y', z, z') E_{bv}(x',y',z') dx'dy'dz'. \quad (29)$$

Therefore, the total scattered electric field in the upper space can be written as

$$E_u^s(x,y,z) = E_{au}^s(x,y,z) + E_{au}^r(x,y,z). \quad (30)$$

$$(u = x,y,z)$$

IV. ELECTRIC FIELD INTEGRAL EQUATIONS FOR BURIED CONDUCTING OBJECTS

See Fig.1, when a plane wave is incident to the interface $z = z_n$ from the upper space, there will be electric current density $\vec{J}(x, y, z)$ excited on the surface of the conducting object. Now we consider an arbitrary point (x, y, z) on the surface $\mathbf{S}$. Suppose that the normal unit vector at point (x, y, z) is $\hat{n}$

$$\hat{n} = \hat{x}\sin\vartheta\cos\varphi + \hat{y}\sin\vartheta\sin\varphi + \hat{z}\cos\vartheta, \quad (31)$$

which is known because the shape of the surface $\mathbf{S}$ is given. In the tangent plane at point (x, y, z), we choose two orthogonal unit vectors $\hat{t}_1$ and $\hat{t}_2$:

$$\hat{t}_1 = \hat{x}\sin\gamma_1\cos\alpha_1 + \hat{y}\sin\gamma_1\sin\alpha_1 + \hat{z}\cos\gamma_1, \quad (32)$$

$$\hat{t}_2 = \hat{x}\sin\gamma_2\cos\alpha_2 + \hat{y}\sin\gamma_2\sin\alpha_2 + \hat{z}\cos\gamma_2 \quad (33)$$

which satify $\hat{t}_1 \times \hat{t}_2 = \hat{n}$. So when one of the angles γ_1, α_1, γ_2 or α_2 is given, the others can be determined.

Because the induced electric current density $\vec{J}(x, y, z)$ is distributed on the surface of the conducting object, we can write $\vec{J}(x, y, z)$ as

$$\vec{J}(x, y, z) = \hat{t}_1 J_1(x, y, z) + \hat{t}_2 J_2(x, y, z). \quad (34)$$

From the results in Section II, the scattered electric field excited by the conducting object can be obtained

$$E^s_{bu}(x, y, z) = -\frac{1}{j4\pi\omega\epsilon_0\epsilon_b}\int_{\mathbf{S}}\sum_{v=x,y,z}[W_{uv}(x-x', y-y', z-z') - \frac{j}{2\pi}F_{uv}(x-x', y-y', z+z')]J_v(x', y', z')dS', \quad (35)$$

where $u = x, y, z$; and

$$J_x = J_1\sin\gamma_1\cos\alpha_1 + J_2\sin\gamma_2\cos\alpha_2, \quad (36)$$

$$J_y = J_1\sin\gamma_1\sin\alpha_1 + J_2\sin\gamma_2\sin\alpha_2, \quad (37)$$

$$J_z = J_1\cos\gamma_1 + J_2\cos\gamma_2. \quad (38)$$

Using the boundary condition of the conducting object, that is the tangent components of electric field equal zero on the surface $\mathbf{S}$, so we have

$$-\sin\gamma_l\cos\alpha_l E^s_{bx}(x, y, z) - \sin\gamma_l\sin\alpha_l E^s_{by}(x, y, z) - \cos\gamma_l E^s_{bz}(x, y, z) = E^i_{t_l}(x, y, z), \quad (39)$$

where $l = 1, 2$; and

$$E^i_{t_l}(x, y, z) = \sin\gamma_l\cos\alpha_l E^i_{bx}(x, y, z) + \sin\gamma_l\sin\alpha_l E^i_{by}(x, y, z) + \cos\gamma_l E^i_{bz}(x, y, z). \quad (40)$$

Substituting (35) into (39), we obtain the electric field integral equations for the induced electric currents $J_1(x, y, z)$ and $J_2(x, y, z)$ on the surface of the conducting object, from which the scattered electric field in the upper space can be formulated

$$E^s_{au}(x, y, z) = \frac{1}{8\pi^2\omega\epsilon_0\epsilon_a}\int_{\mathbf{S}}\sum_{v=x,y,z}Q_{uv}(x-x', y-y', z, z')J_v(x', y', z')dS', \quad (u = x, y, z). \quad (41)$$

V. ELECTRIC FIELD INTEGRAL EQUATIONS FOR MULTIPLE BURIED OBJECTS

For a general case, there supposed to be M dielectric objects $\mathbf{V}_1, \ldots, \mathbf{V}_M$ and N conducting objects $\mathbf{S}_1, \ldots, \mathbf{S}_N$ buried under the multi-layered media. Using the similar procedures to those in Section III and Section IV, and combining them efficiently, we will obtain coupled electric field integral equations for the internal electric fields inside the buried dielectric objects and induced electric currents on the surfaces of the buried conducting objects. Furthermore, the scattered electric field in the upper region $z > z_n$ is also available, which are not written here for pages reason.

VI. CONCLUSIONS

Similar to the two-dimensional cases [4]-[5], the theory presented here is also suitable for lossy case and one-dimensional inhomogeneous medium, and has a clear physical significance.

References

[1] X.B. Xu and C.M. Butler, "Scattering of TM excitation by coupled and partially buried cylinders at the interface between two media," IEEE Trans. Antennas Propagat., vol.AP-35, pp.529-538, 1987.

[2] X.B. Xu and C.M. Butler, "Current induced by TE excitation on coupled and partially buried cylinders at the interface between two media," IEEE Trans. Antennas Propagat., vol.AP-38, pp.1823-1828, 1990.

[3] K.A. Michalski and D. Zheng, "Electromagnetic scattering and radiation by surfaces of arbitrary shape in layered media, Part I: Theory; Part II: Implementation and results for contiguous half-spaces," IEEE Trans. Antennas Propagat., vol.AP-38, pp.335-352, 1990.

[4] T.J. Cui and W. Wiesbeck, "TM wave scattering by multiple two-dimensional scatterers buried under one-dimensional multi-layered media," Proc. IEEE International Geoscience and Remote Sensing Symposium, Lincoln, 27-31 May, 1996.

[5] T.J. Cui and W. Wiesbeck, "TE wave scattering by multiple two-dimensional scatterers buried under one-dimensional multi-layered media," Proc. IEEE International Geoscience and Remote Sensing Symposium, Lincoln, 27-31 May, 1996.

THE MODIFIED RAYLEIGH-GANS APPROACH AND SCATTERING WAVES

Dr. Osman YILDIRIM
Hava Harp Okulu
Department of Electronics
Turkish Airforce Academy,34807 Istanbul,Turkey
Phone:0(212)6632490 Fax:90(212)5741819

Abstract -- The scattering of electromagnetic waves by an homogenous isotropic dielectric shapes has been investigated using a quasistatic approximation. In this study, the modified Rayleigh-Gans approach is developed and applied to a circular thin disc, rod, and sphere whose physical sizes are small compared to wavelength.

The scattered field relationships are used to obtain the radar cross section equations in closed form and also normalized absorption and scatttering cross sections computed by using internal fields.

INTRODUCTION

It is well-known that the atmospheric propagation of millimeter waves is strongly affected by certain meteorological phenomena. The attenuation of electromagnetic waves of centimeter or millimeter wavelengths in a clear atmosphere near ground level is negligible for most practical purposes. The degree of attenuation of millimeter waves is related in a complex way to meteorological conditions along the path of propagation.

Equations for absorption and scattering have been derived by Gustav Mie(1908). Mie's work has been restated by Straton(1941), Golstein(1946), Kerr(1951) and by Van de Hulst(1957).

ANALYSIS

A plane electromagnetic wave incident on an arbitrarily oriented dielectric object. The plane wave is assumed to have polarization $\vec{q}$ and to be propagated in the $\vec{i}$ direction, then

$$\vec{E}_i(\vec{r}) = \vec{q}E_o e^{jk_o\vec{i}.\vec{r}} \tag{1}$$

Where E_o is the magnitude of incident wave, k_o is propagation constant. $\vec{i}$ is the unit vector in the direction of wave propagation whereas $\vec{q}$ is the vector for the direction of its polarization.

An isolated scatterer can be electromagnetically characterized by specifying its far field scattering properties via the scattering amplitude, $F(\vec{o},\vec{i})$. The wave is incident upon a particle whose dielectric constant has both real and imaginar parts. That is, the particle may be lossy and inhomogeneous.

In the case of $R > D^2/\lambda$ the scattered field, E_s, behaves as a spherical wave and is equal to[1]

$$E_s(r) = F(\vec{o},\vec{i})e^{jkR}/R \tag{2}$$

$$F(\vec{o},\vec{i}) = \frac{k^2(\epsilon_r - 1)}{4\pi}\int_V -\vec{o}\wedge[\vec{o}\wedge\vec{E}(\vec{r'})]dV' \tag{3}$$

where $F(\vec{o},\vec{i})$ indicates the amplitude, phase and polarization of the scattered field.

We consider a particle(an ellipsoid) whose surface is given by

$$\frac{x^2}{a^2}+\frac{y^2}{b^2}+\frac{z^2}{c^2} = 1 \tag{4}$$

and the incident field, E_i, has component E_{ix}, E_{iy}, E_{iz} in the x, y, and z directions, respectively. For calculation cross-sections, let us assume that an ellipsoid's axes coinside with x, y, and z axis of cartesian coordinate system which is shown in Fig.1.

We choose $\theta_i = -\pi/2$, than $\vec{x}_o = \vec{h}_o$

$$\vec{i} = \sin\theta_i\vec{y}_o - \cos\theta_i\vec{z}_o \tag{5}$$

Field components of the field inside the particle are given by

$$E_x = \frac{E_{ix}}{[1+\frac{abc}{2}(\epsilon_r-1)A_x]} \tag{6}$$

$$E_y = \frac{E_{iy}}{[1+\frac{abc}{2}(\epsilon_r-1)A_y]} \tag{7}$$

$$E_z = \frac{E_{iz}}{[1+\frac{abc}{2}(\epsilon_r-1)A_z]} \tag{8}$$

0-7803-3068-4/96$5.00©1996 IEEE

The constants A_x, A_y, and A_z are defined as;

$$A_x = \int_0^\infty \frac{ds}{(s+a^2)[(s+b^2)(s+c^2)(s+a^2)]^{1/2}} \quad (9)$$

$$A_y = \int_0^\infty \frac{ds}{(s+b^2)[(s+b^2)(s+c^2)(s+a^2)]^{1/2}} \quad (10)$$

$$A_z = \int_0^\infty \frac{ds}{(s+c^2)[(s+b^2)(s+c^2)(s+a^2)]^{1/2}} \quad (11)$$

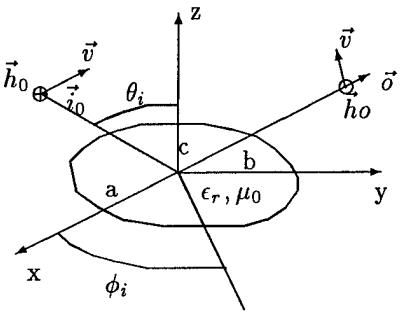


Fig. 1. Geometry of Scattering

We assume that the incident field is initially uniform the internal field within the ellipsoid is also uniform. The polarization factors L_1, L_2, L_3 are defined as [2]

$$L_1 = \frac{abc}{2} A_x \quad (12)$$

$$L_2 = \frac{abc}{2} A_y \quad (13)$$

$$L_3 = \frac{abc}{2} A_z \quad (14)$$

$$L_1 + L_2 + L_3 = 1 \quad (15)$$

By rearranging the above equations, we can obtainthe field inside the ellipsoid as

$$E_y = \frac{E_{iy}}{[1 + L_1(\epsilon_r - 1)]} \quad (16)$$

Since $ka << 1$, the field inside ellipsoid is constant. Then we assume

$$E_x = E_y = \frac{1}{[1 + L_1(\epsilon_r - 1)]} \quad (17)$$

The absorption cross-section is given by [1]

$$Q_{ab} = k\epsilon_r^* \int_V |\vec{E}(\vec{r})|^2 dV \quad (18)$$

where $\vec{E}(\vec{r})$ is the electric field inside the ellipsoid whereas ϵ_r^* is the imaginary part of relative dielectric constant of ellipsoid. By using value of $\vec{E}(\vec{r})$ for ellipsoid, we can obtain

$$Q_{abh} = \frac{k\epsilon^* V}{|1 + L_1(\epsilon_r - 1)|^2} \quad (19)$$

By considering vertical value of electric field inside the ellipsoid, we can write for incident field [3]

$$\vec{E}_v = [|\vec{E}_y|^2 + |\vec{E}_z|^2]^{1/2} \quad (20)$$

In a similiar way, vertical absorption cross-section can be found as

$$Q_{abv} = k\epsilon^* V \left(\frac{\cos^2\theta_i}{|1 + L_1(\epsilon_r - 1)|^2} + \frac{\sin^2\theta_i}{|1 + L_3(\epsilon_r - 1)|^2}\right) \quad (21)$$

where $L_3 = 1 - 2L_1$

We generalize this calculation when θ and ϕ are different from zero. From the geometry of scattering, we can take as a special case $\theta_i = 0$ then

$$Q_s = Q_{sh} = Q_{sv} = \frac{k^4 V^2}{6\pi} \left|\frac{\epsilon_r - 1}{1 + L_1(\epsilon_r - 1)}\right|^2 \quad (22)$$

Clearly, this equation is in agreement with [4]. This agreement is also valid for

$$Q_{abh} = Q_{abv} = k\epsilon_r^* V \left|\frac{1}{1 + L_1(\epsilon_r - 1)}\right|^2 \quad (23)$$

CONCLUSION

Scattering amplitude and cross sections for different isotropic dielectric geometric shapes has been computed under quasi-static approximation. It is so called modified Rayleigh-Gans approximation which is presented to calculate scattering properties of dielectric bodies that are small compared to wave length in at least one direction. For very thin or flat particles, which are arbitrarily oriented, if thinness criterion is satisfied the results are valid in frequency regions.

Numerical results for disc, rod and sphere in horizontal and vertical cases. Results are presented in Fig.2 to 6. Normalized cross sections versus diameter in Fig.2-6 show that horizontal cross section is a little bit greater than vertical case.

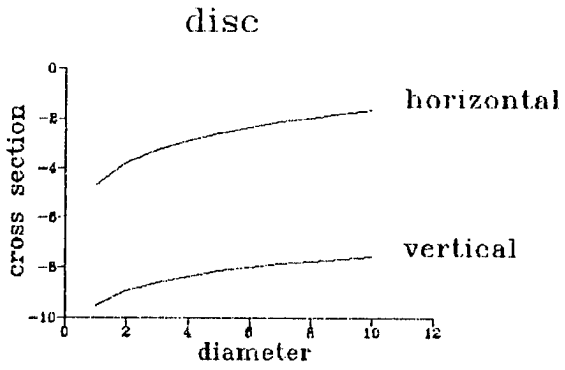


Fig. 2:

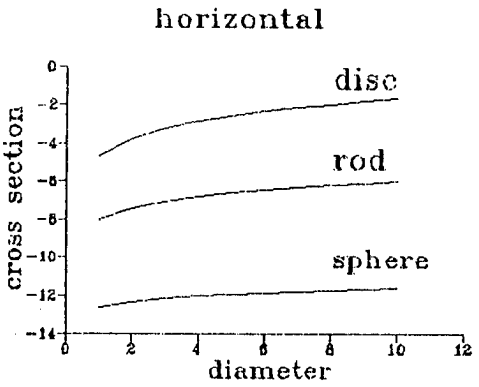


Fig. 5:

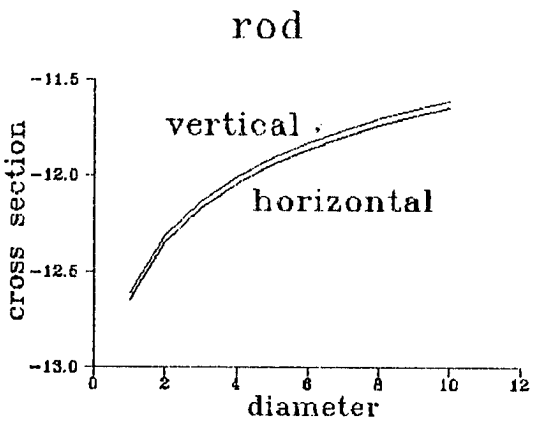


Fig. 3:

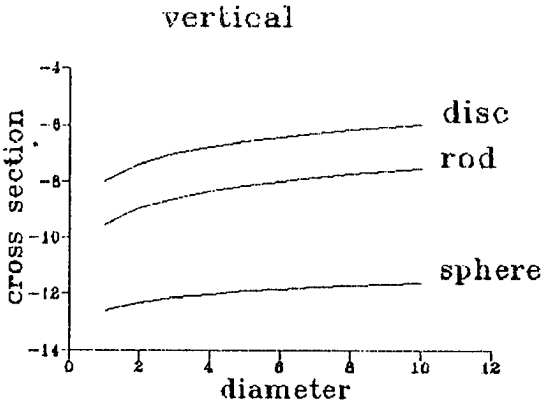


Fig. 6:

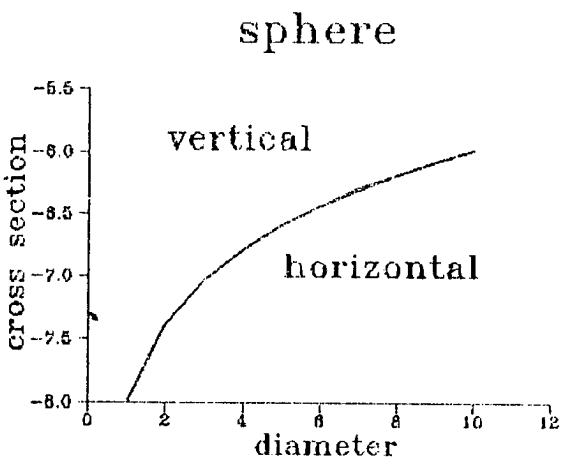


Fig. 4:

REFERENCES

[1] A.Ishimaru, Wave propagation and scattering in random media,Academic Press, New York,1978

[2] H.C.Van de Hulst, Light scattering by small particles, Dover, NewYork, 1957

[3] O.Yildirim, Atmospheric effects due to different particle shapes on propagation, M.Sc.Thesis, Bosphorus University, 1986

[4] D.M.LeVine, The radar cross-section of dielectric discs, IEEE Trans. on Antennas and Propagation, Vol.AP-32,1984

AN INVERSE ALGORITHM FOR INTEGRAL EQUATION FORMULATION OF DIELECTRIC LOADED CAVITIES

K.F. Sabet[1], K. Sarabandi[2], J.G. Yook[2], and L.P.B. Katehi[2]
[1] EMAG Technologies, Inc.
2901 Hubbard Rd., Suite E-116, Ann Arbor, MI 48105
Tel: (313) 769-4587, Fax: (313) 747-6663
[2] Radiation Laboratory
Department of Electrical Engineering and Computer Science
The University of Michigan, Ann Arbor, MI 48109-2122
Tel: (313) 936-1575, Fax: (313) 747-2106

I. INTRODUCTION

In a large number of microwave remote sensing problems, accurate knowledge of the dielectric constant of natural media such as vegetation leaves, branches, stems, and soil is crucial in the estimation of the desired biophysical parameters from the measured data. In the conventional cavity perturbation method, a sample of the test material with dimensions much smaller than the wavelength is placed in a high-quality-factor microwave cavity, and then the resonant frequency and the quality factor of the loaded cavity are measured. Comparing the resonant characteristics of the empty (unloaded) and loaded cavity, one can estimate the real and imaginary parts of the dielectric constant from analytical expressions based on the perturbation theory [1]. Besides practical limitations such as the cavity and sample geometry and size, a major drawback of the cavity perturbation method is its lack of accuracy in measuring the imaginary part of the dielectric constant of low-loss dielectric materials. The change in the quality factor of the cavity is proportional to the total dissipated power in the dielectric sample. When both the dielectric loss tangent and the sample volume are very small, the change in the quality factor becomes extremely small and falls within the measurement errors. To circumvent this difficulty, larger pieces of the material with sizes well beyond the limits of the perturbation theory are needed so that the resulting shift in the cavity characteristics can be measured accurately.

In this paper, we extend the resonant cavity technique for dielectric constant measurement beyond the limitations of the perturbation method. The new approach incorporates a full-wave simulation of the loaded cavity structure into the inverse measurement problem. Thus, the size of the material sample can be taken arbitrarily large as long as it does not disturb the coupling mechanism of the resonator. For the forward measurement problem, an integral formulation of the related boundary value problem is developed and solved numerically using the method of moments (MoM). The MoM results are validated independently by comparing to the results based on the finite element method (FEM). For the inverse measurement problem, a numerically efficient inversion algorithm based on the eigen-analysis of the impedance matrix is employed. In this algorithm the dependence of the complex dielectric constant on the inverse of the impedance matrix is made explicit, thereby establishing simple polynomials relationships between the dielectric constant and the resonant characteristics of the cavity. Both forward and inverse problems are illustrated through simulation examples.

II. THE FORWARD PROBLEM

Fig. 1 shows the geometry of a rectangular dielectric-loaded cavity resonator with typical excitation and observation points. The sample material is also assumed to have a rectangular shape. In the forward measurement problem, the resonant frequency and quality factor of the loaded cavity resonator are to be determined given the complex dielectric constant of the sample. In an integral formulation, the dielectric material can be replaced by an equivalent volume polarization current $\boldsymbol{J_p(r)}$ defined in the following manner:

$$\boldsymbol{J_p(r)} = jk_0Y_0\left[\epsilon(\boldsymbol{r}) - 1\right]\boldsymbol{E(r)}, \tag{1}$$

where k_0 and $Y_0 = 1/Z_0$ are the propagation constant and characteristic admittance of the free space, respectively, $\epsilon(\boldsymbol{r})$ is the relative permittivity as a function of the position vector $\boldsymbol{r}$, and $\boldsymbol{E(r)}$ is the total electric field in the sample. It is clear that $\boldsymbol{J_p(r)}$ vanishes outside the sample volume. By considering the dyadic Green's function of the structure, denoted by $\bar{\bar{G}}_e(\boldsymbol{r} \mid \boldsymbol{r'})$, one can incorporate

0-7803-3068-4/96$5.00©1996 IEEE

the presence of the cavity resonator into the integral formulation [2]. The total electric field at every point inside the cavity is then expressed in the following form:

$$\boldsymbol{E}(\boldsymbol{r}) = -jk_0 Z_0 \int_V \bar{\bar{\boldsymbol{G}}}_e(\boldsymbol{r} \mid \boldsymbol{r}') \cdot \boldsymbol{J}_p(\boldsymbol{r}') dv' + \boldsymbol{E}^i(\boldsymbol{r}), \tag{2}$$

where V denotes the volume occupied by the dielectric sample, and $\boldsymbol{E}^i(\boldsymbol{r})$ is the incident field due to the excitation. Equations (1) and (2) lead to an integral equation, which can be solved numerically using the method of moments. To this end, the unknown electric field inside the sample is discretized using standard brick elements (3-D pulse basis functions). Using Galerkin's technique for testing, the integral equation is reduced to a linear system of the following form:

$$\bar{\bar{\boldsymbol{K}}} \cdot \bar{a} = \bar{b}, \tag{3}$$

where $\bar{\bar{\boldsymbol{K}}}$ is the moment matrix, and $\bar{a}$ and $\bar{b}$ are the amplitude and excitation vectors, respectively. By solving this linear system, the unknown amplitude vector is determined, and from (2) one can compute the electric field at any point inside the cavity.

A rectangular cavity of dimensions 4cm×3cm×2cm loaded with a dielectric sample of permittivity ϵ=6 is considered as an example. Fig. 2 compares the results of the MoM and FEM codes for the resonant frequency of the loaded cavity as a function of the ratio of the sample dimensions to the cavity dimensions. It has been assumed that the material sample is centered on the floor of the cavity, and its dimensions are similar to the cavity dimensions within a scale ratio of $r = a/A = b/B = c/C$. Fig. 3 shows the resonant response of the same cavity loaded with a sample of dimensions 10mm×7.5mm×5mm ($r = 0.25$). In this case, the sample has a complex relative permittivity of $\epsilon = 6 - j0.1$ corresponding to a loss tangent equal to $\tan\delta = 0.0167$. The excitation is applied at the center of the cavity ceiling, and the field response is sampled at the opposite point on the cavity floor. The resonant frequency of the loaded cavity is 5.8428 GHz and its quality factor due to the dielectric loss is 730. Note that in this case the volume fraction of the dielectric sample is 1/64.

III. THE INVERSE PROBLEM

From a transmission measurement one can determine the shift in the resonant frequency and the quality factor of the cavity due to the material loading. Given these information, the unknown complex dielectric constant of the material sample is sought in the inverse measurement problem. The solution of the inverse problem is greatly facilitated if we exploit an interesting feature of the integral formulation as suggested in [3]. Note that by taking the polarization current as the unknown quantity, from (1) and (2) we can derive the following integral equation:

$$\delta\epsilon^{-1}\boldsymbol{J}_p(\boldsymbol{r}) - k_0^2 \int_V \bar{\bar{\boldsymbol{G}}}_e(\boldsymbol{r} \mid \boldsymbol{r}') \cdot \boldsymbol{J}_p(\boldsymbol{r}') dv' = jk_0 Y_0 \boldsymbol{E}^i(\boldsymbol{r}). \tag{4}$$

Now, discretizing equation (4) using a similar MoM expansion and testing it by Galerkin's technique generates a new linear system of the following form:

$$\left[\delta\epsilon^{-1}\bar{\bar{\boldsymbol{I}}} - \bar{\bar{\boldsymbol{Z}}}\right] \cdot \bar{a} = \bar{b}, \tag{5}$$

where $\bar{\bar{\boldsymbol{I}}}$ is the identity matrix, and $\bar{\bar{\boldsymbol{Z}}}$ is another matrix which is computed by the numerical integration of the dyadic Green's function over the brick elements. This latter matrix, however, is independent of the unknown complex permittivity and depends only on the geometry of the structure as well as the frequency.

In the inverse problem we need to compute the $\bar{\bar{\boldsymbol{Z}}}$ matrix only at the resonant frequency f_0 and one 3-dB frequency f_1. We search in the complex ϵ-plane for a point $\epsilon' - j\epsilon''$ which maximizes the cavity response at f_0, and then reduces it by 3 dB at f_1. Noting that $\bar{\bar{\boldsymbol{Z}}}$ is a real and symmetric matrix, it can be decomposed, according to the eigenvalue theory, in the following manner:

$$\bar{\bar{\boldsymbol{Z}}} = \bar{\bar{\boldsymbol{Q}}} \cdot \bar{\bar{\boldsymbol{\Lambda}}} \cdot \bar{\bar{\boldsymbol{Q}}}^{-1}, \tag{6}$$

where $\bar{\bar{\boldsymbol{\Lambda}}}$ is a diagonal matrix. In practice, first $\bar{\bar{\boldsymbol{Z}}}$ is reduced to a tridiagonal matrix using the Householder method, and then we compute the eigenvalues and eigenvectors of the tridiagonal matrix using the QR algorithm [4]. It can be shown that the electric field at any point inside the cavity can be written in the following way:

$$\boldsymbol{E}(\boldsymbol{r}_0) = \bar{\bar{\boldsymbol{H}}} \cdot \bar{\bar{\boldsymbol{Q}}} \cdot \bar{\bar{\boldsymbol{\Gamma}}}(\epsilon) \cdot \bar{\bar{\boldsymbol{Q}}}^{-1} \cdot \bar{b}, \tag{7}$$

where $\bar{\bar{\boldsymbol{H}}}$ is related to the dyadic Green's function and is a function of the observation point $\boldsymbol{r}_0$, and $\bar{\bar{\boldsymbol{\Gamma}}}(\epsilon)$ is a diagonal matrix whose diagonal elements are rational functions of the unknown complex dielectric constant ϵ. In view of equation (7), we now need to maximize $\mid \boldsymbol{E}(\boldsymbol{r}_0, f_0, \epsilon) \mid$ as a function of complex ϵ subject to the condition that $\mid \boldsymbol{E}(\boldsymbol{r}_0, f_1, \epsilon) \mid = \frac{1}{\sqrt{2}} \mid \boldsymbol{E}(\boldsymbol{r}_0, f_0, \epsilon) \mid$. This optimization problem can be easily solved using the conjugate gradient method [4]. As an example, consider the same cavity treated in the forward problem. Given the measured resonant frequency and quality factor of the loaded cavity to be f_0 =5.8428 GHz and Q_d=730, the unknown complex dielectric constant of the sample is found to be

$\epsilon = 6.006 - j0.0996$. The maximization process is illustrated in Fig. 4, which shows the variation of the magnitude of the electric field given by (7) as a function of the the real part of the dielectric constant ϵ'.

IV. CONCLUSION

An efficient full-wave approach has been presented for the solution of the inverse cavity measurement problem. This rigorous approach does not suffer from the limitations of the conventional perturbation theory and is applicable to dielectric samples with arbitrary dimensions and electrical parameters.

ACKNOWLEDGMENTS

This work was supported in part by the U.S. Department of Commerce, National Institute of Standards and Technology.

REFERENCES

[1] R.F. Harrington, *Time-Harmonic Electromagnetic Fields*, pp.321-326, New York: McGraw-Hill, 1961.
[2] C-T. Tai, *Dyadic Green's Functions in Electromagnetics*, New Jersey: IEEE Press, 1994.
[3] K. Sarabandi, "A technique for dielectric measurement of cylindrical objects in a rectangular waveguide," *IEEE Trans. Instrum. Meas.*, vol. 43, no. 6, Dec. 1994.
[4] A. Jennings and J.J. McKeown, Matrix Computation, New York: John Wiley & Sons, 1992.

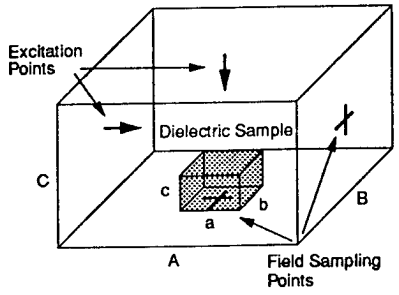


Fig. 1. Geometry of a loaded cavity with typical excitation and sampling points.

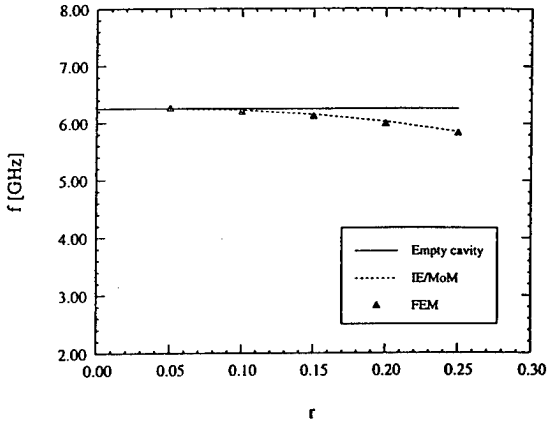


Fig. 2. Variation of the resonant frequency of the loaded cavity as a function of sample size.

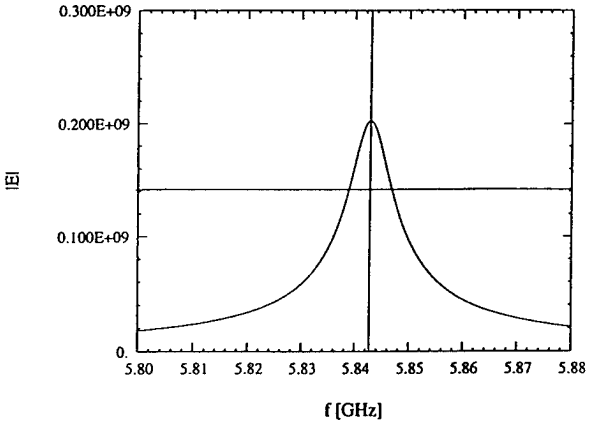


Fig. 3. Cavity response to a lossy dielectric sample.

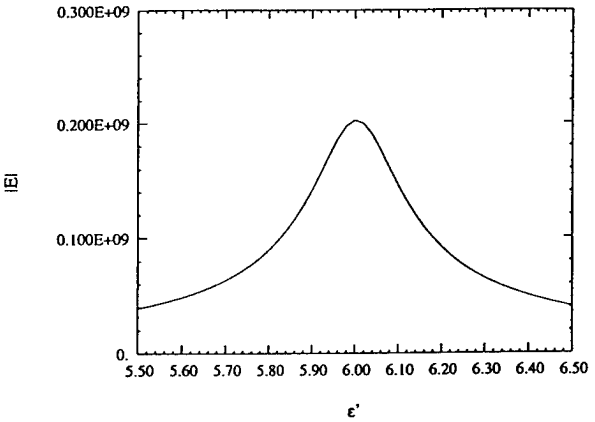


Fig. 4. Variation of cavity response as a function of the real part of dielectric constant in the inverse problem.

Method of Retrieval of Media Structural Parameters from Frequency Dependence of Transmission Coefficient

D.A.Boyarskii
Space Research Institute, Russian Academy of Sciences
Applied Space Physics Department, Profsojuznaya 84/32, Moscow
117810, Russia
Fax. (7-095)-3331056, Email: kub@asp.iki.rssi.ru

Abstract - This paper presents the method of prompt retrieval of average radius and variance of the particle sizes of the medium. The method is based upon the scattering effect of electromagnetic wave by medium consisting of closely packed discrete scatterers, when the wavelength is comparable to scatterer's size. In this case transmission coefficient will depend critically on electromagnetic wavelength.

Here we discuss the application of our method for the retrieval of structure parameters of the test samples of oil-bearing rocks (without oil). It is necessary to know these parameters for prediction of oil outflow. Oil under pressure of water is driven out from rock and this process depends on microstructure of oil-bearing rocks. It is shown that the rock microstructure parameters deduced from our method agree with those obtained from photos processing. This agreement is accurate to 10 %.

INTRODUCTION

We have studied test samples of oil-bearing rocks with different physical parameters (density, average diameter (d_{av}) and variance (σ) of the particle sizes). Samples were circular cylinders with diameter 3 cm, thickness h=1-3 cm and density ρ=1.6-2 g/cm^3. First structure type of samples had single distribution of particle sizes with d_{av}~0.0035cm and σ=30-60% (Fig.1,3). Second type had bimodal distribution with d_{avL}~ 0.005cm, σ_L=40-60% (Fig.2a,4b) and d_{avs}~0.00035cm, σ_s=40-60% (Fig.2b,4a).

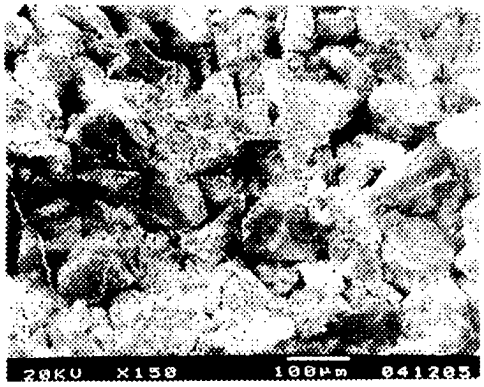


Figure 1. The photograph of the test sample surface with the single distribution of particle sizes.

Microwave spectrometer based upon backward-wave tubes was used for measurement of transmission coefficient P in frequency range 150-600GHz. Detector physical temperature was 4.2K. Experimental equipment made possible the measurement of P from 1 to 10^{-4}.

MODEL OF FREQUENCY DEPENDENCE OF TRANSMISSION COEFFICIENT

Transmission coefficient of medium layer is:

$$P=TS^2,$$

where

$$S=\exp(-(2ks)^2) \quad [1], k=2\pi/\lambda,$$

λ is wavelength, s - the surface roughness variance of the



Figure 2a. The photograph of the test sample surface with the bimodal distribution of particle sizes (magnification-100^x, large particles).

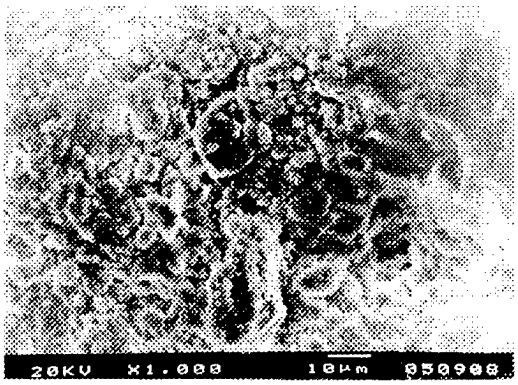


Figure 2b. The photograph of the test sample surface with the bimodal distribution of particle sizes (magnification-1000^x, small particles).

0-7803-3068-4/96$5.00©1996 IEEE

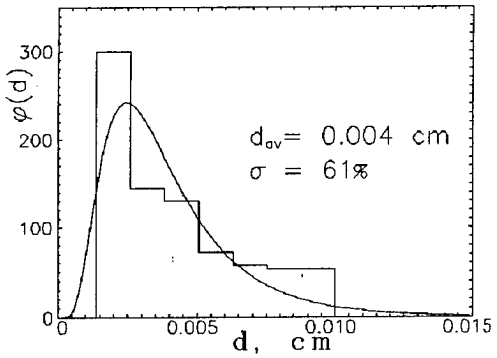


Figure 3. Histogram of particle sizes and its approximation by log-normal distribution for sample with single distribution of particle sizes.

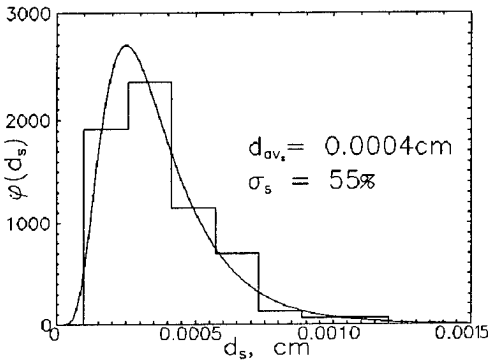


Figure 4a. Histogram of small particle sizes and its approximation by log-normal distribution for sample with bimodal distribution of particle sizes.

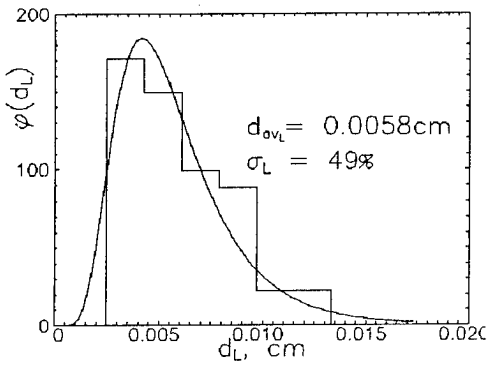


Figure 4b. Histogram of large particle sizes and its approximation by log-normal distribution for sample with bimodal distribution of particle sizes.

sample,

$$T=\frac{(1-r^2)^2\exp(-\tau)}{1+r^4\exp(-2\tau)-2r^2\cos(\delta)\exp(-\tau)}$$

$$\delta=4\pi/\lambda hn',\ \tau=4\pi/\lambda hn''$$

r is the Fresnel reflection coefficient, n' and n" are the real and imaginary parts of the complex refractive index, h is the layer thickness.

In our measurement frequency range it is necessary to take into account the scattering by closely packed medium particles. The model of effective permittivity [2] was used for determination of the complex refractive index. We modeled oil-bearing rock as mixture of spherical particles of quartz (ρ_q=2.6 g/cm^3) with permittivity $\varepsilon=\varepsilon'+i\varepsilon''$, where ε'=4, ε''=0.1-0.001.

Effective permittivity ε_{eff} for medium with single distribution of particle sizes is:

$$\epsilon_{eff}=\left[1-\frac{4\pi n(\epsilon+2)\frac{\langle f\rangle_\omega}{k^2}}{2\epsilon_{eff}+\epsilon}\right]^{-1}$$

where f_ω is the amplitude of the forward scattering of the particles, the angle brackets denote an averaging over the sizes of the ensemble of scatterers, n is the number of particles per unit volume:

$$\frac{\rho}{\rho_q}=n\frac{\pi}{6}\int_0^\infty d^3\phi(d)\,dd$$

where $\phi(d)$ is probability density of log-normal distribution of particle sizes.

Effective permittivity ε_{eff} for medium with bimodal distribution of particle sizes is:

$$\epsilon_{eff}=\left[1-\frac{4\pi(\epsilon+2)\left(n_s\frac{\langle f_\omega\rangle_s}{k^2}+n_L\frac{\langle f_\omega\rangle_L}{k^2}\right)}{2\epsilon_{eff}+\epsilon}\right]^{-1}$$

where $\langle f_\omega\rangle_s$ and $\langle f_\omega\rangle_L$ are the amplitudes of the forward scattering of the small and large particles averaged over the sizes of the ensemble of small and large scatterers, n_s and n_L are the numbers of small and large particles per unit volume:

$$f_s\frac{\rho}{\rho_q}=n_s\frac{\pi}{6}\int_0^\infty d_s^3\ \phi(d_s)\,dd_s$$

$$f_L\frac{\rho}{\rho_q}=n_L\frac{\pi}{6}\int_0^\infty d_L^3\ \phi(d_L)\,dd_L$$

where $\phi(d_s)$and $\phi(d_L)$ is probability density of log-normal distribution, d_s and d_L are the diameters, f_s and f_L are the fractional volumes of small and large particles.

Fig. 5, 6 show frequency dependencies of P from the experiment and those calculated from our model. The drop of the transmission coefficient when wavelength decreases is associated with significant increase of

scattering by medium particles. For comparison frequency dependencies of P calculated from refractive model [3]:

$$\sqrt{\epsilon_{eff}} = (\sqrt{\epsilon} - 1)\, \rho / \rho_q + 1$$

are shown in Fig.5 (dashed line). This model is used usually to find out the effective permittivity of soils in wavelength range 3-60 cm, when scattering by medium particles is small.

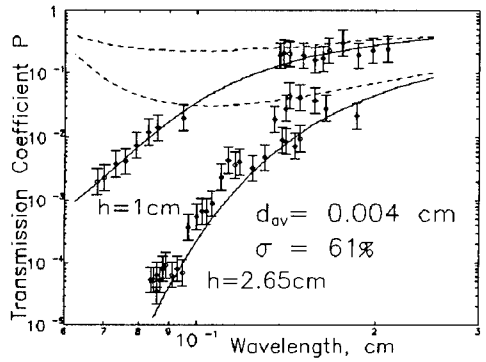


Figure 5. Experimental and calculated frequency dependencies of transmission coefficient for sample with single distribution of particle sizes.

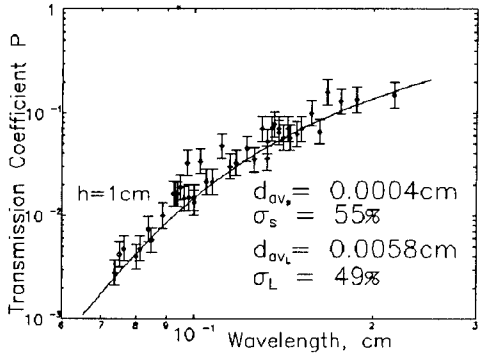


Figure 6. Experimental and calculated frequency dependencies of transmission coefficient for sample with bimodal distribution of particle sizes.

ALGORITHM OF RETRIEVAL OF MEDIUM STRUCTURE PARAMETERS

The problem of retrieval of average diameter and variance of the particle sizes of the medium was solved by minimizing of error function:

$$F(d_{av}, \sigma) = \frac{1}{N}\sum_{n=1}^{N}\left[\frac{P_m(d_{av}, \sigma, \lambda_n) - P_{ex}(\lambda_n)}{P_{ex}(\lambda_n)}\right]^2$$

where $P_m(d_{av}, \sigma, \lambda_n)$ is transmission coefficient at the given parameters d_{av}, σ of optimization at wavelength λ_n, $P_{ex}(\lambda_n)$ is experimental value of transmission coefficient at the same wavelength. To set the boundaries of the retrieval region the following constraints were imposed: $d_{av} > 10^{-4}$cm, $30\% \le \sigma \le 80\%$. These constraints follow from the analysis of structure parameters of samples under investigation.

We applied our algorithm for retrieval of structure parameters of sample with single distribution of particle sizes. For sample with 1 cm thickness the error function has minimum at: d_{av}=0.00365cm and σ=64% of desired parameters. The errors of retrieval of desired parameters are for d_{av} ~ 9% and for σ ~ 5%. Fig.7 shows normalized error function, where F_{max} is maximum value of error function at range $30\% < \sigma < 80\%$.

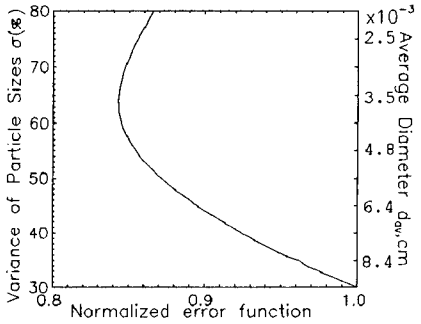


Figure 7. Normalized error functio·

CONCLUSION

Structure parameters of scattering medium are retrievable from frequency dependence of transmission coefficient, when transmission coefficient depends critically on electromagnetic wavelength. Medium microstructure parameters deduced from our method agree with those obtained from photos processing.

ACKNOWLEDGMENTS

Author thanks Prof. E.Gershenzon and Prof. G.Golt'sman for guidance in experiment and V.Tikhonov for computer computation.

REFERENCES

[1] B.Choudhury, T.Schmugge, A.Chang, R.Newton, "Effect of Surface Roughness on the Microwave Emission From Soil," J. of Geophysical Research, 1979, V.84, pp.5699-5706.

[2] D.Boyarskii, V.Tikhonov, N.Kleeorin, V.Mirovski, "Inclusion of Scattering Losses in the Models of the Effective Permittivity of Dielectric Mixtures and Applications to Wet Snow," J. Elect. Waves a n d Appl., 1994, V.8, pp.1395-1410.

[3] J.Birchak, C.Gardner, J.Hipp, M.Victor, "High dielectric constant microwave probes for sensing soil moisture," Proc. IEEE, 1974, V.62, pp.93-98.

EARLY IMAGES FROM THE RADARSAT SYNTHETIC APERTURE RADAR

A.P. Luscombe (Spar Aerospace)*,
R. Gray, N. Shepherd, S. Srivastava (Canadian Space Agency),
D. Meier (MacDonald Dettwiler), W. Jefferies (Radarsat International)
*c/o Spar Aerospace, 21025 Trans-Canada Highway, Sainte-Anne-de-Bellevue, Quebec, H9X 3R2, Canada
Tel. (514) 457-2150 (x3641) Fax. (514) 425-3041 E-mail aluscomb@spar.ca

Abstract -- The Canadian RADARSAT satellite was launched in Autumn 1995, and its Synthetic Aperture Radar (SAR) instrument took its first image 24 days later. This paper presents results obtained from SAR imaging during the Commissioning Phase and early in the Operational Phase. The RADARSAT SAR has been designed to be very versatile in its operations, producing data in a wide range of different modes. Selected images are included in this paper which both illustrate these capabilites and show interesting imaging features.The information presented covers the full range of imaging options from Fine Resolution Beams to the very wide coverage ScanSAR modes.

INTRODUCTION

The RADARSAT satellite was launched on 4th November 1995. The Synthetic Aperture Radar (SAR) sensor on the satellite was first switched into imaging mode on 28th November, and the first image was successfully produced within four hours of the pass. During the Commissioning Phase of the mission, all the imaging modes of the SAR were successfully demonstrated and a large variety of images were produced. The RADARSAT SAR instrument [1,2] was designed to provide a wide range of imaging modes, from Fine Resolution imaging to very wide coverage ScanSAR [3]. The elevation beamforming capabilities of the antenna allow imaging down to incidence angles as low as 10° and as high as 60°. The high data rate recorders on the satellite allow images to be taken anywhere in the orbit for subsequent downlink to a Canadian station.

This images in this paper were obtained in the early stages of the mission, and demonstrate the wide ranging capabilities. Some interesting imaging features shown in the images are discussed.

The authors of this paper represent the companies who designed and built the instrument (Spar) and the ground processor (MDA), and the organisations which manage the satellite operations (CSA) and the distribution of data (RSI).

NADIR AMBIGUITIES

An important requirement of the RADARSAT SAR was that it be capable of imaging any point within a wide 'accessibility region' of over 500km to the right side of the satellite. A set of seven beams were defined to meet this requirement, each covering a swath of over 100km with at least 10km overlap. These beams, and the Pulse Repetition Frequencies (PRFs) to be used with them, were defined so that the pulse returns from the area immediately below the satellite did not coincide with returns from an earlier pulse transmission reflected back by any point within the required swath. The range ambiguities from the nadir region, commonly referred to as 'nadir ambiguities', are potentially very strong because the reflection is specular. In the RADARSAT design, the criterion that was adopted was that the nadir return **after range compression** (i.e. only a fraction of a microsecond in duration) should fall outside the required swath. This is a much less stringent requirement than that adopted in many handbooks (e.g. [4]), where the nadir return before compression (i.e. typically tens of microseconds) must not overlap the return from the swath.

In early imaging operations with RADARSAT, a longer period of the pulse return was sampled than was required to image the nominal swath. This allowed the nadir ambiguity to be examined at the edge of some images. An example is given as Fig. 1. This image shows the region around Vancouver, British Columbia, and was taken with Wide Swath Beam 2. The nominal width of the swath from this beam is 150km, but the receive window had been extended to allow imaging of 160km. The nadir ambiguity line can be seen in the additional coverage at the left of the image. In this image, the nadir ambiguity is only clearly visible against the relatively weak returns of the sea, but in other images it is significantly stronger, varying in strength according to the surface beneath the satellite. In all cases, however, the nadir ambiguity is confined to a very narrow width. This is in accordance with the analysis which underlay the RADARSAT beam and PRF definition, and demonstrates that this is the correct criterion for 'timing-out' the nadir return.

WIDE ANGULAR ACCESS

The RADARSAT SAR was designed to image over a wide range of angles to the side of the satellite so as to increase access to any ground location and to allow choice of an imaging angle which is optimum for a given application. The basic requirement for the SAR was that it be able to image from 20° incidence angle to 50°. This range is extended with a set of High and Low Incidence Beams to cover from 10° to 60°, equivalent to a total accessibility region of about 900km. The value of this wide angular access was demonstrated in late February when a request was received to image the oil spill from the tanker grounded off the coast of Wales. Two images were taken on consecutive days using High Incidence Beam 5 and Standard Beam 1, corresponding to incidence angles of about 57° and 23°. The second of these is shown as Fig. 2. A further four imaging opportunities were available within a week of the request. This pair of images also illustrates the value of a choice of imaging angles. For this application, the steeper angles of the illustrated image are ideal because the oil shows up very clearly against the

0-7803-3068-4/96$5.00©1996 IEEE

sea return, whereas the contrast is lost at the high angles where the sea backscatter is also low. For another application, such as detection of boats, the reverse would be true, and the RADARSAT SAR has the ability to meet both sets of needs.

SCANSAR IMAGING

The ScanSAR imaging mode [3] was incorporated into the RADARSAT SAR design in order to provide very large scale coverage for applications such as ice monitoring. The standard ScanSAR configurations of the system produce images of about 300 and 500km, combining the coverage of two, three or four beams. The first attempt to produce a ScanSAR image was made on 13th December, and a good, geometrically-accurate image was again obtained within hours of the pass. Since early February, a regular supply of ScanSAR images has been provided to the Canadian Ice Centre, who have always been identified as an important customer for RADARSAT data. Examples of this imagery will be shown at the symposium.

FINE RESOLUTION IMAGING

In addition to the standard multi-look images with 20-25m resolution shown in Fig. 1, the RADARSAT SAR can provide fine resolution images using a wide bandwidth pulse. This mode has been shown to provide resolutions better than 8m in each dimension, and has been used extensively during the early months of the mission in combination with the on-board recorders to produce fine scale images of sites around the world for publicity purposes. An example showing the harbour in Osaka, Japan is shown (in negative) as Fig. 3. The suspension bridge produces a particularly interesting image feature, with the raised structure appearing first to the right of the bridge, but also on the far side. This reflected image is so clear in this image because of the very calm water surface, which reflects the pulse on both the path from the satellite to the suspension and on the reverse journey. (Signals reflected just once by the water and once by the suspension coincide with, and are hidden by, signals from the bridge base.)

SUMMARY

Since the first image was taken in late November 1995, the RADARSAT SAR has successfully been producing high quality images in all its modes. Examples of images covering the full ranges of incidence angles, swath widths and resolutions are shown in this paper. At the time of writing, RADARSAT was nearing the end of its Commissioning Phase. Images are already being supplied to customers, and routine service is expected to begin early in Spring 1996.

ACKNOWLEDGEMENTS

The successful implementation of the RADARSAT instrument would not have been possible without the contributions of many people at the authors' companies and organisations, and at subcontractors such as CAL Corp., ComDev, SED and Dornier. All images in this paper are courtesy of RADARSAT International and © Canadian Space Agency.

REFERENCES

[1] R.K. Raney, A.P. Luscombe, E.J. Langham, and S. Ahmed, "RADARSAT", Proc. IEEE, 79, pp. 839-849, 1991.

[2] A.P. Luscombe, I. Ferguson, N. Shepherd, D.G. Zimcik and P. Naraine, "The RADARSAT SAR Development", Canadian J. Remote Sensing, Vol. 19, pp. 298-310, 1993.

[3] A.P. Luscombe, "Taking a Broader View: Radarsat Adds ScanSAR to its Operations, Proc. IGARSS '88, 1027-32.

[4] J.C. Curlander and R.N. McDonough, Synthetic Aperture Radar, Wiley, 1991.

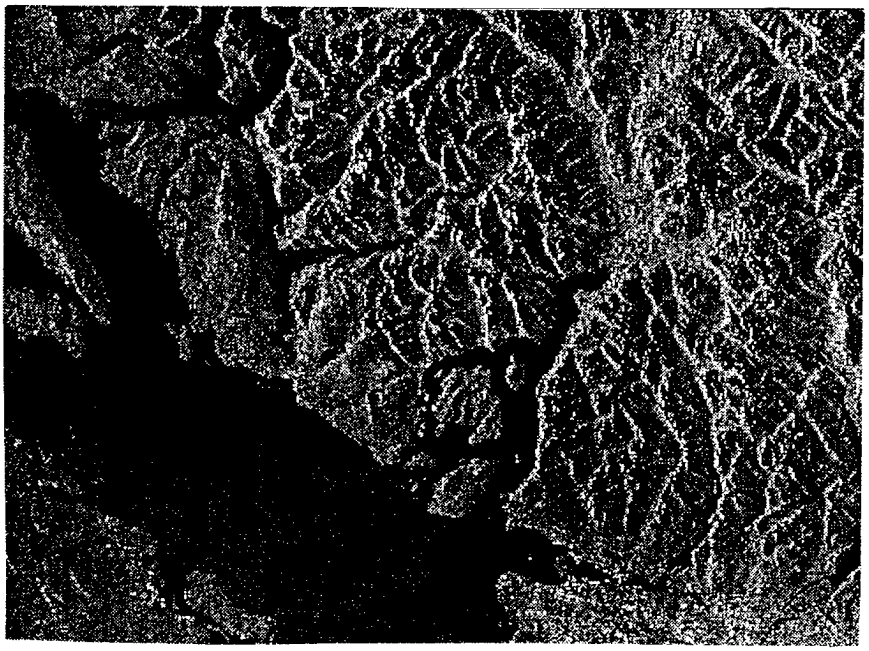


Figure 1: Vancouver, British Columbia

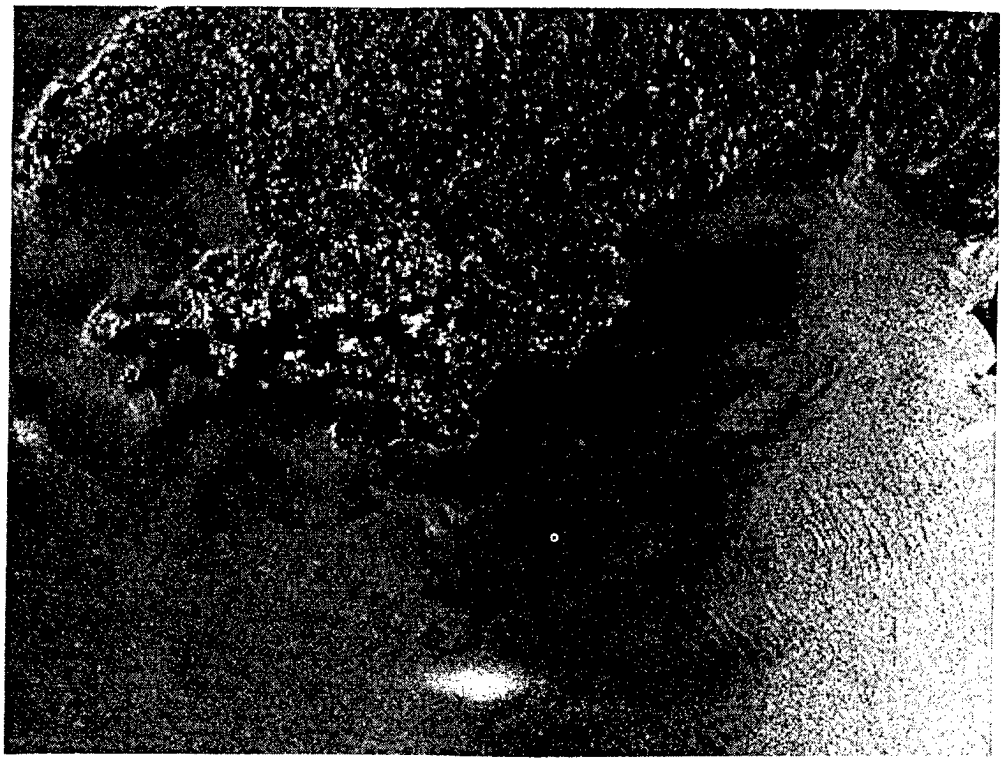


Figure 2: Oil Spill from 23° Incidence

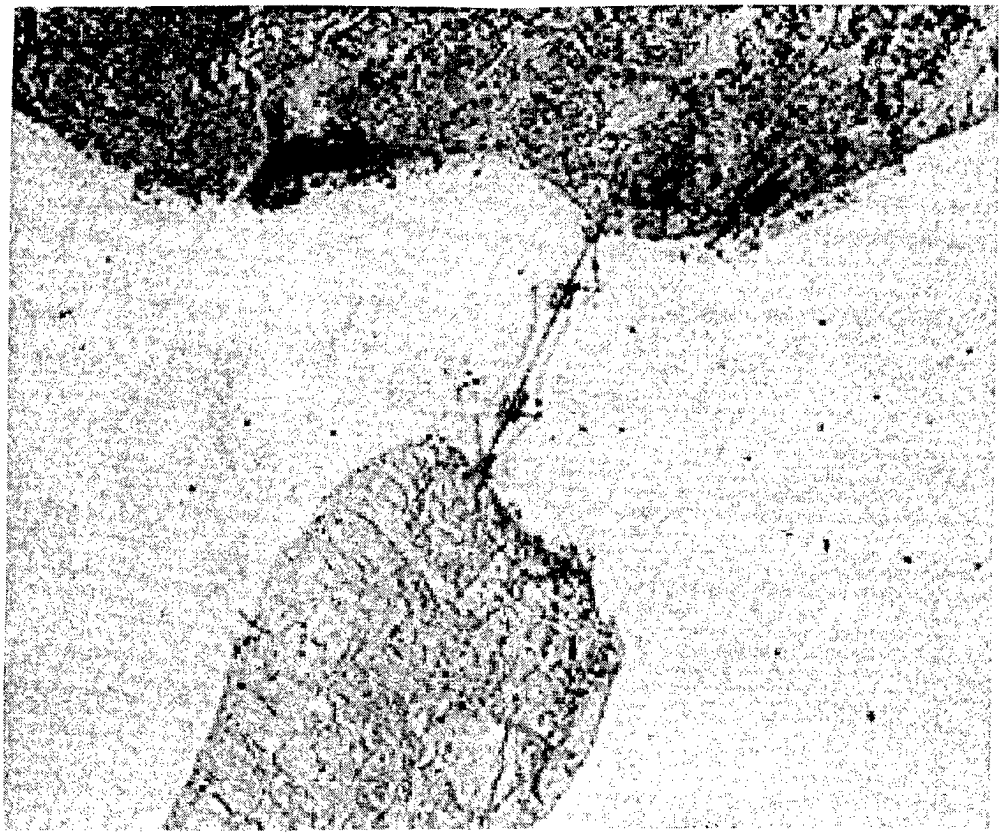


Figure 3: Osaka Suspension Bridge (negative)

THE DEVELOPMENT OF THE ENVISAT-1 ADVANCED SYNTHETIC APERTURE RADAR

P. Mancini, J-L. Suchail, Y-L. Desnos, R. Torres, J. Guijarro and G. Graf

ESA-ESTEC, ENVISAT-1 project, P.O.Box 299, 2200 AG Noordwijk ZH,
The Netherlands
Tel.: (31) 715654552, Fax: (31)7156563649
e-mail: pmancini@vmprofs.estec.esa.nl

Abstract -- The Advanced Synthetic Aperture Radar (ASAR) selected for the ENVISAT-1 mission of the European Space Agency, represents a sensor of paramount importance for the remote sensing community due to its enhanced flexibility with respect to the ERS AMI synthetic aperture radar. The unique combination of different spatial resolutions, incidence angles, swath width sizes and polarisation diversity will reflect in an increased number of operational modes tailored for a large set of scientific and operational applications. The use of an active antenna concept for tailoring the transmit and receive elevation beams to different mode geometry, a digital generation waveform technique for obtaining variable time-bandwidth products and a Block Adaptive Quantization compression scheme are among the innovative design features of this radar. In this paper, the status of the ASAR instrument development will be described, the accomplished project milestones will be highlighted together with preliminary instrument performances.

INTRODUCTION

After the development of the ERS-1/2 SARs, ESA is planning the launch of the ENVISAT-1 ASAR in order to consolidate and enlarge the mission objectives of the previous AMI SARs. The unique capability of imaging a large range of incidence angles with high, medium and low spatial resolutions combined with a multi-polarisation capability and adaptable swath widths will assign to this sensor a role of primary importance among the future microwave imaging sensors.

ASAR will exploit its intrinsic design flexibility through five operational modes. The Image mode will generate high spatial resolution data products (30 m) similar to the AMI SAR, imaging one of the seven swaths located over a range of incidence angles spanning from 15^0 to 45^0. The Wave mode will generate vignette sizes of 5 by 5 km spaced 100 km along-track. The main difference with the previous AMI Wave mode will be the capability to locate the vignette in any of the seven swaths and the introduction of a compression scheme (BAQ) to reduce the data rate and allow on-board storage without the need of on-board range compression. The Wide Swath and Global Monitoring modes are based on Scansar processing and will generate wide swath products (400 km) with spatial resolution of 150 m and 1000 m respectively. These modes will all be operated in one of the two copolar polarisations, HH or VV. The Alternating Polarisation Mode will provide images from the same area in both HH and VV , HH and HV or VV and VH. This mode will utilise the same imaging geometry as the Image mode, similar high spatial resolution but reduced radiometric performances due to the combined operation in the two polarisations.

ASAR FUNCTIONAL DESCRIPTION

The ASAR instrument consists of two main elements: the Central Electronics (CESA) and the Antenna Subassembly (ASA) as shown in Fig. 1. The active antenna contains 20 tiles with 16 Transmit/Receive (T/R) modules each. The instrument is controlled by its Control Subsystem, which provides the command and control interface to the satellite and maintains and manages the distribution and database of operation parameters such transmit pulse, antenna- beam and timing characteristics. The transmit pulse characteristics are set in the Data Subsystem the output of which is an up-chirp pulse centred at the IF carrier (124 MHz). In the RF Subsystem the pulse is amplified and up-converted to the RF frequency (5.331 GHz). The signal is then passed to the Tile Subsystem through a waveguide distribution network and consequently to each individual T/R module using a microstrip corporate feed. The T/R modules apply phase and gain change according to the preselected beam characteristics which have been transmitted from the Control Subsystem and locally stored in each Tile Control Interface Unit. In receiving the reciprocal operation is performed.

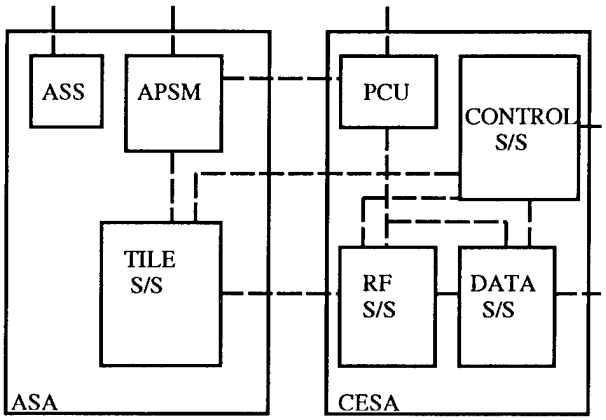


Fig.1 ASAR Functional Diagram

0-7803-3068-4/96$5.00©1996 IEEE

ACTIVE PHASE ARRAY ANTENNA

The ASAR active antenna is a 1.3 m x 10 m phased array. The antenna consists of five 1.3 m x 2 m panels which are folded over for launch. Each panel is formed by four 0.65 m x 1 m tiles mounted together. Each tile consists of 16 linear subarrays of 24 dual-polarised radiating elements. Each subarray is connected to a T/R module with independent connection for the two polarisations.

The Antenna System is broken down in three subsystems: The Antenna Services Subsystem (ASS), the Tile Subsystem (TSS) and the Antenna Power Switching and Monitoring Subsystem (APSM).

Antenna Services Subsystem: The antenna is based on a mechanical structure consisting of five CFRP frames connected by deployment mechanisms with actuators, hinges and latches and hold–down and release mechanisms. The antenna, with the four panels folded over a fixed central one, is held down with eight mechanisms during launch. After release in orbit, the deployment is performed with four stepper motors and four hinge lines up to the final latching with the eight built–in latches. A specific unit contains the electronics for driving and controlling the release, deployment and latching of the antenna once in orbit. The RF distribution is served through a set of CFRP waveguides along the five panels. A parallel waveguide distribution system is used for the calibration channel.

Tile Subsystem: Each of the twenty tiles contains 16 subarrays each one fed by a T/R module. The subarrays and the modules are mounted on a supporting plate, thermally and mechanically decoupled. The subarrays are formed by 24 λ-diameter ring slot radiating elements, electrically coupled to a dual–polarisation low-loss dispersion-free triplate feeding system which provides a constant phase and amplitude illumination.

The measured radiating characteristics of the subarrays are showing a gain of 20.5 dB, loss of 1.5 dB, VSWR of –18 dB and a very good crosspolarisation better than –35 dB for both polarisations.

Transmitter/Receiver Modules. Each module consists of two (H/V) transmit and one common receive chains, which amplify and control the signal of each individual subarray, in phase and amplitude. These functions are implemented using MMIC's. The input Phase Shifter (5 bits) is controlling the Tx/Rx signal, a SP3T selects either Tx (H/V) or Rx chains. On the Tx chain a VGA provides 42 dB of control range, the output power is provided by a Telettra SSPA (10 W at 1 db compression, 30% efficiency). The connection to the subarrays is made via a Circulator/Isolator/Passive-Limiter (0.25 dB insertion loss in Tx, 1 dB in Rx, 35 dB isolation), a 1.3 dB NF LNA (Siemens HEMT's) is connected to the limiter, a SPDT switches the V/H Chain to the common Rx path. For Calibration Purposes, a coupler (-24 dB) has been implemented at the output of the module to the antenna.

The T/R Module is commanded by a serial link consisting of 3 signals: a data signal, a gate control signal and a strobe signal. The temperature of each T/R Module is monitored and used for correction of amplitude and phase setting. The pulse power within the Module is taken from a tantalum capacitor which provides the high currents required by the SSPA during transmit.

The control functions within the Tile are achieved by a Tile Control Interface Unit (TCU) which is carrying out local control of the T/R Modules including temperature compensation and beamforming setting, it is transferring data and interfacing to the Control Subsystem. There is one TCIU per Tile using internal duplication for redundancy purposes.

USE OF DIGITAL TECHNOLOGIES FOR SIGNAL GENERATION AND PROCESSING

Compared to ERS-1&ERS-2 which were using SAW devices for analog chirp generation and On Board Range Compression, ASAR is using more extensively digital technologies for on board chirp generation and data reduction for temporary storage, associated with On Ground Range Compression.

A fundamental advantage of using digital chirp generation in the inherent flexibility of such a design which allows for chirp versatility in terms of pulse duration and bandwidth, thus accommodating efficiently the various requirements associated with the high number of available operational modes and swaths of the instrument.

In the ASAR instrument, the transmit chirp characteristics are set by macrocommand from the Control Subsystem to the Data Subsystem by writing chirp coefficients into the Data Equipment processor. This processor then calculates the In-phase and Quadrature components of the baseband signal to be generated in the form of two digital tables in the Chirp Memory. This memory can store up to 128 chirps of 2040 x 8-bit samples per I & Q channel each. Once the triggering of the transmit chirp occurs, the contents of the two tables corresponding to the selected chirp are sequentially red and transferred to a pair of low glitch impulse DAC operating with a 38.4 MHz clock in order to generate the baseband I & Q signals. These signals are then fed to image rejection mixers for further IF baseband modulation in the Data Subsystem and upconversion to C band in the RF Subsystem.

At reception, the IF echo signal is first demodulated into I & Q components of the IF carrier. These two signals are then both digitised into 8 bit samples at 19.2 MHz following anti-aliasing filtering. It is then possible to perform some digital decimation of the samples by simply transmitting only one in every N samples, if required, in order to reduce the data stream, such as in Global Monitoring mode where the transmit bandwidth is lower than 1 MHz. Following this decimation, a FBAQ scheme is applied for the echo samples.

The developed FBAQ ASIC can be operated in three main modes: Compression mode according to BAQ algorithm, Bypass mode and Noise mode. In compression mode, each 8-bit sample value is compressed to a selectable 4, 3 or 2-bit sample value. By writing into the control register, the operation mode of the ASIC can be selected individually for each data type (echo, calibration and noise). The BAQ Compression mode is selected for echo data, bypass mode (thus preserving the full 8-bit quantization for calibration purposes) for calibration data, noise data.

The Data Equipment also contains a Science Memory where the echo samples are then temporary stored before their transmission to the platform on-board tape recorders in Wave, Global Monitoring and Module Stepping modes (low rate modes). The Science Memory consists of two banks of DRAM memory with 1M x 1 bit each. It is therefore possible to read from one bank while writing into the other.

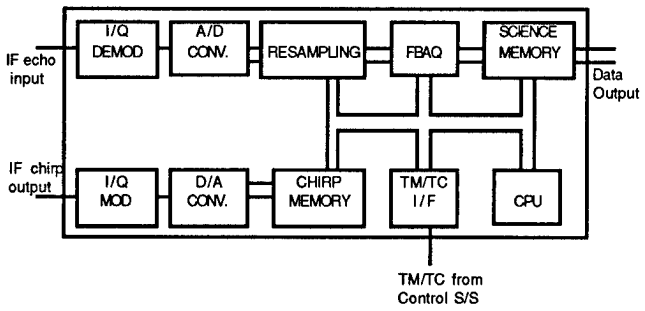


Fig. 2 ASAR DATA Equipment simplified block diagram.

THE ASAR INSTRUMENT CALIBRATION

The internal calibration system objective is to derive instrument internal path transfer function and to perform noise calibration. The internal calibration system provides distinct calibration paths to the 320 T/R modules. This enables transmit pulses at the output of each module to be individually sampled and also allows pulses to be injected in the receive path of any module. The designed calibration loops include all the active circuits of the instrument and allow for monitoring of all drifts, including temperature effects and ageing. Interleaving these calibration pulses with science data during all operational modes and downlinking the sampled calibration pulses and noise measurements with these data will allow for corrections in the ground processor.

Additionally to the internal calibration, an antenna in flight characterisation using the external characterisation mode is performed every 6 months. During this activity, a sequence of transmit pulses is simultaneously sensed by the antenna calibration loop and recorded on ground by a specially built ground receiver in order to provide comparative values for further corrections at ground processor level.

The external calibration objective is to derive the overall calibration scaling factor. The successful methodology developed for ERS-1/2 will be reused for the narrow swath modes. Three specially built high precision transponders with a radar cross section high enough compared to background radar reflectivity and noise will be deployed across ASAR swath and observed several times every 35 day orbit cycle. Images acquired over suitable areas of the amazon rain forest will be used to also derive the in-flight elevation antenna pattern. Absolute calibration factors derived from transponder measurements and across swath correction derived from radar equation will be used to calibrate the final image product.

CONCLUSION

Since ENVISAT-1 programme approval by The European Space Agency in December 1993, ASAR development has significantly progressed. Preliminary EM model subsystems test results are demonstrating the suitability of the selected design approach and FM manufacturing is starting this year.

An Alaska SAR Facility Overview in the Radarsat Era

David Cuddy, Kon Leung
Jet Propulsion Laboratory
California Institute of Technology
MS 300-243
4800 Oak Grove Drive
Pasadena, Ca 91109 USA
Phone: 818-354-2099
Fax: 818-393-0202
EMail: david.cuddy@jpl.nasa.gov

ABSTRACT

With the successful launch of Radarsat in November of 1995, the Alaska SAR Facility (ASF) at the University of Alaska, Fairbanks (UAF) will soon be handling SAR data from four operational satellites (ERS-1, ERS-2, JERS-1, and Radarsat) at the same time. Coming upon the conclusion of 3 years of intensive planning, design, and implementation activities, ASF will be ready mid-1996 to fulfill its role in providing SAR data acquisition, processing, and archive services in support of the Science community.

ASF has been in operations since 1991; initially supporting ERS-1 users. It has grown from the simplicity of handling just one satellite, ERS-1, into a complex organization dealing with multi-national data providers and users. It has also gradually over the years expanded its services and is becoming more user driven in the form of its operations.

This paper chronicles the progression and development of the ASF; with special attention given to its organization and structure in the current Radarsat era. Special treatment is given on describing in detail the end to end system data flow and operations scenarios which serve to provide the Science users insight into fully exploiting the ASF capabilities.

INTRODUCTION

The Alaska SAR Facility (ASF) performs as the ground data system for the acquisition, processing, archives, and distribution of Synthetic Aperture Radar (SAR) and SAR related products for the science community whose interest include polar oceanography, glaciology, geology, hydrology, and ecology. ASF is a cooperative facility between National Aeronautics and Space Administration (NASA) and University of Alaska, Fairbanks (UAF) in which Jet Propulsion Laboratory (JPL) has the system engineering, development, and implementation responsibilities. [1]

Currently, ASF maintains support for three research-oriented satellites which carry a SAR instrument. First was the European Space Agency's (ESA) first Earth Remote Sensing satellite (ERS-1) which was launched in 1991. The second was the National Space Development Agency (NASDA) of Japan's Earth Resources Satellite (JERS-1) which was launched in 1992. The third was ERS-2, which is the follow-on to ERS-1 and was launched in the spring of 1995. On November 4, 1995, Canadian Space Administration (CSA) launched RADARSAT which provides SAR data for scientific applications and for operational missions.

Although the original intensions by ESA were to replace ERS-1 operations with ERS-2, ESA and the science community have found the use of tandem operations of the two SAR instruments invaluable in enhancing the value of the mission data despite the added complexity of doubling the volume of data.

The JERS-1 primary mission of 3 years to map the earth's land surfaces have been achieved by NASDA; however many new science projects have come to take advantage of the L-band SAR data. The volume of new JERS-1 data has not diminished with time.

These satellites continue to challenge ASF by presenting science with a plethora of capabilities including synergism from multi-satellites, added look angles, super wide swath coverage (via ScanSAR), and potential for accurate terrain information (via interferometry). And as one of the Distributed Active Archive Centers (DAAC) that supports interdisciplinary earth science research for the Earth Science Data and Information System (ESDIS), ASF is required to conform to standards and inter-operability requirements adopted by the NASA Earth Science community. [2]

RADARSAT

ASF expects to acquire 120 minutes of data per day and process upon demand up to 80 minutes of that to SAR images and related products. Radarsat distinguishes itself from ERS-1, ERS-2, and JERS-1 with the added capability to electronically steer and spoil the radar beam to achieve wide range of look angles, resolutions, and footprints. Of particular significance is the ScanSAR mode in which various beams are combined to achieve a wider swath of up to 500 KM. Similar to

0-7803-3068-4/96$5.00©1996 IEEE

JERS-1, Radarsat has an on-board recorder which allows it to save the observation data taken almost anywhere on the earth and downlink it later when it passes over one of the receiving stations.

McMURDO STATION

The National Science Foundation in conjunction with NASA has installed a receiving station at the US facility in McMurdo, Antarctica. Although the antenna schedules are managed by Wallops Flight Facility (WFF), ASF however has the responsibility to continue to interface to the various flight agencies for SAR data. Therefore, ASF is required to assemble integrated schedules and satellite orbit information for WFF on a daily basis. Once the data is collected to tape at McMurdo, the reception and tape information are sent from McMurdo via WFF to ASF, who then reports to the flight agencies on the reception activities. The recorded tapes are sent in bulk at a later date to ASF for processing.

FRAMES

Up until now ASF SAR data were divided into images somewhat arbitrarily based on when the first data observations were made. The resulting image frames make the task of overlaying images from repeating orbits one of patchwork at best. ASF now has defined frames which are fixed to earth latitude so that images from repeating orbits will have the same center latitude and longitude. The center latitudes of the images will be fixed relative to the equator at approximately 40 KM spacing between image centers. For 100 KM size images, it is necessary only to order every other frame. For the largest images of 500 KM, it is necessary only to order every 10th frame and still retain a fair overlap between adjacent images.

END-TO-END DATA FLOW

The end-to-end data flow has two major flows representing two ways that user can request data: first, the user can request products by data acquisitions, and second the user can request products by frames. Frame is the unit of data which can be ordered from ASF.

Fig.1 provides a block diagram of the ASF for the Radarsat era. Because Data Acquisition Requests (DARs) parameters include times and areas which can map to many frames that may never get scheduled, ASF has chosen to wait until a DAR is "planned" before the ASF catalog is populated with frames.

In the DAR data flow, the users enter their DARs into the ASF using the User Client software provided as an extension to the EOS Data Information System (EOSDIS) Information Management System (IMS) Version 0 (V0) user interface [3]. The DAR is tracked as a user order and assigned a unique order id. The Acquisition Planning Subsystem (APS, see Fig. 1) retrieves the DARs and with directives from the Acquisition Planner maps the DARs to specific swaths of SAR data that meet the user requirements. These swaths are then sent as request to the flight agencies (ESA, NASDA, or CSA). Once the agencies have planned the swaths, ASF then provides the frames which are computed from the swaths in the ASF catalog. At this point (anywhere from 1 to 8 weeks in advance of the event), the user is able to order products for the frames that are found in the catalog. This feature is one of the main capabilities of the new system that was not available in the older versions of ASF. In the old system, the user needed to wait until the data was collected and processed before the frames appeared in the catalog.

At about 1 day to 1 week in advance of the data observation, the foreign flight agencies will send schedules of datatakes for ASF and McMurdo to the Flight Agency Interface Function (see Fig. 1). These are then turned into a set of integrated schedules by the APS and sent to the appropriate antenna system along with the predicted state vectors. Once the antenna systems have captured the data to a recording media, the user request for the DAR is complete.

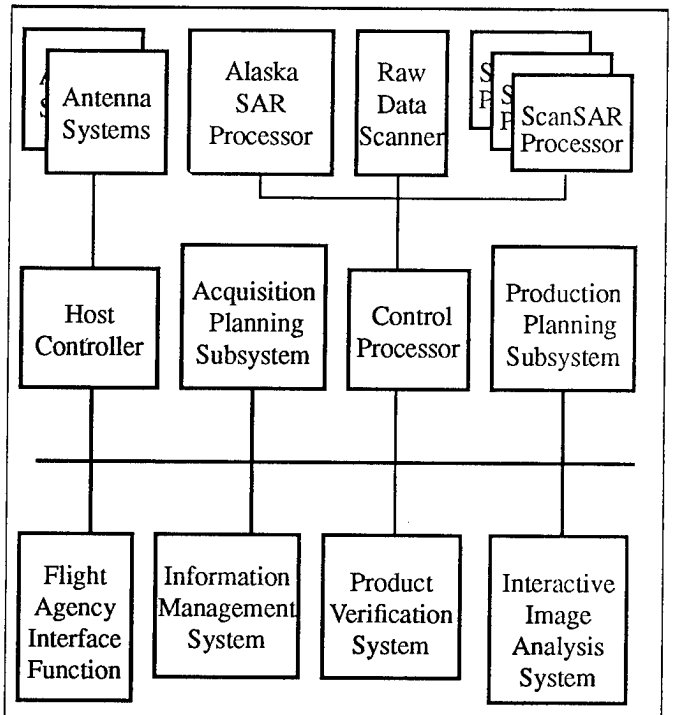


Fig. 1. Block Diagram of ASF for the Radarsat era.

In the frame based request handling, any time after the frames have been catalogued in the IMS, a user through the user client for the EOSDIS IMS V0 searches the catalog, identifies the desired frames, and selects one of the many data sets and packaging options. In Table 1, the list of data sets that are available from ASF in mid-1996 are given. The list will change and grow as ASF continues to evolve.

Table 1: Available ASF data sets in 1996

	ERS-1	ERS-2	JERS-1	Radarsat	
				Continuous	ScanSAR
CCSD	x	x	x		
Complex	x	x	x	x	
Raw Signal Data	x	x	x	x	x
Low Res	x	x	x	x	x
Full Res	x	x	x	x	x
Medium Res					x
Geocoded low res					x
Geocoded full res					x
Geocoded medium res					x
Terrain-corrected low res					x
Terrain-corrected full res					x
Terrain-corrected medium res					x
Ephemeris	x	x	x	x	x
Ice motion vectors	x				
Ice classification	x				
Wave spectra	x				

Processing package specifies processing options, media type, and media format. Processing options are as follows: normal, quicklook, low gain, slant range, subframes, cal-uncomp, cal-comp, or some combination of these. For geocoded and terrain corrected image options, the following projections are possible: Universal Transverse Mercator (UTM), Polar Stereographic (PS), and Lambert. However not all of these options are available for every data set. Data sets can be ordered with various media types as follows: ESA_DCRSi, NASDA_HD_96, RSAT_HD_96, 4-MM 2 GBytes, 4 MM 5 GBytes, 8 MM 2 GBytes, 8 MM 5 GBytes, 9 track 1600 BPI, 9 track 6250 BPI, DISK (electronic/network transfer), dry silver film/paper, and B&W photo film/paper. Again not all media is available with all data sets or with all processing options. Media formats include: CEOS SAR tape, tape archive (tar), CEOS SAR file, 8x10 print, 8x10 positive/negative transparencies, 20x24 2x enlargements, 20x24 5x enlargements. Again not all formats are applicable to all data sets, processing options, and media types.

The IMS will send the request for frames to the Production Planning Subsystem (PPS) which will queue the request until all materials necessary for processing are available locally. IMS will also send request for scanning of tapes to the PPS as the tapes become available locally.

The Control Processor, which provides control of the resources of the various processors retrieves jobs from the PPS queue and executes the job on one of the processors [4]. Amongst these processors, the Alaska SAR Processor produces SAR products for ERS-1, ERS-2, JERS-1, and continuous mode Radarsat; the Raw Data Scanner performs scanning of raw data to determine 'good' data frames that are available and decodes Radarsat ScanSAR data to time-ordered, non-redundant Level 0 data; and the ScanSAR Processors handles all modes of ScanSAR data from Radarsat. Once the products are produced by the processors, the Control Processor provides a quality control function that allows the Production Operator to visually inspect the image and the vital metadata. After the inspection, the product is sent to IMS for distribution to the user.

CONCLUSION

ASF has eliminated the Level 1 archive, but has provided visibility into the planned datatakes and into the Level 0 archive. With judicious processing of only data that is ordered for processing, ASF expects to be able to meet the user needs with similar timeliness exhibited in the pas. The fixed frames scheme will allow users to get repeated orbits with high degree of consistency and overlap.

ACKNOWLEDGMENT

The work described in this paper was carried out at the Jet Propulsion Laboratory, California Institute of Technology, under a contract with the National Aeronautics and Space Administration.

REFERENCES

[1] R.Berwin, D.Cuddy, J.Hilland, and B.Holt, "Design, Test, and Applications of the Alaska SAR Facility," Space Technology, Val. 12, PP 91-104, (1992).

[2] D.Cuddy, T.Bicknell, M.Tankenson, "ASF Design Considerations for Radarsat/ERS-2," , IGARRS'94.

[3] M.Schwaller, B.Krupp, "Science Data Plan for the EOS Data and Information System Covering EOSDIS Version 0 and Beyond", .Version 3, July, 1994.

[4] K.Leung, M.Chen, J.Shimada, A.Chu, "Radarsat Processing System at ASF:", IGARSS'96.

Validation and Ground Truth for TRMM Precipitation Radar Using the MU Radar

Toru Sato, Toshihiro Teraoka and Iwane Kimura
Department of Electronics and Communication, Kyoto University
Kyoto 606-01, Japan
Corresponding Author: T. Sato
Phone: +81-75-753-5960, Fax: +81-75-751-8201
E-mail: tsato@kuee.kyoto-u.ac.jp

INTRODUCTION

The largest advantage of space-borne measurements is in its global coverage, especially in the tropical area, where most of the rainfall occurs. TRMM (Tropical Rainfall Measuring Mission) satellite will be the first one which installs a precipitation radar (PR) onboard, and will be launched in 1997. It is expected to provide essential information in understanding the global water circulation. However, since the planned radar is a single-frequency, single-polarization, and non-Doppler one, the retrieval of rainfall rate from the echo intensity data requires careful interpretation based on sophisticated algorithms which incorporate with peripheral ground validation data.

The objective of this study is to establish a reliable ground truth scheme for the planned TRMM precipitation radar using a ground-based radar, and to validate the rain retrieval algorithm based on the radar data. While most of ground validation sites for TRMM PR use microwave Doppler weather radars, we use the the MU (Middle and Upper atmosphere) radar of Kyoto University, Japan.

GROUND TRUTH USING THE MU RADAR

The MU radar has a unique capability of measuring the vertical profile of the DSD simultaneously with background atmospheric parameters such as winds and turbulence. The vertical wind velocity and the intensity of turbulence provide a reliable measure of distinguishing the convective and stratiform rains. Also, the radar is equipped with an active phased array antenna whose beam steerability roughly covers the footprint of TRMM PR with a much higher horizontal resolution. It is thus possible not only to provide an accurate Z factor versus height, but also to quantitatively evaluate the partial beam filling error of TRMM PR.

We developed a special observation mode with 19 antenna beam directions distributed uniformly within the beam coverage of 30 degrees from the zenith. Table 1 gives the basic parameter of the MU radar for this mode. Fig. 1 shows the arrangement of the radar beams. Large circle shows the footprint of TRMM PR, and small circles are the MU radar beams at 3-km height. These 19 beam directions are switched electronically at the pulse interval of 400μsec in a cyclic manner. Doppler echo power spectra are computed at a height interval of 150m for each beam direction every 10 seconds, and averaged for 1 minutes. Rain dropsize distribution is estimated from the observed spectra by fitting the theoretical spectra assuming the gamma distribution[1]. Background wind and spectral broadening due to atmospheric turbulence are automatically compensated for by simultaneously fitting also the atmospheric component[2].

Fig. 2 is an example of the horizontal distribution of the rain intensity observed during a convective rain event with the 19-beam method. Each shaded hexagon denotes the rain intensity averaged for 1 min in 2-3 km height range at each beam direction shown in Fig. 1. A much larger horizontal variation than the accuracy limit seen in this figure demonstrates the natural variability inside a local rain event. Accumulation of such data will be of crucial importance in evaluating the partial beam-filling (PBF) error of the TRMM PR radar algorithms.

Table 1: Basic parameters of the MU radar for the TRMM validation mode.

Parameter	Value
Location	Shigaraki, Japan (34.85°N, 136.10°E)
Radar system	active-phased-array Doppler radar
Frequency	46.5 MHz
Antenna	circular array of 475 crossed Yagi's
aperture	8330 m^2 (103 m in diameter)
beam width	3.6° (one way; half power)
steerability	steering is completed in each IPP
beam directions	19; 0°–30° off zenith angle
polarizations	linear
Transmitter	475 solid state amplifiers (TR modules; each with output power of 2.4 kW peak)
peak power	1 MW (maximum)
average power	2.5 kW (duty ratio 0.25%)
bandwidth	1.65 MHz (pulse width: 1 μs)
IPP	400 μs
Receiver	
bandwidth	1.65 MHz
IF	5 MHz
A/D converter	12 bits × 8 channels
Pulse compression	none

0-7803-3068-4/96$5.00©1996 IEEE

EVALUATION OF RAIN PROFILING ALGORITHM FOR SPACE-BORNE RADARS

The most essential part of the precipitation radar signal processing is the conversion from the measured reflectivity factor into the rain intensity. At the frequency of TRMM PR of 13.8 GHz, the attenuation due to raindrops makes this conversion much more difficult than at a lower frequency. This rather high frequency was chosen to minimize the antenna size for the required beam width. It is thus necessary to compensate for the attenuation in estimating the rainfall rate at each range gate[3]. The candidate algorithm for the rain profiling (2A-25) will be an extension of the α-adjustment method[4]. It is based on the Hitschfeld-Bordan solution[5], but avoids its instability under strong rain condition by adjusting one of the DSD parameter α using the path-integrated attenuation (PIA). Here we examine the effect of the height variations of DSD using the MU radar data as realistic examples of the given 'truth' in the simulation.

Since the α-adjustment method assumes that the parameters are constant versus height, their height variation may cause errors in the derived rain intensity. Fig. 3 shows the result of simulations using the real DSD profiles observed by the MU radar as model profiles. The upper figure is for stratiform rains, and the lower figure is for convective ones. The stratiform case consists of 135 profiles of 1-min resolution taken on July 2-4, 1990, when a stationary front associated with Baiu was present near the MU radar, and the convective case consists of 43 profiles taken on September 19, 1990, when a typhoon was passing near the MU radar. Determination of the rain type was made

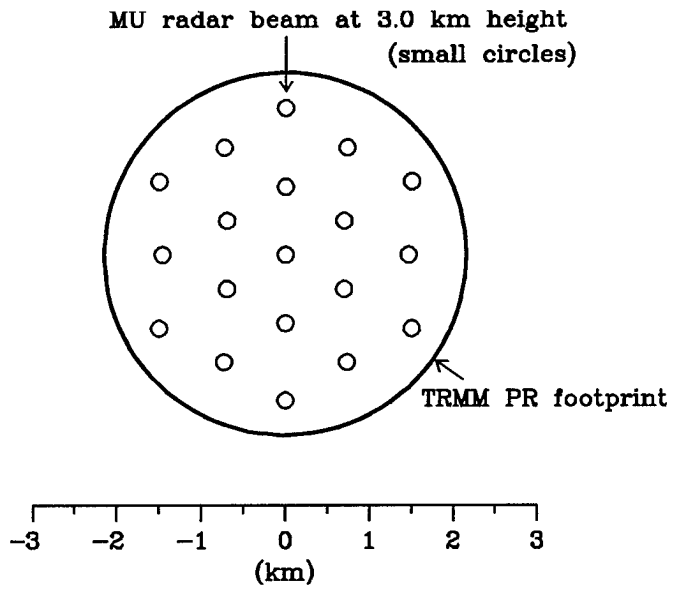


Figure 1: Beam arrangement of TRMM PR and the MU radar at 3 km height.

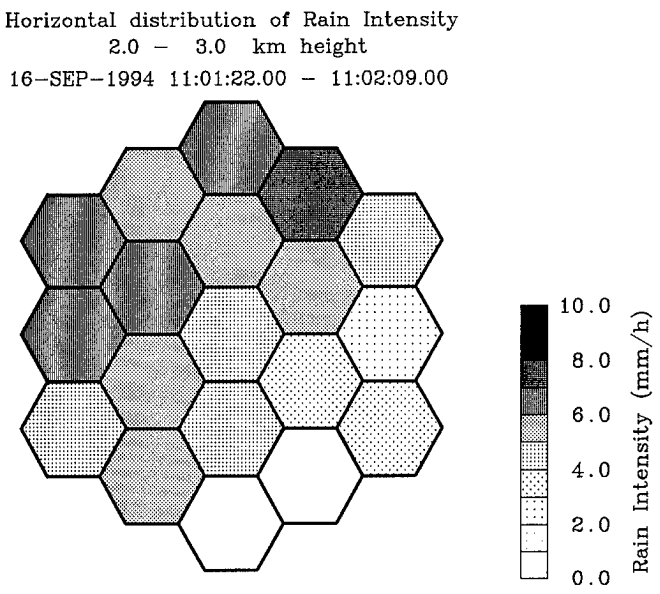


Figure 2: An example of the horizontal distribution of rain intensity.

for individual 1-min profile by whether echoes from rain drops, which have larger Doppler shift than snowflakes, are observed above the freezing level or not. Only those profiles that satisfies this criteria for the stratiform rain for the former data set, and for the convective rain for the latter data set, respectively, are selected.

The attenuation and reflection factors at 13.8 GHz are computed for each range bin from the observed DSD, and then converted to the 'measured' reflectivity profile. In order to avoid additional source of error associated with the bright band, we used the data only below the freezing level. Using these profiles as the given model values, we made numerical simulations. The α-adjustment method is applied to each 1-min profile and the rain intensity is estimated at each range bin. The result is averaged for the entire data set. The error bar put on each estimated value denoted by a circle indicates the standard deviation of the difference between the instantaneous model rain intensity and the estimated one. The error bar for the convective case is about twice larger than the stratiform case, probably due to larger vertical variations of DSD in the convective rain cells.

It should be noted that the vertical variation of DSD also causes positive bias errors even though the α adjustment correctly compensates for the path integrated attenuation. The bias at the sea surface level is 15% and 27% for the stratiform and convective cases, respectively. This bias error is due to the nonlinearity in the $Z - R$ and $k - R$ relations. Although the bias is within the standard deviation, it has a significant meaning for TRMM project whose goal is to provide accurate rain intensity in one-month mean value. It will be effective to make statisti-

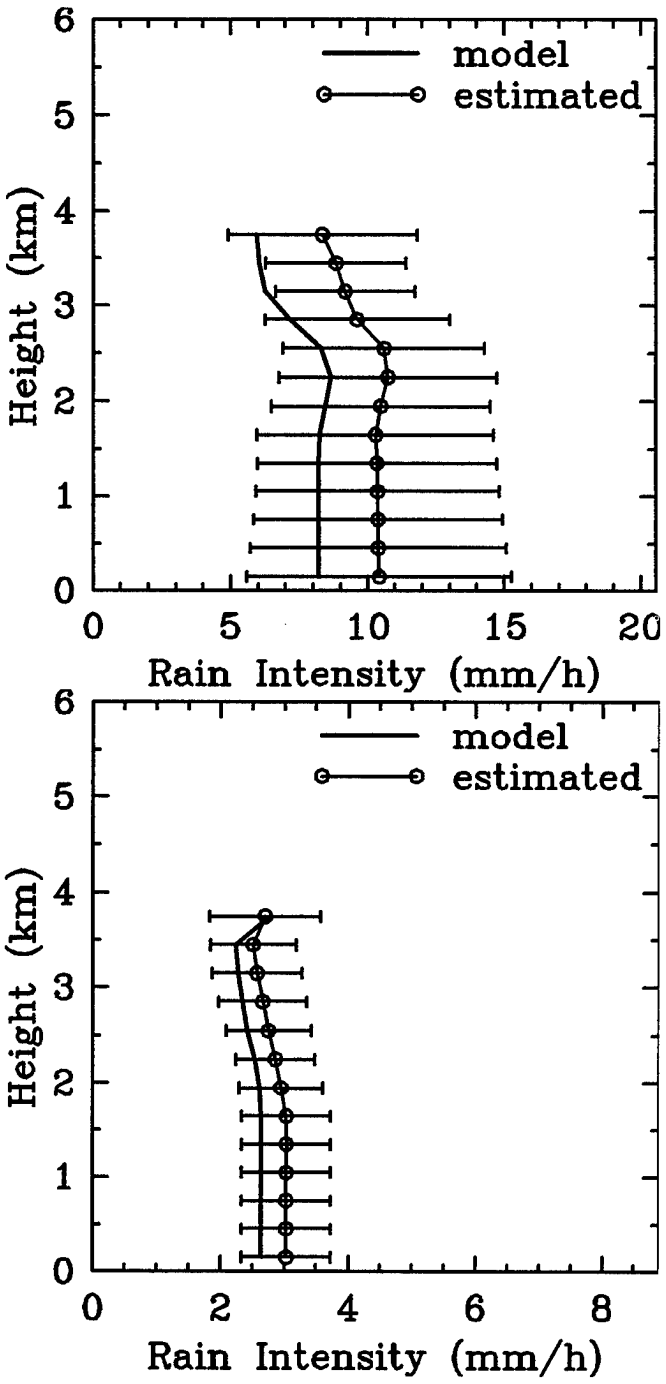


Figure 3: Model and simulation results of rain profiling for the stratiform rain (top) and convective rain (bottom).

cal compensation for this vertical variability of DSD based on ground validation radar data.

SUMMARY

Special 19-beam experiment for the MU radar has been developed for TRMM PR ground validation. Significant horizontal variability over the TRMM PR footprint size (=4km) was found. Effect of such variability on the rain retrieval algorithm has been examined.

The MU radar data are also used in numerical simulations to evaluate the standard rain retrieval algorithm for the TRMM PR data analysis. Effect of the vertical variability of DSD was quantitatively examined, and it was found that it causes a bias of as large as 27% under convective conditions. The proposed scheme for compensating for the PBF error was also examined with a numerical simulation. It was pointed out that although it is possible to make the compensation, its accuracy highly depends on the accuracy of the sea-surface echo.

REFERENCES

[1] T. Sato, M. Sato, H. Chotoku, I. Kimura, H. Ishida, and T. Harimaya, "Evolution of raindrop size distribution observed by a VHF Doppler radar," *Proc. Int. Symp. Antennas Propagat. 1992*, pp. 1049–1052, 1992.

[2] T. Sato, H. Doji, H. Iwai, I. Kimura, S. Fukao, M. Yamamoto, T. Tsuda and S. Kato, "Computer processing for deriving drop-size distribution and vertical air velocities from VHF Doppler radar spectra," *Radio Sci.*, Vol. 25, pp. 961–973, 1990.

[3] R. Meneghini, J. Eckerman, and D. Atlas, "Determination of rain rate from a spaceborne radar using measurements of total attenuation", *IEEE Trans. Geosci. Remote Sens.*, Vol. GE-21, pp. 34–43, 1983.

[4] T. Iguchi, and R. Meneghini, "Intercomparison of single-frequency methods for retrieving a vertical rain profile from airborne or spaceborne radar data," *J. Atmos. Ocean. Tech.*, Vol. 11, pp. 1507-1515, 1994.

[5] W. Hitshfeld, and J. Bordan, "Errors inherent in the radar measurement of rainfall at attenuating wavelengths," *J. Meteor.*, Vol. 11, pp. 58–67, 1954.

Preliminary Results of Ground-Based Rain Measurements with a Dual-Frequency Multiparameter Radar-Radiometer

Hiroaki Horie [1*], R. Meneghini [2], and T. Iguchi [3]
[1] Universities Space Research Association
[1,2] NASA Goddard Space Flight Center
[3] Communications Research Laboratory, JAPAN
Code 975, NASA/Goddard Space Flight Center, Greenbelt MD 20771, USA
+1-301-286-8329(TEL) /+1-301-286-1762(FAX) / horie@meneg.gsfc.nasa.gov

Abstract — Since 1985, a dual-frequency radar-radiometer, built by the Communications Research Laboratory of Japan, has been flown in several NASA-related experiments to test and to develop methods for the estimation of rain rate from space. These measurements have proved useful for developing and justifying methods of rain estimation for the radar to be launched as part of the Tropical Rainfall Measuring Mission. Over this period of time, the instrument was modified to provide, in addition to the usual co-polarized data, cross-polarized measurements at X-band(10 GHz) and Ka-band(34.45 GHz). Additional upgrades have been completed to enable measurements of linear depolarization ratio (L_{DR}) and differential reflectivity ratio (Z_{DR}) at both frequencies for ground-based observations. Plans are presently underway to combine these measurements with the S-band Spandar radar and the microwave and millimeter-wave link experiments located at Wallops Flight Facility. In this paper, we first describe the instrument modifications, then present results taken during a case of light stratiform rain case. Because the calibration of the system is not yet complete, we focus on some of the quantitative features of the data obtained at and near the melting layer.

INSTRUMENT DESCRIPTION

The schematic configuration of the dual-frequency multiparameter radar-radiometer is shown in Fig. 1. The dual-frequency transceiver, radiometer and data acquisition system, enclosed by broken line in Fig. 1, have been installed inside a trailer for the field experiments in the future, with both antennas, polarization switches and antenna controller motors located on the roof. The waveguides from the radar-radiometer to the antennas are connected by rotary joints. The latching circulators and azimuthal and elevation motors are connected by data lines from the control circuitry within the trailer. The original instrument, enclosed by dotted lines in Fig. 1, is controlled independently. The CAMAC data system is used to collect the radar data at both frequencies as well as to record the status data of radar-radiometer. The radiometer data is recorded by a DT2801 A/D conversion card. The card also has a Digital I/O interface, used for controlling the antenna scan motors and selecting the sequence mode at the latching ferrite switch controlling circuitry. The circuitry can change the transmitting and receiving polarization from pulse to pulse. A summary of the instrument characteristics is given in Table 1. The integration number is selectable by the acquisition software on the PC.

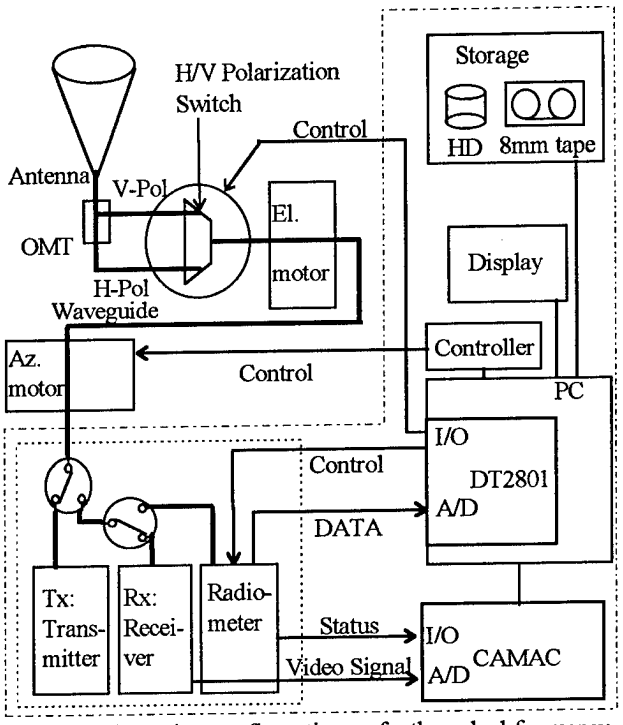


Fig.1 Schematic configuration of the dual-frequency multiparameter radar-radiometer. The original instrument is enclosed by the dotted lines. The instruments enclosed by the hatched line are installed inside the trailer.

* On leave from Communications Research Laboratory, Japan, as a Visiting Scientist Program of USRA.

0-7803-3068-4/96$5.00©1996 IEEE

Table 1. The system specification

	X-band	Ka-band
Center Frequency	10.00 GHz	34.45 GHz
	(3.0cm)	(8.7mm)
Antenna		
Type	Horn lens	Horn lens
Gain	30.3 dB	30.4 dB
HPBW	5.2 deg.	5.1 deg.
Polarization	H and V	H and V
Ferrite Switch		
Isolation	≥30 dB	≥30 dB
Transmitter		
Peak Power	20 kW	10 kW
PRF	440 Hz	440 Hz
Pulse width	0.5 μsec	0.5μsec
Receiver		
NF	5.3 dB	9.6 dB
Detection	Log.	Log.
Dynamic range	80 dB	80 dB
A/D Converter		
Number of bits	8 bits	8 bits
Integration	128	128
Sampling interval	0.2 μsec	0.2 μsec
Radiometer		
Center Frequency	9.86 GHz	34.21 GHz
IF bandwidth	100 MHz	100 MHz
Integ. Time	0.25 sec	0.25 sec
Resolution	0.5 K	0.5 K

RAIN OBSERVATIONS

Fig. 2 shows the range-time profiles of radar images during light stratiform rain obtained by ground-based dual-frequency radar from 16:34 to 16:43 EST on Feb. 8, 1996. Using Z_{PQ} to denote the radar reflectivity factor for transmitted polarization P and receiving polarization Q, the images shown in A), B), C) and D) correspond to Z_{HV}(Ka-band), Z_{HH}(Ka), Z_{HV}(X-band) and Z_{HH}(X), respectively. None of the data were corrected for path attnuation. During the measurement period, the antenna elevation angle was fixed at 45 degrees. The Y axes in Fig.2 correspond to heights between 400 m to 3100 m along the range direction. The X axes represent time in minutes. The grainy nature of the cross-polarized images represent the effect of low signal to noise ratios(SNR). Although the rain was light (less than 1 mm/h according to an optical rain gauge), the images clearly show the melting layer. For the cross-polarization data (Fig. 2 A and C), detectable returns generally occur only in a range of about 0.4 km centered about the melting layer.

Shown in Fig. 3 are range-profiles(A-scope) of the Z_{HH}, Z_{VV} and Z_{HV} at both frequencies at 16:36 EST. Note that in this case a single record consists of a 128-sample average (≈0.6 second). The Z_{HV} at both frequencies are truncated at low SNR. Fig. 4 shows the range-profiles of the Z_{HH}, L_{DR} and Z_{DR} at both frequencies at same time as in Fig. 3.

Comparisons of the Z_{HH}(the X-band and Ka-band) show approximately equal signal strength at ranges below the melting layer, followed by a rapid decrease in the Ka-band signal beginning at the melting layer and continuing into the snow layer. This behavior can be explained by the attenuation through the melting layer and the effect of non-Reyleigh scattering, both of which act to lower the Ka-band return relative to the X-band return. An approximate separation between the two effects can be obtained by examining difference, dBZ_X - dBZ_{Ka}, well above the melting layer; at these ranges, where non-Rayleigh scattering is generally small, the difference is approximately equal to the two-way integrated path attenuation.

The peak values of L_{DR} at both frequencies are slightly less than -10 dB. Moreover a comparison of the peak values of L_{DR} and dBZ(X-band) shows that the former maximum occurs at a slightly lower height. These features of L_{DR} have been observed previously both from ground-based and airborne polarimatric radars [1,2].

Examination of the Z_{DR} values in Fig. 4 at ranges within and just below the melting layer suggest a change in the orientation of the hydrometeor from a random orientation (low Z_{DR} values) to a more ordered orientation (Z_{DR} values of about 1-2 dB). Additional averaging of the data and further tests of the radar calibration are needed, however, to verify these results.

CONCLUSIONS

An existing airborne dual-frequency multiparameter radar-radiometer has been modified for ground-based operation. Upgrades to the switching circuitry provide the capability to measure the LDR and ZDR at X-band and Ka-band frequencies. Measurements in light stratiform rain show features of L_{DR} and dual-frequency ratio (DFR) consistent with previous ground-based and airborne measurements. Future experiments, coordinated with the Spandar radar and the microwave and millimeter-wave link measurements at Wallops Flight Facility, should provide a unique set of measurements for estimating the characteristics of rain.

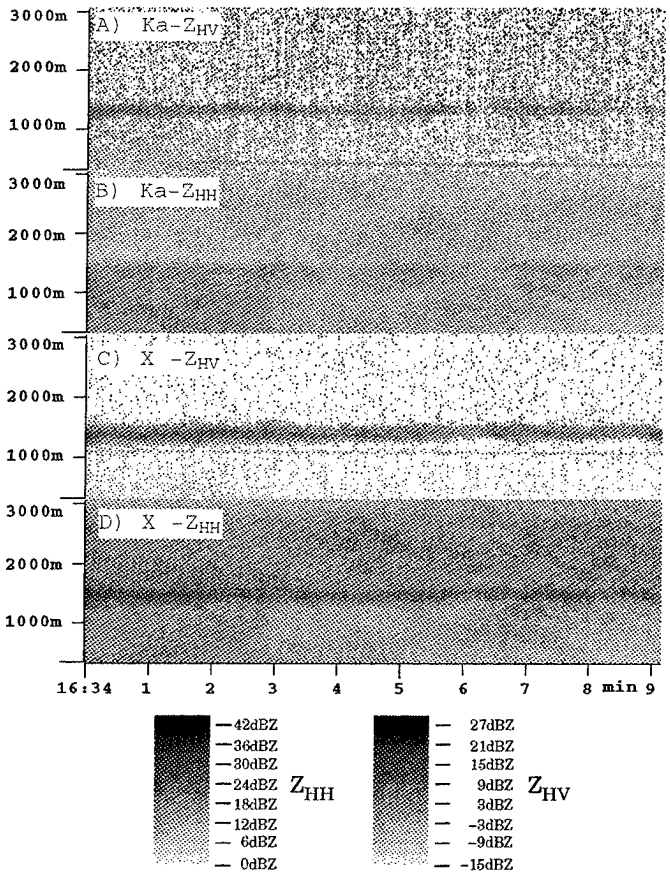


Fig. 2 Range-Time profile obtained during 16:34 - 16:43 EST on Feb. 8, 1996. Antenna elevation angle is 45 degrees. The integration number is 128. Except for the region near the melting layer, the Z_{HV}(X-band and Ka-band) returns are limited by the system noise.

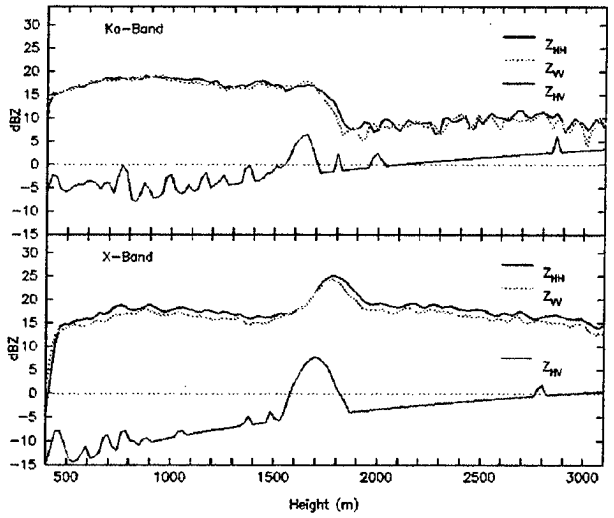


Fig. 3 Range profiles of dBZ_{HH}, dBZ_{VV} and dBZ_{HV} at both frequencies(X and Ka-band) at 16:36 EST on Feb. 8, 1996. Range and time averaging is not performed.

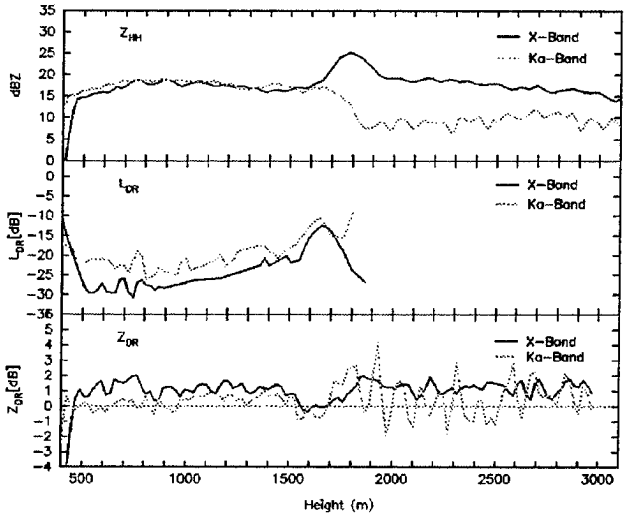


Fig. 4 Range profiles of Z_{HH}, L_{DR} and Z_{DR} at both frequencies (X and Ka-band) at same time as Fig. 3. Range and time averaging is not performed. L_{DR} is truncated at height of around 1900m.

REFERENCES

[1] H. W. J. Russchenberg and L. P. Ligthart, "Backscattering by and Propagation Through the Melting Layer of Precipitation: A New Polarimetric Model", IEEE Trans. Geosci. Remote Sensing, vol. 34, pp. 3-14, Jan. 1996.

[2] R. Meneghini and H. Kumagai, "Characteristics of the Vertical Profiles of Dual-Frequency, Dual-Polarization Radar Data in Stratiform Rain", J. Atmos. Oceanic Technol., Vol. 11, pp. 701, June 1994.

Active and passive microwave for rainfall monitoring

Nativi S., Baldini L., Giuli, D., Mazzetti, P.

Dipartimento di Ingegneria Elettronica, Università di Firenze
via di Santa Marta, 3, 50139, Firenze, Italy
Tel. +39-55-4796370, Fax, +39-55-488883
e-mail: nativi@pinet.ing.unifi.it

Abstract -- This paper reports the experimentation of a joint use of ground-based radars and satellite radiometer in order to obtain more information at diverse spatial and temporal scales to improve quantitative measurement of rainfall over the centre of Italy. In particular the utilisation of radar vertical profile measurements to validate and calibrate passive microwave data is outlined. Experimentation has been conducted on a data set made up of Montagnana multiparameter C-band and DMSP-SSM/I data.

INTRODUCTION

Satellite passive microwave measurements of precipitation are characterised by the presence of larger hydrometeors within clouds, they view the atmosphere from the top downwards and the spatial resolution is very poor; two main issues must be tackled: the beam filling problem and the inversion problem. Surface-based radar measurements of precipitation are based on the estimation of hydrometeors falling from the bases of clouds, they view the atmosphere from the bottom upwards way. The temporal and spatial resolution is very good but there are several physical and technological reasons why the radar estimates may be cumbersome [1]. Investigation of the vertical profile in the presence of precipitation is one of the main topics of interest in radar meteorology, for different kind of applications: micrometeorology, detection and correction of effect due to the presence of bright band in radar rainfall measurements for meteorological application [2], and for predicting attenuation at frequencies used for satellite communication. Even if it is possible to obtain important information from a conventional monoparametric radar, as bright band presence, height and thickness, and Ice Water Content (IWC), the use of polarimetric radar allows the estimate of much more information, such as, hail bulk density, hail detection and a preliminary classification of ice particles. Several parameters have been used to this purpose. Thus, vertical profiles obtained by through polarimetric radar measurements carries a more complete information, with respect to that obtained by using a single parameter radar. Such profiles provides useful information to understand the vertical structure of the observed phenomenon and to aid the comprehension of the inversion topic passive microwave measurements. Information derived from ground-based radar and from satellite radiometer may be integrated and utilised to tackle the passive microwave sources' weaknesses, and through the hydrometeor emission knowledge to improve active microwave source calibration.

Due to the inability of visible and infrared radiation to penetrate the cloud and directly sense precipitation particles, much rainfall algorithms development has been recently based on measurements in the passive microwave regime [3]. Two basic approaches have been used to detect rain using passive microwaves: Regression based algorithms and Physical Inversion algorithms. Regression methods are simple - as far as complexity is concerned - and relatively undemanding of computer resources, but they are not very flexible; The physical inversion algorithms are based on coupled cloud-radiation models, in which the cloud model component is an explicit dynamic-microphysical cloud-mesoscale model (e.g. [4]). They are generally complex and are characterised by large c nputational requirements but they provide flexibility. It is widely accepted that the most satisfactory in the mid-term future are likely to be physical/empirical methods based on good knowledge of cloud physics and use of suitable cloud/rainfall models. Therefore, studies of rain events by both radar and satellite are required, and radar vertical profile information must be particularly considered.

ACTIVE AND PASSIVE MICROWAVE SENSORS

A research project is undertaken between SSM/I data and digital multiparameter radar observations of precipitation, over the centre of Italy. These researches aim at helping build an empirical basis for the quantitative interpretation of microwave radiometric observations of rainfall over land, limited to the Tuscany region, in the centre of Italy. Data sets, derived from the Montagnana multiparameter radar include both Constant Altitude PPI (CAPPI) precipitation maps and Vertical Profiles of Reflectivity (VPR), and DMSP - SSM/I passive microwave data.

DMSP SSM/I

The Special Sensor Microwave Imager (SSM/I) is a passive sensor which detects radiances at four frequencies: 19.35, 22.235, 37.0 and 85.5 GHz. The 19, 37 and 85 channels have dual polarisation (vertical and horizontal), the water vapour line at 22.235 GHz has only vertical polarisation. This instrument is aboard of the operating Defence Meteorological Satellite Program (DMSP) Block 5D-2 Spacecrafts: F10, F11, F13. The seven channels have

0-7803-3068-4/96$5.00©1996 IEEE

different spatial resolutions (i.e. EFOV on earth surface in the cross-track direction) from roughly 43 Km at 19.35 GHz to approximately 13 Km at 85.5 GHz). The passive microwave utilised for the research were acquired from F10, F11 and F13 spacecrafts.

Montagnana Polar 55C radar

The active sensor utilised in this work is the POLAR55C radar system located in Montagnana near Florence. The POLAR55C system is a multiparameter C-Band weather radar operating at 5.5 GHz. The receiver has two incoherent and one coherent channels. In its most common setting the signal processor extracts four parameters which constitute the radar data set: horizontal and differential reflectivity (Z_H, Z_{DR},), mean value and spread of Doppler spectrum (V, σ_V).

THE DATA SET

The present work is based on a data set collected in winter 1995-96. It is relative to some rainfall events observed by POLAR55C radar during the pass of at least one of DMSP satellites. The radar system was set to start the CAPPI acquisition process at the time the satellite began its passing over the region where radar is located, so to have radar data collected some minutes (0 to 5 minutes) after the satellite pass. This should allow a better correlation between the two different methods of measurements.

The table below shows the data set which the work is based on. For every day of radar acquisition the time of a specific satellite pass is shown.

	Pass time (GMT)		
Date	**f10**	**f11**	**f13**
6 Dec 1995		17:24	
23 Jan 1996			16:30
19 Feb 1996	20:46	17:25	16:09
20 Feb 1996		17:11	
21 Feb 1996	10:03	16:59	

DATA PROCESSING

From SSM/I data several parameters related to rainfall over land were achieved. Parameters related to rainfall and to the physical structure of clouds were obtained from radar Zh and Zdr data. Radar and SSM/I parameters maps were processed in order to obtain geographically co-registered images, and to overlay them correlating the diverse information. In particular, both radar and SSM/I images were projected according to the UTM geographical reference system - fuse 32. The radar data were grouped according to a meaningful set of different time lags (involving the times of radar data acquisition and the SSM/I over-passes), and the way the different time lags affect data correlation was examined. The spatial variances related to each SSM/I pixel were estimated through radar data, and their influence on the regression trend (calculated between radar and SSM/I parameters) was considered. The influence of cloud structure parameters on the regression was analysed.

Radar Data Processing

When the meteorological radar is employed within an hydrometeorological monitoring system, whose main objective is to measure rainfall at ground, the main interest lies on the detection of the bright band, and furthermore, deriving its height and thickness, since the presence of bright band generate a peak of radar reflectivity, which provokes overestimation of rainfall, when directly converted into rain. In general vertical variability of the reflectivity field yield two kind of error due the characteristic of radar sampling: the first is related to the discrepancies between radar and ground measurements due to the precipitation sampling performed by radar at a given height above ground. Besides, the radar spatial resolution, though sufficient in the horizontal plane for hydrological applications, is, indeed, extremely scarce in the vertical plane, especially far from radar. Thus, different kind of hydrometers could be intercepted by the radar beam. A method for estimating vertical profile as far the bright band is concerned, have been mainly derived by Smith [2]. When accurate description of variation of reflectivity below bright band is of interest, inversion techniques have to be adopted. The use of multiparameter data is instead necessary when the objective is the identification of particles and the description on layers above the bright band. In fact, although some parameters can be derived through Zh only, such as the Ice Water Content, through a relationship as

$$Zh = a + b \log (IWC);$$

and other from the Zdr such as the ice bulk density [5] through:

$$Zdr = c \cdot \rho^{d} \cdot \log(r);$$

being ρ=ice bulk density; r=axis ratio of ice crystal; Furthermore, Zdr is used to detect hailstones and other particles. Studies and observations are reported in literature and point out the ability of classification of polarimetric radar.

In the case of Polar 55C radar data set, rainrate maps at different heights, projected according to UTM geographical references are obtained through processing of PPI radar maps accounting for ground clutter, attenuation due to C-band propagation and occultation. Further processing includes estimation of vertical profile through inversion method and the computation of parameters characterising ice

particles when the presence of such particles is detected by the use of Zh and Zdr data comparison.

SSM/I Data Processing

SSM/I images were spatially deconvoluted and projected according to UTM system with a resolution of 5x5 Km per cell. They were then processed in order to correct possible navigation errors and are centred on the Montagnana radar site. Snow and cold ground pixels were filtered according to the Ferraro and Grody algorithm [8]. A range of significant passive microwave parameters related to precipitation were then calculated in order to analyse the correlations between the multisensor data sets. Several SSM/I parameters related to precipitation over land have been achieved, among them:
Scatter Index[3]:

$$\begin{cases} SI_{85v} = T_i - T_{b85v}; \\ T_i = a - b \cdot T_{b19v} - c \cdot T_{b22v} + d \cdot T_{b22v}^{\,2}; \end{cases}$$

I and Q Stokes parameters:

$$\begin{cases} I_{85} = \dfrac{T_{b85v} + T_{b85h}}{2}; \\ Q_{85} = \dfrac{T_{b85v} - T_{b85h}}{2}; \end{cases}$$

Polarisation Corrected Temperature [2]:

$$\begin{cases} PCT_{85} = \dfrac{T_{b85v} - \beta \cdot T_{b85h}}{1-\beta}; \\ \beta = \dfrac{1-\varepsilon_v}{1-\varepsilon_h}; \end{cases}$$

$T_{bv,h}$ are the vertical and horizontal brightness temperature measured by the satellite at a single frequency, respectively; $\varepsilon_{v,h}$ are the vertical and horizontal superficial emissivity, respectively.

Statistical Analysis

For the cases analysed, a correlation exists between the radar rainrate and satellite derived parameters, in spite of fundamental differences between the two basic data types, and their different space and time resolutions. In particular, radar 3-D vertical profile parameters provide useful information to invert passive microwave signatures and improve the correlation; that has been particularly true for I_{85} and Q_{85} Stokes and SI parameters. The statistical results point out the importance of the influence that the time lag parameter and the rainfall spatial inhomogeneity exerts on the correlation between the radar and the SSM/I calculated parameters.

CONCLUSIONS AND PERSPECTIVE

The utilisation of Zh and Zdr vertical profiles 3-D maps as well as other derived cloud structure parameter maps, was analysed against the correlation between radar rainrates and estimated passive microwave parameters. This work has established that vertical profile radars maps provide useful information on the structure of the atmosphere which the passive radiometer monitors and should help to improve both the retrieval of precipitation-related parameters from satellite data, and lead to better passive microwave rainfall algorithms, particularly of the physical/empirical type. This methodology must be consolidated and then may be considered operationally to improve regional systems for quantitative estimation of precipitation.

REFERENCES

[1] D.C. Hogg, "Rain, Radiometry, and Radar," IEEE Trans. Geosci. Remote Sensing, vol. 27, No 5 1989, pp. 576-585.

[2] C.J., Smith, "The reduction of errors caused by Bright Band in quantitative rainfall measurements made using radar", in J. of Atmos. Ocean Techn., 3, 1986, pp. 129-141.

[3] E.C. Barrett, and M.J. Beaumont, "Satellite Rainfall Monitoring: an Overview," Remote Sensing Review, vol. 11, pp. 23-48, 1994.

[4] E.A. Smith, A. Mugnai, H.J. Cooper, G.J. Tripoli, and X.W. Xiang, "Foundations for statistical physical precipitation retrieval from passive microwave satellite measurements. Part I brightness temperature properties of a time dependent cloud-radiation model," J. Appl. Meteor., vol. 31, 1992, pp. 506-531.

[5] J. Vivekanandan, V.N. Bringi, M. Hagen, P. Meischner, "Polarimetric radar studies of atmospheric ice particles", IEEE Trans. on Geosci. and Remote Sensing, vol. 32, No 1, 1994, pp. 1-10.

[6] R.R. Ferraro, N.C. Grody, G.F. Marks, "Effect of Surface Conditions on Rain Identification using the DMSP-SSMI," Remote Sensing Reviews, vol. 11, No 14 1994, pp. 195-209.

[7] N.C. Grody, and R.R. Ferraro, "A comparison of Passive Microwave Rainfall Retrieval Methods," 6th Conf. Satellite Meteor. Oceanog., Atlanta, 1992, Amer. Meteor. Soc.

[8] N.C. Grody, "Precipitation monitoring over land from satellite by microwave radiometery," in International Geoscience and Remote Sensing Symposium (IGARSS'84), Strasbourg, France, ESASP-215, 1984, pp. 417-423.

Investigation of Multifrequency / Multipolarization Radar Signatures of Rain Cells, Derived from SIR-C/X-SAR Data

Christian Melsheimer, Werner Alpers, Martin Gade,
Institute of Oceanography, University of Hamburg, D–22529 Hamburg, Germany,
phone: +49 (40) 4123 5432, fax: +49 (40) 4123 5713, e-mail: alpers@ifm.uni-hamburg.de

Abstract – During the two SIR-C/X-SAR missions in April and October 1994, a large number of multifrequency / multipolarization synthetic aperture radar (SAR) images were acquired from the Space Shuttle "Endeavour" which show radar signatures of rain cells over land as well as over the ocean. In this paper we discuss the radar signatures of tropical rain cells that were acquired over the Brasilian rain forest and over the Gulf of Mexico. It is shown that multifrequency / multipolarization radar imagery has the potential to yield valuable information on tropical rain cells,especially on the altitude of the melting layer and the rain rate.

INTRODUCTION

Tropical rainfall is produced by convective processes in the atmosphere that are highly variable in space and time. The rainfall is often confined to isolated cells, called tropical rain cells, that have a diameter of only a few kilometers, but also clusters of rain cells with an extent of several tens of kilometers are quite common. The latent heat that is released into the tropical atmosphere by precipitation is an important heat source for the tropical atmosphere that drives low latitude atmospheric circulations, supplies energy to balance radiation heat losses, and strongly affects the wind system in the middle and high latitudes.

In general, tropical rainfall is associated with a thunderstorm. When the terminal velocity of the large liquid and frozen rain drops inside the clouds (hydrometeors) is higher than the updraft velocity it starts raining and a strong downdraft is generated (mature stage). These downdrafts often have a cylindrical form which, by horizontal spreading, give rise to a divergent radial wind field at the earth surface [1].

Tropical as well as non-tropical rain cells have been studied intensively by ground-based polarimetric weather radars [2,3]. From their data the size of rain cells, the rain rate, and the height of the melting layer (where the temperature is approx. 0 °C) can be determined. When interpreting spaceborne synthetic aperture radar (SAR) images of rain cells, one can therefore recourse to investigations carried out by radar meteorologists who have measured the attenuation and scattering of microwaves by rain drops and ice particles.

In this paper we show that multifrequency / multipolarization SAR imagery is capable of extracting valuable information on rain in the atmosphere as well as on rain imping-

This work has been supported by the German Space Agency (DARA) under contract 01QS9016 / 50QS90165 and by the German Science Foundation under the project SFB 318.

ing on the sea surface. The images were acquired by the X, C, and L band SARs aboard the Space Shuttle "Endeavour" (operating at 9.6, 5.3, and 1.25 GHz, respectively) during the two Spaceborne Imaging Radar-C / X-SAR (SIR-C/X-SAR) missions in April and October, 1994. During these missions, a large set of SAR images has been acquired over tropical areas showing pronounced radar signatures of rain cells, in particular at X band.

IMAGES OF THE RAIN FOREST

Fig. 1 shows signatures of several rain cells on an X band SAR image acquired over the Brasilian tropical rain forest. These signatures are large elongated dark patches with lengths between 8 and 15 km and with a small bright spot at their near-range edge. These bright spots originate from very strong scatterers in the atmosphere (i.e., predominantly ice spheres coated with liquid water) near the melting layer. The dark patches are shadows caused by the attenuation of the microwaves by these strong scatterers. Fig. 2 shows a simultaneously taken hand-held photograph of the same area (note the branch of the Amazon river on the radar image as well as on the photograph). Some of the rain cells visible on the X band SAR image can also be identified on the photograph as distinctive cloud features. One of them is marked by an arrow in both figures.

The L band image (not shown here) of the same area shows no radar signatures of rain cells.

RADAR IMAGE OF THE OCEAN

Radar signatures of rain cells over the ocean are more complex than those of rain cells over rain forests, because they result from a mixture of volume scattering and surface scattering (i.e., the microwaves are backscattered in the atmosphere as well as on the ocean surface). Often it is impossible to disentangle both contributions; however, in some cases they can be separated. Favorable are steep incidence angles.On some SIR-C/X-SAR images radar signatures have been found which must originate from atmospheric (volume) scattering and are not associated with sea surface effects. From these radar signatures an estimate of the height of the melting layer can be derived (typically 4-5 km). As an example, radar signatures that originate from both volume scattering as well as surface scattering are discussed in this paper, in order to show how strongly the signatures of different radars bands and polarizations vary and how information on the rain cell can be extracted from them.

0-7803-3068-4/96$5.00©1996 IEEE

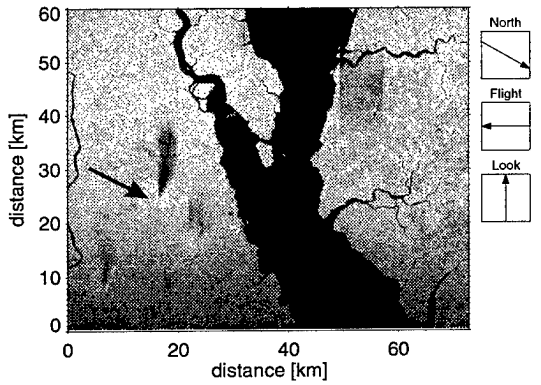


Fig. 1: X band, VV pol., SAR image acquired over the Amazon delta on April 12, 1994, at 18:14 UTC (data take 54.4, image center at 1.5°S, 48.9°W, incidence angle 58.3°) showing the rain forest, a branch of the Amazon river, and several dark and bright patches caused by tropical rain cells.

Fig. 3 shows an X band (left) and an L band (right, both VV pol.) SAR image of a cluster of tropical rain cells over the Gulf of Mexico. The dark and bright structures are much more distinct at X band than at L band, in particular, the bright and dark radar signatures of a rain cell in the lower left-hand section of the X band SAR image are missing in the L band SAR image.

The variations of different parameters characterizing the radar backscattering along the scan lines in Fig. 3 have been determined and are plotted in Fig. 4. These parameters are the effective normalized radar cross sections (NRCS) at X, C, and L band, VV polarization (Panel A), the effective NRCS at C and L band, HV polarization (Panel B), and the phase difference between the HH and the VV backscattered signals (Panel C). Note that surface scattering as well as volume scattering contributes to the effective NRCS.

Panel A of Fig. 4 shows that the variation of the effective

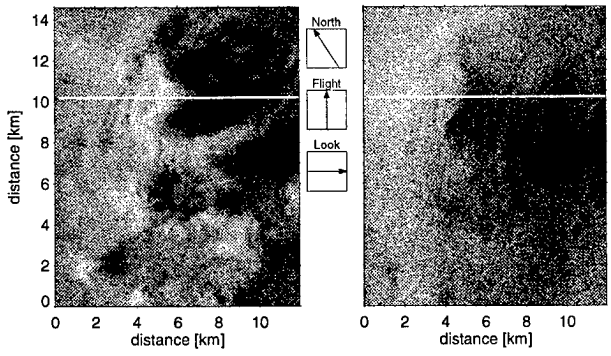


Fig. 3: Composite of two SAR images acquired at X (left) and L band (right), VV pol., on April 18, 1994, at 08:11 UTC over the Gulf of Mexico and showing radar signatures of tropical rain cells (data take 145.12, image center at 25.8°N / 88.6°W, incidence angle 27.4°). Inserted are lines along which the variation of the quantities plotted in Fig. 4 have been determined.

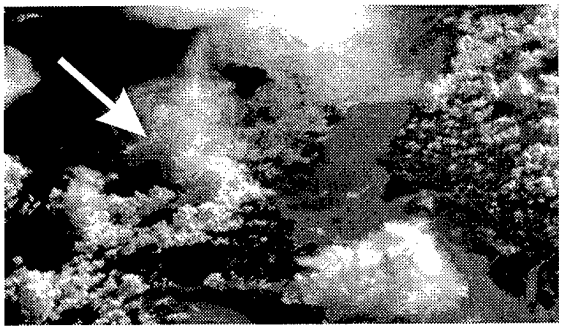


Fig. 2: Quasi-simultaneous photograph taken with a hand-held camera from the Space Shuttle "Endeavor" and covering the same area imaged by the X band SAR (see Fig. 1).

NRCS is largest at X band and smallest at L band. Furthermore, the position where the effective C band NRCS starts to decrease is further to the right (far-range) than the position where the L band NRCS starts decreasing.

THE SCATTERING MECHANISM

The fact that rain cells over tropical rain forests have strong radar signatures at X band, weak signatures at C band, and almost no signature at L band shows that they must be associated with volume scattering at hydrometeors in the atmosphere. The smaller the ratio of the diameter of the hydrometeors to the radar wavelength, the smaller is the scattering and the attenuation of the microwaves. The radar backscattering from the tropical rain forest is practically unaffected by the rain. Thus, by analyzing multifrequency / multipolarization SAR images of rain cells over tropical rain forests, one can obtain information about the height of the melting layer as well as about the distribution of rain drops in the atmosphere.

However, in addition to volume scattering, radar signatures of rain cells over the ocean are also affected by surface scattering. Turbulence induced by rain impinging on the sea surface has a damping effect on the Bragg waves and thus reduces the NRCS [1]. On the other hand, rain impinging on the water surface also generates ring waves which increases the NRCS.

Furthermore, rain cells are often associated with strong winds at the ocean surface which increase the surface roughness and thus the radar backscattering. Therefore, the above mentioned divergent radial wind field can cause nearly circular bright patterns often visible on SAR images acquired over tropical and subtropical ocean areas.

The sketch drawn in Fig. 5 illustrates the geometry of the imaging of a rain cell by a side-looking SAR. The five curves in the lower section qualitatively describe the variation of the image intensities (or effective NRCS) at different frequencies and polarizations as well as the HH-VV phase difference at C band. When the X band radar signal hits the rain drops in the atmosphere, it gives first rise to an increase of the effective NRCS at short ground ranges (according to

the SAR imaging mechanism, atmospheric radar echoes of the same slant range are mapped into the same ground range resolution cell towards near-range). Secondly, it leads to a reduction of the effective NRCS in far-range which is caused by signal attenuation by the rain drops in the atmosphere. This explains the combination of bright spots and dark "shadows" visible in X band SAR images of rain cells (see Fig. 3, left panel) as well as the effective X band NRCS shown in Panel A of Fig. 4.

The radar wavelength is much larger at L band than at X band (24 cm versus 3 cm), and therefore the L band microwaves are practically unaffected by rain in the atmosphere. The decrease of the effective NRCS at L band is thus mainly due to the damping of the Bragg waves by rain-induced turbulences in the upper water layer. Note that the areas of reduced effective NRCS at X, C, and L band are displaced from each other in Fig. 5 which agrees with the respective scan lines shown in Panel A of Fig. 4.

The effective NRCS at C band, cross polarization, (Panel B) is especially large in the transition region (i.e., the region where the X band effective NRCS drops) which shows that, at this range, volume scattering must be the dominant scattering mechanism at C band (the cross polarization NRCS is small for Bragg scattering at the sea surface).

Finally, the change of the phase difference between the HH and the VV signal at C band (Panel C) indicates that the C band microwaves have propagated through rain in the atmosphere. The different influence of the rain on the phases of H and V polarized microwaves causes this phase difference (see [4]).

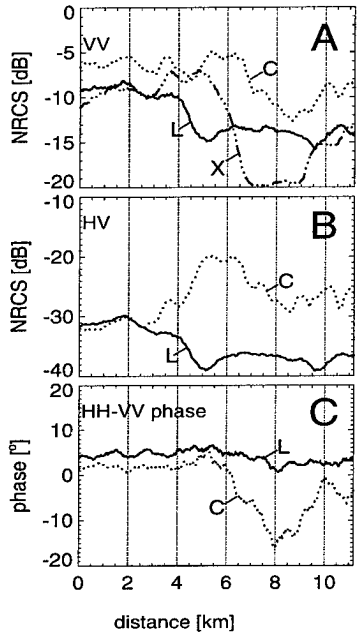


Fig. 4: Variation of the eff. NRCS at VV (Panel A) and HV pol. (Panel B), and of the HH-VV phase difference (Panel C) along the scan line shown in Fig. 3. The solid, dotted, and dashed-dotted lines denote L, C, and X band, respectively.

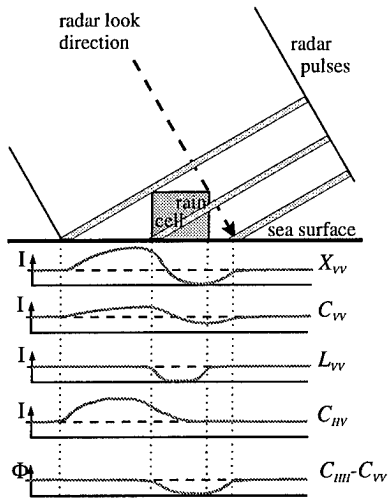


Fig. 5: Sketch of the scattering geometry of a rain cell imaged by a side-looking radar. Below, the intensity variations in range direction at X, C, and L band, VV pol., (X_{VV}, C_{VV}, and L_{VV}), C band, HV pol., (C_{HV}) as well as of the C band HH-VV phase difference (C_{HH}-C_{VV}) are shown qualitatively.

CONCLUSIONS

Multifrequency / multipolarization SAR imagery of (tropical) rain cells acquired over land can be used to obtain information on the distribution of rain in the atmosphere as well as on the height of the melting layer. In addition, if acquired over the ocean it can also be used to extract information on the rain impinging on the sea surface and on the wind gusts associated with them. However, an optimum algorithm for inverting the radar signatures into geophysical parameters has still to be developed.

ACKNOWLEDGMENTS

The authors are grateful to M. Kessler and G. Tanck for their engaged help in processing the SAR data.

REFERENCES

[1] D. Atlas, "Footprints of storms on the sea: A view from spaceborne synthetic aperture radar," J. Geophys. Res., vol.99, 1994, pp.7961-7969.

[2] F.D. Marks, "Radar observation of tropical weather systems," in D. Atlas, Editor, Radar in Meteorology, American Meteorological Society, Boston, 1990, pp.401-425.

[3] R.J.Doviak, D.S.Zrnic, "Doppler Radar and Weather Observations," 2nd. ed., Academic, San Francisco, Calif., 1994.

[4] P. Meischner, I. Dölling, and M. Hagen, "Polarimetrische Radarmessungen in der Meteorologie," in Annalen der Meteorologie, 32, Deutscher Wetterdienst, Offenbach / M (ISSN 0072-4122), 1985, pp.60-73.

Fuzzy Classification Techniques in the Urban Area Recognition

Elena Console (*), Marie Catherine Mouchot (**)
(*) Dipartimento di Matematica e Statistica, Università degli Studi di Napoli "Federico II"
Monte S. Angelo, Via Cinthia, 80126 - Napoli (Italy)
tel.: +39.961.74.75.28/fax: +39.961.72.56.36
e-mail: console_e@abramo.it
(**) Département I.T.I., ENST de Bretagne
Technopôle de Brest-Iroise, BP 832, 29285 Brest Cedex (France)
tel.: +33.98.00.13.58/fax: + 33.98.00.10.98
e-mail: mc.mouchot@enst-bretagne.fr

Abstract -- Determination of scattered urban areas in very heterogeneous environment can prove to be quite difficult using conventional classification techniques of remotely sensed images. On the other hand, fuzzy logic methods enable this difficulty to be overcome by assigning one pixel to more than one class according to a membership grade, determined using a pre-defined function.

In this study, urban area have been classified using fuzzy logic methods. The analysis was performed on a Landsat-TM sub-scene (800X600 pixels) acquired over the province of Catanzaro (Calabria, Italy). The intrinsic characteristics of the ground coverage, as well as the rough topography, contribute to make this area a very heterogeneous one.

The image was classified using a Fuzzy Parallelepiped classifier and membership values, associated to each pixel, were calculated. For each pixel, the classes, which contributed the most, were kept for the determination of the final pixel assignment. Global accuracy of fuzzy classification, estimated on mixed test area (chosen during a 2nd ground truth campaign) reached a level of 0.75

Urban areas were identified analysing the images that represent the combinations of "Urban" class with the other classes.

The fuzzy classification results were compared to image classified using the traditional techniques, minimum distance and maximum likelihood. In terms of global accuracy, fuzzy technique appeared to be more accurate than conventional techniques.

INTRODUCTION

One difficult, although interesting, aspect of remotely sensed images classification is the extraction of urban areas when they appear as heterogeneous scattered patches. Being able to clearly describe these areas is however mandatory for adequate land planning and monitoring.

In the present work, the analysis was performed on a Landsat5 TM sub area of 800x600 pixels (432 km2) acquired over the county of Catanzaro (Calabria, Italy). This area is highly representative of scattered urban settlement, characterized by a mixture of modest inland housing, often abandoned or altered, and more recent coastal housing anarchically erected without any foreseen planification.

Topographically speaking, the area is mainly covered by steep hills quite hard to cultivate. The best arable fields are then intensively used by combining up to three different types of culture at the same location. The radiance reaching the sensor is then modulated by the spectral signature of more than one type of ground cover. In such a very heterogeneous area, conventional methods obviously fail to adequately represent this ground cover; the pixel is authoritatively assigned to the class whose spectral characteristics are the closest, without taking into account the possibility of mixed signatures. On the other hand, fuzzy logic classifiers allow to assign each pixel to more than one class in a proportion given by the membership value of this pixel to all the considered classes.

METHODOLOGY

The first step of a fuzzy logic classification is then to describe the membership functions to each desired class. These classes have been selected according to the one present on the official Italian maps produced by the Istituto Nazionale di Statistica (ISTAT). In our study area, the most representated classes are: *cultivated area* (wheat, oats), *orchards* (olives, oranges), *forest* (deciduous, evergreen), *grass covered area* (pasture, fallow), *non vegetated area* (beach, riverside), and *urban area*. Due to the topographical constraints, it has been necessary to split the forest class into two sub-classes: forest on sunny slopes and forest on shady slopes.

Thereafter, 103 training sites were identified in the field and their spectral signatures calculated. The mixed nature of these pixels was strictly reported for further evaluation of the method. Trapezoidal membership functions were chosen with the core of the function being represented by the interval bounded by the minimum and the maximum values determined for each class using the spectral signatures of the training sites. The functions were defined like this:

if $Min_{i,p} < x_j < Max_{i,p}$, then $\mu_i(x_j) = 1$

0-7803-3068-4/96$5.00©1996 IEEE

if $0 \le x_j \le Min_{i,p}$, then $\mu_i(x_j) = f_1(x_j)$ (1)
if $Max_{i,p} \le x_j \le 255$, then $\mu_i(x_j) = f_2(x_j)$

where:
$\mu_i(x_j)$ = membership value of the *jth* pixel to *ith* class
$Min_{i,p}$, $Max_{i,p}$ = minimum/maximum value in the *pth* band for *ith* class

$$f_1(x_j) = \frac{1}{Min_{i,p}} x_j$$

$$f_2(x_j) = \left(\frac{1}{Max_{i,p} - 255}\right)x_j - \left(\frac{255}{Max_{i,p} - 255}\right)$$

In order to belong to a class, a pixel must comply with the membership function of this class in all spectral bands. The final membership value of a pixel to a given class is then obtained by a t-norm, chosen here according to the Zadeh definition and such as:

$$\mu_i(x_j) = \min_{p=1}^{6} \mu_{i,p}(x_j) \quad (2)$$

where:
i = *ith* class, (i = 1, 7)
p = *pth* band, (p = 1, 6)

RESULTS

Membership values of each class being calculated for all pixels, we first ranked them in descending order and extracted the first two values. The two most contributing classes and their respective contribution are now attached to each pixel. In order to visualize this result, two different types of images were produced. The first one representing the mixed classes and the second one representing, for each mixed class, the degree of mixture.

In the first case encoding was performed as follows. The number of classes being less than 10 each pixel is attributed a 2 digit number. The first digit corresponds to the most contributing class M1 and the second to the second most contributing class M2. If M1=0 the pixel is non classified and, if M2=0, the pixel is considered as being *"pure"*. Using this method a number of 11 mixed classes, among a potential of 15, were identified. They effectively correspond to possible occurrence in the field. As this image does not reflect the degree of membership to each class, 11 more images were created representing the mixed classes.

The degree of membership has been reduced to 5 levels in order to ease the interpretation. Each pixel has been assigned to a 2 digit number. The first digit corresponds to the membership value of class M1 and the second to the membership value of class M2.

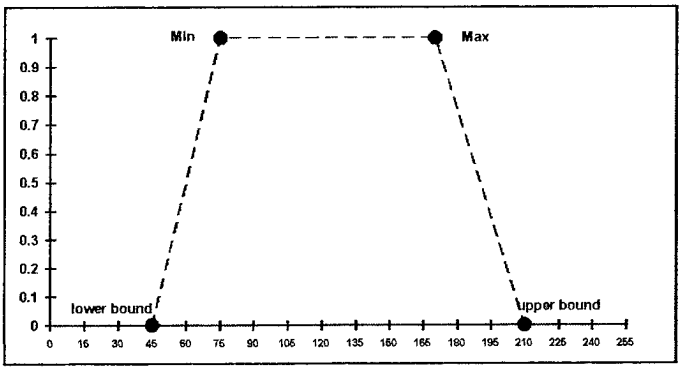


Figure 1: Example of chosen membership function

In order to verify the overall accuracy of the classification the confusion matrix was calculated on a sample of pixels extracted according to the simple sampling method. The global precision index K was equal to 0.75 while it reached 1 for all pure and mixed urban classes.

Finally, the image was also classified using more traditional algorithms such as maximum likelihood and minimum distance. In this case accuracy was evaluated on pure pixels only.

For maximum likelihood, global accuracy was 0.29, going down to 0.17 for the urban class. In the case of the minimum distance, these numbers became 0.23 and 0.30 respectively. Table 1 summarizes the results obtained with the three methods.

CONCLUSION

Fuzzy logic methods have proven to be more adequate than conventional methods for the classification of mixed areas. Both the overall accuracy and the level of intrinsic information have been substantially increased by using fuzzy logic. It should therefore be preferred in all cases of mixed classes interpretation. In the special case of urban area interpretation where mixture is inherent to the class (a town is not a giant block of concrete) it should allow the wider use of remote sensing images for urban planning and monitoring.

Table 1: Comparison between results

PURE CLASSES	MAX.LIK.	MIN.DIST.	FUZZY P.
Orchards	73191	18920	45
Cultivated area	37526	77439	10606
Forest (shady area)	18878	12005	17325
Forest	108156	150650	45127
Grass covered area	91524	10306	-
Urban area	9364	4680	3001
Non vegetated area	5235	1739	4493
MIXED CLASSES			
Orchards+Cultiv. a.	-	-	5517
Orchards+Forest	-	-	6278
Orchards+Urban a.	-	-	143
Cultiv.area+Forest	-	-	96190
Cultiv.a.+ Grass c.a.	-	-	53331
Cultiv.a.+Urban a.	-	-	4171
Cult.a.+Non veget.a.	-	-	1446
Forest+ F.Shady a.	-	-	17981
Forest+Urban area	-	-	4295
Grass cov.a.+Forest	-	-	82827
N. veg.a.+Urban a.	-	-	597
Total pure pixels	**343874**	**275739**	**80597**
Total mixed pixels	-	-	**272776**
Non classified	**310206**	**378341**	**300707**
Total	**654080**	**654080**	**654080**
Global accuracy (K index)	**0.29**	**0.23**	**0.75**

REFERENCES

[1] Congalton R.G., Oderwald R.G. and Mead R.A., (1983), "Assessing Landsat Classification Accuracy Using Discrete Multivariate Analysis Statistical Techniques", in Photogr. Eng. & R. Sens., vol. 49, n. 12, december, pp.1671-1678

[2] Console E. and Mouchot M.C., "A hybrid classification method based on fuzzy logic and conventional techniques", in International workshop on soft computing in remote sensing data analysis, Consiglio Nazionale delle Ricerche, Milano 4-5 december 1995

[3] Mouchot M.C., "Méthodes de classification floue en télédétection", Département Mathématique et Systèmes de Communication, Ecole Nationale Supérieure des Télécommunications de Bretagne, Brest, 1993

[4] Pathirana S. and Fisher P.F., "Combining membership grades in images classification", in Proceegings of ASPRS-ACSM annual meeting, Baltimora, vol. 3, 1991, pp. 302-311

[5] Wang F., "Fuzzy Supervised Classification of Remote Sensing Images", in IEEE Trans. Geos. Rem. Sens., vol. 28, n. 2, mars 1990, pp.194-201

[6] Zadeh L. A., "Outline of a New Approach to the Analysis of Complex Systems and Decision Processes", in IEEE Trans. Sys., Man Cyb., vol. SMC-3, n. 1, january 1973, pp.28-44.

Robust mixed pixel classification using the hypothesis testing Hough transform

P Bosdogianni, M Petrou and J Kittler

Department of Electronic and Electrical Engineering, University of Surrey
Guildford GU2 5XH, United Kingdom
Tel: +44-1483-300800, Fax: +44-1483-34139
E-mails: {p.bosdogianni, m.petrou, j.kittler}@ee.surrey.ac.uk

ABSTRACT

In this paper we present a novel method for mixed pixel classification where the classification of groups of mixed pixels is achieved by using robust statistics. The method is demonstrated using simulated data and is also applied to real Landsat TM data.

1. INTRODUCTION

The motivation of our work is to monitor burned forest regions for several years after the fire so that the regeneration processes can be evaluated. We are interested in assessing the degree of presence of three classes in a region: aleppo pine, bare soil and other vegetation, using Landsat TM images. In the past we addressed the problem of mixed pixel classification when whole regions of mixed pixels have to be classified, by treating the luminance of each pixel as a random variable [2]. In this work we address the same problem but in a way that is applicable to cases that our previous approach is unreliable, namely when outliers are present which is often the case when one has to deal with real data.

2. THE PROPOSED METHOD

In the linear mixing model adopted here, it is assumed that the pixel value in any spectral band is given by the linear combination of the spectral responses of each component within the pixel [1],[6], ie

$$w = ax + by + cz \tag{1}$$

where w is the known spectral reflectance of a mixed pixel, x, y and z are the known spectral reflectances of the three possible cover components within the mixed pixel and a, b and c are the proportions to be estimated for each component contained in the mixed pixel. The method often used for this purpose is that of least squares fitting. It is well known, however, that the method of least squares is particularly sensitive to outliers. What we propose in this paper is the use of a Hypothesis Testing Hough transform.

The linear mixing equation can be considered as the equation of a hyper-plane in luminance space where we measure one type of luminance along each axis. What we are interested in identifying are the parameters a, b, c of this plane. The Hough transform is mainly used to identify straight lines in images, but more generally Hough transform can be thought of as a transformation into the parametric domain where we seek to identify sets of real data that indicate the same values of the parameters for the parametric hyper-surface they define.

In our case this hyper-surface is a plane defined in the 3D domain of the luminances of the three pure classes, which is parameterized by the reflectances of different mixed pixels. The advantage of the Hypothesis Testing Hough transform over the conventional one [3] is that it creates a continuous accumulator function, as opposed to a discrete accumulator array, which can be sampled as densely as it is necessary and which can be calculated at any point with as much accuracy as it is allowed by the data (i.e. the binning error of the conventional Hough is eliminated) [4]. As our proportions have to sum up to 1, our accumulator function is 2D. This array is sampled at a set of chosen (a,b) points. For each hypothesized set of (a,b) values and each triplet of (x,y,z) values drawn from the sets of points that represent the pure classes, we can estimate the reflectance vector w_H using:

$$w_H = z + a(x - z) + b(y - z) \tag{2}$$

The components of this vector then, which are the hypothesized reflectances of the mixed pixel in each of the spectral bands, are compared with the corresponding components of each of the mixed pixels in the mixed pixel set in turn. The hypothesized values (a,b) are confirmed or rejected by each mixed pixel tested according to a kernel function used, that weights the difference between the hypothesized reflectances of the mixture and each of the true reflectances. A suitable kernel function as proved in [4] is given by the following equation.

$$P(\xi) = \prod_{i=1}^{n} Q(\frac{\xi_i}{width}) \tag{3}$$

0-7803-3068-4/96$5.00©1996 IEEE

with

$$Q(x) = \begin{cases} 1 - \frac{m}{m-2}x^2 + \frac{2}{m-2}x^m & \text{for } x < 1 \\ 0 & \text{otherwise} \end{cases}$$

where $i = 1, \ldots, n$ are the bands that are going to be used in the analysis, $\xi_i = w_{H_i} - w_{T_i}$ is the difference between the hypothesized reflectance and the real one, m is an even integer greater than two, in our case we decided to use $m = 4$ and $width$ is the width of the voting kernel.

The width of the voting kernel depends on the uncertainty of our data. We can better explain that by realizing that a given reflectance w of a certain mixed pixel can be created by more than one combinations of values x, y, z, due to the intraclass variability of the pure classes. It can be shown that a suitable width for the voting kernel that reflects this uncertainty would be:

$$width = max(\frac{\sigma_i}{|\overline{x_i} - \overline{z_i}|}, \frac{\sigma_i}{|\overline{y_i} - \overline{z_i}|})$$

where σ_i is the standard deviation of the most diverse class and $\overline{x_i}$, $\overline{y_i}$, $\overline{z_i}$ are the means of the pure classes.

When all possible quadruples of the data have been considered, the highest peak in the accumulator indicates which are the proportions. These values can then be further refined by using a hill climbing method in the accumulator function [5].

3. TESTING OF THE PROPOSED METHOD WITH SIMULATED DATA

Our method is at first assessed using simulated data to represent the pure and the mixed classes. Three distributions were artificially created to represent the three "pure" classes, which were assumed normally distributed in each band. The means and covariance matrices of each of the simulated distributions were chosen to be the same as those computed from real test sites on a remotely sensed image that were known to represent almost pure classes. Next, a mixture distribution was created, from the three pure distributions using the following proportions $a = 30\%$, $b = 60\%$ and $c = 10\%$ and some outliers were added. We represent each distribution by a set of points (30 samples) and we try to estimate the proportions of the classes in the set of mixed pixels. Only two bands were used for all the experiments described below. The sampling of the accumulator function was performed with 5% accuracy.

The parameters that vary in the following experiments are: the type of outliers, the number of outliers and the position of outliers added to the mixed distribution. We can distinguish two main types of outliers, the ones that follow a certain pattern e.g. a cluster (*coherent* outliers) and those that are positioned in random places (*random* outliers).

The results of the Hypothesis Testing Hough Transform (HTHT) method are compared with the solution obtained by the least square error (LSE) [2] method and by the standard Hough Transform (HT) [3]. The results are presented in terms of the relative errors in the computed proportions.

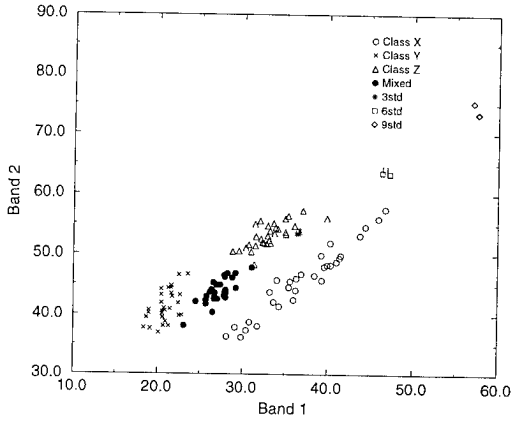


Figure 1: *Outliers placed on a given distance (3,6 and 9 times the standard deviation) from the mixed set.*

At first we will examine *coherent* outliers. Some sets used to represent the "pure" and the "mixed" classes with such outliers are shown in *Fig.* 1.

Each experiment was repeated 100 times, each time a different set of points was drawn to represent the "mixed" class. Then the average and the variance of the errors in estimating the proportions were calculated. The results of these experiments are shown in *Table* 1.

From *Table* 1 we can see that the Hough methods are not affected by the outliers no matter how far they were placed. The Hypothesis Testing Hough gave more accurate results as expected. The LSE method though seems to be affected by the distance, and its performance deteriorates as the outliers were placed further away. The error in estimation of proportion c is the largest one, which was expected since c is small, [2].

So far we examined only coherent outliers now we are going to examine *random* outliers as well. These outliers are randomly chosen at distances in the range between 0 and 12 standard deviations from the mixed set. In this experiment, for a certain number of random outliers, a number of mixed sets were generated and tested. The average and the standard deviation of the errors in proportion estimation based on 100 experiments using different "mixed" sets, are shown in *Table* 2.

The Hough methods performed well, while the LSE method is more significantly affected by the outliers, although not as much as by the presence of the coherent outliers, because the effect of random outliers tends to average out. Thus, the more the outliers are and the more uniformly distributed about the mixed distribution are, the better the LSE method will perform because the mean of the mixture distribution will not be affected by their presence. However, such an improvement in the performance of the classical method is clearly artificial.

Distance	Outliers	HTHT			HT			LSE		
		a	b	c	a	b	c	a	b	c
3	10%	9 (9)	5 (5)	49 (44)	12 (11)	4 (5)	57 (49)	11 (10)	4 (4)	45 (25)
-	20%	10 (11)	5 (6)	61 (46)	13 (11)	5 (5)	68 (46)	24 (17)	7 (5)	82 (54)
-	30%	10 (9)	5 (5)	48 (45)	14 (10)	5 (5)	55 (48)	37 (25)	11 (6)	108 (100)
-	40%	16 (15)	8 (12)	77 (88)	17 (15)	7 (12)	78 (85)	43 (32)	14 (8)	133 (126)
6	10%	11 (10)	4 (5)	53 (39)	14 (11)	4 (5)	59 (49)	24 (20)	8 (6)	86 (70)
-	20%	12 (10)	4 (5)	53 (44)	13 (11)	4 (4)	52 (41)	46 (32)	14 (8)	121 (119)
-	30%	11 (9)	5 (5)	57 (45)	14 (11)	5 (5)	63 (46)	56 (33)	22 (11)	156 (156)
-	40%	11 (9)	5 (5)	51 (40)	13 (10)	4 (5)	54 (41)	66 (34)	28 (14)	171 (183)
9	10%	9 (10)	4 (4)	49 (42)	11 (11)	4 (4)	51 (44)	32 (23)	12 (7)	98 (90)
-	20%	10 (10)	5 (5)	47 (43)	13 (11)	5 (5)	57 (44)	49 (35)	22 (10)	170 (158)
-	30%	12 (10)	6 (5)	57 (47)	14 (10)	5 (5)	59 (47)	75 (32)	33 (17)	229 (231)
-	40%	11 (11)	5 (5)	55 (46)	14 (12)	6 (5)	64 (46)	77 (34)	42 (22)	189 (226)

Table 1: *Effect of coherent outliers present in the mixed distribution. The numbers in the table are the average relative errors over 100 experiments conducted. Inside parentheses are the variances of these errors.*

Outliers	HTHT			HT			LSE		
	a	b	c	a	b	c	a	b	c
10%	11 (9)	4 (4)	50 (41)	13 (9)	4 (5)	56 (41)	11 (10)	5 (5)	46 (36)
20%	11 (8)	4 (5)	50 (45)	13 (9)	4 (5)	57 (45)	18 (18)	7 (7)	61 (57)
30%	9 (10)	4 (5)	50 (44)	13 (10)	4 (5)	59 (44)	22 (23)	7 (6)	82 (80)
40%	13 (11)	6 (5)	60 (50)	15 (13)	6 (5)	65 (54)	30 (27)	8 (8)	103 (106)

Table 2: *Effect of random outliers present in the mixed distribution. The numbers in the table are the average relative errors over 100 experiments conducted and inside parentheses are the variances of these errors.*

4. APPLICATION ON REAL IMAGES

Since the simulation results showed that our model performs well, we then tested it with a real application. The aim was to decide on the type of vegetation in an area located close to Athens, the capital of Greece. The training site data used in this work were collected by the Institute of Mediterranean Forest Ecosystem - National Agricultural Research Foundation (NARF) of Greece for evaluating the potential forest regeneration, risk of erosion and risk of desertification.

As we had no regions solely composed of one class, we derived the attributes of the real pure classes (e.g mean vectors) from sites that we know their composition, using regression techniques [2]. For this purpose we used 39 sites for which ground measurements where available. At the stage of the evaluation of our method we created 30 simulated points to represent the pure classes. Then we tested our model with 14 sites that they had not been used for the derivation of the pure class attributes. From these sites, 9 sites were classified correctly in the sense that the dominant class was identified correctly.

5. CONCLUSIONS

In this paper we discussed the use of Hypothesis Testing Hough Transform for the unmixing problem. With a series of experiments performed with simulated data we showed that HTHT can be very stable. All our results were compared with the classical Least Square Error method which was used as a bench mark. The advantage of the Hough method is its ability to cope with large numbers of outliers in the mixture distribution.

The problem of exponential explosion of the number of quadruples one can use has also to be considered. This is really the limiting factor in our approach: It is not feasible to use it for large data sets or for many "pure" classes.

6. REFERENCES

[1] J.B. Adams, M.O. Smith, P.E. Johnson, "Spectral mixture modeling: A new analysis of rock and soil types at the Viking Lander 1 site", *Journal of geophysical research*, vol.91, no.B8, pp. 8098-8112, 1986.

[2] P. Bosdogianni, M. Petrou, J. Kittler, 1994. "Mixed pixel classification in Remote Sensing". Proceedings of the EUROPTO series, Image and Signal Processing for Remote Sensing, Vol 2315, pp 494–505.

[3] P.Bosdogianni, M.Petrou, J.Kittler, "Robust mixed pixel classification in Remote Sensing", in press *VIII ISPRS-Congress* , Vienna, Austria, July 9-19, 1996.

[4] P.Palmer, M.Petrou, J.Kittler, "A Hough Transform Algorithm with a 2D Hypothesis Testing Kernel", *CVGIP Image Understanding*, Vol. 58, No.2, pp. 221-234, 1993.

[5] P.Palmer, J.Kittler, M.Petrou "An optimising line finder using a hough transform algorithm", in press *CVGIP Image Understanding*, 1996.

[6] M.O. Smith, J.B.Adams and A.R. Gillespie, "Reference endmembers for spectral mixture analysis", 5^{th} *Australian remote sensing conference*, vol.1, pp.331-340, 1990.

Improving Automated Land Cover Mapping by Identifying and Eliminating Mislabeled Observations from Training Data

C. E. Brodley
School of Electrical and Computer Engineering
Purdue University
West Lafayette, IN 47906
brodley@ecn.purdue.edu

M. A. Friedl
Department of Geography and Center for Remote Sensing
Boston University
Boston, MA 02215
friedl@crsa.bu.edu

Abstract – This paper presents a new approach to identifying and eliminating mislabeled training samples. The goal of this technique is to decrease the error of classification algorithms by improving the quality of the training data. The approach employs an ensemble of classifiers that serve as a *filter* for the training data. Using an n-fold cross validation, the training data is passed through the filter. Only samples that the filter classifies correctly are passed to the final classification algorithm. An empirical evaluation of the approach on the task of automated land cover mapping illustrates that the ensemble filter approach is an effective method for identifying labeling errors.

INTRODUCTION

Current information and data related to global land cover is poor and labeling errors in land cover maps arise from a multitude of sources including lack of consistency in the vegetation classification used, variable measurement techniques, and variation in the spatial sampling resolution [1]. This work focuses on improving the quality of the training data for supervised classification algorithms by identifying and eliminating mislabeled samples.

We introduce a method for identifying mislabeled samples that serves as a general method that can be applied to a dataset before feeding it to a specific classification algorithm. The basic idea is to use a set of classification algorithms that serve as a *filter* for the training data. Using an n-fold cross validation, the training data is passed through the filter to remove mislabeled samples.

We present an empirical evaluation of the approach on the task of building classifiers to perform automated land cover mapping from remotely sensed data. Our evaluation shows that removing mislabeled samples by filtering significantly improves predictive accuracy for this domain.

FILTERING TRAINING SAMPLES

This section describes a general procedure for identifying and eliminating mislabeled samples from a training data set. The first step is to identify candidate samples by using m classification algorithms (called *filter algorithms*) to tag samples as correctly or incorrectly labeled. To this end, a n-fold cross-validation is performed over the training data. For each of n subsets, the m algorithms are trained on the other $n-1$ subsets. The m resulting classifiers are then used to tag each sample in the excluded part as either correct or mislabeled. An individual classifier tags an sample as mislabeled if it cannot classify the sample correctly. At the end of the n-fold cross-validation each sample in the training data has been tagged.

The second step is to form a classifier using a new version of the training data for which all of the samples tagged as mislabeled are removed. The filtered set of training samples is provided as input to the *final classification algorithm*. The resulting classifier is the end product of the approach. Specific implementations of this general procedure differ from other filter algorithms in how the filtering is performed, and in the relationship between the filter algorithm(s) and the final algorithm. In our implementation we employ a *consensus filter*. Specifically, we discard only those samples that *all* of the individual classifiers tag as mislabeled.

This method was motivated by the technique of removing *outliers* in regression analysis. An outlier is a case (an sample) that does not follow the same model as the rest of the data, appearing as though is comes from a different probability distribution. Candidates are cases with a large residual error.

Here, we apply this idea by using a set of classifiers formed from part of the training data to test whether samples in the remaining part of the training data are mislabeled. One important difference between our work and previous approaches to outlier detection is that our approach assumes that the errors in the class labels are independent of the particular model being fit to the data. In essence, our method attempts to identify data points that would be outliers in *any* model.

EMPIRICAL EVALUATION

This research was motivated by the nedd for improved methods for identifying labeling errors in land-cover maps of the Earth's surface. In this context, we evaluate the ability of

0-7803-3068-4/96$5.00©1996 IEEE

Table 1: Land Cover Classes

Land Cover Type	Samples
broadleaf evergreen forest	628
coniferous evergreen forest and woodland	320
high latitude deciduous forest and woodland	112
tundra	735
deciduous, evergreen and woodland	57
wooded grassland	212
grassland	348
bare ground	291
cultivated	527
broadleaf deciduous forest and woodland	15
shrubs and bare ground	153

consensus filters to identify mislabeled training samples in remotely sensed data that was labeled using existing land cover maps. Our experiments use three well-known classification algorithms: decision trees [3], k-nearest neighbor [4] and linear discriminant function classifiers [4]. To simulate the type of error that is common to land-cover maps, we artificially introduced noise between pairs of classes that are likely to be confused in the original labels. Our experiments are designed to evaluate the consensus filter's ability to identify mislabeled samples and the effect that eliminating mislabeled samples has on predictive accuracy.

Data

The labeled training data were compiled by Defries and Townsend [5] from three existing maps of global land cover [6, 7, 8]. Only those locations where each of the maps listed above were in agreement were selected as training sites. The spatial resolution of these data is one degree in both the north-south and east-west dimension. These training locations are co-registered with NDVI data from the Advanced Very High Resolution Radiometer. Each one degree pixel is described by a time series of twelve NDVI values at monthly time increments from 1987 and by its latitude, which can be useful for discriminating between classes with otherwise similar spectral properties.

The map overlay procedure that was used by Defries and Townsend is designed to improve the reliability of the training data relative to using only one of the land cover source maps. The fact that only 5% of the data from all three source maps are in agreement (i.e. 3398 out of 180 x 360 pixels) is further evidence of the poor state of knowledge regarding land cover at global scales. The filtering procedure that we describe in this paper is designed to provide a robust and automated method for identifying mislabeled samples that will complement "top-down" training data selection procedures such as the one described above.

Experimental Method

To evaluate the ability of consensus filters to detect mislabeled samples, we introduced random error between the following pairs of classes:

- high latitude deciduous forest and woodland versus tundra
- deciduous, evergreen and woodland versus coniferous evergreen forest and woodland
- wooded grassland versus grassland
- bare ground versus shrubs and bare ground
- broadleaf deciduous forest and woodland versus deciduous, evergreen and woodland

We chose not to simulate all combinations of paired error for two reasons. First, we wanted to simulate the type of error that might occur naturally in a land cover dataset. Second, we wanted to assess the affect of the filter method on the parts of the data that had not been corrupted.

For each of ten runs, the dataset was divided into a training set (90%) and a testing set (10%). For each run, an even distribution over the classes was enforced to reduce variation in performance across different runs. We wanted the data used for both training and testing to mirror the class distribution of the entire data set. After the data was split into independent train and test sets, we then corrupted the training data by introducing labeling errors. For a noise level x, an individual observation whose class is one of the identified pairs has an $x\%$ chance of being corrupted. For example, a sample from class 8 (bare ground) has an $x\%$ chance of being changed to class 11 (shrubs and bare ground), and a sample from class 11 has an $x\%$ chance of being changed to class 8. Using this method the percentage of the entire training set that is corrupted will be less than $x\%$ because only some pairs of classes are considered problematic.

Filtering and Classification Results

For each of five noise levels, ranging from 5% to 40%, we compared the average predictive accuracy of classifiers trained using filtered and unfiltered data. For each of the ten runs that make up the average, we used a four-fold cross-validation to filter the corrupted samples from the training data. The consensus filter consisted of the following base-level classifiers: a decision tree, a linear discriminant function and a k-NN classifier. To assess the ability of the consensus filter to identify the corrupted samples we then trained each of the three algorithms twice: first using the unfiltered dataset then using the filtered dataset. The resulting classifiers were then used to classify the uncorrupted test data.

Table 2 reports the accuracy of the classifiers formed by each of the three algorithms without a filter (none) and with

Table 2: Classification Accuracy of the Test Samples

Noise	k-NN		LDF		DTree	
Level	None	CF	None	CF	None	CF
0	87.3		78.6		85.6	
5	84.4	87.8	76.7	78.9	84.4	86.1
10	81.8	86.4	77.5	79.2	80.1	85.1
20	75.8	83.1	70.2	78.1	75.2	81.8
30	68.6	75.2	63.4	74.0	67.4	74.2
40	58.4	59.9	49.0	54.2	56.9	59.6

a consensus filter (CF) when applied to the uncorrupted test data. Note that separate data were used to construct and test the classifiers. The first row of the table reports the accuracy of each learning method when trained using the original data (hereafter the base-line accuracy). Subsequent rows show the classification accuracy achieved with filtered versus unfiltered training data for increasing amounts of noise.

Filtering significantly improved the classification accuracy (at the 0.05 level of significance using a paired t-test) in all cases except when a linear machine was the final classifier under noise levels 5%, 10% and 40%. For noise levels of 5% and 10% the filter method is able to achieve the same accuracy as the original uncorrupted dataset. At 20% noise the accuracies of the k-NN and the decision tree constructed from the filtered data begin to drop, but not as substantially as when they are constructed from the unfiltered data. For example, applying a decision tree to the unfiltered data set causes a drop of 12.2% ($100 * (85.6 - 75.2)/ 85.6$) from the base-line accuracy versus a 4.4% drop when using the filtered data. At 30% noise, filtering cannot fully overcome the error in the data, but does manage to achieve higher accuracy than using the unfiltered data. Finally, at noise levels of 40% and over, filtering does not help.

A question that arises is whether the consensus filter is just getting rid of those parts of the data that are difficult to classify, thereby achieving higher overall accuracy. In other words, is the filtering procedure throwing out the samples of a particular class, or of a subset of the classes, to achieve higher accuracy on the remaining classes? To test this hypothesis we examined the decision tree's accuracy for classes where noise was not added. For each of these classes (classes 1 and 9) filtering did not decrease accuracy and in some cases increased accuracy. These results show that for this dataset, filtering does not sacrifice the accuracy of some of the classes to improve overall accuracy and that it can retain base-line accuracy in noisy classes for noise levels of up to 20%.

CONCLUSIONS

This article presented a procedure for identifying mislabeled samples. The results of an empirical evaluation demonstrated that the consensus filter method improves classification accuracy for a land-cover mapping task for which the training data contains mislabeled samples. For noise levels up to 20% filtering allows the base-line accuracy to be retained. An evaluation of the precision of the approach shows that consensus filters are conservative in throwing away good data at the expense of keeping mislabeled data.

Finally, the issue of determining whether or not to use the consensus filter method for a given data set must be considered. For the work described here, the data were artificially corrupted. Therefore the nature and magnitude of the labeling errors were known a priori. Unfortunately, this type of information is rarely known in practice. In some situations, it may be possible to use domain knowledge to estimate the amount of label noise in a training data set. For situations where this knowledge is not available, the conservative nature of our filtering procedure dictates that relatively few samples will be discarded for data sets with low levels of labeling error. Therefore, the application of this method to relatively noise free dataset should not significantly impact the performance of the final classification procedure.

REFERENCES

[1] Running, S., Loveland, T. R., Pierce, L. L., Nemani, R. R. , & Hunt, E. R. Jr. (1995). A remote sensing based vegetation classification logic for global land cover analysis. *Remote Sensing of Environment, 51*, 39-48.

[2] Weisberg, S. (1985). *Applied linear regression.* John Wiley & Sons.

[3] Breiman, L., Friedman, J. H., Olshen, R. A., & Stone, C. J. (1984). *Classification and Regression Trees* Belmont, CA: Wadsworth International Group.

[4] Duda, R. O., & Hart, P. E. (1973). *Pattern classification and scene analysis.* New York: Wiley & Sons.

[5] Defries, R. S. , & Townsend, J. R. G. (1994). NDVI-derived land cover classifications at a global scale. *International Journal of Remote Sensing, 15*, 3567-3586.

[6] Matthews, E. (1983). Global vegetation and land use: New high resolution data bases for climate studies. *Journal of Climate and Applied Meteorology, 22*, 474-487.

[7] Olson, J.S., Watts, J., & Allison, L. (1983). *Carbon in live vegetation of major world ecosystems*, (Technical Report W-7405-ENG-26), Oak Ridge National Laboratory, US Department of Energy.

[8] Wilson, M.F. , & Henderson-Sellers, A. (1985). A global archive of land cover and soils data for use in general circulation models. *Journal of Climatology, 5*, 119-143.

An Automatic Technique for Detecting Land-Cover Transitions

S.B. Serpico[1], L. Bruzzone[1], F. Roli[2], and M.A. Gomarasca[3]

(1) Dept. of Biophysical and Electronic Engineering - D.I.B.E.
University of Genoa, Via all'Opera Pia, 11a, I-16145 Genova (Italy)
Phone: +39-10-3532752; Fax.: +39-10-3532134; E-mail: vulcano@dibe.unige.it

(2) Dept. of Electrical and Electronic Engineering
University of Cagliari, Piazza d'Armi, I-09123 Cagliari (Italy)

(3) CNR-IRRS, Remote Sensing Unit
Via Ampère, 56, Milano (Italy)

Abstract -- In this paper, detection of land-cover/land-use transitions by using multitemporal remote-sensing images is addressed. An iterative approach based on a compound classification of multitemporal images is proposed. In particular, a technique to estimate iteratively the probabilities of transitions among classes is presented. The effectiveness of the proposed approach is confirmed by experimental results carried out on multitemporal remote-sensing images acquired by the Thematic Mapper of Landsat over an agricultural area.

INTRODUCTION

Detection of land-cover/land-use changes is one of the most interesting applications of the analysis of multitemporal remote-sensing images [1]. In fact, the availability of images of the earth surface acquired by satellites at different times allows the monitoring of environmental changes occurred [1].

Various approaches to change detection can be adopted. The most widely used ones detect changes by comparing the spectral reflectances of multitemporal raw satellite images [2]. However, these approaches usually do not aim to identify explicitly what kinds of land-cover/land-use transitions have taken place in an area (e.g., the fact that a vegetated area has been urbanized). To this end, techniques based on the classification of multitemporal images (e.g., "post-classification comparison", "direct multidate classification") have to be used [2]. However, these techniques have significant drawbacks: the accuracy provided by the post-classification comparison technique is strongly reduced by classification errors; supervised direct multidate classification technique require the knowledge of multitemporal training samples for all the kinds of transitions (usually it is difficult to have such training data).

In this paper, we address the detection of land-cover/land-use transitions by using multitemporal remote-sensing images. In the next Section, we present an iterative approach based on a compound classification of multitemporal images. In particular, a technique to estimate iteratively the probabilities of land-cover transitions is proposed. Experimental results are reported and discussed in the last Section.

0-7803-3068-4/96$5.00©1996 IEEE

DETECTION OF LAND-COVER TRANSITIONS - AN ITERATIVE APPROACH

Let us consider two multispectral remote-sensing images, acquired at times t_1 and t_2, respectively. Let each couple of pixels (x_1, x_2), made up of a pixel of the multispectral image acquired at time t_1 and of the spatially corresponding pixel of the multispectral image acquired at time t_2, be characterized by the couple of feature vectors (X_1, X_2). For each couple of image pixels, let $\Omega = \{\omega_1, \omega_2, .., \omega_N\}$ be the set of possible land-cover classes at time t_1, and let $W = \{w_1, w_2, .., w_M\}$ be the set of possible land-cover classes at time t_2. For each (x_1, x_2), a "compound classification" [3, 4] can be performed by finding the couple of classes (ω_i, w_j) which provides the following maximum:

$$\max_{\omega_i, w_j} \left\{ p(\omega_i, w_j / X_1, X_2) \right\} . \quad (1)$$

Then land-cover transitions can be detected when $\omega_i \neq w_j$.

It is easy to prove that [4]:

$$\max_{\omega_i, w_j} \left\{ p(\omega_i, w_j / X_1, X_2) \right\} \Leftrightarrow \Leftrightarrow \max_{\omega_i, w_j} \left\{ p(X_1, X_2 / \omega_i, w_j) p(w_j / \omega_i) p(\omega_i) \right\} \quad (2)$$

Unfortunately, a large number of training pixels are required to estimate the joint conditional densities $p(X_1, X_2 / \omega_i, w_j)$ [4]. However, under the hypothesis of class-conditional independence in the temporal domain, the estimation of $p(X_1, X_2 / \omega_i, w_j)$ can be simplified as follows [4]:

$$p(X_1, X_2 / \omega_i, w_j) = p(X_1 / \omega_i) p(X_2 / w_j) . \quad (3)$$

By substituting (3) into (2) and by using the Bayes theorem, it is easy to prove that:

$$\max_{\omega_i,w_j}\left\{p(\omega_i,w_j/X_1,X_2)\right\}\Leftrightarrow$$

$$\Leftrightarrow \max_{\omega_i,w_j}\left\{\frac{p(\omega_i/X_1)p(w_j/X_2)p(w_j/\omega_i)}{p(w_j)}\right\} \quad (4)$$

According to (4), the compound classification requires the estimation of the single-date, multivariate, conditional probabilities $p(\omega_i/X_1)$ and $p(w_j/X_2)$, the a-priori probabilities of the classes $p(w_j)$, and the probabilities of transitions $p(w_j/\omega_i)$. Following the works by Richard and Lippmann [5] and by Gish [6], we propose to estimate $p(\omega_i/X_1)$ and $p(w_j/X_2)$ by two neural networks trained on the data sets available at times t_1 and t_2, respectively. The a-priori probabilities of classes can be easily estimated from the training data. However, a problem arises when one wants to estimate the $N \times M$ probabilities of land-cover transitions, i.e.:

$$\begin{bmatrix} p(w_1/\omega_1) & \cdots & p(w_j/\omega_1) & \cdots & p(w_M/\omega_1) \\ \vdots & \cdots & \vdots & \cdots & \vdots \\ p(w_1/\omega_i) & \cdots & p(w_j/\omega_i) & \cdots & p(w_M/\omega_i) \\ \vdots & \cdots & \vdots & \cdots & \vdots \\ p(w_1/\omega_N) & \cdots & p(w_j/\omega_N) & \cdots & p(w_M/\omega_N) \end{bmatrix} \quad (5)$$

To this end, the training sets at the two dates should be made up of pixels corresponding to the same points on the ground. In many real cases, this does not occur. As an alternative, the probabilities of land-cover transitions could be estimated on the basis of interviews with experts or by analyzing the information contained in historical image databases. However, by using these approaches, it may be difficult to obtain reasonable estimates of all the probabilities of land-cover/land-use transitions.

We propose an iterative approach to estimate the probabilities of transitions. First of all, an initial estimate of each probability of transition can be obtained by classifying separately the images acquired at the two dates (t_1 and t_2) and by comparing the obtained classifications. Then, such an estimate can be iteratively refined by a compound classification of the two-date images (in our case, (4) is iteratively applied). In particular, at each iteration, a new estimate of each probability of transition is computed on the basis of the classifications at the two dates. At the *k-th* iteration, the estimate is updated as follows:

$$\hat{p}_k(w_j/\omega_i) = f_{k-1}(w_j/\omega_i) \quad \forall \omega_i, w_j \quad (6)$$

where $f_{k-1}(w_j/\omega_i)$ is the relative frequency of the transition from ω_i to w_j computed by comparing the classification maps of two times provided by the compound classification at the iteration *k-1*.

The estimation process stops when between two iterations the highest difference among the estimates of all probabilities of transitions is under a selected threshold, i.e.:

$$\max_{\omega_i,w_j}\left\{\left|\hat{p}_k(w_j/\omega_i) - \hat{p}_{k-1}(w_j/\omega_i)\right|\right\} < \varepsilon \quad (7)$$

were $\varepsilon \in [0, 1]$ is a threshold parameter that tunes the estimate accuracy.

EXPERIMENTAL RESULTS

Data set description

The study area is located in the delta of the Po river watershed in the north of Italy. The climate in the area is Xerofil with two main rainy seasons, Autumn and Spring. July is the driest month. The study area is mostly characterized by extended cultivation of wheat, corn, soybean, sugar beet, alpha-alpha, meadows and horticulture. The main phenological cycles studied are referred to wheat, corn, soybean and sugar beet.

We considered two multispectral images (512x512) acquired by the Thematic Mapper (TM) scanner, mounted on board of Landsat, at May 1988 and July 1988, respectively. The images were registered to an average accuracy on the ground control points of about 0.5 pixel. Ground-truth of the the study area was collected in the days of the passages of the Landsat: May 10, and July 29. The available ground truth was used to prepare two thematic maps of the selected test site (one for each date), which were used as reference maps to assess the accuracy in the detection of the land-cover/land-use transitions. For our experiments we considered 3 classes at time t_1 (i.e., bare soil, wheat, and urban) and 5 classes at time t_2 (i.e., sugar beet, corn, soybean, bare soil, and urban). Agricultural fields considered were randomly subdivided in training and test sets: 5795 training pixels and 5793 test pixels were selected. In order to evaluate the performances of our approach, we included in the test set pixels corresponding to the same position on the ground at the two times. Between the two times, the following transitions had taken place (see table 1): bare soil at May became corn or soybean or sugar beet at July, and wheat at May became bare soil at July. Only urban areas did not change.

Results

The performances of the proposed compound-classification (CC) algorithm were compared with those of the post-classification comparison (PCC) algorithm [2]. In particular, in our algorithm, we exploited the proposed iterative

estimation of the probabilities of land-cover/land-use transitions among classes. Table 2 shows the results of the detection of transitions obtained on the test set. In particular, the percentage of false indication of changes (computed with respect to the total number of unchanged pixels) and the percentage of correctly recognized transitions (computed with respect to the total number of changed pixels) are reported. A considerable reduction (i.e., 29.8%) of false indications of changes was obtained by using the CC approach. Improvements were also yielded in the number of correctly recognized transitions (i.e., 3.1%).

The results reported show that our approach allows one to reduce false indications of change and to increase correctly recognized transitions with respect to post-classification comparison. Further experiments are in progress in order to better evaluate the performances of proposed method.

ACKNOWLEDGMENTS

This research was partially conducted within the framework of the cooperative research project "Integrated assessment of environmental degradation connected with forest fires in European areas", funded by the EEC (Environment Programme, Contract N. EV5V CT94 0481) , and partially within the framework of the Italian project "Sviluppo di metodi integrati di classificazione agroecologica tramite dati di telerilevamento per la gestione delle risorse naturali," funded by the Italian Space Agency. Both supports are gratefully acknowledged.

REFERENCES

[1] J.A. Richards, *Remote Sensing Digital Image Analysis*, 2nd edition, Springer-Verlag, New York, 1993.

[2] A. Singh, "Digital change detection techniques using remotely-sensed data", *International Journal of Remote Sensing*, Vol. 10, No. 6, 1989, pp. 989-1003.

[3] R. O. Duda and P. E. Hart, *Pattern Classification and Scene Analysis*, Wiley, New York, 1973.

[4] P.H. Swain, "Bayesian classification in a time-varying environment", *IEEE Transactions on Systems Man and Cybernetics* , Vol. SMC-8, No. 12, December 1978, pp. 879-883.

[5] M. Richard and R. Lippmann, "Neural network classifiers estimate Bayesian a posteriory probabilities", *Neural Computation*, Vol. 3, N. 4, 1991, pp. 461-463.

[6] H. Gish, "A probabilistic approach to the understanding and training of neural network classifiers", *Proc. 1990 Int. Conference on Acoustic, Speech, and Signal Processing*, 3-6 April, 1990, pp. 1361-1364.

Table 1. Ground truth of land-cover/land-use transitions on the test set

Kinds of transitions		Test pixels
May 1988	July 1988	
Bare soil	Sugar beets	218
Bare soil	Soybean	3057
Bare soil	Corn	344
Wheat	Bare soil	1722
Urban	Urban	452
Overall		5793

Table 2. Percentages of false indications of changes and correctly recognized transitions for both the post-classification comparison (PCC) algorithm and the compound classification (CC) algorithm.

Algorithm	False indications of changes (%)	Correctly recognized transitions (%)
PCC	52.4 %	89.1 %
CC	22.6 %	92.2 %

Observations of the ocean surface using an aircraft altimeter, scatterometer and ROWS

D Vandemark[1], D Hines[1], B Chapron[2], J Carswell[3] and W Donnelly[3]

[1] NASA/GSFC
Lab. for Hydrospheric Processes
Wallops Island VA 23337 USA
vandemark@gsfc.nasa.gov
804.824.2038 (V) or 1036 (FAX)

[2] IFREMER/Centre de Brest
DRO/OS, BP 70
29270-Plouzane, France
bchapron@ifremer.fr
33.98.22.43.12

[3] Univ. of Massachusetts
Microwave Remote Sensing Lab.
Knowles Eng. Building
Amherst MA 01003 USA
carswell@alex.ecs.umass.edu

Abstract-- Open-ocean radar measurements acquired from an aircraft are examined. Two Ku-band systems, NASA's Radar Ocean Wave Spectrometer (ROWS) and the Univ. of Massachusetts' Ku-band scatterometer (KUSCAT) were used to derive data on sea surface wind and waves for several long transects over the Atlantic ocean. Noteworthy in this effort is the complete time/space coincidence of data products. This includes scatterometer data at 20°, 30°,40° and 50° incidence as well as altimeter and directional swell measurements. Altimeter- and scatterometer-derived 10 m wind speeds are generated using current satellite geophysical model functions (GMF). The two estimates agree very closely for the available light-to-moderate speeds thus providing further validation of these inversion algorithms. Long wave effects on scatterometer wind direction estimation are examined by comparing off-wind swell to the peak direction derived for near-incidence, 20° KUSCAT data. For the conditions examined, no significant tie is found between swell direction and the scatterometer's peak direction.

AIRBORNE DATA COLLECTION

This paper deals specifically with two Ku-band radars aboard the NASA P-3B aircraft for five Lidar In-space Technology Experiment (LITE) correlative flights. Univ. of Massachusetts' KUSCAT is a VV-polarized scatterometer that combines continuous scanning in azimuth with high-speed stepping between incidence angles of 20°, 30°, 40° and 50° [1]. KUSCAT's pencil beam at each incidence is approximately 5° in both planes and radar power measurements are radiometrically calibrated. The system derives a fully-scanned, stable normalized radar cross section (NRCS) estimate for all incidence angles at 0.8-1.0 km intervals along the flight track. NASA's ROWS is a high-resolution scatterometer, azimuthally-scanned to derive directional swell spectrum based on near-vertical backscatter modulation [2]. ROWS directional wave spectra have 15-30° directional resolution and sensitivity to swell of lengths from 30-400 m. ROWS also continuously collects radar altimeter data that provide backscatter measurements equivalent to satellites such as TOPEX.

Two separate data comparisons are shown below. The first compares wind magnitude estimates from the ROWS altimeter and the four KUSCAT angles. Second, the direction detection capability of KUSCAT is examined when swell direction (as derived by ROWS) is off-wind.

ALTIMETER VS. SCATTEROMETER WIND SPEED

Altimeter and scatterometer wind estimation capability is now well-accepted. For global coverage, scatterometers are preferred for their spatial swath and ability to derive wind direction. The surface wind GMF for both sensors has been derived at Ku-band based on past aircraft and satellite mission data combined with statistical and in situ comparisons. These algorithms are considered to be first-order approximations as they represent the mean or global response to surface wind wave roughening. Theoretically, scattering mechanisms for the altimeter and scatterometer are disparate because of their different incidence angles. Scatterometry is modeled as a resonant interaction (or Bragg scattering) with small-scale ocean ripples through their height spectral density. The Bragg wavenumbers for KUSCAT 20°-50° angles are ~ 3.4 - 1.3 cm. Altimeter backscatter is modeled as quasi-specular scatter from facets of scales large enough to obey high-frequency scattering limits. Succinctly, scatterometers are primarily sensitive to the roughening of small-scale wavelets, while altimeters respond to the overall roughening (or rms slope) across a broader range of wavelengths, nominally 8-200 cm. The coincident LITE data affords an opportunity to see how similarly the two sensors (and scattering mechanisms) respond to the identical sea surface target, and to test agreement between the respective satellite wind algorithms.

0-7803-3068-4/96$5.00©1996 IEEE

To directly compare altimeter and scatterometer data we invert NRCS measurements to wind speed through current GMFs. KUSCAT wind vector estimates at the four incidence angles are derived from NRCS data using the Seasat A scatterometer system (SASS-II) model function adjusted to 10 m using a neutral stability assumption [3]. SASS-II requires that the data be fit to a three term Fourier series as shown in equation 1.

$$NRCS(\phi)=A_0+A_1\cos(\phi)+A_2\cos(2\phi) \qquad (1)$$

In (1), ϕ is the azimuth angle with respect to wind direction. Wind magnitude lies in A_0, and for this data, wind direction was derived by finding the best fit to (1). Expected rms error for SASS-II wind speed is 2 m/s at the light-to-moderate wind speeds encountered here. Altimeter wind speed was derived using the Modified Chelton-Wentz algorithm [4] and ROWS altimeter mean-square-slope estimates as detailed in [1]. Expected rms error for the altimeter is of order 1.5 m/s. Resultant uncertainty is +/- 2.5 m/s.

Figure 1 shows wind speed data from 11 Sept 1994, a flight covering about 3000 km along a track from 34° N to 8° N. A 1:1 correlation line and 2.5 m/s rms lines are also shown. The radar estimated range of 10 m wind speeds is 0-8 m/s. Near-zero biases between scatterometer and altimeter are observed for each of the four KUSCAT incidence angles, indicating consistency between sensor calibrations and the SASS-II and MCW model functions. (We also note that these data agreed with the ECMWF model wind field to within 2 m/s except in the light wind portion of the flight.) For all four angles the scatter between altimeter and scatterometer increases with increasing wind speed. Usually in wind speed comparisons, significant intercomparison uncertainty is due to spatial and temporal differences between estimates. In this case that elusive error source is eliminated. Therefore, deviations observed indicate differences between estimators. For both the scatterometer and altimeter, the wind speed sensitivity is highest at light winds thus differences may be attributed to insensitivity with increasing wind. It is also known that the scatterometer, with its dependence on the small 1-3 cm waves, is more sensitive to changes in local wind than the slope-integrating altimeter. It is likely that a portion of the scatter is attributed to this. In particular, note that the scatter starts in earnest at 5-6 m/s, the region associated with the onset of significant gravity-capillary wave growth.

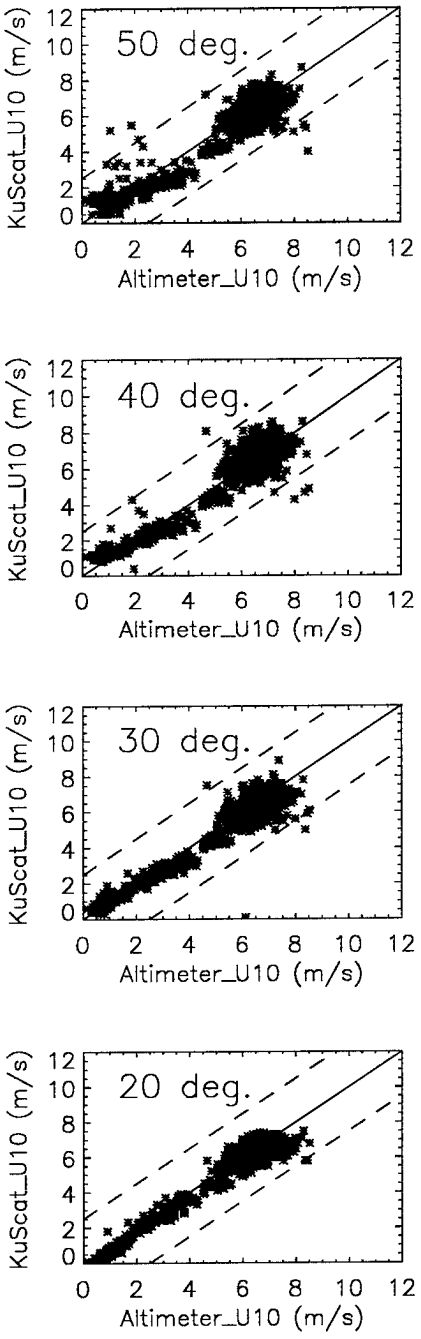


Figure 1 Altimeter vs scatterometer-derived 10 m wind speed.

SCATTEROMETRY AND LONG WAVES

Recently, some emphasis has been given to ascertaining and proposing relationships for the influence of longer waves (swell and sea) on the scatterometer's retrieval of wind vector. These efforts have been directed at examining impacts on both wind amplitude and direction. It is argued that the strongest influence of long waves on scatterometer response should occur at the low-incidence angles (15-30°). This isbecause the second-order long-wave tilting effect on Bragg scatterers is stronger near vertical. Our scatterometer/swell data set may provide information in this area. Note that without in situ estimates of the wind vector, we are precluded from a strict discussion of retrieval errors. However, long-wave spectra measurements coincident with multiple-incidence scatterometer data is a rarity.

Here, we propose to examine possible degradations of scatterometer wind direction detection when swell is at angles other than the wind direction. To do this, we make an assumption that swell impact will be greatest at the lower incidence angles. Therefore, we consider the 40° KUSCAT wind direction to be true wind direction, and will difference that channel with other data. Because evidence suggests that scatterometer direction estimates at all incidence angles can be erratic at light winds, we limit the discussion to data having wind magnitude greater than 3 m/s. Swell direction is derived from ROWS spectra at 15 km intervals along track. The swell mode chosen is the one with the most energy in the wave height spectrum. We note this because on several flights there were multi-mode swell systems. In all cases, the swell were developed to the point of being decoupled from the wind in terms of phase speed. The sea state for all cases was between 1.0 and 2.7 m.

Figure 2 shows normalized histograms of direction differences between the KUSCAT 40° wind direction estimate and KUSCAT 50°, 30°, 20°, as well as ROWS' primary swell mode. The data is derived from all five LITE flights. The bottom right panel in Figure 2 shows a significant amount of cases where swell direction deviated from the scatterometer wind. The KUSCAT difference plots (50°, 30°, and 20°-40°) show closest agreement in direction between 50° and 40° estimates, widening as you go to 30° and to 20°. Some degradation is to be expected because scatterometer sensitivity to wind direction weakens at the lower incidence angles.

The mean direction difference for each KUSCAT histogram in Figure 2 is less than 0.6°. Standard deviations are 4.4°,

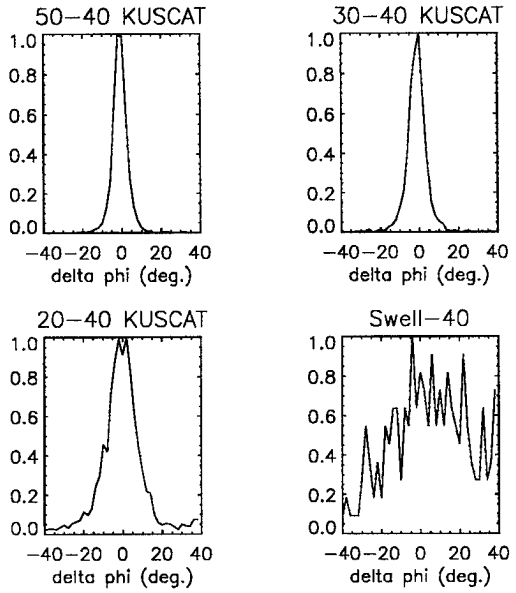


Figure 2 Histograms of direction estimate differences between KUSCAT 40°, the other KUSCAT angles and swell.

5.8°, and 11.5° for the 50°, 30°, and 20° differences respectively. Thus, the KUSCAT 20° direction 'error' still lies primarily within +/- 6°. This indicates that regardless of swell or any other variable, for this data set the degradation of 20° and 30° direction data is not great.

Figure 3 shows a scatter plot between the swell and 20° data of Figure 2. While the histograms indicate no severe problems with 20° direction data, the scatter plot may indicate some relationship between scatterometer direction 'noise' and swell off-wind direction. In particular, it has been suggested that the tilting effect of long waves may cause the 20° scatterometer data to peak up at a direction nearer the swell's direction than the wind's. Such an effect would show up in Figure 3 as a positive slope. Here, this is not the case. There is little correlation (0.03) between the off-wind swell directions and the 20° direction noise, and a linear fit gives a slope of only 0.023.

Clearly, a most exhaustive examination of the behavior of scatterometer models such as SASS-II in presence of swell will be possible with this data set. The full cross section and swell spectra data should permit closer look at how well a 3 term Fourier series holds up under various scenarios. Still,

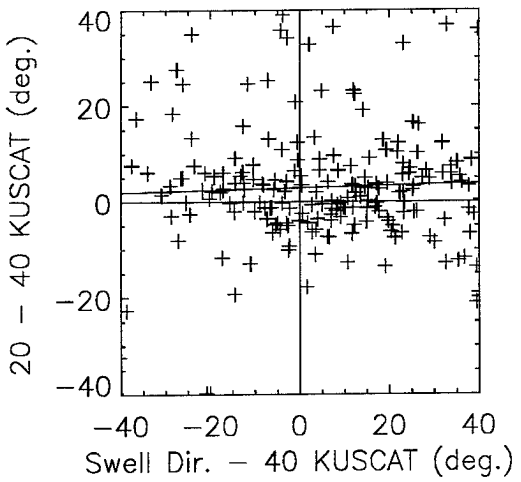


Figure 3 Scatter plot of swell-40° KUSCAT and 20-40° KUSCAT direction estimates. Simple linear regression with slope = 0.023 also shown.

the robust derivation of peak direction from the four KUSCAT scatterometer channels likely indicates less than 2nd order effects due to swell.

SUMMARY

Coincident Ku-band scatterometer and altimeter wind speed estimates are shown to be in close agreement when using the SASS-II and MCW wind speed algorithms. Data collection from the same aircraft platform eliminated typical time/space sampling uncertainties. For wind speeds > 3 m/s, scatterometer wind direction estimates under various off-wind swell conditions show little deviation between the 20°, 30°, 40° and 50° incidence data. No clear tie between off-wind swell direction and noise in the 20° direction data is apparent. We note that this is not conclusive as a full range of possible swell, wind and sea state conditions is by no means available in this data set. Closer examination of the raw NRCS data and directional swell spectra is planned.

REFERENCES

[1] J. Carswell,S. Carson,R. McIntosh,F. Li,G. Neumann,D. McGlaughlin,J. Wilkerson,P. Black, S. Nghiem, "Airborne scatterometers: Investigating ocean backscatter under low- and high-wind conditions", Proc. IEEE, vol. 82, pp. 1835-1860, 1994.

[2] D. Vandemark, F. Jackson, E. Walsh and B. Chapron, "Airborne radar measurements of ocean wave spectra and wind speed during the Grand Banks ERS-1 SAR Wave Experiment", Atmos.-Ocean, vol. 32, pp. 143-178, 1994.

[3] F. Wentz, J.,S. Peteherych and L. Thomas, "A model function for ocean radar cross sections at 14.6 GHz", J. Geophys. Res., vol. 89, pp. 3689-3704, 1984.

[4] D. Witter,and D. Chelton, "A Geosat altimeter wind speed algorithm and a method for altimeter wind speed algorithm development", J. Geophys. Res. vol. 96, pp. 8853-8860, 1991.

Dependence of Altimeter Returns on Wind Stress and Wave Age

T. Elfouhaily, B. Chapron, V. Kerbaol,
J. Gourrion, J. Tournadre, K. Katsaros
IFREMER centre de Brest
DRO/OS, BP 70
29270 Plouzané France
(33).98.22.43.12 (V) or .45.33 (FAX)
Tanos.El.Fouhaily@ifremer.fr (email)

and D. Vandemark
NASA/Goddard Space Flight Center
Wallops Flight Facility
Laboratoy for Hydrospheric Processes
Wallops Island, VA 23337, USA

Abstract -- Much effort has been expended in defining the relationship between wind speed and Normalized Radar Cross Section (NRCS). However, wind stress is known to better describe geophysical processes on the ocean surface than wind speed alone. Using a scattering model and an idealized wavenumber sea spectrum, we present here a wind stress algorithm to interpret altimeter returns. A comparison with measurements from the dual frequency altimeter of TOPEX (Ku and C band) is carried out. Results show that retrieved wind from empirical models is underestimated in presence of young seas such as for on-shore winds near coastal regions.

INTRODUCTION

Capillary-gravity waves on the sea surface which determine to a large extent the air-sea transfer processes, are important roughness elements responsible for the variations in microwave backscattering. For altimeter ocean backscatter measurements, application has been found in the robust empirically-derived wind retrieval algorithm for Ku-band (13.9 GHz) instruments (Witter and Chelton, 1991). Physically-based scattering model studies suggest that a more direct altimeter inference can be made in terms of surface mean square slope (mss) which should parallel the classical optical measurements of ocean mss versus wind speed obtained by Cox and Munk (1954).

We present here a scattering model for altimeter backscatter from the sea including a proposed wind-wave spectrum that is dependent on wind speed and wave age. Wind stress, or friction velocity, is directly related to near-surface wind speed through a drag coefficient. The validity of the proposed spectrum and its implied drag coefficient is checked against a boundary layer model that derives u* from the spectrum.

Resulting predictions for altimeter backscatter are compared to global wind algorithms and TOPEX data to illustrate the promise of dual-frequency data and to point out the effects when inverse wave age is not near the equilibrium value of ~ 0.84.

0-7803-3068-4/96$5.00©1996 IEEE

MODEL PREDICTION

Central to the modeling effort is definition of an idealized sea surface spectrum approximation in the high wavenumber spectral domain. Donelan and Pierson (1987) proposed a model for both the gravity and the gravity-capillary range of the wave spectrum. However, it fails to reproduce well controlled laboratory measurements in the gravity-capillary range obtained by Jähne and its collaborators (1990). Moreover, inferred total mss parameters are not consistent with the Cox and Munk data. In order to improve the Donelan-Pierson model, one can slightly modify its original formulation to match recent spectral forms showing two distinct energy balance regimes, and to be constrained to the optical slope observations. Such a spectrum is wave age dependent, and will exhibit a secondary high-wavenumber peak just before a rapid decay in the capillary region.

Our altimeter backscatter model relies on a two-scale composite Kirchhoff approximation at vertical incidence to treat the dominant quasi-specular scattering and to permit examination of diffraction caused by high-frequency waves. Indeed, Thompson (1988) among others, have advanced that some additional attenuation of near-vertical backscatter can be due to diffraction effects caused by small-scale waves. Using a composite surface model approximation, short-waves below a

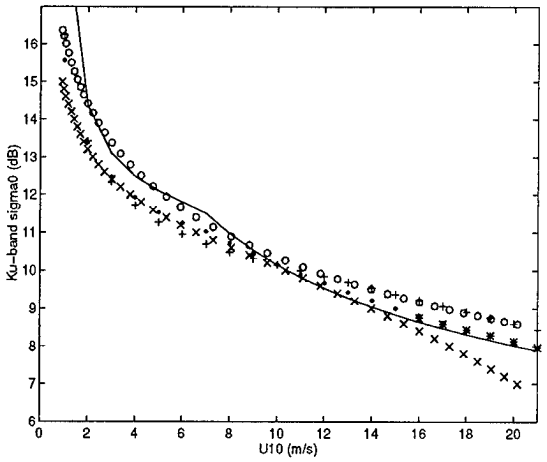


Figure 1: Nadir sigma0 versus wind speed at a height of 10 m (U_{10}). SASS-II 1982 (circles), W&C 1991 (crosses), Jackson 1992 (dotted), Young 1993 (stars), Wu 1995 (plus signs), and e.m. model prediction at ku-band (14 Ghz) (solid).

cut-off limit will diffract radiation in proportion to their height spectral density. This effect will be strongly dependent upon cut-off limits which are incident wavelength dependent.

One test of this physically-based altimeter model should be its ability to reproduce observations and operational algorithms. Here, we consider the Modified Chelton and Wentz (MCW) operational wind speed retrieval algorithm (Witter and Chelton, 1991) for the Ku-band altimeter. Among other empirical operational algorithm, MCW seems to predict the most significant decrease of nadir sigma0 as the wind speed increases. Figure 1 summarizes sigma0 predictions inferred from MCW, SASSII scatterometer wind speed algorithm predictions at nadir, Wu's latest algorithm for a Ku-band instrument (Wu, 1995), Young's high wind branch (1993), Jackson's linear relationship (Jackson et al., 1992) and model results. This comparison shows that our predictions coincide with SASSII at low wind speed, while at higher wind speed model results are close to Jackson's or Young's relationship. In the range of 6 to 15 m/s wind speed, overall agreement between algorithms is observed.

For the highest wind speeds, influence of sea maturity is known to play a major role in relating the radar cross section to surface wind speed (e. g. Lefevre et al., 1994, or Ebuchi et al. 1992). Having an electromagnetic model and a wave spectrum in hand, it is now possible to derive a wind stress relationship to attempt to better describe geophysical phenomena on the ocean surface.

DRAG MODEL

Sea surface roughness is predominantly supported by short waves and is directly related to a significant fraction of the surface stress. A model based on Miles' theory (1957) and Janssen's formulation (1989) that accounts for wind speed and sea state (in terms of the wave spectrum) allows estimation of the surface stress. The approach is based on conservation of momentum in the surface layer. The stress in the surface layer is supported by both turbulent motions of the air and organized wave-induced motions due to the presence of the waves. The latter contribution is mainly determined by the interaction of the air flow with the high frequency part of the wave spectrum (Caudal, 1993; Makin et al., 1995).

Applying the same model spectrum as for scattering prediction, a drag coefficient estimation may be obtained. Figure 2 shows wave age influences. As expected, larger variation would be obtained as the neutral wind speed increases.

TOPEX DATA

A key motivation for this study is the global dual-frequency (C-band (5.5 cm) and Ku-band (2.1 cm)) altimeter data set available from the TOPEX satellite. As presented above, distinct scattering behavior is expected for each instrument when considering diffraction effects. For C-band, the incident wavenumber is nearly three times smaller than for Ku-band, while small-scale height density changes little in this wavenumber range. Therefore, a C-band altimeter should be much less sensitive to changes due to wind entering through diffraction effects.

Selected TOPEX data correspond to a small subset of cycle 70 (10 orbits) acquired over deep-ocean areas. This cycle was chosen for its overall gain stability. Figure 3 presents predicted model results and data. Aside from a shift along the C-band axis (dB), our development reproduces the relationship between the two TOPEX frequency measurements. Discrepancies only appear for the upper branch (lowest sea surface roughness).

This graph clearly reveals a change in sensitivity between C- and Ku-band as sea surface roughness increases. The

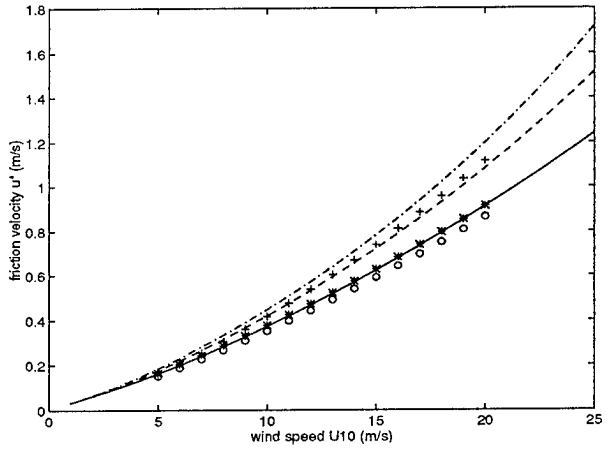


Figure 2: Friction velocity versus neutral wind speed U_{10} for various wave ages; U_{10}/Cp= 0.84 (solid), 2 (dahsed), 3 (dashed dotted). Cp is the peak phase speed. Cd_{10} from Donelan 1982 (plus) ,Garratt 1977 (stars),. Smith 1988 (circles).

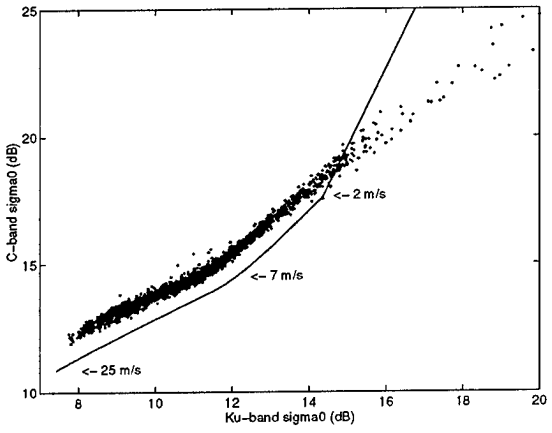


Figure 3: Scatter plot of data from the dual frequency altimeter TOPEX. Ku-band versus C-band sigma0. Solid curve is the predicted model. A break point occurs at about 7 m/s.

change in sensitivity occurs near 7 m/s wind speed. Such a transition may be associated with the transition from aerodynamically smooth to rough flow with onset of increased small scale wave breaking events (Banner and Melville, 1976).

ALTIMETER WIND ALGORITHM

Predictions of altimeter backscatter as function of wind speed and sea state is shown in Figure 4. It can be seen that various wind speeds may correspond to identical value of measured sigma0.

The combination of results shown in Figures 1 and 2 can be used to discuss the effect of changing wave age in Figure 4. The global wind speed algorithms are generated to describe the global or average conditions.Therefore, the retrieved wind speed from empirical models such as MCW is in general lower than the true wind speed in presence of young seas. This is especially true for on-shore winds near coastal regions.

To achieve better accuracy for altimeter wind retrieval algorithm, it seems necessary to include independent measurements such as altimeter significant wave height estimates (Lefevre et al., 1994; Dobson et al., 1987). Moreover, Figure 3 indicates that TOPEX C-band backscatter is less sensitive (than Ku-) to increasing wind stress. It is likely less responsive to steepness associated with young waves. One can envision utilizing the TOPEX significant wave height estimates along with C- and Ku-band data to examine sea state effects at various wind speeds.

CONCLUSION.

In this study, sigma0 for nadir incidence are shown to be related to the wind friction velocity and sea state. Moreover, we observe that C- and Ku-band backscatter measurements show a large departure in the form of the wind-dependence function starting at about 7 m/s. Beyond this wind speed, it is known that generation of small-scale wind waves is responsible for a significant fraction of the mean sea surface wind stress. Simultaneous dual-frequency TOPEX data demonstrate the potential to go beyond empirical wind speed relationships. Therefore, synergetic use of different observed parameters from different satellite instruments (wavelength, incidence angle, passive or active, polarization) can be used to better elucidate various air/sea processes occurring at the interface.

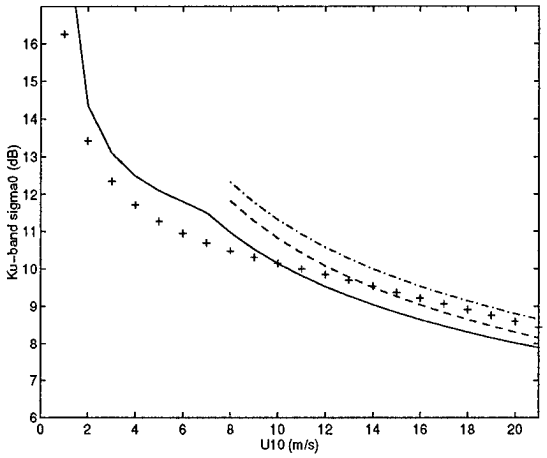


Figure 4: Predicted nadir Ku-band sigma0 versus wind speed for various wave ages: U10/Cp=.84 (solid), 2 (dashed), 3 (dashed dotted). Cp is the peak phase speed. Wu algorithm, 1995, (+) seems to compromise between mature seas at low wind speed and youger seas at high wind speed.

REFERENCES

[1] Miles, J.W., On the generation of surface waves by shear flows, J. Fluid Mech, 3, 185-204, 1957.

[2] Janssen, P.A.E.M., Wave induced stress and the drag of air flow over sea waves, J. Phys. Oceanogr. 19, 745-754,1989.

[3] Banner, M. L. and W. K. Melville, On the separation of air-flow over water waves, J. Fluid Mech., 77, 825-842, 1976.

[4] Witter D.L. and D.B. Chelton. A GEOSAT altimeter wind speed algorithm and a method for altimeter wind speed algorithm development. J. Geophys. Res., 96, 8853-8860, 1991.

[5] Jackson, F. C., W. T. Walton, Walter, W.T., and C. Y. Peng, Sea surface mean square slope from Ku-band backscatter data, J. Geophys. Res., 97, C7, 11.441-11.427, 1992.

[6] Wu, J., Microwave specular reflections from Breaking waves - Measurements of hurricane winds from space , American Meteoro. Society, Vol. 25, 3231-3236, Dec 1995.

[7] Chapron B., Katsaros K., Elfouhaily T. and Vandemark D., A note on relationships between sea surface roughness and altimeter backscatter, Air-Water Gas Transfer, Selected papers from the Third International Symposium on Air-Water Gas Transfer, Heidelberg University, edited by B. Jähne and E. C. Monahan, AEON Verlag and Studio, 63454 Hanau, pages 869-878, July 24-27, 1995.

[8] Cox C.S. and W.H. Munk, Statistics of the sea surface derived from sun glitter, J. Mar. Res., 13, 198-227, 1954.

[9] Donelan, M. A., and W. J. P. Pierson, Radar scattering and equilibrium ranges in wind-generated waves with application to scatterometry, J. Geophys. Res., 92, 4971-5029, 1987.

[10] Jähne B. and K. S. Riemer,1990, Two-dimensional wave number spectra of small-scale water surface waves, J. of Geophys. Res., Vol. 95, No. C7, pages 11,531-11,546, July 15, 1990.

[11] Makin, V.K., V.N. Kudryavtsev and C. Mastenbroek, Drag of the sea surface. Boundary-layer Meteorology, Vol. 73, pp. 159-182, 1995.

[12] Caudal G., Self-consistency between wind stress, wave spectrum and wind-induced wave growth for fully rough air-sea interface, J. Geophys. Res., 98, C12, pages 22.743-22.752, DEC 15, 1993.

[13] Donelan M.A., F.W. Dobson, S.D. Smith, and R.J. Anderson, On the dependence of sea surface roughness on wave development, J. of Physical Oceanography, Vol. 23, 2143-2149, 1993.

[14] Ebuchi N., H. Kawamura and Y. Toba, Growth of wind waves with fetch observed by GEOSAT altimeter in the Japan sea under winter Monsoon, J. of Geophys. Res., 97, C1, 809-819, Jan. 15, 1992.

[15] Lefevre J.M., J. Barckicke, and Y. Ménard, A significant wave height dependent function for TOPEX/POSEIDON wind speed retrieval, J. of Geophys. Res., Vol. 99, No. C12, pp 25.035-25.046, Dec. 15, 1994.

[16] Young I.R., An estimate of the GEOSAT altimeter wind speed algorithm at high wind speeds, J. of Geophys. Res. 98, 20.275-20.285, 1993.

[17] Dobson E., F. Monaldo, J. Goldhirch and J. Wilkerson, Validation of GEOSAT altimeter derived wind speeds and significant wave heights using buoy data, J of Geophys. Res., 92, 10719-10732, 1987

Correcting SeaWinds Scatterometer Measurements for Atmospheric Attenuation

R. K. Moore, N. Kambhammettu, and S. Song
University of Kansas, Radar Systems and Remote Sensing Laboratory
2291 Irving Hill Road, Lawrence, KS 66045-2969, USA
TEL: 913/864-4836 , FAX: 913/864-7789 , E-mail: rmoore@eecs.ukans.edu

Abstract—An attenuation-correction algorithm for the SeaWinds instrument uses the AMSR brightness temperature to find the attenuation experienced by the scatterometer signal. The algorithm uses the concept of excess temperature T_{ex} to evaluate the attenuation. The excess temperature T_{ex} is the difference between the measured brightness temperature and the temperature of the emitting surface. The algorithm uses an iterative scheme. Simulation results show obvious improvement on the scatterometer measurements.

INTRODUCTION

The wind vector on the ocean surface can be determined from measurements of radar backscatter of the ocean by using a spaceborne scatterometer [1]. The global coverage and frequent sampling give the spaceborne scatterometer advantages over other measurements [2]. However, the signal measured by the scatterometer is representative from the sea surface only when dense clouds and precipitation are absent. When heavy clouds and precipitation are present, the signal received at the scatterometer is reduced because of the attenuation of clouds and rain. For accurate determination of the sea surface wind vectors we need to estimate this reduction and make correction in the wind retrieval process.

Using radiometric measurements to make correction on the scatterometric data by combination was presented in [3]. A correction process was developed to evaluate the atmospheric attenuation from SMMR brightness temperature for the Seasat satellite scatterometer. The results showed the correction appeared to improve the accuracy of wind vector determination. However, the non-coincident large footprints of the two instruments negated this improvement in tight storms.

The SeaWinds scatterometer instrument will fly in 1999 as a part of the EOS program on the Japanese ADEOS-II. The scatterometer is a Ku-Band radar. It has antenna beams at two elevation angles giving a conical scan (concentric circles on the surface). The conical design represents a change from the fixed fan-beam antennas of previous spaceborne scatterometers (SeaSat and ERS-1). The on-board Advanced Microwave Scanning Radiometer (AMSR) works at multiple frequencies and also uses a conical scan. The concept of excess temperature is used to develop the correction algorithm for the scatterometer measurements by using the AMSR data. The AMSR and SeaWinds scans are not identical, but the smaller footprints than those on Seasat make comparison more reliable. The AMSR data must be collocated [5] to match the location of the scatterometer measurements.

0-7803-3068-4/96$5.00©1996 IEEE

PRINCIPLES OF THE CORRECTION ALGORITHM

When clouds and rain are present, the scatterometer signal will undergo a two-way attenuation. If we use L to denote the one way attenuation, then the σ^0 measured by the scatterometer will be σ^m and

$$\sigma_m = L^2 \sigma^0 = \sigma^0 e^{-2\alpha} \tag{1}$$

where α is the attenuation factor in nepers. When clouds and rain are present, the radiometer measurements will be

$$T_m = L(T_s + T_r) + T_{atm} \tag{2}$$

where T_s is the sea-surface contribution and T_r is the contribution from the sky emissions reflected by the sea surface. The last term T_{atm} is the contribution from the clouds and rain. The attenuation is denoted by L, as in (1).

The excess temperature is defined as

$$T_{ex} = T_m - T_s \tag{3}$$

From (2), we know that if the surface temperature is known, the excess temperature will depend on L, T_{atm} and T_r. The T_r is small comparing to T_{atm} and can be negligible. Thus the T_{ex} will be determined by the attenuation and the cloud and rain contribution. The relation between attenuation and excess temperature may be expressed by the cubic relation [4]

$$\alpha(dB) = AT_{ex} + BT_{ex}^2 + CT_{ex}^3 \tag{4}$$

From (2)-(4), an iterative process can be established to estimate the attenuation L or α, denoted by L_{est} or α_{est}. Using this factor, we can correct the scatterometer measured σ^0 by simply inverting equation (1)

$$\sigma_c = \sigma_m e^{2\alpha_{est}} \tag{5}$$

However, the sea surface brightness temperature T_s is needed when we calculate the excess temperature T_{ex} by using (2) and (3). This can be obtain by using the following model [1]

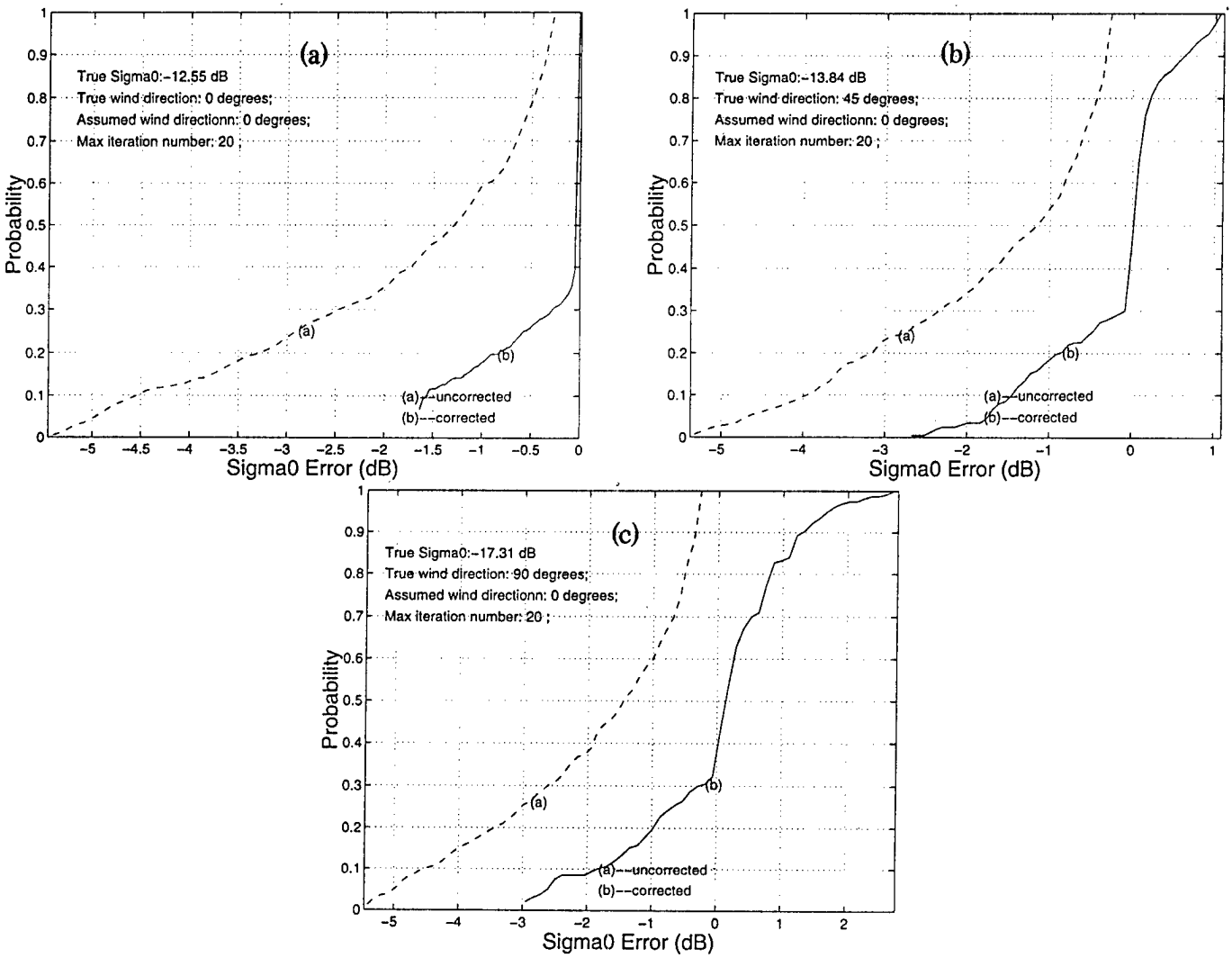


Fig. 1. Examples of error corrections for stratiform rain with different assumptions for wind. (a) Same direction as true wind, (b) 45° from true wind, (c) 90° from true wind.

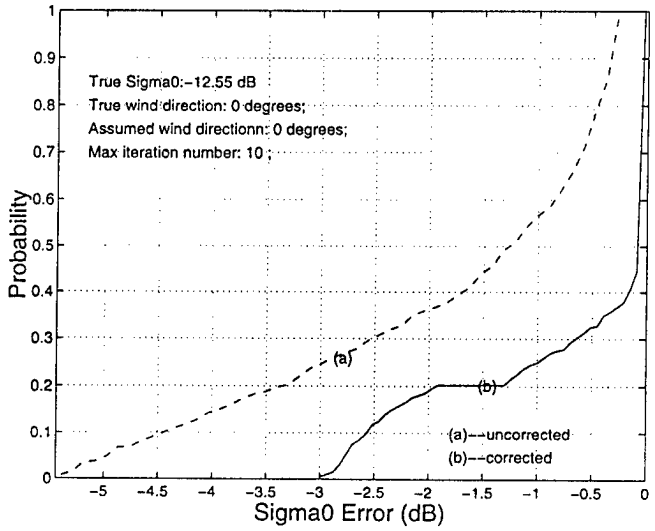


Fig. 2. Example of error correction for convective cells. Four cells in region with r_0 = 7 km. Note errors are small because much of footprint has little or no rain.

$$T_s = 82 + 1.06\,U \tag{6}$$

where U is the sea-surface wind speed, which can be estimated by the scatterometer-measured σ^0 using the SASS model function

$$U_{est} = 10\,\frac{\sigma_c(dB) - 10\,G}{10\,H} \tag{7}$$

where σ^c is from (5). G and H are constants of the model function that depend on the incident angle and the wind direction.

From above we can see how an iterative process can estimate the attenuation and correct the measured σ^0. However, in calculating (7), we need to know the wind direction. There are three possible solutions for this problem:

1. Assuming upwind direction;
2. Obtaining the wind direction using the SeaWinds alias-removal algorithm;
3. Using the previous-cell wind direction.

The second solution has two difficulties. One is that the alias-removal Seawinds algorithm is quite complex and is not suitable for iteration. The other difficulty is the alias-removal SeaWinds algorithm uses a maximum-likelihood method and it needs to combine multi-point measurements of σ^0 to get the wind direction. However, we cannot obtain the accurate wind direction before correction is performed. So we have to use the first or the third solution. Obviously, the third solution is preferred as long as the wind-retrieval method can get accurate wind direction after correction. Simulation results for these two methods are given in the next section.

SIMULATION AND RESULTS

In the correction algorithm described above, we assumed the radiometer data used to estimate the attenuation is located at the same point as the scatterometer measurement. Actually, the measured points on the sea surface for the two instruments overlap but are not coincident. We need to match the scatterometer data with the proper radiometer data. A triangle method [5] is used to do the collocation in simulation. That is, for one scatterometer-measured σ^0 , the nearest three points of AMSR measurements (Tb) will be collocated to this σ^0. Interpolation or weighting techniques are used to get the T_b at the σ^0 point depending on whether the σ^0 point is inside or outside the triangle formed by three T_b points.

In simulation, the cloud and rain distribution for convective storms is characterized by each storm having an exponential excess temperature distribution $T_p \exp(-r/r_0)$, where T_p is the peak temperature at the storm center and r is the distance from the center. The fall-off rate that determines the storm size is r_0. For simulation, the number of storms is set and the peaks and centers of storms are randomly distributed. We ran the correction algorithm 400 times for different cloud and rain distributions to get the statistical results on the correction. Fig. 1 shows the error probability for corrected and uncorrected results for uniform rain throughout the region, as in a stratiform system, and shows the effect of wrong assumptions of direction. For Fig. 1(a) the direction assumed is correct; for 1(b), it is off by 45°, and for 1(c) it is off by 90°. Use of a direction from the preceding wind-vector cell should be well within 45°, and therefore acceptable. Arbitrary assumptions could be 90° off, and the correction poorer. Fig. 2 shows a convective-storm situation with four storms, each with fall-off rate $r_0 = 7$. Even the uncorrected errors are small here, and the correction does improve the results.

CONCLUSIONS

A correction algorithm for the SeaWinds scatterometer, using AMSR estimates of attenuation, was presented. Simulated results show obvious improvement. Best results will be obtained if wind direction from the previous wind-vector cell can be used. Errors can be large with extensive rain unless corrected, but for small convective cells the errors are not large even before correction.

REFERENCES

[1] F. T. Ulaby, R. K. Moore, and A. K. Fung, *Microwave Remote Sensing,* vol. III, Artech House, Inc., Norwood MA, 1985.

[2] F. M. Nader, et al., "Spaceborne radar measurement of wind velocity over ocean-An overview of the NSCAT scatterometer system," *Proc. IEEE,* vol. 79, pp.850-866, 1991.

[3] R. K. Moore, A.H. Chaudhry, and I.J. Birrer, "Errors in scatterometer-radiometer wind measurement due to rain", *IEEE J. Oceanic Eng.,* vol. OE-8, pp. 37-49, 1983.

[4] G. J. Dome, *Oceanic Wind Vector Determination Using SeaSat Satellite,* D. Eng. Thesis, Univ. of Kansas, Lawrence, 1980.

[5] SeaWinds Algorithm Review, JPL, Oct, 1995, unpublished.

Spectrometry of Turbidity in Surface Water

Luoheng Han
Department of Geography
The University of Alabama
Tuscaloosa, AL 35487-0322
(205)348-4981/(205)348-2278/LHAN@gallalee.as.ua.edu

Abstract -- The objective of this paper was to investigate how to measure turbidity of water using surface spectral reflectance. Spectral data from a reservoir were collected using a field spectroradiometer, which contains 512 spectral channels ranging from 350 to 1050 nm. Five replicate scans were taken at each sampling site with a total of 23 such sites selected. The results indicated that wind-induced whitecaps on the surface of water can cause higher overall reflectance and inconsistency among the replicate spectral measurements. As result, it was almost impossible to apply reflectance from any single wavelength to accurately estimate turbidity. It was found that the difference of reflectances between 710 and 720 nm is a better indicator of turbidity.

I. INTRODUCTION

Remote sensing has been proven useful for water quality monitoring. Although satellite remote sensing is widely used for this purpose, its application to inland fresh water has been limited by the spatial, spectral, and radiometric resolutions [3]. In addition, satellite remote sensing is often complicated by a number of extraneous variables such as atmospheric attenuation, angles of illumination and observation, etc. Therefore, it seems to be useful to conduct basic research at close-range, employing the field spectrometry technique. In addition, through measuring spectral signal in hundreds of channels, which is featured in the spectrometry, it is possible to elucidate fundamental relationships between spectral response and water quality conditions. The current research was based on close-range sensing with a spectrometry instrument.

Turbidity of water refers to the optical property of waters that causes light to be scattered and absorbed rather than transmitted through the water. Therefore, turbidity is directly associated with the quantity and quality of suspended particulates in water, e.g., algal solids and inorganic sediments. Since turbidity is the indicator of the clarity of water, measurement of turbidity appeals greatly to resource managers.

As the Secchi disk, the more popular form of turbidity measurement, tends to be subjective, remote sensing has been considered as an alternative tool in measuring turbidity [1][2][3].

The objective of this paper was to investigate how to measure turbidity using surface spectral reflectance.

0-7803-3068-4/96$5.00©1996 IEEE

II. METHODS

This research was conducted at Branched Oak Lake, a flood control reservoir and recreation area, located about 48 kilometers northwest of Lincoln, Nebraska (96°50′56″W to 96°54′7″W and 40°57′32″N to 40°59′53″N). The total uncontrolled drainage area is 154 kilometers^2 and the water area is 7.2 kilometers^2. Agricultural activities, primarily cropland and pasture, dominate land use in the watershed.

To minimize extraneous "bottom reflectance" and maximize depth, two transects for data collection were chosen near stream beds that existed prior to impoundment. The depth of the water along the transects ranged from 5.5 to 7 meters.

Spectral data collection and water sampling were conducted from a 24-foot (7.3-meter) pontoon boat at 23 sampling sites, selected randomly but roughly equidistant from one to the next along the two transects, on July 13, 1995. The time for data collection was between 10:50 a.m. to 1:18 p.m. local daylight saving time, during which the sky remained clear.

An Analytical Spectral Devices (ASD) FieldSpec-UV/VNIR spectroradiometer was used to collect radiance upwelling from the water and a Kodak 18% gray card served as the reference panel. Reflectance (in percentage) was then calculated for each measurement and used in the analysis. The spectroradiometer acquires data in 512 discrete channels ranging from 350 to 1050 nm. For this study, data from 400 to 900 nm (353 channels) were used because of significant noise in the water signal at wavelengths outside this range. The instrument head was attached to a pipe that was pointed south with the boat oriented east-west. The sensor was positioned over the water at a height of 2.5 meters. A nadir view angle and 10° FOV tube were selected for use, resulting in an instantaneous field of view of 0.39 m by 0.39 m on the water surface. Five replicate scans were taken for each spectral sampling.

Water sampling was performed using a Van Dorn sampler, at 0.5 m depth below the surface at each site during the spectral measurements. The turbidity of the water was measured using a Hach model 2100P Portable Turbidometer. The measurements were in Nephelometric Turbidity Units (NTUs). Three samples were measured for each site and the mean of the three was used in the analysis.

III. RESULTS AND DISCUSSION

The averaged spectral reflectance curves over all 23 sampling sites are presented in Fig. 1. The major characteristic spectral features associated with the particulates in water were evident, e.g., the low reflectance between 400 and 500 nm, the high reflectance around 570 nm from algal chlorophyll, coupled with strong backscattering by inorganic suspended sediments, the minimum reflectance at 670 nm caused by chlorophyll absorption, and a prominent reflectance maximum at about 700 nm.

In this study, overall reflectance was strongly influenced by wind, which generated so called whitecap effect [4]. Although the five replicate scans at each site were taken in less than 60 seconds, variations of reflectance were obvious and more directly related to wind speed than turbidity. Figs. 2 and 3 demonstrate the replicate reflectance curves at two sampling sites. It seemed that the overall reflectance and variations among the replicate reflectance increased as the wind speed increased despite lower turbidity occurred.

To investigate the relationship between spectral reflectance (averaged from five replicates) and turbidity at each individual wavelength, a total of 353 correlation coefficients (r) between reflectance and turbidity were computed. The values of r ranged from 0.45 (at 900 nm) and 0.62 (at 700 nm) (Fig. 4). The weak correlations indicated that the averaged reflectance at an individual wavelength is not effective to estimate turbidity in a water body. This is consistent with earlier wind effect analogy.

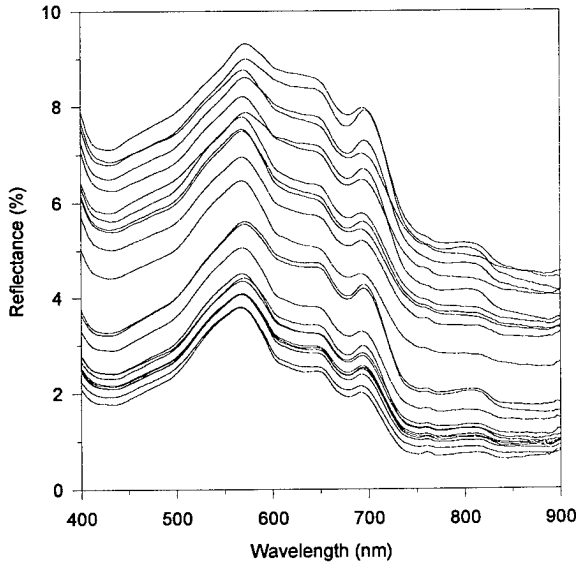


Fig. 1. Averaged spectral reflectance at all 23 sampling sites

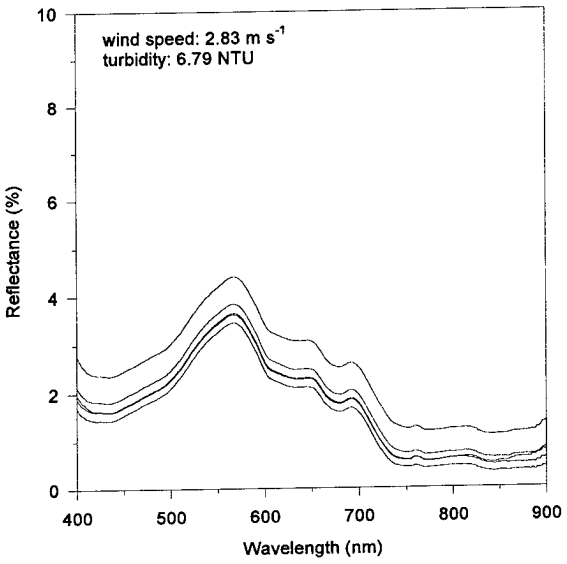


Fig. 2. Five replicate reflectance curves at site #1

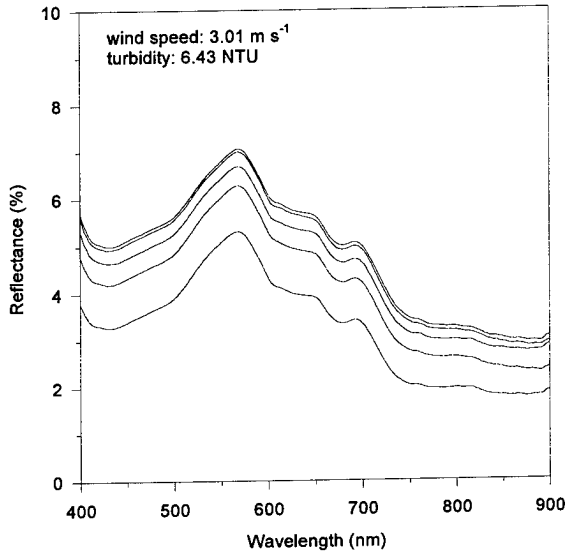


Fig. 3. Five replicate reflectance curves at site #13

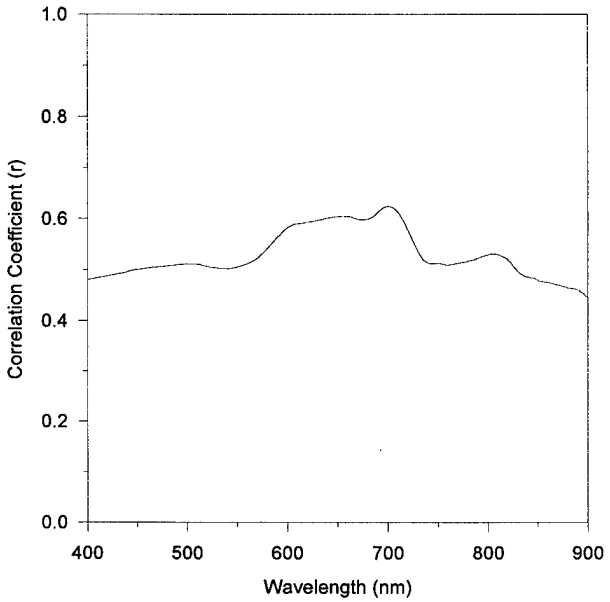


Fig. 4 . Correlation between reflectance and turbidity

Instead of using reflectance at an individual wavelength, it was found that the difference between reflectances at 710 and 720 nm was highly correlated with turbidity. Fig. 5 shows that the correlation coefficient between the two parameters was as high as 0.95. The principle behind this result may be that the gradient of reflectance between 710 and 720 nm is more independent to the wind effect, hence a better indicator of turbidity.

V. CONCLUSIONS

Spectral measurement of water is greatly influenced by external environmental factors, such as wind. Wind-induced whitecaps on the surface of water can cause higher overall reflectance and inconsistency among the replicates. In correlating the reflectance with turbidity, averaging the replicate reflectance did not generate satisfactory results in this study. Differencing the reflectances between 710 and 720 nm , on the other hand, seemed to be a better solution.

ACKNOWLEDGMENTS

The author sincerely thanks Donald C. Rundquist for his support for this research. Thanks also go to Rollie Fraser, Brian Tolk, and Stuart McFeeters for assisting in data collection. The author acknowledges, with appreciation, CALMIT, Conservation and Survey Division at University of Nebraska-Lincoln for providing most of the equipment required for data collection. The High Plain Climate Center at

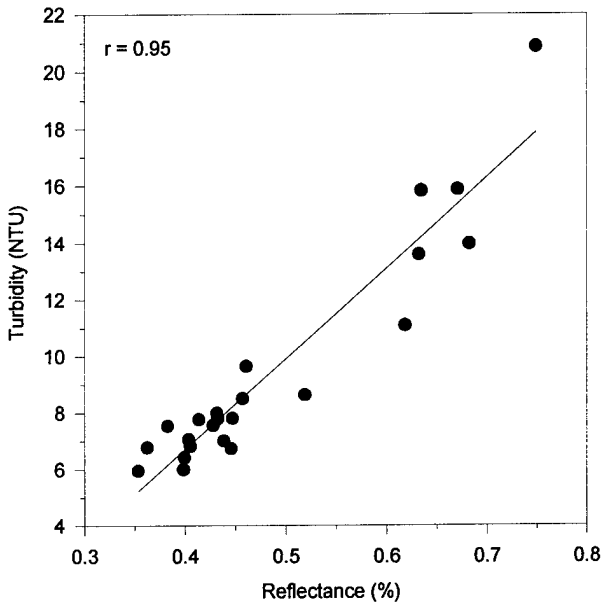


Fig. 5. Correlation between turbidity and difference of Reflectances at 710 and 720 nm

University of Nebraska-Lincoln provided weather information. The author also acknowledges funding support provided by SOMED Grant of The University of Alabama.

REFERENCES

[1] T.T. Alföldi, "Remote sensing for water quality monitoring," In Remote Sensing for Resource Management, C.J. Johannsen and J.L. Sanders, Eds. Iowa: Soil Conservation Society of America, 1982,pp. 317-328.

[2] A.G. Dekker, T.J. Malthus, and Hoogenboom, "The remote sensing of inland water quality," In Advances in Environmental Remote Sensing, F.M. Danson and S.E. Plummer, Eds. New York: John Wiley & Sons, 1995, pp. 123-142.

[3] J. Hilton, "Airborne remote sensing for freshwater and estuarine monitoring," Water Res., vol. 18, no. 10, pp. 1195-1223, 1984.

[4] E.C. Monahan and I.G. O'Muircheartaigh, "Whitecaps and passive remote sensing of the ocean surface," Int. J. Remote Sensing, vol. 7, no. 5, pp. 627-642.

SeaWiFS and MERIS: a comparison of their performance for the estimation of optically active components in ocean water

P. Cipollini[1], G. Corsini[2]
[1] James Rennell Division for Ocean Circulation, Southampton Oceanography Centre
European Way, Southampton SO14 3ZH, UK
Tel. +44-1703-596405 – Fax +44-1703-596400 – E-mail: cipo@soc.soton.ac.uk
[2] Department of Information Engineering, University of Pisa
Via Diotisalvi 2, I-56126 Pisa, Italy
Tel. +39-50-568511 – Fax +39-50-568522 – E-mail: gcorsini@iet.unipi.it

Abstract — SeaWiFS and MERIS capabilities for the estimation of optically active components in ocean waters are analysed by means of a semi-theoretical model of ocean colour which also takes account of the chlorophyll fluorescence signal at about 685 nm. The reflectance curves simulated with the model over various types of water have been integrated over the bands of the two sensors, and a regressive analysis has been used to find the algorithms for the retrieval of the three main classes of optically active components, and the corresponding correlation coefficients. The results show that the availability of SeaWiFS data will give unprecedented capabilities for the retrieval of optically active parameters from satellite imagery, especially over case 1 waters. MERIS will have the same potential in those waters; moreover, the presence of two additional channels in the red region makes this instrument very interesting also for the parameter retrieval over case 2 waters.

INTRODUCTION AND BACKGROUND

In the next 5 years, several ocean colour sensors are planned to be put in orbit. This new interest in ocean colour reflects the ever-growing concern about the mechanisms which regulate the absorption of carbon by the oceans, thus affecting the global balance of this element in the atmosphere and eventually the global climate. In fact, with remote sensing of ocean colour it is possible to estimate productivity through the observation of phytoplankton pigments; moreover, it is in principle possible to estimate the coloured fraction of the dissolved organic matter ('yellow substance'), which is one of the most important reservoirs of reduced carbon.

The optically active components or parameters which can be observed by remote sensing of ocean colour are usually classified into three main groups [2]: pigments contained in the phytoplankton (whose most important is chlorophyll-a), non-chlorophyllous particles including unpigmented cells and mineralized suspended sediments, and yellow substance. Apart from the problems of radiometric and atmospheric corrections of remotely sensed data (which are not addressed here), it seems interesting to study and assess the potential of the new sensors to distinguish among the spectral signatures of the different components on the basis of their spectral characteristics alone. This work aims to evaluate two of the most important instruments, NASA's SeaWiFS (planned for launch this year on board the SeaStar platform) and ESA's MERIS on board ENVISAT-1 which should be available by the end of the century [1].

METHODOLOGY

The approach which we adopt is as follows: first, we use a model of ocean colour to simulate reflectance spectra over a large number of values of the optically active parameter concentrations; then, we integrate the reflectance curves over the bands of the sensors, and finally we perform a regression analysis to find the algorithms for the concentration retrieval. The value of the correlation coefficient for an algorithm is a measure of the effectiveness of that algorithm in estimating the parameter. Thus, the capabilities of the sensor itself can be assessed.

The model we use was originally drawn from that presented in [2] and is of the general form:

$$R(\lambda) = f(C, X, Y) \qquad (1)$$

where $R(\lambda)$ is the reflectance just below the sea surface [3], C is the concentration of chlorophyll-a and phaeopigments in the phytoplankton and thus a measure of phytoplankton concentration itself ($\mathrm{mg\,m^{-3}}$), X is the concentration of non-chlorophyllous particles expressed in terms of their backscattering coefficient at 550 nm ($\mathrm{m^{-1}}$) and Y is the yellow substance absorption at 440 nm ($\mathrm{m^{-1}}$). Wavelength λ goes from 400 to 700 nm in steps of 2 nm.

The reflectance turns out to be approximately proportional to the ratio of the backscattering and absorption coefficients of the water body; these are then expressed as the sum of the

This work has been partially supported by the Commission of European Communities through a Research Training Fellowship to Paolo Cipollini (HCM contract no. ERBCHBGCT930440).

0-7803-3068-4/96$5.00©1996 IEEE

partial contributions due to the water itself and to the three groups of optically active parameters. We have taken the absorption and backscattering of pure sea water from [4]. The absorption of phytoplankton has been modeled as in a recent study by Bricaud et al. [5] to take account of the flattening of the absorption spectra with increasing C. The absorption due to non-chlorophyllous particles has been modeled as an exponential with slope equal to $-0.011\ \mathrm{nm}^{-1}$ according to [6] and specific absorption coefficient at 440 nm equal to 0.042 taken from [2]. For yellow substance the absorption is the classical expression by Morel and Prieur used in [2]. As regards the backscattering by non-chlorophyllous particles, we have adopted a λ^{-1} dependence as in [2], but with a backscattering ratio of 2%.

The backscattering coefficient of phytoplankton gives us the opportunity to introduce into the model a first-order parameterization of chlorophyll fluorescence around 685 nm. On the basis of the results by Ahn et al. [7], we have modeled that coefficient as a constant baseline plus a narrow gaussian curve peaked at 685 nm and with standard deviation of 10 nm. The amplitude of the gaussian is such that the overall peak of the coefficient is ten times the baseline. The expression for the constant baseline is taken from [8] and is:

$$b_{bph-baseline} = 0.002 \cdot 0.30 \cdot C^{0.62} \qquad (2)$$

in which we assume a backscattering ratio of 0.2% for phytoplankton alone according to [9].

With the model, we have generated a large number of reflectance curves extracting the input triplets at random. Following [10], we have chosen a lognormal distribution for C, and we have assumed a similar distribution for the other two parameters as well. We have chosen, somewhat arbitrarily, two different sets (which are presented in table 1) both for the mean values μ and standard deviations σ of the parameter decimal logarithms, and for the correlation r between $\log(C)$ and $\log(X)$ and between $\log(C)$ and $\log(Y)$. The first set of distributions reproduces the values which are believed to be representative of case 1 waters [3], while the second set is more typical of a case1 + case 2 study.

For each set we have simulated 5000 reflectance curves and, finally, they have been integrated over the SeaWiFS and MERIS bands, and the regression analysis performed. Although the MERIS has programmable band position and width, we have used the standard values for oceanographic purposes drawn from [1], that is channels 1-8 in the visible centered at 412.5, 442.5, 490, 510, 560, 620, 665, 681.25 nm with 10 nm bandwidth for channels 1-7 and 7.5 nm bandwidth for channel 8.

RESULTS

The most general form of the algorithms which we have considered is:

$$\log(OAP) = a_o + \sum_i a_i \log(R_i) \qquad (3)$$

where OAP indicates one of the optically active parameters, R_i is the reflectance in the i-th band of the sensor and log is the decimal logarithm. The common reflectance ratio algorithms are also encompassed by the above equation, however it seems reasonable to use the full spectral information given by the sensors in order to obtain the maximum degree of accuracy in the parameter retrieval, apart from radiometric consideration (i.e the signal to noise ratio in some spectral bands can be low and prevent the use of those bands in a practical case).

The results for both the instruments and for the first set of concentration distributions are presented in table 2. The extremely close to unity values for the correlation coefficient r between the logarithms, and the low values of the RMS error e_{RMS} between the logarithms demonstrate the theoretical effectiveness of both the instruments for a case 1 parameter retrieval. Reflectance ratio algorithms can still be regarded as a first approximation for the estimate of C where the yellow substance effects can be neglected. For instance, we have for SeaWiFS:

$$\log(C) = -0.17 - 5.58\log(R_3/R_4) \qquad (4)$$

with $r = -0.929$, but those ratios generally appear to be much more correlated with a cumulative contribution of phytoplankton and yellow substance. In fact we have:

$$\log(C + 7.68Y) = 0.19 - 5.62\log(R_3/R_4) \qquad (5)$$

with $r = -0.989$. This is in agreement with some results obtained from the previous versions of our model [11] [12] [13] [14] (note that in those papers the unit for yellow substance concentration G should read $\mathrm{g\,m^{-3}}$ instead of $\mathrm{mg\,m^{-3}}$).

The results for the case 1 + case 2 set of concentration distributions (set 2) are in table 3. In this case, the lower correlation between the parameters and their larger variability decrease the correlation coefficient for the SeaWiFS phytoplankton retrieval to $r = 0.956$. Although this can still be regarded as a good value, it is worth noting that simple reflectance ratios show higher r values when regressed against the cumulative phytoplankton and yellow substance concentration, for instance:

$$\log(C + 10.35Y) = 1.16 - 1.32\log(R_3/R_6) \qquad (6)$$

with $r = -0.983$. MERIS takes advantage of the presence of two more channels in the red, and the value of r for its phytoplankton algorithm is still very close to unity. In a practical case MERIS should also benefit from the higher S/N ratios in the channels, so it seems to be extremely promising for a separate estimation of all the three optically active components over case 2 waters.

Table 1. Concentration distributions used

statistics	set 1: case 1	set 2: cases 1+2
$\mu_{\log C}, \sigma_{\log C}$	–0.8, 0.3	–0.4, 0.5
$\mu_{\log X}, \sigma_{\log X}$	–1.2, 0.3	–0.7, 0.5
$\mu_{\log Y}, \sigma_{\log Y}$	–1.6, 0.3	–1.0, 0.5
$r_{\log C \log X}, r_{\log C \log Y}$	0.8, 0.8	0.6, 0.6

REFERENCES

[1] M. Rast and J. L. Bézy, "The ESA Medium Resolution Imaging Spectrometer (MERIS): requirements to its mission and performance of its system," Proc. 21st Ann. Conf. of the Rem. Sens. Soc., Southampton (UK), pp. 125-132, 1995.

[2] S. Sathyendranath, L. Prieur and A. Morel, "A three-component model of ocean colour and its application to remote sensing of phytoplankton pigments in coastal waters," Int. J. Rem. Sens., vol. 10, pp. 1373-1394, 1989.

[3] A. Morel and L. Prieur, "Analysis of variations in ocean colour," Limn. Oceanogr., vol. 22, pp. 709-722, 1977.

[4] R. C., Smith and K. S. Baker, "Optical properties of the clearest natural waters," Appl. Opt., vol. 20, no. 2, pp. 177-184, 1981.

[5] A. Bricaud, M. Babin, A. Morel and H. Claustre, "Variability in the chlorophyll-specific absorption coefficients of natural phytoplankton: Analysis and parameterization," J. Geophys. Res., vol. 100 (C7), pp. 13321-13332, 1995.

[6] C. S. Roesler, M. J. Perry and K. L. Carder, "Modeling in situ phytoplankton absorption from total absorption spectra in productive inland marine waters," Limn. Oceanogr., vol. 34, no. 8, pp. 1510-1523, 1989.

[7] Y.-H. Ahn, A. Bricaud and A. Morel, "Light backscattering efficiency and related properties of some phytoplankters," Deep-Sea Res., vol. 39, no. 11/12, pp. 1835-1855, 1992.

[8] H. R. Gordon and A. Morel, "Remote assessment of ocean color for interpretation of satellite visible imagery, a review," in Lecture notes on Coastal and Estuarine Studies, 114 p., Springer-Verlag, New York, 1983.

[9] A. Morel, "Optical modeling of the upper ocean in relation to its biogenous matter content (case I waters)," J. Geophys. Res., vol. 93 (C9), pp. 10749-10768, 1988.

[10] J. W. Campbell, "The lognormal distribution as a model for bio-optical variability in the sea," J. Geophys. Res., vol. 100 (C7), pp. 13237-13254, 1995.

[11] P. Cipollini and G. Corsini, "Interpretation of Parametric Maps Obtained by means of 'Blue to Green Ratio' over Coastal Waters," Proc. IGARSS'94, Pasadena (California), vol. IV, pp. 2106-2108, 1994.

[12] P. Cipollini and G. Corsini, "The Effect of Yellow Substance on Pigment Concentration Retrieval Using 'Blue to Green' Ratio," Proc. IEEE/OES OCEANS 94, Brest (France), vol. I, pp. 772-777, 1994.

[13] P. Cipollini and G. Corsini, "Ocean colour analysis by hyperspectral MIVIS radiometer: model-derived algorithms," Proc. IGARSS '95, Florence (Italy), vol. III, pp. 2081-2083, 1995.

[14] P. Cipollini and G. Corsini, "Model-derived algorithms for marine parameter retrieval from SeaWiFS data," Global Process Monitoring and Remote Sensing of the Ocean and Sea Ice, Proc. SPIE no. 2586, D.W. Deering e P. Gudmandsen eds., Paris (France), pp. 26-31, 1995.

Table 2. Multilinear algorithms for C, X, Y estimateof the form (3) - Case 1 study (distribution set 1)

sensor	parameter	a_0	a_1	a_2	a_3	a_4	a_5	a_6	a_7	a_8	r	e_{RMS}
SeaWiFS	C	3.90	1.75	3.90	–23.44	24.61	–9.14	3.27			0.997	0.022
	X	–0.16	13.40	–35.88	59.27	–49.18	13.45	–0.18			0.997	0.024
	Y	–0.90	–12.02	18.86	–21.15	19.79	–7.32	1.53			0.997	0.023
MERIS	C	1.81	5.25	–10.68	10.52	–6.75	1.18	5.12	–8.46	5.17	0.999	0.011
	X	2.31	7.03	–14.95	15.57	–9.11	0.26	–4.59	10.25	–3.86	0.998	0.019
	Y	–2.29	–7.02	2.43	10.52	–6.80	–0.78	8.24	–11.52	5.00	0.999	0.014

Table 3. Multilinear algorithms for C, X, Y estimate of the form (3) - Case 1 + case 2 study (distribution set 2)

sensor	parameter	a_0	a_1	a_2	a_3	a_4	a_5	a_6	a_7	a_8	r	e_{RMS}
SeaWiFS	C	2.64	14.38	–20.04	–0.05	8.28	–4.22	2.35			0.956	0.146
	X	0.35	7.98	–23.46	39.63	–31.57	8.49	–0.00			0.995	0.051
	Y	–1.06	–10.48	16.90	–16.17	11.00	–2.44	0.84			0.990	0.069
MERIS	C	0.77	9.88	–22.25	23.62	–13.11	0.66	9.21	–13.83	7.07	0.987	0.079
	X	1.01	7.03	–17.59	21.63	–13.33	2.44	0.02	1.71	–0.95	0.996	0.045
	Y	–0.81	–9.77	14.72	–14.74	12.96	–6.21	6.98	–6.46	2.29	0.994	0.055

A Numerical Study of the Composite Surface Model for Ocean Scattering

Joel T. Johnson
Dept. of Electrical Engineering
The Ohio State University
2015 Neil Ave, Columbus, OH 43210
Phone: (614)292-1606
johnson@ee.eng.ohio-state.edu

R. T. Shin, J. A. Kong
Room 26-305, MIT
77 Massachusetts Ave
Cambridge, MA 02139
Phone: (617)253-8535
kong@ewt.mit.edu

L. Tsang, and K. Pak
Dept. of Elect. Eng.
University of Washington
Box 352500
Seattle, WA, 98195-2500
Phone: (206)685-7537

Abstract— A numerical study of ocean backscattering for surfaces rough in two dimensions is presented. The numerical model is based on Monte Carlo simulation using the sparse matrix-flat surface iterative approach with canconical grid (SMFSIA/CAG), which is a more efficient version of the method of moments that allows large two dimensional surfaces to be treated. Backscattering cross sections are illustrated for perfectly conducting power law spectrum ocean surface models at angles from 0 to 60 degrees from normal incidence. Variations with surface spectrum low frequency cutoff (ranging over spatial lengths from 64λ to 2λ) are investigated, and demonstrate the accuracy of the composite surface model.

1. INTRODUCTION

Scattering from the ocean surface has been of interest since the development and application of radar in maritime environments in the 1940's [1]. A combination of the physical optics (PO) or geometrical optics (GO) approximations with the small perturbation method (SPM) for rough surface scattering results in the widely-used composite surface (or "two scale") model [2]-[3] of ocean backscatter. Although the composite surface model has been successful in producing a qualitative agreement with most available ocean scattering data, its basis remains a heuristic one, as the required division of the ocean surface into a "small" and "long" scale remains an unclear process. Selection of the dividing point between these two scales, known as the "cutoff" wavenumber in the ocean spectrum, remains primarily a parametric fit to observed data.

Numerically exact methods for surface scattering can be applied in a Monte Carlo simulation to assess the accuracy of the composite surface model. Such studies have been performed in the past [4]-[5], but were limited to surfaces rough in one dimension only due to the large computational requirements of two dimensional surfaces. A recently developed more efficient version of the method of moments, known as the sparse matrix-flat surface iterative approach with canonical grid (SMFSIA/CAG) [6]-[7], is applied in this paper which allows 2-D surface ocean backscatter simulations to be performed. A Monte Carlo technique is used to produce backscattering predictions for 2-D perfectly conducting random surfaces, described as Gaussian stochastic processes with power law spectra. Comparisons are made with predictions of the SPM, both analytically evaluated and Monte Carlo simulations of PO predictions, and predictions of the composite surface model. In particular, variations in backscattered cross sections with surface low frequency content are investigated to determine the "long" wave spectral portion's influence on overall surface cross sections.

0-7803-3068-4/96$5.00©1996 IEEE

2. NUMERICAL MODEL FOR OCEAN SCATTERING

The SMFSIA/CAG for a perfectly conducting surface is based on solution of the magnetic field integral equation (MFIE) through a point matching method of moments, as described in reference [6]. An iterative approach to solving the MOM matrix equation is adopted, in which the matrix is separated into the sum of a sparse "strong" matrix, which contains the exact coupling between points near to each other on the surface, a "flat-surface" matrix

This work was sponsored by ONR contract N00014-92-J-4098, NASA contract 958461, and a National Science Foundation graduate fellowship. Use of the IBM SP/2 at the Maui High Performance Computing Center is acknowledged, sponsored by the Phillips Laboratory, Air Force Material Command under cooperative agreement F29601-93-2-0001. Opinions, interpretations, conclusions, and recommendations are those of the authors and are not necessarily endorsed by the United States Air Force, Phillips Laboratory, or the U.S. Government.

which contains an approximation to the coupling of points outside the strong matrix region, and a "weak" matrix, which corrects the flat surface approximation. Nested iterations are applied, in which a CG/FFT iterative method is used to solve the strong plus flat surface matrix, and the CG/FFT iterations are iterated to include weak matrix corrections, which are calculated with the FFT through a canonical grid expansion of weak matrix terms. The resulting SMFSIA/CAG technique is order $N \log N$ in complexity, allowing large problems to be solved.

The power law surface model to be investigated in this paper is comprised of a wide range of spatial scales ranging over several orders of magnitude both larger and smaller than the electromagnetic wavelength. Use of a numerical simulation will inherently imply a low and high frequency cutoff wavenumber in the portion of the ocean spectrum simulated, since the finite size of surfaces used limits their low frequency content and the non-zero discretization size used limits their high frequency content. Variations in backscattered cross sections with spectrum low frequency content are considered in this paper, since these variations should illustrate any tilting effects due the "long" wavelength portion of the spectrum simulated.

3. NUMERICAL RESULTS

Simulations were performed for a power law spectrum of

$$\Psi(k,\phi) = a_0 k^{-4} \tag{1}$$

for $k_{dl} < k < k_{du}$ and $\Psi(k,\phi) = 0$ otherwise, where Ψ represents the ocean spectrum amplitude in m^4, k represents the spatial wavenumber of the ocean in $rads/m$, ϕ represents the azimuthal angle of the two dimensional spectrum, and a_0 is a specified constant of 1.273×10^{-3} which roughly corresponds to the overall amplitude of other spectrum models. Surface sizes of 64 by 64 wavelengths were used, giving 524,288 unknowns in the SMFSIA/CAG solution for each realization, and a tapered beam incident field was used to reduce any edge effects. The large number of unknowns in this simulation required weak matrix contributions to be neglected in the SMFSIA/CAG technique, with a resulting error of approximately 1 dB in calculated cross sections. Results were generated for low frequency cutoff wavenumbers varying from 146.6 (2λ) down to 4.58 (64λ), all with a high frequency cutoff of 586.4 ($\lambda/2$). Rms heights σ of the simulated surfaces range from 0.02 to 0.64 electromagnetic wavelengths. A minimum of twenty surface realizations were averaged for each angle, with simulations of independent sets of twenty surface profiles showing convergence to within 1.5 dB. While a larger number of realizations is desirable to reduce this uncertainty, computational limitations prohibited further simulations, so that a final accuracy of approximately 2.5 dB results for this study.

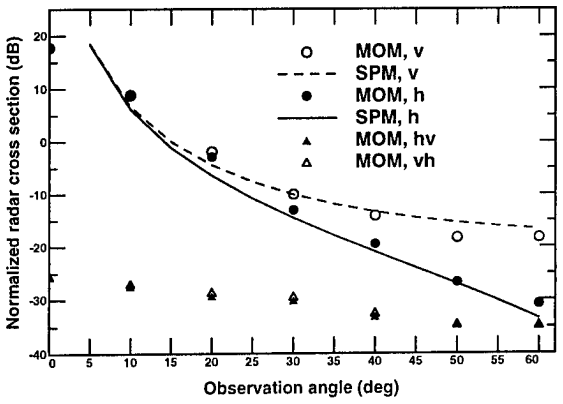


Figure 1: Cutoff wavenumber $k_{dl} = 18.3$, $k_{em}\sigma = 1.0$ Comparison of MOM and SPM backscattering predictions

Figure 1 illustrates SMFSIA/CAG results for backscattered cross sections from surfaces with a low frequency cutoff wavenumber of $k_{dl} = 18.3$, corresponding to a $k_{em}\sigma$ product of 1.0, where k_{em} is the electromagnetic wavenumber. Predictions are compared with those of the SPM alone, with no composite surface model tilting effects included. This figure demonstrates that SPM predictions remain relatively accurate even in this larger $k_{em}\sigma$ product case. Similar results were observed for all of low frequency cutoff cases simulated, with a cutoff effect occuring at angles for which the Bragg wavenumber was cutoff from the surface spectrum. In addition, comparisons were made with numerically evaluated PO integral predictions, which were found to be accurate within 20 degrees of normal incidence for all the surface statistics considered.

The results of the study indicate that SPM predictions indeed remain qualitatively accurate for incidence angles larger than 20 degrees as surface rms heights are increased beyond regions where SPM predictions are expected to hold. In addition, physical optics predictions are observed to be accurate for incidence angles less than 20 degrees regardless of surface rms height. Both of these results favor general assumptions of the composite surface model. More specific aspects are considered in the next section.

4. COMPARISON WITH COMPOSITE MODEL

Although the theoretical basis of the composite surface model has been somewhat justified by the comparisons of the previous section, a more detailed comparison with composite surface model predictions allows further insight into the choice of cutoff wavenumber inherent in the model. For incidence angles greater than 20 degrees, results show very little variation in vv, larger variations in hh, and the largest variation in hv cross sections as surface spectrum

low frequency content is increased. Variations in both vv and hh cross sections are small enough to make their distinction from the 2.5 dB model uncertainty difficult, but variations in hh are clearly larger than their vv counterparts.

Given the success of the physical optics approximation in matching numerical results up to 20 degrees, the primary issue in the 0 to 30 degree region concerns the accuracy of the GO approximation, which is required for non-power law spectra due to the difficulty in evaluating the full PO integral. Figure 2 presents the comparison between GO and PO results using a cutoff spatial wavenumber of $K_d = k/2$ above which contributions to surface slope are neglected in defining the total surface slope for the GO predictions. The choice of K_d is seen to produce a very good comparison with PO predictions up to approximately 20 degrees for the rough surfaces simulated. Alternate choices of K_d were found to produce inferior results, so a choice of $K_d = k/2$ seems optimal for backscattering predictions from a perfectly conducting power law surface. This choice is in agreement with [5], and results in a $k_{em}\sigma$ product of 0.126 for the small scale portion of the spectrum above the cutoff wavenumber K_d.

Comparisons between method of moments results and composite surface model predictions for incidence angles between 30 and 60 degrees are shown in Figure 3 for three of the simulated surfaces. Also included is the corresponding untilted SPM result. A slight underestimation of vv cross sections by the numerical model is observed at higher incidence angles. However, the small variations in vv results with increases in surface slope agree well with the composite surface model. The magnitude of hh variations also agree well with the composite surface model, although again these variations are small enough to make an thorough quantitative assessment difficult. Overall, however, the composite surface model is qualitatively validated by these comparisons.

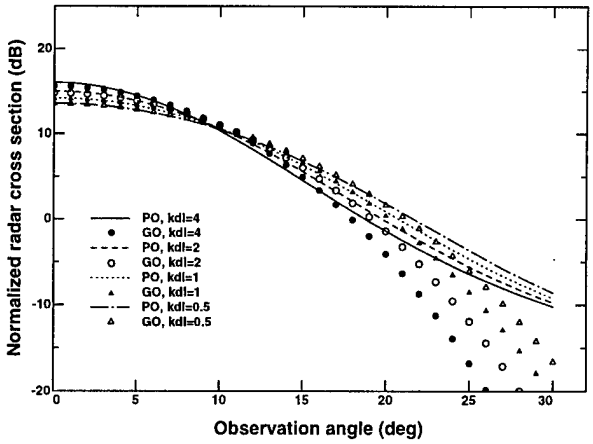


Figure 2: Comparison of PO and GO backscattering predictions using $K_d = k/2$

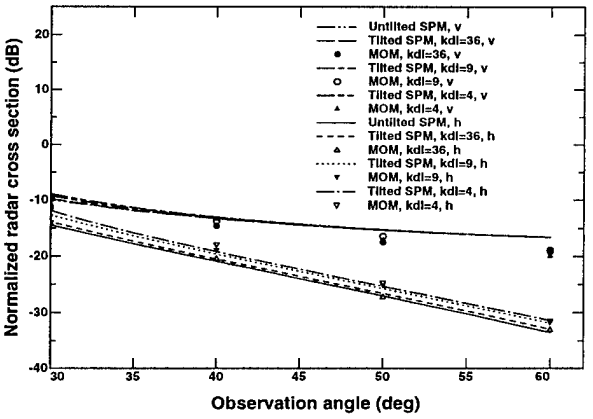


Figure 3: Comparison of MOM and composite surface model co-pol backscatter results

5. REFERENCES

[1] M. I. Skolnik, Introduction to Radar Systems, Second edition, New York: Mcgraw-Hill, 1980.

[2] J. W. Wright, "A new model for sea clutter," IEEE Trans. Ant. Prop., vol. AP-16, pp. 217-223, 1968.

[3] G. R. Valenzuela, "Ocean spectra for the high frequency waves as determined from airborne radar measurements," J. Marine Res., vol. 29, pp. 69–84, 1971.

[4] A. K. Fung and M. F. Chen, "Numerical simulation of scattering from simple and composite random surfaces," J. Opt. Soc. Am. A, vol. 2, pp. 2274–2284, 1985.

[5] S. L. Durden and J. F. Vesecky, "A numerical study of the separation wavenumber in the two scale scattering approximation," IEEE Trans. Geosc. Remote Sens., vol. 28, pp. 271–272, 1990.

[6] K. Pak, L. Tsang, C. H. Chan, and J. T. Johnson, "Backscattering enhancement of electromagnetic waves from 2-D perfectly conducting random rough surfaces based on Monte Carlo simulations," J. Optical Soc. of America, vol. 12, Nov 1995.

[7] J. T. Johnson, L. Tsang, R. T. Shin, K. Pak, C. H. Chan, A. Ishimaru, and Y. Kuga, "Backscattering enhancement of electromagnetic waves from 2-D perfectly conducting random rough surfaces: a comparison of Monte Carlo simulations with experimental data," IEEE Trans. Ant. Prop., May 1996.

Conference Author Index

A

Aarholt, E. 1736
Aas, K. 2307
Abel, P. 1816
Abshire, J. B. 1538
Abuelgasim, A. A. 1426
Adah, T. 700
Advokatov, V. R. 1947
Ahamad, A. 1266
Ahmed, R. H. 2369
Ahola, P. 1998
Ahuja, L. R. 1058
Aiazzi, B. 411, 460, 1042
Akpa, S. *
Alba, P. S. 460, 1042
Alberta, T. A. 1911
Alexander, D. R. 857
Alfoldi, T. T. 324
Alfultis, M. A. 1165, 1504
Alhumaidi, S. M. 1526
Allan, N. 905, 1745
Allen, C. 1932, 2033, 2036
Alparone, L. 411, 460, 1042
Alpers, W. 860, 1370, 1478, 1487
Alumbaugh, D. L. 1941
Alves, M. 830
Amalric, J. *
Amar, F. *
Amodeo, G. 736
Amsbury, D. L. 929
Andary, J. 2160
Anderson, L. E. 1877
Anderson, M. C. 2104, 2358
Anderson, M. R. 959
Anderson, R. *
Andreadis, A. 377
Andres, P. *
Angarkhaeva, L. H. 1945, 1947
Anterrieu, E. 869
Antoniou, A. 990
Arakelian, A. K. 625, 811, 885
Arakelian, K. A. 885
Arbelo, M. *
Arca, G. 520, 854
Armour, B. 339
Arnason, K. 414
Arnaud, A. *
Arnavut, Z. 463
Arnold, D. V. 1475, 1892
Arnon, I. *
Arst, H. 76
Arvidson, T. 2160
Asae, M. 1666
Askari, F. 1141
Asner, G. P. 1663
Atakturk, S. S. 805
Attema, E. 1995
Auer, T. 484
Austin, A. *
Awaya, Y. *
Axelsson, S. R. J. *
Aydin, K. 560, 563
Azimi-Sadjadi, M. R. 1105, 1108

B

Bachem, A. 282
Bachmann, C. M. 356
Baggeroer, P. A. 145
Bahar, E. 1794, 2170, 2177, 2180
Baikalova, T. V. *
Baker, J. *
Bakhanov, V. P. *
Bakhanov, V. V. 609
Baldini, L. 7, 1367
Ballard, J. 2146
Balsiger, F. 1826
Balzer, W. 2291
Bambha, R. 1553
Bamler, R. 1217, 2050
Band, L. E. 212, 420
Banik, R. 1290
Bao, M. 860, 1370
Bara, J. 315, 869
Baraldi, A. 709
Barber, D. G. 953, 1187, 1552, 1992
Barbier, C. 251
Barbosa da Silva, V. 374
Barclay, H. 1873
Barker, J. L. *, 1270, 1276, 1600
Barkerm, J. L. 1273
Barnett, J. 2149
Baronti, S. 411, 460, 1042
Barstow, D. 631, 925
Bartel, L. C. 1935
Barter, J. D. 618, 2201, 2213
Bartoloni, A. *
Barwell, B. R. 1438
Bashkuev, Yu. B. 1945, 1947
Bates, J. J. 1710
Bateson, C. A. 1663
Batista, G. *
Batz, O. 872
Bauer, A. *
Bayma, R. W. 1615
Beach, K. L. 2201, 2213
Beal, R. C. *, 896, 1143
Bearman, G. H. *
Beaven, S. G. *, 115
Becchi, I. 1312
Beh, B. 996, 1266
Belchansky, G. I. 642
Belisle, W. R. 1315
Bellemain, P. *
Belliss, S. 1839
Belongie, M. 1035
Belova, N. I. *
Belward, A. *
Belyaev, B. I. 19, 366
Belyaeva, T. A. 1323
Bencherif, H. 10
Benediktsson, J. A. 63, 414, 1848
Benelli, G. 377
Bennardo, A. *
Bennett, J. C. 2344
Benson, C. S. 2246
Bentamy, A. 805
Bergen, K. M. 580, 1092, 1568
Bergen, Z. D. *
Bergen, Z. 659
Berizzi, F. 1230
Bersano-Begey, T. F. 1520, 2077
Berthod, M. *, 25, 345
Bertram, R. R. 2219
Bertrand, J. 2080
Bertrand, P. 2080
Bessafi, M. 10
Betty, C. L. 2183
Betty, C. 2186
Beus, S. E. 1263
Bhogal, A. S. 1873, 2303
Bianchi, R. *
Bicheron, P. 1901
Bickel, D. L. 2063
Bickel, D. 659
Bidwell, S. W. 402, 1550
Bird, P. 493
Bisson, S. E. 691
Bixler, P. *, 631
Bjerkelund, C. 1155
Bjorgo, E. 932
Blair, J. M. 2361
Blanchard, A. J. *
Blanco, A. 76
Blankenship, C. B. *
Blari, J. B. 1806
Blonda, P. *
Blurton, C. 917
Boback, J. P. 1692
Bobrov, P. P. 2192
Bock, E. J. *
Boehnke, K. *, 839, 2014, 2264
Bogaturov, A. N. 369
Boller, B. D. 269
Bolus, R. L. 1073, 2375
Boncyk, W. C. 1270, 1273
Boncyk, W. 1276
Borak, J. S. 243
Borak, J. 233
Borderies, P. 2167
Borel, C. C. *
Borocz, S. 697
Bosdogianni, P. 1379
Bostater, C. *
Botman, A. M. 324
Bottger, H. 2341
Botti, J. A. 1506
Boucher, D. J. 1704
Bourbigot, K. *
Bourdeau, M. 833
Boutry, J. M. *
Boyarskii, D. A. *
Brakke, T. W. 1657
Brammer, C. *
Brandt, P. 1487

*Author's paper not available at the time of printing.

Braswell, B. H. *
Breaker, L. C. 1712
Bredow, J. W. 863, 947, 2288
Brennan, T. J. 2222
Bresci, E. 1312
Briggs, J. M. 2361
Brisco, B. G. *
Brisco, B. *
Brodley, C. E. 532, 1382
Brown de Colstoun, E. C. 1904
Brown de Coulston, E. 586
Brown, G. S. 2119
Brown, R. A. 805
Brown, R. J. *
Brownsword, C. 1141
Bruegge, C. 1279
Brugman, M. 2255
Bruniquel, J. 387, 662
Bruzzone, L. *
Buckley, J. R. 808
Buckley, J. 1155
Budge, A. *
Bufton, J. L. 423
Bugden, P. *
Bulatov, M. G. 1490
Bulgarelli, B. 1584
Bullock, P. R. 1992
Bundschuh, B. O. 999
Bur, M. C. *
Burgess, M. P. 1618
Burkhart, G. R. 659
Burns, B. E. 2020
Burns, B. 1881
Byrd, M. *

C

Caffey, T. W. H. 2023
Callaghan, G. 796
Cames, A. 869
Campbell, J. W. M. 1146
Campbell, J. W. 1621
Campbell, J. 1155
Capms, A. 315
Capolino, F. 13
Carande, R. E. *, 665, 1211
Carande, R. 659
Carayon, G. 273
Carello, R. 1953
Carlotto, M. J. 34, 2089, 2164
Carpenter, G. A. 529
Carsey, F. 634, 1181, 1775
Carswell, A. I. *
Carswell, J. 1385, 1466
Casar Corredera, J. R. *
Caselles, V. *
Cavalier, D. J. 2246
Cavalieri, D. J. *, 956, 1523, 1529
Cavalli, R. M. *
Cavallo, A. *
Cavayas, F. 236
Caylor, I. J. 1550
Cazaban, F. 387
Cazzaniga, G. 1845
Celani, C. *
Cespedes, E. R. *, 857
Chabert, M. 1842
Chadwick, D. J. 2134
Chadwick, R. B. *
Chagnon, R. *
Chakrabarti, S. 1867
Chan, S. S. 1005
Chan, T. K. 2137, 2140
Chandrasekar, V. 566, 574
Chang, A. T. C. 2011, 2246
Chang, P. *, 1123, 1707
Chang, S. Y. S. 85
Chapman, B. 823, 830
Chapman, R. D. 1736
Chappelle, E. W. 1812
Chapron, B. 600, 606, 612, 621, 1385, 1389
Charlebois, D. 1873, 2303
Chauhan, N. 2146
Che, C. Y. *
Che, X. *
Chen, C. 551
Chen, G. 2240
Chen, H. *
Chen, J. M. 586, 1651
Chen, J. *
Chen, K. S. *, 1297
Chen, L. 1908
Chen, M. *, 43
Chenebault, J. 279
Chenerie, I. 2167
Cheng, H. D. 133
Cheng, S. Y. S. 380
Cherny, I. V. 360, 1968
Cheshire, H. 1609
Cheung, K. 1035
Chiaradia, M. T. 2060
Chinchilla, N. 891
Chiu, T. C. 1070
Chiu, T. 2122
Cho, J. Y. N. 1926
Cho, S. 1977
Choi, J. 469
Choi, M. Y, 628
Choi, S. K. *
Chong, C. C. 180
Choudhury, B. J. 106
Chrien, T. G. *
Chu, A. *, 43
Chubb, S . R. 902, 911
Chugurin, V. V. *
Chun, C. 396
Churilov, V. P. *
Churnside, J. H. 1328
Cialella, A. T. 1904
Cihlar, J. *
Cipollini, P. 91, 1398
Ciucci, A. 520, 854
Clabau, P. 70
Clark, J. H. 1146
Clark, S. 881
Claude, J. 869
Clifford, S. F. 1739
Clift, S. 1293
Clothiaux, E. E. 356
Cloutier, C. *, 1290
Coan, S. M. *
Cohn, S. A. 1914
Coleman, T. L. 1315
Collins, J. D. *
Collins, M. J. 2068
Collins, M. 1141, 2027
Colpitts, B. G. 2189
Coltelli, M. 350
Comiso, J. C. 2008
Compton, M. 1211
Console, E. 1376
Cooper, A. L. 902, 911
Cooper, D. I. *
Cooper, D. *
Coppo, P. 2131
Corbella, I. 315, 869
Corner, B. R. 1920
Cornwall, J. M. 2347
Corp, L. A. 1812
Corsini, G. 290, 1230, 1398
Cowen, R. *
Coyle, D. B. 1806
Crawford, J. P. 1775
Crawford, M. M. *, 263, 1870
Cremers, D. A. *
Cress, D. H. 1935
Crevier, Y. *
Croft, S. K. *
Cromwell, D. 91
Crowley, R. D. 269
Cruz Pol, S. L. 1435
Csillag, F. 2377
Csiszar, I. 1114
Cubero-Castan, E. 457
Cuddy, D. 1358
Cui, T. J. 763, 766, 1340
Cumming, I. 336, 2044, 2255
Cuomo, S. 817
Curlander, J. 1775
Curtis, J. O. 2030, 2282

D

Dabney, P. W. *
Dahl, P. 2270
Dai, X. 1609
Daida, J. M. 891, 1520, 2077, 2219
Dall, J. 276, 1629
D'Amelio, C. *
Damen, M. C. J. 2240
Damiao, D. P. *
Dano, E. B. 2195, 2198
Dano, E. 1158
Daout, F. 615, 746
Das, J. *
Datcu, M. *, 310, 2054
Daughtry, C. S. T. 224, 1803, 1812
Daum, D. R. 1606
Davidson, A. 2377
Davidson, G. W. 2050
Davidson, G. 1217
Davidson, K. L. 1260
Davidson, K. 1158
Davidson, M. W. J. 1980
Davis, C. H. 1783
Davis, F. W. 1077, 1083
Davis, R. E. 254, 754, 757
Davis, R. 591
Davis, S. *
Dawn, D. R. 848
Dawson, M. S. *, 1297
Day, J. L. 1083
De Abreu, R. A. 639
Debinski, D. 2300
De Carolis, G. 1306

Dechambre, M. 833
Dedieu, G. 2366
Deering, D. W. 1654, 1897
DeFries, R. 535
De Grandi, G. 1574, 2086
Dekker, A. G. *
Delaney, P. A. 987
Delignon, Y. 70, 706
Dellepiane, S. 714
Demarest, K. 778
Demarez, V. 1002, 1660
de Matthaeis, P. 736
de Miguel-Vela, G. *
Derksen, C. P. 127
Desachy, J. 2074
Deschaux-Beaume, M. 387
Desjardins, R. 236
Desnos, Y. L. 1217, 1355
De Troch, F. P. 1303
Diak, G. R. 2104, 2358
Diani, M. 1230
Diaz, J. P. *
Di Bisceglie, M. 1580
Dickinson, S. 805
Dietrich, S. *
Diffendal, R. F., Jr. 1017
Dimaio, S. P. 2020
Diner, D. 1279
Ding, K. H. 757, 1208
Dionisio, C. 28
Dmitriev, W. V. 1950
Dobson, F. W. 1155
Dobson, M. C. 580, 1092, 1093, 1568, 2335
Dolash, T. 697
Domanov, M. M. *
Donato, T. 1141
Donelan, M. A. 2210
Donelan, M. *
Dong, Y. 1556
Donnelly, W. 1385, 1466
Douglas, D. C. 642
Doviak, R. J. 1914
Dozier, J. 2002, 2249
Driese, K. L. 186
Drobot, S. D. 1187
Drucker, R. 1190
Du, L. J. 439
Dubayah, R. O. 2149
Dubbert, D. 1881
Dubina, I. N. *
Dufrene, E. 1002
Dugan, J. *
Dunagan, S. E. 2276
Dupont, S. 25, 345
Dutra, L. *
Dwyer, J. L. 547

E

Early, D. S. 124
Eastwood, M. L. *
Ebel, R. *
Echavarria, F. R. *
Eck, T. F. 1897
Edelsohn, C. R. *
Ediriwickrema, D. J. 793
Edson, J. B. *
Ehrismann, J. 339
Eichinger, W. *
Eis, K. E. 1105, 1108
El-Khattib, H. M. 1756
El-Mowilhi, N. M. 1756
El-Shenawee, M. 2170
Elachi, C. *
Elfouhaily, T. 600, 606, 621, 1389
Eloranta, E. *
Emblanch, C. 1067
Emery, W. J. 186, 1138
Emery, W. 192
Ender, J. H. C. *
England, A. W. 2155, 2267, 2270
Engman, E. T. 1058, 1064, 1297, 2237
Entekhabi, D. 1076
Erasmi, S. *
Erbie, E. 2011
Eriksson, M. *
Ersoy, O. K. *
Erxleben, W. H. 1014
Espedal, H. A. 1158
Estes, J. E. 198, 820, 2242, 2321
Etling, D. 1478
Evans, K. *
Exposito, F. J. *

F

Facheris, L. 7, 13
Falls, M. J. 1681
Fang, Y. 496, 1266
Fedele, G. 383
Federici, G. 817
Fedor, L. S. 1450, 1681
Fedoseev, Y. G. *
Fellerhoff, J. R. 659
Fellerhoff, R. 1881
Ferguson, S. 1526
Fernandes, D. 1227
Fernandes, R. 212, 420
Fernandez, D. M. *, 1749
Fernandez, D. *
Ferrare, R. A. 1685
Ferrare, R. *
Ferrazzoli, P. 736
Ferris, M. J. *
Field, C. T. 1800
Filho, O. R. 1986
Firda, J. M. 1
Fischer, A. 2366
Fischer, K. W. 648, 694
Fischer, M. 787
Fiset, R. 236
Fisher, B. 631
Fitzgerald, R. W. *
Fjortoft, R. 457
Flamant, P. H. 4
Floury, N. 836, 842, 975, 1306, 2167
Flynn, T. J. 2057
Fochesatto, G. J. 4
Ford, R. E. 1501
Foresman, T. W. 2242
Foresman, T. 820
Fornaro, G. *, 350, 2047
Forster, B. 1080, 1556
Fortner, R. W. *, 1166
Fortuny, J. *
Foster, J. L. 2011, 2246
Fotedar, L. K. 239
Fowler, C. 73
Franceschetti, G. 51, 350, 680, 2047
Frasier, S. 984, 1730
Frattura, F. 7
Freeman, A. 823, 830
Freemantle, J. *
Frei, M. 1833
Freilikher, V. *
French, N. B. *
Freylikher, V. D. 369
Friedl, M. A. 532, 1382, 2152
Frison, P. L. *
Fritsch, B. *
Frohn, R. C. 2321
Frolind, P. O. 668, 1877
Fromard, F. 733
Frost, E. 925
Frulla, L. A. *
Frulla, L. *
Fuglistaler, S. 342
Fukao, S. 1929
Fung, A. K. *, 772, 947, 1202, 1297, 2008, 2116, 2183, 2186
Furger, M. 399

G

Gade, M. 860
Gagliardini, D. A. *
Gaikovich, K. P. 369
Gaiserl, P. W. *, 1123
Galantowicz, J. F. 1076, 2270
Galbraith, A. E. 683, 1244
Galdi, C. 1580
Galloway, J. 743
Gamba, P. 266, 2071
Garegnani, J. J. 2242
Garello, M. 1584
Garello, R. 612, 621, 1956
Garzelli, A. 377
Gasiewski, A. J. 1120, 1129, 1688
Gasparini, O. 315
Gastellu-Etchegorry, J. P. 1002, 1660
Gatelli, F. 671
Gault, K. A. *, 1221
Gautier, C. 2149
Gazdag, L. 697
Gelautz, M. 31
Gemmill, W. H. 1712
German, M. L. 1441
Gerstl, S. A. W. *, 1642
Geudtner, D. 966, 2255
Giarrusso, J. M. *
Gibas-Tracy, D. R. 2234
Gibbs, D. P. 1541
Gibeaut, J. C. *, 263
Gimond, M. *
Ginzburg, A. I. *
Gird, R. *
Girou, D. *
Gitelson, A. A. *, 2355
Gitelson, A. 209
Giuli, D. 7, 13, 817, 1367
Givri, J. R. *
Gjaja, M. N. 529
Glushko, E. V. 2324
Goblirsch, W. 656

Goel, N. S. 526, 1645
Gogineni, P. 1867
Gogineni, S. P. 115, 1196
Gogineni, S. 1932
Golden, K. M. *
Goldsmith, J. E. M. 691
Golovachev, S. 175
Gomarasca, M. A. *
Gong, P. 2068
Gonzalez, K. D. 1506
Goodberlet, M. A. *
Goodenough, D. G. 1873, 2303
Goodin, D. G. 215
Goodman, N. 2033, 2036
Gopal, S. 529, 538, 787, 1426
Goto, A. 920
Gottfried, J. 1178
Gotwols, B. L. *, 1736
Gouinaud, C. 257, 474
Gourrion, J. 1389
Goutoule, J. M. 869
Gow, A. J. 1184, 1190
Goward, S. N. 1803
Gowda, K. C. 1858
Gower, J. 1146
Graber, W. K. 399
Graf, G. 1355
Grandell, J. *, 583, 1998, 2110
Granhohm, J. 674, 1629
Grankov, A. 175
Grassin, S. 1956
Gray, A. L. 1146, 1155, 1621
Gray, L. 2255
Gray, R. B. 1290
Gray, R. 1352
Green, R. O. *
Greidanus, H. 1633
Grenfell, T. C. 1199
Grindel, M. 999
Grits, Y. 2355
Grodsky, S. A. 1971
Gromov, V. D. 442
Gross, G. 1478
Grunes, M. R. 1574
Guarnieri, A. M. *
Guarnieri, P. 460
Guenther, B. D. 445
Guerra, J. C. *
Guerriero, L. 2060
Guijarro, J. 1355
Guindon, B. *
Guneriussen, T. *
Gurvich, A. S. 369
Gustafson-Bold, C. L. 1283
Gustavsson, A. 1877
Gutierrez, R. O. *, 263
Gutman, S. I. *
Gwilliam, B. L. 1073, 2375

H

Haake, K. 1597
Haas, A. 1080
Haese-Coat, V. 717
Hahn, T. 842
Hall, D. K. 139, 956, 2011, 2246
Hall, F. G. 230, 1657
Hall, K. 254
Hall, S. E. 1498
Hallidin, S. *
Hallikainen, M. *, 484, 583, 1089, 1759, 1998, 2110, 2285
Halthore, R. N. 1904
Haltrin, V. I. 285, 305
Hambaryan, A. K. 625, 811
Hammer, P. D. 2276
Han, L. 1395
Han, Y. 1685
Hanado, H. 487, 512
Hansen, M. 535
Happ, L. 2027
Haptanov, V. B. 1945
Hara, T. *
Hardin, P. J. 827, 848, 1606
Harding, D. J. 1806
Harris, R. 1826
Hart, D. G. 145
Hartnett, J. 1111
Hashimoto, S. 1695
Hassol, S. 1169
Haugen, H. *
Haung, Z. 778
Hautecoeur, O. 204, 1901
Haverkamp, D. 109, 1532
Hawela, F. 1756
Hawkins, R. K. *, 1290, 1621
Hayes, K. *, 1733
Hazen, D. A. 1432
Heer, C. 2341
Hehr, L. H. *
Hein, A. *
Heinrichs, J. 950
Helder, D. L. 1270, 1273
Helder, D. 1276
Hellsten, H. 1877
Hellwich, O. 330, 1836
Henebry, G. M. 166, 195, 215, 448
Henry, J. C. *
Henschel, M. *
Hensley, S. 31
Hensley, W. H. 2063
Hensley, W. 659
Henson, J. M. 254
Herland, E. A. *
Hernandez, P. A. *
Herrera, F. *
Herry, P. *
Hesany, V. *, 888, 1733, 2210
Hesany, *
Hess, L. L. *
Hevizi, L. G. *
Heygster, G. C. 1788
Heymsfield, G. M. 1550
Hicks, M. R. 1504
Hillion, A. 523
Hines, D. 1257, 1385
Hipple, J. 1501
Hirsave, P. P. 1073
Hjartarson, A. 414
Ho, L. L. *
Hochheim, K. P. 1992
Hochschild, G. 436
Hoekman, D. H. 260, 845
Hoffmeyer, P. D. 2030, 2282
Holden, H. M. 427
Holden, H. 88
Holecz, F. 248
Holloway, C. L. 1914
Holt, B. *
Holzworth, R. H. 569
Homer, J. 796
Hood, R. E. 1460
Hoogeboom, P. 1633
Hoogenboom, H. J. *
Hopcraft, G. 1923
Horie, H. 512, 1364
Horn, R. 1624
Hosomura, T. *
Hou, S. 1032
Houzelle, S. *
Howard, S. 246
Howarth, P. J. 1986
Howell, P. B. 1926
Hoyt, P. *
Hsieh, C. Y. 2116
Hsieh, P. 1855
Hsu, A. Y. 1061, 1297
Hsu, A. 1064
Hsu, C. C. 836, 1208
Hu, B. 1587, 1669
Huan, S. 60
Huang, S. *, 1571
Huddleston, J. N. 1718
Huehnerfuss, H. 860
Huemmrich, K. F. 2372
Huete, A. R. *, 157, 1423
Hug, J. F. *
Hughes, W. *, 1221
Huguenin, G. R. 1544
Hummelbrunner, W. *
Hunt, J. 631
Hurlemann, P. *
Hurtaud, Y. 615
Hussein, Z. A. 515
Hwang, J. N. 130
Hyyppa, J. 1089

I

Iacozza, J. 1187
Ignatov, A. *
Iguchi, T. *, 512, 554, 1364
Iisaka, J. *
Inggs, M. R. 454, 2020
Inggs, M. 1889
Iodice, A. 680
Irisov, V. G. 1126, 1450, 1457, 1672
Irons, J. R. *, 1657, 1904, 2161
Irons, J. 2183, 2186
Isernia, T. 1241, 2083
Ishimaru, A. 2128, 2137, 2140
Itten, K. I. 2326
Ivanov, A. Y. 1971
Ivanov, A. Yu. *
Ivanov, V. K. 369
Ivlev, O. V. *
Iwata, Y. 781

J

Jaaskelainen, V. *
Jackson, S. R. 2258
Jackson, T. J. 1058, 1061, 1064
Jacobson, M. D. 1138, 1678

Jain, A. K. 1851
Jakob, G. 31
Jakubauskas, M. E. 2300
Jameson, A. R. 402
Jamsa, S. 2092
Jansen, R. W. 902
Jayaprakash, P. 408
Jayaram Hebbr, K. 784
Jeffries, W. 1352
Jelinski, D. E. *
Jen, L. *
Jenkins, A. D. 1158
Jensen, J. R. 2279
Jenserud, T. 1141
Jessup, A. T. *
Jeyarani, K. 784
Jezek, K. C. 142, 145, 148, 1775
Jezek, K. 118, 1196, 1772
Ji, J. 1300
Ji, W. 2225
Jia, J. C. 180
Jia, S. *, 1423
Jiang, J. 739
Jiang, W. W. *
Jiao, J. *
Jin, M. *
Jin, Y. Q. 2380
Jingli, W. 466
Jingshan, J. 466
Johannessen, J. A. 1158
Johannessen, O. M. 932, 1158
Johansen, B. *
John, H. 2338
Johnsen, H. 1155
Johnson, D. R. *, 1175
Johnson, J. T. *, 1401
Johnson, L. F. 2276
Johnson, P. E. 1721
Johnson, R. S. 808
Jones, M. A. *, 631
Jones, W. L. 1526
Jonsson, T. 1877
Jordan, A. K. 1208
Jordan, L. E., III 2228
Jordan, M. S. 1260
Josberger, E. G. 648
Judge, J. 2270
Jung, M. 1870
Jurczyk, S. 2160
Juying, J. 947

K

Kabashnikov, V. P. 19
Kadygrov, E. N. *
Kaiser, D. *
Kaiser, J. A. C. *, 911
Kaita, E. 1273
Kalb, M. 1175
Kalshoven, J. E. 1797, 1809
Kambhammettu, N. 1392
Kanagaratnam, P. 115, 1196, 1867
Kandus, P. *
Kane, T. J. 993
Kanevsky, M. B. 1493
Kanzieper, E. *
Karaev, V. Y. 1493
Karam, M. A. 154, 594
Karlinsey, T. 1892
Karszenbaum, H. *
Kashkarov, S. S. 369
Kasilingam, D. *
Kassebaum, R. *, 631
Katehi, L. P. B. 1346
Katkovsky, L. V. 19, 366
Kato, Y. 875
Katou, K. *
Katsaros, K. B. 805
Katsaros, K. 1389
Katsev, I. L. *
Katzenberger, J. 1509
Kaupp, V. H. *
Kawata, Y. *, 1250, 1666
Kazandjiev, V. *
Kazmin, A. S. *
Keane, A. N. 603
Keck, C. L. *
Keeler, M. *
Keeler, R. J. 574
Keihm, S. J. 1435
Keithley, C. *, 227
Kellenberger, T. W. 2326
Keller, M. R. *
Keller, M. *, 248
Keller, W. C. *, 888, 1733, 2210
Kellndorfer, J. M. 1093, 2335
Kellndorfer, J. 2329
Kelly, R. E. 1938
Kemarskaya, O. N. 609
Kemppinen, M. 484, 499, 1998, 2285
Kenyi, L. W. 353
Kerbaol, V. 621, 1389
Kerenyi, J. 1114
Kerr, R. B. 686
Kertesz, M. 2377
Kerzner, M. G. 451
Kess, B. L. 1048
Key, J. R. 636
Key, J. 73
Keyte, G. 493
Kheeroug, S. S. 189
Khenchaf, A. 615, 746
Khire, M. V. 430
Khlif, M. S. 857
Khorram, S. 793, 1609
Kiang, R. K. 1864
Kietzmann, H. 1086
Kilic, O. 760
Kim, C. 1977
Kim, E. J. 2267
Kim, H. J. 405
Kim, H. S. 405
Kim, M. S. 1812
Kim, Y. *, 1612
Kimbreau, G. 891
Kimura, I. 775, 1361
Kindscher, K. 2300
Kirchner, C. *
Kirscht, M. 333
Kiselev, S. S. 442
Kishi, A. M. 1704
Kittler, J. 1379
Knapp, A. K. 166, 2361
Knight, A. 869
Knoepfle, W. 2332
Knopfle, W. 802
Knowles, D. S. *
Knudson, C. 296
Knulst, J. 1158
Kobjakova, N. *
Kogan, F. 209
Koh, G. *
Kokhanovsky, A. A. *
Komarov, S. A. *
Komiyama, K. 875
Kong, J. A. *, 757, 836, 1190, 1208, 1401
Kontar, E. A. *
Kooi, P. S. *
Koomen, P. 1633
Koren, H. 2307
Kosmann, D. 2338
Kosov, A. S. 442
Kostina, V. L. 172, 178
Kovalick, W. M. *
Kowk, R. 935
Kozlov, A. I. 299
Kozu, T. *, 512
Kraemer, R. *
Kraft, U. R. 866
Kraft, U. 872
Krasnopolsky, V. M. 1712
Kravtsov, Y. A. 103
Kravtsov, Yu. A. 1454
Krenek, B. *, 1541
Krishen, K. 239
Krishna, A. P. 221
Krivonozhkin, S. N. 369
Kropfli, R. A. 1739
Krueger, D. A. *
Krummell, J. R. 2361
Krupa, R. 436
Kudryavtsev, V. N. 1971
Kuga, Y. 2128, 2137, 2140
Kuhbauch, W. 1980
Kumagai, H. 487, 512
Kumar, S. R. 1858
Kummerow, C. 1429
Kunkee, D. B. 1129
Kuntz, M. 433
Kurtz, J. 2027
Kurvonen, L. 1759
Kusaka, T. *, 1250
Kusneirkeiwicz, D. Y. 1143
Kustas, W. P. 2104
Kutser, T. 76
Kux, H. J. H. *, 195, 374
Kuzmenko, Yu. A. *
Kuzmin, A. V. *, 1454
Kwok, R. *, 1190

L

Labrousse, D. *, 345
la Forgia, V. *
Lahtinen, J. 1998
Lai, S. J. *
Lake, B. M. 2201, 2213
Lalbeharry, R. 1155
Lalonde, M. 1621
Lamont-Smith, T. 1742
Lanari, R. *, 350, 2047
Landgrebe, D. A. 790, 1855
Landgrebe, D. 414
Landry, R. 726

Landsfeld, M. 2149
Lane, J. *
Lang, R. H. 577, 726, 760
Langford, A. O. *
Langford, G. 2276
Langham, C. W. 324
Langlois, P. M. 1917
Langman, A. 2020
Lannes, A. 869
Laroussinie, O. *
Larsen, M. F. 1926
Larsson, B. 1877
Lataitis, R. J. 1914
Lauknes, I. *
Laur, H. 477
Laursen, V. 869
Lavorato, M. B. 4
Lavrenov, I. 1495
Lawrence, S. P. 417, 2158
Lawson, J. *
Lay, W. L. 57
Le, C. T. C. 2128, 2137
Leach, A. *
Leavitt, B. C. 2273
Lebed, L. 209
Leberl, F. 31
Le Ber, J. *
Leblanc, E. 224
Leblanc, S. G. 1651
Lebon, F. 457
Le Caillec, J. M. 612
Le Dantec, V. 1002
LeDrew, E. F. 127, 230, 639, 645, 938
LeDrew, E. P. 427
LeDrew, E. 88
Lee, B. S. 1794, 2180
Lee, J. S. 439, 1162, 1574, 2086
Lee, L. *
Lee, M. E. *
Lee, P. H. Y. 618, 2201, 2213
Lee, R. 118
Le Hegarat-Mascle, S. 1067
Lehmann, F. 2107
Lemaire, P. 251
Leone, A. 1584
Leonelli, J. 697
Leong, M. S. *
Leroy, M. 204, 1654, 1901
Lesht, B. M. 1675
Le Toan, T. 836, 842, 975, 1306, 1983, 2167
Leu, C. H. 160
Leung, K. *, 43, 1358
Leuschen, C. 2033, 2036
Leuskiy, V. Ye. 1672
Leveau, J. 10
Le Vine, D. M. *, 878, 1547
Lewis, J. E. *
Lewis, M. R. *
Lewis, P. 1405, 1408
Lewis, T. B. *
Li, F. K. 1132, 1469, 1959
Li, J. *
Li, L. W. *
Li, L. 1123, 1707
Li, T. L. 1064
Li, X. 293, 591, 1587, 1669, 2173
Li, Z. J. 772
Li, Z. *, 136, 2186
Liang, S. 1648
Liao, L. 16, 554
Liberman, B. 175, 1320
Lieberman, S. H. *
Lightstone, L. *
Liljegren, J. C. 1675
Lim, I. 57, 67
Lin, I. I. 2261
Lin, L. 509
Lin, Y. C. 1334
Lindemer, W. 872
Lindgren, P. D. 1172
Lintz Christensen, E. 1629
Liou, Y. A. 2155
Litovechenko, K. 251
Liu, A. K. 85, 380
Liu, G. *, 1571
Liu, H. 1535
Liu, W. 1515
Livingstone, C. E. 1515, 1621
Llewellyn-Jones, D. T. 417, 2158
Loechel, S. E. 586
Loechel, S. 2149
Loffeld, O. *
Logvin, A. I. 299
Lohi, A. *
Loizzo, R. *
Lombardo, P. 347
Long, D. G. 124, 218, 827, 848, 1463, 1475, 1606, 1715, 1721, 1724, 1892
Longstaff, D. 796
Lopes, A. 387, 457, 662
Lord, R. T. 454
Lou, S. H. 935, 1959
Lou, Y. *, 1612
Loumagne, C. 1067
Loutin, E. A. 299
Loveberg, J. 881
Loveland, T. R. *, 2318
Lu, Y. H. 57, 67
Ludwig, F. L. 891
Lukin, V. P. 1830
Lukin, V. 22
Lukowski, T. I. *, 1290, 1621
Lund, D. E. 2195, 2219
Luong, D. Q. 356
Luscombe, A. P. 1290, 1352
Luvall, J. 1286
Lyzenga, D. R. *, 899, 908, 1158, 2195, 2198, 2219
Lyzenga, D. 1141

M

Ma, W. *
MacArthur, J. L. 1143
Macauley, M. K. 2222
MacDonald, H. C. *
MacDonald, M. C. *, 183
Macelloni, G. 2131
MacGregor, D. *
Mack, J. M. 1938
Madisetti, V. K. 1592
Madsen, S. N. 276, 674, 677, 972, 1629
Magotra, N. 1029
Mahlke, J. 1769
Mahootian, F. *
Maitre, H. 474, 503
Makisara, K. 1010
Makkonen, P. 1998
Makynen, M. 1998
Malaret, E. 1141
Maldonado, L. 1612
Maleev, S. N. 442
Malinovski, V. *
Malliot, H. A. 2349
Manara, G. 290
Mancini, P. L. 279
Mancini, P. 1355
Mandyam, G. 1029
Manninen, T. 583
Manning, W. *
Manohar, M. 1023
Manry, M. T. *
Maotang, L. 466
Marazzi, A. 266, 2071
Marchand, R. 2119
Marechal, N. *, 1233
Marenco, A. L. 1592
Mariani, A. *
Markham, B. L. 586, 1270, 1273, 1276, 1797, 2121
Markina, N. N. 1698
Markus, T. 1247, 1529, 1791
Marmorino, G. O. *
Marra, J. 100, 296
Marthon, P. 457
Martin, S. *, 1190
Martin-Neira, M. 315, 869
Martinez, P. 37
Martinez-Madrid, J. J. *
Marty, G. 1002
Martynov, O. V. *
Marzano, F. S. *
Marzouki, A. 706
Maslanik, J. A. 186
Maslanik, J. 73, 192, 950
Matschke, M. 802, 2332, 2338
Mattar, K. E. 1146
Mattar, K. 1621, 2255
Mattia, F. 1306
Mattikalli, N. M. 1058, 2237
Matwin, S. 1873, 2303
Maupin, P. 1373
Mauser, W. 1974
Mavrocordatos, C. 490
May, G. C. 947, 2288
Mayer, T. S. 993
Mayer, V. J. 1166
Mayor, S. 1911
Mazetti, P. 1367
McBride, W. E., III 285
McCalmont, J. F. 1535
McCleese, D. *
McColl, K. C. 1710
McCoy, W. 1029
McDonald, K. *
McDonnell, J. J. 133
McGee, S. 917
McGuire, J. 631
McIntosh R. E. 1, 984, 1553, 1917, 1923
McIntosh, R. 743, 1466, 1730
McKim, H. A. 1073
McKim, H. L. 2375
McLaughlin, C. D. 929
McLaughlin, D. J. 905, 1745
McLauglin, D. J. *
McMurtrey, J. E. 1812

McNally, T. *
McNeill, S. 1839
Mead, J. B. 1553, 1917, 1923
Meadows, G. A. 2219
Meadows, G. 2195, 2198
Mecocci, A. 2071
Meier, D. 1352
Meier, W. 73
Melack, J. M. *
Melfi, S. H. *, 1257
Melnikov, V. M. *
Melsheimer, C. 1370
Melville, W. K. 2204
Memon, N. D. 1039
Menegasssi Menchik, M. T. *
Meneghini, R. *, 16, 554, 1364
Menon, A. K. 408
Merchant, J. W. 541, 2315
Merzlyak, M. N. 2355
Mesarch, M. A. 1005, 1908
Mesnager, G. 1842
Meyers, R. J. 1506
Michel, T. R. 248
Middleton, E. E. 1005
Miewald, T. 929
Migliaccio, M. *, 680
Migliacio, M. 350
Mikami, T. 1695
Mikheev, P. V. 189
Mikkela, P. 1759
Mikulin, L. *
Miles, M. W. 932
Milillo, G. *
Millar, P. S. 1800
Miller, J. R. *, 212, 1411
Miller, J. 420
Miller, T. 1612
Miller, W. H. 1032
Milovich, J. *
Milshin, A. 175, 1320
Miner, G. F. 1892
Minino, M. *
Minnis, P. 1911
Mironov, V. L. *
Mitchell, S. 2377
Mittermayer, J. 1214, 1217
Mityagina, M. I. *, 103
Miyawaki, M. 1639
Miyazaki, T. 781
Mochi, M. *
Moens, J. B. *
Moghaddam, M. *, 730, 978
Mogili, A. 1266
Mohling, W. *
Mohr, J. J. 677, 972
Moldenhauer, O. 94
Molinaro, F. 10
Moller, D. 984
Monaldo, F. M. 1143, 1149
Mononen, I. 484
Monorchio, A. 290
Montgomery, B. 577
Monti Guarnieri, A. 671, 1845
Moody, A. 544
Moon, C. J. *
Moon, W. M. *
Moore, J. D. 922
Moore, R. K. 496, 996, 1266, 1392
Moore, S. L. *
Mora, F. 541
Morain, S. *
Moran, M. S. 157, 1420
Mordvintsev, I. N. 642
Moreau, L. *, 70
Moreira, A. 1214, 1217
Moreira, J. R. *, 350, 799, 1227
Moreira, J. *
Moreno, J. F. 1823, 1861
Morrison, K. 2344
Moses, R. W. 1938
Mouchot, M. C. 236, 523, 1376, 1753
Mougin, E. *, 733, 1002
Moulin, S. 2366
Mourad, P. D. *
Mozley, E. C. *
Muchoney, D. 233
Mudukutore, A. 574
Mueller, H. J *
Mueshen, B. 2338
Mugnai, A. *
Mukherjee, D. P. *
Mulchi, C. L. 224
Muller, J. 1775
Muller, M. R. 1618
Murata, M. 1639
Murni, A. 1851
Murphy, T. J. *
Myers, R. J. *
Myneni, R. *

N

Nadimi, S. A. 863, 947, 2288
Naeije, M. C. 97
Nagabhushan, P. 1045, 1858
Nagata, H. 1639
Nagatani, G. 628
Nagler, P. L. 1803
Naka, M. 781
Nakajima, M. 390
Nakajima, T. Y. 390
Nakajima, T. 390
Nakamura, K. 512
Nakamura, S. *
Nakamura, T. 1929
Nakonechny, V. P. 1968
Narayanan, R. M. 445, 506, 1017, 1073, 1920, 1926, 2030, 2258, 2282, 2375
Narumalani, S. *, 463
Nash, G. G. *
Nassar, E. 118
Nativi, S. 1367
Naumov, A. P. 1698
Neale, C. M. U. 133, 2369
Nekrasov, V. P. 19, 366, 1441
Nelson, B. *
Nelson, D. H. 393
Nelson, R. F. 1797
Nemani, R. *
Nervi, A. 1603
Neuenschwander, A. 1512
Neumann, G. 1469, 1959
Newman, G. A. 1941
Nezry, E. 1574
Ng, W. E. 57, 67
Ngai, F. M. 665
Nghiem, S. V. 1190, 1208, 1469, 1959
Nguyen, L. 1911
Ni, W. 293, 591
Nichol, J. 2113
Nicolas, J. M. 503
Nielsen, F. 1766
Nielsen, N. B. 686
Niemann, O. 1873
Nikulainen, M. 1998
Nirchio, F. *
Nithack, J. *
Njoku, E. G. 1054
Nocera, L. 25
Nogotov, E. F. 1441
Nohmi, H. 1639
Noll, J. *, 1995
Noltimier, K. F. 142
Norikane, L. 1772, 1775, 2329
Norman, J. M. 2104, 2358
Normand, M. 1067
North, P. R. 1654
Noto, J. 686
Nuesch, D. *
Nunez, M. 1417
Nunnelee, W. M. 1678

O

Oaku, H. 1636
Oden, S. F. 1143
Oertel, D. 2107
Ogor, B. 717
Ohura, Y. 1639
Ojima, D. *
Okamoto, K. *
Okon i'kova, J. A. 609
O'Leary, E. 823
Oleson, K. W. 186
Oleson, K. 192
Oliphant, T. E. 1715, 1721, 1724
Olsen, R. B. *
Olson, W. 1429
O'Neill, P. E. 1061, 1064
O'Neill, P. O. 1297
Onstott, R. G. 944, 1193, 1202, 1520
Onstott, R. 2195
Osharin, A. M. *
Otterman, J. 1657
Oudart, P. 273

P

Paar, G. 31
Paduan, J. D. 1749
Pahl, U. 1478
Painter, T. H. 2249
Pairman, D. 1839
Pak, K. *, 1401, 2125, 2137, 2143
Pal, P. *
Palleschi, V. 520, 854
Palm, S. P. 1257
Palmer, R. D. 1920, 1926, 1929
Paloscia, S. 736, 2131
Pampaloni, P. 736, 2131
Panah, A. A. *
Panegrossi, G. *
Pangburn, T. 1073, 2375
Pankin, A. A. 360

Pantzov, S. Y. 360
Papathanassiou, K. P. *, 350, 799
Paquerault, S. 503
Parishikov, S. V. *
Park, J. D. 1526
Park, S. H. 560
Parkin, S. H. 1102
Parmiggiani, F. 709
Parra, G. A. 1753
Pasaribu, D. P. 372, 1590
Pascazio, V. 1241, 1577, 2083
Pasquali, P. *, 342, 656
Pasquariello, G. *, 1306, 1562, 2060
Payne, B. 321
Payton, S. L. 2273
Pazmany, A. L. 1553
Pazmany, A. 743
Peat, H. 2377
Peczeli, I. 697
Peddle, D. R. 212, 230, 427, 938
Peddle, D. 88
Pellegrini, P. F. 1603
Peltoniemi, J. I. *
Peng, C. Y. 380
Pepin, M. P. 54
Pereira, J. *
Perfiliev, Y. P. 1701
Perona, G. 1584
Perov, A. O. *
Perovich, D. K. 1184, 1190
Peterson, D. L. 2276
Peterson, J. R. *
Petrenko, B. Z. 481
Petrin, R. R. 393
Petrou, M. 1379
Pham, K. 37
Philbrick, C. R. 1253, 1826
Piazza, E. 1603
Picardi, G. 383
Pieczynski, W. 706
Piepmeier, J. R. 1120
Pierce, L. E. 580, 1092, 1568
Pierce, L. 40, 2329
Pierri, R. 1241, 2083
Pignatti, S. *
Pihlflyckt, J. 1998, 2285
Piironen, A. *
Pilant, D. *, 121
Pillai, S. R. 990
Pinel, V. 1660
Piwowar, J. M. 127, 645, 938
Planes, J. G. 387
Plant, W. J. *, 888, 1733, 2210
Plotnizky, S. *
Plumb, R. 778, 2033, 2036
Plummer, S. E. 1654
Plutchak, J. 1498
Poggio, L. 399
Pollard, B. 1923
Pons, I. 257
Porter, D. L. 1152, 2242
Posa, F. 1306
Pospelov, M. N. 1135, 1454
Poulain, D. E. 857
Poulton, M. M. *
Pouwels, H. 1633
Pozdnyakova, V. P. 609
Prakash, H. N. S. 1858
Prati, C. *, 671
Prevosto, M. 1956
Prietzsch, C. 282
Prikhach, A. S. *
Princz, J. *, 1221
Privette, J. L. *, 1663
Proffitt, M. H. *
Proisy, C. 733
Ptichnokov, A. V. 2324
Puglisi, G. 350
Pulliainen, J. 1759
Pullianinen, J. 583, 2110
Pultz, T. J. *
Pungin, V. G. 103
Pyhalahti, T. *

Q

Qi, J. 1420
Qin, P. 1989
Qin, W. 526, 1645
Qiu, Z. 2318
Quagliano, J. R. 393
Quartly, G. D. 91
Quel, E. J. 4
Quick, C. R. 393
Quilfen, Y. 805
Quintanilha, J. A. *

R

Rabine, D. L. 423
Racette, P. 1429
Rackley, K. *, 631
Raev, M. D. 1490
Raggam, H. *, 353
Rague, B. W. 1054
Rahmat-Samii, Y. 515
Rais, J. 1851
Raizer, V. Yu. *
Rall, J. A. R. 1538
Ramamurthy, M. K. 1498
Ramirez, A. *
Rampa, V. 2038
Raney, R. K. 2279
Rango, A. 2011
Ranson, K. J. 577, 1096
Ranzi, R. 266
Rao, C. R. N. *
Rao, K. S. 163, 201, 430
Rao, P. V. N. 163, 201
Rao, Y. S. 163, 201, 430
Rapoport, V. O. *
Rastelli, S. 520, 854
Rautiainen, K. 1998, 2285
Reagan, J. A. 683, 987, 1014, 1244, 1535
Reagan, J. T. 1020
Reed, B. *
Reed, R. 1475
Rees, W. G. 2261
Refice, A. 2060
Refling, J. P. 1102
Reichel, H. 872
Reichenbach, S. E. 1048, 1597
Reiners, W. A. 186
Reinke, D. 1105
Reistad, M. 1158
Remund, Q. P. 827, 848
Ren, Y. 1929
Ressler, M. A. 1886
Rey, L. 273
Reynaud, J. *
Ribbes, F. 842, 1983
Ricci, D. N. 1704
Riccio, D. *, 350, 680
Richard, J. 490
Richter, P. I. 697
Ride, S. *
Rieck, D. R. 448
Riggs, G. 139
Rignot, E. *
Rijkeboer, M. *
Rincon, R. F. 402
Ritter, M. 2204
Roberts, D. A. *
Roberts, M. 227
Rocca, F. *, 671
Rodenas, J. A. 1953
Roeder, R. S. 269
Roenko, A. N. 172, 178
Roli, F. *
Romeiser, R. 597, 981, 1962
Romig P. R., III 1048
Ronsin, J. 717
Roschier, M. 1998
Rosello, J. 1224
Rosenkranz, P. W. *
Rosenthal, W. 2252
Rosich Tell, B. 477
Ross, S. J. 1520, 2077
Rossi, M. *
Rostan, F. 2294
Rosten, D. P. 1809
Roth, A. 802, 2332, 2338
Roth, L. *
Rothrock, D. A. *
Rothrock, D. *
Rott, H. 2125
Rougean, J. L. 1408
Roujean, R. J. 591
Rouvier, S. 2167
Roux, C. 1753
Rozenberg, A. 2204
Rubertone, F. 1571
Rubino, A. 1487
Ruddick, K. G. *
Ruf, C. S. *, 1263, 1435, 1692
Rufenach, C. L. 814
Rungaldier, H. 2201, 2213
Running, S. *
Russell, C. A. *, 648
Russell, M. 1417
Ruzek, M. 1175
Ruzhentsev, N. V. *
Ryzhkov, A. V. *, 557

S

Saatchi, S. S. *, 1861
Saatchi, S. *, 730
Sabet, K. F. 1346
Sabinin, K. D. 103
Sacchini, J. J. 54
Sadjadi, F. 396
Sado, S. *
Saghri, J. A. 1020

Sahr, J. D. 569
Saillard, J. 615, 746
Saint-Joan, D. 2074
Sakurai-Amano, T. *
Salomonson, V. V. 139
Samal, A. 1048
Samuel, P. 1158
Sand, K. *
Sandberg, D. 1181
Sander, G. 1881
Sander, R. K. 393
Sano, E. E. 157
Sansosti, E. 2047
Sarabandi, K. 720, 723, 969, 978, 1070, 1334, 1337, 1346, 2122
Sarita, S. 1045
Sarture, C. M. *
Satalino, G. 1562
Sato, K. 487
Sato, S. 339
Sato, T. 775, 1361, 1612
Sausa, R. C. 851
Savazzi, P. 2071
Savtchenko, A. 2216
Sayler, K. L. 547
Sayood, K. 1026
Sazonov, Y. A. *
Scepan, J. 198
Scharroo, R. 97
Scheiber, R. 1214
Schertzer, D. 37
Schetkin, I. M. 2192
Schiavon, G. 736
Schiller, S. 1286
Schimel, D. S. *
Schirinzi, G. 1241, 1577
Schistad Solberg, A. H. 1484, 2307
Schloss, A. L. 106
Schlueter, N. 1247
Schmidt, G. M. 2101
Schmitt, M. J. 393
Schmugge, T. J. 2101
Schmugge, T. 1051
Schmullius, C. *
Schneider, D. 999
Schoening, V. L. 987
Schuler, D. L. 1162, 2086
Schulze, E. D. *
Schuster, G. L. 1911
Schwabisch, M. *, 350, 802
Schweiger, A. J. 636
Schwemmer, G. *, 1257
Schwichow, H. 339
Seifert, F. M. 1086
Seiferth, J. C. 1600
Sekelsky, S. M. 1, 1553
Seliga, T. A. 551, 569
Sergi, R. *, 1562
Serpico, S. B. *, 714
Servomaa, H. 1998
Sery, F. 457
Sessenrath, G. *
Seu, R. 383
Shaikh, M. A. 1105, 1108
Sharma, A. 1315
Shaw, J. A. 1328
Sheen, D. R. *
Shelton, J. C. 2201, 2213
Shen, C. Y 902
Sheng, Y. 48, 1559
Shepherd, N. W. 1290
Shepherd, N. 1352
Shepherd, P. R. *
Shereshevsky, I. A. 609
Shevtcov, B. M. 369
Shi, J. C. 2125
Shi, J. 136, 754, 2022, 2249
Shih, S. E. 757, 1208
Shimada, J. 43
Shimada, M. 1636
Shin, R. T. *, 1401
Shinme, H. 1639
Shinohara, H. 1639
Shippert, M. M. 169
Shire, H. N. 896
Shirer, H. N. *
Showman, G. A. 1688
Shuchman, R. A. 648
Shuchman, R. 1158
Siddiqui, K. J. 1099
Sieber, A. J. *
Sigismondi, S. 736, 2131
Sikora, T. D. *, 893, 896
Singh, R. *
Siqueira, P. 1337
Skirta, E. A. 603
Skoelv, A. 1141
Skofronick, G. M. 1688
Skotnicki, W. 1612
Skou, N. 674, 749, 869, 1629
Skriver, H. 1300, 1766
Skulachev, D. P. 442
Skvortsov, E. I. 1490
Slatton, K. C. *, 263
Sletten, M. A. 2017, 2207
Small, D. 342
Smirnov, A. I. 1454
Smirnov, A. V. 1481
Smith, G. L. 1414
Smith, J. A. 2146
Smith, M. C. 269
Smith, N. 1414
Smith, R. 1618
Smith, W. H. 2276
Smith, W. L., Jr. 1911
Smits, P. C. 714
Smokty, O. *
Snider, J. B. 1432
Snoeij, P. 1633
Snuttjer, B. R. J. 506
Snyder, W. 2095
So, C. S. *
Soffer, R. 1411
Soh, L. K. 112, 1532, 1565
Sohl, T. 246
Sohn, H. G. 148
Sohus, A. 321
Solaiman, B. 236, 523, 1373, 1562
Solberg, R. *, 1484, 2307
Solimini, D. 736
Solov'ev, D. M. *, 1971
Song, S. 996, 1392
Sosnovsky, Yu. M. 1323
Sottili, F. 13
Souffez, S. H. *
Souffez, S. S. *
Soulis, E. D. 1986
Souyris, J. C. 975, 1306, 2167
Soyris, J. C. 836
Spagnolini, U. 2038
Spencer, M. W. 82, 1463
Spencer, R. W. 1460
Spidaliere, P. 2160
Spinhirne, J. D. 683, 1244
Spring, F. 1515
Sridhar, M. 1498
Srivastava, S. K. 1290
Srivastava, S. 1352
St. Germain, K. M. 1026, 1523
Stacey, N. J. S. 1618
Stacy, N. J. S. *
Stalino, G. *
Stanhope, S. A. 2219
Stanichny, S. V. *
Staples, G. C. *
Starmer, W. J. 198
Steffen, K. 950
Steinauer, R. *
Steingieer, R. 1980
Stenstrom, G. 1877
Stern, H. *
Sternberg, B. K. *
Sterner R. E., II 1736
Stevens, D. 493
Stevens, T. D. 1253
Steyn-Ross, D. A. 94, 1293, 2098
Steyn-Ross, M. L. 94, 1293, 2098
Stiles, J. M. 720, 723
Stogryn, A. 154
Stolz, R. 1974
Stone, R. S. 636
Stork, E. J. 628
Stowe, L. *
Strahler, A. H. 243, 532, 538, 1405, 1426, 1587, 1669
Strahler, A. 233, 293, 591, 2173
Strawa, A. W. 2276
Streck, C. 330, 1836
Stretch, L. *
Strobl, P. 2107
Strukov, I. A. 442
Stuopis, P. A. 254
Sturgess, K. 2027
Sturm, J. M. 2207
Su, H. 2361
Su, Z. *, 1303
Subra, W. 2231
Subramanya, B. 1816
Suchall, J. L. 1355
Sud'bin, A. I. 100
Suga, Y. 1763
Sugawara, M. 1639
Sugimura, T. 79
Suinot, N. 273, 279, 490
Sukhatme, J. S. 430
Sun, C. 133
Sun, G. 577, 1096
Susini, C. 411
Sveinsson, J. R. 63, 1848
Swain, P. H. 1848
Swift, C. T. *, 1547
Sylvester, J. 1205
Syvertson, M. *

T

Taconet, O. 1067
Tadjudin, S. 790
Tait, A. 2005
Takasaki, K. 79
Takemata, K. 1666
Takemura, K. 775
Takeuchi, S. 1763
Talitsky, V. G. *
Tamlourrino, A. 2083
Tamoikin, V. V. *
Tan, S. Y. 67
Tanaka, S. 79
Tang, S. 2216
Tano, F. 1980
Tarchi, D. *
Taskinen, H. 1998
Tauriainen, S. 1998
Teany, L. D. *, 1290
Teraoka, T. 1361
Terre, C. 772
Tesauro, M. 51
Tescher, A. G. 1020
Thames, P. 192
Thayer, J. P. 686
Thiele, O. W. 402
Thomas, A. 953
Thomas, B. H. 1704
Thomas, C. H. 1788
Thomasson, L. 836
Thome, K. J. 1283
Thompson, D. G. 1892
Thompson, D. R. *, 893, 896, 981, 1152
Thompson, H. R., Jr. 2201, 2213
Thompson, L. L. *
Thompson, M. 1881
Thomsen, A. 1300, 1766
Thursby, M. H. 1526
Tian, B. 1105, 1108
Ticehurst, C. 1556
Tiee, J. J. 393
Tierney, M. R. *
Tighe, L. *
Tikhonov, V. V. *
Tikunov, V. S. 2324
Tilton, J. C. 703, 1023
Timchenko, A. I. *
Ting, C. M. *
Tirri, T. 1998
Titov, V. I. 1331
Tjuatja, S. 772, 2008, 2186
Todhunter, J. S. 189
Tognoni, E. 520, 854
Tommervik, H. *
Tomppo, E. 1010
Tong, K. 1035
Torre, A. *, 60, 1571
Torres, F. 315, 869
Torres, R. 1355
Totuka, H. 1639
Tournadre, J. 1389
Tourneret, J. Y. 1842
Touzi, R. 662
Townshend, J. 535
Tracy, B. T. 1073, 2375
Treitz, P. M. 1986
Treuhaft, R. 978
Trimble, J. 823
Trizna, D. B. 905, 2017
Troch, P. A. *, 1303
Trofimov, V. T. *
Troisi, V. J. 651
Troitsky, A. V. *
Trokhimovski, Yu. G. 1126, 1450, 1457, 1672
Troufleau, D. 157
Trump, C. L. *
Tsai, W. Y. 935, 1718
Tsang, L. *, 130, 728, 754, 1401, 2125, 2143
Tsatsoulis, C. 109, 112, 1532, 1565
Tseng, W. Y. 85
Tsu, H. 1763
Tucker, C. J. 1169
Tupin, F. 474
Twarog, E. M. 1745

U

Ueda, K. 1250
Ulaby, F. T. 723, 1070, 1092, 1093, 1568, 2335
Ulaby, F. 2329
Ulander, L. M. H. 668, 1877
Ungar, S. G. *
Usha, P. V. 408

V

Vachon, P. W. 966, 1155, 1621, 2255
Vachon, P. W. 966
Vachon, P. 662
Vadkovsky, V. N. *
Vadon, H. *
Valero, J. L. 336, 2255
Vandemark, D. 1257, 1385, 1389
van den Berg, J. H. 2240
van der Keur, P. 1300
van der Kooij, M. W. A. 339, 963
Vandersteene, F. *
van Gelder, A. 2240
van Halsema, D. 963
van Leeuwen, W. J. D. *, 1423
VanSumeren, H. 2195
Van Woert, M. L. 1117
van Zuidam, R. 2240
van Zyl, J. J. 2294
van Zyl, J. 978, 1612
Vasilevsky, A. F. *
Vasilyev, Yu. F. 172, 178
Vaugh, C. R. 423
Vedel, S. *
Velipasaoglu, E. O. *
Veltroni, M. 1230
Veneziani, N. 2060
Venkataraman, G. 430
Venkataratnam, L. 163, 201
Vermotel, E. R. 1904
Vescoui, F. 1980
Vesecky, J. F. 891, 1520, 2077, 2219, 2347
Vidal, A. 157, 1224
Vidal-Madjar, D. 1067
Vierling, L. A. 1897
Viggian, R. *
Vincent, N. 279, 490
Vishniakov, V. 175
Vogelmann, J. E. 246
Vogelzang, J. *
Volynsky, V. A. *, 100, 296
Von Ahn, J. *
Vorosmarty, C. L. 106

W

Waite, W. P. *
Wakayama, T. 775
Walavalkar, V. 430
Wales, C. 634, 1775, 1777
Walker, B. 1881
Walker, D. T. 2219
Walker, N. 583
Wall, S. *, 51
Wallace, B. 881
Waller, G. 1227
Walsh, T. M. 563
Walter-Shea, E. A. 1005, 1908
Walthall, C. L. 586, 1423, 1797, 1904
Wan, Z. 2095
Wang, B. 1645
Wang, J. R. 956, 1429, 2134, 2246
Wang, J. 1297
Wang, M. X. *
Wang, N. 1989
Wang, Y. *, 1077, 1083
Wanner, W. 1405, 1408, 1411, 1669
Ward, E. 914
Warner, K. K. 1017
Wash, C. H. 1260
Wasrin, U. R. 842
Waters, J. 2231
Way, J. B. *, 628
Weaver, R. L. 651
Wedin, D. 2377
Weeks, R. 2125
Weidemann, A. D. 285, 305
Weinman, J. A. *
Weissman, D. E. 878, 888, 1472
Wergin, W. 2011
Wersinger, J. M. 914
Wessel, G. R. I. 645
Wessman, C. A. 1663
West, J. C. 2207
West, R. D. 1718, 1727
Westwater, E. R. 1138, 1450, 1672, 1681, 1685
Wever, T. 1833
Weydahl, D. J. 151
Weydal, D. *
White, H. P. 212, 1411
White, M. A. *
Whitehead, M. 393
Whiteman, D. *
Whitlock, C. H. 1911
Wick, G. A. *
Wiesbeck, W. 763, 766, 1340, 2294
Wilheit, T. T. *
Wilhelmson, R. B. 1498
Wilkner, D. 881
Williams, D. L. 1797, 2161
Williams, J. 1780
Williams, R. N. 1111
Willis, K. J. 929
Willmott, C. J. 106
Wilson, B. 1772
Wilson, C. J., III 218

Wilson, J. J. 2341
Wilson, L. L. 130
Wilson, W. J. *, 1132
Winebrenner, D. P. 941, 1205
Winokur, R. S. *
Winstead, N. S. *, 893
Winter, R. 966
Wismann, V. R. 839, 2014, 2264
Wismann, V. *
Woelders, K. 276, 674, 1629
Wojtowicz, D. 1498
Wolf, C. 2219
Wolfe, D. E. *
Wolhletz, B. P. 1932
Wood, E. F. 1061, 1064
Woodcock, C. E. 529, 538, 591
Woodcock, C. 293
Woodhouse, I. H. 260, 845
Woodhouse, R. 1279
Wooding, M. 1995
Wu, J. 509, 739, 1965, 2216
Wu, S. T. S. 1309
Wylie, B. 2377

X

Xia, Z. G. 48, 1559, 2310
Xiao, R. 566
Xiong, H. *
Xu, W. 2044
Xu, Y. 2030, 2282
Xuan, J. 700
Xue, Y. 417, 2158

Y

Yacobi, Y. Z. *
Yakin, G. Y. 189
Yakovlev, V. V. *, 103
Yamaguchi, Y. *
Yamanashi, M. 1636, 1929
Yamashita, N. 1695
Yamazaki, A. 1250
Yang, G. 2068
Yang, J. *
Yang, L. 2318
Yang, W. 2315
Yang, X. 1989, 2240
Yang, Y. E. 757
Yankielun, N. E. *
Yanovsky, F. J. 2297
Yanow, G. 321
Yarwood, M. 490
Yea, J. H. 2137
Yee, R. 2201, 2213
Yeh, P. S. 1032
Yeo, T. S. *, 57, 67
Yevtyushkin, A. V. *
Yildirim, O. 1343, 1444
Yonekura, T. 1666
Yook, J. G. 1346
Young, G. S. *, 893, 896
Young, J. 118
Yu, Y. 60
Yueh, S. H. *, 935, 1132, 1190, 1718, 1727
Yueh, S. Y. *
Yushakov, V. N. *
Yutsis, V. V. *

Z

Zagolski, F. 1002
Zaitsev, V. A. 1971
Zaitsev, V. V. *, 363
Zakarin, E. 209
Zakharov, A. I. *
Zamaraev, B. D. 172, 178
Zege, E. P. *
Zeng, Q. *
Zhan, J. 1429
Zhang, B. 1405
Zhang, C. B. 57, 67
Zhang, G. 728, 2143
Zhang, J. 2375
Zhang, N. *
Zhang, Y. 2095, 2177
Zheng, X. *
Zhiqiang, Y. 466
Zhu, K. 2041
Zhukov, B. 2107
Zimmermann, R. *
Zinichev, V. A. *
Zink, M. 1086
Zion, M. 1061
Zlystra, G. J. 547
Zott, J. 2276
Zribi, M. 1067
Zrnic, D. S. 557
Zurk, L. M. 754
Zuykova, E. M. 1331